K.A. Gschneidner, Jr.,

J.-C.G. Bünzli and V.K. Pecharsky

Editors

# HANDBOOK ON THE PHYSICS AND CHEMISTRY OF

# RARE EARTHS

Optical Spectroscopy

Volume 37

North-Holland

HANDBOOK ON THE PHYSICS AND CHEMISTRY
OF RARE EARTHS
VOLUME 37

HANDBOOK ON THE PHYSICS AND CHEMISTRY
OF RARE EARTHS

Advisory Editorial Board

G. ADACHI, *Kobe, Japan*
W.J. EVANS, *Irvine, USA*
S.M. KAUZLARICH, *Davis, USA*
G.H. LANDER, *Karlsruhe, Germany*
M.F. REID, *Christchurch, New Zealand*

Editor Emeritus

LeRoy EYRING✠, *Tempe, USA*

✠Deceased.

HANDBOOK ON THE PHYSICS AND CHEMISTRY OF

# RARE EARTHS

VOLUME 37
Optical Spectroscopy

EDITORS

## Karl A. GSCHNEIDNER, Jr.

*Ames Laboratory–US DOE, and*
*Department of Materials Science and Engineering*
*Iowa State University*
*Ames, Iowa 50011-3020*
*USA*

## Jean-Claude G. BÜNZLI

*Swiss Federal Institute of Technology*
*Laboratory of Lanthanide Supramolecular Chemistry*
*BCH 1402*
*CH-1015 Lausanne*
*Switzerland*

## Vitalij K. PECHARSKY

*Ames Laboratory–US DOE, and*
*Department of Materials Science and Engineering*
*Iowa State University*
*Ames, Iowa 50011-3020*
*USA*

Notice
No responsibility is assumed by the publisher for any injury and/or damage to persons or property as a matter of products liability, negligence or otherwise, or from any use or operation of any methods, products, instructions or ideas contained in the material herein. Because of rapid advances in the medical sciences, in particular, independent verification of diagnoses and drug dosages should be made

For information on all North-Holland publications
visit our website at books.elsevier.com

Printed and bound in The Netherlands

07 08 09 10 11   10 9 8 7 6 5 4 3 2 1

# PREFACE

Karl A. GSCHNEIDNER Jr.,  Jean-Claude G. BÜNZLI and  Vitalij K. PECHARSKY

---

*These elements perplex us in our rearches* [sic], *baffle us in our speculations, and haunt us in our very dreams. They stretch like an unknown sea before us – mocking, mystifying, and murmuring strange revelations and possibilities.*

Sir William Crookes (February 16, 1887)

---

This volume of the *Handbook on the Physics and Chemistry of Rare Earth* begins with a Dedication to late Professor William (Bill) T. Carnall who pioneered the interpretation of lanthanide spectra in solutions in the 1960s and 1970s. The Dedication is written by Drs. James V. Beitz and Guokui Liu from Argonne National Laboratory where Bill Carnall spent his entire 37-year scientific career.

Optical spectroscopy has been instrumental in the discovery of many lanthanide elements. In return, these elements have always played a prominent role in lighting devices and light conversion technologies (Auer mantles, incandescent lamps, lasers, cathode-ray and plasma displays). They are also presently used in highly sensitive luminescent bio-analyses and cell imaging. This volume is entirely devoted to the photophysical properties of these elements. Its five chapters describe various aspects of lanthanide spectroscopy and its applications. Chapter 231 presents state-of-the-art first-principles f–d calculations of lanthanide energy levels and f–d transition intensities. It is followed by a review (chapter 232) on both theoretical and experimental aspects of f–d transitions, a less known field of lanthanide spectroscopy, yet very important for the design of new optical materials. Chapter 233 describes how confinement effects act on the photophysical properties of lanthanides when they are inserted into nanomaterials, including nanoparticles, nanosheets, nanowires, nanotubes, insulating and semiconductor nanocrystals. The use of lanthanide chelates for biomedical analyses is presented in chapter 234; long lifetimes of the excited states of lanthanide ions allow one to take advantage of time-resolved spectroscopy, which leads to highly sensitive analyses devoid of background effects from the autofluorescence of the samples. The last review (chapter 235) provides a comprehensive survey of near-infrared (NIR) emitting molecular probes and devices, from simple chelates to macrocyclic complexes, heterometallic functional edifices, coordination polymers and other extended structures. Applications ranging from telecommunications to light-emitting diodes and biomedical analyses are assessed.

## Chapter 231. First-principles calculations of $4f^n \rightarrow 4f^{n-1}5d$ transition spectra
**by Kazuyoshi Ogasawara, Shinta Watanabe, Hiroaki Toyoshima and Mikhail G. Brik**
**Kwansei Gakuin University, 2-1 Gakuen, Sanda, Japan**
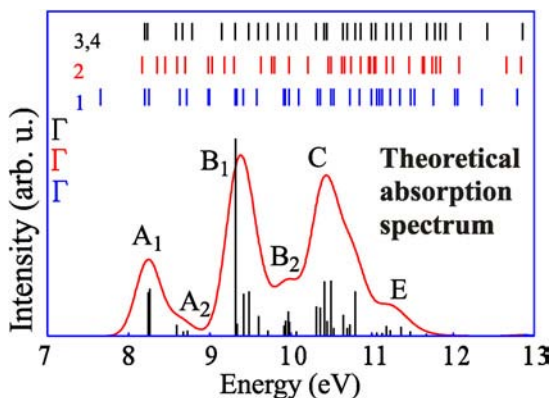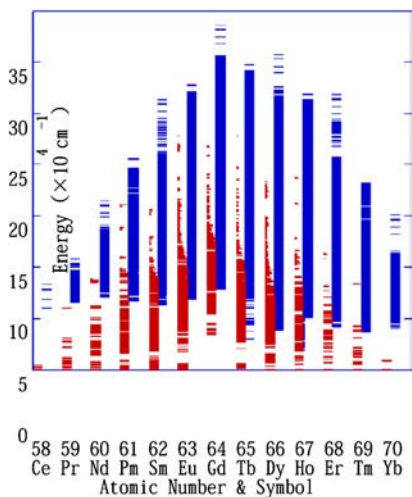


Due to the growing demand for lasers and phosphors operating in UV and VUV regions, a great deal of attention is being paid now to the thorough analysis of high-lying energy levels of lanthanide (R) ions arising from their $4f^n$ and $4f^{n-1}5d^1$ electronic configurations. This chapter reviews the recent development of the first-principles analysis of the $4f^n \rightarrow 4f^{n-1}5d^1$ spectra of R ions in crystals. It starts with a brief review of the commonly used semi-empirical crystal-field calculations and with a historical overview of the first-principles calculations for multiplet states of metal ions in crystals. A detailed description of the relativistic discrete variational multielectron (DVME) method follows, a first-principles relativistic many-electron calculation method developed by the authors. The major part of the chapter is then devoted to the recent achievements on DVME calculations and analyses of the energy level schemes and $4f^n \rightarrow 4f^{n-1}5d^1$ spectra of R ions in a free state and in crystals. The Dieke diagram is theoretically extended and the origins of peaks in the spectra are clarified based on the explicit many-electron wavefunctions. An application to the analysis of a commercially-used blue phosphor, $BaMgAl_{10}O_{17}:Eu^{2+}$ (BAM:$Eu^{2+}$), is also given.

## Chapter 232. $4f^n$–$4f^{n-1}5d$ transitions
**by Gary W. Burdick and Mike F. Reid**
**Andrews University, Berrien Springs, MI, USA and University of Canturbury,**
**Christchurch, New Zealand**

Numerous applications of lanthanide materials, including scintillators, visible ultraviolet (VUV) lasers, and phosphors for fluorescent lighting and plasma displays, make use of the
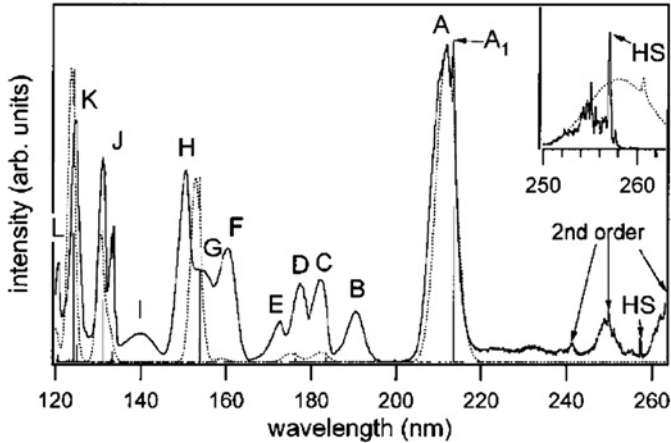
$4f^{n-1}5d$ excited configuration. Obviously, understanding of these states is crucial to the development of advanced materials. This chapter reviews an extension of the parametric model originally developed by Carnall, Wybourne and Dieke to treat $4f^n$ spectra. The authors of this chapter show that the extended model may and has been successfully employed to calculate the absorption and emission spectra for the $4f^{n-1}5d$ configuration. The review illustrates how parametrization can be applied to calculate other properties of interest, such as non-radiative relaxation rates, thus explaining the major features of the UV and VUV spectra for ions across the entire lanthanide series. The chapter concludes with a discussion of the relationship between parametrized calculations and other approaches, such as ab initio calculations.

**Chapter 233. Spectroscopic properties of lanthanides in nanomaterials**
**by Guokui Liu and Xueyuan Chen**
**Argonne National Laboratory, USA and**
**Fujian Institute of Research on the Structure of Matter, Fuzhou, China**

This chapter reviews recent studies on energy levels and excited state dynamics of lanthanides (R) in nano-structures, which include R-doped dielectric nano-crystals, implanted nano-particles of semiconductors, coated core–shell nano-particles, nano-tubes and nano-balls stuffed with R ions. New phenomena such as the action of confinement on ion–phonon interaction and its consequences for electronic transitions, energy transfer, and phase transitions are discussed in the light of experimental and theoretical studies reported in the literature. Although the review aims at being comprehensive and covers all the important aspects in the field, emphasis is given to identification and theoretical analysis of various mechanisms for
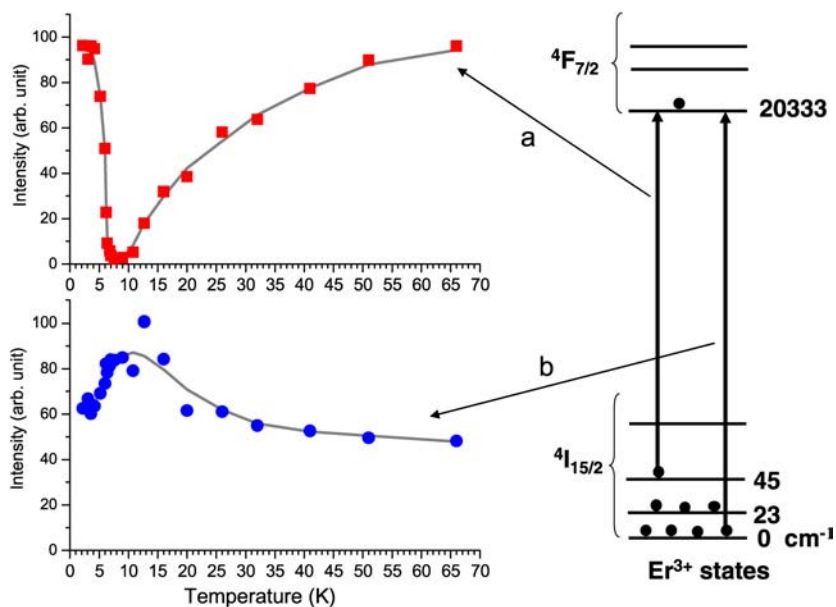
luminescence enhancement, or quenching, and anomalous size- and temperature-dependence of photophysical properties.


## Chapter 234. Lanthanide chelates as luminescent labels in biomedical analyses
## by Takuya Nishioka, Kôichi Fukui, and Kazuko Matsumoto
## Waseda University and Japan Science and Technology Agency, Tokyo, Japan
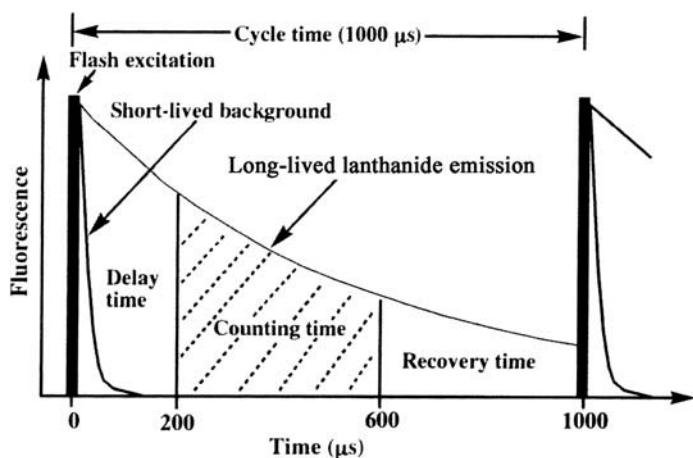
Recent advances in time-resolved spectroscopy (TRS) using luminescent lanthanide labels for biomedical analyses are reviewed. The large Stokes shift and long-lived excited states specific to some lanthanide chelates allow the use of TRS for these analyses, which effectively removes background fluorescence of the samples. This enables the measurement of very small signals which could not be detected in conventional fluorometric analyses based on organic dye labels. The resulting high signal-to-noise ratios leads to the determination of trace amounts of targeted proteins, nucleic acids or any other biomolecules with unusually high sensitivity. The chapter includes a description of the synthesis of luminescent lanthanide chelates and of their physical properties. The advantage of luminescence resonance energy transfer (LRET) and luminescence quenching are explained in relationship to the specific properties of the lanthanide chelates used as luminescent labels. Medical applications of lanthanide chelates in immunoassays, DNA hybridization assays, receptor-ligand binding assays, and imaging are reviewed.

**Chapter 235. Lanthanide near-infrared luminescence in molecular probes and devices by Steve Comby and Jean-Claude G. Bünzli**
**École Polytechnique Fédérale de Lausanne (EPFL), Switzerland**
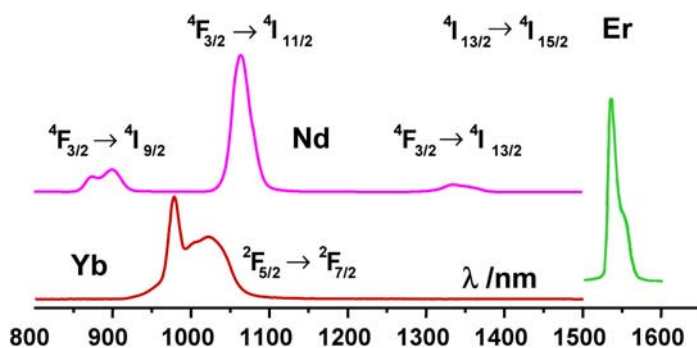


Interest for lanthanide-containing near-infrared (NIR) emitting compounds stemmed initially from the development of lasers, optical fibers and amplifiers for telecommunications. Up-conversion processes have also been the subject of much attention. More recently, it was realized that biological tissues are transparent to light in the range 700–1000 nm, allowing optical detection of tumors. This review concentrates mainly on discrete molecular edifices containing $Nd^{III}$, $Er^{III}$, or $Yb^{III}$, although systems containing other NIR-emitting $R^{III}$ ions are also mentioned. It starts with a general description of the photophysical properties of NIR-emitting lanthanide ions and of their sensitization before systematically reviewing the various classes of compounds used for designing NIR-emitting lanthanide probes. Macrocyclic ligands are described first (porphyrins, coronands, cryptands, cyclen derivatives, calixarenes), followed by acyclic ligands, among them beta-diketonates are a privileged and much studied group of chelates. New strategies are described, which make use of podands, dendrimers,

or self-assembly processes, as well as of sensitization through d-transition metal ions. The overview ends by the description of NIR-emitting ions embedded into extended structures, coordination polymers, inorganic clusters, zeolites, microporous materials, microspheres and nanoparticles. The last part of the chapter focuses on potential applications, including liquid lasers, optical fibers and amplifiers, light-emitting diodes, and analytical applications, including biomedical analyses. As an aid to future work in the field, comprehensive tables compare the effectiveness of the chromophores used to date to sensitize the NIR luminescence of Nd$^{III}$, Er$^{III}$, and Yb$^{III}$.
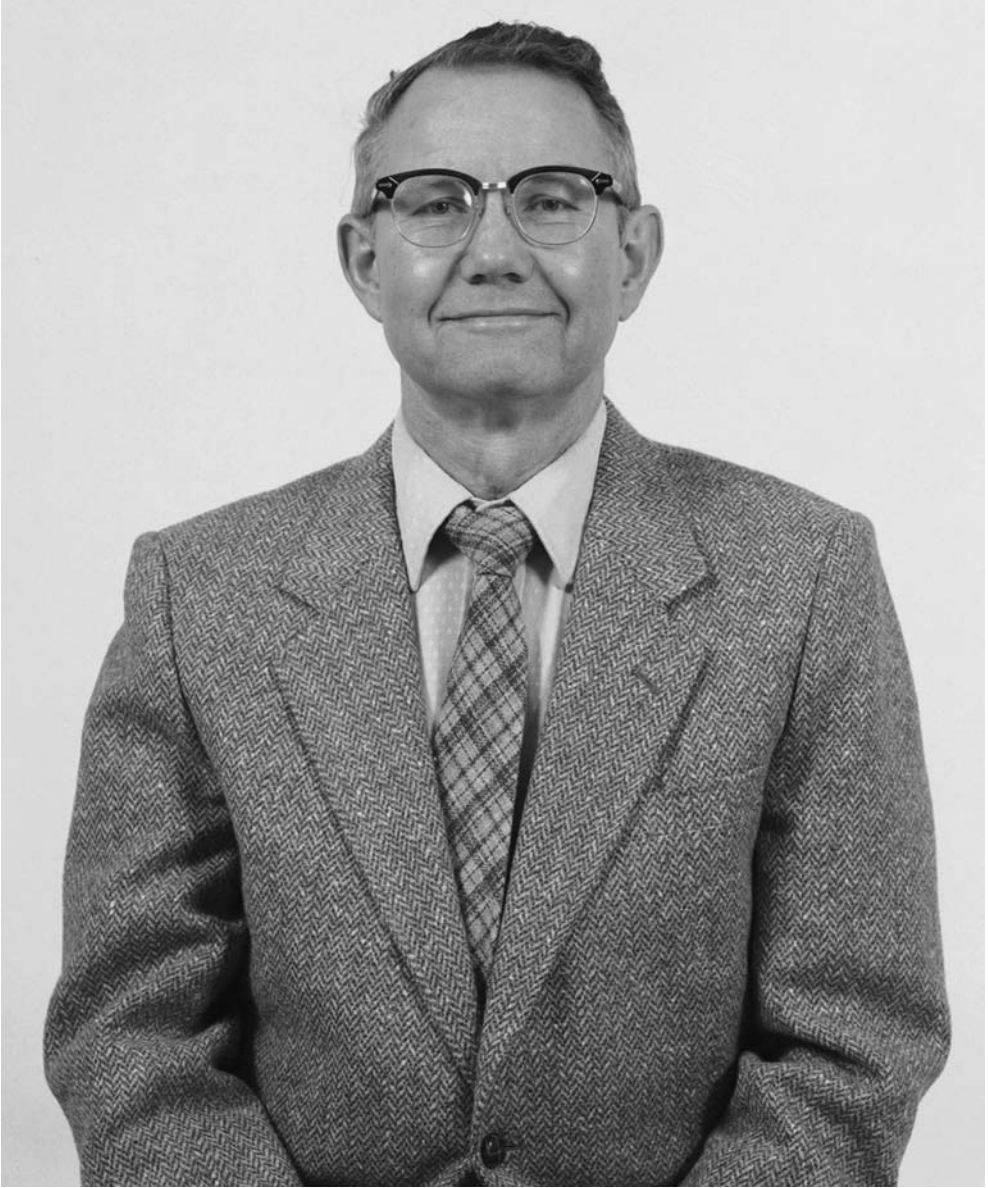
# DEDICATION TO WILLIAM T. CARNALL[*]

James V. BEITZ and Guokui LIU

*Chemistry Division, Argonne National Laboratory, Argonne, IL 60439-4831, USA*

## Contents

---

Dr. William T. Carnall

**William T. Carnall (May 23, 1927–June 22, 2003)**

William Thomas Carnall (known to his many friends as Bill) was born in Denver, Colorado on May 23, 1927. He died at age 76 on June 22, 2003 in an automobile accident. Bill graduated from South High School in Denver, Colorado in 1945. He promptly joined the US Navy in which he served briefly as World War II was ending. He earned his B.S. degree in chemistry from Colorado State University in 1950 with highest honors and married Velaine Vanier. They had three children—Richard, Lisa and Bruce. Bill completed his Ph.D. in physical chemistry with a minor in physics at the University of Wisconsin at Madison in 1954 under the direction Prof. John E. Willard. He then began his productive and distinguished 37 year research career at Argonne National Laboratory in Argonne, Illinois.

At Argonne National Laboratory, development of nuclear reactors was a significant focus of research from the chartering of the Laboratory in 1946. The light lanthanides in particular were recognized early on to be important fission products due to their many radioactive isotopes and their impact on the neutron economy of nuclear reactors due to those lanthanide isotopes with large neutron absorption cross-sections. In addition, the synthetic actinide elements, an essential component of most nuclear reactors, originally had been expected to exhibit lanthanide-like characteristics, including optical spectra, although by the 1950s evidence had accumulated that such was not the case for the most common oxidation states of the light to near mid-series actinide elements. When Bill Carnall joined the Laboratory in 1954 as a chemist in the Chemistry Division, these facts raised a wide variety of issues and opportunities for both fundamental and applied research in areas ranging from separation and removal of lanthanides during reprocessing of spent reactor fuel to development of methods for analysis that were rapid and nondestructive. In addition, significant advances in instrumentation, notably the development and commercialization of dual beam recording spectrophotometers that directly measured optical absorbance, were occurring.

From a basic science perspective, the parallel development of theories concerning f-electron states and their transitions and the reporting of detailed low temperature spectra of many of the lanthanides in a variety of hosts offered opportunities that Bill seized upon early in his scientific career to increase understanding of the origins of the fingerprint-like character of the optical absorption spectra of trivalent lanthanide ions. He was encouraged to pursue such research by two of the leading figures in heavy element research in the Chemistry Division at Argonne National Laboratory, namely Donald C. Stewart and Paul R. Fields. Stewart had a long standing interest in lanthanide spectroscopy as an analytical tool and Fields was leading an effort to discover new actinide elements using such exotic methods as separation and analysis of debris from thermonuclear explosions. A convergence of interests led the U.S. Atomic Energy Commission to fund the building in 1961 of a new hot laboratory research complex in the Chemistry Division that contained not only a suite of chemical laboratories equipped with hoods and gloveboxes designed for radiochemical studies but also a graded series of hot cells that provided the ability to safely handle up to 1 million curies ($3.7 \times 10^{16}$ Bq) of 1 MeV gamma emitting isotopes. This new facility provided space for synthesis of novel radioactive compounds and measurement of their properties, including their optical absorption spectra, and was Bill's research home for most of his scientific career.

Bill's first open literature publication at Argonne National Laboratory in 1958 was on the optical spectroscopy of an aqueous solution of curium, a synthetic element that had become available in sufficient quantity for measurement of absorption spectra. Curium is the 5f analog of the 4f element gadolinium. It was evident in that initial study that the absorption bands of $Cm^{3+}$ occurred at significantly longer wavelengths than is the case for $Gd^{3+}$ but no satisfactory theory existed to interpret this result. An indication of both the greater complexity of 5f electron states of actinides in comparison with 4f states of lanthanides and Bill's persistence in the face of a challenging problem are the additional six papers that he and his collaborators published over the next seventeen years on the subject of the energy level structure and transition intensities of $Cm^{3+}$, culminating in his 1975 paper with Katherine Rajnak which has proven to be the definitive measurement and interpretation of the 5f state optical absorption spectra and transition intensities of aquated $Cm^{3+}$.

Achieving an understanding of lanthanide ion optical spectroscopy and energy level structure was, in Bill's view, both a challenge in its own right and a stepping stone toward addressing the greater complexity of the 5f states of the actinides. He and his coworkers published a series of papers in the 1960s on the optical absorption spectra and band intensities of all of the lanthanide elements, including promethium, as aquated trivalent ions. This provided a new dimension to rare earth spectroscopy in that transition intensities (band areas, not just peak intensities) were measured quantitatively by the then unusual method of resolving overlapping absorption bands using nonlinear least squares adjustment in work that was reported in a series of six papers. His work and that of others provided compelling evidence for a close similarity between the 4f state energy level structure of trivalent lanthanides as aquated ions and those same ions when substitutionally doped into solid lanthanum trichloride or lanthanum trifluoride. This provided synergism with those carrying out spectroscopy at cryogenic temperatures, such as Gerhard H. Diecke and his collaborators at The Johns Hopkins University, who had measured the energies of crystal field split multiplets of 4f states of trivalent lanthanide ions in single crystalline solids, such as lanthanum trichloride, with high accuracy as to wavelength but who achieved only qualitative measurement of band intensities. This burgeoning body of energy level structure and transition intensity data did not go unnoticed by those with an interest in the advancing the theory of the spectroscopy of open shell atoms and ions, but progress occurred most productively in collaborations between experimentalists and theoreticians.

Bill actively sought out and nurtured collaboration with those at the leading edge of development of the predictive theories of f-electron spectroscopy, notably crystal field theory. That work initially focused on understanding the 4f electron energy level structure of lanthanide ions and benefited from the band intensity data that Bill's work provided. The concept of "free ion" states was central to relating aquated lanthanide ion spectra with spectra of the same lanthanide ions substitutionally doped into lanthanum trichloride. A related theory, developed separately by Brian R. Judd and G.S. Ofelt in 1962, together with matrix elements gleaned from energy level structure studies and measured band intensity data from ground state absorption studies, such as those carried out by Bill and his coworkers, provides a basis for calculating the probability of absorption or emission of photons between any f-state multiplets including the case where both multiplets are due to excited electronic states. This

reduces a problem that would otherwise require measuring the intensities of optical transitions whose number is on the order $n!$ down to a problem in which the number of intensities to be measured is on the order $n$ (where $n$ is the number of 4f state multiplets that a particular lanthanide ion possesses). The development of rare earth lasers and lanthanide-based wavelength upconverters has greatly benefited from the insight provided by this body of research.

In the 1970s Bill became group leader of an effort focused on heavy element chemistry research that included a strong spectroscopy component and, in recognition of his scientific accomplishments, was promoted to senior chemist. His studies had convinced Bill that fitting crystal field parameters on a case-by-case basis, as was the practice at the time, likely meant that valuable information about underlying interactions was being lost in comparison with fitting crystal field parameters across the lanthanide elements with a requirement of relatively smooth trend behavior in fit parameter values. This line of reasoning led him to pursue measurement and interpretation of lanthanide 4f state spectra of most lanthanide elements doped into single crystalline lanthanum trifluoride. Unlike lanthanum trichloride, which is relatively soft and so is difficult to polish, and is hygroscopic and must be protected from contact with laboratory air, lanthanum trifluoride is hard, readily polished and unaffected by contact with air. These properties of lanthanum trifluoride permitted more accurate measurement of transition intensities than had been the case in the earlier work on lanthanide ion spectroscopy in lanthanum trichloride which proved valuable in assigning the observed states. A commercial company, Optovac Corporation (Brookfield, Massachusetts), grew the doped lanthanum trifluoride crystals for Bill's studies.

During this same period, actinide elements of increasing atomic number, such as berkelium, californium, and einsteinium, were becoming available in sufficient quantity to permit Bill and his coworkers to synthesize single crystal solid chlorides for optical spectroscopy studies at cryogenic temperature. Comparison of those spectra with spectra recorded in their earlier work on the same ions as aquated species convinced Bill that what had been true of the trivalent lanthanide ions was also true of trivalent heavy actinide ions, namely that the underlying energy level structure of 5f electron "free ion" states was nearly identical for those ions in aqueous solution and doped into lanthanum trichloride. This insight proved particularly valuable in assignment of term symbols to observed bands in optical spectra. The 1970s also marked the beginning of Bill's work on f-elements in the vapor phase with studies on lanthanide chloride–aluminum chloride vapor complexes and isotopically labeled plutonium hexafluoride in the gas phase. He directed and participated in work on laser-induced fluorescence studies of both lanthanide and actinide ions. Bill's contributions to the spectroscopic properties of the lanthanides and actinides led to many requests to write reviews in the 1970s and 1980s, including his extensive and comprehensive critique on "The Absorption and Fluorescence Spectra of Rare Earth Ions in Solution", which was published in 1979 in volume 3 of the *Handbook on the Physics and Chemistry of Rare Earths*, chapter 24, pp. 171–208.

Pursuing a systematic interpretation of the electronic energy level structure of lanthanides and actinides within the framework of crystal-field theory led to the most important accomplishments in Bill's scientific career. In the 1980s, powerful computer programs were devel-

oped by Henry M. and Hanna Crosswhite for Bill that were based on advances in theory achieved by Brian R. Judd, Brian G. Wybourne, Henry M. Crosswhite and others. Those programs addressed much of the complexity of crystal field fitting of the spectra of 5f states of actinide ions in condensed phases. In addition, the speed of execution of those programs was such that Bill achieved his goal of fitting crystal field data for lanthanide ions in a common host across the lanthanide series of elements. This accomplishment was recognized as a milestone in f-element spectroscopy. A key result of that effort was his publication in 1989 of a fifteen page paper in *The Journal of Chemical Physics* (see bibliography, ref. 73) that included an energy level structure diagram for the trivalent lanthanide elements substitutionally doped into lanthanum trifluoride. That diagram was based on both the experimental measurements of Bill and his coworkers and, where necessary, crystal field calculations in which the parameter values across the lanthanide series of elements were fitted to exhibit a relatively smooth trend. The diagram serves as a master map of the energy level structure of trivalent lanthanide ions in condensed phases and now can be found in many review articles and books on lanthanide spectroscopy and materials science.

The systematic approach allowed Bill to reach conclusions as to the underlying interactions that give rise to the observed energy structure of the studied rare earth ions and, as importantly, highlighted remaining deficiencies in the interactions considered. As the 1980s drew to a close, Bill chose to give up group leadership so he could focus his efforts on completing a systematic study of the 5f electron states of trivalent actinide ions doped into lanthanum trichloride that he published in 1992 in a fourteen page paper in *The Journal of Chemical Physics* (see bibliography, ref. 79). This work marked another milestone in systematic and comparative studies of 4f- and 5f-element electronic structure and optical spectroscopy. Based on the model established in analysis of the spectra of trivalent actinide ions, systematic crystal field studies were later extended to the tetravalent actinide ions in cerium tetrafluoride. Bill was the program chair of the 17th Rare Earth Research Conference in 1986 and had the pleasure in 1988 of seeing his long time friend and collaborator Brian R. Judd receive the fifth Frank H. Speeding Award at the 18th Rare Earth Research Conference at Lake Geneva, Wisconsin for which Bill was the general conference chairman.

At present, purely *ab initio* calculation of f-state energy level structure and transition intensities rarely surpass the accuracy of results achieved by crystal field calculations of the type that Bill helped develop. In consequence, most productive results currently are achieved by application of semi-empirical crystal field theory in which parameters of the theory are fitted to observed data that spans only a part of the f-state structure. Due to advances in computer technology, useful crystal field calculations now can be carried out on the simplest of personal computers in a few minutes whereas the systematic calculations that Bill carried out often required an overnight run and all available core memory on Argonne's largest mainframe computer per energy level structure. While he arranged for the wide distribution of the computer programs that he used and helped to develop, Bill was not a computer programmer. He by far preferred studying computed results in the form of stacks of printouts after a run rather than dealing with the mechanics of batch job execution under a time sharing computer operating system. Therefore, he established long term and close collaboration with several theorists in the USA and Europe and hired staff members with expertise in computational

physics. Bill's collaboration with them often stimulated new topics for research and advances in theories. For example, when he realized that an abrupt change occurs in the values of crystal field parameters in the center of the series from $f^6$ to $f^8$ ions, he called Judd's attention to that fact and Judd subsequently developed a more advanced model with two-electron crystal-field operators to account for the observed change. Much of the consequent theoretical analysis in specific topics such as the ground state splitting of $f^7$ ions and the electron correlation in crystal field interaction were based on Bill's achievement in systematic crystal-field modeling.

Following his formal retirement as an Argonne National Laboratory staff member in 1991, Bill continued for several years thereafter to contribute his spectroscopy expertise. He viewed "retired" as meaning too busy to be employed. In "retirement" he was fully involved with and committed to his family which had grown with the marriage of two of his children and the births of his five grandchildren, to his church, and to his community where he served, for example, as Legislative Chairman for the American Association of Retired Persons and a Volunteer Coordinator for the Greater Chicago Food Depository. He was as deeply involved in volunteer community work as he was in his scientific research. On a Thanksgiving Day afternoon, while he and his family and invited guests were preparing the holiday dinner in his suburban home, he made time to distribute donated food in a neighborhood of the City of Chicago.

Bill Carnall's unfailingly good nature and optimism were evident both on bright summer days and those occasional grey winter days filled with snow when, in either case, he could be counted on to greet one with a hearty "A fine day in Chicago." He built the house in which his family grew up, somewhat to the consternation of his children who were awoken some mornings by the sounds of his construction efforts. Bill loved opera for which he had season tickets. He was a dedicated jogger regardless of the weather, an ardent gardener who marked each spring by starting tomato plants on the ledge of his office's south facing window, and a student of several languages who honed his proficiency by trading lessons in English for linguistic pointers from visitors from abroad who were working at Argonne. Bill was always willing to help others in need. For instance, he often drove his pickup truck to collect furniture, kitchen equipment, and dinnerware from his own home and his children's houses for the visiting scholars or postdoctoral associates who came to work temporarily at Argonne where only unfurnished apartments were available locally for housing. For his many fine qualities as a person, his assistance and guidance, and his enduring contributions to science, Bill is fondly and gratefully remembered by us and all others who had the pleasure of knowing him.

## Appendix

***Vita***

*Education*:

| | |
|---|---|
| Colorado State University | 1946–1950 |
| Ft. Collins, Colorado | |
| B.S. in Chemistry (highest honors) | |

|                                                             |           |
|-------------------------------------------------------------|-----------|
| University of Wisconsin, Madison, Wisconsin                 | 1950–1954 |

Ph.D. in Physical Chemistry
Minor in Physics
Advisor: John E. Willard

*Professional employment*

Argonne National Laboratory, Chemistry Division, Argonne, IL

|                                                      |           |
|------------------------------------------------------|-----------|
| Chemist                                              | 1954–1956 |
| Associate Chemist                                    | 1956–1975 |
| Group Leader, Heavy Elements Chemistry Group         | 1972–1989 |
| Senior Chemist                                       | 1975–1991 |
| Retired                                              | 1991–     |

Visiting Research Scientist, Institut für Anorganische Chemie, Universität München, München, Germany (1960–1961).

Visiting Scientist, Institut de Physique Nucléaire, Université de Paris, Orsay, France, September 1983.

Visiting Professor, Institut für Radiochemie, Technische Universität München, Garching/München, Germany, 1984–1990.

Visiting Scientist, USSR Academy of Sciences, Moscow, USSR, April–May 1987.

International Fellowship Award, Council of Scientific and Industrial Research, Republic of South Africa, February 1990.

Visiting Scientist, Khlopin Radium Institute, Leningrad, September 1990.

Visiting Professor, Institut de Physique Nucléaire, Université de Paris, Orsay, France, September 1991.

*Professional and honorary societies*

American Chemical Society
American Nuclear Society
Sigma Xi

*Professional activities*

Committee Memberships

Transplutonium Element Allocation and Program Review Committee, U.S. Department of Energy, Washington, DC (1972–1987)

National Transplutonium Element Program Review Committee, National Research Council, Washington, DC (1983)

External Review Committee, Inorganic and Nuclear Chemistry Division, Los Alamos National Laboratory, Los Alamos, NM (1985–1988)

International Steering Committee, Rare Earth and Actinide Chemistry Conferences (1986–1990)

U.S. Department of Energy Preconceptual Design Review Committee for the Advanced Neutron Source, Oak Ridge National Laboratory, Oak Ridge, TN (1988–1989)

Board of Directors, Rare Earth Research Conferences (1984–1989)

Transplutonium Element Research Assessment Committee, National Research Council (1990)

Scientific Committee of International Conferences

    First International Transplutonium Element Symposium, Argonne, IL, USA, 1963

    Third International Transplutonium Element Symposium, Argonne, IL, USA, 1971

    Fifteenth International Conference on Coordination Chemistry, Moscow, USSR, 1973

    First International Symposium on the Electronic Structure of the Actinides, Argonne, IL, USA, 1974

    Second International Conference on the Electronic Structure of the Actinides, Wroclaw, Poland, 1976

    Symposium on Lanthanide and Actinide Chemistry and Spectroscopy, 178th American Chemical Society Meeting, Washington, DC, USA, 1979

    International Conference on the Actinides, Actinides-81, Asilomar, CA, USA, 1981

    Symposium on Plutonium Chemistry, 184th American Chemical Society Meeting, Kansas City, MO, USA, 1982

    16th Rare Earth Research Conference, Tallahassee, FL, USA, 1983

    International Symposium on Rare Earth Spectroscopy, Wroclaw, Poland, 1984

    Symposium on Actinide Chemistry, 189th American Chemical Society Meeting, USA, 1985

    17th Rare Earth Research Conference, Hamilton, Ontario, Canada, 1986

    Second International Conference on the Basic and Applied Chemistry of f-Elements, Lisbon, Portugal, 1987

    General Chairman, 18th Rare Earth Research Conference, Lake Geneva, WI, USA, 1988

    Third International Conference on the Basic and Applied Chemistry of f-Elements, Leuven, Belgium, 1990

*Editorial boards*

Lanthanide and Actinide Research (1985–1993)

Materials Science (Poland) (1986–1991)

## *Publications*

### *Journals*

1. The Exchange Reaction Between Hydrogen Chloride and Aluminum Chloride, M. Blau, W.T. Carnall, and J.E. Willard, *J. Am. Chem. Soc.* **74**, 5762–5763 (1952).

2. The Absorption Spectrum of Aqueous Curium(III), W.T. Carnall, P.R. Fields, D.C. Stewart, and T.K. Keenan, *J. Inorg. Nucl. Chem.* **6**, 213–216 (1958).

3. A Study of the Complexes of Curium(III) by Absorption Spectrometry, W.T. Carnall and P.R. Fields, *J. Am. Chem. Soc.* **81**, 4445–4449 (1959).

4. The Oxidation State of the Elements and Their Potentials in Fused Salt Solutions. I. The Actinide Elements, D.M. Gruen, R.L. McBeth, J. Kooi, and W.T. Carnall, *Ann. NY Acad. Sci.*, **79**, 941–949 (1960).

5. Absorption Spectra of U(III) and U(IV) in $DClO_4$ Solution, D. Cohen and W.T. Carnall, *J. Phys. Chem.* **64**, 1933–1936 (1960).

6. The Alpha Half-Lives of $Cm^{244}$, $Cm^{245}$, and $Cm^{246}$, W.T. Carnall, S. Fried, and A.L. Harkness, *J. Inorg. Nucl. Chem.* **17**, 12–14 (1961).

7. The Near Infrared Transitions of the Trivalent Lanthanides in Solution. I. Praseodymium (III), Neodymium(III), Samarium(III) and Europium(III) Ions, W.T. Carnall, D.M. Gruen, and R.L. McBeth, *J. Phys. Chem.* **66**, 2159–2164 (1962).

8. Spectrophotometric Analysis of the Lanthanides in Molten Nitrate Media, W.T. Carnall, *Anal. Chem.* **34**, 786–791 (1962).

9. The Visible and Near Infrared Absorption Spectra of Some Trivalent Actinide and Lanthanide Elements in $DClO_4$ and in Molten Salts, W.T. Carnall and P.R. Fields, *Developments in Applied Spectroscopy* **1**, 233–247 (1962).

10. Preparation and Properties of Americium(VI) in Aqueous Carbonate Solutions, J. Coleman, T. Keenan, L. Jones, W.T. Carnall, and R. Penneman, *Inorg. Chem.* **2**, 58–61 (1963).

11. The Near-Infrared Transitions of the Trivalent Lanthanides in Solution. II. $Tb^{3+}$, $Dy^{3+}$, $Ho^{3+}$, $Er^{3+}$, $Tm^{3+}$ and $Yb^{3+}$, W.T. Carnall, *J. Phys. Chem.* **67**, 1206–1211 (1963).

12. Electronic Energy Levels of the Lighter Actinides: $U^{3+}$, $Np^{3+}$, $Pu^{3+}$, $Am^{3+}$ and $Cm^{3+}$, W.T. Carnall and B.G. Wybourne, *J. Chem. Phys.* **40**, 3428–3433 (1964).

13. The Near Infrared Transitions of the Trivalent Lanthanides in Solution. III. $Pm^{3+}$, W.T. Carnall, P.R. Fields and G.E. Toogood, *J. Phys. Chem.* **68**, 2351–2357 (1964).

14. The Low-Lying Energy Levels of Trivalent Curium, W.T. Carnall, P.R. Fields, and B.G. Wybourne, *J. Chem. Phys.* **41**, 2195–2196 (1964).

15. Spectral Intensities of the Trivalent Lanthanides and Actinides in Solution. I. $Pr^{3+}$, $Nd^{3+}$, $Er^{3+}$, $Tm^{3+}$, and $Yb^{3+}$, W.T. Carnall, P.R. Fields, and B.G. Wybourne, *J. Chem. Phys.* **42**, 3797–3806 (1965).

16. Reactions in Molten Salt Solutions. I. Uranate and Neptunate Formation in Molten Lithium Nitrate–Sodium Nitrate, W.T. Carnall, S.J. Neufeldt, and A. Walker, *Inorg. Chem.* **4**, 1808–1813 (1965).

17. The Solution Absorption Spectrum of $Cf^{3+}$, J.G. Conway, S.M. Fried, R.M. Latimer, R. McLaughlin, R.G. Gutmacher, W.T. Carnall, and P.R. Fields, *J. Inorg. Nucl. Chem.* **28**, 3064–3066 (1966).

18. Anhydrous Sodium Polyuranates, W.T. Carnall, A. Walker, and S.J. Neufeldt, *Inorg. Chem.* **5**, 2135–2140 (1966).

19. Reactor Irradiation of Lanthanum Oxide Samples, R.W. Bane, W.T. Carnall, and D.C. Stewart, *Nucl. Appl.* **3**, 270 (1967).

20. Energies and Intensities of Some Low-Lying Levels of Trivalent Curium, W.T. Carnall, *J. Chem. Phys.* **47**, 3081–3082 (1967).

21. Absorption Spectra of $Bk^{3+}$ and $Bk^{4+}$ in Solution, R.G. Gutmacher, E.K. Hulet, R. Lougheed, J.G. Conway, W.T. Carnall, D. Cohen, T.K. Keenan, and R.D. Baybarz, *J. Inorg. Nucl. Chem.* **28**, 2341–2345 (1967).

22. Spectral Intensities of the Trivalent Lanthanides and Actinides in Solution. II. $Pm^{3+}$, $Sm^{3+}$, $Eu^{3+}$, $Gd^{3+}$, $Tb^{3+}$, $Dy^{3+}$ and $Ho^{3+}$, W.T. Carnall, P.R. Fields, and K. Rajnak, *J. Chem. Phys.* **49**, 4412–4423 (1968).

23. Electronic Energy Levels in the Trivalent Lanthanide Aquo Ions. I. $Pr^{3+}$, $Nd^{3+}$, $Pm^{3+}$, $Sm^{3+}$, $Dy^{3+}$, $Ho^{3+}$, $Er^{3+}$, and $Tm^{3+}$, W.T. Carnall, P.R. Fields, and K. Rajnak, *J. Chem. Phys.* **49**, 4424–4442 (1968).

24. Electronic Energy Levels of the Trivalent Lanthanide Aquo Ions. II. $Gd^{3+}$, W.T. Carnall, P.R. Fields, and K. Rajnak, *J. Chem. Phys.* **49**, 4443–4446 (1968).

25. Electronic Energy Levels of the Trivalent Lanthanide Aquo Ions. III. $Tb^{3+}$, W.T. Carnall, P.R. Fields, and K. Rajnak, *J. Chem. Phys.* **49**, 4446–4449 (1968).

26. Electronic Energy Levels of the Trivalent Lanthanide Aquo Ions. IV. $Eu^{3+}$, W.T. Carnall, P.R. Fields, and K. Rajnak, *J. Chem. Phys.* **49**, 4450–4455 (1968).

27. Energy-Level Structure of $Gd^{3+}$ in $CaF_2$, H.M. Crosswhite, R.L. Schwiesow, and W.T. Carnall, *J. Chem. Phys.* **50**, 5032–5033 (1969).

28. Absorption Spectrum of Americium Tricyclopentadienide, R. Pappalardo, W.T. Carnall, and P.R. Fields, *J. Chem. Phys.* **51**, 842–843 (1969),

29. Low-Temperature Optical Absorption of Americium Halides, R.G. Pappalardo, W.T. Carnall, and P.R. Fields, *J. Chem. Phys.* **51**, 1182–1200 (1969).

30. $^1S_0$ Level of $Pr^{3+}$ in Crystal Matrices and Energy-Level Parameters for the $4f^2$ Configuration of $Pr^{3+}$ in $LaF_3$, W.T. Carnall, P.R. Fields, and R. Sarup, *J. Chem. Phys.* **51**, 2587–2591 (1969).

31. Absorption Spectrum of $Tm^{3+}$:$LaF_3$, W.T. Carnall, P.R. Fields, J.C. Morrison, and R. Sarup, *J. Chem. Phys.* **52**, 4054–4059 (1970).

32. Absorption Spectrum of $PuCl_3$, W.T. Carnall, P.R. Fields, and R.G. Pappalardo, *J. Chem. Phys.* **53**, 2922–2938 (1970).

33. Configuration Interaction and the Spectra of $LaCl_3$:$Pr^{3+}$, J.C. Morrison, P.R. Fields, and W.T. Carnall, *Phys. Rev. B* **2**, 3526–3532 (1970).

34. Optical Absorption Spectra of $Gd^{3+}$:$LaF_3$ and $GdCl_3 \cdot 6H_2O$, W.T. Carnall, P.R. Fields, and R. Sarup, *J. Chem. Phys.* **54**, 1476–1479 (1971).

35. Observation and Interpretation of Low Energy Bands in the Solution Absorption Spectra of $Bk^{3+}$ and $Bk^{4+}$, W.T. Carnall, R.K. Sjoblom, R.F. Barnes, and P.R. Fields, *Inorg. Nucl. Chem. Lett.* **7**, 651–657 (1971).

36. Microspectrophotometer Cells of Fused Construction, W.T. Carnall and P.R. Fields, *Appl. Spec.* **25**, 503 (1971).

37. Optical Absorption Spectra of $Er^{3+}$:$LaF_3$ and $ErCl_3 \cdot 6H_2O$, W.T. Carnall, P.R. Fields, and R. Sarup, *J. Chem. Phys.* **57**, 43–51 (1972).

38. The Absorption Spectra of $BkCl_3$ and $CfCl_3$, W.T. Carnall, S.M. Fried, F. Wagner Jr., R.F. Barnes, R.K. Sjoblom, and P.R. Fields, *Inorg. Nucl. Chem. Lett.* **8**, 773–774 (1972).

39. A New Series of Anhydrous Double Nitrate Salts of the Lanthanides. Structural and Spectral Characterization, W.T. Carnall, S. Siegel, J.R. Ferraro, B. Tani, and E. Gebert, *Inorg. Chem.* **12**, 560–564 (1973).

40. Absorption Spectrum of $CfCl_3$, W.T. Carnall, S. Fried, and F. Wagner Jr., *J. Chem. Phys.* **58**, 1938–1949 (1973).

41. Absorption Spectrum of $BkCl_3$, W.T. Carnall, S. Fried, and F. Wagner Jr., *J. Chem. Phys.* **58**, 3614–3624 (1973).

42. Electronic Energy Level and Intensity Correlations in the Spectra of the Trivalent Actinide Aquo Ions. I. $Es^{3+}$, W.T. Carnall, D. Cohen, P.R. Fields, R.K. Sjoblom, and R.F. Barnes, *J. Chem. Phys.* **59**, 1785–1789 (1973).

43. Absorption Spectra of NpCl$_3$ and NpBr$_3$, W.T. Carnall, H.M. Crosswhite, R.G. Pappalardo, D. Cohen, S. Fried, P. Lucas, and F. Wagner Jr., *J. Chem. Phys.* **61**, 4993–5008 (1974).

44. Electronic Energy Level and Intensity Correlations in the Spectra of the Trivalent Actinide Aquo Ions. II. Cm$^{3+}$, W.T. Carnall and K. Rajnak, *J. Chem. Phys.* **63**, 3510–3514 (1975).

45. X-Ray Photoemission Spectroscopy Study of Hexavalent Uranium Compounds, B.W. Veal, D.J. Lam, W.T. Carnall, and H.R. Hoekstra, *Phys. Rev. B* **12**, 5651–5663 (1975).

46. Energy Level Analysis of Pm$^{3+}$:LaCl$_3$, W.T. Carnall, H. Crosswhite, H.M. Crosswhite, and J.G. Conway, *J. Chem. Phys.* **64**, 3582–3591 (1976).

47. Isotope Effects in the Molecular Spectrum of Plutonium Hexafluoride, R. Kugel, C. Williams, M. Fred, J.G. Malm, W.T. Carnall, J.C. Hindman, W.J. Childs, and L.S. Goodman, *J. Chem. Phys.* **65**, 3486–3492 (1976).

48. Deactivation on the Nd$^{3+}$, $^4F_{3/2}$ Level in Neodymium Chloride–Aluminum Chloride Vapor Complexes, R.R. Jacobs, W.F. Krupke, J.P. Hessler, and W.T. Carnall, *Opt. Commun.* **21**, 395–398 (1977).

49. Fluorescence from the TbCl$_3$–AlCl$_3$ Vapor Complex System: A Potential New Gas-Phase Laser, J.P. Hessler, F. Wagner Jr., C. W. Williams, and W.T. Carnall, *J. Appl. Phys.* **48**, 3260–3262 (1977).

50. The Absorption Spectra and Excited State Relaxation Properties of Lanthanide and Actinide Halide Vapor Complexes. I. ErCl$_3$(AlCl$_3$)$_x$, W.T. Carnall, J.P. Hessler, H.R. Hoekstra, and C.W. Williams, *J. Chem. Phys.* **68**, 4304–4309 (1978).

51. Vapor Phase Spectroscopy of Complex Lanthanide Halide–Aluminum Halide Molecular Species, W.T. Carnall, J.P. Hessler, C.W. Williams, and H.R. Hoekstra, *J. Mol. Struct.* **46**, 269–284 (1978).

52. Transition Probabilities in the Absorption and Fluorescence Spectra of Lanthanides in Molten Lithium Nitrate–Potassium Nitrate Eutectic, W.T. Carnall, J.P. Hessler, and F. Wagner Jr., *J. Phys. Chem.* **82**, 2152–2158 (1978).

53. Energy Level Analysis of Np$^{3+}$:LaCl$_3$ and Np$^{3+}$:LaBr$_3$, W.T. Carnall, H. Crosswhite, H.M. Crosswhite, J.P. Hessler, N. Edelstein, J.G. Conway, G.V. Shalimoff, and R. Sarup, *J. Chem. Phys.* **72**, 5089–5102 (1980).

54. The Terbium Chloride–Aluminum Chloride Vapor System. I. Absorption and Excitation Spectra, J.A. Caird, W.T. Carnall, J.P. Hessler, and C.W. Williams, *J. Chem. Phys.* **74**, 798–804 (1981).

55. The Terbium Chloride–Aluminum Chloride Vapor System. II. Fluorescence, J.A. Caird, J.P. Hessler, W.T. Carnall, and C.W. Williams, *J. Chem. Phys.* **74**, 805–812 (1981).

56. The Terbium Chloride–Aluminum Chloride Vapor System. III. Spectral Intensity Analysis, J.A. Caird, W.T. Carnall, and J.P. Hessler, *J. Chem. Phys.* **74**, 3225–3233 (1981).

57. Reply to "Comment on the Energy Level Analysis of Np$^{3+}$:LaCl$_3$ and Np$^{3+}$:LaBr$_3$", W.T. Carnall, H. Crosswhite, H.M. Crosswhite, J.P. Hessler, N. Edelstein, J.G. Conway, G.V. Shalimoff, and R. Sarup, *J. Chem. Phys.* **75**, 3647 (1981).

58. Fluorescence Studies on Neptunium and Plutonium Hexafluoride Vapors, J.V. Beitz, C.W. Williams, and W.T. Carnall, *J. Chem. Phys.* **76**, 2756–2757 (1982).

59. The Synthesis and Characterization of Neptunium Hydroxysulfate, $Np(OH)_2SO_4$, D.W. Wester, J. Mulak, R. Banks, and W.T. Carnall, *J. Solid State Chem.* **45**, 235–240 (1982).

60. Further Investigation of the Spectra of $Pr^{3+}$–$LaF_3$ and $Tm^{3+}$–$LaF_3$, W.T. Carnall and H. Crosswhite, *J. Less-Common Met.* **93**, 127–135 (1983).

61. Availability and Uses of Heavy Elements, W.T. Carnall, *Trans. Am. Nucl. Soc.* **45**, 242 (1983).

62. Electronic Energy Level and Intensity Correlations in the Spectra of the Trivalent Actinide Aquo Ions. III. $Bk^{3+}$, W.T. Carnall, J.V. Beitz, and H. Crosswhite, *J. Chem. Phys.* **80**, 2301–2308 (1984).

63. Radiolytic Oxidation of Am(III) to Am(V) in NaCl Solutions, S. Magirius, W.T. Carnall, and J.I. Kim, *Radiochim. Acta* **38**, 29–32 (1985).

64. Crystal-Field Analysis of $Ho^{3+}$–$LaF_3$ and $Er^{3+}$–$LaF_3$ in $C_{2v}$-Site Symmetry, W.T. Carnall, G.L. Goodman, R.S. Rana, P. Vandevelde, L. Fluyt, and C. Görller-Walrand, *J. Less-Common Met.* **116**, 17–29 (1986).

65. An Optical Study of $\alpha$-$UF_5$ and $\beta$-$UF_5$, H.G. Hecht, J.G. Malm, and W.T. Carnall, *J. Less-Common Met.* **115**, 79–89 (1986).

66. A Systematic View of Optical Absorption Spectra in the Actinide Series, W.T. Carnall, *J. Less-Common Met.* **122**, 1–17 (1986).

67. Analysis of the Absorption Spectra of Complex Pentavalent Actinide Halides. $LiUF_6$, $\alpha$-$NaUF_6$ and $CsUF_6$, H.G. Hecht, J.G. Malm, J. Foropoulus, and W.T. Carnall, *J. Chem. Phys.* **84**, 3653–3662 (1986).

68. Analysis of the Spectrum of $Dy^{3+}$:$LaF_3$ Assuming a $C_{2v}$-Site Symmetry, G.L. Goodman, W.T. Carnall, R.S. Rana, P. Vandevelde, L. Fluyt, and C. Görller-Walrand, *J. Less-Common Met.* **126**, 283–289 (1986).

69. Laser-Induced Fluorescence of $^{249}Bk^{4+}$ in $CeF_4$, G.M. Jursich, J.V. Beitz, W.T. Carnall, G.L. Goodman, C.W. Williams, and L.R. Morss, *Inorg. Chim. Acta* **139**, 273–274 (1987).

70. Crystal-Field Analysis of $Tb^{3+}$:$LaF_3$ and $Gd^{3+}$:$LaF_3$ in $C_{2v}$ Site Symmetry, W.T. Carnall, G.L. Goodman, G.M. Jursich, R.S. Rana, P. Vandevelde, L. Fluyt, and C. Görller-Walrand, *Inorg. Chim. Acta* **139**, 275–276 (1987).

71. Interpretation of Tetravalent Actinide Spectra, W.T. Carnall, G.L. Goodman, C.W. Williams, S. Lam, and G.M. Jursich, *J. Less-Common Met.* **148**, 201–205 (1989).

72. Energy and Intensity Parameterization of the $Nd^{3+}$–$LiYF_4$ Spectrum, C. Görller-Walrand, L. Fluyt, P. Porcher, A.A.S. da Gama, G.F. de Sa, W.T. Carnall, and G.L. Goodman, *J. Less-Common Met.* **148**, 339–348 (1989).

73. A Systematic Analysis of the Spectra of the Lanthanides Doped into Single Crystal $LaF_3$, W.T. Carnall, G.L. Goodman, K. Rajnak, and R.S. Rana, *J. Chem. Phys.* **90**, 3443–3457 (1989).

74. Crystal-Field Analysis of $Am^{3+}$:$LaCl_3$/$AmCl_3$ and Its Relationship to Spectra of Frozen Solutions of $Am^{3+}$ (aquo), W.T. Carnall, *J. Less-Common Met.* **156**, 221–235 (1989).

75. Structure and Luminescence of the $La_{1-x}Gd_xF_3$ System, L.I. Brixner, M.K. Crawford, G. Hyatt, W.T. Carnall, and G. Blasse, *J. Electrochem. Soc.* **138**, 313–317 (1991).

76. Analysis of the Crystal-Field Spectra of the Actinide Tetrafluorides. I. Uranium, Neptunium, and Plutonium Tetrafluorides ($UF_4$, $NpF_4$, and $PuF_4$), W.T. Carnall, G.K. Liu, C.W. Williams, and M.F. Reid, *J. Chem. Phys.* **95**, 7194–7203 (1991).

77. Magnetic Dipole Transitions as Standards for Judd–Ofelt Parameterization in Lanthanide Spectra, C. Görller-Walrand, L. Fluyt, A. Ceulemans, and W.T. Carnall, *J. Chem. Phys.* **95**, 3099–3106 (1991).

78. Synthesis and X-Ray Diffraction Studies of $[N(CH_3)_4]_2BkCl_6$ and $[N(CH_3)_4]_2ZrCl_6$; Absorption Spectra of $Bk^{4+}$ in $[N(CH_3)_4]_2BkCl_6$, L.R. Morss, W.T. Carnall, C.W. Williams, J.A. Fahey, J. Fuger, G. Meyer, and M. Irmler, *J. Less-Common Met.* **169**, 1–8 (1991).

79. A Systematic Analysis of the Spectra of Trivalent Actinide Chlorides in $D_{3h}$ Site Symmetry, W.T. Carnall, *J. Chem. Phys.* **96**, 8713–8726 (1992).

80. Electronic Structure of $U^{4+}$, $Np^{4+}$ and $Pu^{4+}$ Doped into $ThSiO_4$ Single Crystal, J.C. Krupa and W.T. Carnall, *J. Chem. Phys.* **99**, 8577–8584 (1993).

81. Electronic Energy Level Structure of $Tb^{3+}$ in $LiYF_4$, G.K. Liu, W.T. Carnall, R.P. Jones, R.L. Cone, and J. Huang, *J. Alloys Compd.* **207–208**, 69–73 (1994).

82. Analysis of the Crystal-Field Spectra of the Actinide Tetrafluorides. II. $AmF_4$, $CmF_4$, $Cm^{4+}$:$CeF_4$, and $Bk^{4+}$:$CeF_4$, G.K. Liu, W.T. Carnall, G. Jursich, and C.W. Williams, *J. Chem. Phys.* **101**, 8277–8289 (1994).

### *Books and book chapters*

1. The Visible and Near Infrared Absorption Spectra of Some Trivalent Actinide and Lanthanide Elements in $DClO_4$ and in Molten Salts, W.T. Carnall and P.R. Fields. In: *Developments in Applied Spectroscopy*, vol. 1, Plenum Press, New York, 1962, pp. 233–247.

2. Lanthanide and Actinide Absorption Spectra in Solution, W.T. Carnall and P.R. Fields, In: *Lanthanide/Actinide Chemistry*, Advances in Chemistry Series No. 71, P.R. Fields and T. Moeller (Eds.), Am. Chem. Soc., Washington, DC, 1967, pp. 86–101.

3. Low-Temperature Absorption Spectra of Actinide Cyclopentadienides, W.T. Carnall, P.R. Fields, and R.G. Pappalardo. In: *Progress in Coordination Chemistry*. Proceedings of the 11th International Conference on Coordination Chemistry, Haifa and Jerusalem, September 1968. M. Cais (Ed.), Elsevier, Amsterdam, 1969, p. 411.

4. *Gmelin Handbook of Inorganic Chemistry*, vol. 8 (Erganzungswerk zur 8, Auflage, Transurane, Teil A2), G. Koch (Ed.) Verlag Chemie, GmbH, Weinheim, 1973.
     Chapter 8.1. Emission Spectra of the Transuranium Elements, W.T. Carnall, pp. 35–48.
     Chapter 8.2. Absorption and Fluorescence Spectra of the Transuranium Elements, W.T. Carnall, pp. 49–80.
     Chapter 8.3. X-Ray Spectra of the Transuranium Elements, W.T. Carnall, pp. 80–88.

5. Recent Developments in the Interpretation of Trivalent Lanthanide and Actinide Absorption Spectra, W.T. Carnall. In: *Novel in Coordination Chemistry*, Section Lectures of the 13th International Conference of Coordination Chemistry, Cracow–Zakopane, Poland, September 14–22, 1970. B.J. Trzebiatowska and M. Rudolf (Eds.), Państwowe Wydawnictwo Naukowe, Wroclaw, 1974, pp. 89–100.

6. Crystal-Field Calculations for 3+ Actinides in High Symmetry Host Crystals, W.T. Carnall, H.M. Crosswhite, H. Crosswhite, J.P. Hessler, C. Aderhold, J.A. Caird, A. Paszek, and F.W. Wagner Jr. In: *Proceedings of the 2nd International Conference on the Electronic Structure of the Actinides*, Wroclaw, Poland, September 13–16, 1976. J. Mulak, W. Suski, and R. Troć (Eds.), Ossolineum, Wroclaw, 1977, pp. 105–110.

7. XPS Studies on Actinide Materials, B.W. Veal, D.J. Lam, H.R. Hoekstra, H. Diamond, and W.T. Carnall. In: *Proceedings of the 2nd International Conference on the Electronic Structure of the Actinides*, Wroclaw, Poland, September 13–16, 1976. J. Mulak, W. Suski, and R. Troć (Eds.), Ossolineum, Wroclaw, 1977, pp. 145–155.

8. Fluorescence and Excitation Spectra of $Bk^{3+}$, $Cf^{3+}$ and $Es^{3+}$ Ions in Single Crystals of $LaCl_3$, J.P. Hessler, J.A. Caird, W.T. Carnall, H.M. Crosswhite, R.K. Sjoblom, and F. Wagner Jr., In: *The Rare Earths in Modern Science and Technology*, G.J. McCarthy and J.J. Rhyne (Eds.), Plenum Publishing Corp., New York, 1978, pp. 507–512.

9. Investigation of the $HoCl_3$–$AlCl_3$ Vapor Complex as a Potential High Power Laser, H.R. Hoekstra, J.P. Hessler, C.W. Williams, and W.T. Carnall. In: *Proceedings of the Symposium on High Temperature Metal Halide Chemistry*, D.L. Hildenbrand and D.D. Cubicciotti (Eds.), The Electrochem. Soc., Princeton, NJ, 1978, pp. 123–132.

10. Optical Spectroscopy of f-Element Compounds, W.T. Carnall. In: *Organometallics of the f-Elements*, Proceedings, NATO Advanced Study Institute, Sogesto, Italy, September 11–22, 1978, T.J. Marks and R.D. Fischer (Eds.), D. Reidel Publishing Company, Boston, 1979, pp. 281–307.

11. The Absorption and Fluorescence Spectra of Rare Earth Ions in Solution, W.T. Carnall. In: *Handbook on the Physics and Chemistry of Rare Earths*, vol. 3, K.A. Gschneidner Jr. and L. Eyring (Eds.), North-Holland Publishing Co., Amsterdam, 1979, pp. 171–208.

12. Optical Properties of Actinide and Lanthanide Ions, J.P. Hessler and W.T. Carnall. In: *Lanthanide and Actinide Chemistry and Spectroscopy*, ACS Symposium Series No. 131, N.M. Edelstein (Ed.), Am. Chem. Soc., Washington, DC, 1980, pp. 349–368.

13. Uranium Absorption and Luminescence Spectra, W.T. Carnall. In: *Gmelin Handbook of Inorganic Chemistry*, eighth ed., Uranium Supplement Volume A5, chapter 2, K.-C. Buschbeck and C. Keller (Eds.), Springer-Verlag, Berlin, 1982, pp. 69–161.

14. Uranium X-Ray Spectra, H. Crosswhite and W.T. Carnall. In: *Gmelin Handbook of Inorganic Chemistry*, eighth ed., Uranium Supplement Volume A5, chapter 3, K.-C. Buschbeck and C. Keller (Eds.), Springer-Verlag, Berlin, 1982, pp. 162–175.

15. Plutonium Chemistry, ACS Symposium Series, vol. 216, W.T. Carnall and G.R. Choppin (Eds.), Am. Chem. Soc., Washington, DC, 1983.

16. Spectroscopic Properties of the f-Elements in Compounds and Solutions, W.T. Carnall, J.V. Beitz, H. Crosswhite, K. Rajnak, and J.B. Mann. In: *Systematics and the Properties of the Lanthanides*, S.P. Sinha (Ed.), D. Reidel Publishing Company, Boston, chapter 9, 1983, pp. 389–450.

17. Plutonium Hexafluoride Gas Photophysics and Photochemistry, J.V. Beitz, C.W. Williams, and W.T. Carnall. In: *Plutonium Chemistry*, ACS Symposium Series No. 216, W.T. Carnall and G.R. Choppin (Eds.), Am. Chem. Soc., Washington, DC, 1983, pp. 155–172.

18. Measurement and Interpretation of Plutonium Spectra, L. Blaise, M.S. Fred, W.T. Carnall, H.M. Crosswhite, and H. Crosswhite. In: *Plutonium Chemistry*, ACS Symposium Series No. 216, W.T. Carnall and G.R. Choppin (Eds.), Am. Chem. Soc., Washington, DC, 1983, pp. 173–198.

19. Stability and Electronic Spectrum of Cesium Plutonium Hexafluoride, L.R. Morss, C.W. Williams, and W.T. Carnall. In: *Plutonium Chemistry*, ACS Symposium Series No. 216, W.T. Carnall and G.R. Choppin (Eds.), Am. Chem. Soc., Washington, DC, 1983, pp. 199–210.

20. Spectroscopic Studies on the Transplutonium Elements, W.T. Carnall and J.G. Conway. In: *Opportunities and Challenges in Research with Transplutonium Elements*, Report of a National Research Council Workshop, National Academy Press, Washington, DC, 1983, pp. 287–298.

21. A Systematic View of Transition Intensities in the Spectra of Actinides and Lanthanides in Condensed Phases, W.T. Carnall, H. Crosswhite, and K. Rajnak. In: *Rare Earth Spectroscopy*, B.J. Trzebiatowska, J. Legendziewicz, and W. Strek (Eds.), World Publishing Company, Singapore, 1985, pp. 267–297.

22. Optical Spectra and Electronic Structure of Actinide Ions in Compounds and in Solution, W.T. Carnall and H.M. Crosswhite. In: *The Chemistry of the Actinide Elements*, vol. 2, second ed., J.J. Katz, G.T. Seaborg, and L.R. Morss (Eds.), Chapman Hall, New York, 1986, pp. 1235–1277.

23. Photoelectron, Nuclear Gamma-Ray and Infrared Absorption Spectroscopic Studies of Neptunium in Sodium Silicate Glass, B.W. Veal, W.T. Carnall, B.D. Dunlap, A.W. Mitchell, and D.J. Lam (Eds.), In: *High Tech Ceramics*, P. Vincenzini (Ed.), Elsevier Science Publisher, Amsterdam, 1987, pp. 2903–2910.

24. Vibronic interaction and crystal structure distortion in $Cm^{4+}$ in $CeF_4$, G.K. Liu, J.V. Beitz, and W.T. Carnall (Eds.), In *Transuranium Elements A Half Century*, L.R. Morss and J. Fuger (Eds.), Am. Chem. Soc., Washington, DC, 1992, pp. 181–186.

### Research reports

1. The Electronic Energy Levels of the Heavy Actinides: $Bk^{3+}$ ($5f^8$), $Cf^{3+}$ ($5f^9$), $Es^{3+}$ ($5f^{10}$) and $Fm^{3+}$ ($5f^{11}$), P.R. Fields, B.G. Wybourne, and W.T. Carnall, Argonne National Laboratory, Report ANL-6911 (July 1964).

2. Absorption Spectra of $Bk^{3+}$ and $Bk^{4+}$ in Solution, R.G. Gutmacher, E.K. Hulet, R. Lougheed, J.G. Conway, W.T. Carnall, D. Cohen, T.K. Keenan, and R.D. Baybarz, University of California Radiation Laboratory, Report UCRL-70202 (November 1966).

3. Energy Levels and Intensities in the Solution Absorption Spectra of the Trivalent Lanthanides, W.T. Carnall, P.R. Fields, and K. Rajnak, Argonne National Laboratory, Report ANL-7358 (March 1968).

4. Spectroscopic Properties of $Bk^{3+}$ and $Cf^{3+}$, W.T. Carnall, Proceedings of the Symposium Commemorating the 25th Anniversary of Elements 97 and 98, Lawrence Berkeley Laboratory, January 20, 1975, Lawrence Berkeley Laboratory, Report LBL-4366 (July 1976), pp. 61–69.

5. Crystal and Solution Spectroscopy of Einsteinium, W.T. Carnall, Proceedings of the Symposium Commemorating the 25th Anniversary of Elements 99 and 100, Lawrence Berkeley Laboratory, January 23, 1978, Lawrence Berkeley Laboratory, Report LBL-7701 (April 1979), pp. 73–79.
6. Optical Spectra and Electronic Structure of Actinide Ions in Compounds and in Solution, W.T. Carnall and H.M. Crosswhite, Argonne National Laboratory, Report ANL-84-90 (August 1985).
7. A Systematic Analysis of the Spectra of the Lanthanides Doped into Single Crystal $LaF_3$. W.T. Carnall, G.L. Goodman, K. Rajnak, and R.S. Rana, Argonne National Laboratory, Report ANL-88-8 (February 1988).
8. A Systematic Analysis of the Spectra of Trivalent Actinide Chlorides in $D_{3h}$ Site Symmetry, W.T. Carnall, Argonne National Laboratory, Report ANL-89/39 (November 1989).

This page intentionally left blank

# CONTENTS

This page intentionally left blank

# CONTENTS OF VOLUMES 1–36

# INDEX OF CONTENTS OF VOLUMES 1–37

This page intentionally left blank

*Chapter 231*

# FIRST-PRINCIPLES CALCULATIONS OF $4f^n \rightarrow 4f^{n-1}5d$ TRANSITION SPECTRA

Kazuyoshi OGASAWARA[*], Shinta WATANABE, Hiroaki TOYOSHIMA and Mikhail G. BRIK

*Department of Chemistry, Kwansei Gakuin University, 2-1 Gakuen, Sanda, Hyogo 669-1337, Japan*
*E-mail: ogasawara@ksc.kwansei.ac.jp*

## Contents

* Corresponding author.

## Symbols and abbreviations

| | |
|---|---|
| aBR | anti-Beevers–Ross |
| AO | atomic orbital |
| $A_{SO}$ | angular part of spin–orbit interactions |
| $A_{ij}^{pq}$, $B_{ijkl}^{pq}$ | coefficients of one-electron and two-electron integrals in the $(p, q)$ matrix element of the many-electron Hamiltonian |
| BAM | BaMgAl$_{10}$O$_{17}$ |
| BR | Beevers–Ross |
| $B_q^k$ | crystal field parameters |
| $c$ | velocity of light |
| CF | crystal field |
| CFP | crystal field parameters |
| CFT | crystal field theory |
| CI | configuration interaction |
| $C_q^k$ | one-electron spherical tensor operators |
| $C_{ik}$ | the $i$th coefficient of the $k$th molecular orbital |
| DVME | discrete variational multielectron |
| DV-X$\alpha$ | discrete variational X$\alpha$ |
| **e** | unit vector parallel to the electric field vector of the incident light |

| | |
|---|---|
| EPR | electron paramagnetic resonance |
| ESA | excited state absorption |
| $E_i$ | total energy of the $i$th state of a many electron system |
| FWHM | full width at half maximum |
| $f_k$ | angular part of electrostatic interaction |
| $F^k$ | Slater integrals |
| $F^k$(fd), $G^j$(fd) | direct and exchange Slater integrals for the Coulomb interaction element of the many-electron Dirac Hamiltonian between the 4f and 5d electrons, respectively |
| GSA | ground state absorption |
| $h$ | Dirac's one-electron Hamiltonian |
| $H_0$ | spherical part of a free ion Hamiltonian |
| $H_{CF}$ | crystal field Hamiltonian |
| $\tilde{H}$, $\tilde{S}$, $\tilde{C}$ | Hamiltonian, overlap, and eigenvector matrices, respectively |
| $\langle ij|g|kl\rangle$ | two-electron integral |

| | | | |
|---|---|---|---|
| $\langle i|h|j \rangle$ | one-electron integral | YLF | LiYF$_4$ |
| LCAO | linear combination of atomic orbitals | $Z_\mu^{\text{eff}}$ | effective charge of the $\mu$th point charge |
| LDA | local density approximation | $Z_\nu$ | charge of the $\nu$th nucleus |
| $I_{ij}$ | oscillator strength of an electric dipole transition from the $i$th state to the $j$th state | $\tilde{\alpha}$ | and $\tilde{\beta}$ the Dirac matrices |
| | | $\alpha$ | Trees parameter; parameter in the Slater's X$\alpha$ potential |
| mO | mid-oxygen | $\beta, \gamma$ | Trees parameters generalized to higher rank |
| MO | molecular orbital | | |
| $m_h$ | spin–spin interaction operator | $\Gamma_i$ | irreducible representation of the double group (Bethe notations) |
| $M^h$ | strength of $m_h$ | | |
| $\mathbf{p}_i$ | momentum operator of the $i$th electron | $\Gamma_i \times \Gamma_j$ | direct product of two irreducible representations |
| $p_f$ | spin–other orbit interaction term | $\tilde{\varepsilon}$ | diagonal matrix of the energy eigenvalues |
| $P^f$ | strength of $p_f$ | $\varepsilon_k$ | energy of the $k$th molecular orbital |
| RE | rare earth | | |
| $\mathbf{r}_i$ | position vector of the $i$th electron | $\zeta_f$ | spin–orbit interaction constant for the 4f electron |
| $\mathbf{R}_\mu$ | position vector of the $\mu$th point charge | $\zeta(\text{dd})$ | spin–orbit interaction constant for the 5d electron |
| $\mathbf{R}_\nu$ | position vector of the $\nu$th nucleus | $\lambda$ | averaged scaling factor |
| TM | transition metal | $\sigma_{\text{rms}}$ | standard root-mean-squared deviation |
| $t_i$ | three-body interaction operator | $\sigma, \pi$ | polarization of the incident light (perpendicular and parallel to the crystal $c$ axis, respectively) |
| $T^i$ | strength of $t_i$ | | |
| VUV | vacuum ultraviolet | | |
| $V_0(\mathbf{r}_i)$ | potential from the non-explicitly considered electrons | $\rho$ | electron density |
| | | $\phi_k$ | the $k$th molecular orbital |
| $W_{jl}$ | coefficient of the $j$th Slater determinant in the $l$th many-electron wave function | $\Phi_j(\mathbf{r}_1, \ldots, \mathbf{r}_n)$ | the $j$th Slater determinant |
| | | $\omega(\mathbf{r}_p)$ | weight of the $p$th sampling point |

## 1. Introduction

Rare earth (RE) ions have been the subject of intensive investigations for last several decades. A unique combination of their partially filled $4f^n$-electron shell ($1 < n < 14$) (which has a large number of possible energetic states) and screening effect produced by their completely filled $5s^25p^6$-electron shells (which weakens the influence of external electric and magnetic

fields on 4f-electrons) makes them be very attractive for numerous applications, e.g. as activator ions in solid state lasers and phosphors covering a wide spectral range from infrared (IR) to ultraviolet (UV) and vacuum ultraviolet (VUV) spectral regions. First systematic experimental study of the RE energy level schemes, absorption and emission spectra was undertaken by Dieke and Crosswhite (1963) and summarized in the monograph by Dieke (1968). As a result of this work, a diagram of trivalent RE energy levels (which is known now as "Dieke diagram") has been established. Systematic crystal filed analysis for RE ions in several hosts was performed by Carnall et al. (1968, 1997, 1989 and references therein). Recently, the center of experimental researchers' interest is shifted towards high lying energy levels due to the growing demand for the lasers and phosphors operating in UV and VUV regions. Therefore, a great deal of attention is being paid now to the thorough analysis (both experimental and theoretical) of high lying energy levels of RE ions arising from their $4f^n$ and $4f^{n-1}5d$ electron configurations (Dorenbos, 2000a, 2000b, 2000c, 2000d, 2002; Meijerink and Wegh, 1999; Wegh et al., 2000; Reid et al., 2000; van Pieterson et al., 2000; Reid et al., 2002). In these works, the experimental spectra are analyzed based on phenomenological or semiempirical approaches with many fitting parameters involved, and the choice of these parameters is generally quite difficult and not always unique. In contrast to these works, in the present chapter we use a first-principles approach (Ogasawara et al., 2001, 2004, 2005a, 2005b), which would be effective for unambiguous analysis of the experimental spectra or for prediction of optical spectra of unknown materials. Description of the energetic structure of RE ions and their absorption spectra based on first-principles calculations is the main subject of the present chapter, which is organized as follows. First, we give a review of the semiempirical crystal field calculations commonly used for description of the energy level schemes of RE ions in crystals. Second, we describe the basic postulates of the discrete variational multielectron (DVME) method based on the discrete variational $X\alpha$ (DV-$X\alpha$) method (which does not require any empirical parameters to be used). Third, we proceed with giving detailed examples of calculations and analyses of the energy level schemes of RE ions in a free state and in crystals. As an example of practical materials, calculations of absorption spectra of $Eu^{2+}$ ions in a commercially-used blue phosphor $BaMgAl_{10}O_{17}:Eu^{2+}$ (BAM:$Eu^{2+}$) are given. Finally, we conclude the chapter with a summary of the main results obtained.

## 2. Brief review of previous semiempirical and first-principles calculations

### 2.1. *Semiempirical calculations of multiplet structures of REs*

#### 2.1.1. *Semiempirical theory of RE energy levels*
The commonly used Hamiltonian for description of the energy level scheme of $RE^{3+}$ ion in $4f^n$ configurations is as follows (Carnall et al., 1989):

$$H = H_0 + \sum_{k=0,2,4,6} F^k(nf, nf) f_k + \zeta_f A_{SO} + \alpha L(L+1) + \beta G(G_2) + \gamma G(R_7)$$
$$+ \sum_{i=2,3,4,6,7,8} t_i T^i + \sum_{h=0,2,4} m_h M^h + \sum_{f=2,4,6} p_f P^f + H_{CF}. \tag{1}$$

The first term in eq. (1) $H_0$ represents the spherical part of a free ion Hamiltonian and can be omitted without lack of generality. $F^k$'s are the Slater parameters and $\zeta_f$ is the spin–orbit interaction constant; $f_k$ and $A_{SO}$ are the angular parts of electrostatic and spin–orbit interactions, respectively. Two-body correction terms (including Trees' correction) are described by the fourth, fifth and sixth terms, correspondingly, whereas three-particle interactions (for ions with three or more equivalent f electrons) are represented by the seventh term. Finally, magnetic interactions (spin–spin and spin–other orbit corrections) are described by the terms with operators $m_h$ and $p_f$. Matrix elements of all operators entering eq. (1) can be taken from the book by Nielsen and Koster (1963) or from the Argonne National Laboratory's web site (Hannah Crosswhite's data files): http://chemistry.anl.gov/downloads/index.html. In what follows, the Hamiltonian (1) without $H_{CF}$ will be referred to as the free ion Hamiltonian.

Effects of crystal field (if an ion is embedded into a crystal or a glass) give rise to the last term in eq. (1). In the framework of the crystal field theory, the potential created by the crystal lattice at the position of an impurity ion can be expressed in general case as follows:

$$H_{CF} = \sum_{k=2,4,6} \sum_{m=1}^{N} B_0^k C_0^k(m) + \sum_{k=2,4,6} \sum_{q=1}^{k} \sum_{m=1}^{N} \left[ B_q^k \left( C_q^k(m) + (-1)^q C_{-q}^k(k) \right) \right.$$
$$\left. + B_{-q}^k i \left( C_{-q}^k(m) - (-1)^q C_q^k(m) \right) \right]. \tag{2}$$

Here $B_q^k$'s stand for the crystal field parameters (CFP), and $C_q^k(m)$'s are one-electron spherical tensor operators acting on the angular coordinates of the $m$th electron. Here and in what follows the Wybourne notation (Newman and Ng, 2000) is used. Other possible definitions of CFP and operators (e.g. Stevens conventions) and relations between them are dealt with in a series of papers by Rudowicz (1985, 2000, 2004 and references therein). Usually, the $B_q^k$'s are treated as empirical parameters to be determined from fitting of the calculated energy levels to the experimental ones. The number of non-zero CFP depends on the symmetry of the RE$^{3+}$ environment and increases with lowering the symmetry (up to 27 for the monoclinic symmetry), the determination of which is non-trivial (Cowan, 1981). As a result, in the literature there quite different sets of CFP for the same ion in the same host can be found (Rudowicz and Qin, 2004).

There are two types of difficulties in determination of CFP for a given system. The first one is a technical aspect related to the choice of reference systems and fitting algorithms. The second one is an intrinsic aspect related to the possibility to be trapped in various local minima during fitting process.

In order to overcome these difficulties the number of the fitting parameters is often reduced by imposing some restrictions on the range of their values, or by fixing the ratio between two or more parameters.

Another effective approach to reduce the number of fitting parameters is the exchange charge model of crystal field (Malkin, 1987). It allows for calculating CFP from crystal structure data with not more than three parameters (describing the overlap effects between an impurity ion and its nearest environment) which can be easily determined by fitting the calculated energy levels to the observed ones. Application of the exchange charge model to the large number of systems, e.g. LiErF$_4$ (Malkin, 1987), Yb$_2$Ti$_2$O$_7$ and Y$_2$Ti$_2$O$_7$:Yb$^{3+}$ (Malkin et al.,

2004), CsCdBr$_3$:Pr$^{3+}$ (Popova et al., 2001), LiYF$_4$:Er$^{3+}$ (Popova et al., 2000), etc. resulted in relatively good agreement between the calculated and experimental energy level schemes. Also paramagnetic susceptibilies of RE ions, electron paramagnetic resonance (EPR) $g$-factors, etc. can be calculated consistently using the obtained sets of CFP (Shakurov et al. 1998, 2004; Malkin et al., 2000).

The Hamiltonian in eq. (1) described above cannot be used directly to describe the energy levels of the 4f$^{n-1}$5d configurations. To describe the 4f$^{n-1}$5d configuration, one has to use Hamiltonian (1) with the set of parameters corresponding to the 4f$^{n-1}$ configuration and introduce several additional terms, which describe the interaction with one 5d electron. Reid et al. (2000) defined the following additions to the free ion Hamiltonian:

$$H_A(\text{fd}) = \sum_{k=2,4} F^k(\text{fd}) f_k(\text{fd}) + \sum_{j=1,3,5} G^j(\text{fd}) g_j(\text{fd}) + \zeta(\text{dd}) A_{\text{SO}}(\text{dd}). \qquad (3)$$

Here $F^k(\text{fd})$ and $G^j(\text{fd})$ stand for the direct and exchange Slater integrals for the Coulomb interaction between the 4f and 5d electrons (Cowan, 1981). The $\zeta(\text{dd})$ parameter is related to the spin–orbit interaction for the 5d electron. The interaction between 5d electron and crystal field is described by the following term:

$$H_{\text{CF}}(\text{dd}) = \sum_{k=2,4} \sum_{q=-k}^{k} B_q^k(\text{dd}) C_q^k(\text{dd}). \qquad (4)$$

Since the 4f$^n$ and 4f$^{n-1}$5d configurations are of opposite parity, they are not mixed by the Coulomb interaction. However, these configurations can couple by means of the odd-parity crystal field interaction represented as

$$H_{\text{CF}}(\text{fd}) = \sum_{k=1,3,5} \sum_{q=-k}^{k} B_q^k(\text{fd}) C_q^k(\text{fd}). \qquad (5)$$

In the case of Ce$^{3+}$ (having only one 4f electron in the ground state) all the above terms in the Hamiltonian vanish except the third term in eq. (3) and the crystal field term from eq. (4). The last, but not the least term to be taken into account when modeling the energy level schemes of the 4f$^{n-1}$5d configurations is difference between the averaged energies of the 4f$^n$ and 4f$^{n-1}$5d configurations. The average energy of the latter one is higher than the former one. The difference between them arises from several contributions, such as the kinetic energy of electrons, Coulomb effects, etc. (Cowan, 1981). These effects are impossible to distinguish by experimental methods; that is why this factor can be considered as contributing to a single term $\Delta_E(\text{fd})\delta_E(\text{fd})$ in the Hamiltonian. Here the operator $\delta_E(\text{fd})$ is diagonal with unit matrix elements within 4f$^{n-1}$5d configuration and zero matrix elements within 4f$^n$ configuration. Reid et al. (2000, 2002), van Pieterson et al. (2000) using the free ion parameters and 4f$^n$ CFP (Carnall et al., 1989; Duan and Reid, 2003) in their calculations, determined other parameters related to the 4f$^{n-1}$5d configurations by fitting the calculated energy levels to the observed ones. The model for the 4f$^n \rightarrow$ 4f$^{n-1}$5d transitions was proposed by Duan et al. (2002), Ning et al. (2004). It was also successfully used to calculate the f$^n \rightarrow$ f$^{n-1}$d absorption spectra of YPO$_4$:Nd$^{3+}$ (Ning et al., 2004) and LiYF$_4$:U$^{3+}$ (Ning et al., 2003).

Table 1

Main characteristics of the ground and first excited electron configurations of trivalent RE

| Atomic number | Ion | Ground configuration | Ground state $^{2S+1}L_J$ | Total number of states in ground configuration | Excited configuration | Total number of states in excited configuration |
|---|---|---|---|---|---|---|
| 57 | La$^{3+}$ | $4f^0$ | $^1S_0$ | 1 | – | – |
| 58 | Ce$^{3+}$ | $4f^1$ | $^2F_{5/2}$ | 14 | 5d | 10 |
| 59 | Pr$^{3+}$ | $4f^2$ | $^3H_4$ | 91 | $4f^1$5d | 231 |
| 60 | Nd$^{3+}$ | $4f^3$ | $^4I_{9/2}$ | 364 | $4f^2$5d | 1274 |
| 61 | Pm$^{3+}$ | $4f^4$ | $^5I_4$ | 1001 | $4f^3$5d | 4641 |
| 62 | Sm$^{3+}$ | $4f^5$ | $^6H_{5/2}$ | 2002 | $4f^4$5d | 12012 |
| 63 | Eu$^{3+}$ | $4f^6$ | $^7F_0$ | 3003 | $4f^5$5d | 23023 |
| 64 | Gd$^{3+}$ | $4f^7$ | $^8S_{7/2}$ | 3432 | $4f^6$5d | 33462 |
| 65 | Tb$^{3+}$ | $4f^8$ | $^7F_6$ | 3003 | $4f^7$5d | 37323 |
| 66 | Dy$^{3+}$ | $4f^9$ | $^6H_{15/2}$ | 2002 | $4f^8$5d | 32032 |
| 67 | Ho$^{3+}$ | $4f^{10}$ | $^5I_8$ | 1001 | $4f^9$5d | 21021 |
| 68 | Er$^{3+}$ | $4f^{11}$ | $^4I_{15/2}$ | 364 | $4f^{10}$5d | 10374 |
| 69 | Tm$^{3+}$ | $4f^{12}$ | $^3H_6$ | 91 | $4f^{11}$5d | 3731 |
| 70 | Yb$^{3+}$ | $4f^{13}$ | $^2F_{7/2}$ | 14 | $4f^{12}$5d | 924 |
| 71 | Lu$^{3+}$ | $4f^{14}$ | $^1S_0$ | 1 | $4f^{13}$5d | 141 |

## 2.1.2. *Dieke diagram*

The most significant feature of the RE ions is the partial filling of the 4f electron shell. The closed electron shells correspond to a xenon core $1s^2 2s^2 2p^6 3s^2 3p^6 3d^{10} 4s^2 4p^6 4d^{10} 5s^2 5p^6$, which is the ground spectroscopic state of La$^{3+}$ or Ce$^{4+}$. In the following ions electrons are added successively into the 4f shell, until it is full with 14 electrons at Yb$^{2+}$ and Lu$^{3+}$. The number of *LS* terms increases when increasing the number of 4f electrons from 1 to 7 and decreases when increasing the number of 4f electrons from 7 to 14. In the intermediate coupling approximation, all *LS* terms are split by spin–orbit interaction into *JJ* manifolds, the number of which follows the same trend for the *LS* terms above. Each manifold can be split further if an ion is embedded into a crystal or a glass with the number of resulting states depending on the symmetry of the environment (residual double degeneracy of all energy levels which can be removed by magnetic field only remains for the Kramers ions, i.e. Ce$^{3+}$, Nd$^{3+}$, Sm$^{3+}$, Gd$^{3+}$, Dy$^{3+}$, Er$^{3+}$, and Yb$^{3+}$, having odd numbers of 4f electrons). The use of the UV or VUV excitation can promote one of 4f electrons of a RE ion into 5d orbital leading to the change of the electron configuration from $4f^n$ to $4f^{n-1}$5d. Table 1 gives the basic information about the ground and first excited electron configurations of the RE$^{3+}$ ions. Large numbers of states in the ground and first excited configurations (especially for the ions in the middle part of the RE series) open an opportunity for getting an emission in a wide spectral domain, as well as combining different ions to get an effective energy transfer from one to another (provided the resonance condition between the energy levels of interest is fulfilled). In general, since the electronic transitions within the ground configuration are parity forbidden and become allowed only due to the admixture of states of opposite parity, the corresponding absorption and emission lines are very narrow and they are slightly dependent on the environ-
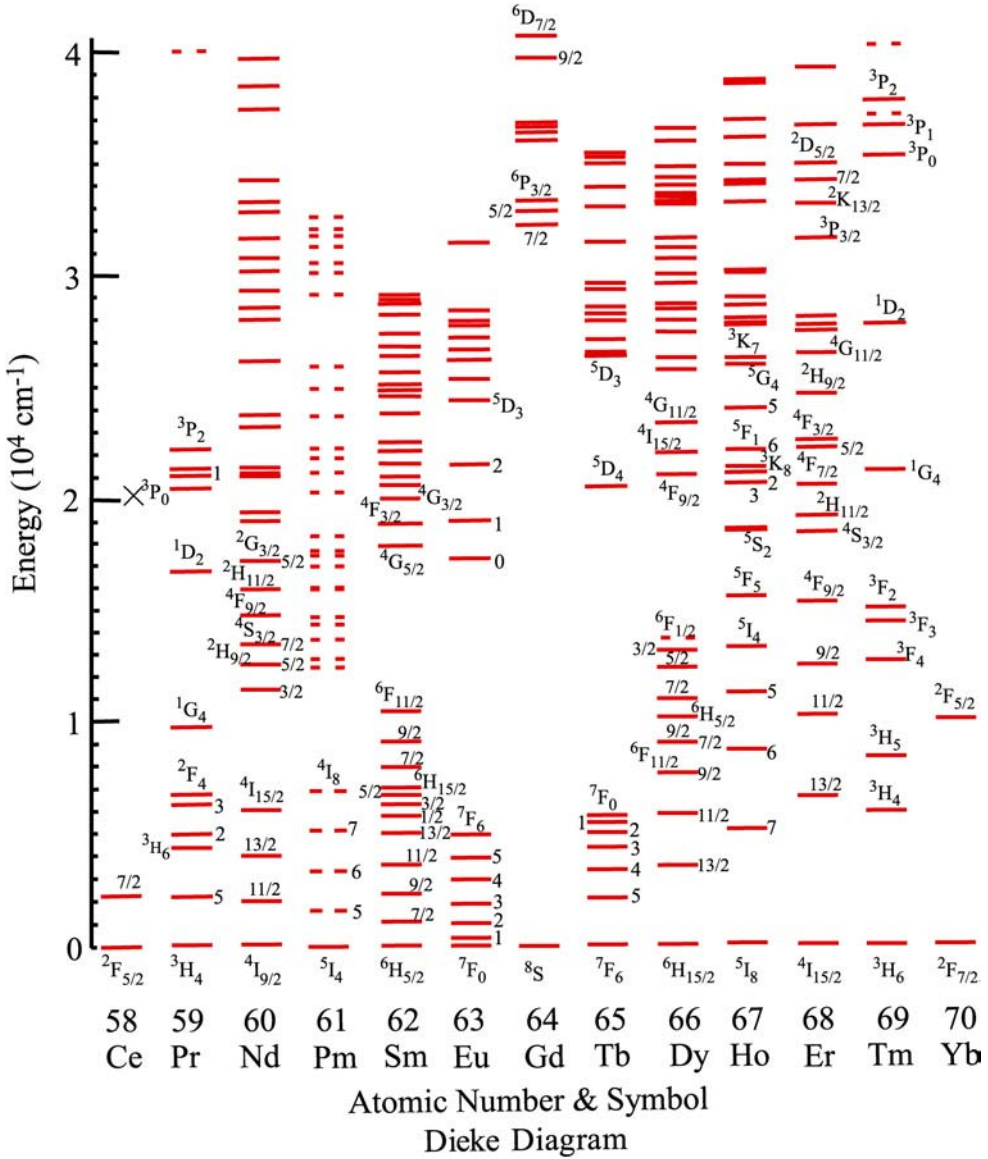
Fig. 1. Dieke diagram (energy levels of free $RE^{3+}$ ions up to 42000 cm$^{-1}$).

ment (because of the screening effect from the outer shells). On the contrary, the absorption spectra ascribing to the interconfigurational $4f^n \rightarrow 4f^{n-1}5d$ transitions are associated with very broad bands and significantly affected by the electron-vibronic interaction.
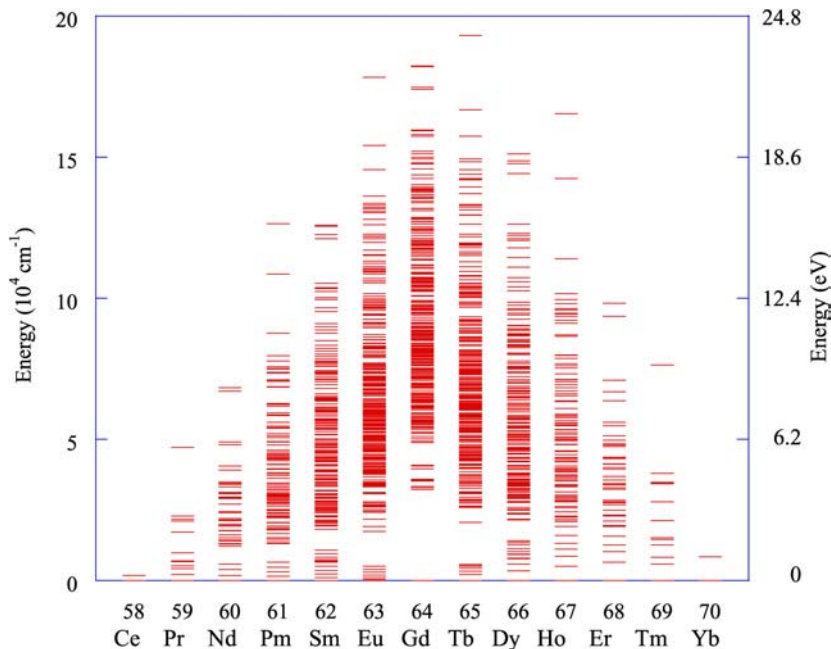
Fig. 2. Complete $4f^n$ energy level diagram for all $RE^{3+}$ ions obtained by semiempirical calculations.

### 2.1.3. *Recent efforts to extend the Dieke diagram*

The energy levels of free trivalent RE ions up to 42000 cm$^{-1}$ measured by Dieke and Crosswhite (1963) are shown in fig. 1, which is the well-known Dieke diagram. This diagram plays a very important role in analyzing the 4f–4f absorption spectra of trivalent RE ions in a free state and in crystals, and it was quite sufficient until recently. However, nowadays there exists a fast growing demand for optical materials operating in the UV or VUV spectral regions, and trivalent RE ions are excellent candidates for this purpose, since they possess a great number of energy levels in this part of spectrum. That is why the problem of extending the Dieke diagram into VUV region is very important. Early attempts to extend it until about 80 000 cm$^{-1}$ were made by Meijerink and Wegh (1999) and Wegh et al. (2000). Complete Dieke diagram with all energy levels of $4f^n$ configurations (fig. 2) was published recently by Ogasawara et al. (2004, 2005a, 2005b), Peijzel et al. (2005). In addition, complete energy level diagram including the $4f^{n-1}5d$ configurations was also obtained by Ogasawara et al. (2004, 2005a, 2005b) and will be presented later.

### 2.2. *First-principles calculations of multiplet structures of metal ions in solids*

Historically the first non-empirical calculation of entire multiplet structures of transition metal (TM) ions in crystals was performed by Watanabe and Kamimura based on the combination of a local density approximation (LDA) calculation and the ligand field theory (Watanabe and

Kamimura, 1987a, 1987b, 1989). They derived an analytic expression of the multiplet energies in $T_d$ symmetry, where all multiplet energies are expressed in terms of ten independent electron–electron repulsion integrals. These integrals were calculated by cluster calculations based on LDA. They investigated the multiplet structures of TM ions in various compound semiconductors and reasonably reproduced the energies of the lower-lying multiplets. However, this type of calculation has not been conducted extensively.

Calculations of multiplet energies based on the density functional method within the framework of the one-electron approximation have been also performed using the symmetry reduction approach developed by Daul (1994). In general, a multiplet state is expressed as a linear combination of Slater determinants. In principle, one-electron calculations can provide only the energy of each Slater determinant. However, Daul et al. obtained multiplet energy levels using analytic relations between multiplet energies and the energies of single Slater determinants. Wissing et al. (1998) also calculated the multiplet structures of $Cr^{4+}$ ion in some oxides by this approach and reproduced the energies of some lower-lying multiplets. However, due to the absence of the corresponding many-electron eigenfunctions, they could not calculate the transition probabilities between the multiplet states. Moreover, the symmetry reduction procedure for the lower symmetry systems is still somewhat ambiguous. Therefore, this approach has been applied to only high symmetry systems such as $O_h$ or $T_d$.

Hartree–Fock (HF) calculations combined with configuration interaction (CI) had been performed by Seijo and coworkers (Moraza et al., 1998). They calculated the multiplet structures of $Ni^{2+}$ ion in MgO (Llusar et al., 1996) and $V^{3+}$ ion in some fluoride crystals (Moraza and Barandiarán, 1996; Moraza et al., 1998), and reasonable agreement with experiment was obtained. Although this approach is mathematically exact, impractically large number of Slater determinants is required for accurate calculations. Due to this computational requirement, only crystals with $O_h$ symmetry have been treated so far. Seijo and coworkers (Moraza et al., 1998) performed recently multiplet structure calculations of $U^{3+}$ ions in $Cs_2NaYCl_6$ incorporating relativistic effects by using two-component configuration interaction (CI) calculations (Seijo and Barandiarán, 2003).

## 3. Method for first-principles calculations

In the present work we first perform molecular orbital (MO) calculations using the relativistic DV-X$\alpha$ method. Then we perform CI calculations using the DVME method to obtain the energy levels and wave functions of a many-electron system, which will be used for calculations and analysis of the optical spectra of RE ions in crystals.

### 3.1. *The relativistic DV-X$\alpha$ method—one-electron calculation*

#### 3.1.1. *The one-electron Dirac Hamiltonian*
If relativistic effects are significant, the electronic states of molecules within the adiabatic approximation can be obtained by solving the one-electron Dirac equation (Dirac, 1928, 1958)

$$h\phi_k(\mathbf{r}) = \varepsilon_k \phi_k(\mathbf{r}), \tag{6}$$

where $\mathbf{r}$ is the position of the electron, and $\phi_k$ and $\varepsilon_k$ are the $k$th MO and its energy, respectively. $h$ represents the Dirac's one-electron Hamiltonian,

$$h = c\tilde{\boldsymbol{\alpha}} \cdot \mathbf{p} + \tilde{\beta}c^2 + V(\mathbf{r}) = -ic\left(\tilde{\alpha}_x \frac{\partial}{\partial x} + \tilde{\alpha}_y \frac{\partial}{\partial y} + \tilde{\alpha}_z \frac{\partial}{\partial z}\right) + \tilde{\beta}c^2 + V(\mathbf{r}), \qquad (7)$$

where $c$ is the velocity of light, $\mathbf{p} = -i\nabla$ is the momentum operator, $\tilde{\boldsymbol{\alpha}}$ and $\tilde{\beta}$ are the Dirac matrices. These matrices are represented by the Pauli's spin matrices, $\tilde{\boldsymbol{\sigma}}$,

$$\tilde{\sigma}_x = \begin{pmatrix} 0 & 1 \\ 1 & 0 \end{pmatrix}, \quad \tilde{\sigma}_y = \begin{pmatrix} 0 & -i \\ i & 0 \end{pmatrix}, \quad \tilde{\sigma}_z = \begin{pmatrix} 1 & 0 \\ 0 & -1 \end{pmatrix} \qquad (8)$$

and 2 by 2 unit matrix, $\tilde{I}$, as

$$\tilde{\alpha}_i = \begin{pmatrix} 0 & \tilde{\sigma}_i \\ \tilde{\sigma}_i & 0 \end{pmatrix} (i = x, y, z), \quad \tilde{\beta} = \begin{pmatrix} \tilde{I} & 0 \\ 0 & -\tilde{I} \end{pmatrix}. \qquad (9)$$

### 3.1.2. The Xα approximation
In the relativistic DV-Xα method (Rosén and Ellis, 1974), the potential $V(\mathbf{r})$ in eq. (7) is expressed using the Slater's Xα potential (Slater, 1974) as

$$V(\mathbf{r}) = -\sum_{\nu} \frac{Z_\nu}{|\mathbf{r} - \mathbf{R}_\nu|} + \int \frac{\rho(\mathbf{r}')}{|\mathbf{r} - \mathbf{r}'|} d\mathbf{r}' - 3\alpha \left\{ \frac{3}{4\pi} \rho(\mathbf{r}) \right\}^{1/3} + \sum_{\mu} \frac{Z_\mu^{\text{eff}}}{|\mathbf{r}_i - \mathbf{R}_\mu|}, \qquad (10)$$

where $Z_\nu$ and $\mathbf{R}_\nu$ are the atomic number and the position of the $\nu$th atom inside the model cluster, respectively, $\rho$ is the electron density, $Z_\mu^{\text{eff}}$, $\mathbf{R}_\mu$ are the effective charge and position of the $\mu$th ion outside the model cluster. The first term represents the interaction between electrons and nuclei, the second term represents the Coulomb interaction between electrons, and the third term represents the exchange-correlation potential. The fourth term describes effective Madelung potential created by point charges. In this work, $\alpha$ is fixed to be 0.7, which was found to be an appropriate value for many solid state systems (Satoko et al., 1978).

### 3.1.3. LCAO method
We regard $\phi_k(\mathbf{r})$ in eq. (6) as MOs. The $k$th MO $\phi_k(\mathbf{r})$ is expressed as a linear combination of atomic orbitals (LCAO) such as

$$\phi_k(\mathbf{r}) = \sum_i C_{ik} \varphi_i(\mathbf{r}), \qquad (11)$$

where $\varphi_i(\mathbf{r})$ is the $i$th atomic orbital (AO) and $C_{ik}$ is the $i$th coefficient of the $k$th MO. Using eq. (11), eq. (6) can be rewritten as the secular equation,

$$\tilde{H}\tilde{C} = \tilde{S}\tilde{C}\tilde{\varepsilon}, \qquad (12)$$

where $\tilde{\varepsilon}$ is a diagonal matrix consisting of the energy eigenvalues, and $\tilde{H}$, $\tilde{S}$, $\tilde{C}$ represent the matrices having the elements, $H_{ij}$, $S_{ij}$, $C_{ik}$, respectively. $H_{ij}$ and $S_{ij}$ are the resonance and

overlap integrals expressed as

$$H_{ij} = \int \varphi_i^*(\mathbf{r}) h(\mathbf{r}) \varphi_j(\mathbf{r}) \, d\mathbf{r}, \quad S_{ij} = \int \varphi_i^*(\mathbf{r}) \varphi_j(\mathbf{r}) \, d\mathbf{r}, \tag{13}$$

respectively. By solving eq. (12), the orbital energy $\tilde{\varepsilon}$ and LCAO coefficients $\tilde{C}$ of MOs are obtained.

### 3.1.4. *Numerical integration of matrix elements*

In the relativistic DV-X$\alpha$ method, all the matrix elements of the Hamiltonian are calculated by the numerical integration using the Diophantine integration scheme (Conroy, 1967; Ellis and Painter, 1970). Using pseudorandom sampling points, the matrix elements are calculated as the weighted sum of the values at the sampling points as

$$H_{ij} = \sum_p \omega(\mathbf{r}_p) \varphi_i^*(\mathbf{r}_p) h(\mathbf{r}_p) \varphi_j(\mathbf{r}_p), \qquad S_{ij} = \sum_p \omega(\mathbf{r}_p) \varphi_i^*(\mathbf{r}_p) \varphi_j(\mathbf{r}_p), \tag{14}$$

where $\mathbf{r}_p$ is the position of the $p$th sampling point and $\omega(\mathbf{r}_p)$ is the weight proportional to the reciprocal of the sampling point density.

### 3.1.5. *Analysis of MO compositions*

In order to evaluate the degree of mixture of AOs in MOs (covalency), we apply an approach analogous to the Mulliken population analysis (Mulliken, 1955). Since the MOs are normalized, the inner product of the $k$th MO with itself can be expanded as,

$$\langle \phi_k | \phi_k \rangle = \left\langle \sum_i C_{ik} \varphi_i \,\middle|\, \sum_j C_{jk} \varphi_j \right\rangle = \sum_i \sum_j C_{ik}^* C_{jk} \langle \varphi_i | \varphi_j \rangle$$

$$= \sum_i \sum_j C_{ik}^* C_{jk} S_{ij} = 1. \tag{15}$$

In this scheme, the contribution of the $i$th AO within the $k$th MO can be represented as,

$$q_i^k \sum_j C_{ik}^* C_{jk} S_{ij}. \tag{16}$$

Summing $q_i^k$ over all possible $i$ yields unity, in accordance with eq. (15).

### 3.1.6. *Calculation of transition oscillator strengths and absorption spectra*

The oscillator strength of an electric dipole transition from the $i$th orbital to the $j$th orbital is given in atomic units as

$$I_{ij} = 2(\varepsilon_j - \varepsilon_i) |\langle \phi_j | \mathbf{r} \cdot \mathbf{e} | \phi_i \rangle|^2, \tag{17}$$

where $\mathbf{e}$ is the unit vector parallel to the electric field vector of the incident light. For easy comparison with the experimental spectra, a theoretical absorption spectrum can be obtained by convoluting oscillator strengths using a Gaussian function. In this work the width of the Gaussian function is determined so that the calculated spectra are in good agreement with experimental ones.

### 3.1.7. *Slater's transition state method*

In principle, the transition energy of an electron is given as the total energy difference $E_f - E_i$ between the final and initial states of a system. According to the Slater's transition state method, the total energy difference can be well approximated by the one-electron (orbital) energy difference, $\varepsilon_f - \varepsilon_i$, in the electron configuration where 0.5 electron is removed from the initial state and added to the final state (Slater, 1974). By performing self-consistent calculations in the Slater's transition state, the effects of orbital relaxation during transitions can also be taken into account.

### 3.2. *The relativistic DVME method*

### 3.2.1. *The many-electron Dirac Hamiltonian*

The eigenstates of a many-electron system (multiplet states for open shell systems) can be obtained by solving the many-electron Dirac equation,

$$H\Psi_l = E_l \Psi_l, \tag{18}$$

where $H$, $\Psi_l$, $E_l$ are the many-electron Dirac Hamiltonian, the $l$th many-electron wave function and the corresponding energy eigenvalue, respectively. In the relativistic DVME method, only relevant electrons and electron configurations are treated explicitly and the other electrons are considered as frozen. Within the Dirac–Coulomb approximation (Schwerdtfeger, 2002), the many-electron Dirac Hamiltonian for explicitly treated $n$ electrons is expressed in atomic units as

$$H = \sum_i^n h(\mathbf{r}_i) + \sum_i^n \sum_{j<i}^n g(\mathbf{r}_i, \mathbf{r}_j), \tag{19}$$

$$h(\mathbf{r}_i) = c\tilde{\boldsymbol{\alpha}} \cdot \mathbf{p}_i + \tilde{\beta}c^2 - \sum_\nu \frac{Z_\nu}{|\mathbf{r}_i - \mathbf{R}_\nu|} + V_0(\mathbf{r}_i) + \sum_\mu \frac{Z_\mu^{\text{eff}}}{|\mathbf{r}_i - \mathbf{R}_\mu|}, \tag{20}$$

$$g(\mathbf{r}_i, \mathbf{r}_j) = \frac{1}{|\mathbf{r}_i - \mathbf{r}_j|}. \tag{21}$$

All the quantities entering the last three equations have been already defined above. The Coulomb repulsion between electrons can be explicitly taken into account by the two-electron operator represented by eq. (21). $V_0(\mathbf{r}_i)$ represents the potential from the other (frozen) electrons expressed as

$$V_0(\mathbf{r}) = \int \frac{\rho_0(\mathbf{r}')}{|\mathbf{r} - \mathbf{r}'|} d\mathbf{r}' + \frac{3}{4} \left[ \frac{\rho(\mathbf{r}) V_{xc}\{\rho(\mathbf{r})\} - \rho_0(\mathbf{r}) V_{xc}\{\rho_0(\mathbf{r})\}}{\rho_1(\mathbf{r})} - V_{xc}\{\rho_1(\mathbf{r})\} \right], \tag{22}$$

where $V_{xc}$ is the Slater's X$\alpha$ potential, $\rho(\mathbf{r})$ is the density of all electrons, $\rho_1(\mathbf{r})$ is the density of the explicitly treated $n$ electrons, $\rho_0(\mathbf{r})$ is the density of the other (frozen) electrons according to Watanabe and Kamimura (1989).

### 3.2.2. *Configuration interaction method*

In the DVME method, the many-electron Dirac Hamiltonian is diagonalized based on the CI approach. In this approach, the $l$th many-electron wave function $\Psi_l$ is represented as a

linear combination of the Slater determinants which are constructed from MOs obtained by the relativistic DV-Xα calculations as

$$\Psi_l = \sum_{j=1}^{K} W_{jl} \Phi_j, \tag{23}$$

$$\Phi_j(\mathbf{r}_1, \ldots, \mathbf{r}_n) = \frac{1}{\sqrt{n!}} \begin{vmatrix} \phi_{j1}(\mathbf{r}_1) & \phi_{j1}(\mathbf{r}_2) & \ldots & \phi_{j1}(\mathbf{r}_n) \\ \phi_{j2}(\mathbf{r}_1) & \phi_{j2}(\mathbf{r}_2) & \ldots & \phi_{j2}(\mathbf{r}_n) \\ \vdots & \vdots & \ddots & \vdots \\ \phi_{jn}(\mathbf{r}_1) & \phi_{jn}(\mathbf{r}_2) & \ldots & \phi_{jn}(\mathbf{r}_n) \end{vmatrix}. \tag{24}$$

In the above equations, $W_{jl}$ is the coefficient of the $j$th Slater determinant in the $l$th many-electron wave function and $K$ is the total number of the Slater determinants used for the linear combination. For example, for $4f^2$ electron configuration, such as ground state configuration of the $Pr^{3+}$ ion, two f electrons occupy 14 MOs. Therefore, the number of possible combinations is $K = 14!/\{2!(14-2)!\} = 91$.

Using eq. (23), eq. (18) can be rewritten in the form of the secular equation,

$$\tilde{H}\tilde{W} = \tilde{W}\tilde{E}. \tag{25}$$

By solving this, the multiplet energies $\tilde{E}$ and the coefficients of the many-electron wave functions are obtained.

A matrix element $H_{pq}$ of the many-electron Dirac Hamiltonian $\tilde{H}$ can be expanded as

$$H_{pq} = \langle \Phi_p | H | \Phi_q \rangle = \sum_{i=1}^{L} \sum_{j=1}^{L} A_{ij}^{pq} \langle i|h|j \rangle + \sum_{i=1}^{L} \sum_{j=1}^{L} \sum_{k=1}^{L} \sum_{l=1}^{L} B_{ijkl}^{pq} \langle ij|g|kl \rangle, \tag{26}$$

where $A_{ij}^{pq}$ and $B_{ijkl}^{pq}$ are the coefficients and $L$ is the total number of considered MOs. $\langle i|h|j \rangle$ and $\langle ij|g|kl \rangle$ are the one-electron and the two-electron integrals, respectively, expressed as

$$\langle i|h|j \rangle = \int \phi_i^*(\mathbf{r}) h(\mathbf{r}) \phi_j(\mathbf{r}) d\mathbf{r}, \tag{27}$$

$$\langle ij|g|kl \rangle = \int \phi_i^*(\mathbf{r}_1) \phi_j^*(\mathbf{r}_2) \frac{1}{|\mathbf{r}_1 - \mathbf{r}_2|} \phi_k(\mathbf{r}_1) \phi_l(\mathbf{r}_2) d\mathbf{r}_1 d\mathbf{r}_2. \tag{28}$$

In the relativistic DVME method, eqs. (27) and (28) are calculated numerically in a similar way to the one-electron calculation such as

$$\langle i|h|j \rangle = \sum_{\alpha} \omega(\mathbf{r}_\alpha) \phi_i^*(\mathbf{r}_\alpha) h(\mathbf{r}_\alpha) \phi_j(\mathbf{r}_\alpha), \tag{29}$$

$$\langle ij|g|kl \rangle = \sum_{\alpha} \sum_{\beta \neq \alpha} \omega(\mathbf{r}_\alpha) \omega(\mathbf{r}_\beta) \phi_i^*(\mathbf{r}_\alpha) \phi_j^*(\mathbf{r}_\beta) \frac{1}{|\mathbf{r}_\alpha - \mathbf{r}_\beta|} \phi_k(\mathbf{r}_\alpha) \phi_l(\mathbf{r}_\beta), \tag{30}$$

where $\mathbf{r}_\alpha$ and $\mathbf{r}_\beta$ are the positions of the $\alpha$th and $\beta$th sampling points, respectively and $\omega(\mathbf{r})$ is weight of the sampling point proportional to the reciprocal of the sampling point density at the position $\mathbf{r}$.

### 3.2.3. *Analysis of many-electron wave function compositions*
In the relativistic DVME method, the interactions among the states represented by the Slater determinants, i.e., the CI can be analyzed using explicit many-electron wave functions expressed by eq. (23). From the orthonormality of the Slater determinants, the inner product of the $l$th many-electron wave function with itself can be expanded as

$$\langle \Psi_l | \Psi_l \rangle = \left\langle \sum_j W_{jl} \Phi_j \middle| \sum_k W_{kl} \Phi_k \right\rangle = \sum_j \sum_k W_{jl}^* W_{kl} \langle \Phi_j | \Phi_k \rangle$$

$$= \sum_j |W_{jl}|^2 \langle \Phi_j | \Phi_j \rangle = \sum_j |W_{jl}|^2 = 1. \tag{31}$$

In this scheme, the contribution of the $j$th Slater determinant $\Phi_j$ within the $l$th many-electron wave function $\Psi_l$ can be simply represented as

$$Q_j^l = |W_{jl}|^2. \tag{32}$$

Summing $Q_j^l$ over all possible $j$ yields unity, in accordance with eq. (31).

### 3.2.4. *Calculation of theoretical absorption spectra*
Since the many-electron wave functions are obtained explicitly as linear combinations of the Slater determinants, the oscillator strengths of an electric dipole transition from the $i$th state to the $j$th state can be calculated by

$$I_{ij} = 2(E_j - E_i) \left| \left\langle \Psi_j \middle| \sum_{k=1}^n \mathbf{r}_k \cdot \mathbf{e} \middle| \Psi_i \right\rangle \right|^2, \tag{33}$$

where $\mathbf{e}$ is the unit vector parallel to the electric field vector of the incident light. For easy comparison with the experimental spectra, the theoretical absorption spectrum can be obtained by convoluting oscillator strengths using a Gaussian function. In this work the width of the Gaussian function is determined so that the calculated spectra are in good agreement with experimental ones.

## 4. Results of first-principles calculations

### 4.1. *Calculations of free trivalent RE ions*

#### 4.1.1. *Comparison with semiempirical calculations for $Pr^{3+}$*
An example of comparison of the results obtained by semiempirical and first-principles methods is given in table 2, which contains energies of the $Pr^{3+}$ ion ($4f^2$ electron configuration). In the results of the semiempirical calculations, two leading contributions to the intermediately coupled eigenstates of the Hamiltonian (1) are given as well. As can be seen from table 2, there is a systematic overestimation (of about 20–30%) of all energy levels $E_2$ obtained by the first principles calculations. This overestimation, presumably due to underestimation of

Table 2

Energy eigenvalues (in cm$^{-1}$) and eigenstates of Pr$^{3+}$. Only two leading *LS* contributions to the wave functions are shown for simplicity

| $J$ | Semiempirical Hamiltonian (eq. (2)) | | | First-principles many-electron Hamiltonian (eq. (6)) | | |
|---|---|---|---|---|---|---|
| | Main term | Wave function | Energy $E_1$ (cm$^{-1}$) | Energy $E_2$ (cm$^{-1}$) | Ratio $E_1/E_2$ | $\lambda_{av} E_2$ (cm$^{-1}$) |
| 4 | $^3H_4$ | $0.986\,|^3H\rangle + 0.163\,|^1G\rangle$ | 0 | 0 | – | 0 |
| 5 | $^3H_5$ | $1.000\,|^3H\rangle$ | 2081 | 2938 | 0.708 | 2203 |
| 6 | $^3H_6$ | $0.998\,|^3H\rangle - 0.055\,|^1I\rangle$ | 4252 | 5963 | 0.713 | 4472 |
| 2 | $^3F_2$ | $0.988\,|^3F\rangle + 0.152\,|^1D\rangle$ | 5185 | 6807 | 0.762 | 5105 |
| 3 | $^3F_3$ | $1.000\,|^3F\rangle$ | 6572 | 8599 | 0.764 | 6449 |
| 4 | $^3F_4$ | $-0.796\,|^3F\rangle + 0.593\,|^1G\rangle$ | 6957 | 8704 | 0.799 | 6528 |
| 4 | $^1G_4$ | $-0.789\,|^1G\rangle - 0.605\,|^3F\rangle$ | 9934 | 12476 | 0.796 | 9357 |
| 2 | $^1D_2$ | $0.944\,|^1D\rangle - 0.293\,|^3P\rangle$ | 17201 | 23492 | 0.732 | 17619 |
| 6 | $^1I_6$ | $0.998\,|^1I\rangle + 0.055\,|^3H\rangle$ | 21100 | 28098 | 0.751 | 21074 |
| 0 | $^3P_0$ | $0.995\,|^3P\rangle + 0.103\,|^1S\rangle$ | 21104 | 29028 | 0.727 | 21771 |
| 1 | $^3P_1$ | $1.000\,|^3P\rangle$ | 21724 | 29847 | 0.729 | 22385 |
| 2 | $^3P_2$ | $0.956\,|^3P\rangle + 0.292\,|^1D\rangle$ | 22911 | 31435 | 0.729 | 23576 |
| 0 | $^1S_0$ | $0.995\,|^1S\rangle - 0.103\,|^3P\rangle$ | 47181 | 63529 | 0.743 | 47647 |

electron correlations, exists for all ions and is considered to be an intrinsic feature of the first-principles CI calculations using only MOs composed mainly of 4f and 5d orbitals.

Table 2 contains corrected energies of Pr$^{3+}$ obtained by multiplication of the $E_2$ values by the averaged ratio $\lambda = 1/N \sum_{i=1}^{N} E_{1i}/E_{2i} = 0.75$ (where $N$ is the total number of $J$ manifolds, $E_{1i}$ and $E_{2i}$ are the $i$th energies obtained by the semiempirical and first principles calculations, respectively). Inclusion of this correction significantly improves the agreement of the first principles results with semiempirical ones as well as with the Dieke diagram (fig. 1).

It should be mentioned here, that there is still an ambiguity regarding the order of the $^1I_6$ and $^3P_{0,1,2}$ levels (Carnall et al., 1989), which are located very close to each other. The order of these levels depends strongly on the parameters of the Hamiltonian. Our results (table 2) based on the Carnall's parameters for free Pr$^{3+}$ ion show different order of the energy levels in very dense group of $^3P_J$, $^1I_6$ states in comparison with that proposed by Sugar (1965). It should be noted that the energetic order obtained by first-principles calculations is consistent with that of our semiempirical calculations. Because of this we will compare the first principles energies with the semiempirical ones in the following sections.

### 4.1.2. *Multiplet energies with introduction of reduction factors*
The eigenvalues of the first-principles Hamiltonian (19) for all RE ions are overestimated with respect to the eigenvalues of the semiempirical Hamiltonian (1) by 20–30%, as we have seen in the case of Pr$^{3+}$ in the previous section. This enabled us to introduce the ion-dependent scaling (reduction) factor by the following equation:

$$\lambda = \frac{1}{N} \sum_{i=1}^{N} \frac{E_{1i}}{E_{2i}}, \tag{34}$$

Table 3
Scaling factors (defined by eq. (34) for all trivalent RE ions)

| Ion | Number of $J$ manifolds | Scaling factor $\lambda$ |
|-----|-------------------------|--------------------------|
| $Ce^{3+}$ | 2 | 0.719 |
| $Pr^{3+}$ | 13 | 0.746 |
| $Nd^{3+}$ | 41 | 0.776 |
| $Pm^{3+}$ | 107 | 0.796 |
| $Sm^{3+}$ | 198 | 0.819 |
| $Eu^{3+}$ | 295 | 0.830 |
| $Gd^{3+}$ | 327 | 0.836 |
| $Tb^{3+}$ | 295 | 0.853 |
| $Dy^{3+}$ | 198 | 0.850 |
| $Ho^{3+}$ | 107 | 0.837 |
| $Er^{3+}$ | 41 | 0.840 |
| $Tm^{3+}$ | 13 | 0.847 |
| $Yb^{3+}$ | 2 | 0.900 |
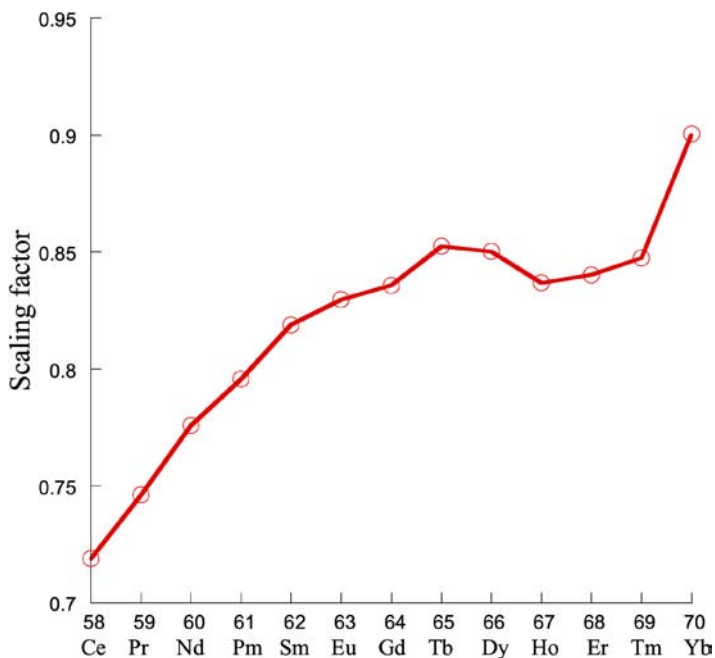


Fig. 3.  Scaling factor defined by eq. (34) as a function of the atomic number.

where $N$ is the total number of $J$ manifolds, $E_{1i}$ and $E_{2i}$ are the eigenvalues of the Hamiltonians (1) and (19), respectively. The values of the scaling factor are given in table 3. The dependence of its value on the atomic number is visualized in fig. 3.
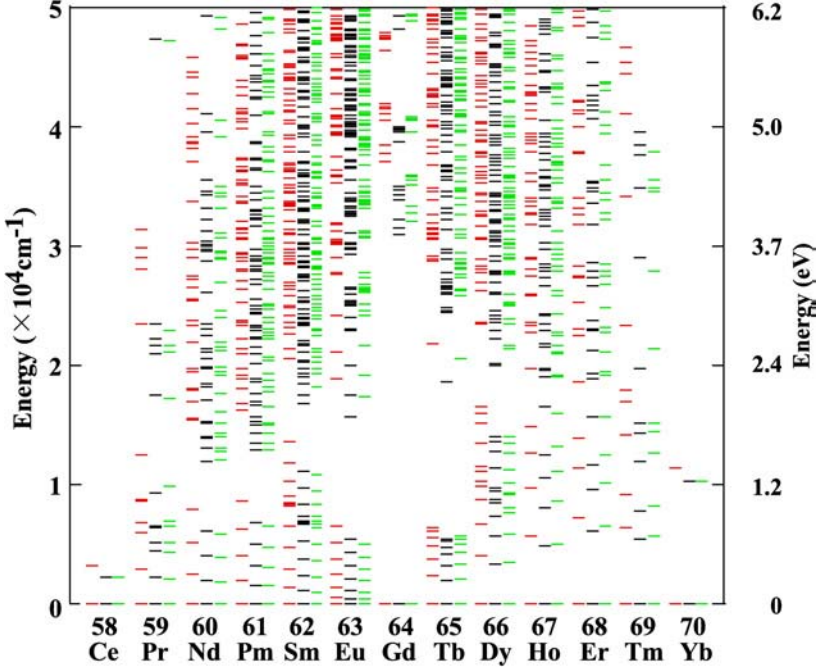
Fig. 4. Calculated multiplet energy levels from 0 to 50000 cm$^{-1}$ obtained by first-principles calculations (left), first-principles calculations considering scaling factors (center) and semiempirical calculations (right) for each trivalent RE ions.

The first-principles results corrected with the scaling factor are shown in figs. 4 and 5 together with the first-principles results without corrections and the semiempirical results. As shown in these figures the calculated multiplet energies are significantly improved by introduction of the scaling factor.

Correspondence between the eigenvalues of both Hamiltonians is quantitatively evaluated by the standard root-mean-square deviation $\sigma_{rms}$ defined as follows:

$$\sigma_{rms} = \sqrt{\frac{\sum_{i=1}^{N}(E_{1i} - E_{2i})^2}{N}}, \tag{35}$$

where the meanings of all variables are the same as in eq. (34).

The values of $\sigma_{rms}$ for all RE ions are listed in table 4. They are given without and with taking into account the scaling factors from table 3.

As seen from table 4, inclusion of scaling factor significantly decreases the value of $\sigma_{rms}$. It is expected to decrease more significantly for RE ions in crystals, since all $J$ manifolds are split by crystal field and number of levels $N$ increases drastically. For example, when similar analysis has been performed for the lowest levels of LaF$_3$:Eu$^{3+}$ by Brik et al. (2006), the value of $\sigma_{rms}$ turned out to be 21.6 cm$^{-1}$. The consistency in energy values and their assignments
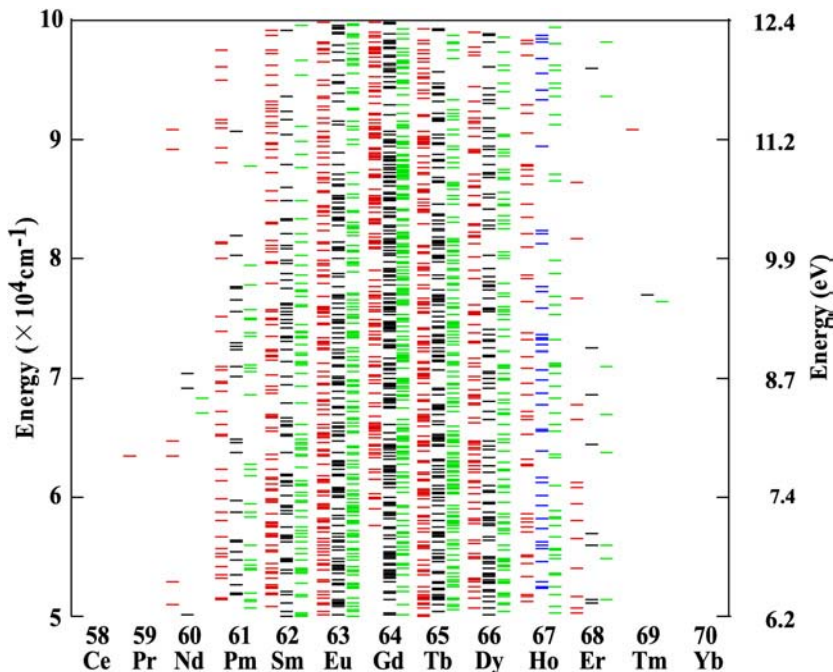
Fig. 5. Calculated multiplet energy levels from 50000 to 100000 cm$^{-1}$ obtained by first-principles calculations (left), first-principles calculations considering scaling factors (center) and semiempirical calculations (right) for each trivalent RE ions.

Table 4
Root-mean-square deviations between eigenvalues of Hamiltonians (1) and (19) without and with scaling factors taken into account

| Ion | Root mean square deviation $\sigma_{rms}$ (cm$^{-1}$) | |
|---|---|---|
| | without scaling factor | with scaling factor |
| Ce$^{3+}$ | 626 | 0 |
| Pr$^{3+}$ | 6663 | 358 |
| Nd$^{3+}$ | 9011 | 714 |
| Pm$^{3+}$ | 12780 | 1375 |
| Sm$^{3+}$ | 13848 | 1866 |
| Eu$^{3+}$ | 16504 | 2158 |
| Gd$^{3+}$ | 22790 | 4165 |
| Tb$^{3+}$ | 15692 | 2661 |
| Dy$^{3+}$ | 13500 | 2216 |
| Ho$^{3+}$ | 12744 | 1374 |
| Er$^{3+}$ | 9024 | 960 |
| Tm$^{3+}$ | 6662 | 1361 |
| Yb$^{3+}$ | 2800 | 0 |
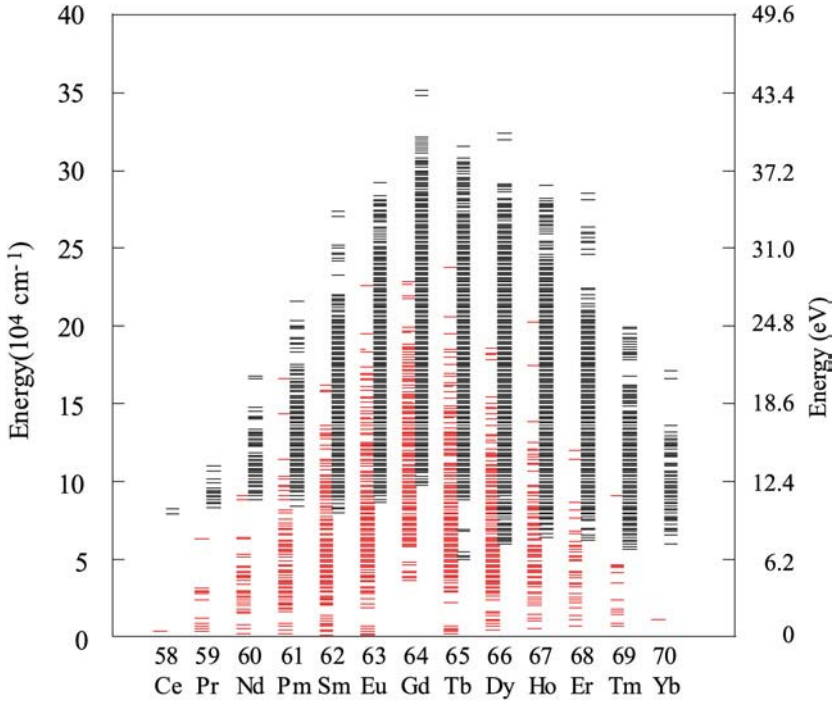
Fig. 6. Complete $4f^n$ (left) and $4f^{n-1}5d$ (right) energy level diagram for all trivalent RE ions.

between the two completely different computational approaches can be considered as a strong basis for highly reliable theoretical analysis.

### 4.1.3. *Multiplets in $4f^n$ and $4f^{n-1}5d$ configurations*

Energy level calculations for $4f^n$ and $4f^{n-1}5d$ electron configurations for all trivalent RE ions have been performed using fully relativistic first-principles many-electron method. The calculated energy levels are shown in fig. 6, which is a complete $4f^n$ and $4f^{n-1}5d$ energy level diagram for trivalent RE ions and can be used in an analysis of high-lying $4f^n \rightarrow 4f^n$ and $4f^n \rightarrow 4f^{n-1}5d$ transitions. The obtained eigenfunctions can be used for the calculation of oscillator strength of electric dipole transitions in absorption spectra, which will be presented below.

### 4.2. *Calculations of trivalent RE ions in LiYF$_4$*

### 4.2.1. *Model clusters for trivalent RE ions in LiYF$_4$*

The crystal structure of LiYF$_4$ (YLF) is shown in fig. 7 (Goryunov and Popov, 1992). The space group is I4$_1$/a, the crystal system is tetragonal and the lattice constants are $a = 5.171$ Å and $c = 10.748$ Å. Considering the ionic radii, valency and charge compensation, trivalent
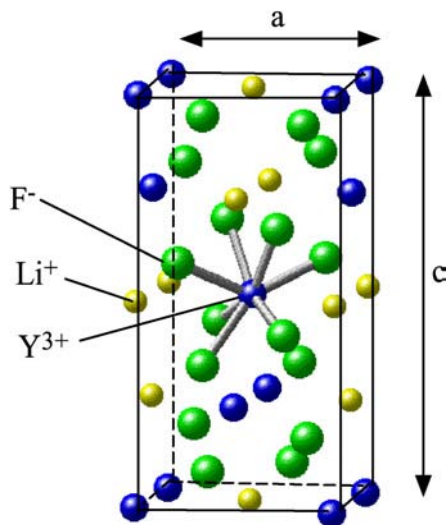
Fig. 7.  Crystal structure of $LiYF_4$.
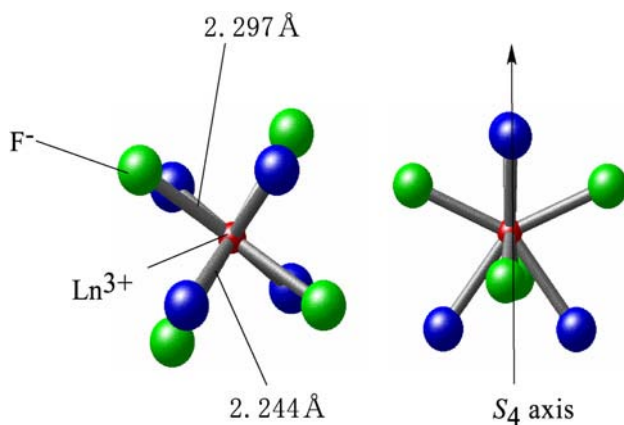


Fig. 8.  Model cluster for trivalent RE ($Ln^{3+}$) in $LiYF_4$.

RE ions ($Ln^{3+}$) are expected to substitute for $Y^{3+}$ ions. Therefore, a model cluster consisting of $Ln^{3+}$ ion coordinated with eight fluorine ions was constructed (fig. 8). The point group of the Y site is $S_4$ and the Y–F bond lengths are 2.247 Å for four fluorine ions and 2.299 Å for another four. The lattice relaxation by the substitution of $Ln^{3+}$ was not considered. In order to take into account the effects of the surroundings of the model cluster, an effective Madelung potential was considered by locating several thousand point charges at atomic sites outside

Table 5
Direct products for $S_4$ point group (Bethe symbols)

| $i$ | $j$ | | | | | | | |
|---|---|---|---|---|---|---|---|---|
| | $\Gamma_1$ | $\Gamma_2$ | $\Gamma_3$ | $\Gamma_4$ | $\Gamma_5$ | $\Gamma_6$ | $\Gamma_7$ | $\Gamma_8$ |
| $\Gamma_1$ | $\Gamma_1$ | $\Gamma_2$ | $\Gamma_3$ | $\Gamma_4$ | $\Gamma_5$ | $\Gamma_6$ | $\Gamma_7$ | $\Gamma_8$ |
| $\Gamma_2$ | $\Gamma_2$ | $\Gamma_1$ | $\Gamma_4$ | $\Gamma_3$ | $\Gamma_7$ | $\Gamma_8$ | $\Gamma_5$ | $\Gamma_6$ |
| $\Gamma_3$ | $\Gamma_3$ | $\Gamma_4$ | $\Gamma_2$ | $\Gamma_1$ | $\Gamma_8$ | $\Gamma_5$ | $\Gamma_6$ | $\Gamma_7$ |
| $\Gamma_4$ | $\Gamma_4$ | $\Gamma_3$ | $\Gamma_1$ | $\Gamma_2$ | $\Gamma_6$ | $\Gamma_7$ | $\Gamma_8$ | $\Gamma_5$ |
| $\Gamma_5$ | $\Gamma_5$ | $\Gamma_7$ | $\Gamma_8$ | $\Gamma_6$ | $\Gamma_3$ | $\Gamma_1$ | $\Gamma_4$ | $\Gamma_2$ |
| $\Gamma_6$ | $\Gamma_6$ | $\Gamma_8$ | $\Gamma_5$ | $\Gamma_7$ | $\Gamma_1$ | $\Gamma_4$ | $\Gamma_2$ | $\Gamma_3$ |
| $\Gamma_7$ | $\Gamma_7$ | $\Gamma_6$ | $\Gamma_6$ | $\Gamma_8$ | $\Gamma_4$ | $\Gamma_2$ | $\Gamma_3$ | $\Gamma_1$ |
| $\Gamma_8$ | $\Gamma_8$ | $\Gamma_5$ | $\Gamma_7$ | $\Gamma_5$ | $\Gamma_2$ | $\Gamma_3$ | $\Gamma_1$ | $\Gamma_4$ |

Table 6
Bethe symbol and Mulliken symbol for the irreducible representation of $S_4$ point group

| Bethe | $\Gamma_1$ | $\Gamma_2$ | $\Gamma_3, \Gamma_4$ | $\Gamma_5, \Gamma_6$ | $\Gamma_7, \Gamma_8$ |
|---|---|---|---|---|---|
| Mulliken | A | B | E | $E_{1/2}$ | $E_{3/2}$ |

the cluster. The number of the sampling points was 100 000 and the atomic orbitals used for the relativistic DV-X$\alpha$ calculation were from 1s to 6p for Ln and from 1s to 2p for F.

### 4.2.2. Irreducible representations in $S_4$ symmetry

When a molecule has a certain point symmetry, MOs or many-electron wave functions can be classified in general into the irreducible representations of the corresponding point group. When spin–orbit coupling is taken into account, double groups should be considered. The irreducible representations specify the transformations of the wave functions under a certain symmetry operation. In the $S_4$ symmetry, each MO corresponds to one of irreducible representations denoted by $\Gamma_1$–$\Gamma_8$ (Bethe symbols), where the pairs ($\Gamma_3$, $\Gamma_4$), ($\Gamma_5$, $\Gamma_6$), and ($\Gamma_7$, $\Gamma_8$) are degenerate, respectively. For one-electron wave functions (MOs) only the $\Gamma_5$–$\Gamma_8$ representations (double group representations) are allowed. The irreducible representations of many-electron wave functions can be easily known from direct products in table 5. In the case of two-electron system such as $Pr^{3+}$, the many-electron wave functions correspond to one of the direct product, ($\Gamma_i \times \Gamma_j$), where $i, j = 5, 6, 7, 8$. The resultant two-electron wave functions correspond to $\Gamma_1$–$\Gamma_4$ as shown in the bottom right part of the direct product table. Similarly, a three-electron system such as $Nd^{3+}$, considering the direct product between the two-electron wave functions and one-electron MO, are represented as the direct product, $\Gamma_i \times \Gamma_j$, where $i = 1, 2, 3, 4$ and $j = 5, 6, 7, 8$. Therefore, only $\Gamma_5$–$\Gamma_8$ are allowed as shown in the upper right part of the direct product table.

In our calculations, the Mulliken symbols are used for MO, and Bethe symbols are used for many-electron wave functions. The correspondence between Bethe and Mulliken symbols is shown in table 6.

Table 7
Selection rules of the electric-dipole transition under $S_4$ symmetry

|  | $\Gamma_1$ | $\Gamma_2$ | $\Gamma_{3,4}$ |  | $\Gamma_{5,6}$ | $\Gamma_{7,8}$ |
|---|---|---|---|---|---|---|
| $\Gamma_1$ | × | $\pi$ | $\sigma$ | $\Gamma_{5,6}$ | $\sigma$ | $\sigma, \pi$ |
| $\Gamma_2$ | $\pi$ | × | $\sigma$ | $\Gamma_{7,8}$ | $\sigma, \pi$ | $\sigma$ |
| $\Gamma_{3,4}$ | $\sigma$ | $\sigma$ | $\pi$ |  |  |  |
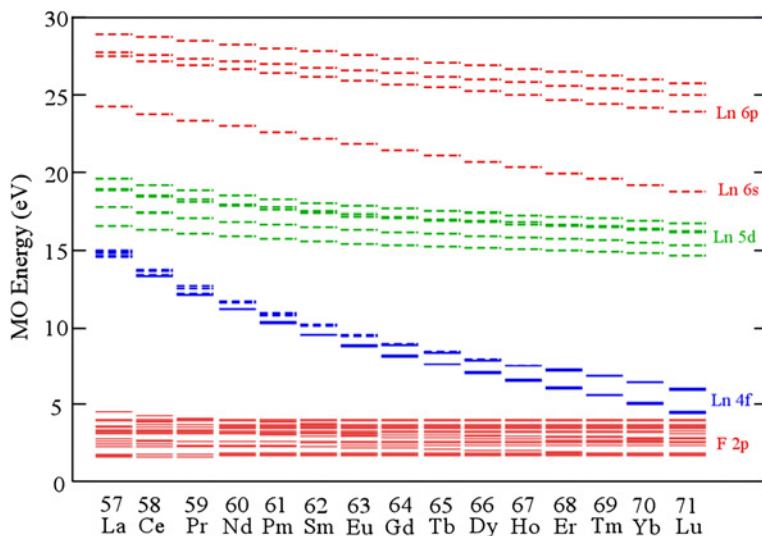


Fig. 9. Calculated MO energy levels for trivalent RE ions in YLF.

### 4.2.3. Selection rules

The electric-dipole transition is determined by the symmetry properties of the initial-state and the final-state wave functions, i.e., their irreducible representations. In the case of electric-dipole transitions, the selection rules shown in table 7 hold true ($\pi$ and $\sigma$ represent the polarizations where the electric field vector of the incident light is parallel and perpendicular to the crystal $c$ axis, respectively. Forbidden transitions are denoted by the "×" sign). In the relativistic DVME method, the Slater determinants are symmetrized according to the Clebsch–Gordan coefficients and the symmetry-adapted Slater determinants are used as the basis functions. Therefore, the diagonalization of the many-electron Dirac Hamiltonian is performed separately for each irreducible representation.

### 4.2.4. Molecular orbital energy levels

The MO energy levels for all RE$^{3+}$ ions in YLF are shown in fig. 9. Each MO is labeled with the name of the most dominant AO. The valence states mainly consist of F-2p orbitals while the conduction band is not reproduced because of the lack of the surrounding cations in the

Table 8
Compositions (%) of the MOs of $CeF_8^{5-}$ cluster

| Energy (eV) | Ce $4f_{5/2}$ | Ce $4f_{7/2}$ | Ce 5d | F 2s and 2p |
|---|---|---|---|---|
| 5.143 | 97.9 | 1.3 | 0.0 | 0.7 |
| 5.169 | 98.4 | 0.2 | 0.5 | 0.8 |
| 5.213 | 93.0 | 5.5 | 0.6 | 0.9 |
| 5.478 | 1.8 | 97.1 | 0.3 | 0.7 |
| 5.486 | 0.0 | 98.9 | 0.2 | 0.7 |
| 5.502 | 0.2 | 98.4 | 0.5 | 0.8 |
| 5.605 | 4.5 | 92.7 | 1.5 | 1.3 |
| 8.159 | 0.0 | 0.0 | 97.0 | 3.0 |
| 9.233 | 0.4 | 1.0 | 93.1 | 5.1 |
| 10.258 | 0.3 | 0.3 | 92.9 | 6.3 |
| 10.354 | 0.2 | 0.4 | 93.0 | 6.3 |
| 10.956 | 0.2 | 0.2 | 92.6 | 6.8 |

present model clusters. The RE 4f orbitals are split due to the spin–orbit interactions and the effects of the crystal field are seen only in the small Stark splittings. On the other hand, RE 5d orbitals split significantly due to the crystal field. Although the RE 5d states can be classified into $\Gamma_{5,6}$ or $\Gamma_{7,8}$, here we name the energy levels as *a–e* in the order of increasing energy. The splittings of RE 5d state into four groups of levels, *a*, *b*, (*c* and *d*), and *e* are due to the crystal field of $S_4$ symmetry while the small splitting between *c* and *d* is due to the spin–orbit interaction. The energy separation between RE 4f and RE 5d states increases as the atomic number increases.

### 4.2.5. *Analysis of MO's compositions for the $CeF_8^{5-}$ cluster*
The analysis of the MO's compositions was performed to investigate the chemical bonding effects for $Ce^{3+}$ in YLF. The composition of each AO with dominant 4f or 5d character for the $CeF_8^{5-}$ cluster is shown in table 8. Concerning the seven levels in the energy range 5.143–5.605 eV, there is quite small mixing between Ce $4f_{5/2}$ and Ce $4f_{7/2}$ states. The composition of Ce 4f is 97.2–99.2% in these MOs and the composition of F 2s and 2p is 0.7–1.3%. These results indicate strong localization of the Ce 4f states. The five levels in the energy range 8.159–10.956 eV correspond to MOs with dominant Ce 5d character. The proportion of the Ce 5d orbital is 92.6–97.0%, while the contribution of F 2s and 2p is 3.0–6.8% in this case. These results indicate a stronger interaction with the ligand orbitals for the Ce 5d orbitals than for the Ce 4f orbitals. Similar analysis has been performed for other $RE^{3+}$ ions in YLF. The compositions of the MOs are almost the same as for $Ce^{3+}$ in YLF.

### 4.2.6. *Multiplet energy levels for $4f^n$ and $4f^{n-1}5d$ configurations*
The results of the relativistic DVME calculations are presented in fig. 10, where the energy levels of $4f^n$ and $4f^{n-1}5d$ configurations for each element are shown on the left and right, respectively. In fig. 10, the lengths of the lines denote the contribution of each configuration. A short line on the left column indicates a partial contribution of the $4f^n$ configuration and
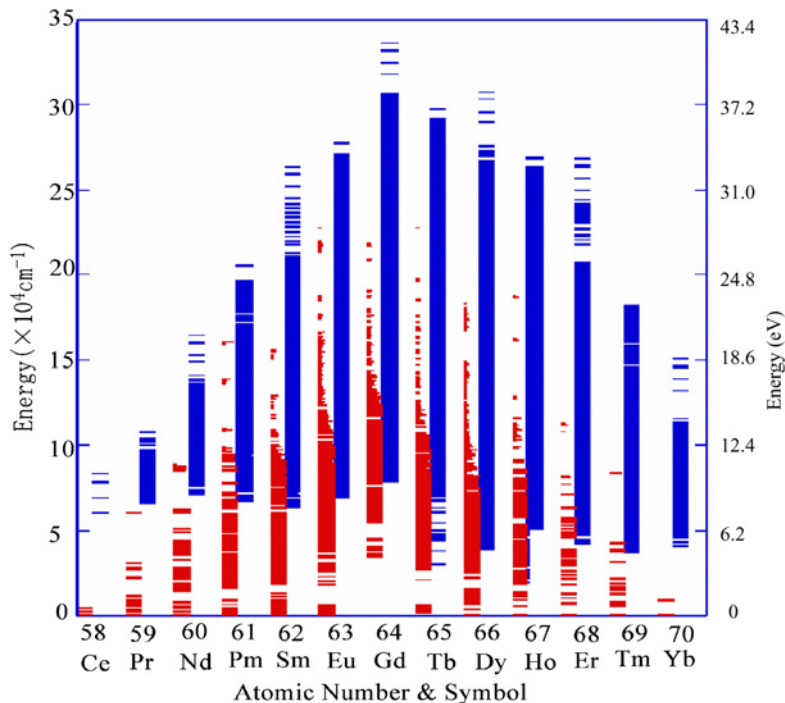
Fig. 10. Complete $4f^n$ and $4f^{n-1}5d$ energy level diagram for all trivalent RE ions in YLF obtained by the first-principles relativistic CI calculations. For each element, the compositions of the $4f^n$ configurations are shown on the left and those of $4f^{n-1}5d$ configurations are shown on the right, respectively. See text for further explanations.

there should be a corresponding short line representing a remaining partial contribution of the $4f^{n-1}5d$ configuration to the state on the right column. Although the short lines on the right columns are buried in a band formed with the full-length lines, we can estimate their contribution from the composition of $4f^n$ configuration. One can note from fig. 10 that, in the case of ions in YLF, there exists a significant mixture between $4f^n$ and $4f^{n-1}5d$ configurations, which is absent in the case of isolated ions due to the difference in parity. The origin of this mixture is the lack of gerade/ungerade representations due to the absence of center of symmetry in the $S_4$ point group. The calculated energy levels are overestimated typically by 20–30%. The major reason for this discrepancy is probably underestimation of electron correlations since only the states mainly composed of RE 4f or RE 5d characters were considered in the CI calculations due to our computational limitations. The inclusion of the other orbitals such as the states mainly composed of F 2p character into the CI active space is expected to reduce this overestimation.

Although the energy levels are overestimated in the first-principles method, if we take into account the element-specific scaling factor estimated from the free ion calculations (Ogasawara et al., 2004, 2005a, 2005b), the results of the first-principles method agree well with
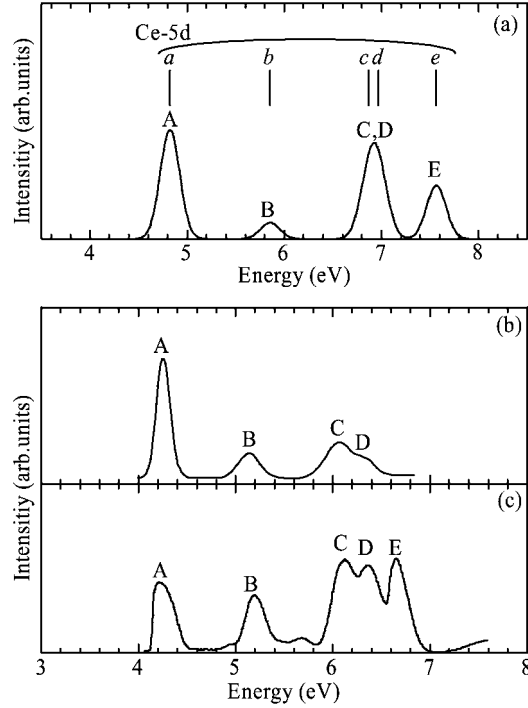
Fig. 11. The absorption spectra of Ce$^{3+}$:LiYF$_4$: (a) theoretical spectra calculated for the CeF$_8^{5-}$ cluster; (b) experimental absorption spectrum (Ehrlich et al., 1979); (c) experimental excitation spectrum (Reid et al., 2000).

those of the semiempirical method and also with the experimental data such as the Dieke diagram. In our work, despite the overestimation of the calculated energy levels, the *relative* energy level intervals are reproduced fairly well, which gives an opportunity for a first-principles prediction of the absorption spectra.

### 4.2.7. *Ce$^{3+}$:YLF*

4.2.7.1. *4f → 5d transition spectrum* In order to reproduce the absorption spectrum, the calculation was performed in the Slater's transition state where 0.5 electron was removed from the lowest Ce 4f$_{5/2}$ level and added to the Ce 5d$_a$ level. The theoretical spectrum was obtained by calculating the oscillator strengths for the transitions from the lowest Ce 4f$_{5/2}$ level to all unoccupied levels and convoluting these values with a Gaussian function with 0.2-eV full-width at half maximum (FWHM).

The theoretical absorption spectrum is compared with the experimental absorption spectrum (Ehrlich et al., 1979) and the experimental excitation spectrum (Reid et al., 2000) in fig. 11. The energy positions of the Ce 5d$_{a-e}$ levels relative to the lowest Ce 4f$_{5/2}$ level are 4.82, 5.85, 6.87, 6.97, 7.56 eV, respectively. Comparing with the experimental absorption spectrum, the relative energy positions and the relative intensity of peak B with respect to

Table 9
Ce–F bond lengths for the relaxed $CeF_8^{5-}$ clusters

| Relaxation rate | Ce–F bond length (1) (Å) | Ce–F bond length (2) (Å) |
|:---:|:---:|:---:|
| 0% | 2.247 | 2.299 |
| +2% | 2.292 | 2.345 |
| +4% | 2.337 | 2.391 |

peak A is well reproduced by the calculation. In higher energy region in addition to peaks C and D, peak E is also observed. Although the positions of the higher energy peaks relative to the lower energy peaks A and B are reproduced to some extent, only two peaks are reproduced in the higher energy region in the theoretical spectrum.

4.2.7.2. *Effects of lattice relaxation*  The overall spectral features are reproduced without any empirical parameters except for the fine structures around peaks C, D, E. However, the separation of the bands is somewhat overestimated. One of the reasons for this overestimation is ignorance of the lattice relaxation effects due to the substitution of $Ce^{3+}$ for $Y^{3+}$. Combes et al. (1997) suggested that the origin of the peaks C, D is a crystal field splitting due to the lowering of the symmetry originating from the substitution of $Ce^{3+}$ for $Y^{3+}$.

The ionic radii of $Ce^{3+}$ and $Y^{3+}$ are 1.143 Å and 1.019 Å, respectively (Shannon, 1976). Therefore, Ce–F bond lengths are expected to be 0.134 Å longer than Y–F bond lengths. Thus we constructed the tentative relaxed $CeF_8^{5-}$ clusters where the Ce–F bond lengths are extended by 2% or 4%. The corresponding bond lengths with this relaxation rate are listed in table 9. An extension by 6% would approximately correspond to the difference in ionic radii. The number of sampling points used for the calculations of these models is 50 000.

The theoretical spectra considering the lattice relaxation effects are shown in fig. 12. The separation between peaks decreases upon expansion of the bond lengths. For example, the separation between peaks A and B is 1.03 eV, 0.87 eV, 0.75 eV for 0%, +2%, +4% relaxed models, respectively. Comparing with the experimental spectrum, the multiplet energy splitting is reproduced best of all for the +2% relaxed model. Contrary to the peak positions, the peak intensities are not significantly influenced by the bonds lengthening.

4.2.8. *Pr:YLF*

4.2.8.1. *$4f^2$ energy levels for isolated $Pr^{3+}$ and $Pr^{3+}$ in YLF*  The theoretical multiplet energy levels of the isolated $Pr^{3+}$ ion are shown in fig. 13. 100 000 sampling points were used for the calculation. The compositions of the $(4f_{5/2})^2$, $(4f_{5/2})(4f_{7/2})$, and $(4f_{7/2})^2$ configurations were analyzed for each level. As shown in the figure, each term has a characteristic composition of electron configuration. Such information is quite important to identify the terms of the RE ions in crystals, as will be shown later.

In order to analyze the $4f \rightarrow 4f$ transitions of $Pr^{3+}$ in YLF, we first consider only MOs with dominant Pr 4f character among the MOs obtained in section 4.2.4 for the $PrF_8^{5-}$ cluster. Therefore, the number of possible electron configurations (number of the Slater determinants) is 91 as shown in table 1.
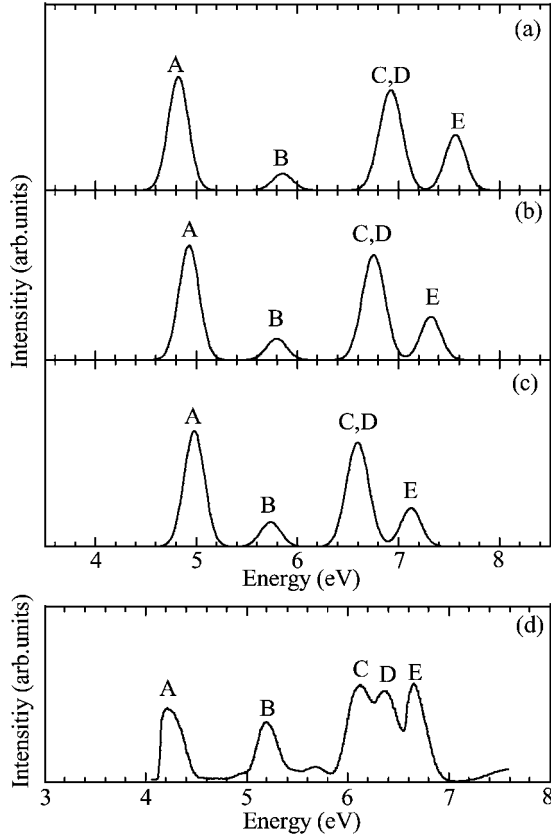
Fig. 12. Variation of the theoretical absorption spectrum of $Ce^{3+}$ in YLF by the lattice relaxation: (a) theoretical spectrum (100%); (b) theoretical spectrum (102%); (c) theoretical spectrum (104%); (d) experimental excitation spectrum (Reid et al., 2000).

   The multiplet energy levels calculated using the $PrF_8^{5-}$ cluster are shown in fig. 14. The experimental energy levels of the $4f^2$ configuration are shown for comparison (Faucher and Moune, 1997). Considering the degeneracy, there are 70 energy levels corresponding to the $4f^2$ configuration. Among them, 52 energy levels are experimentally identified. All theoretical energy levels except $^1S_0$ at 7.65 eV are shown in the figure. Comparing the theoretical energy levels with the experimental ones, the theoretical values are generally overestimated by about 30% as we have seen in section 0. The separation between $^3H_4$, $^3H_5$, $^3H_6$ is also overestimated which indicates that the spin–orbit interactions are also overestimated. However, theoretical energy levels consistently correspond to the experimental energy levels and the overall multiplet structure is reproduced. Here we analyze the many-electron wave functions without introducing any adjustable parameters.
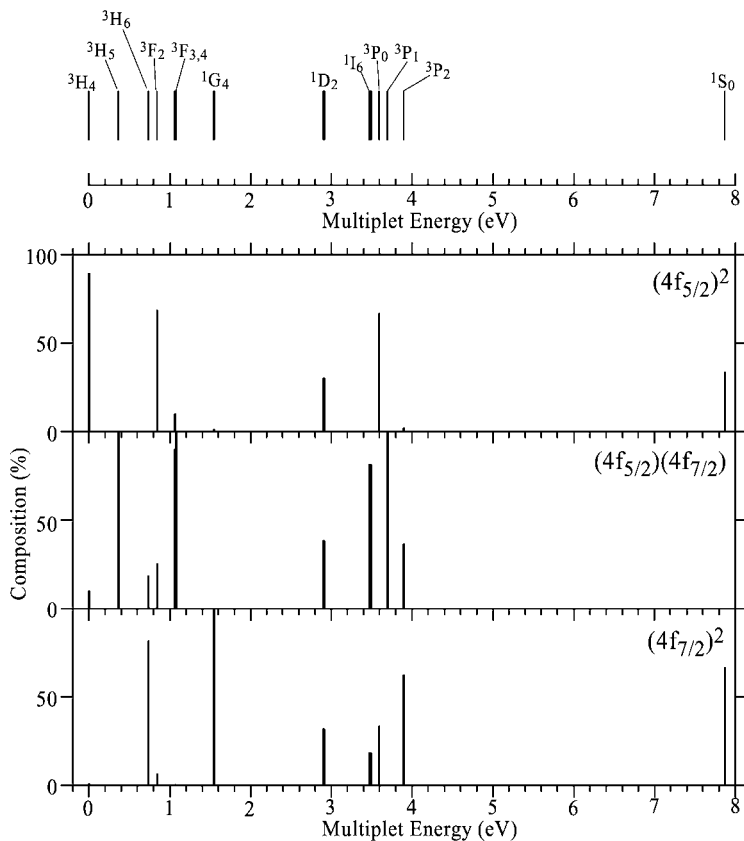
Fig. 13. Theoretical multiplet energy levels and their configuration compositions for isolated $Pr^{3+}$ ion.

Calculation of the $4f^2$ energy levels clearly show the Stark splitting of each term. The compositions of each electron configuration obtained by configuration analysis are shown under the energy levels. As shown in the figure, the configuration compositions for $Pr^{3+}$ in YLF are quite consistent with those of isolated $Pr^{3+}$. Although the terms corresponding to $^1I_6$, $^3P_0$ are energetically overlapping and hard to discriminate, the state which contains about 50% of the configuration was identified as $^3P_0$ by comparison with the calculation of the isolated $Pr^{3+}$ ion and the analysis reported by Laroche et al. (2000).

The theoretical energy values for $^3H_4$, $^1G_4$, $^1D_2$ are shown in tables 10–12 together with the observed values and the values obtained by semiempirical calculations based on crystal field theory (Faucher and Moune, 1997). $\Gamma$'s are the irreducible representations in $S_4$ symmetry. The possible irreducible representations are $\Gamma_1$, $\Gamma_2$, $\Gamma_3$, $\Gamma_4$ for a two-electron system where $\Gamma_3$ and $\Gamma_4$ are degenerate. The theory overestimates Stark splittings of the $^3H_4$ level, compared to the experimental values. One reason for this is the neglect of lattice relaxation
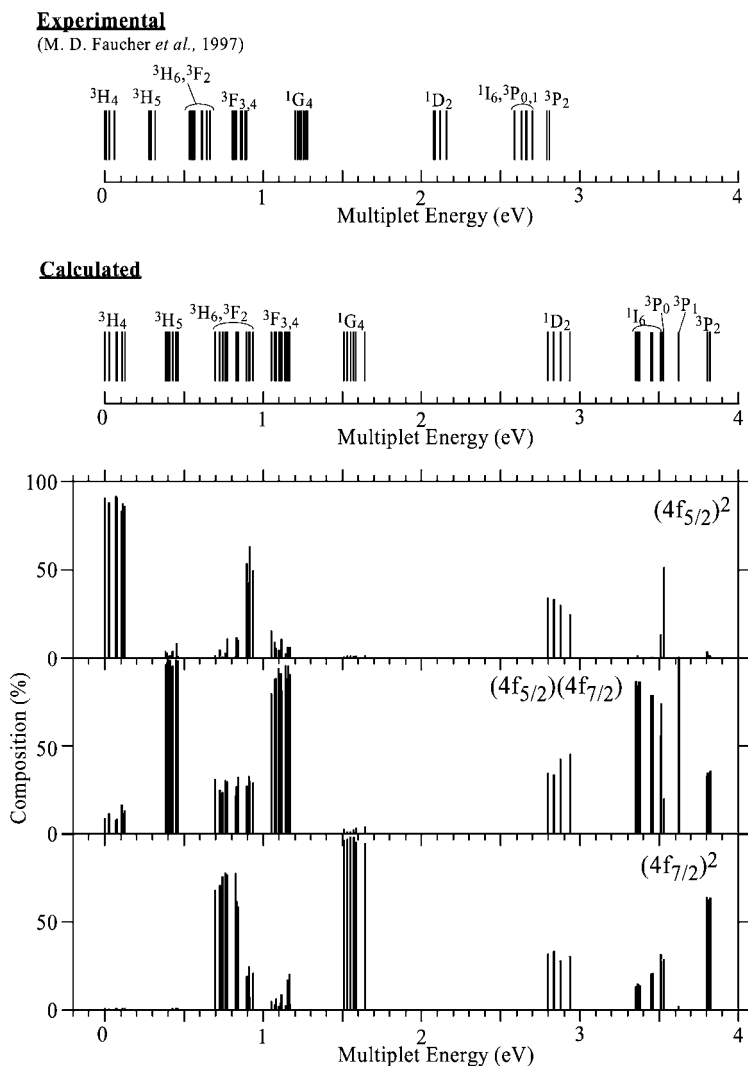
Fig. 14.  Theoretical multiplet energy levels and their configuration compositions for the $PrF_8^{5-}$ cluster.

effects. However, comparing the three lower-lying energy levels, the order of the irreducible representations is consistent with the experimental data. Moreover, the order of all levels is consistent with one predicted by the crystal field theory. Although the energy level splittings are somewhat overestimated, the basic multiplet structure is reproduced without any empirical parameter. In the case of $^1G_4$, the order of irreducible representations in the values obtained by crystal field theory is not consistent with the experimental values, which means that there

Table 10
Energies of the $^3H_4$ multiplet

| Level $^3H_4$ | | | | | |
|---|---|---|---|---|---|
| Expt. | | Calc. (CFT) | | Calc. (DVME) | |
| $\Gamma$ | Energy (eV) | $\Gamma$ | Energy (eV) | $\Gamma$ | Energy (eV) |
| 2 | 0 | 2 | 0 | 2 | 0 |
| 3,4 | 0.0098 | 3,4 | 0.0097 | 3,4 | 0.0272 |
| 1 | 0.0273 | 1 | 0.0289 | 1 | 0.0709 |
| 1 | | 1 | 0.0291 | 1 | 0.0769 |
| 1 | | 1 | 0.0595 | 1 | 0.106 |
| 3,4 | 0.0615 | 3,4 | 0.0606 | 3,4 | 0.110 |
| 2 | | 2 | 0.0631 | 2 | 0.126 |

Table 11
Energies of the $^1G_4$ multiplet

| Level $^1G_4$ | | | | | |
|---|---|---|---|---|---|
| Expt. | | Calc. (CFT) | | Calc. (DVME) | |
| $\Gamma$ | Energy (eV) | $\Gamma$ | Energy (eV) | $\Gamma$ | Energy (eV) |
| 1 | 1.203 | 1 | 1.200 | 1 | 1.510 |
| 3,4 | 1.219 | 3,4 | 1.218 | 3,4 | 1.531 |
| 2 | 1.231 | 2 | 1.232 | 2 | 1.553 |
| 2 | 1.241 | 1 | 1.242 | 1 | 1.571 |
| 3,4 | 1.254 | 2 | 1.242 | 2 | 1.571 |
| 1 | 1.267 | 3,4 | 1.251 | 3,4 | 1.587 |
| 1 | 1.279 | 1 | 1.285 | 1 | 1.642 |

Table 12
Energies of the $^1D_2$ multiplet

| Level $^1D_2$ | | | | | |
|---|---|---|---|---|---|
| Expt. | | Calc. (CFT) | | Calc. (DVME) | |
| $\Gamma$ | Energy (eV) | $\Gamma$ | Energy (eV) | $\Gamma$ | Energy (eV) |
| 2 | 2.075 | 2 | 2.076 | 2 | 2.796 |
| 1 | 2.084 | 1 | 2.081 | 1 | 2.835 |
| 3,4 | 2.118 | 3,4 | 2.120 | 3,4 | 2.876 |
| 2 | 2.158 | 2 | 2.155 | 2 | 2.937 |

are still energy levels not fully understood even in 4f $\rightarrow$ 4f transitions. The calculated values obtained by the relativistic DVME method are also inconsistent with the experimental values but consistent with the values obtained by semiempirical methods. The order of the irreducible representations in $^1D_2$ is consistent with both the experimental and the semiempirical values.

4.2.8.2. *$4f^2 \rightarrow 4f5d$ transition spectrum* In order to analyze the 4f → 5d transitions, multiplet structures for the $4f^2$ and 4f5d configurations were calculated by the relativistic DVME method. The MOs mainly consisting of Pr 4f or Pr 5d states obtained in section 4.2.4 were used in the Slater determinants. The number of states is 91 for the $4f^2$ configuration and 140 for the 4f5d configuration leading to a total of 231 levels as shown in table 1.

The calculated multiplet energy levels and configuration compositions within each multiplet state are shown in fig. 10. All levels within the range 0–7.65 eV correspond to the $4f^2$ configuration and all levels with higher energies correspond to 4f5d configuration. The mixing between the $4f^2$ configuration and the 4f5d configuration is almost negligible, which means there is practically no interaction between the $4f^2$ and 4f5d configurations.

The theoretical ground-state absorption (GSA) spectrum is compared with the experimental spectra in fig. 15. Although the host crystal for the experimental spectrum is $LiLuF_4$, it is still comparable to the theoretical spectrum for YLF, since the crystal structure of $LiLuF_4$ is the same as that of $LiYF_4$ with slightly different lattice parameters. Since the experiment was performed at the room temperature, not only the lowest level (at 0 eV) of $^3H_4$ but also the first excited state at 0.0272 eV were considered as the initial states of the transitions because of thermal population of the latter. The theoretical spectrum was calculated by convoluting the obtained oscillator strengths by a Gaussian functions with 0.30 eV FWHM. It is shown on top of fig. 15 where the thin line represents the transitions for 0 eV ($\Gamma_2$) → 4f5d while the thick line represents transitions for 0.0272 eV ($\Gamma_{3,4}$) → 4f5d. The energy levels for the 4f5d configuration are also shown above the spectrum. The spectra from two different initial states are almost the same, which indicates small temperature dependence of the spectrum. Comparing with the experimental spectrum, peaks $A_1$, $B_1$, C, E are seen both in the observed and the theoretical spectra and relative positions and intensities of these peaks are reproduced. The spectrum shown in the bottom panel is the experimental excitation spectrum. Although the calculated intensities cannot be directly compared with the excitation spectrum, the positions of the peaks $A_1$ and $A_2$ are reproduced in the theoretical spectrum corresponding to absorption from the lowest state (thin line). The peak between the peaks $A_1$ and $A_2$ could not be reproduced in the theoretical spectrum.

In order to clarify the origins of the peaks, we performed a configuration analysis of the many-electron wave functions. The results in the energy range around peaks A and B are shown in fig. 16 while those around peaks C, E are shown in fig. 17. The oscillator strengths, the absorption spectrum for the transitions from the lowest state ($\Gamma_2$) and the configuration compositions for each level are shown in the figure. In fig. 16, the configurations $(4f)(5d_{c,d,e})$ are omitted since contribution from these configurations is negligible. For the same reason, $(4f)(5d_{a,b})$ configurations are omitted in fig. 17. The levels with oscillator strengths greater than $1.0 \times 10^{-3}$ are shown in solid (red in the web version) lines.

The peak $A_1$ corresponds to transitions to the levels at 8.253 eV ($\Gamma_{3,4}$) and 8.261 eV ($\Gamma_1$) and the results of the configuration analysis indicate that the composition of $(4f_{5/2})(5d_a)$ configuration is greater than 90%. On the other hand, peak $A_2$ corresponds to transitions to the three levels at 8.595 eV ($\Gamma_{3,4}$), 8.679 eV ($\Gamma_{3,4}$), and 8.735 eV ($\Gamma_1$). The main component in this peak is $(4f_{5/2})(5d_b)$ with slight contribution of $(4f_{5/2})(5d_a)$. These results indicate that the splitting between peak $A_1$ and $A_2$ originates from the spin–orbit splitting of the Pr 4f levels.
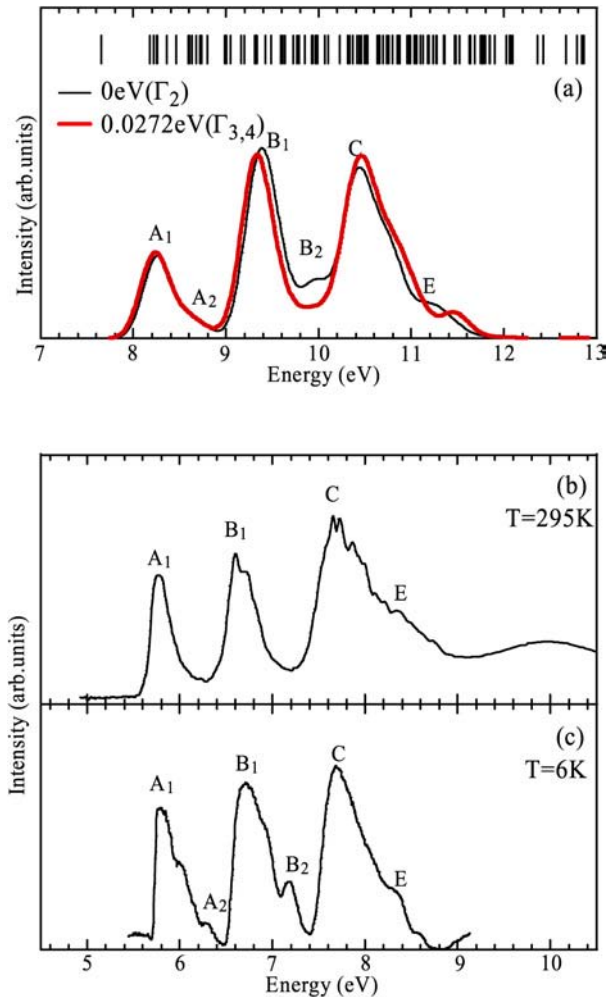
Fig. 15. Ground state absorption (GSA) spectra for $Pr^{3+}$:LiYF$_4$: (a) theoretical spectra for 0 eV ($\Gamma_2$) $\rightarrow$ 4f5d and 0.0272 eV ($\Gamma_{3,4}$) $\rightarrow$ 4f5d; (b) experimental absorption spectrum for $Pr^{3+}$:LiLuF$_4$ (Sarantopoulou et al., 1994); (c) experimental excitation spectrum for $Pr^{3+}$:LiYF$_4$ (Reid et al., 2000).

Similarly, peak B$_1$ corresponds to transitions to the $(4f_{5/2})(5d_b)$ configuration, while peak B$_2$ corresponds to transitions to the $(4f_{7/2})(5d_b)$ configuration. These results also indicate that the splitting between peak B$_1$ and B$_2$ originates from the spin–orbit splitting of Pr 4f levels. Compared with peaks A and B, the compositions of peaks C and E are complicated. Peak C corresponds to transitions to the mixed states of the $(4f_{5/2})(5d_c)$, $(4f_{7/2})(5d_c)$, $(4f_{5/2})(5d_d)$, and $(4f_{7/2})(5d_d)$ configurations which simply corresponds to the transitions from 4f states to
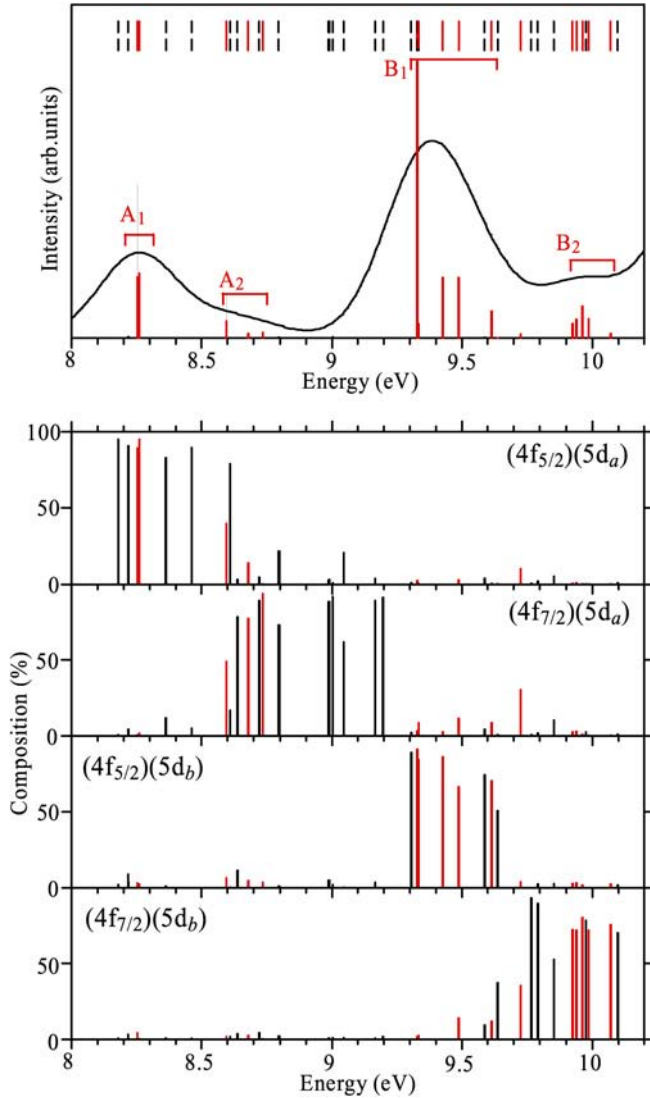
Fig. 16.  Configuration analysis of 4f5d multiplet energy levels for $Pr^{3+}$:LiYF$_4$.

Pr $5d_c$,$5d_d$ states in the one-electron picture. Since the main contribution to peak E are the $(4f_{7/2})(5d_c)$, $(4f_{5/2})(5d_d)$, $(4f_{7/2})(5d_d)$, and $(4f_{5/2})(5d_e)$ configurations, it can be represented as transitions from Pr 4f states to Pr $5d_c$,$5d_d$,$5d_e$ states. In the whole spectra, the results of the configuration analysis clearly indicate that the separations among peaks A, B, C are due to the crystal field splitting of Pr 5d levels.
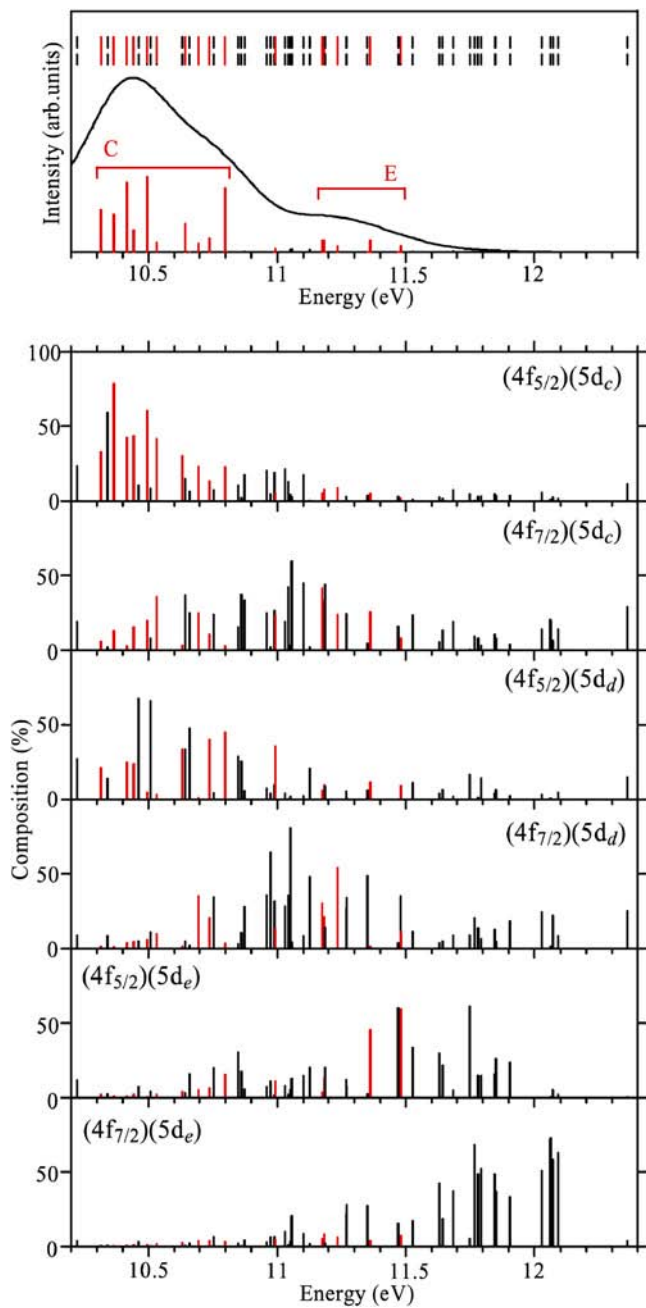
Fig. 17. Configuration analysis of 4f5d multiplet energy levels for $Pr^{3+}$:LiYF$_4$.
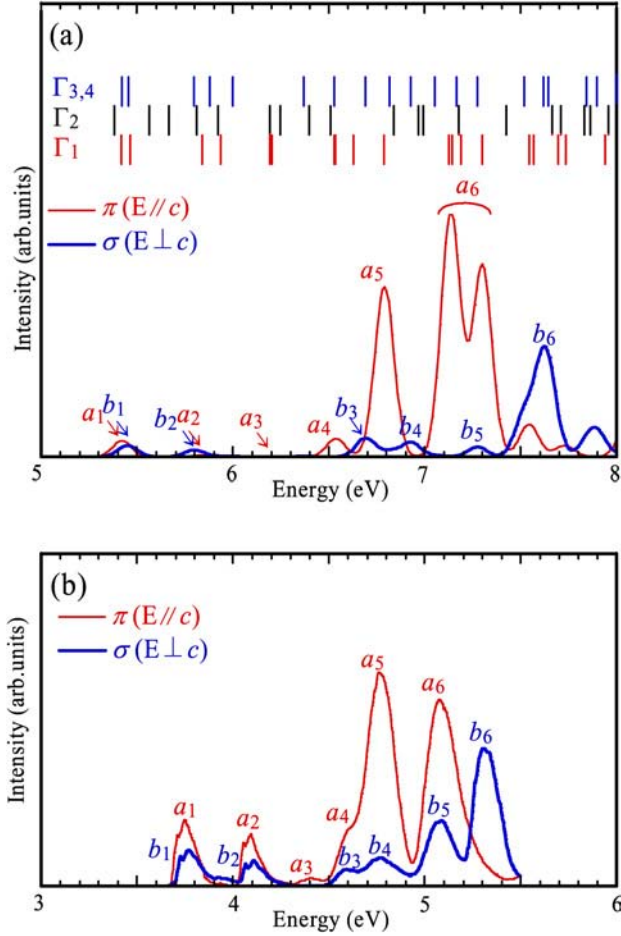
Fig. 18. ESA spectra from $^1D_2$ for $Pr^{3+}$:YLF: (a) theoretical spectra; (b) experimental spectra at $T = 8$ K (Laroche et al., 2000).

4.2.8.3. *$4f^2 \rightarrow 4f5d$ excited state absorption from $^1D_2$* The excited state absorption (ESA) spectra from $^1D_2$ state in the $4f^2$ configuration were also calculated and compared with the experimentally observed ESA spectra in fig. 18. The FWHM of the Gaussian function used for calculating these spectra was 0.10 eV. A two-step excitation using ESA is considered as a potential process for operation of solid-state lasers based on $4f \rightarrow 5d$ transitions pumped by well established light sources in the IR region. ESA can be also considered as an effective tool to investigate the energy level structures in the $4f^{n-1}5d$ configurations. Polarization dependence of these ESA spectra was also experimentally measured. Thus we calculated the spectra for both polarizations $\pi$ and $\sigma$ corresponding to the spectra for the electric field vector of the incident light parallel and perpendicular to the crystal *c*-axis, respectively.
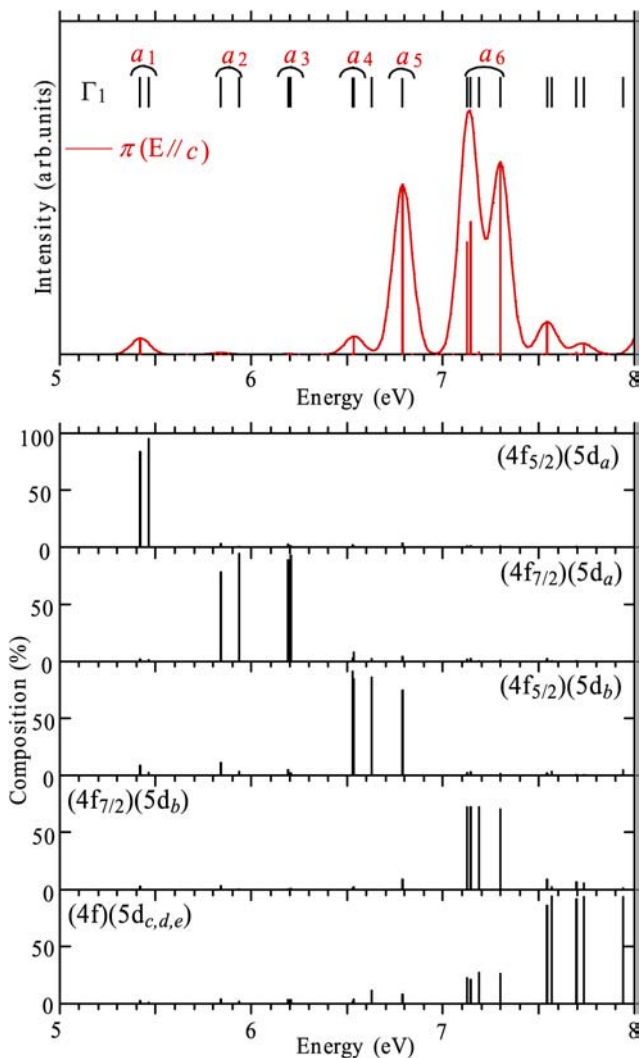
Fig. 19. ESA spectra with $\pi$ polarization (E//c) for $Pr^{3+}$:YLF and configuration analysis of $\Gamma_1$ levels.

Since the experimental ESA spectrum was taken at 8 K, only the lowest state at 2.798 eV ($\Gamma_2$) was taken as the initial state of the transitions. In the $\pi$ spectrum shown in thin (red in the web version) line, the six peaks $a_1$–$a_6$ were observed in the experimental spectrum. In the theoretical spectrum, these six peaks are reproduced and their relative positions and relative intensities are also consistent with the experimental spectrum.

In the experimental $\sigma$ spectrum, six peaks $b_1$–$b_6$ were also observed and they are reproduced in the theoretical spectrum shown in thick (blue in the web version) line. The overall
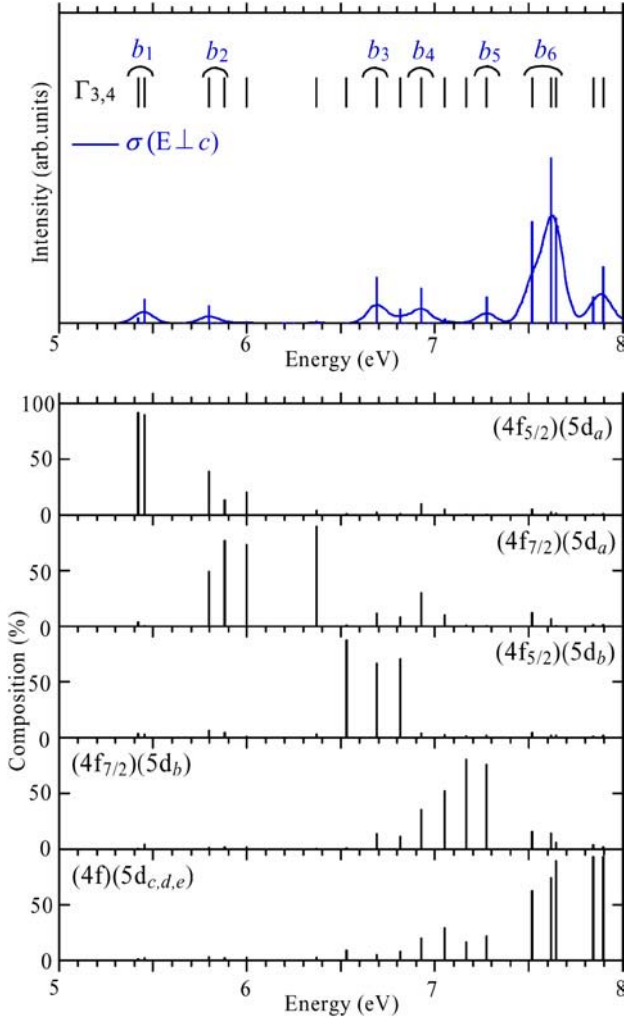
Fig. 20. ESA spectra with $\sigma$ polarization (E⊥c) for $Pr^{3+}$:YLF and configuration analysis of $\Gamma_{3,4}$ levels.

spectral features such as the relative positions and intensities of the peaks, and the polarization dependence are reproduced without using any empirical parameters. Since the lowest $^1D_2$ ($\Gamma_2$) state is the initial state of the transitions, the transitions to $\Gamma_1$ states correspond to the $\pi$ spectrum while the transitions to $\Gamma_{3,4}$ states correspond to the $\sigma$ spectrum. In order to investigate the origins of the peaks, a configuration analysis was performed in a similar way as for the GSA. The results are shown in figs. 19 and 20.

This analysis shows that band $a_1$ corresponds to $(4f_{5/2})(5d_a)$, peaks $a_2$ and $a_3$ correspond to $(4f_{7/2})(5d_a)$, $a_4$, $a_5$ to $(4f_{5/2})(5d_b)$, and $a_6$ to $(4f_{7/2})(5d_b)$. These results indicate that the

separation between peaks $a_1$ and $a_2$ originates from the spin–orbit splitting of the Pr 4f levels while the separation between the peaks $a_2$ and $a_3$ originates from both the spin–orbit splitting of Pr 4f levels and the crystal field splitting of the Pr 5d levels. The separation between peaks $a_4$, $a_5$ and peak $a_6$ also originates from the spin–orbit splitting of Pr 4f levels and the separation between peaks $a_1$, $a_2$, $a_3$ and peaks $a_4$, $a_5$, $a_6$ originates from the crystal field splittings of Pr 5d levels.

In the $\sigma$ spectrum, the effects of the configuration interaction is greater than in the $\pi$ spectrum Peak $b_1$ corresponds only to the $(4f_{5/2})(5d_a)$ configuration while peak $b_2$ corresponds to the $(4f_{7/2})(5d_a)$ configuration with strong mixing with $(4f_{5/2})(5d_a)$ configuration. Peak $b_3$ mainly corresponds to the $(4f_{5/2})(5d_b)$ configuration while peak $b_4$ corresponds to the $(4f_{7/2})(5d_a)$ and $(4f_{7/2})(5d_b)$ configurations with equal contributions. Peak $b_5$ mostly originates from transitions to the $(4f_{7/2})(5d_b)$ configuration. Peak $b_6$ originates from transitions to the $(4f_{5/2})(5d_{c,d,e})$ configurations, and is stronger than the other peaks. In the ESA spectra from the lowest state of $^1D_2$, transitions to $5d_a$ levels hardly contribute to the intensity while the transitions to $5d_b$ levels contribute to intensities only in the $\pi$ spectrum.

4.2.8.4. *$4f^2 \rightarrow 4f5d$ excited state absorption from $^3P_0$* The theoretical ESA spectrum from the $^3P_0$ state was also calculated and compared with the experimental spectrum in fig. 21. The $^3P_0$ level at 3.534 eV ($\Gamma_1$) was taken as the initial state for the transition. In the experimental $\pi$ spectrum shown in thin (red in the web version) line, four peaks $a_1$–$a_4$ were observed which were also reproduced in the theoretical ESA spectrum. In the experimental $\sigma$ spectrum shown in thick (blue in the web version) line, five peaks $b_1$–$b_6$ were observed and they are also reproduced in the theoretical spectrum. Comparing with the experimental spectrum, the intensity of peak $a_2$ with respect to peaks $a_1$ and $a_3$ is underestimated and the separations between peaks $a_1$, $a_2$, $a_3$ are overestimated. A similar trend can be seen for peaks $b_1$–$b_3$. However, the relative positions and intensities of peaks $a_4$, $b_4$, $b_5$, and $b_6$ in the higher energy region are reproduced. According to the selection rules, since the initial state is $^3P_0$ ($\Gamma_1$), the transitions to $\Gamma_2$ correspond to the $\pi$ spectrum, and the transitions to $\Gamma_{3,4}$ correspond to the $\sigma$ spectrum. In order to investigate the origins of the peaks, a configuration analysis was performed. The results are shown in figs. 22 and 23.

The peaks $a_1$, $a_2$ arise from the transitions to $(4f_{5/2})(5d_a)$ configuration, $a_3$ to $(4f_{7/2})(5d_a)$, $a_4$ to transitions to the mixed states of $(4f_{5/2})(5d_b)$ and $(4f_{7/2})(5d_b)$. Therefore, the difference between peaks $a_1$ and $a_2$ originates from the multiplet splitting within $(4f_{5/2})(5d_a)$ configuration, i.e., the interaction between the $4f_{5/2}$ electron and $5d_a$ electron, while the difference between peaks $a_1$, $a_2$ and peak $a_3$ originates from the spin–orbit splitting of the Pr 4f state. Peak $a_4$ arises from the transitions to Pr $5d_b$ levels.

In fig. 23, peak $b_1$ originates from the transitions to $(4f_{5/2})(5d_a)$, $b_2$ to the mixed state of $(4f_{5/2})(5d_a)$ and $(4f_{7/2})(5d_a)$ with comparable contributions, $b_3$ to $(4f_{7/2})(5d_a)$. Compared to the experimental spectrum, the separations of peaks are overestimated in the theoretical spectrum. Peaks $b_4$, $b_5$ correspond to transitions to $(4f_{5/2})(5d_b)$, $b_6$ to $(4f_{7/2})(5d_b)$. Therefore, the separation between peaks $b_4$ and $b_5$ originates from the multiplet splitting within the
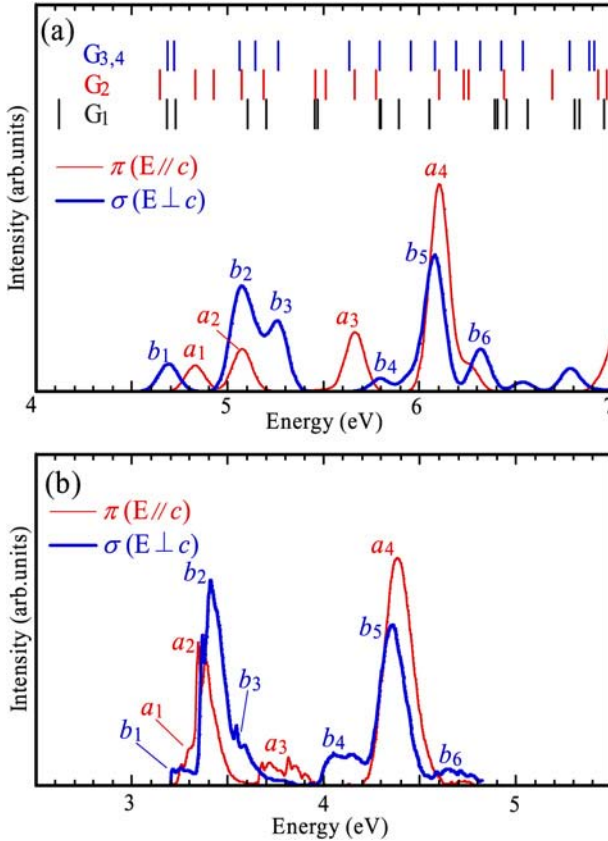
Fig. 21. ESA spectra from $^3P_0$ for $Pr^{3+}$:YLF: (a) theoretical spectra; (b) experimental spectra at $T = 8$ K (Laroche et al., 2000).

$(4f_{5/2})(5d_b)$ configuration while the separation between the peaks $b_4$, $b_5$ and peak $b_6$ originates from the spin–orbit splittings of the Pr 4f levels.

4.2.8.5. *Effects of lattice relaxation* The relation between the Pr–F bond lengths and the absorption spectrum was investigated for $Pr^{3+}$:LiYF$_4$ as done for $Ce^{3+}$:LiYF$_4$ in section 4.2.7.2. The three relaxed model clusters which are similar to those in table 9 were used for the calculations, with 100 000 sampling points. Here the effects of bond lengths are shown only for the $\pi$ ESA spectrum from the $^1D_2$ level.

The theoretical spectra for the three relaxed models are shown in fig. 24. As the bond lengths increase, the separations of the peaks decrease. The theoretical multiplet energy levels for these three models are compared in fig. 25. As shown in the previous section, the separation between peak $a_1$ and peaks $a_2$, $a_3$ originates from the spin–orbit splittings of the Pr 4f levels which are distinguished by red and blue lines. The origin of the separation between peaks $a_4$,
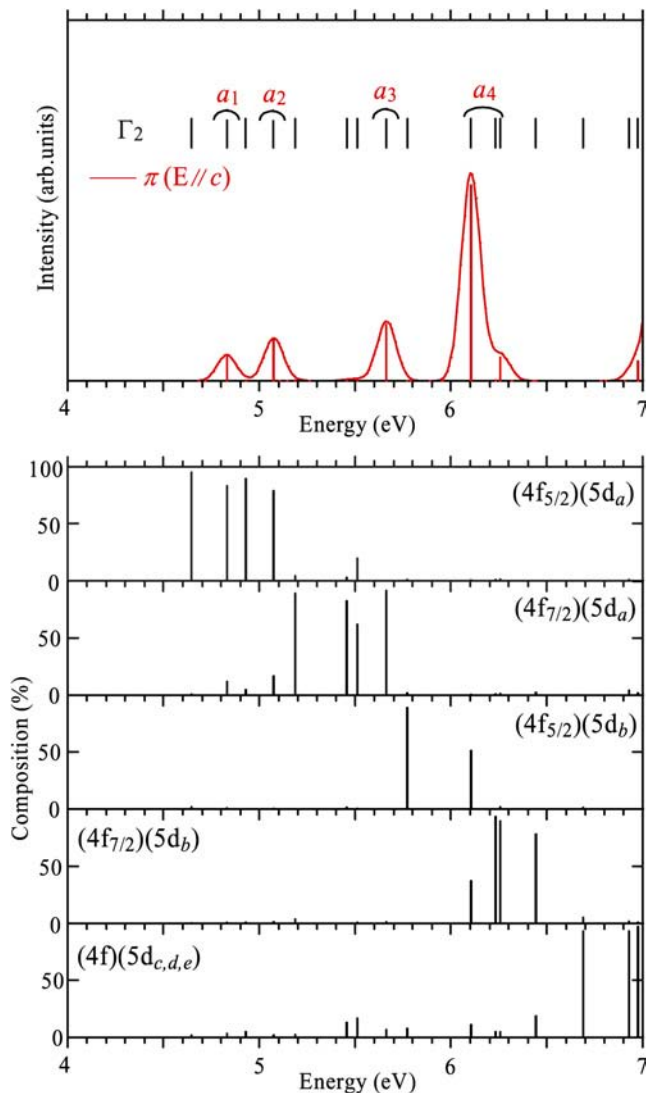
Fig. 22. ESA from $^3P_0$ with $\pi$ polarization (E//c) for $Pr^{3+}$:YLF and configuration analysis of $\Gamma_2$ levels.

$a_5$ and peak $a_6$ is also the same. The separations between peaks $a_1$, $a_2$, $a_3$, peaks $a_4$, $a_5$, $a_6$, and the peaks at higher energy originate from the crystal field splittings of the Pr 5d levels. Comparing the results of the three models, the separation between peaks $a_1$, $a_2$, $a_3$ and peaks $a_4$, $a_5$, $a_6$ decreases as the bond lengths increase. On the other hand, the separation due to the spin–orbit interaction is almost constant for all three models.
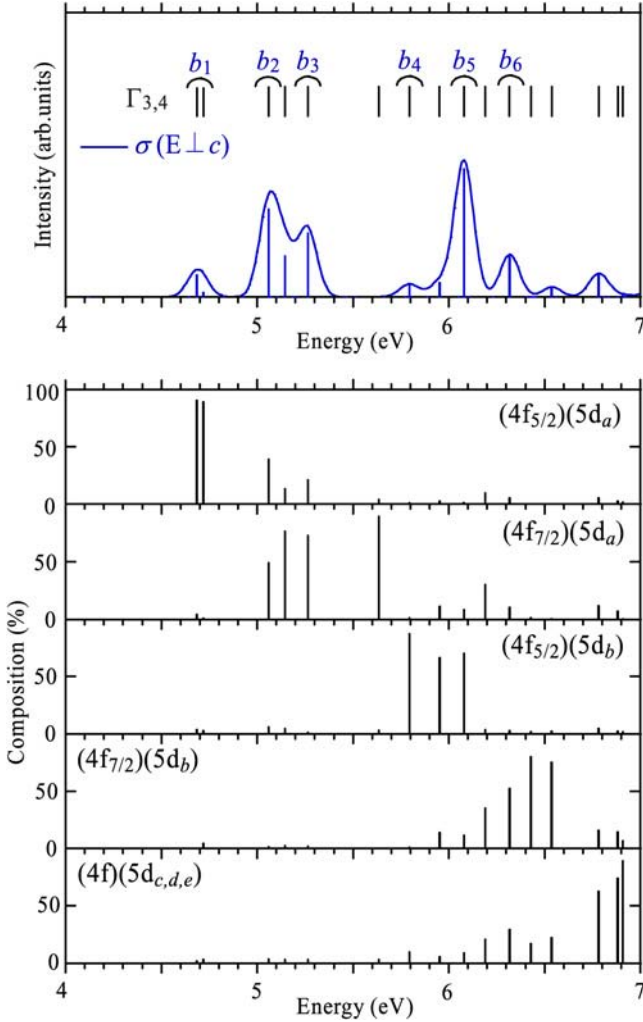
Fig. 23.  ESA from $^3P_0$ with $\sigma$ polarization (E⊥c) for $Pr^{3+}$:YLF and configuration analysis of $\Gamma_{3,4}$ levels.

Comparing the theoretical spectra shown in fig. 24 confirms that as the bond lengths increase, the intensity of peak $a_1$ remains almost unchanged, the intensity of peak $a_2$ decreases, and the intensity of peak $a_3$ increases.

Furthermore, the intensities of peaks $a_4$, $a_5$ are almost unchanged while there is a reversal of the relative intensities of the two peaks denoted as $a_6$ as the bond lengths increase. As shown in this example, the Pr–F bond lengths influence not only the multiplet energy levels but also the peak intensities.
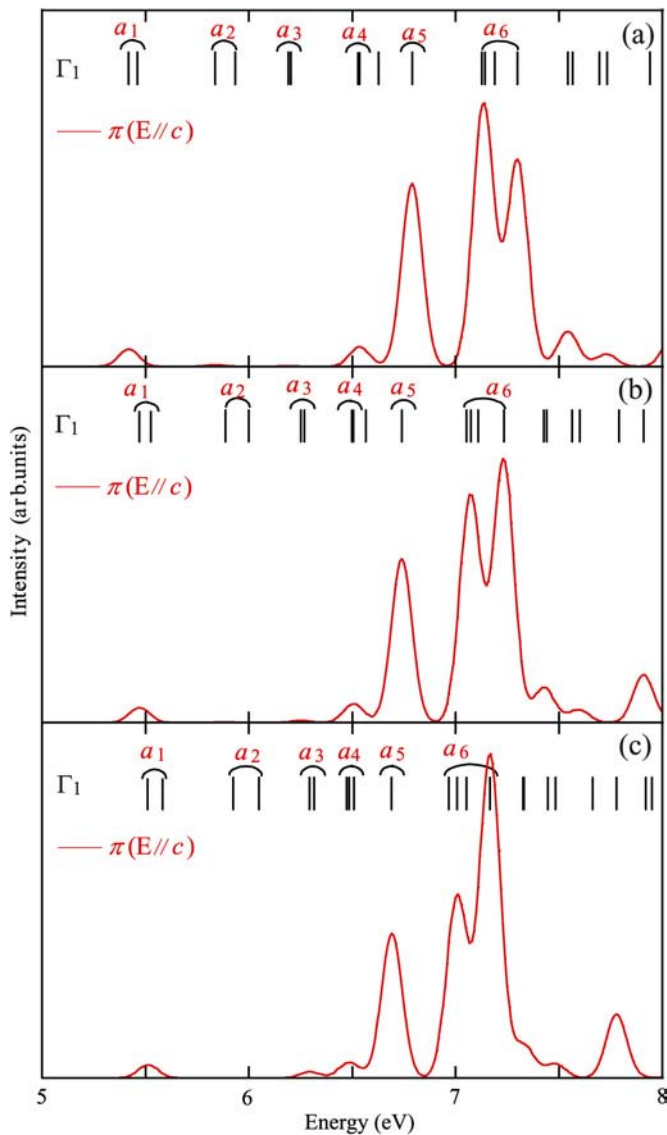
Fig. 24. Influence of the lattice relaxation on the theoretical $\pi$ ESA spectrum: (a) theoretical spectrum for $PrF_8^{5-}$ (100%); (b) theoretical spectrum for $PrF_8^{5-}$ (102%); (c) theoretical spectrum for $PrF_8^{5-}$ (104%).

### 4.2.9. *Nd:YLF*

4.2.9.1. *$4f^3$ energy levels for isolated $Nd^{3+}$ and $Nd^{3+}$ in YLF* The calculated multiplet energy levels for isolated $Nd^{3+}$ ion are shown in fig. 26. The compositions of four configurations, i.e.,
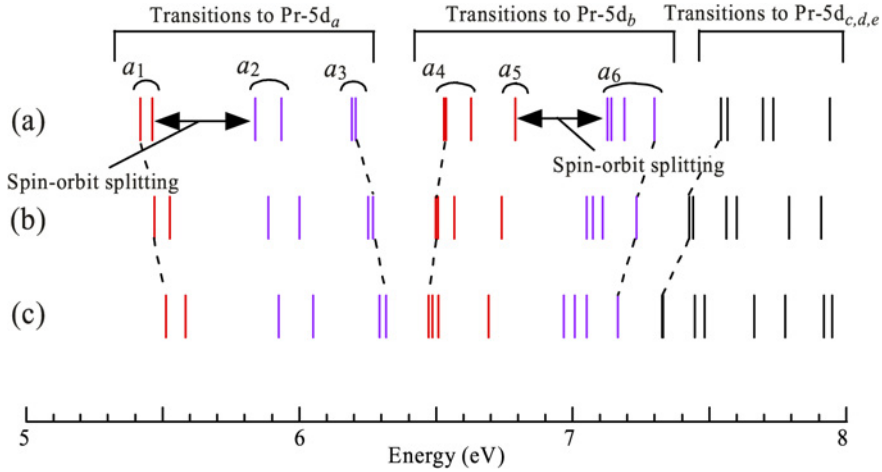
Fig. 25. 4f5d multiplet energy levels of $\Gamma_1$ for unrelaxed and relaxed $PrF_8^{5-}$ clusters: (a) theoretical values for $PrF_8^{5-}$ (100%); (b) theoretical values for $PrF_8^{5-}$ (102%); (c) theoretical values for $PrF_8^{5-}$ (104%).

$(4f_{5/2})^3$, $(4f_{5/2})^2(4f_{7/2})$, $(4f_{5/2})(4f_{7/2})^2$, $(4f_{7/2})^3$ within each energy level are shown below the energy levels. All configurations are distributed in a wide energy range, and there is a strong mixing among them. For example, in the ground state $^4I_{9/2}$ the contribution of the $(4f_{5/2})^3$ configuration is 63%, which is smaller than the contribution of the $4f^2$ configuration in the ground state $^3H_4$ of $Pr^{3+}$, which indicates that the effects of configuration interaction are greater than in $Pr^{3+}$.

In order to analyze the 4f–4f transitions, the MOs mainly consisting of Nd 5d orbitals obtained in section 4.2.4 for $NdF_8^{5-}$ were considered for constructing the Slater determinants.

The theoretical multiplet energy levels obtained for the $NdF_8^{5-}$ cluster are shown in fig. 27, along with the experimental levels for the $4f^3$ configuration (da Gama et al., 1981). Although there are 364 states in the $4f^3$ configuration, considering the degeneracy, we are left with 182 energy levels. On the other hand, the number of observed levels is 128. In the figure, 175 energy levels are shown, representing all the levels, except those from $^2F(1)$ in the 10.66–10.92 eV energy range. Comparing with the results of the isolated ion, the Stark splitting is clearly seen. With respect to the experimental results, the multiplet energies are overestimated by about 30%. However, the overall multiplet structure is reproduced. The configuration compositions for each multiplet level are almost the same as for the isolated ion.

The theoretical energy levels of the ground state $^4I_{9/2}$ are shown in table 13 together with the results of CF calculations and the experimental values. Among the irreducible representations of $S_4$ symmetry, only $\Gamma_5$, $\Gamma_6$, $\Gamma_7$, $\Gamma_8$ are possible for a three-electron system, where $\Gamma_5$ and $\Gamma_6$ or $\Gamma_7$ and $\Gamma_8$ are degenerate. Comparing with the experimental values, the Stark splittings are somewhat overestimated. However, the order of irreducible representations of these five levels is consistent with both the experimental values and those obtained by CFT.
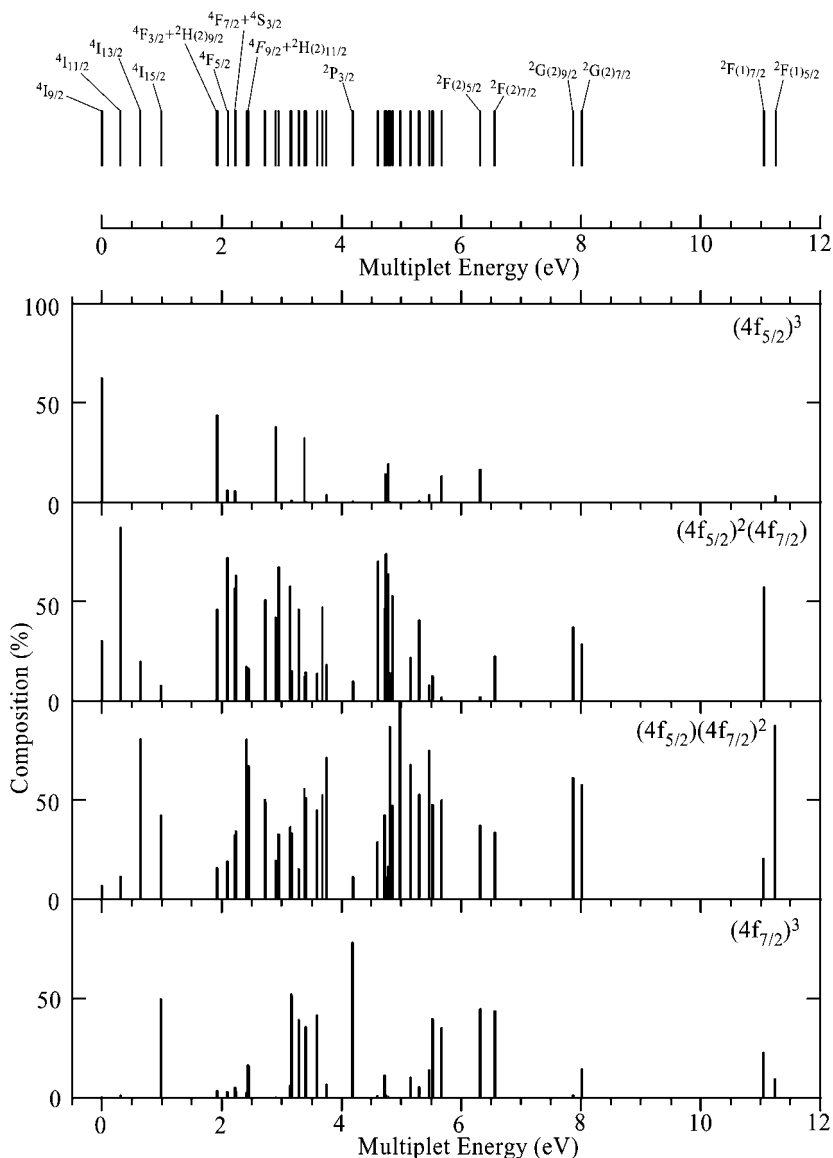
Fig. 26.  Theoretical $(4f)^3$ multiplet energy levels and their configuration compositions for an isolated $Nd^{3+}$ ion.

4.2.9.2. *$4f^3$–$4f^2 5d$ transitions*  In order to analyze the $4f^3 \rightarrow 4f^2 5d$ transition spectrum, the multiplet structure of the $4f^3$ and $4f^2 5d$ configurations was also calculated by the relativistic DVME method. The MOs mainly consisting of Nd 4f orbitals or Nd 5d orbitals were used for
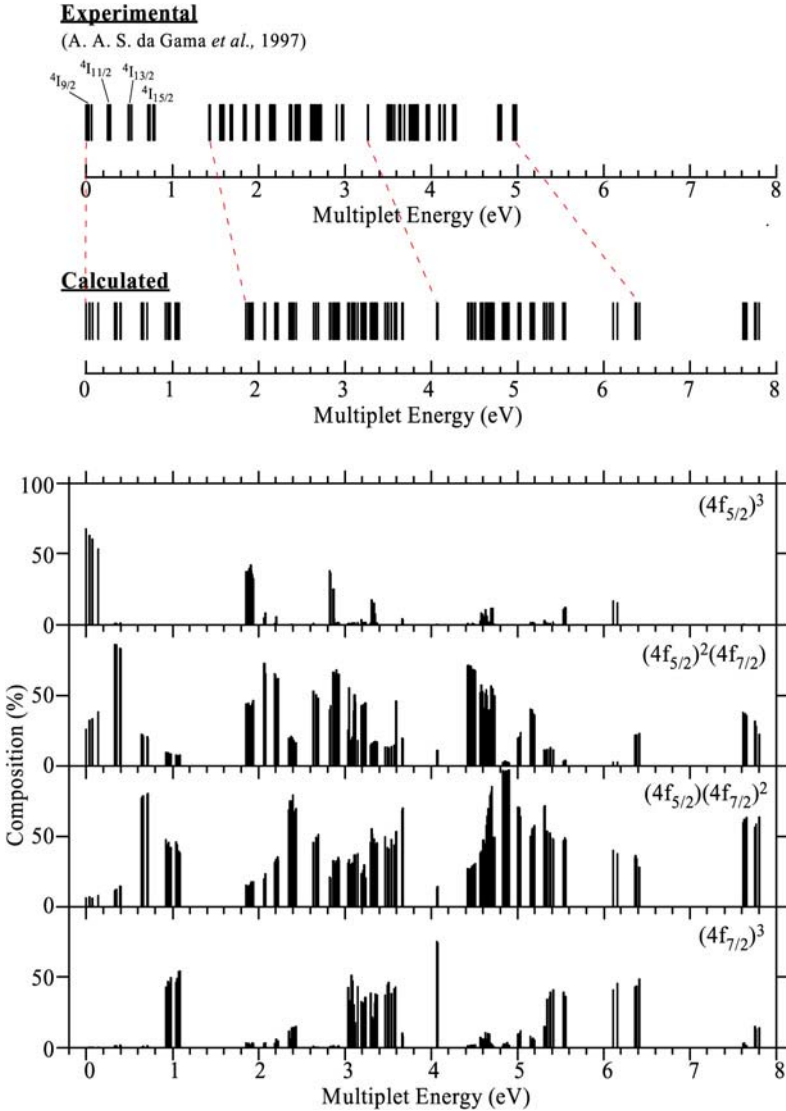
Fig. 27. Theoretical multiplet energy levels and their configuration compositions for the $NdF_8^{5-}$ cluster.

the construction of the Slater determinants. The number of possible electronic levels is 364 for the $4f^3$ configuration and 910 for the $4f^2 5d$ configuration, therefore a total of 1274.

In fig. 10, the calculated multiplet energy levels are shown together with the configuration composition for each level. All the levels in the range of 0–7.80 eV belong to the $4f^3$ configuration, while the $^2F(1)$ level which is the highest term in the $4f^3$ configuration is mixed

Table 13
Energies of the $^4I_{9/2}$ multiplet

| Level $^4I_{9/2}$ | | | | | |
|---|---|---|---|---|---|
| Expt. | | Calc. (CFT) | | Calc. (DVME) | |
| $\Gamma$ | Energy (eV) | $\Gamma$ | Energy (eV) | $\Gamma$ | Energy (eV) |
| 7,8 | 0 | 7,8 | 0.0014 | 7,8 | 0 |
| 7,8 | 0.0164 | 7,8 | 0.0192 | 7,8 | 0.0374 |
| 5,6 | 0.0226 | 5,6 | 0.0242 | 5,6 | 0.0394 |
| 5,6 | 0.0309 | 5,6 | 0.0312 | 5,6 | 0.0716 |
| 7,8 | 0.0648 | 7,8 | 0.0689 | 7,8 | 0.136 |

with the $4f^25d$ configuration. The presence of an interaction between the $4f^n$ and $4f^{n-1}5d$ configurations is in contrast to the case of $Pr^{3+}$.

Next the absorption spectrum from the ground state was also calculated and compared with the experimental spectrum (Kollia et al., 1995). Since the latter was measured at room temperature, we considered not only the lowest state at 0 eV ($\Gamma_{7,8}$) but also the first excited level at 0.0164 eV ($\Gamma_{7,8}$) and the second-excited level at 0.0226 eV ($\Gamma_{5,6}$).

Thus the oscillator strengths for the transitions from these three levels were calculated and the theoretical absorption spectra were obtained by convolution with a Gaussian function with 0.16 eV FWHM (fig. 28). As shown in the figure, the shape of the spectrum strongly depends on the initial states. Therefore, the experimental spectrum taken at room temperature is inappropriate for the analysis of energy level structure in $4f^25d$ configuration. Thus we compare the theoretical spectra with the excitation spectrum measured at 6 K (Reid et al., 2000).

The theoretical spectrum from the lowest state 0 eV ($\Gamma_{7,8}$) is compared with the experimental excitation spectrum in fig. 29. On the experimental spectrum, the positions of peaks A–E for $Nd^{3+}$:YLF are almost the same as peaks A–E for $Pr^{3+}$:YLF. As in the latter case, the bands are labeled as indicated by the arrows in fig. 29.

Although the energy separations between the peaks are somewhat overestimated due to the neglect of lattice relaxation, the relative peak positions are reproduced.

The multiplet energy levels in the range 8–14 eV are shown in figs. 30 and 31, together with the oscillator strengths and the theoretical spectrum for the transitions from the lowest level. The configuration compositions for each level are also shown below. Here the peaks denoted as A–E in fig. 29 are denoted $A_1$, $B_1$, C, D, $E_1$ and the peaks indicated by black arrows are denoted as $A_2$, $A_3$, $B_2$, $B_3$, $E_2$, $E_3$ in fig. 30. The peaks $A_1$, $A_2$ originates from the transitions to the $(4f_{5/2})^2(5d_a)$ configuration. The $(4f_{5/2})^2(5d_a)$ configuration is confined within the range of 8.7–9.2 eV, and there are little interactions with the other configurations. Peak $A_3$ mostly originates from the transition to the $(4f_{5/2})(4f_{7/2})(5d_a)$ configuration. This configuration spreads over a wide energy range and influences much higher levels. For the peaks with energies higher than $B_1$, it is difficult to determine the main component of the configuration since quite large configuration interaction occurs.
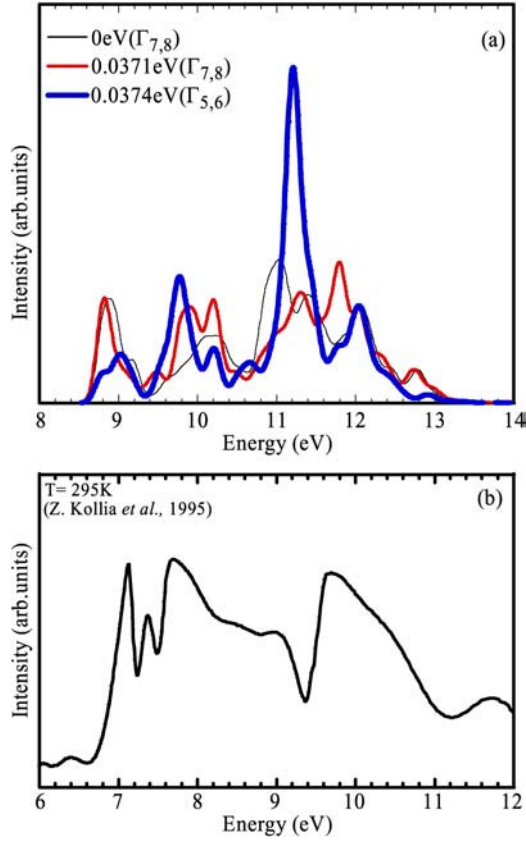
Fig. 28. (a) Theoretical absorption spectra for $Nd^{3+}$:YLF; (b) experimental absorption spectrum for $Nd^{3+}$:YLF.

### 4.2.10. *Ho:YLF*

The theoretical $4f^{10} \rightarrow 4f^9 5d$ absorption spectrum of $Ho^{3+}$ in YLF is calculated and compared with the experimental excitation spectrum (Wegh et al., 1998) in fig. 32. Each level was convoluted by a Gaussian function with 0.1 eV FWHM. Although the $4f^{10} \rightarrow 4f^9 5d$ transition energies are underestimated by about 0.5 eV, the agreement is better than in the case of $Pr^{3+}$. This is probably due to compensation of the overestimation of the energy intervals between the $4f^{10}$ and $4f^9 5d$ configurations by the overestimation of the multiplet splitting of the $4f^9 5d$ configuration. The former would increase the $4f^{10} \rightarrow 4f^9 5d$ transition energies while the latter would decrease the threshold energy of the $4f^{10} \rightarrow 4f^9 5d$ transitions. The experimental spectrum displays five main and broad bands labeled A, B, C, D, and E. There are characteristic features among the intensities of these peaks. The intensity changes alternately until peak D and peak E is the strongest. These features are also reproduced by CF calculations (van Pieterson et al., 2000). According to the first-principles calculations shown in fig. 32,
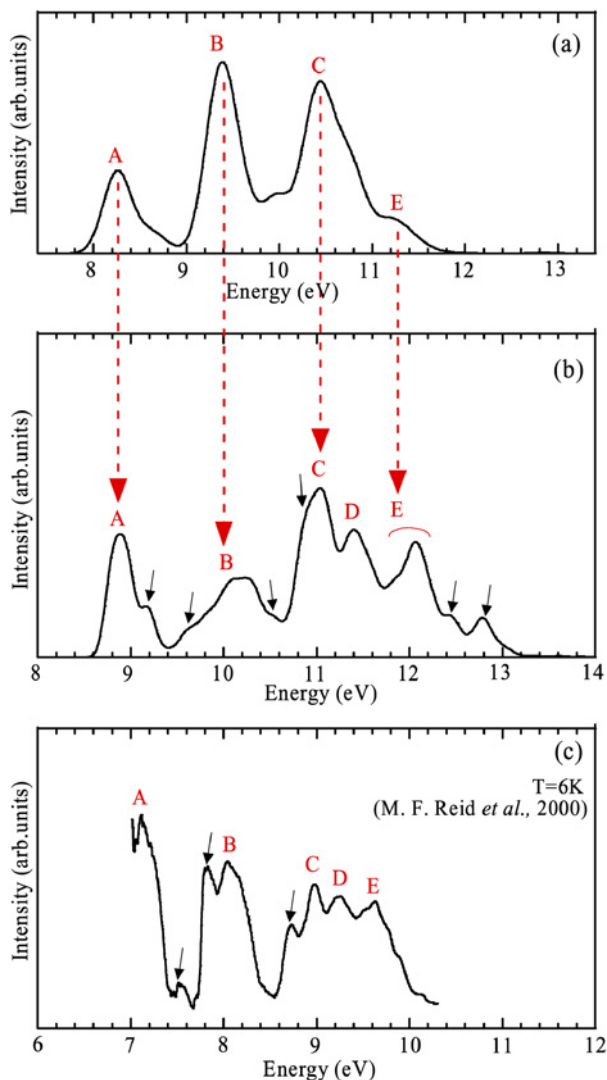
Fig. 29. (a) Theoretical absorption spectrum of $Pr^{3+}$:YLF; (b) theoretical absorption spectrum of $Nd^{3+}$:YLF; (c) experimental excitation spectrum of $Nd^{3+}$:YLF.

the number of energy levels of this configuration is quite large and they almost form a band. However, when the transition probabilities from the ground state to these levels are calculated, only a limited number of states contribute to the transitions. As a result, the characteristic features of the experimental spectrum are well reproduced by the nonempirical relativistic CI calculation.
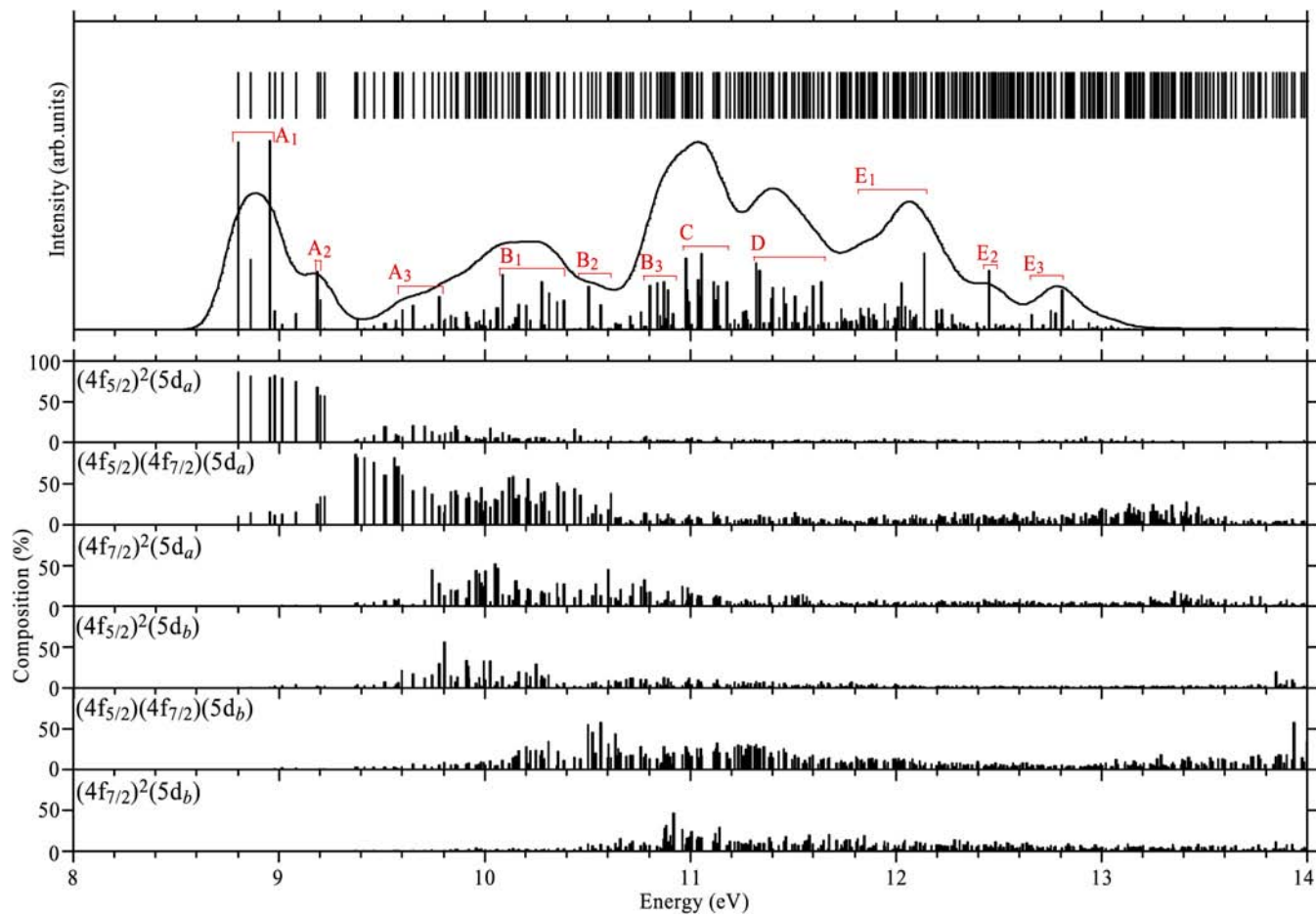
Fig. 30. Configuration analysis of $(4f)^2(5d)$ multiplet levels for $Nd^{3+}$:YLF.
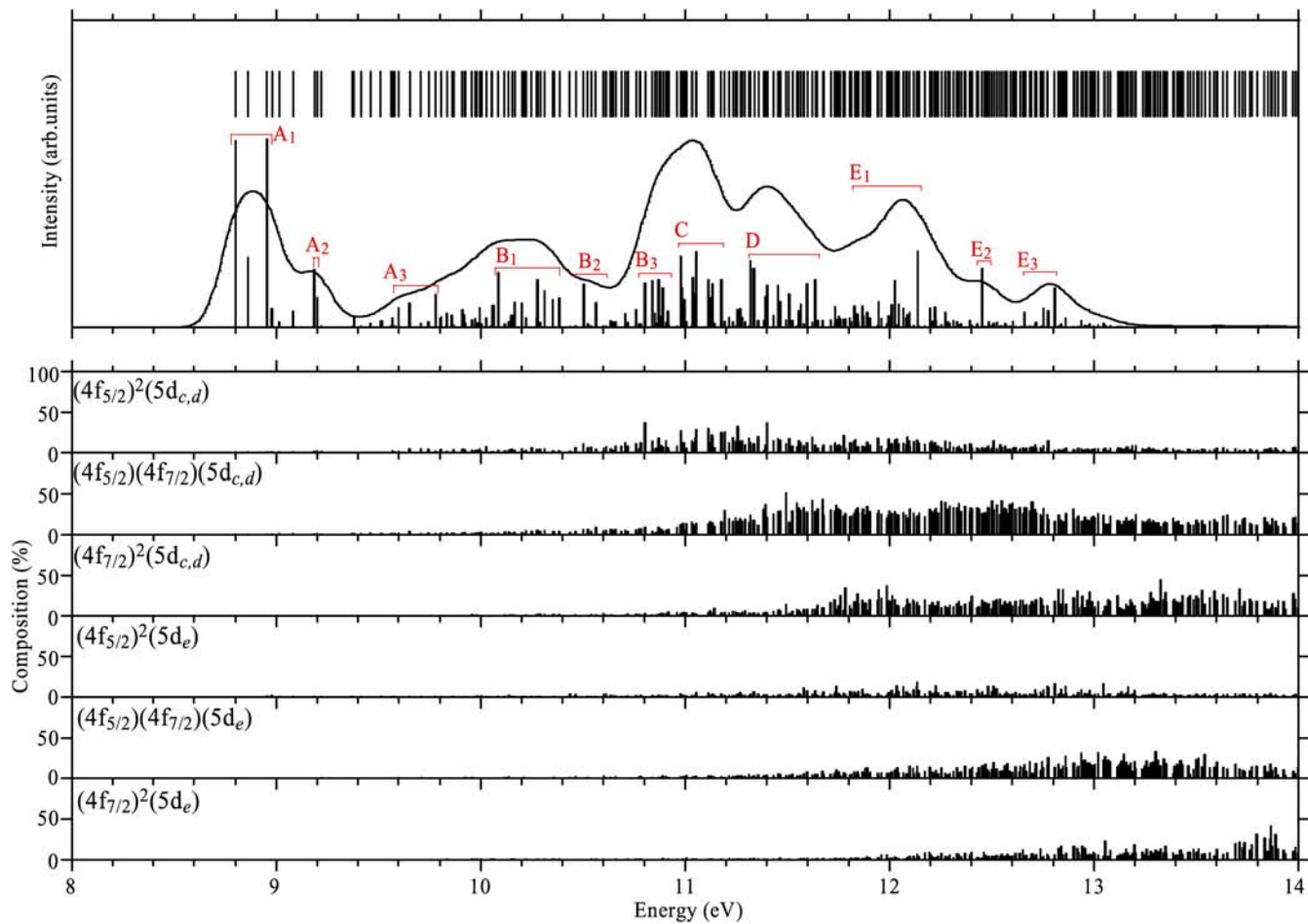
Fig. 31. Configuration analysis of $(4f)^2(5d)$ multiplet levels for $Nd^{3+}$:YLF.
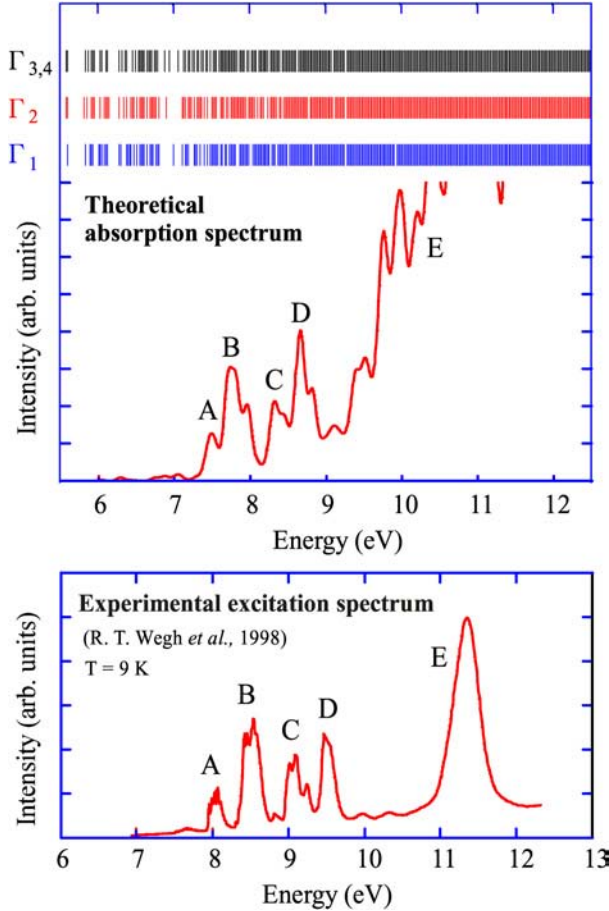
Fig. 32. Theoretical $4f^{10} \rightarrow 4f^9 5d$ absorption spectrum (top) and experimental excitation spectrum (bottom) (Wegh et al., 1998) of $Ho^{3+}$ in YLF.

### 4.2.11. *Tm:YLF*

The theoretical $4f^{12} \rightarrow 4f^{11}5d$ absorption spectrum of $Tm^{3+}$ in YLF is calculated and compared with the experimental excitation spectrum (Wegh et al., 1998) in fig. 33. Each level is convoluted by a Gaussian function with 0.08 eV FWHM. The $4f^{12} \rightarrow 4f^{11}5d$ transition energies are underestimated by about 2.5 eV in this case. Again, this is probably due to compensation between the overestimation of the energy intervals between the $4f^{12}$ and $4f^{11}5d$ configurations and the overestimation of the multiplet splitting of the $4f^{11}5d$ configuration. In this case, the latter is dominant due to the larger number of 4f electrons. Five broad lines labeled A, B, C, D, and E are seen in the experimental spectrum. The intensities of these peaks gradually decrease except the last one (peak E). In the theoretical spectrum the intensity of peak A is underestimated, for a currently unknown reason. A similar underestimation of the
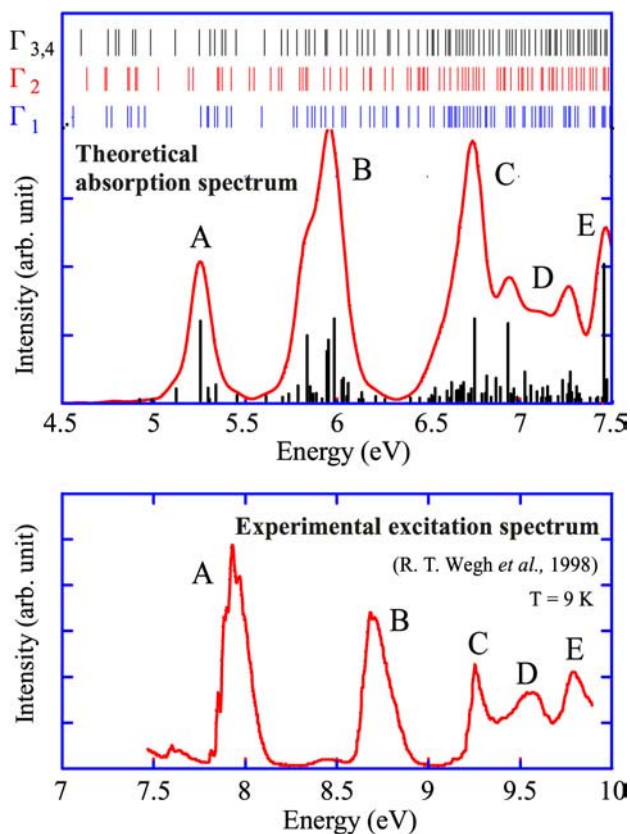
Fig. 33. Theoretical $4f^{12} \rightarrow 4f^{11}5d$ absorption spectrum (top) and experimental excitation spectrum (bottom) (Wegh et al., 1998) of $Tm^{3+}$ in YLF.

intensity of peak A is also reported by van Pieterson et al. (2000), who use CF calculations. Therefore, the intensity variation is difficult to reproduce even by the CF calculation. A possible reason for this discrepancy is the effect of broadening. In this work, we have broadened each peak uniformly. However, the peak widths can be different for each peak. The number of energy levels of this configuration is also quite large. However, when transition probabilities from the ground state to these levels are calculated, only a limited number of states contribute to the peaks in the spectrum and the relative peak positions are well reproduced by the nonempirical relativistic CI calculation.

### 4.3. *Calculations of divalent europium ions in BAM phosphor*

#### 4.3.1. *The BAM phosphor*
$BaMgAl_{10}O_{17}$ activated by $Eu^{2+}$ ($BAM:Eu^{2+}$) is used as a commercial blue phosphor in fluorescent lamps or plasma displays. However this material is relatively unstable against thermal
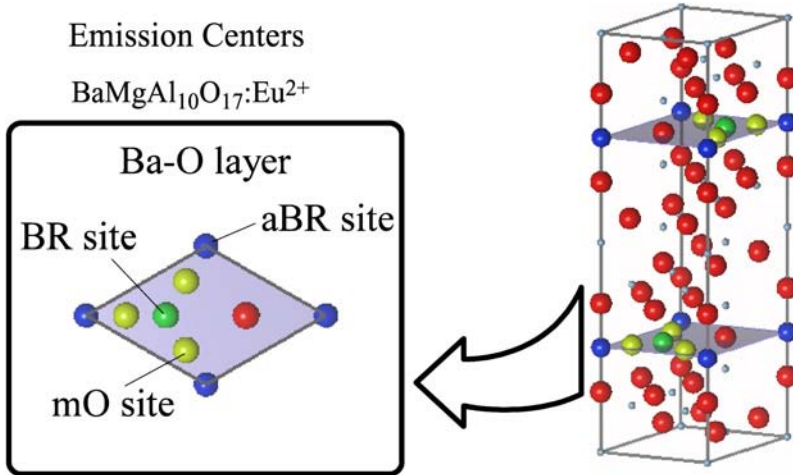
Fig. 34. Crystal structure of BAM. (Drawn with VENUS developed by Dilanian and Izumi.)

degradation and VUV radiation. In order to understand the mechanism of degradation, consideration efforts have been made to clarify the local electronic structure around $Eu^{2+}$ ions. Recently, electronic structure calculations of BAM:$Eu^{2+}$ have been performed by Stephan et al. (2001) and Mishra et al. (2002) using the band structure approach and molecular orbital approach, respectively. Their results indicated that $Eu^{2+}$ ions occupy three different sites called Beevers–Ross (BR), anti-Beevers–Ross (aBR) and mid-oxygen (mO) sites. However, for a more detailed understanding, consideration of multiplet effects beyond one-electron approximation is quite important. In the present work, we have performed first-principles calculations of $4f^7$ and $4f^6 5d$ multiplet states of $Eu^{2+}$ ions in BAM based on the relativistic DVME method and investigated the $4f^7$–$4f^6 5d$ transition spectra.

### 4.3.2. *Crystal structure of BAM*
The crystal structure of BAM is shown in fig. 34. It has the $\beta$-alumina structure with lattice parameters $a = 5.6275$ Å, $b = 22.658$ Å (Iyi et al., 1986). There are layers consisting of $Ba^{2+}$ and $O^{2-}$ ions between the spinel blocks and $Eu^{2+}$ is generally believed to stay within these Ba–O layers. The positions of BR, aBR, and mO sites within this Ba–O layer are shown in fig. 34. The BR site is the substitutional site of Ba and the other two sites are interstitial sites.

### 4.3.3. *Model clusters*
For calculations of $Eu^{2+}$ ions occupying BR, aBR, and mO sites, the $EuO_9^{7-}$, $EuO_5^{3-}$, and $EuO_8^{6-}$ clusters were constructed from the crystal structures of BAM as shown in fig. 35. The lattice relaxations were not considered. In the model cluster for the BR site, $Eu^{2+}$ ions are coordinated by 9 oxygen ions and the Eu–O bond lengths are 3.249 Å (6 bonds) and 2.802 Å
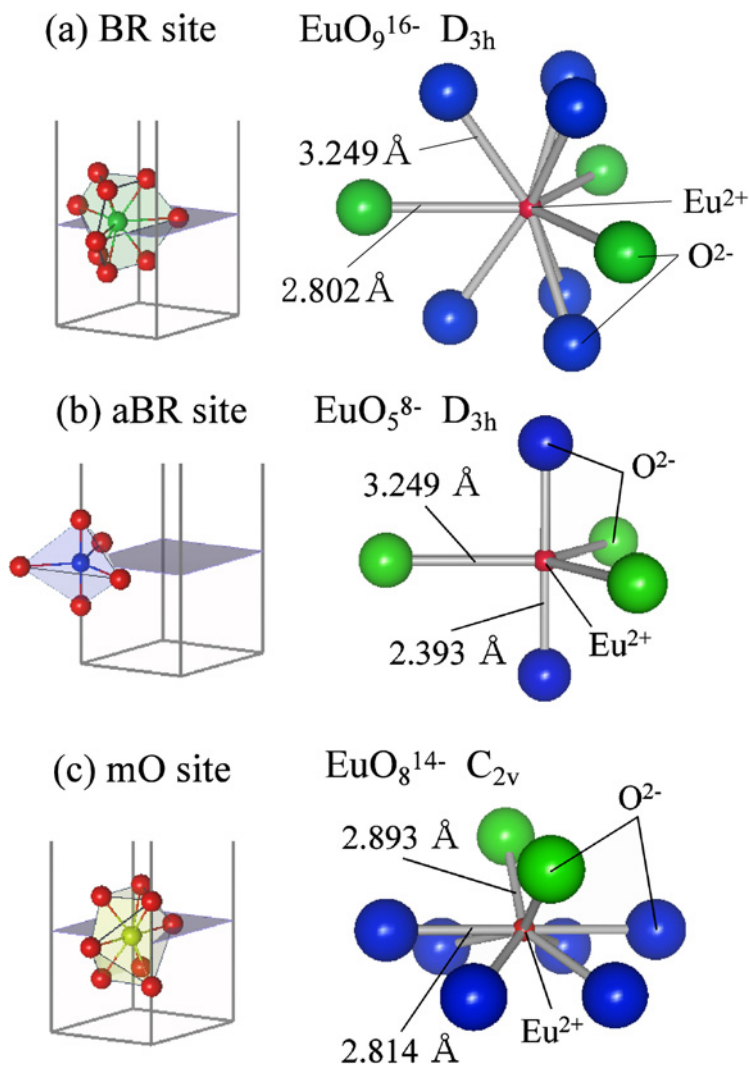
Fig. 35. The model clusters adopted for the calculation of BAM:Eu$^{2+}$ absorption spectra. (Drawn with VENUS developed by Dilanian and Izumi.)

(3 bonds). The point symmetry of the Eu$^{2+}$ site is D$_{3h}$. In the model cluster for aBR site, Eu$^{2+}$ ions are coordinated by 5 oxygen ions and the Eu–O bond lengths are 3.293Å (3 bonds) and 2.393 Å (2 bonds). The point symmetry of the Eu$^{2+}$ site is also D$_{3h}$. In the model cluster for mO site, Eu$^{2+}$ ions are coordinated by 8 oxygen ions and the Eu–O bond lengths are 2.814 Å (6 bonds) and 2.893 Å (2 bonds). The point symmetry of the Eu$^{2+}$ site is C$_{2v}$. These
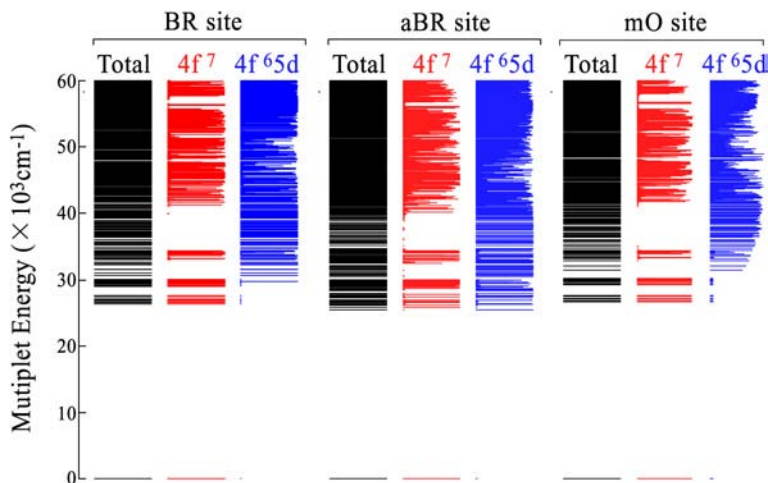
Fig. 36. Calculated multiplet structures of $Eu^{2+}$ in BR, aBR, and mO sites.

clusters were embedded into the effective Madelung potential produced by several thousand point charges.

### 4.3.4. *Multiplet energy levels*

The calculated multiplet structures of $Eu^{2+}$ ions occupying the BR, aBR, mO sites are shown in fig. 36. The energy levels are so numerous that they appear like a band. However, not all energy levels contribute to the spectra and the theoretical spectra characteristic of the $Eu^{2+}$ site can be obtained. The energy of the $4f^65d$ configuration is the lowest for the aBR site. There is significant configuration interaction between the $4f^7$ and $4f^65d$ configurations in the case of mO site.

### 4.3.5. $4f^7 \rightarrow 4f^65d$ *transition spectra*

The theoretical absorption spectra of $Eu^{2+}$ at all three sites in BAM were obtained by broadening the oscillator strengths by a Gaussian function with 0.3-eV FWHM. The calculated spectra in comparison with experimental excitation spectrum are shown in fig. 37. In the experimental excitation spectrum, three main peaks (a–c) and one sub-peak (b′) are clearly identified. The spectrum of the BR site has only one peak whereas the spectra of the aBR and mO sites have two peaks each. For easy comparison, a tentative spectrum consisting of 1:1:1 contribution of each spectrum is also shown in the figure. In this tentative theoretical absorption spectrum, all main features of the experimental spectrum are reproduced without using any empirical parameters.

As shown in the figure, only the aBR site is contributing to peak $a$. These results indicate that in actual material, the occupancy of aBR sites should be greater than the ones of the other sites.
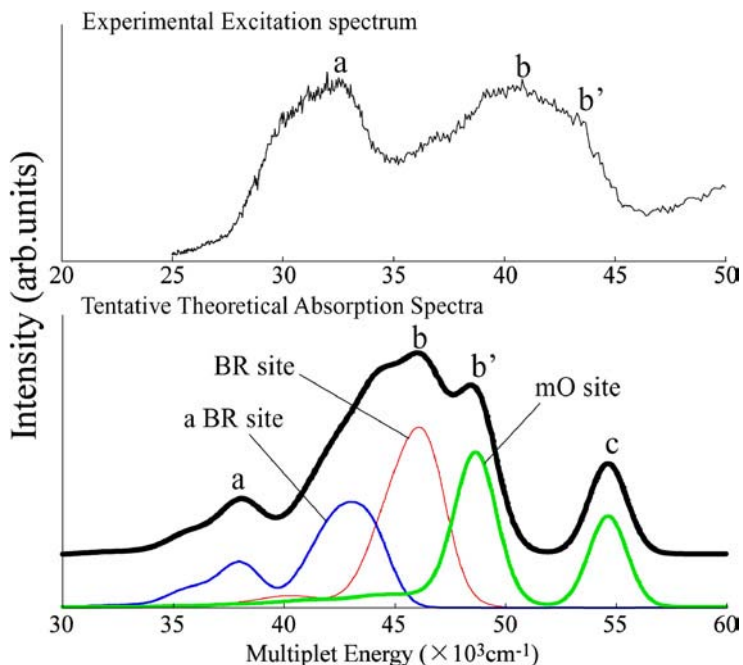
Fig. 37. Experimental excitation spectrum and theoretical absorption spectra for $Eu^{2+}$:BAM. The thickest line is a tentative spectrum produced by summing up the spectra for all three sites with ratio of 1:1:1.

## 5. Summary and perspectives

This chapter is devoted to the first principles calculations of the energy levels and intensities of the $4f^n$–$4f^{n-1}5d$ transitions for trivalent and divalent RE ions. Detailed description of the fully relativistic DVME method without any fitting parameter is given in the present chapter. The main difference between this method and other first-principles calculation techniques is that the former one allows for calculating the multiplets energies within the CI framework. To emphasize a wide area of applicability of the outlined approach, numerous applications of the developed method are presented. As a result of the performed calculations, the Dieke diagram for trivalent RE ions has been extended to include all the states arising from both $4f^n$ and $4f^{n-1}5d$ configurations, thus covering UV and VUV spectral regions. Calculated absorption spectra are compared with experimental results and general trends in the $4f^n$–$4f^{n-1}5d$ transitions in spectra of a number of crystals doped with trivalent and divalent RE ions are discussed. Since the method does not employ any fitting parameters, it can be readily used for prediction of the optical properties of new materials and effective search for new crystals and activator ions for various applications in quantum electronics.

## Acknowledgements

## References

Brik, M.G., Tanaka, I., Ishii, T., Ogasawara, K., Nakamura, A., Watanabe, S., 2006. J. Alloys Compd. **408–412**, 753.

Carnall, W.T., Fields, P.R., Rajnak, K., 1968. J. Chem. Phys. **49**, 4424.

Carnall, W.T., Crosswhite, H.M., Crosswhite, H., Special Rep. 1977. Chemistry Division, Argonne National Laboratory, Argonne, IL.

Carnall, W.T., Goodman, G.L., Rajnak, K., Rana, R.S., 1989. J. Chem. Phys. **90**, 3443.

Combes, C.M., Dorenbos, P., van Eijik, C.W.E., Pedrini, C., Den Hartog, H.W., Gesland, J.Y., Rodnyi, P.A., 1997. J. Lumin. **71**, 65.

Conroy, H., 1967. J. Chem. Phys. **47**, 5307.

Cowan, R.D., 1981. The Theory of Atomic Structure and Spectra. Univ. of California Press, Berkeley, CA.

da Gama, A.A.S., de Sa, G.F., Porcher, P., Caro, P., 1981. J. Chem. Phys. **75**, 2583.

Daul, C.A., 1994. Int. J. Quantum Chem. **52**, 867.

Dieke, G.H., 1968. Spectra and Energy Levels of Rare Earth Ions in Crystals. Wiley–Interscience, New York.

Dieke, G.H., Crosswhite, H.M., 1963. Appl. Opt. **2**, 675.

Dirac, P.A.M., 1928. Proc. R. Soc. London **117**, 610.

Dirac, P.A.M., 1958. The Principles of Quantum Mechanics, fourth edition. Oxford Univ. Press, Berkeley, CA.

Dorenbos, P., 2000a. J. Lumin. **91**, 91.

Dorenbos, P., 2000b. J. Lumin. **91**, 155.

Dorenbos, P., 2000c. Phys. Rev. B **62**, 15640.

Dorenbos, P., 2000d. Phys. Rev. B **62**, 15650.

Dorenbos, P., 2002. Phys. Rev. B **65**, 235110.

Duan, C.K., Reid, M.F., 2003. J. Sol. State Chem. **171**, 299.

Duan, C.K., Reid, M.F., Burdick, G.W., 2002. Phys. Rev. B **66**, 155108.

Ehrlich, D.J., Moulton, P.F., Osgood Jr., R.M., 1979. Opt. Lett. **4**, 184.

Ellis, D.E., Painter, G.S., 1970. Phys. Rev. B **2**, 2887.

Faucher, M.D., Moune, O.K., 1997. Phys. Rev. A **55**, 4150.

Goryunov, A.V., Popov, A.I., 1992. Russ. J. Inorg. Chem. **37**, 126.

Iyi, N., Inoue, Z., Kimura, S., 1986. J. Sol. State Chem. **61**, 236.

Kollia, Z., Sarantopoulou, E., Cefalas, A.C., Nicolaides, C.A., Naumov, A.K., Semashko, V.V., Abdulsabirov, R.Y., Korableva, S.L., Dubinskii, M.A., 1995. J. Opt. Soc. Am. B **12**, 782.

Laroche, M., Doualan, J.L., Girard, S., Margerie, J., Moncorge, R., 2000. J. Opt. Soc. Am. B **17**, 1291.

Llusar, R., Casarrubios, M., Barandiarán, Z., Seijo, L., 1996. J. Chem. Phys. **105**, 5321.

Malkin, B.Z., 1987. Crystal field and electron-phonon interaction in rare-earth ionic paramagnets. In: Kaplyanskii, A.A., Macfarlane, B.M. (Eds.), Spectroscopy of Solids Containing Rare-Earth Ions. North-Holland, Amsterdam, pp. 33–50.

Malkin, B.Z., Leushin, A.M., Iskhakova, A.I., Heber, J., Altwein, M., Moller, K., Fazlizhanov, I.I., Ulanov, V.A., 2000. Phys. Rev. B **62**, 7063.

Malkin, B.Z., Zakirov, A.R., Popova, M.N., Klimin, S.A., Chukalina, E.P., Antic-Fidancev, E., Goldner, P., Aschehoug, P., Dhalenne, G., 2004. Phys. Rev. B **70**, 075112.

Meijerink, A., Wegh, R.T., 1999. Mater. Sci. Forum **315–317**, 11.

Mishra, K.C., Raukas, M., Ellens, A., Johnson, K.H., 2002. J. Lumin. **96**, 95.

Moraza, S.L., Barandiarán, Z., 1996. J. Chem. Phys. **105**, 50.

Moraza, S.L., Seijo, L., Barandiarán, Z., 1998. Phys. Rev. **57**, 11974.

Mulliken, R.S., 1955. J. Chem. Phys. **23**, 1833.

Newman, D.J., Ng, B. (Eds.), 2000. Crystal Field Handbook. Cambridge Univ. Press, Cambridge.

Nielsen, C.W., Koster, G.F., 1963. Spectroscopic Coefficients for the $p^n$, $d^n$, and $f^n$ Configurations. The M.I.T. Press, Cambridge, MA.

Ning, L., Jiang, Y., Xia, S., Tanner, P.A., 2003. J. Phys.: Condens. Matter **15**, 7337.

Ning, L., Duan, C.K., Xia, S., Reid, M.F., Tanner, P.A., 2004. J. Alloys Compd. **366**, 34.

Ogasawara, K., Iwata, T., Koyama, Y., Ishii, T., Tanaka, I., Adachi, H., 2001. Phys. Rev. B **64**, 115413.

Ogasawara, K., Watanabe, S., Sakai, Y., Toyoshima, H., Ishii, T., Brik, M.G., Tanaka, I., 2004. Jpn. J. Appl. Phys. **43**, L611.

Ogasawara, K., Watanabe, S., Toyoshima, H., Ishii, T., Brik, M.G., Ikeno, H., Tanaka, I., 2005a. J. Solid State Chem. **178**, 412.

Ogasawara, K., Watanabe, S., Ishii, T., Brik, M.G., 2005b. Jpn. J. Appl. Phys. **44**, 7488.

Peijzel, P.S., Meijerink, A., Wegh, R.T., Reid, M.F., Burdick, G.W., 2005. J. Solid State Chem. **178**, 448.

Popova, M.N., Chukalina, E.P., Malkin, B.Z., Saikin, S.K., 2000. Phys. Rev. B **61**, 7421.

Popova, M.N., Chukalina, E.P., Malkin, B.Z., Iskhakova, A.I., Antic-Fidancev, E., Porcher, P., Chaminade, J.P., 2001. Phys. Rev. B **63**, 075103.

Reid, M.F., van Pieterson, L., Wegh, R.T., Meijerink, A., 2000. Phys. Rev. B **62**, 14744.

Reid, M.F., van Pieterson, L., Meijerink, A., 2002. J. Alloys Compd. **344**, 240.

Rosén, A., Ellis, D.E., 1974. Chem. Phys. Lett. **27**, 595.

Rudowicz, C., 1985. J. Phys. C **18**, 1415.

Rudowicz, C., 2000. Computer package CST: Conversions, standardization and transformations. In: Newman, D.J., Ng, B. (Eds.), Crystal Field Handbook. Cambridge Univ. Press, Cambridge, pp. 259–268.

Rudowicz, C., Qin, J., 2004. J. Alloys Compd. **385**, 238.

Sarantopoulou, E., Cefalas, C., Dubinskii, A.M., Nicolaides, A.C., Abdulsabirov, R.Y., Korableva, L.S., Naumov, K.A., Semashko, V.V., 1994. Appl. Phys. Lett. **15**, 813.

Satoko, C., Tsukada, M., Adachi, H., 1978. J. Phys. Soc. Jpn. **45**, 1333.

Schwerdtfeger, P., 2002. Relativistic Electronic Structure Theory—Fundamentals. Elsevier, Amsterdam.

Seijo, L., Barandiarán, Z., 2003. J. Chem. Phys. **118**, 5335.

Shakurov, G.S., Tarasov, V.F., Malkin, B.Z., Iskhakova, A.I., Kasatkina, L.A., Heber, J., Altwein, M., 1998. Appl. Magn. Res. **14**, 415.

Shakurov, G.S., Malkin, B.Z., Zakirov, A.R., Okhrimchuk, A.G., Butvina, L.N., Lichkova, N.V., Zavgorodnev, V.N., 2004. Appl. Magn. Reson. **25**, 579.

Shannon, R.D., 1976. Acta Crystallogr. Sec. A **32**, 751.

Slater, J.C., 1974. Quantum Theory of Molecules and Solids, vol. 4. McGraw–Hill, New York.

Stephan, M., Schmidt, P.C., Mishra, K.C., Raukas, M., Ellens, A., Boolchand, P., 2001. Z. Phys. Chem. **215**, 1397.

Sugar, J., 1965. J. Opt. Soc. Am. **55**, 1058.

van Pieterson, L., Reid, M.F., Wegh, R.T., Soverna, S., Meijerink, A., 2000. Phys. Rev. B **65**, 045114.

Watanabe, S., Kamimura, H., 1987a. J. Phys. Soc. Jpn. **56**, 1078.

Watanabe, S., Kamimura, H., 1987b. J. Phys. C **20**, 4145.

Watanabe, S., Kamimura, H., 1989. Mater. Sci. Eng. B **3**, 313.

Wegh, R.T., Meijerink, A., Lamminmäki, R.-J., Hölsä, J., 2000. J. Lumin. **87–89**, 1002.

Wegh, R.T., Donker, H., Meijerink, A., 1998. Electrochem. Soc. Proc. **97–29**, 284.

Wissing, K., Aramburu, J.A., Barriuso, M.T., Moreno, M., 1998. Solid State Commun. **108**, 1001.

This page intentionally left blank

*Chapter 232*

# $4f^n$–$4f^{n-1}$5d TRANSITIONS

Gary W. BURDICK

*Department of Physics, Andrews University, Berrien Springs, MI 49104, USA*
*E-mail: gburdick@andrews.edu*

Michael F. REID

*Department of Physics and Astronomy and MacDiarmid Institute*
*for Advanced Materials and Nanotechnology, University of Canterbury,*
*Christchurch, New Zealand*
*E-mail: mike.reid@canterbury.ac.nz*

## Contents

List of symbols

| | | | |
|---|---|---|---|
| $A_{FI,q}^{ED}$ | Einstein $A$ coefficients | $H_{cf}$ | crystal-field Hamiltonian |
| $\alpha, \beta, \gamma$ | parameters for two-body Coulomb interactions | $H_{ccf}$ | correlation crystal-field Hamiltonian |
| $B_q^k$ | crystal-field parameters | $H_d$ | d-electron portion of the Hamiltonian |
| $C_q^{(k)}$ | many-electron spherical tensor operators | $M^k$ | spin–spin and spin–other–orbit (Marvin) parameters |
| $\delta_q^{(k)}$ | delta-function correlation crystal-field operators | $P^k$ | electrostatically correlated spin–orbit parameters |
| $\Delta_E(\text{fd})$ | energy difference between configurations | $S_{FI}^{ED}$ | dipole strengths |
| $E_{avg}$ | average energy of configuration barycenter above the ground state | $T^i$ | parameters for three-body Coulomb interactions |
| $F^k$ | Slater parameters for direct Coulomb interaction | $f_{FI,q}^{ED}$ | oscillator strengths |
| | | $\tau_{radiative}$ | radiative lifetimes |
| $G^j$ | Slater parameters for exchange Coulomb interaction | FWHM | full width half maximum |
| | | UV | ultraviolet |
| $H$ | complete effective energy level Hamiltonian | VUV | vacuum ultraviolet |
| | | $r^k$ | radial integrals |
| | | $\chi_L$ | local-field refractive index correction |
| | | $\zeta$ | spin–orbit interaction parameter |

# 1. Introduction

The parametric model for determining energy levels within the $4f^n$ configuration of rare earth ions in condensed matter environments was developed in the 1960s (Carnall et al., 1965; Wybourne, 1965; Dieke, 1968) and gained further sophistication through the 1970s and 1980s (Crosswhite and Crosswhite, 1984). This parametric model has been applied with considerable success to hundreds of lanthanide systems, though in some cases, inclusion of two-electron contributions (e.g., Judd, 1977a; Newman, 1977; Burdick and Richardson, 1998; Rukmini et al., 1994) has been needed in order to explain the observed crystal field splitting of certain individual $^{2S+1}L_J$ multiplets. Although major systematic analyses of experimental energy levels seldom went above 40,000 cm$^{-1}$ (see, for example, Carnall et al., 1989), recent interest in the VUV energy levels (Wegh et al., 2000; Peijzel et al., 2005c) have shown that these parametrizations can be extended accurately up to higher energies.

Many applications of lanthanide materials make use of the $4f^{n-1}5d$ excited configuration. These applications include scintillator materials, VUV lasers, and phosphors for fluorescent lighting and plasma displays (Blasse and Grabmaier, 1994; Feldmann et al., 2003). An understanding of these states is crucial to the development of advanced materials.

Transitions to the $4f^{n-1}5d$ excited states of lanthanide ions have been studied for a long time, particularly for divalent ions (McClure and Kiss, 1963) and for Ce$^{3+}$ (Schlesinger and

Whippey, 1968), which have transitions in the UV region. The wide availability of VUV synchrotron radiation from the 1970s allowed systematic experimental studies and some limited calculations to be carried out for the trivalent ions (Elias et al., 1973; Heaps et al., 1976). High-resolution spectra gathered over the past decade have provided enough data to make it now possible to carry out parametrized calculations for the $4f^{n-1}5d$ configuration. Although it is possible to do qualitatively reasonably accurate ab initio calculations (Ogasawara et al., 2005, 2007), parametrized calculations have the advantage of being relatively easy to apply to a large number of ions and hosts.

Though the extension of the parametrized model is straightforward, its application is different for the $4f^{n-1}5d$ configuration for two reasons. Transitions between $4f^n$ and $4f^{n-1}5d$ configurations consist mainly of broad vibronic lines, so interpretation of the spectra is not as straightforward as interpretation of $4f^n \rightarrow 4f^n$ spectra, making accurate determination of the parameters more difficult. In addition, the crystal-field splittings of the $4f^{n-1}5d$ configuration are large compared to the splittings caused by the Coulomb interaction. Whereas for the $4f^n$ configuration the crystal field can be considered as a minor perturbation to the free ion, this is not the case for the $4f^{n-1}5d$ configuration, where the crystal field dominates the spectral structure.

In this Chapter we describe the extension of the parametric model used for $4f^n$ spectra to calculations of absorption and emission spectra for the $4f^{n-1}5d$ configuration. We also illustrate how they can be applied to calculate other properties of interest, such as non-radiative relaxation rates. Finally, we discuss the relationship between parametrized calculations and other approaches, such as ab initio calculations.

## 2. Parametrized energy level calculations

### 2.1. *Introduction*

Detailed modeling of the $4f^n$ and $5f^n$ configurations of lanthanide and actinide ions in crystals was developed in the 1960s (Carnall et al., 1965; Wybourne, 1965; Dieke, 1968) and has become a standard tool for rationalizing spectroscopic measurements. Parameters are available for the entire $4f^n$ and $5f^n$ series for several host crystals (Carnall et al., 1989; Carnall, 1992; Görller-Walrand and Binnemans, 1996). In contrast, calculations for $4f^{n-1}5d$ configurations spanning the lanthanide series have only recently been attempted. In this section, we will cover the major issues encountered in extending the standard model to include the $4f^{n-1}5d$ excited configurations.

Standard crystal field calculations for lanthanides in crystals make use of an "effective Hamiltonian" that acts solely within the $4f^n$ configuration. Rather than solving for the eigenvalues and eigenstates of the full Hamiltonian, the effective Hamiltonian is diagonalized within the model space ($4f^n$ configuration), and the expectation values of the effective operators are evaluated between the model-space eigenvectors. The effective operators implicitly include contributions arising out of configuration mixing of the $4f^n$ configuration with all other configurations having like parity (including the continuum).

It is possible to extend the model space to explicitly include all states of the $4f^{n-1}5d$ configuration as well. In this case, the effective Hamiltonian is diagonalized within the two-configuration model space and additional effective operators are included that act within the $4f^{n-1}5d$ excited configuration. These additional operators also implicitly include contributions arising out of configuration mixing of the $4f^{n-1}5d$ configuration with other configurations having the same parity as $4f^{n-1}5d$.

Parameters for the $4f^n$ configuration are commonly determined by fits to energy levels, with more than 100 identified energy levels for some ions. Transitions between the $4f^n$ and $4f^{n-1}5d$ configurations are dominated by broad vibronic bands, so identification of a large number of energy levels is not possible, despite there being many more $4f^{n-1}5d$ states than $4f^n$ states. Consequently, parametric modeling generally requires a combination of fitting and ab initio calculations. In section 2.2 we will consider the portion of the effective Hamiltonian acting upon $4f^n$ configuration states, followed by a discussion of the portion acting upon $4f^{n-1}5d$ configuration states in section 2.3 This will be followed by a description of the electric-dipole calculations and the inclusion of vibronic lineshapes required to model transition intensities between states of the two configurations in section 2.4.

## 2.2. *$4f^n$ Hamiltonian*

The effective Hamiltonian acting within the $4f^n$ configuration is commonly written (Carnall et al., 1989),

$$H = E_{\mathrm{avg}} + \sum_{k=2,4,6} F^k f_k + \varsigma_{\mathrm{f}} A_{\mathrm{so}} + \alpha L(L+1) + \beta G(G_2) + \gamma G(R_7)$$

$$+ \sum_{i=2,3,4,6,7,8} T^i t_i + \sum_{h=0,2,4} M^h m_h + \sum_{k=2,4,6} P^k p_k + \sum_{k,q} B_q^k C_q^{(k)}, \tag{1}$$

where $E_{\mathrm{avg}}$ is the energy difference between the ground-state energy and the configuration center of gravity (barycenter) and is included to allow the ground-state energy to be set to zero. The Coulomb interaction between the 4f electrons is parametrized by the radial electrostatic integrals, $F^k$, which multiply the angular part of the electrostatic interaction, $f_k$. The coupling of the electron spin magnetic moment and the magnetic field originating in the orbital motion of the electron is represented by the spin–orbit coupling constant, $\zeta_{\mathrm{f}}$, which multiplies the angular part of the spin–orbit interaction, $A_{\mathrm{so}}$.

Higher-order terms in the Hamiltonian include two-electron Coulomb correlation contributions represented by parameters $\alpha$, $\beta$, $\gamma$, where $L$ is the orbital angular momentum and $G(G_2)$ and $G(R_7)$ are Casimir's operators for the groups $G_2$ and $R_7$, respectively (Rajnak and Wybourne, 1963). Three-electron Coulomb correlation contributions are parametrized by $T^i$, with three-body operators $t_i$ given by Judd (1966) and Crosswhite et al. (1968). Three-body operators that take into account higher-order corrections have been tabulated by Hansen et al. (1996), but these terms only arise in higher order perturbations, and their inclusion has not been needed. For the same reason, neither have four-body operators been considered. Magnetically correlated interactions (Judd et al., 1968), representing spin–spin and spin–other–orbit

relativistic corrections are included by the Marvin integrals, $M^k$, and electrostatically corre-lated spin–orbit contributions are represented by the $P^k$.

The parameters discussed above are often called "free ion" parameters for the "atomic Hamiltonian," because they take the same form in the calculations of the free ion as they do in a crystal environment. However, it should be recognized that these parameters are modified by the crystal environment.

The terms in the Hamiltonian that represent the non-spherical part of the interaction with the crystal are modeled using the so-called "crystal-field" Hamiltonian. It is important to recognize that this Hamiltonian is not restricted to electrostatic effects, which form a minor part of the total "crystal-field" effect (Ng and Newman, 1987). When the parameters are fitted to experimental energies, their values reflect all one-electron non-spherical interactions. The crystal-field Hamiltonian is expressed in Wybourne (1965) notation as,

$$H_{cf} = \sum_{h,q} B_q^k C_q^{(k)}, \tag{2}$$

where the $B_q^k$ parameters define the one-electron crystal field interaction and the $C_q^{(k)}$ are many-electron spherical tensor operators for the $4f^n$ configuration. For $f^n$ configurations, $k = 2, 4, 6$, and non-zero values of $q$ depend upon the site symmetry of the lanthanide ion in the host lattice. The total number of crystal field parameters ranges from 27 parameters for $C_1$ or $C_i$ symmetry, down to only two parameters for octahedral or cubic symmetry.

The one-electron crystal field Hamiltonian does not take into account electron correlation effects. For some systems, it has been useful to augment the crystal field Hamiltonian with additional terms representing the two-electron, correlated crystal field. The additional terms most commonly used (see, for example, Peijzel et al., 2005b; Wegh et al., 2003) are from the simplified "delta-function" correlation crystal field model first proposed by Judd (1978) that assumes electron interaction takes place only when two electrons are located at the same position (hence the name "delta-function"). This simplified model, developed by Lo and Reid (1993), adds additional terms, given as,

$$H_{ccf} = \sum_{k,q} D_q^k \delta_q^{(k)}, \tag{3}$$

where $k$ runs over the even integers from 2 to 12 and allowed values of $q$ are determined by the site symmetry. In actual practice, however (Burdick and Richardson, 1998), only the $k = 2, 4$ terms provide significant contributions. This gives two additional parameters, $D_q^2$, and $D_q^4$, with respective operators given by,

$$\delta_q^{(2)} = \frac{35\sqrt{7}}{3\sqrt{2}} g_{2q}^{(2)} - \frac{35\sqrt{7}}{\sqrt{22}} g_{3q}^{(2)} - \frac{28\sqrt{105}}{\sqrt{143}} g_{10q}^{(2)} \tag{4a}$$

and

$$\delta_q^{(4)} = -\frac{21\sqrt{105}}{2\sqrt{11}} g_{2q}^{(4)} + \frac{63\sqrt{105}}{22} g_{3q}^{(4)} + \frac{84\sqrt{42}}{\sqrt{715}} g_{10Aq}^{(4)} + \frac{8232\sqrt{3}}{11\sqrt{1105}} g_{10Bq}^{(4)}, \tag{4b}$$

where the $g$ operators are a subset of the orthogonal correlation crystal field operators of Judd (1977b) and Reid (1987).

### 2.2.1. *Parameters for the $4f^n$ configuration*

The most extensive systematic determination of $4f^n$ parameters for ions across the lanthanide series is by Carnall et al. (1988, 1989) for lanthanides in $LaF_3$. The $4f^n$ free ion parameters are reduced by a few percent in crystals relative to gaseous ions, but do not change very much from one crystalline environment to another. For this reason, the tabulations of Carnall are still used as the starting point for many of the parametrized calculations within the $4f^n$ shell. In most cases, the energy level data are not sufficiently complete to unambiguously determine all of the free ion parameter values, so some of the parameters, such as the three-body parameters, $T^k$, are often kept fixed at Carnall's values. The determination of exactly which parameters to keep fixed, and which to vary, is usually decided on a case-by-case basis, based upon how many multiplets are covered by the data, and upon the indeterminacies that arise during the fitting process itself.

Görller-Walrand and Binnemans (1996) have compiled the most complete listing of 4f-electron crystal field parameters across the lanthanide series. However, additional high quality crystal field level measurements for individual ions have been made since 1996 (see, for examples (De Leebeeck et al., 1999), for $Nd:LiYF_4$, or (Wegh et al., 2003), for $Er:LiYF_4$).

The correlation crystal-field extension to the Hamiltonian becomes more important when many high-energy states are observed. For the $4f^n \rightarrow 4f^n$ transitions, many new energy levels have been observed and identified in the VUV region. The well-known Dieke diagrams (Dieke, 1968) have been extended experimentally from 40 000 up to 65 000 $cm^{-1}$ (Peijzel et al., 2005c), and the standard theoretical models have been well able to handle this increased data. For example, from their synchrotron radiation experiments, Wegh et al. (2003) were able to identify the energy levels of $Er^{3+}:LiYF_4$ up to 63 000 $cm^{-1}$. Peijzel et al. (2005b) identified the energy levels of $Gd^{3+}:LaF_3$ up to 62 000 $cm^{-1}$ using two-photon excited-state absorption techniques. These, and other, VUV $4f^n \rightarrow 4f^n$ spectra are well modeled by the standard calculations described above.

### 2.3. *$4f^{n-1}5d$ Hamiltonian*

The Hamiltonian discussed above for the f-electrons of the $4f^n$ configuration also applies to the $4f^{n-1}$ "core" in the $4f^{n-1}5d$ configuration. Parameter values for the $4f^{n-1}$ "core" are expected to be similar (though not necessarily identical) to the parameter values for the ground $4f^n$ configuration. They are distinguished from parameters for $4f^n$ by appending "(ff)".

With the expansion of the "model space" to include the first excited configuration, $4f^{n-1}5d$, two additional types of terms can arise in addition to the terms that apply to the $4f^{n-1}$ "core". The first type involves effective operators that act *within* the $4f^{n-1}5d$ configuration. Parameters associated with these operators implicitly include contributions involving mixing with other configurations having the same parity as $4f^{n-1}5d$. Since $4f^{n-1}5d$ and $4f^n$ are of opposite parity, these parameters do not include any configuration mixing between the two.

The second type of effective operator acts *between* states of the $4f^n$ and $4f^{n-1}$5d configurations. These configuration-mixing operators may be useful for modeling parity-forbidden electric-dipole transitions within the $4f^n$ configuration (Burdick et al., 1995; Görller-Walrand and Binnemans, 1998; Liu et al., 2006), but have very little effect upon energy levels of either configuration, and thus can be ignored for the calculation of excited-state energy levels. Of course, the electric-dipole operator, to be discussed in section 2.4, has matrix elements between and $4f^n$ and $4f^{n-1}$5d. However, that operator is only used in transition intensity calculations, and is not part of the Hamiltonian.

The additional terms involving the 5d electron may be written as,

$$H_d = \Delta_E(\text{fd}) + \sum_{k=2,4} F^k(\text{fd}) f_k(\text{fd}) + \sum_{j=1,3,5} G^j(\text{fd}) g_j(\text{fd}) + \varsigma(\text{dd}) A_{\text{so}}(\text{d})$$
$$+ \sum_{k=2,4} B_q^k(\text{d}) C_q^{(k)}(\text{d}), \tag{5}$$

where $\Delta_E(\text{fd})$ represents the (barycenter to barycenter) energy difference between the two configurations, and incorporates contributions from both atomic and lattice effects. The $F^k$ and $G^j$ represent the Coulomb interaction of the 5d electron with the $4f^{n-1}$ core and $\zeta(\text{dd})$ represents the spin–orbit interaction of the 5d electron. The $B_q^k(\text{d})$ are crystal-field parameters for the 5d electron. In this case, $k$ is restricted to 2 and 4, and $q$ follows the same restrictions as for the f-electron crystal-field terms. The number of 5d crystal-field parameters ranges from 14 for $C_1$ or $C_i$ symmetry, down to only one parameter for octahedral or cubic symmetry.

Other operators representing higher-order contributions to the Hamiltonian, such as correlation effects involving the 5d electron, are possible. However, these would produce only small corrections which would have small, unobservable, effects.

### 2.3.1. *Parameters for the $4f^{n-1}$5d configuration*

The spectra for transitions within the $4f^n$ configuration consist predominantly of sharp zero-phonon lines, allowing the identification of a large number of energy levels, and thus providing enough information to determine the Hamiltonian parameters by least-squares fitting. In contrast, transitions to the $4f^{n-1}$5d configuration consist of broad vibronic bands, with few if any observable zero-phonon lines. For this reason, fitting of all the Hamiltonian parameters is not generally feasible, and it is therefore crucial to start with good estimates of the parameters, and then use spectroscopic information for different ions to help refine the calculation across the lanthanide series.

Details of the determination of parameters will be given in section 3. However, initial estimates of parameter values are made as follows:

1. Parameters for the $4f^{n-1}$ core are taken from experimentally fitted parameters for the $4f^n$ configuration of the same ion.
2. Atomic interaction parameters involving the 5d electron are taken from ab initio calculations using, for example, the free ion equations of Cowan (1981).
3. Crystal field parameters involving the 5d electron are determined from the $Ce^{3+}$ spectrum.

Table 1

Calculated parameters for the $4f^n$ and $4f^{n-1}5d$ configurations of trivalent lanthanide ions (taken from Reid et al., 2002, with corrections for $r^3$(fd) and $r^5$(fd)). Parameters have units $cm^{-1}$ and radial integrals have units $Å^k$

| Ion | $Ce^{3+}$ | $Pr^{3+}$ | $Nd^{3+}$ | $Pm^{3+}$ | $Sm^{3+}$ | $Eu^{3+}$ | $Gd^{3+}$ | $Tb^{3+}$ | $Dy^{3+}$ | $Ho^{3+}$ | $Er^{3+}$ | $Tm^{3+}$ | $Yb^{3+}$ | $Lu^{3+}$ |
|---|---|---|---|---|---|---|---|---|---|---|---|---|---|---|
| $n$ | 1 | 2 | 3 | 4 | 5 | 6 | 7 | 8 | 9 | 10 | 11 | 12 | 13 | 14 |
| $4f^n$ parameters and radial integrals | | | | | | | | | | | | | | |
| $F^2$ | – | 96682 | 100643 | 104391 | 107970 | 111413 | 114744 | 117979 | 121133 | 124216 | 127237 | 130203 | 133120 | 135993 |
| $F^4$ | – | 60534 | 63029 | 65384 | 67629 | 69785 | 71866 | 73885 | 75850 | 77769 | 79648 | 81490 | 83301 | 85082 |
| $F^6$ | – | 43509 | 45307 | 47003 | 48618 | 50168 | 51663 | 53112 | 54523 | 55899 | 57246 | 58567 | 59864 | 61140 |
| $\zeta_f$ | 681 | 798 | 926 | 1064 | 1213 | 1373 | 1546 | 1732 | 1932 | 2146 | 2376 | 2621 | 2882 | 3161 |
| $r^2$ | 0.3726 | 0.3472 | 0.3216 | 0.2999 | 0.2812 | 0.2648 | 0.2504 | 0.2374 | 0.2258 | 0.2153 | 0.2057 | 0.1969 | 0.1888 | 0.1814 |
| $r^4$ | 0.3155 | 0.2785 | 0.2409 | 0.2113 | 0.1874 | 0.1678 | 0.1514 | 0.1375 | 0.1256 | 0.1153 | 0.1064 | 0.0985 | 0.0916 | 0.0855 |
| $r^6$ | 0.5069 | 0.4297 | 0.3504 | 0.2918 | 0.2472 | 0.2123 | 0.1845 | 0.1620 | 0.1435 | 0.1281 | 0.1151 | 0.1041 | 0.0947 | 0.0866 |
| $4f^{n-1}5d$ parameters and radial integrals | | | | | | | | | | | | | | |
| $\Delta_E$(fd) | 57812 | 65413 | 71773 | 77635 | 82813 | 87401 | 91584 | 95256 | 98526 | 101535 | 104024 | 106306 | 108203 | 109809 |
| $F^2$(ff) | – | – | 108416 | 111922 | 115304 | 118585 | 121778 | 124897 | 127951 | 130948 | 133894 | 136794 | 139653 | 142474 |
| $F^4$(ff) | – | – | 68283 | 70479 | 72594 | 74642 | 76632 | 78573 | 80471 | 82332 | 84159 | 85956 | 87726 | 89472 |
| $F^6$(ff) | – | – | 49197 | 50776 | 52295 | 53765 | 55193 | 56585 | 57945 | 59278 | 60587 | 61873 | 63140 | 64389 |
| $\zeta$(ff) | – | 873 | 1025 | 1167 | 1321 | 1487 | 1665 | 1858 | 2064 | 2284 | 2520 | 2773 | 3041 | 3328 |
| $F^2$(fd) | – | 30271 | 30300 | 30207 | 30111 | 30010 | 29905 | 29795 | 29681 | 29562 | 29439 | 29312 | 29180 | 29044 |
| $F^4$(fd) | – | 15094 | 15038 | 14890 | 14748 | 14611 | 14477 | 14347 | 14219 | 14092 | 13967 | 13843 | 13720 | 13598 |
| $G^1$(fd) | – | 12903 | 12914 | 12739 | 12590 | 12461 | 12348 | 12247 | 12156 | 12073 | 11997 | 11927 | 11861 | 11799 |
| $G^3$(fd) | – | 11160 | 11135 | 10985 | 10851 | 10728 | 10614 | 10508 | 10408 | 10313 | 10221 | 10133 | 10047 | 9963 |
| $G^5$(fd) | – | 8691 | 8659 | 8540 | 8431 | 8330 | 8235 | 8146 | 8060 | 7978 | 7898 | 7821 | 7746 | 7672 |
| $\zeta$(dd) | 1082 | 1149 | 1216 | 1283 | 1351 | 1419 | 1488 | 1557 | 1627 | 1697 | 1768 | 1839 | 1910 | 1982 |
| $r^2$(ff) | – | 0.2945 | 0.2788 | 0.2621 | 0.2474 | 0.2343 | 0.2225 | 0.2119 | 0.2022 | 0.1933 | 0.1852 | 0.1777 | 0.1708 | 0.1644 |
| $r^4$(ff) | – | 0.1875 | 0.1705 | 0.1520 | 0.1366 | 0.1235 | 0.1124 | 0.1029 | 0.0946 | 0.0873 | 0.0809 | 0.0752 | 0.0701 | 0.0656 |
| $r^6$(ff) | – | 0.2221 | 0.1965 | 0.1674 | 0.1444 | 0.1258 | 0.1107 | 0.0981 | 0.0876 | 0.0787 | 0.0711 | 0.0646 | 0.0590 | 0.0541 |
| $r^2$(dd) | 1.6592 | 1.6113 | 1.5676 | 1.5286 | 1.4932 | 1.4609 | 1.4313 | 1.4040 | 1.3788 | 1.3555 | 1.3339 | 1.3138 | 1.2951 | 1.2777 |
| $r^4$(dd) | 4.2618 | 4.0380 | 3.8396 | 3.6679 | 3.5160 | 3.3807 | 3.2594 | 3.1502 | 3.0515 | 2.9620 | 2.8805 | 2.8063 | 2.7384 | 2.6764 |
| $4f^n/4f^{n-1}5d$ radial integrals | | | | | | | | | | | | | | |
| $r^1$(fd) | 0.4350 | 0.4168 | 0.3953 | 0.3771 | 0.3614 | 0.3477 | 0.3356 | 0.3247 | 0.3150 | 0.3062 | 0.2982 | 0.2908 | 0.2841 | 0.2778 |
| $r^3$(fd) | 0.6535 | 0.6029 | 0.5478 | 0.5024 | 0.4643 | 0.4317 | 0.4036 | 0.3791 | 0.3575 | 0.3384 | 0.3213 | 0.3060 | 0.2922 | 0.2798 |
| $r^5$(fd) | 1.4002 | 1.2520 | 1.0939 | 0.9690 | 0.8677 | 0.7842 | 0.7144 | 0.6552 | 0.6045 | 0.5607 | 0.5226 | 0.4893 | 0.4599 | 0.4339 |
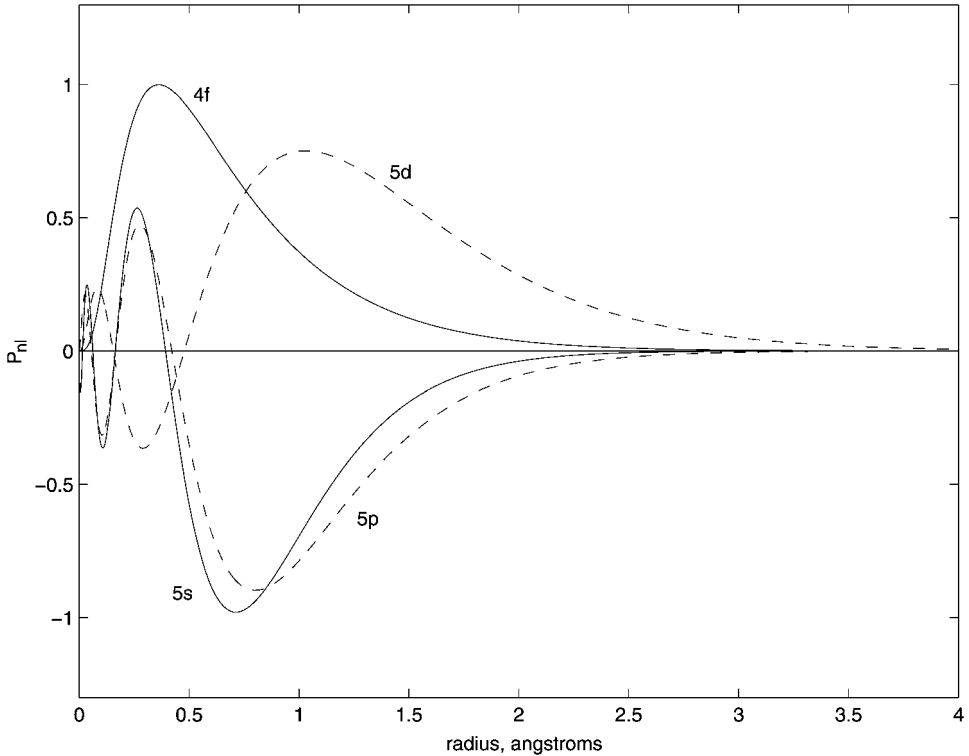
Fig. 1. Radial functions $P_{nl}$ calculated for $Pr^{3+}$ (from Reid et al., 2002). The function for 5s has been multiplied by $-1$ for clarity.

From these initial values, systematic adjustment is made to obtain final parameter sets that give a good representation of $4f^n \rightarrow 4f^{n-1}$5d absorption and $4f^{n-1}$5d $\rightarrow 4f^n$ emission spectra for ions across the lanthanide series.

2.3.1.1. *Parameters for the $4f^{n-1}$5d core*  Table 1 presents atomic parameters and radial integrals for the $4f^n$ and $4f^{n-1}$5d configurations of the trivalent ions across the lanthanide series, with calculated radial functions for $Pr^{3+}$ shown in fig. 1. The top portion of table 1 presents atomic parameters and radial integrals calculated within the $4f^n$ configuration, the second portion parameters and radial integrals calculated within the $4f^{n-1}$5d excited configuration, and the third portion radial integrals calculated between the two configurations. Values were determined using the relativistic Hartree–Fock calculation methods of Cowan (1981).

The ab initio calculations presented in table 1 suggest that parameters for interactions within the $4f^{n-1}$ core of the $4f^{n-1}$5d configuration should have similar values to those for the $4f^n$ configuration for the same ion in the same host crystal. Thus, it is reasonable to use the experimentally determined values for these parameters from the $4f^n$ configuration, discussed in

section 2.2.1, as the initial estimate for these parameters in the $4f^{n-1}5d$ configuration (possibly with an overall scaling factor included, see below).

It is well-known that ab initio calculations overestimate the atomic parameters $F^k$ and $\zeta_f$ for the $4f^n$ configuration (Crosswhite and Crosswhite, 1984; Carnall et al., 1989), with the overestimation particularly large (about 35%) for $F^2$. More elaborate perturbation theory calculations (Morrison and Rajnak, 1971; Cai et al., 1992) can reduce this discrepancy. However, for the most part, extensive perturbation theory calculations are not necessary due to the availability of atomic parameter values fitted from the $4f^n$ configuration energy level data.

The $F^k(ff)$ and $\zeta(ff)$ parameters are calculated to be slightly larger for the $4f^{n-1}5d$ configuration than for $4f^n$. This is a result of the contraction of the 4f orbitals in the $4f^{n-1}5d$ configuration. In order to take this effect into account, the atomic parameters fitted to the $4f^n$ energy level data should be increased by a small scaling factor (about 6%) when applied to 4f orbitals in the excited configuration (van Pieterson et al., 2002b).

2.3.1.2. *Atomic parameters involving 5d electrons* The trends for atomic parameters representing effects involving the 5d electron are markedly different from the trends for $4f^{n-1}$ core parameters, as can be seen from table 1. Whereas the $F^k(ff)$ and $\zeta(ff)$ parameters show a dramatic increase across the lanthanide series from $Pr^{3+}$ to $Lu^{3+}$, due to the contraction of the 4f orbitals for the heavy lanthanides, the $\zeta(dd)$ parameter increases much more slowly. This is due to the fact that the 5d orbitals contract much less across the lanthanide series than do the 4f orbitals. Also, the $F^k(fd)$ and $G^j(fd)$ parameters decrease gradually, due to the reduced overlap between the 4f and 5d orbitals as the 4f orbitals contract. These calculations are useful for estimating the trends in the parameters across the lanthanide series, once they have been determined for a few ions.

As with the case for the $F^k(ff)$ parameters, the $F^k(fd)$ and $G^j(fd)$ parameters for gaseous ions are significantly overestimated by the Hartree–Fock calculations. This may be seen by comparing the calculated parameters listed in table 1 with experimental parameters for gaseous $Pr^{3+}$ (see table 3 of Reid et al., 2002). An additional reduction in these parameters for ions in crystals is also to be expected, due to the nephelauxetic effect, which causes the 5d orbitals to be partially delocalized over the ligands, reducing the interactions with the 4f core. However, this delocalization mainly affects the "tail" of the wavefunctions. The $F^k(fd)$ and $G^j(fd)$ parameters are calculated from integrals involving both 4f and 5d orbitals, and these integrals will not be affected much by changes in the "tail" of the 5d orbitals, because the 4f orbitals are much more localized (see fig. 1). Thus the additional reduction is not as large as might first be suspected.

In many of the calculations described in section 3 the $F^k(fd)$ and $G^j(fd)$ parameters are all scaled equally from their Hartree–Fock values. Comparison of the Hartree–Fock values with the experimental values of table 3 of Reid et al. (2002) shows that the Hartree–Fock calculation overestimates the $F^2(fd)$ and $G^1(fd)$ parameters more than the others. In future calculations, more accurate results might be obtained by using larger scaling factors for these two parameters.

2.3.1.3. *Crystal-field parameters* Crystal-field parameters for the 5d electron are typically 10–20 times the magnitude of the parameters for the 4f electrons. This is due to the fact that the 5d orbital has a much greater overlap with the ligands than does the more localized 4f orbitals, as shown in fig. 1. The 5d crystal field parameters may be determined from the $Ce^{3+}$ spectra and extrapolated to ions across the lanthanide series, as additional electrons in the $4f^{n-1}$ "core" are not expected to have a great influence upon the 5d orbital distribution.

Crystal-field parameters would be expected to change across the series roughly in proportion to the radial integrals $r^2$ and $r^4$ (and $r^6$ for 4f electrons). These integrals decrease dramatically across the lanthanide series for the 4f electrons (because their orbitals contract dramatically) but only by a few percent for the 5d electron. Thus, crystal-field parameters determined for $Ce^{3+}$ may be used across the lanthanide series, with only a small scaling factor for the heavy ions.

## 2.4. *Simulation of spectra*

The $4f^n \rightarrow 4f^{n-1}5d$ transitions are electric-dipole allowed, and it is therefore comparatively easy to calculate the necessary transition matrix elements of the electric-dipole operator,

$$-eD_q^{(1)} = -er^1 C_q^{(1)},$$ 
(6)

where $r^1$ is the 4f–5d radial integral given in table 1, and $C_q^1$ is a spherical tensor operator as defined in Cowan (1981) or Wybourne (1965). In contrast, electric-dipole transitions within the $4f^n$ configuration rely on mixing of the 4f orbitals with opposite parity states on the ion or ligands. This leads to a much more complex parametrization for $4f^n \rightarrow 4f^n$ transitions (Reid and Richardson, 1983; Görller-Walrand and Binnemans, 1998; Reid, 2005).

The measurable quantities of interest for absorption and emission are oscillator strengths and Einstein $A$ coefficients, respectively (e.g., see Henderson and Imbusch, 1989; Reid, 2005). The starting point for the calculations is the electric dipole strength for a particular polarization, $q$,

$$S_{\text{FI},q}^{\text{ED}} = \sum_{i,f} e^2 \big| \langle Ff | D_q^{(1)} | Ii \rangle \big|^2,$$ 
(7)

where the sums are over the components of the initial and final states. For unpolarized light, an isotropic dipole strength may be defined as,

$$\overline{S}_{\text{FI}}^{\text{ED}} = \frac{1}{3} \sum_q S_{\text{FI},q}^{\text{ED}}.$$ 
(8)

Given the calculated electric dipole strength, the absorption oscillator strength is defined as,

$$f_{\text{FI},q}^{\text{ED}} = \frac{2m\omega}{he^2} \frac{\chi_L}{n} \frac{1}{g_I} S_{\text{FI},q}^{\text{ED}}$$ 
(9)

and the Einstein $A$ coefficient for emission of a particular polarization is defined as,

$$A_{\text{FI},q}^{\text{ED}} = \frac{1}{3} \frac{1}{4\pi\varepsilon_0} \frac{4\omega^3}{\hbar c^3} n \chi_L \frac{1}{g_I} S_{\text{FI},q}^{\text{ED}}.$$ 
(10)

In these expressions, $g_I$ is the degeneracy of the initial state, $n$ is the refractive index, and $\chi_L$ is the local correction to the electric field, accounting for the ion being less polarizable than the bulk medium. The local electric field correction may be taken as,

$$\chi_L = \left(\frac{n^2 + 2}{3}\right)^2. \tag{11}$$

It is common to define a $\chi$ that includes both the bulk and local correction factors (i.e., $\chi_L/n$). However, as the exact form of the local correction factor may be significantly more complicated (see Duan et al., 2005b), we consider it more appropriate to maintain the distinction between the two terms.

The sum of the Einstein $A$ coefficients over all possible final emission states and polarizations is the inverse of the radiative lifetime, i.e.,

$$\frac{1}{\tau_{\text{radiative}}} = \sum_F \sum_q A^{\text{ED}}_{\text{FI},q}. \tag{12}$$

Most of the spectra discussed in this Chapter are not normalized, so the magnitude of the dipole moment and the refractive index correction are not of particular interest. We note that when eq. (12) is used to calculate lifetimes, the magnitudes of the dipole moment and the refractive index correction are important. In van Pieterson et al. (2002a), apparently good agreement was obtained between theoretical and experimental lifetimes. However, in those calculations a factor of $\sqrt{3}$ was omitted from the calculation of the dipole moments. When this factor is included the calculated lifetimes are too short by a factor of three. On the other hand, the calculation of radial integrals using Hartree–Fock wavefunctions overestimates the dipole moments. Duan and Reid (2005) estimated that including many-body effects would reduce the dipole moments by about 40%, and hence the dipole strengths by a factor of about 65%. This would increase lifetimes by a factor of about three, restoring agreement with experiment.

The 4f and 5d orbitals have very different interactions with the environment, so the equilibrium positions of the ligands in the excited states are different from the ground state, resulting in the majority of the electric-dipole transition intensity being in vibronic bands (Henderson and Imbusch, 1989; Meijerink et al., 2000). Contrary to the common assumption, the equilibrium bond length in the excited states is not necessarily longer than in the ground state. Ruipérez et al. (2005) performed calculations for lanthanide ions doped into $Cs_2NaYCl_6$. They calculated shorter lanthanide–ligand bond lengths when the lanthanide ion was in the lowest $4f^{n-1}5d$ states than when it was in a $4f^n$ state.

It is possible to model the vibronic bands in some detail. This has been done, for example, by Liu et al. (2004) for the 6d–5f emission spectrum of $Pa^{4+}$ in $Cs_2ZrCl_6$, which is analogous to the emission spectrum of $Ce^{3+}$. However, most of the simulations discussed in this chapter approximate the vibronic band shape with Gaussian bands. The energy level calculations yield zero-phonon line positions, and Gaussian bands are superimposed on the zero-phonon lines in order to reproduce the observed spectra. Peaks of the Gaussian band are offset from the zero phonon line by a constant. Peak offset and band widths, which are mostly host-dependent, may be determined from examination of the lowest 5d level of the $Ce^{3+}$ spectrum, as they will not vary much for different ions in the same host. It is also common to make the standard

approximation that the total intensities of the vibronic bands are proportional to the electric dipole strengths.

## 3. Energy levels of the $4f^{n-1}$5d configuration

In this section we discuss the calculation of energy levels for the $4f^{n-1}$5d configuration and the absorption or excitation spectra. The key to a parametric simulation is the determination of the parameters, so we first describe the strategy for deducing the parameters. We then briefly discuss the analysis of excitation spectra.

Once the parameters are determined, we can calculate other spectroscopic properties for the $4f^{n-1}$5d configuration. These include emission spectra and lifetimes, the presence (or lack of) emission from the $4f^{n-1}$5d configuration, and non-radiative relaxation effects upon the linewidths of $4f^{n-1}$5d and $4f^n$ excited states.

### 3.1. *Determination of parameters*

For the $4f^n$ configuration it is possible to perform detailed parameter fittings. This is not generally the case for the $4f^{n-1}$5d configuration because the broad vibronic bands makes identification of individual transitions difficult. As discussed in the previous section the parameters for the $4f^{n-1}$ "core" are expected to be closely related to the parameters for $4f^n$ configuration for the same ion/host combination, which are usually known. So we need to determine the crystal-field parameters and the free-ion parameters that involve the 5d electron.

#### 3.1.1. *5d crystal field parameters*
A major difference between the 5d and 4f orbitals is that the 5d crystal-field strength remains relatively constant across the lanthanide series. This means that it is usually possible to get a good estimate of the 5d crystal-field parameters from the $Ce^{3+}$ spectrum, though fine-tuning will be necessary. Sometimes it is possible to determine 5d crystal field parameters directly from the $4f^{n-1}$5d spectra, as was done by Laroche et al. (2000) for $LiYF_4$:$Pr^{3+}$. However, values of the 5d crystal field parameters may most easily be determined from examination of the $Ce^{3+}$ spectra, values which can then be applied to ions across the lanthanide series.

This is illustrated in fig. 2, where we present the excitation spectra for $Ce^{3+}$ (top panel), $Pr^{3+}$ (middle panel), and $Nd^{3+}$ (bottom panel) for near-cubic sites in $CaF_2$. In this case, there is a single 5d crystal-field parameter that can be easily estimated from the splitting between the lower (E symmetry) and higher ($T_2$ symmetry) bands. As more f-electrons are added to the system, the spectra become more complex. However, the separation between the principle $^2E$ and $^2T_2$ levels is very similar for these three systems. The calculated spectra in fig. 2 were done using the assumption that the crystal field is constant across the series. It is clear that the calculation slightly overestimates the splitting for $Pr^{3+}$ and $Nd^{3+}$. The small change in the 5d-electron crystal field for heavy lanthanides is to be expected, and is caused by the contraction of the ion across the lanthanide series. However, this change is much smaller than that for the 4f-electron crystal field terms, due to the fact that the 4f wavefunctions contract to
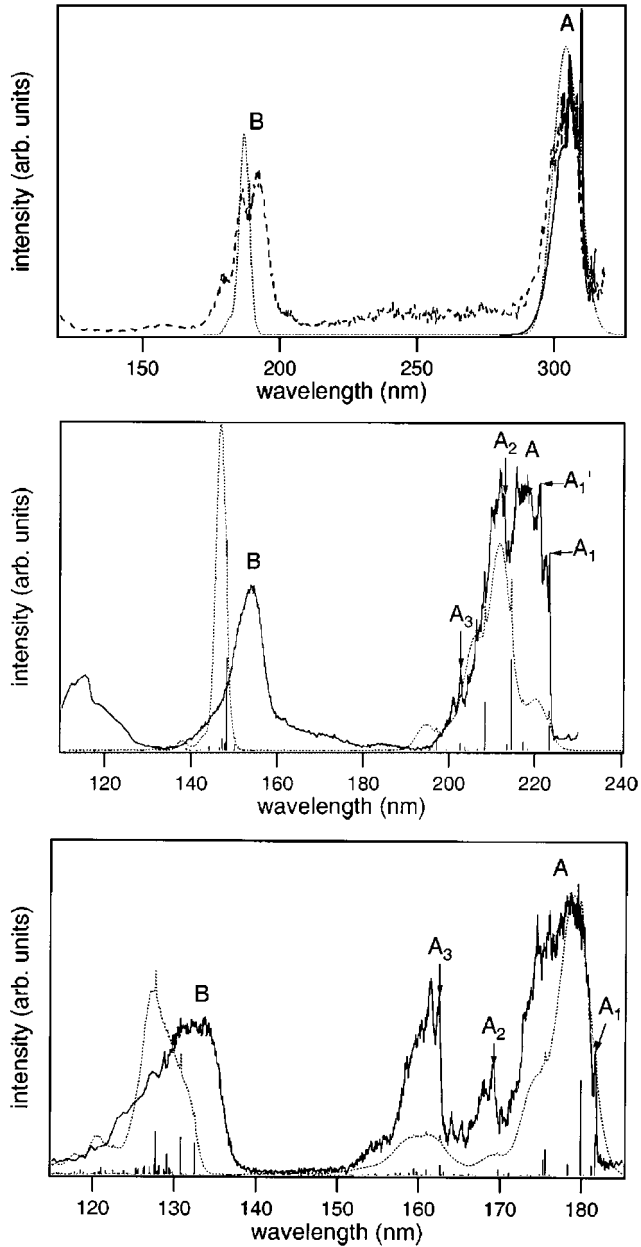
Fig. 2. Experimental and simulated spectra for the $4f^n \rightarrow 4f^{n-1}5d$ excitation of (a) $Ce^{3+}$, (b) $Pr^{3+}$, and (c) $Nd^{3+}$ in $CaF_2$ (from van Pieterson et al., 2002a). In each case, the dotted curve is the simulated spectrum. The experimental spectrum is a dashed curve for $Ce^{3+}$ and a solid curve for $Pr^{3+}$ and $Nd^{3+}$.

Fig. 3. Experimental and simulated spectra for the $4f^n \rightarrow 4f^{n-1}5d$ excitation of $Ce^{3+}$ in (a) LiYF$_4$ and (b) YPO$_4$ (from van Pieterson et al., 2002a). In each case, the solid curve is the experimental spectrum and the dotted curve is the simulated spectrum. Letters A–E indicate peaks of the 5d level bands.

a much greater extent for the heavy lanthanides than do the 5d wavefunctions. Thus, a small linear scaling across the lanthanide series reducing the crystal field parameters for the heavy lanthanides is appropriate.

For near-cubic sites in CaF$_2$ or cubic sites in elpasolite crystals (Tanner et al., 2003a, 2003b) there is only one 5d crystal-field parameter, which is easy to determine from the $Ce^{3+}$ spectrum. However, for sites of lower symmetry the determination is more difficult. The excitation spectra observed for the $Ce^{3+}$ emission in LiYF$_4$:$Ce^{3+}$ (Reid et al., 2000) and in YPO$_4$ (van Pieterson et al., 2002a) are shown in the two panels of fig. 3, respectively. The five strongest bands are assigned to $4f \rightarrow 5d$ vibronic transitions, which are labeled A–E. The zero-phonon line is observed for only the first band. For the other bands, the zero-phonon lines lie in the conduction band, so photo-ionization gives lifetime broadening, making the

Table 2
Experimental and calculated energy levels for the 5d configuration of $Ce^{3+}$ doped in $CaF_2$, $LiYF_4$ and $YPO_4$. The first numeric column for each lattice gives experimental energy levels determined by van Pieterson et al. (2002a) as detailed in the text. All energies in units of $cm^{-1}$

| $CaF_2$ | Octahedral parentage | Cubic | Expt | Calc |
|---|---|---|---|---|
| | $^2E$ | $\Gamma_8$ | 32300 | 32267 |
| | $^2T_2$ | $\Gamma_{8(a)}$ | 51600 | 52857 |
| | $^2T_2$ | $\Gamma_{8(b)}$ | 53300 | 52857 |
| | $^2T_2$ | $\Gamma_7$ | 55200 | 54395 |
| $LiYF_4$ | Octahedral parentage | $D_{2d}$ ($S_4$) | Expt | Calc |
| | $^2E$ | $\Gamma_7$ | 33433 | 33433 |
| | $^2E$ | $\Gamma_6$ | 41101 | 41062 |
| | $^2T_2$ | $\Gamma_6$ | 48564 | 49179 |
| | $^2T_2$ | $\Gamma_7$ | 50499 | 49888 |
| | $^2T_2$ | $\Gamma_7$ | 52790 | 52815 |
| $YPO_4$ | Octahedral parentage | $D_{2d}$ | Expt | Calc |
| | $^2E$ | $\Gamma_7$ | 30698 | 30701 |
| | $^2E$ | $\Gamma_6$ | 40058 | 40095 |
| | $^2T_2$ | $\Gamma_7$ | 41929 | 41562 |
| | $^2T_2$ | $\Gamma_6$ | 43788 | 43668 |
| | $^2T_2$ | $\Gamma_7$ | 48996 | 48814 |

zero-phonon line unobservable. For $LiYF_4$:$Ce^{3+}$, the full width at half maximum (FWHM) of each of the bands is approximately 1200 $cm^{-1}$, and the peak of the first band is offset from the zero-phonon line by 400 $cm^{-1}$. The widths of the bands are constant, so it may be assumed that the peak offset from the (unobserved) zero-phonon lines will also be constant. Following this assumption, the energy levels determined for the 5d states of $Ce^{3+}$ doped $CaF_2$, $LiYF_4$, and $YPO_4$ are presented in the first numeric column of table 2.

Detailed measurements of the 5d levels of $Ce^{3+}$ doped $YPO_4$, $CaF_2$, and $LiYF_4$ have been performed by van Pieterson et al. (2002a), and analyzed using these same assumptions. Resulting energy level diagrams are presented in fig. 4. The nearly cubic symmetry of $CaF_2$:$Ce^{3+}$ results in four crystal-field levels, whereas the (exact) $D_{2d}$ symmetry for $YPO_4$:$Ce^{3+}$ and (approximate) $D_{2d}$ symmetry for $LiYF_4$:$Ce^{3+}$ result in five crystal-field levels. The first, third, and fifth columns of table 3 present the fitted parameters for these three lattices, where the spin–orbit parameter, $\zeta$(dd), was held fixed at its ab initio value for the fluorides or at its measured free-ion value (Wybourne, 1965) for $YPO_4$.

In principle, both the crystal field parameters and the spin–orbit interaction parameter can be determined from the observed 5d levels of $Ce^{3+}$. However, due to the fact that the number of parameters exactly matches the number of experimental energy levels, the "exact" fit may not produce physically meaningful parameter values. For $YPO_4$:$Ce^{3+}$ ($D_{2d}$ site symmetry) and $LiYF_4$:$Ce^{3+}$ ($S_4$ site symmetry), three independent crystal field parameters are allowed, $B_0^2$, $B_0^4$, and $B_4^4$. Technically, for $S_4$ site symmetry, $B_4^4$ is allowed to be complex, seemingly resulting in an additional independently variable parameter. However, it is well understood (see, for example, Rudowicz and Qin, 2004; Burdick and Reid, 2004; Mulak and Mulak, 2005)
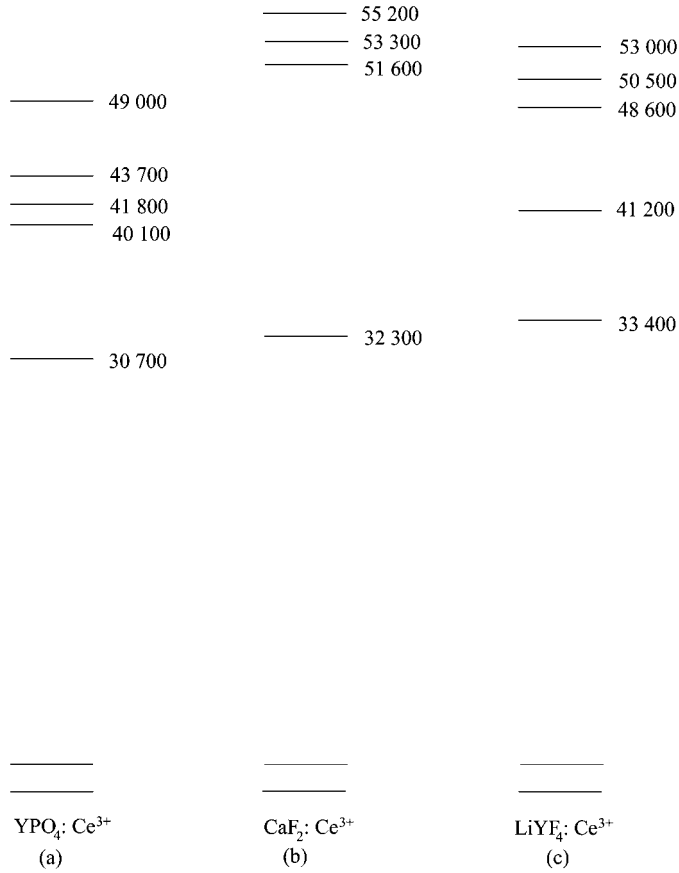
Fig. 4. Energy levels of $Ce^{3+}$ incorporated in (a) $YPO_4$, (b) $CaF_2$, and (c) $LiYF_4$, after van Pieterson et al. (2002a). The position of the zero phonon line is given. For those levels in which no zero phonon line was observed, they have been estimated as constant displacements from the maxima of the observed vibronic bands.

Table 3
Calculated crystal-field parameters for the 5d electron of the $4f^{n-1}$5d excited configuration of $Ce^{3+}$ doped in $YPO_4$, $CaF_2$, $LiYF_4$. Fitted parameters from van Pieterson et al. (2002a), except for the "exact" columns for $CaF_2$, $LiYF_4$ (this work) and $YPO_4$ Peijzel et al. (2005a). Parameters have units of $cm^{-1}$

| Parameter | $CaF_2$:$Ce^{3+}$ | $CaF_2$:$Ce^{3+}$ (exact) | $LiYF_4$:$Ce^{3+}$ | $LiYF_4$:$Ce^{3+}$ (exact) | $YPO_4$:$Ce^{3+}$ | $YPO_4$:$Ce^{3+}$ (exact) |
|---|---|---|---|---|---|---|
| $\Delta_E$(fd) | 43516 | 43516 | 43754 | 43761 | 39488 | 39613 |
| $\zeta$(d) | [1082] | 2044 | [1082] | 3826 | [995.6] | 1188 |
| $B_0^2$(d) | – | – | 4673 | 7994 | 4756 | 4763 |
| $B_0^4$(d) | −44016 | −43134 | −18649 | −4913 | 3010 | 2221 |
| $B_4^4$(d) | −26305 | −25778 | −23871 | −19473 | −22452 | −22568 |

that appropriate orientation of the coordinate axes always allows one complex crystal-field parameter to be made pure real. This means that the true number of independent crystal field parameters for $S_4$ symmetry is reduced to three. In addition to the spin–orbit parameter, $\zeta(dd)$, there is an additional energy parameter, $\Delta_E(fd)$, which represents the barycenter energy of the $4f^{n-1}5d$ configuration above the $4f^n$ configuration. This results in five unknowns to fit five energy levels. For this reason, it has been common practice to leave the spin–orbit parameter, $\zeta(dd)$, fixed in the fit to 5d levels.

Peijzel et al. (2005a) performed an exact fit of the spin–orbit and crystal-field parameters for $YPO_4:Ce^{3+}$ and showed that the parameter values changed very little when the spin–orbit parameter was allowed to vary. We have performed exact transformations of the $LiYF_4:Ce^{3+}$ and $CaF_2:Ce^{3+}$ energy levels to determine just how much the spin–orbit parameter changes when it is fit to the experimental data. As shown in the "exact" columns of table 3, the spin–orbit parameter takes on unphysical values, changing by a factor of two (for $CaF_2$) and a factor of three (for $LiYF_4$), but the crystal-field parameters remain relatively constant. This provides justification for the process of holding the spin–orbit parameter fixed for determining crystal-field parameter values, and provides support for the reliability of the crystal-field parameter values.

### 3.1.2. *Atomic parameters including 5d electrons*

As discussed in the previous section, and shown in fig. 2, the gross structure of the $4f^{n-1}5d$ configuration is determined by the 5d crystal-field levels, with the addition of the $4f^{n-1}$ "core" states giving rise to fine structure. In the absence of the 5d electron the $4f^{n-1}$ states would have an energy-level structure similar to the energy-levels of the previous ion in the lanthanide series. However, the Coulomb interaction between the 5d electron and the 4f electrons, represented by the $F^k(fd)$ and $G^j(fd)$ parameters, modifies this structure. To a first approximation the exchange part of the Coulomb interaction (represented by the $G^j(fd)$ parameters) gives a splitting into lower-energy "high-spin" states (with the maximum possible alignment of electron spins consistent with the Pauli principle) and higher-energy "low-spin" states, with one spin reversed. In the first half of the lanthanide series the "high-spin" states have the same spin as the ground state of the $4f^n$ configuration, and those are the transitions that are observed in figs. 2b and 2c. The "low-spin" states have much smaller intensity and are not generally observed. In the second half of the series, where there are more than 7 4f electrons in the $4f^n$ configuration, the "high-spin" states have a higher spin than the ground state (or any other state) of the $4f^n$ configuration. This is because the Pauli principle only allows 7 4f electrons to have parallel spins, but when one electron is excited to a 5d orbital it is possible to have up to 8 valence electrons with parallel spins. As a consequence, transitions to the lowest-energy states are spin-forbidden. This means that transitions from the ground state to these states have low intensity, but they are readily observable because, in contrast to the case in the first half of the series, they are not obscured by spin-allowed transitions.

Ab initio calculations are expected to overestimate the f–d Coulomb interaction parameters $F^k(fd)$ and $G^j(fd)$ (see section 2.3.1.2). The value of this reduction may be determined from the experimental data.
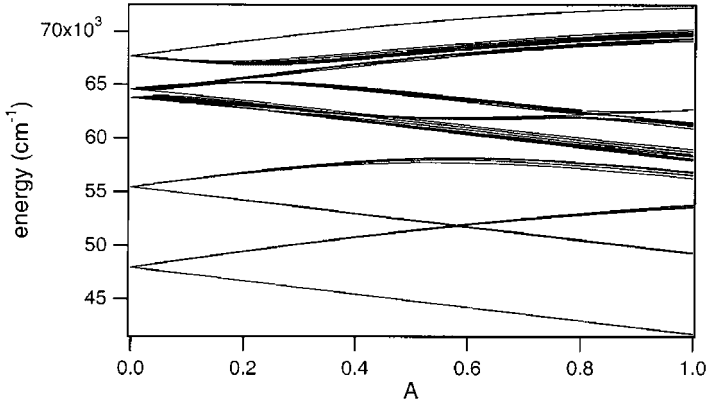
Fig. 5. Splitting of the five $4f^7$5d crystal-field states of $Tb^{3+}$ in $LiYF_4$ (taken from van Pieterson et al., 2002b). The parameter $A$ represents the f–d interactions as explained in the text. On the left ($A = 0$) the parameters for these interactions are set to zero and on the right ($A = 1$) they have the values from Hartree–Fock calculations for the free ion.

van Pieterson et al. (2002a) found that reducing the $F^k$(fd) and $G^j$(fd) parameters to 74% of their calculated values for $LiYF_4$:$Nd^{3+}$ and to 50% for $YPO_4$:$Pr^{3+}$ lead to a significantly better agreement between theory and experiment for their observed $4f^n$ to $4f^{n-1}$5d transitions. The greater reduction in parameter values for $YPO_4$ is to be expected, due to the greater covalency of the $YPO_4$ host lattice, producing a greater delocalization of the 5d electron over the ligands.

A useful measure of the required reduction in $F^k$(fd) and $G^j$(fd) parameter values comes from the "heavy lanthanides", with at least 7 f electrons in the $4f^{n-1}$5d configuration. As discussed above, for heavy lanthanides the lowest $4f^{n-1}$5d states are "high spin" (higher spin than any of the $4f^n$ states) so transitions to these states are spin-forbidden, and rather weak. Transitions to the "low-spin" states are spin allowed and therefore much more intense. The splitting between the lowest high-spin and lowest low-spin states provides a direct measure of the strength of the f–d Coulomb interaction. Fig. 5 (from van Pieterson et al., 2002b) displays this graphically. The vertical axis represents the 5d energy levels (in thousands of $cm^{-1}$) for $LiYF_4$:$Tb^{3+}$ and the horizontal axis represents the scaling factor on the $F^k$(fd) and $G^j$(fd) parameter values ("one" being the ab initio parameter values). The full (unscaled) parameters predict a splitting between high-spin and low-spin states of 11 700 $cm^{-1}$, which is significantly greater than the observed splitting of 8000 $cm^{-1}$ (van Pieterson et al., 2001a), shown in the $LiYF_4$:$Tb^{3+}$ spectrum in fig. 6. The lowest energy high-spin states are labeled "HS" and the lowest energy low-spin states are the band labeled "A". van Pieterson et al. (2002b) found that $A = 0.67$ best reproduced the observed splitting for lanthanides in $LiYF_4$. Using the same methods, van Pieterson et al. also estimated a value of $A = 0.60$ for lanthanides in $YPO_4$. In their studies of $Tb^{3+}$ doped elpasolites, Ning et al. (2005) used an even larger reduction ($A = 0.43$) of the Coulomb parameters in order to correctly reproduce the high to low spin splitting.
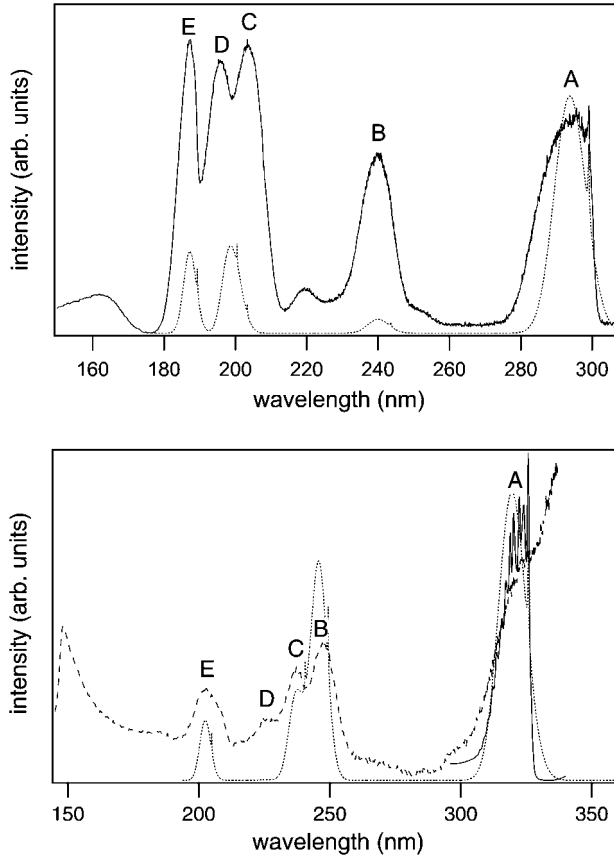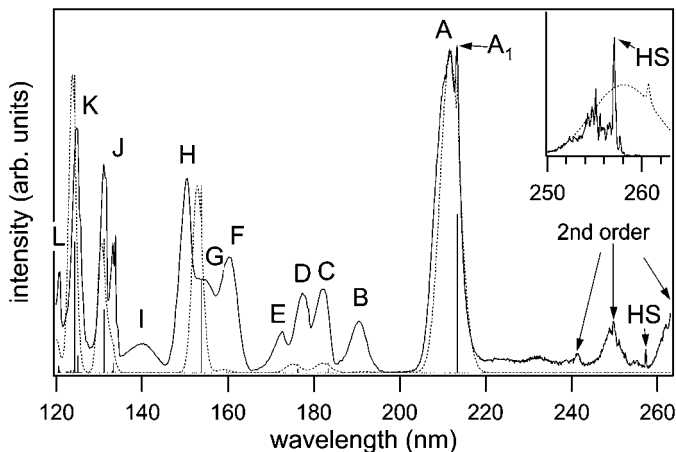
Fig. 6. Experimental and simulated spectra for the $4f^n \rightarrow 4f^{n-1}5d$ excitation of $Tb^{3+}$ in $LiYF_4$ (from van Pieterson et al., 2002b). The solid curve is the experimental spectrum and the dotted curve is the simulated spectrum.

Reid et al. (2002) have shown that parametrizations of gaseous lanthanide ions have much larger reductions in the $F^2$(fd) and $G^1$(fd) parameters from Hartree–Fock values than the other parameters. This would suggest that future calculations might examine specific reductions in these two parameters, rather than the current practice of keeping parameter ratios fixed. However, as of this time, such calculations have not been performed.

The energy parameter $\Delta_E$(fd) represents the barycenter energy of the $4f^{n-1}5d$ configuration above the barycenter energy of the $4f^n$ configuration. As the $E_{avg}$ parameter for the $4f^n$ configuration represents the barycenter energy level of the configuration with respect to the ground state, the sum of these two energy parameters, $E_{avg} + \Delta_E$(fd), presents the barycenter energy of the excited configuration above the ground state. The barycenter energy of the excited configuration is not an easy value to experimentally determine, whereas the lowest energy state of the excited configuration is well-determined experimentally. Thus, once the other parameters are determined, the energy parameter $\Delta_E$(fd) is adjusted so that the calculated and experimental values match for the lowest excited configuration energy level.

### 3.1.3. *Core $4f^{n-1}$ parameters*

For absorption spectra from the ground $4f^n$ state to excited $4f^{n-1}5d$ states, such as the measurements of van Pieterson et al. (2002a, 2002b), the 5d crystal field and spin orbit parameters, along with the 5d–4f Coulomb parameters $F^k$(fd) and $G^j$(fd) provide the dominant contributions to the excited state energy levels and transition intensities. For this reason, van Pieterson et al. (2002a, 2002b) were able to achieve good correlation between experiment and calculation by using "generic" $4f^n$ (and $4f^{n-1}$ "core") atomic parameters from the systematic calculations of Carnall et al. (1989), and 4f crystal field parameters tabulated by Görller-Walrand and Binnemans (1996).

However, for the high resolution emission spectra of Peijzel et al. (2005a, 2005b, 2005c), it was found that much more accurate $4f^n$ wavefunctions were needed in order to accurately reproduce the experimental emission spectra. This is true for two reasons. First, the $4f^{n-1}$ core parameters, along with the Coulomb parameters $F^k(fd)$ and $G^j(fd)$, split the lowest energy 5d state up into a number of components, of which only the lowest energy level is the actual emitting state. Thus, accurate $4f^{n-1}$ core parameters are needed to determine the wavefunction of the emitting state. Second, accurate $4f^n$ parameters are needed to determine the wavefunctions and energy levels of the terminating states of the emission.

Peijzel et al. (2005a) achieved much better agreement between calculated and experimental emission spectra using $4f^n$ parameters that were refit to the best available experimental data for the $4f^n$ energy levels. The top portion of table 4 presents these refit parameter values for $Ce^{3+}$, $Pr^{3+}$, $Nd^{3+}$, $Er^{3+}$ and $Tm^{3+}$ doped into LiYF$_4$. Experimental energy levels for the fits were taken from Burdick and Richardson (1998) for $Pr^{3+}$, da Gama et al. (1981) for $Nd^{3+}$, Couto dos Santos et al. (1998) for $Er^{3+}$, and Jenssen et al. (1975) for $Tm^{3+}$. Parameters for $Ce^{3+}$ were fit to the five observed out of seven crystal-field energy levels which were determined directly from the emission spectra as (0, 216, {547}, 2221, 2316, 2430, {3160} cm$^{-1}$), where the numbers in curly brackets are calculated. Delta-function correlation crystal-field parameters $D^2$ and $D^4$ were included in the fits as they provided a significant improvement to the quality of fit.

## 3.2. *Analyses of absorption and excitation spectra*

The absorption and excitation spectra of $4f^n \rightarrow 4f^{n-1}5d$ transitions in lanthanides have been studied and analyzed since the 1960s (McClure and Kiss, 1963; Loh, 1966). However, in recent years there has been renewed interest in these states and many calculations have been carried out.

Laroche et al. (2000) examined the ground-state and excited-state $4f^2 \rightarrow 4f5d$ absorption spectra of $Pr^{3+}$ in LiYF$_4$, and were able to explain the measured 4f5d energy levels via three adjustable parameters, $B_0^2(d)$, $B_0^4(d)$, and an energy term to vary the position of the 4f5d barycenter energy. In order to simplify the calculation, Laroche et al. followed the simplification that the $B_4^4/B_0^4$ ratio should be the same for the 5d electron as for the 4f electron, an identity that holds in the point-charge model, but may not hold if significant covalent effects are considered (Görller-Walrand and Binnemans, 1998; Marsman et al., 2000). All other parameters were fixed either by fits within the $4f^2$ configuration (for $4f^2$ and $4f^1$ "core" parameters) or by free-ion data (for 5d electron parameters $F^k$, $G^j$, and $\zeta(dd)$). They then independently varied the $B_0^2(d)$ and $B_0^4(d)$ crystal-field parameters until good agreement was achieved between the calculated and experimental spectra. These same methods were used to analyze the spectra of $Pr^{3+}$ in YPO$_4$ (Laroche et al., 2001), and the $Nd^{3+}$ spectra in LiYF$_4$ (Collombet et al., 2003a, 2003b).

Independently, Reid et al. (2000) published their first parametrized analysis of the $4f^n \rightarrow 4f^{n-1}5d$ absorption spectra of $Ce^{3+}$, $Pr^{3+}$ and $Nd^{3+}$ ions doped in LiYF$_4$. The main difference between the early approaches of Laroche et al. and Reid et al. were that Reid employed the $Ce^{3+}$ 5d configuration energy levels to determine the 5d crystal-field parameters to be used

Table 4

Best determined parameters for the $4f^n$ and $4f^{n-1}5d$ configurations of trivalent lanthanide ions doped in $LiYF_4$ (from Peijzel et al. (2005a)). Parameters have units $cm^{-1}$

| Ion | $Ce^{3+}$ | $Pr^{3+}$ | $Nd^{3+}$ | $Er^{3+}$ | $Tm^{3+}$ |
|---|---|---|---|---|---|
| $4f^n$ parameters and $4f^{n-1}$ "core" parameters within $4f^{n-1}5d$ configuration | | | | | |
| $E_{avg}$ | 1517 | 10204 | 24413 | 35806 | 18022 |
| $F^2$ | – | 69025 | 72667 | 97449 | 102215 |
| $F^4$ | – | 50580 | 52737 | 68539 | 72060 |
| $F^6$ | – | 33326 | 35817 | 56051 | 51366 |
| $\alpha$ | – | [23] | 21.49 | 18.27 | 18.2 |
| $\beta$ | – | −649 | −585 | [−580] | −686 |
| $\gamma$ | – | [1371] | 1424 | [1416] | [1820] |
| $\zeta_f$ | 628 | 750.1 | 870.1 | 2374 | [2633] |
| $T^2$ | – | – | 331 | [486] | [400] |
| $T^3$ | – | – | 43 | [43] | [43] |
| $T^4$ | – | – | 84 | [81] | [73] |
| $T^6$ | – | – | −324 | [−327] | [−271] |
| $T^7$ | – | – | 387 | [300] | [308] |
| $T^8$ | – | – | 322 | [346] | [299] |
| $M^0$ | – | [2.00] | 0.66 | 3.91 | 4.67 |
| $P^2$ | – | 215 | 162 | 579 | 720 |
| $B_0^2$ | 316 | 541 | 400 | 306 | 354 |
| $B_0^4$ | [−1150] | −1093 | −1122 | −581 | −631 |
| $B_4^4$ | −1264 | −1327 | −1272 | −917 | −851 |
| $B_0^6$ | [−89] | −45 | −28 | −6 | −171 |
| $B_4^6$ | −821 | −1165 | −1093 | −637 | −627 |
| $D^2$ | – | −15.9 | 4.9 | 5.3 | – |
| $D^4$ | – | 8.8 | 10.1 | 4.0 | – |
| $4f^{n-1}5d$ parameters | | | | | |
| $\Delta_E(fd)$ | 43773 | 50966 | 56684 | 89762 | 94218 |
| $F^2(fd)$ | – | 22703 | 22543 | 19724 | 19639 |
| $F^4(fd)$ | – | 11321 | 11188 | 9358 | 9275 |
| $G^1(fd)$ | – | 9677 | 9608 | 8038 | 7991 |
| $G^3(fd)$ | – | 8370 | 8284 | 6848 | 6789 |
| $G^5(fd)$ | – | 6518 | 6442 | 5292 | 5240 |
| $\zeta(dd)$ | 1082 | 1149 | 1216 | 1768 | 1839 |
| $B_0^2(dd)$ | 4673 | 4626 | 4598 | 4290 | 4252 |
| $B_0^4(dd)$ | −18649 | −18463 | −18351 | −17120 | −16971 |
| $B_4^4(dd)$ | −23871 | −23643 | −23489 | −21914 | −21723 |

in $Pr^{3+}$ and $Nd^{3+}$ ions, rather than fitting the 5d crystal-field parameters directly to the $Pr^{3+}$ 4f5d excited configuration spectrum. The other, relatively minor, difference between the two approaches was that Laroche used established free-ion data, while Reid took advantage of ab initio calculations, to determine the 5d electron parameters $F^k$, $G^j$ and $\zeta(dd)$.

By far the most complete parametrized analysis to date is that of van Pieterson which covers the light lanthanides ($Ce^{3+}$, $Pr^{3+}$, $Nd^{3+}$, $Sm^{3+}$ and $Eu^{3+}$) doped in $YPO_4$, $CaF_2$ and $LiYF_4$

(van Pieterson et al., 2002a) and the heavy lanthanides ($Tb^{3+}$, $Dy^{3+}$, $Ho^{3+}$, $Er^{3+}$, $Tm^{3+}$ and $Yb^{3+}$) doped in the same three lattices (van Pieterson et al., 2002b). Using 5d crystal field parameters from the $Ce^{3+}$ spectra (reduced slightly for the heavy lanthanides), $4f^{n-1}$ splitting parameters from the literature, and f–d Coulomb parameters scaled down from Hartree–Fock calculations, van Pieterson obtained good agreement between the experimental and calculated spectra for the ions across the lanthanide series, reproducing in the calculations most of the complex structure of the excitation spectra. The calculations also correctly reproduced the splitting between high-spin and low-spin $4f^{n-1}5d$ states (for $n > 7$), and reproduced the observed trend that shows a reduction in the high-spin to low-spin splitting for heavy lanthanides.

## 3.3. *Analysis of emission spectra and lifetimes*

Early VUV luminescence spectra for d $\rightarrow$ f transitions using synchrotron radiation excitation were taken at low resolution, which smoothed out a lot of the details (see, for example, Wegh et al., 1998; van Pieterson et al., 2001b). The first high resolution VUV luminescence spectra for these transitions using synchrotron radiation excitation was done on the SUPER-LUMI (Zimmerer, 1991) at the Hamburger Synchrotronstrahlungslabor HASYLAB at DESY, Hamburg, Germany by Chen et al. (2003) for $LiYF_4$:$Er^{3+}$. This work was followed by Kirm et al. (2004, 2005) for Gd and Lu fluorides, and for $LiCaAlF_6$:$Tm^{3+}$ emission, respectively. However, by far the most complete high resolution VUV emission spectra to date is that done by Peijzel et al. (2005a) using fluorine laser excitation at 157 nm, or a fluorine–argon mixture at 193 nm.

The first systematic parametrized modeling of $4f^{n-1}5d \rightarrow 4f^n$ emission spectra was done by van Pieterson et al. (2001a, 2001b) for $Ce^{3+}$, $Pr^{3+}$, $Nd^{3+}$, $Er^{3+}$ and $Tm^{3+}$ ions doped in $LiYF_4$. These are the only lanthanide ions to exhibit $4f^{n-1}5d \rightarrow 4f^n$ emission in $LiYF_4$, as the other ions undergo radiationless transfer from the lowest $4f^{n-1}5d$ state to high-lying $4f^n$ states. Van Pieterson was able to model the emission spectra as well as achieve good agreement between calculated and experimental luminescence lifetimes. This work was then extended by Peijzel et al. (2005a) with much higher resolution measurements and to include emission from $Pr^{3+}$, $Nd^{3+}$, $Er^{3+}$ and $Tm^{3+}$ ions doped in $YPO_4$.

The emission spectra for $LiYF_4$:$Pr^{3+}$ are shown in fig. 7 as an illustration, where the top and bottom panels present the calculated and experimental spectra, respectively. As can be seen from this figure, the calculations correctly reproduce the relative intensities of the emission bands. The calculated spectra are produced by superimposing a Gaussian band that is offset from the zero-phonon line by 600 $cm^{-1}$ on the calculated zero-phonon lines. The FWHM is set to 1000 $cm^{-1}$ for the Gaussian (phonon) bands, and 20 $cm^{-1}$ for the zero-phonon lines. The zero-phonon lines for the 4f5d $\rightarrow$ $^3H_4$ emission are not observed, most likely due to resonant reabsorption.

The calculations do not attempt to model detailed vibronic structure. The simulated spectra are produced by superimposing a Gaussian band on the zero-phonon line, rather than calculating the individual vibronics. For the emission spectra of lanthanides in $LiYF_4$, individual vibronic features are not clearly resolved (see fig. 7), and the calculated broad vibronic bands give a reasonably good description. By contrast, for lanthanides in $YPO_4$, the offset between
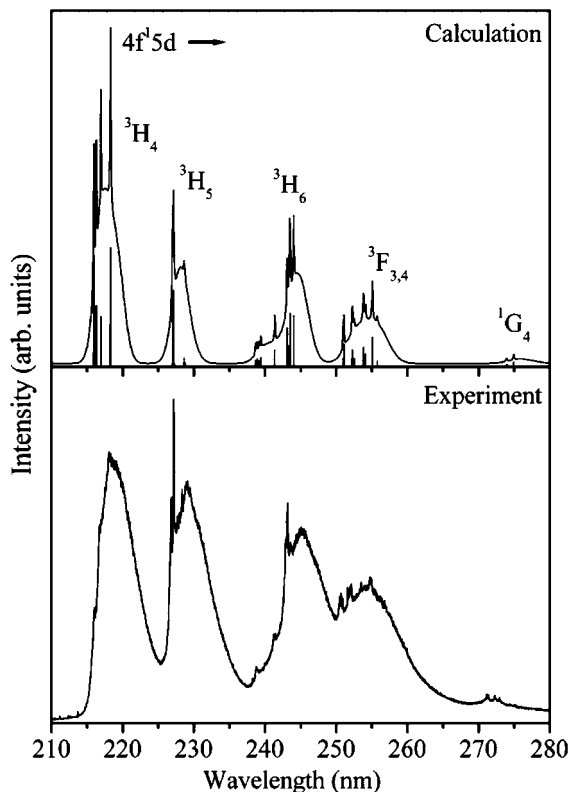
Fig. 7. Calculated and measured emission spectra of $LiYF_4:Pr^{3+}$ from Peijzel et al. (2005a). The bars in the upper spectrum give information on the positions and intensities calculated for the zero-phonon lines, while the spectrum is obtained by superimposing a Gaussian band (offset 600 $cm^{-1}$, width 1000 $cm^{-1}$) on the zero-phonon lines.

the zero-phonon line and the peak of the vibronic band is smaller, resulting in a higher relative intensity of the zero-phonon lines and observation of sharp vibronic lines corresponding to coupling with well-defined vibrational modes. This can be seen in fig. 8 for $YPO_4:Pr^{3+}$, where individual vibronic modes of 148 and 370 $cm^{-1}$ are observed. A detailed analysis of the vibronic structure of the $4f^{n-1}5d \rightarrow 4f^n$ emission bands in $YPO_4$ would be an interesting topic for further studies.

The lifetimes of the lowest $4f^{n-1}5d$ excited states have been measured in a variety of systems. $Ce^{3+}$, $Pr^{3+}$, $Nd^{3+}$, $Er^{3+}$, and $Tm^{3+}$ exhibit emission from the lowest $4f^{n-1}5d$ excited states in $LiYF_4$. These lifetimes have been compared with calculations by van Pieterson et al. (2001a) and Peijzel et al. (2005a). As pointed out in section 2.4, a calculation error in van Pieterson et al. (2001a) cancels out the overestimation of the 4f–5d dipole moments by the Hartree–Fock calculation.

Since the $A$ coefficients are proportional to the cube of the transition energies, and the energy difference between the $4f^{n-1}5d$ and $4f^n$ configurations increases from $Ce^{3+}$ to $Nd^{3+}$,
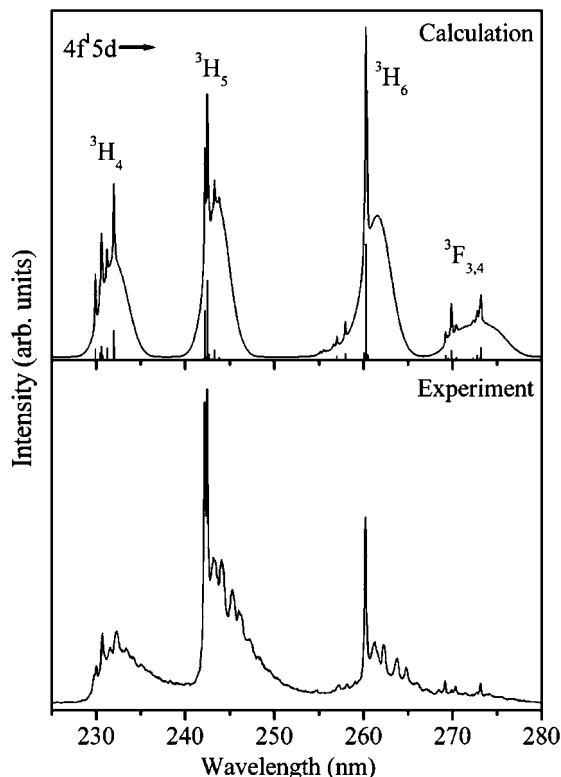
Fig. 8. Calculated and measured emission spectra of $YPO_4$:$Pr^{3+}$ from Peijzel et al. (2005a). The bars in the upper spectrum give information on the positions and intensities calculated for the zero-phonon lines, while the spectrum is obtained by superimposing a Gaussian band (offset 600 $cm^{-1}$, width 1000 $cm^{-1}$) on the zero-phonon lines.

the lifetimes decrease. However, the total splitting of the $4f^n$ configuration also increases, so many of the possible decay pathways have smaller energy factors. As a result the lifetimes do not decrease as much as would be expected if one simply examined the $4f^{n-1}5d$–$4f^n$ separation.

For $Er^{3+}$ and $Tm^{3+}$, emission may be observed from both low-spin and high-spin states. Compared to the low-spin states, with lifetimes of a few nanoseconds, the high-spin states have very long lifetimes (microseconds) because of the spin-forbidden nature of the radiative decay. The lifetimes of the high-spin states may be assumed to be purely radiative, but the low-spin states may also decay non-radiatively (to the high-spin states). The non-radiative decay rate may be calculated from the measured lifetimes of the low-spin and high-spin states and the ratio of the total emission from the low-spin and high-spin states, as has been done by van Pieterson et al. (2001a) and Peijzel et al. (2005a).

It is possible to calculate other spectroscopic details for the $4f^{n-1}5d$ and $4f^n$ configurations. For example, radiative lifetimes for $Eu^{2+}$ typically increase with temperature, rather than

the decrease that is usually expected. Duan et al. (2006) showed that this increase may be explained quantitatively. States with smaller radiative decay rates become populated at higher temperatures, increasing the lifetime.

### 3.3.1. Conditions for $4f^{n-1}5d \rightarrow 4f^n$ emission

The fluorescence properties of lanthanide ions in crystals will vary markedly depending upon the relative energy levels of the excited configuration $4f^{n-1}5d$ states with respect to the $4f^n$ states. That is, for systems with a large energy gap between the bottom of the 5d configuration energy levels and high lying $4f^n$ states, fast efficient 5d → 4f fluorescence may occur, which is useful for UV lasers and scintillators. However, if there are $4f^n$ states close to the lowest-energy 5d energy levels, then non-radiative relaxation will occur between the 5d and the 4f states, and no 5d → 4f emission will occur. In this case, if there is a high lying $4f^n$ state that emits radiation, then there is the potential for quantum cutting (also called "photon cascade emission" or "quantum cascade emission"), getting more than one photon out for every VUV photon absorbed.

The idea of quantum cutting was discussed as early as 1957 by Dexter (1957), and was actually observed for the first time in 1974 independently by two groups, Summerdijk et al. (1974a, 1974b) for $Pr^{3+}$ doped $YF_3$ and $NaYF_4$, and Piper et al. (1974) for $Pr^{3+}$ doped $YF_3$, with back-to-back papers in the Journal of Luminescence. In each case, initial emission came from the $^1S_0$ level of $Pr^{3+}$ after excitation into the 4f5d band. The possibility of quantum cutting has recently attracted great interest due to the technological need for more efficient phosphors for plasma displays and mercury-free fluorescent lamps.

Neodymium systems have the potential for quantum cutting because $Nd^{3+}$ has a high lying $4f^n$ state, $^2G(2)_{9/2}$, at about $47\,000\ cm^{-1}$, which has a $7000\ cm^{-1}$ gap above the next lower level, $^2F(2)_{7/2}$ (Carnall et al., 1988). This energy gap is sufficient to prevent non-radiative relaxation between the two states, and emission from the $^2G(2)_{9/2}$ state can be expected. Exciting the $^2G(2)_{9/2}$ state directly is impractical, due to the very low transition probability from the ground state. However, if efficient absorption into the 5d band occurs, then the $^2G(2)_{9/2}$ state may be populated via non-radiative phonon-assisted relaxation, resulting in $^2G(2)_{9/2}$ emission.

Wegh et al. (2001) studied the $Nd^{3+}$ emission spectra for several phosphate and borate systems upon VUV excitation of the $4f^2 5d$ levels. They observed $4f^2 5d \rightarrow 4f^3$ fluorescence from $LaPO_4$, $4f^3 \rightarrow 4f^3$ fluorescence from $ScPO_4$, $LaBO_3$, $YBO_3$, $LuBO_3$, and $ScBO_3$, and observed a mixture of $4f^2 5d \rightarrow 4f^3$ and $4f^3 \rightarrow 4f^3$ fluorescence from $YPO_4$ and $LuPO_4$. These observations are explained by examination of the energy gap between the lowest $4f^2 5d$ state and the $^2G(2)_J$ states. Fig. 9 presents a graph of the approximate positions of the high lying $4f^3$ states and the onset of the 5d band for each of these systems. Single lines are drawn for each $4f^3$ multiplet, neglecting the crystal-field splitting of these levels for clarity and simplicity. For both the phosphates and the borates, the $4f^2 5d$ onset decreases in energy as the ionic radius of the metal ion decreases: La, Y, Lu, Sc, due to the increasing nephelauxetic effect. This causes the $4f^3$ energy levels to decrease as well, but to a much lesser degree. Furthermore, the smaller ionic radius causes an increase in the 5d crystal field splitting, lowering the $4f^2 5d$ onset even further.
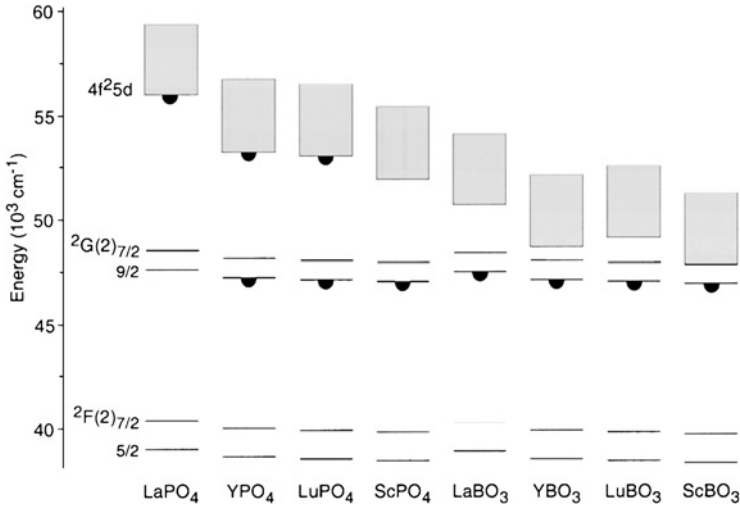
Fig. 9. Schematic energy level diagrams for $Nd^{3+}$ in various $MPO_4$ and $MBO_3$ crystals, showing the positions of the $4f^25d$ and $^2G(2)_J$ levels (from Wegh et al., 2001). Levels exhibiting emission are marked with a semicircle.

Wegh et al. (2001) found that when the energy gap between the lowest $4f^25d$ state and the $^2G(2)_{7/2}$ state was 4000 cm$^{-1}$ or less ($ScPO_4$ and all of the borates), efficient non-radiative relaxation occurred, populating the $^2G(2)_{9/2}$ state and leading to efficient radiation from this $4f^3$ level. When the energy gap was 7000 cm$^{-1}$ or greater ($LaPO_4$), no non-radiative relaxation occurred, and fluorescence was observed only from the lowest $4f^25d$ state. And for the two systems with an energy gap of about 5000 cm$^{-1}$ ($YPO_4$ and $LuPO_4$), both competing processes occurred, and emission from both the lowest $4f^25d$ state and from the $^2G(2)_{9/2}$ state were observed. As the maximum energy of phosphate vibrations is about 1200 cm$^{-1}$, this means that non-radiative processes involving three phonons or less will dominate. For a four or five phonon process, non-radiative and radiative processes have comparable probabilities. And if six or more phonons are needed, the fast radiative emission from the $4f^25d$ state dominates. This result is very similar to that observed for non-radiative relaxation between $4f^n$ levels (Riseberg and Weber, 1976; van Dijk and Schuurmans, 1983), which is not necessarily what would be expected, considering the much stronger electron-phonon coupling in the $4f^25d$ state, compared to the $4f^n$ states. It appears that the much faster radiative rate from the $4f^25d$ state balances the stronger electron-phonon coupling.

### 3.3.2. $Pr^{3+}$ $^1S_0$ emission

By far, the most studied quantum cutting system to date is for praseodymium, where the $4f^2$ $^1S_0$ state lies below the lowest 5d state for many fluorides and some oxides. For most $Pr^{3+}$ doped systems, the nephelauxetic effect and the 5d crystal field splitting are large enough to push the lowest 5d level below the $^1S_0$ state. However, for those systems in which the $^1S_0$
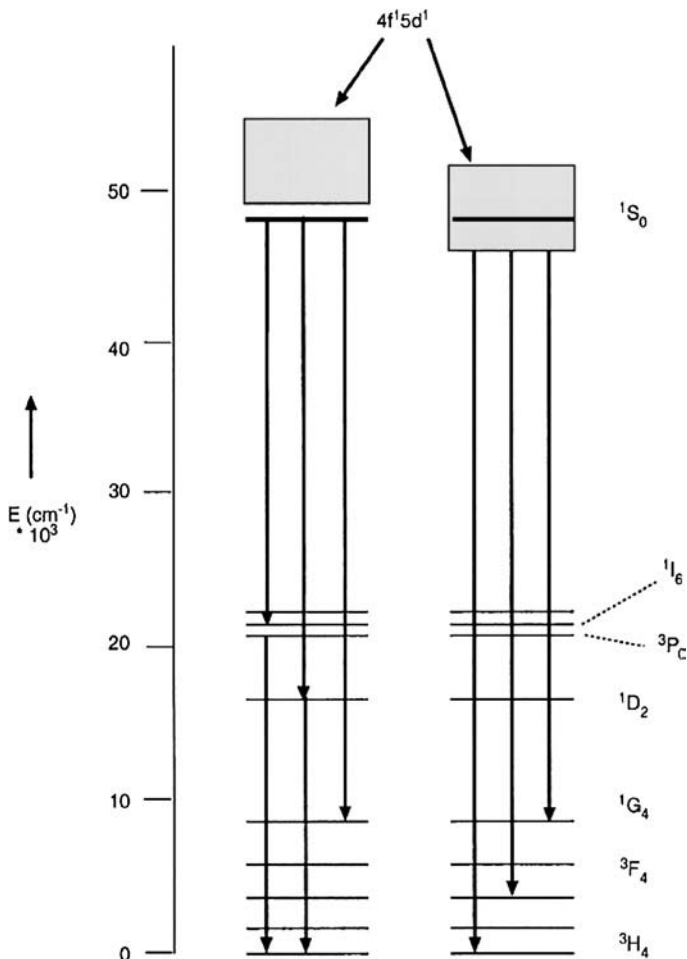
Fig. 10. Energy level scheme of $Pr^{3+}$ showing the $4f^2$ levels and two possibilities for the position of the 4f5d levels (Oskam et al., 2002). On the left the lowest 4f5d level is above the $^1S_0$ level making quantum cutting from the $^1S_0$ level possible. On the right the 4f5d level is situated below the $^1S_0$ level and fast UV 4f5d emission to the lower $4f^2$ levels is possible potentially being a good scintillator or UV laser materials.

state lies below the lowest 5d level, $Pr^{3+}$ provides a nearly ideal system for quantum cutting for the following reasons:

1. Efficient excitation from the ground state to the broad 4f5d bands can occur, followed by non-radiative relaxation to the $^1S_0$ state, allowing efficient population of $^1S_0$.
2. Emission selection rules constrain the emission from $^1S_0$ primarily to excited state levels, rather than directly to the $^3H_J$ ground multiplets, allowing the potential for a second photon to be emitted to the $^3H_J$ states.

Table 5
Systems exhibiting $4f^2$ emission from the $^1S_0$ level of $Pr^{3+}$. References since 2001

| Fluorides | Reference |
| --- | --- |
| $BaF_2$ | Rodnyi et al. (2005b) |
| $BaMgF_4$ | Kück and Sokólska (2002a), Kück et al. (2005a) |
| $BaSiF_6$ | van der Kolk et al. (2002) |
| $CaAlF_5$ | van der Kolk et al. (2004) |
| $CaF_2$ | Oskam et al. (2002), Vergeer et al. (2005b) |
| $Cs_2KYF_6$ | Schiffbauer et al. (2005) |
| $K_5Li_2PrF_{10}$ | Solarz et al. (2004) |
| $KMgF_3$ | Kück et al. (2005a), Sokólska and Kück (2001) |
| $KYF_4$ | Wang et al. (2007) |
| $LaF_3$ | Kück et al. (2005a), Meng et al. (2005), You et al. (2007) |
| $LaZrF_7$ | van der Kolk et al. (2001b) |
| $LaZr_3F_{15}$ | van der Kolk et al. (2001b) |
| $LiBaF_3$ | Vergeer et al. (2005b) |
| $LiCaAlF_6$ | Kück and Sokólska (2002b) |
| $LiSrAlF_6$ | Kück and Sokólska (2002b) |
| $LuF_3$ | Kück and Sokólska (2002a), Kück et al. (2005a) |
| $NaLaF_4$ | Kück et al. (2005a) |
| $NaMgF_3$ | Le Masson et al. (2003), van der Kolk et al. (2004) |
| $NaYF_4$ | Kück et al. (2005a), Wang et al. (2007) |
| $PrF_3$ | Kück and Sokólska (2003), Kück et al. (2005a) |
| $SrAlF_5$ | Potapov et al. (2005), Rodnyi et al. (2003b, 2005a), |
| | van der Kolk et al. (2004), Vink et al. (2002) |
| $SrY_2F_8$ | Meijerink et al. (2006), Vergeer et al. (2005b) |
| $YF_3$ | Kück and Sokólska (2002b), Kück et al. (2005a, 2005b), |
| | Meijerink et al. (2006), Vergeer et al. (2005a, 2005b), |
| | |
| Oxides | |
| $CaAl_{12}O_{19}$ | Wang et al. (2001, 2002) |
| $CaMgAl_{14}O_{23}$ | You et al. (2007) |
| $SrAl_{12}O_{19}$ | Huang et al. (2001, 2003), Liu et al. (2005), Loureiro et al. (2005), |
| | Nie et al. (2006), Rodnyi et al. (2002a, 2002b, 2003b, 2004, 2005a) |
| $SrB_4O_7$ | Chen et al. (2006, 2007), Rodnyi et al. (2003a), van der Kolk et al. (2001a), |
| | Yang et al. (2001) |
| $SrB_6O_{10}$ | Chen et al. (2007), Rodnyi et al. (2003a) |

The quantum cutting process for $Pr^{3+}$ is displayed graphically in fig. 10. The left side of this figure illustrates the situation where the $^1S_0$ state is below the lowest 5d state. Initial emission from the $^1S_0$ state populates the $^3P_0$ and $^1D_2$ states, which then emits a second photon to reach the ground state. By contrast, the right side of this figure illustrates where the $^1S_0$ state lies within the 5d band. In this case, the ion produces UV emission from the lowest 4f5d state which directly populates the ground state.

Table 5 presents a listing of the fluoride and oxide systems for which $^1S_0$ emission has recently been studied (since 2001). van der Kolk et al. (2002) give predictions on what other systems should also exhibit $^1S_0$ emission.

Unfortunately, the first photon emitted from the $^1S_0$ level is in the violet (about 400 cm$^{-1}$). Thus, in order for the quantum-cutting of Pr$^{3+}$ ions to achieve practical usage, it will be necessary to find a mechanism of energy transfer that converts the violet $^1S_0$ emission into more usable wavelengths. Attempts to promote energy transfer from Pr$^{3+}$ to Eu$^{3+}$ were not successful (Zachau, 1998) due to non-radiative relaxation via a metal-to-metal charge transfer, as elucidated by Vergeer et al. (2005a). Vergeer also showed that Yb$^{3+}$ quenched the Pr$^{3+}$ $^1S_0$ level through charge transfer.

The first successful study of such an energy transfer was by Wang et al. (2001, 2002) in their studies of Pr$^{3+}$ and Er$^{3+}$ codoped CaAl$_{12}$O$_{19}$ crystals. They found an energy transfer efficiency of about 25% at room temperature, which was hampered by the large Pr–Er ion separation distance.

Current work has focused on using transition metals, such as Mn$^{2+}$ (van der Kolk et al., 2004; Potapov et al., 2005; Vergeer et al., 2005b; Meijerink et al., 2006; Chen et al., 2006, 2007) and Cr$^{3+}$ (Nie et al., 2006) as energy transfer sites for converting the Pr$^{3+}$ $^1S_0$ emission to useful wavelengths. However, much more work is needed to determine whether any of these proposed mechanisms will be able to produce actual quantum efficiencies higher than 100%.

### 3.4. *Non-radiative relaxation and linewidths*

Fast non-radiative relaxation of excited states leads to broadening of the spectral lines. The amount of broadening gives information about the nature and rate of the relaxation. We will discuss both qualitative and quantitative effects below.

#### 3.4.1. *Linewidths of $4f^{n-1}5d$ states*

It is obvious from figs. 2 and 3 that the fine structure that is observed for the low energy $4f^{n-1}5d$ states is not visible for higher-energy states. This is attributed to non-radiative relaxation. In fig. 2 it is clear that the states where the 5d electron is in the lowest-energy orbital (symmetry $^2E$) have visible fine-structure, whereas the states in which the 5d electron is in a $^2T_2$ orbital do not. The high-energy states are expected to be in the conduction band (Ishii et al., 2001) and the relaxation is presumed to involve ionization to the conduction band.

Remarkably, fine-structure is visible for some very high-energy states in some ions. For example, in fig. 11 we show the excitation spectrum of Tb$^{3+}$ in CaF$_2$, from van Pieterson et al. (2002c). The inset shows that there is fine-structure present around 130 nm. The explanation for this is that in those states the 5d electron is in the lowest-energy ($^2E$) orbital. The "core" $4f^{n-1}$ electrons are arranged in a highly excited state, but there is no non-radiative pathway because those electrons are much more localized than the 5d electron, and there appears to be only weak coupling between the 5d electron and the $4f^{n-1}$ core.

#### 3.4.2. *Linewidths of $4f^n$ states probed by two photon absorption*

Another interesting example of the effect of non-radiative relaxation on linewidths is visible in the two-photon absorption spectrum of Eu$^{2+}$ in CaF$_2$ (Downer et al., 1983). These experiments involve the excitation of $4f^7$ states within the $4f^65d$ band, followed by non-radiative decay to $4f^65d$ states. The excitation was measured by monitoring emission from $4f^65d$ to $4f^7$. It is apparent from the spectra that the linewidths of the $4f^7$ states vary significantly.
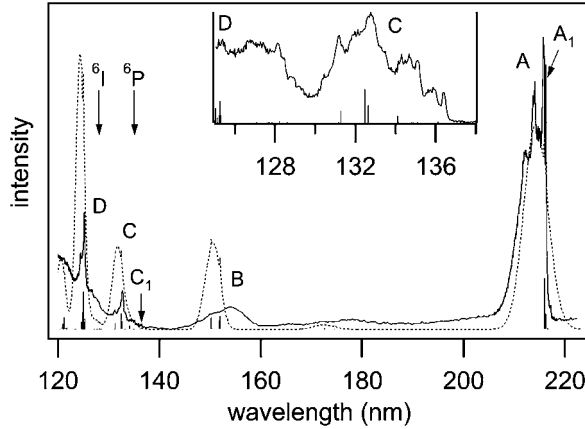
Fig. 11. Excitation spectra for powdered $CaF_2$:$Tb^{3+}$ from van Pieterson et al. (2002c). The solid line shows the excitation spectrum measured at DESY and the dotted line is the calculated spectrum. Positions of the calculated electronic states are indicated by vertical lines. The insert shows high-resolution excitation spectra showing the reappearance of fine structure at high energies.

Non-radiative relaxation rates, and hence linewidths, depend on the existence of $4f^6$5d states of appropriate energies and on the odd-parity vibrations that mediate non-radiative relaxation between the $4f^7$ and $4f^6$5d states. Burdick et al. (2006) showed that the narrow lines for $^8S_{7/2} \rightarrow {}^6P_J$ occur because the only $4f^6$5d states lying below the $^6P_J$ states are high-spin octet states, which are forbidden by the $\Delta S = 0$ selection rule for the odd-parity vibronic operators. This slows down the non-radiative energy transfer, keeping the absorption lines sharp. By contrast, the $^8S_{7/2} \rightarrow {}^6I_J$ transitions showed narrow lines interspersed with broader lines, with experimental line widths varying from 10 $cm^{-1}$ to 50 $cm^{-1}$ (see, for example, fig. 3 of Downer et al., 1983). Using a model developed by Duan et al. (2002) to explain the decay rates, Burdick et al. (2006) showed that the large variation in absorption line-widths for the $^8S_{7/2} \rightarrow {}^6I_J$ transitions could be explained by means of the phonon-coupling selection rules between $^6I_J$ and close lying $4f^6$5d states. The only low-spin sextet states of $4f^6$5d lying below the $^6I_J$ have J $\leqslant$ 9/2. With a $\Delta J \leqslant 3$ selection rule, the $^6I_{17/2}$ states cannot directly connect to the available $4f^6$5d states, and thus are significantly narrower than the other $^6I_J$ states with smaller J. The narrow experimental linewidth of the $^8S_{7/2} \rightarrow {}^6D_{1/2}$ transition can also be explained by these selection rules, as there are no $4f^6$5d states in the acceptable range of energies below $^6D_{1/2}$ with appropriate J values (i.e., J = 5/2 or 7/2).

## 4. Other techniques

### 4.1. *Ab initio calculations*

First-principles (ab initio) analysis methods for ions in solids are often limited in their representation of many-electron effects. Thus, although they have been useful for examining the

spectra of $Ce^{3+}$ in solids (Seijo et al., 2003), it has been difficult to apply these methods for the multi-electron configurations across the lanthanide series. Recently, Ishii et al. (2004a) developed a multi-electron full configuration interaction method that uses the density functional theory in a general molecular orbital cluster calculation. Ishii et al. (2004a) applied this method to the $f^2 + fd$ configurations of Pr:LiYF$_4$ and were able to reproduce qualitatively the energy level spectra of the fd configuration, though not the actual energies. These calculations use a fully relativistic full configuration interaction multi-electron method, in which all the matrix elements of the $4f^2$ and $4f5d$ configurations are numerically calculated. Ishii et al. (2004b) also examined $Pr^{3+}$ ions doped in LaF$_3$ and CaF$_2$ as well as LiYF$_4$. This method has been extended to an analysis of the entire lanthanide series in LiYF$_4$ by Ogasawara et al. (2005, 2007). Although they are able to qualitatively reproduce the energy level spectra of the $4f^{n-1}5d$ configuration, the actual energies are far from the experimental values.

The recent calculations by Ishii, Ogasawara, and co-workers use a cluster that explicitly treats only the lanthanide and the nearest neighbors. An earlier calculation by Ishii et al. (2001) for $Ce^{3+}$:LiYF$_4$ uses a larger cluster and shows that the higher-energy 5d orbitals are strongly mixed with $Y^{3+}$ 4d orbitals, which form the conduction band in these crystals. This confirms the interpretation that high-energy states have large linewidths because they can decay into the conduction band. But it also suggests that interpreting the high-energy regions of the spectra may be more complex than would be supposed from the parametric model.

Due to the inherent difficulties of achieving a reliable ab initio calculation of $4f^{n-1}5d$ energy levels across the lanthanide series, a number of simplified ab initio calculations have been done. Dorenbos has effectively calculated a self-induced dipole contribution to the crystal field, originally proposed by Morrison et al. (1982), and used it to describe $Ce^{3+}$ centroid levels in crystals containing fluorides (Dorenbos, 2000a), chlorides, bromides and iodides (Dorenbos, 2000b), and oxides (Dorenbos, 2001, 2002a). This work has been expanded by Andriessen et al. (2005) to consider anion dipole polarization and dynamic correlation, building upon their earlier work (Dorenbos, 2002b; Andriessen et al., 2002; Dorenbos et al., 2003). An interesting application of this model is given in Dorenbos (2003), where they accurately model the $Ce^{3+}$ ion coordinated to both F$^-$ and O$^{2-}$ ligands. The study of Ruipérez et al. (2005) found that dynamic ligand correlation effects accounted for two-thirds of the depression of the 5d barycenter with respect to the free ion, with the other one-third coming from other effects such as orbital relaxation, charge transfer, and covalency.

Duan et al. (2007) present an alternative approach to these ab initio calculations. They suggest that, rather than attempting to calculate the multitude of 5d energy levels directly, ab initio approaches could concentrate on producing useful parameter values for only the subset of terms in the parametrized Hamiltonian (see section 2) which cannot be experimentally determined. That is, the ab initio calculations could produce reliable values, for example, for the $F^k$(fd) and $G^j$(fd) parameters that could then be incorporated into parametrized calculations. The parameters may then be fine tuned to give a reliable calculation that might be used to investigate other properties of the ions, such as the non-radiative relaxation discussed in section 3.4.

## 4.2. *Simplified models*

One of the problems with comparing calculations and spectra for transitions between $4f^n$ and $4f^{n-1}$5d is that the spectra generally consist of broad bands, with little fine structure visible, and the calculations consist of thousands of individual lines. A straightforward interpretation of the calculated energy levels is difficult because the wavefunctions contain mixtures of many *SLJM* states. Consequently, in most studies the spectra are compared by eye to the simulated spectra. Though the mechanism is different this broadening is reminiscent of solution spectra for transitions within the $4f^n$ configuration. In that case the spectra may be analyzed using just "free ion" parameters and three "Judd–Ofelt" parameters (Carnall et al., 1965; Görller-Walrand and Binnemans, 1998).

For $4f^n$–$4f^{n-1}$5d transitions there is no need for intensity parameters. It would appear that the large 5d crystal field would make a "free ion" calculation impossible. However, if we consider a single 5d crystal-field level it is possible to carry out a "free ion" calculation for the $4f^{n-1}$ part of the states (modified by the influence of the 5d electron). This idea was called the "Simple Model" by Duan et al. (2002) and used to explain selection rules for non-radiative relaxation between $4f^n$ and $4f^{n-1}$5d. It was extended to calculations of energy levels and transition intensities for $4f^n$–$4f^{n-1}$5d transitions by Duan and Reid (2003). As summarized by Xia and Duan (2007), applications to $Nd^{3+}$:$YPO_4$ are given in Ning et al. (2004), $Er^{3+}$:$LiYF_4$ and $CaF_2$ are given in Duan et al. (2005a), and $Nd^{3+}$:$YPO_4$, $CaF_4$, and $LiYF_4$ are given in Xia et al. (2005).

Obviously, simple models such as this cannot replace complete parametrized or ab initio calculations. However, they give valuable insight into selection rules for relative intensities and so provide a way to gain greater *understanding* of the spectra.

## 4.3. *Empirical models for lowest $4f^{n-1}$5d states*

As discussed in section 3.3, one of the most important things to know about the excited $4f^{n-1}$5d configuration is the position of its lowest state. Though $\Delta_E$(fd) increases monotonically across the lanthanide series (table 1; fig. 2 of Reid et al., 2002) the position of the lowest $4f^{n-1}$5d varies widely (fig. 12). This is because some $4f^n$ configurations have particularly low-energy lowest states (e.g., $4f^7$) and some $4f^{n-1}$5d configurations have particularly low-energy lowest states (e.g., $4f^7$5d).

Dorenbos (2000c, 2000d, 2000e) has studied hundreds of lanthanide systems in order to determine an accurate method of prediction for the lowest state of the configuration. Dorenbos discovered that the depression of the 5d level in a given host crystal appears to be the same for all the $Ln^{3+}$ ions, to within about $600 \, cm^{-1}$ (Dorenbos, 2000d). This allows one to predict the position of the lowest $4f^{n-1}$5d state for any ion, given the lowest $4f^{n-1}$5d state for any other ion in the lanthanide series (see fig. 12). In the context of our parametrized calculations this may be understood because the largest contributions to the depression of the lowest 5d level are represented by the 5d crystal field parameters and a change in $\Delta_E$(fd), both of which are expected to be quite constant across the series. Bettinelli and Moncorgé (2001) provide an explanation of Dorenbos' results by invoking work of Morrison (1980) to describe the contribution of ligand polarization to the centroid shift.
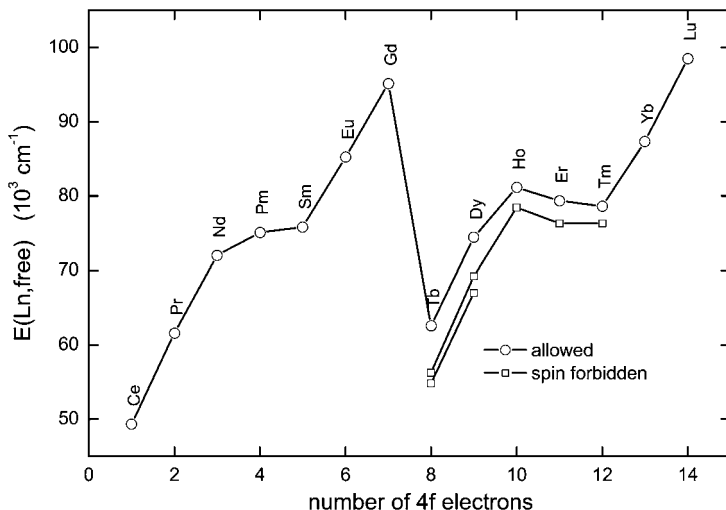
Fig. 12. Predicted lowest energy level of $4f^{n-1}5d$ configuration for gaseous (free) lanthanides (from Dorenbos, 2000e). For lanthanides in solids, the entire graph shifts downward by a constant amount, keeping relative displacements the same.

An interesting result of this analysis, as shown by van der Kolk et al. (2002), is that all crystal lattices that when doped with $Eu^{2+}$ exhibit $^6P_{7/2}$ emission will be the same crystal lattices that when doped with $Pr^{3+}$ exhibit $^1S_0$ emission. This is because the energy difference between $^6P_{7/2}(Eu^{2+})$ and $^1S_0(Pr^{3+})$ is exactly the same as the energy difference between the lowest 5d levels of $Eu^{2+}$ vs $Pr^{3+}$, about $35\,000$ $cm^{-1}$.

There have been other discussions of the separation between the configurations. Thiel et al. (2002) used a two-parameter model to predict these transitions from a systematic study of lanthanide ions in YAG. Using a spin density functional approach, Stephan et al. (2005) have developed a two empirical parameter model for the f–d energy shift. This work was continued in Schiffbauer et al. (2005) in their examination of the quantum cutting potential for $Pr^{3+}$ ions doped in $Cs_2KYF_6$. Dorenbos (2002c) also examined the radial dependence of the crystal field splitting of the 5d configuration for systems with octahedral, cubal, dodecahedral, and cuboctahedral coordination. This work was followed up by Shi et al. (2003), who examined the crystal field splitting of 5d levels in halide hosts.

## 5. Conclusions

In this Chapter we have discussed the use of parametrized models to calculate the energy levels of the $4f^n$ and $4f^{n-1}5d$ configurations of lanthanide ions in condensed-matter environments. Radiative and non-radiative transitions between these configurations have also been

addressed. Using these models it is possible to explain the major features of the UV and VUV spectra for ions across the entire lanthanide series.

Though ab initio calculations continue to improve and we expect them to take a larger role in the future, we do not expect them to totally supersede parametrized models. Parametrized models provide valuable insights into electronic structure and spectra. They also give an efficient way of dealing with a variety of interesting optical properties in a large number of materials.

# References

Andriessen, J., Dorenbos, P., van Eijk, C.W.E., 2002. Nucl. Instrum. Methods Phys. Res. A **486**, 399.

Andriessen, J., Dorenbos, P., van Eijk, C.W.E., 2005. Phys. Rev. B **72**, 045129.

Bettinelli, M., Moncorgé, R., 2001. J. Lumin. **92**, 287.

Blasse, G., Grabmaier, B.C., 1994. Luminescent Materials. Springer-Verlag, Berlin.

Burdick, G.W., Richardson, F.S., 1998. Chem. Phys. **228**, 81.

Burdick, G.W., Richardson, F.S., Reid, M.F., Kooy, H.J., 1995. J. Alloys Compd. **225**, 115.

Burdick, G.W., Reid, M.F., 2004. Mol. Phys. **102**, 1141.

Burdick, G.W., Burdick, A., Deev, V., Duan, C.K., Reid, M.F., 2006. J. Lumin. **118**, 205.

Cai, Z.Y., Umar, V.M., Fischer, C.F., 1992. Phys. Rev. Lett. **68**, 297.

Carnall, W.T., 1992. J. Chem. Phys. **96**, 8713.

Carnall, W.T., Fields, P.R., Wybourne, B.G., 1965. J. Chem. Phys. **42**, 3797.

Carnall, W.T., Goodman, G.L., Rajnak, K., Rana, R.S., 1988. A Systematic Analysis of the Spectra of the Lanthanides Doped into Single Crystal LaF$_3$. Argonne National Laboratory, Argonne, IL.

Carnall, W.T., Goodman, G.L., Rajnak, K., Rana, R.S., 1989. J. Chem. Phys. **90**, 3443.

Chen, Y.H., Kirm, M., Negodin, E., True, M., Vielhauer, S., Zimmerer, G., 2003. Phys. Status Solidi B **240**, R1.

Chen, Y.H., Shi, C.S., Yan, W.Z., Qi, Z.M., Fu, Y.B., 2006. Appl. Phys. Lett. **88**, 061906.

Chen, Y.H., Yan, W.Z., Shi, C.S., 2007. J. Lumin. **122**, 21.

Collombet, A., Guyot, Y., Joubert, M.F., Margerie, J., Moncorgé, R., 2003a. Opt. Mater. **24**, 215.

Collombet, A., Guyot, Y., Joubert, M.F., Laroche, M., Margerie, J., Moncorgé, R., Descroix, E., 2003b. Phys. Rev. B **68**, 035115.

Cowan, R.D., 1981. The Theory of Atomic Structure and Spectra. University of California, Berkeley.

Couto dos Santos, M.A., Antic-Fidancev, E., Gesland, J.Y., Krupa, J.C., Lemaître-Blaise, M., Porcher, P., 1998. J. Alloys Compd. **275**, 435.

Crosswhite, H., Crosswhite, H.M., Judd, B.R., 1968. Phys. Rev. **174**, 89.

Crosswhite, H.M., Crosswhite, H., 1984. J. Opt. Soc. Am. B **1**, 246.

da Gama, A.A.S., de Sá, G.F., Porcher, P., Caro, P., 1981. J. Chem. Phys. **75**, 2583.

De Leebeeck, H., Binnemans, K., Görller-Walrand, C., 1999. J. Alloys Compd. **291**, 300.

Dexter, D.L., 1957. Phys. Rev. **108**, 630.

Dieke, G.H., 1968. Spectra and Energy Levels of Rare Earth Ions in Crystals. Interscience Publishers, New York.

Dorenbos, P., 2000a. Phys. Rev. B **62**, 15640.

Dorenbos, P., 2000b. Phys. Rev. B **62**, 15650.

Dorenbos, P., 2000c. J. Lumin. **87**, 970.

Dorenbos, P., 2000d. J. Lumin. **91**, 91.

Dorenbos, P., 2000e. J. Lumin. **91**, 155.

Dorenbos, P., 2001. Phys. Rev. B **64**, 125117.

Dorenbos, P., 2002a. J. Lumin. **99**, 283.

Dorenbos, P., 2002b. Phys. Rev. B **65**, 235110.

Dorenbos, P., 2002c. J. Alloys Compd. **341**, 156.

Dorenbos, P., 2003. J. Lumin. **105**, 117.

Dorenbos, P., Andriessen, J., van Eijk, C.W.E., 2003. J. Solid State Chem. **171**, 133.

Downer, M.C., Cordero-Montalvo, C.D., Crosswhite, H., 1983. Phys. Rev. B **28**, 4931.

Duan, C.K., Reid, M.F., 2003. J. Solid State Chem. **171**, 299.

Duan, C.K., Reid, M.F., 2005. J. Chem. Phys. **122**, 094714.

Duan, C.K., Reid, M.F., Burdick, G.W., 2002. Phys. Rev. B **66**, 155108.

Duan, C.K., Xia, S.D., Reid, M.F., Ruan, G., 2005a. Phys. Status Solidi B **242**, 2503.

Duan, C.K., Reid, M.F., Wang, Z.Q., 2005b. Phys. Lett. A **343**, 474.

Duan, C.K., Meijerink, A., Reeves, R.J., Reid, M.F., 2006. J. Alloys Compd. **408**, 784.

Duan, C.K., Reid, M.F., Xia, S.D., 2007. J. Lumin. **122**, 939.

Elias, L.R., Heaps, W.S., Yen, W.M., 1973. Phys. Rev. B **8**, 4989.

Feldmann, C., Jüstel, T., Ronda, C.R., Schmidt, P.J., 2003. Adv. Funct. Mater. **13**, 511.

Görller-Walrand, C., Binnemans, K., 1996. In: Gschneidner Jr., K.A., Eyring, L. (Eds.), Handbook on the Physics and Chemistry of the Rare Earths, vol. 23. North Holland, Amsterdam, p. 121.

Görller-Walrand, C., Binnemans, K., 1998. In: Gschneidner Jr., K.A., Eyring, L. (Eds.), Handbook on the Physics and Chemistry of the Rare Earths, vol. 25. North Holland, Amsterdam, p. 101.

Hansen, J.E., Judd, B.R., Crosswhite, H., 1996. At. Data Nucl. Data Tables **62**, 1.

Heaps, W.S., Elias, L.R., Yen, W.M., 1976. Phys. Rev. B **13**, 94.

Henderson, B., Imbusch, G.F., 1989. Optical Spectroscopy of Inorganic Solids. Clarendon, Oxford.

Huang, S.H., Lu, L., Jia, W.Y., Wang, X.J., Yen, W.M., Srivastava, A.M., Setlur, A.A., 2001. Chem. Phys. Lett. **348**, 11.

Huang, S.H., Wang, X.J., Chen, B.J., Jia, D., Yen, W.M., 2003. J. Lumin. **102**, 344.

Ishii, T., Tohei, T., Fujimura, K., Ogasawara, K., Adachi, E., 2001. The 4th Pacific Rim Conference on Lasers and Electro-Optics, vol. 2, p. 80.

Ishii, T., Fujimura, K., Sato, K., Brik, M.G., Ogasawara, K., 2004a. J. Alloys Compd. **374**, 18.

Ishii, T., Brik, M.G., Ogasawara, K., 2004b. J. Alloys Compd. **380**, 136.

Jenssen, H.P., Linz, A., Leavitt, R.P., Morrison, C.A., Wortman, D.E., 1975. Phys. Rev. B **11**, 92.

Judd, B.R., 1966. Phys. Rev. **141**, 4.

Judd, B.R., 1977a. Phys. Rev. Lett. **39**, 242.

Judd, B.R., 1977b. J. Chem. Phys. **66**, 3163.

Judd, B.R., 1978. In: Kramer, P., Rieckers, A. (Eds.), Lecture Notes in Physics. Springer, Berlin, p. 417.

Judd, B.R., Crosswhite, H.M., Crosswhite, H., 1968. Phys. Rev. **169**, 130.

Kirm, M., Krupa, J.C., Makhov, V.N., True, M., Vielhauer, S., Zimmerer, G., 2004. Phys. Rev. B **70**, 241101R.

Kirm, M., Makhov, V.N., True, M., Vielhauer, S., Zimmerer, G., 2005. Phys. Solid State **47**, 1416; erratum, 2203.

Kück, S., Sokólska, I., 2002a. Chem. Phys. Lett. **364**, 273.

Kück, S., Sokólska, I., 2002b. J. Electrochem. Soc. **149**, J27.

Kück, S., Sokólska, I., 2003. Appl. Phys. A **77**, 469.

Kück, S., Sokólska, I., Henke, M., Scheffler, T., Osiac, E., 2005a. Phys. Rev. B **71**, 165112.

Kück, S., Sokólska, I., Henke, M., Osiac, E., 2005b. Chem. Phys. **310**, 139.

Laroche, M., Doualan, J.L., Girard, S., Margerie, J., Moncorgé, R., 2000. J. Opt. Soc. Am. B **17**, 1291.

Laroche, M., Girard, S., Margerie, J., Moncorgé, R., Bettinelli, M., Cavalli, E., 2001. J. Phys.: Condens. Matter **13**, 765.

Le Masson, N.J.M., Vink, A.P., Dorenbos, P., Bos, A.J.J., van Eijk, C.W.E., Chaminade, J.P., 2003. J. Lumin. **101**, 175.

Liu, B., Shi, C.S., Qi, Z.M., Tao, Y., 2005. Chin. Phys. Lett. **22**, 2677.

Liu, F., Zhang, J.H., Lu, S.Z., Liu, S.X., Huang, S.H., Wang, X.J., 2006. J. Lumin. **119**, 492.

Liu, G.K., Chen, X.Y., Edelstein, N.M., Reid, M.F., Huang, J., 2004. J. Alloys Compd. **374**, 240.

Lo, T.S., Reid, M.F., 1993. J. Alloys Compd. **193**, 180.

Loh, E., 1966. Phys. Rev. **147**, 332.

Loureiro, S.M., Setlur, A., Heward, W., Taylor, S.T., Comanzo, H., Manoharan, M., Srivastava, A., 2005. Chem. Mater. **17**, 3108.

Marsman, M., Andriessen, J., van Eijk, C.W.E., 2000. Phys. Rev. B **61**, 16477.

McClure, D.S., Kiss, Z., 1963. J. Chem. Phys. **39**, 3251.

Meijerink, A., Wegh, R.T., van Pieterson, L., 2000. Proc. Electrochem. Soc. **99–40**, 23.

Meijerink, A., Wegh, R., Vergeer, P., Vlugt, T., 2006. Opt. Mater. **28**, 575.

Meng, C.X., Huang, S.H., You, F.T., Tao, Y., Xu, J.H., Zhang, G.B., Wang, X.J., Dejneka, M.J., Yen, W.M., 2005. J. Rare Earths **23**, 319.

Morrison, C.A., 1980. J. Chem. Phys. **72**, 1001.

Morrison, C.A., de Sá, G.F., Leavitt, R.P., 1982. J. Chem. Phys. **76**, 3899.

Morrison, J.C., Rajnak, K., 1971. Phys. Rev. A **4**, 536.

Mulak, J., Mulak, M., 2005. J. Phys. A: Math. Gen. **38**, 6081.

Newman, D.J., 1977. J. Phys. C: Solid State Phys. **10**, 4753; erratum 11, 3742.

Nie, Z.G., Zhang, J.H., Zhang, X., Luo, Y.S., Lu, S.Z., Wang, X.J., 2006. J. Lumin. **119**, 332.

Ning, L., Duan, C.K., Xia, S.D., Reid, M.F., Tanner, P.A., 2004. J. Alloys Compd. **366**, 34.

Ning, L., Mak, C.S.K., Tanner, P.A., 2005. Phys. Rev. B **72**, 085127.

Ng, B., Newman, D.J., 1987. J. Chem. Phys. **87**, 7096.

Ogasawara, K., Watanabe, S., Toyoshima, H., Ishii, T., Brik, M.G., Ikeno, H., Tanaka, I., 2005. J. Solid State Chem. **178**, 412; erratum, 2175.

Ogasawara, K., Watanabe, S., Toyoshima, H., Brik, M.G., 2007. In: Gschneidner Jr., K.A., Bunzli, J.C., Pecharsky, V.K. (Eds.), Handbook on the Physics and Chemistry of the Rare Earths, vol. 37. North Holland, Amsterdam, pp. 1–59 (chapter 1).

Oskam, K.D., Houtepen, A.J., Meijerink, A., 2002. J. Lumin. **97**, 107.

Peijzel, P.S., Vergeer, P., Meijerink, A., Reid, M.F., Boatner, L.A., Burdick, G.W., 2005a. Phys. Rev. B **71**, 045116.

Peijzel, P.S., Vermeulen, P., Schrama, W.J.M., Meijerink, A., Reid, M.F., Burdick, G.W., 2005b. Phys. Rev. B **71**, 125126.

Peijzel, P.S., Meijerink, A., Wegh, R.T., Reid, M.F., Burdick, G.W., 2005c. J. Solid State Chem. **178**, 448.

Piper, W.W., de Luca, J.A., Ham, F.S., 1974. J. Lumin. **8**, 344.

Potapov, A.S., Rodnyi, P.A., Mikhrin, S.B., Magunov, I.R., 2005. Phys. Solid State **47**, 1436.

Rajnak, K., Wybourne, B.G., 1963. Phys. Rev. **132**, 280.

Reid, M.F., 1987. J. Chem. Phys. **87**, 2875.

Reid, M.F., 2005. In: Liu, G.K., Jacquier, B. (Eds.), Spectroscopic Properties of Rare Earths in Optical Materials. Springer, Berlin, p. 95.

Reid, M.F., Richardson, F.S., 1983. J. Chem. Phys. **79**, 5735.

Reid, M.F., van Pieterson, L., Wegh, R.T., Meijerink, A., 2000. Phys. Rev. B **62**, 14744.

Reid, M.F., van Pieterson, L., Meijerink, A., 2002. J. Alloys Compd. **344**, 240.

Riseberg, L.A., Weber, M.J., 1976. In: Wolf, E. (Ed.), Progress in Optics, vol. XIV. North-Holland, Amsterdam, p. 116.

Rodnyi, P.A., Mikhrin, S.B., Dorenbos, P., van der Kolk, E., van Eijk, C.W.E., Vink, A.P., Avanesov, A.G., 2002a. Opt. Commun. **204**, 237.

Rodnyi, P.A., Mishin, A.N., Mikhrin, S.B., Potapov, A.S., 2002b. Tech. Phys. Lett. **28**, 991.

Rodnyi, P.A., Berezovskaya, I.V., Voloshinovskii, A.S., Stryganyuk, G.B., Potapov, A.S., 2003a. Opt. Spectrosc. **94**, 550.

Rodnyi, P.A., Dorenbos, P., Stryganyuk, A.S., Voloshinovskii, G.B., Potapov, A.S., van Eijk, C.W.E., 2003b. J. Phys.: Condens. Matter **15**, 719.

Rodnyi, P.A., Potapov, A.S., Voloshinovskii, A.S., 2004. Opt. Spectrosc. **96**, 862.

Rodnyi, P.A., Potapov, A.S., Voloshinovskii, A.S., Stryganyuk, G.B., 2005a. J. Opt. Tech. **72**, 685.

Rodnyi, P.A., Stryganyuk, G.B., van Eijk, C.W.E., Voloshinovskii, A.S., 2005b. Phys. Rev. B **72**, 195112.

Rudowicz, C., Qin, J., 2004. J. Alloys Compd. **385**, 238.

Ruipérez, F., Barandiarán, Z., Seijo, L., 2005. J. Chem. Phys. **123**, 244703.

Rukmini, E., Jayasankar, C.K., Reid, M.F., 1994. J. Phys.: Condens. Matter **6**, 5919.

Schiffbauer, D., Wickleder, C., Meyer, G., Kirm, M., Stephan, M., Schmidt, P.C., 2005. Z. Anorg. Allg. Chem. **631**, 3046.

Schlesinger, M., Whippey, P.W., 1968. Phys. Rev. **171**, 361.

Seijo, L., Barandiaran, Z., Ordejon, B., 2003. Mol. Phys. **101**, 73.

Shi, J.S., Wu, Z.J., Zhou, S.H., Zhang, S.Y., 2003. Chem. Phys. Lett. **380**, 245.

Sokólska, I., Kück, S., 2001. Chem. Phys. **270**, 355.

Solarz, P., Dominiak-Dzik, G., Lisiecki, R., Ryba-Romanowski, W., 2004. Radiat. Meas. **38**, 603.

Stephan, M., Zachau, M., Gröting, M., Karplak, O., Eyert, V., Mishra, K.C., Schmidt, P.C., 2005. J. Lumin. **114**, 255.

Summerdijk, J.L., Bril, A., de Jager, A.W., 1974a. J. Lumin. **8**, 341.

Summerdijk, J.L., Bril, A., de Jager, A.W., 1974b. J. Lumin. **9**, 288.

Tanner, P.A., Mak, C.S.K., Edelstein, N.M., Murdoch, K.M., Liu, G.K., Huang, J., Seijo, L., Barandiarán, Z., 2003a. J. Am. Chem. Soc. **125**, 13225.

Tanner, P.A., Mak, C.S.K., Faucher, M.D., Kwok, W.M., Phillips, D.L., Mikhailik, V., 2003b. Phys. Rev. B **67**, 115102.

Thiel, C.W., Sun, Y., Cone, R.L., 2002. J. Mod. Opt. **49**, 2399.

van Dijk, J.M.F., Schuurmans, M.F.H., 1983. J. Chem. Phys. **78**, 5317.

van der Kolk, E., Dorenbos, P., van Eijk, C.W.E., 2001a. J. Phys.: Condens. Matter **13**, 5471.

van der Kolk, E., Dorenbos, P., van Eijk, C.W.E., 2001b. Opt. Commun. **197**, 317.

van der Kolk, E., Dorenbos, P., van Eijk, C.W.E., Vink, A.P., Fouassier, C., Guillen, F., 2002. J. Lumin. **97**, 212.

van der Kolk, E., Dorenbos, P., van Eijk, C.W.E., Vink, A.P., Weil, M., Chaminade, J.P., 2004. J. Appl. Phys. **95**, 7867.

van Pieterson, L., Wegh, R.T., Meijerink, A., Reid, M.F., 2001a. J. Chem. Phys. **115**, 9382.

van Pieterson, L., Reid, M.F., Wegh, R.T., Meijerink, A., 2001b. J. Lumin. **94**, 79.

van Pieterson, L., Reid, M.F., Wegh, R.T., Soverna, S., Meijerink, A., 2002a. Phys. Rev. B **65**, 045113.

van Pieterson, L., Reid, M.F., Burdick, G.W., Meijerink, A., 2002b. Phys. Rev. B **65**, 045114.

van Pieterson, L., Reid, M.F., Meijerink, A., 2002c. Phys. Rev. Lett. **88**, 067405.

Vergeer, P., Babin, V., Meijerink, A., 2005a. J. Lumin. **114**, 267.

Vergeer, P., 2005b. Ph.D. Thesis, University of Utrecht, Netherlands (chapter 5); Vergeer, P., Srivastava, A.M., Ronda, C.R., Meijerink, A., submitted for publication.

Vink, A.P., Dorenbos, P., de Haas, J.T.M., Donker, H., Rodnyi, P.A., Avanesov, A.G., van Eijk, C.W.E., 2002. J. Phys.: Condens. Matter **14**, 8889.

Wang, D.W., Huang, S.H., You, F.T., Qi, S.Q., Fu, Y.B., Zhang, G.B., Xu, J.H., Huang, Y., 2007. J. Lumin. **122**, 450.

Wang, X.J., Huang, S., Lu, L., Yen, W.M., Srivastava, A.M., Setlur, A.A., 2001. Opt. Commun. **195**, 405.

Wang, X.J., Huang, S.H., Srivastava, A.M., Setlur, A.A., Lu, L.H., Yen, W.M., 2002. J. Rare Earths **20**, 259.

Wegh, R.T., Donker, H., Meijerink, A., 1998. Phys. Rev. B **57**, R2025.

Wegh, R.T., Meijerink, A., Lamminmäki, R.-J., Hölsä, J., 2000. J. Lumin. **87**, 1002.

Wegh, R.T., van Klinken, W., Meijerink, A., 2001. Phys. Rev. B **64**, 045115.

Wegh, R.T., van Loef, E.V.D., Burdick, G.W., Meijerink, A., 2003. Mol. Phys. **101**, 1047.

Wybourne, B.G., 1965. Spectroscopic Properties of Rare Earths. Wiley, New York.

Xia, S.D., Duan, C.K., 2007. J. Lumin. **122**, 1.

Xia, S.D., Duan, C.K., Deng, Q., Ruan, G., 2005. J. Solid State Chem. **178**, 2643.

Yang, Z., Lin, J.H., Su, M.Z., Tao, Y., Wang, W., Li, G.B., Wang, Y.F., Li, Y.M., 2001. Acta Chim. Sinica (Chinese) **59**, 1372.

You, F.T., Huang, S.H., Meng, C.X., Wang, D.W., Xu, J.H., Huang, Y., Zhang, G.B., 2007. J. Lumin. **122**, 58.

Zachau, M., 1998. In: Proceedings of the Sixth International Conference on Luminescent Materials, Electrochemical Soc. vol. 97-29, p. 314.

Zimmerer, G., 1991. Nucl. Instrum. Methods Phys. Res. A **308**, 178.

*Chapter 233*

# SPECTROSCOPIC PROPERTIES OF LANTHANIDES IN NANOMATERIALS

Guokui LIU

*Chemistry Division, Argonne National Laboratory, Argonne, IL 60439, USA*
*E-mail: gkliu@anl.gov*

Xueyuan CHEN

*Fujian Institute of Research on the Structure of Matter, Chinese Academy of Sciences, Fuzhou, Fujian 350002, China*
*E-mail: xchen@fjirsm.ac.cn*

## Contents

## List of acronyms

| | | | |
|---|---|---|---|
| 1D | one-dimensional | NC | nanocrystal |
| 2D | two-dimensional | NIR | near infrared |
| AMEO | (aminopropyl) triethoxysilane | NT | nanotube |
| BET | Brunauer–Emmett–Teller | NW | nanowire |
| CL | cathodoluminescence | PA | photon avalanche |
| CT | charge-transfer | PL | photoluminescence |
| CW | continuous-wave | PLE | photoluminescence excitation |
| DNA | deoxyribonucleic acid | PDOS | phonon density of states |
| EDTA | ethylenediaminetetraacetic acid | QD | quantum dot |
| EDX | energy dispersive X-ray | RBS | Rutherford backscattering spectroscopy |
| ESA | excited-state absorption | RT | room temperature |
| ET | energy transfer | TEM | transmission electron microscope |
| ETU | energy-transfer upconversion | TLS | two-level-system |
| FED | field emission displays | TM | transition metal |
| FRET | fluorescence resonant energy transfer | RE | rare earths |
| FWHM | full-width at half-maximum | UV | ultraviolet |
| ICDD | International Centre for Diffraction Data | VUV | vacuum ultraviolet |
| | | XRD | X-rays diffraction |
| LED | light emitting devices | YAG | Y$_3$Al$_5$O$_{12}$ |
| LIT | laser-induced thermalization | YAM | Y$_4$Al$_2$O$_9$ |
| LSS | liquid–solid-solution | YAP | YAlO$_3$ |
| LWR | length-to-width ratio | ZPL | zero-phonon line |
| MBE | molecular-beam-epitaxy | | |

## 1. Introduction

Lanthanides activated luminescent materials are widely used for solid-state lasers, luminescent lamps, flat displays, optical fiber communication systems, and other photonic devices. It is because of the unique solid-state electronic properties that enable lanthanide ions in solids to emit photons efficiently in visible and near IR region. Due to the pioneer work by Dieke, Judd, Wybourne, and others in theoretical and experimental studies of the

$4f^n$ electronic structure (Crosswhite and Crosswhite, 1984; Dieke, 1968; Wybourne, 1965; Judd, 1963b), much of the spectroscopic properties of lanthanides are well-understood (Blasse and Grabmaier, 1994; Carnall et al., 1989; Hüfner, 1978; Liu and Jacquier, 2005). Since the rapid advances in nanotechnologies, particularly, the development of new methods of materials synthesis, there have been growing interests in the spectroscopic properties and luminescence dynamics of lanthanide ions in nanomaterials. Promising applications such as nanophosphors for high resolution display devices are driving forces of the research activities. Several review articles and book sections have been published on the optical properties of lanthanide ions doped into insulating nanomaterials (Tissue, 1998; Tanner, 2005; Prasad, 2004; Lebbou et al., 2005). There is also a large member of studies focused on semiconductor nanostructures incorporated with lanthanide ions.

The physical properties of the host materials with nanometer dimensions may differ significantly from that of the bulk materials, therefore affect the luminescence dynamics of an optically active dopant. Understanding the spectroscopic properties of these materials is important for optimizing their emissive properties for technological applications. In lanthanide-doped nanoparticles, particle size may affect emission lifetime, luminescence quantum efficiency, and concentration quenching (Tissue, 1998; Bhargava, 1996). Many of these observed phenomena result from size-reduction induced structure distortion and surface defects that affect the local environments surrounding the doped lanthanide ions. As a result, the site symmetry, crystal field strength, and the index of refraction may be significantly different from that in the bulk materials. Although electronic energy levels shift and excited state lifetime varies as a function of particle size, literally, many of these effects are not considered as a result of nano-confinement on electronic states.

It is well known that in solid phases electrons in the $4f^n$ orbitals of lanthanides are localized, therefore do not exhibit quantum confinement even in nanocrystals. According to crystal field theory, the electronic energy levels for lanthanide ions in nanoparticles may vary because of changes in the strength of local electrostatic field and site symmetry. In nanocrystals, structure disordering and surface defects are inevitable, thus induce more significant inhomogeneous line broadening than that in bulk crystals (Tissue, 1998). However, in the literature, some observed variations in energy levels have been attributed to quantum-confinement effects when the particle diameter is less than 5 nm (Bhargava et al., 1994a; Bhargava, 1997). It is reported that, for nanoparticles doped with transition metal ions such as $Mn^{2+}$:ZnS, the luminescence lifetime becomes shorter by several orders of magnitude. Similar effect has been reported for lanthanide ions in nanosemiconductors (Bhargava et al., 1994b; Chen et al., 2000). Such size-dependent effects are postulated to result from mixing of the s–p electrons of the host with the d–f valence electrons of the activator due to quantum confinement, causing the normally forbidden d–d or f–f transitions to become allowed (Reid, 2000; Rajnak and Wybourne, 1964; Judd, 1963a). Although research in nanostructured semiconductors has long been conducted to produce a clear theoretical picture of these materials, very little theoretical work addressed the size-dependence of localized emissive ions in nanostructured hosts.

Nanophenomena due to size confinement in lanthanide nanoparticles may indeed occur because of ion–phonon coupling that directly affect excited state lifetime and energy transfer. Namely, the size confinement is not on electronic states, but lattice vibra-

tion modes. In a nanocrystal, the density of phonon states becomes discrete and application of Debye approximation of a continuous density function is inappropriate. Moreover, low-frequency acoustic phonon modes are cut off. Nanoparticles not only become thermal insulators, but electron–phonon coupling may be restricted. It is expected in general that the confinement effects on spectroscopy and luminescence dynamics can be induced by inter-ionic electronic and vibronic interactions (Meltzer and Hong, 2000; Liu et al., 2002; Liu et al., 2003b). Significant size dependence of the excited state dynamics and luminescence properties is the most commonly observed nanophenomenon for lanthanide ions in nanomaterials. Given the localized nature of the 4f orbitals of lanthanides in complexes, it is obvious that changes in local environment would influence, mostly through ion–phonon coupling, the dynamics of the 4f–4f transitions, whereas the static energy levels of the 4f states experience less impact. Size effects on electron–phonon interaction are primarily due to the modification of the phonon density of states (PDOS) in a nanocrystal. Discrete phonon spectrum and the low-energy acoustic phonon modes cutoff are the consequence of the size reduction. As a result, luminescence dynamics for lanthanide ions in nanocrystals, particularly nonradiative relaxation and energy transfer efficiency are expected to differ from that in bulk materials.

In this chapter, we review recent studies on the energy level structures and excited state dynamics of lanthanide ions in nanostructures, which include lanthanide-doped dielectric nanocrystals, implanted nanoparticles of semiconductors, coated core–shell nanoparticles, nanotubes and nanoballs stuffed with lanthanide atoms. New nanophenomena such as confinement on ion–phonon interaction and its consequences in electronic transitions, energy transfer, and phase transitions will be discussed based on the experimental and theoretical studies reported in the literature. Although, the review will be comprehensive and cover all important aspects in the field, emphasis will be given to identification and theoretical analysis of various mechanisms for luminescence enhancement (or quenching) and anomalous size- and temperature-dependence. In section 2, we discuss the mechanisms of energy level shifts for lanthanide ions in nanostructures. Whereas the energies of $4f^n$ states exhibit little dependence on particle size, the energy levels of $4f^{n-1}5d$ are quite sensitive to the particle size. In section 3, a survey of theoretical principles is presented for size-dependent luminescence dynamics. Radiative lifetime, nonradiative relaxation, and excitation energy transfer processes are evaluated as a function of particle size. Following the discussion on basic principles and concepts, we report recent advances in spectroscopic characteristics of lanthanides in various nanostructures and different types of materials. This part is organized into three sections, namely, insulating nanocrystals, semiconducting nanocrystals and novel low-dimensional structures. Many related topics are grouped together for convenience. We do not intend to cover all the topics in this area, but focus on the new findings in optical spectroscopy. A review of recent progress in spectroscopic properties of lanthanides in inorganic dielectric nanomaterials is given in section 4.

In the past decade, lanthanide ions doped in nanocrystalline semiconductors have been the subject of numerous investigations. Although quantum size effects are not expected on lanthanide energy level structures, influence of quantum confinement in semiconductor on the luminescence properties of the lanthanides is expected. One of the advantages of lanthanide-doped semiconductor nanocrystals is that the lanthanide luminescence can be efficiently sen-

sitized by exciton recombination in the semiconductor nanocrystals. Potential applications of luminescent lanthanide-doped semiconductor nanocrystals include single color or white light emitting devices (LEDs). In section 5 of this chapter, a review is given on the recent progress in optical properties of lanthanide-doped III–V and II–VI semiconductor nanocrystals prepared by ion implantation, molecular-beam-epitaxy (MBE) or wet chemical syntheses. Although some controversies in this area still exist, many important results have provided insights into a fundamental understanding of the basic physical and chemical properties of lanthanide-doped semiconductor nanocrystals.

The advances in nanotechnology and synthesis methods have enabled nanomaterials to be produced in various shapes and structures. Coating of a luminescent layer activated by lanthanide ions on nanoparticles such as $SiO_2$ or $Al_2O_3$ is one of such approaches to develop new nanophosphors. In section 6, we review recent work on interesting spectroscopic features and luminescence dynamics of lanthanide ions in other novel low-dimensional nanostructures including core–shell, one-dimensional (1D) nanowires and nanotubes, two-dimensional (2D) nanofilms, hollow nanospheres, 2D nanosheet and nanodisk which have also attracted extensive attention.

## 2. Size effects on the structure of electronic levels

In a $4f^n$ configuration electrons in the partially occupied 4f orbitals are shielded by the $5s^2$ and $5p^6$ sub-shells and prevented from interacting with the ligands; therefore they have little participation in chemical bonding. On placing a lanthanide ion in a dielectric crystal, the energy levels split under the influence of the electric field produced by the crystalline environment. The f-electrons have very localized states that are conventionally described within the framework of crystal field theory (Wybourne, 1965). In general, quantum confinement effects on the energy level structure are not expected for the localized electronic states of the lanthanide ions doped in insulating nanocrystals. The electrostatic crystal field which splits the $^{2S+1}L_J$ multiplet of a lanthanide ion up to several hundreds cm$^{-1}$ may be divided into short-range components and long-range electric dipolar interactions.

The crystal field interaction can be treated approximately as a point charge perturbation on the free-ion energy states, which have eigenfunctions constructed with the spherical harmonic functions, therefore, the effective operators of crystal field interaction may be defined with the tensor operators of the spherical harmonics $\mathbf{C}^{(k)}$. Following Wybourne's formalism (Wybourne, 1965), the crystal field potential may be defined by:

$$\mathscr{H}_{CF} = \sum_{k,q,i} B_q^k C_q^{(k)}(i), \tag{1}$$

where the summation involving $i$ is over all the equivalent electrons of the open shell of the ion of interest, the $B_q^k$ are crystal field parameters and the $C_q^{(k)}$ are components of the tensor operators $\mathbf{C}^{(k)}$ that transform like spherical harmonics, for f-electrons, $k$ runs from 0 to 7 and $q$ from 0 to $\pm k$. The $B_q^k$ crystal field parameters depend on ion–ligand distance and symmetry. In the superposition model of crystal field theory proposed by Newman (Newman, 1973),

the distance-dependent parameters $B_k(R_L)$ are referred to as intrinsic crystal field parameters, which by definition are dependent only on the radial distance between the f-ion and the ligand L. Based on the assumption of the point charge model that the ion–ligand electrostatic interaction has a specific power law dependence, the intrinsic parameters can be defined as

$$B_k(R) = B_k(R_0)\left[\frac{R_0}{R}\right]^{\tau_k}, \tag{2}$$

where $R_0$ is the distance between the f-ion and a reference ligand located on the $z$-axis of the crystalline lattice, and $\tau_k$ are power law exponents reflecting the distance dependence of the ion–ligand interaction (Newman and Ng, 2000). $B_k(R_0)$ and $\tau_k$ can be empirically determined as phenomenological parameters. It should be noted that the parameters $\tau_k$ are not generally in agreement with the electrostatic power law components $\tau_2 = 3$, $\tau_4 = 5$, $\tau_6 = 7$. It is obvious that the values of the crystal field parameter for the $k = 4, 6$ components of short range interaction diminish rapidly as the ion–ligand distance increases. On the other hand, the value for the $k = 2$ parameter $B_2(R)$ decreases much slower with $R$. Zhorin and Liu (1998) have calculated the contributions of different shells of ligands to $B_k(R)$. In the $LaCl_3$ lattice the magnitude of lattice contribution to $B_2(R)$ decreases by only 25% from the first to the third shell of ligands and the sign changes between different shells. This result indicates that for nanocrystals with diameters less than 20 times of lattice constants (or approximately 5 nm), the value of $B_2(R)$ becomes size dependent. Considering the variation of particle size and surface defects, line shifts and broadening are expected for lanthanide ions in these small nanocrystals. Because 5d orbitals have a larger radial extension, the size effect on the crystal field splitting is more significant for the excited $4f^{n-1}5d$ states than for the $4f^n$ states. Therefore, we expect the $4f^7$–$4f^65d$ transitions of $Eu^{2+}$ ion exhibits much stronger size dependence than that of the $4f^6$–$4f^6$ transitions of $Eu^{3+}$.

In spectroscopy, excitation energy between the ground state of the impurity and its excited state is dependent on the nanoscopic environment. The energy gap can be tuned by changing the nanoscopic environment. In addition to size effects, the lattice structure and symmetry of the surrounding of the impurity center also lead to additional splitting of the f and d energy levels. The energy level shift may not be significant with respect to the electronic structure of the ion–ligand system. However, such a shift may have a profound effect on the excited state dynamics and luminescence properties. For example, in the case of $Pr^{3+}$, the strength of crystal field interaction determines whether the intensely absorbing $4f^2$–$4f5d$ transition is above or below the $S_0$ level of the $4f^2$ configuration. Because the d orbitals interact more strongly with the surrounding ligands, the energy levels of the 4f5d states are more sensitive to the crystal field than that of the 4f states. This has important consequences in determining the excited state dynamics, especially the luminescence efficiency for applications in the process of quantum cutting or multiphoton phosphors (Chen et al., 2004c; Chen et al., 2000).

For the $4f^7$ configuration of $Eu^{2+}$, the host sensitive energy levels of the $4f^65d$ states are not far from the metastable $4f^7$ $^6P_{7/2}$ multiplet near 27 000 $cm^{-1}$. The strength of crystal field interaction determines whether the lowest $4f^65d$ state is above or below the excited $4f^7$ multiplet, which is insensitive to host lattice. Because there is no 4f state below $^6P_{7/2}$, strong blue luminescence arises from the parity allowed $4f^65d$–$4f^7$ transition. The intensity of the

$4f^6 5d$–$4f^7$ luminescence may vary significantly if the emitting $4f^6 5d$ state shifts above the $4f^7$ $^6P_{7/2}$ multiplet. In the case of $Eu^{2+}$:BaFCl (Liu et al., 2003a), the $Eu^{2+}$ luminescence becomes strongly dependent on temperature, since the $4f^6 5d$–$4f^7$ luminescence from the $4f^6 5d$ state is thermally activated from the metastable $^6P_{7/2}$ state. Without thermal population, the $4f^6 5d$–$4f^7$ luminescence should be quenched by the $4f^7$ $^6P_{7/2}$ multiplet.

Because charge-transfer transitions of lanthanides in complexes involve ligand electrons that participate in chemical bonding at molecular scale, the energy levels of charge-transfer states are more sensitive to environments and particle size than that of the 4f and 5d states. The intensity and energy of charge-transfer transitions vary in nanocrystals as a function of particle size. This subject is covered in a recent review by Tanner (Tanner, 2005).

## 3. Confinement on excited-state dynamics

The nanostructure dependence of the excited state dynamics can be derived from the interaction of the electronic excitation with the surrounding environment and its phonon modes. A variety of nanophenomena, particularly, the lifetime of excited states of lanthanide ions in nanostructures may exhibit strong size-dependence (Prasad, 2004). Energy transfer rate and luminescence efficiency in lanthanide activated phosphors are also sensitive to particle size and surrounding environment.

### 3.1. *Radiative and nonradiative relaxation*

According to Judd–Ofelt theory, one can evaluate the radiative lifetime of any excited state of interest via Einstein spontaneous emission coefficients. The rate of relaxation, $A$, from an initial state $|\psi J\rangle$ to final state $|\psi' J'\rangle$ through radiative processes is given by (Condon and Shortley, 1963; Reid, 2000):

$$A(\psi J, \psi' J') = \frac{64\pi^2 \sigma^3}{3h(2J+1)} (\chi \bar{F}^2 + n^3 \bar{M}^2),$$ (3)

where $\bar{F}^2$ and $\bar{M}^2$ are the matrix elements of the electric dipole and magnetic dipole moments, respectively (Judd, 1962), $\sigma$ (cm$^{-1}$) represents the energy gap between states $|\psi J\rangle$ and $|\psi' J'\rangle$, $\chi = n(n^2+2)^2/9$ is the Lorentz correction for local field with $n$ being the refractive index of the host material. The observed lifetime of a particular excited state, $\tau_T$, is determined by the sum of the inverse of the radiative and nonradiative lifetimes. Thus

$$(\tau_T)^{-1} = A(\psi J) + W_T(\psi J),$$ (4)

where $A(\psi J)$ is the total radiative relaxation rate from state $|\psi J\rangle$, that is, the sum of the rates of radiative decay to all states with energy less than that of $|\psi J\rangle$. If $\tau_R$ is the total radiative lifetime of $|\psi J\rangle$, then $\tau_R = [A(\psi J)]^{-1}$. Similarly, $\tau_{NR} = [W_T(\psi J)]^{-1}$ is a total nonradiative lifetime summed over all nonradiative relaxation processes. The magnitude of the energy gap between a luminescent state and the next lower-energy state plays a major role in determining the nonradiative lifetime of that state.

As a result of ion–phonon interaction, the population of the excited state decreases via nonradiative transition from the excited state to a lower electronic state. The energy difference between the two electronic states is converted into phonon energy. This process of population relaxation is characterized by a relaxation time, $\tau_T$, which depends on the energy gap between the two electronic states, the frequencies of vibration modes, and temperature (Miyakawa and Dexter, 1970; Riseberg and Moos, 1968). At room temperature, the excited state lifetime is dominated by the nonradiative relaxation except in a few cases such as the $^5D_0$ level of $Eu^{3+}$ and $^6P_{7/2}$ level of $Gd^{3+}$ for which the energy gap is much larger than the highest phonon frequency of the lattice vibrations.

With the assumption that the phonons involved are of equal energy, a commonly used expression for the temperature-dependent multiphonon relaxation rate is (Riseberg and Moos, 1968)

$$W(T) = W(0) \left[ \frac{\exp(\hbar\omega_m/kT)}{\exp(\hbar\omega_m/kT) - 1} \right]^{\Delta E/\hbar\omega_m}, \tag{5}$$

where $\hbar\omega_m$ is the maximum phonon energy of the lattice vibrations that couples to the electronic transition of the metal ion, $\Delta E$ is the energy gap between the populated state and the next low-lying state, and $W(0)$ is the spontaneous transition rate at $T = 0$ when the phonon modes are all initially in their ground state. At low temperatures where $\hbar\omega_m \gg kT$, the nonradiative relaxation rate is dominated by $W(0)$, which can be expressed as a simple exponential function depending on the energy gap, $\Delta E$:

$$W(0) = C \exp(-\alpha \Delta E/\hbar\omega_m), \tag{6}$$

where $C$ and $\alpha$ are empirical parameters which are characteristic of the particular crystal. Known as the energy-gap law, this exponential dependence has been used to describe the energy-gap dependence of multiphonon transitions rates for the 4f states (Riseberg and Moos, 1967, 1968).

## 3.2. *Line broadening and shifts*

One of the direct consequences of ion–phonon interaction is a broadening of the line widths of electronic transitions. This temperature-dependent process is called homogeneous line broadening, whereas the structure defect and crystalline strain induced static variation in electronic energy levels and line broadening is named inhomogeneous broadening. In time domain, homogeneous line broadening is a measurement of dephasing of coherence in the excited states, which is characterized by a dephasing time $\tau_2$ given as $\tau_2 = (\pi\Gamma)^{-1}$ where $\Gamma$ is the homogeneous line width. Along with line broadening, the lattice dynamics characterized by electron–phonon interaction leads to temperature-dependent line shift of the electronic transitions. The contributions to homogeneous line broadening and shift generally come from direct one-phonon and multiphonon processes including Raman phonon scattering. Theoretically, the temperature-dependent line width $\Gamma$ and line shifts ($\delta E$) associated with the two levels of an electronic transition can be respectively expressed by the McCumber–Sturge equations

(McCumber and Sturge, 1963):

$$\Gamma \left( \text{cm}^{-1} \right) = \Gamma_0 + \bar{\alpha} \left( \frac{T}{T_D} \right)^7 \int_0^{T_D/T} \frac{x^6 e^x}{(e^x - 1)^2} \, dx \tag{7}$$

and

$$\delta E \left( \text{cm}^{-1} \right) = \alpha \left( \frac{T}{T_D} \right)^4 \int_0^{T_D/T} \frac{x^3}{e^x - 1} \, dx, \tag{8}$$

where the residual width $\Gamma_0$ is temperature independent and due to random crystal strains; $\bar{\alpha}$ and $\alpha$ are the coupling coefficients for the electron–phonon interaction; and $T_D$ is the effective Debye temperature of the phonon distribution. $\bar{\alpha}$, $\alpha$ and $T_D$ are treated as adjustable parameters to get the best fit to the experimental data. The residual width and line position at $T = 0$ K are estimated by extrapolating the experimental data to zero temperature.

In crystals for which the defect-induced inhomogeneous line broadening is dominant, the homogeneous broadening caused by electron–phonon interaction may be determined by nonlinear spectroscopic methods such as hole-burning in frequency domain and photon echoes in time domain experiments. A very narrow excitation source (e.g., from a laser) is used in hole burning to excite a selected site causing saturation or photobleaching, so that this site does not absorb any more. Consequently, a hole appears in the inhomogeneously broadened line shape of the transition. The hole width is limited by the homogeneous broadening. Because of the pumping and probing processes, the hole width is twice the homogeneous line width (MacFarlane and Shelby, 1987).

So far the principles and theoretical models that we discussed for the excited state dynamics including line shifts and broadening were developed originally for ions in bulk solids. Although the 4f electronic states are localized and exhibit little quantum confinement, the dynamics of electronic transitions may be subjected to quantum confinement arising from electron–phonon interactions. Modification of the existing theoretical models is required for their applications to lanthanides in nanomaterials.

### 3.3. Modification of radiative lifetime

Spontaneous emission and radiative lifetime of lanthanide excited state in condensed phases is determined by the electromagnetic field and the index of refraction as shown in eq. (3). In nanocrystals, spontaneous emission of photons is influenced by two mechanisms: (1) the non-solid medium surrounding the nanoparticles that changes the effective index of refraction thus influences the radiative lifetime (Meltzer et al., 1999; Schniepp and Sandoghdar, 2002), (2) size-dependent spontaneous emission rate due to interferences (Schniepp and Sandoghdar, 2002).

The dependence of radiative lifetime on the index of refraction, $n$, arises from the change in the density of states for photons in the medium of reduced light velocity and the modification of the polarizability of the surrounding medium. Since the nanoparticles occupy only a small fraction of the total volume, in order to compare the experimental results with eq. (3) it is necessary to introduce an effective index of refraction for the medium, $n_{\text{eff}}$, which consists of

the nanoparticles surrounded by the media with refractive index $n_{\text{med}}$. One may evaluate an effective index of refraction

$$n_{\text{eff}}(x) = x n_{\text{NP}} + (1 - x) n_{\text{med}}, \tag{9}$$

where $x$ is the "filling factor" showing which fraction of space is occupied by the nanoparticles. For the nanoparticles, $n$ in eq. (3) is consequently replaced by $n_{\text{eff}}(x)$. The use of $n_{\text{eff}}$ is valid when the average size of the particles is much smaller than the wavelength of light.

Interference between the radiation field and the lattice electrostatic field along the radius of emitting ions in spherical nanoparticle results in a coherent effect that leads to resonance in spontaneous decay. One might expect that the presence of nanometer scale material could lead to the scattering of the vacuum field and therefore modification of the spontaneous emission rate. Several theoretical reports have predicted this phenomenon for an atom in the near field of nanoscopic spheroids, sharp tips, and substrates with lateral nanostructures (Chew, 1988; Girard et al., 1995; Gersten and Nitzan, 1981). The variation of spontaneous decay rate along the radius of nanoparticles can be measured using a near-field optical spectrometer to detect the luminescence lifetime of emitters embedded in isolated single dielectric nanospheres (Schniepp and Sandoghdar, 2002). By varying the diameter of the spheres from 100 nm to 2 µm and by modifying their dielectric surrounding, Schniepp et al. have demonstrated a systematic change in the spontaneous emission rate. The experimental results show inhibition of the spontaneous emission up to three times and are in excellent agreement with the results of analytical calculations. The spontaneous emission rate of ions placed in dielectric spheres can be substantially reduced across the border from the superwavelength regime of filed oscillation to the nanoscopic realm of Raleigh scattering.

The spontaneous emission rate of an electric dipole located at an arbitrary location in a sphere of a given diameter has been calculated analytically by Chew (1988). It is shown that the strong oscillations for emitters near the surfaces of the larger spheres are due to the coupling to the natural modes of oscillation of a dielectric sphere (Benner et al., 1980) while the modulations at the center are caused by interference in the radial modes. As it goes from the superwavelength to the subwavelength size regime, however, the oscillations disappear, and the spontaneous emission rate approaches a limiting value below the bulk rate and independent of the dipole orientation and position.

### 3.4. *Modification of phonon density of states and confinement on electron–phonon interaction*

Although no quantum confinement should occur in the electronic energy level structure of lanthanides in nanoparticles because of the localized 4f electronic states, the optical spectrum and luminescence dynamics of an impurity ion in dielectric nanoparticles can be significantly modified through electron–phonon interaction. Confinement effects on electron–phonon interaction are primarily due to the effect that the phonon density of states (PDOS) in a nanocrystal is discrete and therefore the low-energy acoustic phonon modes are cut off. As a consequence of the PDOS modification, luminescence dynamics of optical centers in nanoparticles, particularly, the nonradiative relaxation of ions from the electronically excited states, are expected to behave differently from that in bulk materials.

The most essential property of acoustic vibrations in a nanoparticle is the existence of minimum size-quantized frequencies corresponding to acoustic resonances of the particle. In dielectric nanocrystals, the Debye model is not valid for evaluation of the PDOS if the radius of the nanocrystal is less than 10 nm. The vibrational modes of a finite sphere were analyzed previously by Lamb (1882) and Tamura (1995). A stress-free boundary condition at the surface and a finiteness condition on both elastic displacements and stresses at the center are assumed. These boundary conditions yield the spheroidal modes and torsional modes, determined by the following eigenvalue equations:

$$2\left\{\eta^2 + (l-1)(l+2)\left[\eta\frac{j_{l+1}(\eta)}{j_l(\eta)} - (l+1)\right]\right\}\xi\frac{j_{l+1}(\xi)}{j_l(\xi)} - \frac{1}{2}\eta^4$$
$$+ \left[\eta^2 - 2l(l-1)(l+2)\right]\eta\frac{j_{l+1}(\eta)}{j_l(\eta)} + (l-1)(2l+1)\eta^2 = 0, \tag{10}$$

$$\frac{d}{d\eta}\frac{j_l(\eta)}{\eta} = 0, \tag{11}$$

where for the reduced frequencies of the spheroidal modes and torsional modes, $\xi = \omega R/v_l$ and $\eta = \omega R/v_t$, with $\omega$ being the phonon frequency and $R$ the radius of nanoparticles; $j_l$ is the $l$th order spherical Bessel function; $v_l$ and $v_t$ are the sound velocities of longitudinal and transverse modes, respectively. Fig. 1 compares the phonon spectrum in $Y_2O_2S$ nanocrystals with radii of 5, 10, 20 nm, respectively (Chen et al., 2003b). It clearly shows that the low-frequency phonon modes are significantly reduced with size reduction. Furthermore, there is a cutoff frequency ($\omega_{min}$) in the low frequency side of the phonon spectrum below which all phonon modes are intrinsically eliminated. Thus the luminescence dynamics, especially the phonon-assisted energy transfer processes in nanocrystals is expected to be different from that in their bulk counterparts.

The dependence of $v_{min}$ on the nanoparticle size can be expressed as:

$$v_{min} = \frac{v_t}{2\pi R}\eta_{min}, \tag{12}$$

where $\eta_{min} = 2.05$ ($\xi_{min} = 2.45 > \eta_{min}$) is the minimal reduced frequency determined by the numerical solution of eqs. (10) and (11). It is predicted in fig. 1 that the cutoff phonon frequencies (energies) are approximately 8, 4 and 2 cm$^{-1}$ for the $Y_2O_2S$ nanoparticles with radii of 5, 10 and 20 nm, respectively.

### 3.5. *Energy transfer and upconversion*

As a result of ion–ion interactions, electronic excitation of lanthanide ions in insulating host materials undergoes migration through resonant energy transfer and phonon-assisted energy transfer processes (Miyakawa and Dexter, 1970; Yen, 1987; Huber, 1981). The later is more important because ions imbedded in the lattice of host materials do not have exactly the same energy level in an excited state due to lattice stress and defects. As a result, the line widths of electronic transitions are inhomogeneously broadened, and resonant energy transfer becomes improbable. For excitation migration among the ions with different energy levels due
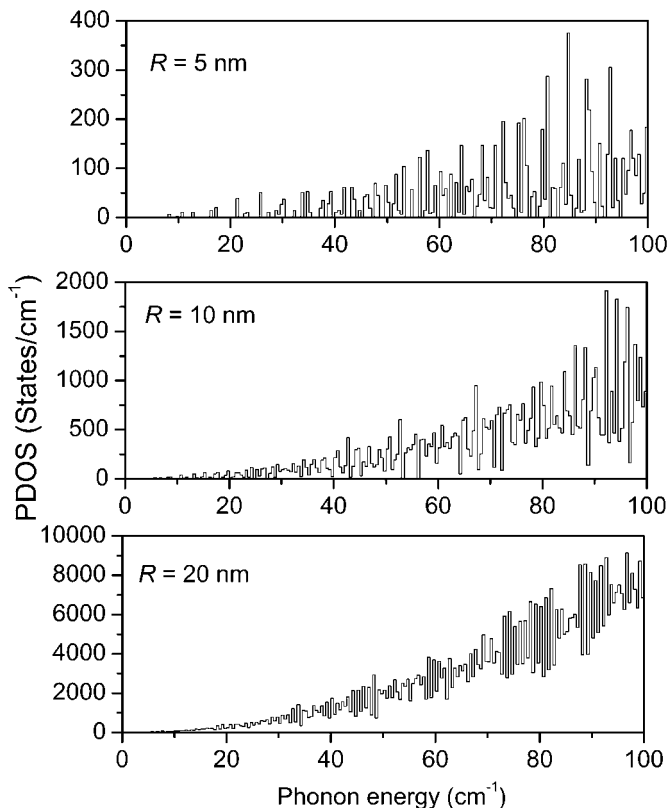
Fig. 1. Calculated phonon density of states in $Y_2O_2S$ nanocrystals with radius of 5 nm, 10 nm, and 20 nm, respectively (redraw after (Chen et al., 2003b)).

to defect induced inhomogeneous broadening, the energy mismatch between a donor and an acceptor is made up by lattice phonons. Phonon assistance is also required in excitation via cross relaxation and upconversion in which energy mismatch in electronic energy levels is made up by lattice phonons. The energy level variation or inhomogeneous broadening is generally more significant in nanostructures than that in bulk crystals. As we discussed in the previous section, the density of phonon states becomes discrete and low frequency phonon modes are absent below a cutoff energy, $E_{cut}$. Energy transfer does not occur when the energy difference between a donor and an acceptor is below $E_{cut}$. Because of the restrictions of phonon density of states in nanocrystals, one expects that both luminescence lifetime and the efficiency of energy transfer will be modified when compared with bulk crystals (Chen et al., 2003b). Moreover, efficiency of cross relaxation and upconversion may also be reduced in nanocrystals.

Based on the classical Dexter–Forster model of inter-ionic interaction induced energy transfer, the excitation probability of ion $i$ can be expressed as (Dexter, 1953; Förster, 1948;

Inokuti and Hirayama, 1965; Miyakawa and Dexter, 1970):

$$\frac{dP_i}{dt} = -\kappa P_i - \sum_{j \neq i} [W_{ij}^{\text{Res}} + W_{ij}^{\text{PA}}] P_i. \tag{13}$$

The first term is due to spontaneous radiative relaxation and nonradiative phonon relaxation as described in eq. (13), where $P_i$ is the probability of ion $i$ in the excited state. The second term is due to energy transfer induced by ion–ion interaction, where $W_{ij}^{\text{Res}}$ and $W_{ij}^{\text{PA}}$ are rates of resonant and phonon-assistant energy transfer, which depend on distance between donor and acceptor $R_{ij}$. For resonant energy transfer

$$W_{ij}^{\text{Res}} = \alpha_0 \left( \frac{R_0}{R_{ij}} \right)^s, \tag{14}$$

where the exponent $s = 6, 8, 10$, for dipole–dipole, dipole–quadrupole and quadrupole–quadrupole interactions respectively. For phonon-assisted energy transfer (Holstein et al., 1976)

$$W_{ij}^{\text{PA}} = \frac{b}{v_s^4} \omega_{ij} \rho(\omega_{ij}) \left( \frac{R_0}{R_{ij}} \right)^{s-2} \left\{ \begin{array}{c} N(\omega_{ij}) + 1 \\ N(\omega_{ij}) \end{array} \right\}, \tag{15}$$

where $\rho$ is the density of phonon states, and $\omega$ is the phonon frequency. The occupation number of the phonon states is given by

$$N(\omega_{ij}) = \left[ e^{\hbar \omega_{ij}/kT} - 1 \right]^{-1}. \tag{16}$$

It is clear from eq. (15) that a modification of the density of phonon states in nanocrystals influences the efficiency of energy transfer. Because the energy transfer rate depends also on the distance between the donor and acceptor, the transfer in very small nanocrystals is restricted. This restriction may be understood based on the fact that the hopping length and the transfer probability are restricted for a donor to find a matching acceptor in the neighborhood of the nanoparticle.

An analytical solution of eq. (13) is generally not available particularly for ions doped into nanocrystals (Liu and Wu, 1994). A Monte Carlo method of simulation may be used in modeling spectral migration of optical centers in inhomogeneously broadened systems (Chen et al., 2003b). It is a simple but useful method for simulating luminescence dynamics of optical centers randomly distributed in crystalline lattice. Use of the Monte Carlo method enables one to "design" a virtual nanocrystal with any size and doping concentration of the luminescent centers. In addition to size restrictions on phonon relaxation, phonon-assisted energy transfer processes may also strongly influence the dynamics of luminescence centers in nanocrystals. Given the discrete phonon density of states and low energy cutoff in nanocrystals, the phonon-assisted energy transfer processes may significantly impact on the luminescence decay at room temperature while they should be negligible at liquid helium temperature. When phonon-assisted energy transfer processes are taken into account, the luminescence decay would show non-exponential characteristics, and size confinement effect is expected.

## 4. Spectroscopy of lanthanide ions doped in insulating nanocrystals

Following the introduction to size-dependent nanophenomena presented in the previous sections, we now focus our attention on the luminescence properties of lanthanide ions at additional sites or distorted structure existing in nanophases. Phenomena of prolonged luminescence lifetime, anomalous thermalization, upconversion luminescence, dynamics of long-range interaction with two-level-systems (TLS), and quantum efficiency are to be discussed.

### 4.1. *Site-resolved luminescence spectra*

As discussed early in this chapter, quantum confinement has little effect on the localized electronic levels of lanthanide ions doped in insulating nanocrystals. But when the particle size becomes very small and approaches to a few nanometers, some exceptions may be observed. The change of lanthanide energy level structure in very small nanocrystals (1–10 nm) is due to a different local environment around the lanthanide ion that leads to a drastic change in bond length and coordination number. Lanthanide luminescence from the new sites generated in nanoparticles can be found experimentally. The most typical case is that observed in nanofilms of Eu:$Y_2O_3$ with a thickness of 1 nm, which exhibits a completely different emission behavior from that of thick films (100–500 nm) (Bar et al., 2003).

In fig. 2, the peak intensity at 611 nm arising from $Eu^{3+}$ ions at regular sites decreases with thinner films and completely vanishes in the case of the 1-nm film. The peak at 612.6 nm, which can be observed in the shoulder of the 611-nm peak in the 500-nm and 100-nm thick films, can be resolved, and its intensity increases. Additionally, a new peak appears at 615.5 nm. The features around 580 nm, the transition $^5D_0 \rightarrow {}^7F_0$ of the $C_2$ site at 579.4 nm, and the transition $^5D_0 \rightarrow {}^7F_1$ of the $C_{3i}$ site at 581.2 nm vanish completely in films with a thickness smaller than 100 nm. The same pattern change of the luminescence spectra was also observed in 1-nm nanofilms of Eu:$Lu_2O_3$ grown on sapphire (Bar et al., 2003). The spectrum evolution suggests that the new emission bands arise from a new site due to the confinement in two-dimensional nanofilms. In a 20-nm-thick film, Bar et al. found that the unit cell of yttria was strongly compressed along the surface by using surface X-ray diffraction measurements (Bar et al., 2005), which to some extent supports the assumption that local environment change leads to the appearance of a new site.

It is worth mentioning that such sharp emission lines from lanthanide ions in an anomalous site in nanocrystals have never been reported previously, and deserves further study including time-resolved/site-selective high-resolution laser spectroscopy to gain more insight into the origin of this new site and its energy level structure. In a separate work these authors reported the excitation spectra in the VUV spectral range (50–350 nm) using synchrotron light (Bar et al., 2005), but their results did not provide additional information on the origin of the new site due to the following reasons: (1) the excitation was limited to VUV range, which we believe should extend to the visible range, especially at 510–580 nm corresponding to the excitation to $^5D_1$ and $^5D_0$. (2) The excitation spectra were obtained by monitoring the peak at 611 nm, which is not suitable for the 5–20 nm films. Instead, all excitation spectra for the 1–5-nm thin films should monitor the anomalous peak at 615.5 nm.
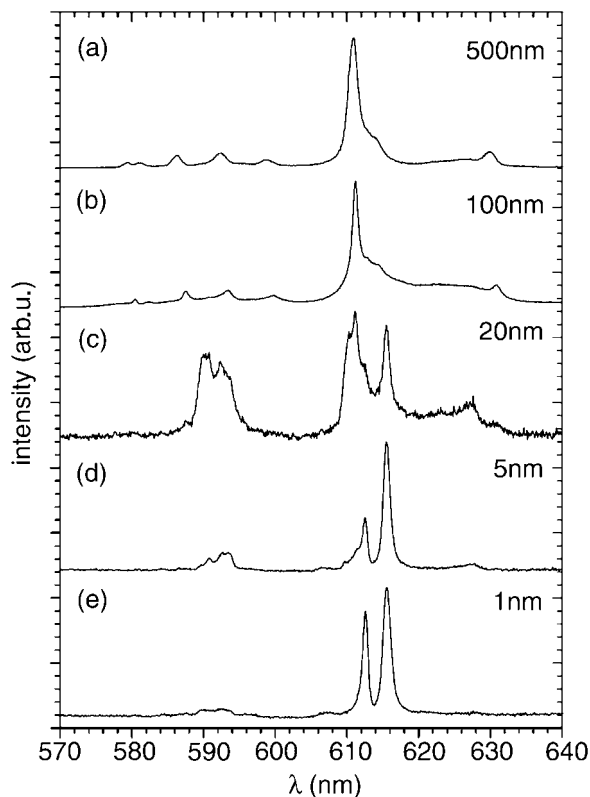
Fig. 2. Emission spectra of Eu(4%):$Y_2O_3$ films with different thicknesses. The excitation wavelength is 243 nm (redraw after (Bar et al., 2003)).

For nanocrystals of $Eu^{3+}$:$Y_2O_3$ with radius in the range of 1–10 nm, the luminescence pattern of the new site looks quite different from that shown in fig. 2e. Moreover, it depends on the synthesis method. In general, the new bands are much broader in nanocrystals than in thin films, possibly arising from surface sites or distorted lattice sites near the surface. For example, two broad bands located at 615 and 622 nm were dominant in the emission spectra of $Eu^{3+}$:$Y_2O_3$ nanocrystals with a size of 9 nm prepared by solution-combustion method (Qi et al., 2002). EXAFS spectra revealed that the local structures around the $Eu^{3+}$ ions drastically change when the particle size is reduced from 40 to 9 nm. Namely, the average Eu–O bond length increases from 0.235 to 0.244 nm and the coordination number increases from 6 to 8, indicating that the $Eu^{3+}$ local environment undergoes structure disordering. Similar results were reported for the 5-nm $Eu^{3+}$:$Y_2O_3$ nanocrystals prepared by the same methods (Zhang et al., 2003), in which emissions from both the normal site and distorted site were superimposed. Another different emission pattern of $Eu^{3+}$ in the $Y_2O_3$ matrix has been observed in well-dispersed $Eu^{3+}$:$Y_2O_3$ nanocrystals (∼6 nm) (Wang, H.Z. et al., 2005), where
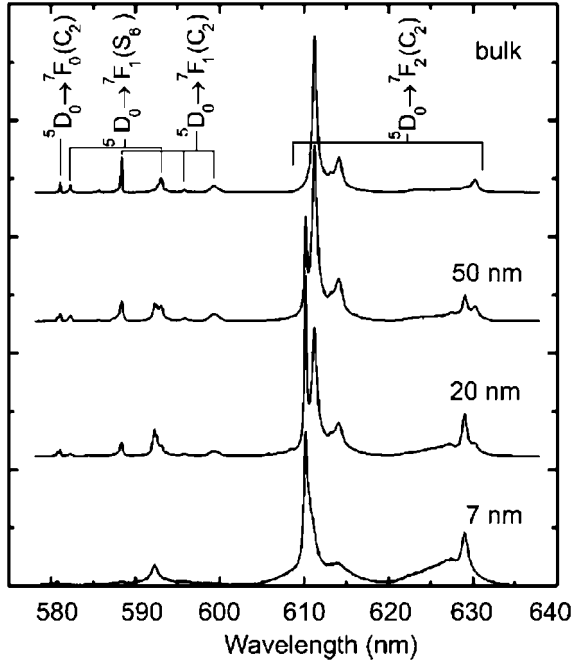
Fig. 3. Emission spectra of Eu:$Gd_2O_3$ (2.5%) nanocrystals with different average diameters excited at 250 nm (reprinted with permission from Mercier et al. (2004)).
© 2004 American Institute of Physics

two broad peaks at 614 and 628 nm with a similar intensity were identified for the $^5D_0 \to {}^7F_2$ transition.

Luminescence from the new $Eu^{3+}$ site in cubic $Gd_2O_3$ nanocrystals prepared by a sol-lyophilization technique was also reported (Mercier et al., 2004). Fig. 3 shows clearly the evolution of the emission lines when the particle size decreases from bulk to 7 nm. As shown in fig. 3, a spectrum dominated by the emission lines typical of $Eu^{3+}$ in a $C_2$ site and the weak $S_6$ site peaks arising from the $^5D_0 \to {}^7F_1$ transition is generally observed for the bulk under ultraviolet excitation at 250 nm. Although the electronic levels of $Eu^{3+}$ in $Gd_2O_3$ are almost the same as in $Y_2O_3$, the luminescence pattern of the new $Eu^{3+}$ site in $Gd_2O_3$ is quite different. The emission pattern of 7-nm nanocrystals is completely different from the bulk. The main peak at 611 nm typical of the regular site gradually diminishes and appears as a shoulder on the main peak at 610 nm typical of the new site. The line positions and intensities drastically change, which indicates a totally different crystal field environment for the $Eu^{3+}$ ions at the new site. The lines of the new site are sharp and comparable to the normal site, reflecting an ordered crystalline change. Note that the line at 593 nm in fig. 3 should be assigned to the $^5D_0 \to {}^7F_1(C_2)$ transition instead of $^5D_0 \to {}^7F_1(S_6)$, according to the energy level analysis.
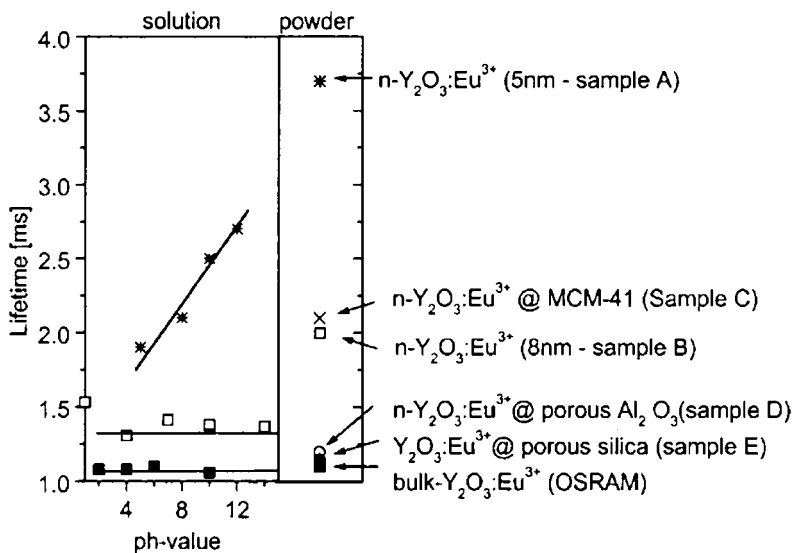
Fig. 4. Lifetime of the $^5D_0$ state of bulk $Y_2O_3$:$Eu^{3+}$ and different nanocrystalline $Y_2O_3$:$Eu^{3+}$ samples found in the dry powder and in aqueous solution of different pH values (reprinted with permission from Schmechel et al. (2001)).
© 2001 American Institute of Physics

## 4.2. *On the nature of lifetime changes*

Luminescence lifetime depends upon radiative and nonradiative decay rates. In nanoscale systems, there are many factors that may affect the luminescence lifetime. Usually the luminescence lifetime of lanthanide ions in nanocrystals is shortened because of the increase in nonradiative relaxation rate due to surface defects or quenching centers. On the other hand, a longer radiative lifetime of lanthanide states (such as $^5D_0$ of $Eu^{3+}$) in nanocrystals can be observed due to (1) the non-solid medium surrounding the nanoparticles that changes the effective index of refraction thus modifies the radiative lifetime (Meltzer et al., 1999; Schniepp and Sandoghdar, 2002); (2) size-dependent spontaneous emission rate increases up to 3 folds (Schniepp and Sandoghdar, 2002); (3) an increased lattice constant which reduces the odd crystal field component (Schmechel et al., 2001).

To investigate the influence of the surrounding environment on the luminescence dynamics of lanthanides in nanocrystalline particles, Schmechel et al. characterized and compared the $Eu^{3+}$ ($^5D_0$) luminescence lifetime in nanocrystals with different size in air or aqueous solution, and inside different caging hosts such as Porous MCM-41, porous silica and porous alumina (Schmechel et al., 2001). Fig. 4 compares the observed lifetimes in different surroundings. Note that the particle size or pore diameter of samples A–E and bulk are 5 nm, 8 nm, 2.7 nm, 80 nm, 15 nm, and 5 μm, respectively. The lifetime of all nanoparticles is, in general, longer when compared to the reference bulk powder (1.1 ms). A general trend can be gathered from fig. 4, namely, the smaller nanocrystals or pores, the longer lifetime ob-

served. Specifically, for the 5-nm nanocrystals in air, the lifetime is found to be up to three times longer than in the bulk, reaching a value of 3.8 ms. Furthermore, the temporal behavior of the lifetime shows only single exponential decay processes, which may exclude the possibility of a superposition of different decays from multiple sites. Combined with their structural characterization, Schmechel et al. assumed that the forced electric dipole transition for $Eu^{3+}$ ($^5D_0$–$^7F_2$) in nanocrystals is hypersensitive to changes in the crystal field, and the increased radiative lifetime may be due to the increased lattice constant in the nanocrystalline samples which thus reduces the odd crystal field components. The strong drop of lifetime in aqueous solution compared to nanocrystals in air is due to the increased nonradiative decay processes involving the vibrational modes of the water molecules at the surface. Unlike the 8-nm nanocrystals and bulk, the lifetime of 5-nm nanocrystals shows a dependence on the pH of the surrounding acid and base, which may be related to the change in the crystal field at $Eu^{3+}$ sites when changing the pH. Obviously, Schmechel et al. ignored another very important contribution to lifetime lengthening, that is, they did not take into account the correction of effective refractive index as Meltzer et al. (1999) did. In fact, the above lifetime behavior can be well explained according to Meltzer's method of "filling factor." The smaller nanocrystals leads to the smaller filling factors in the air thus longer lifetime. That the index of refraction of water (acid or base) is larger than the one of air but smaller than the one of $Y_2O_3$ host may result in a shorter lifetime in the aqueous solution than in the air but larger than in the bulk.

There is another question with respect to the lifetime behavior of lanthanides in nanocrystals. Will the lifetime of all excited states be lengthened? The answer is obviously "no" since the observed lifetime depends on both the radiative and nonradiative relaxation rates. Although the correction of effective refractive index (eq. (9)) may be applicable to all excited states, it affects only the radiative lifetime.

We recently measured the luminescence lifetime of $Eu^{3+}$ ions in $Y_2O_3$–$Al_2O_3$ core–shell nanocrystals (∼7 nm thick nanolayer of cubic-$Y_2O_3$ coating on $Al_2O_3$, with an average size of 60–70 nm) at 3.5 K, 77 K and room temperatures, respectively (Chen, X.Y. et al., 2005). The lifetimes of $Eu^{3+}$ as a function of the temperature are compared with those of the bulk counterparts in fig. 5. Obviously, the lifetime of $^5D_0$ is independent of temperature for both nanocrystals and bulk crystal due to the very large energy gap between $^5D_0$ and $^7F_6$. Similar to the previous case, the lifetime of $^5D_0$ in the nanolayer of cubic-$Y_2O_3$ (1.42 ms) was found to be unusually longer than for the bulk counterparts (0.86 ms). The longer lifetime of $^5D_0$ in the Eu:$Y_2O_3$ nanolayer is most possibly due to the non-solid medium surrounding the nanoparticles that changes the effective index of refraction thus modifies the radiative lifetime. The filling factor, showing which fraction of space is occupied by Eu:$Y_2O_3$ nanocoating particles, is estimated to be approximately 72% by utilizing eq. (9). On the other hand, the $^5D_1$ lifetime is very sensitive to temperature, since it is closely related to the multiphonon relaxation process from $^5D_1$ to $^5D_0$. When the temperature varies from 3.5 to 295 K, the $^5D_1$ lifetime for nanocrystals is significantly shortened from 68 to 13 μs. As shown in fig. 5, the $^5D_1$ lifetime at a specific temperature is much shorter for the nanocrystals than for the bulk counterpart, which may be attributed to surface effects or cross relaxation. The surface defects
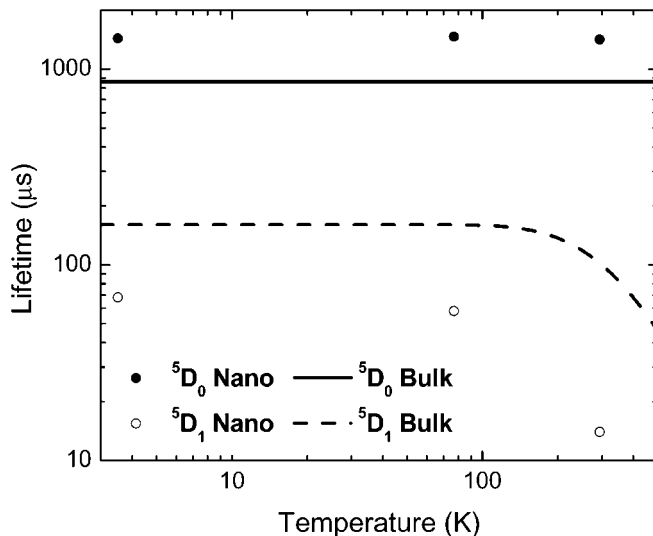
Fig. 5. Comparison of the lifetimes of the $^5D_0$ and $^5D_1$ states of $Eu^{3+}$ between $Eu:Y_2O_3@Al_2O_3$ nanocrystals and bulk crystalline $Eu:Y_2O_3$ crystal (redraw after (Chen, X.Y. et al., 2005)).

of the nanocoating particles act as the nonradiative transition channels, leading to the increase of nonradiative relaxation rates for $^5D_1 \rightarrow {}^5D_0$.

A shortening of the $^5D_1$ lifetime was also observed in $Eu:YAlO_3$ nanocrystals. The lifetime of $^5D_0$ at 3.5 K (1.64 ms) is longer than the value for the bulk counterpart (1.5 ms), which corresponds to a filling factor of $\sim94\%$, but the $^5D_1$ lifetime (45 μs) is much shorter than the value for the bulk (65 μs) in spite of the lower measurement temperature.

For other lanthanide ions doped in nanocrystals, the lifetime behavior may be more complicated. For instance, it was found for $Er^{3+}$ doped in $\sim50$ nm $Lu_2O_3$ nanocrystals that the decay times of the $^4S_{3/2}$ and $^4F_{9/2}$ levels are longer with respect to the bulk sample following upconversion excitation at 980 nm, but shorter with respect to the bulk following direct excitation at 488 nm (Vetrone et al., 2002). This complicated luminescence dynamics results from the competition between two processes: one is the multiphonon relaxation in nanocrystals owing to the presence of contaminants (such as $CO_2$ and $H_2O$) on their surface which increases the nonradiative decay rate; the other is aforementioned change in the effective refractive index in nanocrystals plus the feeding from longer-lived states under upconversion excitation which reduces the radiative rate. For direct pumping, the former prevails over the latter, while the latter is obviously predominant for upconversion pumping.

Energy transfer, particularly, phonon-assisted energy transfer processes must be considered in evaluating lanthanide luminescence decays, because they contribute in many cases to a major part of the observed lifetime. Based on the theoretical models described in section 3, we have conducted Monte Carlo simulations of energy transfer and its effect on luminescence decay for lanthanide ions in nanocrystals and compared the calculated results with experi-
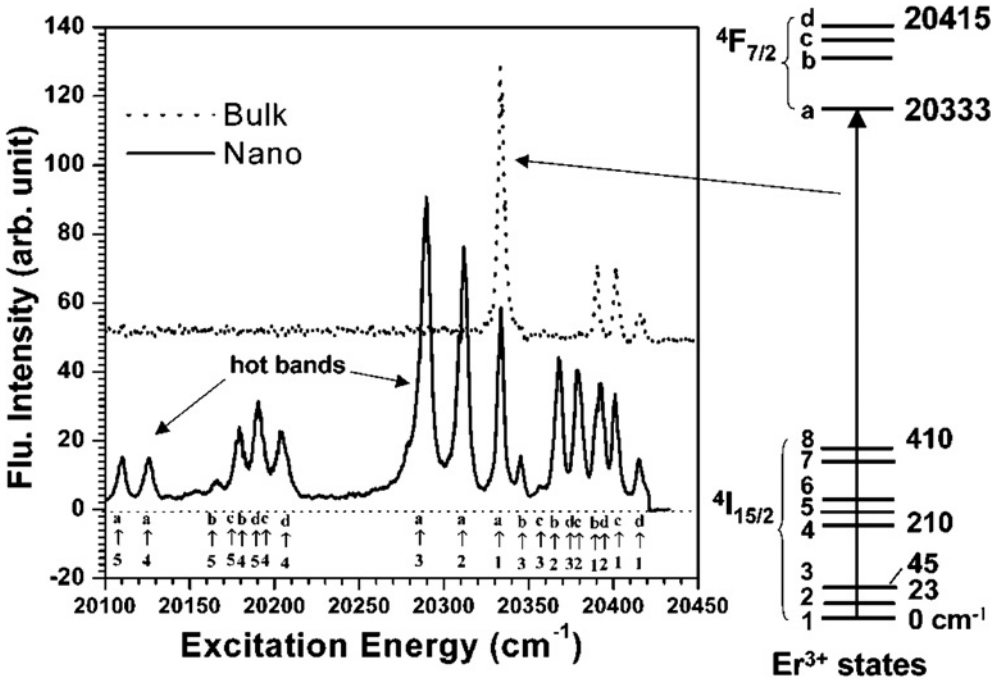
Fig. 6. Excitation spectra of $Er^{3+}$ in 10–40 nm diameter (—) and 400 nm diameters (- - -) nanocrystals of $Y_2O_2S$ at 2.6 K. The optical transition is from the $^4I_{15/2}$ ground state to the $^4F_{7/2}$ excited state while emission from the $^4S_{3/2}$ excited state at 18,248 $cm^{-1}$ is monitored. Vertical lines indicate the electronic transitions from the crystal field sublevels of the ground state to those of the excited state (redraw after (Liu et al., 2002)).

mental measurements on $Er^{3+}$:$Y_2O_2S$ (Chen et al., 2003b). It is demonstrated that how size restriction and the discrete phonon density of states of nanoparticles jointly modify the luminescence decay of the localized electronic states of $Er^{3+}$. The influence of confinement effects on energy transfer processes as a function of nanoparticle size is correctly predicted. The simulations also demonstrate that the size confinement effects on phonon-assisted energy transfer may significantly reduce the transfer rate and upconversion efficiency due to the lack of low-frequency phonon modes in nanocrystals. At the same time, resonant energy transfer is also restricted in nanoparticles.

## 4.3. *Anomalous thermalization*

As discussed early in this chapter, the optical spectrum and luminescence dynamics of an impurity ion in dielectric nanoparticles can be significantly modified through electron–phonon interaction. As a result of confinement on phonon density of states, luminescence dynamics of optical centers in nanoparticles, particularly, the nonradiative relaxation of ions from the electronically excited states, are expected to behave differently from that in bulk materials.

We recently observed anomalous thermalization phenomena in $Er^{3+}$-doped $Y_2O_2S$ nanocrystals of 20-nm diameter at low temperature (Liu et al., 2002). It is well known that the population of the lanthanide ions doped in the host among the energy levels generally obeys the Boltzmann distribution characterized by the Boltzmann factor. For the $i$th level,

$$b_i = g_i \exp(-E_i/k_B T)/\sum_j g_j \exp(-E_j/k_B T), \tag{17}$$

where $k_B$ is the Boltzmann constant; $g_i$ is the degeneracy of the $i$th level and $E_i$ is its energy. Hence, at low temperature (especially below liquid helium temperature, $T < 4.2$ K), one should generally observe the emission or absorption lines from the lowest level of the initial multiplet on which most ions populate, supposing the energy difference between the lowest level and the nearest upper level is much larger than $k_B T$. Nevertheless, we found an "anomaly" during the investigation of optical properties of $Er^{3+}$-doped $Y_2O_2S$ nanocrystals. Fig. 6 shows the low-temperature excitation spectra of $Er^{3+}$ in bulk crystals and nanocrystals, which were obtained by using a 5-ns pulse laser and monitoring the $Er^{3+}$ luminescence from the $^4S_{3/2}$ state at 18248 cm$^{-1}$. Hot bands originating from the upper Stark levels of $^4I_{15/2}$ with an energy gap up to 224 cm$^{-1}$ are observed in the excitation spectrum at 2.6 K.

Fig. 7 shows the evolution of the transitions of $^4I_{15/2}$ (1), (2) and (3) $\rightarrow$ $^4F_{7/2}(a)$ in nanocrystals in a span of temperatures from 2.2 to 66 K, when pumped by a 10 Hz 5-ns laser pulse. Fig. 7 shows a discontinuity at 7.6 K, where the intensity of the hot bands (492.3 and 492.9 nm) reaches a minimum and the intensity of the normal line reaches a maximum. The intensity of the hot band sharply increases and saturates as the sample temperatures decrease from 7.6 to 2.2 K. These anomalous phenomena obviously rule out the possibility that the sample is at an elevated temperature. Note that the above unusual thermalization was not observed in the bulk counterpart ($Er^{3+}$:$Y_2O_2S$ crystal of 400 nm diameter).

The unusual thermalization phenomena take place not only in the $^4I_{15/2} \rightarrow {}^4F_{7/2}$ excitation spectrum but also in the emission spectrum from $^4S_{3/2}$ at low temperature. Fig. 8 shows the $^4S_{3/2} \rightarrow {}^4I_{15/2}$ transition in the nanocrystalline and bulk $Er^{3+}$:$Y_2O_2S$ samples at 3 K. The pump wavelength is 491.8 nm. Only the emission lines from 546.5 to 550.0 nm were measured for comparison, which correspond to the transitions $^4S_{3/2}(a,b) \rightarrow {}^4I_{15/2}(1, 2, 3)$ indicated by arrows in fig. 8. Similarly to situation for the ground state $^4I_{15/2}$, a vast majority of the excited $Er^{3+}$ ions should be in the lower Stark level of $^4S_{3/2}$ at 3 K, since the Boltzmann factor of the upper Stark level (15 cm$^{-1}$ above) is calculated to be only 0.08%. Therefore the normal emission lines of the nanocrystals should be similar to those of the bulk samples with just three peaks arising from the $^4S_{3/2}(a) \rightarrow {}^4I_{15/2}(1, 2, 3)$. In fact, as shown in fig. 7, hot bands corresponding to the emission from the upper level $^4S_{3/2}(b)$ are also observed in the emission spectra of nanocrystals at 3 K.

The luminescence decay from the upper level of $^4S_{3/2}(b)$ was measured to be as long as 3.29 μs at 4 K, nearly identical to that of the lower level, $^4S_{3/2}(a)$. However the decay from $^4S_{3/2}(b)$ cannot be observed in bulk samples due to the rapid direct phonon relaxation process. The unusual long lifetime of $^4S_{3/2}(b)$ in nanocrystals indicates that the ions excited by the pump laser can be efficiently maintained in the upper level $^4S_{3/2}(b)$ even at low temperature,
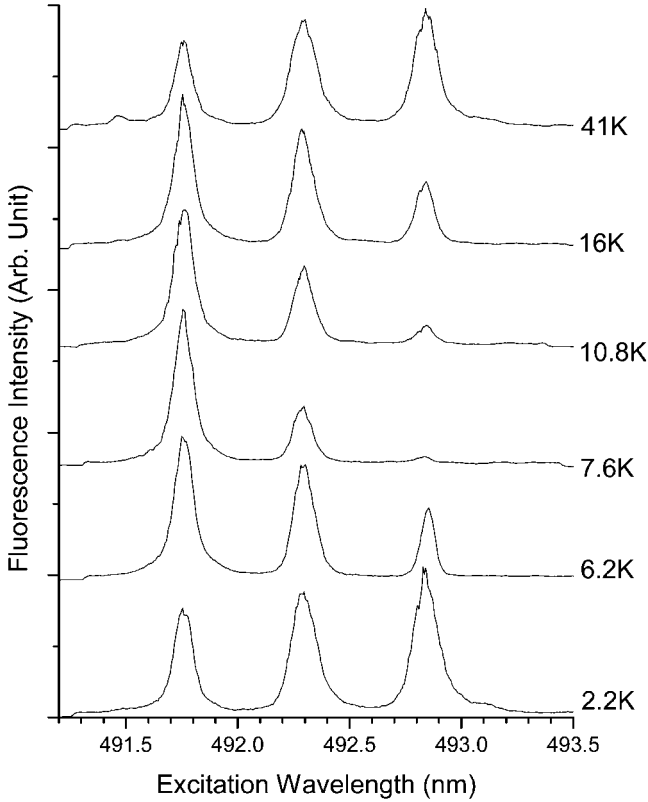
Fig. 7. Excitation spectra of the $^4F_{7/2}(a) \leftarrow {}^4I_{15/2}(1,2,3)$ transitions in $Er^{3+}:Y_2O_2S$ nanocrystals at various temperatures from 2.2 to 66 K, with a pump intensity of 60 kW/cm$^2$.

in line with the appearance of hot bands in the emission spectrum. These results also confirmed the previous conclusion that the decay rates observed in the nanoparticles are drastically reduced compared to those observed in bulk materials because of the lack of low-energy acoustic phonon modes (Yang et al., 1999a, 1999b).

Additional evidence of anomalous thermalization phenomena was found in the excitation spectrum $^2H_{11/2} \leftarrow {}^4I_{15/2}$, $^4S_{3/2} \rightarrow {}^4I_{13/2}$ emission spectrum and upconversion excitation spectrum (monitoring 414 nm or 565 nm), for which similar hot bands were also observed at low temperature.

To gain better understanding of the mechanism of anomalous thermalization in $Er^{3+}:Y_2O_2S$ nanocrystals, the temperature and power dependences of the luminescence intensity in excitation spectra were quantitatively studied. Integrated intensities of excitation spectra at 491.8 and 492.9 nm versus temperature (from 2.2 to 66 K) are shown in fig. 9, where each experimental point represents the integrated intensity of each main peak. The intensity of saturated hot bands in nanocrystals decreases rapidly to zero as temperature increases from 6 to 8 K, and
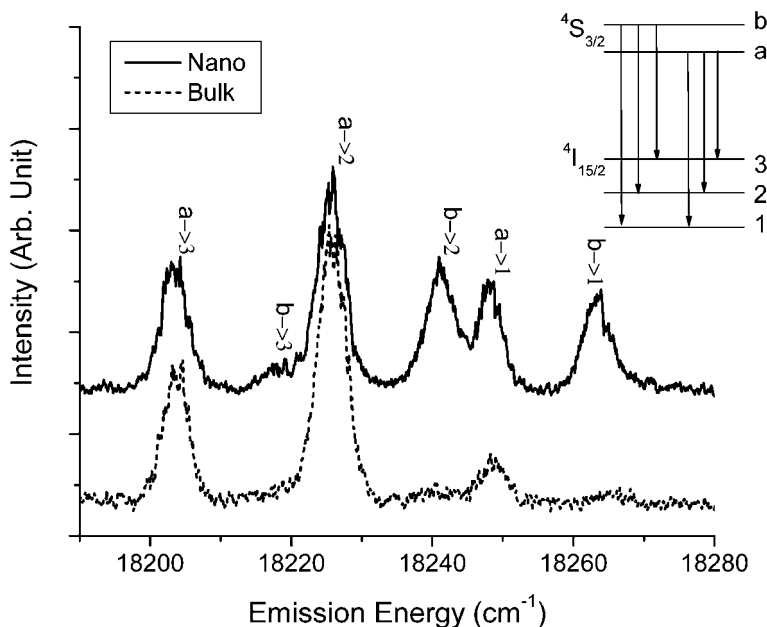
Fig. 8. Comparison of the emission spectra of the transitions $^4S_{3/2} \rightarrow {}^4I_{15/2}$ in nanocrystalline and bulk $Er^{3+}$: $Y_2O_2S$ at 3 K (redraw after (Liu et al., 2003c)).

then increases with temperature reflecting Boltzmann thermalization behavior. The nanocrystals and the bulk crystals exhibit the same thermodynamics above 12 K. The anomaly was still observable at very low pump intensity (5 kW/cm$^2$), indicating that the $Er^{3+}$ population in the ground state can be remarkably depleted by the laser pulse at a peak intensity less than 5 kW/cm$^2$.

The power dependences of the integrated intensity of the three excitation peaks $^4F_{7/2}(a) \leftarrow$ $^4I_{15/2}(1, 2, 3)$ (491.8, 492.3, and 492.9 nm) in $Er^{3+}$:$Y_2O_2S$ nanocrystals at 3 and 20 K were measured (Liu et al., 2003c). As normally expected, the integrated intensity of each excitation peak is proportional to the pump intensity, which is the case at 20 K. But the situation at 3 K is quite different. The hot bands at 492.3 and 492.9 nm exhibit a nonlinear dependence on the pump intensity. At pump intensity lower than 11 kW/cm$^2$, the pump power exponent can be approximately fitted to 1.4 for excitation at 492.9 nm and 1.2 for excitation at 492.3 nm, respectively. The luminescence intensity upon laser excitation at 491.8 nm showed tendency to saturate with increasing pump power, and the exponent was fitted to 0.88.

One question concerning the effect of surface defects still need to be addressed, that is, how the initially empty upper crystal field levels of $^4I_{15/2}$ can be populated at thermal energy far below the energy gaps of the electronic states (up to 200 cm$^{-1}$). In nanocrystals, the influence of lattice defects and contamination of hydrous species in the considerably large area of the surface layer is not negligible. It induces inhomogeneous broadening like in glasses. In the
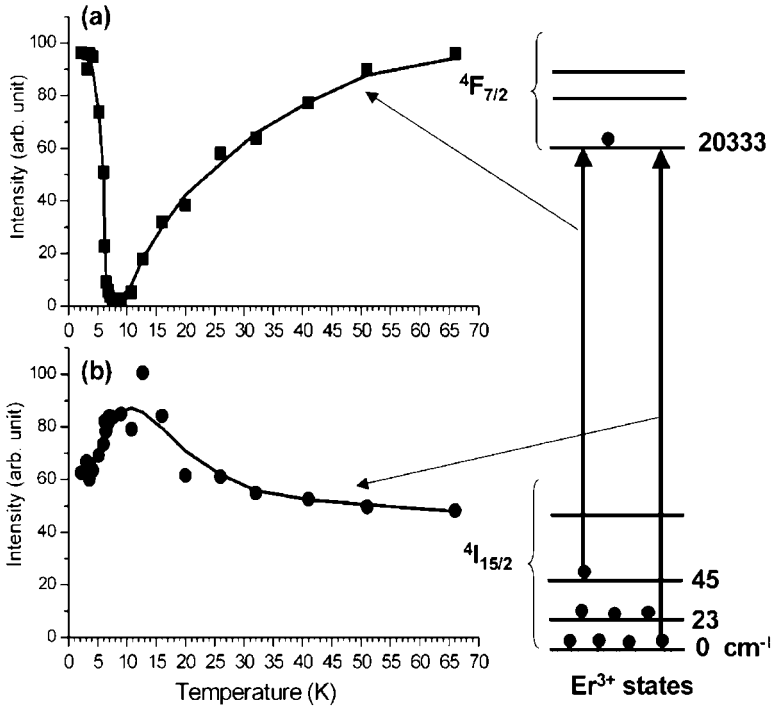
Fig. 9. Temperature dependence of the excitation intensity of $Er^{3+}$ in nanocrystals of $Y_2O_2S$: (a) the hot band originates from the crystal field sublevel 45 cm$^{-1}$ above the ground level, and (b) the normal excitation from the ground level. The dots are the experimental points and the lines are guides to the eyes (redraw after (Liu et al., 2002)).

absence of selective excitation and luminescence line narrowing, the 4f spectra of nanocrystals include contributions from ions in the surface layer as well as in the particle center. The latter should have unperturbed crystalline lattice environment. In fig. 6, the spectrum indicates that the hot bands originating from the upper crystal field levels overlap "accidentally" with the excitation bands of some defect sites from the lowest level in the ground state. Hence, when the laser was tuned to induce a resonant transition apparently from an upper level of the ground state which was initially empty at liquid helium temperature, it actually pumped the $Er^{3+}$ ions at defect sites from the ground level. Through energy transfer and cascade emission of phonons, which occur efficiently in less than 5 ns after the laser pulse, the relaxation of an excited $Er^{3+}$ ion at a defect site may result in populating more than one $Er^{3+}$ ions in the upper levels of the ground state. This describes how an empty level can be populated at low temperature. Then, the $Er^{3+}$ ions in these upper levels can be excited by the same laser pulses, and depending on the rate of nonradiative phonon relaxation of ions in the upper levels, observation of hot bands is possible. This effect is similar to a photon avalanche except that a threshold is not observed.

A possible thermalization mechanism was proposed and a simple model based on the rate-equation approach was established to interpret the above phenomena (Liu et al., 2003c). The equilibrium population in the upper levels of the $^4I_{15/2}$ ground state results from the competition mainly between the laser-induced thermalization (LIT) through nonradiative relaxation in the excited states (populating) and two-phonon Raman process (depopulating). Calculated results are in agreement with the observations. In brief, the anomalous thermalization effect in nanocrystals, which are not observed in the bulk counterparts, can be interpreted within the existing theory by taking into account the facts that the low-frequency phonons are scarce and electronic levels of hot bands can be efficiently populated via laser-induced multiphonon relaxation from the excited states.

The anomalous thermalization effect due to absence of low-frequency phonon modes in nanocrystals discussed above should also occur in other systems. Observation of this effect depends on the energy level structure of the luminescent centers as well as on the sample temperature and crystal size. According to the temperature-dependent multiphonon relaxation rate and the relationship between the cutoff frequency and crystal size, anomalous hot bands from the excited states with higher energies will occur in crystals with smaller size. We believe that the anomalous thermalization observed in $Eu_2O_3$ (Tissue, 1998) nanocrystals is similar to the one as we observed in $Er^{3+}$:$Y_2O_2S$. In the $Eu_2O_3$ nanocrystals, intensive hot bands observed in the excitation spectrum at 12 K are due to excitation of $Eu^{3+}$ from three crystal field levels of the $^7F_1$ excited state (the ground state of $Eu^{3+}$ is a singlet $^7F_0$). Because these excited states are at 300 cm$^{-1}$ and higher above the ground state, diminishing multi-phonon relaxation requires that the crystals have much smaller crystal size so that phonon modes up to 150 cm$^{-1}$ are eliminated or reduced. In Tissue's observation, the hot bands from the $^7F_1$ state are very strong in the 4–6 nm nanocrystals, but become almost not observable in the 12-nm nanocrystals. These results were consistent with our interpretation for the $Er^{3+}$ system. Our hypothesis also predicts that the $^7F_1$ hot bands in the 4–6-nm $Eu_2O_3$ nanocrystals would diminish as temperature increases up to 80 K when one-phonon direct relaxation and two-phonon Raman processes act more predominantly.

Recently, we also observed an anomalous thermalization phenomenon in Er:$Gd_2O_3$ (1 at%) nanocrystals with diameters of 40–50 nm. In the excitation spectra at 2.9 K, hot bands originating from the upper stark level of $^4I_{15/2}$ (38 cm$^{-1}$) were observed. These hot bands disappear when temperature goes up to 5 K. Our preliminary results show that the anomalous thermalization phenomena in this system are more complicated, because they depend on the laser power and temperature. The effect of laser heating or temperature fluctuation in nanocrystals must be ruled out before a definite conclusion can be reached.

## 4.4. *Upconversion nanophosphors*

Upconversion lanthanide-containing nanophosphors, which emit higher-energy photons when excited by lower-energy photons have stirred increasing research interest in recent years. The predominant mechanisms of upconversion in nanophosphors are excited-state absorption (ESA), energy-transfer upconversion (ETU) and photon avalanche (PA) (Prasad, 2004; Auzel, 2005). In the ESA process, two photons are sequentially absorbed by the same ion,

whereas for ETU excitation energy is transferred from one ion to another ion already in its excited state. PA is characterized by a pumping threshold and is completely different from the previous two processes in that the pump beam is nonresonant with the ground state absorption but is resonant with a transition from the intermediate excited state. So far a vast of majority of the studies on upconversion mechanisms in nanophosphors is based on ESA or ETU. The advantages offered by these types of upconversion processes are that they can be induced even by a low-power CW diode laser, without the need of an expensive high-power pulsed laser source such as a mode-locked Ti:sapphire laser used for two-photon upconversion in organic phosphor (Prasad, 2004). Upconversion nanophosphors with a size less than 35 nm can be dispersed in glass or plastic as transparent media for upconverting displays, or they can be coated on a GaAs diode to fabricate highly efficient LED with different colors. They can also be surface-functionalized to be dispersible in an aqueous medium for two-photon confocal-microscope bio-imaging or as sensitive luminescent bio-labels. For example, by using 400 nm $Y_2O_2S$:Yb, Er phosphors as labels, 1 ng/μL DNA was detected, which is four times more sensitive than the test using the traditional cyanine dyes Cy5 label (Van de Rijke et al., 2001). It is expected that the detection sensitivity can be greatly improved if monodispersed upconversion nanophosphors with high luminescent efficiency are used.

A major challenge in this area is to synthesize small homogeneous nanophosphors in the desired size range of less than 50 nm with high upconversion efficiency. Most studies focus on the systems containing Er (Yb), or Tm in hosts with low phonon cutoff frequency such as fluorides in an effort to improve the efficiency by reducing the nonradiative relaxation rate from the metastable excited state. Recently, Yan and Li demonstrated the trichromatic (red, green and blue) upconversion emission in the same Yb/Er co-doped $YF_3$ nanocrystals (20 nm in width and 40–60 nm in length) when excited by a low-power infrared laser diode (980 nm) (Yan and Li, 2005). The nanophosphors were synthesized via a facile sonochemistry-assisted hydrothermal route. The energy levels and possible upconversion scheme in Er and Yb co-doped systems are shown in fig. 10.

Highly efficient multicolor upconversion emission was observed in transparent colloids of lanthanide-doped $NaYF_4$ nanocrystals (Heer et al., 2004). Very strong red and green upconversion bands due to two-photon processes accompanying by a weak blue band due to three-photon process were simultaneously observed in the upconversion emission spectra of colloidal solutions of $NaYF_4$:20% $Yb^{3+}$,2% $Er^{3+}$ nanocrystals (10–17 nm) when pumped by a NIR laser at 974 nm. In $NaYF_4$:20% $Yb^{3+}$,2% $Tm^{3+}$ nanocrystals, a UV band centered at 357 nm resulting from an unusual four-photon upconversion process was observed in addition to the strong red and blue bands. Upconversion nanophosphors of $NaYF_4$:Er,Yb have been utilized as labeling materials in biological detection (Yi et al., 2004). The nanoparticles were prepared by co-precipitation of $Y^{3+}$, $Yb^{3+}$, $Er^{3+}$ with NaF in presence of EDTA, with a size tunable from 37 to 166 nm by varying the amount of EDTA. The biolabeling experiment employed mouse IgG/goat anti-mouse antibody as the model system. The antibody was conjugated to the nanoparticles and IgG was immobilized on a chemically modified glass slide. Before experiment, nanoparticles were first coated with a shell of silica by hydrolysis of tetraethyl orthosilicate to become water soluble. The silica shell was then silanized to introduce functional groups on the particle for antibody conjugation. Binding reaction between
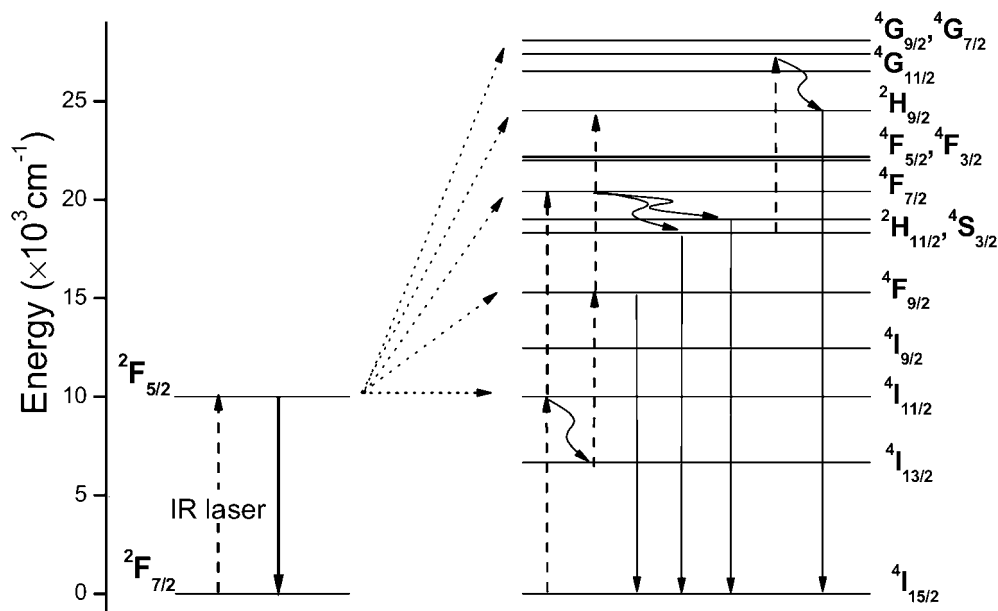
Fig. 10. Energy level and upconversion scheme for the $Er^{3+}$ and $Yb^{3+}$ codoped system. Full, dashed and curved arrows indicate radiative transition, energy transfer and nonradiative relaxation processes, respectively (redraw after (Yan and Li, 2005)).

mouse IgG and antibody would result in the accumulation of surface-confined nanoparticles that could then be detected by upconversion fluorescence. Their preliminary results proved that the upconversion nanophosphors can be used as promising fluorescent labels for the sensitive detection of biomolecules. Similarly, a fluorescence resonant energy transfer (FRET) biosensor has been developed based on hexagonal-phase $Na(Y_{1.5}Na_{0.5})F_6$:$Yb^{3+}$,$Er^{3+}$ upconversion nanophosphors (Wang, L.Y. et al., 2005). The FRET system consists of upconversion luminescent nanoparticles as energy donors and gold nanoparticles as energy acceptors. After surface modification of nanoparticles, the authors have successfully applied this sensor to detect trace amounts of avidin, indicating that the sensor is sensitive and simple for use in biological assays.

The dependence of upconversion luminescence on pumping power exhibits a complicated behavior that reflects the dynamics in the $Er^{3+}$ excited states. The efficiency of upconversion fluorescence for $Er^{3+}$ and $Yb^{3+}$ co-doped into $NaYF_4$ powder crystals has been investigated by Wang et al. (2007) in an attempt at understanding the pump power dependence of the green and red fluorescence bands. For the regular down-conversion cascade relaxation after UV excitation, the green and red luminescence bands have approximately the same intensity. However, in upconversion, the red band is much weaker than the green band because of restricted relaxation channels for populating the red emitting state of $^4F_{9/2}$. The ratio of green and red fluorescence intensities is different between UV excitation and IR excitation. The in-
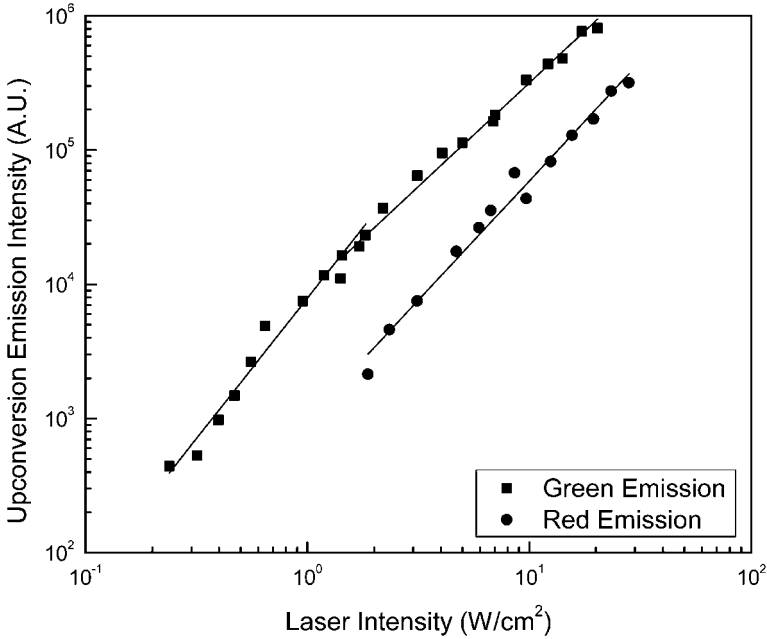
Fig. 11. Log–log plots for the intensities of the green and red upconversion emission of NaYF$_4$:Yb$_{0.2}$/Er$_{0.015}$ as a function of pumping laser intensity (redrawn after (Wang et al., 2007)).

tensity of both green and red upconversion fluorescence bands is affected at high pumping intensities by a low-lying state acting like a bottleneck. It is shown in fig. 11 that the green band and red band have different pumping power dependences. The green emission band and red emission band have different slopes over the same range of high pumping power, 1.55 for the green band and 1.78 for the red band. The effect on upconversion is less significant for the red than for the green. This phenomenon is attributed to cross relaxation and a secondary upconversion processes that only populates the $^4F_{9/2}$ levels. Known as the avalanche process, this effect occurs with pump energies increasing above a threshold (Auzel, 2005). It is expected that for nanophosphors the deviation from quadratic dependence on pumping power is more significant because of changes in phonon modes and surface states.

The upconversion mechanisms in nanophosphors turn out to be more complicated than in the bulk crystals. The effect of Yb$^{3+}$ concentration on the upconversion mechanisms in co-doped Y$_2$O$_3$:Er$^{3+}$,Yb$^{3+}$ nanocrystals has been investigated in details (Vetrone et al., 2004). Vetrone et al. observed green and red upconverted emission following the excitation at 978 nm into the $^2F_{5/2}$ state of Yb$^{3+}$ and subsequent energy transfer from Yb$^{3+}$ to Er$^{3+}$. They also observed significant enhancement of red upconverted emission, the magnitude of which was related to the concentration of Yb$^{3+}$ ions. At high Yb$^{3+}$ levels, green emission was almost entirely suppressed. The authors proposed that a cross-relaxation mechanism between $^4F_{7/2}$ → $^4F_{9/2}$ and $^4I_{11/2}$ → $^4F_{9/2}$ might be in part responsible for red enhancement. However,
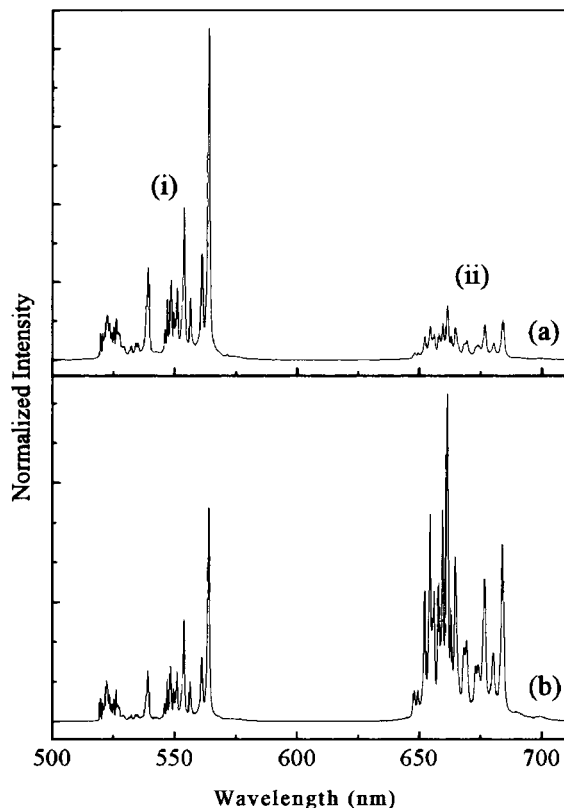
Fig. 12. Comparison of the upconversion spectra of $Y_2O_3$:$Er^{3+}$ (1 at%), $Yb^{3+}$ (1 at%) at room temperature (a) bulk crystals and (b) nanocrystals, where the emission bands correspond to (i) $^2H_{11/2}$, $^4S_{3/2} \rightarrow {}^4I_{15/2}$; and (ii) $^4F_{9/2} \rightarrow {}^4I_{15/2}$. The excitation wavelength is 978 nm (reprinted with permission from Vetrone et al. (2004)). © 2004 American Institute of Physics

this mechanism cannot account for the dramatic difference in the relative green-to-red ratios between identically doped bulk and nanocrystalline $Y_2O_3$:$Er^{3+}$,$Yb^{3+}$ samples, that is, red enhancement is much more pronounced in nanocrystals, as shown in fig. 12. Based on experimental evidence that nanocrystalline lattices can adsorb impurities such as $CO_3^{2-}$ and $OH^-$ on their surface which have vibrational energies of 1500 and 3350 $cm^{-1}$, respectively, they assumed another mechanism as follows (energy levels, see fig. 10): the ground state absorption of 978 nm photons from $Yb^{3+}$ would bring the ion to the $^2F_{5/2}$ state, which in turn would donate its energy to an $Er^{3+}$ ion in close proximity, thereby exciting it to the $^4I_{11/2}$ level. Rapid nonradiative decay from this state would populate the $^4I_{13/2}$ level since the energy gap between $^4I_{11/2}$ and $^4I_{13/2}$ (3600 $cm^{-1}$) could be more easily bridged by the high-energy phonons from the impurities in nanocrystals than in the bulk samples. Subsequent phonon-assisted energy transfer from another $Yb^{3+}$ ion in the excited state would directly populate the $^4F_{9/2}$ level and

result in red enhancement. Following another phonon-assisted ET from an $Yb^{3+}$ ion, the $Er^{3+}$ ion could be further excited into the $^2H_{9/2}$ state. Clearly, increasing the concentration of $Yb^{3+}$ ions resulted in a corresponding increase of red enhancement. At high $Yb^{3+}$ concentration the $^4F_{9/2} \leftarrow {}^4I_{13/2}$ upconversion mechanism could be very efficient and bypasses the $^4S_{3/2}$ state. For example, the green-emission band in $Y_2O_3$:$Er^{3+}$(1%),$Yb^{3+}$(10%) nanocrystals is very weak compared to the red emission. In fact, the $^4S_{3/2}$ level is most probably populated via nonradiative decays from upper states such as $^2H_{9/2}$. This mechanism is supported by the power dependence of the upconversion emission from $^4S_{3/2}$ in $Y_2O_3$:$Er^{3+}$(1%),$Yb^{3+}$(10%) nanocrystals which indicates that the $^4S_{3/2}$ state is populated via a three-photon process instead of a two-photon process as observed for the low $Yb^{3+}$ concentration.

Similarly, a significant enhancement of red upconverted emission was observed with the increase of $Yb^{3+}$ co-doping concentration in $Y_2O_3$:$Er^{3+}$(1 at%),$Yb^{3+}$ nanocrystals (Matsuura, 2002). In Matsuura's upconversion spectra, the green band disappears when the $Yb^{3+}$ concentration reaches 20 at%, while the red band is still present. However, a different story was reported for the upconversion spectra of 50-nm $La_2(MoO_4)_3$:Yb,Er nanocrystals (Yi et al., 2002), where a strikingly enhanced green upconverted emission was observed in nanocrystals in comparison with the bulk counterpart. This change of intensity has been ascribed to surface effects in nanocrystals. The green emission is mainly attributed to the surface $Er^{3+}$ ions while the red emission mainly arises from the internal $Er^{3+}$ ions. The weaker interaction between the surface $Er^{3+}$ ions and their surroundings in nanocrystals results in a longer lifetime of $^4I_{11/2}$ thus in more efficient upconversion.

Other interesting observations of upconversion in nanophosphors have been reported. For instance, Patra et al. (2003a) observed that the upconversion luminescence intensity depends on the crystal structure and particle size of $ZrO_2$ nanocrystals. The nanoparticles annealed at different temperatures showed very different upconversion luminance values, where a significant enhancement of luminance in monoclinic phase was observed in comparison with the tetragonal phase. They ascribed this enhancement to the lower symmetry of the $Er^{3+}$ site in the monoclinic phase in which the optical transition probabilities increase. Comparison of the upconversion spectra of Er:$Lu_2O_3$ and Er:$Y_2O_3$ nanocrystals showed that the upconversion intensity of Er:$Lu_2O_3$ nanocrystals was approximately 100 times greater than that of Er:$Y_2O_3$ although $Er^{3+}$ ions in both hosts have very similar energy level structure (Vetrone et al., 2002). In addition, very different from Er:$Y_2O_3$, noticeable blue upconversion occurs in Er:$Lu_2O_3$ nanocrystals. Vetrone et al. proposed an enhanced intensity-borrowing mechanism that induces mixing of the 4f and 5d orbitals of the $Er^{3+}$ ions via lattice valence-band levels in lutetia for the above findings. For nanophosphors of Na($Y_{1.5}Na_{0.5}$)$F_6$:$Yb^{3+}$,$Er^{3+}$ (50 nm), Wang, L.Y. et al. (2005) observed that the green upconversion luminescence was greatly enhanced and dominant when the cubic nanoparticles were transformed into hexagonal nanoparticles. And the luminescence of the hexagonal phase nanoparticles was stronger when compared to the cubic nanoparticles. This makes the hexagonal nanoparticles an ideal choice for single-emission biolabels. Yang et al. (2006) reported a strange power-dependent and time-dependent upconversion luminescence in $Y_2O_3$:$Ho^{3+}$,$Yb^{3+}$ nanocrystals under the excitation of 978-nm laser. They observed that the upconversion intensity increased as the excitation power increased under lower excitation density but decreased in the case of higher

excitation density, whereas the luminescence intensity decreased with time under high excitation density. The origin of this anomaly is not clarified yet.

## 4.5. *Lanthanide-doped nanocrystals embedded in amorphous matrices*

Although optical spectra of lanthanide-doped insulating nanocrystals embedded in amorphous matrices are very similar to the "free-standing" nanocrystal counterparts, their excited state dynamics behaves very differently from that in simple nanocrystals. Some distinct dynamic properties have recently been found for nanocrystals embedded in polymers or glasses. Simple models for the interaction between lanthanide ions and the matrices were also proposed. However, further studies are needed in order to quantitatively understand the observed size-dependence and dynamic mechanisms.

It is well known that the dynamic properties of lanthanide ions doped into glasses or disordered materials are very different from those in single crystals. In glasses, the dynamic properties are governed by the interactions between the two-level systems (TLS's) and the localized vibrations of the glass matrix (Meltzer et al., 2001). For "free-standing" nanoparticles, the electron–phonon is strongly modified compared to that of the bulk. For example, as previously discussed, the electronic relaxation rate among closely spaced energy levels in small nanocrystals resulting from the single-phonon direct process can experience a significant reduction due to the gap in the acoustic-phonon spectrum and the reduction of PDOS. Optical dephasing resulting from two-phonon Raman processes can be enhanced and its temperature dependence is altered from $T^7$ to $T^3$ due to the modification of PDOS in nanocrystals (Meltzer and Hong, 2000). The optical spectra of lanthanide-doped nanocrystals embedded in amorphous matrices are sharp and nearly identical to those of lanthanide ions in single crystals of the same composition and structure due to the short-range local environment of the lanthanide site, indicating that the electronic structure remains nearly unperturbed. Few studies have been reported on the dynamic properties of lanthanide-doped embedded nanocrystals. It is of great interest to determine whether lanthanide ions separated from the glassy TLS's by the crystalline nanoparticle in which they are contained also exhibit interactions with TLS's when the nanocrystals are embedded in an amorphous matrix such as a glass. In fact, it has been demonstrated that lanthanide doped nanoparticles may serve as efficient probes of many dynamical processes in polymer or glass that cannot be observed when the lanthanide ions are embedded directly in the disordered glass matrix (Meltzer et al., 2002).

Meltzer et al. (2001) showed direct evidence for long-range interactions between lanthanide impurity ions in embedded nanocrystals with the TLS's of the matrix based on hole burning data. The samples were prepared as follows: monoclinic 23 nm $Y_2O_3$:0.1% $Eu^{3+}$ nanocrystals, produced by condensation after laser evaporation, were dispersed in a siloxane polymer. Fig. 13 shows the temperature dependence of the width of spectral holes ($\gamma_{HB}$), which were burned in the $^5D_0 \leftarrow {}^7F_0$ transition of $Eu^{3+}$ ions located on the $c$ sites (582.8 nm) in nanocrystals embedded in polymer, in comparison with the case of the free, as-prepared nanocrystals having the same size. The embedded nanocrystals exhibit a drastic increase in hole width and a very different power-law behavior for the temperature dependence of the hole widths relative to similar isolated nanoparticles. The $T^3$ temperature dependence of the hole width
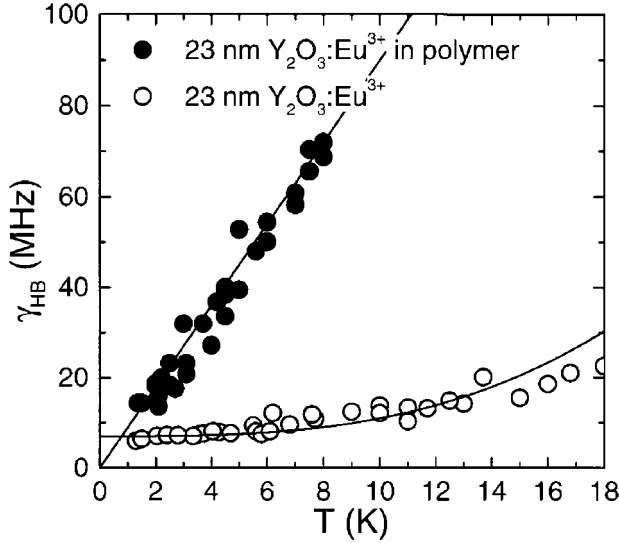
Fig. 13. Temperature dependence of the hole width for $Eu^{3+}$ in $Y_2O_3$ nanocrystals. Solid lines: $\gamma_{HB} \sim T$ (embedded in polymer) and $\gamma_{HB} \sim T^3$ (isolated, as prepared) (reprinted with permission from Meltzer et al. (2001)).
© 2001 American Physical Society

observed for the latter becomes proportional approximately to $T$ for embedded nanocrystals. This nearly linear temperature-dependent behavior of $\gamma_{HB}$ in nanocrystals surrounded by the polymer matrix cannot be explained either by the direct process, two-phonon Raman process or other electron–phonon interactions known for the bulk or observed in isolated $Y_2O_3$ nanocrystals, but is very similar to that observed for $Eu^{3+}$-doped glasses. Therefore Meltzer et al. suggested that the dominant mechanism for the homogeneous broadening of the $^5D_0 \leftarrow {}^7F_0$ transition of $Eu^{3+}$ in $Y_2O_3$ nanocrystals embedded in the polymer is identical to the TLS-lanthanide ion interaction, which is responsible for homogeneous broadening found for ions in glasses. The TLS-lanthanide ion interaction is usually of elastic dipole–dipole nature showing long-range character, with an effective length scale larger than the size of nanocrystals. A similar result was found for Eu- (or Pr-) doped $LaF_3$ nanocrystals embedded in oxyfluoride glass ceramics showing a nearly linear temperature-dependence of hole width (Meltzer et al., 2001). In addition an enhanced optical dephasing was observed when decreasing the size of the embedded nanocrystals. This size dependence can be well explained by a simple model in which the nanocrystal volume containing no TLS is excluded.

Another effects of the interaction with the surrounding disordered matrix is the increase in the one-phonon direct relaxation of $Ho^{3+}$ in oxyfluoride glass ceramics due to coupling to the higher density of low-frequency phonon modes in the glass compared with the crystal (Meltzer et al., 2002). The direct relaxation time between the two lowest $^5F_5$ sublevels (a gap of 14.5 $cm^{-1}$) of $Ho^{3+}$ in nanocrystals of different sizes embedded in oxyfluoride glass ceramics was measured (see fig. 14), under excitation of the second low-
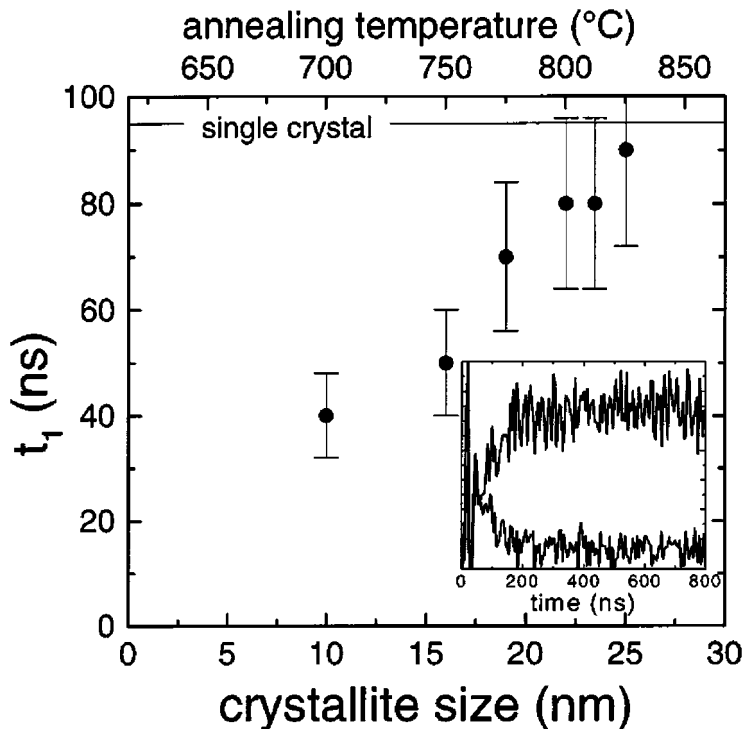
Fig. 14. Times of relaxation between the two lowest $^5F_5$ state sublevels (a gap of 14.5 cm$^{-1}$) of Ho$^{3+}$ in nanocrystals of different sizes embedded in oxyfluoride glass ceramics. Solid line: the relaxation time value for single crystal. Inset: typical time-resolved decay and buildup curves from the second lowest and lowest sublevels of $^5F_5$, respectively (reprinted with permission from Meltzer et al. (2002)).
© 2002 American Physical Society

est sublevel at 640.5 nm. Transitions from both sublevels to one of the ground $^5I_8$ state components were observed in luminescence at 642.6 and 643.2 nm which served as a measure of the sublevel populations. The relaxation times were determined from both the higher sublevel decay and lower sublevel buildup curves (see inset in fig. 14). The relaxation time between those two closely spaced sublevels decreases with a decrease of the nanocrystal size, whereas for the largest nanocrystals (25 nm) it approaches the single crystal value.

Obviously, the modification of the phonon spectrum in nanocrystals due to size confinement effects, which results in the slowing down of the one-phonon direct relaxation in "freestanding" nanocrystals does not play a significant role for the embedded nanocrystals. The observed dependence of the relaxation time on nanocrystal size has been explained assuming an interaction of the electronic states of the lanthanide ions with the low-lying vibrational modes of nonacoustical nature present in the glass matrix. At the frequency of 14.5 cm$^{-1}$ the density of vibrational states of the glass is significantly greater than the density of states

in crystals according to the Debye model. The vibrational modes of the glass may, together with the phonon modes of the nanocrystals, form new mixed vibrational states, which lead to enhanced single-phonon relaxation rates.

According to Meltzer's assumption, the faster relaxation in smaller nanocrystals embedded in glass is possibly due to stronger interaction of the electronic states of lanthanide ions with the larger density of low-frequency vibrational states in the glass, which may circumvent the slowing-down tendency of the relaxation induced by phonon confinement.

The upconversion luminescence of lanthanide-doped nanocrystals embedded in glass is also affected by the mixed vibrational modes of the nanocrystals and glass. For the upconversion spectra of Er:LaF$_3$ nanocrystals embedded in oxyfluoride glass ceramics and pumped by a 980-nm laser, a significantly enhanced red emission at 660 nm was observed compared to the green bands at 540 nm with a decrease in the nanocrystal size (Ma et al., 2006). This is due to the faster multiphonon relaxation rate between $^4S_{3/2}$ and $^4F_{9/2}$, possibly caused by stronger interactions of the Er$^{3+}$ electronic states with the vibrational excitations of the surrounding glass medium and with the mixed vibrational modes of nanocrystals and glass for the system with smaller nanocrystal size.

It is noteworthy that for ions located directly in glass, the measurement of the direct relaxation processes between the closely spaced levels is difficult because of the large inhomogeneous broadening of energy levels. However, utilizing the narrow distribution of energy-levels and the sharpness of the optical transitions of lanthanide ions in nanocrystals, it is possible to tailor the nanocrystal size so as to vary the distance between the probe ions and the modes of the glass to which the lanthanide ions coupled (Meltzer et al., 2002). Therefore embedded nanocrystals with controllable size may serve as a very good probe to investigate the localized vibrational excitations in amorphous matrices.

### 4.6. *Luminescence quantum efficiency*

Luminescence quantum efficiency is defined as the ratio of the number of emitted quanta to the number of absorbed quanta. In the absence of competing radiationless transitions its value is 1 (or 100%). There is a need to develop lanthanide-doped insulating nanophosphors with a luminescence efficiency comparable to their bulk counterparts (or the semiconductor quantum dots) for applications such as flat panel displays, optical amplifiers and bio-labels. However, the quantum efficiency of doped insulating nanocrystals is usually lower than that of the bulk material as a result of energy transfer to the quenching centers at the surface. To significantly increase the quantum yield of nanoparticles by suppressing energy-loss processes at the particle surface, a simple strategy consists in growing a shell of an undoped material with similar lattice constant around each doped nanoparticle. In fact, such surface modification (core–shell) has already been successfully applied to the preparation of high-quantum-yield semiconductor quantum dots.

Haase and co-workers have extensively studied the synthesis of high-quantum-yield nanophosphors such as Eu-, Tb- or Er-doped lanthanide phosphates (Riwotzki et al., 2000, 2001; Lehmann et al., 2004; Kompe et al., 2003; Lehmann et al., 2003). For example, the photoluminescence (PL) quantum yield of the CePO$_4$:Tb core nanocrystals (4–6 nm) diluted

in methanol is 43% for the terbium emission (53% if the Ce emission is taken into account). After the growth of the $LaPO_4$ shell around the core particles, the quantum yield of the core–shell nanoparticles (8–10 nm) can be greatly improved, reaching 70% for the terbium emission (80% for the total emission), which is close to the values for the bulk material (86% for the terbium emission and 93% for the total emission) (Kompe et al., 2003). The quantum efficiency of lanthanide-doped nanocrystals redispersed in colloidal solution depends on the solvent, probably due to the modified nonradiative path via the local vibrational modes of the organic molecules. For comparison, the PL quantum yield of $CePO_4$:Tb nanocrystals (5 nm) redispersed in 2-propanol is reported to be 11% for the terbium emission (16% for the total emission) (Riwotzki et al., 2000). For $LaPO_4$:Ce,Tb nanocrystals (5–6 nm), it was found that the quantum yields of the Ce emission or the Tb emission upon UV excitation of the Ce band were both reduced by 40% if the nanocrystals were dispersed in methanol containing some tetra-$n$-butylammonium hydroxide instead of the usual 1:50 mixture of $N,N$-dimethylformamide and methanol (Riwotzki et al., 2001). On the contrary, it is expected that the quantum efficiency of the core–shell nanoparticles is nearly solvent-independent, since the lanthanide ions in the core are shielded from contact with the organic functional groups in the solution.

So far the optical spectroscopy of Eu:$Y_2O_3$ nanocrystals has been mostly studied due to its versatile applications. However, the reported quantum efficiency for this system is quite inconsistent in the literature owing to the fact that nanocrystals synthesized by different methods may have various structure, particle morphology and surface properties. Schmechel et al. reported that the quantum efficiency of $^5D_0$ emission in $Eu^{3+}$:$Y_2O_3$ decreased from 92% in a commercial bulk (5 μm) sample to less than 10% in 5–10 nm nanocrystals prepared using chemical vapor reaction method (Schmechel et al., 2001). Similarly, Dhanaraj et al. (2001) observed a decrease of quantum efficiency to about 30% for nanocrystals prepared by sol–gel thermolysis in comparison with bulk samples. On the other hand, it has also been reported that the quantum efficiency increases with decreasing particle size. Wakefield et al. (2001) showed that the luminescence efficiency of $Y_2O_3$:$Eu^{3+}$ nanocrystal (70–100 nm) synthesized by a colloid-based route is 10–20% and 50% higher than that in the commercial bulk material, under UV optical excitation and electron beam excitation at 1 kV accelerating voltage, respectively, presumably as a result of the improved crystal quality in nanocrystals. Similarly, Goldburt et al. (1997) reported that the luminescence efficiency of $Y_2O_3$:$Tb^{3+}$ increases with decreasing particle size from 10 to 4 nm, and varies inversely as the square of the particle size. Sharma et al. (1999) reported that the emission intensity of the $^5D_0 \rightarrow {}^7F_2$ transition increases about fivefold as the particle size decreases from 6 μm to 10 nm. Both of them ascribed this variation to a mechanism of quantum size confinement, which now seems questionable. As pointed out by van Dijken et al. (2001) quantum size confinement is not expected to occur in 10 nm $Y_2O_3$ particles because the exciton Bohr radius is much smaller than 10 nm in this insulator. Furthermore, the quantum efficiency of commercial $Y_2O_3$:$Eu^{3+}$ particles having a typical particle size of 5 μm, is almost 100%. It is impossible to increase this efficiency fivefold by decreasing the size from 6 μm to 10 nm. The observed increase in efficiency as a function of particle size is thus related to the poor quality of the micron-size particles employed (van Dijken et al., 2001).

### 4.7. *Other novel optical properties*

Some novel optical properties of lanthanide-doped nanophosphors such as single-ion luminescence have been reported but require further confirmation or theoretical clarification. For example, Barnes et al. (2000) have recently imaged luminescence from single laser-excited $Eu^{3+}$ ions doped in $Y_2O_3$ nanocrystals (5–15 nm) and observed interesting luminescence dynamics such as on-off blinking and multiple discrete luminescence intensity levels (bright states) that closely resemble familiar properties of single molecules or quantum dots. These features of single-ion luminescence were observed for larger particles with multiple chromophores. They first assumed that these effects derived from pump laser-induced fluctuations between different quasi-stable $Eu^{3+}$ sites that effectively modulate the electric dipole transition moment. However recent observation of dipolar emission patterns from isolated $Eu:Y_2O_3$ (3–12 nm) nanocrystals seems to be in contradiction with their own previous assumption (Bartko et al., 2002): these patterns are characteristic of single-quantum emitters whose orientation appears fixed on the measurement time scale. Dipolar emission patterns provide strong evidence of single quantum luminescence, since such patterns are diminished by the presence of multiple chromophores with different orientations. Their studies also showed that, for particles displaying dipolar emission patterns, the luminescence is linearly polarized, also characteristic of single-quantum system behavior. However, the authors noticed that the orientation of the transition moment is invariant with bright levels, which indicates that local symmetry fluctuations are not responsible for the different bright states observed. In view of this observation, they assumed that the novel luminescence dynamics is associated with phonon interactions that enhance both thermal excitation and emission rates. The origin of the observed dipolar emission pattern is not clearly understood.

## 5. Spectroscopy of lanthanide ions in semiconductor nanocrystals

Lanthanides doped into nanocrystalline semiconductors have been the subject of numerous investigations in the past decades. If the size of a semiconductor particle is smaller than the Bohr radius of the excitons, the so-called quantum confinement occurs. As a result, the band gap of the semiconductor increases and discrete energy levels occur at the edges of the valence and conduction bands (Bol et al., 2002; Brus, 1986). These quantum size effects have stimulated extensive interest in both basic and applied research.

Generally, quantum size effects are not expected in lanthanide-doped nanoinsulators such as oxides since the Bohr radius of the exciton in insulating oxides, like $Y_2O_3$ and $Gd_2O_3$, is very small. By contrast, the exciton Bohr radius of semiconductors is larger (e.g., 2.5 nm for CdS) resulting in pronounced quantum confinement effects for nanoparticles of about 2.5 nm or smaller (Bol et al., 2002). Therefore, a possible influence of quantum size effects on the luminescence properties of lanthanide ions is expected in semiconductor nanocrystals.

One of the advantages of lanthanide-doped semiconductor nanocrystals is that lanthanide luminescence can be efficiently sensitized by exciton recombination in the nanocrystals. The photoluminescence efficiency of $Er^{3+}$ in Si nanocrystals in $SiO_2$ increases by more than five

orders of magnitude, which thus enables the fabrication of Er-doped nanocrystal waveguide amplifiers pumped by white light source (Kik and Polman, 2001).

Lanthanide impurities in semiconductor quantum dots have been considered as promising candidates for building a new class of light emitting devices (LEDs). For example, GaN quantum dots doped with Eu, Sm or Pr (red emission), Tm (blue), and Er, Ho, or Tb (green) may have potential applications in full color displays (Hori et al., 2004). It is expected that the strong confinement of carriers in quantum dots will enhance their recombination in the vicinity of lanthanide ions, thus improving luminescence efficiency in the visible range.

Recently, many researchers have paid attention to the optical properties of lanthanide-doped III–V and II–VI semiconductor nanocrystals prepared by ion implantation, molecular-beam-epitaxy (MBE) or wet chemical syntheses. Although some controversies still exist, many important results have been achieved, which may be beneficial to the understanding of the basic physical or chemical properties of lanthanide-doped semiconductor nanocrystals.

### 5.1. *A controversy of lifetime shortening*

With respect to the excited state dynamics of lanthanides in semiconductor nanoparticles, one of the most controversial questions is whether or not the lifetime of transition metal (TM) or lanthanide ions doped in semiconductor nanocrystals can be shortened by several orders of magnitude. In 1994, Bhargava et al. (1994a) reported a remarkable optical property of doped semiconductor nanoparticles. It was argued that the lifetime of the $Mn^{2+}$ emission in nanocrystalline ZnS was shortened from milliseconds to nanoseconds due to quantum size effects. In addition, the luminescence quantum efficiency was reported to increase with decreasing particle size. Bhargava proposed the quantum-confinement-induced ligand-TM hybridization (or sp–d orbital mixing) theory in order to explain the lifetime shortening in nanocrystals of $Mn^{2+}$:ZnS. However, Bhargava's experimental results have been challenged by several authors (Bol and Meijerink, 1998; Murase et al., 1999; Smith et al., 2001; Tanaka et al., 2000) and his ligand-TM hybridization theory lacks clear experimental evidence. It was later shown that lifetime shortening in nanocrystalline ZnS/$Mn^{2+}$ does not occur. The $Mn^{2+}$ emission of nanocrystalline ZnS/$Mn^{2+}$ has a "normal" millisecond lifetime (Bol and Meijerink, 1998). The fast decay component arises actually from the intrinsic and defect-related emission in sulfide compounds (Chen, W. et al., 2005). Furthermore, Tanaka et al. (2000) denied Bhargava's assumption by comparison of the energy levels of $Mn^{2+}$ in nanosized- and bulk-ZnS crystals, showing that the energy levels of $Mn^{2+}$ are almost independent of the ZnS host crystal size.

Similar to their controversial finding on nanocrystals of $Mn^{2+}$:ZnS, Bhargava (1996) has also reported that the $Tb^{3+}$ lifetime was greatly shortened from ∼3 ms in the bulk phosphors to 7 ns in 2–5 nm ZnS nanocrystals on the basis of a similar assumption, the so-called ligand–lanthanide hybridization. Unfortunately in his paper the intensity and line positions of the $^5D_4$ luminescence was not significantly altered, which makes the assumption unconvincing. In brief, the unusually shortened lifetime of $Mn^{2+}$ or $Tb^{3+}$ in ZnS nanocrystals reported by Bhargava et al. has proved to be an artifact, which quite possibly originates from the defects or the ZnS host related emission. As a result, the theoretical model based on quantum-confinement-induced hybridization proposed by Bhargava et al. is also questionable.

## 5.2. *Lanthanides location—are they inside or outside?*

The luminescence mechanism of lanthanides in doped nanocrystals depends on their location in the host lattice. If the lanthanide ions have similar chemical properties (say, the same oxidation state and similar ionic radius), it is easy to incorporate lanthanide ions in the host lattice in replacement of the host metallic ions. This is the case for most of the insulating nanocrystals such as oxide ($Y_2O_3$ and $Gd_2O_3$), phosphate ($LaPO_4$), or fluoride ($LaF_3$, $NaYF_4$). However, an important issue for semiconductor nanocrystals is whether or not lanthanide ions are really incorporated into the lattice sites since their chemical properties usually differ from those of the semiconductor host cations, e.g., II–VI groups cations. For example, for lanthanide doped in ZnS nanocrystals, the trivalent charge of a lanthanide ion on a divalent $Zn^{2+}$ site has to be compensated somewhere in the host lattice. Furthermore the ionic radius of the lanthanide ions is much larger than that of $Zn^{2+}$ (e.g., for coordination number 6, $r(Eu^{3+}) = 0.95$ Å, $r(Zn^{2+}) = 0.75$ Å), which will not favor the substitution of $Zn^{2+}$ either. Bol et al. (2002) proposed a test to confirm if a lanthanide ion is incorporated in a lattice position by observing if the host absorption band appears in the excitation spectrum of the lanthanide emission. They applied this test to $Eu^{3+}$:ZnS, $Eu^{3+}$:CdS, $Tb^{3+}$:ZnS, and $Er^{3+}$:ZnS nanocrystals synthesized under various techniques (such as precipitation in water, methanol, or toluene and inverse micelle techniques) which have been reported to yield ZnS or CdS nanocrystals doped with luminescent lanthanide ions. Upon excitation in the semiconductor host lattice, no or only weak emission was observed from the lanthanide ions. Therefore the authors concluded that the lanthanide ions are not incorporated in the nanocrystalline semiconductor particles but are probably adsorbed on the surface. On the other hand, Liu et al. (2001a, 2001b) observed that the excitation from ZnO hosts is dominant in the excitation spectrum of $Tb^{3+}$:ZnO nanocrystals when monitoring the characteristic emission of $Tb^{3+}$, which indicates ET between $Tb^{3+}$ and ZnO nanocrystals as well as the incorporation of $Tb^{3+}$ in the ZnO lattice. Similarly, Liu, S.M. et al. (2001) found that the excitation from ZnS hosts contributes partly to the excitation spectrum of ZnS:$Tb^{3+}$ sample. Recently Chen, W. et al. (2004b) argued that efficient ET occurs from the host to the dopants in ZnS:$Mn^{2+}$, $Eu^{3+}$ nanocrystals and that both $Mn^{2+}$ and $Eu^{3+}$ ions are incorporated into the ZnS lattice.

Note that the test proposed by Bol et al. (2002) is not always valid since it does not take into account the energy mismatch of ET from the host to lanthanide centers. Specifically, when the energy mismatch is large and the local or lattice phonon energy in nanocrystals is small ($350 \text{ cm}^{-1}$, maximum phonon energy of ZnS), the probability of phonon-assisted ET is small. Hence, this ET will not occur even if the lanthanide ion is incorporated in a lattice site. For example, no energy level of $Eu^{3+}$ is located in the energy range approximately from 28 800 to 30 900 $\text{cm}^{-1}$ (Carnall et al., 1989), which corresponds to an excitation wavelength range from 323 to 347 nm. Coincidently the host excitation of bulk ZnS is centered at 29 400 $\text{cm}^{-1}$ (band gap = 3.65 eV). Although quantum size effect will further blue shift the host excitation of the nanocrystals, the position of the host excitation band still falls above the energy gap of $Eu^{3+}$ unless the nanocrystal size is very small. Thus it is expected that energy transfer from the excited ZnS host to $Eu^{3+}$ is not favored due to energy mismatch. The transfer may however be accomplished with the assistance of phonons; however, phonon-assisted energy transfer is not very efficient when the energy mismatch is large and the phonon energy of

the nanocrystals is small. Such is the case for $Eu^{3+}$:ZnS nanocrystals. For comparison, no energy level of $Tb^{3+}$ locates in an energy interval from approximately 29600–30700 cm$^{-1}$ (Carnall et al., 1988), which corresponds to an excitation wavelength range from 326–340 nm. Obviously, for $Tb^{3+}$:ZnS nanocrystals, a resonant energy transfer with high efficiency from excited ZnS host to $Tb^{3+}$ is possible. This explains the observation by (Liu, S.M. et al., 2001). As for lanthanide doped ZnO nanocrystals, the band gap absorption is blue shifted from the bulk value at 27018 cm$^{-1}$ (3.35 eV). In comparison with ZnS host, energy transfer from excited ZnO host to $Eu^{3+}$ or $Tb^{3+}$ will be more favorable due to the available matching levels.

In brief, the test proposed by Bol et al. (2002) to determine whether the lanthanide ion is incorporated in a semiconductor lattice has to be used with care. A detailed analysis of the energy levels and phonon spectrum may present additional information. In our opinion, it is possible to incorporate the lanthanide ions into lattice sites of semiconductor nanocrystals (e.g., II–VI) if the synthesis method is well designed and the charge-imbalance is compensated.

## 5.3. *Energy transfer from hosts to lanthanide ions*

The effective $Er^{3+}$ excitation cross-section using Si nanocrystal sensitization scheme is a factor of $10^5$–$10^6$ larger than the cross-section for direct optical pumping of $Er^{3+}$ doped $SiO_2$ glass (Kik and Polman, 2001). It is essential to understand the excitation mechanism of lanthanide ions in silicon nanocrystals for designing optical amplifiers and lasers based on these nanocrystals. Franzo et al. (1999) showed that the excited lanthanide ions are not incorporated within the nanocrystals and the energy is transferred at a distance while they are embedded within $SiO_2$. The intense nanocrystal-related luminescence band at 850 nm decreases with increasing lanthanide concentration and the energy is preferentially transferred from the excitons in the nanocrystal to the lanthanide ions which, subsequently, emit radiatively. Interestingly, the nanocrystal luminescence decay time is not affected by the presence of Er. To explain this lifetime "paradox", Franzo et al. (1999) proposed a phenomenological model in which a confined exciton within the nanocrystals excited by the pumping laser transfers its energy either to an intrinsic luminescent centers (emission at 850 nm) or to a lanthanide ion; the two processes are in competition. However, Kik and Polman (2001) disagreed with this model and proposed another scheme for Er excitation (see fig. 15). Previously, Franzo et al. (1999) argued that the model shown in fig. 15a is not consistent with the nanocrystal lifetime behavior they observed since erbium adds a nonradiative decay path for exciton recombination, which should lower the nanocrystal-related luminescence lifetime. Kik and Polman (2001) noticed that the energy transfer to Er occurs well within the nanocrystal decay time at 300 K, thus inferred that a very fast ET from host to lanthanide with a rate up to $10^6$ s$^{-1}$ (the so-called strong-coupling) may occur. As shown in fig. 15b, due to this strong-coupling between the nanocrystal and lanthanide ion, all observed exciton luminescence originates from nanocrystals that do not couple to Er, while nanocrystals that do couple to Er show no luminescence. Thus, the observed lifetime "paradox" can be fully understood.
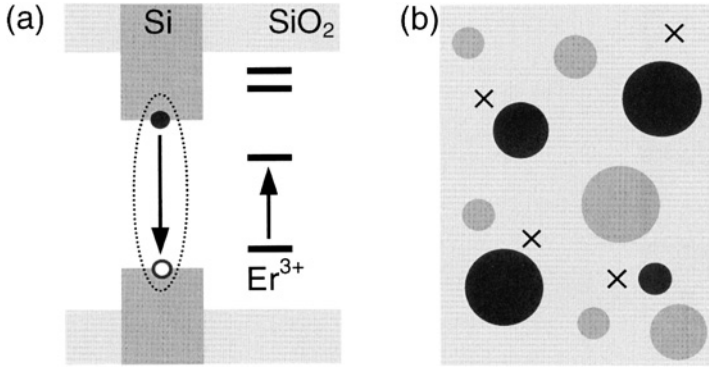
Fig. 15. (a) Schematic Er excitation model, showing the electronic band structure of Si nanocrystall-doped SiO$_2$ and the Er 4f energy levels. An optically generated exciton (dotted line) confined in the nanocrystal can recombine and excite Er$^{3+}$. (b) Schematic representation of SiO$_2$ containing Er (crosses) and nanocrystals (circles). The nanocrystals that couple to Er (filled circles) show no exciton luminescence (redraw after (Kik and Polman, 2001)).

## 5.4. *Lanthanide-doped II–VI semiconductor nanocrystals*

Although Bhargava's mistakes on the shortening of TM lifetime or lanthanide-doped ZnS have been pointed out by other researchers, many scientists still expect that lanthanide-doped II–VI semiconductor nanocrystals may form a new class of luminescent materials. Numerous papers on the luminescence of II–VI semiconductor nanocrystals doped with TM or lanthanide ions have appeared in an effort to achieve high efficient luminescence via ET from II–VI host to lanthanide ions.

### 5.4.1. *Ln:ZnS (Ln = Eu$^{2+}$, Eu$^{3+}$, Tb$^{3+}$)*
Generally nanocrystalline ZnS synthesized at low-temperature belongs to cubic zinc-blended structure (sphalerite-type) instead of hexagonal wurtzite structure. Doped ZnS nanocrystals show distinct optical properties from the conventional bulk material. For ZnS nanocrystals containing Eu$^{2+}$ ions, a size dependence of the emission peak involving the 5d–4f transition in Eu$^{2+}$ has been observed (Chen et al., 2001). It was demonstrated that quantum confinement can modify the energy structure of the nanocrystal host as well as the relative energy levels of the dopants. Specifically, quantum confinement moves the excited states of Eu$^{2+}$ into the band gap of ZnS nanocrystals, thus enables the intra-ion transition of Eu$^{2+}$ in ZnS nanocrystals. By contrast, no intra-ion transition can be observed in Eu$^{2+}$:ZnS bulk due to the photoionization. The emission bands of the 4.2-, 3.2-, and 2.6-nm-size ZnS:Eu$^{2+}$ nanoparticles peak respectively at 670, 580, and 520 nm, as shown in fig. 16. Chen et al. (2001) showed that the decrease in the electron–phonon coupling (or Huang–Rhys parameter $S$) and the crystal field strength are the major factors responsible for the shift of the 4f$^6$5d$^1$(t$_{2g}$)–4f$^7$ emission of Eu$^{2+}$ to higher energies for smaller ZnS:Eu$^{2+}$ nanocrystals.

Typical emission and excitation spectra of ZnS:Eu$^{3+}$ nanocrystals, prepared by using the microemulsion method are shown in fig. 17 (Bol et al., 2002). In the emission spectrum,
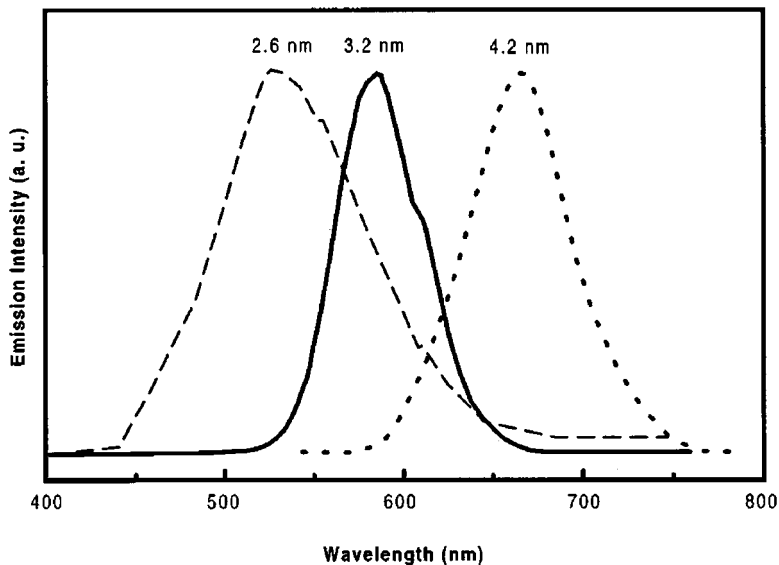
Fig. 16. Emission spectra of ZnS:Eu$^{2+}$ nanocrystals with average size of around 4.2, 3.2, and 2.6 nm, respectively. The excitation wavelength is 260 nm (reprinted with permission from Chen et al. (2001)).
© 2001 American Institute of Physics

the characteristic $^5D_0 \rightarrow {}^7F_J$ emission lines of the Eu$^{3+}$ ion are superimposed on a broad emission band (maximum at ∼465 nm). The excitation spectrum is dominated by intraconfigurational 4f–4f transitions (marked in fig. 17b), the strongest line being the $^5L_6 \leftarrow {}^7F_0$ line at 395 nm as is usually observed for Eu$^{3+}$. The broad excitation band under the sharp lines centered at 375 nm is possibly due to the CT transition of Eu$^{3+}$–S$^{2-}$ or to nanocrystal defects. The ZnS host absorption (<340 nm) is not present in the excitation spectrum. Therefore, Bol et al. (2002) concluded that the Eu$^{3+}$ ions are not incorporated in the ZnS nanocrystals, as we previously discussed. Liu, S.M. et al. (2001) observed a very similar emission spectrum for ZnS:Eu$^{3+}$ nanocrystals prepared by a different method. However, in addition to the sharp f–f transition lines, a very weak host excitation band at 310 nm was observed in the excitation spectrum. They ascribed this low efficient ET to the energy mismatch between the f–f transitions of Eu$^{3+}$ and host band gap absorption. The luminescence lifetime of Eu$^{3+}$ in ZnS:Mn$^{2+}$, Eu$^{3+}$ nanocrystals was determined to be 0.2 and 0.75 ms by a biexponential fit when the exciting Eu$^{3+}$ ions are directly excited at 468 nm (Chen, W. et al., 2004b). Our recent results show that the luminescence lifetime of Eu$^{3+}$ in ZnS nanocrystals prepared by a similar method is about 0.33 ms (Chen, X.Y. et al., 2006). It should be noticed that Ihara et al. (2000) observed a very "neat" emission and excitation spectra for Eu$^{3+}$:ZnS nanocrystals in which the broad bands observed by Bol et al. (2002) are not present. However the spectra of Bol et al. (2002) are in good agreement with those of Ihara et al. (2000) if the broad backgrounds in figs. 17a and 17b are subtracted, respectively.
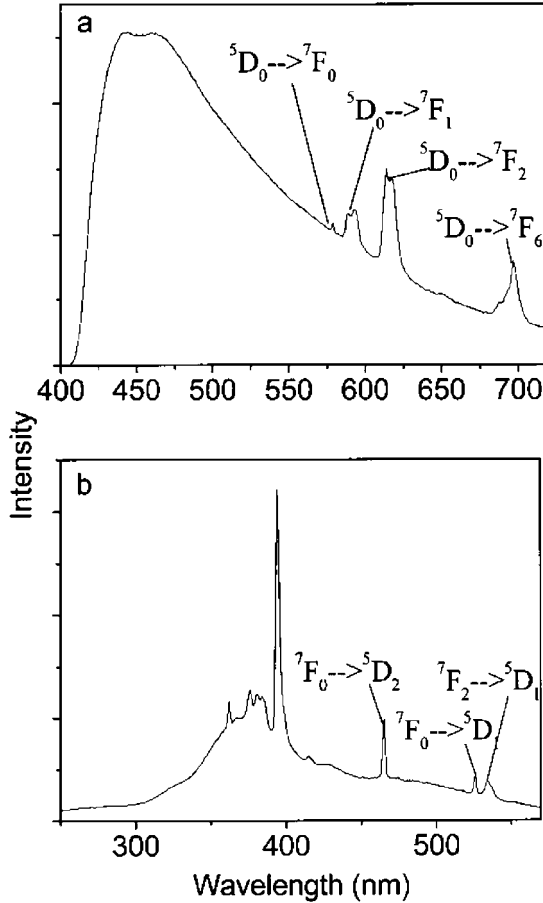
Fig. 17. (a) Emission ($\lambda_{exc}$ = 375 nm) and (b) excitation spectra ($\lambda_{em}$ = 612 nm) of ZnS:Eu$^{3+}$ nanocrystals, prepared by using the microemulsion method, measured at room temperature (redraw after (Bol et al., 2002)).

Strong upconversion luminescence from Eu$^{3+}$ was observed in ZnS: Eu$^{3+}$ nanocrystals upon laser excitation at 929 nm (Chen, W. et al., 2004b). Fig. 18 shows clearly a two-photon resonance in the Eu upconversion spectrum at twice the Eu absorption near 465 nm, which corresponds to the $^{5}D_{2} \leftarrow {}^{7}F_{0}$ excitation. A shift of only one or two nanometers away from the resonant laser wavelength results in a drastic change in the upconversion intensity. Note that there is no energy level of Eu$^{3+}$ in resonance with the one-photon energy at 929 nm. The above upconversion process can only be realized via a virtual intermediate state. The upconversion luminescence showed a quadratic power dependence, indicating that the excitation mechanism is likely through cooperative two-photon absorption.

The optical spectra of Tb$^{3+}$:ZnS nanocrystals have also been well studied since 1994. Upon excitation in the nanocrystalline ZnS host, the well-known $^{5}D_{4} \rightarrow {}^{7}F_{J}$ emission
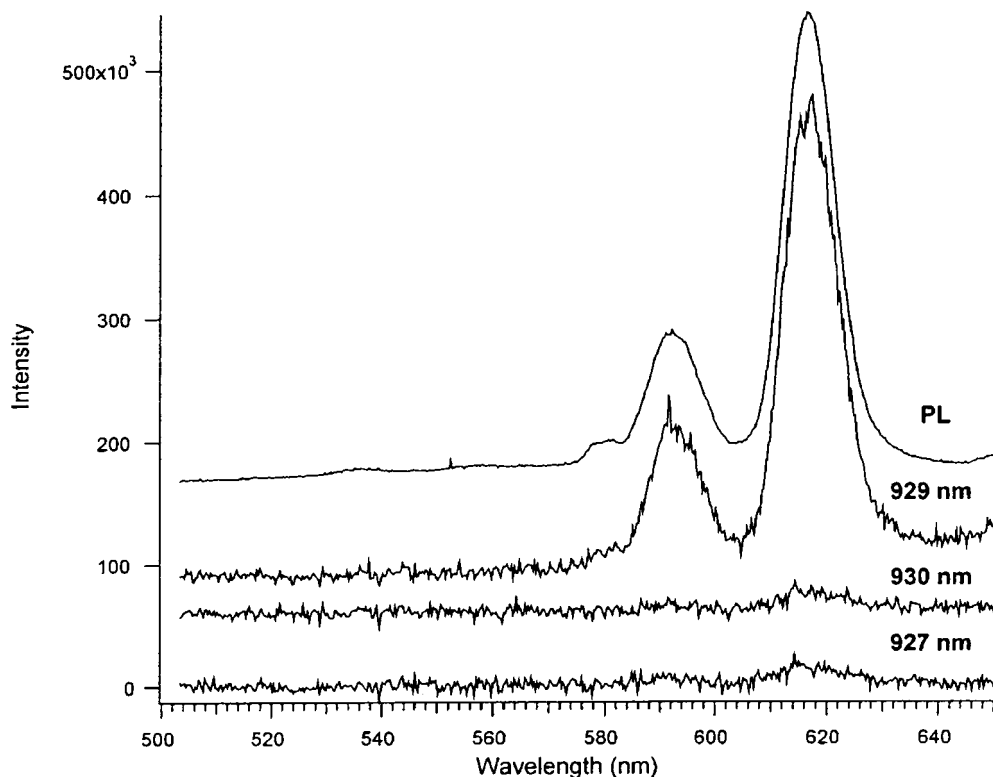
Fig. 18. Upconversion luminescence from ZnS:Eu$^{3+}$ nanocrystals. The emission following excitation at 929 nm is significantly stronger than the emission following excitation only a few nanometers away. For comparison, a PL spectrum is shown as well (reprinted with permission from Chen et al. (2004a, 2004b, 2004c)).
© 2004 American Institute of Physics

of the Tb$^{3+}$ ion around 550 nm was observed (Bhargava, 1996; Bhargava et al., 1994b; Chen, L. et al., 2005; Liu, S.M. et al., 2001). On the contrary, Bol et al. (2002) and Ihara et al. (2000) reported that the Tb$^{3+}$ emission can only be excited via direct excitation of the Tb$^{3+}$ ion, not via ZnS band-gap excitation. Furthermore, Ihara reported that the PL intensities of ZnS:Tb$^{3+}$ and ZnS:Eu$^{3+}$ nanocrystals were 2.5 and 2.8 times higher than those of bulk phosphors. The luminescence efficiency of ZnS:Tb$^{3+}$ and ZnS:Eu$^{3+}$ nanocrystals can be improved 2.5 and 2.2 times, respectively, by taking charge compensation into account. The cathodoluminescence (CL) of ZnS:Tb$^{3+}$ and ZnS:Eu$^{3+}$ nanocrystals was successfully observed for the first time, indicating a potential application for displays (Ihara et al., 2000). As for the lifetime behavior of Tb$^{3+}$ in ZnS nanocrystals, the unusually shortened lifetime from 3 ms for bulk to 7 ns in nanocrystals (Bhargava, 1996) has been pointed out to be a misinterpretation of experimental results. Ihara et al. (2000) observed an efficient lifetime shortening

from 1.15 ms for bulk ZnS:$Tb^{3+}$ to 0.10 ms for ZnS:$Tb^{3+}$ nanocrystals. So far there is no detailed report on the luminescence dynamics of $Tb^{3+}$ or $Eu^{3+}$ doped in ZnS nanocrystals.

Apart from $Eu^{3+}$ and $Tb^{3+}$, few studies have been reported on optical properties of lanthanide ions doped in ZnS nanocrystals. Bol et al. (2002) attempted to incorporate $Er^{3+}$ in ZnS nanocrystal by ion implantation. They annealed the sample at a temperature up to 800 °C to restore the crystal structure around $Er^{3+}$, but no $Er^{3+}$ luminescence was observed. Schmidt et al. (1998) employed a new synthesis strategy to incorporate up to 20 at% $Er^{3+}$ into ZnS (1.5–2 nm) cluster solutions which were stabilized by (aminopropyl)triethoxysilane (AMEO). Ethanolic AMEO-stabilized Er:ZnS clusters in solutions fluoresce 200 times stronger at 1540 nm than that of ethanolic AMEO-Er complexes. This is explained by the very low phonon energies in ZnS QDs, and indicates that $Er^{3+}$ ions are trapped inside chalcogenide clusters. However the exact position of $Er^{3+}$ in ZnS clusters remains unknown. Further spectroscopic and structural analyses are required in order to obtain more detailed information.

### 5.4.2. Ln:ZnO (Ln = $Er^{3+}$, $Eu^{3+}$, $Tb^{3+}$)

Different from ZnS, the nanocrystalline of ZnO synthesized under mild conditions generally belongs to the hexagonal wurtzite structure. Lanthanides ions have been successfully incorporated into its lattice.

### 5.4.2.1. $Er^{3+}$

Optical absorption and NIR luminescence properties of ethanolic $Er^{3+}$:ZnO (3.5–5 nm) colloids have been investigated (Schmidt et al., 1998). A significant band broadening and hyperchromic effect for the hypersensitive transitions to $^4G_{11/2}$ and $^2H_{11/2}$ were observed in the absorption spectrum. For colloids with high ZnO/Er ratio, the hyperchromic term splitting of $^2H_{11/2}$ was obvious, which was possibly related to stronger Er–O orbital overlap within the ZnO-rich ligand field. Similar to Er:ZnS colloids, a strong enhancement of the 1540 nm luminescence of $Er^{3+}$ was achieved in highly concentrated ZnO nanocrystals (ZnO/Er = 40). Recently Wang et al. (2004) also reported the luminescence and visible upconversion properties of $Er^{3+}$ in ZnO nanocrystals. Fig. 19 shows the RT emission spectra of $Er^{3+}$ in ZnO nanocrystals when excited directly into the $^4F_{7/2}$ level (488 nm), where three emission bands in the green, red, and NIR regions correspond to the transitions ($^2H_{11/2}$, $^4S_{3/2}$) $\rightarrow$ $^4I_{15/2}$, $^4F_{9/2} \rightarrow$ $^4I_{15/2}$, and $^4S_{3/2} \rightarrow$ $^4I_{13/2}$. Higher annealing temperature resulted in increased emission intensities and better crystalline structures. A well resolved and sharp emission line due to crystal field splitting can be observed in the emission spectra for the 700 °C annealed sample. This is a very strong evidence that $Er^{3+}$ ions are incorporated into the ZnO nanocrystal lattice. Otherwise, the emission lines would be broadened and unresolved (fig. 19a, similar to the case of lanthanide ions doped in glass), if $Er^{3+}$ ions occupy the surface sites. The average lifetime of $^4S_{3/2}$ is 4.14 μs (Wang et al., 2004), very close to the theoretical fitting value (4.3 μs) for $Er^{3+}$ doped in a fractal ZnO nanolattice (Kohls et al., 2002). The blue ($^2H_{9/2} \rightarrow$ $^4I_{15/2}$), green ($^2H_{11/2}$, $^4S_{3/2} \rightarrow$ $^4I_{15/2}$), and red ($^4F_{9/2} \rightarrow$ $^4I_{15/2}$) upconversion emissions of $Er^{3+}$ ions in the ZnO nanocrystals were observed upon laser excitation at 808 nm (Wang et al., 2004). However the upconversion spectra showed lines with poor resolution compared to those reported in fig. 19d. The green emission is predominant in
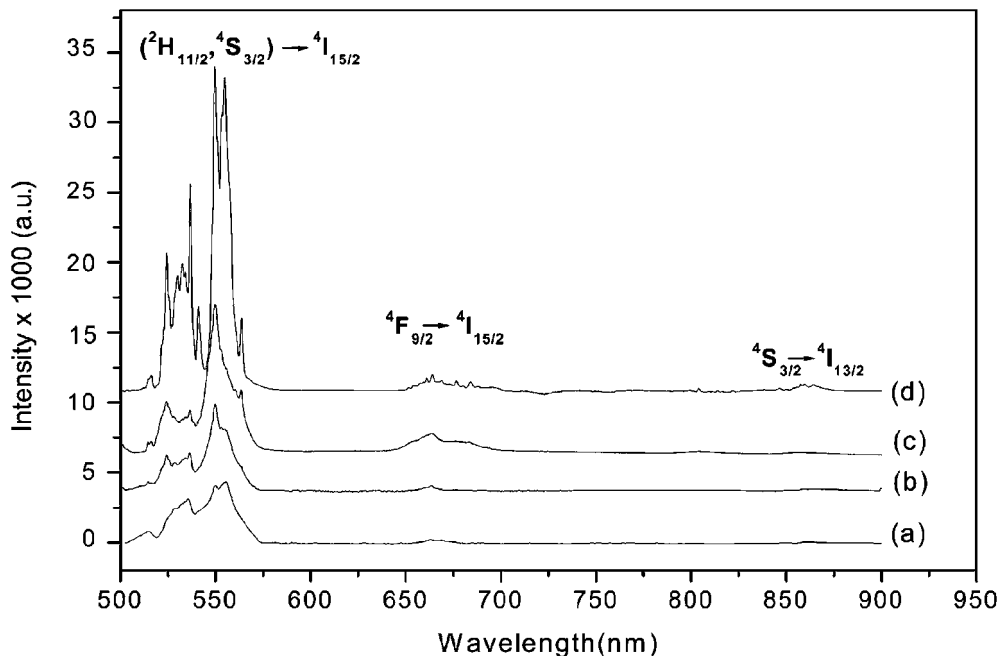
Fig. 19. Room-temperature Stokes emissions of $Er^{3+}$ in the ZnO nanocrystals annealed at (a) 400, (b) 500, (c) 600, and (d) 700 °C upon excitation at 488 nm (reprinted with permission from Wang et al. (2004)).
© 2004 American Chemical Society

the spectrum, much stronger than the blue and red ones. Especially for the sample annealed at 700 °C, the blue and red upconversion bands almost disappear compared to the green one. This behavior was also observed in nanocrystals of $Y_2O_3$:$Er^{3+}$ (<2 mol%) following excitation at 815 nm (Capobianco et al., 2002). For comparison, Xiao et al. (2006) observed a very different upconversion emission pattern in $Er^{3+}$:ZnO bulk powders prepared by fluoride salt decomposition, which exhibited prevailing red emission band over the blue and green ones upon laser excitation at 980 nm. Both the nanocrystal and bulk ZnO showed similar pump power dependence of upconverted red and green integrated intensities (slope = 1.4–1.5 for the red emission, and 1.6–1.7 for the green one). Although a two-photon process is assumed to be responsible for the upconversion, the main ET path resulting in an enhanced population on $^4F_{9/2}$ or $^2H_{11/2}$, $^4S_{3/2}$ levels is expected to be very different in the nanocrystals compared to the case of bulk ZnO.

5.4.2.2. $Eu^{3+}$  Recently, Zhang et al. (2005) observed energy transfer from the host to $Eu^{3+}$ in $Eu^{3+}$-doped ZnO nanocrystals synthesized by high temperature calcination method. The excitation spectrum consists in the strong band of the ZnO host (385 nm) and the characteristic excitation line spectrum of $Eu^{3+}$ when the $Eu^{3+}$ luminescence at 616 or 708 nm is monitored. Note that the latter wavelength was used to avoid the overlap with the host emis-

sion. Furthermore, only $Eu^{3+}$ emissions without the background of the broad emission of ZnO were observed under band-gap excitation at 385 nm. However it is somewhat curious that the observed band-gap absorption was red shifted compared to the bulk ($\sim$370 nm). This is rarely observed since quantum size effect is expected to blue-shift the band gap excitation.

Ishizumi and Kanemitsu (2005) have studied PL properties of $Eu^{3+}$ doped ZnO nanorods fabricated by a microemulsion method. The PL of bound exciton recombination and ZnO defects was observed near 370 and 650 nm under 325-nm light excitation, but no emission of $Eu^{3+}$ occurred. On the other hand, the sharp PL peaks due to the intra-4f transitions of $Eu^{3+}$ ions appeared under nonresonant excitation below the band-gap energy of ZnO (454 and 457.9 nm) in addition to direct excitation to $^5D_2$ (465.8 nm). Therefore the authors concluded that the energy transfer occurs from the ZnO nanorods to $Eu^{3+}$ ions through ZnO-defect states. This energy transfer mechanism seems very different from the previous one and more spectroscopic evidence is required to confirm it.

5.4.2.3. *$Tb^{3+}$* The effect of the doping concentration on the optical spectra of $Tb^{3+}$ in ZnO nanocrystals (5 nm) was investigated in details (Liu et al., 2001b). The PL intensity of $Tb^{3+}$ centers increases with increasing Tb content at the expense of emission from defect states in the ZnO nanocrystals. The characteristic emission of $Tb^{3+}$ at 544 nm is the strongest upon excitation of the ZnO host at 345 nm, which implies an efficient carrier relaxation from ZnO hosts to $Tb^{3+}$ centers. For a 3-nm ZnO sample, the band-gap excitation is blue-shifted to 315 nm due to quantum size confinement. This significant ET from the ZnO nanocrystal host to $Tb^{3+}$ centers confirmed that $Tb^{3+}$ ions can to some extent be effectively incorporated into ZnO nanocrystals.

### 5.5. *Lanthanides doped III–V semiconductor quantum dots*

Quantum dots represent three-dimensional confinement in semiconductor materials. The optical spectroscopy of lanthanides-doped III–V semiconductor QDs has been observed to be very different from the bulk or thick film. For example, carrier confinement in QDs can strongly enhance the radiative quantum efficiency of the lanthanide emission, which thus makes lanthanide-doped III–V semiconductor QDs very promising candidates for full-color LEDs. It is notoriously difficult to dope lanthanide into III–V semiconductor nanocrystals by wet chemical synthesis methods. To date, most of these samples were prepared either by MBE, ion implantation or magnetron co-sputtering.

The optical properties of lanthanides (Eu, Tb, Tm)-doped GaN QDs embedded in AlN or InGaN QDs embedded in GaN grown by plasma-assisted MBE have recently been investigated in detail (Andreev et al., 2005a, 2005b; Hori et al., 2004, 2005). A very important task is to probe the lanthanide location in these materials and get more insight into the PL or CL mechanisms and dynamics. For Eu-doped InGaN QDs/GaN structure, $Eu^{3+}$ ions can occupy lattice sites either in InGaN QDs or in the GaN barrier layer (Andreev et al., 2005b). Fig. 20 shows the PL and PLE spectra from InGaN:Eu QDs measured at 5 K. By analysis of the emission characteristics of the $^5D_0 \rightarrow {}^7F_2$ transition, the 620 and 633.5 nm lines were assigned to $Eu^{3+}$ ions located in the GaN spacer layer, and the 621.6 and 622.3 lines (marked by arrows
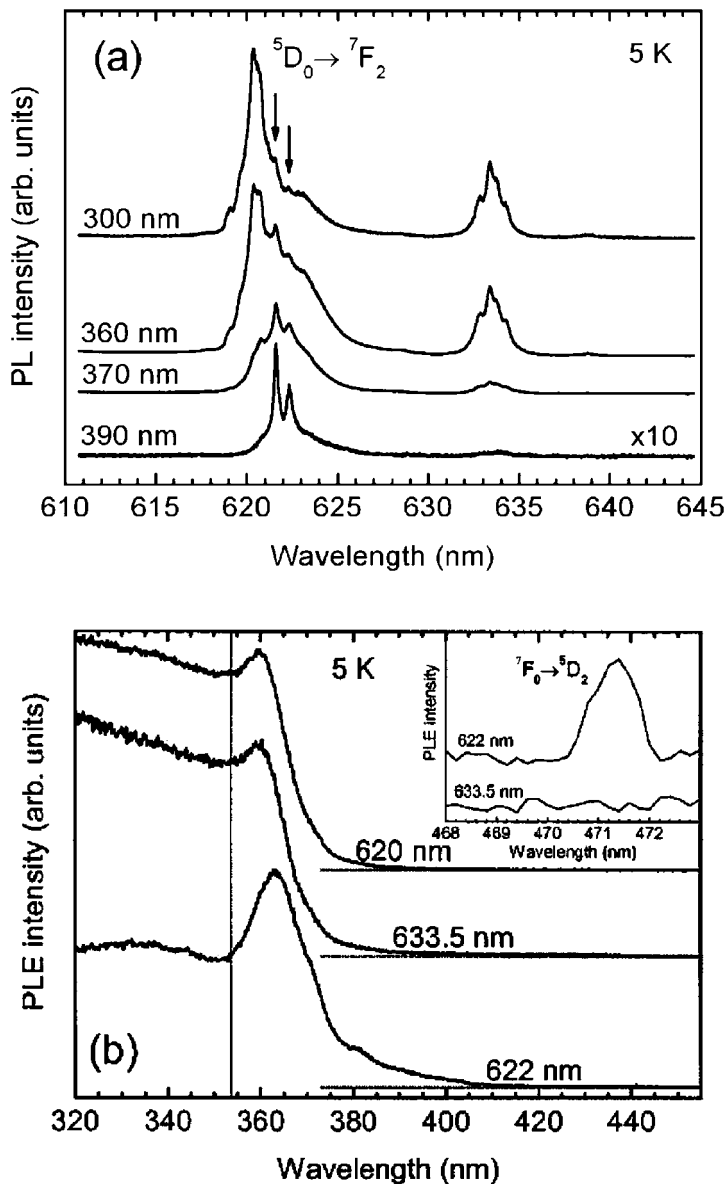
Fig. 20. (a) PL spectra from InGaN:Eu QDs with different excitation wavelengths. The arrows indicate the 622 nm lines assigned to Eu ions inside InGaN QDs. (b) PLE spectra for Eu emissions at 620.0, 622.3, and 633.5 nm in InGaN:Eu QDs. The horizontally dotted lines are PLE base lines. The vertically dotted lines show the band-gap energy of GaN film (3.505 eV). The insets show the PLE spectra of the $^5D_2 \leftarrow {}^7F_0$ transition of $Eu^{3+}$ for emissions at 622 and 633.5 nm. Both (a) and (b) were measured at 5 K (reprinted with permission from Andreev et al. (2005b)). © 2005 American Institute of Physics

in fig. 20a, merging into a 622 nm single line at RT) to $Eu^{3+}$ ions inside InGaN QDs. As shown in fig. 20a, the 620 and 633.5 nm lines are strongly favored by exciting above the band gap of the GaN spacer layer, due possibly to the fact that carriers are created in the spacer layer so that any carrier-mediated ET to $Eu^{3+}$ ions is expected to be more effective for ions located in the spacer than in QDs. When the sample is excited well below the band gap of GaN at 390 nm, only the 621.6 and 622.3 lines are observed. This interesting observation is in good agreement with the PLE spectra to support the above assumption of the $Eu^{3+}$ location. In fig. 20b, one may notice that the PLE band-edge peak for the 622 nm line extends farther in the gap (beyond 400 nm), which reflects the distribution of excited states of an inhomogeneous ensemble of QDs. By contrast, there is almost no contribution to the $Eu^{3+}$ emission at 620 and 633.5 nm upon excitation at 390 nm. The PLE spectra for the 620 and 633.5 nm lines are very similar. The direct excitation to $^5D_2$ only appears in the excitation spectrum of the 622-nm line, as shown in the inset of fig. 20b. All these strongly suggest that the 620 and 633.5 nm lines originate from $Eu^{3+}$ ions located in the same GaN layer. The band-edge peak in the PLE spectra is the most pronounced for the 622 nm line, implying a more efficient ET from the host to the $Eu^{3+}$ ions. This is another evidence for $Eu^{3+}$ location in QDs, since carrier-mediated ET to lanthanide ions is expected to be much more efficient for lanthanide ions located in InGaN QDs than that in GaN layers (Andreev et al., 2005b).

Significant differences in the optical signatures of $Eu^{3+}$ ions were observed between GaN:Eu QDs and GaN:Eu layers (Andreev et al., 2005b): (1) the emission line at 633.5 was not observed in GaN:Eu QDs for unknown reason; (2) the $^5D_0 \rightarrow {}^7F_2$ transition was red shifted by 1.7 nm in QDs compared to the layer sample, which could be induced by a strong internal electric filed in QDs (quantum confinement Stark effect); (3) the PL intensity is almost temperature independent for GaN:Eu QDs, but sensitive to temperature for GaN:Eu layers (Hori et al., 2004).

It was also revealed that $Tm^{3+}$ ions doped in GaN QDs embedded in AlN layer are partially located in the GaN QDs and partially at the GaN/AlN interface by means of structural characterizations such as EXAFS and Rutherford backscattering spectroscopy (RBS) (Andreev et al., 2005a). Consistently, CL spectra (fig. 21) can be well interpreted by assuming that $Tm^{3+}$ is located inside QDs but also in the surrounding AlN spacer. (1) Intense sharp emission lines from the $^1I_6$, $^1D_2$, and $^1G_4$ levels of $Tm^{3+}$ in the blue-green region (450–550 nm), which were absent for the Tm-doped GaN thick layer, were observed in the PL spectrum (fig. 21b). This provides clear evidence for $Tm^{3+}$ ions located in QDs. (2) Compared to the PL spectrum, the CL spectrum of the same GaN:Tm QD sample (fig. 21c) shows additional sharp lines which coincide with those of the CL spectrum of AlN (fig. 21d). Thus it confirms that $Tm^{3+}$ ions are also present in the AlN barrier layer.

Similar to GaN:Eu QDs, transitions of $Tm^{3+}$ inside QDs show constant temperature behavior, a red shift, and broader line widths, resulting from the presence of large internal electric field and strain in QDs (Andreev et al., 2005a).

Full-color CL in a range from UV to visible has been successfully realized by combining three lanthanide ions in a multilayer sample of stacked GaN QD planes (Hori et al., 2005). The sample consists of 3 planes of Eu-doped, 4 planes of Tm-doped and 10 planes of Tb-doped GaN QDs (repeated 5 times). Intense white light was also observed at RT upon exciting the
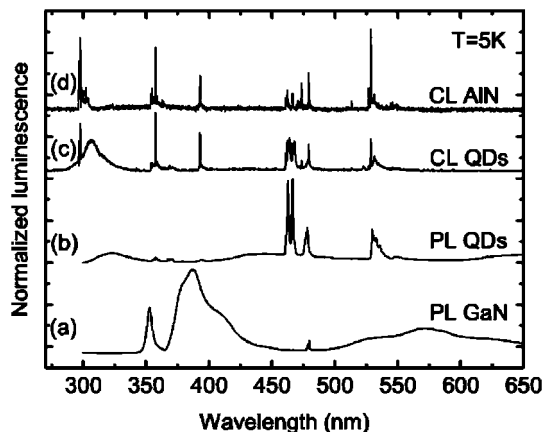
Fig. 21. (a) PL of a GaN:Tm layer; (b) PL of GaN:Tm QDs; (c) CL of GaN:Tm QDs; (d) CL of AlN:Tm at 5 K
(reprinted with permission from Andreev et al. (2005a)).
© 2005 American Physical Society

sample with a 266-nm laser, as a demonstration of potential interest of lanthanides doped III–V QDs for LEDs.

Ideally, lanthanide ions occupy site with $C_{3v}$ symmetry when incorporated into the GaN lattice by substituting the $Ga^{3+}$. However the actual site symmetry is often found lower than $C_{3v}$ due to strain and defects. So far no crystal field analysis has ever been reported for lanthanide-doped III–V QDs, due to the co-existence of multi-sites which complicates the energy level structure and makes crystal field analysis difficult. Site selective spectroscopy is a very useful tool thus proposed to investigate the different crystal field environments of lanthanide ions doped in III–V QDs.

### 5.6. *Lanthanides doped in other semiconductor nanocrystals*

Compared to III–V and II–VI semiconductor nanocrystals, much less work has been performed on lanthanide-doped III–VI (such as $In_2S_3$) or IV–VI (such as $TiO_2$, $SnO_2$) semiconductor nanocrystals. One of the advantages of these hosts over III–V semiconductors is that they can be synthesized by wet chemical methods instead of the sophisticated techniques (e.g., MBE) needed for GaN.

### 5.6.1. *$In_2S_3$*

Chen et al. (2004a) reported full-color emission from cubic 2–3 nm $In_2S_3$:$Eu^{3+}$ nanocrystals. As shown in fig. 22, the positions of sharp emission lines from $Eu^{3+}$ do not shift while the 425-nm blue emission band originating from excitonic recombination of the host shifts to longer wavelengths at higher temperature. The red shift of the blue emission band with increasing temperature is in agreement with the temperature behavior of excitonic emission in semiconductors. The blue band intensity shows a tendency of decreasing from RT to 20 K
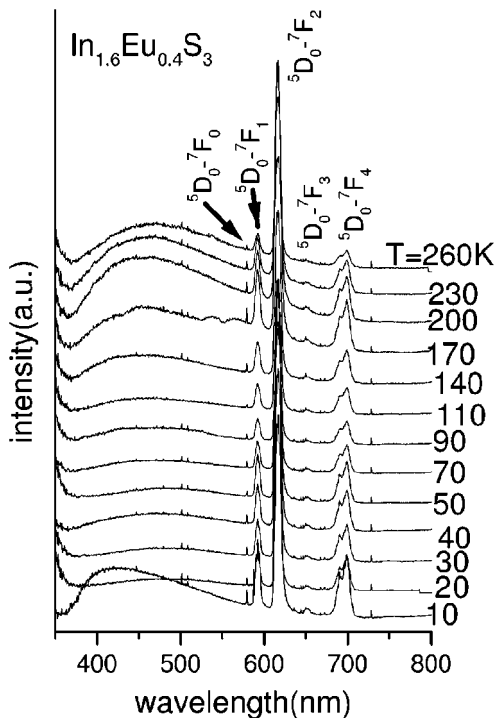
Fig. 22. Emission spectra of $In_{1.6}Eu_{0.4}S_3$ nanocrystals thin films at different temperatures below RT. The excitation is at 325 nm (reprinted with permission from Chen et al. (2004a)).
© 2004 American Chemical Society

then increasing at 10 K, due to the competition between the phonon-induced quenching and ET to $Eu^{3+}$ (Chen et al., 2004a). Luminescence intensity of $Eu^{3+}$ increases with decreasing temperature. The excitation spectrum for the $Eu^{3+}$ emission at 610 nm shows the dominant band gap excitation as well as the relatively weak f–f transition of $Eu^{3+}$, which indicates that $Eu^{3+}$ ions are incorporated in the $In_2S_3$ lattice. The appearance of the $^5D_0 \rightarrow {}^7F_0$ transition at 579.5 nm implies site symmetry not higher than $C_{3v}$ for $Eu^{3+}$ in $In_2S_3$ lattice. It is worthy to mention that the $In_2S_3$ nanoparticle size is significantly smaller than the calculated exciton Bohr radius of 33.8 nm (Chen et al., 2004a). Accordingly, a very large blue shift of the absorption edge (150–220 nm) due to quantum size confinement was observed (Chen et al., 2004a). Such a large shift has never been reported for other systems.

### 5.6.2. *SnO₂*

Yanes et al. (2004) observed a very interesting size selective spectroscopy in 0.4 mol% $Eu^{3+}$:$SnO_2$ nanocrystals (∼4 nm) embedded in $SiO_2$ glass prepared by thermal treatment of sol-gel glasses. The mean size of $SnO_2$ nanocrystals is comparable to the bulk exciton Bohr radius (4.8 nm). Thus the band-gap excitation energy depends on the nanocrystal size.
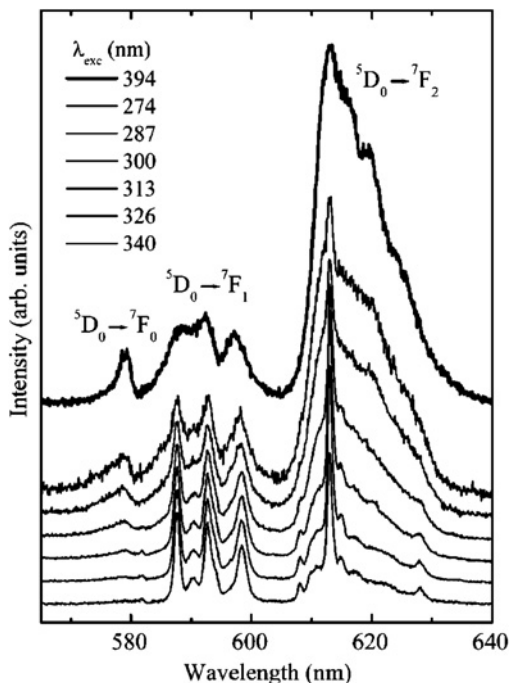
Fig. 23. Emission spectra of the $Eu^{3+}$:$SnO_2$ nanocrystals embedded in $SiO_2$ glass under different excitation wavelength at 13 K (reprinted with permission from Yanes et al. (2004)).
© 2004 American Institute of Physics

For a 4-nm nanocrystal, the band-gap excitation peak for the 613 nm $Eu^{3+}$ emission shifts from 344 nm (bulk) to 320 nm. Note that $Eu^{3+}$ emission can be strongly enhanced by energy transfer from the $SnO_2$ nanocrystals (Nogami et al., 2002), as confirmed by the time-resolved excitation spectra (Del Castillo et al., 2005). Taking advantage of quantum size confinement, it is possible to excite selectively the $Eu^{3+}$ ions inside $SnO_2$ nanocrystals via energy transfer from the host. In fig. 23 the emission spectrum under excitation at 394 nm ($^5L_6 \leftarrow {}^7F_0$ transition) is typical of $Eu^{3+}$ ions in $SiO_2$ glasses, which reveals that only a low percentage of $Eu^{3+}$ is incorporated into the nanocrystals. By contrast, the excitation at the long wavelength side of the band-gap excitation peak (313–340 nm) gives rise to a spectrum with narrow crystal field transition lines indicating a crystalline host for $Eu^{3+}$ ions. When the excitation wavelength decreases, the crystal field transition lines broaden progressively. For an excitation at the short wavelength side such as 287 and 274 nm, the emission spectra become similar to the $Eu^{3+}$ spectra in glasses (Yanes et al., 2004). The above evolution can be well interpreted by considering the nanocrystal size distribution. For longer excitation wavelengths (e.g., 340 nm) the relatively large nanocrystals (>10 nm) are selectively excited, thus efficient energy transfer occurs from the host to the $Eu^{3+}$ ion, and as a result, the predominant environment for the $Eu^{3+}$ ions is crystalline-like. When the excitation wavelength is decreased from 340 to

274 nm, the size of the excited nanocrystals also decreases. For example, a 2-nm nanocrystal corresponds to an excitation wavelength of 274 nm. It is not surprising that a glassy environment is found for the $Eu^{3+}$ ions in such small nanocrystals since most $Eu^{3+}$ ions are close to the surface and inhomogeneous broadening is enhanced due to distortion of the local environment and to the interaction with the $SiO_2$ glass surrounding the nanocrystal (Yanes et al., 2004). The measured lifetime of $^5D_0$ decreases from 2.4 to 1.8 ms when the excitation wavelength decreases from 340 to 274 nm, corresponding to a nanocrystal size decrease from >10 to 1 nm (Yanes et al., 2004). This lifetime decrease for smaller nanocrystals is possibly due to the competition between lifetime lengthening due to the correction of the effective index of refraction in nanocrystals on one hand and lifetime shortening resulting from lower symmetry or distorted environment, and the presence of more defect-related quenching centers in smaller nanocrystals on the other hand.

### 5.6.3. *TiO₂*

Jeon and Braun (2003) developed a new route to synthesize fluorescent $Er^{3+}$-doped $TiO_2$ anatase phase nanoparticles (∼50 nm) through a simple hydrothermal method starting from sol-gel precursors. They observed a remarkably enhanced luminescence from thin films of the nanoparticles by annealing at 500 °C to remove surface hydroxyl groups, whereas the as-deposited films have weaker luminescence. A sharp emission peak at 1532 nm with an full-width at half-maximum (FWHM) of 5 nm was observed, which excludes the possibility that $Er^{3+}$ ions exist under a free oxide form in the $TiO_2$ matrix since the emission band of erbium oxide nanoclusters synthesized through a micro-emulsion technique is centered at 1540 nm with an FWHM of 22 nm (Que et al., 2001). Additional evidence from XRD, and energy dispersive X-ray (EDX) spectra further confirms the incorporation of $Er^{3+}$ into the nanoparticles and the absence of free erbium oxide (Jeon and Braun, 2003). Patra et al. (2003b) reported the upconversion luminescence properties of $Er^{3+}$ in $TiO_2$ nanocrystals. Green and red upconversion emissions at 550 and 670 nm were observed under 975-nm excitation. The effects of the erbium concentration and different processing temperatures on the upconversion emission were investigated. The maximum upconversion emission intensity was found for $TiO_2$:$Er^{3+}$ (0.25 mol%) annealed at 800 °C (∼40 nm) in which both the anatase and the rutile phases are present.

### 5.6.4. *Miscellaneous*

Enhanced luminescence of $SiO_2$:$Eu^{3+}$ by energy transfer from ZnO nanocrystals (3 nm) was recently reported (Bang et al., 2005). The defect-related green emission from ZnO nanocrystals was completely quenched when they were embedded in $SiO_2$ doped with $Eu^{3+}$, indicating a very efficient energy transfer from the embedded ZnO to $Eu^{3+}$. As a result, the f–f emissions from $Eu^{3+}$ were enhanced 5–10 times.

The characteristic 1540 nm emission of $Er^{3+}$ was observed via a silicon exciton-mediated energy transfer for Si:$Er^{3+}$ nanocrystals (12 nm) derived from an erbium amidinate precursor (Ji et al., 2004). Similarly, the PL spectrum of $Er^{3+}$ implanted Si nanocrystals showed two lines at 1535 and 1546 nm, having a much higher intensity when compared to $Er^{3+}$ implanted $SiO_2$ nanocrystals or Er implanted Si nanocrystals (Priolo et al., 2001).

# 6. Spectroscopy of lanthanides doped in core–shell, nanowires, nanotubes, and other novel nanostructures

In the above sections, our attention was primarily focused on the structural and optical properties of lanthanide doped in nanoparticles such as spherical QDs. Lanthanides doped in some other novel low-dimensional nanostructures including core–shell, one-dimensional (1D) nanowires and nanotubes, two-dimensional (2D) nanofilms, hollow nanospheres, 2D nanosheets and nanodisks have also attracted extensive attention. It is expected that their unique structures could result in unusual mechanical, electronic, optical and magnetic properties. So far few papers have been reported for lanthanide ions other than $Eu^{3+}$ in these materials. Much attention is focused on the optical properties of $Eu^{3+}$ ions in view of their very good spectroscopic properties.

## 6.1. *Core–shell or nanolayer structures*

Nowadays the core–shell (or nanocoating) technique is extensively applied to the synthesis of both semiconductor and insulating nanostructures for a variety of purposes. By modification of their nanostructure or surface, one can improve the quantum efficiency of lanthanide optical centers, and design biolabels. In addition, core–shell particles can be used as precursor to produce hollow spheres.

It is possible to alter the intrinsic properties of materials by chemical nanocoating, which cannot be achieved by conventional methods. Generally the core–shell nanostructures are divided into two categories: (1) lanthanides doped in the core; (2) lanthanides doped in the shell. The former are synthesized in order to improve the quantum efficiency of lanthanide ions or design bio-labels, while the latter are meant for the study of surface modifications on the lanthanide luminescence or the synthesis of lanthanide-doped hollow nanospheres.

### 6.1.1. *$Eu_2O_3$ ($Tb_2O_3$) nanocrystals coated on $Al_2O_3$ microcrystals*
Gedanken et al. reported the coating of $Eu_2O_3$ (or $Tb_2O_3$) nanoparticles on micro- or sub-micronmetric $SiO_2$, $Al_2O_3$, $TiO_2$ or $ZrO_2$ by sonochemical synthesis methods (Gedanken et al., 2000a, 2000b; Patra et al., 1999; Pol et al., 2002), and the luminescent properties of the synthesized lanthanide oxide nanolayers were first reported therein. Time-resolved luminescence spectra were measured and compared for $Eu_2O_3$- ($Tb_2O_3$-) coated $Al_2O_3$ micron size spheres and doped $Al_2O_3$ nanoparticles (Gedanken et al., 2000b). The intensity of the $Eu^{3+}$ (or $Tb^{3+}$) luminescence is nearly an order of magnitude stronger for the doped alumina than for coated microspheres. This behavior was ascribed to the concentration quenching of $Eu^{3+}$ in the coated layers. The decay time of $Eu^{3+}$ luminescence in the coated samples showed two components (0.34 ms, 1.55 ms). The longer component is exactly the same as the decay time of $Eu^{3+}$ doped in $Al_2O_3$. Consistently, the concentration quenching may be responsible for the short decay component of the coated samples. A short-lived (tens of nanoseconds) emission band in the range of 380–500 nm was also observed in the coated sample, which was argued to arise from the $Al_2O_3$ substrate.

### 6.1.2. *Eu:Y$_2$O$_3$ nanolayers coated on different dielectric nanoparticles*

Recently, the structural and optical properties of Eu$^{3+}$:Y$_2$O$_3$ films coated on a variety of di-
electric nanoparticles have been investigated using transmission electron microscope (TEM),
X-rays diffraction (XRD) and site-selective laser spectroscopic methods (Chen, X.Y. et al.,
2005; Chen et al., 2003a). Eu$^{3+}$ ions are employed as probes for the study of crystallization
and multi-site structure as well as the luminescent centers in nanolayers. It was found that the
luminescent nanolayers exhibit distinct thermodynamics and luminescence properties.

Nanolayers of Eu$^{3+}$-doped Y$_2$O$_3$ were deposited on the Al$_2$O$_3$, SiO$_2$ and ZnO nanopar-
ticles by chemical deposition. The microscopic structures of Eu:Y$_2$O$_3$ coating films on the
Al$_2$O$_3$ nanoparticles, prepared by three different methods (ammonia-aided hydrolysis, urea-
aided hydrolysis and direct evaporation), have been compared. Eu:Y$_2$O$_3$ nanolayers coated on
alumina nanoparticles synthesized by ammonia-aided hydrolysis, and with main cubic-Y$_2$O$_3$
structure, are more homogeneous than those synthesized by direct evaporation or urea-aided
hydrolysis (Chen, X.Y. et al., 2005).

#### 6.1.2.1. *Al$_2$O$_3$ nanoparticles as cores* Eu:Y$_2$O$_3$ nanolayers (6–8 nm) coated on alumina
nanoparticles were synthesized by ammonia-aided hydrolysis followed by annealing the as-
prepared sample at 750 °C for 12 h. By isomorphic substitution, Eu$^{3+}$ ions in cubic Y$_2$O$_3$
occupy two types of sites, low symmetry sites C$_2$ and high symmetry sites S$_6$. There are
about three times as many ions at the C$_2$ site as at the S$_6$ site. Besides, structural distortion in
nanocrystals is expected because of the large surface-to-volume ratio and surface defects.
The site-selective emission spectra of the sample are compared in fig. 24. The excitation
and absorption spectra of Eu$^{3+}$ in bulk Y$_2$O$_3$ indicate that no absorption occurs at 355 nm
in the bulk crystal. However, when the coated samples were pumped by a 355 nm laser,
typical sharp emission peaks of transition from the $^5$D$_0$ of Eu$^{3+}$ ions at C$_2$ sites superim-
pose on the spectra originating from other sites such as surface sites, as shown in fig. 24a.
This is quite possibly due to (1) energy transfer from the other sites to the C$_2$ site; or (2) a
modification of energy level structure of the Eu:Y$_2$O$_3$ nanolayer induced by structure distor-
tion. The latter seems less possible because of the expected localized electronic structure
of Eu$^{3+}$ in nanocrystals. Some energy levels of Eu$^{3+}$ ions with C$_2$ site symmetry in the
nanolayer were identified from the luminescence spectra from $^5$D$_0$ and $^5$D$_1$ at 77 K, and
shown in table 1. The crystal field levels of $^5$D$_1$ were determined by the excitation spec-
tra monitoring the $^5$D$_0$ to $^7$F$_2$ transition. Most of the observed energy levels in nanocrys-
tals are in good agreement with previous assignment for bulk Y$_2$O$_3$ crystals (Chang, 1963;
Chang and Gruber, 1964), indicating that the localized electronic states remain nearly un-
changed. However, some crystal field levels missing for the bulk were identified in the
nanolayer, and some identified levels differ from the early reported values, which can be
understood because the crystal field environment of Eu$^{3+}$ in nanolayers may be modified to a
certain degree by surface defects and size confinement effects, compared to single crystals.

The excitation wavelength at 533.55 nm in fig. 24b corresponds to the transition from the
first crystal field sublevel of $^7$F$_1$ to $^5$D$_1$ for Eu$^{3+}$ ions occupying the C$_2$ sites of cubic Y$_2$O$_3$.
Fig. 24c shows the typical spectrum of overwhelming C$_2$ sites and minor other-than-C$_2$ sites
even when the laser wavelength is tuned away from the peak of the C$_2$ sites. The excitation
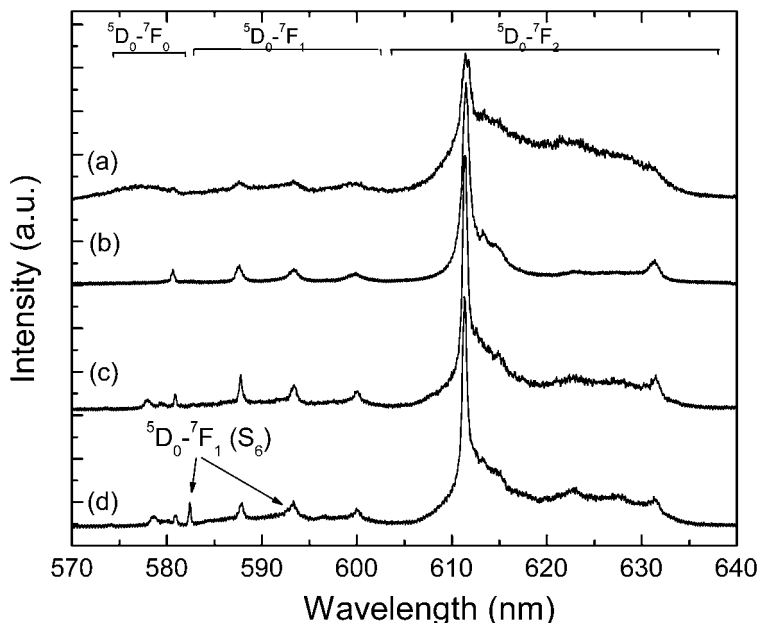
Fig. 24. The RT emission spectra of the core–shell of Eu:$Y_2O_3$/$Al_2O_3$ by site-selective excitation at $\lambda_{exc}$ = (a) 355, (b) 533.55, (c) 525.97, (d) 526.41 nm. The emission was detected using a boxcar integrator that averaged the signal from a cooled PMT with 15 µs gate and 0.3 ms delay from the pump laser pulse (redraw after (Chen, X.Y. et al., 2005)).

Table 1
Energy levels of $Eu^{3+}$ with $C_2$ site symmetry in $Y_2O_3$ nanolayers at 77 K

| Multiplet | Energy ($cm^{-1}$) | | | | | | | | |
|---|---|---|---|---|---|---|---|---|---|
| $^7F_0$ | 0 | | | | | | | | |
| $^7F_1$ | 202 | 361 | 548 | | | | | | |
| $^7F_2$ | 859 | 890 | 908 | 950 | 1378 | | | | |
| $^7F_3$ | 1848 | 1866 | 1907 | 1939 | 2022 | 2129 | 2160 | | |
| $^4F_4$ | 2590 | 2669 | 2801 | 2853 | 3016 | 3062 | 3080 | 3121 | 3182 |
| $^7F_5$ | 3647 | 3757 | 3827 | 3902 | 3941 | 4014 | 4126 | 4294 | |
| $^7F_6$ | 4791 | 5041 | | | | | | | |
| $^5D_0$ | 17216 | | | | | | | | |
| $^5D_1$ | 18936 | 18960 | 19013 | | | | | | |

Note: Only partial crystal field levels were determined for $^7F_5$ and $^7F_6$ because of the extremely weak intensity of the corresponding emission lines.

wavelength at 526.41 nm is resonant with the transition from $^7F_0$ to $^5D_1$ of $Eu^{3+}$ ions at $S_6$ sites of the same cubic structure. For $S_6$ sites, only the magnetic-dipole transitions, such as $^5D_0 \rightarrow {}^7F_1$, are allowed. Due to the coincident overlap of the excitation peak of $C_2$ sites and
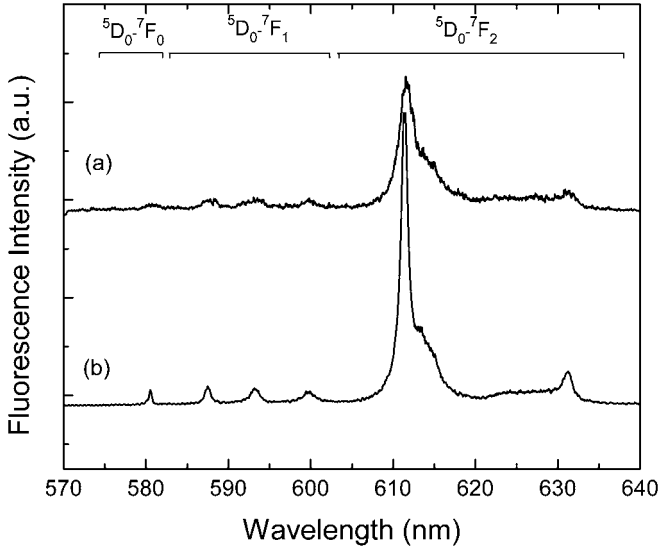
Fig. 25. The RT emission spectra of the core–shell of Eu:$Y_2O_3$/ZnO by selective excitation at $\lambda_{exc} =$ (a) 355 and (b) 533.55 nm (redraw after (Chen, X.Y. et al., 2005)).

other sites, or due to energy transfer, the emission spectrum originates mainly from $C_2$ site when the laser is tuned to excite the $Eu^{3+}$ ions at $S_6$ sites. Despite their weak intensities, two peaks from $S_6$ sites are nevertheless observable, as marked by the arrows in fig. 24d. In brief, luminescence spectra of $Eu^{3+}$ serve as probes to unambiguously demonstrate that the nanolayer has the cubic $Y_2O_3$ crystalline structure, in good agreement with the observations of TEM and XRD. That the multi-site structure is less striking than expected indicates the homogeneity of the coating layer in this sample.

The lifetime behavior for this sample has already been discussed in section 4.2.

6.1.2.2. *ZnO nanoparticles as cores* Homogeneous Eu:$Y_2O_3$ nanolayers (12–14 nm) coated on ZnO nanoparticles can be obtained by urea-aided hydrolysis at an annealing temperature of 600 °C (Chen, X.Y. et al., 2005).

The site-selective emission spectra are shown in fig. 25. They confirm that the nanolayers are homogeneous and have primarily a cubic-$Y_2O_3$ crystalline structure. The sharp emission peaks originating from $Eu^{3+}$ in this sample are exactly the same as those of Eu:$Y_2O_3$ coated on the $Al_2O_3$ core when $Eu^{3+}$ ions at $C_2$ sites are selectively excited at 533.55 nm. The emission spectrum obtained by UV laser pumping (fig. 25a) is similar to fig. 25b, but extremely weak. This similarity indicates the excellent homogeneity of the coating layer, while the decreased line intensity is perhaps closely related to the energy transfer between the ZnO core and nearby $Eu^{3+}$ ions at higher excited states.

The $^5D_0$ decay in Eu:$Y_2O_3$/ZnO fits well to a single exponential, indicating homogeneous environment around $Eu^{3+}$ as observed for the core–shell Eu:$Y_2O_3$/$Al_2O_3$ nanocomposites.
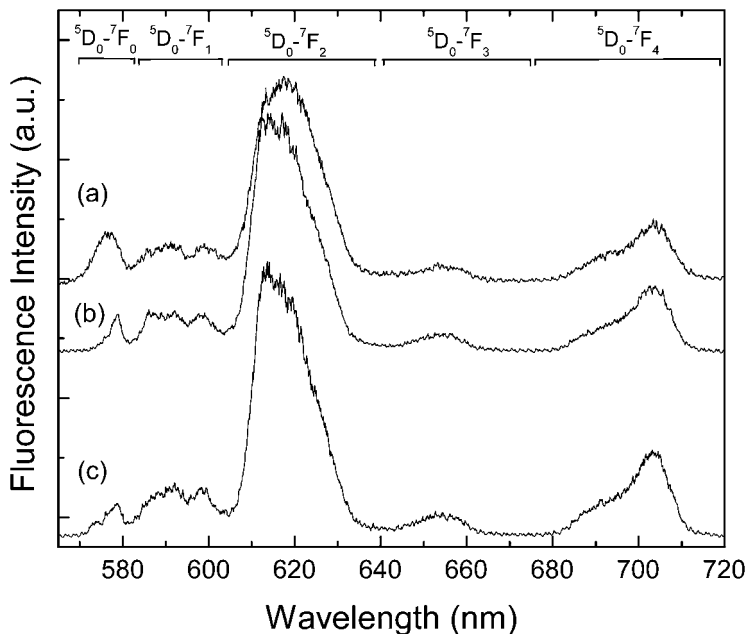
Fig. 26. The RT emission spectra of the core–shell of $SiO_2/Y_2O_3$:Eu by site-selective excitation at $\lambda_{exc}$ = (a) 355; (b) 531.78; (c) 525.88 nm (redraw after (Chen, X.Y. et al., 2005)).

The longer lifetime (1.84 ms) of $^5D_0$ in Eu:$Y_2O_3$/ZnO is most possibly due to the non-solid medium surrounding the nanoparticles that changes the effective index of refraction. The filling factor is estimated to be approximately 58%, smaller than that of Eu:$Y_2O_3$/$Al_2O_3$ (72%). The much shorter $^5D_1$ lifetime (27 µs at RT) compared to the bulk counterpart (90–120 µs) is most possibly related to the enhanced nonradiative multiphonon relaxation induced by surface effects of nanocrystals.

It is noteworthy that the optical properties of the ZnO cores are not affected by the nanocoating process. Their emission spectrum in the UV range is the same as that of uncoated nanoparticles.

6.1.2.3. *$SiO_2$ nanoparticles as cores* Eu:$Y_2O_3$ nanolayers coated on $SiO_2$ nanoparticles prepared by forced hydrolysis method turn out to be mostly amorphous even when annealed at 800 °C for 12 h, according to TEM, XRD and luminescence spectra. As shown in fig. 26 a–c, when pumped by a 355-nm laser, the $Eu^{3+}$ luminescence lines are structureless and broadened, similar to the case of $Eu^{3+}$ ions in glasses. This pattern remains unchanged even under site-selective excitation at 531.78 and 525.88 nm, respectively, confirming the high disorder of the $Eu^{3+}$ crystalline environment in nanolayers. That is, a large portion of the $Eu^{3+}$ ions resides near or at the surface of the nanocrystals. The $^5D_0$ luminescence decay shows double exponential characteristics, in accordance with the behavior of $Eu^{3+}$ in glasses. The fitted

lifetime at RT is 0.54 ms for the short component and 2.12 ms for the long component. However, no rising edge is found at the start of the decay curve. According to the setting of decay measurement, we estimate that the lifetime of $^5D_1$ should be less than 5 μs. This unusual short lifetime of $^5D_1$ indicates a very fast nonradiative relaxation from $^5D_1$ to $^5D_0$ in amorphous core–shell nanostructures.

Similarly, Liu and Hong (2005) and Liu et al. (2004) observed significantly broadened emission peaks in Eu:$M_2O_3$/$SiO_2$ (M = Y, Gd) core–shell nanoparticles, which results from size effects for nanocrystals in the shell.

6.1.2.4. *Crystallization and nanophase transition*  We have observed interesting crystallization and phase transition phenomena in the as-grown Eu:$Y_2O_3$/$Al_2O_3$ core–shell nanophosphors prepared by ammonia-aided hydrolysis (Chen et al., 2003a). It was shown that the coated films of the nanophosphors crystallize at temperatures higher than 600 °C and may be completely converted into a cubic-$Y_2O_3$ nanocrystalline layer at 750 °C. At 900 °C, phase transition occurs across the boundary between the outer coating layer and the inner core. All possible crystallographic phases, including two of solid-state laser ceramics, $YAlO_3$ (YAP), and $Y_3Al_5O_{12}$ (YAG), can be formed in the pseudo-binary $Al_2O_3$–$Y_2O_3$ nanosystem by controlling thermal annealing procedures from 600 to 900 °C, a temperature range far below the conventional solid-state reaction temperature. Obviously, the chemical dynamics in the coated nanoparticles is rather complex, and the thermodynamics for bulk systems are not applicable to the nanoscale systems.

Both XRD and luminescence spectra of the samples annealed at different temperatures were measured. As shown in fig. 27a, the XRD spectrum of the as-grown sample shows the characteristic lines of the $Al_2O_3$ phase and no evidence of the $Y_2O_3$ phase, which indicates that the coating layers of $Y_2O_3$ are amorphous in nature and most of them are actually in the form of yttrium oxyhydroxide (YOOH) (Rao, 1996). The XRD spectrum of the 600 °C sample, fig. 27b, shows clearly the intermediate phases between the crystalline and amorphous phases. It contains a large amount of crystalline phases of the alumina matrix, a small amount of cubic-$Y_2O_3$ and $Y_3O_4Cl$ crystalline phases. The impurity phase $Y_3O_4Cl$ probably formed accidentally during the co-deposition process, which no longer exists in the 750 °C-annealed sample. When the as-grown sample is heated at 750 °C for 12 h, the crystallization is almost complete. As shown in fig. 27c, the XRD spectrum displays exclusively the cubic-$Y_2O_3$ crystal phase, except features arising from the residual matrix of the alumina particles. More curiously, when the as-grown sample is annealed at 900 °C, not only crystallization occurs but also formation of new phases due to efficient transportation of Eu:$Y_2O_3$ and $Al_2O_3$ phases across the interfaces between the shell and the core of the particles. As shown in fig. 27d, approximately 62% of YAP, 38% cubic-YAG, and residual $Al_2O_3$ phases are identified in the XRD spectrum of the 900 °C annealed samples. The ratio between YAP and YAG was estimated by a least-square fit to the standard XRD spectrum. When the as-grown samples are annealed at the same temperature by a step-by-step procedure (600 °C for 10 h, then 900 °C for 10 h), as shown in fig. 27e, another crystalline structure in the $Y_2O_3$–$Al_2O_3$ system, nanocrystalline monoclinic $Y_4Al_2O_9$ (YAM), becomes the dominant component of the final product.
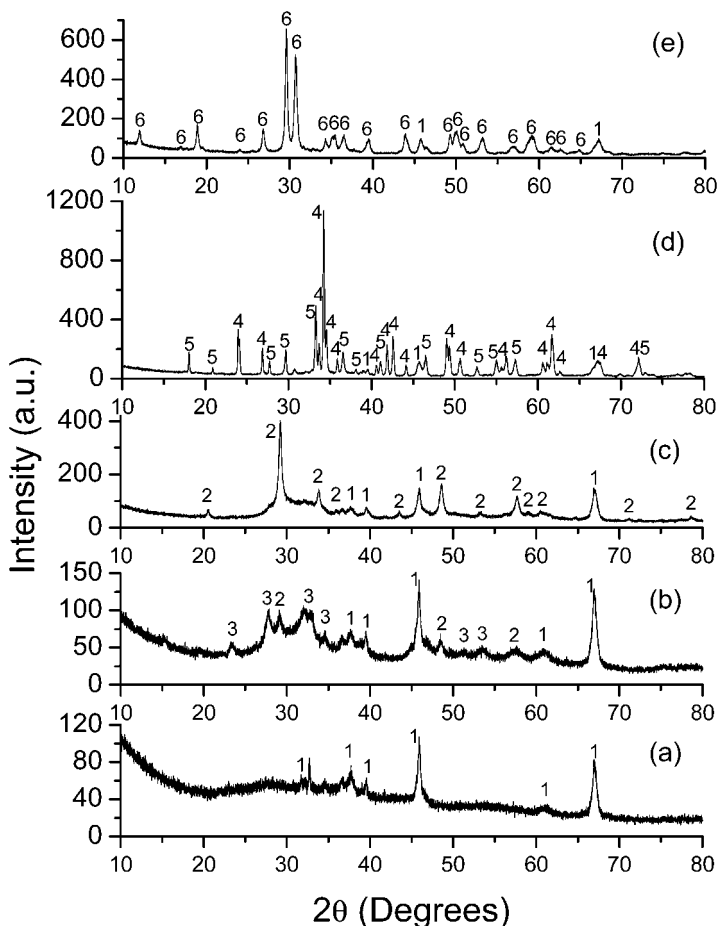
Fig. 27. XRD spectra of the Eu:$Y_2O_3$/$Al_2O_3$ samples (a) as-grown; (b) annealed at 600 °C; (c) annealed at 750 °C; (d) annealed at 900 °C; (e) annealed step by step (600 → 900 °C). All the phases are well identified according to the standard data published by ICDD. (a) $Al_2O_3$ (#77-0403); (b) $Al_2O_3$ (#77-0403) + $Y_2O_3$ (#74-0553) + $Y_3O_4Cl$ (#21-1451); (c) $Y_2O_3$ (#74-0553) + $Al_2O_3$ (#77-0403); (d) YAP (#70-1677) + YAG (#79-1891) + $Al_2O_3$ (#77-0403); (e) YAM (#34-0368) + $Al_2O_3$ (#77-0403). Values in the above parentheses are ICDD numbers. All phases are listed in the order of decreasing intensity. Lines marked by numbers 1, 2, 3, 4, 5, and 6 in the figures correspond respectively to $Al_2O_3$, $Y_2O_3$, $Y_3O_4Cl$, YAP, YAG and YAM crystalline phases (redraw after (Chen et al., 2003a)).

The crystallization behavior and nanophase transitions were further investigated by laser spectroscopy at 3.5 K. As shown in fig. 28a, no $Eu^{3+}$ luminescence is recorded for the as-grown sample possibly due to nonradiative quenching by surface defects. In the sample annealed at 600 °C (fig. 28b), however, luminescence lines are observed, but the line width is much broader than for $Eu^{3+}$ in a crystalline phase, thus suggesting that the $Eu^{3+}$ ions have amorphous environments. In contrast, the narrow peaks in the emission spectrum of the sam-
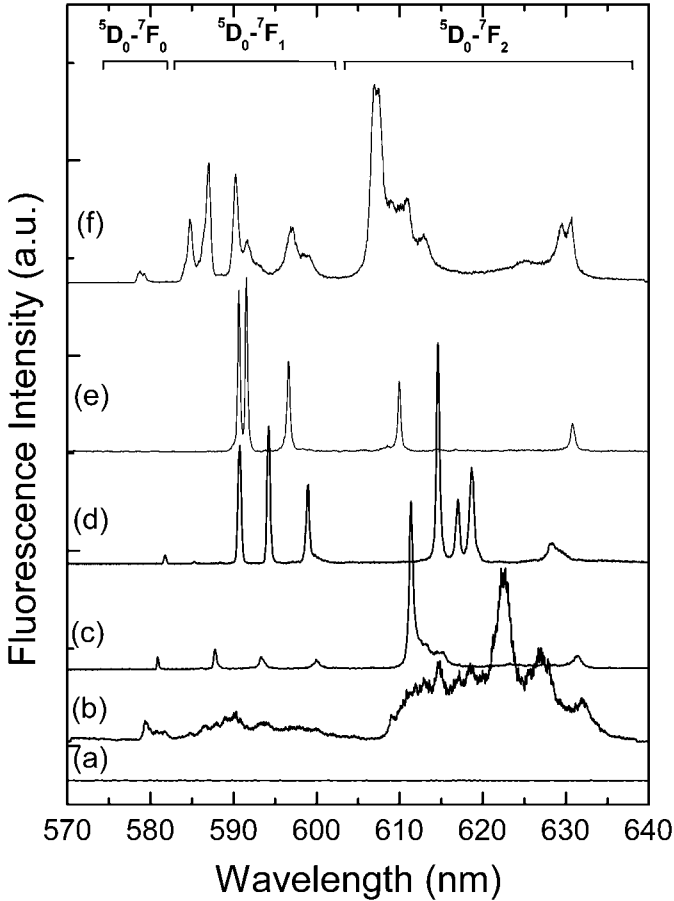
Fig. 28. Emission spectra of the (a) Eu:Y$_2$O$_3$/Al$_2$O$_3$ sample as-grown, $\lambda_{exc}$ = 355 nm; (b) sample annealed at 600 °C, $\lambda_{exc}$ = 526.98 nm; (c) sample annealed at 750 °C (Eu:Y$_2$O$_3$), $\lambda_{exc}$ = 528.09 nm; (d) sample annealed at 900 °C (Eu:YAP), $\lambda_{exc}$ = 528.43 nm; (e) sample annealed at 900 °C (Eu:YAG), $\lambda_{exc}$ = 527.60 nm; (f) sample annealed step by step (600 → 900 °C, Eu:YAM), $\lambda_{exc}$ = 526.61 nm. All spectra were measured at 3.5 K (redraw after (Chen et al., 2003a)).

ples annealed at 750 °C (fig. 28c) are typical of Eu$^{3+}$ ions in the cubic-Y$_2$O$_3$ nanocrystals. For the samples annealed at 900 °C, the spectrum shows that Eu$^{3+}$ ions occupy different lattice sites (YAP and YAG), which have been separately detected using site-selected laser excitation. When the laser was tuned to excite the Eu$^{3+}$ ions ($^5$D$_1$ ← $^7$F$_0$, 528.43 nm) in the YAP lattice (fig. 28d), only emission from Eu$^{3+}$ in YAP sites occurred. When the laser was tuned to excite the Eu$^{3+}$ ions ($^5$D$_1$ ← $^7$F$_0$, 527.60 nm) in YAG sites (fig. 28e), it excited simultaneously a few Eu$^{3+}$ ions in the YAP sites due to the coincident overlap of the excitation peak of Eu:YAP at 527.93 nm. Therefore the emission spectrum (fig. 28e) consists in contributions from two

kinds of $Eu^{3+}$ sites (overwhelming Eu:YAG site and minor Eu:YAP site). As for the sample annealed in two steps (600 and 900 °C, during 10 h each), the emission spectrum at 3.5 K, as shown in fig. 28f, indicates that $Eu^{3+}$ ions occupy at least 3 different sites in the YAM lattice. These results from optical spectroscopy independently identify the crystalline phases formed from annealing of the core–shell nanoparticles, in agreement with the XRD findings. Moreover, the spectroscopic results confirm that each of the crystalline nanophases contains $Eu^{3+}$ ions as luminescent centers.

From the crystallographic point of view, 900 °C is unusually low to enable the growth of binary crystals in the $Y_2O_3$–$Al_2O_3$ system, especially for the YAP crystalline phase. Obviously, the conventional phase diagram of the $Y_2O_3$–$Al_2O_3$ system, which indicates that bulk YAP melts incongruently and is unstable below 1600 °C (Bondar et al., 1984), is not applicable in nanoscale thermodynamics. Note that the as-grown nanocoating layers of Eu:$Y_2O_3$ on the core of alumina particles may have rather high surface energy, which could greatly lower the activation barrier for the reaction between the core and shell. Therefore, it may lead to nonequilibrium phase transition by solid–solid diffusion processes. Generally, the diffusion coefficient $D$ can be expressed as:

$$D = D_0 \exp(-\Delta E / kT),$$

where $\Delta E$ is the activation energy. The latter is closely related to the lattice binding energy, particle size and morphology (surface effects). However, a fundamental understanding of the chemical reaction and solid–solid diffusion processes of nanoscale has not been achieved yet, thus needs future studies. The above statement has been preliminarily verified by some other experiments. Particularly, when the sample annealed at 600 °C was further annealed at 900 °C for 12 h, no YAP or YAG crystalline phases was formed. If we substitute the alumina nanoparticles with the alumina coated with $SiO_2$ prepared by the hydrolysis of tetraethyl orthosilicate during the same ammonia-aided hydrolysis process, which means that the Eu:$Y_2O_3$ nanolayers are isolated by $SiO_2$ layers, no YAP or YAG phase can be found either after heating the as-grown sample at 900 °C. The reason of the former lies in that the surface layer of the 600 °C sample is not "active," while the latter is due to the fact that it cuts off the reaction paths between the outer $Y_2O_3$ layer and the inner core.

By further controlling the composition of the starting materials, deposition and heating processes, it may be possible to obtain more homogeneous and pure phases of YAP (or YAG) crystalline films coated on alumina core at lower annealing temperatures to avoid forming clusters or coalescing.

### 6.1.3. *Dopant site location in core and core–shell nanoparticles*

Lehmann et al. (2004) recently provided direct spectroscopic evidence to identify the dopant site location at the surface and in the interior of $Eu^{3+}$:$LaPO_4$ nanoparticles which were prepared in a high-boiling coordinating solvent mixture. The core–shell nanoparticles belong to the aforementioned category 1. Having compared the site-selective spectroscopy of $Eu^{3+}$:$LaPO_4$ nanocrystals with that of $Eu^{3+}$:$LaPO_4$/$LaPO_4$ core–shell nanoparticles, they concluded that surface sites could be converted completely into bulk sites by overgrowing the nanoparticles with a shell of pure $LaPO_4$.
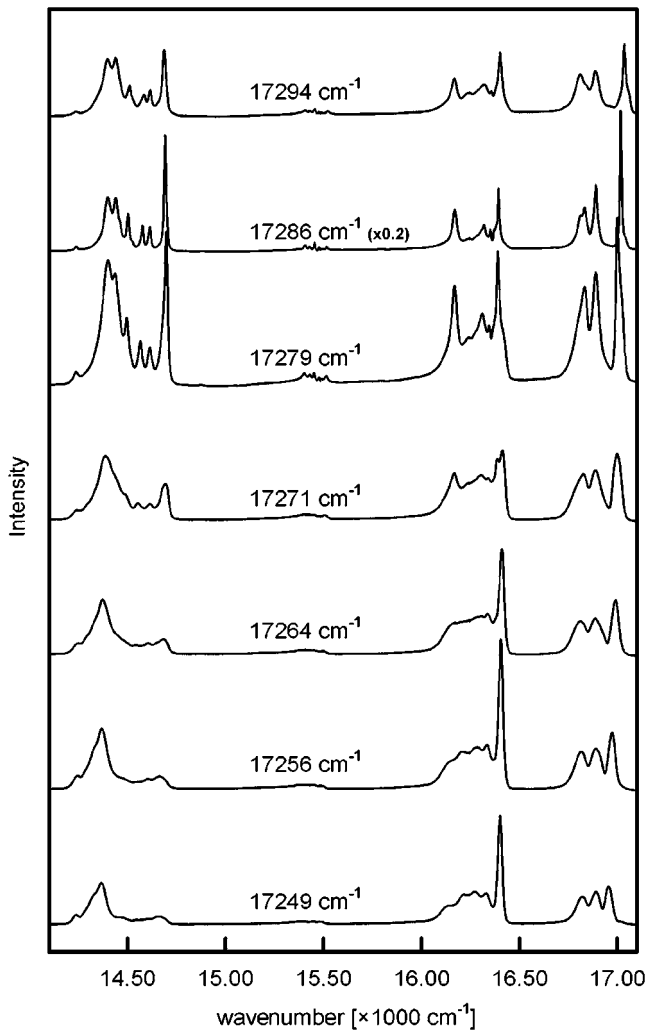
Fig. 29. Site-selective luminescence spectra of LaPO$_4$:Eu$^{3+}$ (5%) nanoparticles without shell, excited at 30 K at the wave numbers indicated. Without the LaPO$_4$ shell, the LaPO$_4$:Eu$^{3+}$ (5%) nanoparticles display spectra of additional Eu$^{3+}$ sites over the entire excitation range (redraw after (Lehmann et al., 2004)).

Fig. 29 shows the spectra of the LaPO$_4$:Eu$^{3+}$ (5%) core nanoparticles before a LaPO$_4$ shell was grown onto them. Site-selective emission spectra for the excitation at 17 294, 17 286, and 17 279 cm$^{-1}$ correspond to the L-, M-, and H-sites in the bulk counterparts respectively. For comparison, no other site than L-, M-, and H-sites were identified in the site-selective emission spectra of Eu$^{3+}$: LaPO$_4$/LaPO$_4$ core–shell nanoparticles over the whole excitation range (17 249–17 294 cm$^{-1}$), indicating that these three sites are located in the interior of

the nanoparticles. Luminescence from additional sites with comparatively broad lines appears over the whole excitation range and has its highest emission intensity under excitation at 17 256 cm$^{-1}$ for the Eu$^{3+}$ doped core nanoparticles, this feature is however absent for the core–shell nanoparticles. The disappearance of this additional emission when a shell is grown onto the nanoparticle surface clearly indicates that it is related to Eu$^{3+}$ in surface sites. To verify the origin of surface sites, Lehmann et al. prepared LaPO$_4$ nanoparticles with Eu$^{3+}$ ions located only on their surface, by reacting Eu$^{3+}$ and phosphate ions with the surface of pure LaPO$_4$ particles in a manner similar to the procedure employed for the growth of LaPO$_4$ shells. They found that surface sites in Eu$^{3+}$:LaPO$_4$ nanoparticles without shell are identical to those LaPO$_4$ nanoparticles with Eu$^{3+}$ on their surface, having the same site-selective emission spectra. They also verified that additional Eu$^{3+}$ sites in LaPO$_4$:Eu$^{3+}$ core nanoparticles are not Eu$^{3+}$ sites of EuPO$_4$ particles that nucleated in solution separately from the doped LaPO$_4$ nanoparticles, showing that the site-selective luminescence spectra of the small and large EuPO$_4$ particles are significantly different from those of the LaPO$_4$/surface Eu$^{3+}$ and LaPO$_4$:Eu$^{3+}$ nanoparticles.

The luminescence lifetimes of the major M-site and surface site of Eu$^{3+}$ (5%) in LaPO$_4$ nanoparticles without shell were measured to be 3.7 ms and 1.6–2.3 ms (multi-exponential decay) at 30 K, respectively (Lehmann et al., 2004). It is not surprising that a shorter lifetime was observed for the surface sites, because the proximity to high energy vibrations of organic ligands may quench the luminescence of Eu$^{3+}$. The luminescence lifetime of the M-site in Eu$^{3+}$:LaPO$_4$/LaPO$_4$ core–shell nanoparticles is 4.2 ms, which is slightly longer than that of the sample without shell, an evidence of improving quantum efficiency.

In brief, the core–shell technique allows one to prepare doped nanoparticles that contain no other dopant sites than those known from the corresponding bulk material, despite their small size, below 15 nm. The quantum efficiency of lanthanide ions can also be improved by surface modification of the nanoparticles.

### 6.1.4. *Core–shell structure with tunable thickness of shells*
To obtain monodisperse spherical core–shell-structured phosphors for field emission displays (FED), Wang, X.Y. et al. (2005) synthesized SiO$_2$/Y$_2$O$_3$:Eu core–shell particles by a Pechini sol–gel process, which belongs to Category 2. The thickness of Eu:Y$_2$O$_3$ shell could be easily controlled by changing the number of deposition cycles, e.g., 60 nm for three deposition cycles. The particles coated three times displayed a strong red emission typical of Eu$^{3+}$ under UV excitation at 250 nm or low-voltage electron beams (2–6 kV). The PL and CL intensity of this phosphor are tunable and depend on the number of coatings or the thickness of Eu:Y$_2$O$_3$ shells on the SiO$_2$ cores (500 nm). An increase in the thickness of the shell results in an increase in PL intensity. The PL intensity of four layer Eu:Y$_2$O$_3$-coated SiO$_2$ core–shell phosphors reaches about 80% of that of pure Eu:Y$_2$O$_3$ prepared in a similar way (Wang, H. et al., 2005). Similarly, the thickness of the Eu:YVO$_4$ shells on SiO$_2$ cores can also be tailored by varying the number of deposition cycles (Yu et al., 2005). For SiO$_2$/YVO$_4$:Eu core–shell particles (60 nm for two deposition cycles), a strong PL dominated by the $^5$D$_0$ → $^7$F$_2$ red emission at 617 nm was observed due to an efficient ET from vanadate groups to Eu$^{3+}$. The

PL intensity of four-layer $Eu^{3+}:YVO_4$ coated $SiO_2$ core–shell phosphor reached about 70% of that of the pure powdered phosphor.

The above core–shell technique may lower the cost of the final phosphors due to the partial substitution of the expensive lanthanide materials for the cheaper silica.

## 6.2. *Hollow nanospheres*

Monodispersed hollow nanospheres containing lanthanide ions have various potential applications such as high-resolution imaging and displays and biolabels due to their large surface areas and hollow characteristics. The luminescence intensity of lanthanide-doped hollow nanophosphors may be the same as that of the solid nanoparticles, while saving raw materials. Wang, X.Y. et al. (2005) reported the synthesis of $Eu^{3+}$-doped $Y_2O_3$, YOF, $La_2O_3$, LaOF hollow nanospheres by a sonochemical-assisted template route, in which the size of hollow spheres can be tailored by selecting different sized-templating carbon spheres. Emission spectra of the $Y_2O_3$, YOF, $La_2O_3$, LaOF hollow spheres doped with $Eu^{3+}$ display dominant $^5D_0 \rightarrow {}^7F_2$ red emission, similar to the bulk ones. However, no detailed spectroscopy including lifetime behavior has been reported for this kind of materials. Note that the templating carbon spheres used by Wang et al. are in the submicrometer range. The luminescence dynamics of lanthanide-doped hollow nanospheres with a size of 1–10 nm is expected to be very distinct compared to the bulk materials or solid nanoparticles, and thus deserves further study.

Liu et al. synthesized hollow nanospheres of $Eu:Y_2O_3$ (20 nm shell thickness) by etching $SiO_2/Y_2O_3:Eu$ core–shell nanoparticles with NaOH solution (Liu and Hong, 2005). No significant difference in emission spectrum was observed for both the hollow nanospheres and their core–shell counterparts.

Interestingly, a series of $LnF_3$ (Ln = Y, La, Pr, Nd, Sm) and $Ln(OH)_3$ (Ln = Y, Sm, Eu, Gd, Tb, Dy, Ho, and Er) fullerene-like nanoparticles have been successfully synthesized by a low-temperature (80–180 °C) hydrothermal method (Wang and Li, 2003). Wang and Li (2003) observed that the formation of fullerene-like nanoparticles is closely related to the hexagonal structure of the corresponding samples, since comparatively fewer fullerene-like nanoparticles are observed in the samples of orthorhombic $YF_3$ and no fullerene-like nanoparticles appear in the orthorhombic samples of other $LnF_3$ (Ln = Eu, Gd, Tb, Dy, Ho, Er, Tm, Yb, and Lu). The hydroxide fullerene-like nanoparticles usually coexist with nanotubes in the final product. The hollow-sphere nature of these samples was further confirmed through Brunauer–Emmett–Teller (BET) surface area measurement, since these samples exhibit a larger surface area than the bulk crystals. The size of hollow spheres can also be tuned via the control of the hydrothermal temperature. For example, the average diameters of $PrF_3$ fullerene-like nanoparticles synthesized at 120 °C were 10 nm, while 30–50 nm for those synthesized at 180 °C. So far no optical properties of these materials have been reported.

## 6.3. *Nanotubes and nanowires*

The optical properties of lanthanide ions in some 1D nanomaterials may behave differently from those of isotropic nanoparticles and bulk materials. Nanowires (NWs) of $Eu:LaPO_4$ phosphors with a diameter of 10–20 nm and a length of several hundred nanometers were

synthesized by the hydrothermal method (Yu et al., 2004b). Site-selective emission spectra indicated that $Eu^{3+}$ ions occupy an additional site besides the main site observed in nanoparticles and microcrystals. The luminescent quantum efficiency of $^5D_0 \rightarrow \, ^7F_J$ transitions, reaches 59%, and is remarkably enhanced compared to that of the corresponding nanoparticles (38%), micrometer particles (47%) and micrometer rods (49%). Curiously, the radiative transition rate from $^5D_1$ (or $^5D_0$) in NWs increases at least 1.5 times over that in nanoparticles and microcrystals. Obviously, the shortened lifetime in NWs cannot be explained by the correction of effective refraction of index as discussed in section 4.2, which leads to a lengthened radiative lifetime. The increase of the radiative transition rate in NWs was therefore attributed to the variation of electric or magnetic dipole field caused by the shape anisotropy (Yu et al., 2004b). In a subsequent report, the same authors reported a shorter $^5D_0$ lifetime with the increasing of length-to-width ratio (LWR) for $Eu:LaPO_4$ NWs. That is, the lifetime of $^5D_0$ decreased from 2.41 ms to 1.70 ms when the LWR of NWs increases from 10 to 30 (Yu et al., 2004a). This trend is in agreement with the above assumption since a large LWR corresponds to larger shape anisotropy. However, no similar trend was observed for cubic $Eu^{3+}:Y_2O_3$ nanotubes (NTs) and NWs synthesized through a similar hydrothermal method at various temperatures (Bai et al., 2005). The nanocrystals prepared at 130 °C yielded NTs with wall thickness of 5–10 nm and outer diameter of 20–40 nm. The nanocrystals prepared at 170 and 180 °C yielded NWs with diameters of $\sim$100 and $\sim$300 nm, respectively. The observed lifetime of $^5D_0$ is 1.36 ms in NTs, 1.91 ms in 100-nm NWs, and 1.65 ms in 300-nm NWs, significantly longer than that in bulk counterparts (0.9 ms). Therefore more evidence including theoretical models is required to confirm the relationship between the shape anisotropy and observed lifetime. Yu et al. (2004a, 2004b) neglected the nonradiative transition from $^5D_0$ and assumed that the observed lifetime of $^5D_0$ is the radiative lifetime since it hardly varied with temperature. However, one should be cautious with the above assumption since the constancy of the observed lifetime with temperature simply reflects that nonradiative de-excitation processes are not temperature-dependent. For instance, the multiphonon relaxation due to the adsorbed impurities (such as water or $OH^-$ with high frequency phonon modes) on the surface of nanoparticles may quench the luminescence from $^5D_0$, however, due to the high phonon energy involed in this quenching process, the resulting observed lifetime shows very weak temperature-dependence. Usually an IR absorption spectrum is needed to determine if such impurity exists in nanoparticles.

Bai et al. (2005) observed a phonon sideband with a frequency shift of 40–50 $cm^{-1}$ located on the low-energy side of the $^5D_0 \leftarrow \, ^7F_0$ zero-phonon line (ZPL) in the 77 K excitation spectrum of $Eu^{3+}:Y_2O_3$ NTs and NWs. However, vibronic sidebands generally appears at the high-energy side of the ZPL in the low-temperature excitation spectra since the vibronic transition involving the creation of a phonon with the annihilation of a photon is much more favored than the annihilation of a phonon at low temperature. The origin of this anomaly sideband remains unknown.

Wang et al. (2003) observed that NTs of lighter lanthanide hydroxide compounds with thinner diameters can be synthesized by the hydrothermal method, while those of the heavier lanthanide hydroxides are obtained with bigger diameters under similar experimental conditions. For example, NTs of $Ln(OH)_3$ (Ln = Y, Yb, Tm, Er, Ho, Dy, Tb) have diameters from around

tens of nanometers to more than one hundred nanometers, while those of lighter lanthanides (Gd, Eu, Sm, Nd, Pr, La) have diameters less than 20 nm. They attributed this difference to the gradual changes in ionic radius of Ln ions and to crystal field changes. Interestingly these NTs have open ends with excellent hydrophilic properties, which open the possibility for the wetting processing of the inner parts with capillary action as the driving force. These NTs can also be further chemically modified to form lanthanide-doped oxysulfide NTs. Excitation and emission spectra of Eu:$Y_2O_2S$ NTs showed typical $S^{2-}$–$Eu^{3+}$ CT band and emission lines of $Eu^{3+}$, respectively. However the assignment of $Er^{3+}$ emission bands in the upconversion and down-conversion spectra of Er, Yb:$Y_2O_2S$ NTs is questionable since either spectrum did not exhibit the typical emission lines of $Er^{3+}$ as observed in other similar nanocrystals (Wang et al., 2003).

### 6.4. *Nanosheets, nanodisks and others*

RE doped in some other nanostructures such as nanosheets and nanodisks were occasionally reported. Jiang et al. (2004) synthesized uniform donut-like assemblies of $YBO_3$:$Eu^{3+}$ via a simple hydrothermal method in absence of any surfactant or template. These microparticles were actually composed of orderly aggregated nanosheets and exhibited improved chromaticity compared with the bulk or the sample calcined at high temperatures. This improvement of chromaticity (higher red/orange ratio in the emission) was ascribed to the distinct microstructure of the assembly, with building blocks-nanosheets having large surface area and high surface energy. Thus results in a high degree of disorder and in lower crystal field symmetry around $Eu^{3+}$ ions. As previously mentioned, well-dispersed $Y_2O_3$:$Eu^{3+}$ nanocrystals could be prepared via a non-hydrolyic route at low temperature (230 °C) (Wang, H.Z. et al., 2005). Similarly, nanodisks of $Y_2O_3$:$Eu^{3+}$ could be synthesized under higher reaction temperature (>270 °C) and without the addition of trioctylphosphine oxide. The nanodisks self-assemble to form (1–3)-dimensional structures under different reaction times.

Very recently, Wang, X. et al. (2005) have developed a general strategy for the fabrication of a series of functional nanocrystals including noble metal, magnetic/dielectric, semiconducting, lanthanide luminescent, biomedical, organic optoelectronic semiconducting and conducting polymer nanoparticles. Their method is based on a general phase transfer and separation mechanism occurring at the interfaces of the liquid–solid-solution (LSS) phases present during the synthesis. In particular, LSS phase-transfer and separation approaches have been applied to synthesize nearly monodisperse lanthanide luminescent nanocrystals. The nanoparticles of $NaYF_4$, $YF_3$, $LaF_3$ and $YbF_3$ are spherical with diameters of 4–12 nm. The $YF_3$ nanoparticles have a rice-like shape with a diameter of 100 nm and length of 500 nm (composed of uniform nanocrystals with a diameter of 5 nm). The $Ln(OH)_3$ nanoparticles are composed of uniform nanorods with a diameter 3–15 nm. When doped with different lanthanide ions these nanocrystals can function as luminescence nanocrystals. The green upconversion of Yb/Er co-doped $NaYF_4$ nanocrystals has been demonstrated upon excitation with a 980-nm laser. Therefore, this LSS strategy provides a simple and convenient route to prepare abundant novel nanostructures containing lanthanide ions for a variety of applications.

## 7. Summary

Research and development of nanoscale luminescent materials are part of the rapidly advancing nanoscience and nanotechnology. Lanthanides, specifically, divalent europium, $Eu^{2+}$, and many trivalent ions such as $Ce^{3+}$, $Pr^{3+}$, $Nd^{3+}$, $Eu^{3+}$, $Tb^{3+}$, $Er^{3+}$, $Tm^{3+}$, and $Yb^{3+}$ have the ability to emit light in NIR, visible and near UV spectral ranges. The electronic properties of these ions in bulk materials have been extensively studied for more than half of a century. Their spectroscopic properties and luminescent dynamics are well understood. Because of the localized electronic states and relatively weak ion–phonon interactions, the spectroscopic properties of the divalent and trivalent lanthanide ions in nanocrystals do not differ significantly from those in bulk crystals. Therefore, doping luminescent lanthanide ions into nanostructures (nanoparticles, thin films, or nanowires) is an ideal approach to developing nanophosphors for various applications. Coating of lanthanide nanophosphors on blue LEDs for white light emission is currently considered for future energy saving lighting devices meant to replace fluorescent lamps. Research on doping of luminescent lanthanide ions into nanosemiconductors many lead to the creation of a new series of highly efficient electro- and photo-luminescent materials.

We have summarized the theoretical principles and models that provide quantitative interpretations of the optical spectra of lanthanide ions in solids in terms of crystal field interactions. For lanthanide ions in nanocrystals of less 5 nm, the crystal field splitting of the electronic energy levels becomes size dependent because of modification of the long-range electrostatic interactions. Since the 5d orbitals extend to a much longer distance than the 4f orbitals do, lanthanide ions in $4f^n 5d$ states exhibit much stronger size dependence. This effect has been observed in the $4f^6 5d$–$4f^7$ electronic transition of $Eu^{2+}$ in various nanostructures. It is possible that in very small nanostructures, ion–lattice interaction may induce stronger 4f/5d mixing than that in bulk crystals, thus increase the cross section of electronic transitions and the luminescence efficiency. Such a mechanism needs further studies. Although, the effects of surface defects cannot be addressed theoretically in detail, inhomogeneous line broadening is generally anticipated in the optical spectra of lanthanide ions in nanoparticles.

Numerous studies have shown that nanoscale size variation has significant effects on the excited state dynamics including radiative and nonradiative lifetimes, energy transfer, and thermalization phenomena. Many of these effects can be interpreted as consequences of modified ion–phonon interactions. We have shown that in nanocrystals, the phonon density of states is no longer continuous, and most of the low-energy phonon (lattice vibration) modes are absent. As a result, the ion–phonon interaction is restricted. In other words, a size confinement is applied to electron–phonon interactions for lanthanide ions in nanocrystals. Such a size confinement has a direct impact on the nonradiative phonon relaxation and phonon-assisted energy transfer processes. Therefore, one expects to observe changes in luminescence decay times, energy transfer efficiency, and efficiency of upconversion luminescence. At low temperatures, due to the cutoff in low-energy phonon states, anomalous hot bands may appear in the luminescence and excitation spectra of lanthanide ions in nanocrystals.

In addition to nanophenomena induced by confinement of the phonon density of states, luminescence decay time and efficiency of lanthanide ions in nanomaterials are also influenced

by variation of local environments that affect the spontaneous photon emission. It has been shown that the variation of index of refraction and the coherent interference of local electric fields at the boundary of nanoparticles must be considered in the evaluation of luminescence intensity and radiative lifetime.

Due to size confinement on electronic interactions and density of phonon states, nano-structured materials exhibit distinct optical, magnetic and thermal properties in comparison with their bulk counterparts. Currently, there is growing interest for understanding how the confinement and other nanoscale mechanisms of electronic interactions in nanophosphors affect luminescence efficiency and photodynamics for such applications as three-dimensional displays, high-performance light emitting devices, and highly sensitive bioassays.

## Acknowledgements

## References

Andreev, T., Hori, Y., Biquard, X., Monroy, E., Jalabert, D., Farchi, A., Tanaka, M., Oda, O., Dang, L.S., Daudin, B., 2005a. Phys. Rev. B **71**, 115310.

Andreev, T., Monroy, E., Gayral, B., Daudin, B., Liem, N.Q., Hori, Y., Tanaka, M., Oda, O., Dang, D.L.S., 2005b. Appl. Phys. Lett. **87**, 021906.

Auzel, F., 2005. In: Liu, G.K., Jacquier, B. (Eds.), Spectroscopic Properties of Rare Earths in Optical Materials. Springer, Berlin, p. 266.

Bai, X., Song, H.W., Yu, L.X., Yang, L.M., Liu, Z.X., Pan, G.H., Lu, S.Z., Ren, X.G., Lei, Y.Q., Fan, L.B., 2005. J. Phys. Chem. B **109**, 15236.

Bang, J., Yang, H., Holloway, P.H., 2005. J. Chem. Phys. **123**, 084709.

Bar, S., Huber, G., Gonzalo, J., Perea, A., Climent, A., Paszti, F., 2003. Mater. Sci. Eng. B Solid **105**, 30.

Bar, S., Huber, G., Gonzalo, J., Perea, A., Munz, M., 2005. Appl. Phys. A Matter **80**, 209.

Barnes, M.D., Mehta, A., Thundat, T., Bhargava, R.N., Chhabra, V., Kulkarni, B., 2000. J. Phys. Chem. B **104**, 6099.

Bartko, A.P., Peyser, L.A., Dickson, R.M., Mehta, A., Thundat, T., Bhargava, R., Barnes, M.D., 2002. Chem. Phys. Lett. **358**, 459.

Benner, R.E., Barber, P.W., Owen, J.F., Chang, R.K., 1980. Phys. Rev. Lett. **44**, 475.

Bhargava, R.N., 1996. J. Lumin. **70**, 85.

Bhargava, R.N., 1997. J. Lumin. **72** (4), 46.

Bhargava, R.N., Gallagher, D., Hong, X., Nurmikko, A., 1994a. Phys. Rev. Lett. **72**, 416.

Bhargava, R.N., Gallagher, D., Welker, T., 1994b. J. Lumin. **60** (1), 275.

Blasse, G., Grabmaier, B.C., 1994. Luminescent Materials. Springer-Verlag, Berlin.

Bol, A.A., Meijerink, A., 1998. Phys. Rev. B **58**, R15997.

Bol, A.A., Van Beek, R., Meijerink, A., 2002. Chem. Mater. **14**, 1121.

Bondar, I.A., Koroleva, L.N., Bezruk, E.T., 1984. Inorg. Mater. **20**, 214.

Brus, L.E., 1986. J. Phys. Chem. **90**, 2555.

Capobianco, J.A., Vetrone, F., Boyer, J.C., Speghini, A., Bettinelli, M., 2002. J. Phys. Chem. B **106**, 1181.

Carnall, W.T., Goodman, G.L., Rajnak, K., Rana, R.S., 1988. A systematic analysis of the spectra of the lanthanides doped into single crystal LaF$_3$, in: Argonne National Laboratory Report No. ANL-88-8, Argonne, Illinois.

Carnall, W.T., Goodman, G.L., Rajnak, K., Rana, R.S., 1989. J. Chem. Phys. **90**, 3443.

Chang, N.C., 1963. J. Appl. Phys. **34**, 3500.

Chang, N.C., Gruber, J.B., 1964. J. Chem. Phys. **41**, 3227.

Chen, L., Zhang, J., Lu, S., Ren, X., Wang, X., 2005. Chem. Phys. Lett. **409**, 144.

Chen, W., Malm, J.O., Zwiller, V., Huang, Y.N., Liu, S.M., Wallenberg, R., Bovin, J.O., Samuelson, L., 2000. Phys. Rev. B **61**, 11021.

Chen, W., Malm, J.O., Zwiller, V., Wallenberg, R., Bovin, J.O., 2001. J. Appl. Phys. **89**, 2671.

Chen, W., Bovin, J.O., Joly, A.G., Wang, S.P., Su, F.H., Li, G.H., 2004a. J. Phys. Chem. B **108**, 11927.

Chen, W., Joly, A.G., Malm, J.O., Bovin, J.O., 2004b. J. Appl. Phys. **95**, 667.

Chen, W., Joly, A.G., Malm, J.O., Bovin, J.O., 2004c. J. Appl. Phys. **95**, 667.

Chen, W., Aguekian, V.F., Vassiliev, N., Serov, A.Y., Filosofov, N.G., 2005. J. Chem. Phys. **123**, 124707.

Chen, X.Y., Yang, L., Cook, R.E., Skanthakumar, S., Shi, D., Liu, G.K., 2003a. Nanotechnology **14**, 670.

Chen, X.Y., Zhuang, H.Z., Liu, G.K., Li, S., Niedbala, R.S., 2003b. J. Appl. Phys. **94**, 5559.

Chen, X.Y., Skanthakumar, S., Liu, G.K., Yang, L., Shi, D., Lian, J., Wang, L.M., Cook, R.E., 2005. In: Dirote, E.V. (Ed.), Nanotechnology Focus. Nova Science Publishers, New York, pp. 141–173.

Chen, X.Y., Liu, Y.S., Luo, W.Q., Ma, E., 2006. Unpublished results.

Chew, H., 1988. Phys. Rev. A **38**, 3410.

Condon, E.U., Shortley, G.H., 1963. The Theory of Atomic Spectra. Cambridge Univ. Press, Cambridge.

Crosswhite, H.M., Crosswhite, H., 1984. J. Opt. Soc. Am. B Opt. Phys. **1**, 246.

Del Castillo, J., Rodriguez, V.D., Yanes, A.C., Mendez-Ramos, J., Torres, M.E., 2005. Nanotechnology **16**, S300.

Dexter, D.L., 1953. J. Chem. Phys. **21**, 836.

Dhanaraj, J., Jagannathan, R., Kutty, T.R.N., Lu, C.H., 2001. J. Phys. Chem. B **105**, 11098.

Dieke, G.H., 1968. Spectra and Energy Levels of Rare Earth Ions in Crystals. Wiley, New York.

Förster, T., 1948. Ann. Phys. (Germany) **2**, 55.

Franzo, G., Vinciguerra, V., Priolo, F., 1999. Appl. Phys. A **69**, 3.

Gedanken, A., Reisfeld, R., Sominski, E., Palchik, O., Koltypin, Y., Panczer, G., Gaft, M., Minti, H., 2000a. J. Phys. Chem. B **104**, 7057.

Gedanken, A., Reisfeld, R., Sominski, L., Zhong, Z., Koltypin, Y., Panczer, G., Gaft, M., Minti, H., 2000b. Appl. Phys. Lett. **77**, 945.

Gersten, J., Nitzan, A., 1981. J. Chem. Phys. **75**, 1139.

Girard, C., Martin, O.J.F., Dereux, A., 1995. Phys. Rev. Lett. **75**, 3098.

Goldburt, E.T., Kulkarni, B., Bhargava, R.N., Taylor, J., Libera, M., 1997. J. Lumin. **72–74**, 190.

Heer, S., Kompe, K., Güdel, H.U., Haase, M., 2004. Adv. Mater. **16**, 2102.

Holstein, T., Lyo, S.K., Orbach, R., 1976. Phys. Rev. Lett. **36**, 891.

Hori, Y., Biquard, X., Monroy, E., Jalabert, D., Enjalbert, F., Dang, L.S., Tanaka, M., Oda, O., Daudin, B., 2004. Appl. Phys. Lett. **84**, 206.

Hori, Y., Andreev, T., Biquard, X., Monroy, E., Jalabert, D., Dang, L.S., Tanaka, M., Oda, O., Daudin, B., 2005. Phys. Status Solidi C **2**, 2373.

Huber, D.L., 1981. In: Yen, W.M., Selzer, P.M. (Eds.), Laser Spectroscopy of Solids. Springer, New York, p. 83.

Hüfner, S., 1978. Optical Spectra of Transparent Rare Earth Compounds. Academic Press, New York.

Ihara, M., Igarashi, T., Kusunoki, T., Ohno, K., 2000. J. Electrochem. Soc. **147**, 2355.

Inokuti, M., Hirayama, F., 1965. J. Chem. Phys. **43**, 1978.

Ishizumi, A., Kanemitsu, Y., 2005. Appl. Phys. Lett. **86**, 253106.

Jeon, S., Braun, P.V., 2003. Chem. Mater. **15**, 1256.

Ji, J.M., Senter, R.A., Tessler, L.R., Back, D., Winter, C.H., Coffer, J.L., 2004. Nanotechnology **15**, 643.

Jiang, X.C., Sun, L.D., Yan, C.H., 2004. J. Phys. Chem. B **108**, 3387.

Judd, B.R., 1962. Phys. Rev. **127**, 750.

Judd, B.R., 1963a. Proc. Phys. Soc. (London) **82**, 874.

Judd, B.R., 1963b. Operator Techniques in Atomic Spectroscopy. McGraw–Hill, New York.

Kik, P.G., Polman, A., 2001. Mater. Sci. Eng. B Solid **81**, 3.

Kohls, M., Bonanni, M., Spanhel, L., Su, D., Giersig, M., 2002. Appl. Phys. Lett. **81**, 3858.

Kompe, K., Borchert, H., Storz, J., Lobo, A., Adam, S., Moller, T., Haase, M., 2003. Angew. Chem. Int. Ed. **42**, 5513.

Lamb, H., 1882. Proc. Math. Soc. London **13**, 187.

Lebbou, K., Perriat, P., Tillement, O., 2005. J. Nanosci. Nanotech. **5**, 1448.

Lehmann, O., Meyssamy, H., Kompe, K., Schnablegger, H., Haase, M., 2003. J. Phys. Chem. B **107**, 7449.

Lehmann, O., Kompe, K., Haase, M., 2004. J. Am. Chem. Soc. **126**, 14935.

Liu, G., Jacquier, B., 2005. Spectroscopic Properties of Rare Earths in Optical Materials. Springer, Berlin.

Liu, G.K., Wu, X., 1994. J. Lumin. **58**, 365.

Liu, G.K., Zhuang, H.Z., Chen, X.Y., 2002. Nano Lett. **2**, 535.

Liu, G.K., Chen, X.Y., Huang, J., 2003a. Mol. Phys. **101**, 1029.

Liu, G.K., Chen, X.Y., Zhuang, H.Z., 2003b. J. Solid State Chem. **171**, 123.

Liu, G.K., Chen, X.Y., Zhuang, H.Z., Li, S., Niedbala, R.S., 2003c. J. Appl. Phys. **94**, 5559.

Liu, G.X., Hong, G.Y., 2005. J. Solid State Chem. **178**, 1647.

Liu, G.X., Hong, G.Y., Sun, D.X., 2004. J. Colloid Interface Sci. **278**, 133.

Liu, S.M., Xu, Z., Liu, F.Q., Xu, X.R., 2001. J. Chin. Rare Earth Soc. **19**, 566.

Liu, S.M., Liu, F.Q., Guo, H.Q., Zhang, Z.H., Wang, Z.G., 2001a. Chin. J. Semiconduct. **22**, 418.

Liu, S.M., Liu, F.Q., Wang, Z.G., 2001b. Chem. Phys. Lett. **343**, 489.

Ma, E., Hu, Z., Wang, Y., Bao, F., 2006. J. Lumin. **118**, 131.

MacFarlane, R.M., Shelby, R.M., 1987. In: Kaplyanskii, A.A., MacFarlane, R.M. (Eds.), Spectroscopy of Solids Containing Rare Earth Ions. North-Holland, Amsterdam, p. 51.

Matsuura, D., 2002. Appl. Phys. Lett. **81**, 4526.

McCumber, D.E., Sturge, M.D., 1963. J. Appl. Phys. **34**, 1682.

Mercier, B., Dujardin, C., Ledoux, G., Louis, C., Tillement, O., Perriat, P., 2004. J. Appl. Phys. **96**, 650.

Meltzer, R.S., Hong, K.S., 2000. Phys. Rev. B **61**, 3396.

Meltzer, R.S., Feofilov, S.P., Tissue, B., Yuan, H.B., 1999. Phys. Rev. B **60**, R14012.

Meltzer, R.S., Yen, W.M., Zheng, H.R., Feofilov, S.P., Dejneka, M.J., Tissue, B.M., Yuan, H.B., 2001. Phys. Rev. B **6410**, 100201.

Meltzer, R.S., Yen, W.M., Zheng, H.R., Feofilov, S.P., Dejneka, M.J., 2002. Phys. Rev. B **66**, 224202.

Miyakawa, T., Dexter, D.L., 1970. Phys. Rev. B **1**, 2961.

Murase, N., Jagannathan, R., Kanematsu, Y., Watanabe, M., Kurita, A., Hirata, K., Yazawa, T., Kushida, T., 1999. J. Phys. Chem. B **103**, 754.

Newman, D.J., 1973. Proc. Rare Earth Res. Conf., 10th **2**, 1135.

Newman, D.J., Ng, B., 2000. In: Newman, D.J., Ng, B. (Eds.), Crystal Field Handbook. Cambridge Univ. Press, Cambridge, p. 140.

Nogami, M., Enomoto, T., Hayakawa, T., 2002. J. Lumin. **97**, 147.

Patra, A., Sominska, E., Ramesh, S., Koltypin, Y., Zhong, Z., Minti, H., Reisfeld, R., Gedanken, A., 1999. J. Phys. Chem. B **103**, 3361.

Patra, A., Friend, C.S., Kapoor, R., Prasad, P.N., 2003a. Appl. Phys. Lett. **83**, 284.

Patra, A., Friend, C.S., Kapoor, R., Prasad, P.N., 2003b. Chem. Mater. **15**, 3650.

Pol, V.G., Reisfeld, R., Gedanken, A., 2002. Chem. Mater. **14**, 3920.

Prasad, P.N., 2004. Nanophotonics. Wiley, New York.

Priolo, F., Franzo, G., Iacona, F., Pacifici, D., Vinciguerra, V., 2001. Mater. Sci. Eng. B **81**, 9.

Qi, Z.M., Shi, C.S., Zhang, W.W., Zhang, W.P., Hu, T.D., 2002. Appl. Phys. Lett. **81**, 2857.

Que, W., Zhou, Y., Kam, C.H., Lam, Y.L., Chan, Y.C., Gan, L.H., Deen, G.R., 2001. MRS Bull. **36**, 889.

Rajnak, K., Wybourne, B.G., 1964. J. Chem. Phys. **41**, 565.

Rao, R.P., 1996. J. Electrochem. Soc. **143**, 189.

Reid, M.F., 2000. In: Newman, D.J., Ng, B. (Eds.), Crystal Field Handbook. Cambridge Univ. Press, Cambridge, p. 190.

Riseberg, L.A., Moos, H.W., 1967. Phys. Rev. Lett. **25**, 1423.

Riseberg, L.A., Moos, H.W., 1968. Phys. Rev. **174**, 429.

Riwotzki, K., Meyssamy, H., Kornowski, A., Haase, M., 2000. J. Phys. Chem. B **104**, 2824.

Riwotzki, K., Meyssamy, H., Schnablegger, H., Kornowski, A., Haase, M., 2001. Angew. Chem. Int. Ed. **40**, 573.

Schmechel, R., Kennedy, M., Von Seggern, H., Winkler, H., Kolbe, M., Fischer, R.A., Li, X.M., Benker, A., Winterer, M., Hahn, H., 2001. J. Appl. Phys. **89**, 1679.

Schmidt, T., Muller, G., Spanhel, L., Kerkel, K., Forchel, A., 1998. Chem. Mater. **10**, 65.

Schniepp, H., Sandoghdar, V., 2002. Phys. Rev. Lett. **89**, 257403.

Sharma, P.K., Jilavi, M.H., Nass, R., Schmidt, H., 1999. J. Lumin. **82**, 187.

Smith, B.A., Zhang, J.Z., Joly, A., Liu, J., 2001. Phys. Rev. B **62**, 2021.

Tamura, A., 1995. Phys. Rev. B **52**, 2688.

Tanaka, M., Qi, J., Masumoto, Y., 2000. J. Lumin. **87–89**, 472.

Tanner, P.A., 2005. J. Nanosci. Nanotech. **5**, 1455.

Tissue, B.M., 1998. Chem. Mater. **10**, 2837.

Van De Rijke, F., Zijlmans, H., Li, S., Vail, T., Raap, A.K., Niedbala, R.S., Tanke, H.J., 2001. Nat. Biotechnol. **19**, 273.

van Dijken, A., Makkinje, J., Meijerink, A., 2001. J. Lumin. **92**, 323.

Vetrone, F., Boyer, J.C., Capobianco, J.A., Speghini, A., Bettinelli, M., 2002. J. Phys. Chem. B **106**, 5622.

Vetrone, F., Boyer, J.C., Capobianco, J.A., Speghini, A., Bettinelli, M., 2004. J. Appl. Phys. **96**, 661.

Wakefield, G., Holland, E., Dobson, P.J., Hutchison, J.L., 2001. Adv. Mater. **13**, 1557.

Wang, H., Lin, C.K., Liu, X.M., Lin, J., Yu, M., 2005. Appl. Phys. Lett. **87**, 181907.

Wang, H.Y., Wang, R.J., Sun, X.M., Yan, R.X., Li, Y.D., 2005. Mater. Res. Bull. **40**, 911.

Wang, H.Z., Uehara, M., Nakamura, H., Miyazaki, M., Maeda, H., 2005. Adv. Mater. **17**, 2506.

Wang, L.Y., Yan, R.X., Hao, Z.Y., Wang, L., Zeng, J.H., Bao, H., Wang, X., Peng, Q., Li, Y.D., 2005. Angew. Chem. Int. Ed. **44**, 6054.

Wang, W., Wu, M., Liu, G.K., 2007. Spectrosc. Lett. **40**, 1.

Wang, X., Li, Y.D., 2003. Angew. Chem. Int. Ed. **42**, 3497.

Wang, X., Sun, X.M., Yu, D.P., Zou, B.S., Li, Y.D., 2003. Adv. Mater. **15**, 1442.

Wang, X., Kong, X.G., Shan, G.Y., Yu, Y., Sun, Y.J., Feng, L.Y., Chao, K.F., Lu, S.Z., Li, Y.J., 2004. J. Phys. Chem. B **108**, 18408.

Wang, X., Zhuang, J., Peng, Q., Li, Y.D., 2005. Nature **437**, 121.

Wybourne, B.G., 1965. Spectroscopic Properties of Rare Earths. Interscience, New York.

Xiao, S., Yang, X., Liu, Z., Yan, X.H., 2006. Opt. Mater. **28**, 285.

Yan, R.X., Li, Y.D., 2005. Adv. Funct. Mater. **15**, 763.

Yanes, A.C., Del Castillo, J., Torres, M., Peraza, J., Rodriguez, V.D., Mendez-Ramos, J., 2004. Appl. Phys. Lett. **85**, 2343.

Yang, H.S., Feofilov, S.P., Williams, D.K., Milora, J.C., Tissue, B.M., Meltzer, R.S., Dennis, W.M., 1999a. Physica B **263**, 476.

Yang, H.S., Hong, K.S., Feofilov, S.P., Tissue, B.M., Meltzer, R.S., Dennis, W.M., 1999b. J. Lumin. **83–84**, 139.

Yang, L., Song, H., Yu, L., Liu, Z., Lu, S., 2006. J. Lumin. **116**, 101.

Yen, W.M., 1987. In: Kaplyanskii, A.A., MacFarlane, R.M. (Eds.), Spectroscopy of Solids Containing Rare Earth Ions. North-Holland, Amsterdam, p. 185.

Yi, G.S., Sun, B.Q., Yang, F.Z., Chen, D.P., Zhou, Y.X., Cheng, J., 2002. Chem. Mater. **14**, 2910.

Yi, G.S., Lu, H.C., Zhao, S.Y., Yue, G., Yang, W.J., Chen, D.P., Guo, L.H., 2004. Nano Lett. **4**, 2191.

Yu, L.X., Song, H.W., Lu, S.Z., Liu, Z.X., Yang, L.M., 2004a. Chem. Phys. Lett. **399**, 384.

Yu, L.X., Song, H.W., Lu, S.Z., Liu, Z.X., Yang, L.M., Kong, X.G., 2004b. J. Phys. Chem. B **108**, 16697.

Yu, M., Lin, J., Fang, J., 2005. Chem. Mater. **17**, 1783.

Zhang, L.L., Guo, C.X., Zhao, J.J., Hu, J.T., 2005. Chin. Phys. Lett. **22**, 1225.

Zhang, W.W., Mei, X., Zhang, W.P., Min, Y., Qi, Z.M., Xia, S.D., Garapon, C., 2003. Chem. Phys. Lett. **376**, 318.

Zhorin, V.V., Liu, G.K., 1998. J. Alloys Compd. **275–277**, 137.

This page intentionally left blank

*Chapter 234*

# LANTHANIDE CHELATES AS LUMINESCENT LABELS IN BIOMEDICAL ANALYSES

Takuya NISHIOKA, Kôichi FUKUI, and Kazuko MATSUMOTO
*Department of Chemistry, Waseda University and Japan Science and Technology Agency, Okubo, Shinjuku-ku, Tokyo 169-8555, Japan*
*E-mail: kmatsu@yf6.so-net.ne.jp*

## Contents

## List of symbols and acronyms

| | | | |
|---|---|---|---|
| AFP | alpha-fetoprotein | BHHCT | 4,4′-bis(1″,1″,1″,2″,2″,3″,3″-heptafluoro-4″,6″-hexane-dione-6″-yl)chlorosulfo-*o*-terphenyl |
| ALP | alkaliphosphatase | | |
| β-NTA | 2-naphthoyltrifluoroacetone | | |
| B/F separation | bound/free separation | | |
| BCPDA | 4,7-bis(chlorosulfophenyl)-1,10-phenanthroline-2,9-dicarboxylic acid | BPMPHD | 1,6-bis(1′-phenyl-3′-methyl-5′-pyrazolon-4′-yl)hexane-1,6-dione |

| | |
|---|---|
| BPTA | $N,N,N^1,N^1$-[2,6-bis(3′-aminomethyl-1′-pyrazoly)-4-phenylpyridine]tetrakis (acetic acid) |
| BSA | bovine serum albumin |
| cAMP | adenosine-3′,5′-cyclic monophosphate |
| CEA | carcinoembryonic antigen |
| cs-124 | 7-amino-4-methyl-2(1H)-quinolinone |
| CTMAB | cetyltrimethylammonium bromide |
| Cy3 | cyanine dye 3 |
| Cy5 | cyanine dye 5 |
| ddATP | dideoxyadenosine 5′-triphosphate |
| ddCTP | dideoxycytidine 5′-triphosphate |
| ddGTP | dideoxyguanosine 5′-triphosphate |
| ddNTP | dideoxyribonucleoside 5′-triphosphate |
| ddTTP | dideoxythymidine 5′-triphosphate |
| DELFIA® | dissociation enhanced lanthanide fluoroimmunoassay |
| DNA | deoxyribonucleic acid |
| DOTA | 1,4,7,10-tetraazacyclododecane-$N,N′,N″,N‴$-tetra(acetic acid) |
| DPLCE | [D-Pen$^2$, L-Cys$^5$]-enkephalin |
| DTPA | diethylenetriamine pentaacetic acid |
| dsDNA | double-stranded DNA |
| dUTP | deoxyuridine 5′-triphosphate |
| EDTA | $N,N,N′,N′$-ethylenediamine tetraacetic acid |
| FITC | fluorescein isothiocyanate |
| FEN | flap endonuclease |
| FLUQ | fluoquinolone |
| FRET | fluorescence (or Förster) resonance energy transfer |
| FWHM | full width at half maximum |
| $G_\alpha$ | G-protein alpha-subunit |

| | |
|---|---|
| $G_{\beta\gamma}$ | G-protein beta- and gamma-subunits |
| GDP | guanosine 5′-diphosphate |
| GPCR | G-protein coupled receptor |
| GTP | guanosine 5′-triphosphate |
| HapMap | haplotype map |
| hMC4R | human melanocortin 4 receptor |
| hNPFF2 | human neuropeptide FF2 |
| HRP | horseradish peroxidase |
| HTRF® | homogeneous time-resolved fluorescence |
| HTS | high-throughput screening |
| IFNγ | interferon γ |
| IgE | immunoglobulin E |
| IL-1α | interleukin-1α |
| LOD | limit of detection |
| MRI | magnetic resonance imaging |
| α-MSH | α-melanocyte-stimulating hormone |
| NBS | $N$-bromosuccinimide |
| NDP-α-MSH | [Nle$^4$, D-Phe$^7$]-α-MSH |
| OLA | oligonucleotide ligation assay |
| PBR | peripheral benzodiazepine receptor |
| PCR | polymerase chain reaction |
| PSA | prostate-specific antigen |
| PTA | pivaloyltrifluoroacetone |
| RBITC | rhodamine B isothiocyanate |
| RNA | ribonucleic acid |
| ROX | rhodamine X |
| SA | streptavidin |
| SDF-1 | stromal cell-derived factor-1 |
| [$^{35}$S]GTPγS | [$^{35}$S]guanosine-5′-O-(3-thio)-triphosphate |
| S/N | signal-to-noise ratio |
| SNP | single-nucleotide polymorphism |
| ssDNA | single-stranded DNA |
| TBP | trisbipyridine cryptand |
| TdT | terminal deoxynucleotidyl transferase |
| TETA | 1,4,8,11-tetraazacyclotetra-decane-1,4,8,11-tetra(acetic acid) |

| $T_m$ | melting temperature | TTA | 2-thenoyltrifluoroacetone |
|---|---|---|---|
| TNF$\alpha$ | tumor necrosis factor $\alpha$ | TTHA | triethylenetetraamine hexaacetic |
| TOPO | trioctylphoshine oxide | | acid |
| TR-FIA | time-resolved | TUNEL | TdT-mediated dUTP nick end |
| | fluoroimmunoassay | | labeling |
| Triton® X-100 | registered name of a surfactant | XL-665 | a modified version of |
| TPA | tris(pyridylmethyl)amine | | allophycocyanin which emits |
| TSH | thyroid stimulating hormone | | fluorescence at 665 nm |
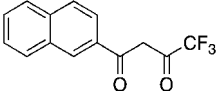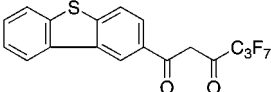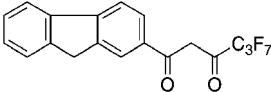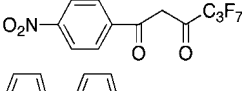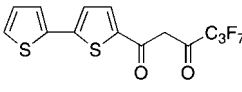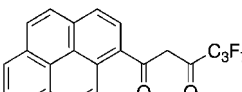
## 1. Introduction

Since Weissman (1942) discovered that $Eu^{3+}$-β-diketonate (ligand 1 in table 1) complex absorbs ultraviolet light and gives visible emission, fluorescent (or luminescent more correctly) chelates of lanthanide ions have been the focus of research and in the rapid growth of biotechnology in recent years, the importance of lanthanide chelates as luminescent labels has been increasingly recognized for detecting biomolecules with high sensitivity, and their application area is expanding. One major feature of lanthanide chelate luminescence is that the excited state lifetime is unusually long compared to those of organic fluorescent compounds, quite often over 1 ms. Therefore, time-resolved fluorometric measurement of lanthanide chelate compounds eliminates undesired background fluorescence, which decays within several nanoseconds, and gives very high sensitivity compared to conventional fluorometric analysis using organic labels such as FITC (fluorescein isothiocyanate). In this chapter, applications of lanthanide chelates as luminescent labels in bioanalysis and biotechnology such as immunoassay, DNA hybridization assay, real-time PCR, SNP typing, and cell imaging are introduced.

Lanthanide elements are 15 elements from lanthanum (La) to lutetium (Lu) corresponding to the progressive filling of the 4f electrons in a subshell. The valence electrons for these elements are 4f electrons, but 4f orbitals have a smaller spatial extension than the larger main quantum number orbitals, 5s, 5p, 5d, and 6s; this results in the shielding of the energetically higher valence 4f electrons by the energetically lower outer 5s, 5p, 5d, and 6s electrons. As a consequence, 4f electrons remain physically and chemically almost undisturbed by the chemical environment of the element or ion and this results in the special features of lanthanide luminescence. Due to the characteristics of this electronic structure and the presence of unpaired electrons in many ions, lanthanide luminescent materials have found industrial applications such as electroluminescent materials in color TV, permanent magnets, and laser light emitters. In addition, $Gd^{3+}$ chelates are used as contrast agents for MRI (magnetic resonance imaging) in medical diagnostics.

Fluorescent lanthanide chelates are divided into three main groups according to their luminescent characteristics that are based on the 4f energy levels. In the strong luminescence group ($Sm^{3+}$, $Eu^{3+}$, $Tb^{3+}$, $Dy^{3+}$ chelates), the excited energy level of the central metal ion is located at lower energy than the ligand triplet level ($T_1$), and can accept the energy transferred from $T_1$. In addition, since there is a large energy difference between the excited level

Table 1

Structure of some β-diketones and luminescence properties of their $Eu^{3+}$ complexes in ethanol

| β-diketone | No. | Absorption ($\lambda_{max}$) | Luminescence intensity |
|---|---|---|---|
| [structure with CF₃] | 1 | 340 nm | Strong |
| [structure with C₃F₇] | 2 | 360 nm | Strong |
| [structure with C₃F₇] | 3 | 363 nm | Strong |
| [O₂N– structure with C₃F₇] | 4 | 382 nm | (–) |
| [structure with C₃F₇] | 5 | 396 nm | (–) |
| [structure with C₃F₇] | 6 | 415 nm | (–) |

and the ground level of these metal ions, non-radiative transitions do not occur easily, so the luminescence quantum yield is high. In the weakly luminescent group ($Ce^{3+}$, $Pr^{3+}$, $Nd^{3+}$, $Pm^{3+}$, $Er^{3+}$, $Tm^{3+}$, $Yb^{3+}$ chelates), the energy difference between the excited and ground levels of the central metal ion is fairly small, so significant portion of the excitation energy is dissipated via non-radiative thermal deactivation processes and the quantum yield is low. In case of $Nd^{3+}$, $Er^{3+}$ and $Yb^{3+}$ chelates, emissions in the near infrared region have been reported. The chelates of the remaining lanthanide elements, i.e., $La^{3+}$, $Gd^{3+}$ and $Lu^{3+}$, are non-luminescent. In this chapter, we focus on luminescent labels of $Eu^{3+}$ and $Tb^{3+}$, since they possess strong luminescence with long lifetimes compared to those of $Sm^{3+}$ and $Dy^{3+}$.

The idea of the use of luminescent lanthanide chelates in bioanalysis can be traced back to the 1980s, when Hemmilä (1985) reported a time-resolved fluorometric system using an Eu labeling reagent, which was commercially produced by Wallac Oy company. The system was intended for immunoassay and included the spectrometer for time-resolved measurements. The basic principle of the immunoassay system (DELFIA®) is shown in fig. 1.

Although this type of analysis was highly innovative and had very high sensitivity, the $Eu^{3+}$ label covalently bound to proteins was itself not luminescent. In the immunoassay described in fig. 1, the $Eu^{3+}$ ion attached to the antibody via the label ligand in an amount proportional to the antigen must be converted into a luminescent compound. The addition of a large excess
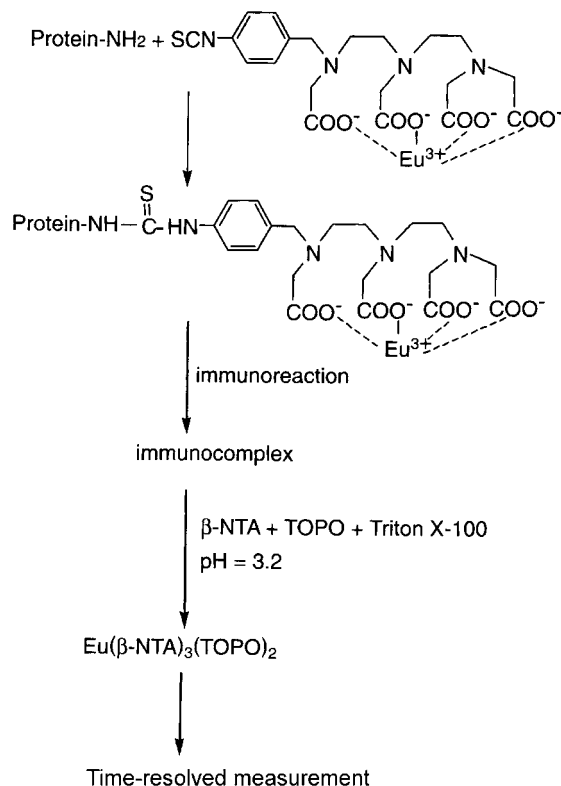
Fig. 1.  Assay principle of DELFIA® system using a non-luminescent $Eu^{3+}$ label.

of free β-diketonato ligand after immuno-complex formation is necessary for this conversion. Since the amount of the luminescent $Eu^{3+}$ β-diketonate is proportional to the initial antigen amount, luminescence measurement of the compound gives the basis for quantitative analysis. The principle is smart, but the procedure is somewhat tedious and suffers the problem of gradual increase of the background level even in time-resolved mode. This background problem is considered to be due to the contamination of $Eu^{3+}$ in the environment, since the large excess of free β-diketonate existing in the solution after formation of the luminescent $Eu^{3+}$ complex gradually binds the $Eu^{3+}$ contaminant and raises background level. Human blood has very low concentration (several ppt, part per trillion) of $Eu^{3+}$, which must come from food and the environment. It seems that very low level of $Eu^{3+}$ exists in the environment.

It naturally occurred to mind that if a luminescent label is developed, a much simpler and faster analysis would be at hand. Actually, such luminescent $Eu^{3+}$ labeling was developed by Diamandis (1988), Diamandis and Christopoulos (1990). The structure of the fluorescent label ($Eu^{3+}$-4,7-bis(chlorosulfophenyl)-1,10-phenanthroline-2,9-dicarboxylate, BCPDA–$Eu^{3+}$) is

**(BCPDA-Eu$^{3+}$)**
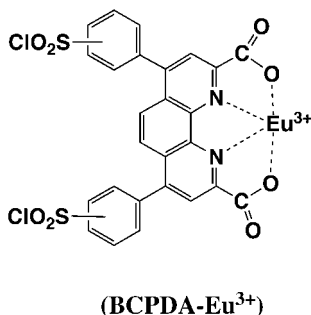
Scheme 1.

shown in scheme 1. The first fluorescent label made a success to a substantial extent in immunoassay, however the fluorescent quantum yield of the labeling reagent was not very high and needed improvement.

## 2. Synthesis and luminescent properties of lanthanide chelates

### 2.1. *Principles of lanthanide luminescence*

Usually aqueous solutions of $Sm^{3+}$, $Eu^{3+}$, and $Dy^{3+}$ ions produce only weak luminescence, so they cannot be used directly in sensitive analyses, whereas $Tb^{3+}$ ion is fairly luminescent with a lifetime of almost 0.5 ms and an intrinsic quantum yield of about 8%. On the other hand, chelates with suitably selected ligands having aromatic groups to absorb near-ultraviolet excitation light, are strongly luminescent in the visible range for all the four ions. Since the luminescence is based on energy transfer from the ligand to the central metal ion, the final emission is almost like atomic emission i.e., the main emission wavelength is, regardless of the ligand, specific to the lanthanide ion ($Sm^{3+}$ 643 nm, $Eu^{3+}$ 615 nm, $Tb^{3+}$ 545 nm, $Dy^{3+}$ 574 nm) with a very sharp peak profile (usually full width at half maximum FWHM of ∼10 nm), whereas the excitation spectrum is largely dominated by ligand absorption bands.

The luminescent mechanism of lanthanide chelates is shown in fig. 2. First, the ligand is excited to the excited state ($S_1$) by ultraviolet light usually in the region 300–350 nm. The absorbed energy is transferred to the triplet state ($T_1$) of the ligand by an intersystem crossing process, and further to the metal excited state(s) (e.g., $^5D$) for $Eu^{3+}$. The $^5D$ state emits in the visible region by transition to the ground state of the metal ion. The scheme of fig. 2 is rather simplified but since lanthanide ions are hard metal ions and their bonds with ligands are of ionic character, the approximation in fig. 2 is sufficient to explain qualitatively the luminescence mechanism. The mechanism also explains why some $Eu^{3+}$ β-diketonates emit strongly, whereas other chelates do not (cf. table 1). Table 2 shows the typical luminescent properties of a lanthanide chelate and those of conventional organic fluorescent labels (fluorescein isothiocyanate, FITC and rhodamine B isothiocyanate, RBITC). The latter two organic
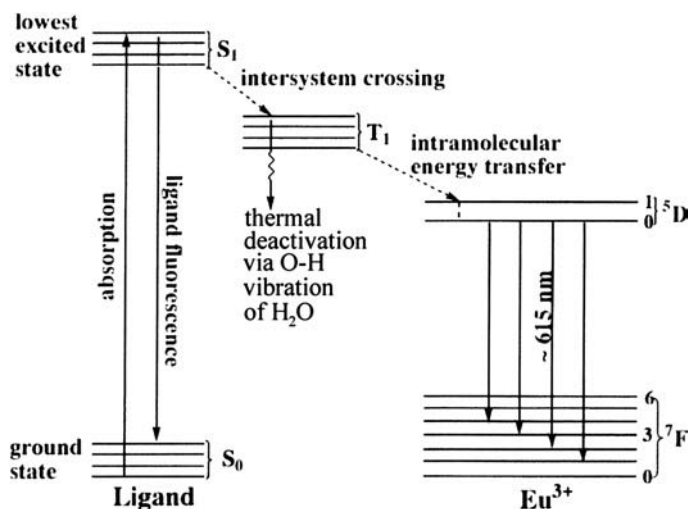
Fig. 2. Mechanism of the luminescence of $Eu^{3+}$ chelates.

Table 2
Photophysical properties of luminescent labels in ethanol

| Compound | Lifetime (ns) | $\lambda_{ex,max}$ (nm) | $\lambda_{em,max}$ (nm) | Stokes shift (nm) |
|---|---|---|---|---|
| FITC | 4.5 | 492 | 518 | 26 |
| RBITC | 3 | 550 | 585 | 35 |
| $[Eu(\beta\text{-NTA})_3]$ | $7 \times 10^5$ | 340 | 613 | 273 |

compounds have a labeling group (–SCN) on the aromatic rings to make covalent bonds with amino groups of proteins, nucleic acids or any other biomolecules, and are used commonly in biotechnology and diagnostics measurements.

The comparison of the excitation and emission spectra of organic and lanthanide compounds is shown in fig. 3.

Table 2 and fig. 3 clearly show that the luminescent properties of lanthanide compounds are quite different from those of fluorescent organic compounds. Actually the luminescence of the lanthanide compounds described here is phosphorescence in an exact terminology because of the mechanism in fig. 2, and all the features of lanthanide-specific properties in table 2 are explained with the emission mechanism sketched in fig. 2. The large Stokes shifts of lanthanide compounds are due to the mechanism in fig. 2. In addition, it explains why ligands with $T_1$ levels higher than the luminescent excited level of the coordinated lanthanide ion give strongly luminescent complexes, whereas ligands with lower $T_1$ levels cannot transfer energy onto the lanthanide ion and lead to weakly luminescent molecules. The sharp peak profiles of lanthanide compounds are due to the nature of the emission, which is essentially
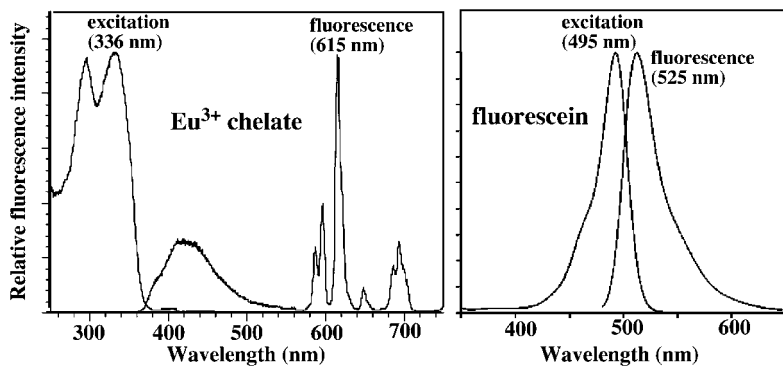
Fig. 3. Excitation and emission spectra of the Eu$^{3+}$ chelate with $N,N,N',N'$-[(4'-phenyl-2,2'; 6',2''-terpyridine-6,6''-diyl)bis(methylenenitrilo)]tetrakis(acetate) (left) and of fluorescein (right).

ionic emission and is not molecular emission. The long lifetimes of lanthanide excited states arise from the forbidden nature of the f–f transitions, both by Laporte's rule and, in the case of the phosphorescent ions, by the spin selection rule ($\Delta s = 0$). Due to the highly protected environment around the 4f electrons, non-radiative deactivation processes, which are usually associated with ligand and solvent vibrations, are minimized and the quantum efficiency of the emission is sometimes quite high.

Improvement of lanthanide labels is still progressing, and their design does not only call for obtaining stronger luminescence, but the current evolution of biotechnology also requires many new specific features for these labels. For instance, PCR (polymerase chain reaction), which is an innovative technology for amplification of DNA, employs a polymerization reaction of labeled mononucleotides, which is catalyzed by the enzyme polymerase. If the labeled mononucleotides are recognized by the enzyme as non-substrate, the polymerase reaction is retarded or does not proceed. This means that every time a new technology using a fluorescent label is invented, the structure and the physicochemical properties must be tuned to that technology, and this is not an easy task as the following sections will show. Up to date many luminescent lanthanide compounds have been synthesized and some of them have really spectacular properties. In order for the compound to be really a useful label, the compound must have a coupling group, and this can be a serious problem in synthesis, since attaching such a group to the luminescent compound quite often dramatically changes its photophysical properties. Even a strongly luminescent compound can lose its intensity drastically after a binding group is attached, and such an effect is often not predictable. In the following sections, both non-label and label luminescent compounds are described.

## 2.2. β-*Diketonates*

The luminescence property of various lanthanide β-diketonates has been reviewed (Binnemans, 2005). In early works, 2-naphthoyltrifluoroacetone (β-NTA), 2-thenoyltrifluoroacetone (TTA) and pivaloyltrifluoroacetone (PTA) (scheme 2) were found to be the best ligands for
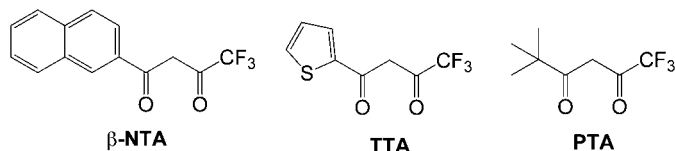
Scheme 2.
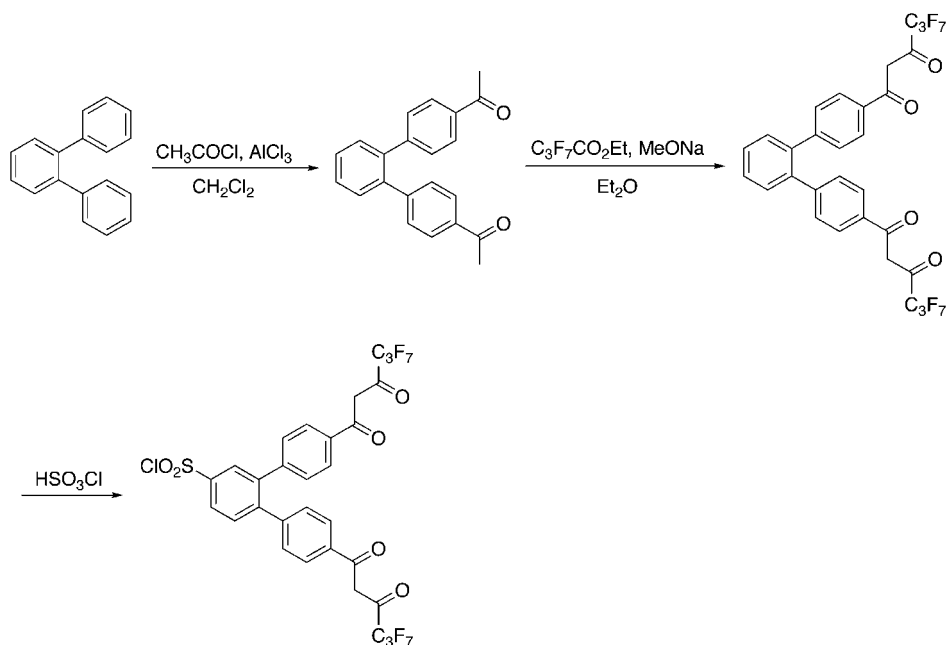


Scheme 3.

fluorescent complexes of $Eu^{3+}$, $Sm^{3+}$, $Tb^{3+}$ and $Dy^{3+}$; among these, β-NTA and TTA are effective only for $Eu^{3+}$ and $Sm^{3+}$, whereas PTA is effective for all four ions at room temperature.

β-Diketones are synthesized by Claisen condensation of appropriate acetyl methyl ketone and ethyl perfluoroalkyl carboxylate. For example, 4,4′-bis(1″,1″,1″,2″,2″,3″,3″-heptafluoro-4″,6″-hexanedion-6″-yl)-chlorosulfo-o-terphenyl (BHHCT) was synthesized from o-terphenyl by three step reactions (scheme 3 (Yuan et al., 1998a, 1998b)). The o-terphenyl are acetylated by acetyl chloride with anhydrous aluminum chloride as a Lewis acid and 4,4′-diacetyl-o-terphenyl is obtained. Then, the 4,4′-diacetyl-o-terphenyl is reacted with perfluoropropionic acid ethyl ester with sodium methoxide as a base. Finally, 4,4′-bis(1″,1″,1″,2″,2″,3″,3″-heptafluoro-4″,6″-hexanedion-6″-yl)-o-terphenyl is chlorosulfonylated by chlorosulfonic acid to form BHHCT.

**β-diketonate-Eu$^{3+}$-TOPO ternary complexes**
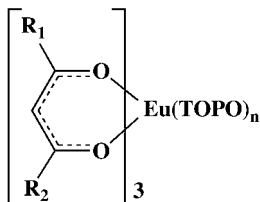


n = 2 for R$_1$ = 2-naphthyl, R$_2$ = CF$_3$ to C$_4$F$_9$,
and R$_1$ = 2-phenanthryl, R$_2$ = CF$_3$.
n = 1.5 for R$_1$ = 2-phenanthryl, R$_2$ = C$_2$F$_5$ to C$_4$F$_9$.

Scheme 4.

As mentioned above, the luminescence properties of lanthanide complexes strongly depend on the structure of the ligands. The structures and the absorption maximum wavelengths ($\lambda_{abs,max}$, in ethanol) of several β-diketones as well as the luminescence intensity of their Eu$^{3+}$ complexes are given in table 1. Although the absorption maximum wavelengths are different, the Eu$^{3+}$ complexes display the same intense emission maximum at ∼615 nm when $\lambda_{abs,max}$ (β-diketone) is less than 380 nm. In contrast, if the β-diketones have $\lambda_{abs,max}$ values larger than 380 nm, the Eu$^{3+}$ complexes are non-luminescent. This phenomenon can be explained by the mechanism shown in fig. 2. It is necessary that the energy of the lowest triplet state level of the ligand is higher than the energy of the Eu$^{3+}$ ion excited state, and the deactivating transitions of the ligand (S$_1$ to S$_0$ and T$_1$ to S$_0$) are minimized.

The quantum yields ($\phi$) and molar absorption coefficients ($\varepsilon$) of Eu$^{3+}$ β-diketonate [Eu$^{3+}$(R$_1$COCHCOR$_2$)] are strongly dependent on the substituents R$_1$ and R$_2$ (see scheme 4 (Sato and Wada, 1970)). When R$_1$ and R$_2$ are alkyl or aryl, the complexes are weakly luminescent. The emission can be strongly enhanced when R$_2$ becomes CF$_3$. With R$_2$ = CF$_3$, the overall emission intensity ($\varepsilon \cdot \phi$) decreases in the order of R$_1$: naphthyl $\geqslant$ thienyl > phenyl > alkyl. When R$_1$ is an aryl group, such as phenyl, naphthyl, thienyl, and phenanthryl, the emission intensity increases in the order of R$_2$: CH$_3$ < CF$_3$ < C$_2$F$_5$ < C$_3$F$_7$ < C$_4$F$_9$. Another factor affecting the luminescence of a lanthanide β-diketonate is the existence of a synergic agent. A synergic agent, such as tri-*n*-octylphosphine oxide (TOPO) or 1,10-phenanthroline, intensifies the emission through the formation of a ternary complex. The relation between the fluorescence properties of the ternary β-diketonate-Eu$^{3+}$–TOPO complexes and the structure of the β-diketonates is shown in table 3 (Yuan and Matsumoto, 1996).

However, the lanthanide β-diketonates shown in scheme 4 cannot be used as labels, since there is no active binding group on the β-diketonate ligands and these complexes are not very stable with stability constants in the order of 10$^3$–10$^6$ only, therefore the complexes dissociate in highly diluted solutions and the luminescence intensity decreases. Recently, three chlorosulfonylated tetradentate β-diketones were synthesized by Yuan and Matsumoto (1996, 1997) and Yuan et al. (1998a, 1998b) (scheme 5). They differ from other β-diketones, because the emission intensity of their Eu$^{3+}$ complexes is not weakened by the presence of the sulfonyl

Table 3
Luminescence properties of Eu(III) β-diketonate ternary complexes with TOPO in benzene.[a] Refer to scheme 4 for formulae

| $R_1$ | $R_2$ | $\lambda_{abs,max}$ (nm) | $\varepsilon_{max}$ ($10^4$ cm$^{-1}$ M$^{-1}$) | $\phi$[b] |
|---|---|---|---|---|
| 2-naphthyl | $CF_3$ | 339 | 5.82 | 0.209 |
| 2-naphthyl | $CF_2CF_3$ | 339 | 6.21 | 0.260 |
| 2-naphthyl | $CF_2CF_2CF_3$ | 339 | 6.39 | 0.335 |
| 2-naphthyl | $CF_2CF_2CF_2CF_3$ | 339 | 6.58 | 0.325 |
| 2-phenanthryl | $CF_3$ | 344 | 8.58 | 0.127 |
| 2-phenanthryl | $CF_2CF_3$ | 346 | 9.00 | 0.178 |
| 2-phenanthryl | $CF_2CF_2CF_3$ | 346 | 9.07 | 0.266 |
| 2-phenanthryl | $CF_2CF_2CF_2CF_3$ | 346 | 9.34 | 0.272 |

[a]The luminescence was measured immediately after the complex was dissolved in benzene.
[b]Quantum yield upon ligand excitation.
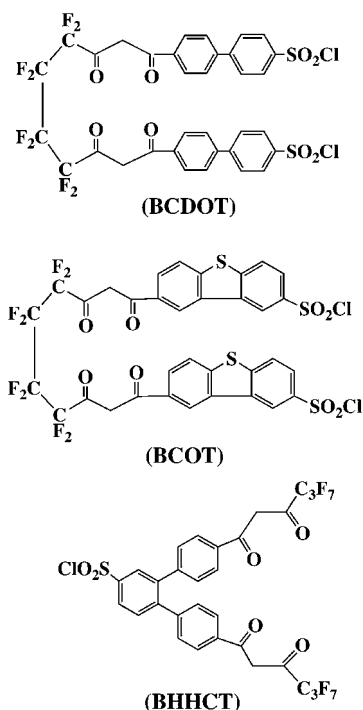


Scheme 5.

chloride group. Compared with bidentate β-diketonates, the tetradentate nature of these ligands can increase not only the stability of their Eu$^{3+}$ complexes but also the luminescence intensity, since less coordinated water molecules are in the first coordination sphere of the Eu$^{3+}$ ion.
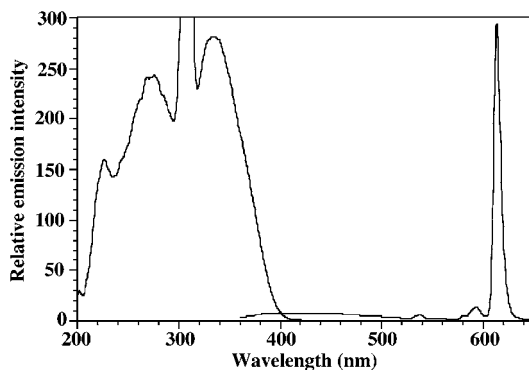
Fig. 4. Excitation and emission spectra of BSA-bound BHHCT–Eu$^{3+}$ in 0.05 M Tris-HCl buffer of pH 9.1. The concentration of the complex is $2.0 \times 10^{-6}$ M.

Among the three ligands, BHHCT yields the most suitable Eu$^{3+}$ label for time-resolved fluorometry. Compared with the others, it has the advantage that (i) it has only one sulfonyl chloride group, therefore cross labeling among several protein molecules does not occur, (ii) its Eu$^{3+}$ complex has a rather long luminescence lifetime (400–700 μs) in several buffers, (iii) the quantum yield, molar absorption coefficient (at 330 nm), and detection limit of the Eu$^{3+}$ complex (bound to bovine serum albumin (BSA)) in 0.05 M Tris-HCl buffer at pH 9.1 are 0.27, $3.0 \times 10^4$ M$^{-1}$ cm$^{-1}$ and $8 \times 10^{-13}$ M, respectively, hence, the relative luminescence intensity ($\varepsilon \cdot \phi$) of the Eu$^{3+}$ complex is considerably larger than those of other europium labels, and (iv) its BSA cojugate (the Eu$^{3+}$ complex bound to BSA) has a relatively large formation constant (about $10^{10}$ M$^{-1}$), therefore the complex is a very stable label in bioassays. The ligand BHHCT is easy to conjugate to proteins through the formation of a sulfonamide linkage (protein–NH–SO$_2$–label). The main drawback of BHHCT is its low solubility in water-based buffers, which makes it unsuitable for direct labeling of small molecules in aqueous solution. However, BHHCT-labeled BSA, the hapten–BSA conjugate, streptavidin (SA), antibodies, and other proteins and nucleic acids are soluble in water-based buffer. Fig. 4 shows the excitation and emission spectra of BSA-bound BHHCT–Eu$^{3+}$.

## 2.3. *Complexes with aromatic amine derivative-type ligands*

This class of ligands mostly consists of derivatives of pyridine, 2,2′-bipyridine, 2,2′,2″-terpyridine, and 1,10-phenanthroline. Scheme 6 shows the structures of four Eu$^{3+}$ chelates with aromatic amine derived ligands, that can be covalently bound to proteins, for time-resolved fluorometry, among which 4,7-bis(chlorosulfophenyl)-1,10-phenanthroline-2,9-dicarboxylic acid (BCPDA)–Eu$^{3+}$ and trisbipyridine cryptate (TBP)–Eu$^{3+}$ are widely used for europium fluorescence labels in TR-FIA.

Recently, many aromatic ligands derived from amines have been synthesized and the luminescence properties of their lanthanide complexes have been investigated. The ligand which is composed of an aromatic amine as a chromophore and tetra(acetic acid) as a chelation
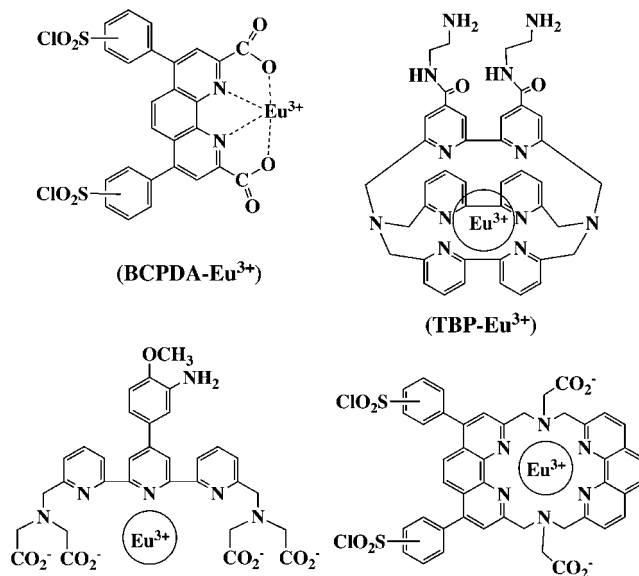
Scheme 6.

site is one of the most widely investigated. For the preparation of these ligands, the aromatic amine moieties are synthesized first, and then the tetra(acetic acid) functions are introduced. Mukkala et al. (1992) reported several different pathways to introduce tetra(acetic acid) moieties. The key intermediates are the bis(halomethyl) derivatives or bis(methylamines). The former are prepared using three different routes starting either from the dimethyl derivatives, directly or via their $N,N''$-dioxides, or from dimethanols. In the most straightforward method, the dimethyl derivatives were halogenated to the bis(halomethyl) derivatives with $N$-halogenosuccinimide, usually $N$-bromosuccinimide (NBS) (scheme 7a). In the case of dimethyldipyrimidenes, they were oxidized with 3-chloroperbenzoic acid into $N,N'$-dioxides, which reacted with phosphorus oxychloride to form the bis(chloromethyl) derivatives (scheme 7b). Bis(bromomethyl) derivatives were also synthesized from dimethanols and tribromophosphine (scheme 7c). Dimethanols were obtained by reduction of dicarbaldehydes or dimethyl dicarboxylates with sodium borohydride. Dimethyl dicarboxylates were synthesized from dimethyl derivatives by oxidation with selenium oxide or from dicarbonitriles by hydrolysis with sulfuric acid followed by esterification with methanol.

In the case of terpyridine and acridine derivatives, the bis(methylamines) are the most convenient intermediates. Substituted 4′-phenyl-2,2′:6′,2″-terpyridines were prepared by reacting ($E$)-propenons and $N$-[2-(pyrid-2′-yl)-2-oxoethyl]pyridinium iodide with ammonium acetate in acetic acid or in methanol. The terminal pyridine moieties were oxidized with 3-chloroperbenzoic acid to $N,N''$-dioxides followed by modified Reisserty–Henze reaction to obtain 6,6″-dicarbonitriles. The bis(methylamines) were obtained by reduction of the 6,6″-dicarbonitriles with borane (scheme 8 (Mukkala et al., 1993)).

a)



b)



c)
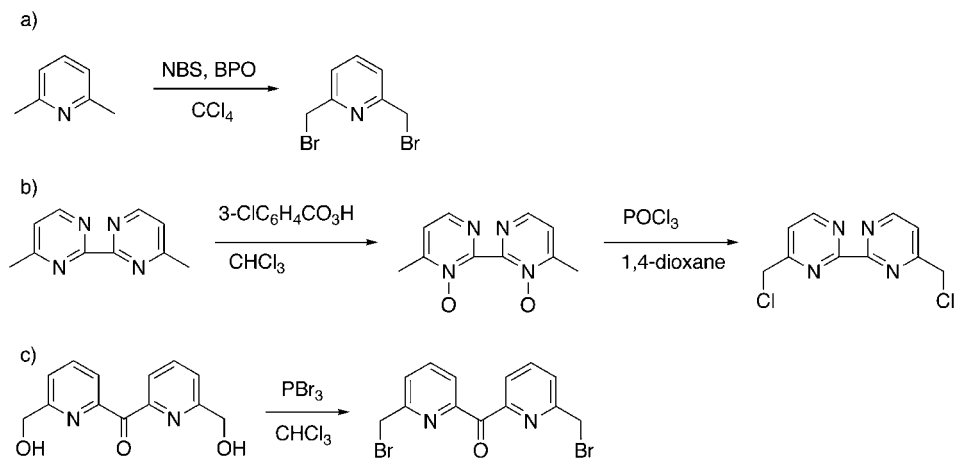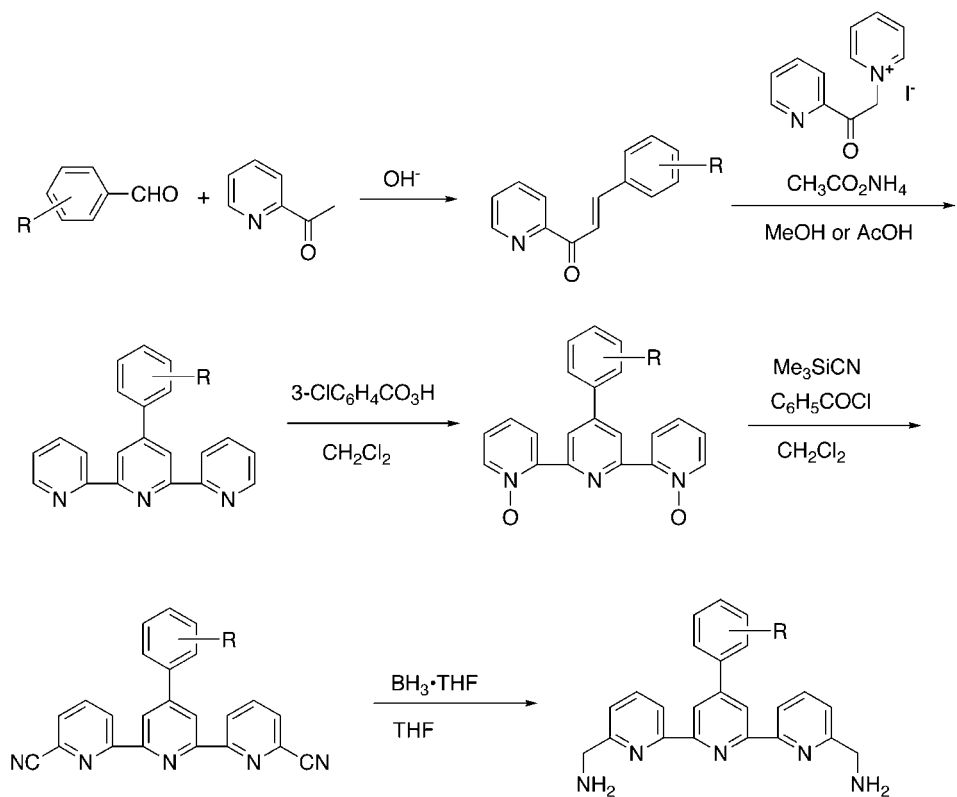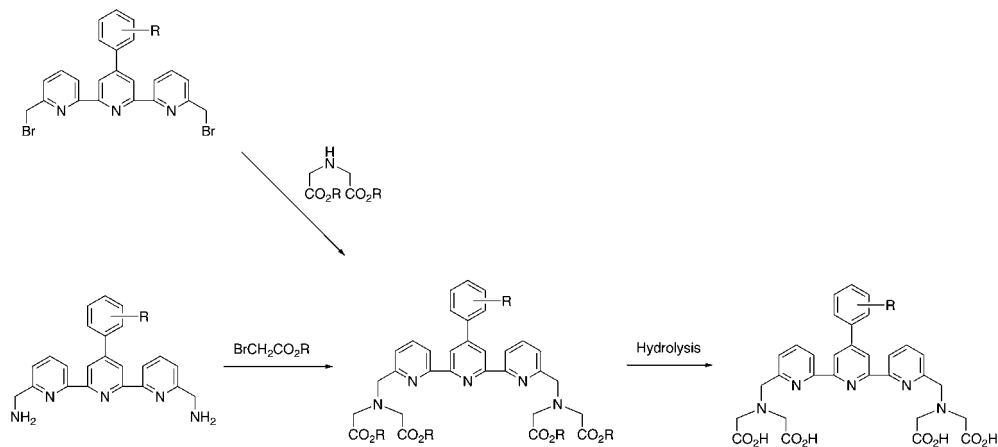


Scheme 7.



Scheme 8.

Scheme 9.
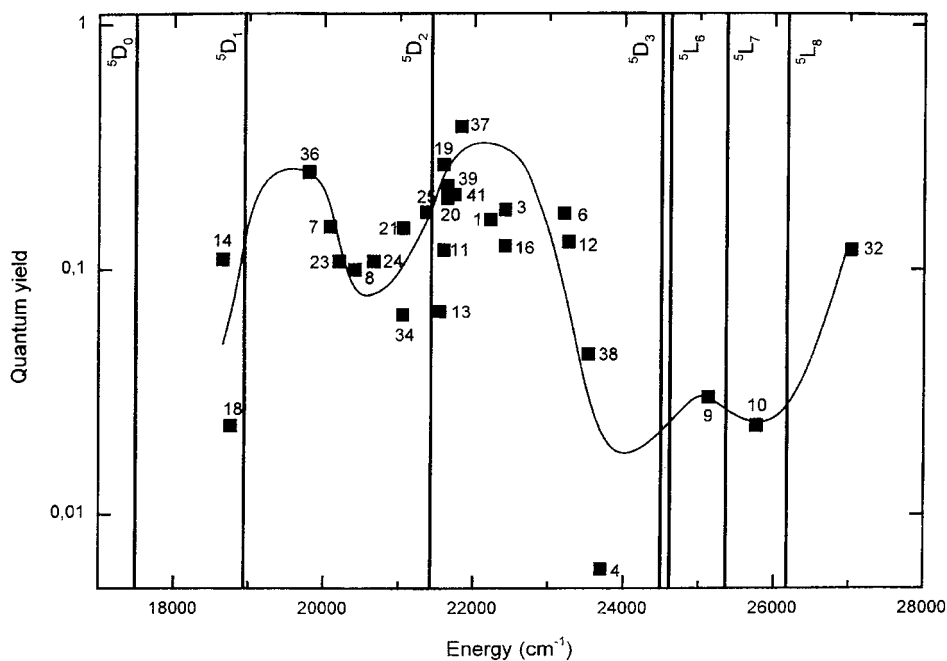


Fig. 5.  The Eu(III) luminescence quantum yields of Eu(III) chelates as a function of the lowest triplet state energy of the ligand. Redrawn, with permission, after Latva et al. (1997).

Finally, the tetraacetate derivatives were synthesized from the bis(halogenomethyl) derivatives and iminobis(acetate) or from the bis(methylamines) and bromoacetate, and then were hydrolyzed to the target tetra(acetic acid) (scheme 9).
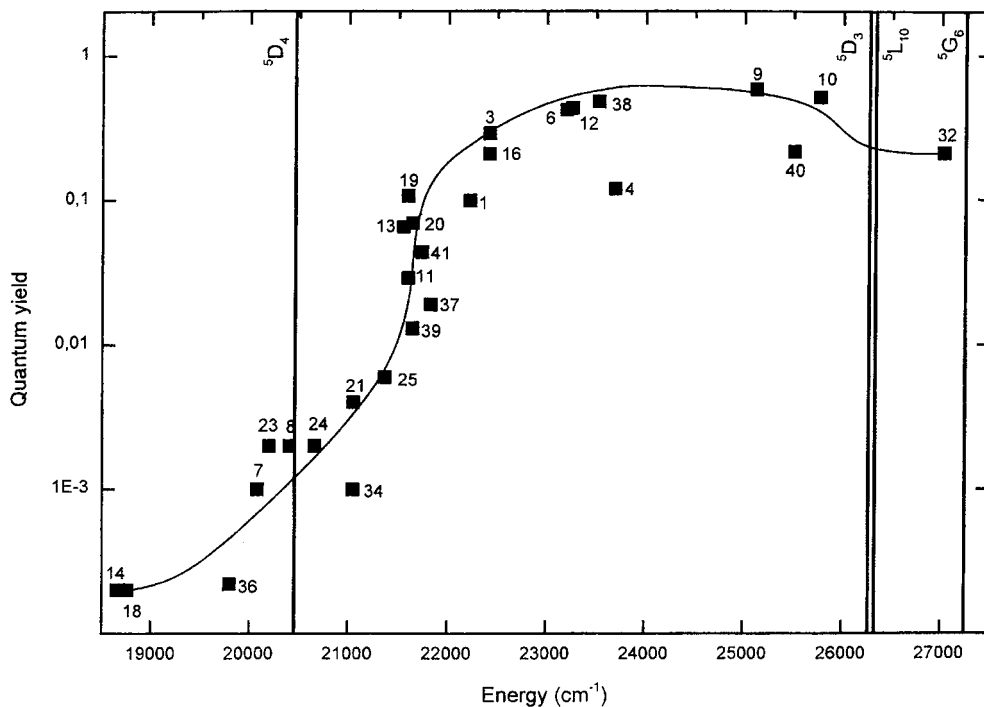
Fig. 6. The Tb(III) luminescence quantum yields of Tb(III) chelates as a function of the lowest triplet state energy of the ligand. Redrawn, with permission, after Latva et al. (1997).

The systematic measurement of the luminescence properties and the ligand triplet energy levels of the $Eu^{3+}$ and $Tb^{3+}$ complexes with 41 aromatic amine–carboxylic acid derived ligands clarified the relationship between the energy of the ligand triplet level and the quantum yield (Latva et al., 1997). The correlation for europium chelates is complicated (fig. 5), but that for terbium chelate clearly shows that the lowest triplet of the ligands should be above $22300 \, cm^{-1}$ (fig. 6), in other words, the energy gap between the lowest triplet energy level of the ligand and the $^5D_4$ level of the terbium ion ($20\,400 \, cm^{-1}$) should be larger than $1850 \, cm^{-1}$ to prevent a decrease in the luminescence quantum yield, due to the energy back transfer from the $^5D_4$ level to the triplet state.

As another class of ligands, conjugates of DTPA (diethylenetriamine pentaacetic acid), TTHA (triethylenetetraamine hexaacetic acid), DOTA (1,4,7,10-tetraazacyclododecane-$N,N',N'',N'''$-tetra(acetic acid)), or TETA (1,4,8,11-tetraazacyclotetradecane-1,4,8,11-tetra-(acetic acid)), with amino derivative of chromophores were synthesized (scheme 10, Li and Selvin, 1995). Among them, the conjugate of DTPA with 7-amino-4-methyl-2(1H)-quinolinone (named DTPA-cs124 by the authors) was widely investigated as a label for time-resolved fluorometry. Its $Eu^{3+}$ and $Tb^{3+}$ complexes are luminescent and have excited state lifetimes of over 1 ms. The DTPA-cs124 can be conjugated to amino compounds by

DTPA-cs124



TTHA-cs124



DOTA-cs124



TETA-cs124
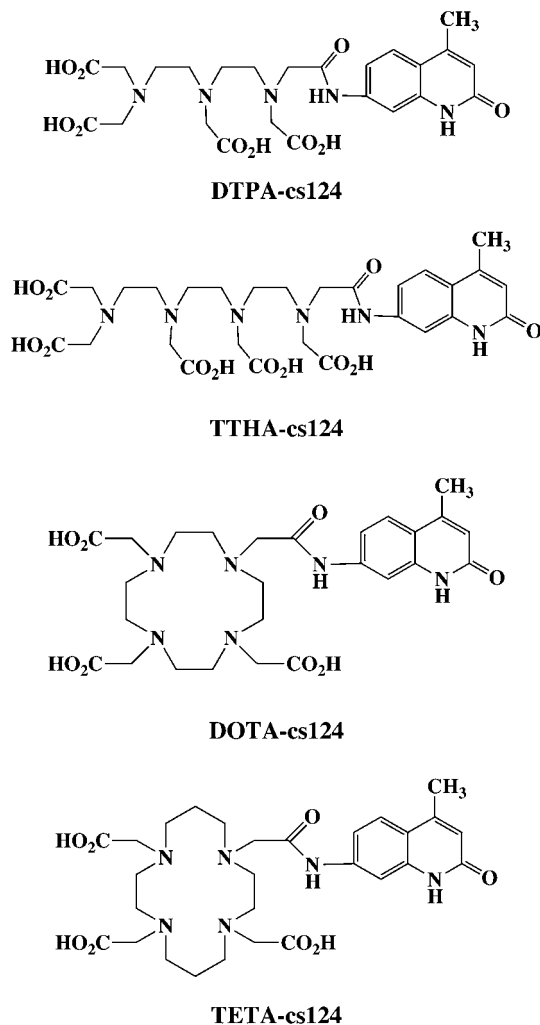
Scheme 10.

using its anhydride form (DTPA anhydride-cs124). Recently, the amino- and thiol-reactive forms of DTPA-cs124 were synthesized by introducing the isothiocyanato and maleimido (or pyridyldithio and bromoacetamide) group onto the molecule, respectively (Li and Selvin, 1997; Chen and Selvin, 1999). The reactivities of the amino- and thiol-reactive DTPA-cs124 as well as the luminescence properties of the $Tb^{3+}$ and $Eu^{3+}$ complexes have been examined. Using a labeled DNA oligomer, the usefulness of DTPA-cs124–$Eu^{3+}$(and $Tb^{3+}$)–labels for fluorescence resonance energy transfer was also examined. The structures of the amino- and thiol-reactive forms of DTPA-cs124 are shown in scheme 11.

**amino-reactive DTPA-cs124**



**thiol-reactive DTPA-cs124**
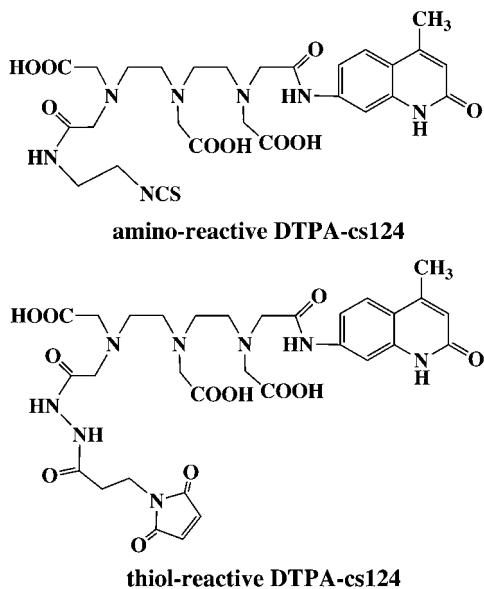
Scheme 11.

## 3. Bioconjugation of lanthanide chelate labels

In order to use the lanthanide complexes for biological assays, they must have a linking group able to bind biomolecules; isothiocyanate, sulfonyl chloride, carboxylate of $N$-hydroxysuccinimide, and maleimide are usually used to couple with DNA, proteins or other biological molecules. These binding groups can be directly bound to an amino group or a thiol group of the biomolecules (scheme 12). Bifunctional bridging reagents are also available for the conjugation of amino or thiol derivatives of lanthanide complexes with biomolecules.

For protein labeling, several $Eu^{3+}$ and $Tb^{3+}$ complexes with aromatic amine-polyamino-polycarboxylic acid derivatives, that can be directly bound to proteins, have been developed (Mukkala et al., 1993; Takalo et al., 1994, 1997; Karilayan et al., 1997). The structures and luminescence properties of these complexes are shown in scheme 13 and table 4. All complexes except those with ligands **2** have metal centered excited state lifetimes of over 1 ms and a relatively strong emission with quantum yields larger than 0.1; the quantum yields of $Eu^{3+}$ complexes **2** are 0.025 and 0.05 when the active groups are isothiocyanato and (4,6-dichloro-1,3,5-triazin-2-yl)amino, respectively (Takalo et al., 1994). It is notable that although the complexes emit the strongest luminescence only with $Eu^{3+}$ or $Tb^{3+}$ listed in table 4, the complexes with some other lanthanide ions also emit at other particular wavelength, i.e., the $Tb^{3+}$ complexes of the ligands **1** and **2**, and the $Eu^{3+}$ complexes of the ligands **3** are also weakly luminescent. This is because the fluorescence quantum yield is dependent on the lowest triplet state energy levels of the ligands and the excited state levels of $Eu^{3+}$ and $Tb^{3+}$. The labels in scheme 13 can be conjugated to pro-

Scheme 12.



R = -NCS (a) or -HN—⟨triazine⟩ (b)
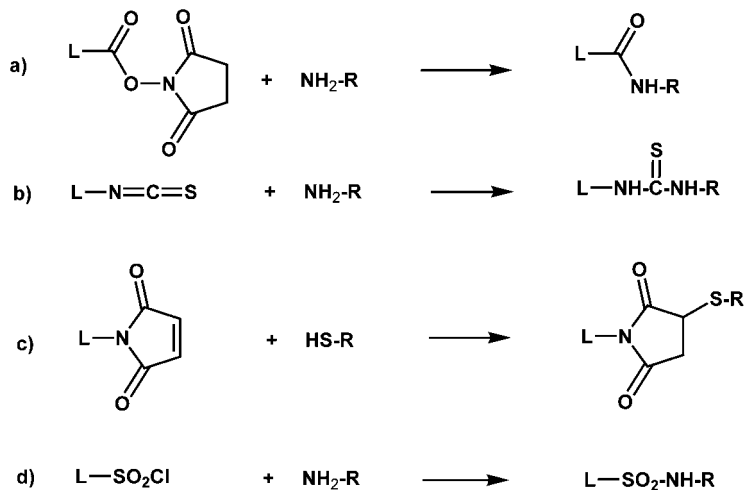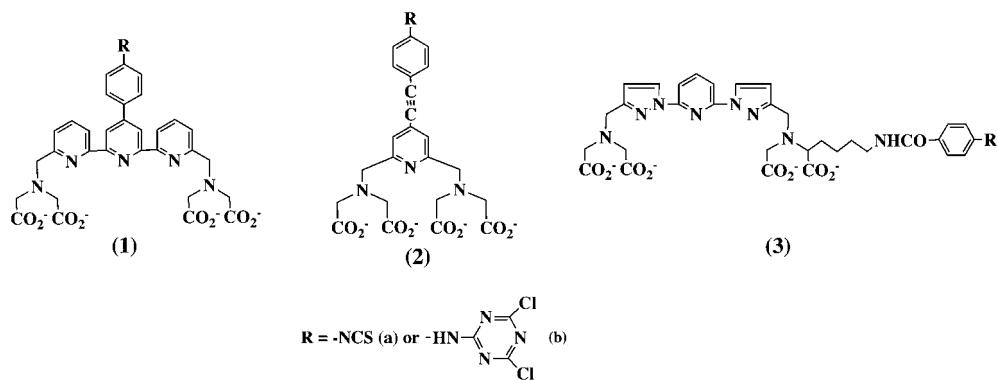
Scheme 13.

Table 4

Photophysical properties of the lanthanide luminescent labels described in scheme 13 and bound to protein

| | Ligands | | | | | |
| | 1a | 1b | 2a | 2b | 3a | 3b |
| Metal ions | $Eu^{3+}$ | $Eu^{3+}$ | $Eu^{3+}$ | $Eu^{3+}$ | $Tb^{3+}$ | $Tb^{3+}$ |
| --- | --- | --- | --- | --- | --- | --- |
| $\lambda_{ex}$ (nm) | 340 | 340 | 330 | 341 | 315 | 310 |
| $\tau$ (μs) | 1400 | 1590 | 380 | 400 | 2930 | 2660 |
| $(\varepsilon \cdot \phi)$ | 2100 | 2600 | 550 | 1100 | 3770 | 4050 |

teins or other amino compounds through their isothiocyanato or (4,6-dichloro-1,3,5-triazin-2-yl)amino group. The labeling reactions with proteins indicated that the (4,6-dichloro-1,3,5-triazin-2-yl)amino group is more efficient than the isothiocyanato group (Mukkala et al., 1993; Karilayan et al., 1997), giving a higher labeling yield.

## 4. Principle of time-resolved luminescence measurement using lanthanide labels

The emission spectra of the $\beta$-pivaloyltrifluoroacetonate complexes of $Tb^{3+}$, $Dy^{3+}$, $Eu^{3+}$ and $Sm^{3+}$ are shown in fig. 7.

The lifetime of course depends on the ligands, but usually the order of the lifetimes is not changed very much even if the ligand is changed, and is always roughly $Eu \approx Tb > Sm > Dy$. With these chelates, time-resolved luminescence measurement is especially effective in removing the undesired background fluorescence whose lifetime is in the range of several to several tens of nanoseconds. The lifetimes of usual materials are totally different from those of the lanthanide chelates, and this makes time-resolved measurement especially effective even with an instrument having relatively low time resolution. Principle of time-resolved measurement is shown in fig. 8, in which a pulse excitation light is used, and after the pulse irradiation, a delay time is enforced. During this time the measurement is not carried out and the background fluorescence decays to almost zero. After a reasonable delay time only the lanthanide luminescence remains and the measurement is started.

By repeating this measurement mode several to hundreds times for accumulation, remarkably high S/N ratios are obtained. The principle enables the measurement of very small signals, which are embedded in the background signal and could not be measured in the normal fluorescence measurement, and thus gives remarkably high sensitivity with very low detection limit. In the authors' laboratory, several proteins were measured in serum for the first time with this method. These will be introduced in a later section. This method is especially effec-
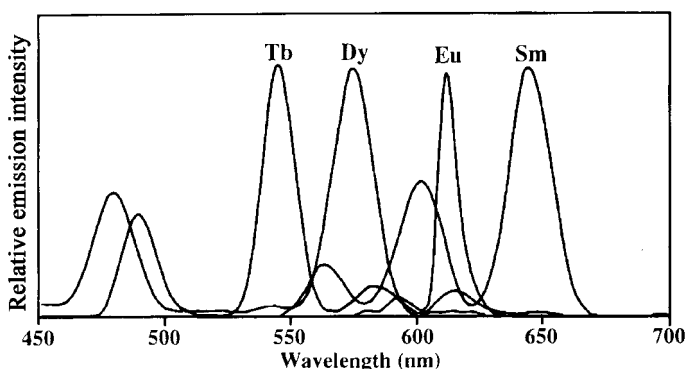


Fig. 7. Emission spectra of the complexes of $Eu^{3+}$, $Sm^{3+}$, $Tb^{3+}$ and $Dy^{3+}$ with PTA (pivaloyltrifluoroacetone) in the presence of 1,10-phenanthroline, Triton® X-100, and $Y^{3+}$.
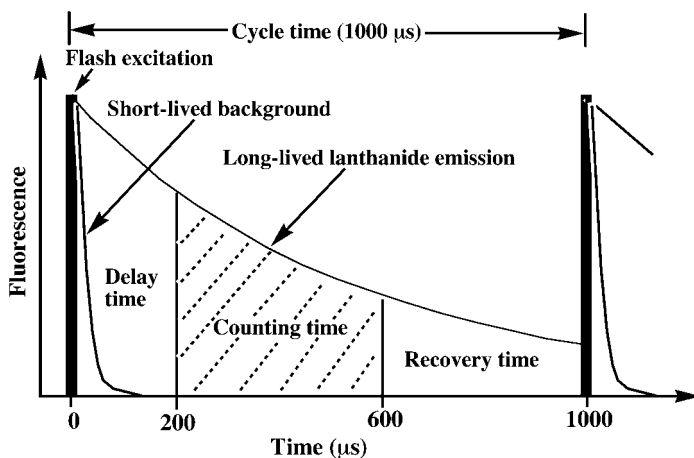
Fig. 8. Principle of time-resolved fluorometric measurement with delay time of 200 μs, counting time of 400 μs, and cycle time of 1000 μs.

tive when the sample contains a lot of coexisting materials as the matrix. Typical example of such sample is serum and time-resolved measurements have produced especially remarkable results in immunoassays of serum.

Since the Stokes shifts of lanthanide compounds are very large when they are excited through ligand levels (over 200 nm for Eu and Tb labels), it may be expected that simple use of a lanthanide label even without time-resolved measurement would give better detection limit, compared to organic fluorescent labels, which have lifetimes in the nanosecond range. But actually this is not the case, since a long lifetime means that the number of photons emitted by unit of time is low. Because the total integrated emission intensity is limited by the quantum yield, the total amount of emitted light is not very much different between organic and lanthanide compounds. Since the detection limit of time-resolved luminescence is so low, it is often misunderstood that the emission of lanthanide chelates must be very strong, but it is not correct. The lanthanide luminescence is rather weak compared to those of organic fluorescent compounds, but when time-resolved measurement is employed, the detection limit becomes superb. This means that the actual luminescence intensity is very low compared to organic fluorescent compounds, and needs a more sensitive instrument to be measured. For normal fluorometry the instrument needs not to be so sensitive, because very small signal is embedded in the background fluorescence and the total detection limit is determined by the level of background. The situation is totally different in time-resolved luminescence of lanthanide compounds, where the background is almost totally removed and so the emission intensity is due almost totally to the lanthanide compounds. In such a case the sensitivity of the instrument determines the detection limit of the analysis.

The selection of the delay time and the measurement time is very important to obtain really high sensitivity. If the delay time is too long, the emission intensity decreases and the total sensitivity is lowered. If the delay time is too short, the background fluorescence still remains

and blurrs the very small signal from the lanthanide ion. Usually, a delay time of 100–200 μs is employed. These values may seem too long considering the lifetimes of the background due to the coexisting materials. But experiment shows that such a delay time is optimum in reducing the background intensity. The pulse width of the excitation light is also an important factor affecting the background intensity level, and the delay time should be chosen in function of the pulse width. It is always a question why the pulse width, typically of several to several tens of microseconds, affects so significantly the background level at the observed wavelength that is very different from the excitation wavelength. Several reasons are conceivable; firstly, since the decay time of the background fluorescence is very short (ns), de-excited molecules can be re-excited in case of a long pulse (μs). Secondly, some "strange" species such as excimer may form which emit with longer lifetimes. Thirdly, since the time-resolved spectrometers used in this field work with either cheap monochromators or with filters, the stray light is very important and contributes substantially to the background fluorescence. This phenomenon is the principal other contribution to the noise and can be amplified if the solution contains colloids (which is often the case of solutions of biological substances).

## 5. Fluorescence resonance energy transfer (FRET) and fluorescence quenching for lanthanide labels

FRET is a commonly used technique in bioscience to detect association of two biomolecules. The principle of FRET is shown in fig. 9, in which the excitation and emission wavelengths of the donor and the acceptor must be suitably selected so that the excitation light is absorbed by the donor but not by the acceptor.

The donor and the acceptor are labeled to two interacting molecules. The energy absorbed by the donor emits fluorescence only if the biomolecule labeled with the donor does not bind to another biomolecule labeled with the acceptor. But when the two biomolecules bind to each other by a specific biological interaction, the donor–acceptor distance becomes short and FRET occurs, i.e., the energy absorbed by the donor is transferred by resonance to the acceptor and the acceptor emits fluorescence. In this case, the emission of the donor is significantly decreased and the emission of the acceptor increases and becomes observable. Since the acceptor is not excited by the excitation light which can excite only the donor, observation of the acceptor fluorescence is a signal that the two biomolecules are close to each other or the two molecules bind to one another. With such a system, one can detect interactions between, for instance, proteins, protein and DNA, a receptor and a ligand, as well as the folding of a large protein. Many specific interactions between two different molecules operate in biological systems and combination of these interactions provides the chemical basis of biological phenomena in living organisms. For instance, gene expression is regulated by binding of specific proteins to specific sites of DNAs. In this case, by detecting binding of the protein to the specific sequence of DNA, initiation of the gene expression is monitored. FRET is also used in homogeneous immunoassays, where antigen–antibody binding reactions are accelerated compared to those of solid state reactions on a cuvette wall. FRET is also used in fluorescence microscopy to observe association of two biomolecules within cells or tissues.

## FRET of Organic-Organic and Lanthanide-Organic Dyes
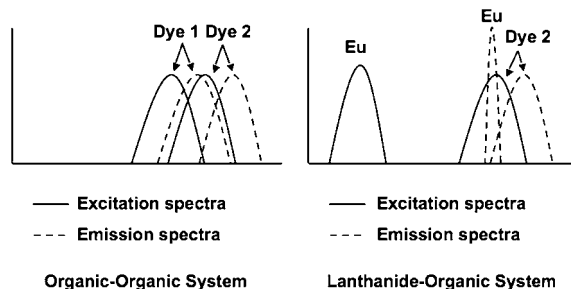


Fig. 9. Principle of FRET between an organic donor and an organic acceptor (left) and between a lanthanide donor and an organic acceptor (right).

FRET intensity can be expressed in function of the distance of the two molecules as shown in eq. (1) assuming a dipole–dipole (Förster's) mechanism for the energy transfer. This gives the basis for calculating the distance of two molecules by measuring FRET intensity:

$$\eta_E = \frac{R^{-6}}{R^{-6} + R_0^{-6}} \tag{1}$$

where $\eta_E$ is the energy transfer efficiency which can be determined from FRET intensity, $R$ is the separation distance between the donor and acceptor molecules, and $R_0$ is the Förster distance which is the characteristic distance between the donor and acceptor when the transfer efficiency is 50%. Alternatively, this yield $\eta_E$ can be calculated by the formula $(1 - \tau/\tau_0)$ where $\tau$ and $\tau_0$ are the lifetimes of the donor in presence and in absence of the acceptor, respectively.

In the conventional FRET using two organic labels, the maximum observable distance is ca. 60 Å. By using a lanthanide label as a donor in FRET, the distance can be extended to ~90 Å, since the lifetime of the donor is much longer than that of an organic donor. Any organic label having a suitable overlap between its absorption spectrum and the emission spectrum of the lanthanide donor can be used. As an example, the corresponding photophysical properties of BPTA–$Tb^{3+}$ and a common organic label Cy3 are shown in fig. 10.

The FRET using this two labels was used to detect a specific DNA sequence in an homogeneous hybridization assay, in which the lifetime of the organic acceptor molecule becomes apparently longer (~ several tens microsecond), and time-resolved measurement can be applied to the organic fluorescence. This is due to the slow population of the excited singlet state by energy transfer from the long-lived lanthanide excited state. In order to avoid confusion, it should be mentioned here that the lifetime of the acceptor excited state is not intrinsically lengthened; it remains unchanged. However, the luminescence decays with the lifetime of the donor, because the population of the acceptor excited state is slow since it is made from the long-lived excited state of the donor. On the other hand, the lifetime of the donor excited state
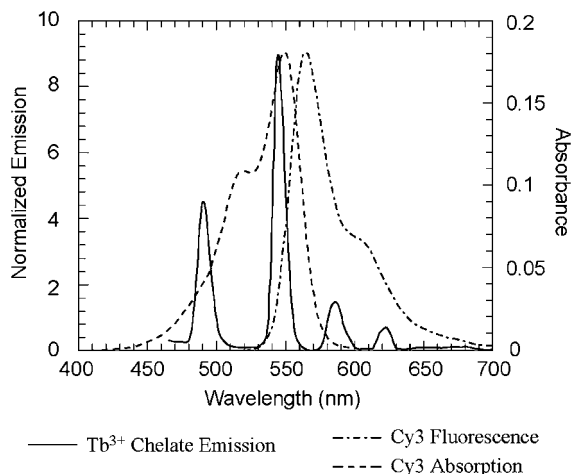
Fig. 10. Overlap between the emission spectrum of the BPTA–Eu$^{3+}$ complex as the donor and the absorption spectrum of the organic acceptor Cy3.



Dabcyl Quencher



Black Hole Quencher (BHQ™)-2
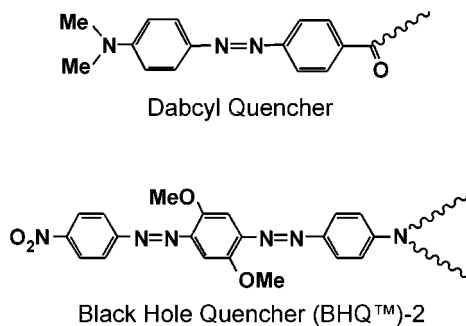
Scheme 14.

is effectively shortened. The merit of using a lanthanide complex as a donor is not limited to the apparent increase of the lifetime of the acceptor, but since the excitation wavelength is far away from the emission of the acceptor, far less background level is attained at the observation wavelength, as compared to the FRET using two organic dyes (fig. 9(left)).

Fluorescence quenching is another technique also using energy transfer, but in this technique, the acceptor is a quencher which absorbs energy from the donor but does not emit light, instead the quencher dissipate the energy as heat. Therefore when the donor and the quencher are in close proximity, the fluorescence of the donor is not observed. For this purpose, several typical quenchers are available, whose structures are shown in scheme 14. These quenchers are effective both for organic and lanthanide luminescent complexes.

## 6. Time-resolved fluorometric immunoassay

Time-resolved lanthanide luminescence was used for the first time for immunoassays. This type of analytical method most effectively removes the background fluorescence, because serum contains many undesired co-existing materials, which raises significantly the background level when the sample is irradiated.

In the first assay format (DELFIA®, fig. 1) developed and commercialized from Pharmacia, a poorly luminescent lanthanide complex was used as the biolabel. As fig. 1 shows, after the antigen binds to antibody having the nonluminescent $Eu^{3+}$ label, the $Eu^{3+}$ ion is removed from the label by addition of an enhancement solution containing the diketone β-NTA in excess to form a luminescent complex. Emission is further enhanced by the presence of TOPO (trioctylphosphine oxide), and Triton X-100 in the enhancement solution. Different from this non-luminescent lanthanide label, the first luminescent label that can be directly bound to biomolecules, europium 4,7-bis(chlorosulfophenyl)-1,10-phenanthroline-2,9-dicarboxylate (BCPDA–$Eu^{3+}$, scheme 1) was commercialized by FIAgen. However, the emission intensity of this reagent was not very high (the detection limit is $10^{-11}$ M). In order to obtain a really high sensitivity in sandwich immunoassay, a lanthanide luminescent label having much higher quantum efficiency was necessary. BHHCT–$Eu^{3+}$ (scheme 5) was synthesized to meet this requirement, and the sandwich-type time-resolved immunoassay carried out for alpha-fetoprotein (AFP) improved the detection limit by about 4 orders of magnitude compared to the conventional immunoassay (Yuan et al., 1998a, 1998b).

Various serum proteins were measured with this labeling reagent, IgE (Yuan et al., 1997), TSH (Yuan et al., 1998a, 1998b), SDF-1 (Ikegawa et al., 2001), IL-1α, TNFα, and IFNγ (Kimura et al., 2001). Reported competitive immunoassays using BHHCT–$Eu^{3+}$ include methamphetamine in human hairs and urines (Kimura et al., 1999), serum p21 protein (Wang et al., 2001), and estradiol and estriol (Majima et al., 2002).

The EDTA–$Tb^{3+}$ complex is poorly luminescent, but becomes strongly emissive when it forms a ternary complex with salicylic acid. By using alkaliphosphatase (ALP) as the label of the antibody, a unique immunoassay system specific to $Tb^{3+}$ was constructed (fig. 11) by Evangelista et al. (1991) and Christopoulos et al. (1992). The enzyme ALP cleaves the phosphoester bond of the substrate and releases 5-fluorosalicylic acid, which binds to EDTA–$Tb^{3+}$ and sensitizes luminescence from $Tb^{3+}$. This method is employed for the determination of serum AFP (α-fetoprotein) and PSA (prostate-specific antigen).

$Eu^{3+}$, $Tb^{3+}$, $Sm^{3+}$, $Dy^{3+}$ complexes have different emission wavelengths with sharp peak profiles, which are suitable for multi-component immunoassay. Several Eu–Sm two-color time-resolved immunoassays have been reported. Since the sensitivity of $Sm^{3+}$ chelates is not high compared to $Eu^{3+}$ and $Tb^{3+}$, Eu–Sm two-color assays are used for the simultaneous determination of a low concentration component (Eu) and a relatively high concentration component (Sm) in serum; the assayed combinations are lutropin and follitropin, myoglobin and carbonic dehydratase, AFP and free β-subunit of human chorionic gonadotrophin (Hemmilä et al., 1987). Use of Eu–Tb is reported by Eriksson et al. (2000) for the simultaneous determination of human serum free and total PSA.
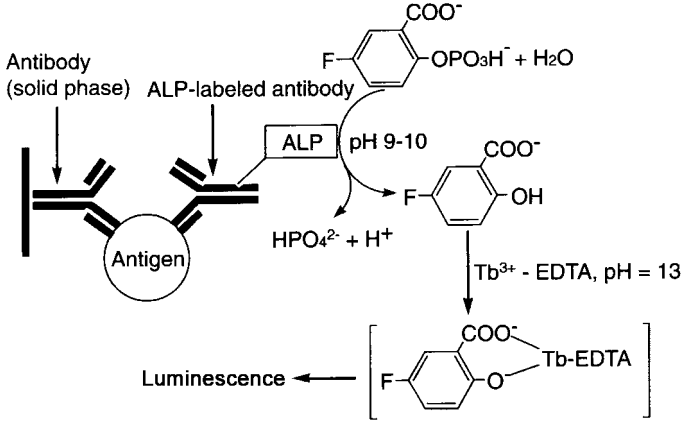
Fig. 11.  Detection principle of enzyme-linked time-resolved immunoassay.
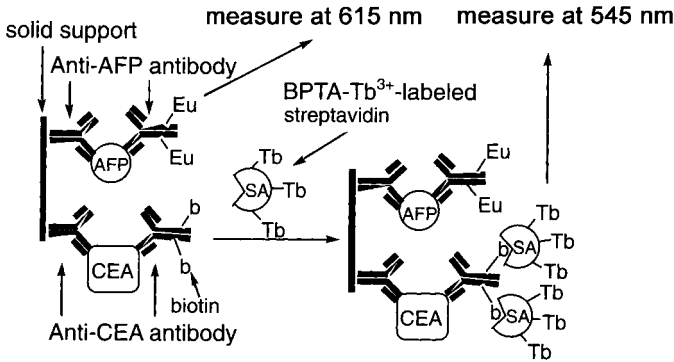


Fig. 12.  Dual-label time-resolved fluoroimmunoassay of AFP and CEA with luminescent lanthanide labels BHHCT–$Eu^{3+}$ and BPTA–$Tb^{3+}$.

In another Eu–Tb two-color immunoassay for two low concentration components, highly luminescent labels, BPTA–$Tb^{3+}$ and BHHCT–$Eu^{3+}$ were used for human serum AFP and CEA (carcinoembryonic antigen) by Yuan et al. (2001) (fig. 12). As shown in fig. 10, a well was coated with AFP and CEA antibodies, and after the serum sample was applied, anti-AFP antibody labeled with BHHCT–$Eu^{3+}$ and anti-CEA antibody labeled with biotin were reacted. After washing the well and measuring the emission of the Eu chelate at 615 nm, SA labeled with BPTA–$Tb^{3+}$ was added and the emission of the Tb chelate at 545 nm was measured. In this system, the detection limits of AFP and CEA were very low, 44 pg/ml and 76 pg/ml, respectively.

Homogeneous immunoassay using FRET is an attractive assay format, since the antigen–antibody binding reaction is much accelerated compared to that of solid phase sandwich im-
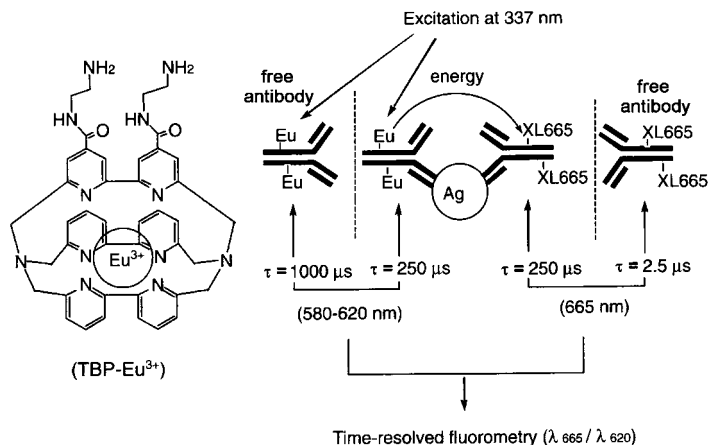
Fig. 13. Structure of TBP–Eu$^{3+}$ and principle of "TRACE" homogeneous time-resolved fluoroimmunoassays.

munoassay. However most homogeneous assays are competitive assays, which is convenient but not very sensitive. Sandwich-type homogeneous assays are desirable, but not easy to carry out, because the bulky antigen molecule sandwiched between two antibody molecules make the distance between the two antibody molecules large and FRET is not usually observed. One example of non-competitive homogeneous immunoassay was reported by Mathis (1993, 1995) and Mathis et al. (1997) and is shown in fig. 13, in which TBP–Eu$^{3+}$ is the donor and a natural dye protein XL665 having quantum yield of 0.7 is used as the acceptor. The emission of XL665 at 665 nm is measured with time-resolved fluorometry, since the lifetime of XL665 becomes long ($\sim n \times 10$ microsecond) due to the FRET from the Eu$^{3+}$ chelate (fig. 11). Many bulky antigens have been measured with this method, e.g., PSA, p53, and the thyrosine protein kinase assay was performed with this technique.

## 7. Applications targeting nucleic acids

### 7.1. *Heterogeneous methods*

Heterogeneous-type assays are analyses which require a washing process to separate the probes bound to targets from unbound free probes (B/F separation). This process is time-consuming and labor-intensive, which sometimes makes this type of assays less attractive than homogeneous-type assays. Nevertheless, the principle is simple, so that many assays are still and will be performed in heterogeneous format. A few recent studies are briefly reviewed below.

Rintamäki et al. (2002) performed heterogeneous hybridization assays to detect *Streptococcus pneumoniae* DNA using an Eu$^{3+}$-labeled probe (table 5). The procedure is as follows: Firstly, usual PCR is performed for *S. pneumoniae* DNA using a forward primer labeled with

Table 5
Lanthanide chelates used in DNA/RNA-targeted applications

| Application type | Chelate | Reference |
|---|---|---|
| Heterogeneous hybridization assay | $Eu^{3+}$–W2014 (Wallac/PerkinElmer) | Rintamäki et al. (2002) |
| | $Eu^{3+}$, $Tb^{3+}$, $Sm^{3+}$–L1 | Samiotaki et al. (1997) |
| Homogeneous hybridization assay | $Eu^{3+}$–BHHCT | Sueda et al. (2000) |
| | $Tb^{3+}$–L3 (BPTA) | Sueda et al. (2002) |
| | $Eu^{3+}$, $Tb^{3+}$– DTPA-cs124–ethylenediamine | Tsourkas et al. (2003) |
| | $Tb^{3+}$–DTPA-cs124 | Root et al. (2004) |
| | $Eu^{3+}$–L2 | Laitala and Hemmilä (2005) |
| Intercalation-based assay | $Tb^{3+}$–L5 | Yegorova et al. (2005) |
| | $Eu^{3+}$–tetracycline | Ci et al. (1995) |
| | $Eu^{3+}$–oxytetracycline | Liu et al. (2002) |
| | $Tb^{3+}$–BPMPHD–CTMAB | Wu et al. (1999) |
| Chemiluminescence-coupled assay | $Tb^{3+}$–FLUQ | Yi et al. (2003) |
| Real-time PCR (TruPoint®-PCR) | $Eu^{3+}$, $Tb^{3+}$–L4 | Nurmi et al. (2000, 2001, 2002), Kiviniemi et al. (2003) |
| | $Eu^{3+}$–L2, $Tb^{3+}$–L4 | Ylikoski et al. (2004) |
| Genotyping | $Eu^{3+}$, $Tb^{3+}$–L4 | Kiviniemi et al. (2003) |
| (Competitive TruPoint®-PCR) | $Eu^{3+}$–L2, $Tb^{3+}$–L4 | Ylikoski et al. (2004) |
| (OLA) | $Eu^{3+}$–TBP | Lopez-Crapez et al. (2001) |
| (Minisequencing) | $Eu^{3+}$–TBP | Lopez-Crapez et al. (2005) |
| (Invader®) | $Eu^{3+}$–L2 (DTBTA), $Tb^{3+}$–L3 (BPTA) | Fukui et al. (2005) |

biotin at the 5′ end. Then the PCR amplicon is introduced into a streptavidin-coated microtiter well and denatured with NaOH, which leaves only the biotin-labeled single-stranded DNA (ssDNA) on the well. An Eu-labeled oligonucleotide probe which is complementary to the biotin-labeled ssDNA is added to the well, and finally the amount of Eu left in the well after washings is determined by DELFIA®. With this assay method, as few as 50 fg of purified *S. pneumoniae* DNA was detected, which corresponded to ∼20 copies of the DNA.

This PCR → hybridization → DELFIA® type of assay can be performed in a multi-color format. Samiotaki et al. (1997) reported this type of assay using seven different hybridization probes, which are three singly-labeled probes (labeled with Eu, Tb, and Sm), three doubly-labeled probes (labeled with Eu and Tb, Eu and Sm, and Tb and Sm), and one triply-labeled probe (labeled with Eu, Tb, and Sm) (see table 5 and scheme 15 for the chelate ligand). After PCR amplification, the PCR product was allowed to hybridize with one of the seven hybridization probes, washed, detected lanthanide ions by DELFIA®, and washed. This cycle was repeated for the remaining six hybridization probes. This procedure enabled detection and identification of seven types of human papilloma virus in one single assay.
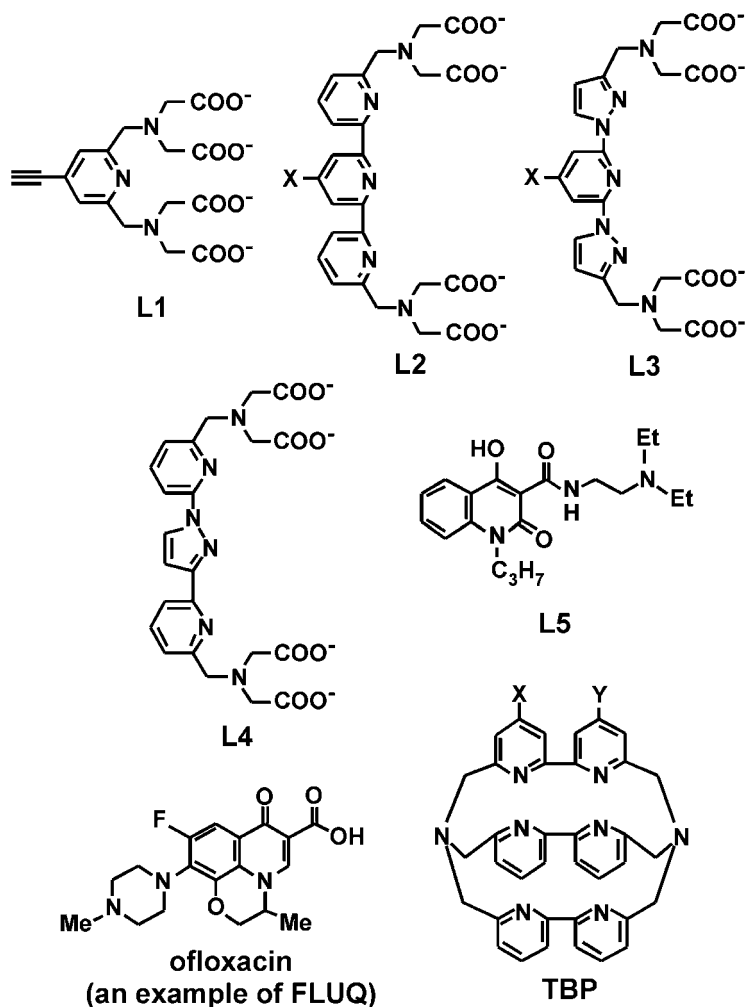
Scheme 15.

## 7.2. *Homogeneous methods*

### 7.2.1. *Homogeneous hybridization assays*

Homogeneous hybridization assays are analyses for the detection of a given DNA/RNA sequence by hybridization without separation processes (B/F separation). These assays form a basis of real-time PCR as described below. Furthermore, sufficiently sensitive homogeneous hybridization assays could be done without PCR and enable, for example, direct detections of certain mRNA forms expressed in cells. This type of experiment has been actually performed with some organic fluorophores (Peng et al., 2005; Santangelo et al., 2006).
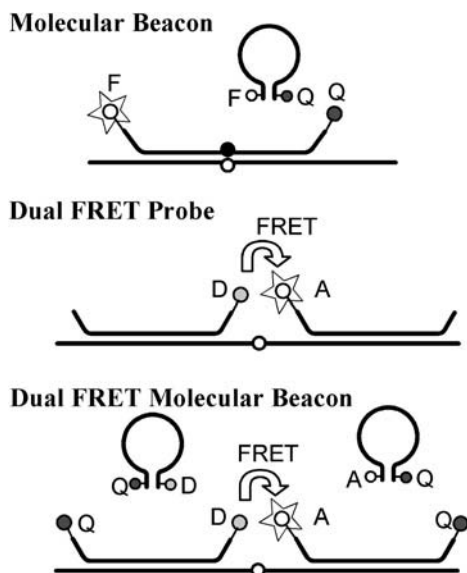
Fig. 14.  Examples of homogeneous hybridization assay methods (F: luminophore, Q: quencher, D: donor, A: acceptor). Thick lines represent DNA strands. Open circles on DNA strands indicate a SNP/mutation site for Molecular Beacon and insertion/deletion sites for dual FRET probe and dual FRET Molecular Beacon when these methods are applied to SNP/mutation typing or deletion/insertion detection. The solid circle on the strand indicates the complementary site.

Various types of homogeneous hybridization assays have been reported, and almost all of them are based on FRET and/or fluorescence quenching technique. FRET and fluorescence quenching reflects interactions of molecules in homogeneous media and thus is suited for homogeneous assays. Molecular beacons and (dual) FRET probes are frequently used oligonucleotide probes based on FRET and fluorescence quenching technique (fig. 14). Molecular beacons are nucleotide probes having a hairpin (stem-loop) structure, where the loop region is designed to be complementary to target DNA/RNA, and the stem region is labeled with a luminophore at one side and a quencher at the other side. Thus the luminescence is quenched without target DNA/RNA. When target DNA/RNA coexists, on the other hand, the molecular beacon is annealed to the target and the luminescence revives. In fact, molecular beacons have been used successfully in PCR, genotyping, DNA/RNA binding or cleavage assay of proteins, and gene expression monitoring (Broude, 2002; Tan et al., 2004; Peng et al., 2005; Santangelo et al., 2006). However, molecular beacons have weak points in that the probes may provide false-positive signals due to (1) degradations by nucleases and (2) interactions with DNA/RNA binding proteins. These points can be problematic particularly when assays are performed with living cells or whole cell lysates. To overcome these points, a dual FRET probe method has been invented (fig. 14). The latter uses a pair of FRET probes, where one is labeled with a donor luminophore and the other is labeled with an acceptor luminophore. The

pair of FRET probes are designed to be complementary to neighboring regions of the targeted DNA/RNA. Hence, when target DNA/RNA coexists, the pair of probes are annealed to the target side by side, which induces FRET from the donor to the acceptor luminophores. On the other hand, no FRET will occur when the probes are digested by nucleases or opened by DNA/RNA binding proteins. A slight modification to the dual FRET probe method is additional conjugation of quenchers to the probes, sometimes referred to as "dual FRET molecular beacon" (fig. 14) (Tsourkas et al., 2003). This quencher conjugation reduces the background signals from unannealed acceptors and donors.

To date, numbers of homogeneous hybridization assays using lanthanide-labeled probes have been reported and improvements in sensitivity have been achieved. When used in FRET-based assays, lanthanide chelates have two particular advantages: One advantage comes from the sharp emission profile of lanthanide chelates. This minimizes the spectral overlap between the emission bands of the donor and the acceptor. Therefore, by choosing an appropriate wavelength for acceptor emission, one can observe the FRET signal almost free of the donor signal even without a quencher. The other advantage comes from relatively large Förster distances for FRET from lanthanide chelates to organic fluorophores, which makes influences of slight fluctuation in the donor-acceptor distance negligible (see section 5).

Sueda et al. (2000, 2002) reported a dual FRET probe assay, where two combinations, Eu-BHHCT–Cy5 and Tb-BPTA–Cy3, were tested for the donor–acceptor combination. They used a pair of 15-mer oligonucleotide probes to detect 31–34 synthetic oligonucleotide targets. As noted above, the emission intensities from $Eu^{3+}$ and $Tb^{3+}$ are negligibly weak at the Cy5 and Cy3 emission wavelengths (669 and 565 nm, respectively). Additionally, the initial emission intensities from Cy3 and Cy5 were quite weak when excited at the excitation wavelengths for the $Eu^{3+}$ and $Tb^{3+}$ chelates (340 and 325 nm, respectively). These properties enabled sensitive detection without quenchers. The detection limits were reported to be ∼200 pM and ∼30 pM for the $Eu^{3+}$–Cy5 and $Tb^{3+}$–Cy3 systems, respectively.

Tsourkas et al. (2003) reported dual FRET molecular beacon assays, where the donor probe was labeled with either $Eu^{3+}$ or $Tb^{3+}$ complex of DTPA-cs124–ethylenediamine (and no quenchers attached). For the $Eu^{3+}$ complex, the acceptor probe was Cy5-labeled (and no quenchers attached); and for the Tb complex, the acceptor probe was labeled with Cy3 or ROX as a fluorophore and with dabcyl as a quencher. They demonstrated that these pairs of probes detected DNA targets (∼50-mer) with high S/N.

Root et al. (2004) reported different dual FRET molecular beacon assays, which used a donor probe labeled with a $Tb^{3+}$ complex and FITC (as a quencher) and an acceptor probe labeled only with Cy5. The donor and acceptor probes were designed to be annealed to a target DNA with a separation of certain nucleotides (14–17 nucleotides) formed between the two probes. They examined the effects of the separation length on the FRET efficiency. The FRET efficiency drastically changed from 0.52 to 0.04 as the number of the intervening nucleotides varied from 14 to 17 (corresponding to a variation from ca. 5.0 to 8.6 Å separation). This change, consistent with the Förster distance of 51 Å evaluated for $Tb^{3+} \rightarrow$ Cy5 FRET, was so drastic that this method was able to distinguish even single nucleotide difference. It is however worth noting that, because of so large Förster distance, rather smaller separations such as 1–5 nucleotide separations could not be distinguished (Sueda et al., 2000). Thus the choice

of the separation length will be crucial for detection of single nucleotide deletion/insertion difference by using this dual FRET molecular beacon method.

An extreme case of high sensitivity was reported by Laitala and Hemmilä (2005), who used "anti-Stokes shift FRET". In their study, the donor probe was labeled with a $Eu^{3+}$ complex, and the acceptor probe was labeled with Alexa Fluor 488, 514, 532, 546, 555, or 647. Alexa Fluor 546, for example, has a fluorescence excitation band in the region of 500–580 nm. On the other hand, the Eu emission bands appear in the region above 580 nm. Thus there is no or very limited spectral overlap between Alexa Fluor 546 and the $Eu^{3+}$ complex. In spite of this fact, they observed strong FRET signal from $Eu^{3+}$ to Alexa Fluor 546. They called this type of FRET "anti-Stokes shift FRET", though in fact the actual excitation wavelength ($\sim$340 nm) is shorter than the Alexa Fluor excitation peak. The advantage of this novel type of FRET is that the emission of the Eu complex at the FRET signal wavelength (572 nm for Alexa Fluor 546) is extremely weak, which permits almost ideal background-free measurements. The detection limit was reported to be 0.8 pM for an assay detecting a synthetic DNA target.

### 7.2.2. *Intercalation-based assay*

Double-stranded DNA (dsDNA) can be detected by intercalation reagents with relatively high sensitivity. Although intercalation-based detection has a disadvantage of non-specificity, this detection method is often used in real-time PCR (e.g., SYBR® Green and PicoGreen®). Several intercalating agents based on luminescent lanthanide complexes have been reported. One recent example is a report by Yegorova et al. (2005). They prepared 9 ligands derived from 2-oxo-4-hydroxy-quinoline-3-carboxylic acid, and selected the best ligand (referred to as L5 here) for DNA detection. The $Tb^{3+}$–L5 complex showed increased luminescence intensity upon addition of DNA. The excitation spectrum also changed with the addition of DNA: The excitation maximum moved by 10 nm from 310 to 320 nm, and a shoulder appeared at 340 nm. Thus the luminescence change was most effectively detected by 340 nm excitation. The limit of detection (LOD) of the $Tb^{3+}$–L5 complex was reported to be 10 ng/ml. This value is similar to those reported for $Eu^{3+}$-tetracyclins (LOD = 11 ng/ml) (Ci et al., 1995; Liu et al., 2002), $Tb^{3+}$–BPMPHD–CTMAB (LOD = 9 ng/ml) (Wu et al., 1999), and ethidium bromide (LOD = 10 ng/ml), but still larger than that for PicoGreen® (LOD = 0.25 ng/ml).

### 7.2.3. *Chemiluminescence-coupled assay*

Yi et al. (2003) combined the Ce(IV)–$Na_2SO_3$ chemiluminescence system and the DNA–$Tb^{3+}$–FLUQ competitive system, where FLUQ is a fluoquinolone such as ofloxacin (scheme 15). The redox reaction between $Ce^{4+}$ and $Na_2SO_3$ produces $SO_2^*$, which can transfer energy to $Tb^{3+}$–FLUQ. Hence chemiluminescence signal can be obtained from the $Ce^{4+}$–$Na_2SO_3$–$Tb^{3+}$–FLUQ system. On the other hand, DNA and FLUQ competes for $Tb^{3+}$. Thus, with the addition of DNA, the luminescent $Tb^{3+}$–FLUQ complex is dissociated and a non-luminescent $Tb^{3+}$–DNA complex forms. Therefore, when DNA is added to the chemiluminescence $Ce^{4+}$–$Na_2SO_3$–$Tb^{3+}$–FLUQ system, the chemiluminescent signal decreases. By using this phenomenon, sensitive detection of DNA was performed. Reported detection limits were 7.8 and 9.5 ng/ml for natural and denatured DNA, respectively.

### 7.2.4. *Real-time PCR (TaqMan® and related techniques)*

PCR is a very powerful technique, providing a sizable amount of DNA from a trace of a DNA sample. Hence it would be natural to expect that the trace amount of starting DNA can be quantitated sensitively from the amount of the finally-obtained PCR product. However, this type of quantitation based on the end-point detection is not reliable because of the saturation effects of PCR. This problem has been overcome by real-time PCR, which monitors PCR amplification in real time and enables accurate quantitation from the kinetics of the exponential phase. Real-time PCR thereby provides a highly sensitive and specific quantitation method for nucleic acids.

At present, roughly two types of methods are available for real-time PCR: (1) the methods using intercalation and (2) the methods using the $5' \rightarrow 3'$ exonuclease activity of DNA polymerases. The former type uses an intercalating agent such as SYBR® Green and PicoGreen® (vide supra). This type of method is quite straightforward, but has a weak point in that it cannot distinguish specific amplifications from non-specific ones. This is inevitable because intercalation itself is a non-specific interaction. The latter type uses the $5' \rightarrow 3'$ exonuclease activity, which is inherent to several DNA polymerases. Such methods allow specific detection of DNA. A typical example is the TaqMan® method (fig. 15), which uses an oligonucleotide probe called TaqMan® probe. This probe has a sequence that is complimentary to a target sequence, and is labeled with a luminophore at one end and a quencher at the other end, exhibiting no (or very weak) luminescence before PCR amplification. In contrast to this, as PCR amplification proceeds, the $5' \rightarrow 3'$ exonuclease activity of the polymerase digests the TaqMan® probe that is annealed to the PCR target, and thus the luminescence from the cleaved luminophore comes to be observed. SNP typing is also possible using TaqMan® probes which are designed to contain the SNP site of interest. Some modifications using luminescent lanthanide complexes have been reported by groups at the University of Turku and PerkinElmer, Inc as described below.

Nurmi et al. (2000) reported a version of real-time PCR which uses a somewhat unique $Tb^{3+}$ complex. This complex has a property that its luminescence becomes notably weak when conjugated to an oligonucleotide. On the other hand, when the $5' \rightarrow 3'$ exonuclease reaction liberates the $Tb^{3+}$ complex from the oligonucleotide, the luminescence of $Tb^{3+}$ increases ($\sim$3 to 4-fold compared to that of the intact probe). One main advantage of this is that no quencher is needed for this $Tb^{3+}$-labeled probe, which simplifies the probe design. It is worth noting that, for usual TaqMan® probes, the quenching efficiency strongly depends on the sequence of the probe, and thus the choice of a suitable sequence is sometimes troublesome. This approach was also employed for SNP typings (Nurmi et al., 2001). This assay however has a weak point that S/N is not good ($\sim$3–4). Furthermore, $Eu^{3+}$ complexes that lose their luminescence when conjugated to oligonucleotides are not yet known. Thus it is difficult to extend this assay to a mutliplex format using exclusively lanthanide chelates.

The Turku University and PerkinElmer group reported a new method named TruPoint®-PCR (Nurmi et al., 2002). They introduced quencher probes, which have a 3'-quencher labeling, in addition to detection probes, which have a 5'-lanthanide-chelate labeling. The quencher probes are designed to be complementary to the detection probes with their $T_m$ values below the PCR annealing temperature (here $T_m$ is the temperature at which 50% of DNA mole-

cules exist as the double-stranded form and the remaining 50% as the single-stranded form). Moreover, each PCR cycle is modified to include an additional low-temperature ($\sim$30 °C) step (called quenching step) after usual denature-anneal-elongation steps. At the elongation step, the detection probes are allowed to be annealed to the target DNA and to be digested by polymerase. Then, at the quenching step, the temperature is lowered and intact undigested detection probes are annealed to the quencher probes. Digested detection probes, on the other hand, are not annealed to the quencher probes. Thus, real-time monitoring of PCR amplification is possible from the luminescence intensity of the lanthanide complexes. This method was used to quantitate prostate-specific antigen mRNA in peripheral blood, and its high S/N and good sensitivity (100 copies of mRNA for this assay versus 1000 copies for usual TaqMan® assay) were demonstrated.

### 7.2.5. *Genotypings (polymorphism/mutation typings)*

In this post-genome era, more and more robust, time-efficient, and cost-effective genotyping methods are demanded to actualize "genome-based medicine" or "personalized medicine." Of particular interest are genotypings of SNPs and point mutations. Numbers of methods including inhomogeneous ones have been reported as Molecular Beacon, TaqMan® (Applied Biosystems, Inc), Invader® (Third Wave Technologies, Inc), BeadArray™ (Illumina, Inc), MassExtend® (Sequenom, Inc), Molecular Inversion Probe (ParAllele, Inc), AcycloPrime™-FP (PerkinElmer, Inc), Oligonucleotide Ligation Assay (OLA), Minisequencing (or Single Nucleotide Primer Extension) (fig. 15). Homogeneous genotyping methods using lanthanide chelates may meet the demands. Several methods have been reported and demonstrated their feasibility and superiority over conventional organic-dye-based non time-resolved methods.

One example for lanthanide-using homogeneous genotyping methods is a PCR-based method named "competitive TruPoint®-PCR" (Kiviniemi et al., 2003; Ylikoski et al., 2004). This method is similar to TruPoint® PCR, which is reviewed above, but distinctive in that this competitive TruPoint®-PCR method is classified as "end-point" detection method. Like TruPoint® PCR, competitive TruPoint®-PCR uses detection probes and quencher probes. However, the quenching step is conducted only after the whole PCR cycles are finished (hence this is classified as "end-point" detection method). Furthermore, asymmetric PCR is performed in competitive TruPoint®-PCR. The detection probes are designed to be complementary to the ssDNA amplified by the asymmetric PCR. Again in contrast to the case in TruPoint® PCR, $T_m$ between the detection probes and the amplified strands is set below the PCR annealing temperature ($\sim$40 °C). Thus the detection probes are not digested in this method. After the asymmetric PCR, the temperature is lowered and the detection probes are allowed to be annealed either to the PCR products or the quencher probes. The detection probes annealed to the quencher probes lose their luminescence whereas the detection probes annealed to the PCR products remain luminescent. On this basis, the amounts of the PCR products are quantitated. This method was applied successfully to SNP typing in a biplex format, where $Tb^{3+}$- and $Eu^{3+}$-labeled detection probes were used simultaneously.

Another example is Oligonucleotide Ligation Assay (OLA), which utilizes an enzyme ligase. The ligase connects oligonucleotide strands annealed side by side, that is with no gap between the two strands. If there is even a one-base gap between them, no (or only suppressed)
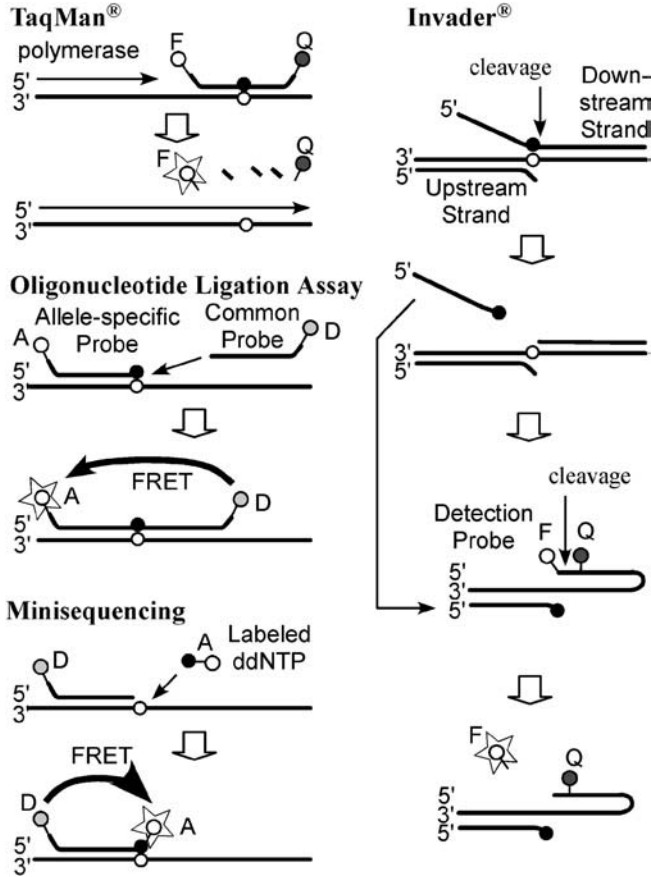
Fig. 15. Examples of SNP/mutation typing methods (F: luminophore, Q: quencher, D: donor, A: acceptor). Thick lines represent DNA strands. Open circles on DNA strands indicate SNP/mutation sites and solid circles their complementary sites.

ligation products are formed (fig. 15). OLA utilizes this ligase property to distinguish one-base difference. A lanthanide-using OLA was reported by Lopez-Crapez et al. (2001). Their method used two oligonucleotide probes, an allele-specific probe and a common probe, where the allele-specific probe has a sequence ending at the site to be typed, and the common probe has a sequence starting one base downstream of this site. The allele-specific probe was labeled with either biotin or Cy5, and the common probe was labeled with Eu-TBP. When the allele-specific probe was biotin-conjugated, XL665- or Cy5-conjugated streptavidin was added for measurement. Then, for the perfect-match case, ligation of the allele-specific and common probes should occur, and induce $Eu^{3+} \rightarrow Cy5$ or $Eu^{3+} \rightarrow XL665$ FRET. For the one-base-mismatch case, on the other hand, no FRET signal should be observed. This method was

applied successfully to the detection of the K-ras codon 12 mutations, which demonstrated its applicability to genotypings.

Lopez-Crapez et al. (2005) also reported a different type of genotyping method based on minisequencing. In minisequencing, the primer is extended by one base, and the incorporated base is identified by FRET (fig. 15). Their system used one nucleotide probe (primer probe) labeled with $Eu^{3+}$–TBP at the 5′ terminus. The primer probe had a sequence ending one base upstream of the site to be typed. It was incubated with one of the four biotin-labeled ddNTPs (ddATP, ddTTP, ddCTP, and ddGTP) in the presence of a DNA polymerase (specifically, thermosequenase™). The biotin-labeled ddNTP is appended to the primer probe if it matches with the base at the site to be typed. After the incubation, XL-665 conjugated streptavidin was added. The $Eu^{3+} \rightarrow$ XL665 FRET signal was observed only when the added biotin-labeled ddNTP matched with the base at the site to be typed. The applicability of this method was demonstrated by applying it to the detection of the p53 gene codon 248 mutations as an example.

The Invader® Method is one of the powerful SNP typing methods, and used actually in the HapMap project. This method employs a well-designed two-step reaction scheme, which allows sensitive SNP typing even from genomic DNA without PCR amplification (Hall et al., 2000). In the Invader® method, a unique nuclease called FEN is used. This nuclease recognizes a unique DNA structure called "overlap-flap" structure and cleaves the 5′-flap. The "overlap-flap" structure is a structure comprised of three DNA strands, where two strands (upstream strand and downstream strand) are annealed to strictly contiguous regions of the remaining one strand with the 3′-region of the upstream strand and the 5′-region of the down-stream strand left unannealed as flaps (fig. 15). The contiguity must be strict: If there is even one nucleotide gap between the two annealing regions, FEN does not cleave the 5′-flap. This property is utilized to distinguish one-base difference in the Invader® method. Because of the well-designed two-step reaction process, the Invader® method offers an extremely sensitive SNP typing method. Use of lanthanide chelates is expected to enhance the sensitivity. Such an attempt was performed by Fukui et al. (2005) and showed notable improvement in S/N and sensitivity, which would enable more reliable SNP typing.

## 8. Applications targeting cells

### 8.1. *Receptor–ligand binding assays*

#### 8.1.1. *DELFIA®-based assays*
Receptors are major targets in drug discovery, and development of high-throughput assay methods for receptor–ligand interactions is desirable for more efficient agonist/antagonist and drug screenings (reviewed, for example, by Hemmilä and Hurskainen, 2002). Receptor–ligand binding assays require high sensitivity, and thus radioactive isotopes are still often used. However, increasing attempts have been made to replace the radioisotopes with luminescent labels such as lanthanide chelates (see review by Handl and Gillies, 2005).

DELFIA®, developed by Wallac/PerkinElmer, Inc, is a quite powerful technique not only in usual immunoassays but also in receptor–ligand binding assays. Quite interestingly,

Table 6
Lanthanide chelates used in cell-targeted applications

| Application type | Chelate | Reference |
|---|---|---|
| Receptor–ligand binding assay | $Eu^{3+}$–DTPA–(peptide); peptide = NDP-$\alpha$-MSH, DPLCE | Handl et al. (2004, 2005) |
| | $Eu^{3+}$–GTP | Engström et al. (2004) Hong et al. (2005) |
| | $Eu^{3+}$–TBP | Gabriel et al. (2003) |
| Apoptosis detection | $Eu^{3+}$–label reagent (Amersham)–(protein); protein = Annexin V | Engbers-Buijtenhuijs et al. (2005) |
| Cell imaging | $\Delta$, $\Lambda$-[$Eu^{3+}$, $Tb^{3+}$–L6] | Frias et al. (2003) |
| | $Eu^{3+}$–L7 | Yu et al. (2006) |
| (Zn sensing) | $Eu^{3+}$–L9 | Hanaoka et al. (2004) |
| (Bimodal receptor imaging) | $Eu^{3+}$–L8 | Manning et al. (2004) |
| Immunohistochemical imaging | $Eu^{3+}$–W1024, $Tb^{3+}$–W14016 (Wallac/PerkinElmer) | Siivola et al. (2000) |
| | $Eu^{3+}$–L2 | Väisänen et al. (2000) |

DELFIA®-based receptor–ligand binding assays are applicable to whole-cell samples. Handl et al. (2004, 2005) investigated the binding of $\alpha$-melanocyte-stimulating hormone ($\alpha$-MSH) to human melanocortin 4 receptor (hMC4R), and the binding of enkephalin to human $\delta$-opioid receptor. Actually, they used superpotent analogs of the ligands, in which some amino acids were replaced with non-natural amino acids such as [Nle$^4$, D-Phe$^7$]-$\alpha$-MSH (NDP-$\alpha$-MSH) and [D-Pen$^2$, L-Cys$^5$]-enkephalin (DPLCE) (table 6). These peptide ligands were labeled with $Eu^{3+}$–DTPA. For the binding assay of NDP-$\alpha$-MSH to hMC4R, for example, $Eu^{3+}$–DTPA-labeled NDP-$\alpha$-MSH was added to hMC4R-overexpressing HEK293 cells. Cells were incubated with the $Eu^{3+}$–DTPA-labeled ligand (or also with the unlabeled ligand for competitive assay) and washed. Then the enhancement solution was added to the system, forcing DTPA to release $Eu^{3+}$ ion and producing a strongly luminescent new $Eu^{3+}$ species (also see fig. 1). From the luminescence intensities, the amounts of the $Eu^{3+}$–DTPA-labeled ligand bound to the receptor were determined. The affinity of the $Eu^{3+}$-labeled ligand was found to be similar to that of the unlabeled ligand. Their results demonstrated that these lanthanide-based assays are highly sensitive and require less time than radioactive assays.

### 8.1.2. G-protein coupled receptor (GPCR)–ligand binding assays

Numbers of drugs target GPCR, which is a class of receptor proteins found ubiquitously as an input window for varieties of signals such as light (rhodopsin), odorants, ions, amino acids, peptides, nucleotides, pheromones, and prostaglandines. Furthermore, the human genome project has revealed the presence of much more GPCRs whose ligands are not yet identified (orphan receptor). Identification of the ligands to these GPCRs will bring new targets for drugs. For this purpose, high-throughput screening (HTS)-compatible methods which can assay the events downstream of the ligand binding are required.
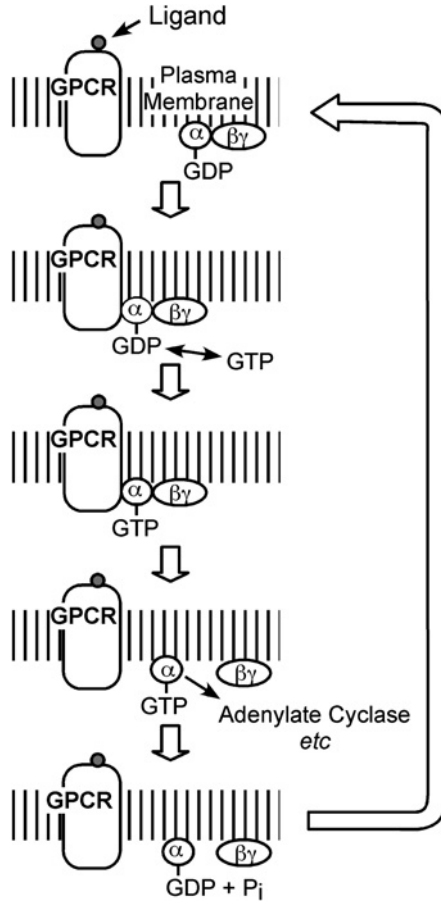
Fig. 16. Schematic drawing outlining the responses of the G-protein coupled receptor (GPCR) and of G-protein induced by ligand binding. The symbols $\alpha$ and $\beta\gamma$ denote the $\alpha$ and $\beta\gamma$ subunits of the G-protein, respectively. Note that the G-protein is situated inside the plasma membrane.

The events followed by the binding of a ligand to GPCR can be outlined as follows (fig. 16): When a ligand is bound to GPCR, the cytoplasmic side of GPCR interacts with a heterotrimer protein called G-protein, $G_{\alpha}(GDP)G_{\beta\gamma}$, which has GDP binding in its resting state. The interaction between GPCR and $G_{\alpha}(GDP)G_{\beta\gamma}$ induces the release of the GDP bound to the G-protein, and promotes alternative binding of GTP (or new GDP). This binding process is not specific to GTP, so that GDP may be bound to the G-protein again. This possibility may influence the results of the assays using radioactive GTP analogues, whose concentrations may be quite low. In live cells, on the other hand, GTP concentration is usually higher than GDP concentration, and thus this process usually leads to the exchange of GDP and GTP. When the G-protein incorporates GTP, GPCR releases the G-protein and furthermore the heterotrimer

becomes dissociated into $G_\alpha(GTP)$ and $G_{\beta\gamma}$. The $G_\alpha(GTP)$ complex interacts with another signal-transducing protein, where the target protein and the effect varies with types of $G_\alpha$. Several types of $G_\alpha$ subunits have been discovered as $G_s$, which stimulates adenylate cyclase; $G_i$, which inhibits adenylate cyclase; $G_q$, which stimulates phospholipase C; $G_t$, which works with rhodopsin in the vision sensory system and stimulates phosphodiesterase. The $G_\alpha$ subunit has an intrinsic GTPase activity, which hydrolyzes the bound GTP to GDP. When this hydrolysis occurs, the $G_\alpha$ becomes inactivated. The GTPase activity of the G-protein is in moderate strength, allowing the activated $G_\alpha(GTP)$ state to last for an appropriate time. After the hydrolysis of GTP, the G-protein returns to its initial resting state $G_\alpha(GDP)G_\beta G_\gamma$. It is important to note that these downstream events occur inside the cell, so that it is quite difficult at least at present to apply assays directly to intact cells.

The binding of GTP to the G-protein would be one of the events suited for assays. Heterogeneous GTP-binding assays based on time-resolved spectroscopy have been developed by PerkinElmer's group (Frang et al., 2003), featured by a non-hydrolyzable luminescent GTP analogue, Eu–GTP. In this assay, membrane samples containing GPCR and the G-protein are added to wells containing the desired concentrations of test ligands. After an appropriate time of incubation, Eu–GTP is added to the wells and allowed to be bound to the G-protein. From the Eu luminescence intensities measured after washing the wells, the amounts of Eu–GTP bound to the G-protein are determined. Engström et al. (2004) applied this assay to screen peptides for a human neuropeptide FF2 (hNPFF2) receptor agonist/antagonist. Results showed that this method is a powerful alternative to the conventional method using the radioactive GTP analogue $[^{35}S]$guanosine-5′-O-(3-thio)triphosphate($[^{35}S]$GTP$\gamma$S). A clear advantage of Eu–GTP over $[^{35}S]$GTP$\gamma$S is that a higher concentration can be used in assays for Eu–GTP, which diminishes the unexpected competition effects between GTP and GDP in the GDP $\leftrightarrow$ GTP exchange process. The authors pointed out that the $K_d$ values obtained using $[^{35}S]$GTP$\gamma$S were systematically lower than those obtained using Eu–GTP because of this competition effect. Attempts to fabricate functional GPCR microarrays using Eu-GTP were reported, and usability of the GPCR microarrays was demonstrated by Hong et al. (2005).

Ligand screenings for GPCR agonists/antagonists are also possible through cAMP assays for the $G_s$ system. Numbers of homogeneous cAMP assay methods are known, and several methods were tested for applicability to GPCR-ligand screening (Gabriel et al., 2003). The report concluded that HTRF® (Cisbio, Inc) and ALPHA Screen™ (PerkinElmer, Inc) methods were found to be sensitive and HTS-compatible for $G_s$-coupled agonist/antagonist screens.

## 8.2. *Apoptosis detection*

Apoptosis (programmed cell death) is a phenomenon involved in many biological events such as organ development, body design, natural anti-tumor activities, and aging. At present there are two typical methods for the detection of apoptosis; Annexin V method and terminal deoxynucleotidyl transferase (TdT)-mediated dUTP nick end labeling (TUNEL) method. An important difference between the two methods is that the Annexin V method detects an early stage of apoptosis whereas the TUNEL method is sensitive to a later stage. The Annexin V method measures a change in plasma membrane, where phosphatidylserine is translocated to

the outer leaflet of the membrane in the early stage of apoptosis. Annexin V is a protein that has a property to bind the translocated phosphatidylserine. Addition of labeled Annexin V therefore enables detection of apoptosis. The TUNEL method, on the other hand, detects cleaved DNA by using an enzyme TdT added externally. When labeled dUTP is added simultaneously, the enzyme TdT attaches the labeled dUTP to the terminal of the cleaved DNA. Detection of apoptosis using $Eu^{3+}$-labeled Annexin V was reported by Engbers-Buijtenhuijs et al. (2005). Specifically, they investigated apoptosis of adherent cells induced by cell detachment (anoikis). High sensitivity of the method allowed direct measurements of adherent cells on a well without a manipulation like trypsinization. This revealed the presence of Annexin V-positive cells also in the group of cells that were still attached to the well. These cells may be in a very early stage of apoptosis.

## 8.3. *Imaging*

### 8.3.1. *Cell imaging*

Cell and tissue imaging using lanthanide chelates is attracting because time-resolved technique is expected to actualize highly sensitive imaging by eliminating the background signal from cell autofluorescence. This possibility, however, does not seem to be explored sufficiently yet. Presumably this is in part because no appropriate time-resolved microscopes are commercially available. (Actually, non time-resolved microscopes were used in most of the studies reviewed below.) Furthermore, the fact that most lanthanide chelates require UV excitation is another disadvantage, which is however progressively improved by continuous efforts to find better chelate–antenna systems. Or multi-photon excitation technique may help overcome this disadvantage (White et al., 2004). Anyway, it is true that non time-resolved imaging is often hampered by background autofluorescence, in particular, for some types of fixed cells or tissues (Tagliaferro et al., 1997; Clancy and Cauller, 1998). This situation must be greatly improved by time-resolved imaging technique.

An example for cell imaging was reported by Frias et al. (2003). They used enantiopure nonacoordinate cationic lanthanide complexes (referred to as $\Delta$[R–L6] and $\Lambda$[R–L6], R $=$ $Eu^{3+}$ and $Tb^{3+}$; see table 6 and scheme 16 for the chelating ligand). Mouse fibroblast NIH 3T3 cells were incubated with an aqueous solution of each complex (1 mM). Microscopic images of the cells after 1–48 h incubations showed migration of the $Eu^{3+}$ and $Tb^{3+}$ complexes through the cytoplasm, across the nuclear membrane, and into nucleus. The migration of the $Tb^{3+}$ complexes from the cytoplasm to the nucleus appeared to be slower than that of the $Eu^{3+}$ complexes. However, it is not clear whether this difference reflects a true difference in migration rate or if it appears because the $Tb^{3+}$ complexes are more sensitive to quenching by nucleic acids in the nucleus. On the other hand, no significant differences were found between the migration behaviors of the $\Delta$- and $\Lambda$-complexes. It is quite interesting that this type of complex (+3 cation and molecular weight >1000) can be taken up by cells, which encourages other attempts for lanthanide-based cell imaging. However, the mechanism by which the cells take up the complexes is not clear. Because of the charge and the bulkiness of the complexes, it is unlikely that the complexes passively penetrate the plasma membrane. The authors suggested that a certain transporter or a pore in the membrane may be involved in
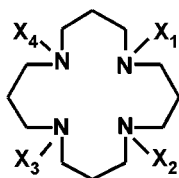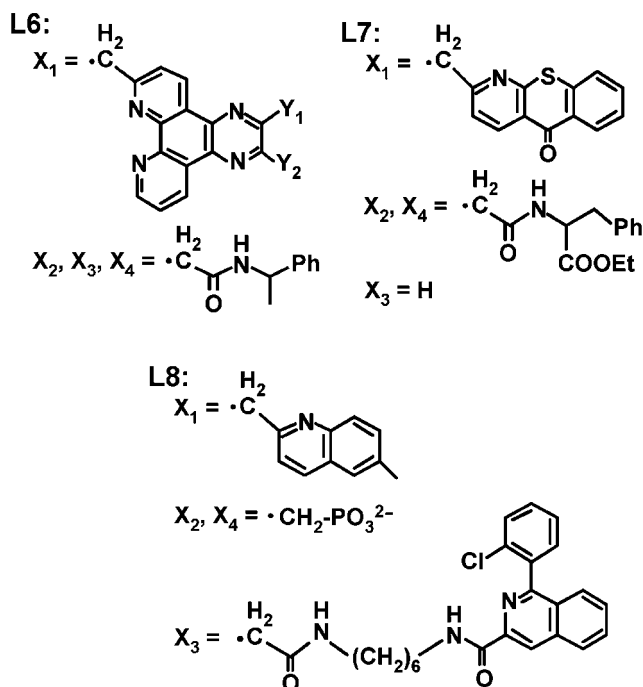
Scheme 16.

the uptake. Another interesting point is that these complexes were able to induce cell death. In vitro studies showed that irradiation of DNA (pBluescript-based plasmid DNA) in the presence of either complex caused damages (nicking and linearization) to the DNA. They also irradiated the cells which were preincubated with the $Eu^{3+}$ complex, and this resulted in 100% cell death. In control experiments, less than 15% cell death was observed in the absence of direct irradiation or in the absence of the complex.

Yu et al. (2006) used an analogous cyclam-based $Eu^{3+}$ complex (Eu–L7) and showed that this complex is useful for selective staining of nucleoli for both live and fixed cells (NIH 3T3, HeLa, and HDF cells). They checked that more than 90% of the cells loaded with the $Eu^{3+}$ complex (100 μM) seemed to remain healthy over 24 h. The amount of $Eu^{3+}$ in cells

**L9**
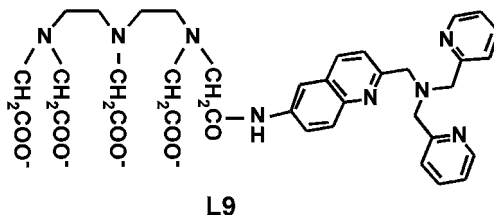
Scheme 17.

which were loaded with 200 μM of the complex for 5 h was estimated by laser-sorting flow-cytometry as $2 \times 10^{-15}$ mol/cell, which corresponded to an intracellular concentration of 0.5 μM. The mechanism of the selective staining is not clear in spite of their efforts including circularly polarized luminescence measurements. They suggested the presence of more than one, possibly protein-bound, $Eu^{3+}$ species in the nucleoli. Nucleoli are nucleus sites where transcription and processing of ribosomal RNA and assembly of ribosome take place. Furthermore, recent studies proposed involvements of nucleoli in other cellular events such as tumorigenesis and aging. Thus the selective staining of nucleoli may find applications in these areas.

Hanaoka et al. (2004) reported an $Eu^{3+}$ complex which can image cellular distribution of chelatable $Zn^{2+}$ ion. The ligand (L9) had a TPA-based moiety where one pyridine was replaced with quinoline for antenna effect (scheme 17). This $Eu^{3+}$ complex exhibited remarkable enhancement of luminescence when the $Zn^{2+}$ ion was ligated to the TPA-based moiety. The luminescence quantum yield changed from $\phi = 0.9\%$ to 7.4% upon Zn addition (while the luminescence lifetime did not change appreciably) with an apparent dissociation constant $K_d = 59$ nM for $Zn^{2+}$. This $K_d$ value may be compared with that of an organic-fluorophore-based Zn sensor (15 nM) (Gee et al., 2002). This $Eu^{3+}$ complex had quite satisfactory Zn specificity, not exhibiting luminescence enhancement with $Na^+$, $K^+$, $Ca^{2+}$, $Mg^{2+}$, $Mn^{2+}$, $Fe^{2+}$, $Fe^{3+}$, $Co^{2+}$, $Ni^{2+}$, or $Cu^{2+}$, but only for biologically irrelevant $Cd^{2+}$ besides $Zn^{2+}$. With this new Zn-sensing complex, the authors performed Zn-imaging of living cells. For this purpose, the $Eu^{3+}$ complex was micro-injected into a living cell (HeLa cell), and the $Zn^{2+}$ ions entering into the cell through exogenously added Zn-selective ionophore, pyrithione, were successfully imaged.

Manning et al. (2004) reported a new type of lanthanide probe which can be used for both magnetic resonance imaging (MRI) and luminescence imaging. Actually the lanthanide probe was a mixture of $Gd^{3+}$ and $Eu^{3+}$ complexes, where the former enhances the proton magnetic relaxation and thus can be visualized clearly by $T_1$ (or $T_2$)-weighted MRI. Specifically, the probe targeted peripheral benzodiazepine receptor (PBR). Benzodiazepines are often used clinically as muscle relaxants, anticonvulsants, anxiolytics, sedative-hypnotics. PBR is one type of the receptors for benzodiazepines, located in mitochondria (though the drug effects are reported to arise mainly from another type of benzodiazepine receptor called central benzodiazepine receptor). The ligand (L8) had a quinoline moiety for antenna effect and a PK11195-based moiety (antagonist of PBR) for receptor binding. Incubations of PBR-overexpressing

C6 glioma cells with the $Eu^{3+}$ complex (10–500 μM, 45 min and 1 h at 37 °C) provided clear images consistent with the localization of the complex at mitochondria. Incubations of the cells at 4 °C, on the other hand, resulted in no probe uptake by the cells, which indicated that the lanthanide probe entered the cells through some biological activities. Finally, the authors performed luminescence and MR imaging experiment by using cocktail mixtures of $Eu^{3+}$ and $Gd^{3+}$ complexes (for example, $Eu^{3+}:Gd^{3+} = 40:60$), and successfully obtained nice luminescence and MR images from the same population of C6 cells.

### 8.3.2. *Immunohistochemical imaging*

Time-resolved immunohistochemical imaging was explored by Väisänen et al. (2000). In conventional immunohistochemical staining, antibodies conjugated to an enzyme such as horse radish peroxidase (HRP) (or antibodies conjugated to biotin, and avidin conjugated to HRP) are used. For the HRP system, antigen–antibody–(biotin–avidin)–HRP complexes are allowed to form, and HRP substrates such as diaminobenzidine and *o*-phenylenediamine are added. Then HRP converts the substrates into insoluble dye products, from the color intensity of which the presence and the quantity of the target is assessed. This method allows highly sensitive detection owing to the high turn-over rate of the conjugated enzyme. However, accurate quantitation of the target antigen is often difficult because the signal amplification by the enzyme may not be linear. Thus, development of a staining method which simply uses a luminophore-labeled antibody and simultaneously has high sensitivity is desirable. With this aim, Väisänen et al. (2000) explored time-resolved immunohistochemical imaging. They examined prostate-specific antigen (PSA) in human prostate tissue specimens and human metastatic prostate adenocarcinoma LNCaP cells. PSA is a protein produced in the prostate gland, and the concentration of PSA in blood is clinically used to check the possibility of prostate cancer. Prostate tissue specimens and LNCaP cells were stained with a $Eu^{3+}$-labeled anti-PSA monoclonal antibody, and imaged on a time-resolved fluorescence microscope. The time-resolved measurements successfully provided images of high S/N by achieving nearly total absence of the background signal. These high S/N images seem to allow much more reliable quantitations than those obtained by conventional staining methods.

## 9. Conclusion and perspectives

Time-resolved fluorometry using lanthanide chelates as luminescent labels is a potentially superior technique for biomedical analyses. In this chapter advantages of the technique have been introduced in comparison with non time-resolved fluorometry using conventional organic dyes. The clearest advantage is that time-resolved fluorometry using lanthanide chelates with long life-time can remove background fluorescence and thus the sensitivity is increased. This advantage is especially clearly observed in assays where the sample contains many co-existing materials in relatively high concentration. Immunoassay of serum is such an example and analyses of target proteins in serum have been reported with high sensitivity. Examples of analyses where time-resolved measurement is less effective in terms of sensitivity compared to immunoassay mentioned above is DNA analyses where DNA is extracted from body samples and the sample solution contains less matrix materials than serum.

The feature of lanthanide chelates, i.e., large Stokes shift over 200 nm and long life-time often more than 1 ms, is specific to lanthanide compounds and is not realized with organic fluorescent dyes. What is considered disadvantage or must be considered more carefully compared to organic dyes is the stability of metal chelates. Since biological samples contain various biomolecules that can act as ligands to lanthanide ions and remove and bind the metal ions from luminescent lanthanide chelates, design of a chelate ligand requires high stability of the metal chelate; usually the complex formation constant should be $10^{13}$ or higher, but in addition, several other aspects of metal chelates must also be considered depending on the application area. Imaging of cells and tissues is a growing area and time-resolved imaging with its high S/N ratio will be an attractive tool to observe structures of cells and tissues. For this purpose, lanthanide chelates should be transported across cell membrane and accumulated in certain organs or structures within a cell or tissues. Permeability of cell membrane is a factor that is strongly required but is not easy to realize for many luminescent labels.

Another desirable factor for certain application is to shift the excitation wavelength as close as possible to 400 nm from the current UV wavelength of about 330 nm. This is important to imaging of living cells where UV light is harmful to cells. If appreciably efficient excitation is possible at longer wavelength, that would make an innovative change to time-resolved instruments, since small cheap solid-state lasers can be used in visible wavelength region above 400 nm, and many instruments in portable size will be available. Excitation with visible light is also preferable to imaging, since UV excitation needs expensive UV lenses in order to suppress the background fluorescence caused by the lens material. Such background problem is much less serious for visible light.

In addition to high sensitivity, possibility of multi-color labeling is also an attractive feature of lanthanide chelate labels. $Eu^{3+}$ and $Tb^{3+}$ chelates are most strongly luminescent compounds, but also $Sm^{3+}$ and $Dy^{3+}$ have been used as relatively strong luminescent chelates. Recently lanthanide chelates that emit in near infrared have been explored, such as $Er^{3+}$ and $Nd^{3+}$. Near infrared is an area where molecules and materials seldom interact with light, therefore spectral background is expected to be very low. The narrow emission peak profiles of lanthanide chelates are especially advantageous in multi-color labeling, and various lanthanide ions will be explored for this purpose, which will eventually lead to new lanthanide chelate biotechnology.

# References

Binnemans, K., 2005. In: Handbook on the Physics and Chemistry of Rare Earths, vol. 35 (chapter 35). Elsevier, Amsterdam.

Broude, N.E., 2002. Trends Biotechnol. **20**, 249.

Chen, J., Selvin, P.R., 1999. Bioconjugate Chem. **10**, 311.

Ci, Y.X., Li, Y.Z., Liu, X.J., 1995. Anal. Chem. **67**, 1785.

Christopoulos, T.K., Diamandis, E.P., 1992. Anal. Chem. **64**, 342.

Clancy, B., Cauller, L.J., 1998. J. Neurosci. Methods **83**, 97.

Diamandis, E.P., 1988. Clin. Biochem. **21**, 139.

Diamandis, E.P., Christopoulos, T.K., 1990. Anal. Chem. **62**, 1149A.

Engbers-Buijtenhuijs, P., Kamphuis, M., van der Sluijs Verr, G., Haanen, C., Poot, A.A., Feijen, J., Vermes, I., 2005. Apoptosis **10**, 429.

Engström, M., Närvänen, A., Savola, J.-M., Wurster, S., 2004. Peptides **25**, 2099.

Eriksson, S., Vehniainen, M., Jansen, T., Meretoja, V., Saviranta, P., Pettersson, K., Lövgren, T., 2000. Clin. Chem. **46**, 658.

Evangelista, R.A., Pollak, A., Templeton, E.F., 1991. Anal. Biochem. **197**, 213.

Frang, H., Mukkala, V.-M., Syystö, R., Ollikka, P., Hurskainen, P., Scheinin, M., Hemmilä, I., 2003. Assay Drug Dev. Tech. **1**, 275.

Frias, J.C., Bobba, G., Cann, M.J., Hutchison, C.J., Parker, D., 2003. Org. Biomol. Chem. **1**, 905.

Fukui, K., Ochiai, Y., Xie, M., Horie, M., Kageyama, Y., Matsumoto, K., 2005. In: Abstract of International Chemical Congress of Pacific Basin Societies (Honolulu, Hawaii; December 15–20, 2005), Program No. 475.

Gabriel, D., Vernier, M., Pfeifer, M.J., Dasen, B., Tenaillon, L., Bouhelal, R., 2003. Assay Drug Dev. Technol. **1**, 291.

Gee, K.R., Zhou, Z.-L., Qian, W.-J., Kennedy, R., 2002. J. Am. Chem. Soc. **124**, 776.

Hall, J.G., Eis, P.S., Law, S.M., Reynaldo, L.P., Prudent, J.R., Marshall, D.J., Allawi, H.T., Mast, A.L., Dahlberg, J.E., Kwiatkowski, R.W., de Arruda, M., Neri, B.P., Lyamichev, V.I., 2000. Proc. Natl. Acad. Sci. USA **97**, 8272.

Hanaoka, K., Kikuchi, K., Kojima, H., Urano, Y., Nagano, T., 2004. J. Am. Chem. Soc. **126**, 12470.

Handl, H.L., Gillies, R.J., 2005. Life Sci. **77**, 361.

Handl, H.L., Vagner, J., Yamamura, H.I., Hruby, V.J., Gillies, R.J., 2004. Anal. Biochem. **330**, 242.

Handl, H.L., Vagner, J., Yamamura, H.I., Hruby, V.J., Gillies, R.J., 2005. Anal. Biochem. **343**, 299.

Hemmilä, I., 1985. Clin. Chem. **31**, 359.

Hemmilä, I.A., Hurskainen, P., 2002. Drug Discovery Today **7**, S150.

Hemmilä, I., Holttinen, S., Pettersson, K., Lövgren, T., 1987. Clin. Chem. **33**, 2281.

Hong, Y., Webb, B.L., Su, H., Mozdy, E.J., Fang, Y., Wi, Q., Liu, L., Beck, J., Ferrie, A.M., Raghavan, S., Mauro, J., Carre, A., Müeller, D., Lai, F., Rasnow, B., Johnson, M., Min, H., Salon, J., Lahiri, J., 2005. J. Am. Chem. Soc. **127**, 15350.

Ikegawa, M., Yuan, J., Matsumoto, K., Herrmann, S., Iwamoto, A., Nakamura, T., Matsushita, S., Kimura, T., Honjo, T., Tashiro, K., 2001. AIDS Res. Hum. Retroviruses **17**, 587.

Karilayan, H., Hemmilä, I., Takalo, H., Toivonen, A., Pettersson, K., Lövgren, T., Mukkala, V.-M., 1997. Bioconjugate Chem. **8**, 71.

Kimura, H., Yuan, J., Wang, G., Matsumoto, K., Mukaida, M., 1999. J. Anal. Toxicol. **23**, 11.

Kimura, H., Suzui, M., Nagao, F., Matsumoto, K., 2001. Anal. Sci. **17**, 593.

Kiviniemi, M., Nurmi, J., Turpeinen, H., Lövgren, T., Ilonen, J., 2003. Clin. Biochem. **36**, 633.

Laitala, V., Hemmilä, I., 2005. Anal. Chem. **77**, 1483.

Latva, M., Takalo, H., Mukkala, V.-M., Matachescu, C., Rodríguez-Ubis, J.C., Kankare, J., 1997. J. Lumin. **75**, 149.

Li, M., Selvin, P.R., 1995. J. Am. Chem. Soc. **117**, 8132.

Li, M., Selvin, P.R., 1997. Bioconjugate Chem. **8**, 127.

Liu, R., Yang, J., Wu, X., 2002. J. Lumin. **96**, 201.

Lopez-Crapez, E., Bazin, H., Andre, E., Noletti, J., Grenier, J., Mathis, G., 2001. Nucleic Acids Res. **29**, e70.

Lopez-Crapez, E., Bazin, H., Chevalier, J., Trinquet, E., Grenier, J., Mathis, G., 2005. Human Mutation **25**, 468.

Majima, K., Fukui, T., Yuan, J., Wang, G., Matsumoto, K., 2002. Anal. Sci. **18**, 869.

Manning, H.C., Goebel, T., Thompson, R.C., Price, R.R., Lee, H., Bornhop, D.J., 2004. Bioconjugate Chem. **15**, 1488.

Mathis, G., 1993. Clin. Chem. **39**, 1953.

Mathis, G., 1995. Clin. Chem. **41**, 1391.

Mathis, G., Socquet, F., Viguier, M., Darbouret, B., 1997. Anticancer Res. **17**, 3011.

Mukkala, V.-M., Sund, C., Kwiatkowski, M., Pasanen, P., Högberg, M., Kankare, J., Takalo, H., 1992. Helv. Chim. Acta **75**, 1621.

Mukkala, V.-M., Helenius, M., Hemmilä, I., Kankare, J., Takalo, H., 1993. Helv. Chim. Acta **76**, 1361.

Nurmi, J., Ylikoski, A., Soukka, T., Karp, M., Lövgren, T., 2000. Nucleic Acids Res. **28**, e28.

Nurmi, J., Kiviniemi, M., Kujanpää, M., Sjöroos, M., Ilonen, J., Lövgren, T., 2001. Anal. Biochem. **299**, 211.

Nurmi, J., Wikman, T., Karp, M., Lövgren, T., 2002. Anal. Chem. **74**, 3525.

Peng, X.-H., Cao, Z.-H., Xia, J.-T., Carlson, G.W., Lewis, M.M., Wood, W.C., Yang, L., 2005. Cancer Res. **65**, 1909.

Rintamäki, S., Saukkoriipi, A., Salo, P., Takala, A., Leinonen, M., 2002. J. Microbiol. Methods **50**, 313.

Root, D.D., Vaccaro, C., Zhang, Z., Castro, M., 2004. Biopolymers **75**, 60.

Samiotaki, M., Kwiatkowski, M., Ylitalo, N., Landegren, U., 1997. Anal. Biochem. **253**, 156.

Santangelo, P., Nitin, N., Bao, G., 2006. Ann. Biomed. Eng. **34**, 39.

Sato, S., Wada, M., 1970. Bull. Chem. Soc. Jpn. **43**, 1955.

Siivola, P., Pettersson, K., Piironen, T., Lövgren, T., Lilja, H., Bjartell, A., 2000. Urology **56**, 682.

Sueda, S., Yuan, J., Matsumoto, K., 2000. Bioconjugate Chem. **11**, 827.

Sueda, S., Yuan, J., Matsumoto, K., 2002. Bioconjugate Chem. **13**, 200.

Tagliaferro, P., Tandler, C.J., Ramos, A.J., Saavedra, J.P., Brusco, A., 1997. J. Neurosci. Methods **77**, 191.

Takalo, H., Mukkala, V.-M., Mikola, H., Liitti, P., Hemmilä, I., 1994. Bioconjugate Chem. **5**, 278.

Takalo, H., Mukkala, V.-M., Meriö, L., Rodríguez-Ubis, J.C., Sedano, R., Juanes, O., Brunet, E., 1997. Helv. Chim. Acta **80**, 372.

Tan, W., Wang, K., Drake, T.J., 2004. Curr. Opin. Chem. Biol. **8**, 547.

Tsourkas, A., Behlke, M.A., Xu, Y., Bao, G., 2003. Anal. Chem. **75**, 3697.

Väisänen, V., Härmä, H., Lilja, H., Bjartell, A., 2000. Luminescence **15**, 389.

White, G.F., Litvinenko, K.L., Meech, S.R., Andrews, D.L., Thomson, A.J., 2004. Photochem. Photobiol. Sci. **3**, 47.

Wu, X., Yang, J.H., Huang, F., Wang, M., Sun, L.M., Xu, G.Y., 1999. Anal. Lett. **32**, 2417.

Yegorova, A., Karasyov, A., Duerkop, A., Ukrainets, I., Antonovich, V., 2005. Spectrochim. Acta Part A **61**, 109.

Yi, L., Zhao, H., Sun, C., Chen, S., Jin, L., 2003. Spectrochim. Acta Part A **59**, 2541.

Ylikoski, A., Elomaa, A., Ollikka, P., Hakala, H., Mukkala, V.-M., Hovinen, J., Hemmilä, I., 2004. Clin. Chem. **50**, 1943.

Yu, J., Parker, D., Pal, R., Poole, R.A., Cann, M.J., 2006. J. Am. Chem. Soc. **128**, 2294.

Yuan, J., Matsumoto, K., 1996. Anal. Sci. **12**, 696.

Yuan, J., Matsumoto, K., 1997. J. Pharm. Biomed. Anal. **15**, 1397.

Yuan, J., Wang, H., Kimura, H., Matsumoto, K., 1997. Anal. Biochem. **254**, 283.

Yuan, J., Wang, G., Kimura, H., Matsumoto, K., 1998a. Anal. Sci. **14**, 421.

Yuan, J., Matsumoto, K., Kimura, H., 1998b. Anal. Chem. **70**, 596.

Yuan, J., Wang, G., Majima, K., Matsumoto, K., 2001. Anal. Chem. **73**, 1869.

Wang, G., Yuan, J., Matsumoto, K., 2001. Anal. Sci. **17**, 881.

Weissman, S., 1942. J. Chem. Phys. **10**, 214.

*Chapter 235*

# LANTHANIDE NEAR-INFRARED LUMINESCENCE IN MOLECULAR PROBES AND DEVICES

Steve COMBY and Jean-Claude G. BÜNZLI

*École Polytechnique Fédérale de Lausanne (EPFL), Laboratory of Lanthanide
Supramolecular Chemistry, BCH 1402, CH-1015 Lausanne, Switzerland
E-mail: jean-claude.bunzli@epfl.ch*

## Contents

## List of abbreviations

| | | | |
|---|---|---|---|
| 8-Q | 8-hydroxyquinolinate | CD | circular dichroism |
| aad | adamantylideneadamantane-1,2-dioxetane | CL | chemiluminescence |
| ac | acetate | CN | coordination number |
| acac | acetylacetonate | CoP | (cyclopentadienyl)tris(diethyl-phosphito)cobaltate(I) anion |
| AMP | amplifying waveguide spiral | | |
| ba | benzoylacetonate | CPL | circularly polarized luminescence |
| bath | monobathophenantholine | CSA | cationic surfactant |
| BCP | bathocuproine | cw | continuous wave |
| bdc | 1,4-benzenedicarboxylate | cyclam | 1,4,8,11-tetraazacyclotetradecane |
| bdc-F$_4$ | 2,3,5,6-tetrafluoro-1,4-benzene-dicarboxylate | cyclen | 1,4,7,10-tetraaza-dodecane |
| bppz | 2,3-bis-(2-pyridyl)pyrazine | dam | diantipyrylmethanate |
| bptz | 3,6-bis-(2-pyridyl)tetrazine | daphm | diantipyrylphenylmethanate |
| bpy | 2,2′-bipyridine | dapm | diantipyrylpropylmethanate |
| bpym | 2,2′-bipyrimidine | dbm | dibenzoylmethanate |
| bpypz | 3,5-di(2-pyridyl)pyrazolate | DEDMS | diethoxydimethylsilane |
| BSA | bovine serum albumin | DEMS | diethoxymethylsilane |
| btfa | benzoyltrifluoroacetonate | dithi | 2-dithienyl-2,2′-bipyridazine |
| | | dme | 1,2-dimethoxy-ethane |

| | | | |
|---|---|---|---|
| dmf | dimethylformamide | HBS | HEPES-buffered saline buffer |
| dmp | dipivaloylmethanate | hCG | human chorionic gonadotropin |
| dmso | dimethylsulfoxide | HEPES | $N$-(2-hydroxyethyl)-piperazine- |
| DNA | deoxyribonucleic acid | | $N'$-2-ethanesulfonic acid |
| dnm | dinaphthoylmethanate | hesa | hexylsalicylate |
| do3a | 1,4,7,10-tetraaza-cyclododecane- | hfa | hexafluoroacetylacetonate |
| | $N,N',N''$-triacetate | HOMO | highest occupied molecular |
| dota | 1,4,7,10-tetraaza-cyclododecane- | | orbital |
| | $N,N',N'',N'''$-tetraacetate | HPLC | high performance liquid |
| dotma | 1R,4R,7R,10R-$\alpha,\alpha',\alpha'',\alpha'''$- | | chromatography |
| | tetramethyl-1,4,7,10-tetraaza- | HSA | human serum albumin |
| | cyclododecane-1,4,7,10-tetra- | HSAB | hard and soft acid and base |
| | acetate | | theory |
| dotp | 1,4,7,10-tetraazacyclododecane- | IgG | immunoglobulin G |
| | 1,4,7,10-tetrakis-methylene- | im | imidazole |
| | phosphonate | ITO | indium tin oxide |
| dpa | pyridine-2,6-dicarboxylate | IUPAC | Internationl Union of Pure and |
| | (dipicolinate) | | Applied Chemistry |
| dpga | diphenylguanidine | LB | Langmuir–Blodgett |
| dpm | dipivaloylmethanate | LCD | liquid crystal display |
| dppm | bis(diphenylphosphinomethane) | LD | laser diode |
| dtpa | diethylenetrinitrilopentaacetate | LED | light emitting diode |
| dtta | diethylenetriaminetetraacetate | LF | ligand field |
| ECL | electrochemically generated | LLCT | ligand-to-ligand charge transfer |
| | luminescence | | state |
| edta | ethylenediamine-$N,N',N'',N'''$- | LMCT | ligand-to-metal charge transfer |
| | tetraacetate | | state |
| ELISA | enzyme-linked immunosorbent | LUMO | lowest unoccupied molecular |
| | assay | | orbital |
| ESA | excited state absorption | MBBA | $N$-($p$-methoxybenzylidene)-$p$- |
| ET | electron transfer | | butylaniline |
| Etonium | 1,2-ethanediaminium, | MCD | magnetic circular dichroism |
| | $N,N'$-bis[2-(decyloxy)-2-oxo- | MDMO-PPV | polyl[2-methoxy-5-($3',7'$-di- |
| | ethyl]-$N,N,N',N'$-tetramethyl- | | methyl-octyloxy)]-$p$-phenylene |
| | dichloride | | vinylene |
| ETU | energy transfer up-conversion | mgl | 1-deoxy-1-(methylamino)glucitol |
| *fac* | facial | MLCT | metal-to-ligand charge transfer |
| FAU | Faujasite | | state |
| fod | 6,6,7,7,8,8,8-heptafluoro-2,2-di- | MMA | methylmethacrylate |
| | methyl-3,5-octadionate | MOF | metal–organic framework |
| fwhh | full width at half height | | (coordination polymer) |
| fx | fluorexon | MRI | magnetic resonance imaging |
| had | hexaaza-triphenylene | NASI | $N$-acryloxysuccinimide |

| | | | | |
|---|---|---|---|---|
| NIR | near infrared | | Quin | 2-methyl-8-hydroxyquinolinate |
| NIT2py | 4,4,5,5-tetramethyl-2-(2′-pyridyl)-4,5-dihydro-1*H*-imidazol-1-oxyl 3-oxide | | RTIL | room temperature ionic liquid |
| | | | SAP | square antiprism |
| | | | SHE | standard hydrogen electrode |
| NMR | nuclear magnetic resonance | | SOMO | single occupied molecular orbital |
| nta | nitrilotriacetate | | stta | mono-thio-thenoyltrifluoro-acetonate |
| NTA | 4,4,4-trifluoro-1-(2-naphthyl)-1,3-butanedionate | | tbo | trimethylenebis(oxamide) |
| OEP | octaethylporphyrinate | | TBP | tetrabenzoporphyrinate |
| OLED | organic light emitting diode | | TEOS | tetraethyl orthosilicate |
| | | | $Tf_2N$ | bis(trifluoromethanesulfonyl)-imide or bis(perfluoromethylsulfonyl)-aminate (pms) |
| Otf | trifluoromethanesulfonate | | | |
| ox | oxalate | | | |
| PAN | 1-(2-pyridylazo)-2-naphthol | | | |
| PAR | 1-(2-pyridylazo)resorcinol | | TGA | thermogravimetric analysis |
| pbs | bis(perfluorobutylsulfonyl)imide, $[C_4F_9SO_2]_2N$ | | thf | tetrahydrofuran |
| | | | TMA | tetramethylammonium |
| Pc | phthalocyanine | | TMOS | tetramethoxysilane |
| pdon | 1,10-phenanthroline-5,6-dione | | topo | trioctylphosphine oxide |
| PEDOT | poly(3,4-ethylene dioxythiophene) | | Tos | tosylate |
| | | | $Tp^H$ | hydridotris(1-pyrazolyl)borate |
| PEG | polyethyleneglycol | | TPD | $N,N$-diphenyl-$N,N$-bis(3-methylphenyl)-[1,1′-biphenyl]-4,4′-diamine |
| PET | photoinduced electron transfer | | | |
| phen | 1,10-phenanthroline | | | |
| PMMA | polymethylmethacrylate | | tpen | tetrakis(2-pyridylmethyl)-ethylenediamine |
| pms | bis(perfluoromethylsulfonyl)-aminate or bis(trifluoromethanesulfonyl)-imide ($Tf_2N$) | | | |
| | | | TPP | tetraphenylporphyrinate |
| | | | tppo | triphenylphosphine oxide |
| | | | tpy | 2,2′:6′,2″-terpyridine |
| poa | perfluorooctanoylacetate | | Tris | 2-amino-2-(hydroxymethyl)-propane-1,3-diol |
| pom | perfluorooctanoylmethanate | | | |
| POM | polyoxometalates | | Trp | tryptophan |
| pos | bis(perfluorooctylsulfonyl)-aminate | | TSAP | twisted square antiprism |
| | | | tta | thenoyltrifluoro-acetylacetonate |
| PS | Phthalexon S | | TTP | tetra-*para*-tolylporphyrinate |
| PSS | polystyrene sulfonate | | UPT | up-converting phosphor technology |
| PVK | poly-($N$-vinylcarbazole) | | | |
| PVV | poly(phenylene–vinylene) | | WDM | wavelength division multiplexer |
| py | pyridine | | Wt% | weight percent |
| P-FiPMA | polyhexafluoroisopropylmeth-acrylate | | YAG | yttrium aluminum garnet |
| | | | YLF | yttrium lithium fluoride |
| qb | 4-(4-(3-triethyoxysilylpropoxy)-phenylazo)-phenyl-diphenyl phosphine oxide | | XO | xylenol orange |

## 1. Outline and scope of the review

Trivalent lanthanide ions offer a wide variety of opportunities to spectrochemists in that their [Xe]4f$^N$ electronic configuration generates numerous electronic levels, up to 3432 for Gd$^{III}$, for instance. These ions display three types of electronic transitions. Charge transfer transitions, both ligand-to-metal (LMCT) and metal-to-ligand (MLCT), are allowed by Laporte's selection rule. Their energy is usually high, so that they appear in the UV above 40 000 cm$^{-1}$, except for the ions which may be relatively easily either reduced to their +2 state (Sm$^{III}$, Eu$^{III}$, Tm$^{III}$, Yb$^{III}$), or oxidized to their +4 state (Ce$^{III}$, Pr$^{III}$, Tb$^{III}$). In these cases, the broad charge transfer transitions may occur at energies as low as 30 000 cm$^{-1}$. To illustrate this point, energies of the 2p(O)–4f LMCT transitions are plotted in fig. 1, using data from the Phosphor Handbook (Shionoya and Yen, 1999). From a practical viewpoint, LMCT transitions are used to pump energy into the lamp phosphors containing Eu$^{III}$ or Tb$^{III}$, for instance. The second kind of transitions corresponds to the promotion of a 4f electron into the 5d sub-shell; such transitions are also allowed by the parity rule, resulting in sizeable oscillator strengths with absorption coefficients in the range $10^{-2}$–$10^3$ M$^{-1}$ cm$^{-1}$, that is, comparable to those of the charge transfer transitions. Their energy depends largely upon the metal environment because 5d orbitals are external and they interact directly with ligand orbitals; however, these transitions are also quite energetic and only those of Ce$^{III}$, Pr$^{III}$ and Tb$^{III}$ are commonly observed below 50 000 cm$^{-1}$. Energies of the 4f–5d transitions in calcium fluoride matrix are reported in fig. 1, from literature data compiled by Dorenbos (2003). Finally, lanthanide trivalent ions display sharp f–f transitions, involving the rearrangement of the electrons in the 4f sub-shell and are therefore forbidden, which explains their faint intensities, with absorption coefficients smaller than 10 M$^{-1}$ cm$^{-1}$ and even often smaller than 1 M$^{-1}$ cm$^{-1}$. These transitions are quite narrow and the barycenter of the ligand-field split bands is fairly insensitive to the metal ion environment. As a consequence, they are easily recognizable and therefore lanthanide ions are ideal candidates for optical probes.

Most of the lanthanide trivalent ions are luminescent, either fluorescent (Pr$^{III}$, Nd$^{III}$, Ho$^{III}$, Er$^{III}$, Yb$^{III}$) or phosphorescent (Sm$^{III}$, Eu$^{III}$, Gd$^{III}$, Tb$^{III}$, Dy$^{III}$, Tm$^{III}$) or both. Their emission covers the entire spectrum (0.3–3 µm), from UV (Gd$^{III}$) to visible (e.g. blue Tm$^{III}$, green Tb$^{III}$, orange Sm$^{III}$, or red Eu$^{III}$), and NIR spectral ranges (see below). The Stokes shifts are extremely small since the rearrangement of the electrons in the 4f sub-shell does not lead to much change in the chemical bond lengths, contrary to what is observed with organic compounds or d-transition metal ions; the configurational coordinate diagrams of fig. 2 depicts these two situations; when the excited state potential energy curve is displaced with respect to the ground level curve, vertical excitation following the Franck–Condon principle leads to vibrationally excited states and the same is valid for deexcitation, resulting in broad band spectra. The contrary holds for Ln$^{III}$ ions and therefore the emission bands are narrow and the radiated colors are rather pure, so that they may be used in trichromatic phosphors for lighting
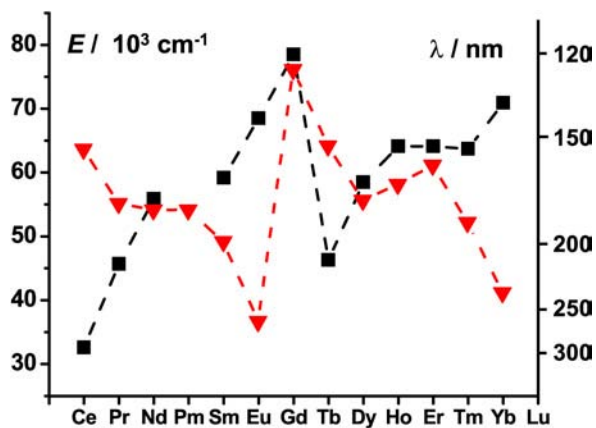
Fig. 1. Energy of the 2p(O)–4f LMCT transitions (▼) (Shionoya and Yen, 1999) and of the 4f–5d transitions of Ln[III] ions in a CaF$_2$ matrix (■) (Dorenbos, 2003).
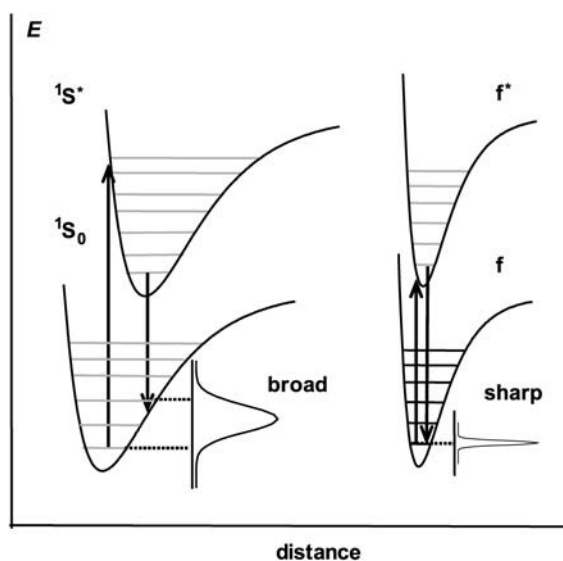


Fig. 2. Sharp emission from Ln[III] ions due to the small offset of the electronic levels as shown from the configurational coordinate diagram (right); as a comparison, the case of an organic molecule is depicted on the left ($^1$S$_0$ = singlet ground state, $^1$S* = singlet excited state).

purposes. Two ions, La[III] and Lu[III], have no f–f transitions and are not luminescent, while Ce[III] displays an intense d–f emission which can be tuned from 290 to 500 nm. Ions in other oxidation states are also luminescent, but in this review we restrict ourselves to trivalent ions.

Initially, interest for NIR emission of lanthanide ions stemmed from the development of optical fibers, lasers and amplifiers for telecommunication (Kido and Okamoto, 2002; Kuriki et al., 2002) and there are a wealth of theoretical and technical papers published in this area. Up-conversion processes have also been the subject of intense investigations (Auzel, 2004). These two areas of research and development mostly deal with purely inorganic compounds or, more recently, with luminescent polymers; they will not be covered in this chapter, with the exception of the latter, which will be partly described.

The large attention noted presently for NIR-emitting molecular compounds originates from needs in medical diagnostic. Imaging technologies developed over the past thirty years, such as magnetic resonance imaging, X-ray or nuclear tomography, have revolutionized clinical medicine. Several parameters influence the final result, resolution, depth penetration, availability of biocompatible and targeted probes, as well as the detection threshold of the latter (Weissleder, 2001). During the past decade, *in vivo* optical detection of tumors by means of near infrared photons has gained momentum (Becker et al., 2001; Kim et al., 2004; Weissleder et al., 1999) because it represents a non-invasive technique allowing the exploration of deeper tissues, the investigation range extending from a few mm up to 20 cm (Weissleder and Ntziachristos, 2003). Indeed, biological tissues have very low absorption coefficients above 700 nm and, in addition, the absorption of water, a major component of biological tissues, diminishes drastically above 900 nm. The development of targeted NIR fluorophores coupled to peptides prompted applications in clinical situations where other imaging techniques are not an option. Until now, most of these clinical applications have made use of organic dyes as probes for NIR imaging and differentiation between the target and background fluorescence has been achieved by molecular switches or beacons (protease-triggered NIR probes) which can be activated *in vivo* by a suitable biochemical reaction (Weissleder, 2001).

An alternate strategy would be to resort to bioprobes incorporating NIR-emitting lanthanide ions (Dossing, 2005; Faulkner et al., 2005). Similarly to the visible-emitting Ln[III] ions, which are well-known optical probes (Bünzli, 2004; Bünzli, 2005; Bünzli and Piguet, 2005), the main advantages of these ions lie in their easily recognizable atom-like spectra and large Stokes shifts when they are excited through the ligand levels. In addition, time-resolved luminescence allows one to achieve a high signal-to-noise ratio since the lifetimes of the Ln[III] emissive states are substantially longer than those of organic material. Synthetic strategies are now at hand to insert Ln[III] ions in a variety of molecular and supramolecular assemblies (Piguet and Bünzli, 1999) which control and even enhance their photophysical properties through the so-called sensitization process since f–f transitions have too small oscillator strengths to yield an efficient excitation path (Bünzli and Piguet, 2005).

In this review, we mainly concentrate on molecular, NIR-emitting compounds containing Nd[III], Er[III], or Yb[III]; discrete molecular edifices containing other ions emitting in this range but less relevant to the problematic dealt with here, namely Pr[III], Sm[III], Dy[III], Ho[III], and Tm[III], have been far less studied and will only be mentioned when relevant. After a brief introduction on the photophysics of near-infrared emitting trivalent lanthanide ions, we describe the various synthetic strategies proposed for encapsulating these ions into molecular edifices and making use of macrocyclic or acyclic ligands or of d-transition metal complexes. Novel approaches

resorting to inorganic clusters, inorganic–organic hybrids (coordination polymers), nanoparticles, or ionic liquids will also be outlined. The chapter ends by a short overview on potential applications, including medical imaging and by a critical evaluation of the chromophores for sensitizing NIR-emitting trivalent lanthanide ions. Separation between the description of NIR-emitting molecular complexes and applications is not always unambiguous, so that in several instances, the motivation for and requirements of applications are described in section 3 rather than in section 4.

Literature is covered up to the end of September 2006.

## 2. Photophysics of near-infrared emitting trivalent lanthanide ions

The photophysics of the NIR-emitting lanthanide ions is not fundamentally different from that of the UV or visible-emitting ions. Intrinsically, f–f transitions are weak and the main objectives of synthetic chemists tailoring adequate environments for luminescent lanthanide ions is firstly to increase the amount of energy which can be pumped into the excited states and secondly to minimize radiationless deactivation processes. For the free ions, the latter are more efficient if the energy gap between the lowest ligand-field sub-level of the excited state and the highest electronic level of the ground state is small. This is unfortunately the case for most of the NIR-emitting ions.

### 2.1. *Near-infrared transitions*

Formally, the NIR spectral range starts at 750 nm and many trivalent lanthanide ions display transitions with wavelengths longer than 750 nm, including, for instance, the red emitter Eu[III] which has a weak transition around 820 nm originating from the $^5D_0$ level ($^5D_0 \rightarrow {}^7F_6$) and several other weak transitions between 2 and 2.6 μm assigned to transitions between the $^7F_J$ sublevels (Carnall et al., 1962). However, known practical applications of NIR luminescence often make use of radiation around 1.32 and 1.55 μm, the so-called telecommunication windows, in which silica is particularly transparent. Praseodymium, neodymium, and possibly dysprosium, cover the first wavelength. Erbium is ideally suited for the second, in particular erbium-doped amplifiers compensate for losses in optical fibers. Neodymium is of course also well known for its 1.06 μm laser line used in the yttrium aluminum garnet (YAG) laser either as spectroscopy light source or for nuclear fusion. For biological tissues, the spectral range of interest is approximately 0.85–1.1 μm, where light transmission is maximized. For these reasons, we shall mostly concentrate on ions emitting sizable luminescence above 850 nm and below 1.6 μm, even if some applications rely on laser lines with longer wavelength, e.g. the holmium transition around 2.1 μm for medical applications. Some relevant electronic levels of NIR-emitting Ln[III] ions are reported in fig. 3, where the luminescent levels are indicated by black down triangles when the transition terminates on one of the sub-levels of the ground state while other transitions are designated by arrows. A list of the main NIR transitions can be found in table 1. With the exception of Pr[III] and Sm[III], the NIR-emitting ions are fluorescent. Several of them have complex photophysical properties (Tanabe, 2002), featuring emission in both visible and NIR spectral
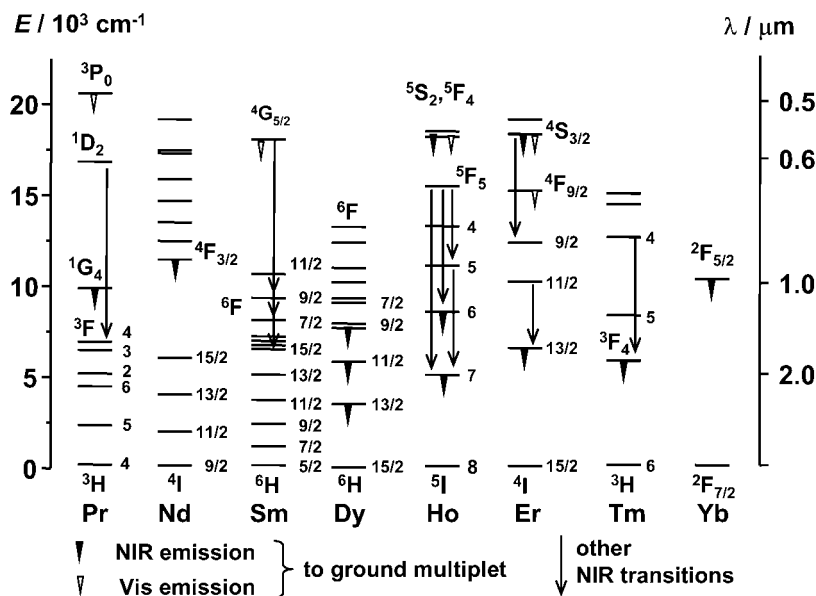
Fig. 3. Partial energy diagrams of NIR-emitting trivalent lanthanide ions. Energies are for the aquo-ions (Carnall et al., 1968; Carnall, 1979).

ranges, that have been thoroughly studied in inorganic matrices (Crosswhite and Moos, 1967; Dieke, 1968) and in solid state materials for the development of lasers (Reisfeld and Jorgensen, 1977), up-conversion devices (Auzel, 2004), optical amplifiers (Kuriki et al., 2002) or organic light emitting diodes (Kido and Okamoto, 2002).

As for the ions of prime interest for this review, $Nd^{III}$ displays fluorescence in three distinct spectral ranges: 0.87–0.92, 1.06–1.09, and 1.32–1.39 µm ($^4F_{3/2} \rightarrow {}^4I_{9/2}$, $^4I_{11/2}$, $^4I_{13/2}$ transitions), the second line being the well known laser line produced by Nd:YAG lasers, which can be doubled (532 nm, green light, e.g. for laser pointers), tripled (355 nm, blue) or quadrupled (266 nm); these lasers enter in a variety of analytical and industrial applications and can reach extremely high powers (up to 20 MW in nuclear fusion machines). The YAG matrix can also be co-doped with other trivalent lanthanide ions, providing a whole range of other interesting emission lines. The longer wavelength line of $Nd^{III}$ occurs in the middle of the first telecommunication window and has drawn attention for amplification of the 1.3 µm signals. $Er^{III}$ has a more complicated photophysics with several emission lines both in the visible (from the $^4S_{3/2}$ excited level) and in the NIR range, in addition to having up-conversion capability (Auzel, 2004); the main line of significance here is however the $^4I_{13/2} \rightarrow {}^4I_{15/2}$ transition around 1.54 µm on which most fiber optic telecommunication amplifiers are based (Weber et al., 1998). Recently, another IR line has been evidenced in yttrium oxide matrix, at 1.75 µm, assigned to the $^4S_{3/2} \rightarrow {}^4I_{9/2}$ transition from $Er^{III}$ in a $C_2$ site (Zhang et al., 2004).

Table 1
Properties of the main NIR-emitting trivalent lanthanide ions

| Ln | G[a] | I[b] | F[c] | $\lambda$ (μm) | $E$ (cm$^{-1}$) | Comment |
|----|------|------|------|----------------|-----------------|---------|
| Pr | $^3H_4$ | $^1D_2$ | $^3F_4$ | 1.01–1.04 | 9890–9600 | |
| | | $^1G_4$ | $^3H_5$ | 1.30–1.33 | 7700–7540 | Telecom line |
| | | $^1D_2$ | $^1G_4$ | 1.44 | 6940 | |
| Nd | $^4I_{9/2}$ | $^4F_{3/2}$ | $^4I_{9/2}$ | 0.87–0.92 | 11 500–10 870 | |
| | | | $^4I_{11/2}$ | 1.06–1.09 | 9430–9170 | Laser line |
| | | | $^4I_{13/2}$ | 1.32–1.39 | 7575–7195 | Telecom line |
| | | | $^4I_{15/2}$ | 1.84–1.86 | 5410–5375 | |
| Sm | $^6H_{5/2}$ | $^4G_{5/2}$ | $^6F_{1/2}$ | 0.88 | 11 385 | |
| | | | $^6F_{7/2}$ | 1.02–1.04 | 9790–9660 | |
| | | | $^6F_{9/2}$ | 1.16–1.17 | 8630–8570 | |
| Dy | $^6H_{15/2}$ | $^6H_{9/2}$, $^6F_{11/2}$ | $^6H_{15/2}$ | 1.28–1.34 | 7810–7575 | Telecom line |
| | | $^6H_{11/2}$ | $^6H_{15/2}$ | 1.7–1.8 | 5880–5555 | |
| | | $^6H_{13/2}$ | $^6H_{15/2}$ | 2.89–3.02 | 3460–3310 | |
| Ho | $^5I_8$ | $^5F_5$ | $^5I_7$ | 0.98–0.99 | 10 250–10 100 | |
| | | | $^5I_6$ | 1.48–1.51 | 6760–6630 | |
| | | | $^5I_5$ | 2.39–2.45 | 4180–4090 | |
| | | $^5I_5$ | $^5I_7$ | 1.63–1.68 | 6120–5965 | |
| | | $^5I_6$ | $^5I_8$ | 1.16–1.19 | 8650–8370 | |
| | | $^5I_7$ | $^5I_8$ | 1.98–2.10 | 5050–4760 | Laser line, medical applications |
| Er | $^4I_{15/2}$ | $^4I_{13/2}$ | $^4I_{15/2}$ | 1.54–1.60 | 6500–6250 | Telecom line |
| | | $^4S_{3/2}$ | $^4I_{9/2}$ | 1.7 | 5880 | Laser line |
| | | $^4I_{11/2}$ | $^4I_{13/2}$ | 2.7 | 3700 | Laser line |
| Tm | $^3H_6$ | $^3F_4$ | $^3H_6$ | 1.75–1.90 | 5730–5260 | |
| | | $^3H_4$ | $^3H_5$ | 2.33 | 4290 | |
| Yb | $^2F_{7/2}$ | $^2F_{5/2}$ | $^2F_{7/2}$ | 0.96–1.03 | 10 400–9710 | |

[a]Ground level.
[b]Initial level.
[c]Final level.

    Finally, Yb$^{III}$ possesses a single emission line in the range 0.98–1.03 μm, owing to its extremely simple electronic structure with one unpaired electron. Typical spectra of these three NIR-emitting ions are presented in fig. 4.

    Among the other NIR-emitting ions, Pr$^{III}$ has two main NIR bands at 1.04 μm ($^1D_2 \rightarrow {}^3F_4$) and 1.3 μm ($^1G_4 \rightarrow {}^3H_5$), the latter being used in telecommunications for amplification of the 1.3 μm signals; it is also often a component of solid state optical materials in view of its ability of generating up-conversion, that is blue emission from its $^3P_0$ level upon two- or three-photon pumping of the $^1G_4$ or $^1D_2$ state. Trivalent samarium Sm$^{III}$ features three spin-forbidden NIR emission lines from the $^4G_{5/2}$ excited state to sublevels of the first excited spectroscopic term, namely $^6F_J$ with $J = 9/2$, 7/2, and 5/2; emission from the same excited level to the ground multiplet yields lines in the visible range, between 560 and 650 nm, and one NIR line at 710 nm ($^4G_{5/2} \rightarrow {}^6H_{11/2}$). Less well known Dy$^{III}$ exhibits three NIR emission bands, one
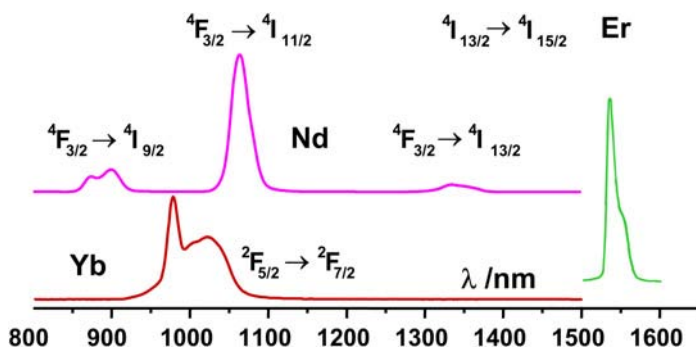
Fig. 4.  Typical NIR emission spectra of $Nd^{III}$, $Er^{III}$, and $Yb^{III}$.

around 1.34 μm ($^6H_{9/2}$, $^6F_{11/2} \rightarrow$ $^6H_{15/2}$) which has been considered as a third candidate for amplification of the 1.3-μm signals (Page et al., 1997), one ($^6H_{11/2} \rightarrow$ $^6H_{15/2}$) at 1.75 μm, and another one at longer wavelength, $^6H_{13/2} \rightarrow$ $^6H_{15/2}$ around 2.9 μm. In addition, dysprosium presents yellow emission from the $^4F_{9/2}$ excited level down to the ground multiplet.

One of the lanthanide ions with the richest spectroscopic properties is $Ho^{III}$, including up-conversion, and only a few of its features are reported in fig. 3; one emission line is close to the second telecommunication window ($^5F_5 \rightarrow$ $^5I_6$, 1.5 μm) while another, at 2.1 μm ($^5I_7 \rightarrow$ $^5I_8$) has generated several medical applications in laser surgery for ophthalmic treatments or for enucleating the prostate for instance (Kuo et al., 2002). The lasers are Q-switched Ho:YAG systems directly pumped into the $^5I_7$ level, $Tm^{III}$ being used as sensitizer thanks to its $^3F_4 \rightarrow$ $^3H_6$ line at 1.8–1.9 μm, itself pumped by a diode laser. $Ho^{III}$ emits a second NIR line around 2.2–2.3 μm ($^5I_4 \rightarrow$ $^5I_6$). With similar purposes, a multi-wavelength laser system has been proposed for precise and efficient tissue ablation under water and was realized by coupling two laser lines, from $Ho^{III}$ at 2.1 μm and $Er^{III}$ at 2.79 μm into a zirconium fluoride optical fiber (Pratisto et al., 1995). In addition to the transition mentioned above, $Tm^{III}$ displays another NIR line at 1.4–1.5 μm, arising from the $^3H_4 \rightarrow$ $^3F_4$ transition.

## 2.2. Sensitization processes

The emissive properties of a lanthanide ion are governed by the facility with which its excited state(s) can be populated and the nonradiative deactivation paths minimized. Most of the electronic transitions of the trivalent $Ln^{III}$ ions involve a redistribution of electrons within the 4f sub-shell. Electric dipole selection rules forbid such transitions but these rules are relaxed by several mechanisms. An important one is the coupling with vibrational modes, where a molecular vibration temporarily changes the geometric arrangement around the metal ion and, therefore, its symmetry. Other mechanisms which cause a breakdown of the selection rules are the J-mixing and the mixing with opposite-parity wavefunctions, such as 5d orbitals, ligand orbitals or charge transfer states. The coupling between the perturbating states and the 4f wavefunctions depends on the strength of the interaction between the 4f orbitals and the surrounding ligands; in view of the shielding of the 4f orbitals, the degree of mixing
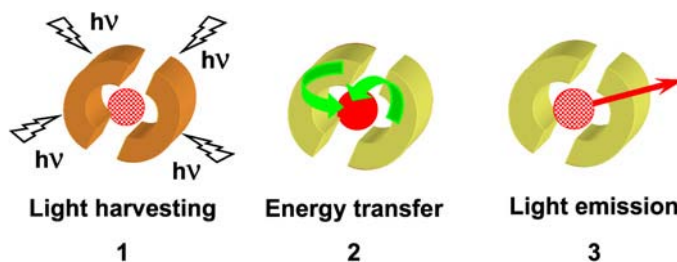
Fig. 5. Schematic representation of the sensitization process of lanthanide luminescence via the surroundings of the metal ion.

remains small, and so are the oscillator strengths of the f–f transitions. As a consequence, even if many lanthanide-containing compounds display a good quantum yield, direct excitation of the Ln$^{III}$ ions rarely yields highly luminescent materials. Indirect excitation, termed sensitization or antenna effect, and discovered by Weissman (1942) has to be used. It proceeds in three distinct steps (fig. 5). Firstly, light is absorbed by the immediate environment of the Ln$^{III}$ ion through the attached organic ligands (chromophores) or the inorganic matrix in case of solid state compounds such as lamp phosphors. Secondly, energy is transferred onto one or several excited states of the metal ion, and, thirdly, de-excitation processes take over and the metal ion emits its characteristic spectrum.

Sensitization via ligand-to-metal charge transfer states or d-transition metal ions can also be envisaged. Charge transfer states essentially operate for Sm$^{III}$, Eu$^{III}$, and Yb$^{III}$; they are often used when these ions are inserted into inorganic matrices and their energy has to be carefully tuned. Indeed, if such LMCT states lie at high enough energy, they can transfer energy into the excited 4f-states; however, when their energy is close to the energy of the emitting level, they act as efficient quenchers of the 4f-luminescence. The second excitation mode relies on energy transfer from a d-transition metal ion. For instance, Cr$^{III}$ is a known activator of the Nd$^{III}$ luminescence in YAG lasers (Seltzer, 1995) and, more recently, this excitation mode has stirred interest for the sensitization of NIR luminescence in molecular complexes (Shavaleev et al., 2005) and for increasing the apparent lifetimes of Nd$^{III}$ and Yb$^{III}$ (Imbert et al., 2003). Sensitization via ligand states is still the commonest strategy and numerous ligands have been designed to meet the stringent requirements pertaining to efficient energy transfers to the Ln$^{III}$ ions.

Although often discussed and modeled in terms of a simple ligand($S_1$) $\rightarrow$ ligand($T_1$) $\rightarrow$ Ln* energy flow which can be optimized by adjusting the energy gap between the lowest ligand triplet state and the Ln$^{III}$ emitting level (Archer et al., 1998; Gutierrez et al., 2004; Latva et al., 1997), sensitization of trivalent lanthanide ions is an exceedingly complex process involving several mechanisms and numerous rate constants (de Sá et al., 2000; Gonçalves e Silva et al., 2000; Gonçalves e Silva et al., 2002). The various contributions to the ligand-to-lanthanide ion energy transfer rates $W_{ET}$ may be described within the frame of Judd–Ofelt theory (Judd, 1962; Ofelt, 1962) by eqs. (1)–(3) in which $J$ is the total angular momentum quantum number of the lanthanide ion while $\alpha$ specifies a 4f spectroscopic term; $G$ is the

degeneracy of the ligand initial state and $S_L$ is the electric dipole strength associated with the transition $\phi \rightarrow \phi'$ in the ligand. The quantities $\langle \| \ \| \rangle$ are reduced matrix elements of the unit tensor operators $U^{(\lambda)}$ (Carnall et al., 1997), and $R_L$ is the distance from the metal ion nucleus to the region of the ligand molecule in which the ligand donor (or acceptor in case of back transfer) state is localized (Malta et al., 1999). The first set of equations describes the contribution of the dipole-$2^\lambda$ pole mechanism:

$$W_{ET}^{mp} = \frac{2\pi}{\hbar} \frac{e^2 S_L}{(2J+1)G} F \sum_\lambda \gamma_\lambda \langle \alpha' J' \| U^{(\lambda)} \| \alpha J \rangle^2, \quad \lambda = 2, 4, \text{ and } 6, \tag{1a}$$

$$\gamma_\lambda = (\lambda + 1) \frac{\langle r^\lambda \rangle^2}{(R_L^{(\lambda+2)})^2} \langle 3 \| C^{(\lambda)} \| 3 \rangle^2 (1 - \sigma_\lambda)^2, \tag{1b}$$

$\langle r^\lambda \rangle$ is the radial expectation value of $r^\lambda$ for 4f electrons, $C^{(\lambda)}$ is a Racah tensor operator, and

$$F = \frac{1}{\hbar \Delta A_L} \sqrt{\frac{\ln 2}{\pi}} \exp\left[ -\left( \frac{\Delta E}{\hbar \Delta A_L} \right)^2 \ln 2 \right], \tag{1c}$$

where $\Delta E$ is the energy difference between the ligand donor level and the lanthanide ion acceptor level and $\Delta A_L$ is the band width at half height of the ligand transition.

The second equation characterizes the dipole–dipole mechanism:

$$W_{ET}^{dp} = \frac{2\pi}{\hbar} \frac{e^2 S_L}{(2J+1)G R_L^6} F \sum_\lambda \Omega_\lambda^{e.d.} \langle \alpha' J' \| U^{(\lambda)} \| \alpha J \rangle^2, \quad \lambda = 2, 4, \text{ and } 6. \tag{2}$$

The third equation represents the exchange mechanism:

$$W_{ET}^{ex} = \frac{8\pi}{3\hbar} \frac{e^2 (1 - \sigma_0)^2}{(2J+1) R_L^4} F \langle \alpha' J' \| S \| \alpha J \rangle^2 \sum_m \left| \left\langle \phi \left| \sum_k \mu_z(k) s_m(k) \right| \phi' \right\rangle \right|^2, \tag{3}$$

where $S$ is the total spin operator of the metal ion, $\mu_z$ is the $z$ component of the electric dipole operator, $s_m$ ($m = 0, \pm 1$) is a spherical component of the spin operator for the ligand electrons, and $\sigma_0$ is a distance-dependent screening factor (Gonçalves e Silva and Malta, 1997). The first term in eq. (3) implies a $R_L^{-4}$ dependence, but the last term depends exponentially on the donor–acceptor distance ($e^{-R_L}$) and this term dominates the overall distance dependence. While the second (Förster) and third (Dexter) mechanisms are well known and documented in the literature, contribution from the multipolar mechanisms are often ignored, despite that they account for a great share of the energy transferred from the surroundings to the lanthanide ions. Dexter's (or exchange) mechanism, involves a double electron transfer and requires a good overlap between the ligand and metal orbitals, while in Förster's (or dipole–dipole) mechanism, the dipole moment associated with the $^3T^*$ state couples with the dipole moment of the 4f orbitals (fig. 6). Due to their respective dependence upon the donor–acceptor distance, Dexter's and the multipolar mechanisms operate at shorter distances than the dipole–dipole mechanism. They are therefore preferred mechanisms for energy transfer from the ligands to the metal ion, whereas dipole–dipole transfers are the main operating mechanisms in metal-to-metal energy transfer processes.
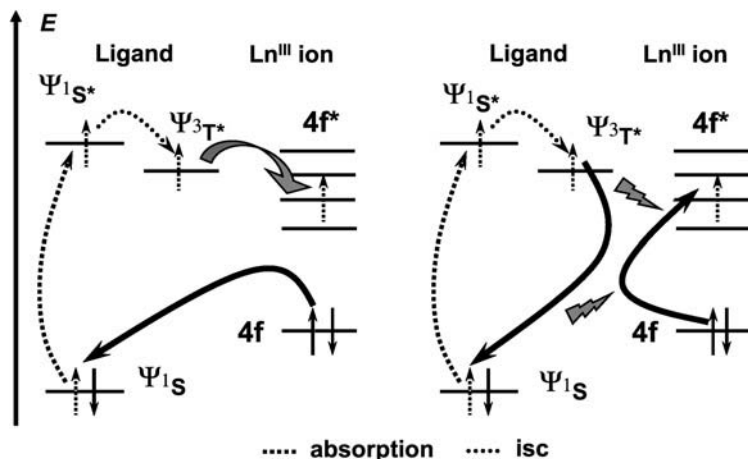
Fig. 6. Schematic representation of Dexter (exchange, left) and Förster (dipole–dipole, right) mechanisms for energy transfer.

When the mechanism is purely dipole–dipolar (Förster mechanism), simplified eqs. (4b) and (4c) allow an estimate of the efficiency of transfer between the donor and the acceptor:

$$\eta_{\text{et}} = 1 - (\tau_{\text{obs}}/\tau_0), \tag{4a}$$

$$\eta_{\text{et}} = \frac{1}{1 + (R_{\text{DA}}/R_0)^6}, \tag{4b}$$

where $\tau_{\text{obs}}$ and $\tau_0$ are the lifetimes of the donor in presence and in absence of acceptor, respectively, $R_{\text{DA}}$ is the distance between the donor and the acceptor and $R_0$ is the critical distance for 50% transfer, which depends on (i) an orientation factor $\kappa$ having an isotropic limit of 2/3, (ii) the quantum yield $Q_D$ of the donor (in absence of the acceptor), (iii) the refractive index $n$ of the absorption (and emitting) medium, and (iv) the overlap integral $J$ between the emission spectrum of the donor and the absorption spectrum of the acceptor:

$$R_0^6 = 8.75 \times 10^{-25} \left( \kappa^2 \cdot Q_D \cdot n^{-4} \cdot J \right). \tag{4c}$$

Considering the above discussion, the fine tuning of the ligand-to-Ln$^{\text{III}}$ transfer process requires the adjustment of several parameters; a comprehensive discussion is not given here, more detailed descriptions being available elsewhere. Both singlet and triplet states of the ligand may transfer energy onto the metal ion (fig. 7) and this transfer may be phonon-assisted; however, since the singlet state is short lived, this process is often not efficient, except in the case of ions such as Nd$^{\text{III}}$ or Er$^{\text{III}}$. Classical qualitative considerations on the ligand-to-metal energy transfer thus take solely the energy of the triplet state into consideration. Or, rather, the energy of the lowest triplet state $^3$T* since elaborate ligands presently designed usually feature several triplet states (as well as several overlapping $^1$S* states). Rules of thumb are that efficient intersystem crossing (isc) from the singlet excited state of the ligand to the triplet state
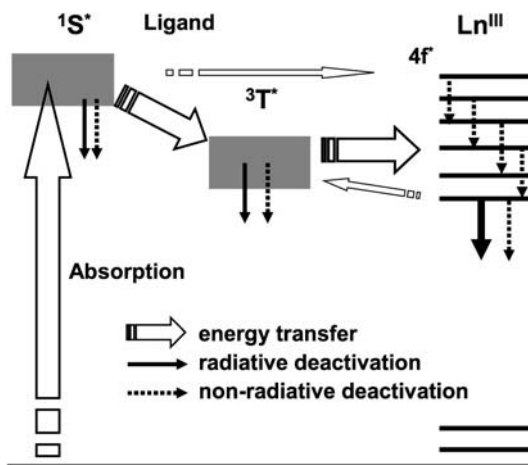
Fig. 7. Simplified diagram showing the main energy flow paths during sensitization of lanthanide luminescence. From (Bünzli and Piguet, 2005), reproduced by permission of the Royal Society of Chemistry.

with the lowest energy occurs when $\Delta E(^1S^*-^3T^*)$ is around 5000 cm$^{-1}$ while high yield transfers from the triplet state to the excited levels of the Ln$^{III}$ ions require $\Delta E(^3T^*-\Gamma^*_{Ln})$ in the range 2500–5000 cm$^{-1}$. When the latter energy gap is larger, the transfer efficiency drops and when it is smaller, back transfer processes become sizeable and reduce the overall efficacy of the transfer process.[1] A simple experiment to assess if the triplet state is implied in the energy transfer is to measure the metal-centered luminescence in absence and in presence of oxygen which is a good quencher of triplet states. If the rate of quenching by oxygen is larger than the rate of the $^3T^*-\Gamma^*_{Ln}$ transfer, which is often the case, then the metal-centered luminescence weakens considerably upon bubbling oxygen into the solution. On the other hand, non quenching does not necessarily means that the triplet state is not involved in the energy transfer mechanism, but can simply point to the rate of transfer being larger than the rate of oxygen quenching (often estimated around $10^7$ s$^{-1}$).

### 2.3. *Erbium sensitization by ytterbium and/or cerium*

One of the big challenges in photonic materials is the design of an efficient, low-noise amplifier operating at the eye-safe telecommunication wavelength of 1.55 µm, a reason why the spectroscopy of Er$^{III}$ has been investigated in details. Three main wavelengths can be used to pump energy into Er$^{III}$, 800 nm ($^4I_{9/2}$), 980 nm ($^4I_{11/2}$), and 1.48 µm (upper ligand-field sublevels of the $^4I_{13/2}$ level). The most favorable is the second one, which is used to pump erbium-doped optical amplifiers displaying large gain efficiency and having a quantum-limited noise level of only 3 dB. Three electronic levels are implied in the amplification process. First,

---

[1]  When evaluating the energy differences, one should take the 0-phonon transitions of $^1S^*$ and $^3T^*$ into account and not the maximum of the band envelope.
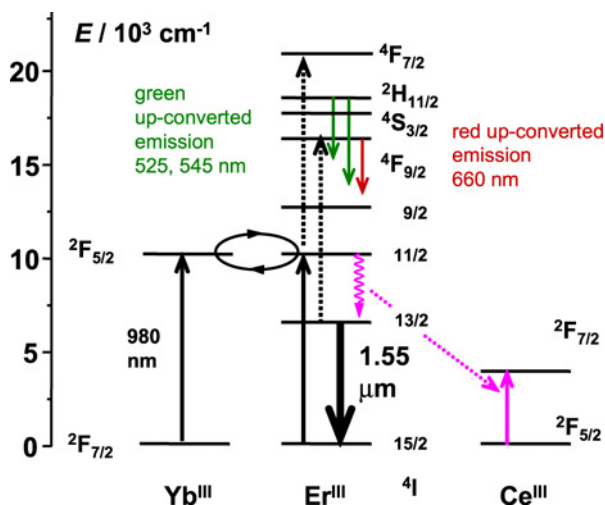
Fig. 8. Transitions of interest for Er[III] and its sensitizers. Internal nonradiative deactivations are not shown for clarity. Dotted arrows represent up-conversion processes. Adapted from (Le Quang et al., 2005).

an electron is promoted into the $^4I_{11/2}$ level, which either de-activates nonradiatively to the metastable $^4I_{13/2}$ level or absorbs a second photon to reach the $^4F_{7/2}$ level (excited state absorption, ESA). This up-conversion phenomenon is responsible for a significant reduction in the efficiency of the Er[III] emission, especially that the $^4I_{13/2}$ level may also absorb a photon to reach the red-emitting $^4F_{9/2}$ state. Since Yb[III] also displays absorption at 980 nm, but with better cross section, it can be used as Er[III] sensitizer. Alternatively, Ce[III] may play a similar role in accelerating the population feeding of $^4I_{13/2}$ from $^4I_{11/2}$ through coupling with its $^2F_{7/2} \leftarrow {}^2F_{5/2}$ transition (fig. 8).

## 2.4. *The special case of ytterbium*

Trivalent ytterbium is a special ion within the lanthanide series in that it possesses only two electronic 4f levels. The fluorescent $^2F_{5/2}$ level lies at around 10 000 cm$^{-1}$ above the $^2F_{7/2}$ ground state. Consequently, ligands with excited (triplet) states having energies around 12–15 000 cm$^{-1}$ are required for sensitizing its NIR luminescence. In this respect, porphyrins are suitable and have been extensively used (*vide infra*, section 3.1.1). On the other hand, antenna effects with ligands having excited states of much higher energy have been observed and there has been some debate regarding the mechanism of this sensitization process. One tempted explanation is that population of the Yb($^2F_{5/2}$) level is achieved by energy transfer from the triplet state *in a phonon-assisted process* (Crosby and Kasha, 1958). Indeed, in [Yb(dbm)$_3$] for instance (dbm is dibenzoylmethanate) the energy difference between Yb($^2F_{5/2}$) state and dbm($^3\pi\pi^*$) is about 13 000 cm$^{-1}$ and direct efficient transfer via exchange or dipole–dipole mechanism is not too plausible. In the phonon-assisted process, the chelate $^3\pi\pi^*$ state transfers energy on high energy vibrational levels of the chelate coupled to the $^2F_{5/2}$ excited state.

The relatively large change in the lowest $^*\pi \leftarrow \pi$ absorption band of the ligand upon complexation, both in energy and intensity, is consistent with a strong vibrational coupling. In more modern terms, this explanation can be translated into a single-configurational coordinate picture, in which the abscissa coordinate $Q$ represents the main expansion coordinate of the $^*\pi \leftarrow \pi$ excitation, that is essentially the breathing mode of the chelate ring ($\approx 1200\ cm^{-1}$). The states are double, coupled metal–ligand states and are therefore doubly labeled; in the following, bold labels refer to excited states. Excitation leads to the coupled state $^2F_{7/2}$–$\mathbf{^1S_1}$, which relaxes first to $^2F_{7/2}$–$\mathbf{^3T_1}$ by isc and to $\mathbf{^2F_{5/2}}$–$^1S_0$; the latter state can then emit NIR light to reach the ground state $^2F_{7/2}$–$^1S_0$. Using Huang–Rhys theory within the Franck–Condon approximation, H. Güdel and collaborators have calculated that the rate constant of the non-radiative $(^2F_{7/2}$–$\mathbf{^3T_1}) \rightarrow (\mathbf{^2F_{5/2}}$–$^1S_0)$ process in $[Yb(dpa)_3]^{3-}$ (dpa is dipicolinate) is seven orders of magnitude larger than for $\mathbf{^3T_1} \rightarrow {^1S_0}$ in the free ligand, so that the nonradiative process leading to excitation of the $Yb^{III}$ ion is quite plausible (Reinhard and Güdel, 2002). In the case of $[Yb(tta)_3(H_2O)_2]$, an efficiency of unity ($\pm15\%$) has been calculated for the $^3T_1 \rightarrow {^2F_{5/2}}$ energy transfer (Venchikov and Tsvirko, 2000). If they have energy comparable to the energy of the lowest triplet state, MLCT states could also be involved in such a phonon-assisted energy transfer.

Another theory put forward is that excitation goes through a long-range electron transfer and involves the divalent oxidation state of ytterbium (deW. Horrocks et al., 1997; Supkowski et al., 1999). This suggestion was motivated by the observation that the 980-nm emission of $Yb^{III}$ is detected in codfish parvalbumin in which the two bound $Ca^{II}$ ions have been replaced with $Yb^{III}$ ions. This calcium-binding protein contains a single tryptophan (Trp) unit which, on the basis of modeling from the known structure of carp parvalbumin, is found to be approximately equidistant from the two metal ion sites with the nearest indole ring atom 8–11 Å from a metal ion site. Excitation of tryptophan at 290 nm results in the NIR luminescence from $Yb^{III}$. In fact, the intensity of the singlet state emission of Trp in $Ln^{III}$-loaded codfish parvalbumin is almost constant for all $Ln^{III}$ ions, except $Eu^{III}$ and $Yb^{III}$ (Breen et al., 1985). At the time, the authors proposed an energy transfer mechanism involving overlap of tryptophan emission with a ligand-to-metal charge-transfer band. However, upon re-examination of the absorption spectra, no such LMCT band could be observed, either for $Eu^{III}$-bound parvalbumin or for the $Yb^{III}$ complex. As a consequence, the electron transfer mechanism depicted in fig. 9 was proposed.

The ground state of the indole sub-unit cannot reduce $Yb^{III}$, but the excited state Trp* can. The driving force, $\Delta G_{Ln}$ for the forward electron transfer (ET) may be estimated with the equation:

$$\Delta G_{Ln} = E\left(Ln^{III}/Ln^{II}\right) + E_{Trp^*} - E\left(Trp^{\cdot+}/Trp\right). \tag{5}$$

The reduction potential of the tryptophan radical cation is estimated to be 1.13 eV, while the energy of Trp in its excited singlet state is 3.9 eV. The reduction potential of the protein-bound metal ion corresponds to the reduction potential ($-1.05$ V for $Yb^{III}/Yb^{II}$) plus a correction of $-0.18$ eV to account for the larger binding constant for $Ln^{III}$ ions to parvalbumin ($\approx100$ times that of $Ln^{II}$ ions). These values yield a driving force for $Yb^{III}$ of $\Delta G = -1.54$ eV
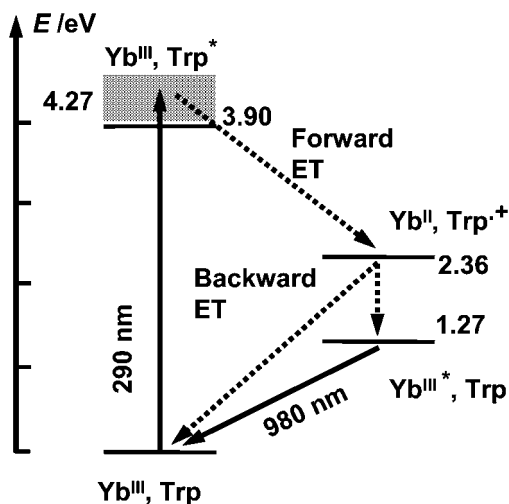
Fig. 9. Proposed electron-transfer mechanism for the sensitization of Yb[III] luminescence by the excited state of tryptophan (Trp). Figures are energies of the states in eV. Redrawn from (deW. Horrocks et al., 1997).

($-148.6\,\text{kJ}\,\text{mol}^{-1}$). The reduction of Yb[III] by tryptophan in its excited singlet state (the forward electron transfer process in fig. 9) produces the tryptophan radical cation $\text{Trp}^{\cdot+}$ and Yb[II]. The former is a strong oxidant, triggering the electron to return onto tryptophan, yielding Yb[III]* and ground state Trp. The Gibbs free energy of the electron transfer back reaction, $\Delta G = E(\text{Ln}^{\text{III}}/\text{Ln}^{\text{II}}) - E(\text{Trp}^{\cdot+}/\text{Trp})$ amounts to $-2.36\,\text{eV}$ ($-227.7\,\text{kJ}\,\text{mol}^{-1}$) and since it is larger than the energy of the $^2F_{5/2}$ state ($1.27\,\text{eV}$, $122.5\,\text{kJ}\,\text{mol}^{-1}$), trivalent ytterbium is thus produced in either the ground or excited state. The fraction of excited Yb[III]* ions formed results in near-infrared luminescence at about 980 nm (deW. Horrocks et al., 1997).

This mechanism is thought to be operative in coordination compounds as well (Beeby et al., 2002c), although in some instances, a fraction of the Yb[III] ions is probably excited via the LMCT state.

## 2.5. Quantum yields and radiative lifetimes

In addition to mastering the various processes leading to electronic excitation of the lanthanide ions, one has to prevent excited states to de-excite via nonradiative processes. The overall deactivation rate constant, which is inversely proportional to the observed lifetime $\tau_{\text{obs}}$, is given by:

$$k_{\text{obs}} = k^{\text{rad}} + \sum_n k_n^{\text{nr}} = k^{\text{rad}} + \sum_i k_i^{\text{vibr}}(T) + \sum_j k_j^{\text{pet}}(T) + \sum_k k_k'^{\text{nr}}, \qquad (6)$$

where $k^{\text{r}}$ and $k^{\text{nr}}$ are the radiative and nonradiative rate constants, respectively; the superscript vibr points to vibrational processes while pet refers to photo-induced electron transfer

processes (De Silva et al., 2000); the rate constants $k'$ are associated with the remaining deactivation paths. The quantum yield is defined as being the number of emitted photons divided by the number of absorbed photons. For an $Ln^{III}$ ion, the intrinsic quantum yield, i.e. the quantum yield obtained by direct excitation into the $4f^*$ levels is simply given by:

$$Q_{Ln}^{Ln} = \frac{\tau_{obs}}{\tau_{rad}} \tag{7}$$

in which $\tau_{rad} = 1/k^{rad}$ is the radiative lifetime of the $Ln^{III}$ ion, that is the inverse of its deactivation rate constant in absence of any quenching and/or nonradiative deactivation processes.

Deactivation through vibrations is especially effective and represents a major concern in the design of both inorganic and organic edifices. Multi-phonon processes are temperature dependent and the deactivation rate constant is also very sensitive to the metal–ligand distance since the interaction is of multipole–multipole nature, wherein the dipole–dipole component is predominant (Hüfner, 1978). In aqueous solutions, interaction with water, both in the inner and outer coordination spheres of the $Ln^{III}$ ion, leads to a severe quenching of the metal luminescence via O–H vibrations. Although detrimental to the design of highly luminescent edifices, this phenomenon can be used to assess the number of water molecules $q$ interacting in the inner coordination sphere and several approximate phenomenological equations have been proposed, based on the assumptions that O–D oscillators do not contribute to deactivation and that all the other deactivation paths are the same in water and in deuterated water, and can henceforth be assessed by measuring the lifetime in the deuterated solvent: (Beeby et al., 1999; Supkowski and deW. Horrocks, 2002):

$$q = A \times (k_{H_2O} - k_{D_2O} - B) - C, \tag{8}$$

where $A$, $B$, and $C$ are phenomenological Ln-depending parameters determined using series of compounds with known hydration numbers. Parameter $A$ describes the inner sphere contribution to the quenching, parameter $C$ the outer sphere contribution of closely diffusing water molecules, while the corrective factor $B$, which has the same units as $k$, accounts for the presence of other de-activating vibrations (e.g. N–H or C–H oscillators). Such relationships, which exist for $Nd^{III}$ (Faulkner et al., 2001), $Sm^{III}$ (Kimura and Kato, 1995), $Eu^{III}$ (Supkowski and deW. Horrocks, 2002), $Tb^{III}$ (Beeby et al., 1999), $Dy^{III}$ (Kimura and Kato, 1995), and $Yb^{III}$ (Beeby et al. 1999), are to be used with care and with the right calibration, given the hypotheses implied. They are nevertheless quite useful and can be extended to other solvents, for instance alcohol. Of interest to this review are the relationships for solvation of $Yb^{III}$ in water and methanol (Beeby et al., 1999), in which the rate constants are expressed in $\mu s^{-1}$:

$$q_{Yb} = 1 \times (k_{H_2O} - k_{D_2O} - B), \quad \text{with } B \text{ between 0.1 and 0.3 } \mu s^{-1}, \tag{9a}$$

$$q_{Yb} = 2.0 \times (k_{CH_3OH} - k_{CD_3OD} - B), \quad \text{with } B \text{ between 0.05 and 0.1 } \mu s^{-1}. \tag{9b}$$

Establishing $q$ for $Nd^{III}$ is more problematic. For instance, an $A$ factor of 342 ns (rate constants are expressed in $ns^{-1}$) can be calculated from lifetime data of the perchlorate salt (table 2), assuming $q = 9$. A similar value is reported for nitrate, 360 ns (Beeby and Faulkner, 1997),

Table 2
Illustration of the energy gap law with respect to quenching of the Ln$^{III}$ luminescence

| Ln | $\Delta E$ (cm$^{-1}$) | Nb of phonons, $n$ | | $\tau$ (µs)[a] | | Reference |
|----|----|----|----|----|----|----|
| | | OH | OD | H$_2$O | D$_2$O | |
| Gd | 32 100 | 9 | 15 | 2300 | n.a. | (Bünzli, 1989) |
| Tb | 14 800 | 4 | 7 | 467 | 3800 | (Bünzli, 1989) |
| | | | | 431 | 4600 | (Kimura and Kato, 1995) |
| Eu | 12 300 | 3–4 | 5–6 | 108 | 4100 | (Bünzli, 1989) |
| Yb | 10 250 | 3 | 4.5 | n.a | 3.95[b] | (Beeby et al., 1997) |
| | | | | 0.17[c] | 5 | (Ermolaev and Sveshnikova, 1979) |
| Dy | 7850 | 2–3 | 3–4 | 2.6 | 42 | (Kimura and Kato, 1995) |
| Sm | 7400 | 2 | 3 | 2.7 | 60 | (Kimura and Kato, 1995) |
| Er | 6600 | 2 | 3 | n.a. | 0.369 | [d] |
| Nd | 5400 | 1–2 | 2–3 | 0.031 | 0.143 | (Beeby and Faulkner, 1997; Lis et al., 2001) |

[a]In dilute solutions of perchlorate salts, at room temperature.

[b]Ytterbium triflate.

[c]Estimated from quantum yield.

[d]Erbium triflate 0.5 M, measured in the authors' laboratory (2006).

while the following equation has been established based on measurements on 4 polyaminocarboxylates (edta, nta, dtpa, and a phosphinate-substituted cyclen, H$_4$**27c**, see section 3.1.4 below):

$$q_{Nd} = 130 \times (k_{H_2O} - k_{D_2O}) - 0.4. \tag{10a}$$

However, this equation does not yield acceptable results in the case of cryptates for instance (Faulkner et al., 2001) and must be used with extreme care. The corresponding equation for methanol solvation is (Beeby et al., 2002a):

$$q_{Nd} = 290 \times (k_{CH_3OH} - k_{CD_3OD}) - 0.4, \tag{10b}$$

but again it has to be used with much caution. The main problem in establishing such a relationship for Nd$^{III}$ is inherent to the presence of C–H vibrations in organic ligands. These vibrations are efficient quenchers even if they lie in the second coordination sphere or even further, so that calibration becomes tricky unless their contribution to the quenching can be established precisely.

The best way to minimize vibration-induced deactivation processes is to design a rigid metal-ion environment, free of high-energy vibrations and protecting the Ln$^{III}$ ion from solvent interaction. Such an environment also contributes to reduce collision-induced deactivation in solution. Further protection may be gained by inserting the luminescent edifice into micelles, a strategy used in some bioanalyses.

Finally, both photo-induced electron transfer from the ligand to the metal ion, resulting in a reduction of Ln$^{III}$ into Ln$^{II}$ with a concomitant quenching of the metal-centered luminescence, and energy back transfer (see fig. 7) have to be avoided by an adequate ligand design positioning the LMCT and triplet states sufficiently away from the emissive state.

In the case of ligand sensitization, the overall quantum yield of a lanthanide-containing molecular edifice is given by

$$Q_{\text{Ln}}^{\text{L}} = \eta_{\text{sens}} \cdot Q_{\text{Ln}}^{\text{Ln}} = \eta_{\text{sens}} \cdot \frac{\tau_{\text{obs}}}{\tau_{\text{rad}}} \tag{11}$$

or $\quad \eta_{\text{sens}} = Q_{\text{Ln}}^{\text{L}} \cdot \frac{\tau_{\text{rad}}}{\tau_{\text{obs}}},$ \hfill (11a)

whereby $Q_{\text{Ln}}^{\text{L}}$ and $Q_{\text{Ln}}^{\text{Ln}}$ are the overall and intrinsic quantum yields resulting from indirect and direct excitation, respectively, while $\eta_{\text{sens}}$ represents the efficacy with which electromagnetic energy is transferred from the surroundings onto the metal ion; $\tau_{\text{obs}}$ is the experimental lifetime of the metal excited state (measured upon direct excitation) and $\tau_{\text{rad}}$ is its radiative lifetime.

The intrinsic quantum yield $Q_{\text{Ln}}^{\text{Ln}}$ essentially depends on the energy gap between the lowest lying excited (emissive) state of the metal ion and the highest sublevel of its ground multiplet. The smaller this gap, the easier is its closing by nonradiative deactivation processes, for instance through vibrations of bound ligands, particularly those with high energy vibrations such as O–H, N–H, or C–H. With the assumption that the de-activating phonons involved have the same energy, the rate temperature-dependent constant $W(T)$ for the quenching of a single excited level is described by the following expression (Hüfner, 1978):

$$W(T) = W(0) \left[ \frac{\exp(\hbar\omega_i / kT)}{\exp(\hbar\omega_i / kT) - 1} \right]^{\Delta E / \hbar\omega_i}, \tag{12a}$$

where $\hbar\omega_i$ is the energy of the de-activating vibration (at maximum of band envelope) and $\Delta E$ the energy gap between the $\text{Ln}^{\text{III}}$ excited state and the terminal low-lying state, $W(0)$ is the spontaneous rate at 0 K, all the vibrations being in their fundamental state. At low temperature, this term dominates the nonradiative deactivation process since $\hbar\omega_i \gg kT$ and therefore eq. (12a) reduces to:

$$W(T) = W(0) = C_1 \cdot \exp(-C_2 \cdot \Delta E / \hbar\omega_i), \tag{12b}$$

with $C_1$ and $C_2$ being empirical parameters characteristic of the $\text{Ln}^{\text{III}}$ environment. In practice, the excited level possesses several crystal-field sublevels, the population of which is in thermal equilibrium. The latter is reached in times short compared to the multiphonon decay time, but since phonon-induced decay rates are significantly slower for the upper levels in view of the larger energy gaps, depopulation of the lower crystal field sub-level is the major contribution to the deactivation process. As a result, the observed lifetime and the quantum yields diminish considerably. A rule of thumb is that radiative de-excitation will compete efficiently with multi-phonon processes if the energy gap is more than 6 quanta of the highest energy vibration present in the molecule.

Multiphonon deactivation is also caused by interaction with alcohol or other vibrations of the solvents, as illustrated in table 3, where $\text{Nd}^{\text{III}}$ lifetime data are reported for various salts in methanol, dmso and their deuterated analogs. One can estimate the rate constant $k_{\text{nr}}$ of the deactivation process assuming that the radiative rate is not affected by deuteration $k^{\text{nr}} =$

Table 3
Lifetimes (ns) of the Nd($^4$F$_{3/2}$) level for solutions of Nd$^{III}$ salts in various solvents. Uncertainties are ±10% for $\tau < 100$ ns and ±5% for $\tau > 100$ ns (Beeby and Faulkner, 1997)

| Salt | H$_2$O | D$_2$O | CH$_3$OH | CH$_3$OD | CD$_3$OD | dmso | dmso-$d_6$ |
|------|--------|--------|----------|----------|----------|------|-----------|
| Nd(ClO$_4$)$_3$·$x$H$_2$O | 30 | 143 | 43 | 191 | 385 | 1726 | 6200 |
| NdCl$_3$·$x$H$_2$O | 29 | 147 | 68 | 245 | 478 | 1692 | 7880 |
| Nd(NO$_3$)$_3$·6H$_2$O | 29 | 152 | 70 | 290 | 476 | 1700 | 9020 |
| Nd(ac)$_3$·H$_2$O | 41 | 158 | 131 | 322 | 517 | 1148 | 2329 |

$k_{obs} - k^{rad}$. From the data for Nd(NO$_3$)$_3 \cdot x$H$_2$O in methanol, the relative changes in $k^{nr}$ induced by substituting O–H and C–H by O–D and C–D are therefore equal to $\Delta k = 1.1 \times 10^7$ s$^{-1}$ and $1.3 \times 10^6$ s$^{-1}$, respectively. Taking into account that there are three C–H groups per O–H, this means that O–H vibrations are de-activating the Nd($^4$F$_{3/2}$) level about 30 times more efficiently than C–H vibrations; this is due to the facts that O–H oscillators are closer to the Nd$^{III}$ ion and that their energy is larger when compared to C–H oscillators (Beeby and Faulkner, 1997). Selected relevant lifetime data for solutions in water and deuterated water are given in table 2, illustrating the quenching effect of O–H vibrations.

Within the frame of the simplified energy transfer model ($^1$S* → $^3$T* → Ln*), eq. (11) can be developed as follows:

$$Q_{Ln}^L = \eta_{isc} \cdot \eta_{et} \cdot Q_{Ln}^{Ln}, \tag{13}$$

with $\eta_{isc}$ representing the efficacy of the intersystem crossing process and $\eta_{et}$ the effectiveness of the $^3$T* → Ln transfer. When excitation of $^3$T* leads to a relatively large expansion of the Ln–L distance, energy transfer occurs as long as the higher vibrational levels of the triplet state are populated, that is the transfer stops when the lowest vibrational level is reached and triplet state phosphorescence takes over. On the other hand, if the Ln–L expansion is small, transfer is feasible as long as the triplet state is populated. If the rate constant of the transfer is large with respect to both radiative and nonradiative deactivation of $^3$T*, the transfer then becomes very efficient ($\eta_{sens} \approx 1$, eqs. (11)). In order to compare the efficiency of chromophores to sensitize Ln$^{III}$ luminescence, both the overall and intrinsic quantum yields have to be determined experimentally. If general procedures are well known for both solutions (Chauvin et al., 2004) and solid state samples (de Mello et al., 1997), measurement of $Q_{Ln}^{Ln}$ is not always easy in view of the very small absorption coefficients of the f–f transitions. This quantity can in principle be estimated differently, from eq. (7), if the radiative lifetime is known. The latter is related to Einstein's expression for the rate of spontaneous emission $A$ from an initial state $|\Psi J\rangle$ characterized by a $J$ quantum number to a final state $|\Psi' J'\rangle$:

$$A(\Psi J, \Psi' J') = \frac{64\pi^2}{3h} \cdot \frac{\tilde{v}_0^3}{(2J+1)} \cdot \left[ \frac{n(n^2+2)^2}{9} \cdot P_{ed} + n^3 \cdot P_{md} \right], \tag{14}$$

where $\tilde{v}$ is the energy of the transition, $n$ the refractive index, $h$ is Planck's constant ($6.63 \times 10^{-27}$ erg s), and $P_{ed}$ and $P_{md}$ are the oscillator strengths of the electric dipole and magnetic

Table 4
Selected Judd–Ofelt intensity parameters for $Ln^{III}$ ions in units of $10^{-20}$ $cm^2$

| Ln | Matrix/anion/solvent | $\Omega_2$ | $\Omega_4$ | $\Omega_6$ | Reference |
|---|---|---|---|---|---|
| Nd | YAG | 0.37 | 2.29 | 5.97 | (Kaminski and Li, 1974) |
| | Aquo ion | 2.25 | 4.08 | 9.47 | (Carnall et al., 1983) |
| | $ClO_4^-$/$CH_3CN$ | 1.2 | 7.7 | 9.8 | (Bünzli and Vuckovic, 1984) |
| | $[Nd(dpa)_3]^{3-}$/$H_2O$ | 7.13 | 3.78 | 13.21 | (Mondry and Starynowicz, 1995) |
| Er | YAG | 1.43 | 1.64 | 1.28 | (Wang et al., 1993) |
| | Aquo ion | 1.34 | 2.19 | 1.88 | (Carnall et al., 1983) |
| | $ErCl_3 \cdot 6H_2O$/EtOH | 5.0 | 2.5 | 0.6 | (Keller et al., 1982) |
| | $[Er(tta)_3]$/MeOH | 34.7 | 1.3 | 2.7 | (Isobe and Misumi, 1974) |
| Yb | Aquo ion | 0.93 | 1.76 | 1.89 | (Carnall et al., 1965) |
| | $LiNO_3$–$KNO_3$ melt | 13.1 | 2.32 | 1.55 | (Carnall et al., 1978) |

dipole contributions to the transitions. According to Judd–Ofelt theory:

$$P_{ed} = e^2 \sum_{\lambda=2,4,6} \Omega_\lambda |\langle J \| U^\lambda \| J' \rangle|^2, \tag{15}$$

with $\Omega_\lambda$ representing the Judd–Ofelt parameters (Judd, 1962; Ofelt, 1962) and $U^\lambda$ doubly reduced matrix elements which are tabulated (Nielson and Koster, 1963).[2] Selected values of $\Omega_\lambda$ parameters for $Nd^{III}$, $Er^{III}$, and $Yb^{III}$ are reported in table 4.

The magnetic dipole contribution can be calculated from:

$$P_{md} = \frac{4\pi^2 e^2 h}{3m^2 c^2} \cdot \frac{\tilde{\nu}_0^3}{(2J+1)} \cdot |\langle J \| L + 2S \| J' \rangle|^2, \tag{16}$$

where $L + 2S$ is the spin–orbit operator which can be evaluated according to published methods (Carnall et al., 1965), and $e$, $m$, $c$ have their usual meaning. Then if the excited state $|\Psi J\rangle$ relaxes to several different states $|\Psi' J'\rangle$, the radiative lifetime $\tau_{rad}$ is equal to:

$$\tau_{rad} = \frac{1}{\sum_{J'} A(\Psi J, \Psi' J')}. \tag{17}$$

The radiative lifetime can therefore be estimated from the spectral intensity that is from eqs. (14)–(17). Except for the special case of $Eu^{III}$ for which a convenient simplified equation can be derived because one transition ($^5D_0 \rightarrow {}^7F_1$) has a pure magnetic origin (Werts et al., 2002), this calculation is not trivial and large errors can occur, including those pertaining to the hypotheses made. In particular it has been assumed that the emitting and receiving levels are really $(2J + 1)$-fold degenerate or, if split by crystal field effects, that all the sublevels are equally populated. This is obviously not true and in the case of $Er^{III}$ this may lead to errors up to 20%. If the absorption spectrum corresponding to an emission spectrum is known however, which may be the case when the luminescence transitions terminate onto the ground level, the

---

[2] Note that eqs. (14) through (18) are given within the frame of the cgs–esu unit system. Oscillator strengths are therefore expressed in $esu^2 cm^2 = debye^2$ while $\Omega_\lambda$ parameters are in $cm^2$.

Table 5
Selected values of radiative lifetimes for Ln$^{III}$ ions

| Ion | Compound | Solvent | Excited state | End state | $\tau_{rad}$ (ms) | Reference |
|-----|----------|---------|---------------|-----------|-------------------|-----------|
| Pr | Doped in Y$_2$O$_3$ | – | $^1G_4$ | $^3H_J$ | 0.58 | (Weber, 1968) |
| Nd | [Nd(dtpa)]$^{2-}$ | D$_2$O | $^4F_{3/2}$ | $^4I_J$ | 0.3–3.4 | (Werts et al., 2002) |
| Sm | [Sm(H$_2$O)$_n$]$^{3+}$ | H$_2$O | $^4G_{5/2}$ | $^6H_J$ | 6.26[a] | (Carnall, 1979) |
| Eu | [Eu(H$_2$O)$_n$]$^{3+}$ | H$_2$O | $^5D_0$ | $^7F_J$ | 9.67[a] | (Carnall, 1979) |
| Tb | [Tb(H$_2$O)$_n$]$^{3+}$ | H$_2$O | $^5D_4$ | $^7F_J$ | 9.02[a] | (Carnall, 1979) |
|    | [Tb(H$_2$O)$_n$]$^{3+}$ | H$_2$O | $^5D_4$ | $^7F_J$ | 5.4[b] | (Bünzli, 1989) |
| Dy | [Dy(H$_2$O)$_n$]$^{3+}$ | H$_2$O | $^4F_{9/2}$ | $^6H_J$ | 1.85[a] | (Carnall, 1979) |
| Ho | [Ho(H$_2$O)$_n$]$^{3+}$ | H$_2$O | $^5S_2$ | $^5I_J$ | 0.37[a] | (Carnall, 1979) |
| Er | [Er(D$_2$O)$_8$]$^{3+}$ | D$_2$O | $^4I_{13/2}$ | $^4I_{15/2}$ | 8.68 | (Werts et al., 2002) |
| Yb | [Yb(dtpa)]$^{2-}$ | D$_2$O | $^2F_{7/2}$ | $^2F_{5/2}$ | 1.21 | (Werts et al., 2002) |

[a]Calculated value from spectral intensities.
[b]Recalculated from $Q_{Ln}^{Ln}$ and $\tau_{obs}$ data reported in the reference.

radiative lifetime is equal to:

$$\frac{1}{\tau_{rad}} = 2303 \cdot \frac{8\pi c n^2 \tilde{v}_0^2}{N_A} \cdot \frac{(2J'+1)}{(2J+1)} \cdot \int \varepsilon(\tilde{v})\, d\tilde{v}, \tag{18}$$

where $c$ is the speed of light in vacuo (in cm s$^{-1}$), $\tilde{v}_0$ is the frequency of the transition in cm$^{-1}$, $n$ is the refractive index of the medium, $N_A$ is Avogadro's number, $\varepsilon(\tilde{v})$ is the absorption spectrum of the transition in M$^{-1}$ cm$^{-1}$ vs wavenumbers (Werts et al., 2002).

There are two important points to be stressed here in order to correct many errors reported in the literature. Firstly, the radiative lifetime is characteristic of one emitting state. If several excited states of an Ln$^{III}$ ion emit light, then each of them will have a characteristic radiative lifetime.

Moreover, the radiative lifetime is not a constant for a given ion and a given electronic level. Indeed, there is a dependence on the refractive index, as clearly shown by eq. (14), so that transposition of a literature value to a specific compound cannot be made directly, which explains the wide range of $\tau_{rad}$ values reported for an individual Ln$^{III}$ ion. As an example, reported radiative lifetimes for Er$^{III}$ range from 3 to 12 ms, even for relatively similar compounds (see table 19 below)! Another hypothesis inherent to Judd–Ofelt theory is that 4f functions do not contain contributions from 5d orbitals, which is not quite the case for Pr$^{III}$ and Tb$^{III}$ for instance. Selected data reported in the literature are listed in table 5.

## 2.6. *Multi-photon absorption and up-conversion*

Up-conversion is a process by which two photons of lower energy are subsequently converted into a luminescence photon of higher energy (typically, two IR photons giving rise to one visible photon, e.g. in Er$^{III}$-containing compounds). This anti-Stokes process is usually observed for ions embedded in solids and is made possible by various mechanisms, such as the now classical excited state absorption mechanism (ESA), or sequential energy transfers (ETU for

energy transfer up-conversion), or cooperative absorption by two or three metal ions. They are very well documented and reviewed (Auzel, 2004) and shall not be discussed here.

On the other hand, many ligands proposed for the sensitization of $Ln^{III}$ luminescence have singlet excited states above $28\,000 \text{ cm}^{-1}$ (below 360 nm), which implies UV excitation. Not only does this feature results in larger costs for routine measurements (instruments, quartz cuvettes) but, in addition, when materials of biological origin are analyzed, photochemical damages can be induced. Henceforth the search was launched by several research groups for ligands able to be excited into the visible range. So far, few ligands have been found fulfilling this condition and only a handful of them can be excited above 400 nm. If, in addition, one takes into account the high transparency of biological materials above approximately 700 nm, a desirable way of exciting the ligands would be to make use of light with wavelengths larger than this limit, which means that one would then probably have to resort to two-photon absorption. This phenomenon is documented for organic molecules and a strategy for the design of molecules with large two-photon absorption cross sections has been recently developed. Indeed, oscillator strengths for two-photon absorption are usually orders of magnitude smaller than those for one-photon absorption. The concept makes use of symmetric charge transfers, from the ends of a conjugated system to the middle, or vice versa, which upon excitation are correlated, resulting in an enhanced value of the cross section for two-photon absorption. Bis(styryl)benzene derivatives with donor–$\pi$–donor, donor–acceptor–donor, and acceptor–donor–acceptor structural motifs exhibit exceptionally large values of two-photon absorption cross sections, up to about 400 times that of trans-stilbene. The combination of large two-photon absorption cross sections and high luminescence quantum yield offers potential for unprecedented brightness in two-photon luminescence imaging or enhanced photosensitivity in two-photon sensitization, respectively (Albota et al., 1998). To date, there are few examples pertaining to the subject of this review in which lanthanide luminescent molecular probes have been excited by a two-photon process. In one related example, $Eu^{III}$ has been directly excited at 796 nm (through the $^5L_6 \leftarrow {}^7F_0$ transition, at 398 nm) in deuterated water for the purpose of using the resulting luminescence for microscopy imaging; in water the intensity is much lower. Trivalent terbium could also been excited via a three-photon process (768 nm) by the same tunable Ti:sapphire laser (Lakowicz et al., 2001). Two- and three-photon excitations of the same ions have been achieved via complexed nucleic acids, proteins, and other fluorescent chelators such as coumarin, carbostyril-124 or methyl anthranilate (Piszczek et al., 2002b). A more recent study proposed a ternary beta-diketonate complex of $Eu^{III}$ for multiphoton excitation (Fu et al., 2005); to our knowledge, such a process has rarely been demonstrated for NIR-emitting molecular complexes.

## 2.7. *Synthetic strategies for ligand and complex design*

In addition to the features relevant to energy-transfer processes and minimization of nonradiative deactivation discussed above, the $Ln^{III}$ environment in a lanthanide-containing luminescent probe must also fulfill several other requirements: high thermodynamic stability, kinetic inertness, and a saturated coordination sphere. Furthermore, in case of bio-analyses, the luminescent probe has to comply with biochemical aspects as well, especially if the probe is to be

used *in vivo*. Given the large lability of lanthanide ions and their need for high coordination numbers (Bünzli, 1998), this poses a real challenge to synthetic chemists who have come up with several strategies to meet, it which are briefly outlined below.

In aqueous solutions, the enthalpy and entropy changes upon complex formation between $Ln^{III}$ cations and many ionic ligands is predominantly influenced by changes in hydration of both the cation and the ligand(s). Complexation results in a decrease in hydration, yielding positive entropy changes favorable to the complexation process. On the other hand, dehydration is endothermic and contribution from bond formation between the cation and the ligand(s) often does not compensate this unfavorable energy contribution to the variation in Gibbs free energy so that the overall complexation process is generally entropy driven. Therefore, it is advantageous to resort to polydentate ligands for building a coordination environment around $Ln^{III}$ ions. During the last decades, inorganic chemists have come up with a number of imaginative strategies to insert $Ln^{III}$ ions into functional edifices using such polydentate ligands.

### 2.7.1. *Linear polydentate and multifunctional ligands*

Numerous ligands fall into this category, so that we shall only mention three large classes of ligands which have produced interesting $Ln^{III}$ complexes. Polyaminocarboxylates have played a special role in $Ln^{III}$ coordination chemistry since publication of the crystal structure of the $La^{III}$ complex with edta (ethylenediamine-$N,N',N'',N'''$-tetraacetate) definitively convinced the chemical community that $Ln^{III}$ ions frequently possess coordination numbers larger than 6 (here 10). With log $K$ in the range 15–20, $[Ln(edta)]^-$ complexes are quite stable and consequently, aminocarboxylate complexing units have been grafted on numerous substrates, including macrocycles, e.g. dota, 1,4,7,10-tetraaza-cyclododecane-$N,N',N'',N'''$-tetraacetate, with log $K$'s in the range 23–25 (Izatt et al., 1991). Stability of these complexes arises from the combination of (i) large entropic effects due to de-solvation of the aqua-ion, (ii) charge compensation occurring upon complexation, (iii) the formation of strong ionic bonds with the carboxylate units, and (iv) the formation of stable five-membered chelate rings (Choppin, 1989).

Another efficient coordinating unit is $\beta$-diketonate. Rare earth $\beta$-diketonates have been prepared as early as 1897 by G. Urbain and they are among the most investigated $Ln^{III}$ coordination compounds, useful in a wealth of applications, ranging from complexation agents in solvent–solvent extraction processes, to NMR shift reagents, luminescent probes for time-resolved immunoassays, and electroluminescent materials. The bidentate nature of the chelating moiety, however, leads often to hexa-coordinated tris-complexes which complete their coordination sphere by adding two water molecules; detrimental to luminescent properties, these molecules can nevertheless be easily replaced with chromophores such as phenanthroline or bipyridine leading to highly luminescent ternary complexes (Binnemans, 2005b).

Acyclic Schiff base derivatives represent a resourceful class of compartmental ligands which are prepared by self-condensation of appropriate formyl and amine precursors. The condensation reaction is simple and generally leads to the desired product in high yield. Literature data on $Ln^{III}$ mono- and bimetallic complexes, as well as on 4f–d transition metal bimetallic entities with these derivatives are abundant and have been reviewed recently (Vigato and Tamburini, 2004). Extension to multimetallic systems and to complexes with 5f elements

is straightforward. Appropriate choice in the number and nature of the coordinating atoms ensures a well defined coordination environment so that multimetallic systems with metal ions at pre-defined distances may be designed.

### 2.7.2. *Macrocyclic receptors* (Sastri et al., 2003)

The idea behind the design of such ligands is to build a pre-organized cavity bearing several donor atoms generating suitable interactions with the metal ion (i.e. hard–hard or soft–soft in HSAB-theory) and with a cavity diameter well adapted to the size of the guest cation (*lock-and-key principle*). In this way, reorganization energy of the ligand upon complexation is minimized. Lanthanide macrocyclic chemistry started in the late 1960's when the need for NMR shift reagents induced the study of lanthanide phthalocyanines and porphyrins (Ng, 2001). Two other classes of macrocyclic receptors were developed soon after as model ligands for the transport of cations through biological membranes, coronands (initially, crown ethers) and cryptands which were tested with variable success with the $Ln^{III}$ ions (Izatt et al., 1985). Indeed, the difference in ionic radius between lanthanum and lutetium amounts to only ca. 0.15 Å (for coordination number 9) while the ionic radius of two consecutive lanthanide ions differs by a mere 0.01–0.015 Å, that is a fine tuning of the receptor to accommodate a specific $Ln^{III}$ ion is out of reach, except possibly for the selective complexation of larger versus smaller ions, or vice versa. This remark is also valid for lanthanide complexes with two series of macrocycles which were studied starting in the mid 1970's: simple calixarenes (Asfari et al., 2001; Bünzli et al., 2000; Roundhill, 1995) and cyclic Schiff base derivatives (Vigato and Tamburini, 2004).

Therefore, another strategy was developed, based on the *induced-fit* concept, which uses flexible receptors in order to optimize the interactions between the donor atoms and the metal ion. In fact, the coordination environment is built upon complexation thanks to the flexibility introduced into the complexation agent, which is now termed "predisposed ligand". These receptors are either large macrocycles able to wrap around the guest or small macrocycles fitted with pendant arms. The latter approach has proved to be very successful, particularly with calixarene (Asfari et al., 2001) and cyclen (1,4,7,10-tetraaza-dodecane) (Lukes et al., 2001) derivatives.

### 2.7.3. *Podands*

The induced-fit approach can also be conducted in an efficient way by designing podands. Here the functionalized pendant arms are no more attached onto a potentially coordinating macrocycle but simply on a single atom (boron, nitrogen, carbon, or transition metal ions) or a small aromatic ring such as benzene or triazine. This strategy is particularly useful when the design of a lanthanide-containing molecular edifice requires bidentate or tridentate pendant arms. Their grafting onto macrocycles is indeed not always straightforward from a synthetic point of view. Ligands with four arms are usually built from small aromatic rings, while tri-armed receptors are often engineered from a single atom. The number of donor atoms can be easily varied by changing both the number of arms and their denticity. However, these ligands are less predisposed than the macrocycles fitted with pendant arms and the orientation of the arms to put the hosting cavity together requires more conformational work, which is

detrimental to the stability of the final molecular edifice. One remedy is to profit from non-covalent interactions, such as H-bonding (Renaud et al., 1999) or $\pi$-stacking interactions, or to start from a transition-metal podate (Piguet et al., 2000) to position the arms in the right conformation prior to complexation.

### 2.7.4. *Self-assembly processes*

In going from pre-organized to pre-disposed receptors, one benefits from simplified synthetic procedures. The next step is to resort to metallosupramolecular chemistry and take advantage of both the high electric field generated by the $Ln^{III}$ ions and weak intermolecular interactions to self-assemble small coordinating units around a metal ion. Application to coordination chemistry is relatively recent (Lehn, 1995). This strategy has been tested in our laboratories to produce large libraries of mono- and di-topic ligands which self-assemble with $Ln^{III}$ ions to yield monometallic and bimetallic 4f–4f, 4f–4f′, as well as d–4f triple-helical edifices under strict thermodynamic control and with predetermined physico-chemical properties (Bünzli and Piguet, 2002). Theoretical and rational modeling of the self-assembly of these helicates is now at hand, which enables a more rational approach (Piguet et al., 2005) as well as extension to multimetallic systems (Floquet et al., 2004), so that self-assembly processes slowly emerge as a privileged strategy for the engineering of elaborate multimetallic edifices and devices.

## 3. NIR-emitting molecular edifices

In this section, lanthanide-containing NIR-emitting compounds are classified according to the synthetic strategy used to encapsulate the metal ion starting with macrocyclic compounds (Korovin and Rusakova, 2001), then moving to acyclic receptors before describing sensitization with transition metal ions and, finally, various other approaches leading to new materials.

### 3.1. *Macrocyclic ligands*

### 3.1.1. *Simple lanthanide porphyrinates*

Tetrapyrrole derivatives such as porphyrins or phthalocyanines (Pc) are highly stable and have exceedingly delocalized $\pi$ systems. Consequently, they exhibit a wide range of intriguing optical, electrical, magnetic, and spectroscopic properties which render them useful in the fields of materials science, catalysis, biology, and medicine. Their combination with trivalent lanthanide ions has been investigated quite early, starting in the mid 1960's and leading to the isolation of $[Ln(Pc)_2]$ complexes (Ln = Pr, Nd, Er, Lu) which are now well known electrochromic materials (Ng, 2001). Regarding NIR sensitization however, no phthalocyanine complexes with metal-centered NIR luminescence have been reported yet, the initial work of Gurevich and Solev'ev in 1961 having demonstrated that no luminescence from $Yb^{III}$ is detected, the energy of the $^3T^*$ state being lower than the energy of the $Yb(^2F_{5/2})$ excited level (Gurevich and Solev'ev, 1961). On the other hand, numerous NIR-emitting lanthanidoporphyrins have been reported, particularly with $Yb^{III}$ in view of the favorable energy of the porphyrin triplet state. Metalloporphyrins display rich photochemical properties. Their absorption spectrum consists usually of two structured bands, in the ranges 400–425 nm ($^1S_2 \leftarrow {}^1S_0$,
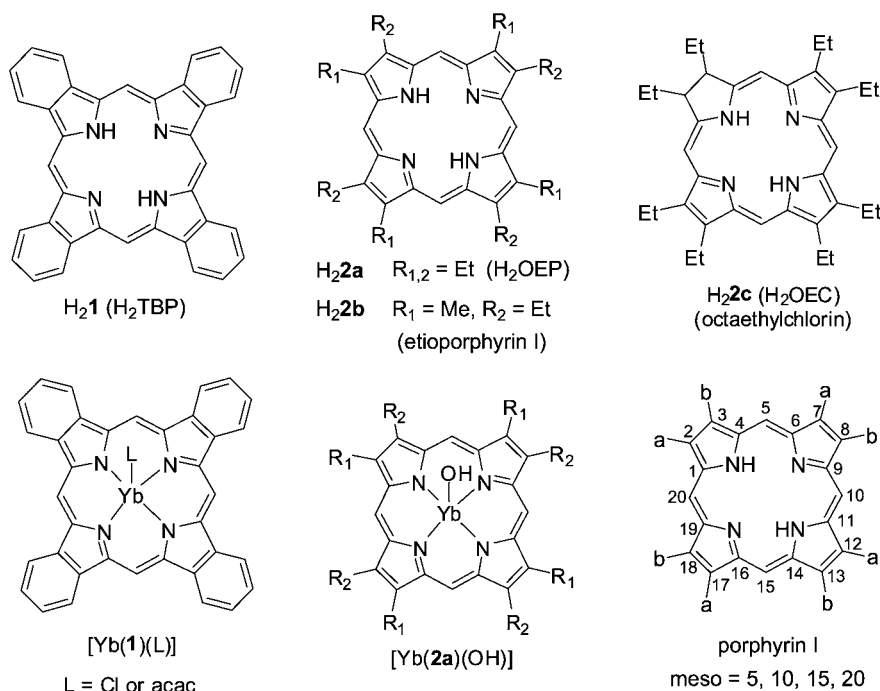
Fig. 10. Free porphyrin ligands (top) and first NIR-emitting lanthanidoporphyrins, along with the numbering adopted for porphyrins (bottom right).

Soret or B-band, $\log \varepsilon \approx 4.5$–$5.5$) and 520–650 nm ($^1S_1 \leftarrow {}^1S_0$, Q-band, $\log \varepsilon \approx 3$–$4$). Fluorescence occurs from both the Soret and Q states since the triplet state $^3T_1$ lies below $^1S_1$.

The nomenclature of porphyrins, which belong to the larger class of tetrapyrrole compounds, is sometimes obscured by historical remnants (e.g. chlorin which does not contain any chlorine substituent, see $H_2$2c in fig. 10, or 2,4-di($\alpha$-methoxyethyl)-deuteroporphyrin for $H_4$4b, see fig. 11 below). IUPAC has published nomenclature rules in 1986[3] and the numbering adopted for the ring is given in fig. 10. The 5, 10, 15, and 20 positions are commonly referred to as *meso* positions; the roman number after a name (I though IV) denotes the relative positions of substituents a and b.

Taking advantage of the fact that the triplet state of metalloporphyrins with tetrabenzoporphyrin ($H_2$TBP or $H_2$1, fig. 10) lies around 12 500 cm$^{-1}$, a team from Minsk succeeded in sensitizing $Yb^{III}$ luminescence in solutions of [Yb(TBP)L], where L = Cl or acac (acetylacetonate), in several solvents like benzene, dimethylformamide (dmf), pyridine, quinoline or a mixture of octane and benzene (Kachura et al., 1974). Energy transfer from the porphyrin chromophore was ascertained by the excitation spectrum of the $Yb^{III}$ luminescence being identical to the absorption spectrum of the complex. In benzene, the quantum yield of

---

3   http://www.chem.qmul.ac.uk/iupac/tetrapyrrole/.

the metal-centered luminescence measured upon ligand excitation amounts to 0.5% with a $Yb(^2F_{5/2})$ lifetime equal to 12 μs. Although this quantum yield is low, only a weak phosphorescence band from the ligand was observed and the Yb[III]-centered luminescence was not quenched by bubbling oxygen into the solution at room temperature. From the photophysical data measured on this system, the authors have estimated the rate constant of the ligand-to-Yb[III] energy transfer to be on the order of $10^7$ s$^{-1}$. Within experimental errors, identical data have been obtained for quantum yield, lifetime and energy transfer rate in the case of the Yb[III] complex with octaethylporphyrin, $H_2OEP$ or $H_2$**2c** (Solovev et al., 1976). The latter authors have also detected a faint luminescence from [Nd(TBP)acac] and [Nd(OEP)acac]. High energy C–H vibrations play an important role in the deactivation of the $Yb(^2F_{5/2})$ level through both inter- and intra-molecular processes (Tsvirko and Kachura, 1975). For instance, the lifetime of the $^2F_{5/2}$ level in [Yb(TBP)(acac)] increases considerably, from 12 to 72.5 μs, when benzene is substituted by carbon disulfide as solvent, removing intermolecular interactions with C–H vibrations. Regarding intramolecular C–H vibrations, the lifetime of [Yb(**2b**)(acac)] in $CS_2$ increases from 71 to 131 μs when etioporphyrin is deuterated four-fold at the methane bridges. Finally, replacing acac with a chloride ion in the deuterated etioporphyrin complex leads to a lifetime of 143 μs.

The photophysical processes in [Ln(TBP)acac] dissolved in ethanol and their correlation with Ln[III] ion characteristics have been later fully investigated by picosecond transient spectroscopy (Tsvirko et al., 1986) for a number of Ln[III] ions including Er[III] and Yb[III]. The non-radiative decay rates of the ligand excited states in the lanthanide-TBP complexes vary by several orders of magnitude depending on the emissive state and the Ln[III] ion: from $2 \times 10^{10}$ to $2 \times 10^{11}$ s$^{-1}$ for $^1S_1$, from $3 \times 10^{11}$ to $2 \times 10^{13}$ s$^{-1}$ for $^1S_2$, and from $6 \times 10^2$ to $3 \times 10^{10}$ s$^{-1}$ for $^3T_1$. The latter deactivation rate constant decreases exponentially when the energy gap $\Delta E(^3T_1$–Ln*) is between 4000 and 14 000 cm$^{-1}$ while it remains more or less constant for $\Delta E < 4000$ cm$^{-1}$. In [Yb(TBP)acac], the $Yb(^2F_{5/2})$ lifetime was found to be 4.5 μs that is, much smaller than the value reported in other non-protic solvents (Kachura et al., 1974).

Soon after the first attempt to sensitize NIR luminescence through the porphyrin triplet state, octaethylporphyrin complexes were synthesized with several rare earth ions (R = Y, Sm, Eu, Gd, Tb, Dy, Ho, Er, Tm, Yb, Lu), by heating free $H_2OEP$ with metal chlorides in an imidazole melt at 210 °C for 2 h, followed by purification steps, including chromatography on a magnesium carbonate column. Chemical analysis and infrared spectroscopy ($\tilde{\nu}_{OH} = 3270$ cm$^{-1}$) established the chemical formula [Ln(OEP)(OH)]. Similar complexes can be prepared from lanthanide acetylacetonates (Gouterman et al., 1976). Although these complexes are not very stable, some of them dissociating readily in methanol, their photophysical properties were established: (i) $f^0$, $f^7$, and $f^{14}$ complexes display fluorescence (0-phonon transition at 575–580 nm) and phosphorescence (0-phonon transition around 700 nm), the latter being especially strong for the Gd[III] complex, (ii) $f^2$–$f^6$ and $f^8$–$f^{12}$ compounds show essentially fluorescence from the organic ligand, both at room and low (77 K) temperature, while (iii) [Yb(OEP)(OH)] emits in three distinct spectral ranges, corresponding to the singlet and triplet state luminescence as described above, and to the $^2F_{5/2} \to {}^2F_{7/2}$ transition. While the quantum yield of the Yb[III]-centered luminescence was not determined, simultaneous detection of ligand fluorescence and phosphorescence points to a less efficient sensitization than

in the TBP analog. The emission spectra of the two porphyrinates [Yb(TBP)(OH)]·2H$_2$O and [Yb(OEP)(OH)]·H$_2$O consist in the intense electronic 4f–4f transition centered at 975 nm and in broad side-bands which are temperature dependent. Their detailed analysis allowed the determination of the ligand–field splitting of both $^2F_{5/2}$ and $^2F_{7/2}$ states (Asano-Someda and Kaizu, 2001).

Porphyrins possess several medically useful properties. The most prominent is their ability to accumulate in cancer cells, or more generally in fast growing tissues, so that they are presently being explored in a number of medical applications ranging from cancer therapy (the best known application), to cardiology, ophthalmology, or dermatology. Starting at the end of the 1970's, patients with breast, lung, prostate and skin cancer have been treated by photodynamic therapy. In this cure, a porphyrin photosensitizer is administrated via intravenous injection and localizes in the cancerous region. Visible (red) light is used to activate the sensitizer and to produce singlet oxygen, the cytotoxic agent. Results were encouraging, with almost 100% of complete or partial response. On the other hand, secondary effects developed, such as burns and skin rashes. Moreover, the early porphyrin treatments were seldom strong enough to kill the entire tumor. Finally, some porphyrins are activated by light that cannot penetrate deep enough into the tumor. Henceforth, the search for new porphyrins with a greater potency and which could be activated by light penetrating deeper in human tissues, in the near-infrared range. Haematoporphyrins accumulate more efficiently in malignant tumor than porphyrins and are therefore privileged target for photodynamic treatment of cancer. On the other hand, they have two disadvantages: (i) a high phototoxicity, which requires protection of patients from the action of light on the skin, and (ii) a low contrast of tumors caused by the masking effect of the background luminescence they generate because of a relatively low efficacy of the intersystem process. These disadvantages can be overcome, at least in principle, by the use of the 1-μm emission line of Yb$^{III}$, since the luminescence of the latter is distinct from the luminescence of the porphyrins and, moreover since the lifetime of the $^2F_{5/2}$ level is relatively long, time-resolved spectroscopy can increase further the signal-to-noise ratio. Therefore, efforts have been undertaken to develop suitable lanthanidoporphyrins with high quantum efficiency. One of the first reports mentioning potential application of Yb$^{III}$ haematoporphyrins H$_4$3 for the diagnosis of malignant tumors uses tetramethyl-haematoporphyrin H$_2$4a, 2,4-di($\alpha$-methoxyethyl)-deuteroporphyrin H$_4$4b, *meso*-tetra(*p*-carboxyphenyl)porphyrin H$_6$4c, and tetrasulfophenylporphyrin H$_6$4e depicted in fig. 11 (Gaiduck et al., 1989; Gaiduck et al., 1990). In view of the poor solubility of the complexes, they were introduced into phosphatidylcholine liposomes. A fiber-laser luminescence spectrometer has been especially designed to monitor the Yb$^{III}$ luminescence from sarcoma-implanted mice. Both the central and peripheral regions of the tumors were measured, as well as surrounding healthy skin, which allowed the determination of a contrast ratio $\gamma_S$ from the total emission areas $S$ (emission from tumor) and $S_0$ (emission from healthy skin):

$$\gamma_S = \frac{S - S_0}{S}. \tag{19}$$

The complexes [Yb(4a)]$^+$ and [Yb(4c)]$^{3-}$ yield a contrast value $\gamma_S = 10 \pm 2$, while the two other complexes are more efficient, with $\gamma_S$ values equal to $19 \pm 4$, and $45 \pm 9$ for [Yb(4b)]$^-$
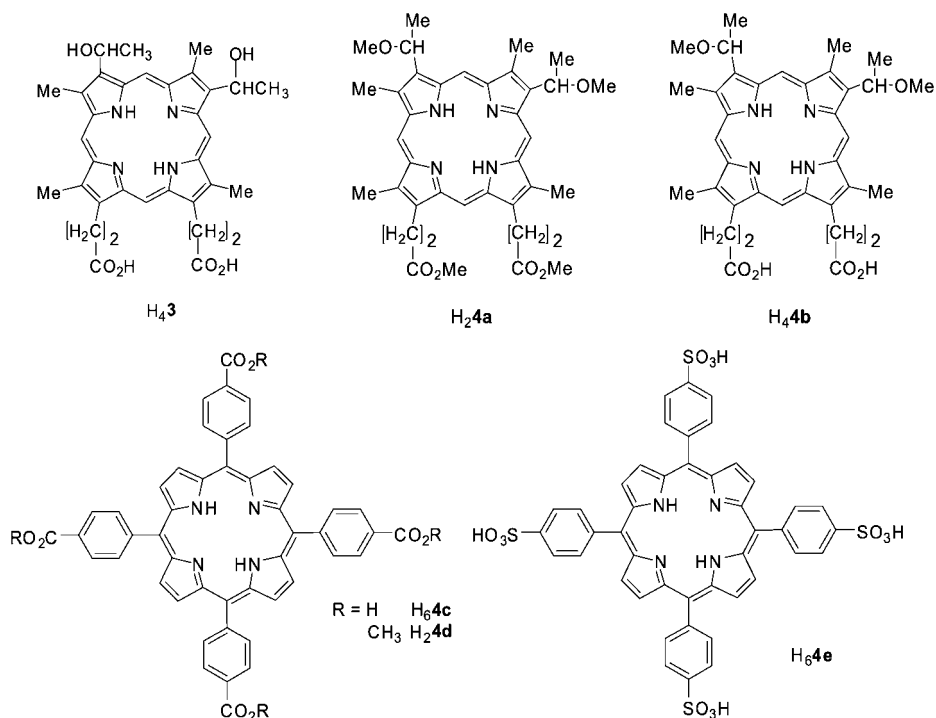
Fig. 11. Structure of haematoporphyrins used to sensitize Yb[III] luminescence in tumors.

and [Yb(**4e**)]$^{3-}$, respectively. In addition to the lower phototoxicity of the lanthanidoporphyri-
nates these contrast data compare most favorably with those obtained with porphyrins alone
(1.1–1.2). The detailed photophysics of these complexes has been elucidated and interpreted
in terms of crystal-field theory (Gaiduck et al., 1991); in liposomes, [Yb(**4b**)]$^{-}$ displays a
lifetime of the metal excited state of 1.5 µs, slightly smaller than in the solid state (1.9 µs).

Sensitization of Yb[III] luminescence by tetraphenylporphyrinate **5c** (TTP, fig. 12) is demon-
strated by a dramatic drop in the quantum yields of the $^1S_1$-level fluorescence of this species
from 0.06% for [Lu(TTP)acac] to less than $3 \times 10^{-3}$% for the Yb[III] derivative. In paral-
lel, the quantum yield of the $^1S_2$-level fluorescence diminishes from 0.15% (Lu[III]) to 0.01%
(Yb[III]). No quantum yield for the metal-centered luminescence is given in this initial work,
but $\tau(^2F_{5/2})$ is reported to be equal to 5 µs (Tsvirko et al., 1980). The quantum yield of
[Nd(TTP)acac] has been determined in benzene and is equal to 0.025% (Shushkevich et al.,
1981). The latter authors have also measured the quantum yields of [Yb(OEP)acac] (0.045%)
and [Yb(**2c**)acac] (0.054%) in the same solvent and undertaken a careful study of the polar-
ization of Nd[III] and Yb[III] emission bands and discussed it with respect to the symmetry of the
complexes. In order to improve the photophysical properties of [Er(TPP)acac] the complex
has been dispersed at concentrations of 5, 17, 28, and 37 wt% into thin films of $\pi$-conjugated
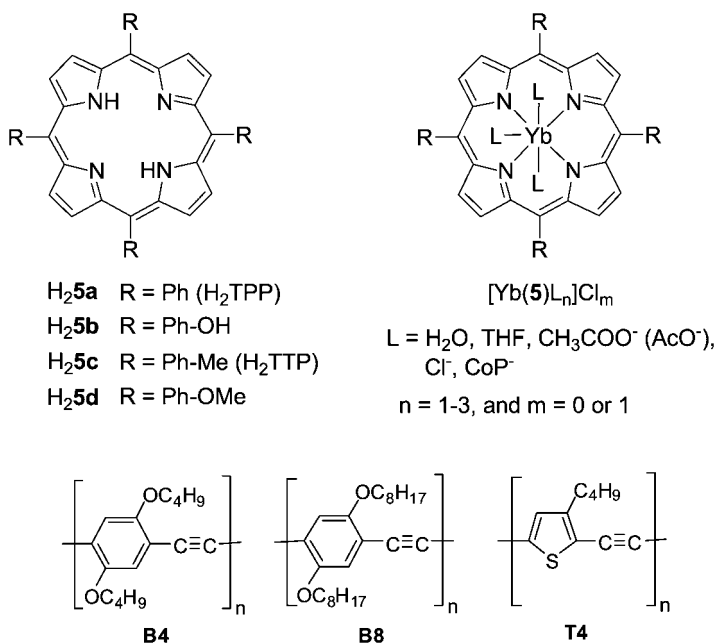
Fig. 12. (Top) [5,10,15,20-tetrakis($p$-(R)phenyl)porphyrins] and their Yb$^{III}$ complexes. (Bottom) $\pi$-conjugated polymers used to host [Er(TPP)acac].

polymers (fig. 12, bottom) obtained by spin coating followed by vacuum annealing. The presence of the lanthanide ion in the porphyrinate produces a strong quenching of the free base visible fluorescence and the NIR quantum yield of a solution of the parent complex $7 \times 10^{-3}$ M in chloroform amounts to 0.04%. In the thin films, of thickness $500 \pm 10$ nm, energy transfer occurs from the $\pi$-conjugated systems because of spectral overlap between the $Q$ absorption band of [Er(TPP)acac] with the fluorescence band of the polymers; interestingly, 5 wt% of the complex quenches 80% of the **B8** polymer fluorescence. A detailed study has been performed along the lines of Förster theory for dipole–dipolar transfer. The donor quantum yield amount to 14, 22, and 1.5% for **B4**, **B8**, and **T4**, respectively, and the critical distance for 50% transfer (eq. (4b)) was estimated to be 2.3, 2.6, and 1.4 Å, respectively. These are quite short and at such distances other mechanisms should also be operative (exchange mechanism for instance), although the authors could satisfyingly fit their data of the fractional quenching of the host luminescence versus the concentration of emitting ions by a theory derived from Förster mechanism. The relative transfer efficiency for 2 wt% of the Er$^{III}$ complex dispersed in thin films amounts to 74 and 21% for **B4** and **T4**, when **B8** is taken as the reference, pointing to the better efficiency of the latter (Pizzoferrato et al., 2004).

In Yb$^{III}$ tetraphenylporphyrinates, the substituent in the *para* position of the phenyl ring plays an important role in the luminescence intensity, as demonstrated for the series of complexes [Yb(**5b**)(AcO)(H$_2$O)$_2$], [Yb(**5c**)(thf)(H$_2$O)$_2$]Cl, [Yb(**5a**)(thf)(H$_2$O)$_2$]Cl,
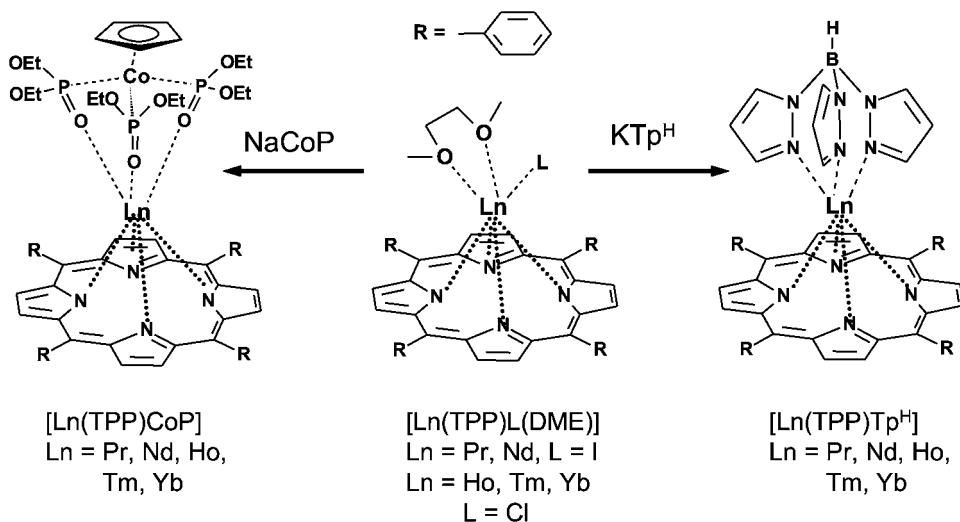
Fig. 13. High-yield syntheses of [Ln(TPP)CoP] and [Ln(TPP)Tp$^H$] (Foley et al., 2003).

[Yb(**5d**)(H$_2$O)$_3$]Cl, and [Yb(**5d**)(CoP) (fig. 12) where CoP is the cyclopentadienyl-tris(dieth-ylphosphito)cobaltate(I) anion (see fig. 13) for which the luminescence intensity increases in the proportions 1:22:36:62:271, upon excitation at 512 nm (Meng et al., 2000). The effect of coordinated water molecules on the metal-centered fluorescence intensity is clearly seen in the more than four-fold enhancement obtained by replacing the three water molecules in [Yb(**5d**)(H$_2$O)$_3$]Cl by CoP; the $^2F_{5/2}$ lifetime of the latter complex (40 μs) is also much longer than lifetimes reported for other Yb$^{III}$ porphyrinates. In addition, the cobaltate anion rigidifies the molecule, which results in a much finer structure of the ligand-field split electronic levels.

Initial synthesis of lanthanide tetraphenylporphyrinates aimed at serving as dipolar probes for nuclear magnetic resonance involved distillation of acetylacetone from a lanthanide acetyl-acetonate in the presence of the dianion TPP$^{2-}$ (**5a**) to give [Ln(TPP)(acac)] in low yield, 10–30% (Wong et al., 1974). The latter arises from the necessary chromatographic purifica-tion which causes hydrolysis of the porphyrinates. A higher yield synthesis was only pro-posed recently, which involves nucleophilic displacement of chloride ions from anhydrous lanthanide trichloride tris(tetrahydrofuran) adducts by the TPP$^{2-}$ dianion under the form of dilithiotetraphenylporphyrin bis(dimethoxyethane); yields up to 85% have been obtained and the crystal structures of the holmium and ytterbium porphyrinate have been solved (Foley et al., 2002). Following a similar synthetic procedure, the same authors have subsequently developed a strategy to isolate in gram quantities [Ln(TPP)L] complexes capped with multi-dentate ligands L such as hydridotris(1-pyrazolyl)borate (Tp$^H$) and CoP (Foley et al., 2003). In methylene chloride, the absorption spectra of the two series of complexes [Ln(TPP)Tp$^H$] and [Ln(TPP)CoP] display the characteristic Soret and $Q$ bands around 425 nm and in the range 550–600 nm, respectively, these bands being slightly red-shifted in going from Tp$^H$
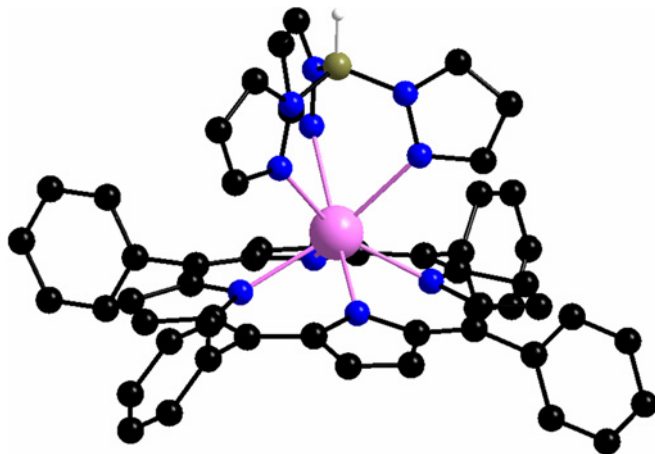
Fig. 14. Molecular structure of seven-coordinate [Yb(TPP)Tp$^H$], redrawn from (Foley et al., 2003).

to CoP. Excitation on the Soret band yields weak emission bands around 650 and 715 nm, assigned to free base H$_2$TPP since all the samples contain this impurity.

In addition, in the case of Nd$^{III}$, Er$^{III}$, and Yb$^{III}$, characteristic Ln$^{III}$ emission is detected. Absolute quantum yields of CH$_2$Cl$_2$ solutions have been determined with respect to both H$_2$TPP (H$_2$**5a**, $Q = 11\%$) and [Zn(TPP)] ($Q = 3.15\%$ in ethanol) and amount to: 0.24, 0.09, and 3.2%, respectively, for the complexes with Tp$^H$ as capping ligand, and 0.2, 0.1, and 2.4%, respectively, for those with CoP. They are small, but generally higher than the yields obtained for other complexes. This arises from the coordination environment (fig. 14) provided by both TPP$^{2-}$ and the capping anion which effectively shields the Ln$^{III}$ ion from interacting with solvent vibrations, particularly C–H vibrations in this case. This explanation is consistent with the quantum yield of [Yb(TPP)Tp$^H$] increasing only from 3.2 to 3.4% in going from CH$_2$Cl$_2$ to CDCl$_3$. The emission quantum yields follow the trend Yb$^{III}$ > Nd$^{III}$ > Er$^{III}$, in line with the energy gap law, and the nature of the capping ion does not affect much the quantum yields. Transient absorption spectra of [Nd(TPP)Tp$^H$] further revealed that excited state absorption in the spectral range 450–500 nm (between the $B$ and $Q$ bands) is stronger than in the case of the Yb$^{III}$ complexes, pointing to an equilibrium population of the TPP$^{2-}$ triplet state produced via thermally activated energy back transfer from the Nd($^4$F$_{3/2}$) state which lies only at about 2000 cm$^{-1}$ below $^3$T$_1$(TPP$^{2-}$). It is noteworthy that in an earlier investigation, no Er-centered luminescence was observed for [Er(TPP)(OH)], [Er(TPP)dpm] (dpm is dipivaloylmethanate), and [Er(OEP)(OH)] solutions in methanol or methanol/ethanol mixtures. On the other hand, these compounds exhibit dual fluorescence from the $^1$S$_1$ and $^1$S$_2$ states while $^3$T$_1$ emission can be detected at low (77 K) temperature (Kaizu et al., 1986).

The beneficial influence of the capping ligand and of aromatic *meso* substituents on the sensitization of Yb$^{III}$ luminescence has been further demonstrated by a systematic study (Rusakova et al., 2004a). In a first step, *n*-alkyl substituted porphyrins have been compared to aromatic- and heteroaromatic-substituted porphyrins. Subsequently, the authors test how

H$_2$**5a**   R$_{1,2,3,4}$ =  (phenyl)          H$_2$**6f**   R$_{1,2,3,4}$ = $n$-C$_4$H$_9$

H$_2$**6a**   R$_{1,2,3,4}$ =  (pyridin-2-yl)     H$_2$**6g**   R$_{1,2,3,4}$ = $n$-C$_9$H$_{19}$

H$_2$**6b**   R$_{1,2,3,4}$ =  (pyridin-3-yl)     H$_2$**6h**   R$_1$ =  (pyridin-4-yl) , R$_{2,3,4}$ = $n$-C$_9$H$_{19}$

H$_2$**6c**   R$_{1,2,3,4}$ =  (pyridin-4-yl)     H$_2$**6i**   R$_{1,3}$ =  (pyridin-4-yl) , R$_{2,4}$ = $n$-C$_9$H$_{19}$

H$_2$**6d**   R$_{1,2,3,4}$ = C$_2$H$_5$          H$_2$**6j**   R$_{1,2}$ =  (pyridin-4-yl) , R$_{3,4}$ = $n$-C$_9$H$_{19}$

H$_2$**6e**   R$_{1,2,3,4}$ = $n$-C$_3$H$_7$      H$_2$**6k**   R$_{1,2,3}$ =  (pyridin-4-yl) , R$_4$ = $n$-C$_9$H$_{19}$
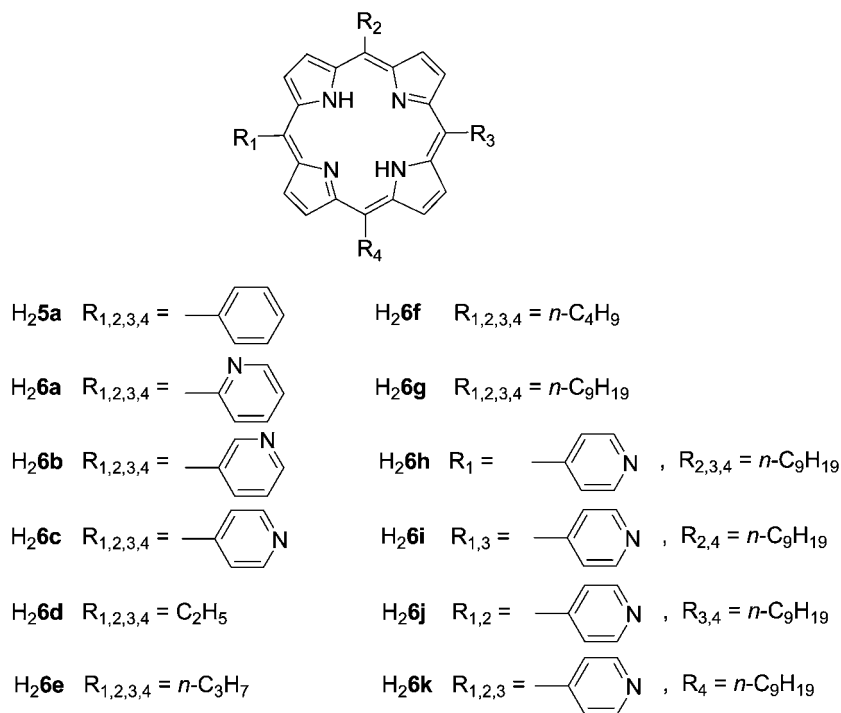
Fig. 15. Porphyrins used in a comparative study to assess the influence of the *meso* substituent and of the capping ligand on Yb[III] luminescence (Rusakova et al., 2004a).

the nature of the capping ligand, chloride, bromide, acetylacetonate (acac), thenoyltrifluoro-acetylacetonate (tta), and benzoylacetonate (ba) affects the quantum yield of the metal-centered luminescence.

Ytterbium complexes with the porphyrins described in fig. 15 were synthesized by re-acting an excess of ytterbium acetylacetonate with the corresponding porphyrin in 1,2,4-tri-chlorobenzene, followed by chromatographic purification on an alumina column. Excitation in the Soret band around 430 nm of methanolic solutions $10^{-5}$–$10^{-4}$ M of the ytterbium porphyrinates, which have high extinction coefficients (log $\varepsilon$ lies in the range 4.2–5.2), re-sults in a very large decrease in the luminescence of the porphyrin fragments (600–640, and 700–720 nm) and in the observation of the Yb($^2$F$_{5/2}$) emission. Excitation spectra of the 4f emission coincide with the absorption spectra of the complexes, confirming the energy trans-fer from the porphyrinates moieties to the metal ion, most probably via the triplet states of the porphyrins, which lie in the range 12 890–12 935 cm$^{-1}$. Results of the analysis of the 12 ytterbium porphyrinates are outlined in fig. 16.

Both the absolute quantum yield (determined with respect to zinc tetraphenylporphyrin in ethanol) and the product of the molar absorption coefficient at the excitation wavelength with the quantum yield, $\varepsilon \cdot Q$, which represents the overall luminescence efficiency follow the
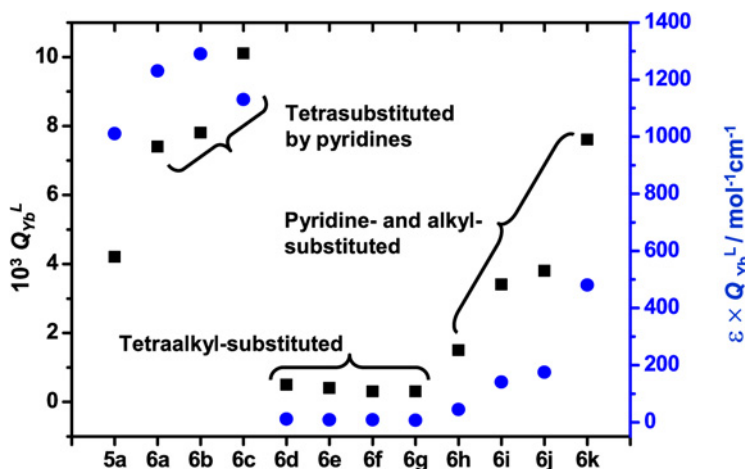
Fig. 16.   Quantum yield ($\blacksquare$, left scale) and overall luminescence efficacy $\varepsilon \cdot Q$ ($\bullet$, right scale) of methanolic solutions of Yb$^{III}$ porphyrinates with ligands depicted in fig. 15 (Rusakova et al., 2004a).

same trend. The latter is also reflected in the $^2F_{5/2}$ lifetimes which vary from about 1 µs for the alkyl-substituted porphyrinates to 12 µs for the complex with **6c**.

Porphyrinates devoid of aromatic *meso* substituents **6d–6g** have clearly very low luminescence, irrespective of the chain length which was increased from $C_2$ in **6d** to $C_9$ in **6g**. The metal-centered photophysical properties improve gradually upon successive replacement of the alkyl chains with a pyridine moiety (**6h–6k**), but the position of the substituents (e.g. $R_{1,3}$ in **6i** vs $R_{1,2}$ in **6j**) has little influence. The effects generated by the aromatic substituents increase almost linearly with the number of substitutions, the quantum yield increasing from 0.03 (**6g**) to 0.15 (**6h**), 0.36 (average of **6i**, **6j**) and 0.76% (**6k**) while the last substitution (**6c**) brings it only up to 1.0%. Among the porphyrinates tetrasubstituted by aromatic rings, the one bearing a simple phenyl group is the less effective in sensitizing the Yb$^{III}$ luminescence. Replacement of the latter with a pyridine unit increases the quantum yield by a factor 2–2.5 depending on the position of the N atom in the ring and indicating that electronic effects are important in determining the efficiency of the ligand-to-metal energy transfer process.

Finally, photophysical properties can also be finely tuned by the nature of the capping anionic ligand. The study conducted on the four aromatic substituted porphyrinates **5a**, **6a–6c** yielded consistent results, the quantum yield of the metal-centered luminescence following the sequence acac > ba > Cl > tta > Br (see fig. 18 for the structure of the capping ligands) for all of the complexes. The surprising position of tta, which usually forms highly luminescent complexes with Ln$^{III}$ ions, is explained by the authors as resulting from the strong Yb–O bonds generated by tta which weaken the Ln–N(porphyrinates) bonds and henceforth diminish the energy transfer efficiency. One notes, however, that the ratio $Q(\text{acac})/Q(\text{Br})$ lies in the range 1.7–2.1, indicating a relatively small effect generated by differences in the anionic capping ligand. Excitation of the porphyrinates in the $Q$-band of porphyrin, which appears as
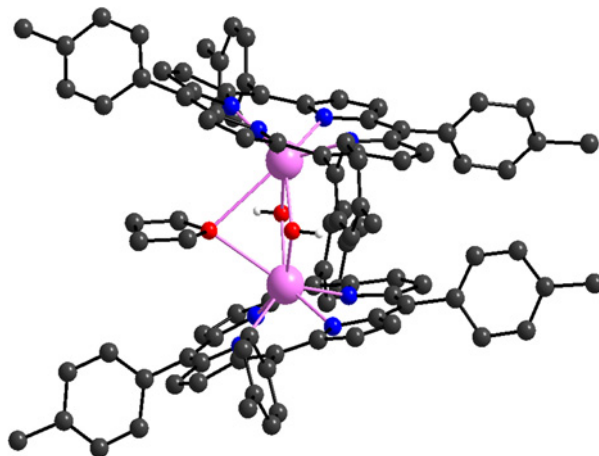
Fig. 17. Molecular structure of the dimer {[Yb(**5c**)($\mu$-OH)]$_2$($\mu$-thf)}·6H$_2$O, redrawn from (H. He et al., 2004c).

a structured four-component absorption band between 510 and 650 nm, is also feasible, but the molar absorption coefficient is one to two orders of magnitude smaller than the one of the Soret band, so that the overall luminescence efficiency is quite small (Rusakova et al., 2004a).

Further studies on the influence of the nature of the *meso* substituent in TPP$^{2-}$ complexes have been published recently. For instance, [Ln(L)(H$_2$O)$_3$]$^+$ complexes with L = **5a**, **5c**, **5d**, and **7a–7c** (fig. 18) exhibit both porphyrinate (650 nm) and Ln$^{III}$ NIR emission (Ln = Er, Yb) in CHCl$_3$ despite the coordination of three water molecules (H.S. He et al., 2004a). In the case of Yb$^{III}$, methyl and methoxy substituents enhance the metal-centered emission, but halogen substituents are detrimental to this luminescence. It is worth mentioning that halogen-substituted porphyrinates are more sensitive to hydrolysis than the others, forming hydroxyl-bridged or halogen-bridged dimers. Photophysical measurements have been performed on dilute solutions ($2 \times 10^{-5}$ M) so that this may well have affected intensity measurements since heavy atom substitutions usually favor intersystem crossing, and therefore are beneficial to the ligand-to-Ln$^{III}$ energy transfer. The intensity of the Yb$^{III}$ emission increases substantially when the three water molecules are replaced with one chloride ion and two dmf molecules (H. He et al., 2004c). Er$^{III}$ emission was extremely weak so that no such effect was observed but, on the other hand, substitution of the coordinated water molecules by thf or dmf resulted in an increase in the luminescence intensity (H. He et al., 2004b, 2004c). Dimerization of the monoporphyrinates [Yb(TPP)(H$_2$O)$_3$]Cl complexes with **5a**, **5c**, and **5d** (fig. 18) occurred when the authors attempted to replace the three water molecules with Tp$^{Me}$ in order to improve the photophysical properties. The dimer {[Yb(**5c**)($\mu$-OH)]$_2$($\mu$-thf)} was obtained (fig. 17), as well as four other ones, [Yb(**5a**)($\mu$-OH)($\mu$-OH$_2$)]$_2$, [Yb(**5d**)($\mu$-Cl)(H$_2$O)]$_2$, [Yb(**5d**)($\mu$-OH)]$_2$, and {[Yb(**5c**)]$_2$($\mu$-OH)($\mu$-Quin)} (Quin = 2-methyl-8-hydroxyquinolinate), depending on the reaction conditions, particularly on the solvent and on the nature of added donor molecules. The intensity of the Yb$^{III}$ emission of [Yb(**5a**)($\mu$-OH)($\mu$-OH$_2$)]$_2$ is comparable to
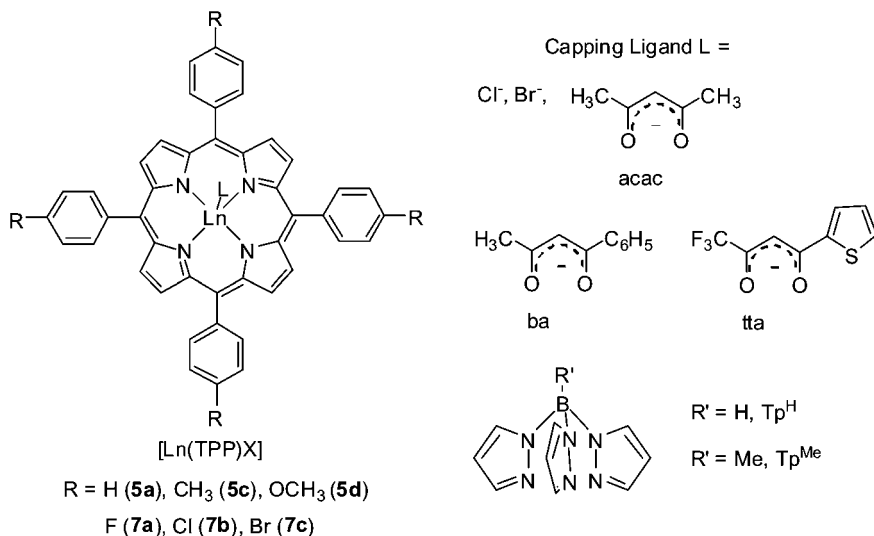
Fig. 18. Lanthanide porphyrinates with substituted TPP$^{2-}$ and anionic capping ligand.

the one of the monoporphyrinate [Yb(**5a**)Cl(dmf)$_2$], while a substantial increase is observed for [Yb(**5d**)($\mu$-Cl)(H$_2$O)]$_2$ and {[Yb(**5c**)]$_2$($\mu$-OH)($\mu$-Quin)} (H. He et al., 2004c). Subsequently, the same authors succeeded in replacing the water molecules with capping anionic ligands such as Tp$^H$ or CoP (fig. 18). With the former capping ligand, the relative intrinsic quantum yields $Q_{Nd}^{Nd}$, determined in toluene from the observed lifetimes, upon excitation in the porphyrinate Q-band at 514 nm, and assuming that the radiative lifetime is the same for all compounds, amount to 1, 0.98, 0.79, 0.31, and 0.98 for porphyrinates **5a** (reference complex), **5c**, **5d**, **7a**, and **7b**, respectively (H. He et al., 2004b).

The substituent effect on $Q_{Nd}^{Nd}$ differs from the one on the total luminescence intensity which follows the same pattern as established for [Yb(TPP)(H$_2$O)$_3$]$^+$ in chloroform (H. Hu et al., 2004b, 2004c). The "absolute" intrinsic yield $Q_{Nd}^{Nd}$ calculated with an estimated $\tau_{rad} = 0.25$ ms amounts to 0.33% for **5a**. Comparing this figure with the value of 0.24% for $Q_L^{Ln}$ in CH$_2$Cl$_2$ (Foley et al., 2003) points to a fairly efficient sensitization of the NIR luminescence by TPP (estimated $\eta_{sens} \approx 0.7$). The solvent influence on the intensity of the Nd$^{III}$ emission follows the trend benzene > dichloromethane > thf > chloroform > acetone > acetonitrile > dmf > methanol, that is, stronger donors probably displace the capping anion and quench the NIR luminescence via their high energy vibrations (O–H in case of methanol). For Yb$^{III}$ complexes, both electron-donating groups (**5c**, **5d**) and halogen substituents (**7a**–**7c**) were found to be detrimental to the metal-centered luminescence, with respect to **5a** while the solvent dependence of the (much weaker) luminescence of the Er$^{III}$ porphyrinates is the same as for the Nd$^{III}$ compounds (H.S. He et al., 2004a).

A similar study has been performed on [Nd(TPP)CoP] complexes with **5a**, **5c**, **5d**, and **7a**–**7c** in toluene with the same conclusions as to the effects of the *meso* substituent and
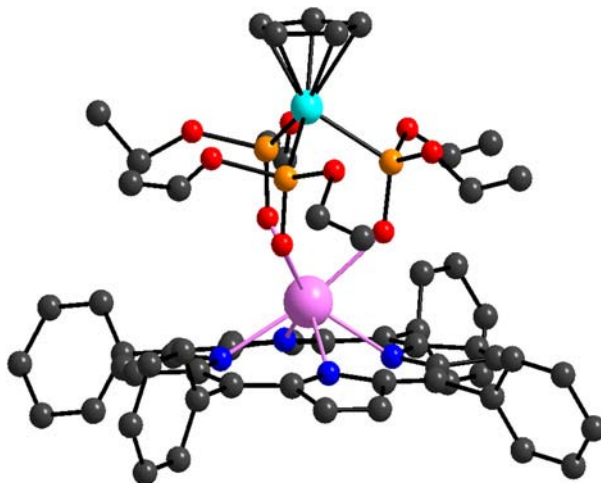
Fig. 19. Molecular structure of seven-coordinate [Er(TPP)CoP$^{Me}$], redrawn from (Wong et al., 2001).

solvent (H. He et al., 2004a). Metal-centered emission has also been reported for [Er(**5a**)CoP] (fig. 19), and [Yb(**5d**)CoP], the latter having $\tau_{obs} = 16$ μs (Wong et al., 2001), as compared to 20 μs for [Yb(**5d**)Tp$^H$] (H.S. He et al., 2004a).

### 3.1.2. *Other lanthanide porphyrinates*

*N*-confused porphyrins are isomers of porphyrins which contain an inverted pyrrole ring linked to the porphyrinic conjugate system through a $\beta$-carbon (fig. 20). Treatment of H$_2$**8** with Ln[N(SiMe$_3$)$_2$]$_3$·[LiCl(thf)$_3$]$_x$ in refluxing toluene, followed by the addition of Na(CoP$^{Me}$) at room temperature results in the crystallization of green complexes with formula [Ln(**8**)CoP$^{Me}$] (Ln = Er, Yb) in 75% yield. According to its X-ray structure, the Yb$^{III}$ compound is eight-coordinate, being bound to the three O-atoms of the capping ligand, to the three N-atoms from the confused porphyrin, as well as to the inner C–H edge of **8** through an agostic $\eta^2$ bond. It displays a weak NIR luminescence upon excitation at 600 nm, the intensity of which is one order of magnitude smaller when compared with [Yb(**5a**)CoP]. This provides further evidence for the formation of the agostic bond, the strong quenching of the luminescence being attributed to the presence of a C–H oscillator in the inner coordination sphere (Zhu et al., 2005).

In order to simplify the synthesis of lanthanide porphyrinates fitted with a capping anionic ligand, W.K. Wong and collaborators have proposed to graft a potentially anionic pendant group on the porphyrin framework which could act as an axial ligand, much as has been done in mimicking cytochrome 450 (H. He et al., 2003). In view of its good coordination properties towards lanthanide ions and, also, its efficient sensitization of the metal-centered luminescence, a $\beta$-diketonate moiety was chosen, more precisely a diethyl malonate group. The latter was linked in *ortho* position of one of the phenyl *meso* substituent through a C$_5$O
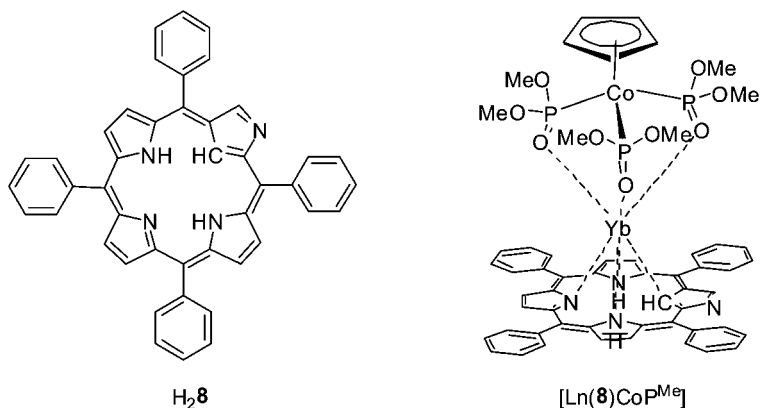
Fig. 20.  *N*-confused tetraphenyl-porphyrin and its Yb[III] complex with a CoP capping anionic ligand.
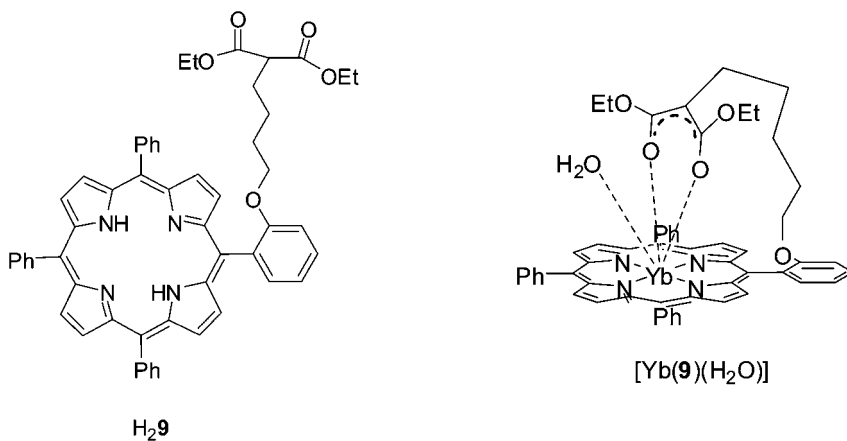


Fig. 21.  Diethyl malonate-appended porphyrin and its Yb[III] complex.

alkyl chain. Air stable porphyrinates [Ln(**9**)(H$_2$O)] (Ln = Nd, Er, Yb) (fig. 21) were isolated and their stability has been ascribed to coordination of the malonate bidentate unit.

The three complexes display NIR luminescence in addition to porphyrinate emission at 650 nm, although Er[III] luminescence is again faint. In addition, the Nd[III] porphyrinate proved to be photosensitive and decomposed under irradiation by the N$_2$-laser (337 nm), so that its photophysical characteristic could not be determined. The lifetime of the Yb($^2$F$_{5/2}$) level amounts to 2.43 µs, that is about ten times smaller than for [Yb(**5d**)Tp$^H$]. Replacement of the water molecule with dmf when the porphyrinate is dissolved in this solvent results in an increase in the intensity of the metal-centered luminescence.
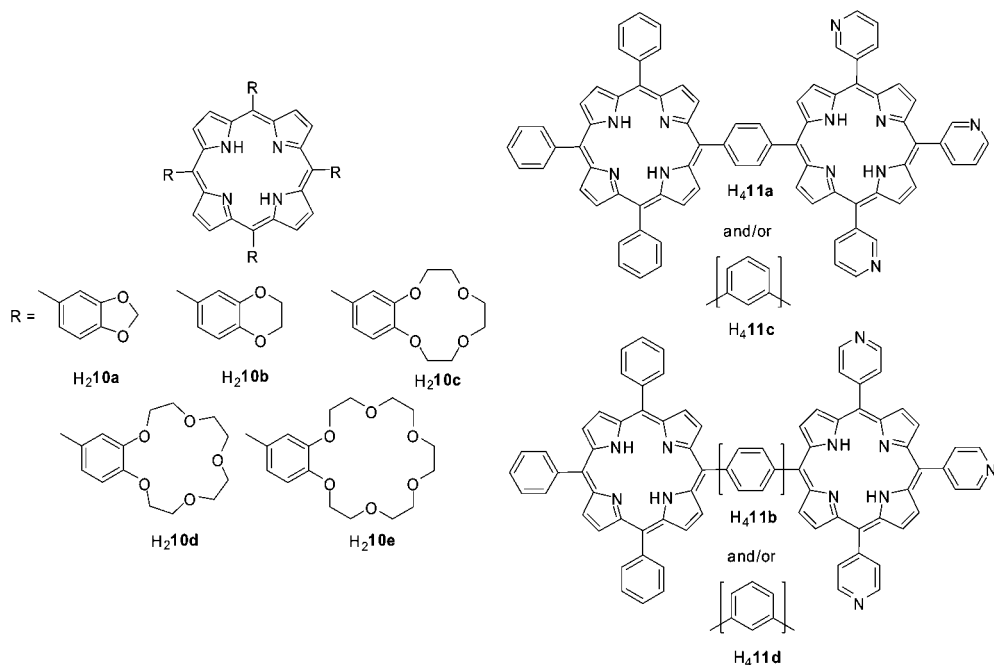
Fig. 22. Crown-ether derivatized porphyrins (left) and bis(porphyrins) (right).

The four *meso* positions of porphyrin have been substituted with several O-containing cycles, including benzodioxolan, benzodioxane, benzo-12-crown-4, benzo-15-crown-5, and benzo-18-crown-6 ethers (fig. 22) in an attempt to determine the influence of coordinated alkali ions on the Yb$^{III}$ photophysical properties (Korovin et al., 2001). The triplet state in the [Yb(**10**)(acac)] complexes lies in the range $13\,775$–$13\,955$ cm$^{-1}$ and upon excitation at 532 nm, the $^5F_{5/2} \rightarrow {}^2F_{7/2}$ transition is seen for all five complexes.

The quantum yields of the metal-centered luminescence $Q_{Yb}^{L}$ (determined in dmf at room temperature with respect to [Zn(**5a**)]) increase from 0.13% for **10a** and **10b**, to 0.19% (**10c**), and 0.27% (**10d**), while it is slightly smaller (0.25%) for **10e**; in parallel, $\tau_{obs}$ ($^2F_{5/2}$) ranges from 3.4 to 5.9 μs. Similarly, the ligand-centered luminescence decreases by 8–13%, confirming the ligand-to-metal energy transfer. Complexation of alkali-metal ions, Na$^I$ with **10c**, K$^I$ with **10d**, and Cs$^I$ with **10e** results in changes in the absorption spectra of the Yb$^{III}$ porphyrinates. They are assigned to the formation of sandwich-type dimers in which two porphyrinates encapsulate eight alkali cations: IR spectra clearly point to the coordination of the alkali cations. A concomitant increase in $Q_{Yb}^{L}$ results: from 0.19 to 0.28% for **10c**, from 0.27 to 0.98% for **10d**, and from 0.25 to 0.70% for **10e**. The four-fold increase for K$^I$ reflects the better stability of the K(benzo-15-crown-5)$_2$ complex with respect to the other alkali complexes.

The same group has also prepared bis(porphyrins) with the purpose of modeling electron-transfer processes (Korovin et al., 2002f). The four asymmetric bis(porphyrins) described in the right part of fig. 22 have been synthesized; one of the porphyrinic ring bears pyridine *meso* substituents since this moiety is favorable to the sensitization of Yb$^{III}$ luminescence as depicted in fig. 16. The Soret band of the bis(porphyrins) is split by 7–11 nm, which suggests a positioning of the two porphyrin rings intermediate between parallel and perpendicular conformations. The bimetallic Yb$^{III}$ bis(porphyrinates) were obtained from Yb(acac)$_3$ and the free bases in 1,2,4-trichlorobenzene, under argon atmosphere. The quantum yields $Q_{Yb}^L$ (measured in dmf) of the compounds with **11a** (0.41%) and **11b** (0.54%) are larger than with **11c** (0.27%) and **11d** (0.35%). That is, 1,3-pyridyl *meso* substituents induce a more efficient sensitization than 1,4-pyridyl moieties, as does the *para* linkage of the two porphyrin units on the central benzene anchor. The quantum yields are comparable to the one determined for **5a**, but smaller than those for the porphyrinates with **6b** and **6c**. Model calculations explain the better luminescence of monoporphyrinates as opposed to bis(porphyrinates) by the absence of Yb$\cdots$Yb interaction in the former. In the dimer, calculations yield Yb$\cdots$Yb distances of 12.0 Å for complexes with **11a** and **11c**, and 10.8 Å for the compounds with **11b** and **11d**.

In summary, despite the adequate match between the energies of the porphyrinate triplet state and the Yb($^2F_{5/2}$) level, the reported quantum yields to date for complexes in organic solvent are usually much smaller than 1%, with three exceptions, [Yb(**6c**)(acac)] (1.01% in methanol), [Yb(**5a**)Tp$^H$] (3.2% in CH$_2$Cl$_2$), and [Yb(**5a**)CoP] (2.4% in CH$_2$Cl$_2$), and protic solvents dramatically decrease these figures. Nevertheless, some applications of NIR-emitting lanthanidoporphyrinates have been proposed (see section 4), including the imaging of cancerous cells described above (Gaiduck et al., 1990), so that interest for these complexes remains high.

### 3.1.3. *Derivatized coronands and cryptands*

A coronand is a cyclic molecule containing several donor atoms in its ring. An archetypal example is the class of cyclic ethers termed crown ethers which contain the repeating –CH$_2$–CH$_2$–O– motif and were proposed by C.J. Perdersen in 1967. Other examples include *N*-containing aza crown ethers and cyclic Schiff base derivatives. The interaction of simple, neutral coronands with Ln$^{III}$ ions in water is often weak, and the resulting coronates are amenable to axial interaction with solvent molecules so that they have often been derivatized in order to increase their coordination properties as well as their functionalities. Another strategy to overcome this problem is to include two amine bridgeheads in the cycle and graft an addition polydentate chain to yield cryptands (Sastri et al., 2003). In this section, we deal with the latter two classes of ligands, including cyclic Schiff bases. Cyclen derivatives and substituted calixarenes are discussed separately, in view of their special importance in lanthanide coordination chemistry.

With respect to heavier lanthanide ions such as Yb$^{III}$, 15-crown-5 has the most adequate cavity size (Bünzli and Pilloud, 1989) and Korovin has fitted this crown ether with an anilinoacridine chromophore which displays cytostatic and/or antiviral activity. If anilinoacridines alone, bearing a hydroxyl or a carboxylic acid substituent in *ortho*, *meta*, or *para* position (fig. 23), are reacted with ytterbium trinitrate, they yield 1:1 complexes with the *ortho*- and
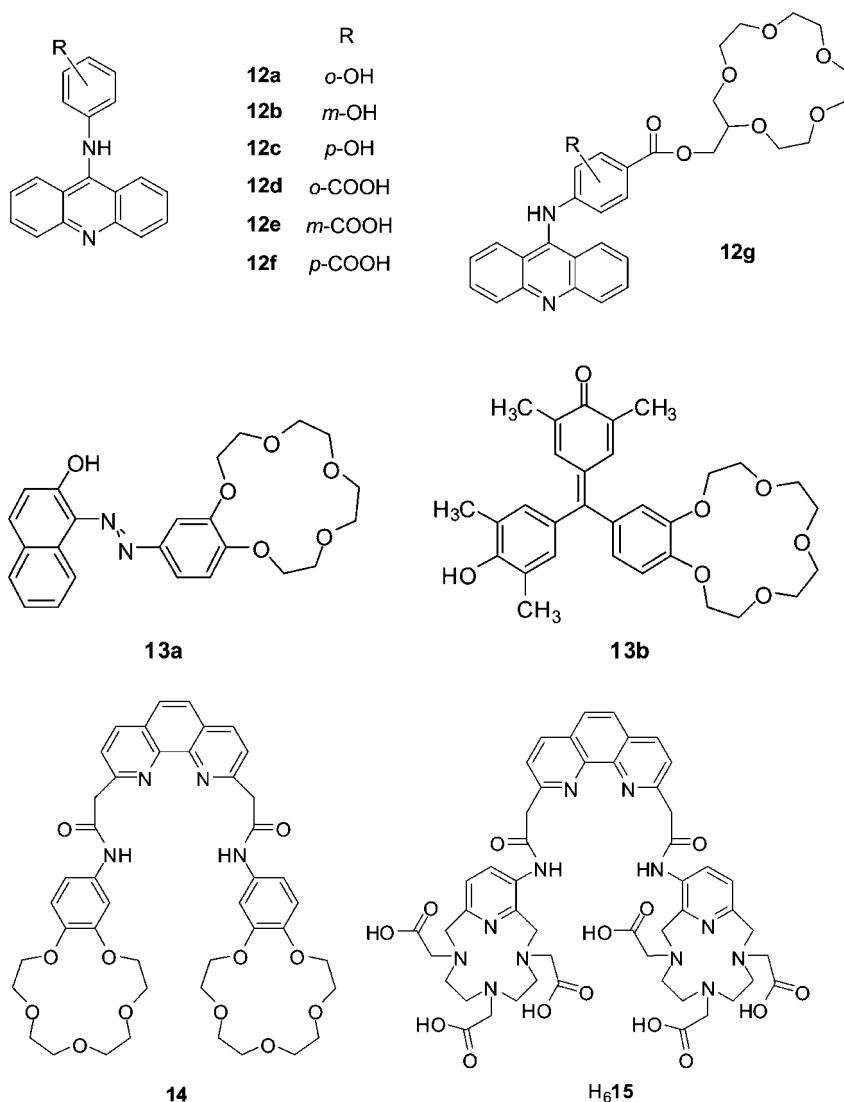
Fig. 23. Derivatized 15-crown-5 and benzo-15-crown-5 ethers, as well as a bis(azacyclic) ligand used to sensitize
Nd[III] and Yb[III] luminescence (Korovin and Rusakova, 2004; Korovin et al., 2002c, 2002d, 2002e; Rusakova et al.,
2004b).

*meta*-substituted ligands whereas the two *para*-substituted ligands **12c** and **12f** lead to the
formation of 1:2 (metal:ligand) complexes. Upon complexation, the broad fluorescence band
of the chromophore appearing in the range 460–540 nm is quenched to an extent of 85–90%,
pointing to energy transfer onto the metal ion. The quantum yields of the metal-centered lu-

minescence in water–ethanol mixtures is the highest for the 1:2 complex while remaining extremely low: 0.0026 and 0.0034% for **12c** and **12f**, respectively (Korovin et al., 2002a). This is understandable because several water molecules still interact in the inner coordination sphere. The latter interaction is somewhat reduced in 1:1 nitrato complexes with macrocyclic ligand **12g** and the quantum yield increases substantially to reach 0.022% (Korovin et al., 2002e). This still low quantum yield arises from the insufficient protection of the $Yb^{III}$ ion by the crown ether: since nitrate ions are displaced by water molecules, axial interaction with the solvent can still occur. Moreover, the energy of the triplet state of the acridine chromophore is around 21 000 cm$^{-1}$ which is too high for an efficient sensitization.

Benzo-15-crown-5 ether has been derivatized with several light-harvesting chromophores with the aim of sensitizing NIR luminescence from $Nd^{III}$ and $Yb^{III}$ in protic solvents. For instance, dyes 1-phenylazo-2-naphthol (cf. **13a**, fig. 23) and xylenol blue (**13b**) with triplet states lying at approximately 16 270 and 15 850 cm$^{-1}$, respectively, have been fused to the polyether macrocycle. The resulting ligands form 1:1 complexes with lanthanide trinitrates, as expected (Bünzli, 1987), and they display a reasonably intense luminescence. The quantum yields determined upon excitation at 532 nm with respect to [Zn(**5a**)] amount to 0.66 and 0.88% for the $Yb^{III}$ complexes with **13a** and **13b**, respectively, and to 0.09 and 0.12% for the corresponding complexes with $Nd^{III}$. According to an initial report (Korovin et al., 2002c), measurements have been carried out in methanol, but in a subsequent paper, the authors report the same figures for solutions in deuterated water (Korovin and Rusakova, 2004). Anyway, whichever the solvent was, the quantum yields for the macrocyclic $Yb^{III}$ complexes are 5–8 times larger than those reported for the complexes with the chromophoric units alone.

Another sensitizing substituent used in conjunction with benzo-15-crown-5 units is 1,10-phenanthroline, which has been linked through its 2 and 9 positions to two macrocycles to yield **14**. The latter forms bimetallic 2:1 complexes with lanthanide nitrates; the quantum yields measured under the same experimental conditions as above, except for the solvent, acetone, are however smaller, 0.39% ($Yb^{III}$) and 0.067% ($Nd^{III}$), due the higher energy of the phenanthroline triplet state (Korovin et al., 2002d). On the other hand, bimetallic complexes with H$_6$**15** are much more stable (log $K \approx 17$) and they provide a tighter environment for the first coordination sphere of the metal ion: [Ln$_2$(**15**)] complexes display the highest quantum yields reported so far for $Nd^{III}$ and $Yb^{III}$ compounds in water: 0.085 and 0.53%, respectively. Lifetime data measured both in water (0.72 μs for $Nd^{III}$ and 4.55 μs for $Yb^{III}$) and deuterated water (1.34 μs for $Nd^{III}$ and 8.86 μs for $Yb^{III}$) point to a relatively weak effect of water molecules on the radiationless de-excitation process: using Beeby's phenomenological equation (9a) for $Yb^{III}$ (Beeby et al., 1999), one gets $q \approx 0.1$ (without applying the second-sphere correction). Data reported for complexes with the ligands depicted on fig. 23 clearly show the importance of optimizing the ligand-to-metal energy transfer process while simultaneously minimizing nonradiative deactivation of the metal-centered excited states.

Lanthanide chemistry with Schiff bases is quite extensive and numerous acyclic, cyclic, monometallic and polymetallic (4f–4f′, 4f–5f, 4f–nd) complexes have been synthesized and studied, in particular with compartmental ligands, owing to the ability of the latter to bind two or more metal ions in close proximity. Asymmetrization of these ligands also provides important diversification of the coordinating sites (Vigato and Tamburini, 2004). On the other
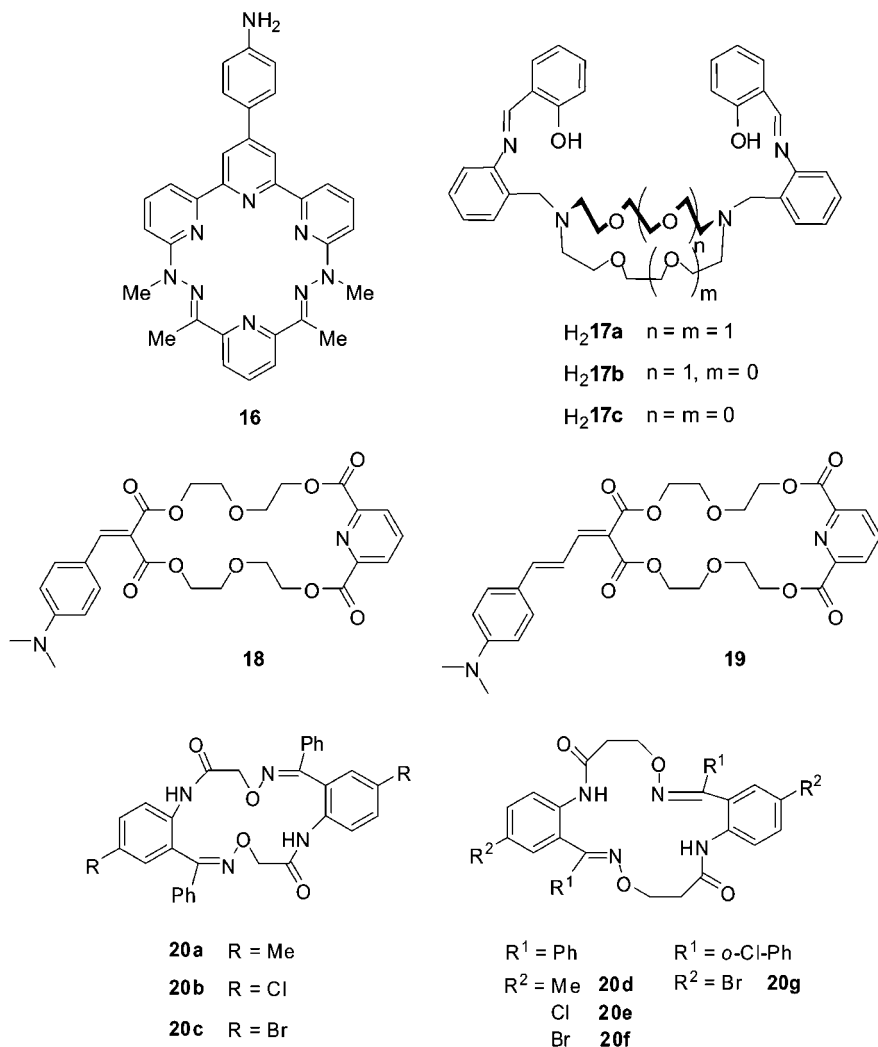
Fig. 24. Coronands and cyclic Schiff bases.

hand, there are only a few examples of sensitization of lanthanide NIR luminescence by such ligands. Interestingly, the complexes with ligand **16** (fig. 24) can be prepared in methanol by template-directed condensation of the terpyridine subunit with 2,6-diacetylpyridine in presence of LnCl$_3$ (Hall et al., 1998). The triplet state of this ligand has too low an energy (0-phonon transition at 18 400 cm$^{-1}$ in EtOH/MeOH glass at 77 K) to sensitize Eu$^{III}$ and Tb$^{III}$ luminescence, but luminescence from [Yb(H**16**)]$^{4+}$ is detected in water, methanol and in their deuterated analogs. From the lifetimes determined at pH (resp. pD) ≈ 5–5.5, 0.32 and 9.1 µs,
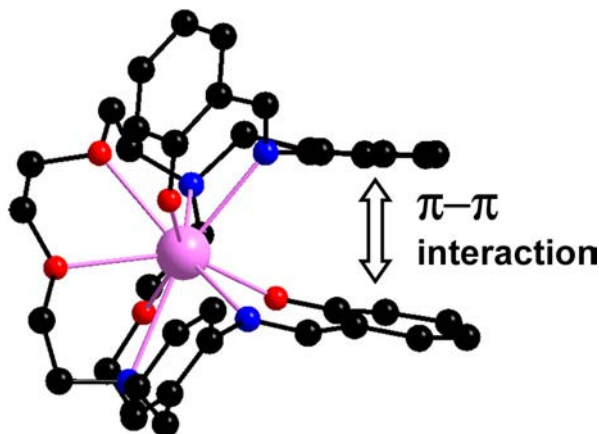
Fig. 25. Molecular structure of [Ce(**17b**)]$^+$, redrawn from (Gonzales-Lorenzo et al., 2003).

the hydration number $q$ could be estimated to $2.8 \pm 0.2$. In presence of 0.1 M NaCl, the hydration number becomes smaller, $2.2 \pm 0.2$ (Beeby et al. 1999) consistent with the X-ray structure of the Eu$^{III}$ complex which reveals two water molecules and one chloride ion bound in the inner coordination sphere. Upon increasing the pH (resp. pD), the Yb($^2F_{5/2}$) lifetime becomes longer and $q$ decreases to eventually reach zero, which is tentatively explained by the successive formation of $\mu$-hydroxo and $\mu$-oxo dimers.

The three Schiff-base bibracchial lariat ethers H$_2$**17a–c** derivatives have been designed for their ability to form a cryptand-like cavity upon reaction with Ln$^{III}$ ions, the size of which can be tuned by varying the number of –CH$_2$–CH$_2$–O– units in the macrocycle. The two 2-salicylaldiminobenzyl pendant arms fold in such a way that $\pi$–$\pi$ interactions between aromatic rings result in the formation of a cryptand-like cavity, as demonstrated by the X-ray structure of the Ce$^{III}$ complex with **17b** depicted on fig. 25 (Gonzales-Lorenzo et al., 2003). The triplet state of the di-anionic receptor is located at 18 750 cm$^{-1}$ (0-phonon component measured on the Gd$^{III}$ complex) so that sensitization of the NIR luminescence is not optimum; nevertheless, Nd$^{III}$ emission could be detected.

The smaller receptor H$_2$**17c** is better suited for the complexation of heavier lanthanide ions. The [Ln(**17c**)]$^+$ complexes with Ln = Ho, Er are isostructural, as shown by X-ray structure determination and have essentially the same molecular arrangement as [Ce(**17b**)]$^+$, except for a smaller coordination number, 8, due to the reduced sized of the macrocycle (Gonzales-Lorenzo et al., 2005). Both Er$^{III}$ and Yb$^{III}$ complexes are emissive in the NIR range in acetonitrile and methanolic solutions. Determination of the lifetime of the Yb($^2F_{5/2}$) level in methanol (2.92 μs) and deuterated methanol (4.65 μs) leads to $q_{CH_3OH} \approx 0.2$ using eq. (9b) so that the induced cavity formed upon reaction of H$_2$**17c** with the smaller lanthanide ions is as protective as the one formed by H$_2$**17b** with the larger Ln$^{III}$ ions. Lifetimes for Er$^{III}$ are shorter, 0.42 μs in methanol for instance. The series of ligands H$_2$**17a–c** provides an original way of forming stable complexes in organic solvents, especially that the induced cavity can

be somewhat tuned to the size of the lanthanide ion. With respect to sensitization of Ln[III] NIR luminescence however, the triplet states of these molecules, around 19 000 cm$^{-1}$, have too high energies to produce efficient ligand-to-metal energy transfers.

The two macrocyclic ligands **18** and **19** (fig. 24) were prepared with the hope of challenging the properties of Er[III] *tris*(8-hydroxyquinolinate) [Er(8-Q)$_3$] which, at the time, was considered for producing organic electroluminescent diodes emitting in the 1.5 μm range. The idea was to extend the absorption edge of [Er(8-Q)$_3$] located at around 460 nm. Indeed, ligand **19** displays an absorption band at 550 nm. Unfortunately, the corresponding Er[III] complex is four times less luminescent than the complex with ligand **18** the absorption edge of which is similar to the one of 8-hydroxyquinolinate. In absence of quantitative photophysical data (quantum yields, lifetimes), a convincing explanation could not be given (Meinardi et al., 2003).

Ligands **20a–c** form stable 1:1 complexes with lanthanide nitrates in dmf, with log $K$ in the range 4.4–4.9. Determination of the hydration number $q$ by lifetime measurements points to values close to two, so that it was inferred that the macrocyclic ligand is not completely bound to the metal ions. Nevertheless, the Yb[III] compounds display NIR luminescence upon ligand excitation, despite a triplet state located at high energy (21 250–21 800 cm$^{-1}$): quantum yields amount to 0.007, 0.041, and 0.003% for complexes with **20a**, **20b**, and **20c**, respectively, while the corresponding lifetimes are 0.2, 1.1, and 0.4 μs. The heavy atom effect may be responsible for the larger values of the latter two quantum yields, although one would have expected the values for the chloro- and bromo-substituted ligands being inverted (Pavlovsky et al., 2004). Replacement of nitrate with chloride leads to smaller values of quantum yield and lifetime for **20a** (0.005%, 0.1 μs) and **20b** (0.030%, 0.8 μs) while the quantum yield of **20c** becomes larger, (0.006%) despite a small shortening in the lifetime to 0.3 μs (Rusakova et al., 2005). Expansion of the 16-membered cycle to 18 atoms results in a large improvement in quantum yields by factors 7, 6, and 21 for the nitrato complexes with **20d**, **20e**, and **20f**, respectively. It is noteworthy that the quantum yield of the nitrato complex [Yb(NO$_3$)$_3$(**20e**)] reaches 0.23% (lifetime = 2.4 μs). A similar effect is observed for the chloro complexes with **20d** and **20f** the quantum yields of which increase by factors seven and eight, while [YbCl$_3$(**20e**)] displays a two-fold reduction in quantum yield compared with [YbCl$_3$(**20b**)]. Finally, *ortho* substitution of the phenyl groups of **20f** by chlorine also increases the quantum yields of both chloro (0.09%, lifetime = 1.3 μs) and nitrato (0.19%, lifetime = 1.9 μs) complexes two to threefold with respect to the unsubstituted compounds; unfortunately, such a substitution has not been probed for **20e** (Rusakova et al., 2005).

The series of ligands **21** derived from 2,6-substituted pyridines (fig. 26) was designed to determine the influence of the number of aromatic chromophoric fragments (between one and four) on the NIR luminescence properties of Nd[III]. Ligands **21a–e** have been prepared by templated condensation of pyridine-2,6-dicarboxyaldehyde and the corresponding diamine in methanol with Nd(NO$_3$)$_3$·6H$_2$O as the templating agent. With respect to the complex with **21c** taken as reference, the luminescence intensity in dmf is approximately twice as large for complexes with ligands having two (**21a**) and three (**21d**, **21f**, **21g**) aromatic chromophores, while it is distinctively larger for those having four such units (**21b**, factor 4.3, and **21e**, factor 4.8). It is noteworthy that other modifications in the cyclic ligands such as the nature of the
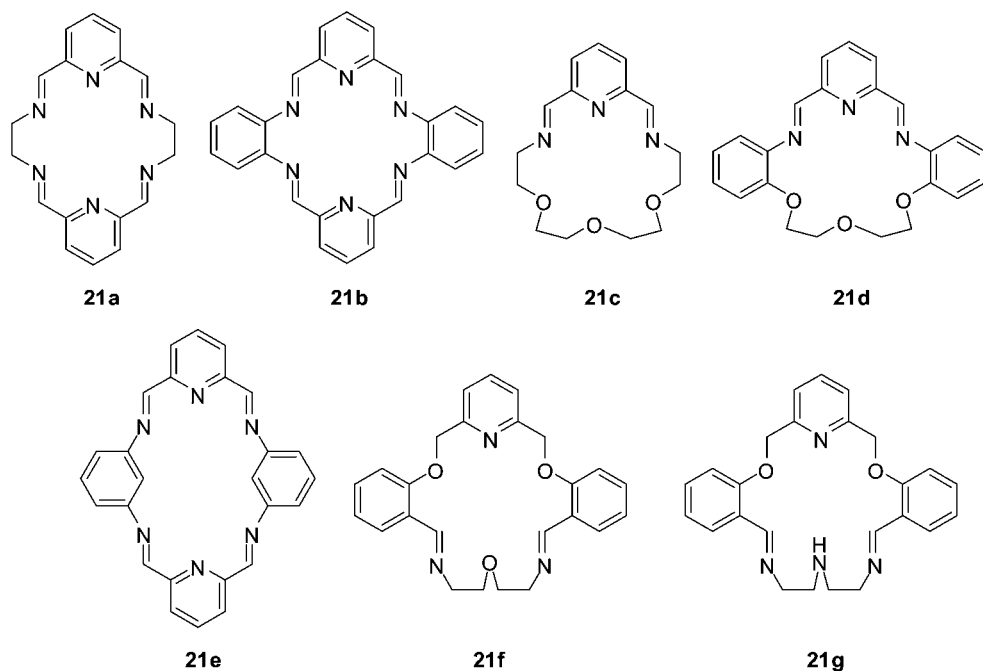
Fig. 26. Aza and oxaza macrocycles.

donor atoms (oxygen versus secondary and/or tertiary amines) have little influence on the overall luminescence intensity (Korovin et al., 2003).

In order to test the behaviour of lanthanide luminescent molecular complexes as optical amplifiers for polymer-based waveguides working in the NIR range, Reinhoudt and collaborators have synthesized $m$-terphenyl-based pre-organized hemispherands and used Eu(III) as a model for studying the effects of the organic ligands on the metal-centered luminescence. The macrocyclic ligands reduce the solvent coordination, as demonstrated for the Eu$^{III}$ complexes with **22a**, $q_{CH_3OH} = 1.9 \pm 0.5$, and **22c**, $q_{CH_3OH} \approx 1$ (Wolbers et al., 1997c), so that these authors subsequently synthesized ligand **22b** (fig. 27) for the sensitization of Nd$^{III}$ with the hope of reducing further solvent interaction in the inner coordination sphere (Wolbers et al., 1997b). Lifetime measurements on a solution of the Eu$^{III}$ complex with the dioxolane-decorated ligand **22b** at a concentration of $10^{-4}$ M in methanol and deuterated methanol yield essentially the same lifetimes (1.42 and 1.56 ms, respectively) so that $q_{CH_3OH}$ is indeed close to zero for this ion. Unfortunately, NIR emission of [Nd(**22b**)] is extremely weak in non-deuterated methanol, with a lifetime shorter than 0.2 µs, whereas it amounts to 0.5 µs in fully deuterated methanol, indicating that solvent molecules still coordinate to this larger lanthanide ion, contrary to Eu$^{III}$.

Further investigations were therefore undertaken with ligands **22c** and **22d**, which sensitize both visible- and NIR-emitting Ln$^{III}$ ions (Wolbers et al., 1998b). Due to the fact that the en-
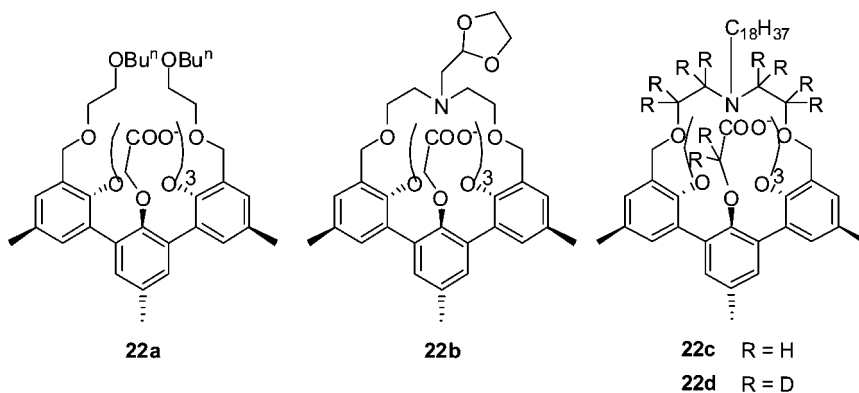
Fig. 27. Hemispherands designed by D.N. Reinhoudt (Wolbers et al., 1997b, 1998b).

ergy gap between $^1G_4$ and $^3F_4$ ($\approx 3000$ cm$^{-1}$) is resonant with a C–H vibration, the Pr($^1G_4 \rightarrow$ $^3H_5$) transition could not be observed. On the other hand, Nd$^{III}$, Er$^{III}$ and Yb$^{III}$ luminescence was detected for complexes with **22a**, **22c** and **22d**, its intensity increasing in the same order. For Nd$^{III}$, lifetime determination in both non-deuterated and deuterated methanol revealed that solvent molecules still interact in the first coordination sphere of the complexes with **22c** and **22d**. Partial deuteration of ligand **22c** resulted in an increase in the luminescence intensity in deuterated methanol by a factor 2.3 while the lifetime increased from 0.79 to 0.89 µs. From these data, the authors estimated the rate constant for quenching by the C–H modes of the ligand to be 142 ms$^{-1}$, as compared to 21 ms$^{-1}$ for Yb$^{III}$ (determined from the luminescence lifetimes of 16 and 24 µs in methanol and deuterated methanol), and 6 ms$^{-1}$ for Sm$^{III}$, emphasizing the large role played by these vibrations in the quenching of Ln$^{III}$ NIR luminescence. The Er$^{III}$ complexes yield a relatively broad emission band in deuterated *n*-butanol, which is of interest for telecommunication applications, although its intensity is very weak and the associated lifetime quite short, 0.8 µs (Wolbers et al., 1998b).

   Cryptands have been somewhat deceptive for both coordination chemistry (Sastri et al., 2003) and photophysical properties of the resulting lanthanide complexes despite some commercial uses (Mathis, 1998), in particular of Lehn's Eu$^{III}$ cryptate with cryptand **23a** (fig. 28). The latter has been tested for the sensitization of the NIR luminescence of Nd$^{III}$ and Yb$^{III}$. Characteristic emission from these two ions is seen upon excitation of the bipyridyl chromophores at 355 nm. Emission from Yb$^{III}$ is reported to be much more intense than the one from Nd$^{III}$ and the authors propose that the excitation mechanism depicted in fig. 9 is operative in this case since no transient absorption corresponding to the formation of the triplet state could be detected (Faulkner et al., 2001). Analysis of lifetime measurements in both water ($\tau(^2F_{5/2}) = 0.52$ µs) and deuterated water (5.21 µs) gives a hydration number $q = 1.5$. Since fitting the luminescence decays to a double exponential function did not improve noticeably the resulting fit, the authors concluded that the non-integer value does not reflect an equilibrium between two different hydration states but, rather, that the distance of close approach of two water molecules is longer: note that comparable experiments on Eu$^{III}$ and Tb$^{III}$
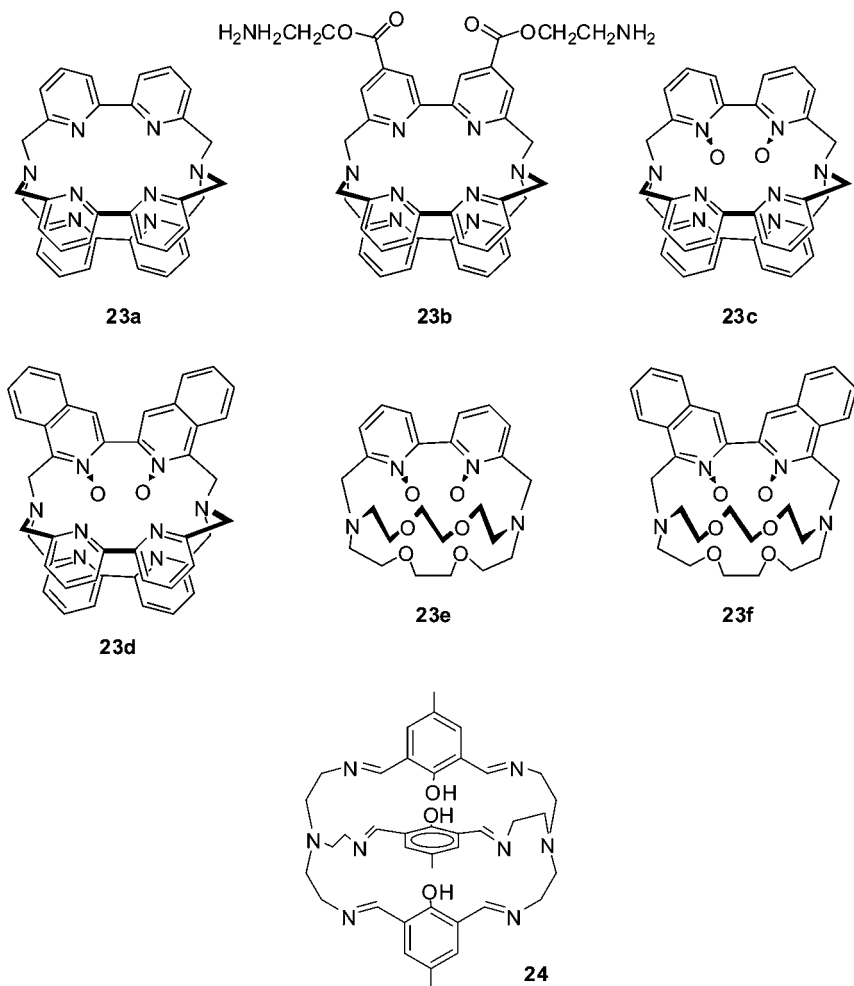
Fig. 28. Some cryptands proposed for the sensitization of NIR luminescence.

cryptates yield $q \approx 2$. Establishing $q$ for the Nd$^{III}$ cryptate proved to be more difficult since no reliable parameters $A$, $B$, and/or $C$ (see eqs. (8) and subsequent discussion above) are published to date. The authors tried to calibrate a relationship by measuring the relevant data for complexes with edta, nta, dtpa, and a cyclen derivative for which $q = 2, 2, 1$, and 0, respectively. When applied to the present case, eq. (10a) yielded $q \approx 0.5$, a value obviously too low, that was explained by the absence, in the cryptate, of a large number of C–H oscillators in the vicinity of the Nd$^{III}$ ion. The Nd$^{III}$ cryptate possesses indeed a relatively long lifetime, 0.1 μs in water and 0.3 μs in deuterated water.

**25**  cyclen

**H$_4$26a**  R = H    H$_4$dota
**H$_4$26b**  R = Me   H$_4$dotma
**H$_4$26c**  R = CH$_2$CH$_2$CO$_2^-$

**H$_3$26d**  H$_3$do3a
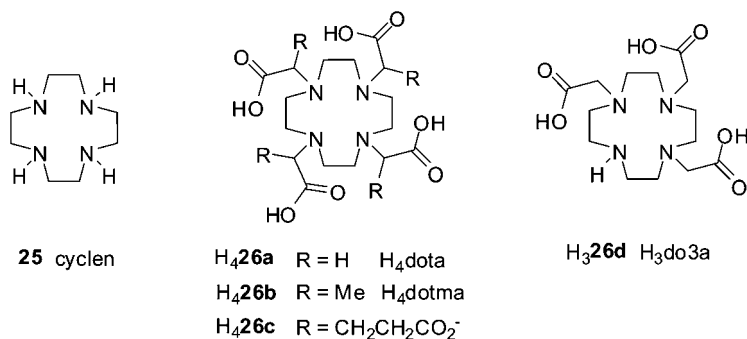
Fig. 29. Basic ligands derived from cyclen.

Following this study, Korovin and coworkers tested cryptands **23b–f** which are used in time-resolved luminescent immunoassays (Mathis, 1993) for the sensitization of Yb$^{III}$ luminescence (Korovin et al., 2002b). From the lifetimes determined in both water and deuterated water, one calculates that the hydration number varies from ≈2 (**23b**), to ≈1.5 (**23a**, **23e**), and finally to ≈1 (**23c**, **23d**, **23f**). Quantum yields were not determined, but luminescence intensities relative to the cryptate with **23a** (in water, at room temperature) point to cryptands **23c** and **23d** being the best sensitizers of the Yb$^{III}$ luminescence with a seven-fold enhancement, while cryptates with **23e** and **23b** are only 1.5- to 1.8-times more luminescent.

The iminocryptate **24**, which can be prepared by a one-pot template reaction, was initially designed for the simultaneous complexation of two 4f ions (Platas et al., 2000) or one 4f ion and one 3d (e.g. Zn$^{II}$, Cu$^{II}$) ion (Rodriguez-Cortinas et al., 2002). Sensitization of Nd$^{III}$ and Yb$^{III}$ was also observed, particularly in the 4f–Zn$^{II}$ heterodimetallic cryptates, for which the crystal field splitting of the 4f levels could be interpreted in terms of a distorted $C_3$ local symmetry.

### 3.1.4. Derivatized cyclens

One of the most studied classes of macrocyclic ligands in lanthanide coordination chemistry is without any doubt the molecules derived from cyclen **25**, a 12-membered ring bearing four amino functions, 1,4,7,10-tetraaza-dodecane (fig. 29). In particular, its tetra-carboxylic derivative H$_4$dota (H$_4$**26a**) was synthesized in 1976 by a German chemist, H. Stetter from the University of Aachen, who isolated complexes with divalent transition metal and alkaline-earth cations (Stetter and Frank, 1976). The tetra-carboxylic acid has p$K_a$ values of 11.1, 9.69, 4.84, and 3.95 (in solutions with $\mu = 0.1$ M KCl). Three years later, a young Belgian chemist, Jean François Desreux from the University of Liège, discovered that dota$^{4-}$ forms highly stable complexes with lanthanide ions, with log $K_1$ in the range 25–28, and that these complexes are also highly kinetically inert.

At that time, the medical industry was looking for good contrast agents able to enhance the sharpness of magnetic resonance images and trivalent gadolinium was an obvious candidate in view of its 7/2 spin. However, Gd$^{III}$ is toxic (the lethal dose, LD$_{50}$, for gadolinium chloride
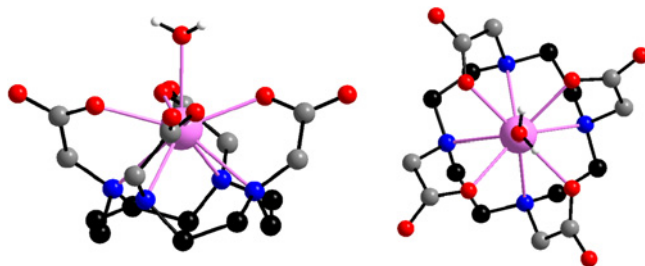
Fig. 30. Two views of the structure of $[Gd(dota)]^-$ showing the encapsulation of the metal ion by the four pendant arms (left) and the $C_4$ symmetry (right, top view). Redrawn from (Chang et al., 1993).

is 0.4 mmol kg$^{-1}$ for mice) because its ionic radius is almost equal to that of Ca$^{II}$, resulting in replacement of the latter in a number of calcium-dependent systems. Many proteins exhibit a binding affinity up to 1000-fold higher for Gd$^{III}$ compared with Ca$^{II}$ in view of the higher charge density of the former cation. As a consequence, Gd$^{III}$ had to be inserted into a very stable and highly inert complex before being injected to patients. Henceforth the choice of dota$^{4-}$ was made by a French company, Guerbet SA, which filed a patent in 1988 for meglumine gadoterate, $[Gd(dota)(H_2O)]^-(mgl)^+$, under the registered trade mark Dotarem$^{TM}$ (meglumine is 1-deoxy-1-(methylamino)glucitol, MeHN–$(CH_2)$–$(CHOH)_4$–$(CH_2OH)$).

The structure of $[Gd(dota)]^-$ is shown in fig. 30. The coordination cavity is achieved by the four nitrogen atoms of the ring and by four additional oxygen donor atoms located on each dangling arm. With respect to the commonly observed 9-coordination of the trivalent lanthanide ions in aqueous solution, one position remains free for interaction with water, an essential feature in the design of contrast agents. The four carboxylate groups are folded, yielding a monocapped square antiprismatic coordination (SAP) with a twist angle of about 40° that is close to the ideal value of 45°. In fact, in solution, two species coexist, which are in slow exchange on the NMR time scale. These species differ in the position of the bound acetates relative to the macrocycle, with the major isomer, denoted M and which predominates for Nd–Lu complexes with dota, having the square antiprismatic geometry illustrated above. The other isomer, m, possesses a twisted square antiprismatic coordination geometry (TSAP), with a twist angle ranging between 15° and 30°. It is of prime importance to note that the SAP isomer bears one coordinated water molecule (coordination number CN = 9), while the TSAP isomer is devoid of water coordination (CN = 8). The relative concentration of the two isomers depends of the specific ligand: if the M isomer predominates for dota complexes (for Yb$^{III}$, the ratio is about 4:1) the situation is reverse for dotma compounds for which the m isomer is the most abundant.

The formation of the $[Ln(dota)(H_2O)]^-$ species is rather slow since it corresponds to considerable stiffening of the ligand. Detailed kinetic studies unveiled the following reaction mechanism (Wu and deW. Horrocks, 1995; Lincoln, 1997):

$$Ln^{3+}(aq) + H_2dota^{2-}(aq) \leftrightarrows [Ln(H_2dota)(H_2O)_5]^+(aq), \quad K \approx 10^6 \, M^{-1}. \qquad (20)$$
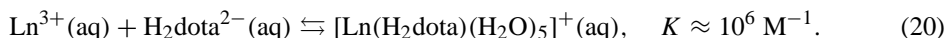
In a first step, intermediate species form rapidly upon mixing the lanthanide ion with $H_4$dota. Both excited state luminescence lifetime determinations for the $Eu^{III}$ complex (Chang et al., 2001) and molecular mechanics calculations are consistent with a structure in which the lanthanide ion is coordinated to four carboxylate groups, well away from the nitrogen atoms of the macrocycle, two of which are protonated. This intermediate may react with a hydroxide group to form monoprotonated neutral species in a rapid equilibrium.

$$[Ln(H_2dota)(H_2O)_5]^+(aq) + OH^- \leftrightarrows [Ln(Hdota)(H_2O)_5](aq) + H_2O. \qquad (21)$$

Finally, the monoprotonated species rearrange into the final product:

$$[Ln(Hdota)(H_2O)_5](aq) \leftrightarrows [Ln(dota)(H_2O)]^- + 4H_2O + H^+. \qquad (22)$$
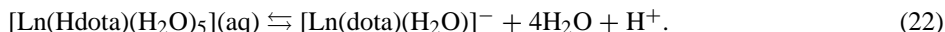
The rate of conversion of $[Ln(H_2dota)(H_2O)_5]^+(aq)$ into $[Ln(dota)(H_2O)]^-$ is pH-dependent and ranges from $7.2 \times 10^{-4}$ to $7.9 \times 10^{-2}$ $s^{-1}$ for Ln = Eu as the pH is raised from 3.8 to 5.8; similar values are obtained for Ln = Gd. Dissociation of the Gd-dota complex is also very slow and its half-life in a 0.1 M solution of hydrochloric acid is larger than one month.

The usual dose for a MRI experiment is 0.1 mmol $kg^{-1}$, there are few side effects and excretion is reasonably fast (75% in 3 h). Given these properties, the cyclen framework has been also used for designing potential luminescent bioprobes emitting either in the visible or in the NIR spectral ranges. Since luminescence probes do not necessarily require four chromophores, a common synthetic pathway is to start from $H_3$do3a ($H_3$**26d**, fig. 29), or from its analog with protected carboxylic acid groups, now commercially available, and to derivatize the remaining secondary amine function with the desired chromophore. Another framework with interesting properties is $H_8$dotp (fig. 31). Its complexes have been studied in details with regard to their solution and magnetic properties, and their potential as high-resolution NMR shift reagents for protein structure determination. The thulium complex $[Tm(dotp)]^{5-}$ induces a particularly large paramagnetic shift. The thermodynamic stability constants with the first half of the lanthanide series (La–Gd) are in the range $\log K = 28.9$–$29.6$, as determined by a competitive method with the dye arsenazo III (Sherry et al., 1996). They are slightly larger than those for $[Ln(dota)]^-$ and the complexes display only one isomer in solution, on the NMR time scale, as opposed to two for $[Ln(dota)]^-$, see above. The only drawback of the dotp complexes is the larger negative charge, which may be a problem for *in vivo* applications, by increasing substantially the osmotic pressure. This is a reason why phosphinic acid derivatives (fig. 31) are often preferred since their complexes bear only one negative charge, similarly to dota complexes.

The first study using a cyclen derivative to sensitize the NIR emission of $Yb^{III}$ appeared in 1997. David Parker (Beeby et al., 1997) found that the tetrabenzyl phosphinate complex $[Yb(\mathbf{27c})]^-$ which, according to X-ray and relaxometry investigations, contains no bound water (Aime et al., 1997), displays a longer $Yb(^2F_{5/2})$ lifetime (4.5 μs in $H_2O$) than $[Yb(\mathbf{27d})]$ (1.87 μs in $H_2O$). In deuterated water, the lifetime of $[Yb(\mathbf{27c})]^-$ increases to 8.9 μs; using eq. (9a) without the second sphere correction, one gets $q \approx 0.1$, that is the residual quenching effect can be assigned to a contribution from closely diffusing, unbound water molecules ("outer-sphere" effect). The $Nd^{III}$ complex with **27c** has a lifetime of 0.16 μs in water and 0.33 μs in deuterated water (Faulkner et al., 1999), and use of eq. (10a) yields indeed $q \approx 0$.
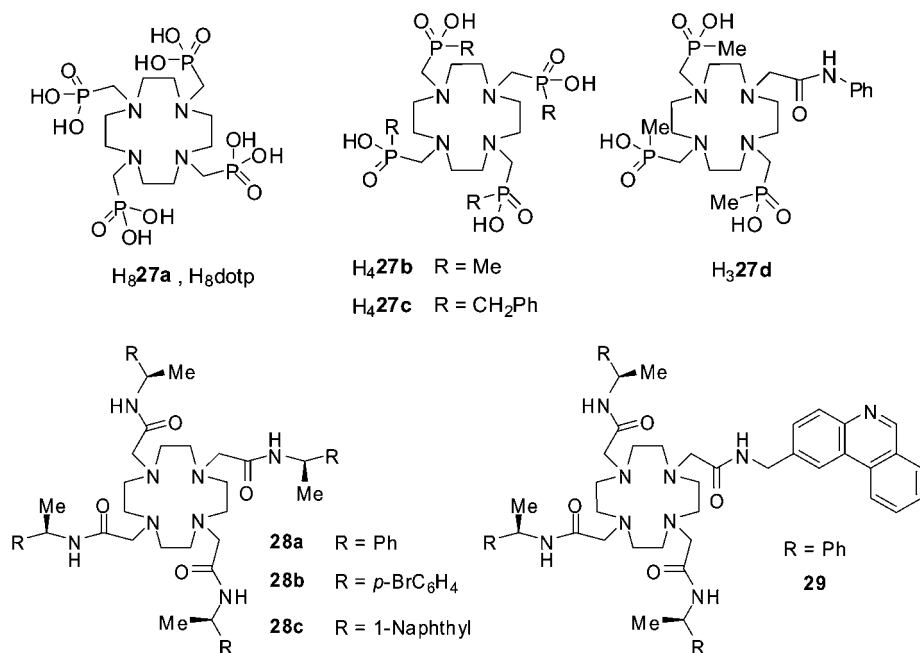
Fig. 31. Phosphonic and phosphinic acid derivatives of cyclen (top), and tetraamide derivatives (bottom).

The shorter lifetime of the related mono-amide triphosphinate complex [Yb(**27d**)] (6.7 µs in D$_2$O) leads to $q \approx 0.4$ (without the correction) or $q \approx 0.15$ if the correction in eq. (9a) is taken into account. This apparent hydration number can be explained by the presence of a hydrogen bonded water molecule, as demonstrated for the Eu$^{III}$ and Tb$^{III}$ complexes (Aime et al., 1996). On the other hand, the lifetimes of the related complexes with the tetraamide ligands **28a–c** (fig. 31) are much shorter (0.7–0.8 µs in H$_2$O and 5.0–7.5 µs in D$_2$O) reflecting the presence of bound water molecules, in line with known crystal structures with other lanthanide ions. The rate of water dissociation in [Ln(**28a**)(H$_2$O)]$^{3+}$ is 500-fold faster for Ln = Yb, compared to Eu, as ascertained by NMR data: $k_{dis} = (1.9 \pm 0.7) \times 10^6$ s$^{-1}$ ($\Delta G^0 = 34.6 \pm 2.6$ kJ mol$^{-1}$). The rate constants for the decay of the Yb($^2$F$_{5/2}$) excited level amount to $1.6 \times 10^5$ s$^{-1}$ ($\tau_{obs} = 6.25$ µs) in D$_2$O and $1.4 \times 10^6$ s$^{-1}$ ($\tau_{obs} = 0.71$ µs) in H$_2$O at room temperature, that is close to the water exchange rate constant. Therefore, single exponential decays are observed at this temperature. At lower temperature, a single decay is still observed for the D$_2$O solution, but in water, the decay becomes bi-exponential, the faster process being ascribed to the 9-coordinate monohydrated species and the slower one to the 8-coordinate non-hydrated complex (Batsanov et al., 1999).

The quenching effect of proximate OH, NH, and CH vibrations on Yb$^{III}$ luminescence (see eq. (9a)) has been determined by measuring the rate constants for the depopulation of the $^2$F$_{5/2}$ state of complexes with edta$^{4-}$, dtpa$^{5-}$, (H**16**)$^+$ (fig. 24), (**26a**)$^{4-}$, (**26c**)$^{4-}$ (fig. 29),

Table 6

Comparison between actual ($q$) and calculated ($q_{corr}$) hydration states for $Yb^{III}$ complexes with cyclen derivatives (Beeby et al., 1999)

| Complex | $q^a$ | $\Delta k_{obs}$ ($\mu s^{-1}$)[b] | $A \times \Delta k_{corr} = q_{corr}^c$ |
|---|---|---|---|
| $[Yb(27c)]^-$ | 0 | 0.11 | 0 |
| $[Yb(27b)]^-$ | 0 | 0.24 | 0.04 |
| $[Yb(26a)]^-$ | $0.8^d$ | 0.50 | 0.30 |
| $[Yb(26c)]^-$ | 0 | 0.74 | 0.54 |
| $[Yb(28a)]^{3+}$ | 1 | 1.27 | 1.07 |
| $[Yb(28c)]^{3+}$ | 1 | 1.00 | 0.80 |
| $[Yb(28b)]^{3+}$ | 1 | 1.17 | 0.97 |
| $[Yb(H16)]^{4+}$ | 3 | 2.98 | 2.78 |
| $[Yb(27d)]$ | 0 | 0.38 | 0.18 |

[a] As determined by NMR or X-ray diffraction.

[b] $\Delta k_{obs} = k_{H_2O} - k_{D_2O}$.

[c] $A = 1$ μs; $\Delta k_{corr} = \Delta k_{obs} - 0.20$ $\mu s^{-1}$, except for **27c**.

[d] Taking into account the 4:1 $M{:}m$ isomer proportion.

($\textbf{27b}$)$^{4-}$, ($\textbf{27c}$)$^{4-}$, ($\textbf{27d}$)$^{3-}$, and $\textbf{28a–c}$ (fig. 31) in both water and deuterated water (Beeby et al., 1999). Deuterated analogs have been synthesized as well, particularly for replacing the N–H group in the amide ligands **28** with N–D functions, and for substituting some of the ring $CH_2$ groups of dota. In fact NH/ND exchange does occur rapidly on the experimental timescale and double exponential decays were observed for the cationic complexes with amides **28**. The main results for the evaluation of the effect of proximate water molecules are reported in table 6.

Given the uncertainty of $\pm 15\%$ affecting the lifetime measurements, an average uncertainty of $\pm 0.3$ can be assigned to the $q_{corr}$ values. Except in the cases of the anionic complexes with ($\textbf{26a}$)$^{4-}$ and ($\textbf{26c}$)$^{4-}$, agreement between the values calculated from the lifetimes and the values estimated from other data is good. In fact, additional corrections should apply, in particular for the presence of N–H oscillators in the tetraamide complexes (0.06 $\mu s^{-1}$) and for the CH oscillators (0.088 $\mu s^{-1}$). Equation (9a), in which $B$ is set to 0.25 $\mu s^{-1}$ and $C$ to 0, takes these contributions partially into account.

Circularly polarized luminescence (CPL) from chiral molecular systems is the emission analog of circular dichroism (CD) and as such reflects the chirality of the excited state in the same manner as CD probes reflect the chirality of the ground state (Riehl and Muller, 2005). For lanthanide ions, large CPL (and/or CD) signals are expected for f–f transitions obeying magnetic dipole selection rules, in particular $\Delta J = 0, \pm 1$; $Eu(^5D_0 \rightarrow {}^7F_1)$, $Tb(^5D_4 \rightarrow {}^7F_4$, $^5D_4 \rightarrow {}^7F_5)$, $Dy(^4F_{9/2} \rightarrow {}^6H_{11/2})$, $Yb(^2F_{5/2} \rightarrow {}^2F_{7/2})$ emissions are typical examples. Recent advances in instrumentation permit the detection of very small differences in the intensity of left versus right circular polarization, opening the field for measurements of $Yb^{III}$ complexes. In CPL, results are usually reported in term of the dissymmetry ratio $g_{lum}$:

$$g_{lum} = \frac{\Delta I(\lambda)}{(1/2)I(\lambda)} = \frac{2[I_L(\lambda) - I_R(\lambda)]}{I_L(\lambda) + I_R(\lambda)}, \tag{23}$$
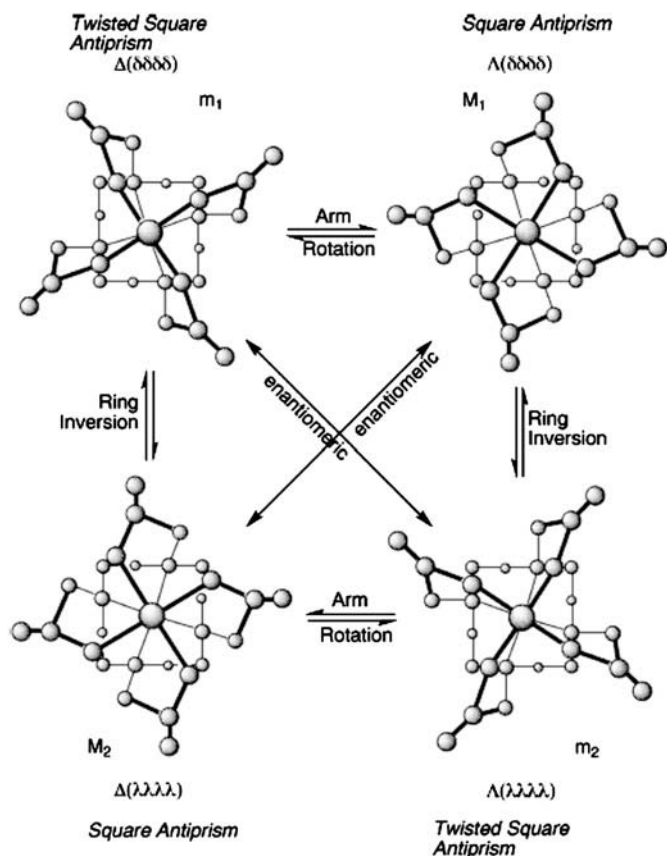
Fig. 32. Schematic representation of the isomers of cyclen-based complexes, with chirality and potential exchange mechanisms between them. From (Dickins et al., 1998), reproduced with permission of the Royal Chemical Society (RSC) on behalf of the Centre National de la Recherche Scientifique (CNRS).

in which R and L stands for right polarized and left polarized emission intensity, respectively. The dissymmetry factor provides useful information concerning the structural changes that take place on the timescale of the light emission. Complexes with cyclen derivatives display rich chiral properties, induced both by the positioning of the arms, indicated by $\Delta$ for a clockwise or by $\Lambda$ for an anti-clockwise arrangement, and the cycle which can adopt two enantiomeric conformations in the complex, $\lambda\lambda\lambda\lambda$ or $\delta\delta\delta\delta$ in each 5-member chelate ring according to Corey and Bailar's classification (fig. 32). The ring inversion of [Yb(dotma)]$^-$ (fig. 29), $\Lambda(\lambda\lambda\lambda\lambda) \leftrightarrows \Lambda(\delta\delta\delta\delta)$, in methanol, is a slow process on the NMR timescale and the equilibrium is in favor of the m isomer over the M form (in a proportion of about 13:1), with $K(298) = 0.075$, $\Delta H^0 = -4 \text{ kJ mol}^{-1}$, $\Delta S^0 = -35 \text{ J K}^{-1} \text{ mol}^{-1}$. The NIR CD spectrum of the $^2F_{5/2} \leftarrow {}^2F_{7/2}$ transition shows several well-resolved transitions with a very high
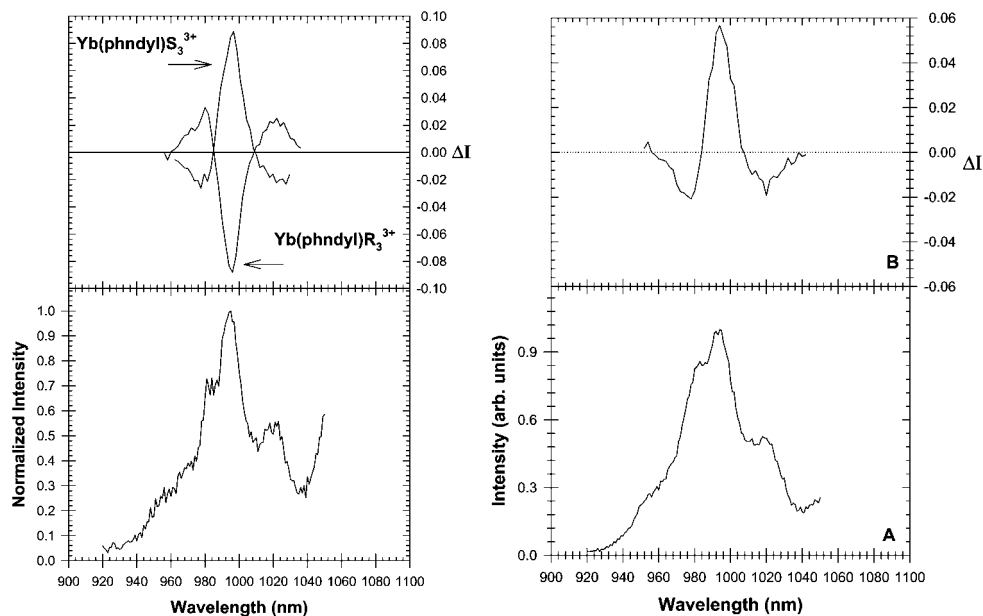
Fig. 33. Total luminescence spectra (B) and circularly polarized spectra (A) of the Yb($^2F_{5/2} \rightarrow {}^2F_{7/2}$) transition for [Yb(*S*-**29**H)]$^{4+}$, [Yb(*R*-**29**H)]$^{4+}$ 1 mM in D$_2$O (left) and [Yb(*S*-**28b**)]$^{3+}$ 0.5 mM in D$_2$O (right). Reproduced with permission from (Maupin et al., 1998). Note: phndylR$_3$ and phndylS$_3$ correspond to *R*-**29**H$^+$ and *S*-**29**H$^+$, respectively.

© 1998 American Chemical Society

dissymmetry factors. The ligand field splitting and population of the LF sub-levels have been determined as a function of temperature (Di Bari et al., 2000a).

In the first study of CPL emission of optically active Yb$^{III}$ complexes with tetra-amide derivatives of cyclen, the authors have selected ligands **28b** and **29** (fig. 31), the latter bearing a phenanthridyl chromophore for better sensitization of the Yb$^{III}$ luminescence when it is protonated (Maupin et al., 1998). The two enantiomers *R* and *S*, with each chiral amine having the same conformation produce $C_4$-symmetrical complexes with, as a consequence, a splitting of the Yb$^{III}$ levels into three ($^2F_{5/2}$) and four ($^2F_{7/2}$) ligand-field sub-levels. This splitting is reflected in the total emission spectrum of [Yb(**29**H)] 1 mM in D$_2$O containing trifluoroacetic acid; as required by symmetry, two opposite CPL spectra are obtained for the two complexes with the two enantiomers and the dissymmetry factors calculated for the three main peaks of the spectra $|g_{lum}|$ are >0.1, that is analogous to those reported for similar complexes with Eu$^{III}$ and Tb$^{III}$. The sign pattern in the CPL spectrum of [Yb(*S*-**28b**)]$^{3+}$ is identical to the one displayed by [Yb(*S*-**29**H)]$^{4+}$ while the dissymmetry factor is somewhat smaller (fig. 33). This is evidence that the replacement of one of the chiral amines with the achiral phenanthridyl group does not change the $C_4$ arrangement around the central metal ion.

Further studies reported similar CPL spectra for [Yb(**28a**)]$^{3+}$, as compared to [Yb(**28b**)]$^{3+}$ (Dickins et al., 1999), with dissymmetry factor $g_{lum}$ for the peak corresponding to the maximum of luminescence (at 995 nm) of $-0.18$ (Maupin et al., 2000). A quantitative comparison with the CD spectrum for which the absorption dissymmetry factor $g_{abs} = -0.11$ is difficult in view of the spectral overlap of various transitions from differently populated LF sub-levels, as demonstrated in a previously cited study (Di Bari et al., 2000a). However, such a comparison is useful to verify the sign of the CPL emission:

$$g_{abs} = \frac{\Delta \varepsilon}{(1/2)\varepsilon} = \frac{2(\varepsilon_L - \varepsilon_R)}{\varepsilon_L + \varepsilon_R}. \tag{24}$$

$C_4$-symmetric species are prime targets for developing useful correlations between CPL spectra and chemical structure, and the sign (and magnitude) of the CPL signals have been correlated to the degree of helical twist of the complex, the strength of the ligand field, and the polarisability of the axial donor group (Di Bari et al., 2000b; Dickins et al., 2003; Lisowski et al., 2004). The local helicity at the lanthanide center can also be related to the angle between the electric dipole and magnetic dipole transition moments and therefore to the rotary strength of a given transition; however, most of the CPL studies associated with this correlation have been performed on Eu$^{III}$ and Tb$^{III}$ $C_4$-symmetrical species (Riehl and Muller, 2005).

As mentioned above, the phenanthridyl chromophore is more efficient in sensitizing Yb$^{III}$ emission when it is protonated, so that [Yb(**29**H)]$^{4+}$/[Yb(**29**)]$^{3+}$ can act as a switchable luminescent couple in function of pH. In fact this corresponds to two different mechanisms for the sensitization of Yb$^{III}$ luminescence (Beeby et al., 2002c). As depicted in fig. 9, a rapid, sequential electron exchange mechanism is thought to be responsible for the sensitization of Yb$^{III}$ luminescence at least when both electron transfer steps are thermodynamically feasible, which is the case here. Indeed the triplet state energies are $\approx$22 000 cm$^{-1}$ for the phenanthridine chromophore and $\approx$21 300 cm$^{-1}$ for the phenanthridinium moiety and both have negligible overlap with the $^2F_{5/2}$ excited state. Since the rate of the backward electron transfer Yb$^{II} \rightarrow$ Yb$^{III*}$ is fast, one can simplify the mechanism by writing:

$$\text{Phen*} + \text{Yb}^{III} \xrightarrow{k_{et}} \text{Phen} + \text{Yb}^{III*} \xrightarrow{k_{lum}} \text{Phen} + \text{Yb}^{III} + h\nu. \tag{25}$$
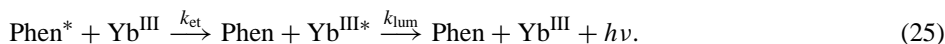
Therefore, the intensity of the emitted light is given by:

$$I(t) \propto \frac{k_{et}}{k_{lum} - k_{et}} \cdot \left( e^{-k_{et}t} - e^{-k_{lum}t} \right). \tag{26}$$

From eq. (26), one sees that if $k_{et} \gg k_{lum}$, the growth of the metal-centered luminescence will mirror the decay of the triplet state, $k_T$, while the decay of the metal-centered luminescence will be determined by $k_{obs} = k_{lum}$. On the other hand, if $k_{et} \ll k_{lum}$, that is when the energy transfer step is rate determining, the observed decay rate constant will reflect the decay of the triplet state, $k_{obs} = k_T$, and therefore $k_{obs}$ will depend on the degree of aeration of the solution; the growth of the Yb$^{III}$-centered luminescence will be independent of the presence of oxygen but conversely it will depend on the nature of the solvent. The kinetics of the energy transfer has been investigated by time-resolved luminescence of the metal
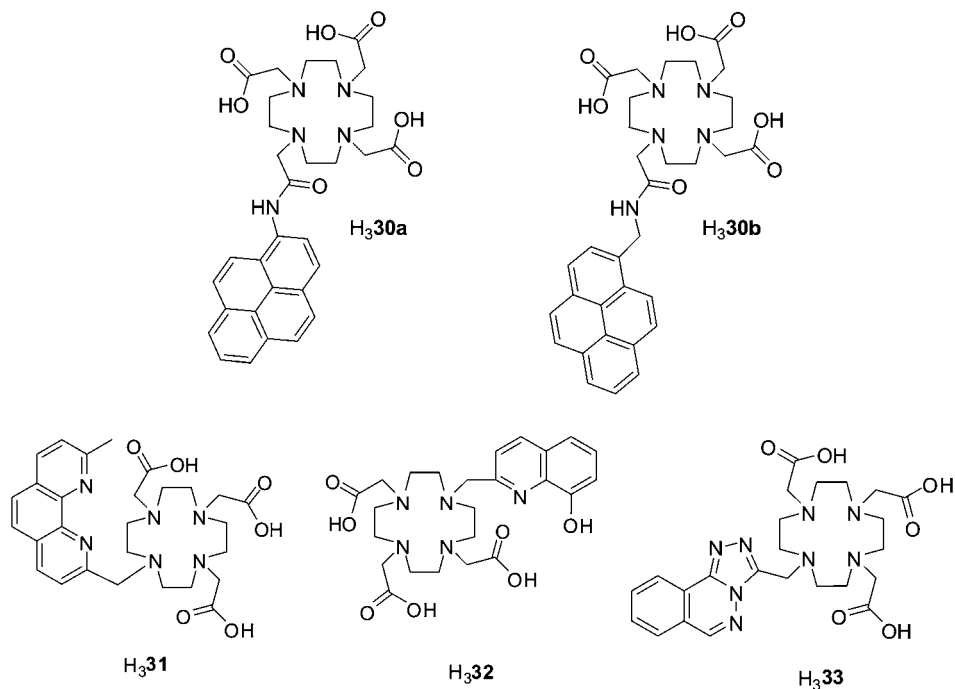
Fig. 34. Chromophore-appended dota ligands.

ion, as well as by fluorescence and triplet–triplet absorption data for the phenanthridine chromophore in both acidic and neutral water and deuterated water. In addition, it was established that the presence of oxygen decreased the luminescence intensity of Yb[III] by a factor 4–5 for the protonated complex while it did not affect the non-protonated compound. Since it is well established that oxygen does not quench directly lanthanide excited states, the effect of oxygen on the metal-centered luminescence reveals a quenching of the triplet state. From these data, the authors could establish that the protonated complex [Yb(29H)]$^{4+}$ follows a classical behaviour with direct sensitization of the Yb[III] luminescence through energy transfer from the triplet state. The profile of the time-resolved luminescence for the un-protonated complex [Yb(29)]$^{3+}$ which is the major species for pH > 6 is very different, with a luminescent decay independent of aeration, pointing to a sensitization mechanism following the double electron transfer depicted in fig. 9. A similar investigation for [Nd(29H)]$^{4+}$ ruled out the latter mechanism for the sensitization of Nd[III] (Beeby et al., 2001), which is in line with Nd[II] not being readily accessible in water ($E_{red}^0 < -2.5$ V).

Other chromophores have been grafted onto the dota framework (fig. 34). Both pyrene-sensitized Nd[III] and Yb[III] emissions have been observed with ligands H$_3$30a and H$_3$30b; lifetime determinations in H$_2$O and D$_2$O led to $q_{Nd} = 0.8$ and 1.0, respectively, while data for Yb[III] yielded 1.1 and 0.5, respectively. Interestingly, quantum yields for [Ln(30a)] in which

the pyrene chromophore is directly bound to the amide coupling group are 1.6-fold larger than for [Ln(**30b**)] in which the pyrene sensitizing group is linked by a methylene spacer. In line with this observation, the rise time in complexes with $H_3$**30b** is longer (70 ns for $Nd^{III}$ and 125 ns for $Yb^{III}$) than in complexes with $H_3$**30a** (<5 ns for $Nd^{III}$ and 15 ns for $Yb^{III}$), implying a less efficient energy transfer with increasing separation of the chromophore and the metal ion (Faulkner et al., 2004).

A way of expelling the interacting water molecule out of the first coordination sphere is to use a bidentate pendant chromophore such as *o*-phenanthroline in ligand $H_3$**31**, which will saturate the coordination sphere of the metal ion. As a matter of fact, the hydration number of [Eu(**31**)] proved to be zero and the antenna is reasonably efficient in sensitizing the europium luminescence ($Q_{Eu}^L = 30\%$ in $D_2O$ as determined with respect to [Ru(bpy)$_3$]$^{2+}$ in aerated water, $Q = 2.8\%$). Despite a close to 1 value of $\eta_{sens}$ for the $Er^{III}$ complex, the quantum yield in $D_2O$ remains extremely weak for this compound, $Q_{Er}^L = 5 \times 10^{-4}\%$, in line with the difficulty of preventing nonradiative deactivation for this ion (Quici et al., 2004). The complex with 8-hydroxyquinoline-fitted ligand $H_3$**32** also emits a weak $Er^{III}$ luminescence in water at pH 7, but no quantitative data are at hand (Rizzo et al., 2004). Lifetimes only are reported for [Ln(**33**)] (Ln = Nd, Eu, Er, Yb) in $H_2O$ and $D_2O$ ($q_{Eu} = 0.9$) and the $Er^{III}$ luminescence in water is said to be very weak (Burton-Pye et al., 2005).

Instead of grafting a coordinating chromophore on the macrocyclic framework, which sometimes requires the recourse to relatively complicated synthetic routes, another strategy was tested, which forms ternary complexes in situ. An example is pyrene acetic acid H**34** (fig. 35) which reacts with [Ln(**26d**)($H_2O$)$_2$] to form kinetically labile ternary complexes [Ln(**26d**)(**34**)($H_2O$)$_x$], Ln = Nd, Yb (Faulkner et al., 2004). Metal-centered luminescence occurs upon pyrene excitation. However, according to lifetime measurements for $Yb^{III}$, 0.72 and 2.52 μs in $H_2O$ and $D_2O$, respectively, and the use of eq. (9a), $q = 0.9$, which suggests that a pyrene acetic acid molecule is coordinated to the metal center expelling one water molecule, but not the second one. That is, the ternary complex does not represent an improvement over [Yb(**30a**)].

Another potential ancillary ligand is tetrathiafulvalene carboxylic acid H**35a**. Indeed, the sulfur-based heterocycle tetrathiafulvalene is a highly efficient electron donor which can be oxidized sequentially to the radical cation and dication and which is incorporated in various materials applications. Ligand H**35a** effectively acts as a sensitizer for $Yb^{III}$ luminescence and lifetime measurements on [Yb(**35a**)$_3$] in methanol (0.50 μs) and deuterated methanol (3.67 μs) point to $q_{CH_3OH} = 3.25$ (cf. eq. (9b)), whereas the ternary complex [Yb(**26d**)(**35a**)] has $q_{CH_3OH} = 0.2$ ($\tau_{H_2O} = 2.02$ μs, $\tau_{D_2O} = 3.49$ μs). In the latter, sensitization occurs through the double electron redistribution mechanism outlined in fig. 9, as substantiated by electrochemical data leading to an estimated $\Delta G \approx 2.37$ eV for the electron back transfer (Faulkner et al., 2002). S.J.A. Pope has further screened several other mono- and di-anionic ligands, **35b–e** (fig. 35); all of the ternary complexes [Ln(**26d**)(**35b–e**)] (Ln = Nd, Yb) are emissive, some of them weakly, while luminescence from $Er^{III}$ species is faint which prevented lifetime determination. Lifetimes for methanolic solutions are in the range 1.4–2 ms for $Yb^{III}$ and **35a**, **c**, **e** while no emission is observed for **35b**; for $Nd^{III}$, lifetimes range from 108 to 237 ns for **35a–e**. From the $q_{MeOH}$ values deduced from lifetime data for $Yb^{III}$, carboxylates appear to
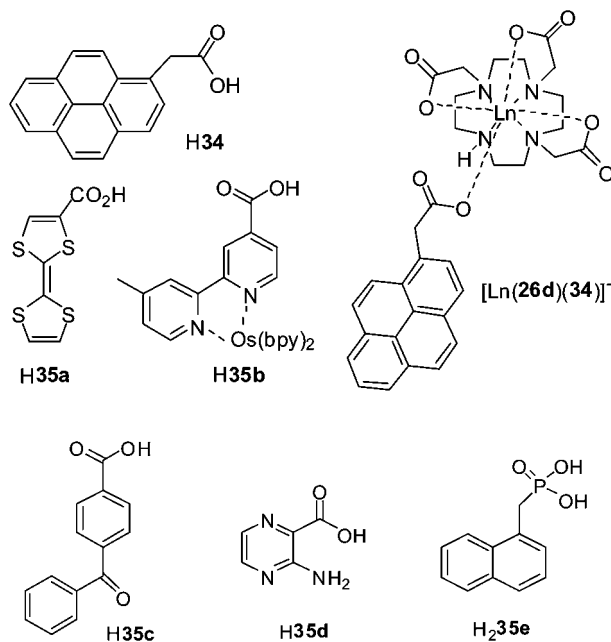
Fig. 35. Ancillary chromophoric ligands for the formation of ternary complexes.

behave as monodentate ligands and their replacement with phosphate anions is quite easy; by contrast, phosphonate derivatives are more robust, being bound in a bidentate fashion (Pope et al., 2006). Altogether, however, it seems that the strategy of producing ternary complexes in situ has not yielded better sensitization efficacy compared to 1:1 complexes with octa- or nona-dentate ligands.

Finally, there are also some reports of $Nd^{III}$ and $Yb^{III}$ bimetallic complexes in which two cyclen moieties are coupled together by a chromophoric unit (fig. 36). Korovin and Rusakova have screened a series of seven dyes, with triplet state energy in the range 13 750–14 320 $cm^{-1}$, for their ability to sensitize $Nd^{III}$ and/or $Yb^{III}$ luminescence. The best one proved to be phthalexon S, with quantum yields in $D_2O$ of 0.41% for $Yb^{III}$ and 0.025% for $Nd^{III}$ and consequently, ligand $H_7\mathbf{36}$ was synthesized by a Mannich reaction involving phenol red, do3a, and formaldehyde in 1:3:3 proportion (Korovin and Rusakova, 2002). Complexes with 2:1 Ln:L stoichiometry (Ln = Nd, Yb) are soluble in water and both the quantum yields and lifetimes are noticeably larger than those for the 1:1 complexes with the dye, or with do3a. For the bimetallic $Yb^{III}$ complex, $Q^L_{Yb} = 1.45\%$ in $D_2O$ measured with respect to [Zn(TPP)], which is indeed one of the largest quantum yields reported for an ytterbium complex in solution. The corresponding lifetime amounts to 12.6 μs and decreases to 6.8 μs in $H_2O$ which corresponds, according to eq. (9a), to $q \approx 0$, a surprising result at first, but the inexistent hydration may be traced back to the lipophilicity of the linkage unit. The corresponding data for $Nd^{III}$ are $Q^L_{Nd}(D_2O) = 0.23\%$, $\tau_{H_2O} = 0.75$ μs and $\tau_{D_2O} = 1.45$ μm. Under the same
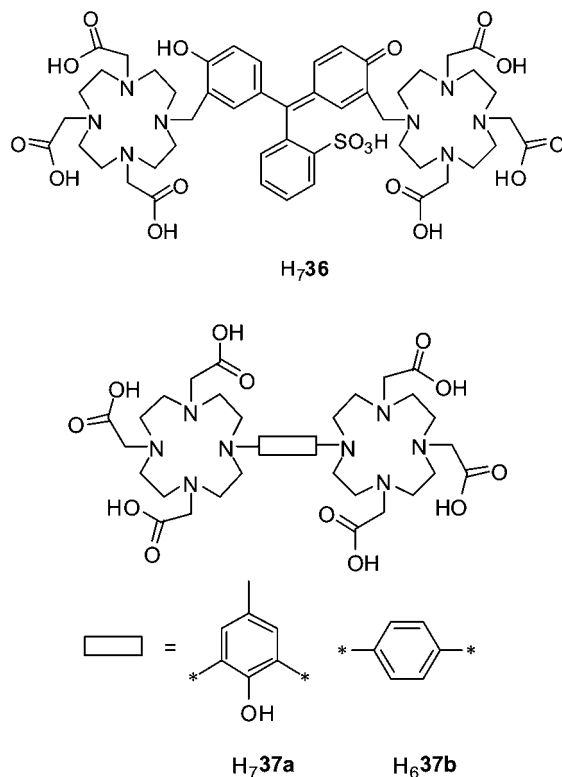
Fig. 36.  Cyclen-based ditopic ligands for bimetallic complexes.

excitation conditions (532 nm), luminescence for the bimetallic $Er^{III}$ complex could only be observed in dmso-$d_6$ ($\tau = 1.8$ µs) (Korovin and Rusakova, 2004).

Reaction of the ditopic ligand $H_7\mathbf{37a}$ with ytterbium triflate yields a well defined, kinetically stable bimetallic complex. Its photophysical properties demonstrate that two different $Yb^{III}$ environments are present on the luminescence timescale. For instance, luminescence decays upon excitation at 337 nm are bi-exponential, with lifetimes of 0.51 and 1.67 µs in water and 1.17 and 4.95 µs in $D_2O$. The corresponding $q$ values are 0.3 and 1.0 (eq. (9a)). There are essentially two possibilities, either the formation of one bimetallic complex with two different binding sites or the co-existence of two forms of the complex in solution. From a coordination viewpoint, a reasonable assumption if the first hypothesis is valid would be that both sites are 8-coordinate, by the seven donor atoms of each macrocycle and by either a water molecule or a phenol oxygen, since the bulk of the macrocycles prevents the two metal ions from sharing the latter donor atom (Pope et al., 2003b). When the phenol linkage group is replaced with a simpler $p$-xylene unit in $H_6\mathbf{37b}$, the Yb($^2F_{5/2}$) decay is a single exponential function corresponding to lifetimes of 1.45 µs in water and 6.07 µs in deuterated water, hence

to $q = 0.4$ (eq. (9a)). The two binding sites are now equivalent, as further demonstrated by the NMR spectrum and the hydration is close to zero, with a somewhat unusual coordination number of 7, again possibly due to the hydrophobicity of the coupling group (Pope et al., 2003a).

### 3.1.5. *Derivatized calixarenes and resorcinarenes*

Calix[*n*]arenes are a family of macrocycles prepared by condensation reactions between *n* *para*-substituted phenols and *n* formaldehyde molecules under either base or acid catalysis. Different sizes of the macrocycles can be obtained ($n = 4$–20) (Stewart and Gutsche, 1999) depending on the exact experimental conditions, which were mastered in the 1960's (Gutsche, 1998), but the most common receptors are those with $n = 4, 6, 8$ (macrocycles with an odd number of phenol units are more difficult to synthesize). We use here the simplified nomenclature in which the number of phenolic units is indicated between square brackets and *para* substituents are listed first.[4] Calixarenes, which can be easily derivatized both on the *para* positions of the phenolic units and on the hydroxyl groups, have been primarily developed for catalytic processes and as biomimics, but it was soon realized that they can also easily encapsulate metal ions and the first complexes with d-transition metal ions were isolated in the mid-1980's (Olmstead et al., 1985). Jack Harrowfield characterized the first lanthanide complex with a calixarene in 1987, a bimetallic europium complex with *p-tert*-butylcalix[8]arene (Furphy et al., 1987).

Calix[4]arenes can adopt several conformations. The most usual one is when the four alkyl substituents are on the same side, resulting in a cone conformation, stabilized by strong hydrogen bonds between the intra-annular OH groups. Initially, the rim bearing the alkyl substituents was termed "upper rim"; however, to avoid potential confusions, the current practice is to name it "wider rim". The other conformers are the partial cone one in which one alkyl substituent lies opposite to the three other ones, the 1,2-alternate and the 1,3-alternate. Most of the lanthanide complexes with calix[4]arene derivatives contain the ligand in the cone conformation. The calixarene framework can be regarded as a platform with two rims onto which functional groups can be separately grafted to modify either the coordination behaviour or the lipophilicity, which is important for solubility. The size of the induced cavity can be modulated both by adjusting the number *n* of phenolic units and/or the size of the pendant-arm substituents. Simple calix[*n*]arenes bearing no substituent on the narrower rim and *p-tert*-butyl groups on the wider rim form complexes with lanthanide ions with the following Ln:L stoichiometry: 2:2 for $n = 4$ and 5, 1:2 for $n = 6$, but one ligand molecule is not coordinated, and 2:1 for $n = 8$ (Bünzli et al., 2000). Some 1:1 complexes with the latter are also known (Bünzli and Besançon, 2005), and this stoichiometry is often seen with derivatized calix[4]arenes. When phenol is replaced with resorcinol, similar cyclic compounds are obtained, which have the same four conformational possibilities as calix[4]arene, but which are more fluxional in absence of intra-annular OH groups (fig. 37).

---

[4]  *p-tert*-Butylcalix[4]arene for instance is 5,11,17,23-tetra-4-*tert*-butyl-25,26,27,28-tetrahydroxycalix[4]arene or for a complete description, pentacyclo[19.3.1.13,7.19,13.115,19]octacosa-1(25),3,5,7(28),9,11,13(27),15,17,19(26), 21,23-dodecaene-25,26,27,28-tetrol, 5,11,17,23-tetrakis(1,1-dimethylethyl).

| | R | $R_1$ | $R_2$ |
|---|---|---|---|
| $H_8$38a | $C_6H_5$ | $CH_2$-$N(C_2H_5)_2$ | H |
| $H_8$38b | $CH_3$ | $CH_2$-$N(C_2H_5)_2$ | H |
| $H_8$38c | $CH_3$ | H | H |
| 38d | $CH_3$ | H | $COCH_3$ |
| $H_8$38e | $C_6H_5$ | H | H |
| 38f | $C_6H_5$ | H | $COCH_3$ |
| 38g | $CH_3$ | Br | $COCH_3$ |

| | n | $R_1$ | R |
|---|---|---|---|
| $H_4$39a | 1 | H | H |
| 39b | 1 | $CH_3$ | $R_1$ |
| 39c | 1 | $H_2CHC=CH_2$ | $R_1$ |
| $H_4$39d | 1 | $CH_2COOH$ | $R_1$ |
| 39e | 1 | $CH_2COOCH_3$ | $R_1$ |
| $H_2$39f | 1 | $CH_2CONHC_6H_5$ | H |
| $H_8$40 | 5 | H | H |



$H_8$38c



$H_4$39a
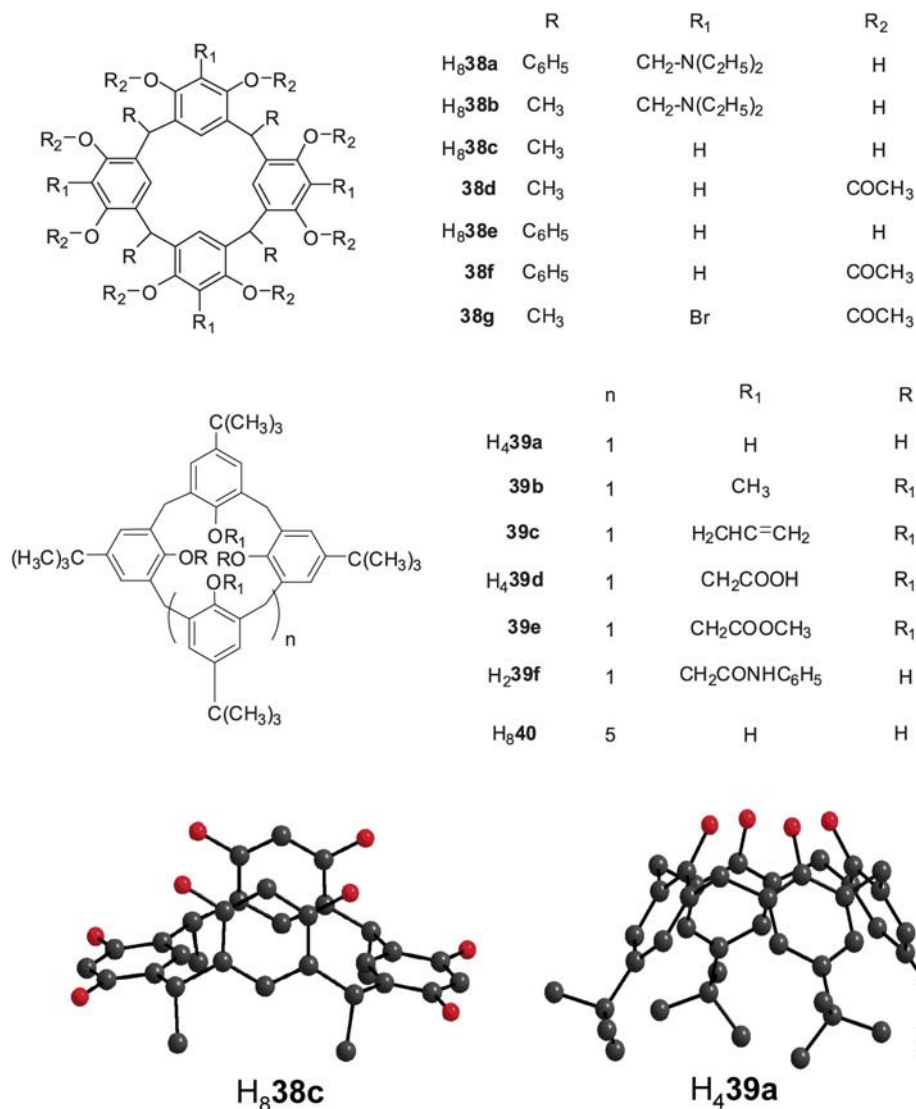
Fig. 37.  (Top) Formulae of calix[4]resorcinarenes; (middle) formulae of calix[n]arenes; (bottom) X-ray structures of (left) calix[4]resorcinarene (MacGillivray et al., 2001) and (right) *p-tert*-butylcalix[4]arene (Ungaro et al., 1985).

Shevchuk and coworkers have performed systematic investigations of Nd[III] and Yb[III] 1:1 complexes with a series of calix[4]resorcinarenes and calix[4]arenes. A first study aimed at establishing an analytical procedure for the determination of these two ions in organic solvents. The intrinsic luminescence of the ligand is quenched when Yb[III] chloride is added to the so-

| Ligand | Solvent | $E_T$ (cm$^{-1}$) | $Q_{Nd}$ (%)[a] | $Q_{Yb}$ (%) | Refs. |
|--------|---------|---------|---------|---------|-------|
| H$_8$**38a** | dmf (Nd)[b] | 18 400 | 0.028 (0.053) | 0.095 | [c] |
| H$_8$**38b** | Ethanol (Yb) | 19 000 | 0.013 (0.027) | 0.086 | |
| H$_8$**38c** | | 18 800 | 0.043 (0.075) | 0.068 | |
| **38d** | | 19 500 | 0.026 (0.049) | 0.061 | |
| H$_8$**38e** | | 18 200 | 0.065 (0.107) | 0.037 | |
| **38f** | | 18 500 | 0.056 (0.084) | 0.033 | |
| **38g** | | 19 000 | 0.012 (0.026) | 0.026 | |
| H$_4$**39a** | dmf | | 0.080 | 0.120 | [d] |
| **39b** | | | 0.090 | 0.180 | |
| **39c** | | | 0.060 | 0.090 | |
| H$_4$**39d** | | 20 600–23 500 | 0.180 | 0.220 | |
| **39e** | | | 0.070 | 0.120 | |
| H$_2$**39f** | | | 0.240 | 0.610 | |

[a]Determined taking into account only the $^4F_{3/2} \rightarrow {}^4I_{11/2}$ transition (1.06 μm). Values in parentheses take into account
the two transitions $^4F_{3/2} \rightarrow {}^4I_{11/2}, {}^4I_{9/2}$.
[b]Whether measurements were performed in dmf or ethanol is not clear.
[c](Shevchuk et al., 1998b, 1999).
[d](Shevchuk et al., 1998a; Korovin and Rusakova, 2001).

lution and the maximum of metal-centered luminescence for macrocycles H$_8$**38a** and H$_8$**38b**
occurs when a 1:1 stoichiometric ratio is reached. The nature of the solvent has a large influ-
ence on the luminescence intensity, the best ones being dmf for the first complex and ethanol
for the second, with an approximate 12-fold increase in luminescence intensity over water.
The presence of the phenyl group in H$_8$**38a** is beneficial to the sensitization process and linear
relationships were obtained in the concentration ranges 0.1–10 μg ml$^{-1}$ and 0.5–5 μg ml$^{-1}$, for
H$_8$**38a** and H$_8$**38b**, respectively. The estimated detection limit for the Yb[III]/H$_8$**38a**/dmf system
is 0.09 μg ml$^{-1}$, but other Ln[III] ions interfere (Shevchuk et al., 1997). The quantum yields of
the Yb[III] complexes with the calix[4]resorcinarenes reported in fig. 37, which possess triplet
states between 17 700 and 19 500 cm$^{-1}$ as determined from the phosphorescence spectra of
the Lu[III] solutions, range from 0.026% for **38g** to 0.095% for H$_8$**38a** in ethanol (for a detailed
listing, see table 7). The influence of the various substituents is not clear, for instance the ex-
change of the phenyl group by a methyl group does not produce the same change in the pairs
H$_8$**38a/b**, **38c/e**, and **38d/f**, and surprisingly, the introduction of a bromine substituent in **38g**
decreases the quantum yield with respect to **38d**, possibly pointing to a sensitization mech-
anism involving the singlet state of the ligand since the presence of the bromine substituent
increases the efficiency of the isc process; as a consequence, the population of the singlet state
decreases. However, the reported quantum yields, measured on 10$^{-4}$ M solutions with respect
to [Zn(TPP)], should be considered with some care since the authors did not establish the
speciation in these solutions (Shevchuk et al., 1998b). A study conducted on Nd[III] solutions

Table 8

Partial quantum yields[a] of $Nd^{III}$ and quantum yields of $Yb^{III}$ luminescence upon ligand excitation (300 nm) in homo-
and hetero-bimetallic complexes with *p-tert*-butylcalix[8]arene in dmf, at room temperature (Korovin et al., 2000)

| Compound | $Q_{Nd}$ (%) | Compound | $Q_{Yb}$ (%) | Compound | $Q_{Nd}$ (%) | Compound | $Q_{Yb}$ (%) |
|---|---|---|---|---|---|---|---|
| $Nd_1Nd_1$ | 0.088 | $Yb_1Yb_1$ | 0.432 | $Nd_{1.8}Tb_{0.2}$ | 0.207 | $Yb_{1.95}Nd_{0.05}$ | 0.522 |
| $Nd_{1.8}Sm_{0.2}$ | 0.185 | $Yb_{1.9}Sm_{0.1}$ | 0.629 | $Nd_{1.5}Tb_{0.5}$ | 0.135 | $Yb_{1.9}Nd_{0.1}$ | 0.503 |
| $Nd_{1.5}Sm_{0.5}$ | 0.152 | $Yb_{1.8}Sm_{0.2}$ | 0.612 | $Nd_1Tb_1$ | 0.042 | $Yb_{1.8}Nd_{0.2}$ | 0.374 |
| $Nd_1Sm_1$ | 0.052 | $Yb_{1.5}Sm_{0.5}$ | 0.534 | $Nd_{0.2}Tb_{1.8}$ | 0.011 | $Yb_{1.8}Pr_{0.2}$ | 0.007 |
| $Nd_{1.8}Eu_{0.2}$ | 0.177 | $Yb_1Sm_1$ | 0.356 | $Nd_{1.8}Yb_{0.2}$ | 0.012 | $Yb_{1.8}Dy_{0.2}$ | 0.021 |
| $Nd_{1.5}Eu_{0.5}$ | 0.105 | $Yb_{1.8}Eu_{0.2}$ | 0.078 | $Nd_{1.5}Yb_{0.5}$ | 0.005 | $Yb_{1.8}Ho_{0.2}$ | 0.012 |
| $Nd_1Eu_1$ | 0.057 | $Yb_{1.8}Tb_{0.2}$ | 0.051 | $Nd_{0.2}Yb_{1.8}$ | 0.003 | | |
| $Nd_{0.2}Eu_{1.8}$ | 0.007 | $Yb_{1.5}Tb_{0.5}$ | 0.014 | | | | |

[a]Determined taking into account the two $^4F_{3/2} \rightarrow {}^4I_{11/2}, {}^4I_{9/2}$ transitions only.

led to similar conclusions with quantum yields in the range 0.026 to 0.107% (Shevchuk et
al., 1999). In addition, the number of bound dmf molecules in the inner coordination sphere
was assessed by measurement of the luminescence intensity in various dmf/dmf-$d_7$ mixtures;
it amounts to one for H$_8$**38a**, H$_8$**38b**, and **38g**, and to two for the other ligands.

The higher energy of the triplet states in calixarenes **39a–f** (fig. 37), 20 600–23 500 cm$^{-1}$,
allows sizeable sensitization of Eu$^{III}$ and Tb$^{III}$ luminescence. Compared with calix[4]resorcin-
arenes, better quantum yields are also obtained for the Nd$^{III}$ and Yb$^{III}$ 1:1 complexes (table 7),
0.06–0.24%, and 0.09–0.61%, respectively. However, the solvent is not the same, dmf as
compared to ethanol, which may explain the difference. As for the calix[4]resorcinarene com-
plexes, the speciation in solution has not been established, but in this case, the 1:1 complexes
have been isolated and gave satisfactory elemental analyses (Korovin and Rusakova, 2001;
Shevchuk et al., 1998a). The best quantum yields are obtained with H$_2$**39f** which bears two
phenylamide chromophores on the narrower rim and these substituents are directly coordi-
nated onto the lanthanide ion, which understandably increases the efficiency of the energy
transfer process.

When reacted with lanthanide nitrates in dmf or dmso in presence of a base such as tri-
ethylamine, *p-tert*-butylcalix[8]arene (H$_8$**40**) can host two different Ln$^{III}$ ions at a quite short
distance ($\approx$3.8 Å) by adopting a chair-like configuration (Bünzli et al., 2000). The mecha-
nism of energy transfer between Ln$^{III}$ ions can therefore be tested by inserting two different
metal ions in the macrocycle (Froidevaux and Bünzli, 1994). Korovin and coworkers have
synthesized two series of Nd$_{2-x}$Ln$_x$ (Ln = Nd, Sm, Eu, Tb, Yb) and Yb$_{2-x}$Ln$_x$ (Ln = Pr,
Nd, Sm, Eu, Dy, Ho, Yb) complexes with H$_8$**40** and determined the corresponding quantum
yields in dmf (table 8). The Nd$^{III}$ luminescence is enhanced by a factor 2–2.5 with respect
to [Nd$_2$(H$_2$**40**)(dmf)$_5$] by the presence of ions such as Sm$^{III}$, Eu$^{III}$, and Tb$^{III}$, when they are
in small quantity ($x = 0.2$). Increasing their molar fraction to 0.5 systematically lowers the
luminescence intensity and when $x = 1$, the luminescence intensity is smaller than the one
displayed by the homobimetallic species. On the other hand, Yb$^{III}$ acts as an efficient quencher
of the Nd$^{III}$ luminescence. In the case of Yb$^{III}$, most of the Ln$^{III}$ ions quench the $^2F_{5/2}$ lumi-
nescence, except Nd$^{III}$ ($x = 0.05–0.1$), Sm$^{III}$ ($x = 0.5–1.0$), and Tb$^{III}$ ($x = 0.2–0.5$) which
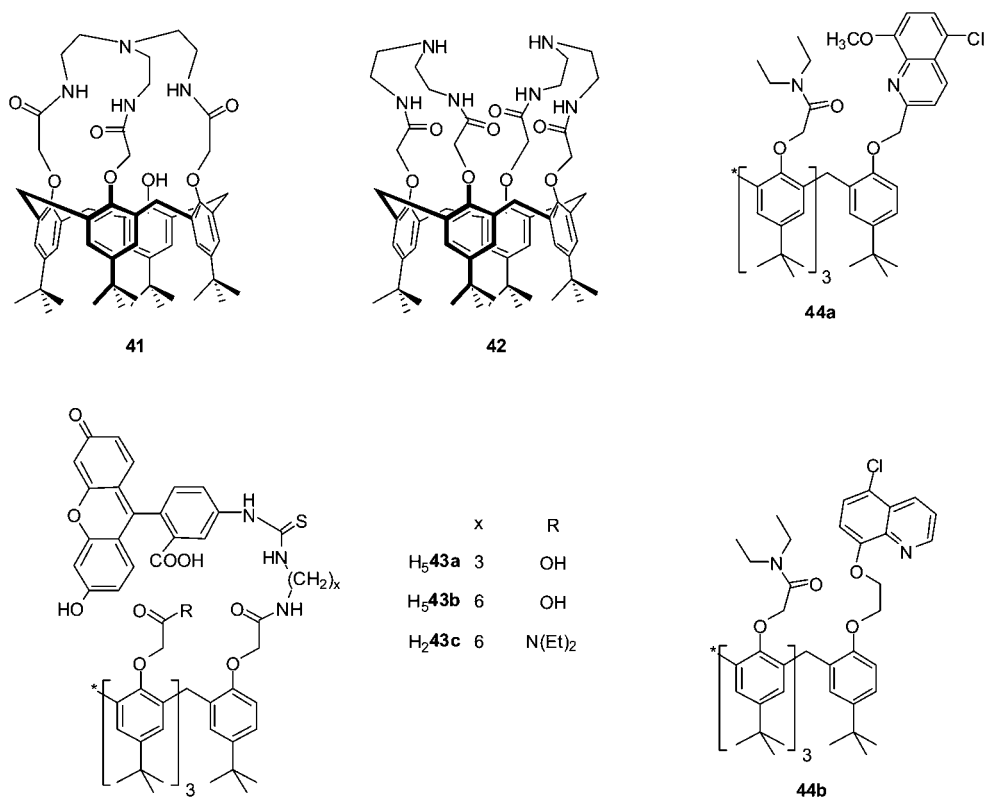
Fig. 38. Calix[4]azacrowns (top left), calix[4]arenes fitted with fluorescein (bottom left) and with chloroquinoline (top right, bottom right).

cause some enhancement. Both intra- and intermolecular energy transfers occur, the latter being less important as demonstrated by measuring the variation of the luminescence intensity in mixtures of homobimetallic complexes (Korovin et al., 2000).

The calix[4]azacrowns **41** and **42** (fig. 38), capped with aminopolyamide bridges bind $Ln^{III}$ ions and form both 1:1 and 1:2 (Ln:L) complexes with stability constants in the ranges $\log \beta_1 \approx 5$–6 and $\log \beta_2 \approx 10$–11 in acetonitrile for **42**, while the stability of the complexes with **41** is about two orders of magnitude smaller. Hydration numbers around 1 were found for the $Eu^{III}$ and $Tb^{III}$ complexes, but the ability of the ligands to sensitize $Ln^{III}$ luminescence is very weak, except in the $Tb^{III}$ complex with **42**. No $Er^{III}$ luminescence could be evidenced, but some $Nd^{III}$ emission was recorded, which is 12 times larger with ligand **42** than with receptor **41** (Oueslati et al., 2006).

To improve the photophysical properties of the calixarene receptors, the team of D. Reinhoudt has covalently grafted one adequate chromophore, fluorescein, on the narrower rim of calix[4]arene via either a propyl ($H_5$**43a**) or a hexyl ($H_5$**43b**) bridge; simultaneously strongly

coordinating carboxylic acid or diethylamide groups were introduced on the remaining three phenolic functions. In fact, receptors **43a–c** (fig. 38) were designed so that the resulting 1:1 complexes are sufficiently lipophilic and therefore can dissolve in organic solvents, a prerequisite for the preparation of thin films by spin-coating or for their introduction into polymer layers as active optical components.

The intrinsic triplet yield of fluorescein, which absorbs in the green part of the visible spectrum (515 nm), is only 2% but the presence of the lanthanide ion increases considerably the efficacy of the intersystem crossing rate. In complexes of the three NIR-emitting lanthanide ions with dtpa-fluorescein for instance, the fluorescence intensity of the chromophore is reduced by 65–85%, pointing to an enhanced isc process (Hofstraat et al., 1998). $Nd^{III}$ and $Yb^{III}$ luminescence is sensitized by exciting both at 310 (phenolic groups) and 515 nm (fluorescein), the latter excitation mode yielding more intense luminescence, while $Er^{III}$ only emits upon excitation of the fluorescein. Although $Yb^{III}$ luminescence is sensitized by both ligands $H_5$**43a** and $H_5$**43b**, the authors only fully tested $Nd^{III}$ and $Er^{III}$ complexes in both aerated and de-aerated methanol-$d_4$ and dmso because they were interested in developing devices for telecommunication purposes.[5] No significant change in luminescence intensity was detected upon removal of oxygen, which implies a strong interaction between the chromophore and the lanthanide ion, in line with a substantial red shift observed in the absorption spectrum of fluorescein upon complexation. Indeed, fluorescein contains a deprotonated carboxylic acid group under the experimental conditions used and can fold over the lanthanide ion and coordinate to it, protecting it from further solvent interaction. Moreover this observation allows one to estimate the rate of ligand to metal energy transfer being larger than $3 \times 10^8$ $s^{-1}$ in the two solvents. Lifetimes for the $Er^{III}$ complexes are 0.8–0.9 µs in methanol-$d_4$ and 1.6–1.7 µs in dmso. On the basis of the other measured photophysical properties (molar absorption coefficients, energy transfer rates, triplet yields), a rough calculation was made of the gain which may be reached using the calixarene-based materials as the medium for optical amplifiers. For a 2-µm core waveguide doped with the $Er^{III}$ calixarene complexes, a 1.7-dB $cm^{-1}$ gain would be obtainable with only 1.4-mW pumping, which would mean a significant improvement over inorganic glass-based Er-doped fiber amplifiers, despite the lifetimes being shorter by approximately three orders of magnitude. It is noteworthy that the length of the alkyl chain connecting fluorescein to the calix framework does not play a decisive role in the values of the lifetimes, but the overall luminescence is more intense for the $Nd^{III}$ complex with $H_5$**43a** compared to the one with $H_5$**43b**. Based on the only photophysical parameter reported, the $Nd(^4F_{3/2})$ lifetime, receptor **43c** appears to be less interesting than the two tricarboxylic ligands (Hofstraat et al., 1998; Wolbers et al., 1998a). In inorganic optical amplifiers, sensitization of the $Er^{III}$ luminescence is often achieved by co-doping $Yb^{III}$ in the matrix because this ion has a broad charge-transfer absorption band and, additionally, it efficiently transfers energy onto erbium. In organic matrices, the excitation efficiency of $Yb^{III}$ is largely increased by the antenna effect (by 3–4 orders of magnitude). Since calixarenes **43** (see fig. 38) were shown to be reasonably good hosts for $Er^{III}$ luminescence, the Dutch team at Twente has tried to combine both advantages by designing ditopic bis(calixarene) ligands with various coupling groups (fig. 39). Another motivation

---

[5] On the other hand, no NIR emission was detected for $Pr^{III}$.
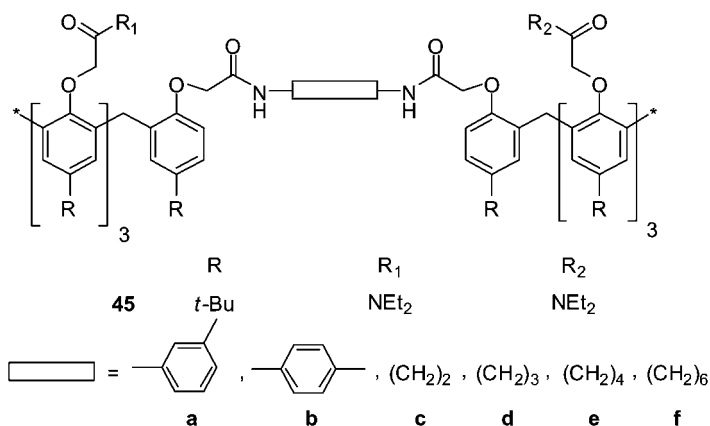
Fig. 39. Bis-calix[4]arenes (Wolbers et al., 1997a).
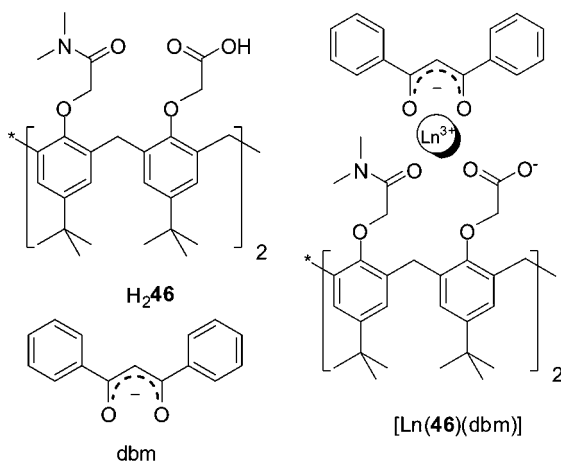


Fig. 40. Ternary complex with an amide-acid calixarene and dbm (Hebbink et al., 2001a).

was the study of metal-to-metal energy transfer, which was performed for [NdEu(**45b**)] in several solvents. The lifetime of the Eu($^5D_0$) level is shorter in the heterobimetallic NdEu complex than in the EuEu compound in chloroform, acetonitrile, and thf, which is indicative of a Eu$^{III} \rightarrow$ Nd$^{III}$ energy transfer. The yield of transfer, calculated as $100(1 - \tau_{obs}/\tau_0)$ where $\tau_0$ is the lifetime in absence of energy acceptor, i.e. in the EuEu compound, amounts to about 50–65% (Wolbers et al., 1997a).

Another chromophore, 8-alkoxy-5-chloroquinoline, was appended to the narrower rim of a calix[4]arene triamide, **44a** and **44b** (see fig. 38). If Nd$^{III}$, Er$^{III}$, and Yb$^{III}$ nitrates are added to acetonitrile solutions of these receptors, quenching of the methoxyquinoline luminescence oc-

curs and is accompanied by a sizeable increase in the metal-centered luminescence; however, no quantitative data were reported (Casnati et al., 2003).

Although this strategy has not been much tested, the appended chromophoric arm can be replaced by the formation of a ternary complex with an adequate strongly coordinating antenna, e.g. dibenzoylmethanate (fig. 40), as seen previously for cyclen-based complexes. Deuterated dichloromethane solutions of [Ln(**46**)(dbm)] (Ln = Nd, Er, Yb) exhibit the typical emission spectra of these ions upon excitation of the dbm antenna at 360 nm. Lifetimes are in the microsecond range, 0.9, 1.3, and 12.5 μs for $Nd^{III}$, $Er^{III}$, and $Yb^{III}$, respectively (Hebbink et al., 2001a).

## 3.2. *Acyclic ligands*

### 3.2.1. *Beta-diketonates and related chelates*

From the first synthesis of rare-earth $\beta$-diketonates in 1897 by Urbain until now, hundreds of different complexes formed by reaction between $Ln^{III}$ ions and $\beta$-diketone derivatives have been described in the literature. Interest for this type of complexes comes from their potential application in numerous and diverse domains. These complexes can be used for example as extractants in solvent–solvent extraction processes or as active compounds for the development of chelate lasers or liquid lasers. But they can also find applications in NMR as shift reagents or as electroluminescent materials in organic light-emitting diodes (OLEDs) (Binnemans, 2005b).

In presence of lanthanide ions, $\beta$-diketonates generally form neutral tris complexes, [Ln($\beta$-diketonate)$_3$], the delocalization of the negative charge of the ligand leading to the formation of stable six-membered chelate rings. Since lanthanide ions frequently adopt coordination numbers of 8 or 9 in solution, the coordination sphere of the lanthanide ion in these six-coordinate complexes is not complete. Therefore the presence of one or several molecules of solvent in the first coordination sphere is often observed, giving complexes of general formula [Ln($\beta$-diketonate)$_3$(solv)$_n$], with solv = $H_2O$, dmf, dmso and $n = 1$–3. Stable ternary complexes [Ln($\beta$-diketonate)$_3$(L)$_n$] can also be formed in presence of bidentate ($n = 1$) Lewis bases (L) such as 2,2′-bipyridine or 1,10-phenanthroline, or monodentate ($n = 2$) ones such as triphenylphosphine oxide (tppo) or tri-$n$-octylphosphine oxide (topo). Additionally, apart from tris complexes, tetrakis complexes with general formula [Ln($\beta$-diketonate)$_4$]$^-$ can be obtained in which the lanthanide ion is surrounded by four $\beta$-diketonate ligands and which are more luminescent than the tris complexes.

As it is well known, sensitization of Ln-centered luminescence can be achieved via an intramolecular energy transfer upon excitation of organic ligands, instead of using direct excitation of the weak $Ln^{III}$ absorption bands. This phenomenon now called "antenna effect" or "luminescence sensitization" has first been observed in 1942 by Weissman for europium(III) complexes formed with salicylaldehyde and with $\beta$-diketonates, more particularly benzoylacetonate (ba, **48a**), dibenzoylmethanate (dbm, **48b**) and *meta*-nitrobenzoylacetonate (**47a**, fig. 41) (Weissman, 1942).

At the end of the 1950's, Crosby and Kasha reported the rather exceptional case of near-infrared luminescence of trivalent ytterbium ion in an 1:3 (Ln:L) chelate occurring after intramolecular energy transfer between the organic ligand, in this case dbm (**48b**), and the lan-

R$_1$ = CH$_3$, R$_2$ = m-C$_6$H$_5$NO$_2$ (**47a**)

R$_{1,2}$ = CH$_3$ (acac, **47b**), CF$_3$ (hfa, **47c**)

        tC$_4$H$_9$ (dpm, **47d**)

R$_1$ = tC$_4$H$_9$, R$_2$ = CF$_3$ (**47e**)

R$_1$ = CH$_3$, R$_2$ = CF$_3$ (**47f**)

R$_1$ = CH$_3$, R$_2$ = C$_3$F$_7$ (**47g**)

R$_1$ = tC$_4$H$_9$, R$_2$ = C$_3$F$_7$ (fod, **47h**)

R$_1$ = (C$_2$H$_5$)$_2$CH, R$_2$ = C$_3$F$_7$ (**47i**)

R$_1$ = CF$_3$, R$_2$ = anthryl (**47j**)

R$_{1,2}$ = (**47k**)

R$_1$ = (47l) R$_2$ =

R$_1$ = R$_2$ = C$_6$H$_5$ (**47m**)

R$_1$ = N-(CH$_2$)$_4$O-*  R$_2$ = C$_6$H$_5$ (**47n**)

R$_1$ = t-Bu-  R$_2$ = (47o)

R =   CH$_3$ (ba, **48a**), C$_6$H$_5$ (dbm, **48b**)

        CF$_3$ (btfa, **48c**), C$_3$F$_7$ (**48d**)

        C$_6$F$_{13}$ (**48e**), C$_8$F$_{17}$ (**48f**)

        CF$_3$OCF$_2$ (**48g**), CF$_3$O(CF$_2$)$_2$ (**48h**)

        C$_3$F$_7$OCF(CF$_3$) (**48i**)

        CF$_3$O(CF$_2$)$_3$OCF(CF$_3$) (**48j**)

R =   CF$_3$ (**49a**, tta), C$_3$F$_7$ (**49b**)

        C$_6$F$_{13}$ (**49c**), CF$_3$OCF$_2$ (**49d**)

        C$_3$F$_7$OCF(CF$_3$) (**49e**)

Fig. 41. $\beta$-Diketonate ligands.

thanide ion. At 77 K, in a 1:1:1 mixture of ethyl ether, isopentane, absolute ethanol and under excitation in the absorption band of the $\beta$-diketonate at 365 nm, an intense luminescence emission at 971 ± 4 nm corresponding to the $^2F_{5/2} \rightarrow {}^2F_{7/2}$ transition of the Yb$^{III}$ ion was observed. The efficiency of the intramolecular energy transfer is quite remarkable given that the triplet $^3\pi\pi^*$ state of the chelate lies at 20 500 cm$^{-1}$, that is at about 10 000 cm$^{-1}$ above the $^2F_{5/2}$ acceptor level of the Yb$^{III}$ ion (Crosby and Kasha, 1958). This opened new perspectives in the understanding and determination of ligand-field effects in Yb$^{III}$ complexes. Indeed, until this work, emission spectra were most of the time unavailable for ytterbium so that only the splitting of the upper $^2F_{5/2}$ level could be determined. Ligand-field calculations are easily achievable with tris($\beta$-diketonates), the symmetry around the ion being well defined. As a consequence new calculations performed by Perkins showed good agreement

between the experimentally observed Yb$^{III}$ energy levels and those calculated according to the electrostatic ligand-field theory (Perkins and Crosby, 1965). After these first studies, interest in $\beta$-diketonate complexes emitting near-infrared light died out until Meshkova and her Ukrainian research group published a series of works at the end of the 1980's and beginning of the 1990's. At this time determination of lanthanide impurities in compounds of other lanthanides became necessary since high-purity lanthanide compounds were extensively used in advanced materials.

Determination of lanthanide ions with a fairly low detection limit of $10^{-5}$–$10^{-6}$ wt% is achieved with Ln$^{III}$ $\beta$-diketonates. Relying on this fact new, rapid, selective, and highly sensitive analytical methods essentially based on the luminescence properties of these complexes have been developed. After a preliminary work on Sm$^{III}$ and Eu$^{III}$ chelates (Topilova et al., 1989), interest focused on NIR-emitting lanthanides, more particularly on Nd$^{III}$ and Sm$^{III}$ ions since they are often present as impurities in lanthanide oxides. A first study dealt with the determination of trace amounts in europium oxide using thenoyltrifluoroacetonate (tta, **49a**, fig. 41) and diantipyrylpropylmethane, dapm, see fig. 44 below (Meshkova and Rusakova, 1990). Mixing these ligands with lanthanide ions in ethanol yields 1:3:1 (Ln:tta:dapm) complexes which are precipitated and put into suspension in a 0.5% solution of gelatin. Under excitation in the absorption bands of tta or dapm at 340 or 270 nm, respectively, luminescence is observed at 878 and 903 nm for Nd$^{III}$ ($^4F_{3/2} \rightarrow {}^4I_{9/2}$ transition) and at 950 nm for Sm$^{III}$ ($^4G_{5/2} \rightarrow {}^6F_{5/2}$ transition). In order to obtain a better sensitivity the Eu$^{III}$ luminescence has to be masked, the band at 820 nm ($^5D_0 \rightarrow {}^7F_6$) being quite close to the Nd$^{III}$ $^4F_{3/2} \rightarrow {}^4I_{9/2}$ transition. One way to achieve this consists in reducing Eu$^{III}$ into Eu$^{II}$, which is not luminescent in this spectral range, using Jones reducing agent since other lanthanides are not reduced with amalgamated zinc. However Eu$^{II}$ is quite sensitive to traces of oxygen and it is necessary to stabilize the europium ion in its bivalent oxidation state. For this purpose the authors suggested to isolate Eu$^{II}$ ions from the solution by addition of sulfate and precipitation of EuSO$_4$. Optimizing the different parameters, such as solution pH, contact time with the reducing agent, and sulfate ion concentration finally allowed to reach detection limits of $3.2 \times 10^{-4}$ and $2.2 \times 10^{-4}$ wt% for Nd$^{III}$ and Sm$^{III}$, respectively. A series of fluorine-containing $\beta$-diketonates, with an ether function in the fluorinated alkyl chain (**48d**, **48g–i** and **49b**, **49d**, **49e**) were synthesized to improve the detection limit of Nd$^{III}$ in lanthanide sesquioxides Ln$_2$O$_3$ (Ln = Y, La, Gd, Lu). By analyzing the $^4F_{3/2} \rightarrow {}^4I_{11/2}$ (1.06 μm) transition of Nd$^{III}$ in complexes formed with ligands **48g**, **48h**, or **49d** and dapm, a detection limit of $5 \times 10^{-5}$ wt% was achieved. A complete study of the photophysical properties of a large series of this kind of Nd$^{III}$ $\beta$-diketonates was also performed (Topilova et al., 1991).

Meshkova et al. have investigated the influence of the substituents grafted on ligands **47b**, **c**, **e**, **g**, **i**, **48a–h**, and **49a**, **b**, **d**, **e** on the optical characteristics of Nd$^{III}$ in tris $\beta$-diketonates and related ternary complexes with 1,10-phenanthroline or other organic bases (Meshkova et al., 1992b; Rusakova et al., 1992b; Rusakova et al., 1992a). Samples were measured as suspensions in aqueous ethanol containing 0.5% of gelatin to stabilize the suspended particles. The luminescence properties of the Nd$^{III}$ complexes, namely intensities, quantum yields, and lifetimes increase in going from symmetrical to asymmetrical $\beta$-diketonates. For example the quantum yield of the tris complex with symmetrical dbm (**48b**) is 0.031% whereas replac-
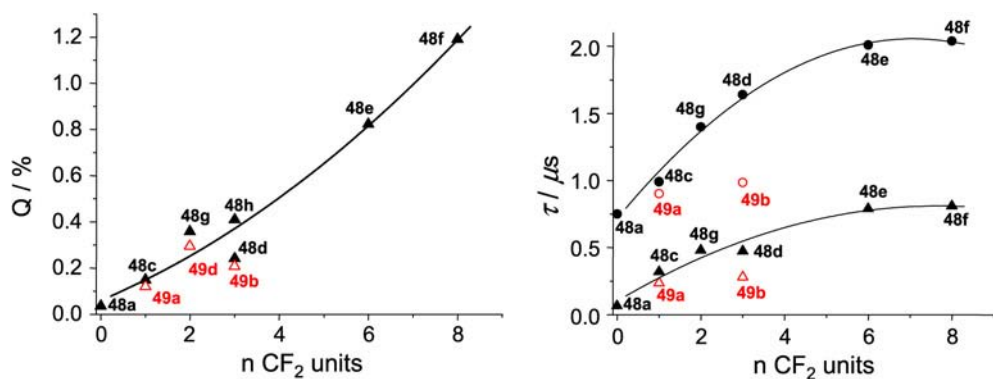
Fig. 42. (Left) Partial luminescence quantum yields ($^4F_{3/2} \rightarrow {}^4I_{11/2}$ transition) of $Nd^{III}$ tris($\beta$-diketonates). (Right) Luminescence lifetimes of tris and ternary $Nd^{III}$ complexes as a function of the fluorinated radical chain length. Filled and opened triangles stand for tris complexes with benzoylacetonate and thienylacetonate derivatives, respectively; filled and opened circles for the corresponding ternary complexes formed with phen.

ing one phenyl with a $CH_3$ (**48a**) or a $CF_3$ (**48c**, btfa) group gives quantum yields of 0.036 and 0.149%, respectively. The same trend is observed when fluorine-containing ligands are used compared to non-fluorinated ones. Additional enhancement of the luminescence quantum yields and lifetimes can be achieved by lengthening the chain of the fluorinated residue, as can be visualized on fig. 42 for benzoyl and $\alpha$-thienyl acetonate derivatives. However branching of the fluorinated chains, even if they are lengthened, causes a decrease in the spectroscopic properties of the complexes; a potential explanation is the steric hindrance becoming considerable and resulting in a lengthening of the Ln–O bonds and consequently in a weaker $Nd^{III}$–diketonate interaction.

Moreover $\beta$-diketonates featuring an aryl residue, in this case a phenyl group, have better luminescent properties than the corresponding complexes with alkyl or thienyl substituents. This arises from the additional stabilization brought by the formation of a single $\pi$-electronic conjugation chain between the aryl ring and the six-member ring of the enolic tautomer. Another way to enhance the luminescent characteristics of these complexes consists in introducing an oxygen atom, that is, an ether function, in the fluorinated radical chain. This effect can be explained by the flexibility of the C–O–C bond ensuring better shielding of the central ion from quenching action of water molecules. An alternative hypothesis tested was the coordination of a fluorine atom belonging to the terminal trifluoromethyl group. However, conformational analysis of $La^{III}$ and $Nd^{III}$ perfluoro-$\beta$-diketonates done both by molecular mechanics calculations and by NMR spectroscopy clearly showed no evidence of additional coordination of a fluorine atom (Meshkova et al., 1998). As a consequence, the increase in luminescence properties of $Ln^{III}$ $\beta$-diketonates with the elongation of the fluorinated radical chain was explained by the enhanced lipophilicity of these ligands, which form a highly hydrophobic shell around the $Ln^{III}$ ion, thus eliminating strong luminescence quenchers such as OH oscillators, both from the inner and outer coordination spheres. This assumption was

Table 9
Luminescence properties (lifetimes and intrinsic quantum yields) of $Nd^{III}$ $\beta$-diketonates
with dbm derivatives ($\tau_0(Nd) = 0.25$ ms)

| Complex | $\tau$ ($\mu$s) | $Q_{Nd}^{Nd}$ (%) |
|---|---|---|
| [Nd(dbm)$_3$(phen)] | 0.707 (62.9%) | |
| | 21.5 (37.1%) | 8.6 |
| [Nd(dbm)$_3$(bath)] | 0.670 (52.3%) | |
| | 20.2 (47.7%) | 8.1 |
| [Nd(**47n**)$_3$(bath)] | 0.803 (28.6%) | |
| | 14.0 (71.4%) | 5.60 |
| [Nd(**47k**)$_3$(bath)] | 0.845 (11.6%) | |
| | 24.5 (88.4%) | 9.81 |
| [Nd(**47m**)$_3$(bath)] | 0.864 (7.8%) | |
| | 24.2 (92.2%) | 9.69 |
| [Nd(**47o**)$_3$(bath)] | 0.994 (6.7%) | |
| | 24.9 (93.3%) | 9.95 |

confirmed with fluorinated ligands possessing much higher lipophilicity and lower surface tension than the corresponding un-fluorinated $\beta$-diketonates.

In an effort to sensitize $Nd^{III}$ and $Er^{III}$, J.G. Kang and coworkers have designed the asymmetrical $\beta$-diketonate **47j** (fig. 41) bearing an anthracene antenna. In dmf, the fluorescence of the latter has a quantum yield of 3.62% in the $Gd^{III}$ tetrakis compound [Gd(**47j**)$_4$]$^-$, which is drastically reduced to 0.89 and 1.70% in the $Nd^{III}$ and $Er^{III}$ complexes, indicating energy transfer onto these ions. Indeed, NIR emission is seen, with lifetimes equal to 0.83 $\mu$s ($Nd^{III}$) and 1.53 $\mu$s ($Er^{III}$). Similar effects are observed in chloroform and 2-methyltetrahydrofuran (Nah et al., 2006). Recently, L.F. Yang et al. studied a series of novel $\beta$-diketonates formed with dbm derivatives, featuring functionalized aromatic moieties (see fig. 41, ligands **47k**–**47o**) (L.F. Yang et al., 2006). The absorption spectra of the free ligands measured in $CH_2Cl_2$ display strong absorption bands between 300–400 nm, attributed to intramolecular $\pi$–$\pi^*$ transition. The absorptions of the dbm derivatives are red-shifted compared to the 342 nm band of dbm, the largest shift (about 33 nm) being observed for ligands **47m** and **47o**, due to the extended conjugation system. This additional conjugation is also responsible for the lowering of the singlet state energy of the ligands from 433 nm for dbm to 507 nm for **47o**. However, in the case of ligand **47n**, introduction of a donor carbazole group on the dbm framework through a flexible chain does not influence the $\pi$ system of the molecule. Phosphorescence spectra of the $Gd^{III}$ complexes allowed the determination of the triplet states energy, which is between 20 410 and 18 520 cm$^{-1}$.

All the ternary $Nd^{III}$ complexes, [Nd($\beta$-diket)$_3$(bath)], formed with these ligands and with bath (monobathophenanthroline) exhibit the characteristic metal-centered NIR luminescence. The photophysical properties of these chelates are compared to those of [Nd(dbm)$_3$(phen)] in table 9.

All the luminescence decays are biexponential, but since the complexes are quite hygroscopic, the shortest lifetime has been attributed by the authors to hydrated species and therefore only the longer lifetime has been taken into consideration. The longest lifetime is ob-

2-acetyl-1,3-indandione                2-benzoyl-1,3-indandione
            (aid)                                      (bid)
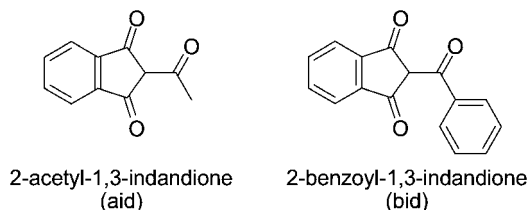
Fig. 43. Cyclic $\beta$-diketones.

served for [Nd(**47o**)$_3$(bath)] with a value of 24.9 µs, which is almost 2-fold larger than the smaller one, 14.0 µs, observed for [Nd(**47n**)$_3$(bath)].

Measurements on complexes formed with cyclic $\beta$-diketones (fig. 43) demonstrated that for identical molar absorption coefficient values, higher luminescence intensities were observed for cyclic $\beta$-diketonates compared to aliphatic ones. This indicates a more efficient energy transfer to the Nd$^{III}$ ion on account of the rigid structure of these cyclic $\beta$-diketonates in which the central ion is well shielded from interaction with water molecules.

To complete the study on Nd$^{III}$ $\beta$-diketonates, ternary complexes formed with various organic bases (fig. 44) have also been considered. Addition of a second ligand results in all cases in an enhancement of the luminescence properties compared to the corresponding tris complexes since water molecules are removed from the first coordination sphere of the Ln$^{III}$ ion. For example, lifetimes are 2–3 times longer when 1,10-phenanthroline is used as ancillary ligand (fig. 42). Luminescence intensities are also enhanced, up to 6-fold, depending on the organic base used. However this increase is less important for $\beta$-diketonates containing long fluorinated alkyl chains or for cyclic ligands because of their higher lipophilicity. Changes occurring in luminescence intensities as a function of the nature of the organic base acting as ancillary ligand (fig. 44) have been investigated and the luminescence enhancements observed in going from tris to ternary complexes are summarized on fig. 45 for the most representative $\beta$-diketonates (see fig. 41 for formulae).

The solvent also influences the luminescence intensity and the largest enhancement was achieved with dmso or dmf, which are known to coordinate strongly to Ln$^{III}$ ions and thus favor the removal of water molecules from the first coordination sphere. Smaller enhancements were observed when ethanol or a protic solvent was used. The amount of solvent used for producing the suspensions is also crucial and the authors showed that the maximal luminescence intensity occurs for a concentration of the solvent of 20 vol%, above which the suspension decomposes thus leading to decreasing intensities.

In summary, this series of studies on Nd$^{III}$ $\beta$-diketonates demonstrate that luminescence properties are enhanced when the fluorinated chain is lengthened. As a consequence, attempts have been made to use the benzoylacetonate derivatives **48e** and **48f** in luminescence determination of lanthanides in order to improve the sensitivity of the method. Luminescence intensities for Nd$^{III}$ and Yb$^{III}$ chelates formed with **48e** and **48f** are higher by a factor 1.2–1.6 than those observed for the ternary complexes formed with tta and phen. Although highly sensitive detection of Nd$^{III}$ and Yb$^{III}$ can also be achieved using tris complexes only, ternary
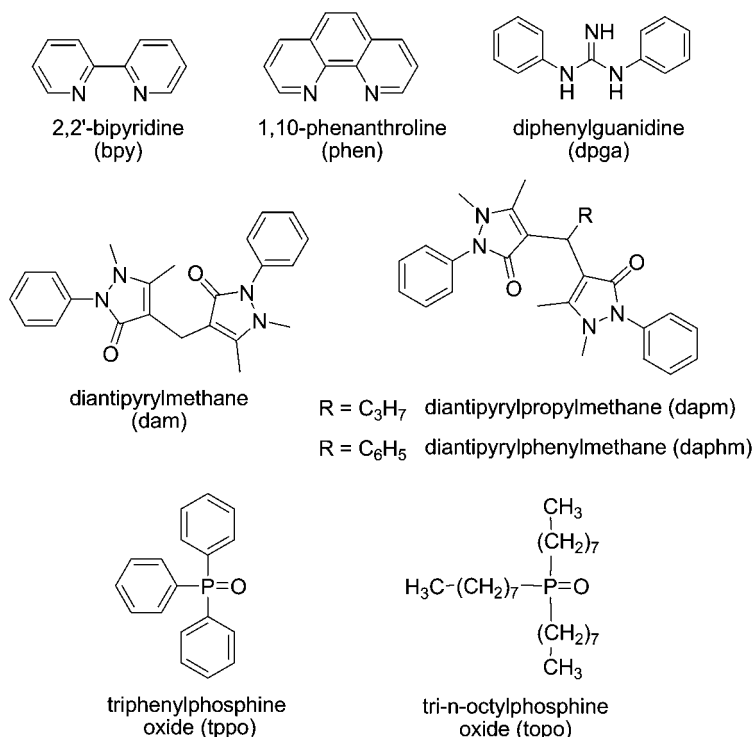
Fig. 44.  Organic bases used as second ligand in ternary $\beta$-diketonate complexes.
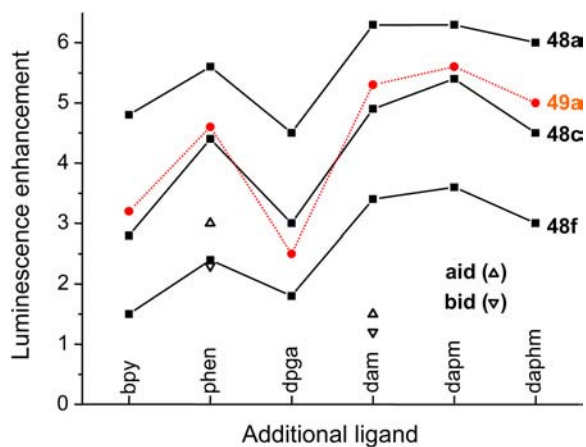


Fig. 45.  Enhancement factors of the luminescence intensity between some tris($\beta$-diketonates) and their corresponding ternary complexes.
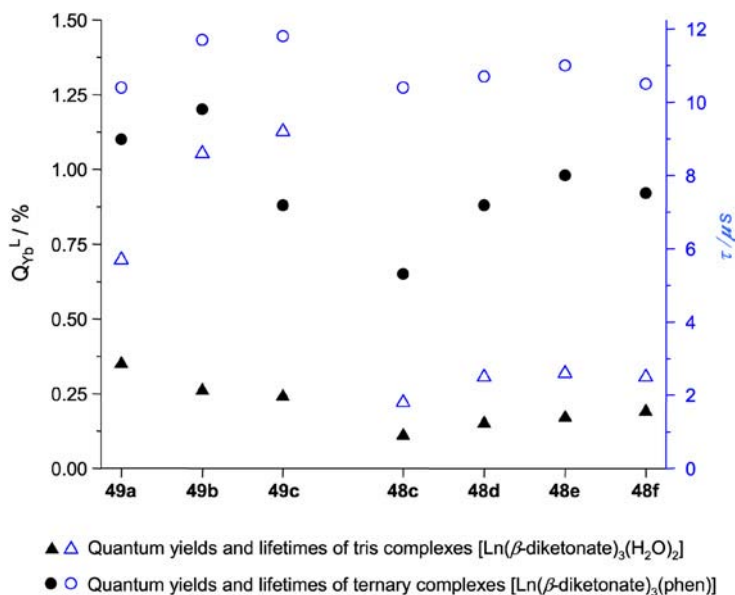
Fig. 46. Quantum yields (▲, ●, left scale) and lifetimes (△, ○, right scale) of Yb$^{III}$ $\beta$-diketonates in toluene.

complexes are preferentially used. Detection limits are as low as $3 \times 10^{-5}$ and $7 \times 10^{-5}$ wt% for Nd$^{III}$ and Yb$^{III}$, respectively (Meshkova et al., 1997).

The luminescence properties of Yb$^{III}$ $\beta$-diketonates generally parallel the trends observed for Nd$^{III}$ complexes. For instance, an increase in luminescence intensity was observed in going from thienyl to benzoyl derivatives, from fluorine-free to fluorine-containing $\beta$-diketonates and in this case with increasing fluorinated alkyl chain length. However replacement of a CF$_2$ unit with an ether function leads to a small decrease of the luminescence intensity contrary to what was observed for Nd$^{III}$ chelates. Adding dmso or dmf to the suspension also results in sizeable increase in luminescence intensity. When compared to Nd$^{III}$, however, the Yb$^{III}$ complexes seem to be more stable since concentration of dmso or dmf can be increased up to 80 vol% before partial decomposition of the suspended complexes. Studies on ternary complexes were also performed and the luminescence enhancement observed in going from tris to ternary complexes is similar to what was reported for their Nd$^{III}$ analogs. The greatest enhancement was observed for the complex formed with **48c** and topo, the ratio $I_{\text{ternary}}/I_{\text{tris}}$ reaching seven (Bol'shoi et al., 1997; Topilova et al., 1997).

This work was followed by a more detailed study including determination of quantum yields and lifetimes for the Yb$^{III}$ $\beta$-diketonates formed with fluorinated benzoyl (**48c–j**, fig. 41) and thienyl (**49a–e**) derivatives of acetylacetonate and for their corresponding ternary complexes with phen (Meshkova et al., 1999; Tsvirko et al., 1999). Complexation of 1,10-phenanthroline induces 3- to 6-fold increases in quantum yields, which amount to 0.11–0.35% for the tris complexes while they reach 0.65–1.20% for the ternary complexes (fig. 46). A par-
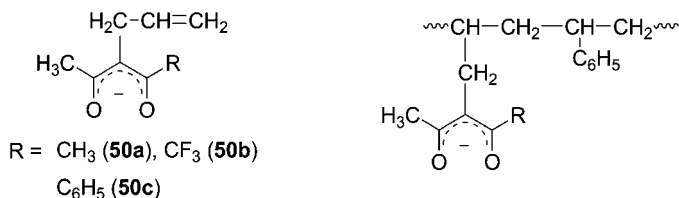
Fig. 47. Allyl-derivatized $\beta$-diketonates (left) and copolymer formed with styrene (right).

allel evolution is observed for the lifetimes, as expected since lifetimes increase when phenanthroline is used as second ligand. However the increase is less important in complexes with thienyl derivatives, for which enhancement factors of 1.5–1.8 were observed, compared to enhancement factors of 4–6 for benzoyl derivatives. Analysis of these data (fig. 46) gives useful information about the role played in deactivation processes by the main and secondary ligands. As seen in section 2.5, the sensitization efficacy of the ligand can be written as:

$$\eta_{\text{sens}} = Q_{\text{Ln}}^{\text{L}} \cdot \frac{\tau_{\text{rad}}}{\tau_{\text{obs}}}. \tag{11a}$$

Assuming $\tau_{\text{rad}} \approx 1$ ms (see table 5) the authors estimate $\eta_{\text{sens}} > 0.6$. As a consequence, the low quantum yield values are explained mainly by deactivation of the $Yb^{\text{III}}$ excited state occurring through high-frequency vibrational modes of both ligand and solvent. In order to minimize these vibrational deactivations, allyl derivatives **50a–c** (fig. 47) of ligands **47b**, **47f**, and **48a** (fig. 41) have been synthesized and luminescence intensities of $Nd^{\text{III}}$ and $Yb^{\text{III}}$ complexes have been studied either in their monomeric form or in their co-polymeric form with styrene or methylmethacrylate (MMA) (Meshkova, 2000).

It turned out that incorporation of tris complexes into the polymeric chain is difficult, the predominant complex then becoming the less luminescent 1:2 (Ln:L) species. Despite this, the luminescence intensities in $Nd^{\text{III}}$ and $Yb^{\text{III}}$ complexes attached to styrene are one order of magnitude higher than those observed in solutions of tris complexes formed with the corresponding $\beta$-diketonates, derivatized or not. This can be explained by the rigid structure of the copolymer and also by the important decrease in the energy losses due to thermal deactivations, the molecular mass of the $Ln^{\text{III}}$ copolymers being significantly larger when compared to the tris complexes. Compound $[Ln(\mathbf{50c})_3\text{-styrene}]_n$ displays the best luminescence with an intensity 2–5 times higher with respect to the corresponding diketonates with **50a** and **50b**. Such copolymeric compounds can be useful for the luminescence determination of lanthanides in highly quenching environments. To fully understand the nonradiative deactivation processes occurring in $Yb^{\text{III}}$ $\beta$-diketonates, the luminescence characteristics of dibenzoylmethanate and thenoyltrifluoroacetonate, as well as their deuterated analogs dbm-$d_1$ and tta-$d_1$ (fig. 48) were studied in toluene and partly in carbon tetrachloride and dmso-$d_6$ (Tsvirko et al., 2001). Complexes of general formula, $[Yb(\beta\text{-diketonate})_3(H_2O)_2]$ are formed in solvents with low coordinating ability like toluene, the two water molecules remaining in the first coordination sphere of the metal ion. The contribution of these water molecules to nonradiative deactiva-
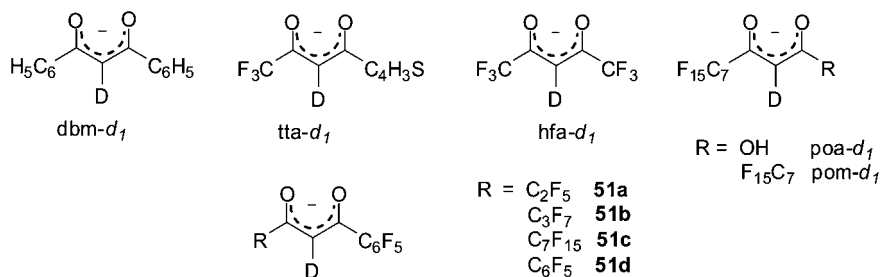
Fig. 48. Some deuterated $\beta$-diketonates.

tion considerably exceeds the total contribution of all the other de-activating groups. This is why little or no increase in luminescence is observed upon deuteration of the central CH group of the ligands. On the other hand, the replacement of $H_2O$ by $D_2O$ in tris $Yb^{III}$ complexes with tta (**49a**, fig. 41) leads to a $\approx$1.5-fold increase in the luminescence quantum yield, demonstrating that the exclusion of the water molecules from the inner coordination sphere is essential for optimized luminescence properties. This can be easily achieved (i) by using a solvent like dmso or better, dmso-$d_6$, with much superior coordinating properties towards $Ln^{III}$ ions than toluene, (ii) by forming ternary complexes through the addition of an organic base, like 1,10-phenanthroline or trioctylphosphine oxide. Following the first strategy, using dmso-$d_6$ as solvent instead of toluene, yielded [Yb($\beta$-diketonate)$_3$(dmso-$d_6$)$_2$] complexes with quantum yields 18–32 times larger than the hydrated complexes. For example [Yb(tta)$_3$(H$_2$O)$_2$] has a quantum yield of 0.12% and a lifetime of 1.19 μs, whereas the respective values for [Yb(tta)$_3$(dmso-$d_6$)$_2$] are 2.14% and 27.3 μs. Such an increase was also observed in presence of phen but to a lesser extent, with quantum yield and lifetime for [Yb(tta)$_3$(phen)] reaching 1.60% and 15.8 μs, respectively.[6]

Once water molecules are removed, deuterating the central C–H group of the $\beta$-diketone further increases the quantum yields and lifetimes by approximately 17% in the ternary complexes. Another source of nonradiative deactivation that should not be neglected comes from diffusing solvent molecules in the second sphere which contain high-frequency C–H vibrations. As a consequence, replacement of toluene with carbon tetrachloride leads to a further slight increase in the luminescence lifetimes of [Yb(dbm-$d_1$)$_3$(phen)] and [Yb(tta-$d_1$)$_3$(phen)] (table 10).

Nonradiative deactivation of the Yb($^2F_{5/2}$) excited state occurs through vibrational states of surrounding molecular groups. Since the contributions of these molecular groups to the overall nonradiative deactivation rate constant are known to be additive, the following equation can be written:

$$\frac{1}{\tau_{obs}} = k^{rad} + k^{nr} \approx k^{rad} + k(\text{diket}) + k(\text{CH, CD}) + k_\alpha + k_\beta, \tag{27}$$

---

[6] The same authors had previously reported different values for [Yb(tta)$_3$(H$_2$O)$_2$] ($Q^L_{Yb} = 0.35\%$, $\tau = 6.7$ μs) and [Yb(tta)$_3$(phen)] ($Q^L_{Yb} = 1.11\%$ , $\tau = 10.4$ μs) (Meshkova et al., 1999; Tsvirko et al. 1999, 2001).

Table 10
Quantum yields and lifetimes of the $^2F_{5/2} \rightarrow {}^2F_{7/2}$ transition of Yb$^{III}$ in $\beta$-diketonate complexes (Tsvirko et al., 2001)

| Complex | dbm | | tta | |
| --- | --- | --- | --- | --- |
| | $Q_{Yb}^L$ (%) | $\tau$ (µs) | $Q_{Yb}^L$ (%) | $\tau$ (µs) |
| [Yb($\beta$-diketonate)$_3$(H$_2$O)$_2$][a] | 0.023 | 1.0 | 0.12 | 1.16 |
| [Yb($\beta$-diketonate)$_3$(phen)][a] | 0.59 | 10.3 | 1.60 | 15.8 |
| [Yb($\beta$-diketonate-$d_1$)$_3$(phen)][a] | 0.69 | 12.1 | 1.86 | 18.6 |
| [Yb($\beta$-diketonate-$d_1$)$_3$(phen)][b] | 0.69 | 13.6 | 2.14 | 22.8 |
| [Yb($\beta$-diketonate)$_3$(dmso-$d_6$)][c] | 0.73 | 17.4 | 2.14 | 27.3 |
| [Yb($\beta$-diketonate-$d_1$)$_3$(dmso-$d_6$)][c] | 1.26 | 30.1 | 6.10 | 71.8 |

[a]Solution in toluene.
[b]Solution in CCl$_4$.
[c]Solution in dmso-$d_6$.
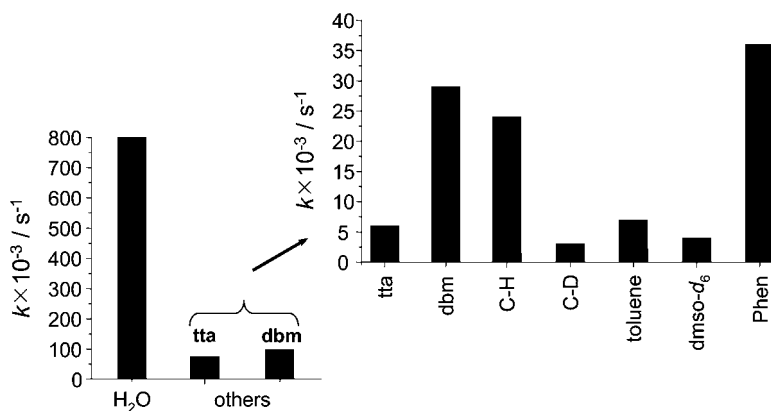


Fig. 49. Nonradiative deactivation rate constants of Yb$^{III}$ ion in tris or ternary $\beta$-diketonate complexes for various molecular groups (Tsvirko et al., 2001).

where $k^{rad}$ is the radiative rate constant for the $^2F_{5/2} \rightarrow {}^2F_{7/2}$ transition while the rate constants for nonradiative deactivation are denoted as follows: $k$(diket) is associated with the $\beta$-diketonate anions, except for the central CH group, $k$(CH) and $k$(CD) correspond to deactivation through vibrations from the central CH and CD bonds; finally, $k_\alpha$ is the rate constant associated with neutral ligands or solvent molecules L coordinated to the central ion, and $k_\beta$ includes contributions from solvent molecules in the second coordination sphere. Making use of the data reported in table 10 and assuming $k^{rad} \approx 1000$ s$^{-1}$, Tsvirko et al. have been able to estimate the different contributions of each molecular groups (fig. 49). It is noteworthy that the contribution of coordinated water molecules ($k_{H_2O}^{nr} \approx 8 \times 10^5$ s$^{-1}$) greatly exceeds the total contribution of all remaining molecular groups ($k_{tot}^{nr} \approx 7.3 \times 10^4$ s$^{-1}$ for [Yb(tta)$_3$phen]

or $9.6 \times 10^4$ s$^{-1}$ for [Yb(dbm)$_3$phen] in toluene. The next largest contribution comes from the $\beta$-diketonates themselves, with tta quenching less ($k_{\text{diket}} + k_{\text{CH}} = 3 \times 10^4$ s$^{-1}$) than dbm ($5.3 \times 10^4$ s$^{-1}$).

Thus if one wants to improve the overall quantum yield of $\beta$-diketonate complexes, removal of coordinated water molecules is absolutely necessary. By means of the estimated nonradiative deactivation rate constants, calculations showed that removal of these water molecules allows one to reach a maximum quantum yield of 2.6% in toluene for the Yb$^{\text{III}}$-tta complex. However, water molecules are usually replaced with a coordinating secondary ligand, such as phenanthroline, which also contributes to the nonradiative deactivation ($k_{\text{phen}} \approx 3.6 \times 10^4$ s$^{-1}$), but to a much lesser extent than water molecules. Further improvement can be reached by deuteration of the central C–H group in the $\beta$-diketonate: in [Yb(tta-$d_1$)$_3$(phen)] for instance, deactivation due to C–H oscillators occurs eight times faster when compared to C–D oscillators.

By taking advantage of the keto–enol equilibrium, [Yb(hfa-$d_1$)$_3$] was prepared in methanol-$d_4$ and its luminescence properties were determined in several solvents, methanol-$d_4$, thf-$d_8$, PO(OMe)$_3$, and dmso-$d_6$. Emission intensity is the largest in the latter solvent, by a factor 2.5 with respect to deuterated methanol and the Yb($^2$F$_{5/2}$) lifetime reaches 66 μs, as compared to 10 μs in methanol-$d_4$ (Kim and Park, 2003).

Further enhancement of luminescence properties is possible through halogenation of the C–H group. With this improvement, the maximum theoretical quantum yield achievable (without water molecules and secondary ligand) is 14%, corresponding to a Yb($^2$F$_{5/2}$) lifetime of 140 μs (Tsvirko et al., 2001).

Quenching of the Er($^4$I$_{13/2}$) luminescence by O–H and C–H vibrations has been quantified for tris and tetrakis complexes with hexafluoroacetylacetonate (hfa) presenting various degrees of hydration and deuteration (Winkless et al., 2006). Hydrated [Er(hfa)$_3$(H$_2$O)$_2$], Cs[Er(hfa)$_4$] and Cs[Er(hfa)$_4$] dissolved in CD$_3$OD show single exponential decay with lifetimes of 100 ns, 1.8, and 1.6 μs, respectively. When [Er(hfa)$_3$(H$_2$O)$_2$] is dried under vacuum (1 mbar), the decay becomes bi-exponential with associated lifetimes of 132 ns (17%) and 1.8 μs (83%), demonstrating the large effect of O–H vibrations. The lifetime of the tetrakis complex is still quite short and reflects the quenching effect of the four C–H oscillators which are at a distance of about 4.7 Å from the erbium ion. When this compound is almost fully deuterated (98%), its decay is bi-exponential, with lifetimes of 11 μs (96.4%) and 106 μs (3.64%). The latter is assigned to ions with no hydrogen atoms in their coordination sphere and surrounded by nearest neighbour molecules with no hydrogen atoms. The population analysis based on the contribution of the two exponential to the fluorescence decay points to Er$^{\text{III}}$ sites for which the 160 nearest hydrogen atoms are fully deuterated, that is to Er$^{\text{III}}$ sites surrounded by 40 fully deuterated [Er(hfa)$_4$]$^-$ entities. This corresponds to a fully deuterated shell with 20 Å diameter. This figure is comparable to the one calculated for Er$^{\text{III}}$ 8-hydroxyquinolinates by the "continuous medium approximation" (Quochi et al., 2006), about 30 Å.

Kazakov and coworkers determined the influence of water on the luminescence of [Ln($\beta$-diketonate)$_3$(H$_2$O)$_2$] in toluene (Ln = Nd, Sm, Tb, Dy, and Yb) (Voloshin et al., 2000c; Voloshin et al., 2000d). Addition of water quenches the NIR luminescence of the Nd$^{\text{III}}$ and

Yb[III] chelates with ligands **48c** and **49a** whereas the opposite effect, i.e. an enhancement of the luminescence, is observed for the corresponding Sm[III] complexes and for Tb[III] diketonates with **47b** and **48c**. This behavior was explained by significant concentration quenching due to formation of dimers $[Ln(\beta\text{-diketonate})_3(H_2O)_n]_2$ occurring at high concentrations of chelate. These dimers have lower luminescence properties compared to monomers since quenching is caused by deactivation of the ligand excited state before the L → Ln energy transfer and by cross-relaxation in the Ln[III] ions. Addition of water causes dissociation of the poorly luminescent dimers to give more luminescent monomers.

The effect of fluorination of the alkyl chains of deuterated $\beta$-diketonates, as well as of the deuterated solvent on Nd[III] luminescence is described in several papers and the main results are reported in table 11. Generally speaking, the more fluorine substituents on the alkyl chains, the largest the intrinsic quantum yield $Q_{Nd}^{Nd}$, e.g. the series acac-$d_1$–hfa-$d_1$–pom-$d_1$ in dmso-$d_6$ for which the quantum yield increases from 0.8 to 1.1, and 3.2%, respectively. Some care has to be exercised in interpreting these data since values for the same compound may vary widely. This is demonstrated by $Q_{Nd}^{Nd}$ data for hfa-$d_1$ in thf-$d_8$ which varies from 0.5 to 1.5% depending on the authors. One reason could be concentration at which measurements have been carried out. Too low a concentration leads to dissociation of the complex, while larger concentration induces quenching. For instance, Y. Hasegawa and collaborators have shown that the quantum yield of $[Nd(pom\text{-}d_1)_3]$ in dmso-$d_6$ is fairly constant at ≈3.2% in the concentration range $1–7 \times 10^{-2}$ M while it drops to ≈1.2% for a 0.3 M solution. Similarly, the quantum yield of $[Nd(hfa\text{-}d_1)_3]$ in the same solvent drops from 2.5% for a $10^{-2}$ M solution to 0.6% at 0.5 M, a range overlapping the values reported in table 11. For the systems tested, concentration quenching occurs through collisions and is therefore diffusion controlled. Assuming pure dipole–dipole interaction of the colliding molecules, the estimated critical distance for 50% transfer, $R_0$, is 11.7 Å, while the average distance between molecules in a 0.1 M solution is around 14 Å (Hasegawa et al., 1996b). Thus the large emission efficiency of the pom chelate is due to the suppression of cross relaxation as nonradiative energy transfer by maintaining the distance between Nd[III] ions at the limit of the diffusional collision. As far as solvents are concerned, dmso-$d_6$ is the best, the quantum yield in this medium being at least two times larger than in the other tested solvents. A last point of interest is the comparison between symmetrical and asymmetrical ligands, the latter having the tendency to induce a stronger luminescence. The improvement in quantum yield is relatively modest when asymmetry arises from different fluorinated alkyl chains grafted on the acac substrate or when it is closer to the inner coordination sphere of the metal ion, compare for instance symmetric pom-$d_1$ with asymmetric poa-$d_1$. However, in the latter case, the oscillator strength of the hypersensitive transition is 2.5 times higher, so that the solution is more luminescent (Iwamuro et al., 1998). It is noteworthy that tetrakis chelates have much larger $\Omega_2$ parameter than tris analogs (cf. data for btfa); the corresponding parameter for $[Er(btfa)_4]^-$ amounts to $26.1 \times 10^{-20}$ cm$^2$ and simulations on $[Sm(btfa)_4]^-$ dissolved in methylmethacrylate, a precursor of PMMA, demonstrate the feasibility of an optical amplifier working at 650 nm, a wavelength corresponding to the absorption minimum of PMMA. Based on the data collected, a gain of 20 dB is predicted for a 60-cm fiber (Koeppen et al., 1997).

Table 11
Judd–Ofelt parameter $\Omega_2$, Nd($^4F_{3/2}$) lifetimes and quantum yields of various fluorinated tris($\beta$-diketonates). See fig. 48 for ligand formulae

| Diketonate | Solvent | $\Omega_2$ ($10^{-20}$ cm$^2$) | $\tau$ ($^4F_{3/2}$) (μs) | $Q_{Nd}^{Nd}$ (%)[a] | $Q_{Nd}^{L}$ (%)[b] | Refs. |
|---|---|---|---|---|---|---|
| acac-$d_1$ | dmso-$d_6$ | 22.2 | 3.3 | 0.8 | n.a. | c,d |
| tfa-$d_1$ | dmso-$d_6$ | 19.1 | 5.7 | 1.1 | n.a. | c |
| hfa-$d_1$ | acetone-$d_6$ | 16.3 | 1.71 | 0.4 | n.a. | c,d,e |
| | methanol-$d_4$ | 14.8 | 0.70 | ≈0.1 | n.a. | c,e |
| | thf-$d_8$ | 17.5 | 2.33 | 0.5 | n.a. | c,e |
| | | 23.8 | 1.9 | 0.7 | n.a. | g |
| | | 23.8 | 2.1 | 1.51 | 0.30 (20) | f |
| | dmf-$d_7$ | n.a | 2.86 | 0.6 | n.a. | c,e |
| | dmso-$d_6$ | 9.2 | 6.3 | 1.1 | n.a. | c,e |
| btfa[h] | acetone-$d_6$ | 61.6 | 417[i] | n.a. | n.a. | j |
| pom-$d_1$ | methanol-$d_4$ | 2.2 | 1.6 | 0.7 | n.a. | c |
| | dmso-$d_6$ | 1.4 | 14.5 | 3.2 | n.a. | c |
| poa-$d_1$ | methanol-$d_4$ | 22.3 | 1.4 | 0.7 | n.a. | g |
| | acetone-$d_6$ | 18.0 | 1.7 | 0.8 | n.a. | g |
| | thf-$d_8$ | 19.3 | 2.5 | 0.8 | n.a. | g |
| **51a** | thf-$d_8$ | 26.5 | 2.7 | 1.34 | 0.30 (22) | f |
| **51b** | thf-$d_8$ | 26.9 | 2.4 | 1.29 | 0.30 (23) | f |
| **51c** | thf-$d_8$ | 30.4 | 4.5 | 1.70 | 0.42 (25) | f |
| **51d** | thf-$d_8$ | 31.3 | 2.8 | 1.44 | 0.52 (35) | f |

[a]Intrinsic total quantum yield ($^4F_{3/2} \rightarrow {}^4I_J$, $J$ = 9/2, 11/2, 13/2) under excitation at 585 nm.
[b]Quantum yield upon ligand excitation (350–395 nm), $\eta_{sens} = 100 \times Q_{Nd}^{L}/Q_{Nd}^{Nd}$ in parentheses.
[c](Hasegawa et al., 1998).
[d](Hasegawa et al., 1996c).
[e](Hasegawa et al., 1996a).
[f](Iwamuro et al., 2000b).
[g](Iwamuro et al., 1998).
[h]Tetrakis chelate.
[i]Radiative lifetime.
[j](Koeppen et al., 1997).

Sulfur-containing asymmetric $\beta$-diketonates, such as mono-thio-thenoyltrifluoroacetonate (stta, **52**, fig. 50), give intensely colored, air and moisture stable complexes [Ln(stta)$_3$(tppo)$_2$] (Ln = Nd, Yb) which emit in the near-infrared (Voloshin et al., 2001b). However thio substitution results in lower thermal stability and lower luminescence efficiency for Nd$^{III}$ and Yb$^{III}$ chelates when compared to the diketonates obtained with the non-sulfonated analog tta. Despite this, the advantage of stta chelates lies in their ability to sensitize Ln$^{III}$ emission with visible blue light (465 nm) whereas the corresponding tta complexes have to be excited with UV light.

Bis(perfluoroalkylsulfonylaminates) bear some resemblance with diketonates and their Nd$^{III}$ complexes with alkyl chain length ranging from 1 to 8 have been measured in deuterated acetone and dmso, as well as in un-deuterated acetone. While all these complexes
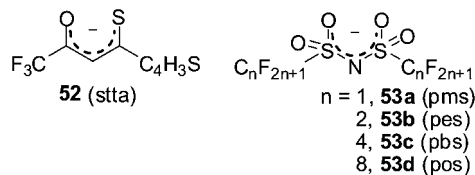
Fig. 50. Mono-thio-thenoyltrifluoroacetonate (stta) and bis(perfluoroalkylsulfonyl)aminate.

have identical quantum yield of 3.3% in dmso-$d_6$, [Nd(pos)$_3$] (fig. 50) is the most luminescent in acetone-$d_6$ ($\tau = 13$ μs, $Q_{\mathrm{Nd}}^{\mathrm{Nd}} = 3.2\%$) and un-deuterated acetone ($\tau = 12$ μs, $Q_{\mathrm{Nd}}^{\mathrm{Nd}} = 3.0 \pm 0.5\%$), the order of the quantum yields being [Nd(pos)$_3$] > [Nd(pbs)$_3$] > [Nd(pes)$_3$] > [Nd(pms)$_3$]. The identical quantum yields (and lifetimes) in dmso-$d_6$ most probably arise from the replacement of the ligands with dmso molecules. Coordination of three pos ligands to Nd$^{\mathrm{III}}$ builds a relatively symmetric environment around the metal ion, so that Judd–Ofelt parameter $\Omega_2$ is small, $0.1 \times 10^{-20}$ cm$^2$ (Hasegawa et al., 2000; Yanagida et al., 2000a).

Strong erbium luminescence with a full-width at half-maximum of 100 nm is also generated by the ternary complex [Er(pos)$_3$phen] upon excitation in the ancillary ligand band at 333 nm. With respect to direct Er$^{\mathrm{III}}$ excitation into the $^2$H$_{11/2}$ level at 520 nm, the photoluminescence signal increases by a factor 20 (Van Deun et al., 2004b).

Very few studies are available on the near-infrared luminescence of praseodymium diketonates in solution. One of these deals with the influence of the ligand triplet state energy on the luminescence of the Pr$^{\mathrm{III}}$ chelates formed with ligands **47b**, **d**, **h**, **48c**, and **49a** (Voloshin et al., 2001a). For Pr$^{\mathrm{III}}$, emission can take place from three different levels, $^3$P$_0$ (green), $^1$D$_2$ (red and NIR) and $^1$G$_4$ (NIR); in addition some papers report luminescence from $^3$P$_1$ as well. On the other hand, emission from $^1$G$_4$ is rarely seen in solution, contrary to solid state, as shown for the trinitrate [Pr(NO$_3$)$_3$(X$_2$O)$_6$] (X = H, D) in dmso and dmso-$d_6$ which emits light only from $^3$P$_1$, $^3$P$_0$, and $^1$D$_2$ (Sveshnikova and Timofeev, 1980). The studied $\beta$-diketonates can be classified into three groups depending on the energy of the triplet state $E(^3\pi\pi^*)$, larger, approximately equal, or smaller than $E(^3$P$_0)$. Chelates formed with ligands **47b**, **d**, and **h** belong to the first group ($E(^3\pi\pi^*) > {}^3$P$_0$) and as a consequence they emit blue and red light from both $^3$P$_0$ and $^1$D$_2$ excited states. The second group includes ligand **48c** which fulfils the condition $E(^3\pi\pi^*) \approx E(^3$P$_0)$ and displays very weak luminescence from this excited state which is depopulated by metal-to-ligand energy back transfer. However red and near-infrared emission from unquenched $^1$D$_2$ state is clearly observed at 605, 890, and 1060 nm. The energy corresponding to the latter band also matches the energy of the $^1$G$_4 \rightarrow {}^3$H$_4$ transition, but the assignment could not be ascertained. The chelate with ligand **49a** belongs to the third group, $E(^3$P$_0) > E(^3\pi\pi^*) \geqslant E(^1$D$_2)$. Excitation of [Pr(**49a**)$_3$(H$_2$O)$_2$] at 365 nm results in red and near-infrared luminescence of Pr$^{\mathrm{III}}$ originating only from the $^1$D$_2$ level. In dmso, luminescence in the near-infrared is more intense than the red luminescence, with partial quantum yields of <0.18% (1060 nm) and 0.006% (605 nm). It results from this study that emission

of $Pr^{III}$ in organic chelates from two and/or one excited state(s) can be tuned by choosing a ligand with a triplet state having the appropriate energy relative to the $^3P_0$ and $^1D_2$ levels.

In an attempt to sensitize $Er^{III}$ luminescence by partial energy transfer from $Yb^{III}$, these two ions have been co-crystallized in a 1:1 ratio to yield $[Er_{1/2}Yb_{1/2}(\mathbf{47c})_3(tppo)_2]$. The molar ratio Er:Yb has been ascertained by energy dispersion X-ray spectroscopy and their photophysical properties were studied in reference to those of their monometallic analogs, $[Er(\mathbf{47c})_3(tppo)_2]$ and $[Yb(\mathbf{47c})_3(tppo)_2]$ (Zhong et al., 2006). The luminescence measurements have been performed at room temperature on bulk microcrystalline powders under excitation at 355 nm. At this wavelength, tppo does not absorb much, so that one can consider that the excitation energy goes mainly into the hfa levels. The triplet state of the latter is located at 22 200 cm$^{-1}$ and is almost resonant with the $Er^{III}$ $^4F_{5/2}$ (22 100 cm$^{-1}$), $^4F_{7/2}$ (20 400 cm$^{-1}$), and $^2H_{11/2}$ (19 100 cm$^{-1}$) levels, which ensures a sizeable energy transfer efficiency. Erbium emission at 1530 nm is effectively observed in pure $[Er(\mathbf{47c})_3(tppo)_2]$ and is enhanced in the Er–Yb co-crystallized complex (about two to three-fold), with a concomitant decrease of the $Yb^{III}$ luminescence intensity at 980 nm when compared to $[Yb(\mathbf{47c})_3(tppo)_2]$. Therefore, $Yb^{III}$ contributes to the $Er^{III}$ emission by energy transfer from the $Yb(^2F_{5/2})$ level to (probably) the resonant $Er(^4I_{11/2})$ excited state. Due to the larger absorption cross-section of $Yb^{III}$ ions at 980 nm compared to $Er^{III}$, a usual method to improve the pumping efficiency of $Er^{III}$ ions consists in using an Yb-based 980 nm semiconductor laser diode (LD). Thus excitation of the Er–Yb co-crystallized complex at 980 nm with an LD source also exhibited significant near-infrared luminescence enhancement (two to three-fold) for the $Er^{III}$ ion with respect to the pure monometallic complex. In fact indirect excitation of the $Er^{III}$ ions occurs via energy transfer from the $^2F_{5/2}$ level of the $Yb^{III}$ ion to the $^4I_{11/2}$ $Er^{III}$ level, before subsequently decaying to a lower level, $^4I_{13/2}$, from which near-infrared emission takes place ($^4I_{13/2} \rightarrow {^4I_{15/2}}$ transition). However the efficiency of this process is modest, as demonstrated by lifetime measurements. All luminescence decays obtained under excitation at 355 nm proved to be single exponential functions from which $Yb(^2F_{5/2})$ lifetimes equal to 89.1 and 83.7 μs could be extracted for $[Yb(\mathbf{47c})_3(tppo)_2]$ and co-crystalline $[Er_{1/2}Yb_{1/2}(\mathbf{47c})_3(tppo)_2]$, respectively, while the lifetime of $Er(^4I_{13/2})$ remains the same at ≈61 μs. Using eq. (4a), the slight decrease in $Yb^{III}$ lifetime translates into an efficiency of about 6% only for the Yb → Er energy transfer. Calculated quantum yields of 0.43 and 0.44% for $Er^{III}$ and 4.5 and 4.2% for $Yb^{III}$, in pure and co-crystallized complexes, respectively, were obtained using eq. (7) with radiative lifetimes of 14 ms ($Er^{III}$) and 2 ms ($Yb^{III}$).

So far in most of the afore-mentioned studies the $\beta$-diketonates played the role of both coordination and sensitization unit. This is also true for the second ligand in ternary complexes, but this ligand may be more specifically designed so that the photophysical functionality becomes more important. Apart from the widely used phenanthroline, luminescence sensitization has been achieved using organic dyes with large absorption cross sections. One example is Nile red (fig. 51), which reacts with $\beta$-diketonates $[Ln(\mathbf{47h})_3(solv)]$ (Ln = Er, Yb) in benzene yielding NIR luminescent solutions (Werts et al., 1999b).

Another example is IR5 with a triplet state energy at ≈7700 cm$^{-1}$ closely matching the acceptor $^4I_{13/2}$ level of the $Er^{III}$ ion at 6500 cm$^{-1}$ (H.S. Wang et al., 2004). Moreover, excitation in the near-infrared spectrum is compatible with optical communication applications based on
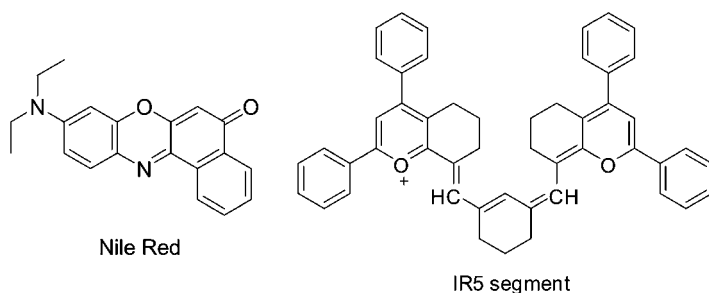
Fig. 51. Organic dyes used in ternary $\beta$-diketonate complexes.

silica fibers, in which a 980 nm semiconductor laser diode is typically used as pumping source. In view of the involved organic synthesis procedures needed to obtain an IR5-functionalized ligand, the authors decided in favor of ternary complexes formed by ion association of an anionic tetrakis $\beta$-diketonate, in this case [Er(**47c**)$_4$]$^-$, with the IR5 basic dye which possesses a large cationic segment (fig. 51). Luminescence of a bulk powdered sample of [Er(**47c**)$_4$IR5] has been studied at two different wavelengths using as excitation sources, an Ar$^+$ laser with (488 nm) and a 980 nm semiconductor LD. Upon excitation at both wavelengths two-fold and ten-fold luminescence enhancements were observed when compared to the parent anionic K[Er(**47c**)$_4$] complex, respectively. Indirect excitation mechanisms for the investigated complex are deduced to be mainly $^1S_2 \rightarrow {}^1S_1 \rightarrow {}^3T_1 \rightarrow Er^{III}(^4I_{13/2})$ for 488 nm excitation and $^1S_1 \rightarrow {}^3T_1 \rightarrow Er^{III}(^4I_{13/2})$ for 980 nm excitation. In the former case, $^1S_2$ deactivates to $^1S_1$ rather than to $^3T_2$ since the internal conversion $S_2 \rightarrow S_1$ takes place extremely fast compared to the intersystem crossing from $^1S_2$ to $^3T_2$. Regarding the interest for applications in telecommunications, the efficient sensitization of the Er$^{III}$ luminescence in [Er(**47c**)$_4$IR5] complex pumped at 980 nm let foresee its possible incorporation into polymers or hybrid inorganic–organic matrices for the fabrication of planar amplifiers. Use of a long-wavelength source for excitation is advantageous both for optical devices and medical imaging.

On the other hand, highly luminescent ternary complexes formed with bpy or phen can only be excited by UV radiation. To circumvent this drawback, S. Faulkner and M.D. Ward (Shavaleev et al., 2003c) have synthesized new compounds in which the diimine ligand, 3,6-bis(2-pyridyl)tetrazine (bptz, fig. 52), plays simultaneously the role of a coordinating and sensitizing group. Contrary to other $N,N'$-bidentate ligands such as bpy and phen, the absorption maximum of the tetrazine unit lies at relatively low energy (18 200 cm$^{-1}$, $\approx$550 nm). In order to maximize the sensitization process, the chromophoric unit has been directly coordinated to the metal center, which is further bound to three thenoyltrifluoroacetonate anions. Reaction of the potentially bis-bidentate bridging ligand bptz with two equivalents of various Ln$^{III}$ complexes [Ln(tta)$_3$(H$_2$O)$_2$] (Ln = La, Nd, Gd, Er, and Yb) in aqueous ethanol yielded either monometallic complexes [Ln(tta)$_3$(bptz)] (Ln = La, Nd) or bimetallic entities [{Ln(tta)$_3$}$_2$($\mu$-bptz)] (Ln = Gd, Er, Yb) (fig. 52). It is not well understood yet why the larger lanthanides ions only give monometallic species while the smaller lanthanides give bimetallic complexes, since the stepwise binding constants corresponding to the association of one and
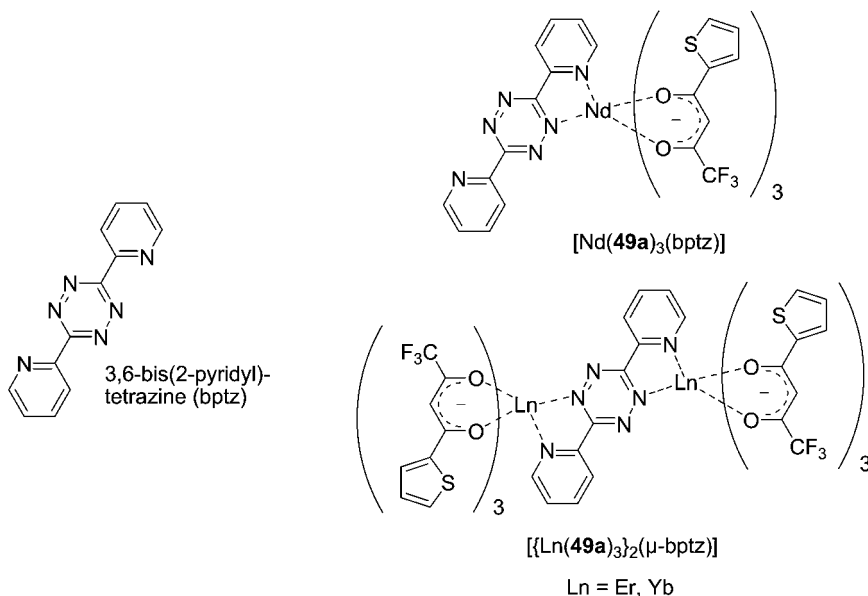
Fig. 52. Monometallic and bimetallic Ln[III] complexes formed with 2,6-bis(2-pyridyl)-tetrazine (bptz).

two Ln(tta)$_3$ units, respectively, are similar for La and Yb, amounting to ca. $K_1 = 10^6$ M$^{-1}$ and $K_2 = 10^5$ M$^{-1}$. Excitation of the complexes formed with near-infrared emitting Ln[III] ions has been performed both on tta and bptz ligands at 337 and 520 nm, respectively. For the Nd[III] monometallic complex in solution in CH$_2$Cl$_2$, single exponential decays were observed under both excitation wavelengths, with lifetimes amounting to 0.76 and 0.78 μs, respectively. This clearly indicates that the ternary complex does not dissociate in dichloromethane since excitation on the bptz ligand leads to NIR luminescence only if the complex [Nd(tta)$_3$(bptz)] remains intact. In solid state, absence of solvent-based quenching results in a longer lifetime ($\tau = 1.25$ μs).

Under excitation of the Er[III] and Yb[III] bimetallic complexes at 337 nm bi-exponential decays were obtained resulting from the dissociation of the bimetallic complex into the monometallic species. According to the binding constants, 11% dissociation is expected, but further dissociation yielding free bptz and [Ln(tta)$_3$(solv)] is also envisaged by the authors. Therefore three distinct luminescent species are present in solution; however the best fit is obtained using a two-component model indicating that bimetallic and monometallic complexes have similar lifetimes. For the Yb[III] ion the lifetimes are 13.3 and 1.0 μs. The longer-lived emission is assigned both to the bi- and monometallic complex and the shorter-lived emission to solvated Yb(tta)$_3$. The bimetallic Er[III] complex shows similar behavior, i.e. under 337 nm excitation a longer-lived emission (1.70 μs) corresponding to intact [{Er(tta)$_3$}$_2$(μ-bptz)] and to some [Er(tta)$_3$(bptz)] while the shorter lifetime (0.15 μs) is attributed to the solvated Er(tta)$_3$. The lifetimes of solid samples of [{Yb(tta)$_3$}$_2$(μ-bptz)] and [{Er(tta)$_3$}$_2$(μ-bptz)]
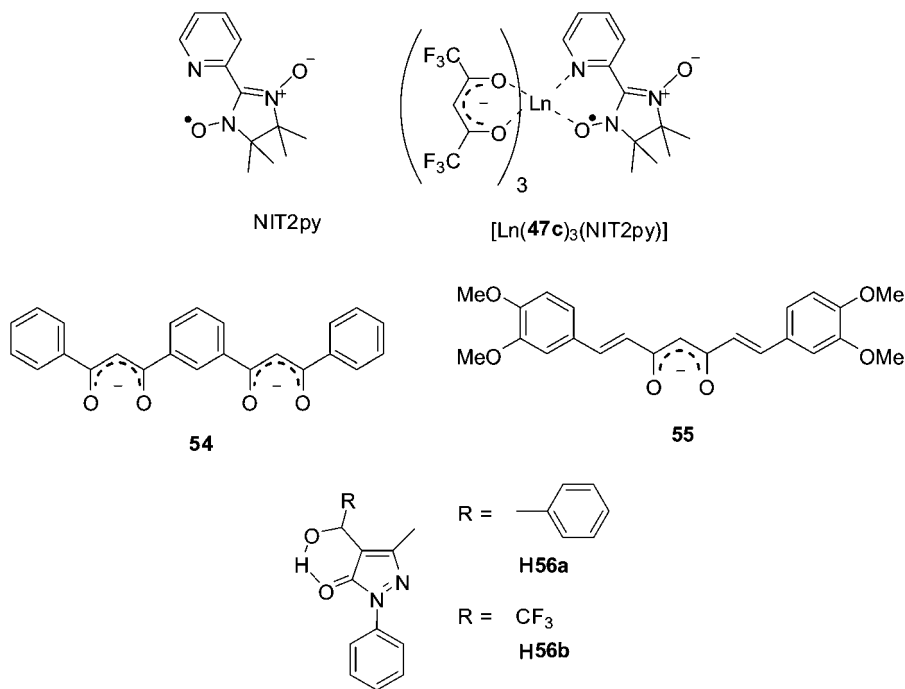
Fig. 53. (Top) Ligand 4,4,5,5-tetramethyl-2-(2′-pyridyl)-4,5-dihydro-1*H*-imidazol-1-oxyl-3-oxide (NIT2py) and its ternary complexes with hfa (**47c**). (Middle) Bis(diketonate) and non-phenolic derivatives of natural curcumin. (Bottom) Pyrazolones.

are 14.1 and 2.0 μs, respectively. Intrinsic quantum yields have also been calculated from the observed and radiative lifetimes (assumed to be 0.25, 14 and 2 ms, respectively) and amount to 0.3, 0.012, and 0.7% for $Nd^{III}$, $Er^{III}$, and $Yb^{III}$, respectively.

Recently, sensitization of the NIR luminescence of $Nd^{III}$, $Tm^{III}$, and $Yb^{III}$ was achieved through energy transfer from the single occupied molecular orbital $\pi^*$ (SOMO) of the nitroxide radical of ligand NIT2py (see fig. 53) (Kaizaki et al., 2005). This ligand was used as secondary ligand for the formation of ternary complexes $[Ln(\mathbf{47c})_3(NIT2py)]$ with trishexafluoroacetylacetonate chelates (Ln = Nd, Sm, Eu, Tm, Yb, and Lu) (fig. 53). In the solid state at 15 K, $Ar^+$ laser excitation (514.5 nm) of the $Nd^{III}$ and $Yb^{III}$ complexes leads to the observation of their typical NIR luminescence. More unusual is the NIR luminescence exhibited by the $Tm^{III}$ complex at $10\,000$ cm$^{-1}$ ($^3H_4 \rightarrow {}^3H_6$) and $12\,500$ cm$^{-1}$ ($^3F_3 \rightarrow {}^3H_6$). On the contrary, $[Eu(\mathbf{47c})_3(NIT2py)]$ only gives the intraligand doublet–doublet luminescence of the SOMO $\pi^*$ excited state, probably due to its lower lying position compared to the emissive 4f energy levels of $Eu^{III}$ ions.

So far only diketonates containing one binding site have been investigated. One way to increase the luminescence is to develop ligands containing multiple binding sites, such as

1,3-bis(3-phenyl-3-oxopropanoyl)benzene (H$_2$**54**, fig. 53) which consists in two conjugated benzoyl $\beta$-diketone sites linked by a 1,3-phenylene spacer (Bassett et al., 2004). Reaction of H$_2$**54** with LnCl$_3$·6H$_2$O in a 3:2 ratio in the presence of triethylamine leads to the formation of a single species, the triple-stranded helicates [Ln$_2$(**54**)$_3$·$n$H$_2$O] (Ln = Nd, Sm, Eu) with high molar absorption coefficients ($\approx$1.3 × 10$^5$ M$^{-1}$ cm$^{-1}$). Excitation in the ligand absorption band (358 nm) of a dmf-$d_7$ solution of [Nd$_2$(**54**)$_3$] yielded three narrow bands corresponding to the typical Nd$^{III}$ $^4$F$_{3/2}$ → $^4$I$_{9/2}$, $^4$I$_{11/2}$ and $^4$I$_{13/2}$ transitions. Analyzing the emission decay monitored at 1054 nm resulted in a lifetime of 1.5 μs which can be compared to the reported lifetime of 2.86 μs for [Nd$^{III}$(hfa)$_3$(solv)] in dmf-$d_7$ (Hasegawa et al., 1996a). Taking into account a radiative lifetime of 270 μs, the intrinsic quantum yield of the Nd$^{III}$ ion is 0.6%.

Lanthanide complexes formed with most of the $\beta$-diketonates, like acac, dbm or tta, have relatively high energy triplet excited states (20 000–25 000 cm$^{-1}$) compared to the principal emissive states of NIR emitting Ln$^{III}$ ions. In order to allow a better sensitization of Ln$^{III}$ luminescence, efforts have been made in the synthesis of ligands possessing triplet states that are more energetically suitable. Following this idea a non-phenolic analog of curcumin (**55**, fig. 53) was synthesized (Seltzer et al., 2005). Curcumin (bis(4-hydroxy-3-methoxyphenyl)-1,6-heptadiene-3,5-dione) is a natural product with an enolic form functionally similar to substituted $\beta$-diketonates in terms of metal complexation, but with more extensive $\pi$-electron conjugation and consequently longer wavelength absorption and lower triplet state energy ($\sim$14 000 cm$^{-1}$ for the enolate form in dioxane). Since the absorption spectrum of the non-phenolic curcuminoid in methanol solution is almost similar to the one of natural curcumin, the authors reasonably assume that the energy of the triplet states of **55** and curcumin are similar. Excitation of [Yb(**55**)$_3$(phen)] at 418 nm results in the typical Yb$^{III}$ emission. In order to determine if the sensitization occurs through an intramolecular energy transfer or via photo-induced electron transfer (PET) mechanism, the free enthalpy $\Delta G^0$ of the electron transfer reaction has been calculated and compared with the values obtained for tryptophan and dbm, for which PET mechanism is known to be favored. In the case of ligand **55**, fluorescence sensitization occurs exclusively through intramolecular energy transfer. It is also the case for the Nd$^{III}$ ternary complex since no divalent oxidation state is available for neodymium. Even if the phenanthroline unit is not involved in the sensitization process, excitation being performed at 418 nm, luminescence enhancement in going from the tris complex to the ternary compound is nevertheless observed because of the exclusion of water molecules from the first coordination sphere of the Ln$^{III}$ ion.

3.2.1.1. *Chemiluminescence (CL)* Chemiluminescence can be generated by decomposition of adamantylideneadamantane-1,2-dioxetane (aad), which is an energy-rich four-member cyclic peroxide. It decomposes into adamantanone, produced both as its singlet and triplet excited states. The resulting chemiluminescence spectrum consists of a broad-band extending from 350 to 550 nm, which overlaps the absorption spectrum of thenoyltrifluoroacetonate in [Ln(tta)$_3$(H$_2$O)$_2$] (Ln = Nd, Yb). Singlet–singlet energy transfer from adamantanone onto tta is followed by the usual energy migration to the triplet state of the $\beta$-diketonate and the 4f levels, so that NIR emission matching the photoluminescence spectra is observed in toluene (Voloshin et al., 2000b). The rate constants for the quenching of aad chemiluminescence are

$7.9 \times 10^9$ and $8.9 \times 10^9$ s$^{-1}$ for Nd$^{III}$ and Yb$^{III}$, respectively. Both the above-described intermolecular mechanism, as well as an intramolecular pathway in the ternary complex with aad which forms in solution, are responsible for the observation of NIR luminescence in these systems. Addition of water to the toluene solutions quenches the NIR luminescence, while it enhances the visible CL emission of the corresponding solution of Eu$^{III}$ and Tb$^{III}$ (Voloshin et al., 2000c). Neodymium and ytterbium tris(benzoyltrifluoroacetonates) display the same CL as tta complexes, although for Yb$^{III}$ its intensity is about 2.5 times lower than for the tta chelate. On the other hand, almost no CL is detected for acetylacetonate complexes (Voloshin et al., 2000a). Thermal or photochemical decomposition of aad also triggers CL from [Pr(dpm)$_3$] and Pr(fod)$_3$, both in the visible (from the $^3P_1$, $^3P_0$, and $^1D_2$ levels) and in the NIR at 850 nm ($^1D_2 \rightarrow {}^3F_2$ transition) and 1100 nm ($^1D_2 \rightarrow {}^3F_4$ transition). The excited chelate [Pr(fod)$_3$]$^*$ also initiates decomposition of aad by branched quantum chain reaction (Kazakov et al., 1998).

3.2.1.2. *Electroluminescence* Lanthanide $\beta$-diketonates are extensively used for the design of electroluminescent devices or for the development of optical amplifiers in telecommunications. These applications are not specifically reviewed here, but some of them will be presented in section 4.

3.2.1.3. *Pyrazolones* 4-Acyl-pyrazolones H**56** (fig. 53, bottom) are a class of heterocyclic ligands bearing similarities with $\beta$-diketonates. These ligands are mainly known as extractants for a variety of metals, including 4f-elements. Langmuir–Blodgett film-forming properties of A[Ln(**56a**)$_4$], where A = $N$-alkyl-4-(2-(4-(dimethylamino)phenyl)ethenyl)pyridinium and Ln = La, Nd, Dy, Yb are comparable to those of hemicyanine iodide but the lanthanide complexes display largely enhanced second-order hyperpolarizability as determined from second harmonic generation experiments (Huang et al., 1995). Attention was drawn to these lanthanide complexes in 1998, when it was demonstrated that the ternary Tb$^{III}$ complex with the 4-isobutyryl derivative and triphenylphosphine oxide (tppo) possesses a much higher green electroluminescence intensity than aluminum tris(8-hydroxyquinolinate), [Al(8-Q)$_3$] (Gao et al., 1998). Reaction of Ln(NO$_3$)$_3 \cdot x$H$_2$O with H**56a** and KOH in a 1:1 mixture of ethanol and water yields air-stable 8-coordinate tris complexes [Ln(**56a**)$_3$(H$_2$O)(EtOH)] for the entire lanthanide series. The Nd$^{III}$ compound crystallizes in the triclinic $P\bar{1}$ space group and the coordination environment of the metal ion is fairly close to a square antiprismatic geometry. A $5 \times 10^{-4}$ M solution in acetonitrile (Nd$^{III}$) displays NIR luminescence at 0.88 and 1.06 μm upon excitation at 337 nm. Similarly the $^1D_2 \rightarrow {}^3F_4$ emission from Pr$^{III}$ is detected for solutions of the complexes with both **56a** and **56b** in dmso, although it is much weaker than Nd$^{III}$ fluorescence, especially in the case of the second complex (Pettinari et al., 2002).

3.2.2. *Quinolinates*
8-Hydroxyquinoline (8-quinolinol or 8-HQ) and its halogenated derivatives (see fig. 54) are bidentate ligands possessing good coordination properties towards a wide range of metal ions, including rare earths. For a long time, 8-HQ has been essentially used as reagent for gravimetric analysis; the first report for Ln$^{III}$ analysis appeared in 1936 (Pirtea, 1936).
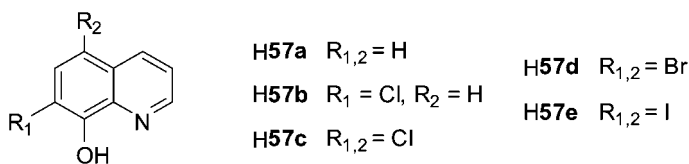
Fig. 54. 8-Hydroxyquinoline-based ligands.

In view of the poor solubility of metal hydroxyquinolinates in aqueous media, 8-HQ also found applications as extraction reagent. These first two applications only take advantage of the coordination properties of the bidentate ligand, but 8-HQ also possesses useful photophysical properties, with a triplet state located around 17 100 cm$^{-1}$ (585 nm). For instance, the Al$^{III}$ tris(8-hydroxyquinolinate) complex [Al(8-Q)$_3$] exhibits intense green electroluminescence and is certainly the most investigated quinoline-based chelate. Indeed, interest in [Al(8-Q)$_3$] complexes started in 1987 when C.W. Tang and S.A. Van Slyke demonstrated its usefulness as active medium in organic light emitting diodes (OLEDs) operating in the visible region around 510 nm (Tang and Van Slyke, 1987). Moreover, [Al(8-Q)$_3$] is commonly used as the electron transport/emitting layer in electroluminescent devices and much effort is still focused on the optimization of its performance, particularly its luminescence efficiency and long-term stability. Optical devices based on organic materials emitting in the visible region are well known and are routinely incorporated in electroluminescent devices. NIR-emitting lanthanide chelates based on 8-hydroxyquinoline have also attracted much attention during the last decade because of their potential use as active components in optical amplifiers or OLEDs operating at telecom wavelengths. Current optoelectronic devices are often composed of silica optical fibers which have two main windows in their transmission loss spectra in the 1.3 and 1.5 μm wavelength regions. The 1.5 μm window is one of the standard telecommunication windows, therefore Er$^{III}$ chelates have been extensively tested for this purpose since the Er($^4$I$_{13/2}$ → $^4$I$_{15/2}$) transition has the right wavelength. Moreover, use of organic materials instead of traditional inorganic optoelectronic components offers some advantages, such as solution processing, flexibility and low cost. W.P. Gillin and R.J. Curry were first to demonstrate that replacement of the [Al(8-Q)$_3$] chelate with its Er$^{III}$ analog is achievable from a technological point of view, yielding a 1.5 μm light source which can be integrated directly within silicon devices (Curry and Gillin, 1999; Gillin and Curry, 1999).

After this first report of NIR electroluminescence using Er$^{III}$ hydroxyquinolinate, H. Suzuki et al. investigated the luminescence characteristics of this complex under different sample forms which can further be used as NIR emissive materials. Three types of samples have been prepared: vacuum-deposited thin-films, doped spin-coated IR polymer films and doped polymer microparticles (Suzuki et al., 2003). Typical NIR luminescence of the Er$^{III}$ ion was observed at 1.55 μm for each sample form and with higher intensities when excitation was performed in the ligand absorption bands instead of directly in the Er$^{III}$ excited levels. This clearly indicates that sensitization of Er$^{III}$-centered luminescence occurs through ligand-to-metal energy transfer. For the doped monodispersed PMMA microparticles the lower lumi-

nescence intensity is explained by the lower chelate concentration and by the host polymer PMMA which has a much larger absorption cross section than the other two materials in this spectral range. A great advantage of the [Er(8-Q)$_3$] chelate that makes it suitable for application in optical amplifier is its luminescence bandwidth, which is, for each sample form, larger than those of Er$^{III}$ in various inorganic glass matrices exhibiting optical amplification. Indeed large bandwidth is necessary to get a wide gain bandwidth for optical amplification. Luminescence bandwidths ranging from 79 nm for the vacuum-deposited thin-film to 97 nm for doped PMMA microparticles have been obtained, which compare favorably with bandwidths of 7.94 nm in pure silica fiber and 63.8 nm in fluorohafnate glass. The larger bandwidths originate from the more inhomogeneous nature of the sample, including the Er$^{III}$ chelate and/or the polymer matrices. For a better understanding of the emission process occurring in this kind of material, time-resolved studies have been performed on Er$^{III}$ tris(8-hydroxyquinolinate) under the form of powder, thin-film blend with polycarbonate, evaporated film, and in solution in dmso-$d_6$ (Magennis et al., 2003). In all the cases, the $^4I_{13/2} \rightarrow {}^4I_{15/2}$ transition displays biexponential decays with mean luminescence lifetimes of 0.2 µs for the powder, 0.6 µs for the thin-film blend, 1.03–1.37 µs for evaporated film depending on the film thickness, and 2.7 µs in solution. For the solution, a rise time of ca. 30 ns has also been observed. The biexponential decays reflects the presence of different local environments around the Er$^{III}$ ions and is attributed to the different numbers of solvent molecules that can be coordinated to tris complexes. It is noteworthy that longer lifetimes have been obtained in solution than in the solid state. This is due to the replacement of bound water or methanol molecules with more coordinating dmso-$d_6$ molecules, which possess vibrations with much lower energy and thus provide less efficient quenching of the Er$^{III}$ luminescence. By assuming a radiative lifetime $\tau_{rad} = 8$ ms, which the authors report as being an average of radiative lifetimes published for erbium complexes, and taking into account the mean lifetimes $\tau_{mean} = A_1 \cdot \tau_1 + A_2 \cdot \tau_2$, where $A_i$ are the pre-exponential factors, luminescence quantum yield have been estimated to ca. 0.002% for the powder, 0.005% for the thin-film blend with polycarbonate, 0.01% for evaporated film and 0.03% for solution in dmso-$d_6$. These small quantum yields suggest that the low efficiency of 0.01% estimated by R.J. Curry and W.P. Gillin for an [Er(8-Q)$_3$] based OLED device may actually be close to the maximum efficiency achievable when such an Er$^{III}$ organic chelate is used as the emissive material (Curry et al., 2000).

The 1:3 stoichiometry of lanthanide 8-hydroxyquinolinates was taken for granted for a long time until R. van Deun et al. became interested in the relationship between the structure of these compounds and their luminescence and discovered that three types of 8-hydroxyquinolinates and of their halogenated derivatives can be isolated depending on the experimental conditions: (i) hydrated tris complexes [Ln(**57**)$_3$·$x$H$_2$O], (ii) tetrakis complexes [ALn(**57**)$_4$] and (iii) trimeric complexes [Ln$_3$(**57**)$_8$B], where A and B are monovalent cation and anion, respectively (Van Deun et al., 2004a). Monomeric anhydrous tris complexes could not be obtained from syntheses in solutions. The syntheses of lanthanide 8-hydroxyquinolinates were repeated following the most frequently used synthetic procedures found in literature and instead of 1:3 complexes, mixtures of different species were obtained in most of the cases. The first procedure, listed as method A in table 12, consists in mixing an ethanolic solution of the ligand and an aqueous solution of Ln$^{III}$ nitrate, to which a slight

Table 12

Summary of the synthetic procedures commonly used in literature to yield rare-earth quinolinates (Van Deun et al., 2004a)

| Method (year) | Ligand (solvent) | LnX$_3$ (solvent) | Base | Complexes |
|---|---|---|---|---|
| A (1971) | H**57a** (EtOH) H**57c**, **d**, **e** (EtOH) | Ln(NO$_3$)$_3$ (H$_2$O) | NH$_4$OH | tris/trimeric tris/tetrakis |
| B (2001) | H**57** (H$_2$O/MeOH, 20/80) | LnCl$_3$ (H$_2$O) | – | trimeric (>90%) |
| C (1957) | H**57a**, **b** (acetone) H**57c**, **d**, **e** (acetone) | LnCl$_3$ (H$_2$O) | CH$_3$CO$_2$NH$_4$ | trimeric tris/tetrakis |
| D (2004) | H**57** (EtOH) | LnCl$_3$ (EtOH) | NaOH | tetrakis |

excess of an ammonium hydroxide solution is added, thus causing the precipitation of the complex. Elemental analyses of the complexes lead to the conclusion that they correspond to the general formula [Ln(**57**)$_3$·$x$H$_2$O]. However the presence of another, trimeric species [Ln$_3$(**57**)$_8$(solv)]$^+$ is suggested by mass spectrometry and confirmed by X-ray analysis of Er$^{III}$ single crystals. In this trimeric complex, the two peripheral erbium ions each coordinate to four 8-hydroxyquinolinate ligands. An additional hydroxide anion is bound to one of the peripheral erbium ions, while a water molecule is coordinated to the other one. Each ligand coordinates in a bidentate fashion and bridges the erbium ions via the oxygen atom except for two peripheral ligands. The synthetic method B, which is the most currently used method to produce active emitting materials for OLEDs, resulted in the formation of pure trimeric complexes (in >90% yields). The last method investigated (method C, see table 12) uses ammonium acetate as a base leading for ligands **57a** and **57b** to the formation of trimeric species in which the two peripheral erbium ions are both surrounded by four ligands and linked to the central erbium ion, this latter being coordinated to six oxygen atoms and to one acetate counterion (fig. 55, right).

With halogen-disubstituted ligands, a mixture of tris and tetrakis complexes is obtained, but no longer the trimeric species. In the tris complex, erbium coordination consists of three bidentate 8-hydroxyquinolinates and two water molecules, the latter forming strong hydrogen bonds with the oxygen atoms of two ligands of a second tris complex and thus leading to the formation of dimerized tris complexes (fig. 55, upper left). To summarize, ligands **57a** and **57b** form primarily trimeric complexes, while disubstituted ligands **57c**, **57d**, and **57e** yield tris/tetrakis mixtures.

New synthetic routes have therefore been developed in order to improve the purity of the precipitates. Thus pure tetrakis complexes (see fig. 55, bottom) could be isolated using ligand **57** in ethanol with a large excess of sodium ions in slightly basic conditions (method D, table 12), whereas method B seems to be the more appropriate synthetic way to obtain pure trimeric complexes. Pure tris complexes could not be isolated; however mixtures with up to 75% of tris complex could be obtained by using as little ammonium hydroxide as possible and a mixture of dichloromethane and water as biphasic solvent (improved A method).
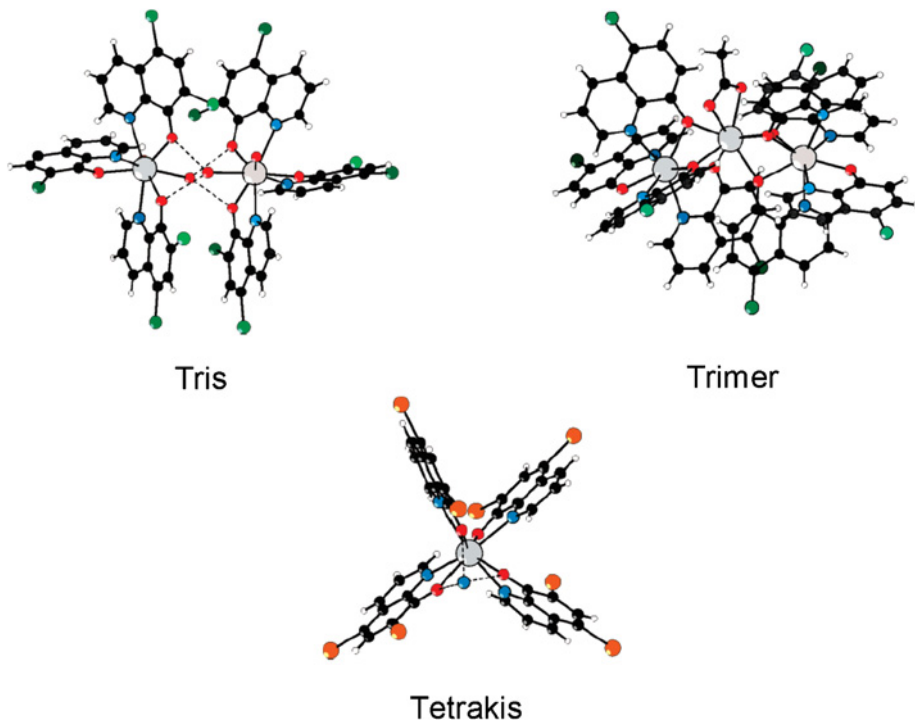
Fig. 55. The three types of structures observed for rare-earth 8-hydroxyquinolinates. Reproduced with permission from (Van Deun et al., 2004a).
© 2004 American Chemical Society

Before these findings, Van Deun et al. had investigated the luminescence properties of $Er^{III}$ tris-8-hydroxyquinolinate complexes in dmso upon ligand excitation around 400 nm (Van Deun et al., 2003a). Since dmso molecules coordinate to the $Er^{III}$ ion expelling the water molecules from the first coordination sphere, the most efficient quencher in such complexes is the aromatic C–H stretching vibration, which is located at 3060 cm$^{-1}$. As a consequence, the second overtone almost matches the energy of the $Er(^4I_{13/2} \rightarrow {}^4I_{15/2})$ transition ($\approx$6500 cm$^{-1}$). Thus by substituting the aromatic proton with a heavy atom the stretching frequency should be significantly lowered, so that higher overtones would be required for efficient quenching, a process less likely to occur. Indeed, halogen substitution of the 5,7-hydrogen atoms in the quinoline moiety results in an increase of the luminescence intensity by not less than 30%, with lifetimes going from 1.2 μs for the unsubstituted ligand **57a** to 1.9 and 1.8 μs for ligands **57c** and **57d**, respectively. However, it has to be noted that the tris complex has been synthesized according to method A (see table 12) and thus most likely consisted of a mixture of tris and tetrakis species. In fact, the emission intensity of trimeric and tetrakis species with the same ligand is almost identical, whereas the tris species, due to coordinated solvent molecules, are less luminescent. Taking this observation into account, pure tetrakis complexes

have been synthesized with disubstituted ligands and showed a luminescence enhancement of 50% instead of 30% (Van Deun et al., 2004a). Lifetimes of the tris and tetrakis complexes with ligand **57c** amount to 2.2 and 2.3 μs, respectively, whereas lifetime of pure [Er(**57a**)$_4$]$^-$ is 1.5 μs.

More recently, a fourth type of structure with general formula [Er$_3$(**57a**)$_9$] has been elucidated by X-Ray analysis (Artizzu et al., 2005). In this trimetallic complex, each erbium ion presents a distorted antiprismatic geometry; the two outer ions being bound by four nitrogen and four oxygen atoms while the inner ion is coordinated to one nitrogen and seven oxygen atoms. The overall structure is strengthened by $\pi$–$\pi$ stacking interactions occurring between quinolinate anions. Mass spectrometry and UV–vis–NIR spectroscopy clearly show that the structure of the trimetallic complex is maintained in dmso solution. Two bands are observed in the diffuse reflectance spectrum, a first one around 1.5–1.55 μm assigned to the $^4I_{13/2} \leftarrow$ $^4I_{15/2}$ transition and a second one near 1.68 μm corresponding to the absorption of the first overtone of the stretching mode of the aromatic quinolinate C–H groups. As a consequence, Er$^{III}$ luminescence quenching in the [Er$_3$(**57a**)$_9$] complex is also only due to the aromatic C–H vibrations of the ligand. Despite the presence of two distinct sites in the complex, nearly single exponential decay was observed within the available dynamic range. This can be explained by the fact that the Er$^{III}$–Er$^{III}$ energy migration occurs much faster (10-ns time scale) than the Er$^{III}$ nonradiative decay time, 2.2 μs for a crystalline sample; as a result, the excitation energy migrates and is delocalized over the three ions, so that only an average emission spectrum is observed.

The quenching of the NIR-emitting Er($^4I_{13/2}$) level induced by resonant dipolar interaction between the metal ion and high frequency vibrations of the organic ligand has been modeled by means of a "continuous medium approximation" using the erbium quinolinate complexes described above (Artizzu et al., 2005; Van Deun et al., 2004a) as test compounds (Quochi et al., 2006). In this model, the quenching process is assumed to follow Förster's mechanism with a $1/r^6$ dependence on the dipole–dipole distance and the discrete acceptor distribution (i.e. C–H, C–C, C–O vibrations) is replaced with a continuous and homogeneous distribution $\rho_A$, representing an average acceptor density. The non-radiative rate constant can therefore be estimated as

$$k_{nr} = \frac{k_r}{(2\pi n)^4 R_{min}^3} \int F_D(\lambda)\alpha_A(\lambda)\lambda^4 \, d\lambda \cong \frac{\lambda_{em}^4}{(2\pi n)^4} \cdot \frac{k_r \langle \alpha_A \rangle_{Er}}{R_{min}^3}, \tag{28}$$

where $n$ is the refractive index, $R_{min}$ is the minimum distance between the Er$^{III}$ ion and the acceptor (calculated from the crystal structure), $F_D(\lambda)$ is the normalized Er$^{III}$ emission spectrum, $\alpha_A = \sigma_A \rho_A$ is the vibrational absorption coefficient of the acceptor distribution where $\sigma_A$ is the absorption cross section. The radiative rate constant $k_r$ is given by the Strickler–Berg expression:

$$k_r = 8\pi n^2 c \int \frac{\sigma_E(\lambda)}{\lambda^4} \, d\lambda \tag{29}$$

in which $\sigma_E(\lambda)$ is the emission cross section. Therefore, $k_{nr}$ depends on two spectroscopic quantities only: the radiative rate constant $k_r$ and the vibrational absorption averaged over the

$Er^{III}$ emission, $\langle \alpha_A \rangle_{Er}$. The model works well (within $\pm 10\%$) because $R_{min}$ is relatively large ($\approx 3.4$ Å for the chosen hydroxyquinolinate). In $[Er_3(\mathbf{57a})_9]$ for instance, $\tau_r = 5 \pm 0.5$ ms and $\langle \alpha_A \rangle_{Er} = 1 \pm 0.3$ cm$^{-1}$; with $n \approx 1.5$, the calculated non-radiative lifetime becomes $\tau_{nr} = 2.6$ μs, in reasonably good agreement with the experimental value of 2.3 μs. One way of decreasing the influence of the vibrational quenching is to increase $R_{min}$; however, assuming $\langle \alpha_A \rangle_{Er} \approx 1$ cm$^{-1}$, one sees that $R_{min}$ should be larger than 30 Å for $k_{nr}$ to be smaller than $k_r$. Another mean is the reduction of the vibrational absorption $\langle \alpha_A \rangle_{Er} = \langle \sigma_A \rangle_{Er} \cdot \rho_A$, which is achievable by using halogenated ligands and by reducing the density of vibrational quenching groups. Again, for $k_{nr}$ to be smaller than $k_r$, one can calculate that $\langle \sigma_A \rangle_{Er}$ should be smaller than $5 \times 10^{-4}$ cm$^{-1}$, a value two thousand times smaller than the one measured for the unsubstituted complexes. Such values, however, are close to the ones calculated for fluorinated polymers.

8-Hydroxyquinolinates are also well-suited for the sensitization of $Nd^{III}$ luminescence since their triplet state emission centered at $\approx 585$ nm overlaps the $Nd^{III}$ absorption band with the highest transition probability ($^2G_{7/2}$, $^4G_{5/2} \leftarrow {}^4I_{9/2}$). Examples are the series of neodymium complexes formed with 8-hydroxyquinolinate-based ligands **57** depicted on fig. 54 (Iwamuro et al., 1999; Iwamuro et al., 2000a). Excitation performed on the absorption band of the ligand (425 nm for ligand **57a** and 447 nm for ligands **57c**, **d**, **e**) leads to the typical $Nd^{III}$ luminescence at 890, 1070 and 1350 nm. As for the corresponding $Er^{III}$ complexes, substitution of the hydrogen atoms in the 5- and 7-position of the 8-hydroxyquinoline by halogen atoms leads to an increase in the luminescence quantum yields in dmso-$d_6$ by more than a factor of two: $Q_{Ln}^L = 0.4, 1.0, 1.0$, and $0.9\%$ for ligands **57a**, **c**, **d**, and **e**, respectively (Iwamuro et al., 2000a). Intrinsic quantum yields and lifetimes have also been measured and follow the same trend, i.e. an increase is observed in going from 8-hydroxyquinolinate to its halogenated derivatives. Calculations of the overlap integral $J$ between the phosphorescence spectrum of the ligand and the absorption spectrum of $Nd^{III}$ according to the Dexter exchange-interaction theory give large values as expected from the above discussion, confirming the reason for the intense NIR luminescence observed with all these complexes.

Lanthanides 8-hydroxyquinolinates are promising materials for the design of electroluminescent devices and further applications will be discussed in section 4.

### 3.2.3. *Terphenyl-based ligands*

Acyclic *m*-terphenyl-based ligands form another class of chelating agents which encapsulate efficiently $Ln^{III}$ ions via the formation of 1:1 complexes (Ln = Nd, Sm, Eu, Gd, Tb, Dy, Er, and Yb) and, at the same time, act as antenna-chromophores since they have a high rate of intersystem crossing (Steemers et al., 1995). Their macrocyclic analogs (ligands **22b**, **c**, and **d**) have already been discussed in section 3.1.3. In search of suitable ligands for the sensitization of $Ln^{III}$ NIR luminescence, F.C.J.M. Van Veggel and collaborators have synthesized *m*-terphenyl-based ligands bearing amido (ligands **58a**, **b**) and sulfonamido (ligand **58c**) functionalities (Klink et al., 2000b). Each of these ligands, which are represented on fig. 56, provides eight oxygen donor atoms: three ether and three carboxylate functions from the three oxyacetate groups, and two additional donors from amide or sulfonamide groups. Coordina-
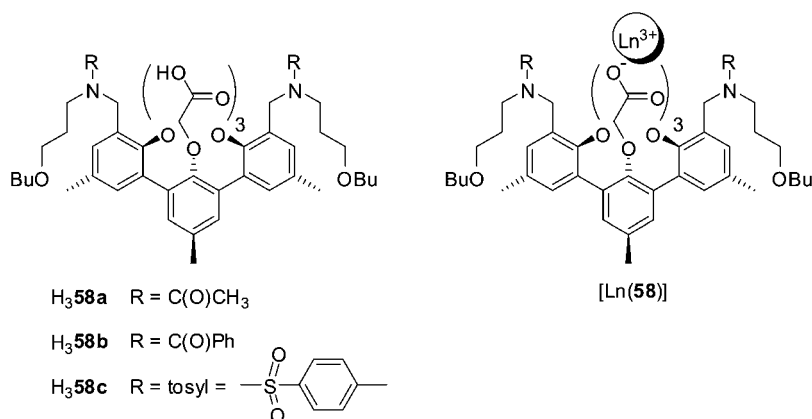
Fig. 56. Terphenyl-based ligands bearing amido and sulfonamido pendant arms and their corresponding $Ln^{III}$ complexes.

tion of the latter to the lanthanide ion has been evidenced by NMR measurements of the $Y^{III}$ complexes in dmso-$d_6$.

From the luminescence lifetimes obtained in methanol and methanol-$d_1$ for the $Eu^{III}$ and $Tb^{III}$ complexes, it has been established that only one methanol molecule is coordinated to the $Ln^{III}$ ion in [Ln(**58a–b**)] complexes, leading to 9-coordinate complexes. For the compounds [Ln(**58c**)], $q_{MeOH}$ is between one and two, which suggests the presence of an equilibrium between two differently solvated species. In spite of the high lying triplet states of the terphenyl-based ligands ($\approx 24\,600$ cm$^{-1}$), sensitized NIR emission of $Nd^{III}$, $Er^{III}$ and $Yb^{III}$ complexes with ligands **58b** and **58c** occurs in dmso after laser excitation at 350 nm. Using dmso-$d_6$ instead of dmso leads to a significant increase in the lifetimes, indicating that in such complexes C–H oscillators of the solvent molecules are effective quenchers of the $Ln^{III}$ excited states. The quenching rate constants calculated for complexes [Ln(**58b–c**)] amount to $\approx 4.5 \times 10^5$, $1.5 \times 10^5$ and $6 \times 10^4$ s$^{-1}$ for Ln = $Nd^{III}$, $Er^{III}$, and $Yb^{III}$, respectively. The same experiment has been repeated on $Eu^{III}$ complexes and the calculated rate constants are two to three orders of magnitude smaller ($\approx 100$ s$^{-1}$). These results are in agreement with the well-established energy gap law. Taking radiative lifetimes of 0.25, 14, and 2 ms for Nd, Er and Yb, respectively, gives intrinsic quantum yields of 0.84, 0.02, and 0.78% in dmso-$d_6$. These low values are caused essentially by the presence of C–H oscillators in the ligand. As a consequence, deuteration of the ligand $H_3$**59a** has been achieved to yield $H_3$**59b** (see fig. 57), where all the C–H groups that contribute to quenching have been deuterated (Hebbink et al., 2001b). In order to determine which C–H oscillators are responsible for the quenching, average distances between hydrogen atoms and the $Ln^{III}$ ion have been calculated using molecular dynamics simulations. Since the quenching rate is exponentially related to the distance between donor and acceptor, C–H groups lying at 6 Å and further away from the $Ln^{III}$ ion will not significantly contribute to the quenching and thus do not have to be deuterated. This is the case for all the hydrogen atoms of the *m*-terphenyl moiety, whereas all the other groups have to
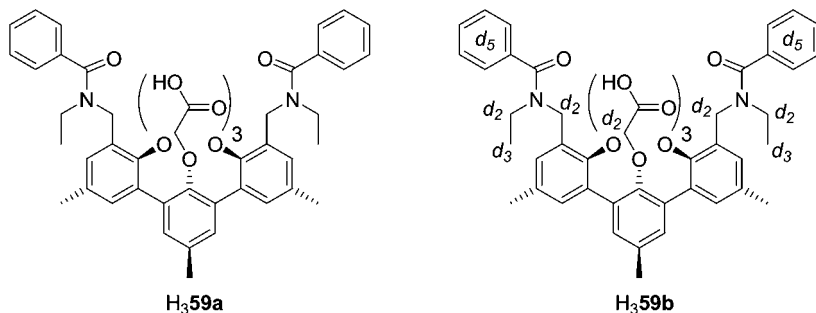
Fig. 57. Terphenyl-based ligand and its deuterated analog.

be deuterated. The lifetimes obtained in dmso-$d_6$ with non-deuterated ligand **59a** amount to 2.5, 3.3, and 19.0 μs for Nd, Er, and Yb, respectively, while the corresponding lifetimes for the deuterated ligand **59b** are 5.5, 5.4, and 52.3 μs, leading to intrinsic quantum yields of 2.0, 0.04, and 3.0%, assuming the same radiative lifetime as above, for Nd[III], Er[III], and Yb[III], respectively. The enhancement factor upon deuteration of the ligand is therefore 2- to 3-fold.

One great advantage of all these *m*-terphenyl-based ligands comes from their rather easy functionalization by incorporating different sensitizer units at the amide and sulfonamide positions, without changing either the synthetic route or the coordinating nature of the ligand. Therefore a series of new terphenyl-based ligands containing additional chromophoric units possessing relatively high intersystem crossing quantum yield, such as organic dyes (see fig. 58), have been synthesized in view of practical applications. Indeed, with this approach, it is hoped that the excitation wavelength can be shifted into the visible region up to around 530 or even 630 nm, where very compact and relatively cheap green or red diode lasers can be used as excitation sources. Moreover in such complexes the antenna chromophore is positioned in close proximity to the Ln[III] ion because of the coordination of the amide carbonyl. The first example of a terphenyl-based ligand fitted with a dye antenna is derivative H$_3$**60a** depicted in fig. 59 (Klink et al. 1999, 2000a). It exhibits an isc quantum yield of 89%, but for this ligand, excitation has to be performed in the UV, between 300 and 350 nm.

Upon excitation of the triphenylene antenna, the typical line-like emission of NIR emitting Ln[III] ions is observed for all [Ln(**60a**)] complexes in dmso-$d_6$ with lifetimes of 2.5, 3.4, and 18.6 μs for Ln = Nd, Er and Yb, respectively, whereas lifetimes measured in non-deuterated dmso are 1.4–2 times smaller. This decrease clearly shows the extreme sensitivity of NIR emitting Ln[III] ions toward quenching by C–H oscillators, in this case from the solvent molecules. Quenching rate constants of these C–H oscillators range from 0.5 to $3.1 \times 10^5$ s$^{-1}$ with the higher value for the [Nd(**60a**)] complex, in agreement with the energy gap law. The radiative rate constants calculated from the radiative lifetimes, amount to 4000, 71, and 500 s$^{-1}$ for Nd, Er, and Yb, respectively. Since the observed rate constant $k$ is the sum of both the radiative and nonradiative rate constants and in view of the values obtained, it is clear that for NIR emitting Ln[III] ions the rate constant $k$ is dominated by nonradiative deactivation of the luminescent state.
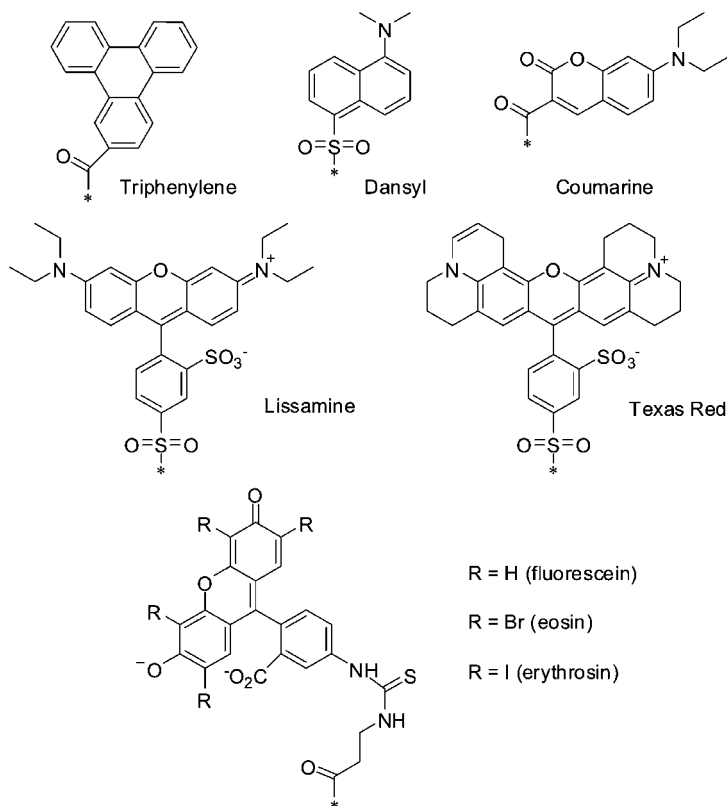
Fig. 58. Organic dyes used as antenna chromophore in terphenyl-based ligands.



R =   triphenylene (H₃**60a**), dansyl (H₃**60b**),
       coumarine (H₃**60c**), lissamine (H₃**60d**),
       Texas Red (H₃**60e**)

R =   dansyl (H₃**60f**), coumarine (H₃**60g**)
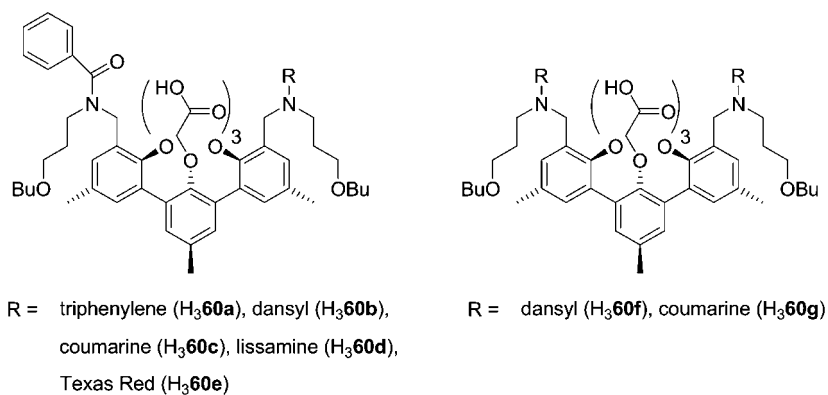
Fig. 59. Dye-functionalized derivatives of terphenyl-based ligands.

Although an internal redox mechanism is possible for the sensitization of $Yb^{III}$ luminescence, it has been shown that it cannot occur in such complexes and that as a consequence, the usual energy transfer pathway ($^1S \rightarrow {}^3T \rightarrow Ln^*$) is operative in these $Yb^{III}$ complexes. Oxygen quenching of the triphenylene triplet state and energy transfer to the $Ln^{III}$ ion are in competition. Therefore the luminescence intensity is enhanced by 35% for [Nd(**60a**)], 120% for [Er(**60a**)], and 90% for [Yb(**60a**)] upon de-oxygenation of the dmso-$d_6$ solutions. A good estimate of the energy transfer rate can be achieved from this oxygen dependence by using the following Stern–Volmer equation:

$$\frac{I_0}{I} = 1 + k_{\text{diff}} \cdot \tau_T \cdot [O_2], \tag{30}$$

where $I_0$ and $I$ are the $Ln^{III}$ luminescence intensities in the absence and presence of oxygen, respectively, $k_{\text{diff}}$ is the diffusion-controlled quenching rate constant, $\tau_T$, the lifetime of the triphenylene triplet state, and [$O_2$], the oxygen concentration in dmso. Taking $k_{\text{diff}} = 10^{10}$ M$^{-1}$ s$^{-1}$ and [$O_2$] = 0.47 mM, and assuming that in deoxygenated solutions the lifetime of the triphenylene triplet state is mainly governed by the energy transfer rate constant $k_{\text{et}} = 1/\tau_T$. The energy transfer rate constants obtained for the different complexes reach $1.3 \times 10^7$, $3.8 \times 10^6$, and $5.1 \times 10^6$ s$^{-1}$ for Nd, Er, and Yb, respectively. These values are of the same order of magnitude as the oxygen quenching rate ($\approx 5 \times 10^6$ s$^{-1}$) so that the slowest the energy transfer is, the largest the oxygen quenching and thus the lowest energy transfer quantum yield. This is corroborated by the experimental observations. Thus the $Nd^{III}$ complex, in which the energy transfer is the fastest, is less influenced by the presence of oxygen and exhibits the lowest luminescence enhancement after de-oxygenation, whereas the reverse situation is observed for the $Er^{III}$ complex. As a consequence, the energy transfer quantum yields amount to 74, 45, and 53% for the Nd, Er, and Yb complexes, respectively. Although energy transfer is quite efficient in the $Nd^{III}$ complex, the intrinsic quantum yield is relatively low, only 1% in dmso-$d_6$, meaning that the overall quantum yield is also low. For the $Er^{III}$ and $Yb^{III}$ complexes, intrinsic quantum yields of 0.02 and 0.93%, respectively, were calculated.

Keeping in mind the development of a polymer-based optical amplifier, for which $Nd^{III}$ and $Er^{III}$ ions are suitable as the optical active component, a series of six dye-functionalized $Nd^{III}$ complexes have been synthesized and their luminescence properties investigated (Klink et al., 2001). The study focused on complexes with $Nd^{III}$ since it exhibits larger intrinsic quantum yields than $Er^{III}$ in organic environments. Four different fluorescent dyes, namely dansyl, coumarine, lissamine and Texas Red (see figs. 58 and 59) were used for the sensitization of the $Nd^{III}$ luminescence. Bis-functionalized ligands with dansyl (H$_3$**60f**) and coumarine (H$_3$**60e**) have also been synthesized to investigate the influence of an additional chromophore on the efficiency of the sensitization process. All these fluorescent dyes have broad and intense bands ranging from the near-UV to the visible region, with absorption maxima at 345 nm for dansyl, 400 nm for coumarine, 568 nm for lissamine, and 590 nm for Texas Red. For the six $Nd^{III}$ complexes, excitation of the antenna chromophore resulted in the observation of the typical NIR $Nd^{III}$ emission, the lifetimes of which are around 2.2 µs in dmso-$d_6$. Taking into account the absorbance of the samples and differences in the excitation intensity as a function of the wavelength, the recorded emission intensities showed that in the series of investigated dyes,

dansyl (H$_3$**60b**) is the most efficient sensitizer, followed by lissamine (H$_3$**60d**) and Texas Red (H$_3$**60e**), while coumarine (H$_3$**60c**) is the least efficient one. Moreover, incorporation of a second antenna chromophore in ligands H$_3$**60f** and H$_3$**60g** does not increase the luminescence quantum yield of the system. For most of the complexes, oxygen has no influence on their luminescence intensities, except for [Nd(**60c**)] and [Nd(**60g**)] formed with coumarine functionalized ligands for which de-oxygenation of the samples leads to a 20% increase in luminescence intensity. According to the authors, this indicates that the transfer of energy from coumarine to Nd$^{III}$ is slower than for the other antenna chromophores. The presence of the Nd$^{III}$ ion leads to a significant reduction of the antenna fluorescence intensity in the complex when compared to the free ligand. The most important decrease is observed for dansyl chromophore (80%) whereas for coumarin only a 40% decrease occurs. At first, the authors explained the reduction in the fluorescence intensity of the antenna by an external heavy atom effect induced by the presence of the heavy and paramagnetic Nd$^{III}$ ion, which enhances the intersystem crossing process and thus hinders the radiative process, i.e. the fluorescence of the antenna. However more detailed work performed on dansyl- and lissamine-functionalized Nd$^{III}$ complexes clearly showed that this explanation is not correct and that the observation of sensitized Nd$^{III}$ luminescence in such complexes results from a direct energy transfer from the singlet excited state of the dye to the lanthanide ion (Hebbink et al., 2002a). As seen previously, the dansyl chromophore is a better sensitizer with the emission intensity of the lissamine-functionalized complex [Nd(**60d**)] being approximately 70% of that of the dansyl one, [Nd(**60b**)]. Lifetimes are in the range 2.1–2.2 μs in dmso-$d_6$, whereas they are almost two times shorter in dmso (1.1–1.2 μs). Moreover as stated before, the luminescence of these two complexes is not influenced by oxygen, which is known as an efficient triplet-state quencher, implying two possible explanations; the triplet state is either (i) depopulated relatively fast, meaning that the energy transfer from the triplet state to the Ln$^{III}$ ion is too fast ($>10^7$ s$^{-1}$) to compete with oxygen quenching, or (ii) is not involved at all, indicating that the energy transfer occurs from the singlet state. Measurements performed on the Gd$^{III}$ complexes show that quantum yields and lifetimes of the dye fluorescence are the same for the complexes and for free ligands H$_3$**60b** and H$_3$**60d**. This implies that no external heavy atom effect from the lanthanide ions is operative on the dansyl and lissamine moieties. As a consequence, the decrease of the antenna fluorescence in the Nd$^{III}$ complexes can only be attributed to a direct energy transfer from the singlet state to the Nd$^{III}$ ion. Furthermore no phosphorescence could be observed at 77 K in an ethanol/methanol glass, indicating that the formation of triplet states is insignificant.

Er$^{III}$ and Yb$^{III}$ complexes have also been studied, but upon antenna excitation no sensitized NIR luminescence was observed, and the lifetimes of the antenna fluorescence in these complexes are the same as those measured for the free ligands. It is obvious that for a fast energy transfer the antenna singlet excited state and the accepting Ln$^{III}$ energy level should have a non-zero spectral overlap integral. Based on the large energy gap between the Yb$^{III}$($^2$F$_{5/2}$) level lying at 10 200 cm$^{-1}$ and the singlet excited state of both the dansyl ($E(^1\pi\pi^*) \approx 17200$ cm$^{-1}$) and lissamine ($E(^1\pi\pi^*) \approx 23\,500$ cm$^{-1}$) moieties, the energy transfer will be slow and cannot compete with the rate of radiative deactivation by fluorescence. Both Nd$^{III}$ and Er$^{III}$ ions possess several energy levels able to accept the excitation en-
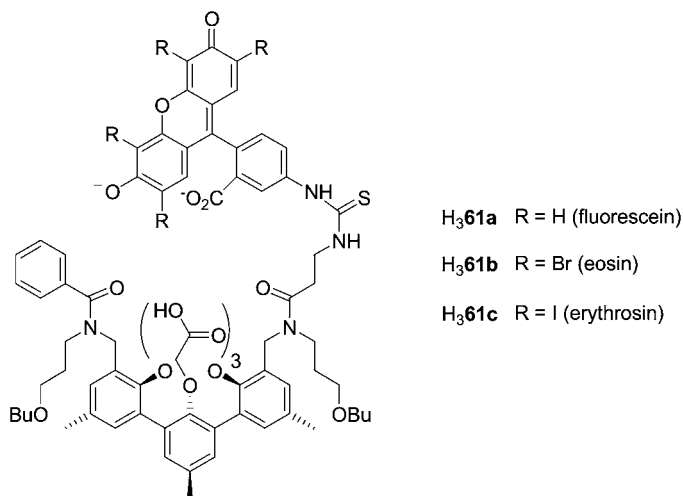
Fig. 60. Xanthene-functionalized terphenyl-based ligands for the sensitization of NIR emitting $Ln^{III}$ ions.

ergy from the singlet excited state of dansyl and lissamine units. However these levels should satisfy the selection rules for 4f–4f transitions accompanying the energy transfer process. Since Dexter-type mechanisms have the highest probability, the selection rule $|\Delta J| = 0, 1$ ($J = J' = 0$ excluded) allowing this type of transfer has to be followed. In these conditions, only the $Nd^{III}$ ion possesses levels allowing energy transfer from the lissamine and dansyl units. The only excited level of $Er^{III}$ meeting this selection rule is $^4I_{15/2}$, lying at 6400 cm$^{-1}$, for which the energy gap is too large to allow fast energy transfer. Even though the best results were obtained with the dansyl-functionalized ligand $H_3$**60b**, the lissamine-containing ligand $H_3$**60d** is more suitable for applications since it allows excitation up to 570 nm, whereas with the dansyl unit the excitation window is limited to 400 nm.

Three other *m*-terphenyl-based ligands have been prepared which incorporate dyes that are structurally very similar to the xanthene moiety (Hebbink et al., 2003). The dyes used are fluorescein, eosin and erythrosin (see figs. 58 and 62) linked to the terphenyl moiety via a $\beta$-alanine spacer and possessing absorption maxima in methanol at 505, 535, and 545 nm, respectively. The great advantage of these dyes compared to the previous ones comes from their carboxylate group that coordinates to the $Ln^{III}$ ion, reducing the distance between the donor and the acceptor, and thus allowing more efficient energy transfer. Furthermore, in such complexes the $Ln^{III}$ ion is coordinated by four carboxylates, two amides, and three ether oxygen atoms, leading to a coordination number of 9, henceforth saturating the first coordination sphere and preventing solvent molecules to interact directly with the $Ln^{III}$ ion. Molecular dynamics calculations clearly evidenced the coordination of the carboxylate anion, and the average distances between the $Ln^{III}$ ion and the xanthene unit were found to be 6.1–6.2 Å.

The complexes of general formula [Ln(**61**)] (Ln = Nd, Er and Yb) (see fig. 60) exhibit the typical NIR luminescence of each $Ln^{III}$ ion upon excitation in the antenna chromophore. The overall quantum yields have been determined in deuterated methanol and by using the $Nd^{III}$

Table 13
NIR emission properties of [Ln(**61**)] complexes in methanol-$d_1$

| Ln | Ligand | $Q_{Ln}^{L}$ (%) | $Q_{Ln}^{Ln}$ (%)[b] | $\eta_{sens}$ (−) |
|----|--------|-----------------|----------------------|-------------------|
| Nd | **61a** | 0.03 | 0.16 | 0.19 |
|    | **61b** | 0.014 | 0.16 | 0.09 |
|    | **61c** | 0.012 | 0.15 | 0.08 |
| Er | **61a** | 1.0[a] | 0.0065 | |
|    | **61b** | 0.51[a] | nd[c] | |
|    | **61c** | 0.43[a] | nd[c] | |
| Yb | **61a** | 0.23 | 0.55 | 0.42 |
|    | **61b** | 0.14 | 0.56 | 0.25 |
|    | **61c** | 0.17 | 0.58 | 0.29 |

[a]Relative quantum yields, $Q([\text{Er}(\textbf{61a})]) = 1.0$.
[b]Calculated from $Q_{Ln}^{Ln} = \tau_{obs}/\tau_{rad}$, with $\tau_{rad} = 0.25$, 14, and 2 ms for Nd, Er, and Yb, respectively.
[c]Not determined, no accurate decay trace obtained.

and Yb[III] complexes formed with fluorexon (Fx, see fig. 64 in section 3.2.4 below) as standards for the Nd[III] and Yb[III] complexes. For the Er[III] complexes, the quantum yields are given relative to the complex [Er(**61a**)], for which the quantum yield has been fixed to unity. From data reported in table 13, it is clear that the highest quantum yields are obtained for complexes formed with H$_3$**61a** which contains the fluorescein antenna; this was difficult to predict since the intersystem crossing yield is much higher in erythrosin (82%) or eosin (18%) than in fluorescein (2%). In fact, the isc quantum yields of the antenna has less influence than expected since the external heavy atom effect provided by the Ln[III] ion diminishes drastically this difference. Moreover, for Nd[III] complexes the accepting energy level is $^4F_{9/2}$ (at 15 000 cm$^{-1}$) and not the $^4F_{7/2}$ level located at 13 400 cm$^{-1}$. Therefore, energy back transfer occurring from the accepting Nd[III] level to the triplet state of eosin and erythrosin is more pronounced than for fluorescein, the energy gap being larger in the latter case. For Er[III] complexes, the authors postulate that relaxation of the selection rules allows additional pathways, which may be the reason for the sensitization of this ion. For instance, the more efficient sensitization observed in the fluorescein complex [Er(**61a**)] can be attributed to a pathway involving the Er[III] $^4F_{9/2}$ level at 15 500 cm$^{-1}$.

The quantum yields are rather low despite the fact that deuterated methanol-$d_1$ was used. This is mainly due to vibrational deactivations occurring in the complex itself, especially C–H oscillators as seen above. From the lifetimes obtained in methanol and deuterated methanol it is possible to calculate the rate constant of solvent quenching in these complexes. A value smaller or equal to $3 \times 10^4$ s$^{-1}$ was found for the Yb[III] complexes, whereas for the corresponding Yb[III] complex formed with ligand H$_3$**58b** this quenching rate constant is one order of magnitude higher ($3 \times 10^5$ s$^{-1}$). This shows that the ligand shield effectively the Ln[III] ion from the solvent, which is in accordance with the molecular modeling studies. Rate constants of $\leqslant 1 \times 10^6$ s$^{-1}$ were found for Nd[III] complexes, caused by solvent molecules present in the second coordination sphere, whereas this value reaches $2.3 \times 10^6$ s$^{-1}$ in the correspond-

ing complex [Nd(**58b**)], which has solvent molecules in the first coordination sphere. Thus, second-sphere solvent molecules play a greater role in the deactivation of $Nd^{III}$ ions when compared to $Yb^{III}$, since the energy gap between the excited and ground states is much larger for the latter. Moreover $Nd^{III}$ ions are slightly bigger than $Yb^{III}$ ions allowing more space for second sphere quenchers. Concerning the energy transfer rate constant, it was estimated to be at least $10^8$ $s^{-1}$.

### 3.2.4. *Polyaminocarboxylates*

Polyaminocarboxylates yield stable 1:1 complexes with lanthanide ions in view of the strong ionic bonds between the carboxylate anions and the $Ln^{III}$ cation, and due to the formation of five-membered chelate rings. The simplest ligands belonging to this class are nitrilotriacetic acid ($H_3$nta), ethylenediaminetetraacetic acid ($H_4$edta), and diethylenetriaminepentaacetic acid ($H_5$dtpa), which are depicted in fig. 61. In the case of nta or edta, formation of 1:2 (Ln:L) complexes is also possible. The remarkable stability of the 1:1 complexes is exploited in complexometric titrations (Schwarzenbach, 1957), in the determination of stability constants by competitive measurements, or in the design of contrast agents for medical imaging.

In absence of chromophoric substituents, no sensitization of $Ln^{III}$ luminescence occurs, either in the visible or in the near-infrared ranges (Beeby et al., 1997; Beeby and Faulkner, 1997). On the other hand, complexation of the chelating agent removed the inner-sphere water molecules, resulting in a considerably enhanced intrinsic quantum yield. Two strategies have been probed to improve the photophysical properties of lanthanide polyaminocarboxylates, (i) electrochemically generated luminescence (ECL) and (ii) the functionalization of polyaminocarboxylate with dyes. Conversely, aminocarboxylate groups are often grafted on luminescence sensitizers to improve their coordinative properties, as seen elsewhere in this review.

Ala-Kleme and collaborators have probed the ability of six heptadentate, one octadentate, and three nonadentate polyaminocarboxylates to sensitize $Yb^{III}$ emission by an electrochemically generated process (fig. 62). In these experiments, peroxidisulfate is added to the chelate solutions and electric pulses generate hydrated electrons ($E^0 = -2.9$ V vs SHE) which trigger the following reactions:

$$S_2O_8^{2-} + e^-(aq) \rightarrow SO_4^{\cdot-} + SO_4^{2-}, \tag{31a}$$

$$YbL + SO_4^{\cdot-} \rightarrow Yb(L^\cdot)^+ + SO_4^{2-}, \tag{31b}$$

$$YbLn(L^\cdot)^+ + e^-(aq) \rightarrow YbL^* \rightarrow Yb^*L. \tag{31c}$$
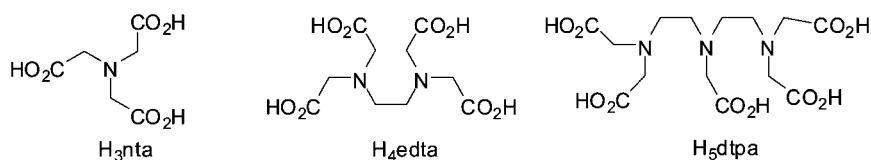


Fig. 61.  Simple polyaminocarboxylic acids.
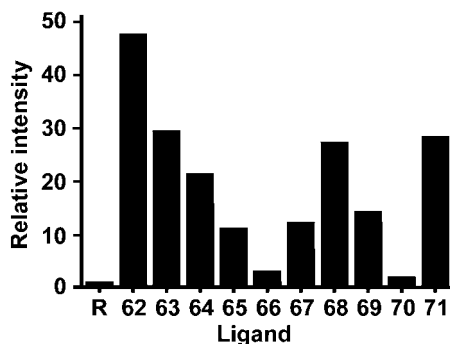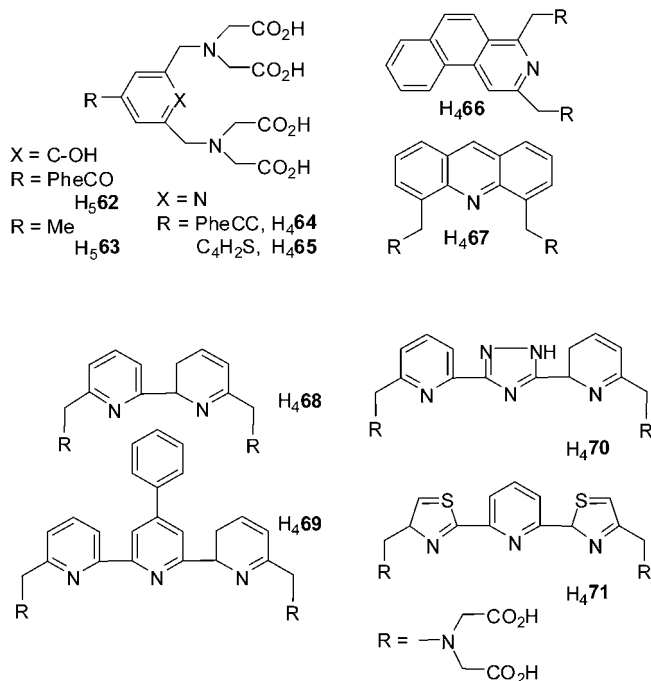
Fig. 62. Aromatic polyaminocarboxylate ligands for ECL (top) and relative ECL emission for Yb$^{III}$ complexes $10^{-5}$ M at pH 9.2 (bottom); R is the reference edta chelate.

Sulfate radicals are formed ($E^0 = +3.49$ V vs SHE), which oxidize the aromatic moieties of the polyaminocarboxylate ligands into Yb(L$^{\cdot}$)$^{+}$. In turn, the latter species is easily reduced by aqueous electrons leading to an excited ligand (YbL*). This reaction is fast enough to produce the excited singlet or triplet states of the aromatic unit, provided that the net reaction enthalpy exceeds the energy difference between the ground state and the excited state of the organic ligand. This is effectively the case here, $-\Delta H^0$ being estimated to $\approx$4.1 eV, while
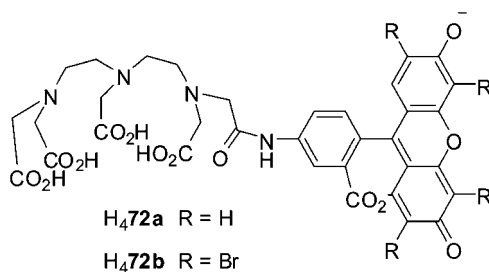
Fig. 63. Xanthene-modified diethylenetriaminepentaacetic acid (dtpa) derivatives.

$E(^1\pi\pi^*) \approx$ 3.7–4.1 eV and $E(^3\pi\pi^*) \approx$ 2.8–3.3 eV. The excited ligand subsequently transfers energy onto the metal ion (Yb*L). The process is sometimes called "oxidation-initiated reductive excitation". Alternatively, a competing "reduction-initiated oxidative excitation" could occur in which the aqueous electron that reduces the chelate (YbL$^-$) is produced first and then reacts with the sulfate radical to produce YbL*. Energy considerations, however, indicate that the preferred excitation is the first mechanism. Several of the tested chelates have sizeable Yb$^{III}$-centered ECL as shown on fig. 62 in which [Yb(edta)]$^-$ is taken as reference (R). The advantage of these systems, beside generating NIR ECL luminescence in water, is that the blank electrochemically generated luminescence of the oxide-covered aluminum cathode (the so-called F-center ECL) is practically zero in this spectral range leading to a high signal-to-noise ratio (Ala-Kleme et al., 1999).

Polyaminocarboxylates are often used as building blocks for designing more elaborate ligands in which, for instance, an antenna chromophore is grafted on one of the tertiary amine of the aliphatic skeleton. This results in a new type of receptors which are well suited for the sensitization of Ln$^{III}$ luminescence since they combine the coordinating properties of polyaminocarboxylate moieties and the light harvesting efficiency of dyes. With a judicious choice of the chromophore, efficient sensitization of NIR emitting Ln$^{III}$ ions can be achieved with visible light. For instance, xanthene derivatives such as fluorescein and eosin, which have absorption maxima near 500 nm, have been attached onto dtpa, yielding ligands H$_4$**72a** and H$_4$**72b** depicted on fig. 63 (Hofstraat et al., 1998; Werts et al., 1997). As expected, both ligands form stable, water-soluble 1:1 complexes with Ln$^{III}$ ions (Ln = Nd, Er, and Yb), but the complexation does not change their absorption spectra, the maxima being still observed at 491 nm for the fluorescein-containing ligand and at 519 nm for the eosin-containing one. Excitation at 488 nm of 10$^{-6}$ M solutions of the chelates in deuterated Tris-DCl buffer (Tris is 2-amino-2-(hydroxymethyl)propane-1,3-diol) leads to the typical NIR lanthanide emission. The relatively good sensitization of Ln$^{III}$ NIR luminescence in [Ln(**72a**)] complexes, whereas the isc quantum yield of fluorescein is only 2% in water, can be explained by the heavy atom effect produced by the lanthanide ion. Enhancement of the isc yield could not be quantitatively determined, but it is confirmed by the large decrease in fluorescence intensity of the antenna upon complexation. The luminescence of all the solutions is more or less oxygen sensitive, clearly indicating the implication of the xanthene triplet state in the sensitization process. Luminescence enhancement factors of 1.1
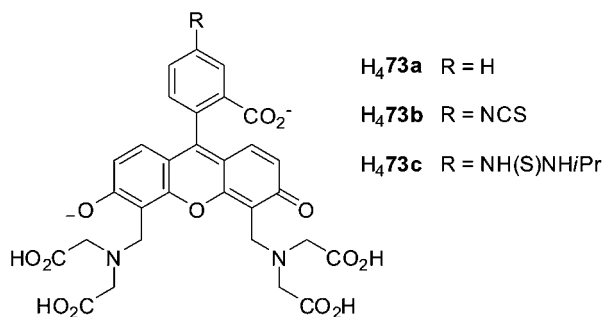
Fig. 64. $4',5'$-bis[$N,N$-bis(carboxymethyl)aminomethyl]fluorescein, also called fluorexon (fx, R = H) and thio-derivatives.

for [Er(**72a**)] to 5.8 and 6.4 for the Yb$^{III}$ chelates with H$_4$**72a** and H$_4$**72b**, respectively, have been observed upon de-oxygenation of the solutions. Therefore, the ligand-to-metal energy transfer in the Yb$^{III}$ complex is much slower than the corresponding process in the Nd$^{III}$ and Er$^{III}$ compounds. This is relatively easy to understand since energy transfer occurs between two states separated by a large energy gap $\approx$5000 cm$^{-1}$, the excited triplet state of the dye lying at $\approx$15000 cm$^{-1}$. In some cases $^1O_2$ ($^1\Delta_g \rightarrow {}^3\Sigma_g$) phosphorescence at 1275 nm has been detected, the latter species resulting from a triplet–triplet annihilation process occurring when the sensitizer triplet state interacts with molecular oxygen.

The lifetimes measured for Ln$^{III}$ complexes with ligand H$_4$**72a** amount to 0.6, 1.0, and 8.5 µs for Nd$^{III}$, Er$^{III}$, and Yb$^{III}$, respectively, and are comparable to the lifetimes generally found for organic complexes, but still remain short compared to those obtained in inorganic glasses, which are in the millisecond range. This demonstrates once more the effectiveness of high-energy vibrational modes in deactivation of the excited states of those NIR emitting Ln$^{III}$ ions. Multi-photon excitation mechanism is another way to further shift the excitation wavelength into the visible or near-infrared region, for which low-cost excitation sources can be used. The first case of sensitization of NIR emitting lanthanide via multi-photon excitation has been demonstrated on Nd$^{III}$ and Yb$^{III}$ complexes formed with H$_4$**72a** (Piszczek et al., 2002a). NIR emission is sensitized via two-photon excitation of the fluorescein-containing ligand at 800 or 840 nm for Yb$^{III}$ and Nd$^{III}$, respectively. The four-fold decrease in the emission intensity when the excitation is attenuated two-fold clearly demonstrates two-photon absorption.

The xanthene dye sensitizers used in the studies cited above feature a fused three-ring system acting as the chromophoric unit which is oriented almost perpendicular to the phenyl ring. As a result, the distance between the chromophoric unit and the lanthanide ion is long, which is detrimental for the overall sensitization process, the exchange interaction being weakened. To circumvent this drawback, a fluorescein derivative, $4',5'$-bis[$N,N$-bis(carboxymethyl)aminomethyl]fluorescein, commonly named calcein or fluorexon (fx, H$_4$**73a**) has been prepared (Werts et al., 2000a). This ligand and related derivatives are depicted on fig. 64; they consist of a fluorescein dye, in which the xanthene moiety has been directly functionalized with polyaminocarboxylate arms. By doing so, the binding site of the

lanthanide ion is in closer proximity of the chromophore than in complexes with ligands H$_4$**72a** and H$_4$**72b**.

Under stoichiometric conditions, fluorexon and its derivatives form 1:1 complexes with Ln$^{III}$ ions. However when the ratio Ln:Fx is increased, complexes with other stoichiometries are observed, the exact nature of which has not been determined. On the other hand, luminescence data of solutions with a ratio Yb$^{III}$:Fx $\leqslant$ 1 clearly indicate the presence of only one luminescent species, the 1:1 complex. Monoexponential luminescence decays are observed corresponding to a lifetime of 1.9 µs, whereas multi-exponential decays are measured when the Yb$^{III}$:Fx ratio is increased. Further proof of the existence of 1:1 complexes has been brought by mass spectrometry. Competitive titration with edta has been followed by monitoring the Yb$^{III}$ luminescence, since the edta complex is non-luminescent, contrary to the chelate formed with Fx. After addition of 5 equivalents of edta to a solution of [Yb(fx)] in Tris-HCl buffer, the Yb$^{III}$ luminescence intensity decreases to 12% of its initial value. The thermodynamic stability of the fluorexon chelate is, therefore, comparable to [Yb(edta)]$^-$. In addition, the luminescence decay after addition of edta aliquots is relatively slow, the estimated rate constant being $7.1 \times 10^4$ s$^{-1}$, indicating a reasonably high kinetic stability of the fluorexon chelate.

As for the chelates formed with ligands H$_4$**72a** and H$_4$**72b**, the fluorescence intensity of the dye is drastically reduced upon complexation with Nd$^{III}$, Er$^{III}$, and Yb$^{III}$, the corresponding quantum yield decreasing from 85% for the free ligand to less than 1% in the complexes. The quenching of the antenna fluorescence can be explained by three different mechanisms; (i) energy transfer from the singlet state to the Ln$^{III}$ ion, (ii) electron transfer (especially for Yb$^{III}$ ion which is easily reduced) and (iii) improved intersystem crossing. Since the quenching is identical in the complexes with the three NIR-emitting ions and with Gd$^{III}$, the first two mechanisms can be discarded and thus an enhancement of the intersystem crossing due to the paramagnetic and heavy atom effects is the most likely cause of the fluorescence quenching. The intersystem crossing rate constant can be estimated to be $>10^{10}$ s$^{-1}$. Moreover, study of the photophysical properties of the Gd$^{III}$ complex gives direct information on the triplet state of the chromophore, especially its lifetime, which is found to be short (3.1 µs). Deoxygenation of the solution, results in an increase of this lifetime to 21 µs. For the complexes with the NIR-emitting Ln$^{III}$ ion, only the typical metal-centered luminescence is observed in each case, indicating an efficient energy transfer from the triplet state of the antenna to the Ln$^{III}$ ion. Furthermore, the overall NIR luminescence quantum yield is independent of the oxygen concentration contrary to what was observed in complexes with H$_4$**72a**. This implies that both the intersystem crossing and the $^3\pi\pi^* \rightarrow$ Ln$^{III}$ energy transfer rates are fast since oxygen quenching, which occurs at a rate of $\approx 10^7$ s$^{-1}$, cannot compete. This results in high sensitization efficiencies, which reach estimated values of 50, 100, and 90% for Ln = Nd$^{III}$, Er$^{III}$, and Yb$^{III}$, respectively. However the lifetimes are still in the microsecond range (0.25–10.4 µs) and similar to what is usually observed in other organic complexes, corresponding to small intrinsic quantum yields, so that despite the high sensitization efficacy, the overall quantum yields (table 14) remain small, the highest value reaching 0.09% for the Yb$^{III}$ complex in Tris-HCl 0.1 M (0.45% in deuterated Tris-DCl).

Table 14

Lifetimes, intrinsic and overall quantum yields, and sensitization efficiency for 1:1 complexes formed with ligands H$_4$**73a** and H$_4$**74** in aqueous solution

| Ln | Ligand[a] | | $\tau$ (µs) | $Q_{Ln}^{Ln}$ (%)[b] | $Q_{Ln}^{L}$ (%) | $\eta_{sens}$ (–)[c] |
|---|---|---|---|---|---|---|
| Nd | H$_4$**73a** | H$_2$O[a] | 0.25 | 0.03 | 0.017 | 0.5 |
| | | D$_2$O[a] | 0.58 | 0.07 | 0.038 | 0.5 |
| | H$_4$**74** | H$_2$O | <0.2 | <0.03[d] | 0.004 | 0.1[d] |
| | | D$_2$O | 0.4 | 0.05[d] | 0.02 | 0.4[d] |
| Er | H$_4$**73a** | H$_2$O[a] | – | – | – | – |
| | | D$_2$O[a] | 1.46 | 0.02 | 0.019 | 1.0 |
| | H$_4$**74** | H$_2$O | – | – | – | – |
| | | D$_2$O | 1.2 | 0.02[d] | 0.004 | 0.2[d] |
| Yb | H$_4$**73a** | H$_2$O[a] | 1.91 | 0.1 | 0.089 | 0.9 |
| | | D$_2$O[a] | 10.4 | 0.5 | 0.45 | 0.9 |
| | H$_4$**74** | H$_2$O | 2.5 | 0.13[d] | 0.02 | 0.2[d] |
| | | D$_2$O | 10.0 | 0.50[d] | 0.10 | 0.2[d] |

[a]Tris-HCl and deuterated Tris-DCl 0.1 M solutions.

[b]Calculated from $Q_{Ln}^{Ln} = \tau_{obs}/\tau_{rad}$, with $\tau_{rad}$ = 0.8, 8, and 2 ms for Nd$^{III}$, Er$^{III}$, and Yb$^{III}$, respectively.

[c]Calculated from $Q_{Ln}^{L} = \eta_{sens} \cdot Q_{Ln}^{Ln}$.

[d]Recalculated from the data of (Quici et al., 2005) using the radiative lifetimes given under[b].

This work clearly demonstrates that a fluorescent chromophore is not necessarily a bad antenna for lanthanide ions. Indeed, high fluorescence quantum yields indicate the absence of nonradiative deactivation and thus, if the Ln$^{III}$ ion is sufficiently close to the chromophore, a significant intersystem crossing enhancement can occur, leading to an efficient sensitization of the Ln$^{III}$ luminescence. The authors extended the study further by functionalizing ligand H$_4$**73a** with a reactive group, in this case isothiocyanate (see ligands H$_4$**73b** and **73c**, fig. 64) for coupling with biological molecules in view of developing near-infrared luminescent probes for fluoroimmunoassays and fluorescence microscopy, as discussed in section 4.3 (Werts et al., 2000b).

The simpler phenanthroline chromophore has also been tested by grafting it onto diethylenetriaminetetraacetic acid, H$_4$dtta or H$_4$**74**, depicted on fig. 65 (Quici et al., 2005). Stable, water-soluble 1:1 complexes form with Ln$^{III}$ ions and $^1$H NMR and luminescence studies performed on the [Eu(**74**)] chelate clearly indicate that the two nitrogen atoms of the phenanthroline are involved in the coordination of the lanthanide ion, thus that no solvent molecule is present in the first coordination sphere. As already observed with the previous ligands, complexation with lanthanide ions leads to a quenching of the antenna fluorescence and hence to an enhancement of the intersystem crossing process. In the case of phen, the high value of the isc quantum yield in the free ligand (85%) suggests that it should be close to unity in the chelates.

Upon excitation of phen in the UV, at 279 nm, the typical luminescence of Pr$^{III}$, Nd$^{III}$, Sm$^{III}$, Eu$^{III}$, Tb$^{III}$, Dy$^{III}$, Ho$^{III}$, Er$^{III}$, and Yb$^{III}$ is observed. Thus ligand H$_4$**74** is able to sensitize the
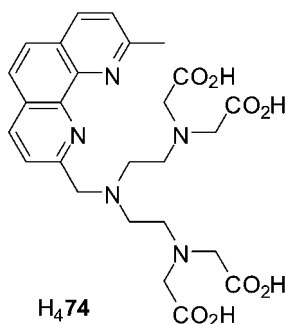
Fig. 65. Phenanthroline-functionalized diethylenetriaminetetraacetic acid (dtta).

whole range of emitting lanthanide ions in aqueous solution, which is quite exceptional especially for $Sm^{III}$, $Dy^{III}$, and $Ho^{III}$, the NIR luminescence of which is rarely observed in solution. Regarding NIR emitting $Ln^{III}$ ions (Nd, Er, and Yb) the lifetimes of the $Nd^{III}$, $Er^{III}$, and $Yb^{III}$ excited levels are exactly in the same range of values as those observed for complexes formed with $H_4$**73a**; i.e. from 0.2 to 10 μs (see table 14). However the overall quantum yields are smaller, with a maximum value of 0.1% in $D_2O$ obtained for the [Yb(**74**)] chelate. It has to be noted that a potential cause of luminescence quenching for NIR emitting $Ln^{III}$ ions in aqueous solutions can be water reabsorption of the emitted light. For instance, $Er^{III}$ complexes with $H_4$**73a** and $H_4$**74** undergo complete quenching in water and their emission can only be detected in deuterated water.

Another completely different approach consists in choosing a dye, that already possesses aminocarboxylate functions (Meshkova et al., 1992a), such as triphenylmethane dyes. The latter can be used for selective luminescent determination of $Nd^{III}$ and $Yb^{III}$ in samarium oxide, for instance. As previously described in the section devoted to $\beta$-diketonates (section 3.2.1), the triplet excited states of $\beta$-diketonates lie at energies $>20\,000$–$25\,000$ cm$^{-1}$, above most of the accepting levels of $Ln^{III}$ ions. As a consequence, determination of $Nd^{III}$ and $Yb^{III}$ in europium or samarium oxides is difficult using $\beta$-diketonates since these two ions exhibit luminescence in the NIR, especially $Sm^{III}$ with emission lines at 908, 930, 950, and 1038 nm close to the analytical lines of $Nd^{III}$ and $Yb^{III}$. Therefore, the detection limit of $Nd^{III}$ and $Yb^{III}$ in samarium compounds by luminescence of their ternary complexes with tta and phen is only 0.1–1 wt%.

In order to solve this problem, Meshkova et al. used triphenylmethane dyes, especially phthalexon S (PS, $H_4$**75a**, fig. 66) and xylenol orange (XO, $H_4$**75c**), since their triplet states (12 800–14 600 cm$^{-1}$) are higher in energy than the $^4F_{3/2}$ and $^2F_{5/2}$ excited levels of $Nd^{III}$ and $Yb^{III}$, respectively, but lower than the $^4G_{5/2}$ excited state of the $Sm^{III}$ ion. Following this strategy and using XO as colored reagent, detection limits of $Nd^{III}$ and $Yb^{III}$ in samarium oxide could be brought down to $2.5 \times 10^{-3}$ and $3.0 \times 10^{-4}$ wt%, respectively.

Ligands $H_4$**75a** and $H_4$**75c** form 1:1 and 1:2 complexes with $Ln^{III}$ ions, and to avoid quenching by water molecules, a surfactant was added. The subsequent formation of micelles led to 7- to 12-fold increases in $Nd^{III}$ luminescence intensity (Rusakova et al., 1984).
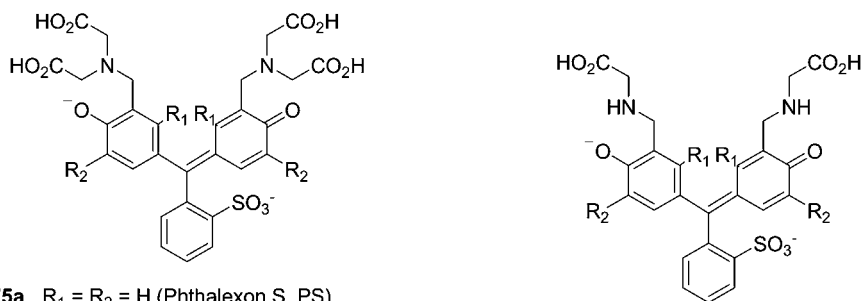
H$_4$**75a**   R$_1$ = R$_2$ = H (Phthalexon S, PS)

H$_4$**75b**   R$_1$ = H, R$_2$ = Br

H$_4$**75c**   R$_1$ = H, R$_2$ = CH$_3$ (xylenol orange, XO)

H$_4$**75d**   R$_1$ = CH$_3$, R$_2$ = *i*-Pr (methylthymol blue)

H$_4$**76a**   R$_1$ = H, R$_2$ = CH$_3$ (glycinecresol red)

H$_4$**76b**   R$_1$ = CH$_3$, R$_2$ = *i*-Pr (glycinethymol blue)

Fig. 66.  Triphenylmethane dyes.

Cationic surfactants cause the greatest increase, whereas anionic or nonionic surfactants influence the luminescence intensity to a much lesser extent. With PS or XO as colored reagent and the cationic surfactant Etonium (1,2-ethanediaminium, $N,N'$-bis[2-(decyloxy)-2-oxoethyl]-$N,N,N',N'$-tetramethyl-dichloride), the smallest concentration of Nd$^{III}$ that yields observable NIR luminescence reaches 0.1 µg ml$^{-1}$. Further triphenylmethane dyes were tested, such as H$_4$**75b**, **d** and H$_4$**76a**, **b** (fig. 66), the two last ligands possessing iminoacetate functions instead of iminodiacetate ones (Rusakova and Meshkova, 1990). The solvent also influences the emission intensity and with respect to water, the largest enhancement occurs when dmso is added (up to 70%), followed by dmf and alcohols, whereas with acetone and acetonitrile, the emission is enhanced up to addition of 60% solvent and then drops due to decomposition of the complexes. In view of these results, a new selective method for determining Nd$^{III}$ in rare-earth oxides has been proposed based on a Nd$^{III}$ complex with xylenol orange in the presence of Etonium and dmso. The Nd$^{III}$ detection limit in Sm$^{III}$ and Pr$^{III}$ oxides is $2.5 \times 10^{-3}$ wt%, whereas in La$^{III}$ and Y$^{III}$ oxides it reaches $1 \times 10^{-3}$ wt%. Similar results have been obtained for Yb$^{III}$ (Meshkova et al., 1985; Poluektov et al., 1984) and the most important photophysical characteristics of the two series of complexes with ligands H$_4$**75** and H$_4$**76** in water and deuterated water are summarized in table 15.

Because of the higher sensitivity of Nd$^{III}$ ions towards deactivation through O–H oscillators, the complexes with this lanthanide have much lower quantum yields and lifetimes when compared to Yb$^{III}$. The best photophysical properties are obtained with phthalexon S and since complexes with PS contain 4–5 water molecules, depending on the lanthanide ion, it is quite clear that exclusion of these water molecules from the first coordination sphere will lead to much enhanced luminescent properties. This is indeed demonstrated by bis(cyclen)-substituted PS, H$_7$**36** (see fig. 36), which increases quantum yields to 0.23 and 1.45% in D$_2$O for Nd$^{III}$ and Yb$^{III}$, respectively (Korovin and Rusakova, 2002).

Table 15

Photophysical properties of some Nd$^{III}$ and Yb$^{III}$ complexes with triphenylmethane dyes in water (Korovin and Rusakova, 2002)

| Ln | Ligand | $E(^3\pi\pi^*)$ (cm$^{-1}$) | $Q_{Ln}^L$ (%)$^a$ | $\tau$ (µs) H$_2$O | D$_2$O |
|----|--------|------|------|------|------|
| Nd | H$_4$**75a** | 14 060 | 0.025 | 0.07 | 0.35 |
|    | H$_4$**75c** | 13 950 | 0.021 | 0.06 | 0.30 |
|    | H$_4$**75d** | 13 750 | 0.008 | 0.05 | 0.25 |
| Yb | H$_4$**75a** | 14 110 | 0.411 | 0.70 | 3.15 |
|    | H$_4$**75c** | 14 030 | 0.496 | 0.60 | 2.70 |
|    | H$_4$**75d** | 13 870 | 0.190 | 0.40 | 1.60 |
|    | H$_4$**76a** | 14 015 | 0.020 | 0.15 | 0.80 |
|    | H$_4$**76b** | 13 905 | 0.036 | 0.20 | 1.15 |

$^a$Overall luminescence quantum yields of D$_2$O solutions determined with [ZnTPP] as standard ($Q = 3.15\%$ in ethanol).
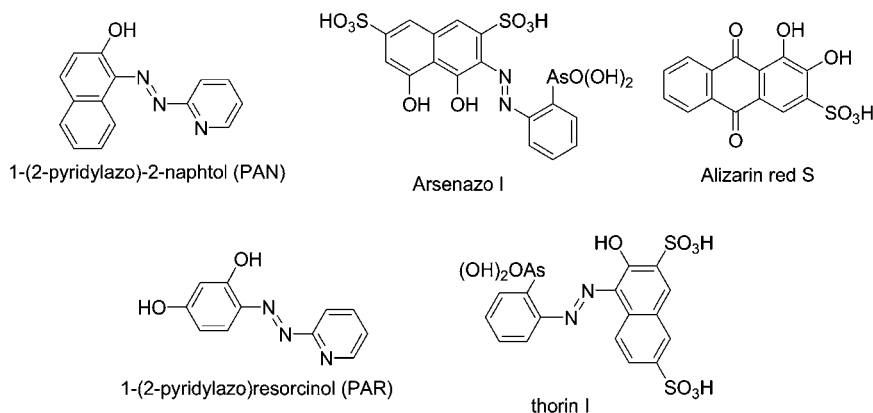


Fig. 67. Some of the dyes investigated as colored reagents.

### 3.2.5. *Other chelating agents*

3.2.5.1. *Dyes* Following a strategy similar to the one described above, other types of dyes have been proposed for analytical purposes. For instance, Korovin et al. have investigated the possibility of using a 1:2 (Yb:L) ytterbium complex with 1-(2-pyridylazo)-2-naphthol (PAN, fig. 67) for the determination of Yb$^{III}$ in solutions of its salts. The luminescence intensity varies linearly over an Yb$^{III}$ concentration range from 0.1 to 10.0 µg ml$^{-1}$, whereas the detection limit reaches 0.05 µg ml$^{-1}$ (Korovin et al., 1984). One disadvantage of using dyes as ligands comes from the fact that most of the time the first coordination sphere of the Ln$^{III}$ ion is not saturated, leaving space for one or several bound solvent molecules. This leads to a consequent quenching of the NIR luminescence and thus decreases the detection limit. To circumvent this problem, Meshkova et al. turned to ternary complexes, as often encountered
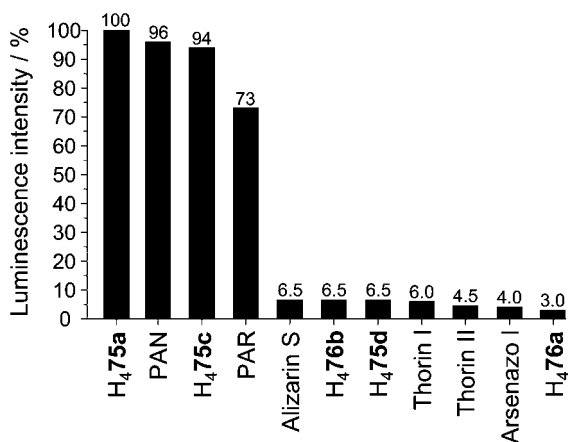
Fig. 68. Relative intensities of luminescence of Yb[III] ion in complexes with colored organic reagents; values taken from (Poluektov et al., 1984).

with $\beta$-diketonates, using an organic base, such as phen, bpy or pyridine as second ligand (Meshkova et al., 1987).

The luminescence characteristics of four complexes formed with arsenazo (I and II) and thorin (I and II) dyes (fig. 67) as well as those of the corresponding ternary complexes with phen have been investigated in aqueous solution. In presence of Yb[III] ions, 1:1 complexes are formed, except for thorin I, which yields a 1:2 (Yb:L) complex. As a consequence, for thorin I only one phen molecule is present, yielding a 1:2:1 (Yb:L:phen) ternary complex, while 1:1:2 stoichiometries are observed for the three other complexes. Addition of phen results in a significant enhancement (2- to 7-fold) of the luminescence quantum yields, which reach a maximum value of 0.13% for the complex with arsenazo I. As a consequence, the detection limits are lowered by similar factors, from 2 to 8.

Hydroxyanthraquinone derivatives, especially alizarine red S (fig. 67), also form 1:1 complexes with Yb[III] ions (Korovin et al., 1988). The observed lifetimes are very short, around 0.3 µs, but comparable to those listed in table 15 for the complexes with triphenylmethane dyes. The relative luminescence intensities of Yb[III] complexes with several different dyes are summarized in fig. 68. The intensities are given relative to the more luminescent complex, with phthalexon S. It is noteworthy that all these complexes have absorption maxima at wavelengths longer than 500 nm, between 505 nm for thorin I and 590 nm for methylthymol blue $H_4$**75d**, and can thus be excited by the 546 nm-emission line of a mercury lamp.

F.J. Steemers and coworkers followed a similar approach, but designing organic chromophores derived from azatriphenylene (fig. 69) instead of organic dyes (Steemers et al., 1998). In acetonitrile and in presence of Ln[III] ions, formation of 1:1 complexes occurs with diazatriphenylene **77** and with two of the tetraazatriphenylene ligands, **78a** and **78b**, while ligand **78c** yields 1:2 (Ln:L) complexes. Sensitization of the NIR luminescence of Nd[III], Er[III], and Yb[III] ions is achieved through excitation in the ligand absorption bands. Azatriphenylene
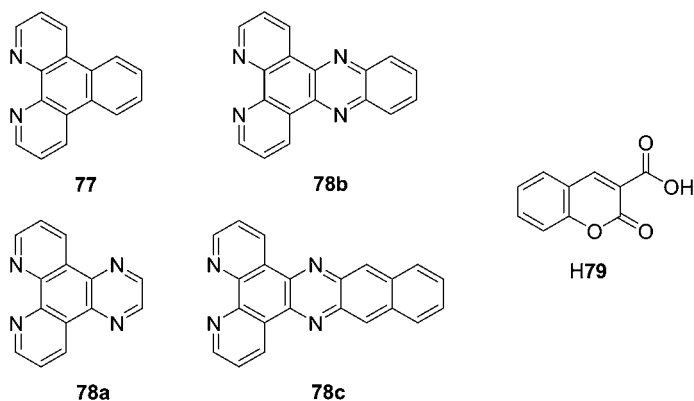
Fig. 69. Azatriphenylene (**77**–**78c**) and coumarin (H**79**) derivatives.

derivatives possess several absorption bands and can be excited in a spectral range extending from 280 to 375 nm, or even up to 450 nm for ligand **78c**. However their triplet excited states lie at relatively high energy, between 18 500 (**78b**) and 23 800 cm$^{-1}$ (**77**) compared to the accepting levels of Nd$^{III}$, Er$^{III}$, and Yb$^{III}$. As a consequence, energy transfer to the Ln$^{III}$ ion is not sufficiently fast to avoid competition with triplet state deactivation due to oxygen quenching. This is evidenced by an emission band appearing at 1275 nm, which is attributed to the phosphorescence of singlet oxygen, the latter resulting from energy transfer between the excited triplet state of the chromophore and molecular oxygen. Ln$^{III}$ luminescence is, therefore, enhanced upon de-oxygenation of the samples. For tetraazatriphenylene **78c**, for which the triplet state lies at the lowest energy, the influence of oxygen is strongly reduced, indicating a faster energy transfer in complexes formed with this ligand. The lifetimes measured for all the complexes in acetonitrile are around 0.5, 2 and 8 µs for Nd$^{III}$, Er$^{III}$, and Yb$^{III}$ ions, respectively.

A completely different approach consists in resorting to rather simple molecular frameworks functionalized with carboxylate groups, since these groups strongly coordinate Ln$^{III}$ ions. The first example lies at the border of the two last approaches since the ligand H**79** (fig. 69) is based on a coumarin dye, functionalized in position 3 by a carboxylic acid (Roh et al., 2004b). In view of potential advanced photonic applications, interest has focused on the Er$^{III}$ tris complex, [Er(**79**)$_3$(H$_2$O)$_3$], in which three water molecules are needed to saturate the first coordination sphere. The photophysical properties of this chelate 10$^{-5}$ M in dmso proved to be moderately interesting, the presence of the fluorescence band of the ligand between 375 and 550 nm indicating that energy transfer is not very efficient.

3.2.5.2. *Carboxylates* With the aim of developing highly luminescent Er$^{III}$ complexes for advanced photonic applications, some of the research concentrates on the synthesis of new ligands, based on simple molecular frameworks such as alkyl chains or benzene rings fitted with carboxylate groups for coordination to the lanthanide ions. For instance, the photophys-

ical properties of Er$^{III}$ complexes formed with ligands H**80** and H**81** (see fig. 70) have been studied in the solid state by direct excitation of the Er$^{III}$ ion (Li et al., 2005). Ligand H**80**, commonly named stearic acid, possesses a long C$_{18}$-alkyl chain and forms a tris complex [Er(**80**)$_3$], which exhibits a Er($^4$I$_{13/2}$) lifetime of 2.69 μs. Assuming a radiative lifetime of 14 ms, which corresponds to the typical value observed for Er$^{III}$ in silica, an intrinsic quantum yield of 0.02% can be calculated for this compound. Since C–H oscillators are efficient quenchers of Er$^{III}$ luminescence, the authors tried to address this problem by synthesizing ligand H**81**, in which the C–H groups of the C$_8$-alkyl chain are completely fluorinated. As for ligand H**80**, one can expect the formation of a tris complex, but the photoluminescence decay of the Er$^{III}$ compound with ligand H**81** turned to be a multi exponential function, indicating the presence of several species, which were assumed to be the tris and tetrakis species [Er(**81**)$_3$] and [Er(**81**)$_4$]$^-$. Depending on the pumping wavelength, intrinsic quantum yields ranging from 0.4 to 4.3% were obtained, again assuming a radiative lifetime of 14 ms. Therefore a considerable enhancement in the intrinsic quantum yield is observed compared to the typical value of 0.02% for usual Er$^{III}$ organic complexes.

In a similar way, the luminescence properties of Er$^{III}$ complexes with benzoic acid (H**82a**) and pentafluorobenzoic acid (H**82b**), as well as their ternary complexes with bipyridine (fig. 70) have been investigated (Roh et al., 2004a). Thermogravimetric analyses (TGA) performed on tris complexes clearly show the presence of three water molecules in the first coordination sphere of the Er$^{III}$ ion, as was previously observed in complexes with coumarin-3-carboxylic acid, H**79**. In the corresponding ternary complexes with bpy, TGA revealed the absence of coordinated water molecule and thus the formation of saturated 8-coordinate Er$^{III}$
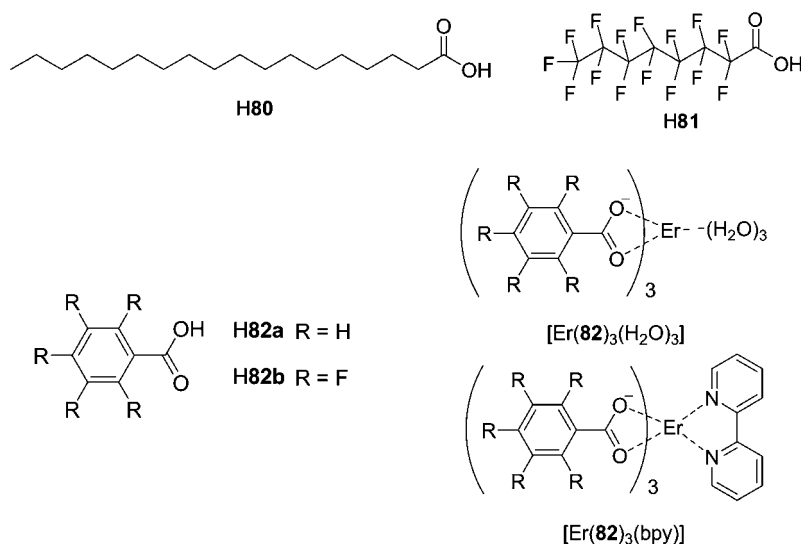


Fig. 70. (Top) Carboxylate-functionalized alkyl and perfluoroalkyl ligands; (bottom) benzoate and pentafluoro-benzoate ligands and their tris and ternary complexes.
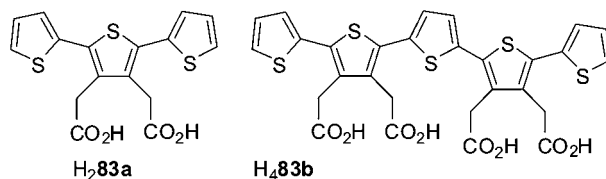
Fig. 71. Oligothiophene ligands.

complexes, [Er(**82**)$_3$(bpy)]. Upon excitation in the ligand levels, the typical NIR luminescence of Er$^{III}$ ion is observed in both tris and ternary complexes. As expected, the luminescence intensity of ternary complexes is much higher than that of the hydrated tris chelates. NIR luminescence is also much more intense (up to 80 times in ternary complexes) when indirect excitation is performed instead of direct Er$^{III}$ excitation at 488 nm. Furthermore the probability of multi-phonon relaxation is essentially related to the energy difference between the upper and lowers levels of the Ln$^{III}$ ion ($\Delta E \approx 7000$ cm$^{-1}$ for Er$^{III}$) and to the harmonic vibration energy of the metal ion surroundings. In complexes with pentafluorobenzoate, this probability is very low because the harmonic vibration energy of C–F bonds is much smaller than the energy gap, whereas one overtone of C–H vibration almost matches the energy difference, leading to a much higher probability in multi-phonon relaxation. As a consequence, the luminescence intensity is much stronger in fluorine-containing complexes. For instance [Er(**82b**)(bpy)] is four times more luminescent than its analog formed with ligand **82a**. The same photophysical study has been performed on the dimeric Er$^{III}$ complex, [Er$_2$(**82a**)$_6$(bpy)$_2$], synthesized through a ligand-exchange reaction using erbium chloride in the presence of bipyridine and potassium benzoate salt. According to the crystal structure, four bridging and two chelating benzoate as well as two bipyridine ligands are involved in the coordination of the two 8-coordinate Er$^{III}$ ions (Roh et al., 2005).

One of the problems pertaining to the development of Er$^{III}$ electroluminescent devices is the relatively low solubility of lanthanide complexes. To overcome this drawback, organic polymers (PMMA, PVK) are used in the blend of the active luminescent materials, or organic ligands are attached onto polymeric chains. Examples of the latter are oligothiophene ligands with carboxylate functionalities (fig. 71) which have the following advantages: (i) good solubility in organic solvents, facilitating the production of devices, for instance by spin-coating, (ii) good transport properties, and (iii) efficient isc process combined with the possibility of excitation in the visible range for H$_4$**83b**.

Er$^{III}$ complexes with 1:2 stoichiometries are isolated by reaction of the sodium salts of the two oligothiophene ligands with erbium chloride under anhydrous conditions. No analytical data are reported to prove this stoichiometry, but both compounds Na[Er(**83a**)$_2$] and Na$_5$[Er(**83b**)$_2$] display the 1.54 μm emission in anhydrous pyridine upon excitation at 353 nm. The emission intensity of [Er(**83a**)$_2$]$^-$ is comparable to the fluorescence intensity of [Er(8-Q)$_3$] recorded under the same experimental conditions, while emission intensity of the pentathiophene complex is about half that. This is explained by the more efficient triplet state production in shorter oligothiophenes than in longer ones (Destri et al., 2003).

2,6-Pyridine-dicarboxylic acid ($H_2$dpa) is a well known chelating agent for both d- and f-transition metal ions. It reacts in water with lanthanide ions to yield 9-coordinate tris complexes with $D_3$ symmetry. The tris complexes have appreciable stability, with log $\beta_3$ in the range 18–22, and they are also highly luminescent upon excitation into the ligand level, so that they are used as luminescent stains in analytical processes, for instance [Tb(dpa)$_3$]$^{2-}$ for the detection of bacterial endospores, such as anthrax (Pellegrino et al., 1998). Crystals of Na$_3$[Yb(dpa)$_3$]·13H$_2$O have an Yb($^2F_{5/2}$) lifetime of 2.5 μs at 15 K and the ligand-field splitting of the $^2F_{5/2}$ (3 sub-levels, total splitting 268 cm$^{-1}$) and $^2F_{7/2}$ (4 sub-levels, 348 cm$^{-1}$) is in line with the trigonal symmetry. In aqueous solution at room temperature, the lifetime decreases to 2 μs; no up-conversion process could be evidenced either for the crystals or for the solution (Reinhard and Güdel, 2002).

Substitution of the 4-position of the pyridine ring of dpa with OH or Cl has been achieved and the resulting Nd$^{III}$ complexes formed with these derivatives showed better luminescence properties than the corresponding dpa complexes (Curry et al., 2005).

3.2.5.3. *Tropolonates* In view of their moderately low-lying excited triplet states ($\approx$16 800 cm$^{-1}$), tropolone-based ligands are well-suited for efficient energy transfer to the low-energy accepting levels of several NIR emitting lanthanide ions such as Nd$^{III}$, Ho$^{III}$, Er$^{III}$, Tm$^{III}$, and Yb$^{III}$. Moreover tropolonates provide strong coordination to Ln$^{III}$ ions since two oxygen donors are available, forming stable 5-membered chelate rings. Therefore 2-hydroxycyclohepta-2,4,6-trien-1-one, known as tropolone (H**84a**, fig. 72), has been chosen for the development of NIR emitting Ln$^{III}$ complexes (Zhang et al., 2005). X-ray structures of {K[Ln(**84a**)$_4$]·dmf}$_\infty$ (Ln = Tb, Dy, Ho, Er, Tm, Yb, Lu) clearly show the Ln$^{III}$ ion being surrounded by four bidentate tropolonates, while the potassium ion plays a significant role in the packing pattern of the complexes in the crystal.

UV–vis titrations in dmso indicate that 1:1, 1:2, 1:3, and 1:4 (Ln:L) complexes are successively formed in solution. Under the conditions leading to tetrakis [Ln(**84a**)$_4$]$^-$ complexes and when excitation is performed in the ligand absorption band at 340 nm, typical NIR luminescence is monitored for all the complexes, indicating efficient sensitization of the Ln$^{III}$ luminescence via energy transfer from the tropolonate moieties. Not only are the well-known emission bands from Nd$^{III}$, Er$^{III}$, and Yb$^{III}$ ions observed, but also the less-common Tm$^{III}$ bands at 796 ($^3F_4 \rightarrow {}^3H_6$) and 1465 nm ($^3F_4 \rightarrow {}^3H_4$), and the ones from Ho$^{III}$ around 975, 1160, and 1479 nm, which are assigned to $^5F_5 \rightarrow {}^5I_7$, $^5I_6 \rightarrow {}^5I_8$, and $^5F_5 \rightarrow {}^5I_6$ transitions, respectively. However the presence of ligand-centered emission in all these complexes clearly indicates that the ligand-to-lanthanide energy transfer process is not complete. To quantify the intramolecular energy transfer, the overall luminescence quantum yields have been determined in different solvents and are summarized in table 16.

The $^4G_{5/2} \rightarrow {}^6H_{9/2}$ transition of Sm$^{III}$ (2-hydroxyisophthalamide) macrobicyclic complex with $Q^L_{Ln} = 0.073\%$ in 0.01 M tris buffer (Petoud et al., 2003) has been used as a reference for the [Yb(**84a**)$_4$]$^-$ complex, this latter being itself taken as standard for the quantum yield measurements of Nd$^{III}$ and Er$^{III}$ complexes. For Ho$^{III}$ and Tm$^{III}$, the [Er(**84a**)$_4$]$^-$ complex was used as standard because of their comparable luminescence intensities. The quantum yields obtained are clearly dependent on the nature of the solvent, suggesting that the Ln$^{III}$
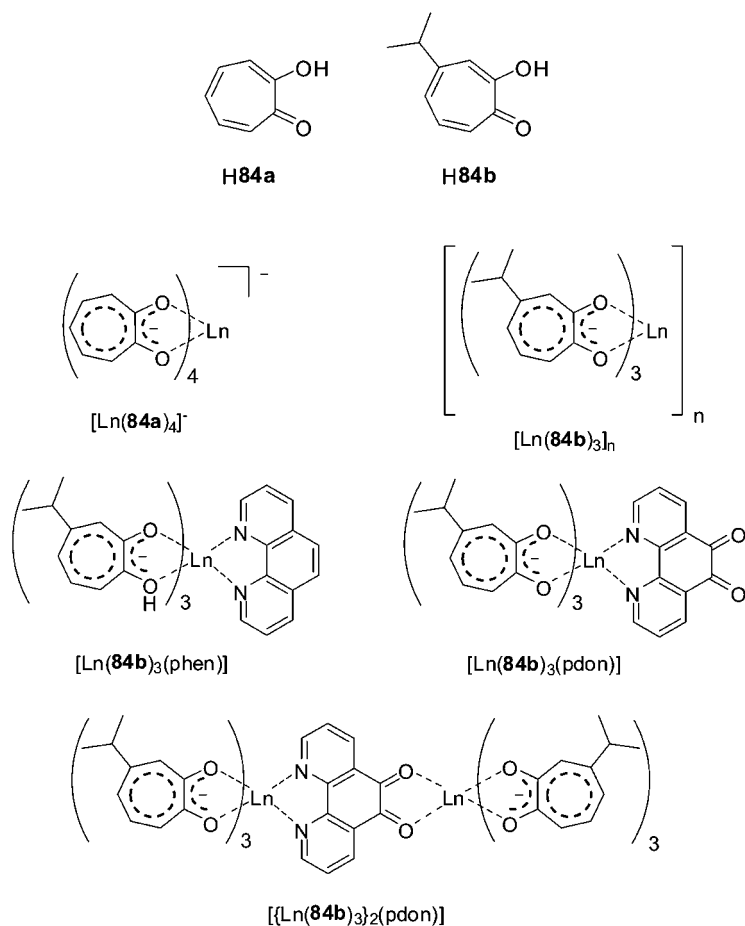
Fig. 72. (Top) Tropolone-based ligands and (bottom) their Ln$^{III}$ complexes with and without secondary ligand.

Table 16
Overall luminescence quantum yields for [Ln(**84a**)$_4$]$^-$ in organic and aqueous media ($\lambda_{ex}$ = 340 nm)

| Ln | Solvent | $Q^L_{Ln}$ (%) | $Q^L_{Ln}$ (%)[a] |
|---|---|---|---|
| Nd | dmso | 0.21 | 0.36 |
| Ho | dmso | $2.3 \times 10^{-3}$ | $2.4 \times 10^{-3}$ |
| Er | dmso | $1.7 \times 10^{-2}$ | $3.2 \times 10^{-2}$ |
| Tm | dmso | $3.8 \times 10^{-3}$ | $5.7 \times 10^{-3}$ |
| Yb | dmso | 1.9 | 2.2 |
| | MeOH | 0.13 | 1.6 |
| | H$_2$O | $2.4 \times 10^{-2}$ | 0.74 |

[a]Overall luminescence quantum yields measured in the corresponding deuterated solvent.

ion is not completely shielded from solvent molecules by the four tropolonate ligands. Using eq. (9a) with Yb$^{III}$ lifetimes of 0.75 and 10.03 µs in H$_2$O and D$_2$O, respectively, one finds $q_{H_2O} = 1.1$; the same value is obtained for $q_{CH_3OH}$. Thus the structure in solution is different from that in the solid state in which no solvent molecules are coordinated to the lanthanide ion.

According to elemental, thermogravimetric and IR analyses, the tris-tropolonato Ln$^{III}$ complexes of the 4-isopropyl derivative H**84b** (fig. 72), obtained by reaction of a methanolic solution of H**84b** with NaOH and LnCl$_3$·6H$_2$O, have no coordinated solvent molecules (Bertolo et al., 2006). However, the authors suppose that, in order to complete the first coordination sphere of the Ln$^{III}$ ion, the complexes are in the form [Ln(**84b**)$_3$]$_n$ ($n = 2$ or 3). These polymeric forms easily react with a secondary ligand to form ternary complexes with phen or 1,10-phenanthroline-5,6-dione (pdon) as secondary ligand. The latter is a suitable ditopic ligand for the formation of bimetallic complexes since it contains two well separated coordination sites. The various adducts, [Ln(**84b**)phen], [Ln(**84b**)pdon], and {[Ln(**84b**)]$_2$pdon} are depicted on fig. 72. Upon excitation in the absorption bands of the ligand at 355 nm, the characteristic Er$^{III}$ emission is observed for all the complexes. The quantum yield of the IR emission is on the order of a few hundredths of percent, which is comparable with the data obtained for the tris 8-hydroxyquinolinate Er$^{III}$ complex. On the other hand, the lifetimes measured in dmso are in the range 2.11–2.15 µs and are somewhat longer when compared to [Er(8-Q)$_3$] (1.80 µs). The tris-tropolonato Yb$^{III}$ complex, [Yb(**84b**)$_3$]$_n$ exhibits the typical NIR emission near 1 µm when excited at 355 nm. Even though no quantitative data are presented in this work, the authors, in view of the luminescence intensity, estimated a quantum yield of about two orders of magnitude larger than the one measured for the corresponding Er$^{III}$ complex. The photoluminescence decay is again monoexponential and lifetimes as long as 70–80 µs were obtained, suggesting a good protection of the Ln$^{III}$ ion from nonradiative deactivation processes in this complex.

3.2.5.4. *Imidophosphinates* Sterically bulky bidentate imidodiphosphinates present an ideal framework for the minimization of nonradiative deactivation processes because of the formation of a lipophilic shell around the Ln$^{III}$ ion avoiding the coordination of solvent molecules and the lack of high-energy oscillators in close proximity to the lanthanide ion. In view of these characteristics, Bassett et al. (2005) have synthesized a tetraphenyl imidodiphosphinate ligand, H**85a** (fig. 73), and studied the photophysical properties of its neutral tris Ln$^{III}$ complexes (Ln = Nd, Er and Yb) in solution in CH$_3$CN or in the solid state. X-Ray analysis of single crystals of [Er(**85a**)$_3$] shows two symmetrically independent arrangements, in which the Er$^{III}$ ion is hexa-coordinated by the oxygen atoms of the three ligands. The difference between these two complexes lies in the geometry around the Er$^{III}$ ion, which is a distorted octahedron in one complex and a distorted trigonal prism in the other one. However in both cases, the three ligands are symmetrically equivalent around the Ln$^{III}$ ion, as further demonstrated for all the complexes by $^{31}$P NMR. It is also important to note that the presence of intramolecular CH–$\pi$ interactions between the 12 phenyl rings of the same ligand may stabilize the hydrophobic shell around the Ln$^{III}$ ion.

H**85a**  R = H

H**85b**  R = F
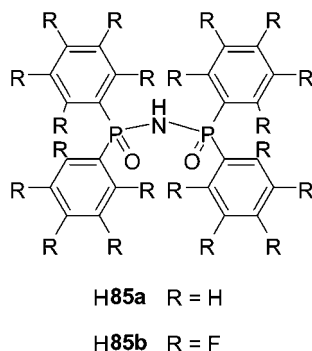
Fig. 73.  Imidodiphosphinate ligand and its perfluorinated analog.

Upon excitation in the phenyl absorption band of the ligand at 266 nm, all the complexes exhibit near-infrared emission in both solution and solid state. The lifetimes measured in dry acetonitrile solutions are quite long, amounting to 2.7, 6.5, and 52.8 μs for Nd$^{III}$, Er$^{III}$, and Yb$^{III}$, respectively. These values are comparable with the ones obtained for complexes with fully fluorinated $\beta$-diketonate ligands, in line with an efficient shielding of the Ln$^{III}$ ion by the three imidodiphosphinate ligands. Adding an excess of water ([H$_2$O] = 10 M) to the acetonitrile solutions results in a large decrease in the emission lifetimes reaching 81% for Nd$^{III}$, whereas the lifetimes diminish only by 17 and 24% for [Er(**85a**)$_3$] and [Yb(**85a**)$_3$], respectively. The corresponding data measured on powdered samples are 1.2, 2.3, and 17.8 μs for Nd$^{III}$, Er$^{III}$, and Yb$^{III}$, respectively. According to the authors, the shortening of the lifetimes with respect to solutions may be attributed to lattice vibrations or cross-relaxation mechanisms between the closely positioned lanthanide ions in the solid state. To further improve emission intensity, fluorination of the imidodiphosphinate ligand has been performed, yielding ligand H**85b** (Mancino et al., 2005). The authors investigated only the Er$^{III}$ tris complexes formed with fluorinated and non-fluorinated ligands, in CDCl$_3$ and in the solid state both as powder and as 500 nm thin film. The intrinsic quantum yields of Er$^{III}$ in [Er(**85b**)$_3$] complexes calculated using a radiative lifetime of 8 ms amount to 0.4% in solution and to 1.8 and 1.71% for powder and thin-film samples, respectively. These values are significantly larger (from 7, up to 43 times) than the ones obtained for the corresponding complex with the non-fluorinated ligand. However the luminescence decays for all the complexes is best described by a biexponential process, which is in contradiction with the monoexponential decays observed for [Er(**85a**)$_3$] by Bassett et al. (2005). Moreover the lifetime values for the Er$^{III}$ powdered samples are not in agreement from one study to the other.

3.2.5.5. *Pyrazoylborates* Tetradentate (**86**) and hexadentate (**87**) pyrazoylborates (see fig. 74) form a range of 1:1 and 1:2 complexes with Ln$^{III}$ ions, as well as ternary 1:1:1 adducts with dibenzoylmethanate, which have coordination number between 8 and 12. In the case of visible-emitting lanthanide ions, large quantum yields have been recorded, up to 50% for Tb$^{III}$ for instance (Armaroli et al., 1997). With Nd$^{III}$ and Yb$^{III}$, four types of complexes
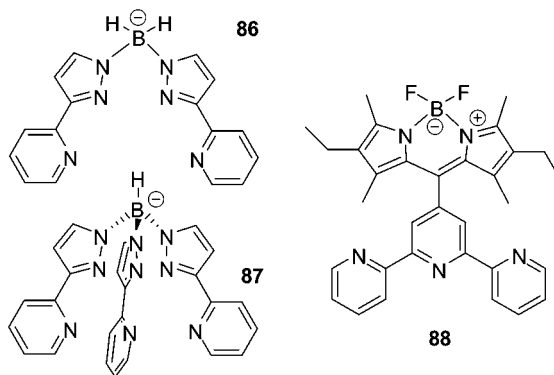
Fig. 74. Pyrazoylborate (left) and boradiazaindacene-substituted terpyridine (right).

have been characterized, 8-coordinate $[Ln(\mathbf{87})(dbm)_2]$, 10-coordinate $[Ln(\mathbf{87})(NO_3)_2]$ and $[Ln(\mathbf{86})_2(NO_3)]$, and 12-coordinate $[Ln(\mathbf{87})_2]BPh_4$ in which the metal center is bound by two interpenetrating hexadentate podands (Beeby et al., 2002a). Lifetimes have been determined in methanol and are relatively long, 0.15–1.6 μs for $Nd^{III}$ and 0.45–2.9 μs for $Yb^{III}$, in view of the few C–H vibrations close to the metal ion. Using relationships (9b) and (10b), solvation numbers have been calculating and, with the exception of $[Yb(\mathbf{87})_2(NO_3)]$, they are in the range 0–1.

It was demonstrated later that $[Nd(\mathbf{87})(dbm)_2]$ rearranges to $[Nd(\mathbf{87})_2][Nd(dbm)_4]$ upon re-crystallization, with the latter entity having almost perfect $O_8$ coordination. Besides, $Pr^{III}$ emission assigned to $^1D_2 \rightarrow {}^3F_4$ is observed at 1.02 μm for $[Pr(\mathbf{87})(dbm)_2]$ in methanol (lifetime: 13 ns), as well as the 1.53 μm fluorescence (lifetime 0.85 μs) of the isostructural $Er^{III}$ complex (Davies et al., 2004). In addition to visible emission from $^3P_0$, praseodymium luminescence at 1.44 μm was also detected in the case of $[Pr(\mathbf{87})(NO_3)_2]$ and $[Pr(\mathbf{86})_2(NO_3)]$ and was assigned to the $^1D_2 \rightarrow {}^1G_4$ transition which fits exactly with the expected energies of these levels; further evidence for this assignment comes from the lifetimes determined while monitoring the two NIR bands and which were found to be the same, within experimental errors; they amount to 54 and 73 ns for the complexes with **86** and **87**, respectively (Davies et al., 2005a).

The terpyridine-substituted difluoroborondipyrromethene dye **88** is a singlet emitter at 540 nm ($18\,500$ cm$^{-1}$) and its triplet state emission extends from 550–750 nm ($18\,200$–$13\,300$ cm$^{-1}$), which makes it a potential sensitizer of lanthanide NIR luminescence. In $[Yb(NO_3)_3(\mathbf{88})]$ (see fig. 75), the lanthanide ion is bound to the terdentate terpyridine and to three bidentate nitrate counterions, in a distorted tricapped antiprismatic geometry. The $Ln^{III}$ complexes (Ln = La, Nd, Er, Yb) have large absorption coefficients ($65\,000$ M$^{-1}$ cm$^{-1}$ at 529 nm) and upon complexation with lanthanide ions, the quantum yield of the $^1\pi\pi^*$ emission decreases from 79% for the free ligand in dichloromethane to 54% for the $La^{III}$ complex, due to the heavy atom effect favoring the isc process. With $Nd^{III}$, $Er^{III}$, and $Yb^{III}$ the quantum yield further decreases to 15–20% while NIR emission appears, indicating energy transfer
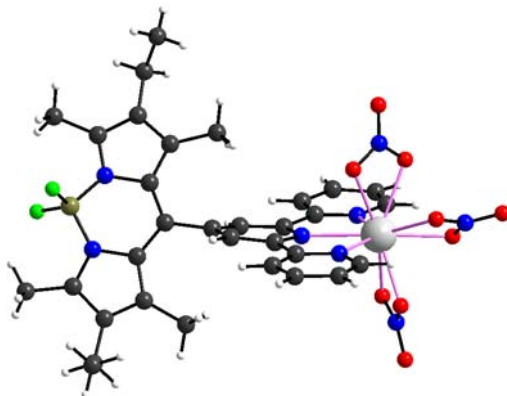
Fig. 75.  Structure of [Yb(NO$_3$)$_3$(**88**)], redrawn from (Ziessel et al., 2006).

from the ligand to the metal ions. In the same solvent, at a concentration of $10^{-4}$–$10^{-7}$ M, the quantum yields of the metal-centered luminescence are 0.016 and 0.31% for Nd$^{III}$, and Yb$^{III}$, respectively. Calculations of the sensitization efficiency of the indacene dye moiety based on an estimate of the intrinsic quantum yields via lifetimes ($\tau_{rad}$ taken as 0.8 and 2.0 ms, respectively) lead to $\eta_{sens} = 47$ and 63%, respectively. These comparatively low values, despite favorable energy gaps, may be traced back to the relatively long distance between the metal ion and the indacene unit which can be estimated to be about 9 Å, and to the unfavorable orientation of the chromophore which is tilted by about 60° with respect to the terpyridine coordination unit (Ziessel et al., 2006).

3.2.6. *New synthetic strategies podands, dendrimers, self-assembly processes*
In addition to the systems described in sub-sections 3.2.1–3.2.5, some innovative strategies for sensitizing the luminescence of NIR-emitting lanthanide ions are emerging. We describe three of these new approaches in this section, which call on the design of podands or dendrimeric ligands, as well as on the use of self-assembly processes.

3.2.6.1. *Podands*  A good way to reach efficient energy transfer from the ligand to the NIR-emitting metal ion while simultaneously achieving thermodynamic stability and kinetic inertness of the resulting molecular edifice is to resort to multidentate podands fitted with one or several sensitizer arms (Beeby et al. 2002a, 2002b). It is essential that the targeted chelating agents offer a good protection against solvent interactions and are devoid of coordinating groups possessing high energy vibrations. Until now, there are only few examples, most of them stemming out of our laboratory, of such a molecular construction in which a sensitizing unit is attached onto small backbones or on atoms.

A first example is heptadentate 2,2′,2″-tris(salicylideneimino)-triethylamine, H$_3$**89** (fig. 76), which forms an isomorphous series of complexes [Ln(**89**)] (Bernhardt et al., 2000). A crystal field analysis based on polarized absorption and emission spectra of the trigonal
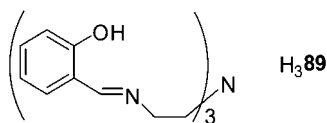
Fig. 76.  Salicylidene-imino podand.

crystals [Er(**89**)] was performed. The $C_3$ site symmetry of the metal ion requires eight ligand-field parameters for a full description within the one-operator model. All the 4f–4f transitions could be reliably assigned and the compound shows unusually large splittings of the multiplets. In fact, the heptadentate ligand imparts one of the largest ligand field reported for Er$^{III}$ complexes with organic ligands (Flanagan et al., 2001). The ligand-field splitting was also interpreted in terms of the angular overlap model and a similar analysis was reported subsequently for Nd$^{III}$ (Flanagan et al., 2002).

Another design for a tetrapodal ligand (H$_8$**90**, fig. 77) relies on a short 1,2-diaminoethane backbone fitted with four 8-hydroxyquinolinate moieties, the corresponding anion being known to be an efficient sensitizer of lanthanide NIR luminescence, as seen in section 3.2.2 (Kido and Okamoto, 2002; Rizzo et al., 2004). The spacer bears an amide coupling function and its length has been chosen to achieve a tight coordination around the Ln$^{III}$ ion saturating its first coordination sphere; the same reason prevailed to the choice of a tetrapodal instead of a more common tripodal ligand. Finally, sulfonate groups have been grafted onto the 8-hydroxyquinoline building block to improve solubility in water (Imbert et al., 2005). The ligand possesses 14 protonation sites, four pyridinium nitrogen atoms, two tertiary amines, four hydroxyl groups (p$K_a$'s in the range 1.8–12.2), and four sulfonate groups. It interacts fairly strongly with trivalent lanthanide ions in water yielding 1:1 podates with pLn values in the range 15–16.[7] Several species are in equilibrium and the speciation depends upon the pH. Fortunately, the 1:1 [Ln(H$_2$**90a**)]$^{3-}$ species is largely dominant in the pH range 6–8, and particularly at physiological pH 7.4, as shown from quantitative spectrophotometric and potentiometric data collected on the Eu$^{III}$/H$_8$**90a** system (fig. 77, bottom).

The Nd$^{III}$ and Yb$^{III}$ podates are quite luminescent, while Er$^{III}$ gives rise to somewhat fainter emission. Their photophysical properties are gathered in table 17. The hydration numbers calculated from eqs. (10a) and (9a) are very small, 0.37 and 0.15 for Nd$^{III}$ and Yb$^{III}$, respectively. They could arise either from partial dissociation of the (probably) 8-coordinate podates or from second-sphere interaction with diffusing water molecules and/or the N–H oscillators. To settle this point, the tetrapodal podand H$_8$**90b** in which the secondary amine groups are methylated has been synthesized. Its acid–base and coordination properties are not much changed with respect to H$_8$**90a**, but now, the calculated hydration numbers for both Nd$^{III}$ and Yb$^{III}$ are close to zero, being even slightly negative. In another experiment, the podates have been inserted into Triton X-100 micelles, which in principle protect the complex entities from interacting with water molecules and no changes at all were detected in lifetime data or in quantum yields. This clearly proves the deleterious action of the four secondary amine groups

---

[7] The pLn values are defined as $-\log_{10}$[Ln]$_{free}$ at pH 7.4 and for [Ln]$_{tot} = 10^{-6}$ M and [L]$_{tot} = 10^{-5}$ M (Raymond et al., 1984).
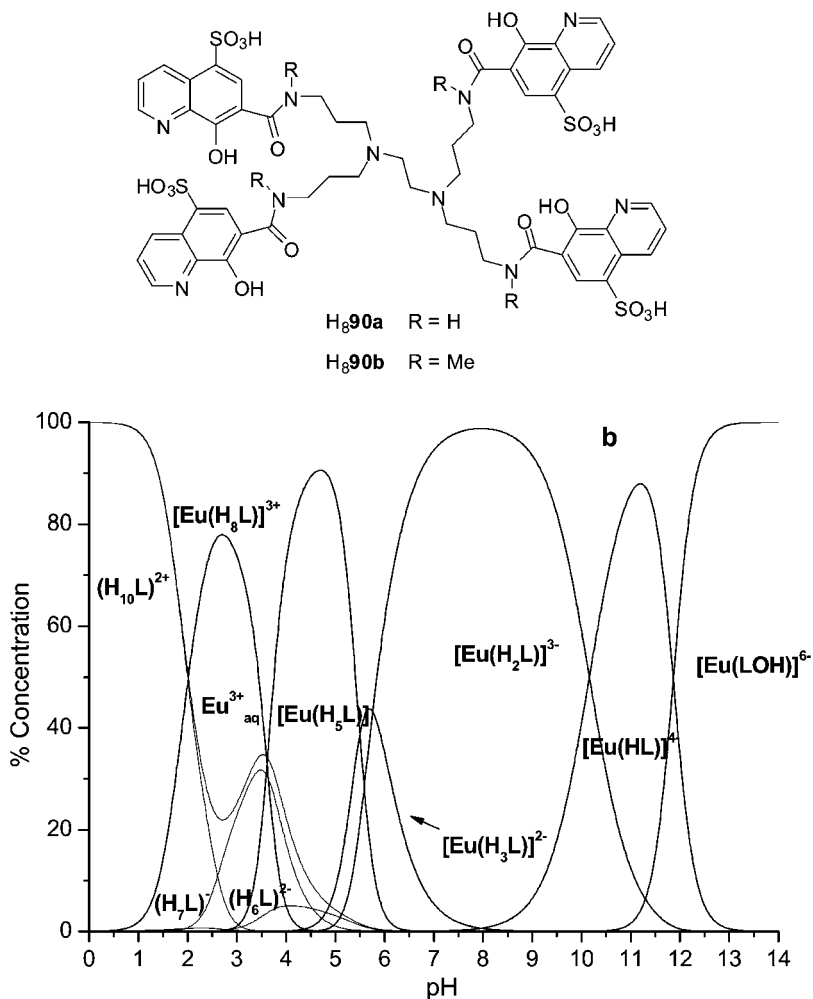
Fig. 77. (Top) Quinoline-fitted podands. (Bottom) Speciation for the $Eu^{III}$/$H_8$**90a** ($= H_8L$) system. Reproduced with permission from (Comby et al., 2006b).
© 2006 American Chemical Society

on the emissive properties, as corroborated by the quantum yield values increasing by a fac-tor of two when $H_8$**90a** is replaced with $H_8$**90b** in the $Yb^{III}$ podates. Another conclusion is that the coordination environment provided by the podand is tight enough to effectively pre-vent solvent molecules to interact with the metal ion, as planned in the ligand design. The quantum yield obtained for $Yb^{III}$ is so far the largest reported for a molecular compound in aqueous solution. It is 4- and 15-fold larger than the quantum yields reported for complexes with fluorexon (Werts et al., 2000b) and tropolonate (Zhang et al., 2005), for instance. The

Table 17

Absolute quantum yields measured upon ligand excitation (relative error: ±10%), lifetimes (standard deviation in parentheses), and associated hydration numbers of the $[Ln(H_2\mathbf{90})]^{3-}$ podates, $6 \times 10^{-5}$ M in aqueous solutions at 295 K and pH 7.4 (Comby et al., 2006b)

| Ln | $\lambda_{an}$ (nm) | $\tau$ (μs) $H_2O$ | $Q_{Ln}^L$ (%) $H_2O$ | $\tau$ (μs) $D_2O$ | $Q_{Ln}^L$ (%) $D_2O$ | $q^a$ |
|---|---|---|---|---|---|---|
| $H_8\mathbf{90a}$ | | | | | | |
| Nd | 1063 | 0.13(1) | 0.02 | 0.58(2) | 0.10 | 0.37 |
| Er | 1540 | 0.23(1) | $3.7 \times 10^{-5}$ | 1.39(2) | $5.4 \times 10^{-3}$ | – |
| Yb | 976 | 2.21(1) | 0.18 | 10.0(1) | 0.81 | 0.15 |
| $H_8\mathbf{90b}$ | | | | | | |
| Nd | 1063 | 0.25(3) | 0.04 | 0.61(1) | 0.11 | −0.09 |
| Er | 1540 | 0.67(1) | $4.0 \times 10^{-5}$ | 2.31(2) | $7.1 \times 10^{-3}$ | – |
| Yb | 976 | 5.79(1) | 0.37 | 14.6(1) | 0.90 | −0.1 |

[a]Calculated with eqs. (9a) (Yb$^{III}$, corrective factor $B = 0.2$ μs$^{-1}$) and (10a) (Nd$^{III}$).
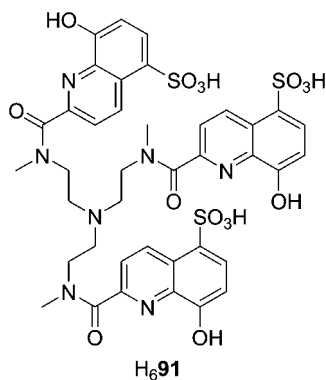


Fig. 78. Quinoline-containing tripodal ligand.

overall luminescence efficiency of the $[Yb(H_2\mathbf{90})]^{3-}$ podate, $\varepsilon \cdot Q_{Ln}^L$, reaches 70 M$^{-1}$ cm$^{-1}$ for an excitation at 344 nm and excitation up to 580 nm is possible. On the other hand, methylation has far less influence on the quantum yields of the Nd$^{III}$ and Er$^{III}$ podates, which is understandable since other nonradiative deactivation processes are much more efficient than in the Yb$^{III}$ complex (Comby et al., 2006b). The $[Yb(H_2\mathbf{90})]^{3-}$ podate has been successfully introduced into a glass matrix using a two-step sol–gel method and thin films of this material display even better photophysical properties than the aqueous solutions, with an average quantum yield of 0.45%, which is encouraging with respect to potential applications (Comby et al., 2006a).

Following a slightly different strategy, the same authors have designed another tripodal ligand, $H_6\mathbf{91}$ (fig. 78), consisting of a triamine anchor bearing three 8-hydroxyquinoline units

Table 18

Absolute quantum yields measured upon ligand excitation, lifetimes (standard deviation in parentheses), and associated hydration numbers of the $Ln^{III}$ podates with $H_6 \mathbf{91}$, $6.5 \times 10^{-5}$ M in aqueous solutions at 295 K and pH 7.4. From (Comby et al., 2007)

| Ln | $\lambda_{an}$ (nm) | $\tau$ (µs) $H_2O$ | $Q^L_{Ln}$ (%) $H_2O$ | $\tau$ (µs) $D_2O$ | $Q^L_{Ln}$ (%) $D_2O$ | $q^a$ |
|---|---|---|---|---|---|---|
| $H_6 \mathbf{91}$ | | | | | | |
| Nd | 1063 | 0.15(1) | 0.03 | 0.91(2) | 0.08 | 0.31 |
| Er | 1540 | 0.24(1) | n.a. | 2.55(1) | $3.5 \times 10^{-3}$ | – |
| Yb | 976 | 2.47(3) | 0.13 | 26.0(2) | 1.5 | 0.16 |

[a]Calculated with eqs. (9a) ($Yb^{III}$, corrective factor $B = 0.2$ µs$^{-1}$) and (10a) ($Nd^{III}$).

which are tailored to behave as tridentate receptors. As for ligands $H_8 \mathbf{90a}$ and $H_8 \mathbf{90b}$, sulfonation of the 8-hydroxyquinoline subunits leads to relatively highly water-soluble podates. In addition to the three sulfonate groups, which are always deprotonated in the experimental conditions used, the ligand possesses seven protonation sites, three pyridinium nitrogen atoms, one tertiary amine, and three hydroxyl groups ($pK_a$'s range from 3.7 to 10.2). In presence of $Ln^{III}$ ions, stable and water-soluble 1:1 complexes are formed, as demonstrated by NMR titration of a tris-DCl solution of $H_6 \mathbf{91}$ with $Ln^{III}$ (Pr and Lu) solutions prepared in $D_2O$.

The three $Nd^{III}$, $Er^{III}$, and $Yb^{III}$ chelates display sizeable metal-centered NIR luminescence in HBS-buffered (pH 7.4) aqueous solutions. Their photophysical characteristics are summarized in table 18. The hydration numbers calculated from eqs. (10a) and (9a) are very small, 0.31 and 0.16 for $Nd^{III}$ and $Yb^{III}$, respectively, and compare well with the results obtained for the tetrapodal ligand $H_8 \mathbf{90a}$. The overall luminescence quantum yields in aqueous solution are comparable to those obtained for $H_8 \mathbf{90a}$, but smaller than those determined for chelates with $H_8 \mathbf{90b}$ (compare tables 17 and 18). Upon deuteration of the solvent, from 3- to 10-fold increases are observed in the luminescence quantum yields. Moreover cytotoxicity studies on several cell lines have shown the $Yb^{III}$ chelate to be non-toxic, opening the way for applications in cell imaging (Comby et al., 2007).

3.2.6.2. *Dendrimers* Dendrimer chemistry can be thought of as being a branch of polymer chemistry in which highly branched monomers are uniformly assembled to yield a tree-like or generational structure. Preparing such polymers demands a high level of synthetic control which is achieved through stepwise reactions, building the dendrimer one monomer layer, or "generation", at a time. Each dendrimer consists of a multifunctional core molecule with a dendritic wedge attached to each functional site. The core molecule is referred to as "generation 0". Each successive repeat unit along all branches forms the next generation, generation 1 (G1), generation 2 (G2), and so on until the terminating generation. Interest in lanthanide dendrimers stems from nuclear magnetic imaging for which contrasts agents with large molecular weight are thought to be more efficient (Fulton et al., 2006; Wiener et al., 1994). Few reports deal with visible (Cross et al., 2004; Kawa and Frechet, 1998) or NIR luminescence (Kim et al., 2005) and, generally speaking, lanthanide dendrimer chemistry is still in its infancy.
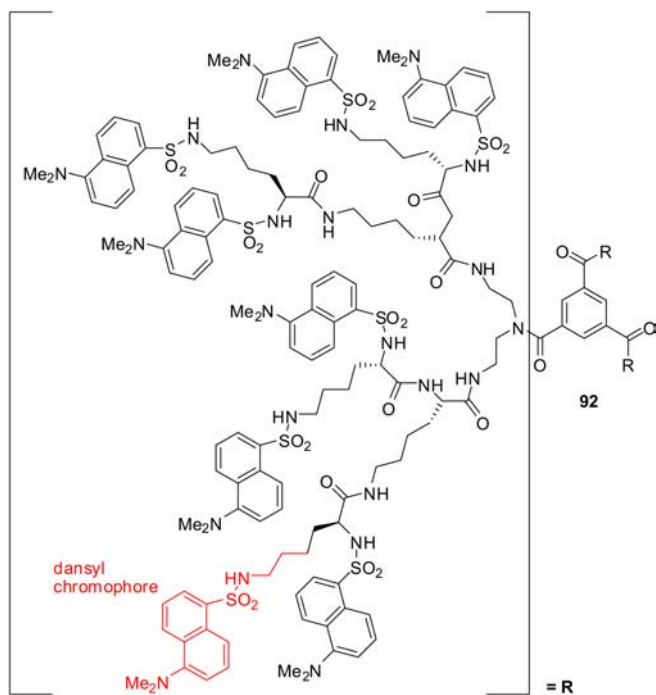
Fig. 79. Benzene-cored dendrimer fitted with dansyl chromophores.

The polylysin dendrimer depicted on fig. 79 consists of a benzene core branched in 1, 3, and 5 positions; each branch starts with a (dialkyl)carboxamide-type unit and carries six aliphatic amide groups and eight 5-dimethylamino-1-naphthalenesulfonamido (dansyl) chromophores. Therefore the interior of the dendrimer contains 18 amide groups which are known to strongly bind to lanthanide ions, as well as 24 light-harvesting moieties on the periphery, leading to molar absorption coefficients of $3 \times 10^5$ (253 nm) and $9.2 \times 10^4$ (338 nm) $M^{-1} cm^{-1}$. The photophysical properties of the dansyl groups in the dendrimer are close to those displayed by the monomeric dansyl group, so that little interaction between the chromophores is antici-pated. Titration of a 4.2 μM solution of the dendrimer in acetonitrile/dichloromethane by $Nd^{III}$ nitrate causes a quenching of the broad-band ligand fluorescence extending from 420 through 650 nm ($Q = 28\%$ in absence of metal ion) with decrease of the singlet state lifetime from 15 to 6 ns and a concomitant increase in the metal-centered NIR luminescence. The overall quantum yield of the metal-centered luminescence, obtained by a comparison method with $[Nd(hfa)]_3$ in $D_2O$, amounts to 0.27%. Combined with the large absorption coefficients of the dendrimer, this makes this dendrimeric complex a relatively efficient NIR emitter (Vögtle et al., 2001). Sensitized emission of $Eu^{III}$, $Tb^{III}$, $Er^{III}$, and $Yb^{III}$ also occurs with this dendrimer, the latter two ions emitting only moderately (Vicinelli et al., 2002).
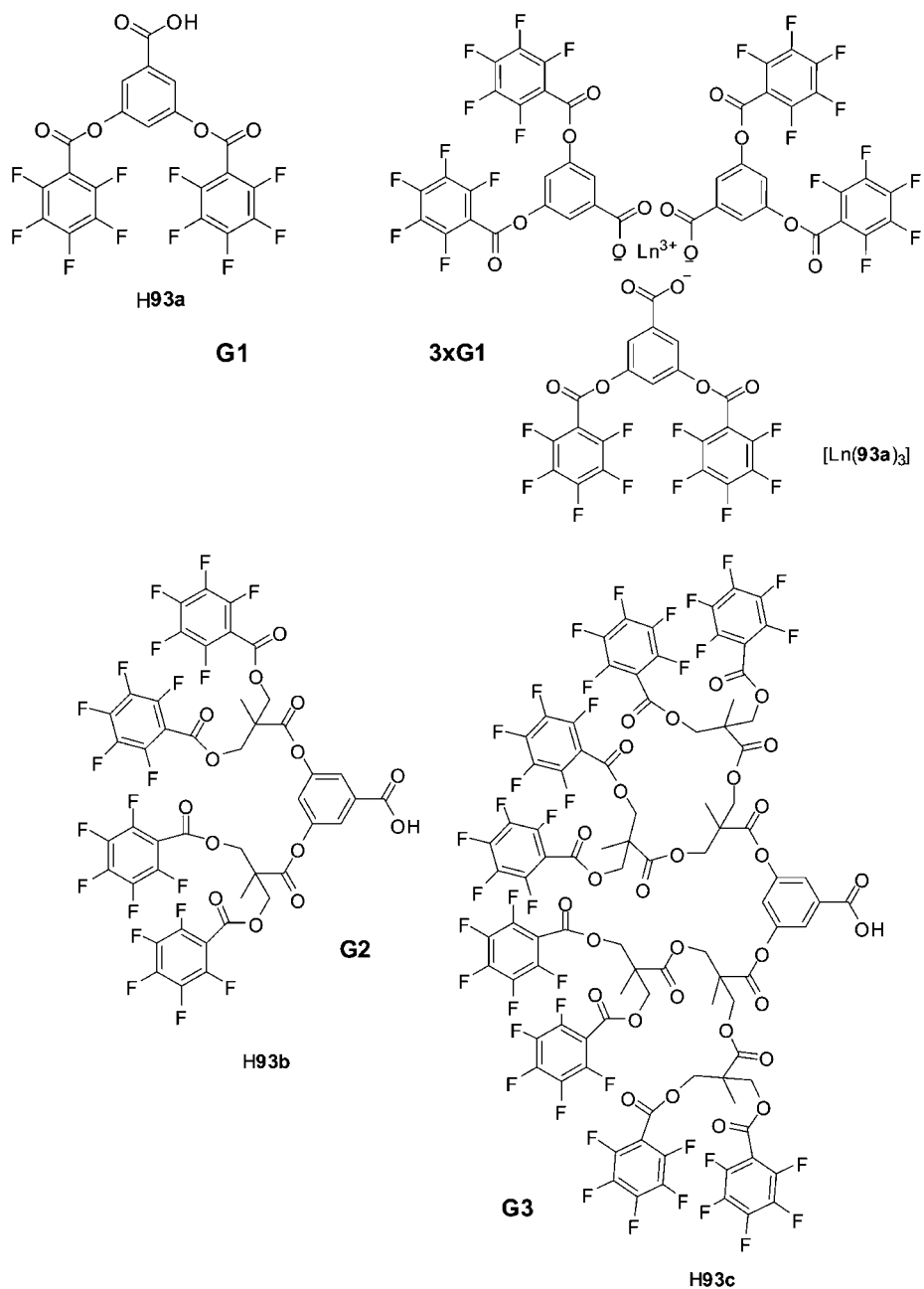
Fig. 80.  Fluorinated dendrons and corresponding lanthanide dendrimer of first generation.

In order to minimize nonradiative losses, a fluorinated dendrimeric system has been designed in which the lanthanide ions act as the core. The dendrons are derived from benzenecarboxylic acid substituted in positions 3 and 5 by a pentafluorinated phenyl group, the linker being an ester group. First (H**93a**), second (H**93b**) and third (H**93c**) generations of these dendrons (see fig. 80) have been prepared. When reacted with lanthanide acetate in a dry and oxygen-free atmosphere, three dendrons assemble around the core $Ln^{III}$ ion (Ln = Pr, Nd, Er). Sensitized luminescence was only observed for [Nd(**93b**)$_3$] and [Er(**93c**)$_3$], 2.7 and 0.73 mM, respectively, in methylene chloride. The former compound can be excited at 805 nm ($^4F_{5/2}$ ← $^4I_{9/2}$ transition). On the other hand, no luminescence could be detected for the $Pr^{III}$ dendrimers (Pitois et al., 2003) while the same systems sensitize $Eu^{III}$ and $Tb^{III}$ emission (Pitois et al., 2005).

Cyclam, or 1,4,8,11-tetraazacyclotetradecane is a popular macrocyclic ligand for d-transition metal coordination chemistry. It also coordinates to lanthanide ions, although much less strongly than the better size-adapted cyclen. As for the latter, however, derivatization of the amine functions by amide, carboxylate, or phosphinate groups considerably improves the coordination ability of the macrocycle.

Disregarding this aspect, and since cyclam is an interesting core for constructing dendrimers because it can be easily functionalized and because despite its absence of spectroscopic properties, it can interact in such a way with dendrons as to modify their photophysical properties, the interaction of lanthanide ions with cyclam-based dendrimers has been investigated. The dendrimers are constructed from the cyclam core fitted with four dimethoxybenzene and eight naphthyl units (generation 1, fig. 81); second generation introduces a total of 12 dimethoxybenzene and 16 naphthyl moieties. Coordination to $Ln^{III}$ ions occurs in acetonitrile/methylene chloride (Ln = Nd, Eu, Gd, Tb, and Dy), but no sensitized Ln-luminescence was observed (Saudan et al., 2004). Another example of a macrocycle-based dendrimer is discussed below in section 3.3.2.

The large light-harvesting ability of dendrimeric ligands is an attractive asset and in an attempt to obtain highly emitting NIR systems, aryl ether dendrons have been combined with a carboxylic acid derivatized diphenyl anthracene coordinating unit. The resulting complexes are protected from nonradiative deactivation by further binding of an ancillary ligand, namely tpy (fig. 81, bottom). These elaborate ligands **G*n*An** are synthesized in five steps from 9,10-dibromoanthracene and **G*n*-Br**. Efficient energy transfer is observed between the dendritic units and the anthracene moiety with photoluminescence quantum yields ranging from 62% for $n = 1$ to 80% for $n = 3$. Thin films of the resulting $Ln^{III}$ complexes (Ln = Nd, Er, Yb) display NIR luminescence with concomitant decrease in the anthracene fluorescence intensity. The intensity of the metal-centered luminescence is independent of the presence of oxygen and no phosphorescence could be evidenced at low temperature for the corresponding $Gd^{III}$ complexes. As a consequence, it is assumed that the ligand-to-metal energy transfer essentially involves singlet states of the dendritic ligands. The quantum yields of the [Ln(G3-An)$_3$(tpy)] dendrimers calculated from the lifetimes, assuming $\tau_{rad}$ = 0.25, 8, and 2 ms for $Nd^{III}$, $Er^{III}$, and $Yb^{III}$, respectively, amount to 0.28, 0.025, and 0.55%, with $\tau_{obs}$ = 0.7 ($Nd^{III}$), 2 ($Er^{III}$), and 11 ($Yb^{III}$) μs. These figures remain modest but in view of the large absorption displayed by the dendritic ligands, the overall emission intensity is large (Baek et al., 2006).

**94a**

**94b-G1**          **94b-G2**          **94b-G3**

{Ln-[G*n*-An]₃(tpy)}      *n* = 0, 1, 2, and 3
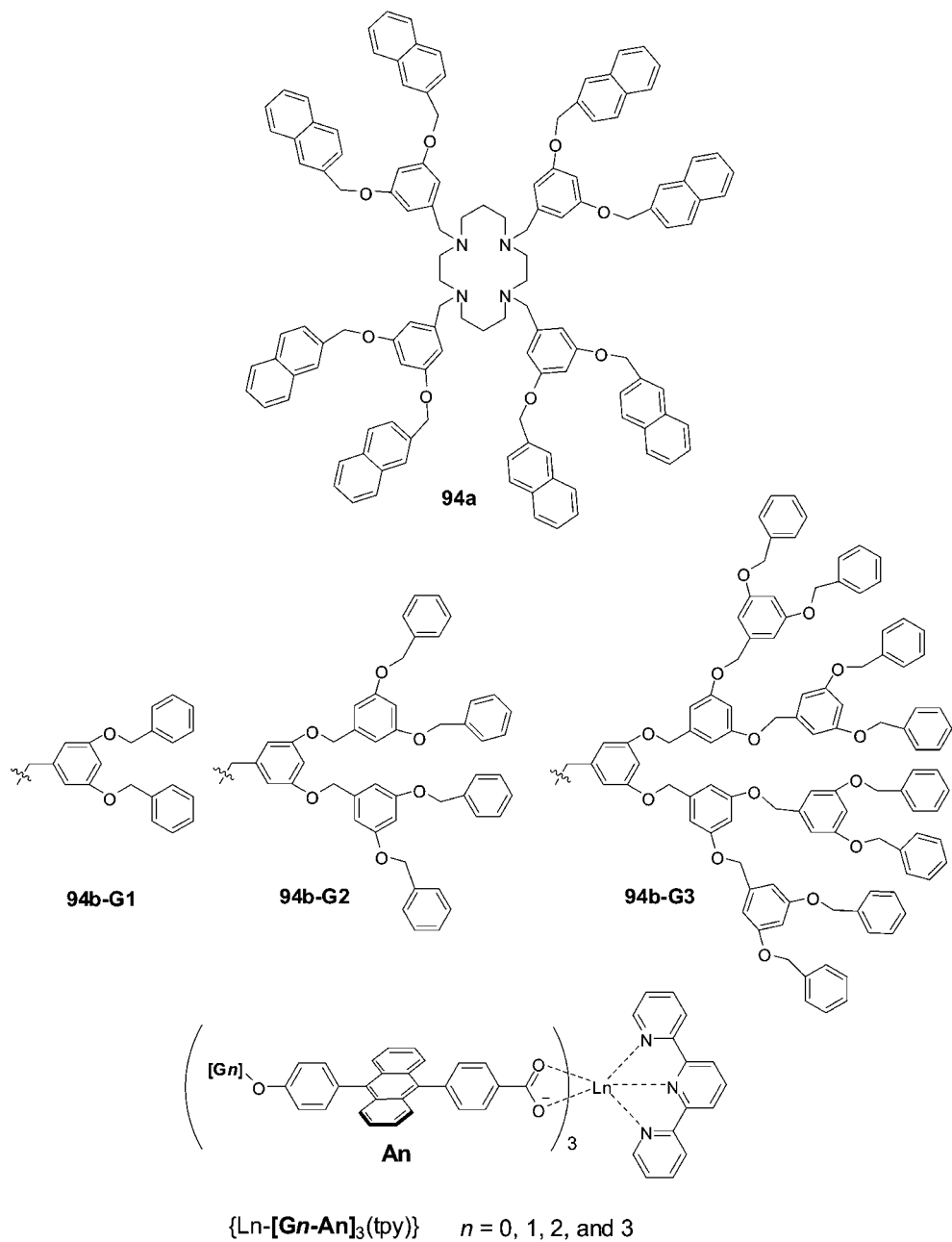
Fig. 81.  (Top) Cyclam-based dendrimer of first generation. (Bottom) Dendritic 9,10-diphenylanthracene ligands and their Ln complexes.
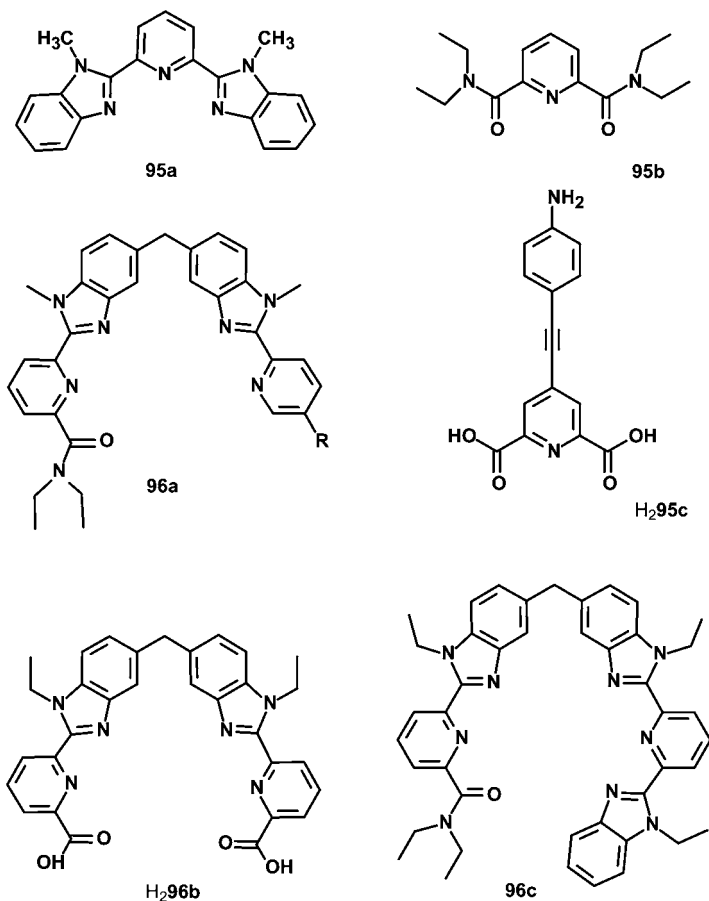
Fig. 82. Ligands for helical monometallic and bimetallic complexes.

3.2.6.3. *Self-assembly processes*  Self-assembly processes imply the formation of an induced coordination cavity around the targeted metal ion from tailored ligand strands possessing adequate donor atoms and some conformational flexibility. The difference between a simple coordination reaction, e.g. formation of a tris($\beta$-diketonate), and a self-assembly process is sometimes blurred and because self-assembly is fashionable, this term is often misused. An important factor in a self-assembly process is the concept of recognition: the induced cavity should be tailored for a specific metal ion. That is the targeted self-assembled species form preferentially among various possibilities. This is illustrated by the ligands described in fig. 82. For instance, three ligand strands **95a** self-assemble with lanthanide ions in acetonitrile to yield triple helical complexes which are stabilized by nine ion-dipole Ln$^{III}$–N bonds and by additional strong $\pi$-stacking interactions between ligand strands. As a result, the sys-

tem shows a larger selectivity for the cations in the middle of the lanthanide series than for the heavier lanthanide ions (Petoud et al., 1997). On the other hand, although the dipicolinic acid derivative **95b** also forms helical tris complexes, a simple electrostatic trend prevails for their stability constants, and no interstrand interaction contributes to their energetics; the resulting complexes are simple coordination compounds. This is also the case for the axial $[Ln(\mathbf{95c})_3]^{3-}$ complexes, the relatively low lying triplet state of which ($\approx 18\,000$ cm$^{-1}$) sensitizes Nd$^{III}$ luminescence (Platas et al., 2001).

In contrast, the three ligands **96** are designed for the simultaneous recognition of a 4f–3d metal ion pair (**96a**) (Piguet et al., 1996), a homopair of 4f ions (H$_2$**96b**) (Elhabiri et al., 1999), or a heteropair of 4f ions (**96c**) (André et al., 2002). For instance, under stoichiometric conditions, $[M^{II}Ln^{III}(\mathbf{96a})_3]$ is the only species formed out of a potential mixture of at least six species (three M$^{II}$- and two Ln$^{III}$-containing complexes were identified in solutions with a single metallic species). The photophysical and energy-transfer properties of Cr$^{III}$Ln$^{III}$ and Ru$^{II}$Ln$^{III}$ (Ln = Nd, Yb) helicates is described below in section 3.3.4.

Stable triple-stranded homobimetallic helicates are self-assembled in water from H$_2$**96b**, which feature large thermodynamic stability and excellent protection of the nine-coordinate Ln$^{III}$ ions lying in pseudo tricapped trigonal prismatic coordination environments. The $[Yb_2(\mathbf{96b})_3]^{3-}$ helicate is faintly emissive in water, so that its photophysical properties have been investigated in deuterated water in which the quantum yield of the metal-centered luminescence amounts to 1.8%, upon ligand excitation, and the Yb($^2$F$_{5/2}$) lifetime is equal to $40 \pm 2$ µs. Analysis of the crystal-field splitting of both $^2$F$_{5/2}$ and $^2$F$_{7/2}$ levels confirm the $D_3$ symmetry of the self-assembled helicate. Up-conversion was looked for, but was not observed, possibly a consequence of the relatively large separation of the two Yb$^{III}$ ions, 9.1–9.3 Å (Gonçalves e Silva et al., 2002).

A helical triple-decker complex of Yb$^{III}$ has been self-assembled in 25% yield from ligand H$_2$**99b** (see fig. 84 below), YbCl$_3\cdot$6H$_2$O and Zn(OAc)$_2\cdot$2H$_2$O in methanol/acetonitrile (X.P. Yang et al., 2006a). The solid-state structure of this compound reveals a complex supramolecular architecture involving cross-linked one-dimensional strands of chiral trimetallic molecules linked by $\pi$–$\pi$ stacking interactions. Each Yb$^{III}$ ion is eight-coordinate and intermetallic distances range between 3.7 and 3.8 Å. A solid-state sample and a solution in acetonitrile exhibit metal-centered NIR luminescence while solutions in methanol and deuterated methanol are less luminescent, probably due to some dissociation of the complex. When compared to the emission of a solution of $[ZnYb(\mathbf{99b})(NO_3)_2(OAc)]$ in acetonitrile having the same absorbance, the fluorescence intensity of $[Yb_3(\mathbf{99b})Cl(OAc)_2]$ at 976 nm is larger by a factor 2.7, which supports the idea that the helical ligand framework in the trimetallic complex provides improved shielding of the metal ions.

Other examples of self-assembled, NIR-emitting triple helical complexes are described in section 3.3.4.

## 3.3. *Heterometallic functional assemblies: taking advantage of d-transition metal ions*

The synthesis of heteropolymetallic d–f complexes is well documented and understood because the two metal ions display highly different stereochemical preferences. Valence

d-orbitals are external and interact strongly with ligand orbitals, whereas the shielding of 4f-orbitals by the filled $5s^2$ and $5p^6$ subshells results in spherical $Ln^{III}$ ions with little co-valency in their binding with organic ligands. Heteropolymetallic d–f molecular edifices (or coordination polymers) are appealing because the communication between metal ions is an additional tool for the synthetic chemist for tuning the inner coordination sphere of the metal ions and therefore their electronic properties (Piguet et al., 2000). Three types of intermetallic interactions have been evidenced: mechanical coupling, interactions based on orbital over-lap, and electrostatic communication. Intermolecular mechanical coupling between metal-lic centers is well established, particularly for $Fe^{II}$-containing discrete oligomers in which the triggering of the iron spin-crossover properties has been unambiguously demonstrated in heterobimetallic triple-stranded helicates (Edder et al., 2000). Orbital overlap is a route for intermetallic interaction; when 4f elements are involved though, the distance between the two metal ions must be short because the 4f–nd coupling is very small in view of the limited expansion of the 4f orbitals. This type of interaction is mainly involved in mag-netic coupling (e.g., between $Cu^{II}$ and $Gd^{III}$, with an exchange integral on the order of a few $cm^{-1}$), although it may also influence the flow of energy between the two metal ions (Bünzli and Piguet, 2002). Finally, long-distance energy transfer processes often occur via multipolar through-space mechanisms and both $4f \rightarrow 3d$ and $3d \rightarrow 4f$ energy transfer processes have been evidenced (Brayshaw et al., 1995; Cantuel et al., 2002; Edder et al., 2001); it is noteworthy that in solid-state devices, $Cr^{III}$ acts as a good sensitizer of the lumi-nescence of several $Ln^{III}$ ions, including $Nd^{III}$ in YAG lasers, $Er^{III}$ or $Tm^{III}$ (Shen et al., 2000; Tröster, 2003).

With respect to NIR luminescence, we are mostly interested in the latter communication mode, for two reasons. The first is that d-transition metal ions have larger molar absorption coefficients than 4f ions and, additionally, they may be excited through charge transfer states; subsequent directional transfer to 4f ions will consequently provide an efficient way of sensi-tizing their luminescence. Moreover, $Ln^{III}$ ions displaying NIR luminescence have compara-tively shorter lifetimes ($10^{-9}$–$10^{-6}$ s) than the visible-emitting ions ($10^{-3}$ s), which somewhat limits the efficiency of time-resolved experiments. This disadvantage can be overcome by the use of long-lived excited states of d-transition metal ions for populating the excited states of the 4f ions (Imbert et al., 2003; Torelli et al., 2005).

The various roles of d-transition metal ions in the elaboration of lanthanide-containing lu-minescent edifices, as well as some of the structural motifs described to date are schematically depicted in fig. 83. Among the heteropolymetallic d–f edifices reported to date, some make use of a transition metal ion because they build convenient counterions; this function discussed previously (cf. section 3.1.1, fig. 13) is not represented in fig. 83. In fig. 83a, the transition metal ion is a component of the ligand but assumes no essential role, apart from stabiliz-ing the ligand structure. In the second case (fig. 83b), transition ion complexation affects the electronic properties of the ligand, allowing a better energy transfer or a more convenient ex-citation mode. In the molecular edifice sketched on fig. 83c, directional energy transfer from the d-transition metal ion populates the excited state of the 4f ion, therefore controlling its photophysical properties. The latter two situations are combined in fig. 83d, in that complex-ation of the d-transition metal ion induces ligand-to-metal charge transfer states which will
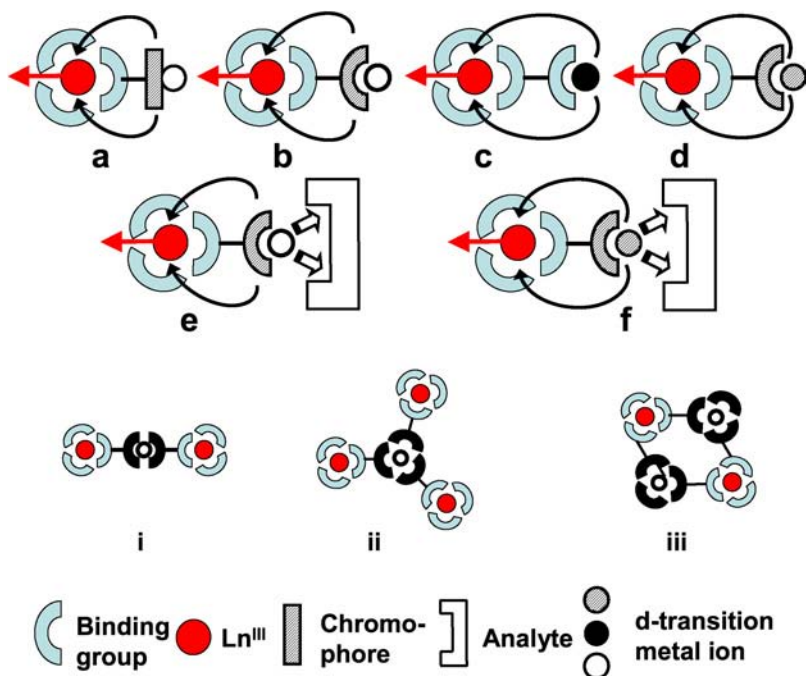
Fig. 83.  Various roles (a through f) and structural motifs (i through iii) in d–f functional edifices.

transfer energy to the 4f ion. The last two cases (e, f) make use of the transition metal moiety of the edifice for the recognition of the analyte (e.g. DNA intercalation of Pt-complexes, see below); the d-transition metal ion can play no further role, or modify the electronic properties of the ligand (fig. 83e), or take part in the energy transfer through $^3$MLCT states (fig. 83f). Depending on the edifices, intermediate situations between those described in fig. 83 can also be foreseen.

In view of the strong stereochemical preferences of the d-transition metal ions, several structural motifs are at hand, for instance with the d-metal ion unit acting as bridging ligand (i), or as templating agent for larger edifices (in fig. 83ii, a triangular motif is depicted, but others are possible, for instance, star-like or dendrimer-like arrangements), or with d- and f-metal ions arranging themselves in 2D grids as depicted in fig. 83iii, or in more elaborate 3D coordination polymers.

### 3.3.1. $Zn^{II}$ as structure stabilizer

The zinc Schiff base complex $N,N'$-bis(3-methoxysalicylidene)ethylene-1,2-diamine, [Zn(**97a**)] fig. 84), reacts with lanthanide trinitrates giving neutral trimetallic complexes with formula [Zn(NO$_3$)($\mu$-**97a**)(Ln(NO$_3$)$_2$(H$_2$O)] (Ln = Nd, Ho, Er, Yb). X-ray crystallography of the Ho$^{III}$ complex reveals that the Zn$^{II}$ ion is located in the N$_2$O$_2$ cavity and is 5-coordinate,

H$_2$**97a**    R = H

H$_2$**97b**    R = $p$-C$_6$H$_4$CH$_3$

H$_2$**98**

[Zn$_2$Yb$_2$(**98**)$_2$($\mu$-OH)$_2$]Cl$_4$

X = NO$_3$$^-$

H$_2$**99a**    R = H

H$_2$**99b**    R = Br

L = MeOH

[Nd$_2$Zn$_2$(**99a**)$_2$($\mu$-Cl)$_2$Cl$_4$(MeOH)$_2$]
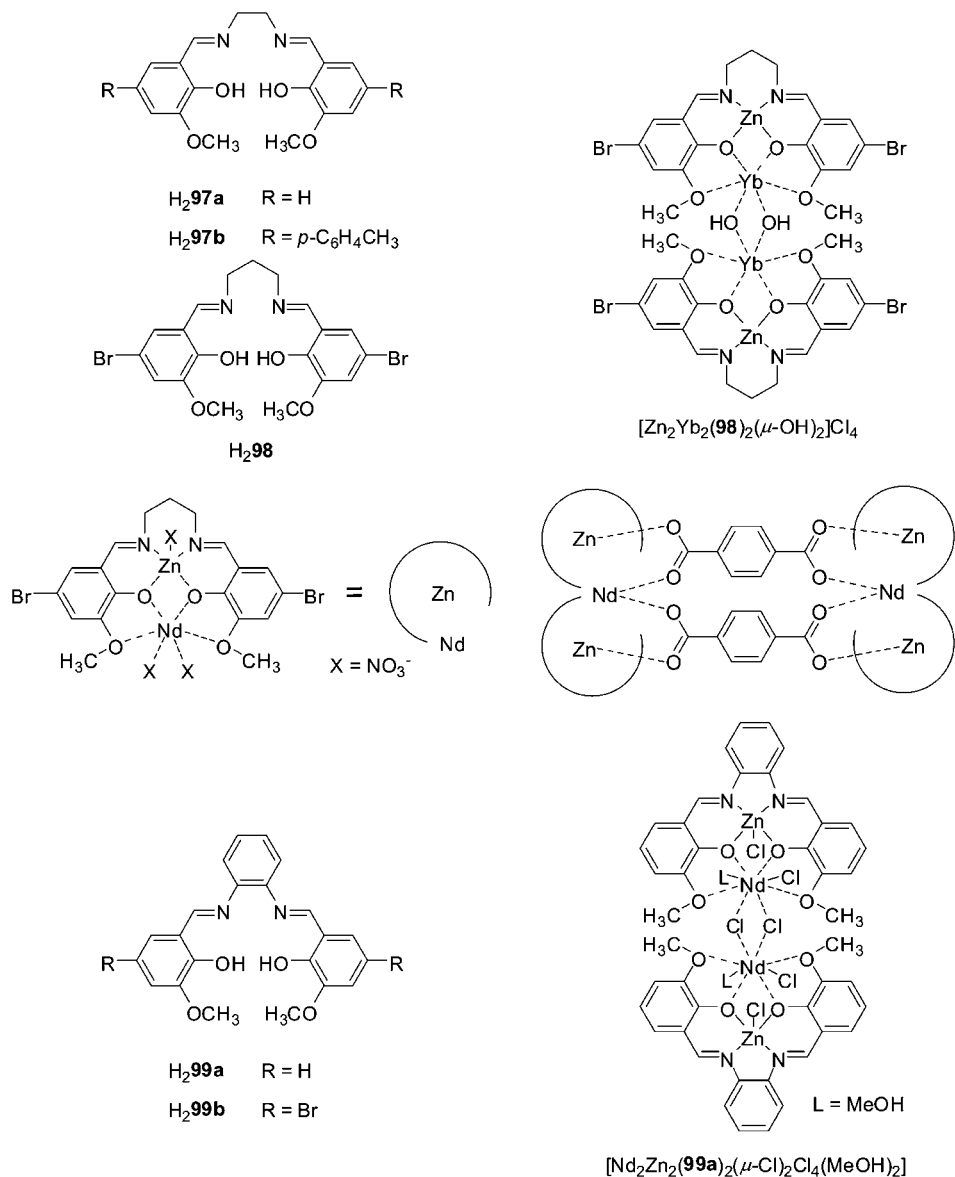
Fig. 84.  Schiff-base derivatives for Zn–Ln heterometallic edifices.

with a distorted square pyramidal geometry, by the additional coordination of a monoden-tate nitrate ion. The Yb$^{III}$ ion is 9-coordinate being bound to two bidentate nitrate ions, two bridging phenolate groups, two methoxy oxygen atoms and one water molecule. In methanol,

the complexes behave as 2:1 electrolytes, owing to the dissociation of two nitrate ions while they are non-electrolytes in acetonitrile. Upon excitation either at about 280 nm or 350 nm, ligand fluorescence occurs at 460–475 nm with a quantum yield of 3.37% for Ln = Gd. This quantum yield is smaller in the other complexes (0.72, 1.33, 2.77, and 1.37% for Nd, Ho, Er, and Yb, respectively) indicating energy transfer onto the $Ln^{III}$ ion. Indeed, apart from the $Ho^{III}$ compound, the complexes exhibit characteristic $Ln^{III}$ NIR luminescence in methanol, with lifetimes of 1.33 μs for $Nd^{III}$ and 1.31 μs for $Yb^{III}$ (Wong et al., 2002). Similar complexes were isolated with H$_2$**97b**, [Zn(NO$_3$)$_{3-y}$($\mu$-**97b**)(Ln(NO$_3$)$_y$(H$_2$O)$_x$] ($x = 2$, $y = 3$, Ln = La, Nd; $x = 1$, $y = 2$, Ln = Gd, Ho, Er, and Yb). The molecular structures of La, Nd, Er, and Yb elucidated by X-ray crystallography are very similar to the structure of the $Ho^{III}$ complex with H$_2$**97a**, except for the coordination number which varies from 9 (Er, Yb, one bound H$_2$O, two bidentate nitrate ions) to 10 (Nd, one bound H$_2$O, one monodentate and two bidentate nitrate ions) and 11 (La, one bound H$_2$O and three bound bidentate nitrate ions). In acetonitrile, the Yb($^2F_{5/2}$) lifetime is larger than for the solid state samples, reaching 14.6 μs, while the $Nd^{III}$ lifetime remains the same (Lo et al., 2004).

Modification of the Schiff-base ligand by introduction of two bromine substituents in H$_2$**98** resulted in the isolation of a tetrametallic species {[YbZn(**98**)]$_2$($\mu$-OH)$_2$} (fig. 84) when the zinc complex was treated with ytterbium trichloride. Typical Yb($^2F_{5/2}$) emission takes place upon ligand excitation, both in acetonitrile and in methanol, with an intensity larger than the one exhibited by the related bimetallic complex [Zn(**98**)(ac)Yb(NO$_3$)$_2$] (Yang et al., 2005).

The interest of ligand H$_2$**98** is its two dissimilar metal-binding sites. In bimetallic complexes, the metal ions are roughly located in a planar deprotonated ligand set. The mononegative ligand X (see middle of fig. 84) often occupies an axial site of the 3d metal ion, resulting in a distorted square-based pyramidal configuration. In {[YbZn(**98**)]$_2$($\mu$-OH)$_2$}, this axial ligand has disappeared in favor of two bridging hydroxyl units spanning the two metal ions. This suggests that the nuclearity of the complexes could be increased by carefully choosing multidentate ligands able to occupy the axial and bridging sites of each 3d–4f pair. 1,4-Benzenedicarboxylate (bdc) fulfils these requirements, and reaction of equimolar quantities of H$_2$**98**, zinc acetate, neodymium nitrate and H$_4$bdc in ethanol afforded a remarkable hexametallic assembly comprised of two Zn$_2$Nd(**98**)$_2$ fragments connected by two bdc dianions each carboxylate unit of which spans a Zn–Nd pair. The assembly is stable in methanol and displays Nd($^4F_{3/2}$) emission upon UV excitation (275–330 nm). In a semi-quantitative assay, the authors determine that the emission intensity is 5–6 times larger than the one exhibited by [Zn(**98**)(ac)Yb(NO$_3$)$_2$] (X.P. Yang et al., 2006b).

Reaction of equimolar quantities of neodymium trichloride and Zn(**99a**) in methanol leads to the isolation of the tetrametallic species {[NdZn(**99a**)]$_2$($\mu$-Cl)$_2$Cl$_4$(MeOH)$_2$} in which the zinc Schiff base acts as a tetradentate ligand for 8-coordinate $Nd^{III}$ (fig. 84, bottom right). Upon replacement of neodymium chloride with neodymium nitrate, bimetallic species are isolated—[Zn(**99a**)(MeCN)Nd(NO$_3$)$_3$]—featuring 10-coordinated $Nd^{III}$. On the other hand, trimetallic species form when the stoichiometric ratio is increased to 1:2 (Nd:Zn): {Nd[Zn(**99a**)(H$_2$O)(NO$_3$)]·H$_2$O·NO$_3$·EtOH}, in which one methoxy group of each Schiff base binds $Nd^{III}$ in addition to the two bridging phenolates, and {[Nd(Zn(**99a**))$_2$Cl$_2$(H$_2$O)$_3$]· Cl·2MeOH·5H$_2$O} with 9-coordinate $Nd^{III}$. All these species are NIR emitters, the bet-

ter intensity being obtained for the bimetallic species (Wong et al., 2006). Finally, di-bromination of **99a** does not seem to affect the luminescence intensity, since [Nd(Zn(**99b**)(μ-ac)(NO$_3$)$_2$(H$_2$O)] was found to be only weakly emitting (X.P. Yang et al., 2006c).

### 3.3.2. *Transition metal ions as modifiers of ligand electronic properties and/or recognition units*

Erbium-doped silica amplifiers are widely used in telecommunication systems. However, Er$^{III}$ cations are poorly soluble in inorganic media, leading to poor amplification properties. One way to circumvent this problem is to develop polymer-based fiber optic systems, in which Er$^{III}$ complexes would be fairly soluble. With this in mind, H.K. Kim has proposed to use a substituted tetraphenylporphyrin H$_3$**100a**, or more precisely the corresponding metallopor-phyrins H**100b–c** in order to achieve complexation of the lanthanide ion by the carboxylic acid function and not by the porphyrinic core (fig. 85). Since the tris complex, which can be classified as a dendrimer (see section 3.2.6.2), would only fill six of the coordination sites of the lanthanide ion; a ternary complex with terpyridine has been prepared. In addition to the non-coordinating nature of the macrocyclic core, the another advantage of metalloporphyrins over free porphyrins lies in a larger symmetry resulting in only two components for the Q ab-sorption band. The benefit of Pt$^{II}$ over Zn$^{II}$ is the occurrence of a strong interaction between the unoccupied 5d orbitals of the metal ion and the $\pi$ orbitals of the porphyrin, resulting in appreciable shifts in both the UV absorption spectrum and the red emission. Upon excitation at 430 nm for instance, the Zn porphyrin H**100b** displays a moderate emission band at 596 nm and a strong band at 646 nm, while the photoluminescence spectrum of the platinum porphyrin H**100c** shows a strong band at 653 nm and a moderate one at 713 nm. The photoluminescence spectrum of the ternary complex [Er(**100c**)(tpy)] recorded under excitation at 488 nm displays the characteristic $^4$I$_{15/2} \rightarrow {}^4$I$_{13/2}$ emission at 1.525 μm while this band is hardly seen for the corresponding tris(hydrated) metalloporphyrinate or for the zinc-based ternary complex in thf (Oh et al. 2004, 2005). The quenching of this NIR luminescence by oxygen proves the role of the porphyrin triplet state in the sensitization process.

In addition to facile quenching by proximate vibrations, Er$^{III}$ ions sustain concentration quenching that is well documented. This limits for instance the concentration of Er$^{III}$ ions in doped silica optical fibers and consequently the maximum gain achievable (to about 30 dB). To minimize similar quenching process in the metalloporphyrinate complexes, the same au-thors have fitted the benzo substituents of the Pt-porphyrinate with a second generation aryl-ether dendron used to produce dendrimers, leading to receptor H**100d**. The resulting micelle-like entities with a Ln$^{III}$ core effectively display a larger luminescence intensity when com-pared with [Er(**100c**)(tpy)], both in tetrahydrofuran (10$^{-5}$ M) and in the solid state where it is 7-fold larger (Oh et al., 2005).

Palladium porphyrinates have appealing properties in that they feature long-lived triplet states: they are subject to very efficient quenching by molecular oxygen, they bind deoxyri-bonucleic acid (DNA), and this intercalation process curbs the oxygen quenching so that emission from the triplet state is enhanced considerably. In an effort to explore the sensi-tizing ability of the Pd-porphyrinate moiety, Beeby et al. (2000) has prepared a porphyrinate conjugate linked to a chiral lanthanide moiety (**101b**). Reaction of the porphyrinate iodoac-
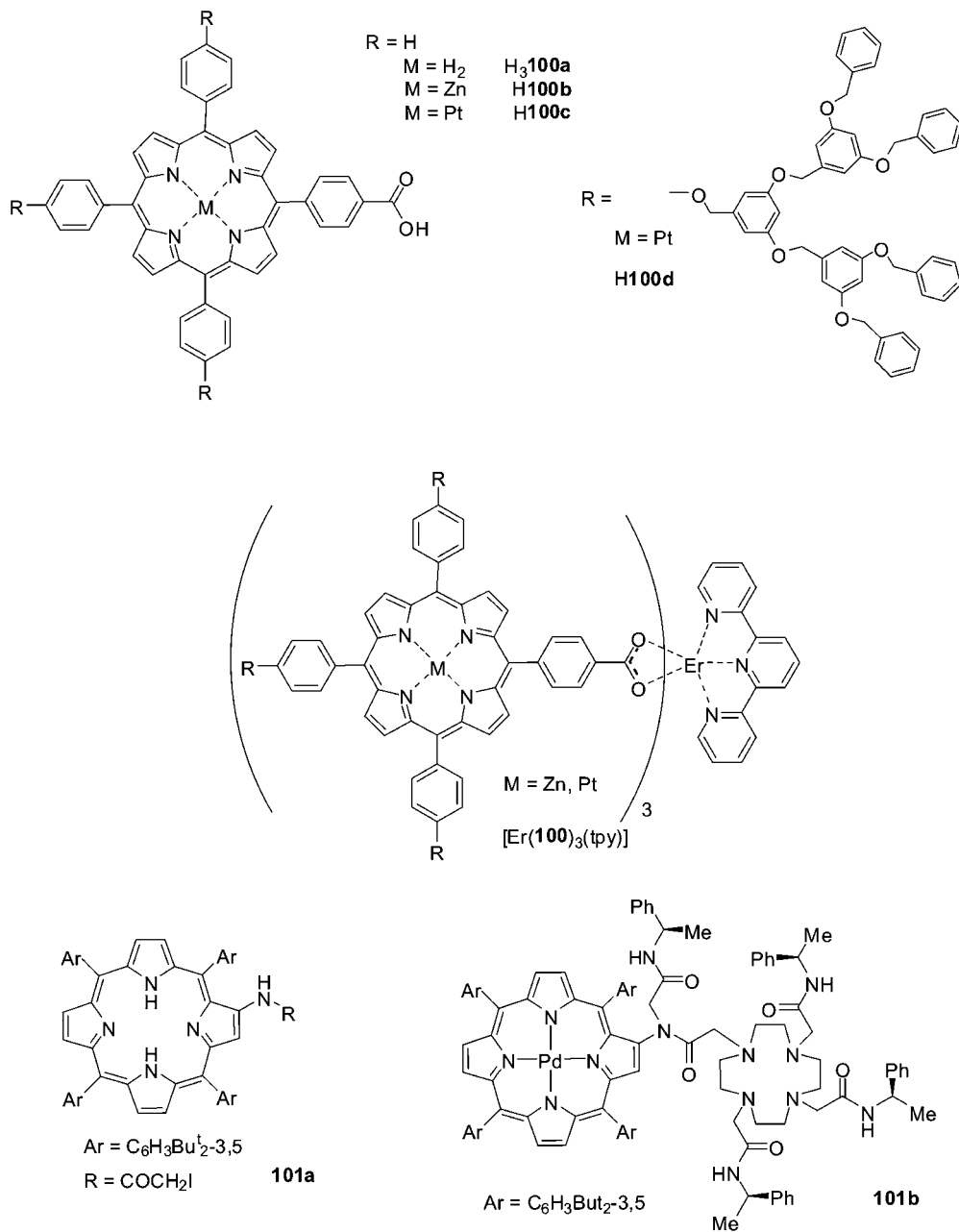
Fig. 85. (Top) Metalloporphyrins and corresponding $Er^{III}$ complexes. (Bottom) Modified palladium metalloporphyrin.
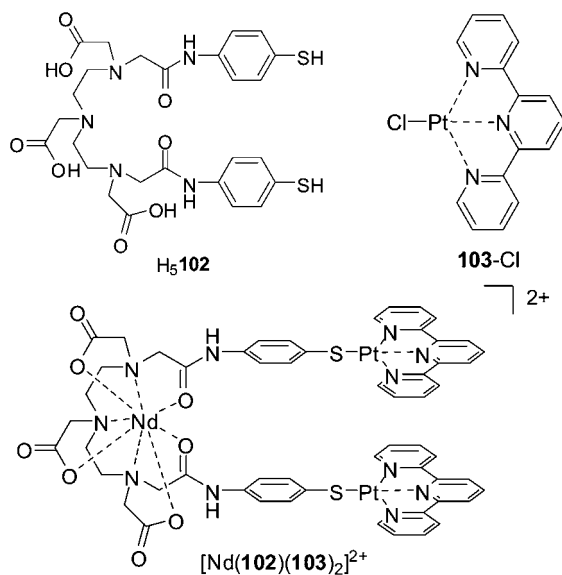
Fig. 86. Hairpin-shaped complex for DNA intercalative recognition (Glover et al., 2003).

etamide **101a** with an excess of cyclen in thf gave the monosubstituted Pd-porphyrinate in almost quantitative yield. The three chiral pendant arms were then introduced with either chirality (*RRR*) or (*SSS*) and subsequent reaction with lanthanide trifluoromethanesulfonates yielded the cationic complexes $[Ln(\mathbf{101b})]^{3+}$ (Ln = Nd, Yb). Their CD spectra are dominated by the porphyrinate chromophore, with $g_{abs}$ values (eq. (24)) at 560 nm of $+1.7 \times 10^4$ for both the Nd and Yb complexes. With $(RRR)$-$[Yb(\mathbf{101b})]^{3+}$ weak CPL signals were observed at 985 nm ($g_{lum} = -0.04$, see eq. (23)) and 963 nm ($g_{lum} = +0.05$); the Nd$^{III}$ complex exhibits an even weaker CPL signal ($g_{lum} = -0.006$ at 1055 nm). In de-aerated methanol–water (5 μM, CD$_3$OD/D$_2$O 80/20), the phosphorescence of the porphyrinate moiety appears as weak bands at 735 and 800 nm, in addition to metal-centered luminescence, which is not the case for aerated solutions. Removal of oxygen from the solutions results in an enhancement of the NIR luminescence by a factor 2 for Nd$^{III}$ and 7 for Yb$^{III}$. Since excitation spectra nearly perfectly match the absorption spectra of the complexes, the ligand-to-metal energy transfer rate is competitive with the rate of triplet state quenching by oxygen; the latter is $10^9$ s$^{-1}$ for Pd-porphyrinate; monitoring the decay of the porphyrinate triplet emission as well as the grow-in and decay of the Ln$^{III}$ luminescence by time-resolved experiments allowed the rate constant for oxygen quenching to be calculated as being $5 \times 10^8$ s$^{-1}$ (Ln = Nd). The addition of an oligonucleotide such as $[(CG)_6]_2$ or of calf-thymus DNA to an aerated solution of $(RRR)$- or $(SSS)$-$[Yb(\mathbf{101b})]^{3+}$ leads to an increase of about 30% in the luminescence intensity of the porphyrinate and the Yb$^{III}$ ion, with respect to a de-aerated solution. The sensitivity of Nd$^{III}$ and Yb$^{III}$ luminescence to $pO_2$ is of interest for potential mapping of regions of organisms with low oxygen pressure.

Following the same motivation of DNA tagging, but using a very different approach, Pikramenou and coworkers (Glover et al., 2003) have self-assembled a LnPt$_2$ complex featuring a hard binding core H$_5$**102** for Ln complexation via five oxygen and three nitrogen atoms and bearing two soft thiol substituents for coordination to Pt$^{II}$ (see fig. 86). Platinum terpyridyl moieties **103** were chosen for their ability to intercalate in DNA. The reactants **102**, NdCl$_3$·$x$H$_2$O, and **103** were mixed into 1:1:2 stoichiometric ratio and the solution in methanol was simply refluxed during 2 h, yielding the desired heterotrimetallic complex in quantitative yield. The absorption spectrum of [Nd(**102**)(**103**)$_2$]$^{2+}$ is the sum of the spectra of the individual components, [Nd(H$_2$**102**)] and **103**–Cl, with a slight shift of the aromatic thiolate, plus a new band at 515 nm which is attributed to a ligand-to-ligand charge transfer (LLCT) state, p$\pi$(RS$^-$) $\rightarrow$ $\pi^*$(tpy). Sensitization of the Nd$^{III}$ luminescence occurs through this state (as well as through states centered on the thiophenyl units) and the relative emission intensity remains constant upon addition of calf-thymus DNA. The binding to the latter has been further evidenced by linear dichroism and the corresponding constant estimated to be on the order of 10$^8$ M$^{-1}$. The Nd$^{III}$ unit acts as a luminescent reporter of the intercalation despite its relatively low quantum yield (0.25% in dmso-$d_6$, as estimated from eq. (7) with $\tau_{obs} = 670$ ns and assuming $\tau_0 = 270$ μs).

### 3.3.3. *d-Transition metal ions as luminescence sensitizers*

In the following, chromophores containing transition metal ions, namely Cr$^{III}$, Fe$^{II}$, Ru$^{II}$, Re$^{I}$, Os$^{II}$, and Pt$^{II}$ are inserted into heterometallic edifices and sensitize Ln$^{III}$, mainly Nd$^{III}$ and Yb$^{III}$, luminescence through either directional dipole–dipole transfer, MLCT states, or a sequential process involving both mechanisms. The energy of the MLCT states largely depends on the d-metal ion environment and can therefore be tuned by modifying the hosting ligands. The first excitation mode does not require a direct chemical link between the two communicating metals, whereas the second does and several bridging ligands have been described for this purpose. For instance, S. Kaizaki has developed a series of stable heterobimetallic complexes by linking lanthanide hydridotris(1-pyrazolyl)borates with a mixed Cr$^{III}$ complex with acetylacetonate and oxalate: [Cr(acac)(μ-ox)Ln(Tp$^H$)$_2$] (fig. 87). Red emission arising from the Cr($^2$E) excited state is seen for the complexes with Tb$^{III}$ and Lu$^{III}$, but not with Yb$^{III}$ for which the Cr$^{III}$ $\rightarrow$ Yb$^{III}$ transfer is complete owing to the ideal energy gap ($\approx$2500 cm$^{-1}$) between the Cr($^2$E) and Yb($^2$F$_{5/2}$) levels (Sanada et al., 1998b); the lifetime of the Yb($^2$F$_{5/2}$) level amounts to 48 μs at 10 K. NIR emission also occurs for the complexes with Nd$^{III}$, Ho$^{III}$ ($^5$I$_{5,4} \rightarrow$ $^5$I$_8$, $^5$I$_7 \rightarrow$ $^5$I$_8$ transitions, 1.2–1.6 μm), Er$^{III}$, and Tm$^{III}$ ($^3$F$_3$, $^3$H$_4 \rightarrow$ $^3$H$_6$, $\approx$800 nm), simultaneously with Cr$^{III}$ luminescence (Subhan et al., 2003). The series of chiral complexes (Ln = Nd, Sm, Dy, Ho, Er, and Yb), has also been extensively studied by NIR circular dichroism and NIR magnetic circular dichroism (Subhan et al., 2001; Subhan et al., 2002). Replacing oxalate with trimethylenebis(oxamide) (tbo) and Cr$^{III}$ by Ni$^{II}$ resulted in the isolation of a trimetallic complex {[Ni($\mu^2$-tbo)][Yb(Tp$^H$)$_2$]$_2$}, the crystal structure of which was solved, but no metal-centered luminescence was detected (Sanada et al., 1998a). Another bridging ligand is 3,5-di(2-pyridyl)pyrazolate (bpypz) which yields [Cr(acac)$_2$(μ-bpypz)Ln(hfa)$_3$] complexes (fig. 87) in which the Ln ion (Ln = Yb) is 8-coor-

[Cr(acac)$_2$(μ-ox)Ln(Tp$^H$)$_2$]     [Cr(acac)$_2$(μ-bpypz)Ln(hfa)$_3$]

[(Tp$^H$)$_2$Yb(μ-C$_6$Cl$_2$O$_4$)Yb(Tp$^H$)$_2$]
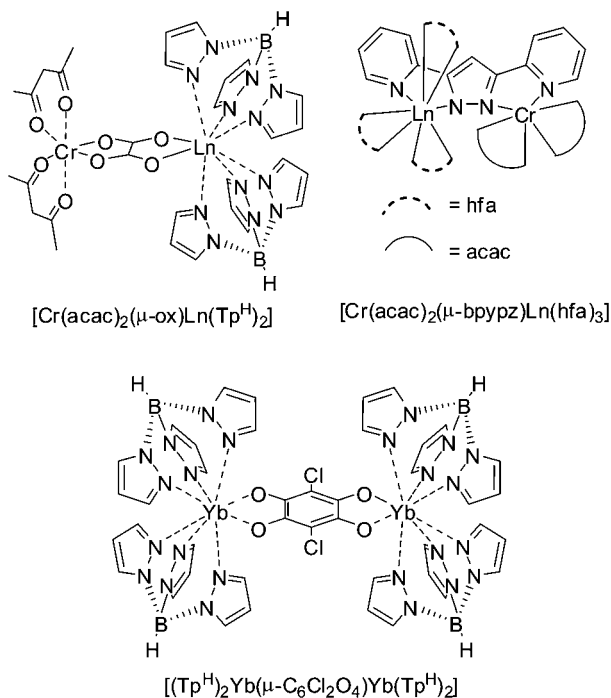
Fig. 87. Bridged Cr–Ln and Ln–Ln bimetallic complexes.

dinate in a bicapped trigonal prismatic geometry (Kawahata et al., 2003). Since the Cr–Yb distance is shorter (4.65 Å) in [Cr(acac)$_2$(μ-bpypz)Yb(hfa)$_3$] than in [Cr(acac)(μ-ox)Yb(Tp$^H$)$_2$], emission from the Yb($^2$F$_{5/2}$) level only occurs for the former compound, even at 10 K and the corresponding lifetime amounts to 155 μs (solid state). The Nd$^{III}$ analog also shows exclusively 4f–4f emission. When bpypz is replaced with chloranilate, a tetradentate ligand acting as bridging bis(bidentate)unit, a homobimetallic Yb$^{III}$ complex forms, with formula [(Tp$^H$)$_2$Yb(μ-C$_6$Cl$_2$O$_4$)Yb(Tp$^H$)$_2$]. The deep-violet complex crystallizes in the $P2_1/n$ space group and the two 8-coordinate Yb$^{III}$ ions linked by the planar bis(bidentate) chloranilate are separated by 8.56 Å. The complex displays strong Yb-centered emission which is traced back to energy transfer from the triplet state of chloranilate: the excitation spectrum indeed presents a band at around 600 nm due to the intraligand singlet–singlet n–π* transition of chloranilate, shifted from 568 nm in the absorption spectrum and from 511 nm in the absorption spectrum of free chloranilate (Abdus et al., 2004).

   The first example of Nd$^{III}$ and Yb$^{III}$ luminescence sensitized by Ru$^{II}$ and ferrocene appeared in 2000. The authors noticed that [Ru(bpy)$_3$]$^{2+}$ has an intersystem crossing yield near unity and that it enables excitation with visible light up to 500 nm. On the other hand, ferrocene has weaker absorption bands in the visible spectrum, but its low-lying triplet state (≈13 300 cm$^{-1}$) matches fairly well the Nd$^{III}$ ($^4$F$_{3/2}$, 11 300 cm$^{-1}$) and Yb$^{III}$ ($^2$F$_{5/2}$,
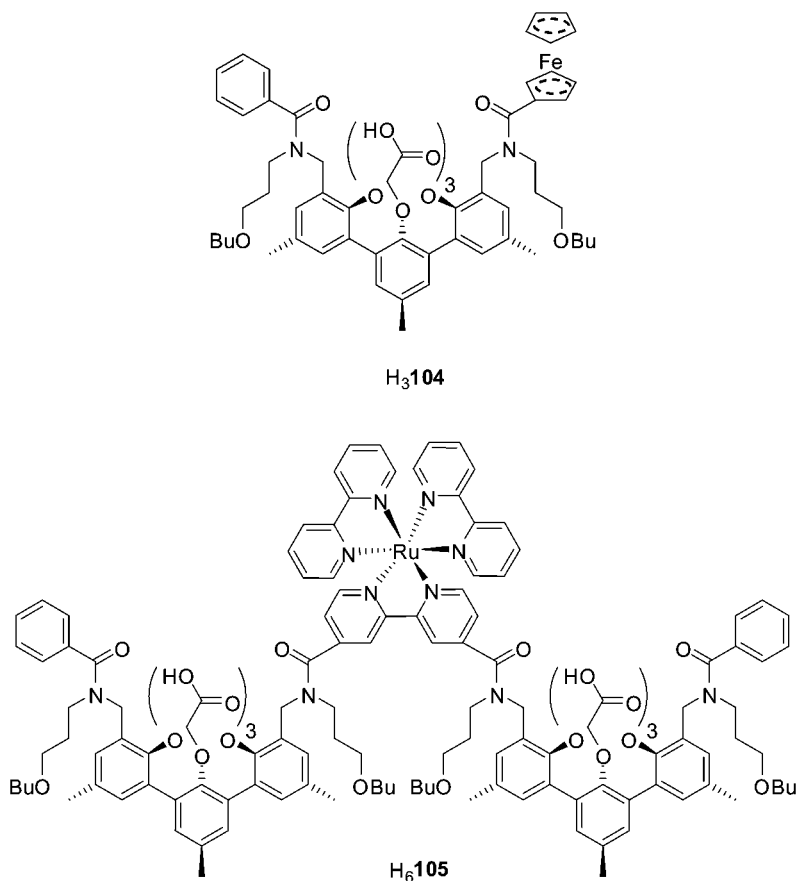
Fig. 88. Ferrocene and $Ru^{II}$ chromophore for the sensitization of $Nd^{III}$ and $Yb^{III}$ luminescence.

10 300 cm$^{-1}$) excited states. Terphenyl-based $Ln^{III}$ complexes were covalently linked to the transition metal complexes (fig. 88). De-oxygenated solutions of dmso-$d_6$ of the ferrocene-functionalized complexes with $Nd^{III}$ and $Yb^{III}$ (10$^{-4}$ M) display the typical metal-centered emission upon ferrocene excitation at 320 nm; the lifetimes are 2.0 ± 0.2 μs for [Nd(**104**)] and 18.8 ± 0.2 μs for [Yb(**104**)]. The trimetallic complexes [Ln$_2$(**105**)] also displayed metal-centered luminescence upon visible light excitation. Time-resolved luminescence data on the $Nd^{III}$ system proved that energy transfer involves a $^3$MLCT state of the $Ru^{II}$ chromophore: the $Nd^{III}$ luminescence intensity rises with a lifetime (420 ± 20 ns) equal to the lifetime of the chromophore triplet state (420 ± 10 ns, emission at 660 nm) and decays with a lifetime equal to 2.1±0.2 μs. Both the intensity of the $Ru^{II}$ chromophore luminescence and its lifetime (770 ± 20 ns) are larger in the corresponding $Gd^{III}$ reference compound; the energy transfer rate to $Nd^{III}$ can then be estimated to $k_{et} = 1.1 \times 10^6$ s$^{-1}$. On the other hand, both the triplet

state intensity and lifetime of the Yb[III] trimetallic complex are equal to the corresponding data for Gd[III], meaning that the rate of the energy transfer process in [Yb$_2$(**105**)] is at least one order of magnitude smaller than the decay rate of the triplet state (i.e., $< 10^5$ s$^{-1}$). This points to an electron transfer mechanism for the excitation of the Yb($^2$F$_{5/2}$) state, the lifetime of which amounts to $18.2 \pm 0.8$ µs in dmso-$d_6$ (Klink et al. 2000c, 2002).

More elaborate molecular edifices have been proposed (fig. 89, note that the "outer"-sketched substituents of calix[4]arene are in fact located on the narrower rim). For instance, a star-like receptor featuring a central [Ru(bpy)$_3$]$^{2+}$ core unit to which six functionalized cal-ixarene receptors are covalently linked (Beer et al., 2004). Addition of lanthanide nitrate (Ln = Nd, Eu, Tb) to solutions of the Ru[II] complexes causes substantial changes in the absorption spectra, confirming complexation of the trivalent ions, although not always complete. Analysis of the UV–visible titrations yields the final following stoichiometries (Nd:L): 1:1 for receptor H$_3$**106** (log $K = 5.2$ in acetonitrile), 2:1 for H$_6$**107** (log $\beta_2 = 13.4$), and at least 5:1 for H$_{18}$**108** (no stability constant could be determined). During the titrations, a decrease of the $^3$MLCT emission of ruthenium at 610 nm parallels an increase in the typical 4f–4f emission of Nd[III] as the metal ion concentration increases. In the case of [Nd(**106**)], the rate constant for the $^3$MLCT $\rightarrow$ Nd($^4$F$_{3/2}$) could be estimated to be $2.4 \times 10^6$ s$^{-1}$. On the other hand, excitation spectrum of the Ru[II] emission at 610 nm does not display the band corresponding to the calixarene receptor, while this band is markedly present in the excitation spectrum of Nd[III]; in fact, since the latter ion lies closer to the calixarene than Ru[II], this proximity gives rise to a fast energy transfer to the 4f-metal ion.

Starting from the same [Ru(bpy)$_3$]$^{2+}$ chromophore, S. Faulkner and coworkers (Pope et al., 2004b) have modified one of the bipyridine moiety in L$^1$ = 4′-methyl-2,2′-bipyridyl-4-carboxylic acid, (H**109a**, fig. 89) and have extended the study to the [Os(bpy)$_2$L$^1$]$^{2+}$ antenna (H**109b**) as well as to the facial complex *fac*-[ReCl(CO)$_3$L$^1$] (H**109c**). Ternary complexes of the type {[M(bpy)$_2$(L$^1$)][Ln(do3a)]}$^{2+}$ (M = Ru, Os) or {[ReCl(CO)$_3$(L$^1$)][Ln(do3a)]}, Ln = Nd, Er, Yb, are formed in methanol by simple mixing of the two metal-containing components. The idea behind this design was to complete the coordination sphere of the do3a complexes by the carboxylate moiety of L$^1$ and to be able to screen a large number of chromophores by simple interaction with the known stable complexes of do3a. If the latter idea proved to be successful, some residual solvation remains, as evidenced by the $q$ values obtained on the basis of lifetime measurements in methanol and deuterated methanol: $q_{Yb} = 0.6$, (Re[I]) 0.7 (Ru[II]) and 1.1 (Os[II]). Somewhat smaller values were obtained for Nd[III], which is surprising in view of the larger ionic radius of this ion, but relationship (10b) is known to be less reliable than the relationship for $q_{Yb}$. Er[III] luminescence could hardly be detected in methanol and the short-emissive MLCT states based on Re[I] and Os[II] proved to be more suitable as donor chromophores when compared to the Ru[II] moiety.

The ternary complex strategy is appealing, but the stability of the complexes may be a problem, a reason why the same authors have covalently grafted chromophores H**109a–c** on a dtpa core to yield ligands H$_3$**110a**, H$_3$**110b**, and H$_3$**111** (fig. 90). The existence of trimetallic complexes [Ln(**110**)]$^{n+}$ ($n = 4$, Ru[II], Os[II]; $n = 0$, Re[I]) in methanolic solution is ascertained by mass spectrometry. In the same solvent, the $^3$MLCT emission maximum shifts from 630 in H$_3$**110a** to 637 nm in its complexes with Nd[III], Er[III], and Yb[III]. In parallel, the $^3$MLCT lifetime
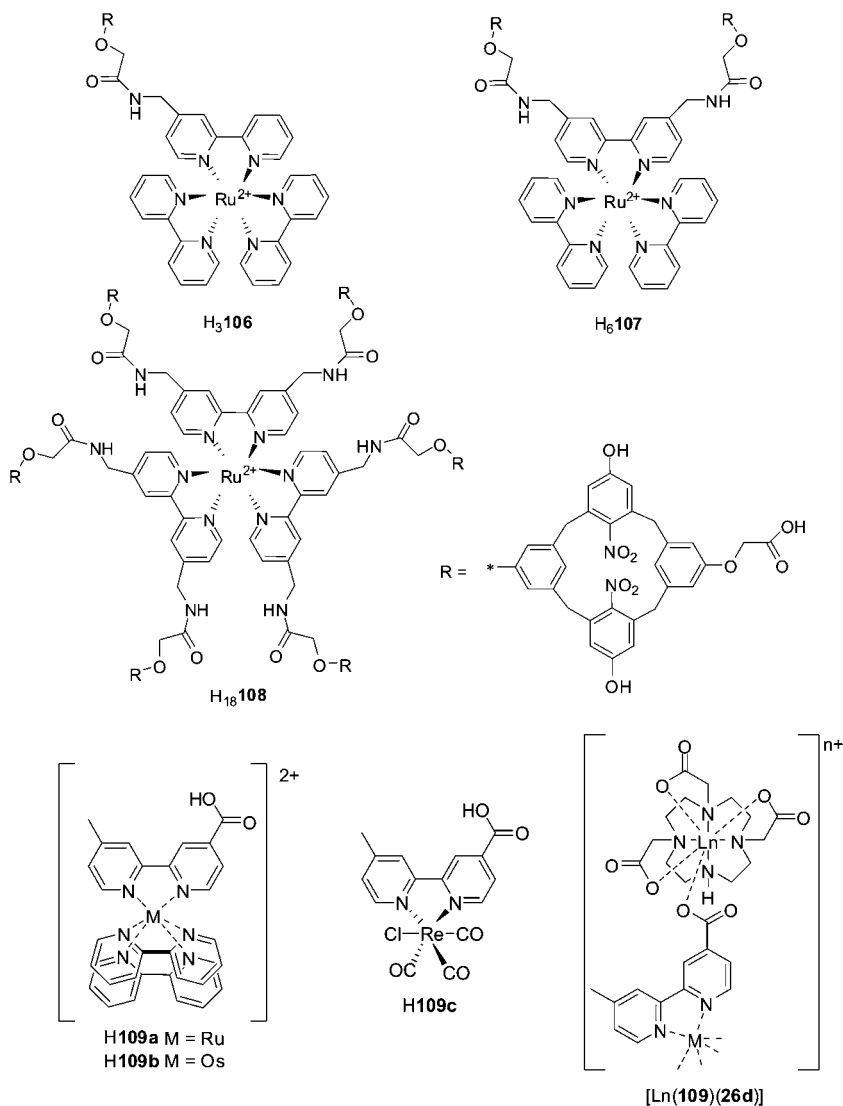
Fig. 89. (Top and middle) Calix[4]arene-fitted [Ru(bpy)$_3$]$^{2+}$. (Bottom) Ru$^{II}$, Os$^{II}$, and Re$^{I}$ chromophores and ternary complexes with do3a.

(309 ns) decreases to 240, 275, and 294 ns, respectively, indicative of an energy transfer onto the lanthanide ion. From the measured rise time, $\approx$200 ns for both Nd$^{III}$ and Er$^{III}$, this transfer is however rather inefficient. In the case of Yb$^{III}$, the NIR emission of $^3$MLCT and the 4f ion could not be clearly separated so that no quantitative data are at hand. The Os$^{II}$ trimetallic
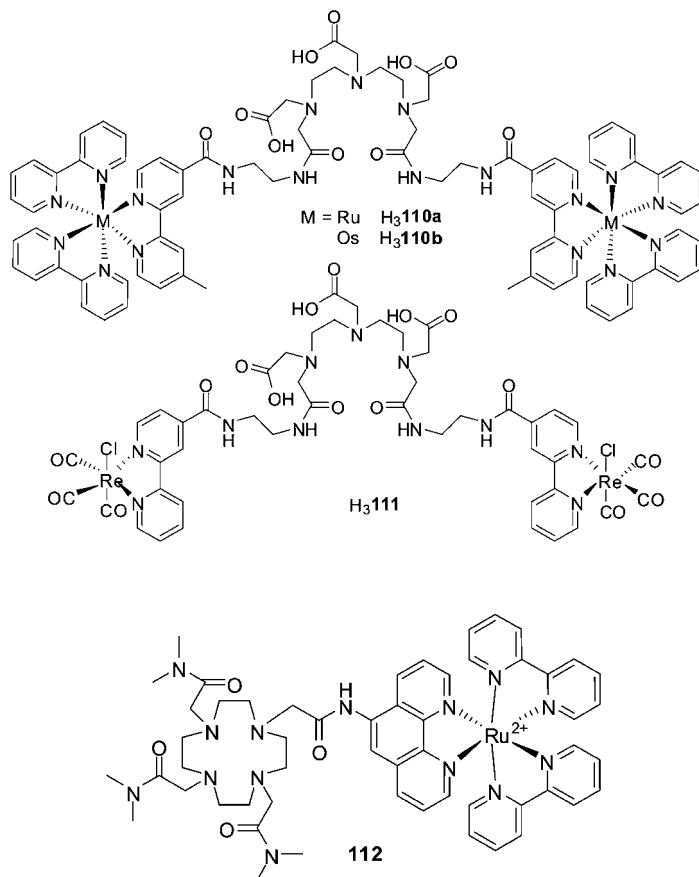
Fig. 90. d-Transition metal chromophores fitted on dtpa (top and middle) and do3a (bottom).

complexes also show attenuation of the $^3$MLCT emission when compared to H$_3$**110b**, as well as a red shift from 745 to 757 nm. The triplet state lifetime of H$_3$**110b** (34 ns in methanol) is much shorter compared to H$_3$**110a** and it shortens to 24–26 ns in the trimetallic complexes. Again, the chromophore emission interferes with Yb$^{III}$ luminescence so that deconvolution methods have to be used to extract the lifetimes. The *fac*-[ReCl(CO)$_3$(L$^1$)] complex emits at 625 nm, much as the Ru$^{II}$ chromophore and this emission is not shifted in the trimetallic complexes. The $^3$MLCT lifetime (13 ns) is also not much affected by lanthanide complexation (10–13 ns) but the emission intensity decreases by about 30%, again indicative of energy transfer. The lifetimes of the Ln$^{III}$ excited states amount to 0.51, 0.54, and 8.3 μs for Nd$^{III}$, Er$^{III}$, and Yb$^{III}$, respectively. These values are comparable to those obtained with the other two chromophores, but the grow-in of the emission is very fast. The determination of hydration numbers leads to values between 0.1 and 0.3 for Nd$^{III}$ in the three complexes, consistent
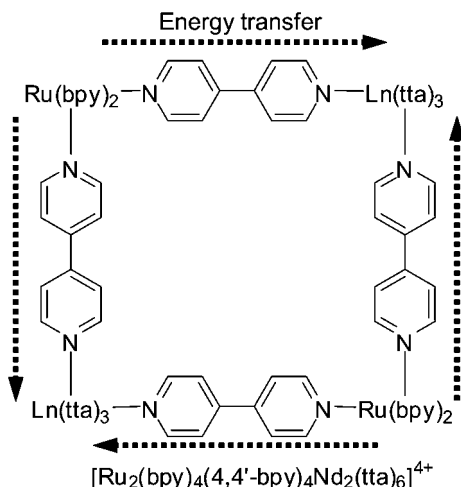
Fig. 91. Tetrametallic complex exhibiting $Ru^{II}$-to-$Ln^{III}$ (Ln = Nd, Yb) directional energy transfer (Guo et al., 2004).

with an octadentate coordination environment. As for the ternary complexes, none of the $Er^{III}$ complexes produces detectable emission in methanol, but emission is observed in deuterated methanol. An intriguing aspect of this work is the comparison of the apparent energy transfer efficiencies; energy transfer rates lie between 3.5 and $5.8 \times 10^7$ s$^{-1}$ for the $Re^I$ chromophore, almost one order of magnitude faster than for the $Os^{II}$ chromophore ($6.2$–$9.4 \times 10^6$ s$^{-1}$) and two orders of magnitude larger when compared with $Ru^{II}$ ($3.8 \times 10^5$ s$^{-1}$). Since the energies of the donor $^3$MLCT state are close for $Re^I$ and $Ru^{II}$ (15 700 and 16 000 cm$^{-1}$, respectively), and the linker between the dtpa coordination site and the transition metal ion chromophore comprises a saturated ethylene linker, rendering through bond energy transfer unlikely, the spatial proximity between the donor and the acceptor will play a key role. The less sterically hindered $Re^I$ chromophore is therefore a better donor than the more crowded $Ru^{II}$ one (Pope et al. 2004b, 2005).

Following a similar line, T. Gunnlaugsson has covalently attached the $[Ru(bpy)_2]^{2+}$ chromophore on a cyclen-amide derivative via a phenanthroline moiety (**112**, fig. 90). Excitation of the latter, at 285 nm, or of the $^3$MLCT state, at 450 nm, results in sensitized emission. The $Ru^{II}$ lifetime (202 ns) remains constant in water and deuterated water, which is not the case of the Nd($^4$F$_{3/2}$) level: its lifetime decreases from 192 ns in $D_2O$ to 30 ns in water; similarly, $\tau(Yb^{III})$ decreases from 6.4 to 2 μs, signifying a quenching by the solvent (Gunnlaugsson and Leonard, 2005).

In order to improve the $Ru^{II}$-to-$Ln^{III}$ energy transfer, Guo et al. have proposed interesting tetrametallic square $Ru_2Ln_2$ complexes (fig. 91). The $^3$MLCT emission at 610 nm is clearly visible in the reference $Gd^{III}$ assembly, but fades considerably for $Yb^{III}$ and even more for $Nd^{III}$, being ten times smaller than in the reference compound. In parallel, the metal-centered emission grows considerably, demonstrating the energy transfer (Guo et al., 2004); unfortunately, no quantitative data have been reported. This type of work on d–f complex prefigures
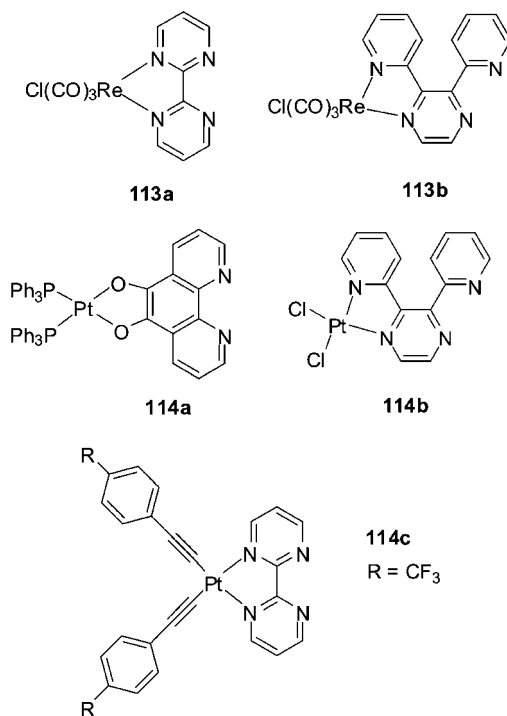
Fig. 92. Rhenium and platinum chromophores.

the development of coordination polymers in which sensitization of NIR luminescence occurs (see section 3.4).

Monovalent rhenium carbonyl complexes with 2,2′-bipyrimidine (**113a**, bpym) or 2,3-bis-(2-pyridyl)pyrazine (**113b**, bppz) have also been tested as potential sensitizing groups (fig. 92). The available bidentate coordination unit is simply coupled to a lanthanide $\beta$-diketonate complex, such [Ln(tta)$_3$] or [Ln(fod)$_3$]. The 650-nm emission of the $^3$MLCT state is quenched in the ternary adducts with Nd$^{III}$, Er$^{III}$, and Yb$^{III}$, demonstrating the energy transfer (Shavaleev et al., 2002). Metal-centered luminescence is consequently observed in methylene chloride upon excitation at 460 nm with lifetimes of <0.5 μs (Nd$^{III}$, Er$^{III}$), and 6.7 μs (Yb$^{III}$); quantum yields for solid state samples remain very small, 0.24, 0.02, and 0.79% for Nd, Er, and Yb, respectively, estimated from lifetime measurements and assuming $\tau_{rad} = 0.25$, 14, and 2 ms, respectively (Shavaleev et al., 2005). The same authors have designed similar chromophores by replacing Re$^I$ with Pt$^{II}$ (**114a–c**, cf. fig. 92). The ternary complexes [Ln(tta)**114a**] display slightly improved photophysical properties with respect to the Re chromophore, with lifetimes, in methylene chloride, equal to 0.99 (Nd$^{III}$), 2.52 (Er$^{III}$), and 10.6 μs (Yb$^{III}$), and quantum yields (solid state, from lifetimes) of 0.4, 0.018, and 0.53%, respectively (Shavaleev et al., 2003a). Replacing chromophore **114a** with the pyrazine derivative **114b** and/or the $\beta$-diketonate tta with btfa, (benzoyltrifluoroacetonate) does not change sub-
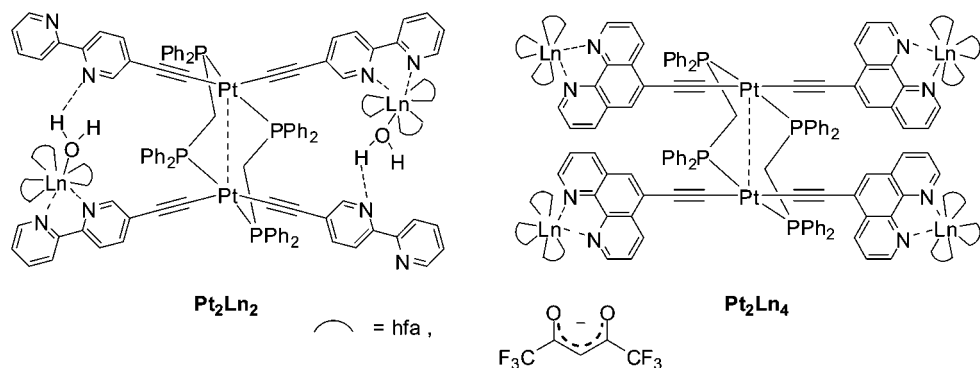
Fig. 93. Diplatinum chromophores forming tetra- and hexa-metallic complexes with Ln$^{III}$ ions (Xu et al., 2006).

stantially the photophysical properties and both lifetimes and quantum yields remain close to the figures listed above (Shavaleev et al., 2003b). This is also true for chromophore **114c**: the lifetime of [Nd(hfa)$_3$**114c**] is smaller than 0.5 μs and the quantum yield estimated from the lifetime of a solid sample (1 μs, $\tau_{rad} = 0.36$ ms) amounts to 0.27% (Shavaleev et al., 2005).

Another example of bifunctional bridging ligand is the diplatinum alkynyl chromophore depicted on fig. 93 (Xu et al., 2006). It is based on an acetylide-functionalized diimine (a commonly used building block for the design of multicomponent assemblies featuring redox and/or photoactive units) and the coordination sphere of the Pt$^{II}$ ion is completed by binding to bridging bis(diphenylphosphinomethane) (dppm) units. It forms 5d–4f heterometallic arrays with a nuclearity of four when reacted with luminescent lanthanide $\beta$-diketonates (hfa in this case, Ln = Nd, Eu, Yb). If the bipyridine unit is replaced with a 1,10-phenanthroline group, hexametallic arrays are isolated with the same lanthanide $\beta$-diketonates. In the case of Pt$_2$Eu$_2$, the association constant for the binding of the Eu$^{III}$ diketonate to the bipyridyl sites is $3 \times 10^7$ M$^{-2}$. According to X-ray analysis, the Pt$_2$Nd$_2$ array is composed of [Pt$_2$(μ-dppm)$_2$(bpy-ethynyl)$_4$] units incorporating [Nd(hfa)$_3$(H$_2$O)$_2$] complexes through 2,2′-bipyridyl chelates; they are stabilized by strong intramolecular hydrogen bonds and the intramolecular Pt···Nd distance is 8.8 Å, that is favorable to dipole–dipole (through space) energy transfers. Upon irradiation in the diplatinum $^3$MLCT band (250–450 nm), all of the isolated complexes exhibit metal-centered emission, both in the solid state and in methylene chloride. Lifetimes of the Nd($^4$F$_{3/2}$) level are 0.21 (Pt$_2$Nd$_2$) and 0.49 μs (Pt$_2$Nd$_4$) in the solid state (emission in solution is too weak for lifetime measurements), while Yb($^2$F$_{5/2}$) lifetimes amount to 11–13 μs for the two edifices, either in the solid state or in solution. The quantum yields of the solid samples calculated from the lifetimes, with $\tau_{rad} = 0.25$ ms (Nd) and 2 ms (Yb), are 0.08% for Pt$_2$Nd$_2$, 0.20% for Pt$_2$Nd$_4$, and 0.57 and 0.64% for the corresponding Yb$^{III}$ complexes.

Building on their technique for assembling [2]pseudorotaxanes through anion templation, P.D. Beer and S. Faulkner have designed supramolecular d–f heterometallic assemblies in which the luminescence of the lanthanide ion is sensitized by a d-transition metal ion (fig. 94).
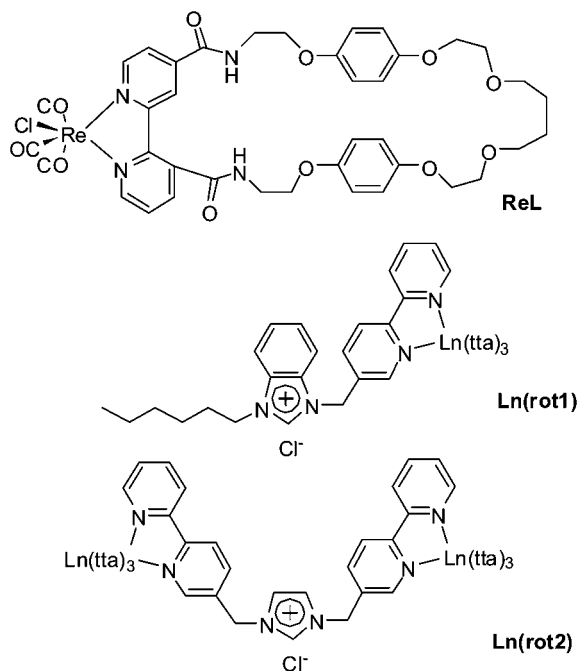
Fig. 94. Macrocycle (top) used to host the lanthanide-containing pseudo-rotaxane threads (middle and bottom) (Sambrook et al., 2006).

The threading component is comprised of a benzimidazolium or an imidazolium chloride stoppered by a tris(thenoyltrifluoroacetonate) lanthanide unit. The rhenium-containing macrocycle **ReL** contains a rhenium(I) bipyridyl group as sensitizer, in combination with an amide cleft for chloride recognition and electron rich hydroquinone groups for potential $\pi-\pi$ stacking interactions. It allows the penetration of the benzimidazolium or imidazolium chloride into its cavity and therefore the formation of **Ln(rot)** $\subset$ **ReL** (Ln = Nd, Gd, Yb) occurs through anion recognition and is signaled by sensitized NIR emission (Sambrook et al., 2006). Association constants are $\log K_a = 4.2$ and 4.8 in methylene chloride for **Gd(rot1)** $\subset$ **ReL** and **Gd(rot2)** $\subset$ **ReL**, respectively. Upon complexation to the Gd$^{III}$ threads, the lifetime of the Re$^I$($^3$MLCT) emission increases from 31 ns for the free macrocycle to 215 ns. Replacement of Gd$^{III}$ by Nd$^{III}$ or Yb$^{III}$ threads results in a severe quenching of the rhenium emission, when compared with the emission of the Gd$^{III}$ analogs. This evidences energy transfer from the Re$^I$($^3$MLCT) state located at 25 900 cm$^{-1}$ onto the emissive Ln$^{III}$ states. The lifetimes of the latter amount to 0.8 µs for Nd($^4F_{3/2}$) and 11.1 µs for Yb($^2F_{5/2}$).

### 3.3.4. *d-Transition metal ions for extending the apparent Ln$^{III}$ lifetime*

When the donor d-transition metal ion and the accepting Ln$^{III}$ ion lie relatively close, typically at distances <5 Å, several mechanisms are operative to achieve the energy transfer,
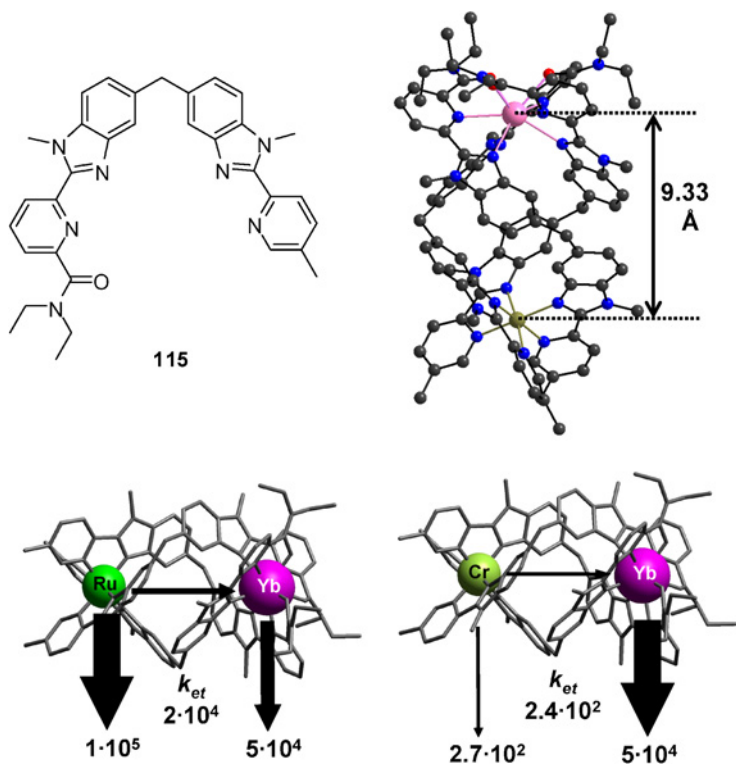
Fig. 95. (Top left) Ditopic ligand for the self-assembly of discrete M–Ln edifices. (Top right) Structure of $[CrYb(\mathbf{115})_3]^{6+}$, redrawn from (Imbert et al., 2003). (Bottom) Schematic representation of the energy migration paths occurring in the RuYb and CrYb edifices, with associated rate constants in $s^{-1}$ (Torelli et al., 2005).

particularly in the case of $Yb^{III}$ for which both an electron exchange pathway and phonon-assisted processes are feasible. The possible simultaneous occurrence of these mechanisms in the same heterobimetallic edifice, combined with the difficulty in separating the exchange from the multipolar contributions to the ligand-to-metal energy transfer limits the efficiency of molecular programming and the tuning of the electronic properties of the 4f ion, henceforth intensity of its NIR luminescence. In this context, discrete nd–4f heterobimetallic edifices have been designed and produced by strict self-assembly of a pentadentate ditopic ligand $\mathbf{115}$ based on benzimidazolepyridine units. The molecule belongs to a class of compounds comprising both hexadentate and pentadentate synthons, which self-assemble under stoichiometric conditions to produce $Ln_2L_3$, $LnLn'L_3$ or $MLnL_3$ triple-stranded helicates with approximate $D_3$ symmetry (Bünzli and Piguet, 2002). In these edifices, the three ligands are arranged in a head-to-head-to-head fashion (HHH), that is, the same three coordinating units are connected to the same metal ion. In the structure shown in fig. 95, $Yb^{III}$ is 9-coordinate by six nitrogen atoms and three oxygen atoms from the three amide groups, in an approximate tricapped trig-

onal prismatic geometry, whereas the smaller $Cr^{III}$ ion is 6-coordinate in a slightly distorted octahedral arrangement. The intermetallic distance of 9.33 Å ensures that the energy transfer mechanism is mainly of dipole–dipolar origin.

When one metal ion is used as a donor for sensitizing the emission of a second accepting metal ion, the characteristic lifetimes $\tau$ of their excited states, which are related to their deactivation rates by $\tau = k^{-1}$, are affected by the metal-to-metal communication process. This situation can be simply modeled for the special case of an isolated d–f pair, in which the d-block chromophore (M) sensitizes the neighboring lanthanide ion (Ln) thanks to an energy transfer process described by the rate constant $k_{et}^{M,Ln}$. In absence of energy transfer, excited states of the two isolated chromophores decay with their intrinsic deactivation rates $k^M$ and $k^{Ln}$, respectively, which provides eqs. (32) and (33) yielding eqs. (34) and (35) after integration:

$$d\big[M^*(t)\big]/dt = -\big(k_{et}^{M,Ln} + k^M\big) \cdot \big[M^*(t)\big]^2, \tag{32}$$

$$d\big[Ln^*(t)\big]/dt = k_{et}^{M,Ln} \cdot \big[M^*(t)\big] - k^{Ln}\big[Ln^*(t)\big], \tag{33}$$

$$\big[M^*(t)\big] = \big[M^*(0)\big] \cdot e^{-(k_{et}^{M,Ln}+k^M)\cdot t}, \tag{34}$$

$$\big[Ln^*(t)\big] = \big[M^*(0)\big] \cdot \frac{k_{et}^{M,Ln}}{k^{Ln} - (k_{et}^{M,Ln} + k^M)} \cdot \Big(e^{-(k_{et}^{M,Ln}+k^M)\cdot t} - e^{-k^{Ln}\cdot t}\Big). \tag{35}$$

The decay rate of the excited state of the d-block donor M* increases when it transfers energy to an acceptor. The experimental decay rate thus corresponds to the sum of the two deactivation rate constants and translates into a reduced lifetime:

$$k_{obs}^M = k^M + k_{et}^{M,Ln}, \quad \tau^M = \big(k_{obs}^M\big)^{-1} = \big(k^M + k_{et}^{M,Ln}\big)^{-1}. \tag{36}$$

Interpretation of eq. (35) is less straightforward, because the magnitude of $k_{et}^{M,Ln}$ controls the feeding rate of the excited state of the acceptor. Therefore, the variation of $[Ln^*]$ over time, after initial excitation of the donor, strongly depends on the relative magnitudes of the rate constants $k_{obs}^M$ and $k^{Ln}$ and two limiting cases can be described:

(i) $k_{obs}^M > k^{Ln}$

The Ln* level is almost completely populated before any significant Ln-centered deactivation occurs. As a consequence, the experimental Ln-centered deactivation rate $k_{exp}^{Ln}$ mirrors that found in absence of metal-to-metal communication, $k^{Ln}$. Introducing the specific condition $k_{obs}^M \gg k^{Ln}$ in eq. (35) produces eq. (37), whereby the time dependence of the decay profile indeed corresponds to $k_{exp}^{Ln} = k^{Ln}$:

$$\big[Ln^*(t)\big] = \big[M^*(0)\big] \cdot \frac{k_{et}^{M,Ln}}{k_{et}^{M,Ln} + k^M} \cdot e^{-k^{Ln}\cdot t}. \tag{37}$$

This situation is encountered for a large number of d–f pairs, because the intrinsic deactivation rates of the d-block donor $k^M$ are often considerably larger than the deactivation of the Ln-centered 4f excited states. For instance, it occurs for the Ru $\rightarrow$ Yb transfer in $[RuYb(\mathbf{115})_3]^{5+}$ (fig. 95). As expected, the experimental decay rate $k_{obs}^{Ru} =$

$1.2 \times 10^5$ s$^{-1}$ is larger compared to $k^{\text{Ru}} = 1.0 \times 10^5$ s$^{-1}$ (in [RuGd(**115**)$_3$]$^{5+}$). Since $k_{\text{obs}}^{\text{Ru}} = 1.2 \times 10^5$ s$^{-1} > k^{\text{Yb}} = 5 \times 10^4$ s$^{-1}$ (in [ZnYb(**115**)$_3$]$^{5+}$), eq. (35) predicts that the experimental Yb-centered decay rate recorded in [RuYb(**115**)$_3$]$^{5+}$ should roughly mirror $k^{\text{Yb}}$, and this is indeed observed with an experimental value of $k_{\text{exp}}^{\text{Yb}} = 4.4 \times 10^4$ s$^{-1}$.

(ii) $k_{\text{obs}}^{\text{M}} < k^{\text{Ln}}$

Here, the Ln-centered excited state relaxes almost instantaneously as long as it is slowly populated by the donor and deactivation of the d-block ion controls the overall deactivation process. As a consequence, the experimental Ln-centered deactivation rate $k_{\text{exp}}^{\text{Ln}}$ should mirror $k_{\text{obs}}^{\text{M}}$. Introduction of the condition $k_{\text{obs}}^{\text{M}} < k^{\text{Ln}}$ into eq. (35), provides a simplified eq. (38), which demonstrates that the time dependence of the decay profile would indeed correspond to $k_{\text{exp}}^{\text{Ln}} = k_{\text{obs}}^{\text{M}}$:

$$\left[\text{Ln}^*(t)\right] = \left[\text{M}^*(0)\right] \cdot \frac{k_{\text{et}}^{\text{M,Ln}}}{k^{\text{Ln}}} \cdot e^{-(k_{\text{et}}^{\text{M,Ln}}+k^{\text{M}})\cdot t} = \left[\text{M}^*(0)\right] \cdot \frac{k_{\text{et}}^{\text{M,Ln}}}{k^{\text{Ln}}} \cdot e^{-k_{\text{obs}}^{\text{M}}\cdot t}. \quad (38)$$

The replacement of Ru$^{\text{II}}$ with Cr$^{\text{III}}$ as the donor in [CrYb(**115**)$_3$]$^{6+}$ illustrates this second situation. The combination of the intrinsic deactivation rate of the Cr-centered donor levels $k^{\text{Cr}} = 2.7 \times 10^2$ s$^{-1}$ (in [CrGd(**115**)$_3$]$^{6+}$), with the rate of energy transfer $k_{\text{et}}^{\text{Cr,Yb}} = 2.4 \times 10^2$ s$^{-1}$ gives $k_{\text{obs}}^{\text{Cr}} = k^{\text{Cr}} + k_{\text{ET}}^{\text{Cr,Yb}} = 5.1 \times 10^2$ s$^{-1}$. This remains small compared to the intrinsic rate of deactivation of Yb($^2$F$_{5/2}$) ($k^{\text{Yb}} = 5 \times 10^4$ s$^{-1}$ in [ZnYb(**115**)$_3$]$^{5+}$), and therefore $k^{\text{Yb}} \gg k_{\text{obs}}^{\text{M}}$ (fig. 95). Experimentally, the decay rate of the Yb($^2$F$_{5/2}$) level amounts to $k_{\text{exp}}^{\text{Yb}} = 5.1 \times 10^2$ s$^{-1}$, which perfectly mirrors the slow deactivation of the Cr$^{\text{III}}$ chromophore. These rate constants can be transformed into characteristic excited lifetimes, thus leading to $\tau_{\text{exp}}^{\text{Yb}} = 23$ μs, when Yb$^{\text{III}}$ is sensitized by Ru$^{\text{II}}$ in [RuYb(**115**)$_3$]$^{5+}$, and $\tau_{\text{exp}}^{\text{Yb}} = 1960$ μs (1.96 ms) when Yb$^{\text{III}}$ is sensitized by Cr$^{\text{III}}$ in the isostructural complex [CrYb(**115**)$_3$]$^{6+}$. Such apparent extension of the Ln-centered NIR luminescence, which is also observed for Nd$^{\text{III}}$ (Imbert et al., 2003), by two or three orders of magnitude (from the microsecond to the millisecond range) may be valuable for improving the sensitivity of time-gated homogeneous luminescent immunoassays, provided a judicious choice of the donor chromophore is made.

### 3.3.5. *4f-Transition metal ions as luminescence sensitizers*

Energy transfers between lanthanide ions are well documented, either in solid state, for instance for the sensitization of laser materials, or in solution of metal-containing proteins in which the replacement of Ca$^{\text{II}}$ or Zn$^{\text{II}}$ with different Ln$^{\text{III}}$ ions allows the determination of the metal-to-metal distances by measuring the yield of energy transfer. Diffusion limited energy transfer from Tb$^{\text{III}}$ to NIR emitting ions, particularly Nd$^{\text{III}}$ (Bünzli and Vuckovic, 1983; Kandpal et al., 1979) and Er$^{\text{III}}$ (Kandpal and Tripathi, 1979), in organic solvents such as acetone, acetonitrile, dmf, or dmso is also well documented. On the other hand, energy transfer between 4f ions in discrete molecular assemblies has been less studied because of the lack of suitable synthetic methods for producing pure heteropolymetallic complexes; as a consequence, studies have often been performed on statistical mixtures (Froidevaux and Bünzli,
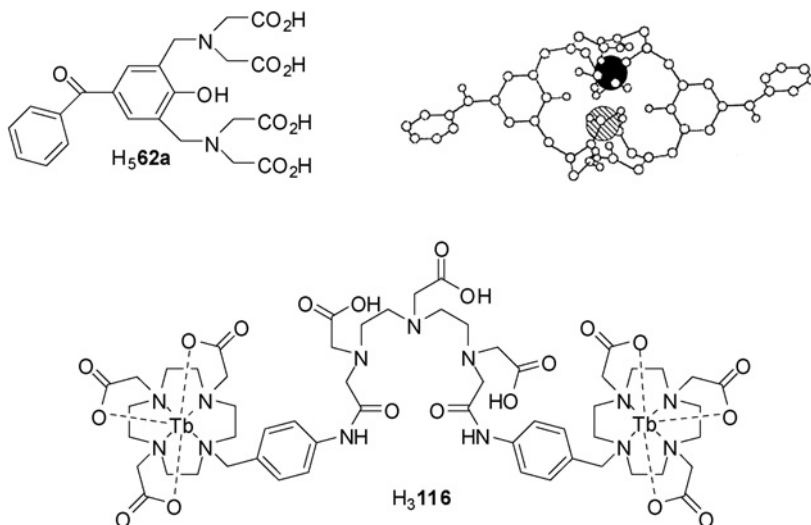
Fig. 96. (Top) Polyaminocarboxylic acid for producing $Ln^{III}Ln^{III}$ dimeric species, with a calculated structure; reproduced from (Ala-Kleme et al., 2000). (Bottom) Bis(do3a)-modified dtpa for sensitization of $Yb^{III}$ by convergent energy transfers from two $Tb^{III}$ ions.
© 2000 with permission from Elsevier

1994; Piguet et al., 1993). One example pertains to the sensitization of $Nd^{III}$ and $Yb^{III}$ by energy transfer from $Tb^{III}$ in dimeric polyaminocarboxylates. The dimeric species $Tb^{III}Tb^{III}$, $Ln^{III}Ln^{III}$, and $Tb^{III}Ln^{III}$ (Ln = Y, Nd, Dy, Yb) were prepared by diluting appropriate amounts of $Ln^{III}$ ions in an equimolar solution of the potentially heptadentate ligand 2,6-bis[$N,N$-bis(carboxymethyl)-aminomethyl]-4-benzoylphenol, $H_5$**62a** (fig. 96), adjusted to pH 9.2 in a borate buffer in order to ensure complete deprotonation of the ligand (Ala-Kleme et al., 2000). The solutions were placed in a quartz cuvette containing an oxide-covered aluminum working electrode having a surface of $\approx 0.8$ cm$^2$ and a thickness of $\approx 4$ nm, as well as a platinum counter electrode; peroxodisulfate was added. Electrochemically generated luminescence was observed for $Tb^{III}$ and $Dy^{III}$. Intensity of the $Tb^{III}$ luminescence progressively decreases when the $Ln^{III}$ (Ln = Nd, Yb) proportion is increased in the $Tb^{III}/Ln^{III}$ systems, clearly pointing to energy transfer onto the NIR emitting ions. The corresponding luminescence was however not observed due to instrumental limitations.

It is only recently that S. Faulkner took advantage of the kinetic inertness of $Ln^{III}$ cyclen macrocyclic complexes for producing the neutral pure heterotrimetallic compound [Yb(**116b**)] (fig. 96) in which convergent directional intramolecular $Tb^{III} \rightarrow Yb^{III}$ processes are responsible for the sensitization of the NIR Yb($^2F_{5/2}$) emission (Faulkner and Pope, 2003). The complex is stable in water and according to the lifetime measured (1.83 and 4.22 μs in $H_2O$ and $D_2O$, respectively), the hydration number of $Yb^{III}$ is close to zero ($q_{Yb} = 0.2$) while $q_{Tb} = 1.4$ is obtained, in line with its complexation by the heptadentate cyclen derivative.

The Yb($^2F_{5/2}$) lifetime is independent of the excitation mode, through the aryl chromophore or through the Tb$^{III}$ ion (488 nm).

### 3.4. *NIR luminescence in extended structures and various materials*

The aim of this chapter is to review NIR-emitting *molecular* edifices. If the last complexes discussed belong to this category, while completely inorganic Nd:YAG materials are clearly excluded, there is a range of compounds and materials which are between these two aspects of lanthanide science. They include extended mono-dimensional or poly-dimensional structures, both inorganic or organic, composite porous materials, and nanoparticles. Since these compounds are more and more tested for practical applications, either in telecommunications, lighting, or medical diagnostic (bioanalyses and imaging), we discuss them here with varying extent of coverage, the more inorganic-like systems being less dealt with. We have also added a section on ionic liquids, another emerging field of today's chemistry.

### 3.4.1. *Coordination polymers*

The assembly of metal–organic infinite frameworks via the coordination of metal ions by multi-functional bridging ligands provides the possibility of bringing metal ions in close proximity, henceforth facilitating metal-to-metal communications, as well as of increasing the number of metal ions per unit cell, improving the performance of functional materials. Introduction of lanthanide ions in one- (1D-), two- (2D-), or three- (3D-) dimensional networks is expected to be more difficult to control than their d-block metal analogs due to the higher coordination numbers of lanthanide ions and the absence of strong specific steric requirements. On the other hand, the inherent flexibility of lanthanide coordination geometry leads to the synthesis of unprecedented structures.

The connecting ligand dictates, to some degree, the dimensionality of the array. For instance, cyanide or d-metal cyanides help constructing 1D arrays; a judicious combination of small ligands such as cyanide and carbonyl results in 2D grid-like materials, while benzene polycarboxylates or derivatized bipyridines often lead to 3D arrangements (Bünzli and Piguet, 2002). Although the number of reported lanthanide-containing coordination polymers (sometimes referred to as metal–organic frameworks, MOF) is steadily increasing (Guillou and Daiguebonne, 2004), relatively few have been specifically designed for NIR luminescence and all of these examples are fairly recent.

In order to bring Ru$^{II}$ close to an NIR-emitting Ln$^{III}$ ion, M. Ward and coworkers (Davies et al., 2005b; Miller et al., 2004) have co-crystallized the cyanoruthenate chromophore K$_2$(**117**) (K$_2$[Ru(CN)$_4$(bpy)], fig. 97) with lanthanide chlorides (Ln = Pr, Nd, Gd, Er, Yb) in water, which afforded oligomers and networks in which the [Ru(CN)$_4$(bpy)]$^{2-}$ unit is connected to the lanthanide ion via Ru–CN–Ln bridges. Two main structural types of coordination polymers crystallize. In the first one, depicted in the middle of fig. 97, the chromophoric unit is connected to a single Ln$^{III}$ ion by individual cyanide bridges, yielding trimetallic fragments, $\{[Ru(CN)_4(bpy)]_2[Ln(H_2O)_x][K(H_2O)_y]\cdot zH_2O\}_n$ ($x = 7$, 6, 6 for Ln = Pr, Er, Yb, respectively), denoted as RuLnK. The second type contains 2D sheets of interconnected, cyanide-bridged Ru$_2$Ln$_2$ squares and corresponds to the general formula
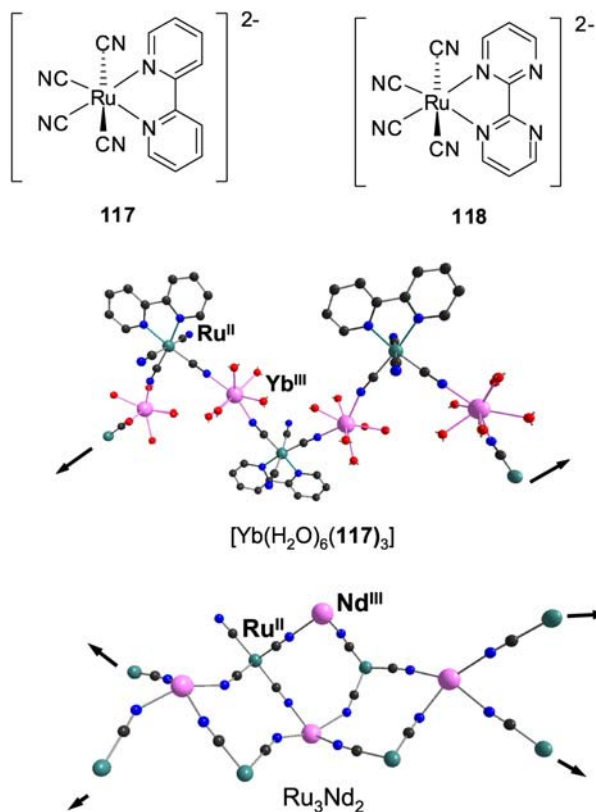
Fig. 97. (Top) Ru$^{II}$ synthons for building coordination polymers; (middle) Ru–CN–Yb bridged coordination polymer. (Bottom) Sketch of the 2D sheet structure in the Ru$_3$Nd$_2$ compound. Redrawn from (Davies et al., 2005b; Miller et al., 2004).

$\{[Ru(CN)_4(bpy)]_3[Ln(H_2O)_4]_2 \cdot zH_2O\}_n$ (Ln = Nd, Gd); it is denoted Ru$_3$Ln$_2$. The Ru$^{II}$-based luminescence observed upon excitation at 337 nm in the Ru$_3$Gd$_2$ largely fades off in the networks containing NIR-emitting Ln$^{III}$ ions with concomitant appearance of the typical 4f–4f transitions, even the Pr$^{III}$ ($^1D_2 \rightarrow {}^3F_4$) transition at 1.01 μm. For solid state samples, the $^3$LMCT lifetime decreases from 550 ns in the Ru$_3$Gd$_2$ compound to 197 ns in Ru$_2$YbK, 76 ns in Ru$_2$ErK, 22 ns in Ru$_2$PrK and 5 ns in Ru$_3$Nd$_2$. The Ru$^{II}$-to-Ln$^{III}$ energy transfer rates could be estimated and range from $3 \times 10^6$ s$^{-1}$ in Ru$_2$YbK, to $1 \times 10^7$ s$^{-1}$ in Ru$_2$ErK, $4 \times 10^7$ s$^{-1}$ in Ru$_2$PrK, and $2 \times 10^8$ s$^{-1}$ in Ru$_3$Nd$_2$. These fast rates are explained by the vicinity of the Ru–Ln pairs (5.4–5.5 Å in RuLnK and 5.4–5.7 Å in Ru$_3$Ln$_2$ polymers). Indeed they are about two orders of magnitude larger than those reported for the molecular complexes with receptors H$_3$**104**–H$_6$**105** (fig. 88). The increasing order of transfer rates, Nd > Pr > Er > Yb can further be rationalized on the basis of the overlap of the f–f absorption bands with the emission spectrum from the donor $^3$MLCT state.

In an extension of this work, bipyridine in $[Ru(CN)_4(bpy)]^{2-}$ has been replaced with 2,2′-bipyrimidine (bpym, see formula **118**, fig. 97) for two reasons: bpym has a lower triplet state than bpy and its two additional nitrogen atoms may coordinate to $Ln^{III}$ ions (Herrera et al., 2006a). Simple evaporation of an aqueous solution containing $K_2[Ru(CN)_4(bpym)]$ and hydrated $Ln(NO_3)_3$ in a 1:5 molar ratio results in the crystallization of two types of isostructural coordination polymers: (i) $\{[Ru(CN)_4(bpym)][Ln(NO_3)(H_2O)_5]\}_n$ for Ln = Nd, Sm, Gd (denoted RuLn), in which 1D helical chains along the $c$ axis consist of alternating $[Ru(CN)_4(bpy)]^{2-}$ and $[Ln(NO_3)(H_2O)_5]$ units linked by cyanide bridges, and (ii) $\{[Ru(CN)_4(bpym)]_2[Ln(NO_3)(H_2O)_2][Ln(NO_3)_{0.5}(H_2O)_{5.5}](NO_3)_{0.5}(H_2O)_{5.5}\}_n$ for Ln = Er, Yb (denoted Ru₂Ln), which form complicated 2D networks. Sensitized NIR emission from Nd, Er, and Yb was observed for all of the crystalline samples grown in $D_2O$ (to minimize quenching by O–H vibrations) upon excitation either at 337 nm or at 430 nm ($^1$MLCT state). For $Nd^{III}$, the lifetime of the lanthanide-based excited state is about the same in RuNd and Ru₂Nd (64 and 66 ns at room temperature), while it is much longer in RuYb (587 ns) than in Ru₂Yb (245 ns). For $Er^{III}$, the decay had to be fitted with a bi-exponential function ($\tau_{obs}$ = 43 and 300 ns). The $^3$MLCT lifetime of the donor amounts to 80 ns, which means that the energy transfer rates are fast; they have been estimated to be larger than $10^8$ s$^{-1}$, that is somewhat faster when compared to the rates determined for the coordination polymers based on the $[Ru(CN)_4(bpy)]^{2-}$ donor. A similar coordination polymer based on hexaaza-triphenylene (hat) with overall formula $\{Nd_2[Ru(CN)_4]_3(\mu^3\text{-hat})\cdot23H_2O\}_n$ contains 9-coordinate $Nd^{III}$ ions bound to five water molecules and four cyanide ions. It displays strong MLCT absorption and transfers energy onto the 4f-ion, the lifetime of the $^4F_{3/2}$ level being around 100 ns (Herrera et al., 2006b). Although interesting from the point of view of energy transfer efficiency, these materials however present a severe drawback in that several water molecules remain coordinated on the lanthanide ion and as a result, nonradiative deactivations stay important.

The influence of fluorination on $Er^{III}$ luminescence has been demonstrated with 1,4-benzenedicarboxylate (bdc) and 2,3,5,6-tetrafluoro-1,4-benzenedicarboxylate (dbc-F₄) organic frameworks (Chen et al., 2006). A mixture of hydrated erbium nitrate and the desired dicarboxylic acid in dimethylformamide/ethanol is introduced into a vial which is sealed and heated for 24 h at 80 °C, yielding light purple crystals. The structure of $[Er_2(bdc)_3(dmf)_2(H_2O)_2]\cdot H_2O$ consists in bimetallic $Er^{III}$ units as building blocks, bridged by two carboxylates from two bdc anions; the coordination sphere of each $Er^{III}$ ion is completed through coordination from two bidentate carboxylates and terminal dmf and water molecules. The bimetallic units are connected by six bdc anions and form a 3D distorted primitive cubic framework. The structure of $[Er_2(bdc-F_4)_3(dmf)(H_2O)]\cdot dmf$ is different, consisting in a 1D rod-like framework, but the number of $Er^{III}$ ions per unit volume, 1.14 per 1000 Å$^3$, is similar when compared to the un-fluorinated coordination polymer (1.24), so that comparing emission intensities has some meaning: the fluorescence intensity is four times larger for the fluorinated compound.

Amino–carboxylic and phosphonic acids are known to form open frameworks (i.e. porous materials), particularly with first-row transition metal ions. Lanthanide diphosphonates with 3D pillared-layer structure are also known and several classes of ligands such as sim-
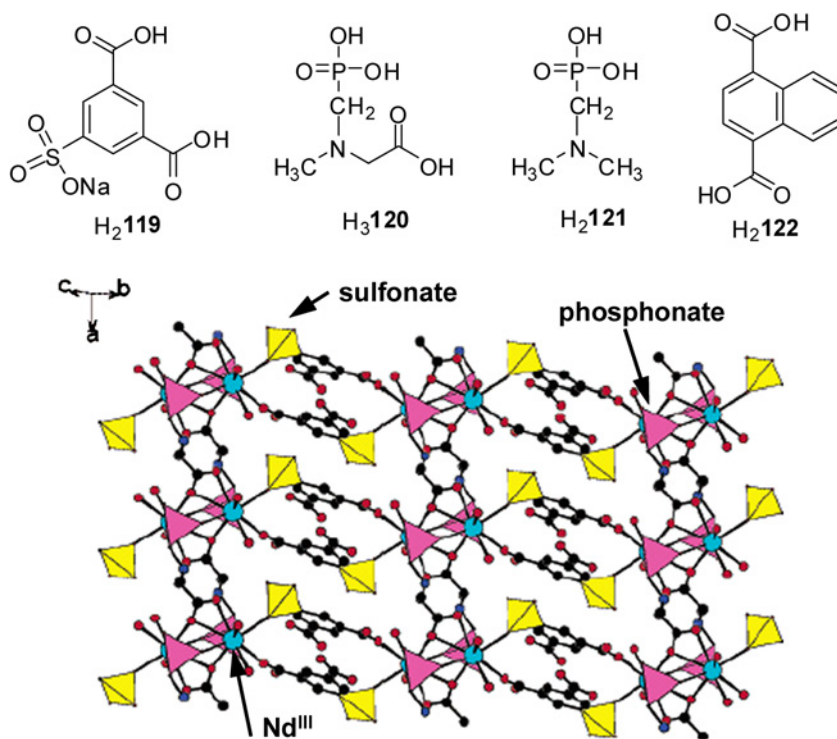
Fig. 98. (Top) Ligands based on sulfonic, phosphonic and carboxylic acids. (Bottom) ⟨011⟩ layer in [Nd(**119**)(H$_2$**120**)(H$_2$O)$_2$]·H$_2$O; reproduced with permission from (Song et al., 2004).
© 2004 American Chemical Society

ple aromatic derivatives, aminoacids, calixarenes and cyclens have been decorated with phosphonate groups. Jiang-Gao Mao and his collaborators have chosen the sodium salt of 5-sulfoisophthalic acid (H$_2$**119**, fig. 98) and one carboxylic-phosphonic acid, *N*-(phosphonomethyl)-*N*-methylglycine (H$_3$**120**) to produce, by hydrothermal methods, phosphonate–sulfonate hybrids of general formula [Ln(**119**)(H$_2$**120**)(H$_2$O)$_2$] (Ln = La, Pr, Nd, Gd) and having an isomorphous layered architecture (see fig. 98 for an example). While the Gd compound possesses a single emission band at 416 nm arising from the ligand states, the Nd coordination polymer displays, in addition, its typical emission from the $^4F_{3/2}$ state, the intensity of which is much enhanced upon de-hydration of the hybrid material (Song et al., 2004). Replacing 5-sulfoisophthalate with oxalate (ox), results in the crystallization of three series of tridimensional networks with the following formulae: {[Ln(ox)(H$_2$**120**)]·0.5H$_2$O}$_n$ (Ln = Nd, Eu, Gd), {[Ln$_4$(ox)$_5$(**121**)$_2$(H$_2$O)$_4$]·2H$_2$O}$_n$ (Ln = La, Nd), and {[Ln$_3$(ox)$_4$(**121**)(H$_2$O)$_6$]·6H$_2$O}$_n$ (Ln = Gd, Er). Both Nd$^{III}$-containing materials, as well as the Er$^{III}$ compound are luminescent, and the emission intensity again increases upon removal of the lattice water molecules. The advantages of these materials are their high
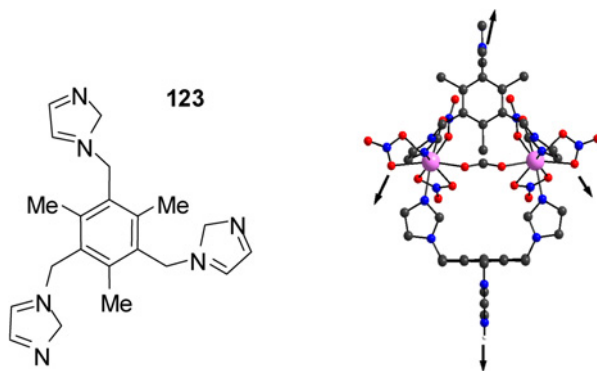
Fig. 99. (Left) Tripodal ligand for the building of a lanthanide–organic framework. (Right) Yb[III] dimeric unit with arrows indicating the directions of the H-bonds in the 2D network. Redrawn from (Zhang et al., 2006).

solubility and good crystallinity due to the introduction of the oxalate anion (Song and Mao, 2005).

Aromatic polycarboxylates easily form 2D or 3D networks, for instance [Nd$_2$(**122**)$_3$(dmf)$_4$]· H$_2$O which present a 2D structure in which the 1,4-naphthalenedicarboxylate anions link Nd[III] ions of two adjacent double chains keeping them at a short distance of about 4.1 Å (J. Yang et al., 2006). This allows up-conversion to take place, albeit with very low efficiency: a blue emission is seen at 449.5 nm upon excitation at 580 nm (corresponding to the $^4G_{5/2} \leftarrow {}^4I_{9/2}$ transition) and from the structure and the magnetic properties an energy-transfer up-conversion mechanism involving no excited state absorption is more likely.

Another way of realizing extended networks is to program weak interactions between discrete complex molecules, for instance hydrogen bonds or $\pi$–$\pi$ stacking interactions. One example of such a network is given by W.-Y. Sun et al. (Zhang et al., 2006) who reacted the tripodal ligand 1,3,5-tris(imidazole-1-ylmethyl)-2,4,6-trimethylbenzene (**123**, fig. 99) with hydrated lanthanide nitrate in presence of triethylorthoformate in methanol and obtained bimetallic complexes [Ln$_2$(NO$_3$)$_6$($\mu$-HCO$_2$)($\mu$-**123**)($\mu$-**123**H)]·3MeOH (Ln = Eu, Gd, Tb, Dy, Er, and Yb). The structure of the Gd[III] compound reveals dimeric species in which the two metal ions are connected by bidentate bridging **123** units (fig. 99) and the formate ions. The tripodal ligand uses only two of the three imidazole groups, the third one being uncoordinated; one ligand adopt a *cis, cis, cis* conformation while the other one is protonated with a *cis, trans, trans* conformation. The dimeric units are connected into a 2D network by hydrogen bonds between the nitrate O-atoms and the C–H bonds of the methyl groups of the anchor, as well as between the protonated NH$^+$ and the unprotonated amine function of an uncoordinated imidazole (fig. 99); according to the authors, a further much weaker interaction between benzene rings ensures a 3D dimensionality (distance between aromatic cores ≈3.8–4 Å, far from the generally agreed upon distance of 3.5 Å). The cavity holes host three methanol molecules (not shown on fig. 99). Near-infrared emission is reported for the Yb[III] complex 1 mM in dmso-$d_6$.
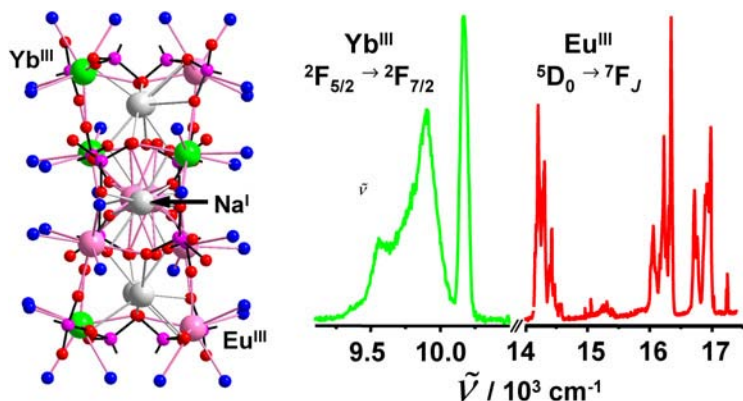
Fig. 100. (Left) Structure of the Eu $\subset$ Na$_6$Eu$_{8-x}$Yb$_x$ cluster ($x = 4$) and (right) dual emission in the visible and NIR. Redrawn from (Comby et al., 2006c).

### 3.4.2. *Inorganic clusters*

The exploration of lanthanide-containing discrete polymetallic frameworks with high and controlled nuclearity is a field which is not yet mature, except maybe in the cases of dendrimeric structures for MRI contrast agents (Pierre et al., 2005) and of metallacrowns (Stemmler et al., 1999). Such clusters have, however, large potential interest as precursors for doped materials or for studying (and implementing) metal–metal interactions, e.g. energy transfers or magnetic interactions (Zaleski et al., 2004). Research on these clusters has usually focused in obtaining wheel- or cage-like edifices, some of them acting as supramolecular receptors for anions or cations. They can be assembled using different synthetic strategies, the key being to avoid the extension of the structure into a coordination polymer and, possibly, to control the nuclearity (i.e. the number of metal ions in the core, $m$) or the global complexity $m + n$ of [Ln$_m$L$_n$] (Senegas et al., 2005). This can be achieved with simple polydentate ligands leaving some coordination vacancies around the metal ion, such as 5′-methyl-2,2′-bipyridyl-6-phosphonic acid (H$_2$L). Monoclinic crystals of composition [Na$_6$Ln$_9$L$_{16}$(H$_2$O)$_4$]·(OH)·47H$_2$O (Ln = Eu, Gd, Tb, Er) crystallize upon slow diffusion of acetone into aqueous solutions with a 1:3 Ln$^{III}$:H$_2$L stoichiometric ratio and adjusted to pH 7.4 (Comby et al., 2006c). The crystallization process is strictly controlled and any change in the experimental conditions fails to produce the desired material. The clusters contains eight eight-coordinate peripheral Ln$_p^{III}$ ions arranged in the corners of two parallel parallelepipeds; the ninth Ln$^{III}$ ion lies in the middle of the assembly, is also eight-coordinate, but four water molecules are bound in its inner coordination sphere. The Na$_6$Ln$_9$ clusters are held together by an intricate network of bridging phosphonate groups and sizeable $\pi$–$\pi$ stacking interactions.

Mixed clusters Eu $\subset$ Na$_6$Eu$_{8-x}$Yb$_x$, with $x = 4$ or 5 (see fig. 100), in which the central site is occupied by Eu$^{III}$ whereas the Yb$^{III}$ ions are statistically distributed in the peripheral sites, are isostructural with the Na$_6$Ln$_9$ species. They display dual luminescence from Eu$^{III}$ and Yb$^{III}$, an interesting property despite the fact that the quantum yield of the Yb$^{III}$ luminescence

remains modest at $0.22 \pm 0.02\%$ while the $^2F_{5/2}$ lifetime amounts to $9.3 \pm 0.1$ μs at room temperature (the quantum yield of the $Eu^{III}$ luminescence is $20 \pm 2\%$).

Ytterbium luminescence has also been seen for a nonametallic cluster assembled from hexylsalicylate (hesa) and with overall formula $H_{10}[Yb_9(hesa)_{16}(\mu-O)_{10}(NO_3)]$. The cluster has two fused square-pyramidal pentametallic units assembled via an apical metal ion. The two square pyramids are twisted $45°$ and the cluster core is stabilized by hydroxide bridges. The luminescence decay of the $Yb^{III}$ cluster is bi-exponential, with lifetimes of 0.2 and 0.6 μs, reflecting the two types of cations (Manseki et al., 2006).

Polyoxometalates are important reagents in analytical chemistry and they also find applications in catalysis, molecular biology, materials sciences, and medicine. A recent study of nine $Nd^{III}$ polyoxometalates (POM) showed their aqueous 5 mM solutions to be weakly luminescent, whereas no luminescence at all is seen for the aquo ion. In particular, the bis(POM) complexes better protect the $Nd^{III}$ ion from nonradiative deactivations, for instance $\tau(^4F_{3/2}) = 411 \pm 6$ ns for $[Nd(PW_{11}O_{39})_2]^{11-}$ and $67 \pm 2$ ns for $[Nd(As_4W_{40}O_{140})]^{25-}$ (But et al., 2005).

The 1.5 μm emission line of $Er^{III}$ is useful for amplifying optical fiber signals. Its performance depends on a range of properties, stimulated emission cross section, effective bandwidth of the emission band, and fluorescence lifetime, i.e. intrinsic quantum yield. As seen previously, silica matrices in which the ion is simply doped have the disadvantage that the doping percentage must remain low to avoid concentration quenching; purely inorganic compounds are sparingly soluble in apolar solvents used to produce polymer-based devices. Organic complexes can transfer efficiently energy onto $Er^{III}$ but the presence of numerous deactivating vibrational modes, mainly the energetic O–H, N–H, or C–H vibrations, is difficult to avoid without deuterating or fluorinating the molecules at high cost, and even in these cases, the result is not always rewarding. As an alternative, J.G. Brennan has proposed cluster compounds which are soluble in organic solvents and are relatively devoid of high-energy vibrational modes, while providing a reasonable concentration of $Ln^{III}$ ions per unit volume. The most successful Ln cluster syntheses rely on chalcogenide derivatives, such as $Ln(EPh)_3$, which are oxidized by elemental E (E = S, Se, Te). Common to all the clusters is the presence of at least one ancillary, neutral ligand binding the $Ln^{III}$ ion and therefore allowing the formation of discrete architectures.

In one synthesis, metallic Er, $PhSe_2Ph$, iodine, and mercury were combined in thf at room temperature; after all the lanthanide metal had reacted, elemental sulfur was added. Pink crystals of the hexametallic $[Er_6S_6I_6(thf)_{10}]\cdot6thf$ cluster (**Er$_6$S$_6$**) crystallized out of the solution. The compound has a double cubane framework, with one face of an $Er_4S_4$ cubane cluster capped by an $Er_2S_2$ layer. Single terminal iodides are connected to all six $Er^{III}$ ions while the remaining octahedral coordination sites are occupied by thf molecules (fig. 101). When the starting Ln:$I_2$ ratio is increased from 1:0.5 to 10:3 while simultaneously replacing S with a mixture of S and Se, a yellow decametallic cluster $[Er_{10}S_6(Se_2)_6I_6(thf)_{14}]\cdot3thf$ (**Er$_{10}$S$_6$**) crystallized, in which the central $Er_6S_6$ core is capped on two opposite sides by $Er_2(Se_2)_3$ units (Kornienko et al., 2005b). The two inner $Er^{III}$ ions are therefore entirely surrounded by chalcogenide ligands (4 $S^{2-}$ and 4 $Se^-$). Absorption spectra of these two clusters in thf, as well as of $[Er(SC_6F_5)_3(dme)_2]$ (**ErS$_3$**) have been recorded and oscillator strengths calculated
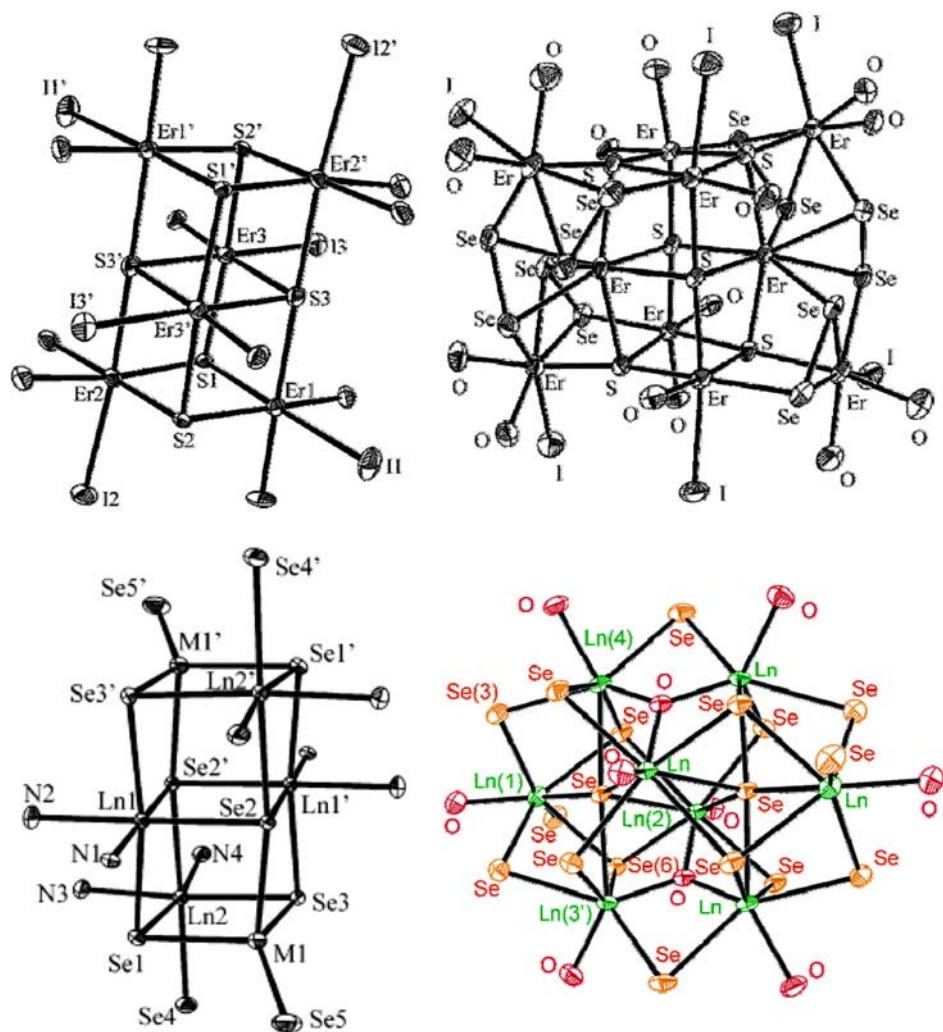
Fig. 101. (Top) Double cubane structures of the clusters [Er$_6$S$_6$I$_6$(thf)$_{10}$]·6thf (left) and [Er$_{10}$S$_6$(Se$_2$)$_6$I$_6$(thf)$_{14}$]·3thf (right). Reproduced with permission from (Kornienko et al., 2005b) ©2005 American Chemical Society. (Bottom) Double cubane structures of the cluster [Ln$_4$M$_2$Se$_6$(SePh)$_4$(py)$_8$] (left) reproduced with permission from (Kornienko et al., 2005a) ©2005 American Chemical Society, and structure of [Ln$_8$O$_2$Se$_2$(SePh)$_{16}$(thf)$_8$] (right), reproduced with permission from (Banerjee et al., 2005) ©2005 American Chemical Society.

(Kumar et al., 2005). In turn the Judd–Ofelt parameters were calculated and the radiative life-time estimated from eqs. (14)–(18). It is noteworthy that Judd–Ofelt parameters reproduce the observed spectra well. Photophysical data are listed in table 19 along with the emission cross section and the lifetime of the Er($^4$I$_{13/2}$) level. The emission spectra were obtained by exci-

Table 19
Photophysical parameters of the clusters with double cubane structure. Data are from (Kornienko et al., 2005b; Kumar et al., 2005)

| Property | $Er_6S_6$ | $Er_{10}S_6$ | $ErS_3$ | $Er:LaF_3$ |
|---|---|---|---|---|
| Ions/cm$^3$ | $8.7 \times 10^{20}$ | $3.5 \times 10^{20}$ | $1.26 \times 10^{18}$ | $22.6 \times 10^{20}$ |
| Emission cross section, $\sigma_e$ (cm$^2$) | $4.1 \times 10^{-21}$ | $1.6 \times 10^{-20}$ | $0.76 \times 10^{-20}$ | $3.3 \times 10^{-21}$ |
| Emission bandwidth, $\Delta\lambda$ (nm) | 61 | 76 | 104 | 73 |
| Radiative lifetime, $\tau_{rad}$ (ms) | 3.85 | 3.85 | 3.85 | 12.3 |
| Observed lifetime, $\tau_{obs}$ (ms) | 3.0 | 3.0 | 2.88 | 12.3 |
| Intrinsic quantum yield (%) | 78 | 78 | 75 | 100 |

tation either at 800 nm or at 980 nm (by a diode laser). All these properties are remarkable, particularly the large quantum yield, ranging between 75 and 78%, especially when compared to the corresponding data for Er-doped lanthanide trifluoride. These are the highest values reported for Er$^{III}$-containing molecular compounds and they are attributable to the absence of any O–H and C–H vibrations close to the emitting center: the second-order vibrational energy of the latter is indeed almost resonant with the energy of the $^4I_{13/2} \rightarrow {}^4I_{15/2}$ transition. In the clusters, the only C–H bonds are those of thf molecules; they are distant from the Er$^{III}$ and, moreover, the solvent molecule is only loosely bound to the metal ion. The more luminescent cluster is **Er$_{10}$S$_6$** and comparing it with **ErS$_3$**, this results from the higher ionic concentration in the unit cell. Analysis of the energy transfer between nearby Er$^{III}$ ions in **Er$_{10}$S$_6$** by Monte-Carlo simulations reveals a strong multipolar interaction between these ions; the critical separation for the dipole–dipole interaction ($R_0$) is estimated to 15.5 Å. Because the shortest and the longest separation between two metal centers in this cluster (3.9 and 10.25 Å, respectively) are both shorter than this distance, there is always a multipolar interaction between two Er$^{III}$ ions quenching part of the luminescence, which explains why the quantum yield is smaller than 100%. In fact the luminescence decay can be simulated taking into account both cooperative energy transfer up-conversion and excited state absorption (Kumar et al., 2005). It is noteworthy that the obtained photophysical properties compared very favorably with those reported for chalcogenide glasses, As$_2$O$_3$ and As$_{24}$S$_{38}$Se$_{38}$, doped with Er$^{III}$: due to their high refractive indices, the emission cross sections amount to $1.5 \times 10^{-20}$, but the lifetimes of the $^4I_{13/2}$ level is only 2.3 ms (Fick et al., 2000).

Similarly, hetero hexametallic clusters containing Ln$^{III}$ ions (Ln = Er, Yb, Lu) and group 12 M$^{II}$ divalent ions (M = Cd, Hg), [Ln$_4$M$_2$Se$_6$(SePh)$_4$(py)$_8$] (Ln = Er, Yb and M = Cd, Hg), **Ln$_4$M$_2$Se$_6$**, have been isolated (Kornienko et al., 2005a). Their structure (fig. 101, bottom left) is also derived from a double cubane framework. With respect to **Er$_{10}$S$_6$**, the emission intensity of **Ln$_4$Cd$_2$Se$_6$** and **Ln$_4$Hg$_2$Se$_6$** is 45% smaller and the observed lifetimes are shorter (1.41 and 0.71 ms, respectively). This is attributed to a lesser number of Er$^{III}$ ions per unit volume and the quenching effect of the C–H vibrations of the SePh units.

Ln$_x$E$_y$ clusters are air-sensitive, a definite obstacle in composite materials synthesis. Air-stable O-containing ligands (e.g. O$^{2-}$) could be another solution but the resulting clusters react with water to form hydroxides. Selenium oxide is an alternative soluble source of oxo ligands, giving for instance [Ln$_8$($\mu_3$-O)$_2$($\mu_5$-Se)$_2$(SePh)$_{16}$(thf)$_8$]·6thf clusters (fig. 101, bot-

tom right), in which the strong Ln–O bond does not impact negatively the $Nd^{III}$ emissive properties (Banerjee et al., 2005). On the contrary, the emission intensity of this oxoseleno cluster (upon 800-nm pumping) is larger when compared to $[Nd(SC_6F_5)_3(dme)_3]$. In particular, the transitions to $^4I_{15/2}$ (1.8 μm) and $^4I_{13/2}$ (1.35 μm) are clearly visible, the latter being relevant to the telecommunication windows. However, strong luminescence quenching still occurs in the cluster (quantum yield = 16%), again, because of interactions between $Nd^{III}$ ions and the presence of C–H vibrations in thf, dme, and SePh.

### 3.4.3. *Zeolites and composite mesoporous materials (inorganic–organic hybrids)*

This section describes systems which are at the border of what has been defined as being the scope of this review and therefore does not pretend to be comprehensive. Indeed, if there is a wealth of strictly inorganic materials and glasses into which NIR-emitting lanthanide ions have been incorporated and which are clearly excluded from the review, there also exist a continuum between these materials and molecular entities, for instance coordination polymers and clusters which have been described in the two preceding sections. In continuity with these concepts are micro- and mesoporous materials into which lanthanide salts or complexes can be incorporated or attached. These are essentially zeolites and sol–gel materials, either conventional or the so-called inorganic–organic hybrids, as well as polymers.

3.4.3.1. *Zeolites*  The zeolites are framework silicates consisting of interlocking tetrahedrons of $SiO_4$ and $AlO_4$ with a ratio (Si + Al)/O equal to 1/2. The alumino-silicate structure is negatively charged and has large vacant spaces or cages that allow space for large cations, such as alkali, alkaline-earth or lanthanide cations and even relatively large molecules such as water, ammonia, carbonate ions and nitrate ions. In the more useful zeolites, the spaces are interconnected and form long wide channels of varying sizes depending on the mineral, which allow easy movement of the guest ions and molecules into and out of the structure. Zeolites are characterized by their ability to lose and absorb water without damage to their crystal structures. The term zeolite includes natural silicate zeolites, synthetic materials, and phosphate minerals that have a zeolite like structure. The complexity of this combined group is extensive with over 120 structural variations and more are being discovered or made every year. Zeolites should be suitable host materials for NIR emitting lanthanide ions because their walls consist of Si–O–Al and Si–O–Si framework with low vibrational energies; on the other hand, their ability to host hydroxyl groups or water molecules may be detrimental to the sought after property. A series of interesting zeolites are faujasites (FAU) which have a 3-dimensional structure with pores running perpendicular to each other in the *x*, *y*, and *z* directions. The pore (supercage) entrance is large with a diameter of 7.4 Å, being defined by a 12-member oxygen ring; it leads into a larger cavity of diameter 12 Å (fig. 102) which is surrounded by smaller sodalite cages. S. Yanagida has prepared nanocrystalline faujasite containing tetramethylammonium cations ($TMA^+$) and with particles sizes 50–80 nm (n-FAU-TMA). Treatment of these particles in water containing neodymium chloride yielded a Nd-exchanged zeolite, 85–95% of the sodium ions being replaced with $Nd^{III}$ ions. The $TMA^+$ cations remain in the smaller sodalite cages and prevents lanthanide ions to penetrate into these voids. Further treatment included the replacement of the anions with bis(perfluoromethylsulfonyl)aminate
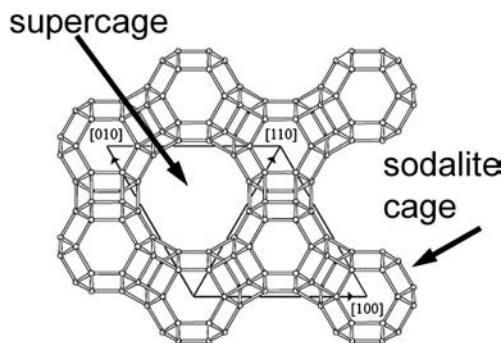
Fig. 102. Schematic representation of a Faujasite.

(pms)[8] and exposition to $D_2O$ vapor to convert O–H oscillators. The number of complexes was estimated to 1–2 per supercage and excitation of the $Nd(^2G_{7/2})$ level at 585 nm of both powdered samples and dispersions in dmso-$d_6$ resulted in characteristic $Nd^{III}$ emission. Dispersions of the doped nanocrystalline particles into dmso-$d_6$ have a high quantum yield of $9.5 \pm 1\%$, compared to 3.3% for solutions of $[Nd(pms)_3]$ in the same solvent. The former yield is the highest reported for a "molecular" neodymium compound (Ryo et al., 2004; Wada et al., 2000). The $Nd(^4F_{3/2})$ lifetime of the powdered samples depends on the $Nd^{III}$ loading level: at low level, water molecules remain coordinated to the metal ion ($\tau < 40$ μs); when more neodymium salt is inserted, the lifetime increases to 100 μs, which is assigned to anhydrous $[Nd(pms)_3]$ entities. Concentration quenching then occurs through energy migration among the $Nd^{III}$ ions, which are separated by 8 Å when two molecules are inserted into the same cage. At this distance, cross relaxation is suppressed (it is operative at distances $<4$ Å), but energy migration is still effective. This concentration quenching can be removed by diluting the $Nd^{III}$ ions with $La^{III}$ (Ryo et al., 2003). The variation of Judd–Ofelt parameters, particularly $\Omega_2$ versus the temperature treatment of the samples indicates a lowering in site symmetry when the temperature is increased from 293 to 473 K; a higher symmetry is regained at temperatures between 473 and 623 K (Ryo et al., 2002).

U. Kynast has proposed another strategy adapted from works on visible $Ln^{III}$ luminescence, in which $Ln^{III}$-loaded faujasite in absence of $TMA^+$ cations is thermally converted into sodalite (the so-called Hauyne phase) by heating at 660–1000 °C in presence of molybdate $MoO_4^{2-}$ (Ln = Eu) or tungstate $WO_4^{2-}$ (Ln = Tb). Excitation of the luminescent centers via the LMCT state (O $\rightarrow$ $W^{VI}$, 254 nm) results in high quantum yields (e.g. 55% for $[Eu_4(Al_8SAl_4O_{24})(MoO_4)_2]$). $[La_xLnYb_{3-x}(Al_8SAl_4O_{24})(WO_4)_2]$ (Ln = Ho, Er, $x = 1, 2$) samples have been prepared by the same method (Lezhnina and Kynast, 2004). Unfortunately, excitation into the LMCT band did not result in NIR luminescence. On the other hand, upconversion was observed upon excitation at 980 nm. For the $Yb^{III}/Er^{III}$ couple, twofold resonant energy transfers initially yield an excited $Er^{III}$ ion ($^4F_{7/2}$), which vibronically relaxes to $Er(^2H_{11/2})$. Subsequent emission from this state is observed at 526 nm (see fig. 103). Some

---

[8]  This anion is also designated $NTf_2$ and named bis(trifluoromethanesulfonyl)imide.
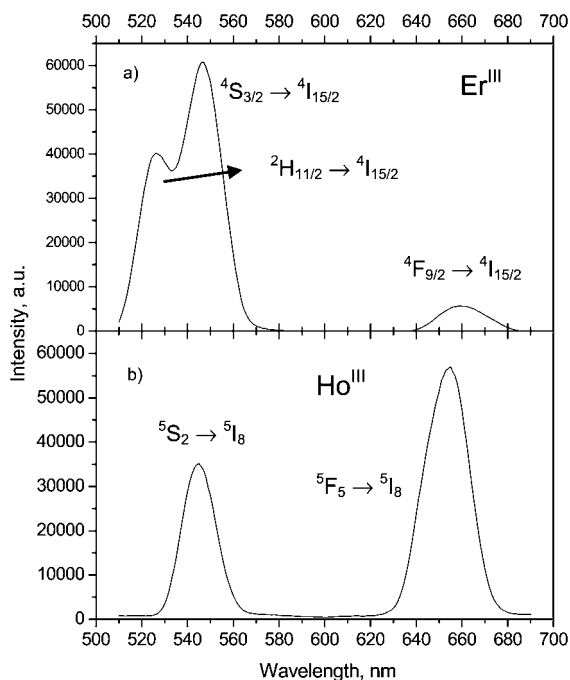
Fig. 103. Up-conversion spectra obtained under excitation at 980 nm of the Yb($^2$F$_{5/2}$) level for (a) [La$_2$ErYb-(Al$_8$SAl$_4$O$_{24}$)(WO$_4$)$_2$] and (b) [LaHoYb$_2$(Al$_8$SAl$_4$O$_{24}$)(WO$_4$)$_2$]. Reproduced from (Lezhnina and Kynast, 2004). © 2004 with permission from Elsevier

of the energy is transferred onto the green emitting $^4$S$_{3/2}$ state (548 nm, most intense band in the up-conversion spectrum) while further relaxation ends to the red-emitting state $^4$F$_{9/2}$ (648 nm). In the corresponding Ho$^{III}$ sodalite, excitation of Yb($^2$F$_{5/2}$) at 980 nm is followed by a transfer onto Ho($^5$I$_6$) which, in turn, populates the luminescent Ho($^5$S$_2$) state emitting at 544 ($^5$S$_2 \rightarrow {}^5$I$_8$) and 654 ($^5$F$_5 \rightarrow {}^5$I$_8$) nm. The internal relaxation $^5$S$_2 \rightarrow {}^5$F$_5$ is quite efficient, as proved by the larger intensity of the red emission when compared to the green one.

Similar up-conversion also takes place for fluoride complexes inserted in zeolites and luminescence from Nd$^{III}$ occurs for [La$_2$Nd$_x$Gd$_{2-x}$(Al$_8$SAl$_4$O$_{24}$)(WO$_4$)$_2$] or [La$_{4-x}$Nd$_x$ (Al$_8$SAl$_4$O$_{24}$)(WO$_4$)$_2$] sodalites upon pulsed diode laser excitation at 803 nm. The optimum content of neodymium maximizing the 1.06 μm emission in the second material is 0.2 Nd$^{III}$ ion per unit cell (Lezhnina et al., 2006; Lezhnina and Kynast, 2005).

3.4.3.2. *Simple silica matrices* To further illustrate the limit of this chapter, we briefly discuss one type of materials that will not be systematically reviewed: layered lanthanide silicates obtained by hydrothermal synthesis. An alkaline solution of sodium silicate and lanthanide chlorides was stirred to produce a gel which was subsequently put into an autoclave under pressure at 230 °C during seven days, a procedure during which lamellar photoluminescent silicates

form, $K_3[Ln'_{1-a}Ln_a Si_3O_8(OH)_2]$ ($Ln' =$ Y, Eu, Gd, Tb, Er; Ln = Eu, Gd, Tb, Er), which are denoted Ln-AV-22. The materials contain crystallographically unique $LnO_6$ centers with slightly distorted octahedral geometry and connected to six $SiO_4$ tetrahedra. The photoluminescence spectra of homometallic Er-AV-22 at 300 and 75 K display well resolved ligand-field split emission bands. Interestingly, the integrated intensity increases with increasing temperature, particularly above 225 K, for a 2.7-fold total increase between 75 and 300 K, due to redistribution of population between the Stark levels of the fundamental multiplet (Ananias et al., 2004).

Attempts to incorporate relatively large lanthanide complexes in silica matrix by sol–gel procedure have also been successful. For instance, neodymium tris(dipicolinate), $Na_3[Nd(dpa)]_3$), has been encapsulated into a silicate sol–gel monolith at room temperature. The $Nd^{III}$ ions are shielded from hydroxyl interaction by the dipicolinate anions. The emission of the doped gels exhibit inhomogeneous broadening typical of metal ions in a disordered environment and the longest lifetime recorded is around 3 μs (Lai et al., 1996). Other examples are erbium (Clark et al., 1999) and neodymium (Cervantes et al., 2002) tetraphenylporphyrinates, [Ln(TPP)(acac)], which have been introduced in a tetraethylorthosilicate matrix with, as a result, the production of gels having high optical quality. They present both visible and near IR emission and the bandwidth of the erbium emission is five- to six-fold narrower in the gel when compared to solutions or to silica glasses. Dibenzoylmethanate ternary complexes with phenanthroline, [Ln(dbm)$_3$phen], Ln = Nd, Yb, have been introduced in the same matrix by an in situ sol–gel synthesis with the aim of designing laser materials (Sun et al., 2005). A Judd–Ofelt analysis of the radiative properties performed on the $Nd^{III}$-containing material revealed that the stimulated emission cross section of the $^4F_{3/2} \rightarrow ^4I_{11/2}$ transition (1.06 μm) amounts to $1.4 \times 10^{-20}$ cm$^2$, a value comparable to those found in glasses, while its radiative lifetime is 0.52 ms, making this transition a potential candidate for laser action.

Sol–gel chemistry leads to inorganic polymerization reactions and offers a possibility of controlling both the micro- and macro-structures of the host matrix. It presents great potential for manufacturing low cost optical devices because large areas can be covered with good homogeneity and surface planarity. A common synthetic method is the hydrolysis of a silane derivative, such as diethoxymethylsilane, [SiH(OEt)$_2$(CH$_3$)] referred to as DEMS, in presence of a metal alkoxide. This leads to the formation of a siloxane network with concomitant evolution of hydrogen gas as a result of the cleavage of Si–H bonds. The advantage of the method is that the synthesis is performed at lower temperature compared with conventional chemical reactions and therefore organic components can be inserted in the oxide gel matrix without decomposition. It is particularly well suited when coatings or thin films are needed. In an early study on luminescent coatings, sols were prepared by reacting DEMS in ethanol with $Zr(OPr^n)_4$ and a lanthanide methoxyethoxide (Ln = Nd, Sm, Dy, Er, Tm), generating Zr–Ln-containing particles embedded in the siloxane structure (fig. 104). Thin layers of 50–100 μm were then deposited on a glass plate, and all of the coatings presented photoluminescence, including those containing the NIR emitting $Nd^{III}$ and $Er^{III}$ ions (Koslova et al., 1993). In the case of $Nd^{III}$ both the absorption and emission spectra were analyzed in details in terms of Judd–Ofelt theory and the Nd($^4F_{3/2}$) lifetime was shown to decrease from 160 μs for $4 \times 10^{19}$ ions cm$^{-3}$ (quantum yield estimated from the lifetimes was 35%)
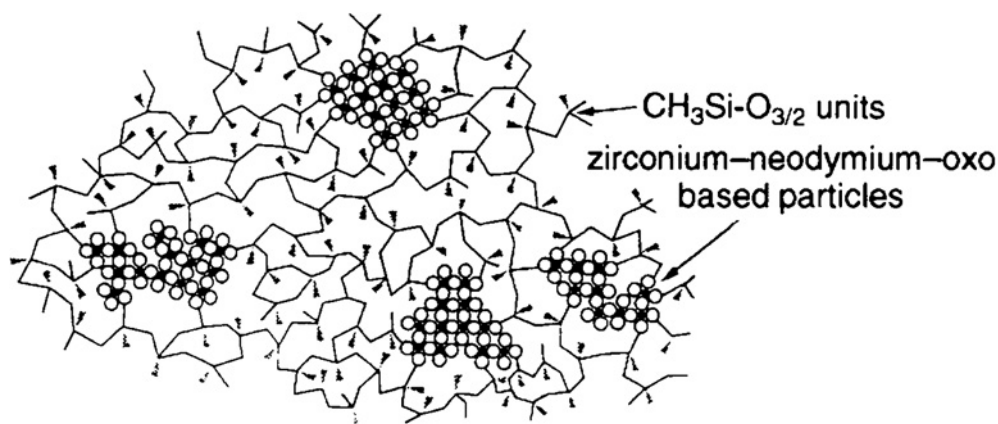
Fig. 104. Schematic structure of hybrid siloxane–metal oxide materials. From (Viana et al., 1995), reproduced with permission from the Royal Society of Chemistry.

to 0.2 µs for a concentration of $4 \times 10^{21}$ ions cm$^{-3}$ (quantum yield $< 0.01\%$) in view of cross-relaxation processes; in addition, the Nd$^{III}$ ions are well encapsulated inside the Zr-oxo core at low concentrations and are therefore far from the surface and protected from interactions with the residual hydroxy groups (Viana et al., 1995). Co-doping the Nd$^{III}$-containing particles with rhodamine 6G which emits a broad band centered at 570 nm, results in energy transfer from the latter to the 4f ion. The process is however not efficient because rhodamine 6G is hydrophobic and interacts with the methyl groups of the siloxane polymer, so that the dye molecules lie too far away from the acceptor ion.

Despite the inherent advantages of the sol–gel procedure no commercial waveguides based on this technology are available at the time of the writing of this review, despite numerous attempts made around the world. Two reasons can be invoked, the layer thickness (1–2 µm is needed) and the difficulty in handling large volumes of solution at the industrial scale. The first issue is not easy to address because 25–35 successive coatings are necessary to reach the desired thickness and mechanical problems can arise during the process. In order to obtain crack-free thick films, an improved method has been proposed in which the films are obtained by dispersion of silica–hafnia nanoparticles into a binder solution, spin-coating followed by thermal treatment. The hafnia nanoparticles allow a control of the refractive index. The resulting films present good optical quality and the required thickness for a fiber matching single mode waveguide. Thick films obtained by this method and doped with 0.3 mol% erbium and 0.7 mol% ytterbium (as sensitizer) support two transversal electric modes at 1.55 µm and possess low birefringence, as indicated by the very small difference between the transversal electric and magnetic modes, with corresponding refractive indices equal to 1.4730 and 1.4735, respectively. The ligand-field splitting reflected in the Er($^4I_{13/2} \rightarrow {}^4I_{15/2}$) transition is typical of a cubic environment for the metal ion, henceforth indicating the presence of erbium in the cubic phase of HfO$_2$ nanoparticles. Up-conversion of the Er($^4F_{3/2} \rightarrow {}^4I_{15/2}$) transition has been obtained upon continuous wave excitation at 980 nm (Sigoli et al., 2006).
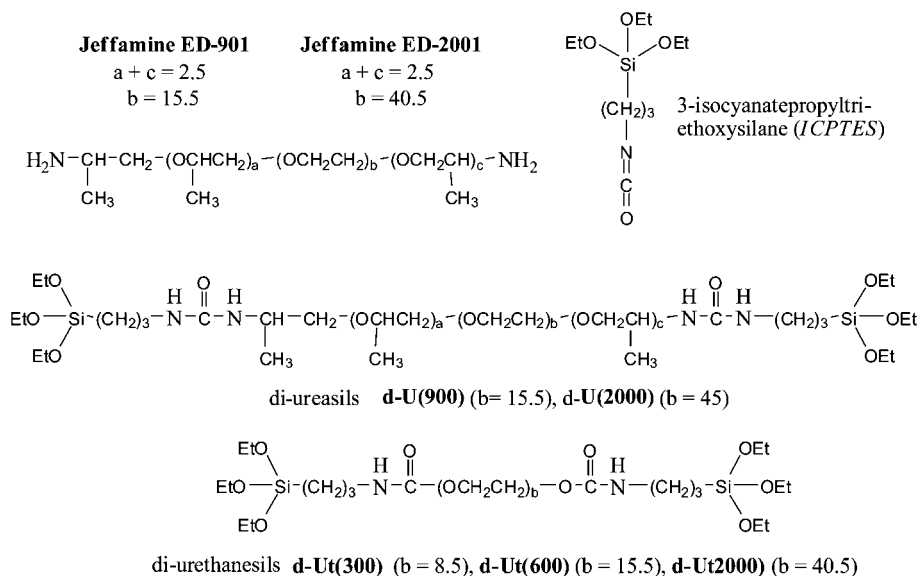
Fig. 105. Some components and precursors of di-ureasil inorganic–organic hybrids.

Silica-polyethyleneglycol (PEG) hybrids present an increased solubility for lanthanide complexes. In view of the large ability of dipicolinate (dpa) and calcein, $4',5'$-bis-$[N,N$-bis(carboxymethyl)aminomethyl]fluorescein ($H_4$**73a**, fig. 64), to sensitize the NIR luminescence of lanthanide ions, the corresponding complexes $[Ln(dpa)_3]^{3-}$ and $[Ln(calcein)]^{2-}$ (Ln = Pr, Nd, Sm, Dy, Er, Ho, Yb) have been doped in a matrix prepared from tetramethylorthosilicate and PEG-200 (Driesen et al., 2004b). Intense $Yb^{III}$ luminescence was observed for both complexes, while only calcein sensitized $Nd^{III}$ and $Er^{III}$ luminescence to an acceptable extent, especially when the gel was dried. Indeed, the produced gels contain unreacted silanol groups as well as water molecules which reduce strongly the NIR emission and shorten the lifetime. The lifetime of the $Nd(^4F_{3/2})$ level is $139 \pm 4$ ns ($280 \pm 4$ ns after drying the gel), as compared to 250 ns for the same complex in water. For the calcein complex, the lifetime of the $Yb(^2F_{5/2})$ level is $1.83 \pm 0.02$ µs ($3.72 \pm 0.02$ µs after drying), as compared to 1.9 µs in water.

3.4.3.3. *Xerogels: ureasilicates and urethanesilicates* One class of investigated compounds in the development of polymeric electrolytes for various types of electrochemical devices (fuel cells, rechargeable batteries, solar cells, for instance) are ureasilicates, also termed di-ureasils, di-urethanesils, or ormosils. They possess good mechanical and thermal stability in addition to being optically transparent. In these materials, urea (or urethane) bridges are used to graft diamines containing oxyethylene segments of two different molecular weights onto a silica network (fig. 105). The preparation of lanthanide-doped materials goes through the reaction of 3-isocyanatepropyltriethoxysilane with a diamine, $\alpha,\omega$-diaminepoly(oxyethylene-co-oxypropylene), commercially designated as Jeffamine ED-Y (Y = 901 or 2001, for in-

Table 20

Lifetimes (ms, at 14 K) of the di-ureasils emitting centers and efficiency (%) of the energy transfer to the $Nd^{III}$ ion in **d-U(Y)$_n$Nd(Otf)$_3$** xerogels; percentages within parentheses indicate the $Nd^{III}$ content with respect to the total mass
(Sa Ferreira et al., 2003)

| | U(900)$_n$Nd(Otf)$_3$ | | | | U(2000)$_n$Nd(Otf)$_3$ | | | |
|---|---|---|---|---|---|---|---|---|
| | $n = \infty$ | $n = 100$ (1.5%) | $n = 60$ (2.4%) | $n = 40$ (3.4%) | $n = \infty$ | $n = 100$ (2.1%) | $n = 60$ (3.4%) | $n = 40$ (4.7%) |
| $\tau_{NH}$ | $122 \pm 7$ | $103 \pm 12$ | $38 \pm 5$ | $21 \pm 7$ | $160 \pm 7$ | $98 \pm 9$ | $79 \pm 5$ | $49 \pm 4$ |
| $\tau_{Si}$ | $3.7 \pm 0.4$ | $3.1 \pm 0.2$ | $3.2 \pm 0.1$ | $2.8 \pm 0.2$ | $3.6 \pm 0.1$ | $2.1 \pm 0.4$ | $0.9 \pm 0.3$ | $0.5 \pm 0.1$ |
| $\eta_{NH}$ | – | 16 | 69 | 83 | – | 39 | 51 | 70 |
| $\eta_{Si}$ | – | 5 | 8 | 35 | – | 40 | 74 | 86 |

stance) in thf, to yield ureapropyltriethoxysilane or urethanepropyltriethoxysilane precursors. A lanthanide salt LnX$_3$ (usually a triflate) dissolved in ethanol/water is then added to the solution of the precursor. Slow evaporation of the solvent results in gelation and after drying and aging for a sufficient time (3–4 weeks), a rigid and brittle elastomeric film is obtained, which is called a xerogel. The designation codes for the materials are as follows: **d-U(Y)$_n$LnX$_3$** or **d-Ut(Y)$_n$LnX$_3$** where **d-U** and **d-Ut** stand for di-ureasil and di-urethanesil, respectively, **Y** depends on the stoichiometric coefficient b (see fig. 105) and indirectly indicates the length of the oxyethylene chains, and $n$ = O/Ln represents the ratio of (O–CH$_2$–CH$_2$–) monomers units per Ln ion (Bermudez et al., 1998).

The undoped xerogels are luminescent by themselves. For instance, **d-U(2000)** emits a blue-green band with a maximum around 540 nm, but extending from 375 to 630 nm, upon excitation at 460 nm. The luminescence originates both from the urea moiety (NH-emission, due to photoinduced proton transfer between NH$_2^+$ and N$^-$ defects) and from electron–hole recombinations in the inorganic siliceous backbone. When neodymium triflate is doped into the material (with $n$ = 100, 60, 40, and 20) dips appear in this emission band, which correspond to absorptions from the $Nd^{III}$ ion. As a result, Nd($^4F_{3/2}$) emission is detected in the NIR range, the intensity of which shows an intricate dependence upon $Nd^{III}$ concentration and temperature (Carlos et al., 2000). The lifetimes of the di-ureasil emitting centers and the efficiency of the energy transfer between them and $Nd^{III}$, calculated according to eq. (4a), have been determined for a series of **d-U(Y)$_n$Nd(Otf)$_3$** xerogels (**Y** = 900, 2000, $n$ = 40, 60, 100, and $\infty$). They are reported in table 20. The efficiency of the two energy transfer processes increases with the concentration of incorporated $Nd^{III}$ ions for both host materials. At the doping concentration tested, no or little concentration quenching occurs (Sa Ferreira et al., 2003).

Room-temperature NIR emission has also been reported for the di-urethanesils **Ut(600)$_3$-Er(Otf)$_3$** and **Ut(900)$_n$Nd(Otf)$_3$** ($n$ = 80, 60), indicating that this hybrid framework protects the lanthanide ions from nonradiative deactivation processes equally efficiently when compared with the di-ureasils (Carlos et al., 2004). In fact, the most noticeable difference between the $Nd^{III}$-doped di-ureasils and di-urethanesils is the energy difference between the undoped host and the doped hybrids which, in the case of **Ut(600)$_n$**, for instance, is concentration dependent (Gonçalves et al., 2005).

Ormosil spin-coated thin films obtained from vinyltriethoxysilane and doped with $\beta$-diketonates have been recently investigated by H. Wang and collaborators. Both hydrated chelates and ternary complexes with phen and tppo were doped at a concentration of 5 mol% (relative to Si) by a multi step sol–gel method. Out of the 12 compounds tested, [Nd(tta)$_3$(tppo)$_2$] yielded the best results but no quantitative luminescence data are given, preventing comparison with materials of known properties (Wang et al., 2005).

3.4.3.4. *Covalently-linked luminescent hybrid materials* Hybrid materials combine inorganic, organic, and even biochemical properties in a tailored matrix. They possess inorganic pores with adjustable size and their surface can be modified by organic or bio-active functions. The possibility of processing mesoporous hybrid materials into thin films adds to their applicability, especially when optical devices are targeted. The chemical synthesis of hybrid materials implies essentially a combination between sol–gel chemistry of the inorganic precursors (alkoxide or inorganic salts, for instance) and the self-assembly features of the organic pore templates, e.g. surfactants (Soler-Illia and Innocenzi, 2006).

One of the problems with the previously described systems is the presence of either water molecules or hydroxyl groups which can induce de-complexation of the doping complexes. Moreover, the lanthanide-containing compounds are only bonded to the matrix through weak interactions (van der Waals forces, hydrogen bonds or weak electrostatic effects, for instance), which gives little control over the clustering of emitting centers and leads to inhomogeneous dispersion, itself a cause of leaching of the photoactive centers in the material. A strategy to overcome these difficulties consists in attaching a coordinating group onto the porous framework which simultaneously acts as a sensitizer. Several such examples deal with ternary complexes of lanthanide $\beta$-diketonates (fig. 106). In one example, the glass matrix was prepared by first reacting 5-amino-1,10-phenanthroline with 3-(triethoxysilyl) propyl isocyanate. The resulting compound, tetramethoxysilane (TMOS) and diethoxydimethylsilane (DEDMS) were hydrolyzed and condensed at a neutral pH to a sol–gel glass. A tris(2-thenoyltrifluoroacetonato) europium(III) dihydrate complex was then covalently attached to the phen groups on the silica gel (fig. 106a). The sol–gel glass doped with Sm$^{III}$ shows luminescence both in the visible ($^4G_{5/2} \rightarrow {}^6H_J$, $J = 5/2$–9/2) and in the near-infrared range ($^4G_{5/2} \rightarrow {}^6H_{15/2}$, $^6F_{5/2-9/2}$ transitions), with a lifetime of 65 µs. Luminescence from the other NIR-emitting ions could also be detected: Nd$^{III}$, lifetime of $^4F_{3/2} = 0.26$ µs, Er$^{III}$, lifetime of $^4I_{13/2} = 0.99$ µs, and Yb$^{III}$, lifetime of $^2F_{5/2} = 13$ µs after drying the sample (Lenaerts et al., 2005b). In order to simplify the cumbersome synthesis of the 1,10-phenanthroline-derivatized matrix, the same authors have resorted to a 2-substituted imidazo[4,5-f]1,10-phenanthroline linking group (fig. 106b), which allowed them to detect NIR luminescence from Nd$^{III}$ ($^4F_{3/2} \rightarrow {}^4I_{9/2-13/2}$, lifetime = 0.32 µs), Sm$^{III}$ ($^4G_{5/2} \rightarrow {}^6H_{15/2}$, $^6F_{5/2-9/2}$ lifetime = 40 µs), Ho$^{III}$ ($^5S_2 \rightarrow {}^5I_6$, 975 and 1020 nm), Er$^{III}$ ($^4I_{13/2} \rightarrow {}^4I_{15/2}$, lifetime = 0.95 µs), and Yb$^{III}$ ($^2F_{5/2} \rightarrow {}^2F_{7/2}$, lifetime = 12 µs) at room temperature and from Pr$^{III}$ ($^1D_2 \rightarrow {}^3F_4$, 1.03 µm) at 77 K. Emission from the Ho$^{III}$ compound was too weak to measure the lifetime. Thin films were produced by spin-coating and displayed more intense luminescence than the bulk materials: the Er($^4I_{13/2}$) lifetime could be determined as being 1 µs (Lenaerts et al., 2005c). The same $\beta$-diketonates were covalently attached to a cross-linked chloromethylated polystyrene (Mer-
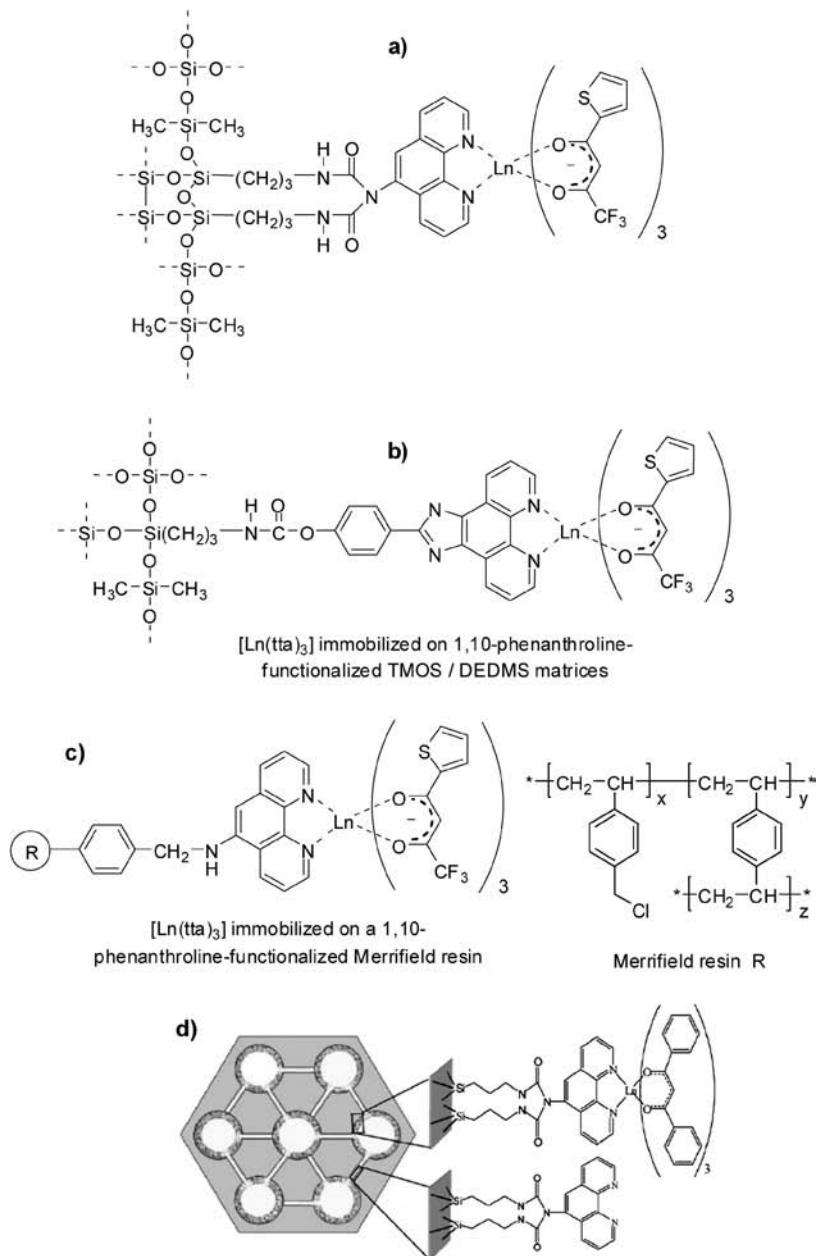
Fig. 106. Immobilized $\beta$-diketonate complexes in mesoporous materials. Part (d) is reproduced with permission from (Sun et al., 2006).
© 2006 American Chemical Society
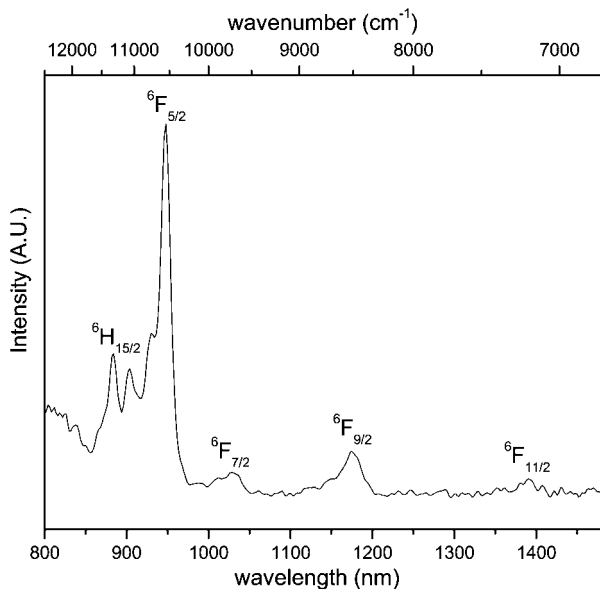
Fig. 107. NIR region of the photoluminescence spectrum ($\lambda_{exc}$ = 370 nm) of [Sm(tta)$_3$] immobilized on a phen-derivatized Merrifield resin (fig. 106c). Reproduced with permission from (Lenaerts et al., 2005a).
© 2005 American Chemical Society

rifield resin) through a 1,10-phenanthroline linker (fig. 106, bottom) and again, NIR emission could be detected at room temperature from Nd$^{III}$, Sm$^{III}$ (fig. 107), Er$^{III}$, and Yb$^{III}$ with lifetimes longer than the previous ones: 0.4, 70, 1.4, and 10 μs, respectively (Lenaerts et al., 2005a).

Mesoporous materials similar to the one described in fig. 106a, but possessing a hexagonally-ordered silicate structure, have been described in 1992 (Kresge et al., 1992). A typical example is MCM-41 which is obtained by reacting the surfactants hexadecyltrimethylammonium hydroxide with tetramethylammonium silicate in presence of alumina and precipitated silica at 150 °C during 2 days, followed by calcination at 540 °C. The resulting material shows regular hexagonal arrays of uniform channels similar to the arrangement found in lyotropic liquid crystals. Its pores have a diameter of about 40 Å, that is, much larger than those found in zeolites, and can be tuned by varying the size of the surfactant alkyl chain. The MCM-41 material has been functionalized by 1,10-phenanthroline units in order to bind lanthanide $\beta$-diketonates and the resulting compounds are written [Ln(dbm)$_3$phen-MCM-41$_{XY}$] with $X$ denoting the Ln$^{III}$/phen-MCM-41 molar ratio and $Y$ the reaction time (in hours) for the complexation to the mesoporous material; $X$ = 12 and $Y$ = 6 proved to be optimum (Sun et al., 2006). A similar functionalization has been performed on a related material, SBA-15, obtained from alkyl poly(ethylene oxide) oligomeric surfactants and poly(alkylene oxide) block copolymers (Zhao et al., 1998), yielding [Ln(dbm)$_3$phen-SBA-15] compounds. The excitation spectra of Er$^{III}$-doped materials are very similar and extend from 250 to 450 nm; they

are narrower than for the parent $\beta$-diketonate and blue shifted, due to the change in polarity in the mesoporous materials. The $^4I_{13/2} \rightarrow {}^4I_{15/2}$ transitions are broad with a full width at half height (fwhh) equal to 76 and 72 nm for MCM-41 and SBA-15, respectively, enabling wide gain bandwidth for optical amplification. The Nd$^{III}$- and Yb$^{III}$-doped materials present the same excitation spectra. The [Ln(dbm)$_3$phen-SBA-15] materials which have a lower lanthanide ion content present slightly longer lifetimes of the NIR luminescence (0.28 vs 0.23 μs for Nd$^{III}$, 2.40 vs 2.29 μs for Er$^{III}$, and 12.3 vs 12.1 μs for Yb$^{III}$) and higher emission intensity per lanthanide ion (factor 9.6, 7, and 3.9 for Nd$^{III}$, Er$^{III}$, and Yb$^{III}$, respectively) than the corresponding [Ln(dbm)$_3$phen-MCM-41], probably in view of the larger number of residual surface silanol groups in the latter (Sun et al., 2006).

### 3.4.4. *Microspheres and nanoparticles*

Silica-based glasses doped with lanthanide ions are optically active materials widely used for photonic applications. As mentioned previously, their properties are however limited, for instance, by concentration quenching, and several alternative solutions are being investigated, including the materials described in the preceding section. One of these solutions is the synthesis of nanoscale particles doped with Ln$^{III}$ luminescent centers. The main advantage of such an approach is that physical and electronic properties of the particles can be modulated by varying their size and shape, a definite plus for the design of microlasers, thin-film devices or active photonic band-gap materials, or luminescent nanosensors. Moreover, this approach opens the way for the use of luminescent inorganic compounds in organic environment since most of the nanoparticles can be dispersed in apolar organic solvents and/or in polymers. As for the previous section, description of nanoparticle-based NIR luminescent materials is not intended to be comprehensive since the field is at the border of the matter covered in this chapter. Selected examples will be presented, highlighting their fundamental aspects, while a more detail account can be found in another chapter of this volume (Liu and Chen, 2007). The substrates used in the various studies range from simple silica microspheres to lanthanide fluorides, phosphates, oxides, borates, vanadates, and titanium oxide. They will be described in this order. The parameters influencing the optical properties are the size and size distribution of the particles, the doping rate of the luminescent centers, as well as the presence of a co-dopant. As far as excitation mode is concerned the nanoparticles described up to now fall into two classes: those for which direct 4f–4f excitation is required and those for which excitation makes use of a sensitization process involving TiO$_2$ or vanadate (e.g. LaVO$_4$).

Control of the particle size is critical and heavily depends on the preparation method. Sonochemistry has been tried, for instance for the reaction of lanthanide nitrates with tetraethyl orthosilicate (TEOS), but a large fraction of the nanoparticles agglomerated in clusters with irregular shapes and sizes, while the doping density could not be controlled satisfyingly. Despite this somewhat deceptive result, silica (and alumina) particles doped with Eu$^{III}$ and Tb$^{III}$ displayed emission intensities comparable to those of the commercial phosphors (Patra et al., 1999). Ion implantation is an alternative, but only a few particles can be doped at one time and the level of doping is not homogeneous. Therefore chemical methods were tested which proceed either by base- or by acid-catalyzed growth of silica particles. In fact, base-catalyzed growth is inadequate because of the easy formation of lanthanide hydroxides. On the other

hand, the acid-catalyzed method proved to be quite successful. First, 0.5–2% of $LnCl_3 \cdot 6H_2O$ are dissolved into an aqueous solution of acetic acid and TEOS is rapidly added; after initial stirring during a few seconds, the solution is left reacting for half an hour and the doped nanoparticles sediment and are separated by centrifugation. To eliminate unreacted TEOS, the particles are re-dispersed several times in ethanol before being thermally treated to 750 °C; this treatment not only eliminates solvents and acetate groups, but it also promotes more complete condensation of the surface and interior silanol groups, which should reduce the luminescence quenching by O–H vibrations. On the other hand, the treatment leaves enough hydroxyl groups on the surface to maintain the hydrophilic nature of the particles and to allow for future surface functionalization (e.g. surface coating by alkoxysilanes). In absence of lanthanide dopant, most of the particles (up to 85%) are "necked", whereas spherical, discrete particles are obtained in presence of the lanthanide salt. For a given ratio TEOS: acetic acid: water, usually in the range 1:(4–8):(1.5–5), the polydispersity of the particles is controlled by the concentration of the lanthanide salts and the reaction time. At a concentration of 1% $LnCl_3 \cdot 6H_2O$ a sample of doped microparticles with an average size of 2.8 μm and a standard deviation of less than 10% was isolated after only 5 min. In fact, if the reaction is stopped after the nucleation and growth of the first generation of nuclei, more monodisperse (or, better, uniform) samples can be obtained. The resulting Ln-doped (Ln = Pr, Er) samples were highly luminescent, with emission from $^1D_2$ and $^3P_0$ for $Pr^{III}$ and from $^4I_{13/2}$ in the NIR for $Er^{III}$ (Moran et al., 2001). The same synthetic route has been used by M.J.A. de Dood for producing monodisperse Er-doped colloidal silica microspheres. In addition, a seeded growth process is described in which a thin shell of Er-doped silica is grown on existing monodisperse silica colloids (de Dood et al., 2002). The luminescence decay of the annealed particles is a single exponential function and the associated lifetime amounts to 13.2 ms which corresponds to an estimated intrinsic quantum yield of ≈70%.

Lanthanide trifluoride has very low vibrational energies, with the highest phonon energy around 350 $cm^{-1}$, and is thus an ideal host for the study of lanthanide spectroscopy, particularly erbium (Hüfner, 1978; Weber, 1967a; Weber, 1967b). The $LaF_3$ nanoparticles are prepared by heating a solution of ammonium di-*n*-octadecyldithiophosphate with NaF in ethanol/water and adding a solution of lanthanum nitrate and of the desired lanthanide nitrate. After centrifugation and re-dispersion in dichloromethane for purification purposes, the particles with diameter between 5 and 10 nm are simply dried in vacuum for two days. They can be dispersed in apolar solvent such as chloroform, dichloromethane, or toluene. Near-infrared emission was observed for the dispersed particles doped with 5% of $Ln^{III}$: for $Nd^{III}$, upon excitation at 514 nm, the luminescence decay is bi-exponential corresponding to lifetimes of the $^4F_{3/2}$ level equal to 240 and 40 μs; for $Ho^{III}$, under excitation at 448 nm, both $^5F_5 \rightarrow {}^5I_7$ (966 nm) and $^5F_5 \rightarrow {}^5I_6$ (1.46 μm) transitions are observed (lifetimes: 340 and 30 μs); for $Er^{III}$, upon excitation at 488 nm, the emission at 1.53 μm shows a wide bandwidth, but the decay is a single exponential function corresponding to a lifetime of 220 μs. The authors explain the occurrence of two lifetimes by the presence of luminescent ions in the center and at the surface of the nanoparticles; a possible explanation for observing only one lifetime in the case of erbium is that the metal ions are located closer to the surface due to a stronger ligand–$Er^{III}$ interaction (Stouwdam and Van Veggel, 2002). Using $Eu^{III}$ as structural local
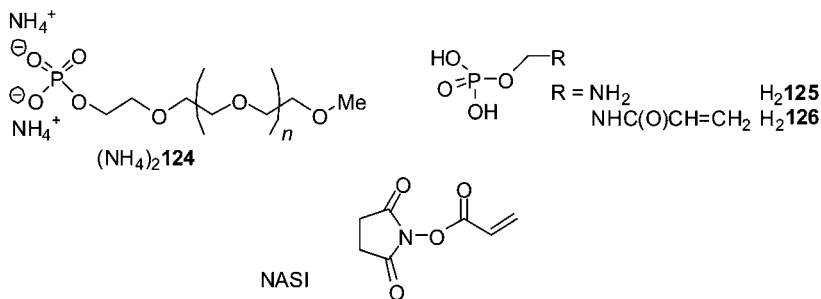
Fig. 108. Ligands used for the formation of Ln$^{III}$-doped LaF$_3$ nanoparticles.

probe, the site symmetry of the dopant ion has been established to be $C_2$ and the luminescence decays were calculated theoretically with a shell model considering the quenching at the surface by the solvent (10 shells were taken into account) and which reproduced correctly the longer lifetime of the core–shell nanoparticles (Stouwdam et al., 2003). Further improvement of the photophysical properties, particularly of Er$^{III}$, could be obtained by preparing, by sol–gel technique, thin films with Ln$^{III}$-doped LaF$_3$ nanoparticles stabilized by citrate. Lifetimes of the Er($^4$I$_{13/2}$) level up to 10.9 ms could be obtained (Sudarsan et al., 2005), indicating the absence of clustering of the Er$^{III}$ ions. This value is close to the 17 ms lifetime measured for Er$^{III}$ in ion-implanted (350 keV) silica colloidal particles with a size of 240–360 nm and for which the intrinsic quantum yield was estimated to be around 80% based on a radiative lifetime of 20–22 ms (Slooff et al., 2000a).

  In view of potential applications as biolabels, F.C.J.M. van Veggel and collaborators have prepared six types of water-soluble, highly luminescent Ln$^{III}$-doped (5 mol%, Ln = Eu, Er) LaF$_3$ nanoparticles from one-pot syntheses using the ligands reported in the upper part of fig. 108 (Diamente and Van Veggel, 2005). The phosphate monoester group limits the size of the nanoparticles to <20 nm in view of the electrostatic repulsion generated by the doubly charged anion, while the PEG substituent in **124** is intended for covalently attaching the nanoparticles to biological macromolecules. In addition to the hydrophilic nature of PEG, rendering the nanoparticles water soluble, this group suppresses antigenic and immunogenic epitopes, preventing recognition and degradation of the nanoparticles by proteolytic enzymes. Ligand H$_2$**125** was tested to demonstrate that with an amine-terminated ligand, the nanoparticles can be modified at their surface, for instance with N-acryloxysuccinimide (NASI) while retaining their photophysical properties. The optical properties of the PEG-based nanoparticles in water were investigated using Eu$^{III}$ as a spectroscopic probe and according to luminescence decay analysis three different metal ion environments (core and surface) are present; one with a long lifetime (2.7 ms) corresponds to the luminescent centers embedded in the particle cores while the other two arise from surface-located Eu$^{III}$ ions ($\tau$ = 0.6 and 0.2 ms). For Er$^{III}$, NIR luminescence is only seen in deuterated water and the corresponding decay is also tri-exponential, with the longer lifetime equal to 50 μs, indicating still significant quenching (compare $\tau_{rad} \approx$ 20 ms). Nanoparticles grown with H$_2$**125** have bi-exponential luminescence decay with longer lifetimes, 118 and 17 μs. When these nanoparticles are reacted with NASI,

their solubility in water decreases due to the presence of vinyl groups, but the overall photo-physical properties are maintained.

Although lanthanum phosphate possesses higher energy phonons ($\approx$1050 cm$^{-1}$) than lan-thanide fluoride it is also a convenient medium for preparing Ln-doped nanoparticles, starting from tris(2-ethylhexyl)phosphate and following a procedure similar to that used for the flu-oride nanoparticles. Some transitions not seen in the fluoride materials could be recorded in the phosphate medium, possibly because the metal ion sites have lower symmetry, $C_1$ (Stouwdam et al., 2003). This is the case of the 980-nm emission from erbium ($^4I_{11/2} \rightarrow {}^4I_{15/2}$) and of Pr$^{III}$ emission not observed in the fluoride particles upon excitation at 476 nm. For the latter, transitions from the $^1D_2$ level to the $^3F_J$ manifold ($J$ = 2, 3, and 4, in the range 800–1100 nm) and to the $^1G_4$ level (1.4–1.55 μm) were identified; incorporation of LnPO$_4$:Ln nanoparticles in poly(methylmethacrylate) is feasible and the photophysical prop-erties are retained (Hebbink et al., 2002b). Similarly, the LaPO$_4$ nanoparticles can be incor-porated into 3-(trimethoxysilyl)propyl methacrylate (Jung et al., 2005). On the other hand, Ho$^{III}$ emission could not be observed in LaPO$_4$ particles, contrary to the fluoride medium while co-doping Yb$^{III}$ and Er$^{III}$ led to increased erbium emission in both materials in view of the energy transfer process discussed previously (Jung et al., 2005; Lehmann et al., 2003; Stouwdam et al., 2003).

Since oxide materials are extensively used in practical devices such as lamp phosphors or laser materials, their behavior at the nanoscale level has also been investigated. The size of yttrium oxide nanoparticles Y$_2$O$_3$:Ln can be finely tuned by glycine-nitrate combustion synthesis. The overall equation of the exothermic reaction can be expressed as:

$$6\,Ln(NO_3)_3 + 10\,NH_2CH_2CO_2H + 18\,O_2 \rightarrow 3\,Ln_2O_3 + 5\,N_2 + 18\,NO_2$$
$$+ 20\,CO_2 + 25\,H_2O. \tag{39}$$
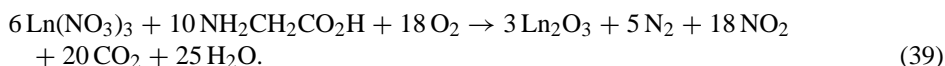
Combustion of the lanthanide nitrate and glycine spontaneously starts at 240 °C and the re-sulting voluminous powder is annealed at 600 °C. The particle size depends on the annealing temperature and time, as well as on the glycine/Ln(NO$_3$)$_3$ ratio and can be tuned accordingly between 15 and 70 nm, the smallest particles being the most luminescent. Thin films of these particles inserted into PMMA polymer matrix obtained by spin-coating have been produced and the authors showed that the optimal parameters with respect to integrated emission inten-sity are a concentration of 1 mol% of Er$^{III}$ (to minimize ESA) and co-dopant concentrations of 1 mol% Ce$^{III}$ or 5 mol% Yb$^{III}$ (see fig. 8). The net gain of the PMMA/Er:Yb:Y$_2$O$_3$ system reaches 30 dB cm$^{-1}$ for a pump intensity of 12.5 W cm$^{-2}$ (Le Quang et al., 2005).

Lamellar nanohybrids composed of Ln$_2$O$_3$ layers regularly separated from each other by organic layers of intercalated benzoate molecules can be obtained by a one-pot procedure (Karmaoui et al., 2006), the benzyl alcohol route. Lanthanide isopropoxides are simply dis-solved in benzyl alcohol and reacted at high temperature (250–300 °C), resulting in the isola-tion of nanoparticles of 50-nm mean size. Eu$^{III}$-doped nanohybrids have better radiance char-acteristics than the standard phosphor Y$_2$O$_3$:Eu while both yttrium- and gadolinium-based nanomaterials doped with Nd$^{III}$ display intense NIR luminescence, with a Nd($^4F_{3/2}$) lifetime of 49 μs in the case of the yttrium nanohybrid (Sa Ferreira et al., 2006).

Yttrium orthoborate nanoparticles Y$_{1-x}$Nd$_x$BO$_3$ have been less studied. They can be prepared by hydrothermal synthesis from boric acid, urea, yttrium nitrate, and neodymium
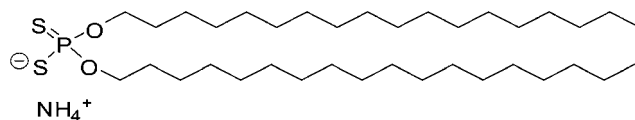
Fig. 109. Dithiophosphate ligand used in the synthesis of LaVO$_4$:Ln nanoparticles.

sesquioxide in dilute nitric acid. The Nd$^{III}$ ions lie in two different metal ion sites with the same $C_3$ symmetry and therefore have similar emission properties, leading to narrow emission bands. The luminescence intensity of these particles having diameter in the range 40–60 nm is maximized when the Nd$^{III}$ doping concentration reaches 10 mol% (F. Wang et al., 2004).

Concentrated aqueous colloidal solutions of well dispersed YVO$_4$:Ln (Ln = Nd, Yb) nanocrystals with an average size of 8 nm were obtained by precipitation of lanthanide citrates with sodium orthovanadate and heating at 60 °C for 30 min (Buissette et al., 2003). Aqueous suspensions of these nanocrystals have luminescence properties which are not as good compared to the bulk materials (e.g. smaller lifetimes). Thermal treatment at 600 °C yields silica-capped nanoparticles for which the initial luminescent properties are restored. In particular, the co-doped YVO$_4$:Er,Yb material exhibits green up-conversion luminescence, in addition to the 1.55 μm NIR emission. The two-photon process is demonstrated by the square-power dependence of the green emission intensity at 550 nm. A noteworthy result is that the up-conversion efficiency (0.4%) is not affected by the nanometric size of the crystallites. To make vanadate nanoparticles soluble in organic solvents, F.C.J.M. van Veggel et al. have proposed to coordinate negatively charged ligands at their surface, such as dithiophosphate substituted with a C$_{18}$ alkyl chain (fig. 109). The doped vanadate nanoparticles are synthesized by heating a solution of the dithiophosphate with sodium orthovanadate, lanthanum nitrate, and 5 mol% of the dopant lanthanide nitrate in ethanol/water at 75 °C, followed by the usual treatment, re-dispersion, and drying at room temperature.

One advantage of the vanadate system is its V–O charge-transfer state around 35 700 cm$^{-1}$ (280 nm) which can be used to populate the Ln$^{III}$ excited states. In this way, NIR emission form Nd$^{III}$, Ho$^{III}$, and Er$^{III}$ is observed in chloroform solutions, upon excitation at 280 nm (Stouwdam et al., 2005).

Stable luminescent suspensions of Er$^{III}$-doped titania (TiO$_2$) nanoparticles with an average size of 50 nm display only faint luminescence from the $^4I_{13/2}$ level upon pumping at 795 nm if no thermal treatment is applied. Simple drying at 100 °C improves their photophysical properties and treatment at 500 °C results in further luminescence enhancement. The nanoparticles can be assembled into thin films and inserted into photonic crystals (Jeon and Braun, 2003). Energy transfer from titania is also instrumental in exciting the Ln$^{III}$ levels, as demonstrated on very small (3–5 nm) TiO$_2$ nanoparticles doped with NIR-emitting Ln$^{III}$ ions and prepared from thermal decomposition of an organometallic precursor in trioctylphosphine oxide. Diluted dispersions in dichloromethane of the particles doped with Nd$^{III}$, Er$^{III}$, or Yb$^{III}$ emit the characteristic NIR luminescence and the corresponding excitation spectra show the same broad band with an onset at 350 nm, proving sensitization by the inorganic matrix (Stouwdam and Van Veggel, 2004).

### 3.4.5. *Fullerenes*

The fact that fullerenes may host additional atoms in their structure, particularly metal atoms, has been demonstrated by mass spectrometry on samples obtained by laser vaporization of lanthanum-impregnated graphite. Another method of obtaining lanthanide-containing fullerenes is arc vaporization of cored carbon rods packed with lanthanide oxide and graphite powder, followed by extraction by carbon disulfide or 1,2-dichlorobenzene and purification by high performance liquid chromatography (HPLC). Rare earth atoms do not enter easily into $C_{60}$ although La@$C_{60}$, has been evidenced, as well as a few other compounds. They are more likely to be found in larger cages, such as $C_{82}$ and $C_{84}$, the former being favored because its tri-anionic form is stabilized by the additional electrons. Despite the stunning properties of the metallofullerenes (magnetic properties, superconductivity for instance) few spectroscopic studies are reported, mainly because of the difficulty in producing pure materials in reasonable yield (Bethune et al., 1993). Undoped fullerenes dissolved in toluene have a deep red appearance and the onset of absorption shift to longer wavelengths when the cage becomes larger. For instance, $C_{60}$ starts to absorb strongly at 400 nm while the corresponding absorption onset lies at 500 nm for $C_{82}$. In the case of La@$C_{82}$, two isomers have been identified which present extended absorption spectra to the NIR range down to 2 μm, with a weak and broad absorption at 1.5 μm for the major isomer and 1.35 μm for the minor isomer. In addition, other sharp feature are seen at about 1 μm and 700 nm (Yamamoto et al., 1994). As far as NIR luminescence is concerned the most studied ion is $Er^{III}$ trapped in endohedral fullerenes and we shall limit the discussion to these systems.

Thin films of a mixture of fullerenes are reported to present an emission spectrum at 20 K in the range 700–1400 nm upon excitation with an argon laser (457 nm). Two sets of vibrational progressions could be identified, the relative intensities of which change drastically from sample to sample, which were assigned to $C_{60}$. When the fullerenes are doped with $Er^{III}$, the general shape of this emission remains similar, although the intensities of the vibrational features are modified; in addition a very well resolved $^4I_{13/2} \rightarrow {}^4I_{15/2}$ transition appears in the range 1.45–1.65 μm. The authors however could not identify the species (Er@$C_{60}$ or Er@$C_{82}$) responsible for this emission spectrum (Hoffman et al., 1995). In a subsequent study, the same authors produced Er@$C_{82}$ and $Er_2$@$C_{82}$ by the carbon arc method. Time-of-flight mass spectrometry suggested that the bimetallic species is the most abundant metallofullerene in the samples. Low-temperature photoluminescence spectra display at least three lines attributable to lanthanide emission (1.520, 1.526, and 1.545 nm). It was concluded from molecular orbital calculations that this emission arises mainly from the bimetallic species, because the lowest unoccupied molecular orbital (LUMO) of the $C_{82}^{3-}$ fullerene lies at 5000 cm$^{-1}$, that is lower than the Er($^4F_{13/2}$) level. This is not the case for $C_{82}^{6-}$ for which the energy of the LUMO has been measured at 9000 cm$^{-1}$ for a $Sc^{II}$ fullerene, $Sc_3$@$C_{82}$, so that energy transfer from the cage to the metal ion is feasible for $Er_2$@$C_{82}$ (Hoffman et al., 1998). This result has been confirmed later by two other groups (Ding et al., 1997a; Ding et al., 1997b; MacFarlane et al., 1997). In particular, MacFarlane produced three different isomers of $Er_2$@$C_{82}$, separated by repeated HPLC passes. One isomer was isolated with >96% purity and was dissolved in carbon disulfide and in a mixture of *cis* and *trans* decalin (decahydro-naphthalene) which forms a glass when frozen. The room-temperature

absorption spectrum of the carbon disulfide solution extends down to 1.3 μm, with distinct features at 1.1 μm, 900 nm, and 700 nm. The emission spectra of the decalin glass and of the frozen $CS_2$ solution at 1.6 K exhibit the characteristic $Er^{III}$ emission centered at 1.57 μm. A fine structure assigned to an exchange coupling between the two encaged $Er^{III}$ ions has been identified on the 1.51 μm component of the transition. Although the $Er(^4I_{13/2})$ lifetime could not be measured, an upper limit, <50 μs, could be determined, corresponding to an intrinsic quantum yield of less than 0.1% (MacFarlane et al., 1997). In fact, it has been shown that vacuum sublimation of the soot at low temperature (350–430 °C) leads to a mixture with $Er@C_{60}$ as the main component. The metallofullerene can then be isolated in good purity by HPLC, as shown by time-of-flight mass spectrometry (Ogawa et al., 2000). In light of this result, Hoffman and Conley re-investigated their initial system, producing thin films under various conditions, avoiding any contact with air. Fluorescence from two samples generated by vacuum sublimation at 430 and 850 °C was compared to the emission of a sample obtained directly from the toluene extract. The latter clearly shows a line at 1.519 μm, typical of $Er_2@C_{82}$ while the film obtained at high-temperature displays, in addition, two lines at 1.511 and 1.526 μm, typical of $Er@C_{60}$. The film sublimated at low temperature is devoid of the line corresponding to $Er_2@C_{82}$ (Hoffman and Conley, 2001). This demonstrates that sample preparation is very crucial for metallofullerene and sometimes difficult to control precisely, especially that the purity of the isolated samples is rarely larger than 95%, opening the way to artifacts generated by minor species.

Erbium has also been introduced into another family of endohedral fullerenes, namely $Ln_xSc_{3-x}N@C_{80}$. This system is interesting because it possesses icosahedral $I_h$ symmetry, as demonstrated for $Sc_3N@C_{80}$ by NMR spectroscopy (Stevenson et al., 1999). Moreover, the synthesis mainly produces one isomer and the entire $Er_xSc_{3-x}@C_{80}$ is available for $x = 0-3$. The crystal structure of $ErSc_2N@C_{80}$ points to triangular tri-metal nitride $R_3N^{6+}$ groups inside $C_{80}^6$-cages (Olmstead et al., 2000); extended Hückel calculations indicate that the $C_{80}$ edifice is greatly stabilized by the addition of six electrons. Lifetimes of the $Er(^4I_{13/2})$ levels have been measured at 1.6, 77, and 300 K for the three compounds with $x = 1, 2,$ and 3; they lie between 1.1 and 1.6 μs, with a marked difference between the species with $x = 3$ and the two other compounds. Analysis of the narrow multiplet arising from ligand-field splitting allows one to further characterize each particular species. The quantum yield estimated from the lifetimes is on the order of $10^{-4}$, that is comparable to the one determined for glassy or crystalline hosts (MacFarlane et al., 2001).

### 3.4.6. *Ionic liquids and liquid crystal phases*

Room temperature ionic liquids (RTIL) are non-flammable, non-volatile liquids which can potentiality replace usual organic solvents in almost every field of chemistry (e.g. catalysis, synthesis, or electrochemistry). A working definition of an ionic liquid is a salt with a melting temperature below the boiling point of water. Both the cationic and the anionic components of these liquids can be easily varied and they can therefore be tailored for specific applications or sets of properties. As a consequence, RTIL's represent an environmental-friendly, "green" alternative to volatile organic solvents. They were discovered at the beginning of the 19th century but they remained laboratory curiosities until the 1960's when
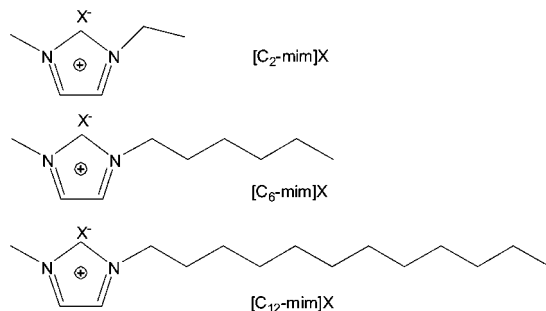
Fig. 110. Examples of methylimidazolium ionic liquids.

aluminates were developed as electrolytes for fuel cells and batteries. The interest for these compounds with respect to broader applications only developed in the 1990's but today a large number of these compounds have been synthesized and tested (Moutiers and Billard, 2004; Wasserscheid and Welton, 2005). Several ionic liquids are colorless and are transparent through almost the whole visible and NIR spectral ranges. Together with their excellent chemical stability, this makes them quite adequate as optical solvents. The spectroscopy of lanthanide ions in these media is not yet well known, but initial studies demonstrated novel aspects, with, in addition, the ability of some RTILs to stabilize $Ln^{II}$ divalent states (Billard et al. 2003, 2004). One of the most studied classes of ionic liquid derives from the 3-methylimidazolium cation substituted in position 1 by an alkyl chain of variable length (fig. 110). Another advantage of the RTILs is that a wide range of anions can be tested, particularly large non-coordinating anions, such as triflate (Otf), bis(trifluoromethanesulfonyl)imide $(Tf_2N)$ or bis(perfluorobutylsulfonyl)imide, $[C_4F_9SO_2]_2N^-$ (pbs). On the other hand, precautions have to be taken in that the properties of RTILs are very sensitive to their water content and most of the ionic liquids are highly hygroscopic.

Neodymium salts with $Br^-$, $Otf^-$, and $Tos^-$ (tosylate) as anions have been dissolved in the ionic liquids with the corresponding anions, $[C_6\text{-mim}]Br$ and $[C_2\text{-mim}]X$ (X = Otf, and Tos), and the Judd–Ofelt parameters $\Omega_2$, $\Omega_4$, and $\Omega_6$ were calculated from the absorption spectra. The $\Omega_2$ parameter is associated with short-range coordination effects, while the two other parameters depend on long-range effects. The first parameter for the investigated salts amounts to 5.2, 4.8, and $8.5 \times 10^{-20}$ cm$^2$ for Br, Otf, and Tos, respectively that is 2–3 fold larger than for the aquo ion ($2.25 \times 10^{-20}$ cm$^2$, cf. table 4), despite the weak binding properties of the anions. NIR luminescence was observed for the three systems upon direct excitation in the $^4G_{5/2} \leftarrow {}^4I_{9/2}$ transition at 586 nm (Driesen et al., 2004a) and the lifetimes of the Nd($^4F_{3/2}$) level are 1.51, 0.38, and 0.80 µs for Br, Otf, and Tos, respectively. Neutral and anionic lanthanide complexes are also stable in ionic liquids as demonstrated by an extensive physico-chemical study of $[Ln(tta)_n]^{(n-3)-}$ ($n = 3$, 4) in $[C_4\text{-mim}]Tf_2N$/water biphasic system (Jensen et al., 2003): the $[Nd(tta)_4]^-$ absorption and emission spectra in this RTIL match those recorded for the same species in o-xylene, for instance. Similarly, the tetrakis($\beta$-diketonate) complex of Nd$^{III}$ with 4,4,4-trifluoro-1-(2-naphthyl)-1,3-butanedionate, $[Nd(NTA)_4]^-$, in $[C_6\text{-mim}]Br$

displays the characteristic Nd$^{III}$ NIR emission under excitation into the diketonate levels, and a similar observation has been made for [Nd(pbs)$_3$(phen)] in [C$_6$-mim]pbs (Driesen et al., 2004a).

With respect to the water content of RTILs, the detrimental influence of water on the spectroscopic properties of LnI$_3$ salts (Ln = Nd, Er) dissolved in [C$_{12}$-mim] Tf$_2$N is evidenced by the disappearance of the NIR luminescence as soon as the samples are exposed to air. On the other hand, the quantum yield of an anhydrous solution of the Nd$^{III}$ salt amounts to $1.5 \pm 0.2$%, a quite high value, which compares favorably with those obtained in *deuterated* organic solvents (see table 21 below). The corresponding lifetime is $\tau(^4F_{3/2}) = 15.3$ μs; the luminescence intensity of the Er$^{III}$ salt was too low to determine the quantum yield, but the $^4I_{13/2}$ lifetime is in the microsecond range, 10.4 μs (Arenz et al., 2005). Interestingly, the dysprosium NIR absorption $^6F_{11/2}$, $^6H_{9/2} \leftarrow {}^6H_{15/2}$ in the range 7000–9000 cm$^{-1}$ is seen in this solvent and the lifetime of the visible emitting level $^6H_{15/2}$ is similar to the one found in deuterated water, 63 μs (Mudring et al., 2006).

Other ionic liquids of interest are those displaying simultaneously liquid crystalline properties (Binnemans, 2005a). Indeed, liquid crystalline phases provide anisotropic media which are used in displays (LCD) and succeeding in producing emissive LCDs by rendering the liquid crystalline phase luminescent would be a definitive advantage. Several strategies have been proposed for the design of lanthanide-containing liquid crystalline phases (Terazzi et al., 2006). With respect to the NIR spectral range, mesomorphic materials could be useful in optical communications by acting as switchable light-converting devices. The first near-infrared photoluminescent liquid–crystalline material has been made by doping the nematic liquid–crystalline matrix $N$-($p$-methoxybenzylidene)-$p$-butylaniline (MBBA) with [Ln(dbm)$_3$(phen)], Ln = Nd, Er, Yb. The photoluminescence intensity of the Yb$^{III}$ sample increases by 100% when the isotropic phase is cooled to the nematic phase, due to the birefringence nature of the liquid crystalline phase, which better diffuses light and leads to enhanced excitation of the lanthanide ion (Van Deun et al., 2003b). Imidazolium chlorides with long alkyl chains, e.g. [C$_{12}$-mim]Cl, form lamellar arrays in the crystalline phase and an enantiomeric smectic crystalline phase (termed SmA$_2$) at room temperature. The crystal-to-SmA$_2$ transition temperature depends on the hydration of the ionic liquid, ranging from $-2.8\,°C$ for anhydrous [C$_{12}$-mim]Cl to $+44.5\,°C$ for the monohydrated species. Lanthanide salts, such as chlorides, nitrates, triflates, or perchlorates can be doped into the liquid crystalline phases without disturbing the mesomorphic properties of the ionic liquid, up to a concentration of 10 mol% (Guillet et al., 2004). A similar strategy was adopted to insert 1 mol% of highly luminescent $\beta$-diketonate complexes [Ln(tta)$_3$phen] (Ln = Nd, Er, Yb) into the same ionic liquid (Puntus et al., 2005). Due to the relative sensitivity of the complexes to thermal decomposition, thermal treatment of the resulting materials could not be made at temperatures allowing complete dehydration and the transition temperature was in the range 6–12 °C. On the other hand, the smectic A$_2$ phase is retained after introduction of the complexes, as ascertained by differential scanning calorimetry and small-angle X-ray diffraction data. Despite the low concentration of the lanthanide complexes, all three samples displayed NIR luminescence with an intensity comparable or larger than the one exhibited by the solid state samples. This is particularly true for the Yb$^{III}$ mesophase, with an associated quantum yield
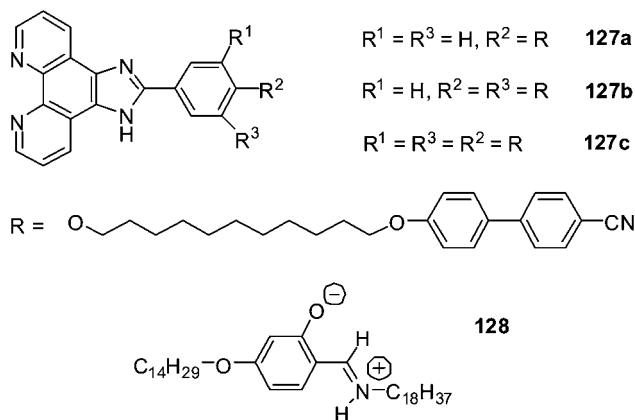
Fig. 111. (Top) Imidazo[4,5-f]1,10-phenanthroline ligands for metallomesogens. (Bottom) Salicylaldimine Schiff base for low temperature lanthanidomesogens.

of $2.1 \pm 0.3\%$, as compared to $1.6 \pm 0.2\%$ for microcrystalline [Yb(tta)$_3$phen] (Puntus et al., 2005) or to $1.1 \pm 0.1\%$ for its solution in toluene (Meshkova et al., 1999). Interestingly, these NIR-emitting mesophases can be excited up to 410 nm, in the visible.

Liquid crystalline phases containing lanthanide ions are also obtained by the design of suitable ligands. The resulting complexes are termed lanthanidomesogens and the nature of the liquid crystalline phases obtained depends on the ligand design (Piguet et al., 2006). Few systems deal with luminescent lanthanidomesogens and among them only a couple report NIR luminescence. To obtain nematic phases containing lanthanide ions, K. Binnemans and coworkers (Cardinaels et al., 2005) have decoupled the mesogenic groups from the metal-coordinating group by a flexible spacer (fig. 111). The lanthanide $\beta$-diketonates [Ln(tta)$_3$] are simply dissolved in the liquid–crystal host and phase separation is prevented by the covalent link between the metal ion and the mesogenic moiety (here through the phenanthroline group). All of the [Ln(tta)$_3$**127**] complexes present a crystalline-to-nematic transition around 75–92 °C depending on the metal ion and mesogenic ligand; the nematic phases exist over a temperature range of 35–50 °C. The Nd$^{III}$ ternary complex with **127a** and the Er$^{III}$ and Yb$^{III}$ ternary complexes with **127b** display an intense and well characterized NIR emission at room temperature. NIR luminescence is also seen for [Sm(tta)$_3$**127b**] in the range 880–950 nm, corresponding to the $^4G_{5/2} \rightarrow {}^6F_J$ transitions ($J = 7/2, 5/2$), and around 1180 nm, assigned to $^4G_{5/2} \rightarrow {}^6F_{9/2}$. In order to obtain lanthanide mesophases close to room temperature, the same authors have prepared $\beta$-diketonate ternary complexes with a salicylaldimine Schiff base derivative, [Ln(tta)$_3$(**128**)$_2$] and [Ln(btfa)$_3$(**128**)$_2$]. The transition temperatures from initial glassy states to smectic A phases occur between 20 and 24 °C for La$^{III}$ to Er$^{III}$ complexes with thenoyltrifluoroacetonates while the corresponding benzoyltrifluoroacetonates display somewhat lower transition temperature, around 18–19 °C. Thin films of [Nd(tta)$_3$(**128**)$_2$] and [Nd(btfa)$_3$(**128**)$_2$] emit in the NIR and the lifetimes of the Nd($^4F_{3/2}$) level amount to 0.44 and 0.38 μs, respectively. The luminescence from the Er$^{III}$ compounds is much weaker but can

nevertheless be observed at room temperature, with lifetime of 0.66 µs (tta) and 0.56 µs (btfa) for the $^4I_{13/2}$ level (Y.T. Yang et al., 2006).

## 4. Overview of potential applications

Potential applications of lanthanide-induced NIR emission essentially lie in two main fields: optical and electro-optical devices on one hand, including laser materials, amplifiers, and light emitting diodes, and biomedical analysis on the other hand. While the latter field is in its infancy, optical applications are numerous and we do not intend to cover them thoroughly. Moreover, keeping to our working principle, purely inorganic systems, such as glasses or nanocrystalline silicon thin films which have generated a wealth of publications during the last 30 years or so, are excluded from the review, and we concentrate on systems using lanthanide chelates.

### 4.1. *Inorganic liquid lasers*

Crystals and glasses containing trivalent neodymium ion have been widely used as laser materials. Since single-crystal growing and shaping were complicated techniques at the end of the 1960's and beginning of the 1970's, many researchers focused on lanthanide-doped liquids exhibiting laser action at room temperature, and thus providing a potential alternative to solid-state lasers (Batyaev, 1971; Heller, 1968a). Some initial studies focused on solutions of $\beta$-diketonates (Binnemans, 2005b) or fluorinated propionates (Heller, 1967), but it became rapidly evident that efficient nonradiative deactivation by vibrations of the organic ligands was difficult to overcome, so that researchers turned to purely inorganic systems. This field of research appears now to be abandoned, but we nevertheless review it, at least as far as neodymium lasers are concerned, so as to bring some of the accumulated data to the knowledge of younger readers.

   In order to allow the accumulation of ions in the metastable state, for instance, the Nd($^4F_{3/2}$) level, and thus achieve population inversion, a fundamental requirement for these liquids is minimization of radiationless relaxation paths. Deactivation through vibrations can be prevented following two different strategies. The first one consists in using laser active materials possessing strongly allowed transitions, like fluorescent organic dyes. In this case the radiative deactivation occurs at rates which are fast relative to the nonradiative ones. The second strategy is based on the weakening of the vibrations in the environment of the laser active ion so that they do not compete with the lanthanide transitions. This can be achieved either by totally excluding high-energy vibrations from the system or by shielding the ion from its environment by the coordination of one or several ligands having no such high-energy vibrations.

### 4.1.1. *Neodymium in selenium oxychloride*
A number of solvent systems have been screened for potential ionic (uncomplexed) $Nd^{3+}$-based liquid lasers. These systems must meet several requirements: they should (i) not contain

light atoms, particularly hydrogen and deuterium, (ii) be devoid of vibrations with frequency exceeding 2000 cm$^{-1}$, (iii) have high dielectric constants to allow the complete dissolution of the lanthanide salts and (iv) be transparent in the pumping range (500–900 nm) and emission range (1000–1400 nm) of Nd$^{3+}$. Selenium oxychloride, SeOCl$_2$, meets all these requirements and has therefore been used in numerous studies. Since no lighter atoms than oxygen is present, there are no vibrations of sufficient energy to accept the energy corresponding to the gap between the excited and ground multiplets. Indeed the highest vibration of selenium oxychloride is 955 cm$^{-1}$, whereas the smallest possible gap for Nd$^{III}$ amounts to 5500 cm$^{-1}$. In spite of the high dielectric constant of selenium oxychloride, neodymium oxide and chloride dissolve only to a limited extent in this solvent. One way to increase the concentration of Nd$^{3+}$ in such systems consists in designing neutral or acidic solutions, by adding aprotic acids, like SnCl$_4$, TiCl$_4$, SbCl$_5$, for instance. This leads to the formation of a Lewis acid–selenium oxychloride adduct, $(MCl_6)^{n-}(SeOCl^+)_n$, which further decomposes to provide the strong acid species SeOCl$^+$. This species then reacts with neodymium oxide or chloride, solubilizing it:

$$SnCl_4 + 2SeOCl_2 \rightleftharpoons SnCl_6^{2-} + 2SeOCl^+,$$

$$SbCl_5 + SeOCl_2 \rightleftharpoons SbCl_6^- + SeOCl^+,$$

$$6SeOCl^+ + Nd_2O_3 \rightleftharpoons 2Nd^{3+}(solv) + 3SeOCl_2 + 3SeO_2,$$

$$3SeOCl^+ + NdCl_3 \rightleftharpoons Nd^{3+}(solv) + 3SeOCl_2,$$
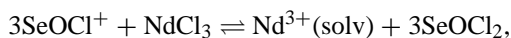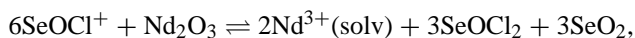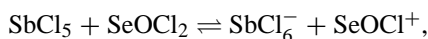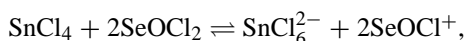
where Nd$^{3+}$(solv) represents in fact the solvated ion with several selenium oxychloride molecules coordinated in the first coordination sphere, that is $[Nd(SeOCl_2)_m]^{3+}$. The anions $(MCl_6)^{n-}$ of the aprotic acid are coordinated in the outer sphere of Nd$^{3+}$(solv). Indirect evidence for this outer shell coordination is given by the electronic absorption spectra of the Nd$^{3+}$ f–f transitions which are independent of the aprotic acid used.

In such laser solutions the most undesirable impurities are hydrogen-containing compounds, since hydrogen atoms are known to provide highly energetic oscillators (O–H or N–H, for instance). As a consequence these compounds have to be eliminated and this can be done either by using extremely pure solvents or by separating the undesired products during the preparative steps (Heller, 1968c). Since the extreme solvent purification techniques required are tedious, the second way is generally followed and hydrogen-containing compounds are removed by distillation along with part of the solvent. The obtained mixture is usually deep brown owing to the presence of reduction products such as selenium or diselenium dichloride Se$_2$Cl$_2$. The brown products interfere with the optical pumping of the laser solutions and are eliminated by oxidation with KClO$_3$. Finally, vacuum removal of the dissolved gases (chlorine or chlorine dioxide) formed during the chlorate treatment yields solutions that contain only selenium dioxide, tetrachloride, or oxychloride, which do not absorb in the spectral range used for optical pumping.

The laser liquids prepared by these techniques possess properties, such as high gain and sharpness of the emission, that are more characteristic of crystalline hosts (Nd$^{3+}$:CaWO$_4$ or Nd$^{3+}$:YAG) than glass lasers (Heller, 1966; Heller, 1968a; Lempicki and Heller, 1966). Moreover, under identical excitation conditions, the solutions have $^4F_{3/2} \rightarrow {}^4I_{11/2}$ emission

intensity exceeding the emittance of the best neodymium-doped sodium-compensated calcium tungstate laser crystals. In systems containing $SeOCl_2$, the lifetimes of the $Nd(^4F_{3/2})$ level ranges between 150 and 255 μs, depending on the conditions used for preparing the solution. Basic solutions, prepared without addition of Lewis acids, exhibit the lowest lifetime, whereas the system $SbCl_5$:$SeOCl_2$ possesses the longest one ($255 \pm 10$ μs). Tin tetrachloride gives a very similar lifetime of $240 \pm 10$ μs. Since the viscosity of the solutions are quite high, and increases with increasing amounts of neodymium salt and Lewis acid, attempts have been made to reduce it. For the system $SnCl_4$:$SeOCl_2$, this can be done by removing the excess of acid by fractional distillation, leading to solutions with lower viscosity, referred to as "neutral" solutions. However, the luminescence characteristics of these neutral solutions are not as good as the ones of acidic solutions. This can be explained by the enhancement of diffusion-assisted quenching processes since the liquid is less viscous. The best lifetimes obtained for the neutral solutions reach only $200 \pm 10$ μs.

The quantum yields of fluorescence of the different systems have also been determined relative to a single crystal of neodymium-doped YAG for which a quantum yield of unity has been assumed (Heller, 1968a). The quantum yields obtained, even if they are accurate only within a factor of two, follow the same trend as for the lifetimes, with the highest values for the acidic solutions; 0.70 and >0.75 in presence of $SnCl_4$ and $SbCl_5$, respectively. Neutral and basic solutions are less luminescent and have quantum yields of 0.5 and 0.4, respectively. Identical measurements performed on a sodium-compensated neodymium-doped calcium tungstate crystal lead to a value of 0.5. The high quantum efficiency and the low threshold (between 2 and 40 J) of these $Nd^{3+}$:$SeOCl_2$ systems clearly demonstrate that liquids are not inherently inferior to solids as laser materials.

In all the studies described above, the stimulated emission originates in the $^4F_{3/2} \rightarrow {}^4I_{11/2}$ transition of $Nd^{3+}$ ion near 1.06 μm. The possibility of observing stimulated emission from other $Nd^{3+}$ transitions has also been explored (Heller and Brophy, 1968). Stimulated emission from the $^4F_{3/2} \rightarrow {}^4I_{13/2}$ transition at 1.33 μm can indeed be achieved at room temperature whereas such a phenomenon is not observed for the $^4F_{3/2} \rightarrow {}^4I_{9/2}$ transition. However the cross section for stimulated emission at 1.33 μm is 11-fold smaller than the stimulated emission at 1.06 μm and the threshold required is one order of magnitude larger.

From a more technical point of view, liquid lasers solutions containing $Nd^{3+}$ in $SeOCl_2$ display an unusual and interesting phenomenon, referred to as self Q-switching. It consists in the generation of highly energetic pulses with peak powers in the range of 300–500 MW (Samelson et al. 1968b, 1968a; Samelson and Lempicki, 1968). Such output powers are achieved without the aid of any devices, like Pockel or Kerr cells, saturable absorbers, for instance.

### 4.1.2. *Neodymium in phosphorus oxychloride*

Selenium oxychloride is not the only inorganic solvent used for liquid lasers, several studies use as solvent phosphorus oxychloride, $POCl_3$ (Blumenthal et al., 1968; Brecher and French, 1969; Brinkschulte et al., 1972). Although this solvent is a worse host for ionic salts due to its lower dielectric constant, it is much more attractive for liquid laser uses since it is far less toxic and corrosive than $SeOCl_2$. The approach for the preparation of $POCl_3$ solutions is slightly

different from that described for $SeOCl_2$. With $POCl_3$, the dissolution of neodymium oxide can be described by the following equation:

$$Nd_2O_3 + 3SnCl_4 + 6POCl_3 \rightleftharpoons 2Nd^{3+}(solv) + 3SnCl_6^{2-} + 3P_2O_3Cl_4.$$
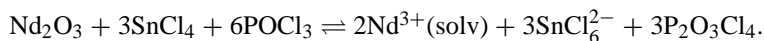
However, due to the much lower solubility of rare earth salts in $POCl_3$, concentrations of $Nd^{3+}$ needed for laser solutions cannot be achieved in pure and completely anhydrous solvent. The addition of water to acidified $POCl_3$ in a molar ratio of about 1:10 increases dramatically the solubility of $Nd^{3+}$. It is believed that one of the compounds resulting from the reaction of water with phosphorus oxychloride enhances the solubility of $Nd^{3+}$ in $POCl_3$:$SnCl_4$. The difficulty consists in returning to the aprotic state without destroying the compound responsible for the solubility enhancement. This has been done by boiling off a sufficient fraction of the solution to remove all the residual HCl and $H_2O$ and finally by adding anhydrous $POCl_3$ and $SnCl_4$ to reach the desired concentration. A 0.3 M $Nd^{3+}$ solution in $POCl_3$:$SnCl_4$ prepared in this way has a fluorescence decay time of 245 μs whereas the corresponding laser solution with $SeOCl_2$:$SnCl_4$ has a lifetime of 260 μs. The comparison of the $SeOCl_2$ and $POCl_3$ aprotic solvents leads to the conclusion that the differences between the two liquid laser systems are not large (Brecher and French, 1969). In addition to its lower corrosiveness and toxicity the $POCl_3$ system has the advantage over selenium oxychloride solutions that the $^4F_{3/2} \rightarrow \, ^4I_{11/2}$ has larger intensity whereas the resonant $^4F_{3/2} \rightarrow \, ^4I_{9/2}$ transition is less intense. Thus the proportion of energy reaching the $^4F_{3/2}$ excited state and being emitted in the desired spectral range is much greater for $POCl_3$ solutions. This leads to a decrease of the overall transition probability from this state and hence makes potentially a more efficient laser system. However, comparison of the measured lifetime with the one calculated from spectroscopic considerations shows it to be about 20% smaller than the calculated value (310 μs) and thus points to nonradiative losses from the emitting state. For the $SeOCl_2$ system, the measured and calculated lifetimes are nearly identical (280 μs), indicating the absence of losses and hence a quantum efficiency close to unity. Vibrational coupling is a possible explanation for nonradiative deactivation in the $POCl_3$ system. Indeed a rather intense absorption is present in the infrared spectrum in the region of the first overtone of the P–O stretching vibration, whereas only a very weak second overtone of the Se–O vibration is observed in the corresponding $SeOCl_2$ system. Except for these differences, the two systems are quite similar and the choice of one or the other depends mainly on experimental conditions.

Different Lewis acids are used to facilitate the dissolution of relatively high amounts of $Nd^{3+}$ salts in the inorganic phosphorus oxychloride. Except well-known tin tetrachloride, acids such as $TiCl_4$, $AlCl_4$, $ZrCl_4$ or $BBr_3$ have been used to develop suitable systems showing laser action (Brinkschulte et al., 1972; Schimitscheck, 1968). The $POCl_3$:$ZrCl_4$ system has been studied in more details in the work of Hongyo et al. (1972) and Brecher and French (1973).

### 4.1.3. *Other lasing ions*

Erbium and ytterbium ions also display NIR emission in selenium oxychloride (Heller, 1968b). Simple $Nd^{3+} \rightarrow Yb^{3+}$ and double $Nd^{3+} \rightarrow Yb^{3+} \rightarrow Er^{3+}$ energy transfers have been investigated. In selenium oxychloride solutions, energy transfer processes depend to a

greater extent of the acidity of the medium, the more acidic solutions exhibiting the poorer energy transfer efficiency. In this respect, basic solutions are most suited. However, due to the lower solubility of rare earth salts in basic media, neutral solutions were preferred. Upon excitation at 578 nm, a wavelength absorbed only by $Nd^{3+}$, the characteristic $Yb^{3+}$ fluorescence is observed in parallel to $Nd^{3+}$ emission in the binary solution. Using the same excitation wavelength for the ternary solution, simultaneous emission of the three ions, $Nd^{3+}$, $Yb^{3+}$ and $Er^{3+}$ occurs. The $Er^{3+}$ luminescence is particularly well sensitized by the $Yb^{III}$ $^2F_{5/2} \rightarrow$ $^2F_{7/2}$ transition, which fully overlaps the $Er^{III}$ ($^4I_{11/2} \leftarrow {}^4I_{15/2}$) absorption band. In absence of sensitizing ion, no $Er^{3+}$ luminescence is observed.

### 4.1.4. *A second try*

Although numerous studies have been performed on selenium oxychloride or phosphorus oxychloride as inorganic solvent for liquid lasers, systems based on these solvents have no longer been developed and utilized for almost twenty years because of their high toxicity and corrosiveness toward structural materials. At the end of the 1980's, attempts have been made in order to develop inorganic liquid lasers with low toxicity, using mixtures of bromides (e.g. $AlBr_3$–$SbBr_3$–$PBr_3$–$NdBr_3$) or chlorides ($SOCl_2$–$AlCl_3$, $SOCl_2$–$GaCl_3$). The lasing properties of $NdCl_3$ in $SOCl_2$–$GaCl_3$ are comparable ($\tau = 240$ µs) to the $SeOCl_2$- or $POCl_3$-based lasers, but with lower toxicity and viscosity (Batyaev et al., 1989b). The same binary aprotic solvent has been used to study energy transfer in solution occurring between $Yb^{III}$ and $Er^{III}$ ions (Batyaev et al., 1989a). In 1995, Han et al. (1995) studied the possible use of a $Nd^{3+}$ solution in ethyleneglycol as amplifier gain medium for a $Nd^{3+}$:YLF (yttrium lithium fluoride) laser. Since this study, no improvement has been achieved anymore.

### 4.2. *Optical fiber amplifiers and waveguides*

In optical telecommunication systems, light carries information between several users. Optical links consisting in single-mode silica optical fibers are now used in telecommunications and have the ability of providing high-bandwidth and long-distance communication. The manipulation of the optical signals on a local scale requires splitters, couplers, multiplexers, de-multiplexers, and amplifiers. These devices are easy to make and can be integrated on one planar substrate with a technology called integrated optics, a basic element of which is the planar optical waveguide. It consists of a high refractive index guiding core layer of typical dimension $2 \times 1$ µm$^2$, sandwiched between two lower-index cladding layers (fig. 112 gives an example for a PMMA device). The optical signal travels in the guiding layer and total internal reflection at the interface between the core and cladding maintains it in the waveguide. The increasing demand for optical links in the office and at home is generating interest for cheap optical devices which can be directly installed by the end-user, a reason why plastic optical fibers receive presently a lot of attention. Indeed, they have clear technical advantages over glass fibers: a better flexibility and a large core diameter enabling efficient coupling. If the guiding layer of an optical fiber is doped with an active element, optical gain results upon adequate pumping. Typical low-cost plastic optical fibers of 100 m length have an attenuation of 100 dB km$^{-1}$ and a bandwidth around 5.1 GHz. More importantly, fluorinated fibers are
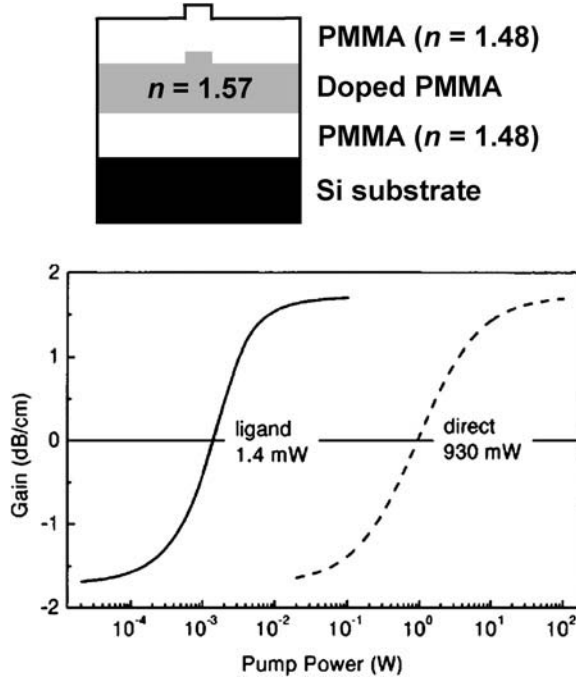
Fig. 112. (Top) Polymer channel waveguide for optical gain. (Bottom) Calculated differential optical gain for an Er-doped devices (organic complex, $2 \times 1\ \mu m^2$ core section) as a function of pump power for direct (- - -) and ligand (—) excitation; reproduced with permission from (Slooff et al., 2002).
© 2002 American Institute of Physics

at hand, with an optical transmission range extending in the NIR range (Kuriki et al., 2002). This has triggered a large number of projects aiming at developing polymers containing highly luminescent lanthanide complexes, mostly $\beta$-diketonates.

Under direct $Ln^{III}$ excitation and assuming that the population of the ground state ($N_g$) of the emitting 4f ion decays rapidly to populate the first excited state ($N_e$), the rate equations reduce to those of a two-level system, and further assuming steady state, one gets

$$N_g = \frac{W_e}{W_e + R} \cdot N \quad \text{and} \quad N_e = \frac{R}{W_e + R} \cdot N \quad \text{with } R = \frac{\sigma_a P \lambda}{hca}, \tag{40}$$

where $W_e$ is the $Ln^{III}$ decay rate, $N$ the $Ln^{III}$ concentration, $P$ the pump power in the waveguide, $\sigma_a$ the absorption cross section, $\lambda$ the excitation wavelength, and $a$ the waveguide core cross section. The differential optical gain (OG, in dB cm$^{-1}$) is given by:

$$\text{OG} = 10 \times {}^{10}\log\frac{I}{I_0} = 10 \times {}^{10}\log(e^{kx}) \quad \text{with } k = \sigma_e \cdot (N_e - N_g) \cdot \alpha, \tag{41}$$

in which $I_0$ is the light intensity at the beginning of the waveguide and $I$ the intensity along the waveguide, $k$ is the optical gain factor, $\sigma_e$ the emission cross section, and $\alpha$ the fraction

of incident light confined in the core of the waveguide. In the case of Er$^{III}$, Slooff et al. (2002) have calculated the gain factor versus the pump power with the following parameters: $W_e = 1.25 \times 10^6$ s$^{-1}$ (corresponding to $\tau_{obs} = 0.8$ μs), $\sigma_a = 1.1 \times 10^{-20}$ cm$^2$ at $\lambda = 488$ nm, $\sigma_e = 1.1 \times 10^{-20}$ cm$^2$ at 1.54 μm, $a = 2$ μm$^2$, $N = 9 \times 10^{19}$ cm$^{-3}$, $\alpha = 0.4$. The threshold power, that is the power at which $k$ becomes positive is 930 mW (fig. 112, dashed curve) which is much higher than the minimum power needed in Er$^{III}$-doped glasses or alumina amplifiers. This can be traced back to the very small quantum yield of Er$^{III}$ in organic media. But this threshold power can be dramatically reduced if excitation is made in the ligand levels for which the absorption cross section is much larger ($\approx 10^3$-fold). Taking the ligand-to-Ln$^{III}$ ion energy transfer into consideration and assuming than the isc ($^1$S $\rightarrow$ $^3$T) process is fast, calculation of the gain proceeds as follows:

$$\frac{dN_\ell}{dt} = R_\ell N_{g\ell} - W_{\ell r} N_\ell - W_{\ell nr} N_\ell N_g \quad \text{with } R_\ell = \frac{\sigma_\ell P \lambda}{hca}, \tag{42}$$

$$\frac{dN_e}{dt} = -W_e N_e + W_{\ell nr} N_\ell N_g, \tag{43}$$

in which $N_\ell$ and $N_e$ are the population fractions of the excited states of the ligand and Ln$^{III}$ ion, respectively, while $N_{g\ell}$ and $N_g$ are the corresponding values for the ground states, $W_{\ell n}$ is the ligand radiative decay rate, $W_{\ell nr}$ is the ligand nonradiative (transfer) rate, and $\sigma_\ell$ is the ligand absorption cross section. In the case of the triphenylene-based organic complexes of Er$^{III}$ (see section 3.2.3), $\sigma_\ell = 8.5 \times 10^{-18}$ cm$^2$, $W_{\ell r} = 2 \times 10^8$ s$^{-1}$, and $W_{\ell nr} = 10^9$ s$^{-1}$, resulting in the plain curve in fig. 112 and in a threshold power of only 1.4 mW. Note however that these calculations do not take up-conversion and excited state absorption into account, which may increase the pump power needed for amplification (Polman and Van Veggel, 2004; Slooff et al., 2002).

The main problem for lanthanide-containing NIR optical fibers is the minimization of non-radiative deactivation of the excited states. Several groups, including industrial laboratories, have devoted a large effort to develop strategies addressing this problem along several lines: (Hasegawa et al., 2004; Slooff et al., 2002; Yanagida et al., 1998).

(i) Suppression of vibrational deactivation (including the one induced by water molecules). This problem has been discussed in section 3.2.1 and is usually dealt with by adding long perfluorinated lateral chains on the $\beta$-diketonate, by deuterating the C–H bridge and by working in deuterated solvents. The longer the perfluorinated chain, the less water molecules penetrate into the inner coordination sphere. They are also expelled by coordination of strong donor such as dmso. Despite these improvements, the intrinsic quantum yields remain small, for instance, they do not exceed 3% for Nd$^{III}$ in acetone, a solvent with C–H vibrations.

(ii) Inhibition of energy migration between luminescent centers and of up-conversion processes. Diffusion of Ln$^{III}$ chelates in solution induces collisions between molecules, leading to energy transfer via cross-relaxation and excitation migration (see fig. 113 for an illustration in the case of Nd$^{III}$). Both processes are based on dipole–dipole interactions. In cross relaxation, energy is partially transferred to a neighboring ion, leaving
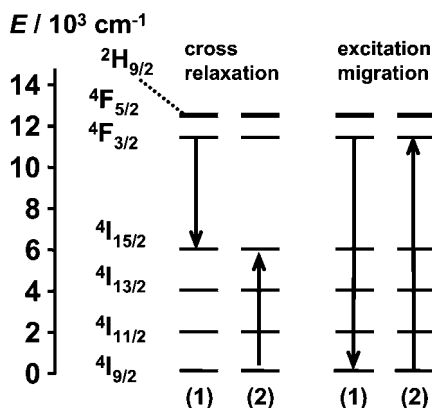
Fig. 113. Radiationless transitions via energy migration in Nd[III] samples.

both ions in a lower energy level, e.g. $Nd(^4I_{15/2})$, from which they relax easily in a non-radiative way to the ground level. Migration of energy by hopping onto a neighboring ion does not quench luminescence by itself, but it enhances the probability of quenching by permitting the energy to finally migrate onto a site where more rapid nonradiative decay takes place. The only way of avoiding this "concentration quenching" is to keep luminescent centers enough apart ($r_{Ln–Ln} > R_0$) so that the probability of transfer is reduced. This can be done either by having large complexes, e.g. $[Nd(pom)_3]$ (fig. 48) which possesses long fluorinated alkyl chains, or by dispersing them into polymer matrices.

One problem with polymers such as polymethylmethacrylate (PMMA) though is the presence of C–H bonds so that the use of polymers with low percentages of C–H bonds is recommended. One example is polyhexafluoroisopropylmethacrylate (P-FiPMA). Additionally, dmso-$d_6$ can be added to improve the quantum yield. For instance, the intrinsic quantum yield of $[Nd(hfa-d_1)_3(D_2O)_2]$ incorporated in PMMA (weight percentage of H-atom: 8%) is only 0.1%, that is comparable to the yield measured in methanol-$d_4$ (see table 11). When 6.6 wt% of dmso-$d_6$ is added, it increases to 0.5%, and finally, reaches 0.7% with P-FiPMA/dmso-$d_6$ (containing 2.5 wt% of C–H bonds), a value still lower than in pure dmso-$d_6$, 1.1%, see table 11 (Hasegawa et al., 1999; Yanagida et al., 2000b). The chelates $[Nd(pms)_3]$ and $[Nd(pes)_3]$ (fig. 50) have been similarly incorporated into PMMA/dmso-$d_6$ and P-FiPMA/dmso-$d_6$ leading to intrinsic quantum yields of $0.9 \pm 0.2\%$ for both complexes in the first matrix and of $1.3 \pm 0.1$ and $1.6 \pm 0.1\%$, respectively, in the second matrix. The authors judge that these values are large enough to prepare working devices for the 1.3 μm telecommunication window (Hasegawa et al., 2003).

Up-conversion and excited state absorption are the main gain-limiting factors in Er[III]-doped planar optical amplifiers, either glass- or polymer-based. Up-conversion increases the pump power required to achieve a certain degree of population inversion, up to factors

5–10. The ESA cross section is strongly material dependent and this phenomenon also increases the pump power needed, so that when both gain-limiting factors are present, pump powers of 10–100 mW are required, which considerably increases the cost of optical amplifiers. It is hoped that the introduction of sensitizers such as $Yb^{III}$, $Ag^{I}$ or silicon nanocrystals into inorganic optical fibers will help solving this problem. Organic chelates in polymer fibers may also be an alternative (Polman and Van Veggel, 2004).

(iii) Optimization of the sensitization ability of the ligand and of the emission intensity. As seen in section 3.2.1, $\eta_{sens}$ is between 20 and 30% and is larger with unsymmetrical ligands compared with symmetrical ones. Adding a second ligand to form a ternary complex, or a dye to transfer energy on the metal ion, can improve the sensitization, although it is difficult to go beyond a factor of two, possibly three. An example of such a strategy is the use of dichromated gelatin, a water-soluble volume hologram emulsion with a wide transmission bandwidth between 300 and 2700 nm. This photolime gelatin was doped by neodymium chloride hexahydrate ($6.7 \times 10^{19}$ ions cm$^{-3}$) and chlorophenol red (23%). All the active components were dissolved in a mixed solvent and no aggregation was observed in the obtained waveguide. The latter consisted in a layer of the doped gel sandwich between an Al layer deposited on glass, and an indium tin oxide (ITO) layer covered with glass. The waveguide was pumped by a tunable Ti:sapphire laser, while the signal beam was provided by a Nd:YAG laser (1.06 μm) and an optical gain of 3.8 dB was obtained at this wavelength. The optical gain heavily depends on the $Nd^{III}$ concentration, reaching a peak in the range $4–8 \times 10^{19}$ cm$^{-3}$. The waveguide also generated an optoelectronic effect (An et al., 1998). Therefore, the real problem resides in the low intrinsic quantum yields (see the two points above).

(iv) Choice of an adequate host medium and defect-free fabrication of the waveguide. The ideal host should disperse the luminescent centers sufficiently to avoid concentration quenching while simultaneously allowing high enough concentration of these centers and minimizing optical losses. Losses can come from several sources: scattering is a major one and arises from imperfections in the waveguide, such as rough sidewalls or defects in the core material. Another loss mechanism is the mismatch between the device waveguide mode and the incident light source mode. Finally, in a waveguide doped with a chromophoric organic complex, absorption of both the chromophore and the polymer backbone also contributes to the loss. The host material should also not modify the complex, or at least not the inner coordination sphere, and not provide nonradiative deactivation paths, henceforth the many fluorinated polymers and functionalized zeolites were tested.

Interestingly, attempts are also made to use optical fibers in nuclear power plants, especially for monitoring radioactivity. However, when measurements of high rate radioactive doses are performed in this way, this induces losses in the optical fibers. To remedy this problem, the use of NIR emission from rare earths ions instead of visible light has been suggested, particularly when they are inserted into inorganic matrices, such as $Gd_2O_2S:Ln^{III}$ (Ln = Pr, Nd, Yb). For instance, linear relationship between dose rate and peak counts has been demonstrated in the case of $Pr^{III}$ (Takada et al., 1998).
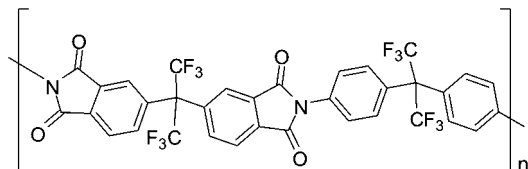
Fig. 114. Generic formula for the polyimide Ultradel®-9000.

### 4.2.1. *Neodymium-doped polymers*

Optical amplification in a silica fiber containing $Nd^{III}$ has been demonstrated in 1961 (Snitzer, 1961) and since many active high-performance integrated optical devices have been fabricated in purely inorganic matrices. The first organic $Nd^{III}$-containing optical amplifier appeared in 1993 and was built from photolime gel doped with 5 wt% of neodymium chloride leading to a concentration of $Nd^{III}$ ions equal to $1.03 \times 10^{20}$ $cm^{-3}$: a gain of 8.5 dB was observed over a waveguide length of 2.2 cm using a tunable Ti:sapphire laser as the pump and a Nd:YAG laser as the source (Chen et al., 1993). Contrary to the system described under point (iii) above, no sensitizing dye was used.

Among other systems tested, neodymium octanoate doped into PMMA shows a high-transmission window between 50 and 620 nm, with the minimum loss occurring at 570 nm (27 dB $km^{-1}$). The fibers made with a fiber-drawing method have a coupling efficiency of 20% for a 25-cm length and a core diameter of 60 μm. Neodymium fluorescence at 575 nm occurs through a three-level system, the pump light (514.5 nm) populating the $Nd(^4G_{7/2}, ^4G_{9/2})$ levels, which decay rapidly to the $^4G_{5/2}$ level emitting orange light. Excited state absorption from the $^4G_{5/2}$ to the $^2F_{5/2}$ level has a much smaller transition probability. The threshold pump energy is relatively large, at 85 mW and the transition originating from $^4F_{3/2}$ are not seen, mainly because the transmission window of the fiber is not suitable under the experimental conditions used (Zhang et al., 1998). Observation of the orange emission from $Nd^{III}$ has, however, been challenged and assigned to dye impurities in the fiber (Werts et al., 1999a). On the other hand, photoluminescence from the $Nd(^4F_{3/2})$ level has been reported for $[Nd(hfa-d_1)_3]$ doped into all-deuterated PMMA under pumping by a dye laser at 580 nm (Kuriki et al., 2000).

Since hermetic packaging of polymer optical devices is expensive, manufacturers prefer environmentally stable polymers such as epoxy or polyimide polymers, which are not water soluble. However, incorporating the $Ln^{III}$ ion under the form of a salt into such matrices is often difficult, even with techniques such as spin- or spray-coating. This is easier with organic chelates, which dissolve in the polymer solution. A combination of choices, meeting many of the requirements for an optimum optical device, is the incorporation of $[Nd(hfa)_3]$ into fluorinated polyimides such as Ultradel®-9000 (fig. 114). The doped fluorinated polyimide was spin coated and the film baked at 100 °C for a few minutes to remove the solvents before being exposed to a UV mercury lamp to crosslink the polymer. A final heat treatment under nitrogen (175 °C during 30 min) afforded a uniform film of 3 μm thickness. Several kinds of single-mode and multi-mode devices were prepared having $N_{Nd}$ in the range $0.2–1.0 \times 10^{20}$ $cm^{-3}$ (about half the value in glass hosts), which have an absorption cross section of

about $10^{-20}$ cm$^2$ at 799 nm. The photoluminescence signal is about 20 dB higher than the pump power (Lin et al., 1996).

A multilayer waveguide structure with alternate layers of undoped and Nd$^{III}$-doped Ultradel$^®$ polyimides of the series 9000 was fabricated. Ultradel$^®$ 9020 was chosen for the top layer since it has a refractive index lower than Ultradel$^®$ 9120 used for the doped layer. The layer of undoped polyimide renders the doped polyimide layer more planar, thus reducing surface scattering losses. Channels in the active layer (50 μm × 7 μm × 5 cm) were defined by photolithography. Photoluminescence spectra are broad (fwhh = 27 nm) which is beneficial to the operation of the waveguide. A gain of 8 dB has been obtained when a continuous-wave Ti–sapphire laser operating at 800 nm was used as the pump source and a cw Nd-YAG laser operating at 1.06 μm as the signal beam. The channels were multimode at the pump and probe wavelengths and the density of Nd$^{III}$ ions was about $10^{20}$ per cm$^3$, corresponding to 2.2 wt% (Karve et al., 2000).

As seen above, one way to improve the properties of optical amplifiers is to increase the ligand cross section, e.g. by grafting dye moieties on the chelating agent. For example, a terphenyl-based chelating agent has been functionalized with lissamine, a derivative of rhodamine, and the photophysical properties of both [Nd(**58b**)] (fig. 56) $10^{-2}$ M and [Nd(**60d**)] (fig. 59) $10^{-6}$ M were determined in dmso-$d_6$. When monitored at 1.06 μm, the photoluminescence intensity of the lissamine-modified chelate is very different from the reference compound, particularly in the range 475–525 nm clearly indicating energy transfer from the xanthene unit of the dye. The measured absorption cross section is in the range $10^{-17}$ cm$^2$, that is, four orders of magnitude higher than the typical intra-4f transitions of Nd$^{III}$ (at 515 nm, the optical absorption is almost identical for the two solutions). The lissamine-functionalized chelate was introduced into fluorinated polycarbonate waveguides at concentrations varying between 1 and 10 wt%. Partially fluorinated polycarbonates are ideally suited for planar waveguide applications because the background loss at the Nd$^{III}$ emission wavelengths is <0.05 dB cm$^{-1}$ at 1.06 μm and 0.08 dB cm$^{-1}$ at 1.34 μm. The waveguides were made by spin-coating a solution of polycarbonate and the chelate onto a silicon substrate covered with a 3 μm thick, thermally grown layer of silica, followed by thermal annealing at 190 °C in vacuum for one hour. The absorption cross section at 580 nm, as determined from ellipsometry and refractive index measurements, amounts to $4.5 \times 10^{-16}$ cm$^2$, while the lifetime of the Nd($^4F_{3/2}$) level is only 0.8 μs, a substantial reduction from the 2.2 μs observed in dmso-$d_6$. Since the emission is not quenched by the presence of oxygen, the authors estimated that the rate of energy transfer between lissamine and Nd$^{III}$ is faster than $10^7$ s$^{-1}$. The distance between lissamine and the Nd$^{III}$ ion is about 7–8 Å, whereas the effective Bohr radius for the excited lissamine and unexcited metal ion is about 2.5 Å. According to Dexter theory, this means that only 3% of the maximum possible energy transfer is reached. There are two ways of improving this figure, either by shortening the lissamine–Nd$^{III}$ distance, which is not easy to achieve, or by increasing the spectral overlap between the donor and the acceptor. In the present case, the energy of the lissamine $^3\pi\pi^*$ state matches with the 14 600 cm$^{-1}$ absorption band of the metal ion, which has a low cross section. Red-shifting the triplet state energy by 1000 cm$^{-1}$ would result in an overlap with the much stronger absorption $^4S_{3/2} \leftarrow {}^4I_{9/2}$. Another problem to address is the strong photo-degradation occurring upon continuous illumination, which might be due to the
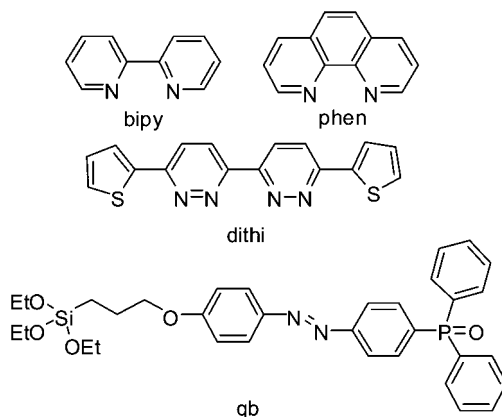
Fig. 115.  Aza aromatic ligands.

presence of oxygen in the polymer film or to radicals formed upon photo-excitation (Slooff et al., 2000b).

### 4.2.2. *Erbium-doped polymers*

Thin films of simple $Er^{III}$ complexes with aza aromatic ligands such as 2,2′-bipyridine (bpy), 1,10-phenanthroline (phen) or 2-dithienyl-2,2′-bipyridazine (dithi, fig. 115) doped into poly-methylmethacrylate (PMMA), or polyl[2-methoxy-5-(3′,7′-dimethyl-octyloxy)]-*p*-phenylene vinylene (MDMO-PPV) have been fabricated. The dithi complex is the most promising, with the strong luminescence of the MDMO-PPV matrix quenched by a factor 100 upon doping (Koppe et al., 2001). No other quantitative data are however reported.

In an erbium-doped planar optical amplifier, pump and signal beams are coupled into the device through separate input waveguides and combined into a wavelength division multi-plexer (WDM) to which a few-centimeter long $Er^{III}$-doped waveguide section is hooked. The latter is rolled up on a small area forming a spiral structure (amplifying waveguide spiral, AMP). After this section, signal and pump are separated in a second WDM and a splitter is added. The total device area is mostly determined by the size of the AMP. By using high refractive index waveguide cores, the spiral dimension can be kept as small as 1 mm$^2$; for instance, a 4-cm spiral of $Er^{III}$-doped alumina has a net gain of 2.3 dB for a pumping power of 10 mW at 1.48 μm and a signal wavelength of 1.53 μm (Polman and Van Veggel, 2004).

The photophysical properties of terphenyl-based acyclic (**22a**) and cyclic hemispherands (**22c**, **22d**, see fig. 27) have been investigated in organic solvents and in KBr pellets (1 wt%) with the purpose of introducing them later in optical amplifiers (Slooff et al., 1998). Absorp-tion cross sections for the 1.54 μm emission, which is quite broad with fwhh = 70 nm, amount to 0.62, 1.1, and 0.93 × 10$^{-20}$ cm$^2$ for [Er(**22a**)], [Er(**22c**)] and [Er(**22d**)], respectively. The best photoluminescence intensities are obtained with the cyclic ligands. The optical gain of the complexes doped into a polymer channel waveguide is on the order of 1.7 dB cm$^{-1}$, while the threshold power is as low as 1.4 mW.

Hybrid organic–inorganic channel waveguides can also be envisaged and the proof of principle has been given for an Er-doped material prepared by using a highly reactive siloxane precursor, methyl-trimethoxysilane or methyl-diethoxysilane, associated with colloidal silica stabilized into tripropylene glycol diacrylate. The $Er^{III}$ $\beta$-diketonate (2,4-pentanedionate) was introduced in 1.6 wt% and buried channel waveguides were made of a three-layer structure deposited by dip-coating on a silicon substrate: a buffer layer, the active guiding layer, and a protective layer. The resulting waveguides were typically from 2 to 10 μm wide and 2.5-cm long. Light is highly confined in these structures and compensation of energy losses was reached (Etienne et al., 2000).

To solubilize $Er^{III}$ in a transparent matrix while minimizing interactions between adjacent metal ions by keeping them sufficiently apart, complex $[Er(NO_3)_3(qb)_3]$ has been designed (see fig. 115) and introduced into PMMA. Polymer thin films have been obtained by spin coating, as well as single-mode waveguides, and their physical and photophysical properties have been investigated versus erbium concentration. With a 980-nm excitation, the intensity of the 1.542 μm emission from erbium increases regularly with doping concentration, up to ten weight percent (wt%), and then decreases, indicating self-quenching. The fluorescence decay significantly deviates from single exponential behaviour at concentration larger than 10 wt% and analysis of the lifetimes of $Er(^4I_{13/2})$ versus concentration yields a quenching concentration (i.e. the concentration at which the actual lifetime is half that for the zero concentration limit) of 13.4 wt%; the zero concentration lifetime amounts to 4.6 ms, while the lifetime at ten weight percent concentration is 3.46 ms (Le Quang et al., 2007).

The widespread distribution of fiber optics built from $Er^{III}$-doped fiber amplifiers has stirred a need for predicting the characteristics of such materials, in particular their gain, noise factor and absorption and emission spectra of erbium. Several models are available, among them a so-called "black-box" model for which a detailed knowledge of the structure of the optical material is not needed. With this model, determination of the gain is a simple one-parameter problem. A recent extension of this model has been proposed in which the "input noise approach" used for calculating the characteristics of active electronic devices has been implemented. This allowed the calculation of the limiting spectral efficiency of information transfer, which is in the range 6.0–6.7 bits per second and per Hz for an erbium amplifier with 20 dB signal-to-noise ratio (Varaksa et al., 2006a; Varaksa et al., 2006b).

## 4.3. *NIR organic light-emitting diodes (OLEDs)*

A landmark in the development of OLED is the finding in 1987 of the bright green emission of aluminum tris(8-hydroxyquinolinate), $[Al(8-Q)_3]$, in thin organic layers (Tang and Van Slyke, 1987). This device has a luminance of 1000 cd m$^{-2}$ below 10 V and a quantum efficiency of 1 photon per 100 electrons injected. Presently, electroluminescent devices can be made of a single layer of a $\pi$-conjugated polymer, such as poly(phenylene–vinylene), PVV, between two electrodes (Kido and Okamoto, 2002). Thin films OLEDs consist of multiple organic and/or metallic layers on an indium–tin oxide (ITO) covered glass deposited by various known methods, plasma deposition, thermal evaporation, Langmuir–Blodgett deposition, or spin-coating from solutions. It is important that the layers are chemically stable
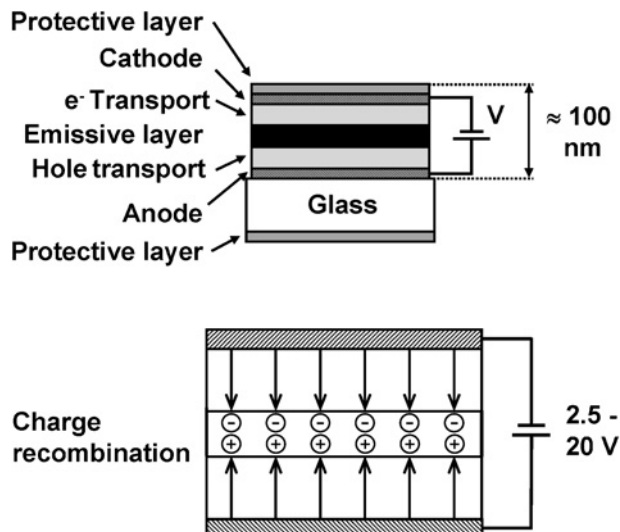
Fig. 116. Scheme of a typical electroluminescent device (OLED).

and highly transparent to the emitted light. The devices can have a single or a triple active layer. The latter case is shown on fig. 116: a voltage bias is applied to the ITO electrodes and electrons and holes are injected in the electron- and hole-transport layers by the cathode and anode, respectively. The voltage bias is not large, but since the layers are very thin (typically a few nm thick) the electric field is in the range $10^5$–$10^7$ V cm$^{-1}$. Therefore, the injected charges migrate against each other, meet and recombine in the emissive layer. The hole-transport layer mainly transports holes within the highest occupied molecular orbital (HOMO) and to a lesser degree within the lowest unoccupied molecular orbital (LUMO). Consequently the corresponding materials should have a high hole mobility and a low ionization potential. Additionally, after charge recombination, the hole-transporting layer should also block the migration of excitons from the emitting layer, that is, it should have higher exciton energy than the emissive layer. Finally, it should also be transparent to the radiation emitted by the emissive layer. Among potential materials are poly-($N$-vinylcarbazole) (PVK) and $N,N$-diphenyl-$N,N$-bis(3-methylphenyl)-[1,1′-biphenyl]-4,4′-diamine (TPD). Electron-transporting materials widely used are 2-(4-biphenyl)-5-(4-$tert$-butylphenyl)-1,3,4-oxadiazole or the tris(8-hydroxyquinolinate)aluminum complex. The charge recombination energy is transferred to the material of the emissive layer, a polymer doped with luminescent centers. In OLEDs, 25% of the excitation energy leads to singlet states and 75% to triplet states. As a consequence, it is desirable that the luminescent centers are good triplet quenchers, which is the case of some transition metal ions and of lanthanide ions. Amazingly the exploitation of the triplet state energy was ignored until 1998 (Baldo et al., 1998) but is now a major goal in the development of these lighting devices. A main challenge in OLEDs is the design of efficient, white-emitting diodes and a recent example demonstrated the feasibility of

a lanthanide-based device using up-conversion to produce simultaneous emission of Tm[III] at 475 nm, Er[III] at 525, 550, and 675 nm, as well as of Eu[III] at 590 and 620 nm, upon excitation at 980 nm. The device consists in a sol–gel derived thin film made with Ln[III]-doped lanthanum fluoride nanoparticles (Ln = Eu, Er, Tm, Yb); the Yb[III] ions serve as Er[III] sensitizer (Sivakumar et al., 2005). Here we concentrate on NIR emission and the following descriptions are classified according to the Ln[III] luminescent ion. In several instances, the emissive layer and the electron-transporting layers are combined into a single thin film built up from the luminescent complex. The performances of OLEDs are tested by measuring the current density–voltage and the luminance–voltage characteristics. The turn-on voltage is defined as the voltage needed to produce a luminance of 1 cd m$^{-2}$. The luminance increases with increasing bias voltage up to a certain value from which saturation occurs leading ultimately to a decrease in luminance. Finally, the external electroluminescence quantum efficiency is defined as the ratio of the emitted photons to the number of charge carriers generated in the device.

### 4.3.1. *Neodymium OLEDs*

The feasibility of room-temperature Nd[III] electroluminescence was demonstrated on a doped gallium arsenide semiconductor; the external quantum yield of $5 \times 10^{-7}$ is close to the one exhibited by similar Er[III]-doped LED, but about three orders of magnitude smaller than for Yb:InP (Chang, 1995). To our knowledge, the first Nd[III]-containing three-layer OLED has been proposed by S. Yanagida and collaborators. The 50-nm thick hole-transporting layer is a diamine derivative, TPD, the electron-transporting layer (50 nm thick) is [Al(8-Q)$_3$], and the emitting layer (25 nm thick) contains the ternary $\beta$-diketonate [Nd(dbm)$_3$bath], where bath is monobathophenanthroline (fig. 117). The device not only emits the characteristic Nd[III] light with a threshold voltage of about 15 V, but also a pale bluish-green luminescence arising from [Al(8-Q)$_3$]. The luminescence properties of the device are very sensitive to the layer thickness. When the emitting layer is thinner than 15 nm, the dominant emission is from [Al(8-Q)$_3$], for instance. Moreover, the device degrades fairly rapidly upon illumination at 390 nm (Kawamura et al., 1999).

A similar ITO/TPD (see fig. 117) OLED was built, with [Nd(8-Q)$_3$] as luminescent active layer; the device has an operative voltage of 30 V, corresponding to a current density of 78 mA cm$^{-2}$; the threshold voltage is 13 V ($\approx$0.23 mA cm$^{-2}$) and no visible luminescence is emitted (Khreis et al., 2000).

Another early system for Nd[III] OLED relies on a tetrakis(pyrazolonate) complex the negative charge of it is compensated by an hemicyanine-based cation (fig. 118), (**130**)[Nd(**129**)$_4$]. The complex has very good film-forming as well as second-harmonic generation properties (Pavier et al., 1996). Electroluminescence of 15-Langmuir–Blodgett monolayers deposited on ITO and fitted with an Al electrode occurs with voltage thresholds in the range 4–7 V. The corresponding complex with Dy[III] also displays electroluminescence. These materials can be used to produce OLEDs (Weaver et al., 1996).

9-Hydroxyphenalen-1-ones have been employed as sensitizer ligands because they are soluble in a wide range of organic solvents and possess adequate photophysical properties. For instance, the isc efficiency is nearly equal to one, due to the $\alpha, \beta$-conjugated carbonyl groups.
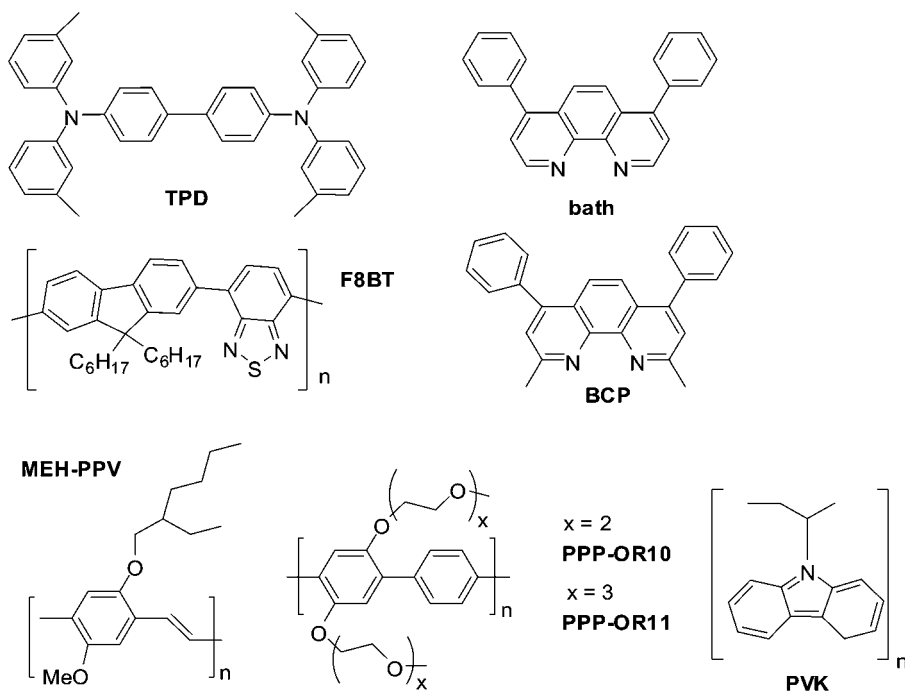
Fig. 117. Formula of various hole- and electron-injection and transport materials, as well as of the ancillary ligand bath used in Ln$^{III}$-containing OLEDs.
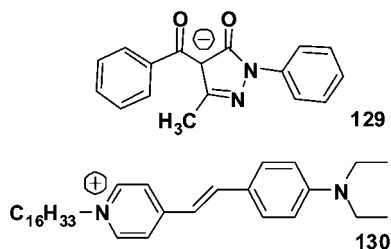


Fig. 118. Pyrazolonate ligand and hemicyanine-based counterion.

Doped PVK thin films display intense electroluminescence from the Nd$^{III}$ ion and OLED devices fabricated with this active material have a maximum irradiance of 8.5 nW mm$^{-2}$ and an external quantum yield of 0.007%. Further refinement of the processing will hopefully lead to a still better optimization of the performance of these Nd$^{III}$-doped polymeric emissive layers (O'Riordan et al., 2006).

The lissamine-sensitized terphenyl Nd$^{III}$ chelate [Nd(**60d**)] (fig. 59) has been introduced in the host polymer F8BT (fig. 117) and the latter is efficiently quenched by the chelate. Lis-

samine acts as a charge trapping site owing to its low energy gap between HOMO and LUMO and, moreover, has a fast isc rate ($4.4 \times 10^8$ s$^{-1}$). A device made of ITO electrodes, poly(3,4-ethylene dioxythiophene), PEDOT, doped with polystyrene sulfonate, PSS, as hole injection layer, and of the Nd$^{III}$ chelate in F8BT as emissive layer shows intense electroluminescence; F8BT has very high photoluminescence efficiency in the solid state ($\approx$60%), a good solubility in common organic solvents, and a high electron affinity ($\approx$2.9 eV), which facilitates electron injection. Finally, there is considerable overlap between its emission spectrum and the absorption spectrum of Nd$^{III}$, so that efficient Förster-type energy transfers are operative in this doped material. For a 2 mm$^2$ area and an 80-nm thick active layer, the threshold voltage is around 15 V at $\approx$0.01 cd m$^{-2}$. The electroluminescence is about four-fold larger than photoluminescence of the lissamine-functionalized chelates in polycarbonate waveguides (Slooff et al., 2001).

The $\beta$-diketonate [Nd(dbm)$_3$bath] (see figs. 41 and 117) has a photoluminescence quantum efficiency of 0.33% in dmso-$d_6$ solution at a 1 mM concentration. It has been introduced as the active 20-nm thick layer into an OLED having an ITO electrode with a sheet resistance of 40 $\Omega$ cm$^{-2}$, TPD as hole transporting layer with a thickness of 40 nm, and bathocuproine (BCP) (40 nm) as the electron injection and transporting layer (see fig. 117). The electroluminescence spectrum is identical to the photoluminescence emission; the luminescence intensity at 1.07 µm versus current density curve deviates from linearity from approximately 10 mA cm$^{-2}$ on, due to triplet–triplet annihilation. Near-IR electroluminescent efficiency $Q_{EL}$ has been determined by comparison with [Eu(dbm)$_3$bath] for which the total photoluminescence quantum yield in dmso-$d_6$ at a concentration of 1 mM is $Q_{PL} = 6\%$ upon ligand excitation, while its external electroluminescence efficiency is 0.14% (3.2 cd m$^{-2}$ at 1 mA cm$^{-2}$):

$$Q_{EL} = \eta_e \cdot \eta_r \cdot Q_{PL}, \tag{44}$$

where $\eta_e$ is the fraction of emitted photons coupled out of the device and $\eta_r$ is the fraction of injected charge carriers that form excitons. Therefore, for similar devices:

$$Q_{EL}(\text{Ln}) = Q_{EL}(\text{Eu}) \cdot \frac{Q_{PL}(\text{Ln})}{Q_{PL}(\text{Eu})}. \tag{45}$$

In the case of the [Nd(dbm)$_3$bath] OLED, the estimated $Q_{EL}$(Nd) amounts to $7 \times 10^{-5}$ neglecting deactivation effects at the metal cathode; this figure is low but larger than the quantum efficiency of the Nd:GaAs LED, $5 \times 10^{-7}$ at 77 K (Kawamura et al., 2001).

Electroluminescence of [Nd(TPP)CoP$^{Me}$] (see figs. 18 and 19) dispersed in a polystyrene host in a 2:1 (complex:host) ratio has also been reported (Kang et al., 2003b).

### 4.3.2. *Erbium OLEDs*

The systems of interest here entail either 8-hydroxyquinolinate, $\beta$-diketonate, or porphyrin complexes. Upon excitation at 351 nm, tris(8-hydroxyquinolate) [Er(8-Q)$_3$] shows a broad emission band at room temperature in the range 380–750 nm, with a maximum at 600 nm, which is red-shifted by about 80 nm with respect to group III (e.g. Al$^{III}$) quinolinates. In addition, a bright 1.54-nm emission is seen upon excitation with an argon laser at 457 nm the intensity of which varies linearly with the excitation power in the range 1–100 mW (Gillin

and Curry, 1999). The same bands, although narrower, are emitted by a multi-layer device containing an ITO-coated glass with a sheet resistance of 20 $\Omega \, cm^{-2}$, a 60-nm thick TPD hole-transporting layer (see fig. 117), a 60-nm film of [Er(8-Q)$_3$], and an aluminum electrode, upon excitation by a driving voltage of 25 V. Interestingly, the blue electroluminescence is considerably weaker when compared to the one observed under the same operating conditions for OLEDs with groups III chelates. The current–voltage characteristics of the Er-containing OLED point to a relatively high turn-on voltage of 12 V, which is indicative of poor injection at the contact electrode. The device appears to be robust, not breaking down under reverse voltages up to −30 V (Curry and Gillin, 1999). The use of silicon as the hole injection contact is also feasible (Curry et al. 2000, 2001). On the other hand, the electroluminescent properties of the Er-containing OLED are dependent on the deposition conditions (Curry and Gillin, 2000). As for many similar devices, a decrease in efficiency with increasing current is explained by the quenching of the excited lanthanide ion state with injected charge carriers (polarons). Triplet–triplet annihilation plays an important role in this process (Curry and Gillin, 2001). [Er(8-Q)$_3$]-doped monodisperse microparticles ($\approx$20 μm) seem to have some potential for OLED devices as well, besides organic red-emitting dyes (Suzuki et al., 2004; Suzuki, 2004).

A single-layer OLED with [Er(acac)$_3$phen] doped into a 80-nm thick film of PVK (see fig. 117) prepared by spin-coating and deposited on an ITO electrode, and with a 100-nm lithium-doped (0.1%) aluminum cathode has also been tested and shows an onset voltage of about 12 V for electroluminescence (Sun et al., 2000). [Er(dbm)$_3$bath] has a photoluminescence quantum yield of 0.007% in dmso-$d_6$ at 1 mM concentration; the OLED based on this compound and similar to the one described above for Nd$^{III}$ has a NIR external electroluminescence efficiency of $1 \times 10^{-6}$ (Kawamura et al., 2001).

Another approach takes advantage of the high degree of spectral overlap between the emission band of MEH-PPV (fig. 117) and the Q-absorption bands of tetraphenylporphyrin (TPP) to transfer energy from the host polymer to [Ln(TPP)(acac)], Ln = Er, Yb, or between the fluorescence of PPP-OR11 (fig. 117) and the Soret band of the same complexes. Near-IR electroluminescent devices were fabricated starting with an ITO glass electrode coated with a special hole-transporting layer; the polymer:[Ln(TPP)(acac)] (5 mol%) blend was then spin-coated from a 1% solution in toluene. After drying under vacuum, a 5-nm thick layer of calcium, followed by a 150-nm layer of aluminum were deposited and the whole OLED was encased in epoxy to minimize exposure to air, i.e. oxygen and moisture. Erbium electroluminescence is clearly seen when a 13 V voltage is applied for both MEH-PPV (Harrison et al., 2001) or PPP-OR11 devices (Schanze et al., 2003).

### 4.3.3. Ytterbium OLEDs

Proposed Yb$^{III}$-containing OLEDs contain either $\beta$-diketonates or porphyrin complexes. With respect to the first class of compounds, [Yb(dbm)$_3$bath] (see figs. 41 and 117), which has a photoluminescence quantum yield of 1.4% in dmso-$d_6$ at a 1 mM concentration, has been introduced into a three-layer electroluminescent device, TPD (50 nm thick)/[Yb(dbm)$_3$bath] (25 nm)/[Al(8-Q)$_3$] (50 nm), with ITO and Mg:Al (10:1) electrodes. Bright luminescence is recorded with a threshold voltage of 15 V and only saturates when the voltage reaches 24 V.

One drawback of the device though is the poor charge injection ability of the Yb[III] diketonate, so that at 20 V bias, the current density only reaches 9.7 mA cm$^{-2}$ (Kawamura et al., 2000). Replacing [Al(8-Q)$_3$] with BCP increases the efficiency of the device, although it shows a more marked decrease in emitted intensity and electroluminescence efficiency with current density, when compared to the corresponding Nd[III] OLED (see above). For instance, the current densities giving 10% of the initial efficiency are 55 and 230 mA cm$^{-2}$ for Yb[III] and Nd[III], respectively. On the other hand, the external electroluminescent efficiency is the largest for Yb[III] ($3 \times 10^{-4}$) in comparison with Nd[III] ($7 \times 10^{-5}$) and Er[III] ($1 \times 10^{-6}$) (Kawamura et al., 2001). Another design using the same emissive complex, ITO/TPD (40 nm)/[Yb(dbm)$_3$bath]:TPD (weight ratio 1:1, 40 nm)/[Yb(dbm)$_3$bath] (60 nm)/Ag:Mg (150 nm) has a onset voltage of about 6 V while saturation starts around 12 V, corresponding to a current density of about 250 mA cm$^{-2}$; in fact the maximum emission efficiency is in the range 1–10 mA cm$^{-2}$ (Hong et al., 2001b). Similarly to the Nd[III] OLED, Yb[III] tris(hydroxyquinolinate) emissive material was used in an ITO/TPD/[Yb(8-Q)$_3$]/Al device, in which the luminescent layer was deposited on ITO by sublimation at $10^{-6}$ mbar pressure. The electroluminescence spectrum is turned on at current densities above 5 mA cm$^{-2}$, which corresponds to a drive voltage of 17 V; it displays a sharp peak at 977 nm on top of a broader feature (Khreis et al., 2001). Further treatment of the ITO layer by oxygen plasma may considerably lower the turn-on voltage, as observed for the corresponding devices with Nd[III] (Khreis et al., 2000) and Er[III] (Curry and Gillin, 1999).

The performances of two Yb[III] complexes, [Yb(dbm)$_3$phen] and [Yb(dnm)$_3$phen] (dnm is dinaphthoylmethanate) have been compared in OLEDs based on two blue emitting oligoether-functionalized poly($p$-phenylenes), PPP-OR10 with $Q_{PL} = 44\%$ and PPP-OR11 with $Q_{PL} = 92\%$ (fig. 117). The structure of the electroluminescent devices comprises an Al:Ca electrode, the emissive complex (1–20 mol%): PPP-OR11 layer, a hole-injection film of poly(3,4-ethylene dioxythiophene), PEDOT doped with polystyrene sulfonate, and an ITO glass electrode. Quenching of the polymer fluorescence as well as the NIR irradiance are clearly more important with dnm than with dbm. The turn-on voltage is only 5 V for 10 mol% [Yb(dnm)$_3$phen] doped into PPP-OR11, but the emissive layer must contain more than 10 mol% of the dnm complex for the NIR emission to be larger than the blue polymer fluorescence. Depending on the conditions used, the external quantum efficiencies are between $10^{-5}$ and $10^{-4}$, which is comparable to the previous device (Kang et al., 2003a).

On the other hand, external electroluminescence efficiencies about ten times larger are obtained with the PPP-OR11-based OLED doped with 5 mol% [Yb(TPP)CoP$^{Me}$] and which has an onset voltage of 6 V: at 7 V, $Q_{EL}(Yb) = 4 \times 10^{-4}$ (Schanze et al., 2003). This device has better characteristics than the one based on [Yb(TPP)acac] (Harrison et al., 2001). Possible reasons are the higher photoluminescence quantum yield of [Yb(TPP)CoP$^{Me}$] (3.2% in CHCl$_3$) compared to [Yb(dnm)$_3$phen] (0.1% in the same solvent), an improved host fluorescence/dopant absorption spectral overlap, and an enhanced carrier transport through the porphyrin (Kang et al., 2003a). The porphyrinate complex has been blended into polystyrene and PVK at concentrations of 50–80 wt%. The devices with the first polymer have a turn-on voltage of only 4 V and near-IR irradiance of 0.2–0.6 µW cm$^{-2}$ for bias voltages between 10 and 15 V. The external electroluminescence efficiency peaks at about $10^{-3}$ for very low

current density, on the order of 1 mA cm$^{-2}$, and with the lowest loading of the emissive complex (50 wt%); as soon as current density is increased the efficiency drops to a constant value of $2 \times 10^{-4}$, a phenomenon likely due to saturation effects caused by the long 50 μs lifetime of Yb($^2F_{5/2}$). Conversion of electron–hole pair recombination events into luminescence is estimated to approximately 10% in these devices. Replacing polystyrene with PVK does not alter the characteristics of the OLEDs, meaning that charge transport in both devices is dominated by the [Yb(TPP)CoP$^{Me}$] complex, regardless of its electroactive host (Kang et al., 2003b). The same authors have fabricated OLEDs based on [Yb(TPP)CoP$^{Me}$] blended into PPP-OR11 and investigated energy-transfer processes in the corresponding devices from the polymer to the luminescent complex. If a dipole–dipole transfer is assumed to be the main operative mechanism, the donor–acceptor distance for 50% transfer amounts to 4.6 nm. Light absorbed by PPP-OR11 produces a singlet exciton on the host which transfers energy on the TPP complex and generates the TPP $^1\pi\pi^*$ state; in turn, the latter rapidly decays by isc to the TPP $^3\pi\pi^*$ state, followed by transfer onto the 4f-centered excited state. The OLED tested, ITO/PEDOT-PSS/PPP-OR11:[Yb(TPP)CoP$^{Me}$]/Ca:Al, turns on between 4 and 5 V bias voltage and the electroluminescence intensity peaks at 9 V. The NIR irradiance at 9 V depends on the doping concentration and ranges from 1.6 (5 mol%) to 10.0 (15 mol%) μW cm$^{-2}$ at current densities of 100 and 315 mA cm$^{-2}$, respectively. At a current density of 100 mA cm$^{-2}$, the external electroluminescence efficiency is around 10$^{-4}$ for doping concentrations equal or larger than 10%. The efficiency of the electron–hole recombinations converted into light is between 1 and 10%. The authors explain these values by the hole injection being more efficient and the hole transport more rapid compared to electron injection and transport, henceforth a mismatch detrimental to the overall efficiency of the OLED. The ability of non-conjugated polymers such as PMMA to produce OLEDs with similar properties has been demonstrated, which opens up opportunities for lowering the cost of the devices with these inexpensive polymers (Harrison et al., 2004).

### 4.3.4. OLEDs with other lanthanide ions

Both metal-centered visible (608 nm, $^1D_2 \rightarrow {}^3H_6$) and near-IR (890 nm, $^1D_2 \rightarrow {}^3F_2$; 1.015 μm, $^1D_2 \rightarrow {}^3F_3$; 1.065 μm, $^1D_2 \rightarrow {}^3F_4$; 1.55 μm, $^1D_2 \rightarrow {}^1G_4$) light is emitted by [Pr(dbm)$_3$bath] in bi- and tri-layer devices containing TPD, in addition to broad exciplex fluorescence from the polymer host. The visible emission at 608 nm is favored when the concentration of the Pr$^{III}$ complex is increased and NIR emission starts when the voltage bias is 8 V corresponding to a current density of 4.5 mA cm$^{-2}$ (Hong et al., 2001a). When the Ho$^{III}$ β-diketonate is doped into TPD, near-IR luminescence is observed at 980 nm ($^5F_5 \rightarrow {}^5I_7$), 1.20 μm ($^5I_6 \rightarrow {}^5I_8$), and 1.50 μm ($^5F_5 \rightarrow {}^5I_6$), the turn-on voltage being around 10 V (Zang et al., 2004b). Similarly, the 1.2 μm emission was observed with the PPP-OR11:[Ho(TPP)CoP$^{Me}$] OLED (Schanze et al., 2003). Thulium electroluminescence at 800 nm ($^3F_4 \rightarrow {}^3H_4$) and 1.4 μm ($^3F_4 \rightarrow {}^3H_6$) is generated in OLEDs containing one of the β-diketonates, [Tm(dbm)$_3$phen], [Tm(dbm)$_3$bath], [Tm(acac)$_3$phen], or [Tm(acac)$_3$bath]. Electroluminescence from the latter two complexes is, however, very weak because the triplet state of acetylacetonate lies at about 25 500 cm$^{-1}$, resulting in a preferred population of the $^1G_4$ level which radiatively relaxes by emitting 480 nm photons. In the case of dbm, the en-

ergy of the triplet state is smaller than the energy of the $^1G_4$ level and the $^3F_{4,3,2}$ levels are populated by the energy transfer process, despite a relatively large energy mismatch. Simultaneous introduction of [Tm(dbm)$_3$bath] and [Er(dbm)$_3$bath] in the emissive layer resulted in a broad band emission extending from 1.4 to 1.6 μm, an interesting property for applications in optical communications (Zang et al., 2004a).

### 4.4. *Analytical applications*

In addition to the elemental analyses performed with $\beta$-diketonates and mentioned in section 3.2.1, NIR luminescent lanthanide complexes start to be used as responsive probes for the analysis of cations and anions.

Ligand **131** contains both cryptate and crown ether binding units. It reacts with neodymium triflate to give a 1:1 cryptate [Nd $\subset$ **131**]$^{3+}$ exhibiting NIR luminescence upon excitation at 355 nm. The lifetime of the Nd($^4F_{3/2}$) level is 347 and 711 ns in methanol and methanol-$d_4$, respectively, which translates to $q_{MeOH} \approx 0$ using eq. (10b). When barium ions are added to a solution of this complex in acetonitrile, the intensity of the 1.06 μm emission band is reduced substantially, while the lifetime of the Nd($^4F_{3/2}$) level remains unchanged at about 470 ns. The Nd$^{III}$ ion is therefore not displaced from the cryptand cavity, while its luminescence is modulated by the presence of the Ba$^{2+}$ ions bound by the crown ether (Coldwell et al., 2006).

Anion sensing using visible-emitting lanthanide probes has proven successful (Tsukube et al., 2006) and this work is now being extended to Yb$^{III}$ probes, particularly for the detection of thiocyanate. The latter is the principal metabolite of cyanide anion and exists in human serum, saliva, and urine. The luminescent probe is a complex of hexadentate tetrakis(2-pyridylmethyl)ethylenediamine (tpen, see fig. 119) which bears two water molecules, [Yb(tpen)(H$_2$O)$_2$](Otf)$_3$. In absence of anion coordination, the 980-nm luminescence is quenched, but the replacement of the water molecules with thiocyanate or other anions such as acetate, nitrate or halogenides removes the quenching, which makes the complex a responsive probe. The largest effect (a six-fold increase in luminescence) is obtained for thiocyanate, followed by acetate and nitrate (3.5-fold) and chloride (two-fold).

A more elaborate sensor consists in a dendrimeric-like complex featuring eight quinoline units **132** (fig. 119, bottom), allowing the complexation of four Yb$^{III}$ ions and yielding a 8.5-fold increase in the 980-nm emission upon thiocyanate complexation (Tsukube and Shinoda, 2006).

Asymmetrically substituted cyclen derivatives (**133**, see fig. 119) have been developed to prepare a series of photoactive donor–acceptor quencher triads based on Nd$^{III}$ and Yb$^{III}$ complexes. Two successive nitrogen atoms of the cyclen scaffold are fitted with a rhodamine B antenna and a nucleoside quencher serving as chelator for the metal ion. This ensures close proximity of the antenna-quencher pair, facilitating their interaction. The rhodamine antenna can be excited in its whole absorption range, from 355 to 700 nm, which is a definite advantage. The remaining two nitrogen atoms are alkylated with coordinating arms to enhance the stability of the complexes. The resulting complexes, [Ln(**133-B**)]Cl$_3$ (Ln = Nd, Yb; B = U, A), display essentially no luminescence in methanol, because the uridine or adenosine group quenches the emission from rhodamine B, preventing energy transfer onto the 4f ion. When
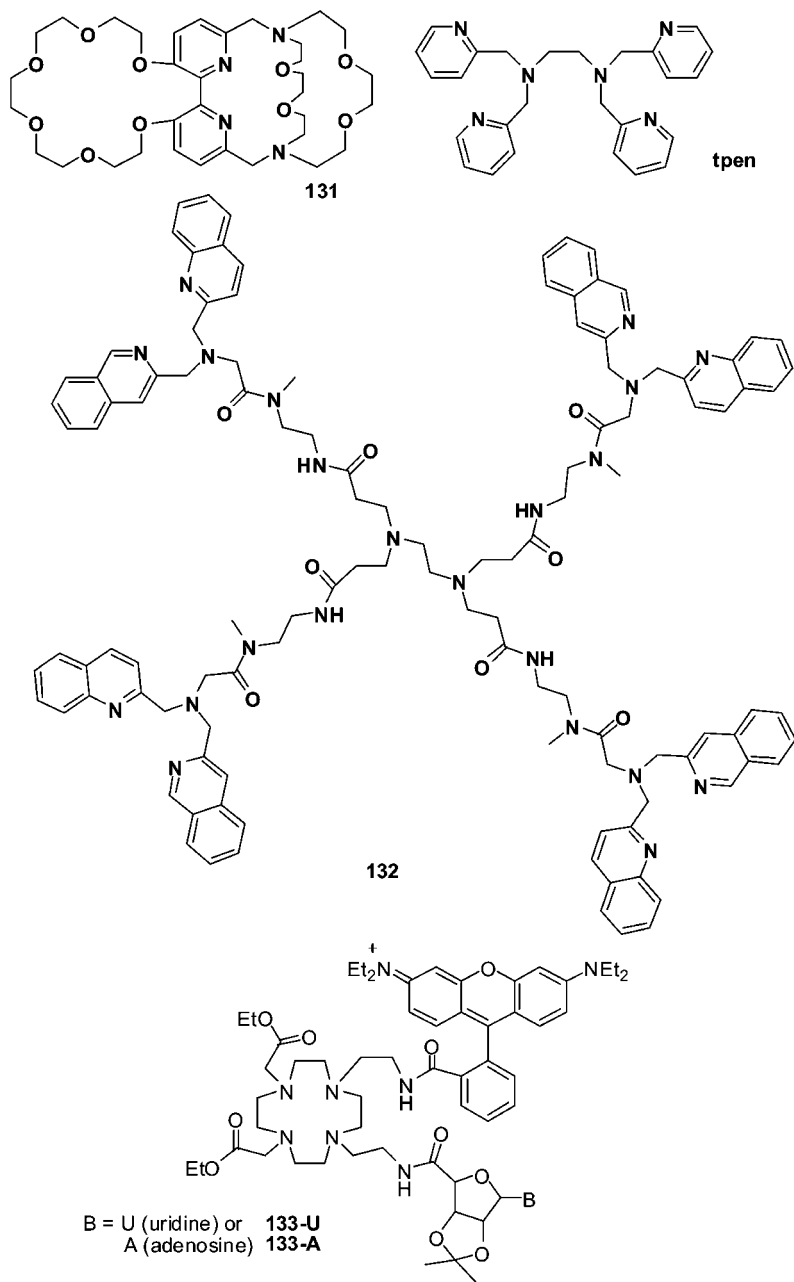
Fig. 119. (Top) Crown-cryptand for the analysis of barium and ethylenediamine ligand for anion sensing (tpen). (Bottom) Dendrimer-like ligand for anion sensing.

a complementary nucleoside base, uridine or adenosine, was added to the solution, quenching of the rhodamine fluorescence decreased and energy transfer between rhodamine and the Ln$^{III}$ ion was restored. For the Nd complexes this also translated into a longer lifetime. For instance, in the case of [Nd(**133-A**)]$^{3+}$, $\tau(^4F_{3/2})$ increased from non-measurable (too short) in absence of complementary base to 0.23 μs in presence of one equivalent of complementary base. The change in lifetime was more marked when uridine was present (increasing from 0.09 to 0.47 μs). For Yb$^{III}$ complexes, an opposite trend was observed and has been attributed by the authors to the susceptibility of Yb$^{III}$ to reduction by the added nucleoside (Supkowski et al., 1999). In conclusion, this work demonstrates the possibility of regulating the extent of energy transfer between the antenna and the lanthanide by an external chemical stimulus (Borbas and Bruce, 2006).

### 4.5. *Biomedical applications*

Although bioanalyses and bio-imaging have been the driving force of many investigations during the last ten years, very few systems have made it up to real applications at least as far as NIR luminescence is concerned (Faulkner et al., 2005). On the other hand, the use of CD spectroscopy of Yb$^{III}$ for determining the configuration of chiral diols (Di Bari et al., 2002; Tsukube and Shinoda, 2002) or biological substrates is well established. We have also described the CPL properties of some Yb$^{III}$ complexes with cyclen derivatives in section 3.1.4. There are two major applications for which NIR probes are being developed: luminescent immunoassays and diagnosis of tumors (cell imaging). Immunoassays rely on a biochemical reaction between an antigen (analyte) and a specific antibody. In luminescent assays, the latter is labeled by a lanthanide chelate. There are two types of luminescent immunoassays, heterogeneous and homogeneous (fig. 120). In the first ones, the Ln-labeled antibody is reacted with the antigen (step 1), the non-reacted reagents are washed, and the pH is lowered to de-complex the Ln$^{III}$ probe before re-complexing it with another chelating agent (step 2), inserting it into a micelle and reading the luminescence intensity in time-resolved mode. Homogeneous assays necessitate less handling: the antigen is reacted with two different but specific antibodies, one labeled with the Ln$^{III}$ luminescent chelate and the other with an (organic) acceptor. Upon excitation (often by UV light), energy is transferred first from the triplet state of the chelating agent onto the Ln$^{III}$ ion and subsequently onto the acceptor molecule which emits characteristic light. The resonant energy transfer only occurs when the Ln$^{III}$ chelate (the donor) and the acceptor lie at a reasonably short distance, i.e. when they are attached to the same antigen molecule, so that there is no need to separate the various chemical species in solution before reading the luminescence intensity. The same principle can be used to detect protein-protein interactions and DNA hybridization (Bünzli and Piguet, 2005). The most usual Ln$^{III}$ probes used to date are visible-emitting Ln$^{III}$ ions with detection limit in time-resolved mode as low as $10^{-15}$ M (Matsumoto and Yuan, 2003). Since Yb$^{III}$ is the NIR-emitting ion having usually the best quantum yield, all the biomedical applications published to date use this ion. One incentive for trying to use NIR-emitting probes rather than visible-emitting ones is the fact that the former may be more easily excited by visible light, instead of UV-light which may damage biological molecules.
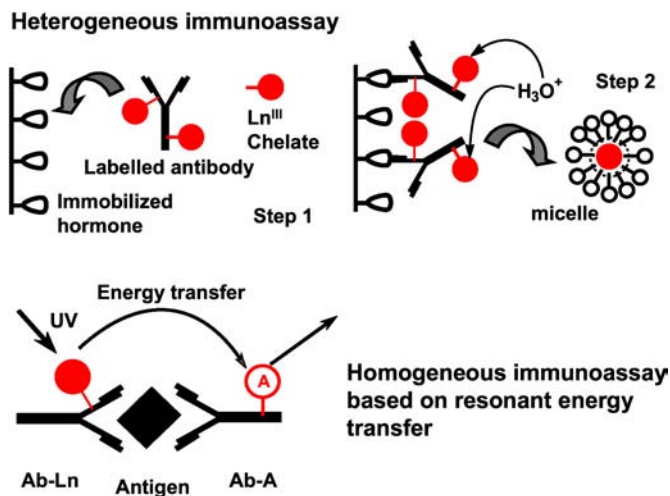
Fig. 120. Principle of heterogeneous (top) and homogeneous (bottom) immunoassays.

To allow coupling with biological material, the fluorescein-substituted polyaminocarboxy-late ligand $H_4$**73a** has been functionalized with an isothiocyanate group, leading to $H_4$**73b** (see fig. 64). The latter is reactive towards amine functions, allowing easy coupling to pro-teins. Avidin was chosen for a proof of principle (Werts et al., 2000b). This glycoprotein of molecular weight 68 kDa is synthesized in the hen oviduct and represents about 0.05% (w/w) of the total protein content of the hen egg white. The great affinity of avidin for bi-otin ($K_{assoc} = 10^{15}$ M) results in a great number of applications in biochemistry, immunoas-says, receptor and histochemical studies, bacteriophage inhibitions, for instance. Excitation at 514 nm of the avidin-[Yb(**73b**)] conjugate containing on average 3.2 labels per protein leads to metal-centered luminescence with a quantum yield and a lifetime (2.0 µs) equal to those of [Yb(**73a**)]. The quantum yield drops by 20% however when the number of labels per protein is increased to 5.2. The authors point out that the Yb$^{III}$ label compares favorably with the Eu$^{III}$ luminescent cryptate used in a commercial diagnostic and for which the product $\varepsilon \cdot Q$ amounts to 100 M$^{-1}$ cm$^{-1}$ when light from a nitrogen laser (337 nm) is used for excitation: the avidin-[Yb(**73b**)] conjugate achieves the same figure for excitation at 514 nm. The robustness of the Yb$^{III}$ label was also tested in a known medical pregnancy test making use of a heterogeneous immunoassay of human chorionic gonadotropin (hCG). The analyte containing 5 international units of hCG was sandwiched between an anti hCG antibody immobilized on a nitrocellulose membrane and an antibody labeled with [Yb(**73b**)]. Luminescence was observed with a scan-ning near-IR microscope and clearly revealed the spots corresponding to a positive test. On the other hand, an attempt to conjugate Nd$^{III}$- and Er$^{III}$-doped LaF$_3$-based nanoparticles with avidin proved unsuccessful, since no metal-centered luminescence was observed (Diamente et al., 2006).

Protein concentration in solutions and in physiological fluids such as blood plasma can be determined by the changes occurring in the NIR fluorescence intensity during the highly specific reaction between an antigen and an antibody in Langmuir–Blodgett (LB) films. An immunosensor based on LB films of ytterbium tetraphenylporphyrinate, [Yb(TPP)(X)] (the nature of X is not specified in the article) has been proposed by G.K. Chudinova and the antigen–antibody reaction tested used rabbit immunoglobulin G (IgG), which is a polyclonal antibody against human serum albumin (HSA). IgG was labeled with benzoyltrifluoroacetone isothiocyanate, while HSA was conjugated with [Yb(TPP)(X)]. Labeled IgG was mixed with a lipid (phosphatidylcholine), a monolayer produced and transferred onto a quartz plate coated with stearic acid. Depending on the number of stearic acid layers, the working surface is either polar (10 layers) or non-polar (11 layers). The interaction between the immobilized and labeled IgG and the HSA-[Yb(TPP)(X)] conjugate results in an amplification of the $Yb^{III}$ luminescence intensity due to energy transfer from benzoyltrifluoroacetone and the non-polar system gives the best results. In fact, due to concentration quenching, the luminescence intensity increases when the concentration of the conjugate decreases from $10^{-7}$ to $10^{-11}$ M. The sensitivity achieved by the sensor for protein detection in blood plasma is $10^{-11}$ M. As a comparison, enzyme-linked immunosorbent assays (ELISA) have a detection limit of $10^{-9}$ M and require a much longer reaction time, 2 h versus 6 min. In addition to serum albumin, the immunosensor described here can be adapted to the detection of other proteins, provided that the corresponding specific antibody can be immobilized in an LB film (Nagovitsyn and Chudinova, 2002).

We would also like to mention the elegant technology proposed by a group from Leiden University who has developed a luminescent reporter for the sensitive detection of antigens in tissue sections or on cell membranes, although it does not use NIR luminescence but rather NIR excitation followed by up-conversion. It consists of phosphor microcrystals (0.2–0.4 μm) made of yttrium oxysulfide doped with two different lanthanides exhibiting strong emission in the visible (blue, green, and red). The microparticles are surface-labeled with avidin or antibodies and can bind specifically to antigens on intact cells or in tissue sections. The phosphor microparticles exhibit visible luminescence by up-converting infrared to visible light. The method is termed up-converting phosphor technology (UPT) and has been tested on the prostate-specific antigen in tissue sections and the CD4 membrane antigen on human lymphocytes (Zijlmans et al., 1999), as well as for various other assays (Kuningas et al., 2006).

The possibility of using $Yb^{III}$ luminescence from porphyrinate complexes for the diagnosis of tumors has been described in 1989 already, but does not seem to have been followed by practical applications (see section 3.1.1, fig. 11). The affinity of porphyrin for cancer cells increases when metalloporphyrin-albumin conjugates are used and therefore, [Yb(H$_3$**4c**)(im)$_2$] (see fig. 11, im is imidazole) has been conjugated with bovine serum albumin (BSA) which contains free amino groups from lysine residues located at its surface. Conjugation was achieved in two steps, the first being the preparation of the succinimide ester of the porphyrinate under anhydrous conditions. The second step involved conjugation with the protein in water–organic medium at pH 9–9.3. The number of porphyrin molecules per protein is in the range 5.4–6.6. With respect to [Yb(H$_3$**4c**)(im)$_2$], which has a quantum yield of 0.6% in

water at pH 9.2 and at a concentration of 0.1 M, which doubles in Triton X-100 micelles, the fluorescence of the BSA conjugate is three-fold larger (Chudinov et al., 2004).

## 5. Comparison of the chromophores
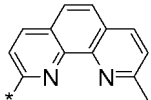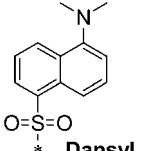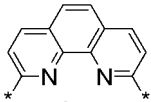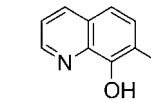
In order to evaluate the efficacy of the chromophores used by various authors for the sensitization of the NIR emission of $Ln^{III}$ ions, the photophysical properties, lifetimes and quantum yields, of the complexes described in the previous sections are listed in table 21 for $Nd^{III}$, table 22 for $Er^{III}$, and table 23 for $Yb^{III}$. Within a table, data are listed in order of increasing excitation wavelength. *Only ligands substituted by a specific chromophore are listed in these tables*. That is for instance, parent calix[n]resorcinarenes and calix[n]arenes are not included since relevant data are given in tables 7 and 8. The same remark is valid for simple tris($\beta$-diketonates) for which quantitative data are listed in figs. 42, 45, and 46, tables 10 and 11, as well as for triphenylmethane dyes (tables 14 and 15).

### 5.1. *Note on quantum yields*

Complete data are not available for all the chromophores. Moreover, one has to exercise some care with quantum yield data. They are among the most difficult photophysical parameters to determine experimentally and require adequate standards when a comparative method is used, which are not always easily at hand as far as NIR luminescence is concerned. It is of course essential that the same detector is used for measuring the luminescence from the standard and from the unknown solution. If these two solutions are not in the same solvent, the refractive index correction has to be applied (Chauvin et al., 2004). Sometimes all the NIR bands of $Nd^{III}$ are not measured because of detector response: few detectors are able to measure simultaneously the three $^4F_{3/2} \rightarrow {}^4I_J$ transitions ($J = 13/2, 11/2, 9/2$), so that *partial quantum yields* are given taking into account only one or two transitions. There is also some confusion about the nature of the quantum yield and a clear distinction has to be made between the overall quantum yield obtained upon ligand excitation and the intrinsic quantum yield obtained upon direct metal-ion excitation (see eq. (11)). Henceforth all the quantum yields estimated using lifetime measurements are intrinsic quantum yields. Moreover, the value of the radiative lifetime is not a constant for a given lanthanide ion and it varies depending on the compound and emitting level. It should therefore be calculated from eq. (17) and not taken from "literature data". Intrinsic quantum yields estimated in this way are highly susceptible to bear larger errors.
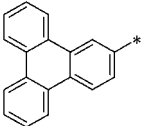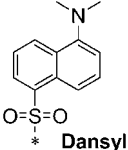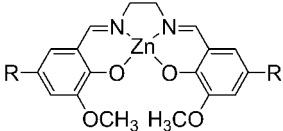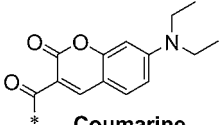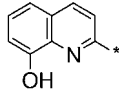
The best procedure for quantum yield determination is the absolute method of Wrighton, using an integration sphere (de Mello et al., 1997; Wrighton et al., 1974) and which is operative for both powdered samples and solutions (Gumy and Bünzli, 2006). In any case, whether a comparative or absolute method is used, excellent instrumental functions should be at hand to correct the measured spectra. These functions should be re-determined often, especially if excitation is in a spectral range in which the lamp has a low luminance or if the emission lines fall in a low-response range of the detector. In photon counting mode, saturation of the

<div align="center">

Table 21

Photophysical properties of Nd$^{III}$-containing compounds

</div>

| Nd | | Experimental conditions | | | | | |
|---|---|---|---|---|---|---|---|
| Antenna[a] | Major unit | $\lambda_{ex}$ (nm) | Nature/solvent | $Q_{Ln}^{L}$ (%) | $Q_{Ln\ or\ rel}^{Ln}$ (%)[b,c,d,e,f,g] | $\tau$ ($\mu$s)[h,i,j] | Reference |

*Complexes for which quantum yields ($Q_{Ln}^{L}$, $Q_{Ln\ or\ rel}^{Ln}$) have been measured or estimated*

| Antenna | Major unit | $\lambda_{ex}$ | Nature/solvent | $Q_{Ln}^{L}$ | $Q_{Ln\ or\ rel}^{Ln}$ | $\tau$ | Reference |
|---|---|---|---|---|---|---|---|
|  **phen** | Polyamino-carboxylates H$_4$**74** | 279 | H$_2$O | $4 \times 10^{-3}$ | | <0.2 | (Quici et al., 2005) |
| | | | D$_2$O | 0.02 | | 0.4 | |
|  **Dansyl** | Dendrimer | **92** | 297 | CH$_3$CN/ CH$_2$Cl$_2$ (5:1) | 0.27 | | – | (Vögtle et al., 2001) |
|  **phen** | Crown ether | **14** | 300 | Acetone | 0.07[k] | | 0.64 | (Korovin et al., 2002d) |
| | | | | Acetone-$d_6$ | 0.10[k] | | 1.17 | |
| | | H$_6$**15** | | H$_2$O | 0.09[k] | | 0.72 | |
| | | | | D$_2$O | 0.18[k] | | 1.34 | |
|  **8-Hydroxyquinoline** | Podands | H$_8$**90a** | 344 | H$_2$O | 0.02 | 0.03[c] | 0.13[j] | (Imbert et al., 2005) |
| | | | | D$_2$O | 0.10 | 0.14[c] | 0.58[j] | |
| | | H$_8$**90b** | 344 | H$_2$O | 0.04 | 0.06[c] | 0.25[j] | (Comby et al., 2006b) |
| | | | | D$_2$O | 0.11 | 0.15[c] | 0.61[j] | |

| Nd | | | Experimental conditions | | | | | |
|---|---|---|---|---|---|---|---|---|
| Antenna[a] | | Major unit | $\lambda_{ex}$ (nm) | Nature/solvent | $Q_{Ln}^{L}$ (%) | $Q_{Ln\ or\ rel}^{Ln}$ (%)[b,c,d,e,f,g] | $\tau$ ($\mu$s)[h,i,j] | Reference |
|  Triphenylene | | Terphenyl-based ligands | H$_3$60a | 350 | dmso-$h_6$ dmso-$d_6$ | | 0.56[b] 1.00[b] | 1.4[i] 2.5[i] | (Klink et al. 1999, 2000a) |
|  Dansyl | | Terphenyl-based ligands | H$_3$60b H$_3$60f | 350 | dmso-$h_6$ dmso-$d_6$ dmso-$d_6$ | | – 1.0[g] 0.95[g] | 1.10[i] 2.21[i] 2.15[i] | (Klink et al., 2001; Hebbink et al., 2002a) |
|  | | Zn Schiff base | H$_2$97a H$_2$97b | 355 | CH$_3$OH CH$_3$CN | | – 0.52[b] | 1.33 1.31 | (Wong et al., 2002; Lo et al., 2004) |
| [G3-An] (cf. fig. 81) | | Dendrimer | 94b-G3 | 390 | thin film | | 0.28[b] | 0.7 | (Baek et al., 2006) |
|  Coumarine | | Terphenyl-based ligands | H$_3$60c H$_3$60g | 400 | dmso-$d_6$ | | 0.29[g] 0.26[g] | 2.16[i] 2.39[i] | (Klink et al., 2001) |
|  8-Hydroxyquinoline | | Podands | H$_6$91 | 410 | H$_2$O D$_2$O | 0.03 0.08 | | 0.15[j] 0.91[j] | (Comby et al., 2007) |
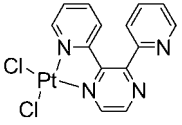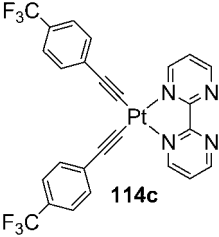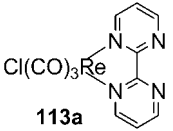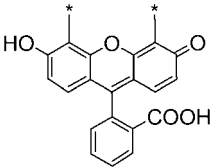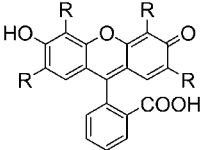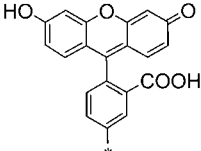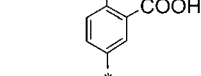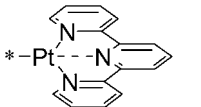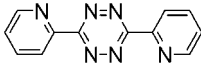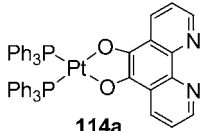
Table 21, *continued*

| Nd | | | Experimental conditions | | | | | |
|---|---|---|---|---|---|---|---|---|
| Antenna[a] | Major unit | | $\lambda_{ex}$ (nm) | Nature/solvent | $Q^L_{Ln}$ (%) | $Q^{Ln}_{Ln\ or\ rel}$ (%)[b,c,d,e,f,g] | $\tau$ ($\mu$s)[h,i,j] | Reference |
|  **114b** | $\beta$-Diketonates (Ternary complex) | **tta** **btfa** | 440 | CH$_2$Cl$_2$ Solid CH$_2$Cl$_2$ Solid | – – | – – 0.33[b] – | – 0.94 0.82 1.02 | (Shavaleev et al., 2003b) |
|  **114c** | $\beta$-Diketonates (Ternary complex) | **hfa** | 460 | CH$_2$Cl$_2$ Solid | – | – 0.27[b] | <0.5[j] 1.0[j] | (Shavaleev et al., 2005) |
|  **113a** | $\beta$-Diketonates (Ternary complex) | **fod** | 460 | CH$_2$Cl$_2$ Solid | – | – 0.24[b] | <0.5[j] 0.9[j] | (Shavaleev et al., 2005) |
|  | Polyamino-carboxylates | H$_4$**73a** | 480 | H$_2$O D$_2$O | 0.017 0.038 | 0.031[d] 0.073[d] | 0.25[i] 0.58[i] | (Werts et al., 2000a) |

| Nd | | | Experimental conditions | | | | | |
|---|---|---|---|---|---|---|---|---|
| Antenna[a] | | Major unit | $\lambda_{ex}$ (nm) | Nature/solvent | $Q_{Ln}^{L}$ (%) | $Q_{Ln\,or\,rel}^{Ln}$ (%)[b,c,d,e,f,g] | $\tau$ (µs)[h,i,j] | Reference |
|  R = Br **Eosin** | | Polyamino-carboxylates H$_4$**72b** | 488 | D$_2$O Degassed D$_2$O | | 1.0[f] 1.5[f] | – – | (Werts et al., 1997; Hofstraat et al., 1998) |
|  **Fluorescein** | | Polyamino-carboxylates H$_4$**72a** Terphenyl-based ligands H$_3$**61a** | 488 505 | D$_2$O Degassed D$_2$O CH$_3$OH CH$_3$OD | 0.030 | 0.71[f] 0.86[f] 0.10[b] 0.16[b] | 0.6 – 0.24[i] 0.41[i] | (Werts et al., 1997; Hofstraat et al., 1998) (Hebbink et al., 2003) |
|  | | Polyamino-carboxylates H$_5$**102** | 515 | H$_2$O | | 0.25[e] | 0.670[i] | (Glover et al., 2003) |
|  **bptz** | | β-Diketonates (Ternary complex) **tta** | 520 | CH$_2$Cl$_2$ CH$_2$Cl$_2$ Solid | | 0.3[b] | 0.76[i] 0.78 1.25[i] | (Shavaleev et al., 2003c) |
|  **114a** | | β-Diketonates (Ternary complex) **tta** | 520 | CH$_2$Cl$_2$ Solid | | 0.40[b] | 0.99 – 0.95 | (Shavaleev et al., 2003a, 2003b) |

| Nd | | | Experimental conditions | | | | | |
|---|---|---|---|---|---|---|---|---|
| Antenna[a] | Major unit | | $\lambda_{ex}$ (nm) | Nature/solvent | $Q^L_{Ln}$ (%) | $Q^{Ln}_{Ln \text{ or rel}}$ (%)[b,c,d,e,f,g] | $\tau$ ($\mu$s)[h,i,j] | Reference |
|  **1-phenylazo-2-naphtol** | Crown ether | **13a** | 532 | $D_2O$ | 0.09 | | 0.8 | (Korovin et al., 2002c; Korovin and Rusakova, 2004) |
|  **Xylenol Blue derivative** | Crown ether | **XB** **13b** | 532 | $D_2O$ | – 0.12 | | – 0.9 | (Korovin et al., 2002c; Korovin and Rusakova, 2004) |
|  **Phthalexon S derivative** | Cyclen | **PS** $H_7$**36** | 532 | $H_2O$ $D_2O$ $H_2O$ $D_2O$ | – 0.07 – 0.23 | | 0.07 0.35 0.75 1.45 | (Korovin and Rusakova, 2002, 2004) |
|  **b** R = Br   **Eosin** **c** R = I   **Erythrosin** | Terphenyl-based ligands | $H_3$**61b** $H_3$**61c** | 535 545 | $CH_3OH$ $CH_3OD$ $CH_3OH$ $CH_3OD$ | – 0.014 – 0.012 | 0.14[b] 0.16[b] 0.10[b] 0.15[b] | 0.36[i] 0.41[i] 0.25[i] 0.37[i] | (Hebbink et al., 2003) |

| Nd | | | Experimental conditions | | | | | |
|---|---|---|---|---|---|---|---|---|
| Antenna[a] | Major unit | | $\lambda_{ex}$ (nm) | Nature/solvent | $Q^L_{Ln}$ (%) | $Q^{Ln}_{Ln \text{ or rel}}$ (%)[b,c,d,e,f,g] | $\tau$ ($\mu s$)[h,i,j] | Reference |
|  **lissamine** | Terphenyl-based ligands | H$_3$**60d** | 570 | dmso-$h_6$<br>dmso-$d_6$<br>Polymer host | | —<br>0.75[g]<br>— | 1.16[i]<br>2.21[i]<br>0.8[i] | (Klink et al., 2001; Hebbink et al., 2002a; Slooff et al., 2000b) |
|  **Texas Red** | Terphenyl-based ligands | H$_3$**60e** | 590 | dmso-$d_6$ | | 0.53[g] | 2.26[i] | (Klink et al., 2001) |
| *Complexes for which only lifetimes have been determined* | | | | | | | | |
|  **Ferrocene** | Terphenyl-based ligands | H$_3$**104** | 320 | dmso-$d_6$ | — | | 2.0[i] | (Klink, et al. 2000c, 2002) |
|  **Pyrene acetic acid (H34)** | Cyclen<br><br>(Ternary complex) | **do3a** | 337 | H$_2$O<br><br>D$_2$O | —<br> | | 0.15<br><br>0.75 | (Faulkner et al., 2004) |
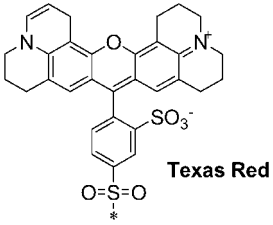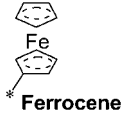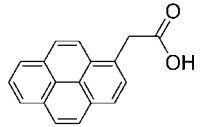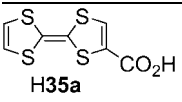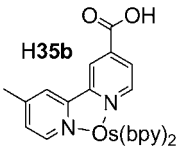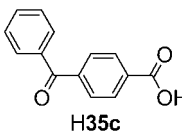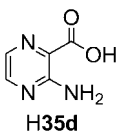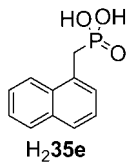
Table 21, *continued*
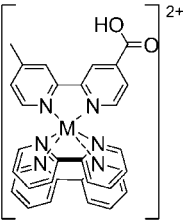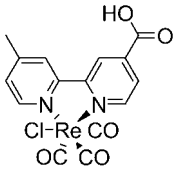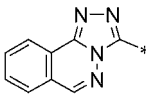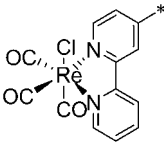
| Nd | | | Experimental conditions | | | | | |
|---|---|---|---|---|---|---|---|---|
| Antenna[a] | Major unit | | $\lambda_{ex}$ (nm) | Nature/solvent | $Q^L_{Ln}$ (%) | $Q^{Ln}_{Ln\ or\ rel}$ (%)[b,c,d,e,f,g] | $\tau$ ($\mu$s)[h,i,j] | Reference |
|  H**35a** | Cyclen (Ternary complex) | **do3a** | 337 | CH$_3$OH CD$_3$OD | – | | 0.12 0.46 | (Pope et al., 2006) |
|  H**35b** | Cyclen (Ternary complex) | **do3a** | 337 | CH$_3$OH CD$_3$OD | – | | 0.24 0.57 | (Pope et al., 2006) |
|  H**35c** | Cyclen (Ternary complex) | **do3a** | 337 | CH$_3$OH CD$_3$OD | – | | 0.13 0.59 | (Pope et al., 2006) |
|  H**35d** | Cyclen (Ternary complex) | **do3a** | 337 | CH$_3$OH CD$_3$OD | – | | 0.11 0.55 | (Pope et al., 2006) |
|  H$_2$**35e** | Cyclen (Ternary complex) | **do3a** | 337 | CH$_3$OH CD$_3$OD | – | | 0.16 0.60 | (Pope et al., 2006) |

| Nd | | | Experimental conditions | | | | | |
|---|---|---|---|---|---|---|---|---|
| Antenna[a] | Major unit | | $\lambda_{ex}$ (nm) | Nature/solvent | $Q_{Ln}^{L}$ (%) | $Q_{Ln\ or\ rel}^{Ln}$ (%)[b,c,d,e,f,g] | $\tau$ ($\mu$s)[h,i,j] | Reference |
|  M = Ru (H**109a**), Os (H**109b**) | Cyclen (Ternary complex) | H**109a** | 337 | $CH_3OH$ | – | | 0.174 | (Pope et al., 2004b) |
| | | | | $CD_3OD$ | | | 0.413 | |
| | | H**109b** | | $CH_3OH$ | | | 0.237 | |
| | | | | $CD_3OD$ | | | 0.565 | |
|  H**109c** | Cyclen (Ternary complex) | H**109c** | 337 | $CH_3OH$ | – | | 0.353 | (Pope et al., 2004b) |
| | | | | $CD_3OD$ | | | 0.754 | |
|  **Triazolophthalazine** | Cyclen | H$_3$**33** | 337 | $H_2O$ | – | | 0.09 | (Burton-Pye et al., 2005) |
| | | | | $D_2O$ | | | 0.33 | |
|  | Polyamino-carboxylates | H$_3$**111** | 337 | $CH_3OH$ | – | | 0.237 | (Pope et al., 2004a, 2005) |
| | | | | $CD_3OD$ | | | 0.512 | |
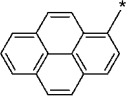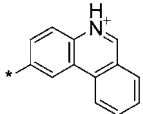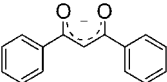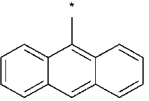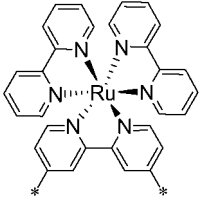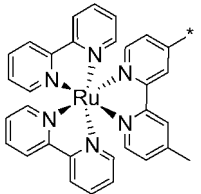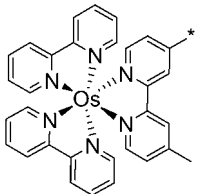
Table 21, *continued*

| Nd | | | Experimental conditions | | | | | |
|---|---|---|---|---|---|---|---|---|
| Antenna[a] | Major unit | | $\lambda_{ex}$ (nm) | Nature/solvent | $Q^L_{Ln}$ (%) | $Q^{Ln}_{Ln \text{ or rel}}$ (%)[b,c,d,e,f,g] | $\tau$ ($\mu$s)[h,i,j] | Reference |
|  Pyrene | Cyclen | H₃**30a** | 355 | H₂O<br>D₂O | – | | 0.080<br>0.320 | (Faulkner et al., 2004) |
| | Cyclen | H₃**30b** | 355 | H₂O<br>D₂O | – | | 0.220<br>0.310 | (Faulkner et al., 2004) |
|  Phenanthridinium | Cyclen | **29** | 355 | H₂O<br>H₂O degassed<br>D₂O<br>D₂O degassed | – | | 0.189<br>0.182<br><br>0.357<br>0.345 | (Beeby et al., 2001) |
|  dbm, **48b** | Calix[4]arene (Ternary complex) | H₂**46** | 360 | CD₂Cl₂ | – | | 0.9 | (Hebbink et al., 2001a) |
|  anthryl | $\beta$-Diketonates | **47j** | 366 | dmf<br>CHCl₃<br>Me-thf | – | | 0.93<br>0.63<br>0.87 | (Nah et al., 2006) |
|  | Cyclen | **112** | 450 | H₂O<br>D₂O | – | | 0.03<br>0.192 | (Gunnlaugsson and Leonard, 2005) |

| Nd | | | Experimental conditions | | | | | |
|---|---|---|---|---|---|---|---|---|
| Antenna[a] | Major unit | | $\lambda_{ex}$ (nm) | Nature/solvent | $Q_{Ln}^{L}$ (%) | $Q_{Ln \text{ or rel}}^{Ln}$ (%)[b,c,d,e,f,g] | $\tau$ ($\mu$s)[h,i,j] | Reference |
|  [Ru(bpy)$_3$]$^{2+}$ | Terphenyl-based ligands | H$_6$**105** | 450 | dmso-$d_6$ | – | | 2.1 | (Klink et al., 2000c, 2002) |
|  [Ru(bpy)$_3$]$^{2+}$ | Polyamino-carboxylates | H$_3$**110a** | 450 | CH$_3$OH CD$_3$OD | – | | 0.22 0.50 | (Pope et al., 2005) |
|  [Os(bpy)$_3$]$^{2+}$ | Polyamino-carboxylates | H$_3$**110b** | 490 | CH$_3$OH CD$_3$OD | – | | 0.27 0.55 | (Pope et al., 2005) |
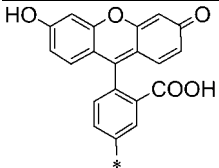
Table 21, *continued*

| Nd | | | Experimental conditions | | | | | |
|---|---|---|---|---|---|---|---|---|
| Antenna[a] | Major unit | | $\lambda_{ex}$ (nm) | Nature/solvent | $Q^L_{Ln}$ (%) | $Q^{Ln}_{Ln \text{ or rel}}$ (%)[b,c,d,e,f,g] | $\tau$ ($\mu s$)[h,i,j] | Reference |
|  **Fluorescein** | Calix[4]arene | $H_5$**43a** | 515 | $CD_3OD$ | – | | $0.86^i$ | (Wolbers et al., 1998a; |
| | | | | dmso | | | $1.23^i$ | Hofstraat et al., 1998) |
| | | $H_5$**43b** | | $CD_3OD$ | | | $0.80^i$ | |
| | | | | dmso | | | $1.26^i$ | |
| | | $H_2$**43c** | | $CH_3CN$ | | | $0.73^i$ | |

[a]The attachment point of the antenna is indicated by —∗; in case of ternary complexes, the sketched molecule acts both as the ternary ligand and antenna.

[b]Intrinsic quantum yields ($Q^{Ln}_{Ln}$) estimated from a radiative lifetime $\tau_0(Nd) = 0.25$ ms.

[c]Intrinsic quantum yields ($Q^{Ln}_{Ln}$) estimated from a radiative lifetime $\tau_0(Nd) = 0.42$ ms.

[d]Intrinsic quantum yields ($Q^{Ln}_{Ln}$) estimated from a radiative lifetime $\tau_0(Nd) = 0.8$ ms.

[e]Intrinsic quantum yields ($Q^{Ln}_{Ln}$) estimated from a radiative lifetime $\tau_0(Nd) = 0.27$ ms.

[f]Quantum yields relative to the one of [Nd (**72b**)] ($Q^{Ln}_{rel}$) in aerated $D_2O$ (Tris-DCl buffer); fixed to unity.

[g]Quantum yields relative to the one of [Nd (**60b**)] ($Q^{Ln}_{rel}$) in dmso-$d_6$; fixed to unity.
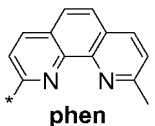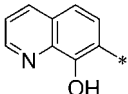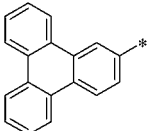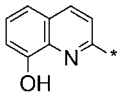
[h]Measured under excitation at the wavelength given in column 3, or otherwise stated.

[i]$\lambda_{ex} = 337$ nm.

[j]$\lambda_{ex} = 355$ nm.
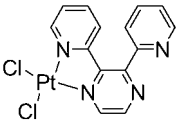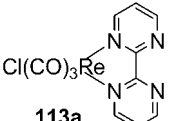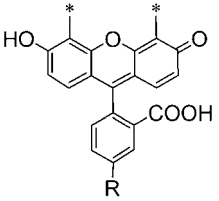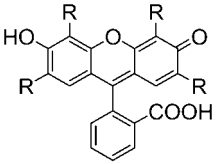
[k]Partial quantum yields ($^4F_{3/2} \rightarrow {}^4I_{9/2}$ and $^4F_{3/2} \rightarrow {}^4I_{11/2}$ transitions).

Table 22
Photophysical properties of $Er^{III}$-containing compounds

| Er | | | Experimental conditions | | | | | |
|---|---|---|---|---|---|---|---|---|
| Antenna[a] | Major unit | | $\lambda_{ex}$ (nm) | Nature/solvent | $Q^L_{Ln}$ (%) | $Q^{Ln}_{Ln \text{ or rel}}$ (%)[b,c,d,e,f] | $\tau$ (μs)[g,h,i] | Reference |
| *Complexes for which quantum yields ($Q^L_{Ln}$, $Q^{Ln}_{Ln \text{ or rel}}$) have been measured or estimated* | | | | | | | | |
|   **phen** | Cyclen  Polyamino-carboxylates | H$_3$**31**  H$_4$**74** | 278  279 | D$_2$O  H$_2$O  D$_2$O | $5 \times 10^{-4}$  –  $4 \times 10^{-3}$ | | –  –  1.2 | (Quici et al., 2004)  (Quici et al., 2005) |
|   **8-Hydroxyquinoline** | Podands | H$_8$**90a**  H$_8$**90b** | 344  344 | H$_2$O  D$_2$O  H$_2$O  D$_2$O | $3.7 \times 10^{-5}$  $5.4 \times 10^{-3}$  $4.0 \times 10^{-5}$  $7.1 \times 10^{-3}$ | 0.035[c]  0.21[c]  0.10[c]  0.35[c] | 0.23[i]  1.39[i]  0.67[i]  2.31[i] | (Imbert et al., 2005; Comby et al., 2006b) |
|   **Triphenylene** | Terphenyl-based ligands | H$_3$**60a** | 350 | dmso-$h_6$  dmso-$d_6$ | | 0.02[b]  0.02[b] | 2.4[h]  3.4[h] | (Klink et al., 1999, 2000a) |
| [**G3-An**] (cf. fig. 81) | Dendrimer | **94b-G3** | 390 | thin film | | 0.025[d] | 2 | (Baek et al., 2006) |
|   **8-Hydroxyquinoline** | Podands | H$_6$**91** | 410 | H$_2$O  D$_2$O | –  $3.5 \times 10^{-3}$ | | 0.24[i]  2.55[i] | (Comby et al., 2007) |
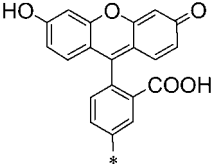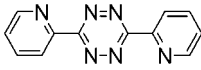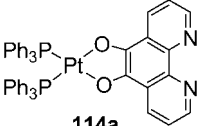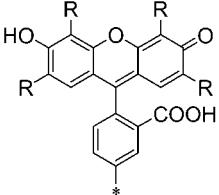
Table 22, *continued*

| Er | | | | Experimental conditions | | | | |
|---|---|---|---|---|---|---|---|---|
| Antenna[a] | | Major unit | | $\lambda_{ex}$ (nm) | Nature/solvent | $Q_{Ln}^{L}$ (%) | $Q_{Ln\ or\ rel}^{Ln}$ (%)[b,c,d,e,f] | $\tau$ ($\mu$s)[g,h,i] | Reference |

| Antenna | Major unit | | $\lambda_{ex}$ | Nature/solvent | $Q^L$ | $Q^{Ln}$ | $\tau$ | Reference |
|---|---|---|---|---|---|---|---|---|
|  **114b** | $\beta$-Diketonates (Ternary complex) | **tta** | 440 | CH$_2$Cl$_2$ | | – | – | (Shavaleev et al., 2003b) |
| | | | | Solid | | – | 1.59 | |
| | | **btfa** | | CH$_2$Cl$_2$ | | 0.011[b] | 1.50 | |
| | | | | Solid | | – | 1.41 | |
|  **113a** | $\beta$-Diketonates (Ternary complex) | **fod** | 460 | CH$_2$Cl$_2$ | | – | <0.5[i] | (Shavaleev et al., 2005) |
| | | | | Solid | | 0.02[b] | 1.6[i] | |
|  **Fluorescein** | Polyamino-carboxylates | H$_4$**73a** | 480 | H$_2$O | – | – | – | (Werts et al., 2000a) |
| | | | | D$_2$O | 0.019 | 0.018[d] | 1.46[h] | |
|  R = Br  **Eosin** | Polyamino-carboxylates | H$_4$**72b** | 488 | D$_2$O | | 0.083[e] | – | (Werts et al., 1997; Hofstraat et al., 1998) |
| | | | | Degassed D$_2$O | | 0.30[e] | – | |

| Er | | | Experimental conditions | | | | | |
|---|---|---|---|---|---|---|---|---|
| Antenna[a] | Major unit | | $\lambda_{ex}$ (nm) | Nature/solvent | $Q^L_{Ln}$ (%) | $Q^{Ln}_{Ln \text{ or rel}}$ (%)[b,c,d,e,f] | $\tau$ ($\mu$s)[g,h,i] | Reference |
|  **Fluorescein** | Polyamino-carboxylates | H$_4$**72a** | 488 | D$_2$O Degassed D$_2$O | | 0.28[e] 0.31[e] | 1.0 – | (Werts et al., 1997; Hofstraat et al., 1998; Hebbink et al., 2003) |
| | Terphenyl-based ligands | H$_3$**61a** | 505 | CH$_3$OD | | 1.0[f] | 0.91 | |
|  **bptz** | $\beta$-Diketonates (Ternary complex) | **tta** | 520 | CH$_2$Cl$_2$ CH$_2$Cl$_2$ solid | | 0.012[b] | 1.70[h] 1.69 2.0[h] | (Shavaleev et al., 2003c) |
|  **114a** | $\beta$-Diketonates (Ternary complex) | **tta** | 520 | CH$_2$Cl$_2$ Solid | | 0.018[b] – | 2.52 1.56 | (Shavaleev et al., 2003a, 2003b) |
|  **b** R = Br **Eosin** **c** R = I **Erythrosin** | Terphenyl-based ligands | H$_3$**61b** H$_3$**61c** | 535 545 | CH$_3$OD CH$_3$OD | | 0.51[f] 0.43[f] | – – | (Hebbink et al., 2003) |

| Er | | | | | | | | |
|---|---|---|---|---|---|---|---|---|
| | | | **Experimental conditions** | | | | | |
| Antenna[a] | Major unit | | $\lambda_{ex}$ (nm) | Nature/solvent | $Q_{Ln}^{L}$ (%) | $Q_{Ln \text{ or rel}}^{Ln}$ (%)[b,c,d,e,f] | $\tau$ (µs)[g,h,i] | Reference |
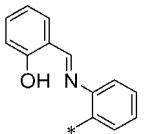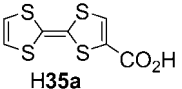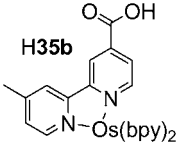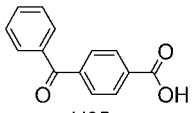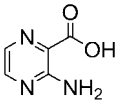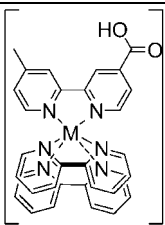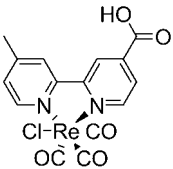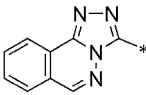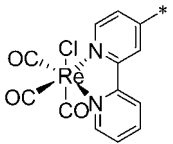
*Complexes for which only lifetimes have been determined*

| Antenna | Major unit | | $\lambda_{ex}$ | Nature/solvent | $Q^L$ | $Q^{Ln}$ | $\tau$ | Reference |
|---|---|---|---|---|---|---|---|---|
|  2-salicylal-diminobenzyl | Crown ether | **17c** | 337 | CH$_3$CN CH$_3$OH CD$_3$OD | - | | 0.78 0.42 0.78 | (Gonzales-Lorenzo et al., 2005) |
|  H**35a** | Cyclen (Ternary complex) | **do3a** | 337 | CH$_3$OH CD$_3$OD | – | | – 0.44 | (Pope et al., 2006) |
|  H**35b** | Cyclen (Ternary complex) | **do3a** | 337 | CH$_3$OH CD$_3$OD | – | | – 0.49 | (Pope et al., 2006) |
|  H**35c** | Cyclen (Ternary complex) | **do3a** | 337 | CH$_3$OH CD$_3$OD | – | | – 0.41 | (Pope et al., 2006) |
|  H**35d** | Cyclen (Ternary complex) | **do3a** | 337 | CH$_3$OH CD$_3$OD | – | | – 0.56 | (Pope et al., 2006) |

| Er | | | Experimental conditions | | | | | |
|---|---|---|---|---|---|---|---|---|
| Antenna[a] | Major unit | | $\lambda_{ex}$ (nm) | Nature/solvent | $Q^L_{Ln}$ (%) | $Q^{Ln}_{Ln \text{ or rel}}$ (%)[b,c,d,e,f] | $\tau$ ($\mu$s)[g,h,i] | Reference |
|   M = Ru (H**109a**), Os (H**109b**) | Cyclen (Ternary complex) | H**109a**  H**109b** | 337 | CH$_3$OH CD$_3$OD CH$_3$OH CD$_3$OD | – | | – 0.427 – 0.490 | (Pope et al., 2004b) |
|   H**109c** | Cyclen (Ternary complex) | H**109c** | 337 | CH$_3$OH CD$_3$OD | – | | – 0.398 | (Pope et al., 2004b) |
|   **Triazolophthalazine** | Cyclen | H$_3$**33** | 337 | H$_2$O D$_2$O | – | | <0.02 1.3 | (Burton-Pye et al., 2005) |
|  | Polyamino-carboxylates | H$_3$**111** | 337 | CH$_3$OH CD$_3$OD | – | | – 0.54 | (Pope et al., 2004a, 2005) |

Table 22, *continued*

| Er | | | Experimental conditions | | | | | |
|---|---|---|---|---|---|---|---|---|
| Antenna[a] | Major unit | | $\lambda_{ex}$ (nm) | Nature/solvent | $Q_{Ln}^{L}$ (%) | $Q_{Ln\ or\ rel}^{Ln}$ (%)[b,c,d,e,f] | $\tau$ ($\mu s$)[g,h,i] | Reference |
|   dbm, 48b | Calix[4]arene  (Ternary complex) | H$_2$**46** | 360 | CD$_2$Cl$_2$ | – | | 1.3 | (Hebbink et al., 2001a) |
|   anthryl | $\beta$-Diketonates | **47j** | 366 | dmf CHCl$_3$ Me-thf | – | | 1.53 1.57 1.87 | (Nah et al., 2006) |
|   [Ru(bpy)$_3$]$^{2+}$ | Polyamino-carboxylates | H$_3$**110a** | 450 | CH$_3$OH CD$_3$OD | – | | _$^h$ 0.85$^h$ | (Pope et al., 2005) |
|   [Os(bpy)$_3$]$^{2+}$ | Polyamino-carboxylates | H$_3$**110b** | 490 | CH$_3$OH CD$_3$OD | – | | _$^h$ 1.16$^h$ | (Pope et al., 2005) |

| Er | | | Experimental conditions | | | | | |
|---|---|---|---|---|---|---|---|---|
| Antenna[a] | Major unit | | $\lambda_{ex}$ (nm) | Nature/solvent | $Q_{Ln}^{L}$ (%) | $Q_{Ln\ or\ rel}^{Ln}$ (%)[b,c,d,e,f] | $\tau$ ($\mu$s)[g,h,i] | Reference |
|  **Fluorescein** | Calix[4]arene | H$_5$**43a** | 515 | CD$_3$OD dmso | – | | 0.76[h] 1.71[h] | (Wolbers et al., 1998a; Hofstraat et al., 1998) |
| | | H$_5$**43b** | | CD$_3$OD dmso | | | 0.88[h] 1.63[h] | |
|  **Phthalexon S derivative** | Cyclen | H$_7$**36** | 532 | dmso-$d_6$ | – | | 1.8 | (Korovin and Rusakova, 2004) |

[a]The attachment point of the antenna is indicated by —∗; in case of ternary complexes, the sketched molecule acts both as the ternary ligand and antenna.

[b]Intrinsic quantum yields ($Q_{Ln}^{Ln}$) estimated from a radiative lifetime $\tau_0$(Er) = 14 ms.

[c]Intrinsic quantum yields ($Q_{Ln}^{Ln}$) estimated from a radiative lifetime $\tau_0$(Er) = 0.66 ms.

[d]Intrinsic quantum yields ($Q_{Ln}^{Ln}$) estimated from a radiative lifetime $\tau_0$(Er) = 8 ms.

[e]Quantum yields relative to the one of [Nd (**72b**)] ($Q_{rel}^{Ln}$) in aerated D$_2$O (Tris-DCl buffer); fixed to unity.
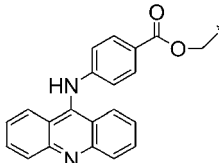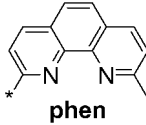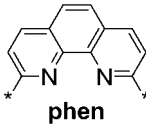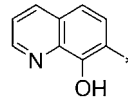
[f]Quantum yields relative to the one of [Nd (**61a**)] ($Q_{rel}^{Ln}$) in CH$_3$OD; fixed to unity.

[g]Measured under excitation at the wavelength given in column 3, or otherwise stated.

[h]$\lambda_{ex}$ = 337 nm.
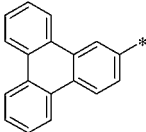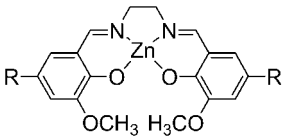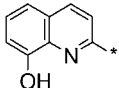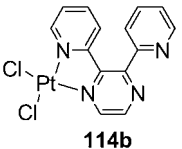
[i]$\lambda_{ex}$ = 355 nm.

Table 23
Photophysical properties of Yb[III]-containing compounds

| Yb | | Experimental conditions | | | | | |
|---|---|---|---|---|---|---|---|
| Antenna[a] | Major unit | $\lambda_{ex}$ (nm) | Nature/solvent | $Q^L_{Ln}$ (%) | $Q^{Ln}_{Ln\ or\ rel}$ (%)[b,c] | $\tau$ ($\mu$s)[d,e,f] | Reference |

*Complexes for which quantum yields ($Q^L_{Ln}$, $Q^{Ln}_{Ln\ or\ rel}$) have been measured or estimated*

| | | | | | | | |
|---|---|---|---|---|---|---|---|
|  9-(4-carboxyphenyl- amino)acridine | Crown ether | 12g | 254 | $H_2O$–$C_2H_5OH$ | 0.022 | | – | (Korovin et al., 2002e) |
|  phen | Polyamino-carboxylates | H$_4$74 | 279 | $H_2O$ $D_2O$ | 0.02 0.10 | | 2.5 10.0 | (Quici et al., 2005) |
|  phen | Crown ether | 14 H$_6$15 | 300 | Acetone Acetone-$d_6$ $H_2O$ $D_2O$ | 0.39 0.58 0.53 0.86 | | 2.20 3.86 4.55 8.86 | (Korovin et al., 2002d) |
|  8-Hydroxyquinoline | Podands | H$_8$90a H$_8$90b | 344 344 | $H_2O$ $D_2O$ $H_2O$ $D_2O$ | 0.18 0.81 0.37 0.90 | 0.11[b] 0.50[b] 0.29[b] 0.73[b] | 2.21[f] 10.0[f] 5.79[f] 14.6[f] | (Imbert et al., 2005; Comby et al., 2006b) |
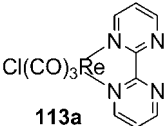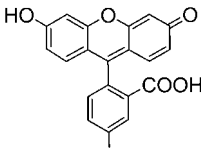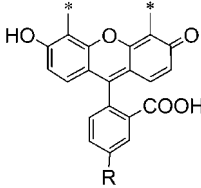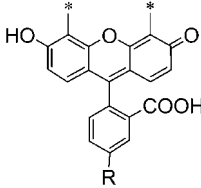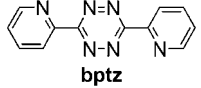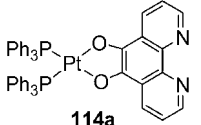
*continued on next page*

| Yb | | | Experimental conditions | | | | | |
|---|---|---|---|---|---|---|---|---|
| Antenna[a] | | Major unit | $\lambda_{ex}$ (nm) | Nature/solvent | $Q^L_{Ln}$ (%) | $Q^{Ln}_{Ln \ or \ rel}$ (%)[b,c] | $\tau$ ($\mu$s)[d,e,f] | Reference |
|   **Triphenylene** | | Terphenyl-based ligands  H$_3$**60a** | 350 | dmso-$h_6$  dmso-$d_6$ | | 0.47[b]  0.93[b] | 9.4[e]  18.6[e] | (Klink et al., 1999;  Klink et al., 2000a) |
|  | | Zn Schiff base | H$_2$**97a**  H$_2$**97b** | 355 | CH$_3$OH  CH$_3$CN | | –  0.73[b] | 1.31  14.59 | (Wong et al., 2002;  Lo et al., 2004) |
| [**G3-An**] (cf. fig. 81) | | Dendrimer | **94b-G3** | 390 | Thin film | | 0.55[b] | 11 | (Baek et al., 2006) |
|   **8-Hydroxyquinoline** | | Podands | H$_6$**91** | 410 | H$_2$O  D$_2$O | 0.13  1.5 | | 2.47[f]  26.0[f] | (Comby et al., 2007) |
|   **114b** | | $\beta$-Diketonates  (Ternary complex) | **tta**   **btfa** | 440 | CH$_2$Cl$_2$  Solid  CH$_2$Cl$_2$  Solid | | 0.37[b]  –  0.48[b]  – | 7.30  11.5  9.50  11.0 | (Shavaleev et al.,  2003b) |

| Yb | | | Experimental conditions | | | | | |
|---|---|---|---|---|---|---|---|---|
| Antenna[a] | Major unit | | $\lambda_{ex}$ (nm) | Nature/solvent | $Q_{Ln}^{L}$ (%) | $Q_{Ln \text{ or rel}}^{Ln}$ (%)[b,c] | $\tau$ (µs)[d,e,f] | Reference |
|  **113a** | $\beta$-Diketonates (Ternary complex) | **fod** | 460 | $CH_2Cl_2$ Solid | | – 0.79[b] | 6.7[f] 9.6[f] | (Shavaleev et al., 2005) |
|  **Fluorescein** | Polyamino-carboxylates | H$_4$**72a** | 488 | $D_2O$ Degassed $D_2O$ | | 0.08[c] 0.46[c] | 8.5 – | (Werts et al., 1997; Hofstraat et al., 1998) |
| | Terphenyl-based ligands | H$_3$**61a** | 505 | $CH_3OH$ $CH_3OD$ | – 0.23 | 0.49[b] 0.55[b] | 9.8[e] 11.1[e] | (Hebbink et al., 2003) |
|  | Polyamino-carboxylates | H$_4$**73a** | 480 | $H_2O$ $D_2O$ | 0.09 0.45 | 0.10[b] 0.52[b] | 1.91[e] 10.4[e] | (Werts et al., 2000a, 2000b) |
| | | H$_4$**73c** | 510 | $H_2O$ | ≈0.05 | 0.09[b] | 1.8[e] | |
|  **bptz** | $\beta$-Diketonates (Ternary complex) | **tta** | 520 | $CH_2Cl_2$ $CH_2Cl_2$ solid | | 0.70[b] | 13.3[e] 14.5 14.1[e] | (Shavaleev et al., 2003c) |
|  **114a** | $\beta$-Diketonates (Ternary complex) | **tta** | 520 | $CH_2Cl_2$ Solid | | 0.53[b] – | 10.6 11.0 | (Shavaleev et al., 2003a, 2003b) |

| Yb | | | | Experimental conditions | | | | |
|---|---|---|---|---|---|---|---|---|
| Antenna[a] | Major unit | | $\lambda_{ex}$ (nm) | Nature/solvent | $Q^{L}_{Ln}$ (%) | $Q^{Ln}_{Ln\ or\ rel}$ (%)[b,c] | $\tau$ ($\mu$s)[d,e,f] | Reference |
| **1-phenylazo-2-naphtol** | Crown ether | **13a** | 532 | $D_2O$ | 0.66 | | 3.8 | (Korovin et al., 2002c; Korovin and Rusakova, 2004) |
| **Xylenol Blue derivative** | Crown ether | **XB** **13b** | 532 | $D_2O$ | 0.11 0.88 | | 0.6 4.2 | (Korovin et al., 2002c; Korovin and Rusakova, 2004) |
| **Phthalexon S derivative** | Cyclen | **PS** | 532 | $H_2O$ $D_2O$ | – 0.41 | | 0.70 3.15 | (Korovin et al., 2002c; Korovin and Rusakova, 2004) |
| | | **H$_7$36** | | $H_2O$ $D_2O$ | – 1.45 | | 6.80 12.60 | |
| **b**  R = Br  **Eosin** | Polyamino-carboxylates | **H$_4$72b** | 488 | $D_2O$ $D_2O$ degassed | | 1.4[c] 9.0[c] | – – | (Werts et al., 1997; Hofstraat et al., 1998) |
| **c**  R = I  **Erythrosin** | Terphenyl-based ligands | **H$_3$61b** | 535 | $CH_3OH$ $CH_3OD$ | – 0.14 | 0.58[b] 0.56[b] | 11.6[e] 11.2[e] | (Hebbink et al., 2003) |
| | | **H$_3$61c** | 545 | $CH_3OH$ $CH_3OD$ | – 0.17 | 0.51[b] 0.58[b] | 10.2[e] 11.5[e] | |
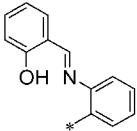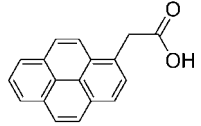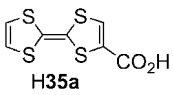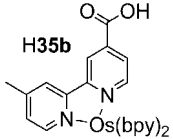
Table 23, *continued*

| Yb | | | Experimental conditions | | | | | |
|---|---|---|---|---|---|---|---|---|
| Antenna[a] | Major unit | | $\lambda_{ex}$ (nm) | Nature/solvent | $Q^L_{Ln}$ (%) | $Q^{Ln}_{Ln \text{ or rel}}$ (%)[b,c] | $\tau$ ($\mu$s)[d,e,f] | Reference |

*Complexes for which only lifetimes have been determined*

| | | | | | | | | |
|---|---|---|---|---|---|---|---|---|
|  * **Ferrocene** | Terphenyl-based ligands | H₃**104** | 320 | dmso-$d_6$ | – | | 18.8[e] | (Klink et al., 2000c, 2002) |
|  **2-salicylal-diminobenzyl** | Crown ether | **17c** | 337 | CH₃CN CH₃OH CD₃OD | – | | 4.34 2.92 4.65 | (Gonzales-Lorenzo et al., 2005) |
|  **Pyrene acetic acid (H34)** | Cyclen (Ternary complex) | **do3a** | 337 | H₂O D₂O | – | | 0.72 2.52 | (Faulkner et al., 2004) |
|  **H35a** | Cyclen (Ternary complex) | **do3a** | 337 | CH₃OH CD₃OD | – | | 2.02 3.49 | (Faulkner et al., 2002; Pope et al., 2006) |
|  **H35b** | Cyclen (Ternary complex) | **do3a** | 337 | CH₃OH CD₃OD | – | | 1.38 8.19 | (Pope et al., 2006) |

| Yb | | | Experimental conditions | | | | | |
|---|---|---|---|---|---|---|---|---|
| Antenna[a] | | Major unit | $\lambda_{ex}$ (nm) | Nature/solvent | $Q_{Ln}^{L}$ (%) | $Q_{Ln\ or\ rel}^{Ln}$ (%)[b,c] | $\tau$ ($\mu s$)[d,e,f] | Reference |
|  **H35d** | | Cyclen (Ternary complex) | **do3a** | 337 | CH₃OH CD₃OD | – | | 1.43 7.02 | (Pope et al., 2006) |
|  M = Ru (H**109a**), Os (H**109b**) | | Cyclen (Ternary complex) | **H109a** **H109b** | 337 | CH₃OH CD₃OD CH₃OH CD₃OD | – | | 2.00 9.60 1.38 8.19 | (Pope et al., 2004b) |
|  H**109c** | | Cyclen (Ternary complex) | **H109c** | 337 | CH₃OH CD₃OD | – | | 1.85 4.76 | (Pope et al., 2004b) |
|  **Triazolophthalazine** | | Cyclen | **H₃33** | 337 | H₂O D₂O | – | | 1.87 7.88 | (Burton-Pye et al., 2005) |

| Yb | | | Experimental conditions | | | | | |
|---|---|---|---|---|---|---|---|---|
| Antenna[a] | Major unit | | $\lambda_{ex}$ (nm) | Nature/solvent | $Q_{Ln}^{L}$ (%) | $Q_{Ln\ or\ rel}^{Ln}$ (%)[b,c] | $\tau$ ($\mu$s)[d,e,f] | Reference |
|  **phenol** | Cyclen | H$_7$**37a** | 337 | H$_2$O site I<br>H$_2$O site II<br>D$_2$O site I<br>D$_2$O site II | – | | 1.67<br>0.51<br>4.95<br>1.17 | (Pope et al., 2003b) |
|  **p-xylene** | Cyclen | H$_6$**37b** | 337 | H$_2$O<br>D$_2$O | – | | 1.45<br>6.07 | (Pope et al., 2003a) |
|  **Pyrene** | Polyamino-carboxylates | H$_3$**111** | 337 | CH$_3$OH<br>CD$_3$OD | – | | 1.88<br>8.30 | (Pope et al., 2004a, 2005) |
|  **Pyrene** | Cyclen | H$_3$**30a**<br><br>H$_3$**30b** | 355 | H$_2$O<br>D$_2$O<br>H$_2$O<br>D$_2$O | –<br><br>– | | 0.74<br>7.45<br>1.34<br>7.40 | (Faulkner et al., 2004) |
|  **Phenanthridine** | Cyclen | **29** | 355 | H$_2$O<br>H$_2$O degassed<br>D$_2$O<br>D$_2$O degassed | – | | 5.0<br>24.4<br>5.9<br>26.3 | (Beeby et al., 2002c) |
|  **Phenanthridinium** | | | | H$_2$O<br>H$_2$O degassed<br>D$_2$O<br>D$_2$O degassed | – | | 0.9<br>0.9<br>7.7<br>7.7 | |

| Yb | | | Experimental conditions | | | | | |
|---|---|---|---|---|---|---|---|---|
| Antenna[a] | Major unit | | $\lambda_{ex}$ (nm) | Nature/solvent | $Q_{Ln}^L$ (%) | $Q_{Ln\ or\ rel}^{Ln}$ (%)[b,c] | $\tau$ ($\mu$s)[d,e,f] | Reference |
|  dbm, **48b** | Calix[4]arene (Ternary complex) | H$_2$**46** | 360 | CD$_2$Cl$_2$ | – | | 12.5 | (Hebbink et al., 2001a) |
|  | Cyclen | **112** | 450 | H$_2$O D$_2$O | – | | 2.0 6.37 | (Gunnlaugsson and Leonard, 2005) |
|  [Ru(bpy)$_3$]$^{2+}$ | Terphenyl-based ligands | H$_6$**105** | 450 | dmso-$d_6$ | – | | 18.2 | (Klink, et al. 2000c, 2002) |
|  [Ru(bpy)$_3$]$^{2+}$ | Polyamino-carboxylates | H$_3$**110a** | 450 | CH$_3$OH CD$_3$OD | – | | –[e] 7.39[e] | (Pope et al., 2005) |
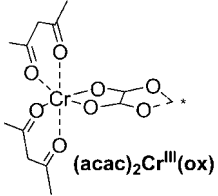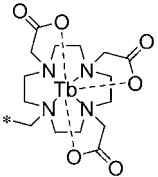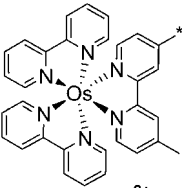
Table 23, *continued*

| Yb | | Experimental conditions | | | | | |
|---|---|---|---|---|---|---|---|
| Antenna[a] | Major unit | $\lambda_{ex}$ (nm) | Nature/solvent | $Q_{Ln}^L$ (%) | $Q_{Ln\ or\ rel}^{Ln}$ (%)[b,c] | $\tau$ ($\mu$s)[d,e,f] | Reference |
|   (acac)$_2$Cr$^{III}$(ox) | Cr$^{III}$–Ln$^{III}$ assembly | 488 | Solid | – | | 48 | (Subhan et al., 2003) |
|  | Polyamino-carboxylates  H$_3$**116** | 337  488 | H$_2$O  D$_2$O  D$_2$O | – | | 1.83  4.22  4.22 | (Faulkner and Pope, 2003) |
|   [Os(bpy)$_3$]$^{2+}$ | Polyamino-carboxylates  H$_3$**110b** | 490 | CH$_3$OH  CD$_3$OD | – | | –[e]  5.33[e] | (Pope et al., 2005) |

[a]The attachment point of the antenna is indicated by —∗; in case of ternary complexes, the sketched molecule acts both as the ternary ligand and antenna.

[b]Intrinsic quantum yields ($Q_{Ln}^{Ln}$) estimated from a radiative lifetime $\tau_0$(Yb) = 2 ms.

[c]Quantum yields relative to the one of [Nd(**72b**)] ($Q_{rel}^{Ln}$) in aerated D$_2$O (Tris-DCl buffer); fixed to unity.

[d]Measured under excitation at the wavelength given in column 3, or otherwise stated.

[e]$\lambda_{ex}$ = 337 nm.

[f]$\lambda_{ex}$ = 355 nm.

detected signal should also be avoided (signal $<5 \times 10^5$ cps). Accuracies better than $\pm 10$–20% are anyway difficult to achieve.

For Nd[III], the overall quantum yields exhibited by molecular complexes with organic ligands remain small. The best chromophores seem to be un-symmetric fluorinated $\beta$-diketonates, for which partial quantum yields up to 1.2% are obtained in organic solvents that are boosted to 3–4% in the corresponding ternary complexes. The largest quantum yields for complexes with calixarenes and calixresorcinarenes are in the range 0.1–0.2% in dmf. The use of sensitization groups such as 8-hydroxyquinolinate, 1,10-phenanthroline, dansyl or phthalexon S, or xylenol blue leads to quantum yields in the range of 0.1 to 0.3% in deuterated water or acetonitrile and 0.04 to 0.09% in water. It should be stressed here that the intrinsic quantum yield rarely exceeds 2–4%, so that the sensitization process is not the only limiting factor.

Quantum yields for Er[III] are much smaller and no data are reported for $\beta$-diketonates. Among the few other quantitative figures reported, we note a quantum yield of 0.02% in deuterated water with fluorescein as the antenna chromophore, while all the other quantum yields are far below $10^{-3}$%. As for neodymium, 1,10-phenanthroline and 8-hydroxyquinolinate are among the best sensitizers.

Ytterbium is a more rewarding ion in that quantum yields in the range 0.2–0.5% are reported in water, these values reaching 0.4–1.45% in deuterated water and in some organic solvents. Calixarene derivatives have quantum yields in the range 0.1–0.6% in dmf and ternary complexes with $\beta$-diketonates reach quantum yields of 1–2% in organic solvents and up to 6% in deuterated solvents and when the C–H bridge of the diketonate unit is deuterated. As far as sensitizing moieties are concerned, the best ones are again 1,10-phenanthroline and 8-hydroxyquinolinate and the best dyes are fluorescein, 1-phenylazo-2-naphthol, phthalexon S, and xylenol blue.

## 6. Conclusions

The number and variety of molecular systems tested for the encapsulation and sensitization of the NIR-emitting trivalent lanthanide ions Nd[III], Er[III], and Yb[III] which are described in sections 3 and 4 of this review are vivid proofs of the interest for these luminescent centers triggered by potential applications in telecommunications, lighting devices, and more recently medical diagnostic and analyses. The starting point of NIR luminescence in lanthanide-containing complexes with organic ligands is the report by Crosby and Kasha (1958) on the sensitization of ytterbium luminescence by $\beta$-diketonates, followed by the report of Gurevich and Solev'ev (1961) on the luminescence of ytterbium porphyrinate, but the field really took off in the mid 1970's only so that most of the information described in this chapter has been gathered during the last twenty years. We note that the contribution of Bill Carnall, to whom this volume of the Handbook is dedicated, on the NIR transitions of trivalent lanthanide ions in solution which appeared in 1962 has also to be considered as one of the activators of this research field (Carnall et al., 1962).

## 6.1. *Is sensitization of the NIR luminescence a problem?*

When designing a host system for NIR-emitting lanthanide ions, chemists have two problems to solve: (i) sensitization of the lanthanide luminescence, taken in a restrictive sense that is optimization of the ligand-to-metal energy transfer, and (ii) protection against nonradiative deactivation. The first problem is not difficult to cope with, and the answer to the question stated above is clearly no, since $\eta_{sens}$ values larger than 60% can routinely be obtained with many chromophoric ligands. The numerous detailed photophysical studies performed on many systems have clearly evidenced the various mechanisms for energy transfer, which depend on the specific lanthanide ion, and they have also demonstrated that the simplistic scheme $^1S \rightarrow {}^3T \rightarrow Ln^*$ is not the only mechanism to take into account. This has fruitful consequences in that the simplistic model calls for organic ligands having as little fluorescence as possible and a large intersystem crossing yield. In fact, ligands with large fluorescence intensity and poor isc yield may also be excellent sensitizers for two reasons. The first one is that some ions, particularly the fluorescent $Nd^{III}$ ion, can be easily excited by direct transfer from the singlet state. The second is that complexation of paramagnetic lanthanide ions to the organic chromophore results in a large "heavy atom" effect favoring the isc process to the expense of ligand fluorescence. Furthermore, in the case of $Yb^{III}$ excitation, more elaborate mechanisms are operative, involving either a phonon-assisted transfer or a double electron exchange mechanism in which the ytterbium ion is momentarily reduced into its divalent oxidation state. And to render this mechanism operative, considerations other than singlet and triplet state energies have to be included, especially free Gibbs energy of the redox processes. Finally, $Er^{III}$ excitation is also an example for which alternative mechanisms may be developed, such as up-conversion. Additionally, two-photon absorption, which has yet to be demonstrated for organic complexes of the NIR emitting $Ln^{III}$ ions, may also be considered in the future.

## 6.2. *Preventing nonradiative deactivation: the real problem*

All organic ligands possess a large distribution of phonon states. Careful tailoring of the ligands to meet the criteria of thermodynamic stability (and possibly kinetic inertness), protection from inner-sphere solvent interaction, as well as efficient energy transfer onto the metal ion excited state is not sufficient to produce a highly luminescent lanthanide complex. The inner coordination sphere must be devoid of high energy vibrations such as O–H and N–H and C–H and, worse, these vibrations should ideally also be absent from the second and subsequent coordination spheres. This is especially true for $Nd^{III}$ and $Er^{III}$ complexes since the energy gap for these ions is very small. If O–H and N–H vibrations can be reasonably well dealt with, see for instance the replacement of water molecules with non O–H donors in $\beta$-diketonate ternary complexes (Rusakova et al., 1992a) or the substitution of N–H by N–Me demonstrated for quinolinate-based podands (Comby et al., 2006b), C–H vibrations are much more difficult to eliminate. In the case of $Er^{III}$, recent modeling of their quenching effect indicates that the environment of the metal ion must be devoid of C–H vibrators up to distances ranging between 20 and 30 Å for the radiative rate constant to be larger than the nonradiative one (Quochi et al., 2006; Winkless et al., 2006). The only alternative is either deuteration or fluorination of the ligands and both methods are expensive and time-consuming. In

addition if the ligands are deuterated, then deuterated solvents should be used to avoid hydrogen exchange. Similarly, deactivation by the solvent can be curtained only by replacing C–H containing solvents with halogenated solvents such as carbon tetrachloride or by deuterating them.

### 6.3. *Best complexation agents and chromophores*

Amid the relatively simple chelating agents, aminocarboxylates, $\beta$-diketonates, and 8-hydroxyquinolinate are the best. The advantage of aminocarboxylates is their large stability in water, but unless suitably substituted, they do not provide any antenna effect. On the other hand, $\beta$-diketonates are among the best sensitizers of NIR luminescence, but they are not stable enough in water. The ideal compromise seems to stem from 8-hydroxyquinolinates, the stability of which in water is only slightly smaller than the one of polyaminocarboxylates and which provide an antenna effect comparable or better than the sensitization afforded by $\beta$-diketonates. Generally speaking, macrocyclic receptors have not produced highly luminescent entities, with a few exceptions, and they must be considered for special applications only. For instance, the ability of porphyrins and related compounds to selectively bind cancer cells is important for the development of cancer imaging or for the monitoring of cancer cell apoptosis. Another promising application of porphyrinates is electroluminescence owing to their electron conducting ability. Other applications of macrocycles could involve the encapsulation of ions in the kinetically inert environment of cyclen derivatives, or the design of luminescent sensors with a special compartment for the complexation of alkali cations, for instance. When dealing with more elaborate ligands, one wishes to substitute a strong complexing agent with chromophores having low-energy singlet and triplet states. The best molecules and dyes tested so far are clearly the dansyl chromophore, fluorescein, phthalexon S, 1-phenylazo-2-naphthol, and xylenol blue; in any case, the sensitizing moiety has to be brought close to the $Ln^{III}$ ion in order to maximize the efficiency of the energy transfer process.

Excitation of the $Ln^{III}$ ion by a d-transition metal ion is an alternative to chromophore-substituted ligands, and proof of principle has been demonstrated for several systems. The lack of quantitative data, however does not allow an evaluation of their real potential, except for their main advantage, which is the control of the luminescent properties of the 4f-metal ion by directional energy transfer. In this context, we note the emergence of self-assembly processes to build new edifices, particularly bi-metallic edifices, by the simultaneous recognition of two metal ions. This relatively unexplored area has already resulted in the design of edifices in which the rate of population, and therefore the apparent lifetime, of a 4f-excited state can be fine-tuned by energy transfer from a d-transition metal ion (Torelli et al., 2005).

### 6.4. *The future of NIR-emitting $Ln^{III}$ ions in applications*

There is no doubt that despite the low quantum yields achieved to date for $Nd^{III}$ and $Er^{III}$ organic materials, polymer optical fibers will be an alternative to silica fibers in the telecommunication windows, mainly in view of their intrinsic advantages cited in section 4, including low cost. A similar conclusion can be drawn for NIR-emitting OLEDs and the availability of fluorinated polymers and $\beta$-diketonates with low vibrations will certainly help boosting

developments in this area. Encaging the luminescent centers in porous materials has proved rewarding as well, with the astonishingly large quantum yield of 9.5% attained for [Nd(pms)$_3$] doped into TMA$^+$-containing faujasite zeolite nanocrystallites dispersed in dmso-$d_6$ (Ryo et al., 2004).

While we do not foresee wide applications of Nd$^{III}$ and Er$^{III}$ for biology-related problems, except for up-converting phosphor technology (Kuningas et al., 2006), Yb$^{III}$ probes are luminescent stains with a large potential in this field. Technical developments in instrumentation for imaging of NIR-emission signals are still ongoing, but some proofs of principle are at hand, for instance, the NIR-image of a [Yb(TPP)Trp] device in polystyrene captured using a commercial video camera with NIR capability (Harrison et al., 2004). Indeed, the possibility of exciting NIR luminescent probes by visible light makes it inevitable that NIR-labels will be accepted as bioprobes in a near future, much as their visible counterparts, especially if quantum yields of 1–3% can be achieved for Yb$^{III}$ under physiological conditions. This target should be within reach in a near future, possibly with 8-hydroxyquinolinate-based systems. Another direction for future research in NIR biolabels is *in cellulo* probing and imaging. The prerequisite is that the complex must be non-toxic and cell-permeable with, preferably, targeting ability. That is, the complex should localize in a given organelle. Bio-conjugation is a major tool towards this goal since the localization of the probe in the cell will then be determined by the nature of the protein or peptide vector used. The problem of localization is however relatively complex since the bio-conjugates often recognize a cell surface receptor, so that the conjugates reside then in an endosome or a related vesicle structure. Solving this problem is a real challenge which will only be met by a close collaboration between biochemists and chemists.

## 6.5. *Concluding statement*

The wealth and variety of results reviewed in this chapter show both the potential of organic complexes and materials for NIR-luminescent probes and the difficulty in achieving reasonable emission efficiency, especially with the very difficult-to-solve problem of C–H vibrations. Alternatives between purely inorganic systems such as glasses and organic complexes and polymers may well be clusters which combine the advantages of both, as demonstrated with Er$^{III}$ polymetallic assemblies having a double cubane structure (Kumar et al., 2005), or functionalized nanoparticles, e.g. doped LaF$_3$ nanoparticles (Slooff et al., 2000a). In these systems, intrinsic quantum yields reach values as high as 70–80% and therefore the main problem hindering the development of NIR-emitting lanthanide-containing probes is elegantly overcome. Furthermore, the possibility of derivatizing nanoparticles and their binding to biomolecules opens the way for their application in targeted biomedical analyses, including multiplexed detection of protein cancer markers, and cell imaging (Diamente et al., 2006). Other promising systems for inclusion of NIR-emitting Ln$^{III}$ ions are ionic liquids in which tetrakis($\beta$-diketonates) act as the anion or doped ionogels generated by the confinement of ionic liquids within a porous silica matrix. Not only do these gels have excellent mechanical, thermal and optical properties but in addition, they feature high ionic conductivity, a key factor for electroluminescent devices (Neouze et al., 2005).

# References

Abdus, S., Kawahata, R., Nakata, H., Fuyuhiro, A., Tsukuda, T., Kaizaki, S., 2004. Inorg. Chim. Acta **357**, 3139.

Aime, S., Botta, M., Parker, D., Williams, J.A.G., 1996. J. Chem. Soc., Dalton Trans., 17.

Aime, S., Batsanov, A.S., Botta, M., Dickins, R.S., Faulkner, S., Foster, C.E., Harrison, A., Howard, J.A.K., Moloney, J.M., Norman, T.J., Parker, D., Royle, L., Williams, J.A.G., 1997. J. Chem. Soc., Dalton Trans., 3623.

Ala-Kleme, T., Haapakka, K., Latva, M., 1999. Anal. Chim. Acta **395**, 205.

Ala-Kleme, T., Latva, M., Haapakka, K., 2000. Anal. Chim. Acta **403**, 161.

Albota, M., Beljonne, D., Bredas, J.L., Ehrlich, J.E., Fu, J.Y., Heikal, A.A., Hess, S.E., Kogej, T., Levin, M.D., Marder, S.R., McCord-Maughon, D., Perry, J.W., Rockel, H., Rumi, M., Subramaniam, C., Webb, W.W., Wu, X.L., Xu, C., 1998. Science **281**, 1653.

An, D.C., Yue, Z.Z., Chen, R.T., 1998. Appl. Phys. Lett. **72**, 2806.

Ananias, D., Kostova, M., Almeida Paz, F.A., Ferreira, A., Carlos, L.D., Klinowski, J., Rocha, J., 2004. J. Am. Chem. Soc. **126**, 10410.

André, N., Scopelliti, R., Hopfgartner, G., Piguet, C., Bünzli, J.-C.G., 2002. Chem. Commun., 214.

Archer, R.D., Chen, H.Y., Thompson, L.C., 1998. Inorg. Chem. **37**, 2089.

Arenz, S., Babai, A., Binnemans, K., Driesen, K., Giernoth, R., Mudring, A.-V., Nockemann, P., 2005. Chem. Phys. Lett. **402**, 75.

Armaroli, N., Balzani, V., Barigelletti, F., Ward, M.D., McCleverty, J.A., 1997. Chem. Phys. Lett. **276**, 435.

Artizzu, F., Deplano, P., Marchio, L., Mercuri, M.L., Pilia, L., Serpe, A., Quochi, F., Orru, R., Cordella, F., Meinardi, F., Tubino, R., Mura, A., Bongiovanni, G., 2005. Inorg. Chem. **44**, 840.

Asano-Someda, M., Kaizu, Y., 2001. J. Photochem. Photobiol. A Chem. **139**, 161.

Asfari, Z., Böhmer, V., Harrowfield, J.M., Vicens, J., 2001. Calixarenes 2001. Kluwer Academic Publishers, Dordrecht.

Auzel, F., 2004. Chem. Rev. **104**, 139.

Baek, N.S., Kim, Y.H., Roh, S.G., Kwak, B.K., Kim, H.K., 2006. Adv. Funct. Mater. **16**, 1873.

Baldo, M.A., O'Brien, D.F., You, Y., Shoustikov, A., Sibley, S., Thompson, M.E., Forrest, S.R., 1998. Nature **395**, 151.

Banerjee, S., Huebner, L., Romanelli, M.D., Kumar, G.A., Riman, R.E., Emge, T.J., Brennan, J.G., 2005. J. Am. Chem. Soc. **127**, 15900.

Bassett, A.P., Magennis, S.W., Glover, P.B., Lewis, D.J., Spencer, N., Parsons, S., Williams, R.M., De Cola, L., Pikramenou, Z., 2004. J. Am. Chem. Soc. **126**, 9413.

Bassett, A.P., Van Deun, R., Nockemann, P., Glover, P.B., Kariuki, B.M., Van Hecke, K., Van Meervelt, L., Pikramenou, Z., 2005. Inorg. Chem. **44**, 6140.

Batsanov, A.S., Beeby, A., Bruce, J.I., Howard, J.A.K., Kenwright, A.M., Parker, D., 1999. Chem. Commun., 1011.

Batyaev, I.M., 1971. Russ. Chem. Rev. (Engl. Transl.) **40**, 622.

Batyaev, I.M., Danil'chuk, N.V., Kabatskii, Y.A., Shapovalov, V.N., Shilov, S.M., 1989a. J. Appl. Spectrosc. (Engl. Transl.) **51**, 1262.

Batyaev, I.M., Kabatskii, Y.A., Mokhova, E.A., Sviridov, V.V., 1989b. J. Appl. Spectrosc. (Engl. Transl.) **50**, 394.

Becker, A., Hessenius, C., Licha, K., Ebert, B., Sukowski, U., Semmler, W., Wiedenmann, B., Grotzinger, C., 2001. Nat. Biotechnol. **19**, 327.

Beeby, A., Faulkner, S., 1997. Chem. Phys. Lett. **266**, 116.

Beeby, A., Dickins, R.S., Faulkner, S., Parker, D., Williams, J.A.G., 1997. Chem. Commun., 1401.

Beeby, A., Clarkson, I.M., Dickins, R.S., Faulkner, S., Parker, D., Royle, L., de Sousa, A.S., Williams, J.A.G., Woods, M., 1999. J. Chem. Soc., Perkin Trans. **2**, 493.

Beeby, A., Dickins, R.S., FitzGerald, S., Govenlock, L.J., Maupin, C.L., Parker, D., Riehl, J.P., Siligardi, G., Williams, J.A.G., 2000. Chem. Commun., 1183.

Beeby, A., Faulkner, S., Parker, D., Williams, J.A.G., 2001. J. Chem. Soc., Perkin Trans. **2**, 1268.

Beeby, A., Burton-Pye, B.P., Faulkner, S., Motson, G.R., Jeffery, J.C., McCleverty, J.A., Ward, M.D., 2002a. J. Chem. Soc., Dalton Trans., 1923.

Beeby, A., Bushby, L.M., Maffeo, D., Williams, J.A.G., 2002b. J. Chem. Soc., Dalton Trans., 48.

Beeby, A., Faulkner, S., Williams, J.A.G., 2002c. J. Chem. Soc., Dalton Trans., 1918.

Beer, P.D., Szemes, F., Passaniti, P., Maestri, M., 2004. Inorg. Chem. **43**, 3965.

Bermudez, V.D., Carlos, L.D., Duarte, M.C., Silva, M.M., Silva, C.J.R., Smith, M.J., Assuncao, M., Alcacer, L., 1998. J. Alloys Compd. **277**, 21.

Bernhardt, P.V., Flanagan, B.M., Riley, M.J., 2000. Aust. J. Chem. **53**, 229.

Bertolo, L., Tamburini, S., Vigato, P.A., Porzio, W., Macchi, G., Meinardi, F., 2006. Eur. J. Inorg. Chem., 2370.

Bethune, D.S., Johnson, R.D., Salem, J.R., de Vries, M.S., Yannoni, C.S., 1993. Nature **366**, 123.

Billard, I., Mekki, S., Gaillard, C., Hesemann, P., Moutiers, G., Mariet, C., Labet, A., Bünzli, J.-C.G., 2004. Eur. J. Inorg. Chem., 1190.

Billard, I., Moutiers, G., Labet, A., El Azzi, A., Gaillard, C., Mariet, C., Lützenkirchen, K., 2003. Inorg. Chem. **42**, 1726.

Binnemans, K., 2005a. Chem. Rev. **105**, 4148.

Binnemans, K., 2005b. Rare earth $\beta$-diketonate complexes: functionalities and applications. In: Gschneidner Jr., K.A., Bünzli, J.-C.G., Pecharsky, V.K. (Eds.), Handbook on the Physics and Chemistry of Rare Earths, vol. **35**. Elsevier, Amsterdam (chapter 225).

Blumenthal, N., Ellis, C.B., Grafstei, D., 1968. J. Chem. Phys. **48**, 5726.

Bol'shoi, D.V., Meshkova, S.B., Topilova, Z.M., Lozinskii, M.O., Shapiro, Y.E., 1997. Opt. Spectrosc. (Engl. Transl.) **83**, 627.

Borbas, K.E., Bruce J.I., 2006. Chem. Commun., 4596.

Brayshaw, P.A., Bünzli, J.-C.G., Froidevaux, P., Harrowfield, J.M., Kim, Y., Sobolev, A.N., 1995. Inorg. Chem. **34**, 2068.

Brecher, C., French, K.W., 1969. J. Phys. Chem. **73**, 1785.

Brecher, C., French, K.W., 1973. J. Phys. Chem. **77**, 1370.

Breen, P.J., Hild, E.K., deW. Horrocks Jr., W., 1985. Biochemistry **25**, 4991.

Brinkschulte, H., Fill, E., Lang, R., 1972. J. Appl. Phys. **43**, 1807.

Buissette, V., Huignard, A., Gacoin, T., Boilot, J.P., Aschehoug, P., Viana, B., 2003. Surf. Sci. **532**, 444.

Bünzli, J.-C.G., 1987. Complexes with synthetic ionophores. In: Gschneidner Jr., K.A., Eyring, L. (Eds.), Handbook on the Physics and Chemistry of Rare Earths, vol. **9**. Elsevier Science Publ., Amsterdam, pp. 321–394 (chapter 60).

Bünzli, J.-C.G., 1989. Luminescent probes. In: Bünzli, J.-C.G., Choppin, G.R. (Eds.), Lanthanide Probes in Life, Chemical and Earth Sciences. Theory and Practice. Elsevier Science B.V., Amsterdam, pp. 219–293 (chapter 7).

Bünzli, J.-C.G., 1998. Coordination chemistry of the trivalent lanthanide ions: an introductory overview. In: Saez Puche, R., Caro, P. (Eds.), Rare Earths. Editorial Complutense, Madrid, pp. 223–259.

Bünzli, J.-C.G., 2004. Luminescent lanthanide probes as diagnostic and therapeutic tools. In: Sigel, A., Sigel, H. (Eds.), Metal Complexes in Tumor Diagnosis and as Anticancer Agents, vol. **42**. Marcel Dekker, New York, pp. 39–75 (chapter 2).

Bünzli, J.-C.G., 2005. Rare earth luminescent centers in organic and biochemical compounds. In: Liu, G.K., Jacquier, B. (Eds.), Spectroscopic Properties of Rare Earths in Optical Materials. Springer Verlag, Berlin, pp. 462–499 (chapter 11).

Bünzli, J.-C.G., Besançon, F., 2005. Phys. Chem. Chem. Phys. **7**, 2191.

Bünzli, J.-C.G., Piguet, C., 2002. Chem. Rev. **102**, 1897.

Bünzli, J.-C.G., Piguet, C., 2005. Chem. Soc. Rev. **34**, 1048.

Bünzli, J.-C.G., Pilloud, F., 1989. Inorg. Chem. **28**, 2638.

Bünzli, J.-C.G., Vuckovic, M.M., 1983. Inorg. Chim. Acta **73**, 53.

Bünzli, J.-C.G., Vuckovic, M.M., 1984. Inorg. Chim. Acta **95**, 105.

Bünzli, J.-C.G., Besançon, F., Ihringer, F., 2000. Bimetallic lanthanide supramolecular edifices with calixarenes. In: Lumetta, G.J., Rogers, R.D., Gopalan, A. (Eds.), Calixarenes for Separations, vol. **757**. American Chemical Society, Washington, DC, pp. 179–194 (chapter 14).

Burton-Pye, B.P., Heath, S.L., Faulkner, S., 2005. Dalton Trans., 146.

But, S., Van Deun, R., Parac-Vogt, T.N., Görller-Walrand, C., Binnemans, K., 2005. Spectrochim. Acta A **62**, 478.

Cantuel, M., Bernardinelli, G., Imbert, D., Bünzli, J.-C.G., Hopfgartner, G., Piguet, C., 2002. J. Chem. Soc., Dalton Trans., 1929.

Cardinaels, T., Driesen, K., Parac-Vogt, T.N., Heinrich, B., Bourgogne, C., Guillon, D., Donnio, B., Binnemans, K., 2005. Chem. Mater. **17**, 6589.

Carlos, L.D., Ferreira, R.A.S., Bermudez, V.D., 2000. Electrochim. Acta **45**, 1555.

Carlos, L.D., Ferreira, R.A.S., Silva, N.J.O., Amaral, V.S., Goncalves, M.C., Bermudez, V.D., 2004. Adv. Mater. Forum **455–456**, 564.

Carnall, W.T., 1979. The absorption and fluorescence spectra of rare earth ions in solution. In: Gschneidner Jr., K.A., Eyring, L. (Eds.), Handbook on the Physics and Chemistry of Rare Earths, vol. **3**. North Holland, Amsterdam, pp. 172–208 (chapter 24).

Carnall, W.T., Gruen, D.M., McBeth, R.L., 1962. J. Phys. Chem. **66**, 2159.

Carnall, W.T., Fields, P.R., Wybourne, B.G., 1965. J. Chem. Phys. **42**, 3797.

Carnall, W.T., Fields, P.R., Rajnak, K., 1968. J. Chem. Phys. **49**, 4424.

Carnall, W.T., Hessler, J.P., Wagner, F.J., 1978. J. Phys. Chem. **82**, 2152.

Carnall, W.T., Beitz, J.V., Crosswhite, H.M., Rajnak, K., Mann, J.B., 1983. Spectroscopic properties of the f-elements in compounds and solutions. In: Sinha, S.P. (Ed.), Systematics and the Properties of Lanthanides. Reidel, Dordrecht, pp. 389–450 (chapter 9).

Carnall, W.T., Crosswhite, H., Crosswhite, H.M., 1997. Energy Level Structure and Transition Probabilities of the Trivalent Lanthanides in LaF$_3$. Argonne National Laboratory, Argonne, USA.

Casnati, A., Sansone, F., Sartori, A., Prodi, L., Montalti, M., Zaccheroni, N., Ugozzoli, F., Ungaro, R., 2003. Eur. J. Org. Chem., 1475.

Cervantes, M., Clark, A., Terpugov, V., Medrano, F., 2002. J. Opt. Technol. **69**, 61.

Chang, C.A., Francesconi, L.C., Malley, M.F., Kumar, K., Gougoutas, J.Z., Tweedle, M.F., Lee, D.W., Wilson, L.J., 1993. Inorg. Chem. **32**, 3501.

Chang, C.A., Liu, Y.-L., Chen, C.-Y., Chou, X.-M., 2001. Inorg. Chem. **40**, 3448.

Chang, S.J., 1995. J. Appl. Phys. **78**, 4279.

Chauvin, A.-S., Gumy, F., Imbert, D., Bünzli, J.-C.G., 2004. Spectrosc. Lett. **37**, 517. Erratum: 2007, **40**, 193.

Chen, B., Yang, Y., Zapata, F., Qian, G., Luo, Y., Zhang, J., Lobkovsky, E.B., 2006. Inorg. Chem. **45**, 8882.

Chen, R.T., Lee, M., Natarajan, S., Lin, C., Ho, Z.Z., Robinson, D., 1993. IEEE Phot. Technol. Lett. **5**, 1328.

Choppin, G.R., 1989. Chemical properties of the rare earth elements. In: Bünzli, J.-C.G., Choppin, G.R. (Eds.), Lanthanide Probes in Life, Chemical and Earth Sciences. Theory and Practice. Elsevier Science, Amsterdam, pp. 1–41 (chapter 1).

Chudinov, A.V., Rumyantseva, V.D., Lobanov, A.V., Chudinova, G.K., Stomakhin, A.A., Mironov, A.F., 2004. Russ. J. Bioorg. Chem. (Engl. Transl.) **30**, 89.

Clark, A., Terpugov, V., Medrano, F., Cervantes, M., Soto, D., 1999. Opt. Mater. **13**, 355.

Coldwell, J.B., Felton, C.E., Harding, L.P., Moon, R., Pope, S.J.A., Rice, C.R., 2006. Chem. Commun., 5048.

Comby, S., Gumy, F., Bünzli, J.-C.G., Saraidarov, T., Reisfeld, R., 2006a. Chem. Phys. Lett. **432**, 128.

Comby, S., Imbert, D., Chauvin, A.-S., Bünzli, J.-C.G., 2006b. Inorg. Chem. **45**, 732.

Comby, S., Scopelliti, R., Imbert, D., Charbonnière, L.J., Ziessel, R., Bünzli, J.-C.G., 2006c. Inorg. Chem. **45**, 3158.

Comby, S., Imbert, D., Vandevyver, C., Bünzli, J.-C.G., 2007. Chem. Eur. J. **13**, 936.

Crosby, G.A., Kasha, M., 1958. Spectrochim. Acta **10**, 377.

Cross, J.P., Lauz, M., Badger, P.D., Petoud, S., 2004. J. Am. Chem. Soc. **126**, 16278.

Crosswhite, H.M., Moos, H.W., 1967. Optical Properties of Ions in Crystals. Interscience Publishers, New York.

Curry, R.J., Gillin, W.P., 1999. Appl. Phys. Lett. **75**, 1380.

Curry, R.J., Gillin, W.P., 2000. Synth. Met. **111**, 35.

Curry, R.J., Gillin, W.P., 2001. Curr. Opin. Solid State Mater. Sci. **5**, 481.

Curry, R.J., Gillin, W.P., Knights, A.P., Gwilliam, R., 2000. Appl. Phys. Lett. **77**, 2271.

Curry, R.J., Gillin, W.P., Knights, A.P., Gwilliam, R., 2001. Opt. Mater. **17**, 161.

Curry, R.J., George, M.R., Grossel, M.C., 2005. The potential of pyridine-2,6-dicarboxylic acid based organolanthanide complexes for efficient near infrared emission. In: Zajya, H., Kafafi, H., Lane, P.A. (Eds.), Proc. SPIE, pp. 59371R-1–59371R-9.

Davies, G.M., Aarons, R.J., Motson, G.R., Jeffery, J.C., Adams, H., Faulkner, S., Ward, M.D., 2004. Dalton Trans., 1136.

Davies, G.M., Adams, H., Pope, S.J.A., Faulkner, S., Ward, M.D., 2005a. Photochem. Photobiol. Sci. **4**, 829.

Davies, G.M., Pope, S.J.A., Adams, H., Faulkner, S., Ward, M.D., 2005b. Inorg. Chem. **44**, 4665.

de Dood, M.J.A., Berkhout, B., van Kats, C.M., Polman, A., van Blaaderen, A., 2002. Chem. Mater. **14**, 2849.

de Mello, J.C., Wittmann, H.F., Friend, R.H., 1997. Adv. Mater. **9**, 230.

de Sá, G.F., Malta, O.L., Donega, C.D., Simas, A.M., Longo, R.L., Santa-Cruz, P.A., da Silva, E.F., 2000. Coord. Chem. Rev. **196**, 165.

De Silva, A.P., Fox, D.B., Huxley, A.J.M., Moody, T.S., 2000. Coord. Chem. Rev. **205**, 41.

Destri, S., Porzio, W., Meinardi, F., Tubino, R., Salerno, G., 2003. Macromolecules **36**, 273.

deW. Horrocks Jr., W., Bolender, J.P., Smith, W.D., Supkowski, R.M., 1997. J. Am. Chem. Soc. **119**, 5972.

Di Bari, L., Pintacuda, G., Salvadori, P., 2000a. J. Am. Chem. Soc. **122**, 5557.

Di Bari, L., Pintacuda, G., Salvadori, P., Dickins, R.S., Parker, D., 2000b. J. Am. Chem. Soc. **122**, 9257.

Di Bari, L., Lelli, M., Pintacuda, G., Salvadori, P., 2002. Chirality **14**, 265.

Diamente, P.R., Van Veggel, F.C.J.M., 2005. J. Fluoresc. **15**, 543.

Diamente, P.R., Burke, R.D., Van Veggel, F.C.J.M., 2006. Langmuir **22**, 1782.

Dickins, R.S., Howard, J.A.K., Maupin, C.L., Moloney, J.M., Parker, D., Peacock, R.D., Riehl, J.P., Siligardi, G., 1998. New J. Chem. **22**, 891.

Dickins, R.S., Howard, J.A.K., Maupin, C.L., Moloney, J.M., Parker, D., Riehl, J.P., Siligardi, G., Williams, J.A.G., 1999. Chem. Eur. J. **5**, 1095.

Dickins, R.S., Parker, D., Bruce, J.I., Tozer, D.J., 2003. Dalton Trans., 1264.

Dieke, G.H., 1968. Spectra and Energy Levels of Rare Earth Ions in Crystals. Interscience Publishers, New York.

Ding, X.Y., Alford, J.M., Wright, J.C., 1997a. Chem. Phys. Lett. **269**, 72.

Ding, X.Y., Geng, L., Lascola, R., Wright, J.C., 1997b. J. Lumin. **72–74**, 553.

Dorenbos, P., 2003. J. Phys.: Condens. Matter **15**, 575.

Dossing, A., 2005. Eur. J. Inorg. Chem., 1425.

Driesen, K., Nockemann, P., Binnemans, K., 2004a. Chem. Phys. Lett. **395**, 306.

Driesen, K., Van Deun, R., Görller-Walrand, C., Binnemans, K., 2004b. Chem. Mater. **16**, 1531.

Edder, C., Piguet, C., Bernardinelli, G., Mareda, J., Bochet, C.G., Bünzli, J.-C.G., Hopfgartner, G., 2000. Inorg. Chem. **39**, 5059.

Edder, C., Piguet, C., Bünzli, J.-C.G., Hopfgartner, G., 2001. Chem. Eur. J. **7**, 3014.

Elhabiri, M., Scopelliti, R., Bünzli, J.-C.G., Piguet, C., 1999. J. Am. Chem. Soc. **121**, 10747.

Ermolaev, V.L., Sveshnikova, E.B., 1979. J. Lumin. **20**, 387.

Etienne, P., Coudray, P., Porque, J., Moreau, Y., 2000. Opt. Commun. **174**, 413.

Faulkner, S., Pope, S.J.A., 2003. J. Am. Chem. Soc. **125**, 10526.

Faulkner, S., Beeby, A., Dickins, R.S., Parker, D., Williams, J.A.G., 1999. J. Fluoresc. **9**, 45.

Faulkner, S., Beeby, A., Carrié, M.-C., Dadabhoy, A., Kenwright, A.M., Sammes, P.G., 2001. Inorg. Chem. Commun. **4**, 187.

Faulkner, S., Burton-Pye, B.P., Khan, T., Martin, L.R., Wray, S.D., Skabara, P.J., 2002. Chem. Commun., 1668.

Faulkner, S., Carrié, M.-C., Pope, S.J.A., Squire, J., Beeby, A., Sammes, P.G., 2004. Dalton Trans., 1405.

Faulkner, S., Pope, S.J.A., Burton-Pye, B.P., 2005. Appl. Spectrosc. Rev. **40**, 1.

Fick, J., Knystautas, E.J., Villeneuve, A., Schiettekatte, F., Roorda, S., Richardson, K.A., 2000. J. Non-Cryst. Sol. **272**, 200.

Flanagan, B.M., Bernhardt, P.V., Krausz, E.R., Luthi, S.R., Riley, M.J., 2001. Inorg. Chem. **40**, 5401.

Flanagan, B.M., Bernhardt, P.V., Krausz, E.R., Luthi, S.R., Riley, M.J., 2002. Inorg. Chem. **41**, 5024.

Floquet, S., Borkovec, M., Bernardinelli, G., Pinto, A., Leuthold, L.-A., Hopfgartner, G., Imbert, D., Bünzli, J.-C.G., Piguet, C., 2004. Chem. Eur. J. **10**, 1091.

Foley, T.J., Abboud, K.A., Boncella, J.M., 2002. Inorg. Chem. **41**, 1704.

Foley, T.J., Harrison, B.S., Knefely, A.S., Abboud, K.A., Reynolds, J.R., Schanze, K.S., Boncella, J.M., 2003. Inorg. Chem. **42**, 5023.

Froidevaux, P., Bünzli, J.-C.G., 1994. J. Phys. Chem. **98**, 532.

Fu, L.M., Wen, X.F., Ai, X.C., Sun, Y., Wu, Y.S., Zhang, J.P., Wang, Y., 2005. Angew. Chem. Int. Ed. **44**, 747.

Fulton, D.A., Elemento, E.M., Aime, S., Chaabane, L., Botta, M., Parker, D., 2006. Chem. Commun.

Furphy, B.M., Harrowfield, J.M., Kepert, D.L., Skelton, B.W., White, A.H., Wilner, F.R., 1987. Inorg. Chem. **26**, 4231.

Gaiduck, M.I., Grigoriants, V.V., Mironov, A.F., Roitman, L.D., Chissov, V.I., Rumiantseva, V.D., Sukhin, G.M., 1989. Dokl. Acad. Nauk SSSR **309**, 980.

Gaiduck, M.I., Grigoriants, V.V., Mironov, A.F., Rumyantseva, V.D., Chissov, V.I., Sukhin, G.M., 1990. J. Photochem. Photobiol. B Biol. **7**, 15.

Gaiduck, M.I., Grigoriants, V.V., Mironov, A.F., Rumyantseva, V.D., 1991. Eesti Teaduste Akadeemia Toimetised, Fuusika, Matemaatika **40**, 198.

Gao, X.C., Cao, H., Huang, C.H., Li, B.G., Umitani, S., 1998. Appl. Phys. Lett. **72**, 2217.

Gillin, W.P., Curry, R.J., 1999. Appl. Phys. Lett. **74**, 798.

Glover, P.B., Ashton, P.R., Childs, L.J., Rodger, A., Kercher, M., Williams, R.M., De Cola, L., Pikramenou, Z., 2003. J. Am. Chem. Soc. **125**, 9918.

Gonçalves e Silva, F.R., Malta, O.L., 1997. J. Alloys Compd. **250**, 427.

Gonçalves e Silva, F.R., Longo, R.L., Malta, O.L., Piguet, C., Bünzli, J.-C.G., 2000. Phys. Chem. Chem. Phys. **2**, 5400.

Gonçalves e Silva, F.R., Malta, O.L., Reinhard, C., Güdel, H.U., Piguet, C., Moser, J.E., Bünzli, J.-C.G., 2002. J. Phys. Chem. A **106**, 1670.

Gonçalves, M.C., Silva, N.J.O., de Zea Bermudez, V., A sà Ferreira, R., Carlos, L.D., Dahmouche, K., Ostrovskii, D., Correia Vilela, I.C., Craievich, A.F., 2005. J. Phys. Chem. B, 20093.

Gonzales-Lorenzo, M., Platas-Iglesias, C., Avecilla, F., Geraldes, C.F.G.C., Imbert, D., Bünzli, J.-C.G., de Blas, A., Rodriguez-Blas, T., 2003. Inorg. Chem. **42**, 6946.

Gonzales-Lorenzo, M., Platas-Iglesias, C., Avecilla, F., Faulkner, L.R., Pope, S.J.A., de Blas, A., Rodriguez-Blas, T., 2005. Inorg. Chem. **44**, 4254.

Gouterman, M., Schumaker, C.D., Srivastava, T.S., Yonetani, T., 1976. Chem. Phys. Lett. **40**, 456.

Guillet, E., Imbert, D., Scopelliti, R., Bünzli, J.-C.G., 2004. Chem. Mater. **16**, 4063.

Guillou, O., Daiguebonne, C., 2004. Lanthanide-containing coordination polymers. In: Gschneidner Jr., K.A., Bünzli, J.-C.G., Pecharsky, V.K. (Eds.), Handbook on the Physics and Chemistry of Rare Earths, vol. **34**. Elsevier North Holland, Amsterdam (chapter 221).

Gumy, F., Bünzli, J.-C.G., 2006, unpublished results.

Gunnlaugsson, T., Leonard, G.A., 2005. Chem. Commun., 3114.

Guo, D., Duan, C., Lu, F., Hasegawa, Y., Meng, Q., Yanagida, S., 2004. Chem. Commun., 1486.

Gurevich, M.G., Solev'ev, K.N., 1961. Dokl. Acad. Nauk SSSR **5**, 291.

Gutierrez, F., Tedeschi, C., Maron, L., Daudey, J.P., Poteau, R., Azéma, J.L., Tisnes, P., Picard, C., 2004. Dalton Trans., 1334.

Gutsche, C.D., 1998. Calixarenes Revisited. Monographs in Supramolecular Chemistry. The Royal Society of Chemistry, Cambridge.

Hall, J., Häner, R., Aime, S., Botta, M., Faulkner, S., Parker, D., de Sousa, A.S., 1998. New J. Chem. **22**, 627.

Han, K.G., Kong, H.J., Kim, H.S., Um, G.Y., 1995. Appl. Phys. Lett. **67**, 1501.

Harrison, B.S., Foley, T.J., Bouguettaya, M., Boncella, J.M., Reynolds, J.R., Schanze, K.S., Shim, J., Holloway, P.H., Padmanaban, G., Ramakrishnan, S., 2001. Appl. Phys. Lett. **79**, 3770.

Harrison, B.S., Foley, T.J., Knefely, A.S., Mwaura, J.K., Cunningham, G.B., Kang, T.-S., Bouguettaya, M., Boncella, J.M., Reynolds, J.R., Schanze, K.S., 2004. Chem. Mater. **16**, 2938.

Hasegawa, Y., Kimura, Y., Murakoshi, K., Wada, Y., Kim, J.-H., Nakashima, N., Yamanaka, T., Yanagida, S., 1996a. J. Phys. Chem. **100**, 10201.

Hasegawa, Y., Murakoshi, K., Wada, Y., Kim, J.H., Nakashima, N., Yamanaka, T., Yanagida, S., 1996b. Chem. Phys. Lett. **260**, 173.

Hasegawa, Y., Murakoshi, K., Wada, Y., Yanagida, S., Kim, J.-H., Nakashima, N., Yamanaka, T., 1996c. Chem. Phys. Lett. **248**, 8.

Hasegawa, Y., Iwamuro, M., Murakoshi, K., Wada, Y., Arakawa, R., Yamanaka, T., Nakashima, N., Yanagida, S., 1998. Bull. Chem. Soc. Jpn. **71**, 2573.

Hasegawa, Y., Sogabe, K., Wada, Y., Kitamura, T., Nakashima, N., Yanagida, S., 1999. Chem. Lett., 35.

Hasegawa, Y., Ohkubo, T., Sogabe, K., Kawamura, Y., Wada, Y., Nakashima, N., Yanagida, S., 2000. Angew. Chem. Int. Ed. **39**, 357.

Hasegawa, Y., Sogabe, K., Wada, Y., Yanagida, S., 2003. J. Lumin. **101**, 235.

Hasegawa, Y., Wada, Y., Yanagida, S., 2004. J. Photochem. Photobiol. C: Photochem. Rev. **5**, 183.

He, H., Wong, W.-K., Guo, J., Li, K.-F., Wong, W.-Y., Lo, W.-K., Cheah, K.-W., 2004a. Inorg. Chim. Acta **357**, 4379.

He, H., Wong, W.-K., Guo, J., Li, K.-F., Wong, W.-Y., Lo, W.-K., Cheah, K.-W., 2004b. Aust. J. Chem. **57**, 803.

He, H., Zhu, X., Hou, A., Guo, J., Wong, W.-K., Wong, W.-Y., Li, K.-F., Cheah, K.-W., 2004c. Dalton Trans., 4064.

He, H.S., Zhao, Z.X., Wong, W.K., Li, K.F., Meng, J.X., Cheah, K.W., 2003. Dalton Trans., 980.

He, H.S., Guo, J.P., Zhao, Z.X., Wong, W.K., Wong, W.Y., Lo, W.K., Li, K.F., Luo, L., Cheah, K.W., 2004a. Eur. J. Inorg. Chem., 837.

He, H.S., Wong, W.K., Li, K.F., Cheah, K.W., 2004b. Synth. Met. **143**, 81.

He, H.S., Wong, W.K., Li, K.F., Cheah, K.W., 2004c. Synth. Met. **145**, 103.

Hebbink, G.A., Klink, S.I., Oude Alink, P.G.B., Van Veggel, F.C.J.M., 2001a. Inorg. Chim. Acta **317**, 114.

Hebbink, G.A., Reinhoudt, D.N., Van Veggel, F.C.J.M., 2001b. Eur. J. Org. Chem., 4101.

Hebbink, G.A., Klink, S.I., Grave, L., Alink, P.G.B.O., Van Veggel, F.C.J.M., 2002a. Chem. Phys. Chem. **3**, 1014.

Hebbink, G.A., Stouwdam, J.W., Reinhoudt, D.N., Van Veggel, F.C.J.M., 2002b. Adv. Mater. **14**, 1147.

Hebbink, G.A., Grave, L., Woldering, L.A., Reinhoudt, D.N., Van Veggel, F.C.J.M., 2003. J. Phys. Chem. A **107**, 2483.

Heller, A., 1966. Appl. Phys. Lett. **9**, 106.

Heller, A., 1967. J. Am. Chem. Soc. **89**, 167.

Heller, A., 1968a. J. Mol. Spectrosc. **28**, 101.

Heller, A., 1968b. J. Mol. Spectrosc. **28**, 208.

Heller, A., 1968c. J. Am. Chem. Soc. **90**, 3711.

Heller, A., Brophy, V., 1968. J. Appl. Phys. **39**, 4086.

Herrera, J.M., Pope, S.J.A., Adams, H., Faulkner, S., Ward, M.D., 2006a. Inorg. Chem. **45**, 3895.

Herrera, J.M., Ward, M.D., Adams, H., Pope, S.J.A., Faulkner, S., 2006b. Chem. Commun., 1851.

Hoffman, K.R., Conley, W.G., 2001. J. Lumin. **94–95**, 187.

Hoffman, K.R., DeLapp, K., Andrews, H., Sprinkle, P., Nickels, M., Norris, B., 1995. J. Lumin. **66–67**, 244.

Hoffman, K.R., Norris, B.J., Merle, R.B., Alford, M., 1998. Chem. Phys. Lett. **284**, 171.

Hofstraat, J.W., Wolbers, M.P.O., Van Veggel, F.C.J.M., Reinhoudt, D.N., Werts, M.H.V., 1998. J. Fluoresc. **8**, 301.

Hong, Z.R., Liang, C.J., Li, R.G., Zang, F.X., Fan, D., Li, W.L., Hung, L.S., Lee, S.T., 2001a. Appl. Phys. Lett. **79**, 1942.

Hong, Z.R., Liang, C.J., Li, R.G., Zhao, D., Fan, D., Li, W.L., 2001b. Thin Solid. Films **391**, 122.

Hongyo, M., Ueda, K., Sasaki, T., Yamanaka, C., Nagao, Y., 1972. IEEE J. Quantum Electron. QE **8**, 192.

Huang, C.H., Wang, K.Z., Xu, G.X., Zhao, X.S., Xie, X.M., Xu, Y., Liu, Y.Q., Xu, L.G., Li, T.K., 1995. J. Phys. Chem. **99**, 14397.

Hüfner, S., 1978. Optical Spectra of Transparent Rare Earth Compounds. Academic Press, New York.

Imbert, D., Cantuel, M., Bünzli, J.-C.G., Bernardinelli, G., Piguet, C., 2003. J. Am. Chem. Soc. **125**, 15698.

Imbert, D., Comby, S., Chauvin, A.-S., Bünzli, J.-C.G., 2005. Chem. Commun., 1432.

Isobe, T., Misumi, S., 1974. Bull. Chem. Soc. Jpn. **47**, 281.

Iwamuro, M., Adachi, T., Wada, Y., Kitamura, T., Yanagida, S., 1999. Chem. Lett., 539.

Iwamuro, M., Hasegawa, Y., Wada, Y., Murakoshi, K., Nakashima, N., Yamanaka, T., Yanagida, S., 1998. J. Lumin. **79**, 29.

Iwamuro, M., Adachi, T., Wada, Y., Kitamura, T., Nakashima, N., Yanagida, S., 2000a. Bull. Chem. Soc. Jpn. **73**, 1359.

Iwamuro, M., Wada, Y., Kitamura, T., Nakashima, N., Yanagida, S., 2000b. Phys. Chem. Chem. Phys. **2**, 2291.

Izatt, R.M., Bradshaw, J.S., Nielsen, S.A., Lamb, J.D., Christensen, J.J., 1985. Chem. Rev. **85**, 271.

Izatt, R.M., Pawlack, K., Bradshaw, J.S., Bruening, R.L., 1991. Chem. Rev. **91**, 1721.

Jensen, M.P., Neuefeind, J., Beitz, J.V., Skanthakumar, S., Soderholm, L., 2003. J. Am. Chem. Soc. **125**, 15466.

Jeon, S., Braun, P.V., 2003. Chem. Mater. **15**, 1256.

Judd, B.R., 1962. Phys. Rev. **127**, 750.

Jung, H.K., Oh, J.S., Seok, S.I., Lee, T.H., 2005. J. Lumin. **114**, 307.

Kachura, T.F., Sevchenko, A.N., Solov'ev, K.N., Tsvirko, M.P., 1974. Dokl. Acad. Nauk SSSR **217**, 1121.

Kaizaki, S., Shirotani, D., Tsukahara, Y., Nakata, H., 2005. Eur. J. Inorg. Chem., 3303.

Kaizu, Y., Asano, M., Kobayashi, H., 1986. J. Phys. Chem. **90**, 3906.

Kaminski, A.A., Li, L., 1974. Phys. Status Solidi A **26**, K21.

Kandpal, H.C., Tripathi, H.B., 1979. Solid State Commun. **29**, 139.

Kandpal, H.C., Agarwal, A.K., Tripathi, H.B., 1979. J. Lumin. **20**, 207.

Kang, T.S., Harrison, B.S., Bouguettaya, M., Foley, T.J., Boncella, J.M., Schanze, K.S., Reynolds, J.R., 2003a. Adv. Funct. Mater. **13**, 205.

Kang, T.S., Harrison, B.S., Foley, T.J., Knefely, A.S., Boncella, J.M., Reynolds, J.R., Schanze, K.S., 2003b. Adv. Mater. **15**, 1093.

Karmaoui, M., Ferreira, R.A.S., Mane, A.T., Carlos, L.D., Pinna, N., 2006. Chem. Mater. **18**, 4493.

Karve, G., Bihari, B., Chen, R.T., 2000. Appl. Phys. Lett. **77**, 1253.

Kawa, M., Frechet, J.M.J., 1998. Thin Solid Films **331**, 259.

Kawahata, R., Tsukuda, T., Yagi, T., Subhan, M.A., Nakata, H., Fuyuhiro, A., Kaizaki, S., 2003. Chem. Lett. **32**, 1084.

Kawamura, Y., Wada, Y., Hasegawa, Y., Iwamuro, M., Kitamura, T., Yanagida, S., 1999. Appl. Phys. Lett. **74**, 3245.

Kawamura, Y., Wada, Y., Iwamuro, M., Kitamura, T., Yanagida, S., 2000. Chem. Lett., 280.

Kawamura, Y., Wada, Y., Yanagida, S., 2001. Jpn. J. Appl. Phys. I **40**, 350.

Kazakov, V.P., Voloshin, A.I., Shavaleev, N.M., 1998. J. Photochem. Photobiol. A Chem. **119**, 177.

Keller, B., Bukietynska, K., Jezowska-Trzebiatowska, B., 1982. Chem. Phys. Lett. **92**, 541.

Khreis, O.M., Curry, R.J., Somerton, M., Gillin, W.P., 2000. J. Appl. Phys. **88**, 777.

Khreis, O.M., Gillin, W.P., Somerton, M., Curry, R.J., 2001. Org. Electron. **2**, 45.

Kido, J., Okamoto, Y., 2002. Chem. Rev. **102**, 2357.

Kim, H.K., Oh, J.B., Baek, N.S., Roh, S.G., Nah, M.K., Kim, Y.H., 2005. Bull. Korean Chem. Soc. **26**, 201.

Kim, J.-H., Park, Y.-P., 2003. J. Korean Phys. Soc. **43**, 277.

Kim, S., Lim, Y.T., Soltesz, E.G., De Grand, A.M., Lee, J., Nakayama, A., Parker, J.A., Mihaljevic, T., Laurence, R.G., Dor, D.M., Cohn, L.H., Bawendi, M.G., Frangioni, J.V., 2004. Nat. Biotechnol. **22**, 93.

Kimura, T., Kato, Y., 1995. J. Alloys Compd. **225**, 284.

Klink, S.I., Hebbink, G.A., Grave, L., Van Veggel, F.C.J.M., Reinhoudt, D.N., Slooff, L.H., Polman, A., Hofstraat, J.W., 1999. J. Appl. Phys. **86**, 1181.

Klink, S.I., Grave, L., Reinhoudt, D.N., Van Veggel, F.C.J.M., Werts, M.H.V., Geurts, F.A.J., Hofstraat, J.W., 2000a. J. Phys. Chem. A **104**, 5457.

Klink, S.I., Hebbink, G.A., Grave, L., Peters, F.G.A., Van Veggel, F.C.J.M., Reinhoudt, D.N., Hofstraat, J.W., 2000b. Eur. J. Org. Chem. **10**, 1923.

Klink, S.I., Keizer, H., Van Veggel, F.C.J.M., 2000c. Angew. Chem. Int. Ed. **39**, 4319.

Klink, S.I., Alink, P.O., Grave, L., Peters, F.G.A., Hofstraat, J.W., Geurts, F.A.J., Van Veggel, F.C.J.M., 2001. J. Chem. Soc., Perkin Trans. **2**, 363.

Klink, S.I., Keizer, H., Hofstraat, H.W., Van Veggel, F.C.J.M., 2002. Synth. Met. **127**, 213.

Koeppen, C., Yamada, S., Jiang, G., Garito, A.F., Dalton, L.R., 1997. J. Opt. Soc. Am. B Opt. Phys. **14**, 155.

Koppe, M., Brabec, C.J., Sariciftci, N.S., Eichen, Y., Nakhmanovich, G., Ehrenfreund, E., Epstein, O., Heiss, W., 2001. Synth. Met. **121**, 1511.

Kornienko, A., Banerjee, S., Kumar, G.A., Riman, R.E., Emge, T.J., Brennan, J.G., 2005a. J. Am. Chem. Soc. **127**, 14008.

Kornienko, A., Emge, T.J., Kumar, G.A., Riman, R.E., Brennan, J.G., 2005b. J. Am. Chem. Soc. **127**, 3501.

Korovin, Y.V., Rusakova, N.V., 2001. Rev. Inorg. Chem. **21**, 299.

Korovin, Y.V., Rusakova, N.V., 2002. J. Fluoresc. **12**, 159.

Korovin, Y.V., Rusakova, N.V., 2004. J. Alloys Compd. **374**, 311.

Korovin, Y.V., Meshkova, S.B., Poluektov, N.S., 1984. J. Anal. Chem. USSR (Engl. Transl.) **39**, 234.

Korovin, Y.V., Meshkova, S.B., Poluektov, N.S., 1988. Zh. Prikl. Spektrosk. (Engl. Transl.) **48**, 45.

Korovin, Y.V., Shevchuk, S.V., Bacherikov, V.A., Rusakova, N.V., Alekseeva, E.A., Gren', A.I., 2000. Russ. J. Inorg. Chem. (Engl. Transl.) **45**, 1383.

Korovin, Y.V., Zhilina, Z., Rusakova, N.V., Kuz'min, V., Vodzinsky, S., Ishkov, Y., 2001. J. Porphyrins Phthalocyanines **5**, 481.

Korovin, Y.V., Rusakova, N.V., Kostenchuk, M., Rusakova, M., Suveyzdis, Y., 2002a. Pol. J. Chem. **76**, 901.

Korovin, Y.V., Rusakova, N.V., Popkov, Y.A., 2002b. J. Appl. Spectrosc. (Engl. Transl.) **69**, 89.

Korovin, Y.V., Rusakova, N.V., Popkov, Y.A., 2002c. Russ. Chem. Bull. (Engl. Transl.) **51**, 2303.

Korovin, Y.V., Rusakova, N.V., Popkov, Y.A., Dotsenko, V.P., 2002d. J. Appl. Spectrosc. (Engl. Transl.) **69**, 841.

Korovin, Y.V., Rusakova, N.V., Suveyzdis, Y.I., 2002e. Russ. J. Inorg. Chem. (Engl. Transl.) **47**, 1398.

Korovin, Y.V., Rusakova, N.V., Zhilina, Z.I., Ishkov, Y.V., Vodzinsky, S.V., Dotsenko, V.P., 2002f. Mendeleev Commun., 151.

Korovin, Y.V., Lozitskaya, R.N., Rusakova, N.V., 2003. Russ. J. Gen. Chem. (Engl. Transl.) **73**, 1641.

Koslova, N.I., Viana, B., Sanchez, C., 1993. J. Mater. Chem. **3**, 111.

Kresge, C.T., Leonowicz, M.E., Roth, W.J., Vartuli, J.C., Beck, J.S., 1992. Nature **359**, 710.

Kumar, G.A., Riman, R.E., Torres, L.A.D., Garcia, O.B., Banerjee, S., Kornienko, A., Brennan, J.G., 2005. Chem. Mater. **17**, 5130.

Kuningas, K., Ukonaho, T., Pakkila, H., Rantanen, T., Rosenberg, J., Lovgren, T., Soukka, T., 2006. Anal. Chem. **78**, 4690.

Kuo, R.L., Paterson, R.F., Siqueira, T.M., Derdak, S., Steele, R.E., Simmons, G.R., Lingeman, J.E., 2002. J. Urol. **167**, 295.

Kuriki, K., Kobayashi, T., Imai, N., Tamura, T., Nishihara, S., Tagaya, A., Koike, Y., Okamoto, Y., 2000. IEEE Phot. Technol. Lett. **12**, 989.

Kuriki, K., Koike, Y., Okamoto, Y., 2002. Chem. Rev. **102**, 2347.

Lai, D.C., Dunn, B., Zink, J.I., 1996. Inorg. Chem. **35**, 2152.

Lakowicz, J.R., Piszczek, G., Maliwal, B.P., Gryczynski, I., 2001. ChemPhysChem **2**, 247.

Latva, M., Takalo, H., Mukkala, V.-M., Matachescu, C., Rodriguez-Ubis, J.-C., Kankare, J., 1997. J. Lumin. **75**, 149.

Le Quang, A.Q., Besson, E., Hierle, R., Mehdi, A., Reyé, C., Corriu, R., Ledoux, I., 2007. Opt. Mater. **29**, 941.

Le Quang, A.Q., Zyss, J., Ledoux, I., Truong, V.G., Jurdyc, A.M., Jacquier, B., Le, D.H., Gibaud, A., 2005. Chem. Phys. **318**, 33.

Lehmann, O., Meyssamy, H., Kompe, K., Schnablegger, H., Haase, M., 2003. J. Phys. Chem. B **107**, 7449.

Lehn, J.-M., 1995. Supramolecular Chemistry. Concepts and Perspectives. VCH, Weinheim.

Lempicki, A., Heller, A., 1966. Appl. Phys. Lett. **9**, 108.

Lenaerts, P., Driesen, K., Van Deun, R., Binnemans, K., 2005a. Chem. Mater. **17**, 2148.

Lenaerts, P., Ryckebosch, E., Driesen, K., Van Deun, R., Nockemann, P., Görller-Walrand, C., Binnemans, K., 2005b. J. Lumin. **114**, 77.

Lenaerts, P., Storms, A., Mullens, J., D'Haen, J., Görller-Walrand, C., Binnemans, K., Driesen, K., 2005c. Chem. Mater. **17**, 5194.

Lezhnina, M., Kynast, U., 2004. J. Alloys Compd. **380**, 55.

Lezhnina, M., Laeri, F., Benmouhadi, L., Kynast, U., 2006. Adv. Mater. **18**, 280.

Lezhnina, M.M., Kynast, U.H., 2005. Phys. Sol. State **47**, 1485.

Li, Y.G., Yang, H., He, Z., Liu, L.Y., Wang, W.C., Li, F.Y., Xu, L., 2005. J. Mater. Res. **20**, 2940.

Lin, S.H., Feuerstein, R.J., Mickelson, A.R., 1996. J. Appl. Phys. **79**, 2868.

Lincoln, S.F., 1997. Coord. Chem. Rev. **166**, 255.

Lis, S., Kimura, T., Yoshida, Z., 2001. J. Alloys Compd. **323**, 125.

Lisowski, J., Ripoli, S., Di Bari, L., 2004. Inorg. Chem. **43**, 1388.

Liu, G.K., Chen, X.Y., 2007. Spectroscopic properties of lanthanides in nano materials. In: Gschneidner Jr., K.A., Bünzli, J.-C.G., Pecharsky, V.K. (Eds.), Handbook on the Physics and Chemistry of Rare Earths, vol. **37**. Elsevier, Amsterdam (chapter 233).

Lo, W.-K., Wong, W.-K., Guo, J., Wong, W.-Y., Li, K.-F., Cheah, K.-W., 2004. Inorg. Chim. Acta **357**, 4510.

Lukes, I., Kotek, J., Vojtisek, P., Hermann, P., 2001. Coord. Chem. Rev. **216**, 287.

MacFarlane, R.M., Wittmann, G., vanLoosdrecht, P.H.M., de Vries, M., Bethune, D.S., Stevenson, S., Dorn, H.C., 1997. Phys. Rev. Lett. **79**, 1397.

MacFarlane, R.M., Bethune, D.S., Stevenson, S., Dorn, H.C., 2001. Chem. Phys. Lett. **343**, 229.

MacGillivray, L.R., Reid, J.L., Ripmeester, J.A., 2001. Chem. Commun., 1034.

Magennis, S.W., Ferguson, A.J., Bryden, T., Jones, T.S., Beeby, A., Samuel, I.D.W., 2003. Synth. Met. **138**, 463.

Malta, O.L., Gonçalves e Silva, F.R., Longo, R.L., 1999. Chem. Phys. Lett. **307**, 518.

Mancino, G., Ferguson, A.J., Beeby, A., Long, N.J., Jones, T.S., 2005. J. Am. Chem. Soc. **127**, 524.

Manseki, K., Hasegawa, Y., Wada, Y., Ichida, H., Kanematsu, Y., Kushida, T., 2006. J. Lumin. **122–123**, 262.

Mathis, G., 1993. Clin. Chem. **39**, 1953.

Mathis, G., 1998. Biological applications of rare earth cryptates. In: Saez Puche, R., Caro, P. (Eds.), Rare Earths. Editorial Complutense, Madrid, pp. 285–297.

Matsumoto, K., Yuan, J.G., 2003. Lanthanide chelates as fluorescent labels for diagnostics and biotechnology. In: Sigel, A., Sigel, H. (Eds.), Metal Ions in Biological Systems, vol. **40**. Marcel Dekker, New York, pp. 191–232 (chapter 6).

Maupin, C.L., Parker, D., Williams, J.A.G., Riehl, J.P., 1998. J. Am. Chem. Soc. **120**, 10563.

Maupin, C.L., Dickins, R.S., Govenlock, L.G., Mathieu, C.E., Parker, D., Williams, J.A.G., Riehl, J.P., 2000. J. Phys. Chem. A **104**, 6709.

Meinardi, F., Colombi, N., Destri, S., Porzio, W., Blumstengel, S., Cerminara, M., Tubino, R., 2003. Synth. Met. **137**, 959.

Meng, J.X., Li, K.F., Yuan, J., Zhang, L.L., Wong, W.K., Cheah, K.W., 2000. Chem. Phys. Lett. **332**, 313.

Meshkova, S.B., 2000. J. Fluoresc. **10**, 333.

Meshkova, S.B., Rusakova, N.V., 1990. J. Anal. Chem. USSR (Engl. Transl.) **45**, 737.

Meshkova, S.B., Korovin, Y.V., Poluektov, N.S., 1985. Russ. J. Phys. Chem. (Engl. Transl.) **59**, 1012.

Meshkova, S.B., Korovin, Y.V., Poluektov, N.S., Demeshko, D.V., 1987. J. Anal. Chem. USSR (Engl. Transl.) **42**, 385.

Meshkova, S.B., Rusakova, N.V., Bol'shoi, D.V., 1992a. Acta Chim. Hung. **129**, 317.

Meshkova, S.B., Rusakova, N.V., Topilova, Z.M., Lozinskii, M.O., Kudryavtseva, L.S., 1992b. Russ. J. Coord. Chem. (Engl. Transl.) **18**, 183.

Meshkova, S.B., Topilova, Z.M., Lozinskii, M.O., Rusakova, N.V., Bol'shoi, D.V., 1997. J. Anal. Chem. USSR (Engl. Transl.) **52**, 852.

Meshkova, S.B., Shapiro, Y.E., Kuz'min, V.E., Artemenko, A.G., Rusakova, N.V., Pykhteeva, E.G., Bol'shoi, D.V., 1998. Russ. J. Coord. Chem. (Engl. Transl.) **24**, 669.

Meshkova, S.B., Topilova, Z.M., Bol'shoi, D.V., Beltyukova, S.V., Tsvirko, M.P., Venchikov, V.Y., 1999. Acta Phys. Pol. A **95**, 983.

Miller, T.A., Jeffery, J.C., Ward, M.D., Adams, H., Pope, S.J.A., Faulkner, S., 2004. Dalton Trans., 1524.

Mondry, A., Starynowicz, P., 1995. J. Alloys Compd. **225**, 367.

Moran, C.E., Hale, G.D., Halas, N.J., 2001. Langmuir **17**, 8376.

Moutiers, G., Billard, I., 2004. Techniques de l'Ingénieur, Report AF 6, 712.

Mudring, A.V., Babai, A., Arenz, S., Giernoth, R., Binnemans, K., Driesen, K., Nockemann, P., 2006. J. Alloys Compd. **418**, 204.

Nagovitsyn, I.A., Chudinova, G.K., 2002. Dokl. Biochem. Biophys. **382**, 16.

Nah, M.K., Cho, H.G., Kwon, H.J., Kim, Y.J., Park, C., Kim, H.K., Kang, J.G., 2006. J. Phys. Chem. A **110**, 10371.

Neouze, M.A., Le Bideau, J., Leroux, F., Vioux, A., 2005. Chem. Commun., 1082.

Ng, D.K.P., 2001. Half-sandwich tetrapyrrole complexes of rare earths and actinides. In: Gschneidner Jr., K.A., Eyring, E.M., Lander, G.H. (Eds.), Handbook on the Physics and Chemistry of Rare Earths, vol. **32**. Elsevier Science B.V., Amsterdam, pp. 611–653 (chapter 210).

Nielson, C.W., Koster, G.F., 1963. Spectroscopic Coefficients for $p^n$, $d^n$, and $f^n$ Configurations. MIT Press, Cambridge, MA.

O'Riordan, A., O'Connor, E., Moynihan, S., Nockemann, P., Fias, P., Van Deun, R., Cupertino, D., Mackie, P., Redmond, G., 2006. Thin Solid Films **497**, 299.

Ofelt, G.S., 1962. J. Chem. Phys. **37**, 511.

Ogawa, T., Sugai, T., Shinohara, H., 2000. J. Am. Chem. Soc. **122**, 3538.

Oh, J.B., Paik, K.L., Ka, J.-W., Roh, S.-G., Nah, M.K., Kim, H.K., 2004. Mater. Sci. Eng. C, Biomimet. Supramol. Syst. **C24**, 257.

Oh, J.B., Kim, Y.H., Nah, M.K., Kim, H.K., 2005. J. Lumin. **111**, 255.

Olmstead, M.M., de Bettencourt-Dias, A., Duchamp, J.C., Stevenson, S., Dorn, H.C., Balch, A.L., 2000. J. Am. Chem. Soc. **122**, 12220.

Olmstead, M.M., Sigel, G., Hope, H., Xu, X., Power, P.P., 1985. J. Am. Chem. Soc. **107**, 8087.

Oueslati, I., Sa Ferreira, R.A., Carlos, L.D., Baleizao, C., Berberan-Santos, M.N., de Castro, B., Vicens, J., Pischel, U., 2006. Inorg. Chem. **45**, 2652.

Page, R.H., Schaffers, K.I., Payne, S.A., Krupke, W.F., 1997. J. Lightwave Technol. **15**, 786.

Patra, A., Sominska, E., Ramesh, S., Koltypin, Y., Zhong, Z., Minti, H., Reisfeld, R., Gedanken, A., 1999. J. Phys. Chem. B **103**, 3361.

Pavier, M.A., Weaver, M.S., Lidzey, D., Richardson, T., Searle, T.M., Bradley, D.D.C., Huang, C.H., Li, H., Zhou, D., 1996. Thin Solid Films **285**, 644.

Pavlovsky, V.I., Kulikov, O.V., Rusakova, N.V., Andronati, S.A., Korovin, Y.V., 2004. Russ. Chem. Bull. (Engl. Transl.) **53**, 791.

Pellegrino, P.M., Fell, N.F., Rosen, D.L., Gillespie, J.B., 1998. Anal. Chem. **70**, 1755.

Perkins, W.G., Crosby, G.A., 1965. J. Chem. Phys. **42**, 407.

Petoud, S., Bünzli, J.-C.G., Renaud, F., Piguet, C., Schenk, K.J., Hopfgartner, G., 1997. Inorg. Chem. **36**, 5750.

Petoud, S., Cohen, S.M., Bünzli, J.-C.G., Raymond, K.N., 2003. J. Am. Chem. Soc. **125**, 13324.

Pettinari, C., Marchetti, F., Pettinari, R., Drozdov, A., Troyanov, S., Voloshin, A.I., Shavaleev, N.M., 2002. J. Chem. Soc., Dalton Trans., 1409.

Pierre, V.C., Botta, M., Raymond, K.N., 2005. J. Am. Chem. Soc. **127**, 504.

Piguet, C., Bünzli, J.-C.G., 1999. Chem. Soc. Rev. **28**, 347.

Piguet, C., Bünzli, J.-C.G., Bernardinelli, G., Hopfgartner, G., Williams, A.F., 1993. J. Am. Chem. Soc. **115**, 8197.

Piguet, C., Bünzli, J.-C.G., Bernardinelli, G., Hopfgartner, G., Petoud, S., Schaad, O., 1996. J. Am. Chem. Soc. **118**, 6681.

Piguet, C., Edder, C., Rigault, S., Bernardinelli, G., Bünzli, J.-C.G., Hopfgartner, G., 2000. J. Chem. Soc., Dalton Trans., 3999.

Piguet, C., Borkovec, M., Hamacek, J., Zeckert, K., 2005. Coord. Chem. Rev. **249**, 705.

Piguet, C., Bünzli, J.-C.G., Donnio, B., Guillon, D., 2006. Chem. Commun., 3755.

Pirtea, Th.I., 1936. Z. Anal. Chem. **107**, 191.

Piszczek, G., Gryczynski, I., Maliwal, B.P., Lakowicz, J.R., 2002a. J. Fluoresc. **12**, 15.

Piszczek, G., Maliwal, B.P., Gryczynski, I., Dattelbaum, J., Lakowicz, J.R., 2002b. J. Fluoresc. **11**, 101.

Pitois, C., Vestberg, R., Rodlert, M., Malmstrom, E., Hult, A., Lindgren, M., 2003. Opt. Mater. **21**, 499.

Pitois, C., Hult, A., Lindgren, M., 2005. J. Lumin. **111**, 265.

Pizzoferrato, R., Lagonigro, L., Ziller, T., Di Carlo, A., Paolesse, R., Mandoj, F., Ricci, A., Lo Sterzo, C., 2004. Chem. Phys. **300**, 217.

Platas, C., Avecilla, F., de Blas, A., Rodriguez-Blas, T., Geraldes, C.F.G.C., Tóth, E., Merbach, A.E., Bünzli, J.-C.G., 2000. J. Chem. Soc., Dalton Trans., 611.

Platas, C., Piguet, C., André, N., Bünzli, J.-C.G., 2001. J. Chem. Soc., Dalton Trans., 3084.

Polman, A., Van Veggel, F.C.J.M., 2004. J. Opt. Soc. Am. B Opt. Phys. **21**, 871.

Poluektov, N.S., Meshkova, S.B., Korovin, I.V., 1984. Dokl. Acad. Nauk SSSR (Engl. Transl.) **273**, 960.

Pope, S.J.A., Kenwright, A.M., Boote, V.A., Faulkner, S., 2003a. Dalton Trans., 3780.

Pope, S.J.A., Kenwright, A.M., Heath, S.L., Faulkner, S., 2003b. Chem. Commun., 1550.

Pope, S.J.A., Coe, B.J., Faulkner, S., 2004a. Chem. Commun., 1550.

Pope, S.J.A., Coe, B.J., Faulkner, S., Bichenkova, E.V., Yu, X., Douglas, K.T., 2004b. J. Am. Chem. Soc. **126**, 9490.

Pope, S.J.A., Coe, B.J., Faulkner, S., Laye, R.H., 2005. Dalton Trans., 1482.

Pope, S.J.A., Burton-Pye, B.P., Berridge, R., Khan, T., Skabara, P.J., Faulkner, S., 2006. Dalton Trans., 2907.

Pratisto, H., Ith, M., Frenz, M., Weber, H.P., 1995. Appl. Phys. Lett. **67**, 1963.

Puntus, L., Schenk, K.J., Bünzli, J.-C.G., 2005. Eur. J. Inorg. Chem., 4739.

Quici, S., Cavazzini, M., Marzanni, G., Accorsi, G., Armaroli, N., Ventura, B., Barigelletti, F., 2005. Inorg. Chem. **44**, 529.

Quici, S., Marzanni, G., Forni, A., Accorsi, G., Barigelletti, F., 2004. Inorg. Chem. **43**, 1294.

Quochi, F., Orru, R., Cordella, F., Mura, A., Bongiovanni, G., Artizzu, F., Deplano, P., Mercuri, M.L., Pilia, L., Serpe, A., 2006. J. Appl. Phys. **99**, 053520-1.

Raymond, K.N., Müller, G., Matzanke, F., 1984. Top. Curr. Chem. **123**, 49.

Reinhard, C., Güdel, H.U., 2002. Inorg. Chem. **41**, 1048.

Reisfeld, R., Jorgensen, C.K., 1977. Lasers and Excited States of Rare Earths. Springer-Verlag, Berlin.

Renaud, F., Piguet, C., Bernardinelli, G., Bünzli, J.-C.G., Hopfgartner, G., 1999. J. Am. Chem. Soc. **121**, 9326.

Riehl, J.P., Muller, G., 2005. Circularly polarized luminescence spectroscopy from lanthanide systems. In: Gschneidner Jr., J.-C.G., Bünzli, K.A., Pecharsky, V.K. (Eds.), Handbook on the Physics and Chemistry of Rare Earths, vol. **34**. Elsevier, Amsterdam, pp. 289–357 (chapter 220).

Rizzo, F., Papagni, A., Meinardi, F., Tubino, R., Ottonelli, M., Musso, G.F., Dellepiane, G., 2004. Synth. Met. **147**, 143.

Rodriguez-Cortinas, R., Avecilla, F., Platas-Iglesias, C., Imbert, D., Bünzli, J.-C.G., de Blas, A., Rodriguez-Blas, T., 2002. Inorg. Chem. **41**, 5336.

Roh, S.G., Oh, J.B., Nah, M.K., Baek, N.S., Lee, Y., Kim, H.K., 2004a. Bull. Korean Chem. Soc. **25**, 1503.

Roh, S.G., Baek, N.S., Hong, K.-S., Kim, H.K., 2004b. Bull. Korean Chem. Soc. **25**, 343.

Roh, S.G., Nah, M.K., Oh, J.B., Baek, N.S., Park, K.M., Kim, H.K., 2005. Polyhedron **24**, 137.

Roundhill, D.M., 1995. Prog. Inorg. Chem. **43**, 533.

Rusakova, N.V., Meshkova, S.B., 1990. J. Anal. Chem. USSR (Engl. Transl.) **45**, 1371.

Rusakova, N.V., Meshkova, S.B., Poluektov, N.S., 1984. Dokl. Acad. Nauk SSSR (Engl. Transl.) **279**, 404.

Rusakova, N.V., Meshkova, S.B., Venchikov, V.Y., Pyatosin, V.E., Tsvirko, M.P., 1992a. J. Appl. Spectrosc. (Engl. Transl.) **56**, 488.

Rusakova, N.V., Topilova, Z.M., Meshkova, S.B., Lozinskii, M.O., Gevaza, Y.I., 1992b. Russ. J. Inorg. Chem. (Engl. Transl.) **37**, 63.

Rusakova, N.V., Korovin, Y.V., Zhilina, Z.I., Vodzinskii, S.V., Ishkov, Y.V., 2004a. J. Appl. Spectrosc. (Engl. Transl.) **71**, 506.

Rusakova, N.V., Popkov, Yu.A., Dotsenko, V.P., 2004b. J. Appl. Spectrosc. (Engl. Transl.) **69**, 841.

Rusakova, N.V., Pavlovsky, V.I., Kulikov, O.V., Andronati, S.A., Korovin, Y.V., Kost, S.S., 2005. Russ. J. Inorg. Chem. (Engl. Transl.) **50**, 1516.

Ryo, M., Wada, Y., Okubo, T., Nakazawa, T., Hasegawa, Y., Yanagida, S., 2002. J. Mater. Chem. **12**, 1748.

Ryo, M., Wada, Y., Okubo, T., Hasegawa, Y., Yanagida, S., 2003. J. Phys. Chem. B **107**, 11302.

Ryo, M., Wada, Y., Okubo, T., Yanagida, S., 2004. Res. Chem. Intermed. **30**, 191.

Sa Ferreira, R.A., Carlos, L.D., de Zea Bermudez, V., Molina, C., Dahmouche, K., Messaddeq, Y., Ribeiro, S.J.L., 2003. J. Sol–Gel Technol. **26**, 315.

Sa Ferreira, R.A., Karmaoui, M., Nobre, S.S., Carlos, L.D., Pinna, N., 2006. ChemPhysChem **7**, 2215.

Sambrook, M.R., Curiel, D., Hayes, E.J., Beer, P.D., Pope, S.J.A., Faulkner, S., 2006. New J. Chem. **30**, 1133.

Samelson, H., Lempicki, A., 1968. J. Appl. Phys. **39**, 6115.

Samelson, H., Lempicki, A., Brophy, V., 1968a. J. Appl. Phys. **39**, 4029.

Samelson, H., Lempicki, A., Brophy, V.A., 1968b. IEEE J. Quantum Electron. **4**, 849.

Sanada, T., Suzuki, T., Kaizaki, S., 1998a. J. Chem. Soc., Dalton Trans., 959.

Sanada, T., Suzuki, T., Yoshida, T., Kaizaki, S., 1998b. Inorg. Chem. **37**, 4712.

Sastri, V.S., Bünzli, J.-C.G., Rao, V.R., Rayudu, G.V.S., Perumareddi, J.R., 2003. Modern Aspects of Rare Earths and Complexes. Elsevier B.V., Amsterdam.

Saudan, C., Ceroni, P., Vicinelli, V., Maestri, M., Balzani, V., Gorka, M., Lee, S.K., van Heyst, J., Vögtle, F., 2004. Dalton Trans., 1597.

Schanze, K.S., Reynolds, J.R., Boncella, J.M., Harrison, B.S., Foley, T.J., Bouguettaya, M., Kang, T.S., 2003. Synth. Met. **137**, 1013.

Schimitscheck, E.J., 1968. J. Appl. Phys. **39**, 6120.

Schwarzenbach, G., 1957. Complexometric Titrations. Chapman & Hall, London.

Seltzer, M.D., 1995. J. Chem. Educ. **72**, 886.

Seltzer, M.D., Fallis, S., Hollins, R.A., Prokopuk, N., Bui, R.N., 2005. J. Fluoresc. **15**, 597.

Senegas, J.-M., Koeller, S., Bernardinelli, G., Piguet, C., 2005. Chem. Commun., 2235.

Shavaleev, N.M., Bell, Z.R., Ward, M.D., 2002. J. Chem. Soc., Dalton Trans., 3925.

Shavaleev, N.M., Moorcraft, L.P., Pope, S.J.A., Bell, Z.R., Faulkner, S., Ward, M.D., 2003a. Chem. Commun., 1134.

Shavaleev, N.M., Moorcraft, L.P., Pope, S.J.A., Bell, Z.R., Faulkner, S., Ward, M.D., 2003b. Chem. Eur. J. **9**, 5283.

Shavaleev, N.M., Pope, S.J.A., Bell, Z.R., Faulkner, S., Ward, M.D., 2003c. Dalton Trans., 808.

Shavaleev, N.M., Accorsi, G., Virgili, D., Bell, Z.R., Lazarides, T., Calogero, G., Armaroli, N., Ward, M.D., 2005. Inorg. Chem. **44**, 61.

Shen, Y.R., Riedener, T., Bray, K.L., 2000. Phys. Rev. B **61**, 11460.

Sherry, A.D., Ren, J., Huskens, J., Brucher, E., Tóth, E., Geraldes, C.F.G.C., Castro, M.M.C.A., Cacheris, W.P., 1996. Inorg. Chem. **35**, 4604.

Shevchuk, S.V., Rusakova, N.V., Turianskaya, A.M., Korovin, Y.V., Nazarenko, N.A., Gren, A.I., Shapiro, Y.E., 1997. Anal. Commun. **34**, 201.

Shevchuk, S.V., Alekseeva, E.A., Rusakova, N.V., Korovin, Y.V., Bacherikov, V.A., Gren, A.I., 1998a. Mendeleev Commun., 112.

Shevchuk, S.V., Rusakova, N.V., Turianskaya, A.M., Korovin, Y.V., Nazarenko, N.A., Gren, A.I., 1998b. J. Fluoresc. **8**, 225.

Shevchuk, S.V., Rusakova, N.V., Turianskaya, A.M., Korovin, Y.V., Nazarenko, N.A., Gren, A.I., 1999. Asian J. Spectrosc. **3**, 155.

Shionoya, S., Yen, W.M., 1999. Principal phosphor materials and their optical properties. In: Shionoya, S., Yen, W.M. (Eds.), Phosphor Handbook. CRC Press Inc., Boca Raton, FL 33431, USA, pp. 177–230 (chapter 3).

Shushkevich, I.K., Dvornikov, S.S., Kachura, T.F., Solov'ev, K.N., 1981. J. Appl. Spectrosc. (Engl. Transl.) **35**, 1109.

Sigoli, F.A., Gonçalves, R.R., Messaddeq, Y., Ribeiro, S.J.L., 2006. J. Non-Cryst. Solids **352**, 5194.

Sivakumar, S., van Veggel, F.C.J.M., Raudsepp, M., 2005. J. Am. Chem. Soc. **127**, 12464.

Slooff, L.H., Polman, A., Wolbers, M.P.O., Van Veggel, F.C.J.M., Reinhoudt, D.N., Hofstraat, J.W., 1998. J. Appl. Phys. **83**, 497.

Slooff, L.H., de Dood, M.J.A., van Blaaderen, A., Polman, A., 2000a. Appl. Phys. Lett. **76**, 3682.

Slooff, L.H., Polman, A., Klink, S.I., Hebbink, G.A., Grave, L., Van Veggel, F.C.J.M., Reinhoudt, D.N., Hofstraat, J.W., 2000b. Opt. Mater. **14**, 101.

Slooff, L.H., Polman, A., Cacialli, F., Friend, R.H., Hebbink, G.A., Van Veggel, F.C.J.M., Reinhoudt, D.N., 2001. Appl. Phys. Lett. **78**, 2122.

Slooff, L.H., van Blaaderen, A., Polman, A., Hebbink, G.A., Klink, S.I., Van Veggel, F.C.J.M., Reinhoudt, D.N., Hofstraat, J.W., 2002. J. Appl. Phys. **91**, 3955.

Snitzer, E., 1961. Phys. Rev. Lett. **7**, 444.

Soler-Illia, G.J.A.A., Innocenzi, P., 2006. Chem. Eur. J. **12**, 4478.

Solovev, K.N., Tsvirko, M.P., Kachura, T.F., 1976. Opt. Spectrosc. (Engl. Transl.) **40**, 391.

Song, J.L., Lei, C., Mao, J.G., 2004. Inorg. Chem. **43**, 5630.

Song, J.L., Mao, J.G., 2005. Chem. Eur. J. **11**, 1417.

Steemers, F.J., Verboom, W., Hofstraat, J.W., Geurts, F.A.J., Reinhoudt, D.N., 1998. Tetrahedron Lett. **39**, 7583.

Steemers, F.J., Verboom, W., Reinhoudt, D.N., Vandertol, E.B., Verhoeven, J.W., 1995. J. Am. Chem. Soc. **117**, 9408.

Stemmler, A.J., Kampf, J.W., Kirk, M.L., Atasi, B.H., Pecoraro, V.L., 1999. Inorg. Chem. **38**, 2807.

Stetter, H., Frank, W., 1976. Angew. Chem. **88**, 760.

Stevenson, S., Rice, G., Glass, T., Harich, K., Cromer, F., Jordan, M.R., Craft, J., Hadju, E., Bible, R., Olmstead, M.M., Maitra, K., Fisher, A.J., Balch, A.L., Dorn, H.C., 1999. Nature **401**, 55.

Stewart, D.R., Gutsche, C.D., 1999. J. Am. Chem. Soc. **121**, 4136.

Stouwdam, J.W., Van Veggel, F.C.J.M., 2002. Nano Lett. **2**, 733.

Stouwdam, J.W., Van Veggel, F.C.J.M., 2004. Chem. Phys. Chem. **5**, 743.

Stouwdam, J.W., Hebbink, G.A., Huskens, J., Van Veggel, F.C.J.M., 2003. Chem. Mater. **15**, 4604.

Stouwdam, J.W., Raudsepp, M., Van Veggel, F.C.J.M., 2005. Langmuir **21**, 7003.

Subhan, M.A., Suzuki, T., Kaizaki, S., 2001. J. Chem. Soc., Dalton Trans., 492.

Subhan, M.A., Suzuki, T., Kaizaki, S., 2002. J. Chem. Soc., Dalton Trans., 1416.

Subhan, M.A., Nakata, H., Suzuki, T., Choi, J.H., Kaizaki, S., 2003. J. Lumin. **101**, 307.

Sudarsan, V., Sivakumar, S., Van Veggel, F.C.J.M., Raudsepp, M., 2005. Chem. Mater. **17**, 4736.

Sun, L.N., Zhang, H.J., Meng, Q.G., Liu, F.Y., Fu, L.S., Peng, C.Y., Yu, J.B., Zheng, G.L., Wang, S.B., 2005. J. Phys. Chem. B **109**, 6174.

Sun, L.N., Zhang, H.J., Peng, C.Y., Yu, J.B., Meng, Q.G., Fu, L.S., Liu, F.Y., Guo, X.M., 2006. J. Phys. Chem. B **110**, 7249.

Sun, R.G., Wang, Y.Z., Zheng, Q.B., Zhang, H.J., Epstein, A.J., 2000. J. Appl. Phys. **87**, 7589.

Supkowski, R.M., deW. Horrocks Jr., W., 2002. Inorg. Chim. Acta **340**, 44.

Supkowski, R.M., Bolender, J.P., Smith, W.D., Reynolds, L.E.L., deW. Horrocks Jr., W., 1999. Coord. Chem. Rev. **186**, 307.

Suzuki, H., 2004. J. Photochem. Photobiol. A Chem. **166**, 155.

Suzuki, H., Hattori, Y., Iizuka, T., Yuzawa, K., Matsumoto, N., 2003. Thin Solid Films **438**, 288.

Suzuki, H., Yokoo, A., Notomi, M., 2004. Polym. Adv. Technol. **15**, 75.

Sveshnikova, E.B., Timofeev, N.T., 1980. Opt. Spektrosk. **48**, 503.

Takada, E., Hosono, Y., Kakuta, T., Yamazaki, M., Takahashi, H., Nakazawa, M., 1998. IEEE Trans. Nucl. Sci. **45**, 556.

Tanabe, S., 2002. Comptes Rendus Chim. **5**, 815.

Tang, C.W., Van Slyke, S.A., 1987. Appl. Phys. Lett. **51**, 913.

Terazzi, E., Suárez, S., Torelli, S., Nozary, H., Imbert, D., Mamula, O., Rivera, J.-P., Guillet, E., Benech, J.-M., Bernardinelli, G., Scopelliti, R., Donnio, B., Guillon, D., Bünzli, J.-C.G., Piguet, C., 2006. Adv. Funct. Mater. **16**, 157.

Topilova, Z.M., Gerasimenko, G.I., Kudryavtseva, L.S., Lozinskii, M.O., Meshkova, S.B., 1989. Russ. J. Inorg. Chem. (Engl. Transl.) **34**, 1265.

Topilova, Z.M., Rusakova, N.V., Meshkova, S.B., Lozinskii, M.O., Kudryavtseva, L.S., Kononenko, L.I., 1991. J. Anal. Chem. USSR (Engl. Transl.) **46**, 618.

Topilova, Z.M., Meshkova, S.B., Bol'shoi, D.V., Lozinskii, M.O., Shapiro, Y.E., 1997. Zh. Neorg. Khim. **42**, 99.

Torelli, S., Imbert, D., Cantuel, M., Bernardinelli, G., Delahaye, S., Hauser, A., Bünzli, J.-C.G., Piguet, C., 2005. Chem. Eur. J. **11**, 3228.

Tröster, T., 2003. Optical studies of non-metallic compounds under pressure. In: Gschneidner Jr., K.A., Bünzli, J.-C.G., Pecharsky, V.K. (Eds.), Handbook on the Physics and Chemistry of Rare Earths, vol. **33**. Elsevier, Amsterdam, pp. 515–589 (chapter 217).

Tsukube, H., Shinoda, S., 2002. Chem. Rev. **102**, 2389.

Tsukube, H., Shinoda, S., 2006. Near infrared emissive lanthanide complexes for anion sensing. ICFE'6 Conference, Wroclaw, September 4–9, 2006, paper AI-5.

Tsukube, H., Onimaru, A., Shinoda, S., 2006. Bull. Chem. Soc. Jpn. **79**, 725.

Tsvirko, M.P., Kachura, T.F., 1975. J. Appl. Spectrosc. (Engl. Transl.) **23**, 907.

Tsvirko, M.P., Stelmakh, G.F., Pyatosin, V.E., Solovyov, K.N., Kachura, T.F., 1980. Chem. Phys. Lett. **73**, 80.

Tsvirko, M.P., Stelmakh, G.F., Pyatosin, V.E., Solovyov, K.N., Kachura, T.F., Piskarskas, A.S., Gadonas, R.A., 1986. Chem. Phys. **106**, 467.

Tsvirko, M.P., Meshkova, S.B., Venchikov, V.Y., Bol'shoi, D.V., 1999. Opt. Spectrosc. (Engl. Transl.) **87**, 866.

Tsvirko, M.P., Meshkova, S.B., Venchikov, V.Y., Topilova, Z.M., Bol'shoi, D.V., 2001. Opt. Spectrosc. (Engl. Transl.) **90**, 669.

Ungaro, R., Pochini, A., Andreetti, G.D., Domiano, P., 1985. J. Chem. Soc., Perkin Trans. **2**, 197.

Van Deun, R., Fias, P., Driesen, K., Binnemans, K., Görller-Walrand, C., 2003a. Phys. Chem. Chem. Phys. **5**, 2754.

Van Deun, R., Moors, D., De Fre, B., Binnemans, K., 2003b. J. Mater. Chem. **13**, 1520.

Van Deun, R., Fias, P., Nockemann, P., Schepers, A., Parac-Vogt, T.N., Van Hecke, K., Van Meervelt, L., Binnemans, K., 2004a. Inorg. Chem. **43**, 8461.

Van Deun, R., Nockemann, P., Görller-Walrand, C., Binnemans, K., 2004b. Chem. Phys. Lett. **397**, 447.

Varaksa, Y.A., Sinitsyn, G.V., Khodasevich, M.A., 2006a. J. Appl. Spectrosc. (Engl. Transl.) **73**, 309.

Varaksa, Y.A., Sinitsyn, G.V., Khodasevich, M.A., 2006b. Opt. Spectrosc. (Engl. Transl.) **100**, 946.

Venchikov, V.Y., Tsvirko, M.P., 2000. J. Appl. Spectrosc. (Engl. Transl.) **67**, 745.

Viana, B., Koslova, N.I., Haschehoug, P., Sanchez, B., 1995. J. Mater. Chem. **5**, 719.

Vicinelli, V., Ceroni, P., Maestri, M., Balzani, V., Gorka, M., Vögtle, F., 2002. J. Am. Chem. Soc. **124**, 6461.

Vigato, P.A., Tamburini, S., 2004. Coord. Chem. Rev. **248**, 1717.

Vögtle, F., Gorka, M., Vicinelli, V., Ceroni, P., Maestri, M., Balzani, V., 2001. Chem. Phys. Chem. **2**, 769.

Voloshin, A.I., Shavaleev, N.M., Kazakov, V.P., 2000a. J. Lumin. **91**, 49.

Voloshin, A.I., Shavaleev, N.M., Kazakov, V.P., 2000b. J. Photochem. Photobiol. A Chem. **131**, 61.

Voloshin, A.I., Shavaleev, N.M., Kazakov, V.P., 2000c. J. Photochem. Photobiol. A Chem. **136**, 203.

Voloshin, A.I., Shavaleev, N.M., Kazakov, V.P., 2000d. J. Photochem. Photobiol. A Chem. **134**, 111.

Voloshin, A.I., Shavaleev, N.M., Kazakov, V.P., 2001a. J. Lumin. **93**, 199.

Voloshin, A.I., Shavaleev, N.M., Kazakov, V.P., 2001b. J. Lumin. **93**, 115.

Wada, Y., Okubo, T., Ryo, M., Nakazawa, T., Hasegawa, Y., Yanagida, S., 2000. J. Am. Chem. Soc. **122**, 8583.

Wang, F., Fan, X.P., Pi, D.B., Wang, M.Q., 2004. J. Solid State Chem. **177**, 3346.

Wang, H., Qian, G., Zhang, J., Luo, Y., Wang, Z., Wang, M., 2005. Thin Solid Films **479**, 216.

Wang, H.S., Qian, G.D., Wang, M.Q., Zhang, J.H., Luo, Y.S., 2004. J. Phys. Chem. B **108**, 8084.

Wang, Q.Y., Zhang, S.Y., Jia, Y.Q., 1993. J. Alloys Compd. **202**, 1.

Wasserscheid, P., Welton, T., 2005. Ionic Liquids in Synthesis. Wiley–VCH, Weinheim.

Weaver, M.S., Lidzey, D.G., Pavier, M.A., Mellor, H., Thorpe, S.L., Bradley, D.D.C., Richardson, T., Searle, T.M., Huang, C.H., Lui, H., Zhou, D., 1996. Synth. Met. **76**, 91.

Weber, J.K.R., Felten, J.J., Cho, B., Nordine, P.C., 1998. Nature **393**, 769.

Weber, M.J., 1967a. Phys. Rev. **157**, 262.

Weber, M.J., 1967b. Phys. Rev. **156**, 231.

Weber, M.J., 1968. Phys. Rev. **171**, 283.

Weissleder, R., 2001. Nat. Biotechnol. **19**, 316.

Weissleder, R., Ntziachristos, V., 2003. Nat. Med. **9**, 123.

Weissleder, R., Tung, C.H., Mahmood, U., Bogdanov, A., 1999. Nat. Biotechnol. **17**, 375.

Weissman, S.I., 1942. J. Chem. Phys. **10**, 214.

Werts, M.H.V., Hofstraat, J.W., Geurts, F.A.J., Verhoeven, J.W., 1997. Chem. Phys. Lett. **276**, 196.

Werts, M.H.V., Verhoeven, J.W., Hofstraat, J.W., 1999a. Appl. Phys. Lett. **74**, 3576.

Werts, M.H.V., Duin, M.A., Hofstraat, J.W., Verhoeven, J.W., 1999b. Chem. Commun., 799.

Werts, M.H.V., Verhoeven, J.W., Hofstraat, J.W., 2000a. J. Chem. Soc., Perkin Trans. **2**, 433.

Werts, M.H.V., Woudenberg, R.H., Emmerink, P.G., van Gassel, R., Hofstraat, J.W., Verhoeven, J.W., 2000b. Angew. Chem. Int. Ed. **39**, 4542.

Werts, M.H.V., Jukes, R.T.F., Verhoeven, J.W., 2002. Phys. Chem. Chem. Phys. **4**, 1542.

Wiener, E.C., Brechbiel, M.W., Brothers, H., Magin, R.L., Gansow, O.A., Tomalia, D.A., Lauterbur, P.C., 1994. Magn. Reson. Med. **31**, 1.

Winkless, L., Tan, R.H.C., Zheng, Y., Motevalli, M., Wyatt, P.B., Gillin, W.P., 2006. Appl. Phys. Lett. 89, Art. 111115, Sept. 11, 2006.

Wolbers, M.P.O., Van Veggel, F.C.J.M., Heeringa, R.H.M., Hofstraat, J.W., Geurts, F.A.J., Vanhummel, G.J., Harkema, S., Reinhoudt, D.N., 1997a. Liebigs Ann. Chem., 2587.

Wolbers, M.P.O., Van Veggel, F.C.J.M., Hofstraat, J.W., Geurts, F.A.J., Reinhoudt, D.N., 1997b. J. Chem. Soc., Perkin Trans. **2**, 2275.

Wolbers, M.P.O., Van Veggel, F.C.J.M., Snellink-Rüel, B.H.M., Hofstraat, J.W., Geurts, F.A.J., Reinhoudt, D.N., 1997c. J. Am. Chem. Soc. **119**, 138.

Wolbers, M.P.O., Van Veggel, F.C.J.M., Peters, F.G.A., Van Beelen, E.S.E., Hofstraat, J.W., Geurts, F.A.J., Reinhoudt, D.N., 1998a. Chem. Eur. J. **4**, 772.

Wolbers, M.P.O., Van Veggel, F.C.J.M., Snellink-Rüel, B.H.M., Hofstraat, J.W., Geurts, F.A.J., Reinhoudt, D.N., 1998b. J. Chem. Soc., Perkin Trans. **2**, 2141.

Wong, C.-P., Venteicher, R.F., deW. Horrocks Jr., W., 1974. J. Am. Chem. Soc. **96**, 7149.

Wong, W.K., Hou, A.X., Guo, J.P., He, H.S., Zhang, L.L., Wong, W.Y., Li, K.F., Cheah, K.W., Xue, F., Mak, T.C.W., 2001. J. Chem. Soc., Dalton Trans., 3092.

Wong, W.K., Liang, H.Z., Wong, W.Y., Cai, Z.W., Li, K.F., Cheah, K.W., 2002. New J. Chem. **26**, 275.

Wong, W.K., Yang, X., Jones, R.A., Rivers, J.H., Lynch, V., Lo, W.K., Xiao, D., Oye, M.M., Holmes, A.L., 2006. Inorg. Chem., 4340.

Wrighton, M.S., Ginley, D.S., Morse, D.L., 1974. J. Phys. Chem. **78**, 2229.

Wu, S.L., deW. Horrocks Jr., W., 1995. Inorg. Chem. **34**, 3724.

Xu, H.-B., Shi, L.-X., Ma, E., Zhang, L.-Y., Wei, Q.-H., Chen, Z.-N., 2006. Chem. Commun., 1601.

Yamamoto, K., Funasaka, H., Takahashi, T., Akasaka, T., Suzuki, T., Maruyama, Y., 1994. J. Phys. Chem. **98**, 12831.

Yanagida, S., Hasegawa, Y., Murakoshi, K., Wada, Y., Nakashima, N., Yamanaka, T., 1998. Coord. Chem. Rev. **171**, 461.

Yanagida, S., Hasegawa, Y., Iwamuro, M., Kawamura, Y., Wada, Y., 2000a. J. Org. Synth. Chem. Jpn. **58**, 945.

Yanagida, S., Hasegawa, Y., Wada, Y., 2000b. J. Lumin. **87–89**, 995.

Yang, J., Yuo, Q., Li, G.D., Cao, J.J., Li, G.H., Chen, J.S., 2006. Inorg. Chem. **45**, 2857.

Yang, L.F., Gong, Z.L., Nie, D.B., Lou, B., Bian, Z.Q., Guan, M., Huang, C.H., Lee, H.J., Baik, W.P., 2006. New J. Chem. **30**, 791.

Yang, X.P., Jones, R.A., Lynch, V., Oye, M.M., Holmes, A.L., 2005. Dalton Trans., 849.

Yang, X.P., Jones, R.A., Oye, M.M., Holmes, A.L., Wong, W.-K., 2006a. Cryst. Growth Des. **6**, 2122.

Yang, X.P., Jones, R.A., Wong, W.K., Lynch, V., Oye, M.M., Holmes, A.L., 2006b. Chem. Commun., 1836.

Yang, X.P., Jones, R.A., Wu, Q.Y., Oye, M.M., Lo, W.K., Wong, W.K., Holmes, A.L., 2006c. Polyhedron **25**, 271.

Yang, Y.T., Driesen, K., Nockemann, P., Van Hecke, K., Van Meervelt, L., Binnemans, K., 2006. Chem. Mater. **18**, 3698.

Zaleski, C.M., Depperman, E.C., Kampf, J.W., Kirk, M.L., Pecoraro, V.L., 2004. Angew. Chem. Int. Ed. **43**, 3912.

Zang, F.X., Hong, Z.R., Li, W.L., Li, M.T., Sun, X.Y., 2004a. Appl. Phys. Lett. **84**, 2679.

Zang, F.X., Li, W.L., Hong, Z.R., Wei, H.Z., Li, M.T., Sun, X.Y., Lee, C.S., 2004b. Appl. Phys. Lett. **84**, 5115.

Zhang, J., Badger, P.D., Greib, S.J., Petoud, S., 2005. Angew. Chem. Int. Ed. **44**, 2508.

Zhang, Q.J., Wang, P., Sun, X.F., Zhai, Y., Dai, P., Yang, B., Hai, M., Xie, J.P., 1998. Appl. Phys. Lett. **72**, 407.

Zhang, X.X., Li, K.F., Cheah, K.W., Zhou, X.J., Tanner, P.A., 2004. Chem. Phys. Lett. **400**, 331.

Zhang, Z.H., Song, Y., Okamura, T., Hasegawa, Y., Sun, W.Y., Ueyama, N., 2006. Inorg. Chem. **45**, 2896.

Zhao, D., Huo, Q., Feng, J., Chmelka, B.F., Stucky, G.D., 1998. J. Am. Chem. Soc. **120**, 6024.

Zhong, Q., Wang, H., Qian, G., Wang, Z., Zhang, J., Qiu, J., Wang, M., 2006. Inorg. Chem. **45**, 4537.

Zhu, X.J., Wong, W.K., Lo, W.K., Wong, W.Y., 2005. Chem. Commun., 1022.

Ziessel, R., Ulrich, G., Charbonnière, L.J., Imbert, D., Scopelliti, R., Bünzli, J.-C.G., 2006. Chem. Eur. J. **12**, 5060.

Zijlmans, H.J.M.A., Bonnet, J., Burton, J., Kardos, K., Vail, T., Niedbala, R.S., Tanke, H.J., 1999. Anal. Biochem. **267**, 30.

# AUTHOR INDEX

# SUBJECT INDEX

This page intentionally left blank